HB2016

2016 HB

Proceedings of the 57th ICFA Advanced Beam Dynamics Workshop on High-Intensity and High-Brightness Hadron Beams

Scandic Triangeln Hotel, Malmö, Sweden
2016 July 3-8

EUROPEAN SPALLATION SOURCE

Welcome to HB2016

Welcome to Malmö and to the 57^{th} ICFA advanced beam dynamics workshop on high-intensity and high-brightness hadron beams.

HB, High-Brightness High-Intensity Hadron Beams workshop series is and has been a network for scientists and engineers involved in the study, design, development or operation of hadron accelerators.

Since the first HB within the ICFA's (International Committee for Future Accelerators) ABDW (Advanced Beam Dynamics Workshops) series, there has been a giant leap in the size and power of high intensity hadron accelerators, and our community has successfully broken one record after another. At the time of the first HB, the highest power accelerator had not yet reached a megawatt of power; today we have accelerators operating above 1 MW, making the hard challenges look easy. On the energy frontier we have passed the 10 TeV (c.o.m.) energy for protons and the 1 PeV for ions. This wouldn't have been possible without extensive study of the beam dynamics, halo production mechanisms, developments in diagnostics devices, loss measurement and activation, and of course the availability of high power targets. Today our community is proposing accelerators with powers above 10 MW, and to make that proposal a reality; we should look at how we made it past the MW threshold and see how to take the next steps. The HB has been and still is the forum to discuss our ideas, cherish our successes together, and share our failures and the lessons we have learned from them.

The HB starts with a day of plenary talks, and the first day ends with a poster session. In the next three days two sessions will be held in parallel, covering Beam Dynamics in Rings (WG-A), Beam Dynamics in Linacs (WG-B), Accelerator Systems (WG-C), Commissioning and Operations (WG-D) and Beam Instruments and Interactions (WG-E). On the last day of the workshop there will be a plenary summary and discussion on parallel sessions and we will end the workshop with a bus tour (optional to participate) to the ESS construction site (WG-E). The program of the HB is set by the International Organizing Committee (IOC), which also selects the plenary speakers and working group conveners. The speakers of the parallel sessions are invited by the working group conveners and are selected from the submitted abstracts. These committees have done an excellent work in setting up the program, and without their help this workshop would have been impossible.

Malmö is the third largest city in Sweden though small compared to many cities in the rest of the world. On the other hand Malmö is home to people from more than 175 nationalities, is an eco-friendly city and one of the greenest cities in Europe.

We very much look forward to your active participation in the workshop. Once again, welcome to Malmö and HB2016.

Mamad Eshraqi
HB2016 Chairman

Contents

Committees

International Organizing Committee

Mohammad Eshraqi	(ESS, Sweden)
Alex Chao	(SLAC, USA)
Andrea Pisent	(INFN, Italy)
Bill Weng	(BNL, USA)
Christopher Prior	(RAL, UK)
Hideaki Hotchi	(J-PARC, Japan)
Hongwei Zhao	(IMP, China)
In Soo Ko	(Postech, Korea)
Ingo Hofmann	(GSI, Germany)
Jean-Michel Lagniel	(GANIL, France)
Ji Qiang	(LBL, USA)
Ji-Ho Jang	(IBS, Korea)
Jia-er Chen	(Peking University, China)
Jie Wei	(FRIB, USA)
Jingyu Tang	(IHEP, China)
Jiuqing Wang	(IHEP, China)
John Galambos	(ORNL, USA)
Jose Manuel Perez	(CIEMAT, Spain)
Lawrence Rybarcyk	(LANL, USA)
Mike Seidel	(PSI, Switzerland)
Ronald Davidson	(PPPL, USA)
Sergey Ivanov	(IHEP, Russia)
Shinian Fu	(IHEP, China)
Simone Gilardoni	(CERN, Switzerland)
Srinivas Krishnagopal	(Bhabha, India)
Stephen Holmes	(FNAL, USA)
Thomas Roser	(BNL, USA)
Todd Satogata	(JLAB, USA)
Weiren Chou	(FNAL, USA)
Yong Ho Chin	(KEK, Japan)
Yoshi Mori	(Kyoto University, Japan)
Yoshishige Yamazaki	(FRIB, USA)

Local Organizing Committee

Abril Qaraeen	(ESS, Sweden)
Danéle Gous	(ESS, Sweden)
Garry Trahern	(ESS, Sweden)
Henno Gous	(ESS, Sweden)
Inga Tejedor	(ESS, Sweden)
Johan Olander	(ESS, Sweden)
Juliana Pranke	(ESS, Sweden)
Mikael Johansson	(ESS, Sweden)
Mohammad Eshraqi	(ESS, Sweden)
Ryoichi Miyamoto	(ESS, Sweden)
Søren Pape Møller	(Aarhus University, Denmark)
Theodor Lindquist	(ESS, Sweden)
Yngve Levinsen	(ESS, Sweden)
Alexander Lauge Pedersen	(ESS, Sweden)
Oscar Elmqvist Sandvik	(ESS, Sweden)

Editorial Team

Denéle Gous	(ESS, Sweden)
Michaela Marx	(DESY, Germany)
Raphael Mueller	(GSI, Germany)
Johan Olander	(ESS, Sweden)
Volker RW Schaa	(GSI, Germany)
Garry Trahern	(ESS, Sweden)

Conveners

WG-A: Beam Dynamics in Rings

Giuliano Franchetti	(GSI, Germany)
Wolfram Fischer	(BNL, USA)
Yong Ho Chin	(KEK, Japan)

WG-B: Beam Dynamics in Linacs

Alessandra Lombardi	(CERN, Switzerland)
Masanori Ikegami	(FRIB, USA)
Yuan He	(IMP, China)

WG-C: Accelerator Systems

Sarah Cousineau	(SNS, USA)
Jean-Luc Biarrotte	(CNRS-IN2P3, France)
Sheng Wang	(IHEP, China)
Luc Perrot	(IN2P3, France)

WG-D: Commissioning and Operations

Fernanda Garcia	(FNAL, USA)
Angelina Parfenova	(PSI, Switzerland)
Hideaki Hotchi	(JAEA, Japan)

WG-E: Instrumentation and Beam Interactions

Michiko Minty	(BNL, USA)
Hee Seock Lee	(Postech, Korea)
Tom Shea	(ESS, Sweden)

THE LINAC4 PROJECT

A. M. Lombardi for the LINAC4 team , CERN, Geneva, Switzerland

Abstract

Linac4 is a normal conducting, 160 MeV H- ion accelerator that is being constructed within the scope of the LHC injectors upgrade project. Linac4 will be connected to the Proton Synchrotron Booster (PSB) during the next long LHC shut-down and it will replace the current 50 MeV hadron linac, Linac2. Linac4 is presently being commissioned, with the aim of achieving the final energy at the end of the year. A test of the injection chicane and a reliability run will follow. The beam commissioning, in steps of increasing energy, has been prepared by an extended series of studies and interlaced with phases of installation. In this paper we will detail the beam dynamics challenges and we will report on the commissioning results.

INTRODUCTION

Linac4 is a 160 MeV H^- linear accelerator presently under construction at CERN. It will replace the present 50 MeV proton Linac2 as injector of the CERN PS Booster, as a first step of the LHC Injector Upgrade project. A sketch of Linac4 and a detailed description of the layout and beam dynamics can be found in [1,2].

The pre-injector includes a source followed by a Low Energy Beam Transport at 45 keV, a Radio Frequency Quadrupole which accelerates the beam to 3MeV and a Medium Energy Beam Transport line (MEBT). The MEBT, 3.6 m in length, houses a fast chopper with the purpose of removing selected micro-bunches in the 352 MHz sequence and therefore avoid losses at capture in the CERN PSB (1MHz). Presently the preferred scheme envisages to chop out 133 bunches over 352 with a resulting average current reduced by 40%. The beam is then further accelerated to 50 MeV by a conventional Drift Tube Linac (DTL) equipped with Permanent Magnet Quadrupoles (PMQ), to 100 MeV by a Cell-Coupled Drift Tube Linac (CCDTL) and to 160 MeV by a π-mode structure (PIMS). The focusing after 100 MeV is provided by Electromagnetic Quadrupoles (EMQ) whereas between 50 and 100 MeV by a combination of PMQs and EMQs. The nominal beam delivered by Linac4 consist of an H- pulse 400μsec in duration and with peak current during

LINAC4 machine layout- 352MHz					
Pre-injector (9m)		DTL (19m)		CCDTL (25m)	Π-mode (23m)
3MeV		50 MeV		100 MeV	160 MeV
SOURCE Plasma Generator Extraction e-Dump LEBT 2 solenoids Pre chopper	RFQ CHOPPER LINE 11 EMQ 3 Cavities 2 Chopper units In-line dump	3 Tanks 3 Klystrons : 5 MW 1 EMQ 114 PMQ 2 steerers		7 Modules 7 Klystrons : 7 MW 7 EMQ + 14 PMQ 7 steerers	12 Modules 8 Klystrons: 12MW 12 EMQ 12 steerers
Beam Commissioning stages					
45 keV	3 MeV	12 MeV	50 MeV	105 MeV	160 MeV
Not yet the final source	Octobre2013	August 2014	November 2015	June 2016	Octobre 2016 (foreseen)

Figure 1: Layout of Linac4 and key stages of the beam commissioning.

ISBN 978-3-95450-185-4

the pulse of 40 mA. As a fall back, a beam of 600μsec and 30mA would give the same performance in the PSB for the LHC type beams [3].

The machine layout and the key stages of the beam commissioning are shown in Figure 1

Linac4 is equipped with 7 beam transformers, 7 wire scanners, 7 profile harps, 7 beam position monitors and phase probes.

At the time of writing a beam of 25 mA peak current (vs 50 mA nominal) and 100 MeV has been observed on the measurement bench at the end of the first PIMS structure. The normalised transverse emittance of the beam is estimated at 0.3 π mm mrad rms, corresponding to expectations.

RF Cavities

The pre-injector of Linac4 [4] [5] [6] has been described in many references and it is working reliably since 2014. The status and challenges of the remaining RF cavities is detailed in the following.

The DTL [7] has been designed for reliable operation with up to 10% duty cycle, it is composed of rigid self-supporting steel tanks assembled from segments less than 2 m in length. The tank design is almost without welds, heat-treated after rough machining. The Permanent Magnet Quadrupoles are in vacuum for streamlined drift tube assembly. The philosophy of the design is "adjust & assemble": tightly-toleranced Al girders w/o adjustment mechanism once assembled.

The tank mounting mechanism (easy to use) has been patented. To guarantee reliability of operation, the first cells of tank1 (shorter) present an increased gap spacing to reduce the chance of breakdown which could be enhanced by the PMQ fields.

All the above choices have paid off, with a smooth conditioning and an excellent availability during the commissioning phase.

The CCDTL [8] has been constructed by the Russian Scientific Research Institute for Technical Physics (VNIITF) and the Budker Institute of Nuclear Physics. The quadrupoles are located outside of the RF structure. The structures are made of copper plated stainless steel, and because of high number of C-shaped metal seals, the assembly process is rather time consuming.

Each cavity needed around 1 month of conditioning to clean surfaces, after which the full gradient was established without problems. All drift tube centres are aligned within ±0.1 mm, for increased acceptance. The Linac4 CCDTL is first-ever CCDTL in a working machine! Its performance so far have been up to specification..

The last of the Linac4 RF structure, the PIMS [9], is made out of bulk copper, it doesn't present RF seals, and discs and rings that constitute the cells are tuned and electron-beam welded at CERN

The PIMS were constructed within a CERN-NCBJ-FZ Jülich collaboration and assembled and tuned at CERN. Series production could start only after a qualification period of almost 3 years. The critical point was the required precision machining on large pieces of copper (10 - 20 um on 500 mm diameter pieces). The conditioning of the prototype was extremely swift, it took only 24 hours. The PIMS will be the first low-beta π-mode structure to go into an operational machine. Beam commissioning through the PIMS is foreseen for fall 2016

COMMISSIONING

The commissioning of Linac4 has been staged in 6 phases of increasing energy with the aim of matching the schedule of the RF cavities delivery and to be able to assess the beam qualities after each structure with the help of extra diagnostics located on a movable bench. This approach has allowed to progress in beam commissioning before complete installation of the hardware and to optimise the beam throughput at each stage. Most important it has also allowed to cross check the information from the permanent diagnostics against more detailed information coming from the temporary diagnostics and therefore validate a strategy to set-up and diagnose possible faults when the Linac4 will be operational as the sole proton injector to the CERN Proton Synchrotron Booster [3], currently scheduled for the LHC Long Shutdown 2 in 2019.

The 6 phases of commissioning include dedicated beam measurements at the energy of 45keV, 3 MeV, 12 MeV, 50 MeV, 100 MeV and finally 160 MeV. The 100 MeV stage has recently been completed. The 160 MeV stage will begin after the summer.

Two benches have been used during the Linac4 commissioning. A "low-energy" bench, used at 3 and 12 MeV which allows direct measurement of the transverse emittance with a slit and grid (or laser and diamond detector) [10] and direct measurement of the energy spread with a 28 degrees bending magnet followed by a profile harp[4]. A "high-energy" bench has been employed for the measurements at 50 and 100 MeV, it contains a) three profile harps and 3 wire scanners at the appropriate phase advance (about 60degrees) for an indirect emittance measurement b) a Bunch Shape Monitor and a lasing station (which allows transverse profile measurement via stripping) and c) two monitors for Time- of- Flight and beam centre position.

Direct Measurements

Some of these measurements have been already reported in [6] [11] [12] and are repeated here for sake of completeness. The important results of the campaign at 3 and 12 MeV is that the direct method of slit-and-grid (or laser-diamond) and the indirect method based on emittance reconstruction from profiles give the same overall value for the emittance. Even more important, both the direct and indirect emittance measurements give the same orientation of the emittance within a range of 10% which is a very important information for the matching of the beam to the structures downstream. With this result we have validated the model of the machine on which emittance reconstruction techniques rely and the correspondence between direct and indirect methods. The success of this campaign is due as well to the method applied for the

ISBN 978-3-95450-185-4

reconstruction which are more sophisticated than the standard matrix inversion. In particular in the framework of Linac4 we have developed the "forward-method" [13] which extends the accuracy of the classic emittance reconstruction techniques to space charge dominated regimes, and the tomographic method which allows phase space density information to be calculated from the profile [14]. These two methods combined allow for a full knowledge of the beam parameters without relying on direct emittance measurements. Example of a direct emittance measurement compared with a reconstructed emittance is given in Figure 2.

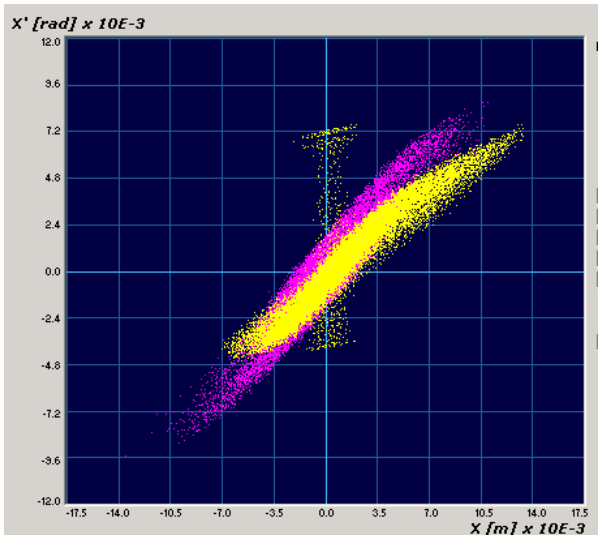

Figure 2: Transverse emittance measured with slit-and grid (yellow) compared to expectation (pink) at 12 MeV.

Indirect Measurements

Following the measurements performed after the first DTL tank at 12 MeV [6], a period of installation of about 10 months has brought to the second type of measurement campaign. After the installation of the remaining DTL structures, the beam energy of 50MeV no longer allows direct emittance and energy spread measurements. Several RF structure are installed in one period and the beam is passed through unpowered RF structure to measure its quality at each energy step. This part of the commissioning has been accompanied by very accurate simulation as the beam in certain cases would travel 20 meters without any acceleration before being measured in the bench. Backtracking techniques have also been employed and a combination of backtracking/forward tracing has been employed to verify the consistency of the measurement. As of today we had two such campaigns, after the DTL from October to December 2015) and after the CCDTL from May 2016 to present. In the first case we were able to transport the 12 MeV DTL beam for 12 meters to the bench and measure its characteristics, as well as a 30 MeV beam. Emittance measured on the high energy bench is deduced from three (or more) profile measurements, a typical example shown in Figure 3. An optimal phase advance between the profiles, located at 0.7 and 0.9 m from each other allows for a very accurate reconstruction. Emittance measured at 50 and 80 MeV are shown in Figure 4 and 5 respectively.

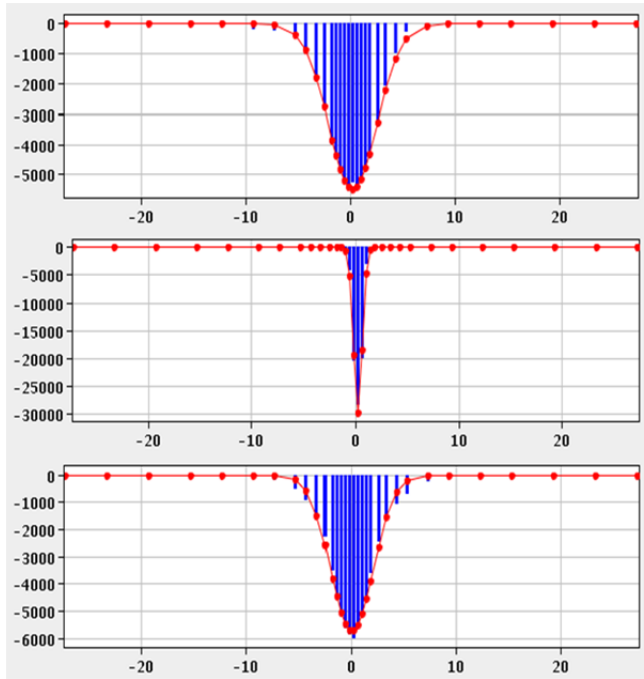

Figure 3: Typical transverse profiles (units of mm) obtained on the profile harps located on the high-energy measurement bench. The distance between the three profile- harp is 0.7 m and the corresponding phase advance is suitable for emittance reconstruction.

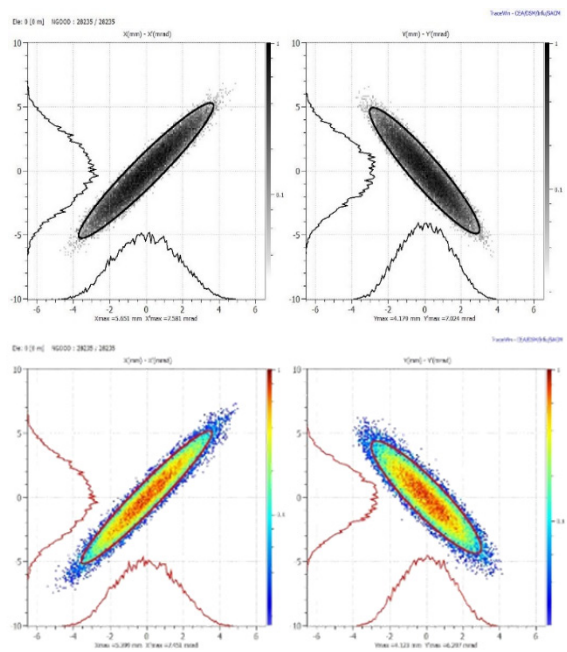

Figure 4: Transverse emittance measured at 50 MeV (bottom), compared to expectation (top).

ISBN 978-3-95450-185-4

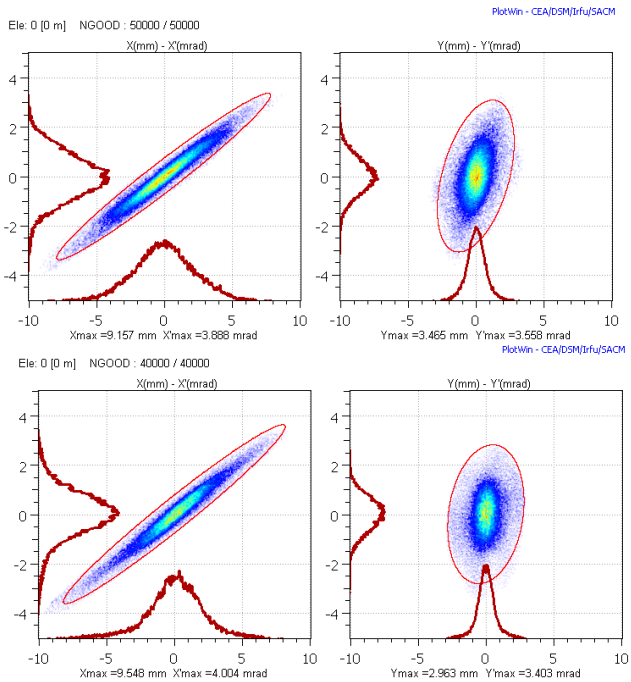

Figure 5: Transverse emittance measured at 80 MeV (bottom), compared to expectation (top).

In general the agreement between the transverse measurement be it emittance profile or steering is very good which is a key for a swift and successful commission and for being able to plan efficiently the beam time and the necessary ancillary services. In the author's opinion this is due to several factors including an accurate model of the machine, a fruitful exchange of essential information with the equipment responsible , a direct participation of RF and Beam Instrumentation experts to the commissioning and most important of all a thorough description of the input beam at the low energy end (after the source and the matching line to the RFQ) which has been gained by back tracing to the source a number of measurements taken under different condition therefore creating a beam representative of what is generated from the source, not only in term of distribution but also in terms of source variability.

Setting of RF Cavities' Phase and Amplitudes

One of the challenges of Linac4 during operation is to be able to set 22 phases and 23 amplitudes of the RF cavities without dedicated longitudinal beam diagnostics. To address this issue a dedicated campaign of finding beam-based signatures (indirect measurements of beam longitudinal parameters) has been put in place after each structure. For the RFQ, amplitude a characteristics curves based on the transmission as a function of the RF voltage is sufficient to find the nominal amplitude. For the bunchers a combination of beam loading observations, (to find the two RF zero crossings) and transverse beam sizes on a wire scanners allows to identify the correct phase. Transmission through the DTL RF bucket [6] is a good indication of the buncher amplitude and phase. For the DTL,CCDTL and in the future for the PIMS a system based on measuring the average beam energy as a function of the cavity phase has been validated as an accurate method to complement RF pick-up calibrations. In particular a simple yet surprisingly precise method of measuring the beam energy gain through a cavity is the measurement of the beam loading. As the cavity is regulated such to have a constant voltage, the low level RF systems responds to the presence of the beam depending on the phase between the cavity and the beam. The LLRF system will increase/decrese the power in the cavity (Power forward) depending whether the beam is accelerated and therefore takes power from the cavity or is decelerated and therefore gives power to the cavity. Figure 6 shows the power to the cavity as the beam passes through at the accelerating phase or at the decelerating phase. By measuring the difference in power (ΔP) and the beam current (I) at a downstream transformer the energy gain ΔE can be calculated via the formula

$$\Delta E = \frac{\Delta P}{I}$$

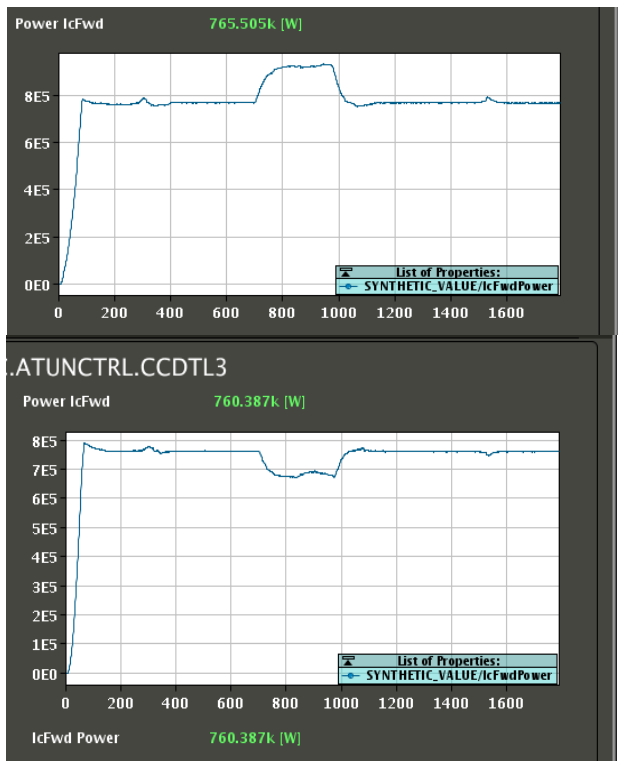

Figure 6: Forward power in CCDTL cavity number 3 when the beam is at the accelerating phase (top) or at the decelerating one (bottom).

Applying the above technique to the Linac4 CCDTL, has allowed to cross calibrate phase and amplitudes of the seven cavities. An example is shown in Figure 7.

For increased precision the same measurement has been repeated with a pair of pick-ups which allow the measurement of the time of flight. Some pick up are located in between cavities and some are located on the bench. During the measurements all the cavities downstream the one being measured have been switched off and detuned. The results are shown in Figure 8.

ISBN 978-3-95450-185-4

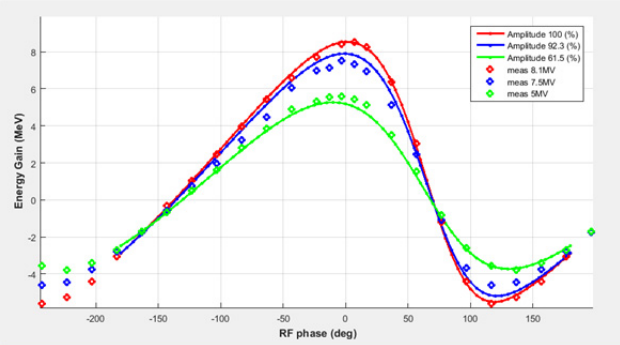

Figure 7: Energy gain in CCDTL cavity number 3 for three different amplitude as a function of phase. Solid lines are simulation and dots are energy measurements deduced from beam loading observations.

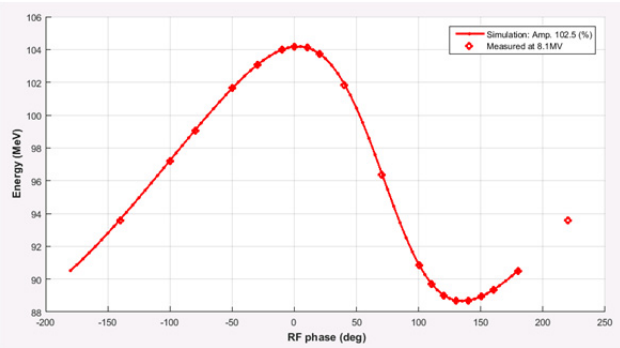

Figure 8: Energy gain in CCDTL cavity number 7 for three different amplitude and varying phase. Solid lines are simulation and dots are energy measurements deduced from Time-of-Flight measurements.

HIGHLIGHTS

During the last six months a very useful tool has been deployed at Linac4. It is a system which will regulate the source parameters (e.g. the gas injection and the RF power) while watching some given observables like the electron/H- ratio with the aim of delivering a constant flat pulse of current of the desired intensity and duration. It is important to stress that this system is not a random optimiser but rather an intelligent Autopilot which contains the knowledge and expertise of beam source expert developed during years. This autopilot is used also to guide the monthly caesiation needed for the correct functioning of the source.

OUTLOOK AND POTENTIAL

The next steps are the commissioning to the final energy of 160MeV followed by a reliability run. From October part of the 160 MeV beam will be deviated towards the half-sector test (HST,[15]) which aims at testing half of the injection chicane into the PSB. The reason for this test is to gain experience on H- injection, and in general to mitigate the risks for future PSB H- injection, namely to study in time to steer the design of some critical components like the H- stripping foil unit, the H0/H- monitor and dump for unstripped/partially stripped particles and the relative instrumentation.

Linac4 is a machine with an enormous potential for upgrade: the peak current limit for beam stability is 80mA – 3 times what we run today, the beam duty cycle limit is 5% - 10 times what we run today and the chopping pattern (sequence of 352MHz micro-bunches) is extremely flexible and can be repeated at frequency up to 20MHz. The potential will be fully exploitable only if the beam formation, extraction and transport through the pre-injector are studied in more details and solution to the present limitation and bottlenecks are found.

ACKNOWLEDGMENT

I wish to thank the member of the commissioning team from BE/ABP. Members of the RF, BI, VAC, CO, RP and EPC groups were always there when needed, to all of them goes my thanks.

REFERENCES

[1] F. Gerigk, M. Vretenar (eds.), Linac4 Technical Design Report, CERN-AB-2006-084.
[2] A.M. Lombardi, *et al.*, “Beam Dynamics in Linac4 at CERN”, in *proc. HB’08*, Nashville, Tennessee, Aug. 2008, paper WGB14.
[3] E. Benedetto, “Space Charge effects and Mitigation in the CERN PS Booster, in view of the upgrade”, presented at HB2016, Malmö, Sweden, July 2016, paper THPM6X01
[4] G Bellodi *et al.,* “3 MeV Test Stand commissioning report”,CERN-ACC-2013-0259.
[5] M. Paoluzzi *et al.,* CERN-AB-Note-2008-040 (2008) F.Caspers *et al.,* “The CERN-SPL Chopper Concept and Final Layout”, EPAC’04, Luzern, Switzerland (2004)
[6] A.M. lombardi., “Commissioning Of The Low-Energy Part Of Linac4”, in *Proc. Linac’14*, Geneva, Switzerland, Sept. 2014, paper MOIOA02.
[7] S. Ramberger , “CERN Linac4 Drift Tube Linac Manufacturing and Assembly”, in *Proc. Linac’14*, Geneva, Switzerland, Sept. 2014, paper THPP036.
[8] A. Tribendis , “Construction and RF Conditioning of the Cell-Coupled Drift Tube Linac (CCDTL) for Linac4 at CERN” in *Proc. Linac’14*, Geneva, Switzerland, Sept. 2014, paper WEIOA01.
[9] F. Gerigk, “The Hot Prototype of the PI-Mode Structure for Linac4” , *in Proc.* Linac’10, Tsukuba, Japan, Sep. 2010, paper MOP071.
[10] S. M. Gibson, *et al.*, “A Fibre Coupled, Low Power Laserwire Emittance Scanner at CERN Linac4”, IPAC’14, Dresden, Germany, May 2014, paper THPME190.
[11] V. Dimov *et al.,* “Beam commissioning of Linac4 up to 12MeV”, in *Proc. IPAC’15,* Richmond, VA, USA, May 2015, pp. 3886-3889.
[12] G. Bellodi *et al.,* “Longitudinal beam profile measurements in Linac4 commissioning”, in *Proc. Linac’14*, Geneva, Switzerland, Sept. 2014, 108-110.
[13] J.B. Lallement *et al.,* “Linac4 transverse and longitudinal emittance reconstruction in the presence of space charge”, in *Proc. Linac’14*, Geneva, Switzerland, Sept. 2014, 913-915.
[14] V. Dimov, “Emittance Reconstruction Techniques in Presence of Space Charge Applied duringLinac4”, presented at HB2016, Malmö, Sweden, July 2016, paper WEPM1Y01.
[15] W. Bartmann *et al.,* New PSB H− Injection and 2 GeV Transfer to the CERN, in *Proc. HB 2014*, East-Lansing, USA, Nov. 2014, paper WEO4AB02.

ISBN 978-3-95450-185-4

THE ESS ACCELERATOR

Håkan Danared, Mohammad Eshraqi and Morten Jensen,
European Spallation Source, Lund, Sweden

Abstract

The European Spallation Source, ESS, is now in construction in Lund, Sweden. It will be a long-pulse spallation source, using a 2 GeV superconducting proton linac to deliver a 5 MW beam onto a rotating, helium-gas-cooled tungsten target. ESS is a partnership between, at present, 11 European nations. According to current planning, the accelerator will be ready for beam in 2019, and by 2023 ESS will start operating as a user facility. This paper reviews the current status of the accelerator project.

INTRODUCTION

Construction work at the ESS site started in the summer of 2014, and now, two years later, the accelerator tunnel is cast, the front-end building, klystron gallery and cold-box building are nearing completion, and piling for the target building is in progress. Work on instrument halls and laboratory and office buildings has begun or will begin in the near future.

At the same time, accelerator, target and neutron-instrument hardware is being designed, prototyped and built at the more than 100 partner institutions around Europe that will deliver in-kind contributions to ESS.

One of the top-level parameters of the ESS project [1] is the 5 MW average beam power. This will be achieved with a 62.5 mA peak beam current at 2 GeV energy, a 14 Hz pulse-repetition rate and a 2.86 ms pulse length.

This beam will hit a spallation target made from tungsten. It is a wheel with 36 sectors, rotating so that consecutive beam pulses will hit adjacent sectors. The wheel is cooled by gaseous helium.

The design of moderators and reflectors is essential for the performance of the neutron source. This design has gone through successive generations. An optimized configuration together with the long-pulse concept gives an unprecedented neutron brightness, and ESS will in total be up to 100 times more powerful than existing neutron sources.

There will be 16 neutron instruments built within the 1,843 M€ construction budget of ESS (plus another 90 M€ from the Swedish government for infrastructure), and another six instruments are included in the complete facility.

Before all instruments are built, however, ESS is expected to start operating as a user facility in 2023.

IN-KIND

A major fraction of the linac hardware is provided as in-kind contributions from accelerator laboratories across Europe or in collaboration with institutions in the host countries Sweden and Denmark that have agreed to provide all their funding as cash. Exceptions are mainly expensive, purely commercial equipment such as cryo plants and RF sources, where there is little academic interest for a potential in-kind partner but a substantial economic risk.

In this in-kind model, ESS in Lund is responsible for the overall design of the accelerator, largely expressed as requirement documents in several levels down to individual work packages. Detailed design, prototyping and manufacturing are then made at the partner laboratories, while ESS in Lund monitors progress through earned-value management and runs regular reviews of work packages and work units. When components arrive to the site, also a substantial fraction of the installation work will be done by in-kind labour. Continuous knowledge transfer during the course of the project is evidently important, since ESS will eventually take full ownership and responsibility of the facility.

Currently, work on the accelerator is under way at 23 partner institutions in 10 countries. The value of this work represents a little above 50% of the 510 M€ accelerator construction budget.

In-kind partners and their main contributions are: Aarhus University: Beam delivery system; Atomki, Debrecen: RF local protection system; University of Bergen: Ion source expertise; CEA Saclay: RFQ, elliptical cavities, cryomodules, beam diagnostics; Cockcroft Institute, Daresbury: Target imaging; DESY, Hamburg: Beam diagnostics; Elettra, Trieste: Spoke RF power, beam diagnostics, magnets, magnet power converters; ESS-Bilbao: MEBT, warm-linac RF, beam diagnostics; University of Huddersfield: RF distribution; IFJ PAN, Krakow: Manpower for installation and tests; INFN Catania: Ion source, LEBT; INFN Legnaro: DTL; INFN Milan: Medium-beta cavities; IPN Orsay: Spoke cavities, cryomodules, cryo distribution; Lodz University of Technology: LLRF; Lund University: LLRF, test stand; NCBJ, Swierk: LLRF, gamma blockers; University of Oslo: Beam diagnostics; STFC Daresbury Laboratory: High-beta cavities, vacuum; Tallinn University of Technology: Power converters; Uppsala University: Test stand; Warsaw University of Technology: LLRF, phase reference line; Wroclaw University of Technology: Cryo distribution.

Since no institution has expressed interest in either the accelerator cryo plant or the test stand and instruments cryo plant, the project schedule has forced ESS in Lund to procure these. (The cryo plant cooling the moderators will however be an in-kind contribution to the target.)

Also, there are no partners for klystrons, IOTs or the modulator production yet. Prototypes have been procured or built by ESS, but the series production is still open for in-kind contributions.

ISBN 978-3-95450-185-4

LINAC

If the design goals for a spallation-source linac should be stated in only one sentence, it may be to produce the highest possible beam power at the lowest possible cost. The most important additional requirements for the ESS linac are that the machine has to operate safely and reliably, such that users as little as possible will have to return back home without data because the accelerator had a problem, and it is also required that beam losses are small, in order to minimize radiation doses to the staff and to allow hands-on maintenance of the accelerator components.

Physics puts additional constraints on the design, and basic beam-physics rules-of-thumb tell that the betatron phase advance in each of the three planes has to be less than 90 degrees, that the average phase advance has to change smoothly throughout the linac, and that the tune depression should be greater than 0.4.

Also technological limitations have to be taken into account. Among those are limits to acceleration gradients and power couplers. For example, the maximum electric surface field in the elliptical cavities is set to 45 MV/m, and the maximum instantaneous power to the beam per coupler in these cavities is 1.1 MW.

Given the relatively low duty factor of 4%, room-temperature acceleration structures are economical at low energy. At ESS, they are used up to an energy of 90 MeV. Acceleration to 75 keV is achieved from the ion-source platform, up to 3.6 MeV in an RFQ, and then by five DTL tanks up to 90 MeV. Superconducting structures at 2 K then take over. Double-spoke cavities are used up to 216 MeV, medium-beta (β = 0.67) elliptical cavities take the beam to 571 MeV and high-beta (β = 0.86) elliptical cavities to the full energy of 2 GeV. The RF frequency is 352.21 MHz up through the spoke section, and then it doubles to 704.42 MHz in the elliptical cavities.

An optimization [2] with respect to criteria like the ones just mentioned results in a power to the beam per cavity as in Fig 1.

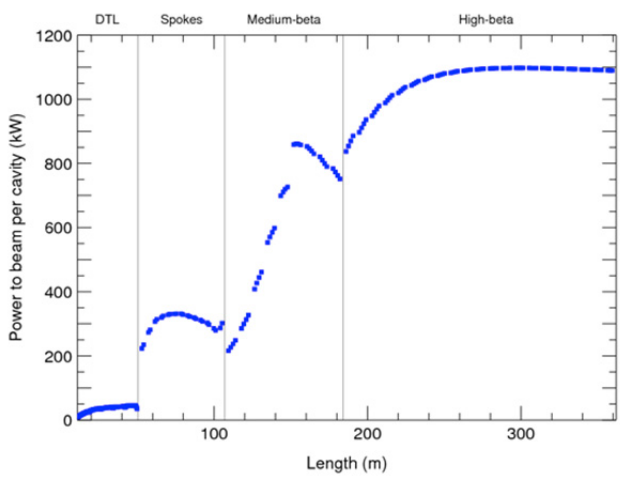

Figure 1: Power to the beam per cavity from the DTL through the superconducting linac.

One of the outputs of the optimization and this energy-gain curve is the length of the accelerator, which both through real-estate and a component count is closely related to the construction cost.

RF DEVELOPMENTS

The majority of the power delivered to the beam comes from the high power amplifiers in the 704 MHz parts of the linac. The medium-beta linac will have 36 klystrons capable of delivering up to 1.5 MW at saturation. ESS has placed three contracts for prototypes from three different vendors. Due to the spread in power requirements in the medium-beta part of the linac, the klystrons have been optimized to allow them to be operated at reduced voltage, and in addition each klystron is being tested with a variable mismatch in the output line. The first klystron has already been tested and delivered to ESS and demonstrated an efficiency of > 65% at saturation at 600 kW and at 1.5 MW.

The high-beta linac will have 84 RF sources. ESS are working with industry to deliver two technology demonstrators of multibeam (MB) IOTs, each capable of delivering 1.2 MW during the flat top pulse. The key advantage of the MB-IOT is that it maintains high efficiency over a broad output power range at the point of operation, critical to enable ESS to meet its stringent energy targets. Both MB-IOT designs are complete, and each contains 10 individual beams combined in a single toroidal output cavity. The first IOT by L3 Communications Electron Devices, shown in Fig 2, is under test in the factory and has already demonstrated high efficiency and 1.2 MW RF output power. The second IOT being manufactured by a consortium of Thales Electron Devices (TED) and Communications & Power Industries (CPI) will start testing in November 2016.

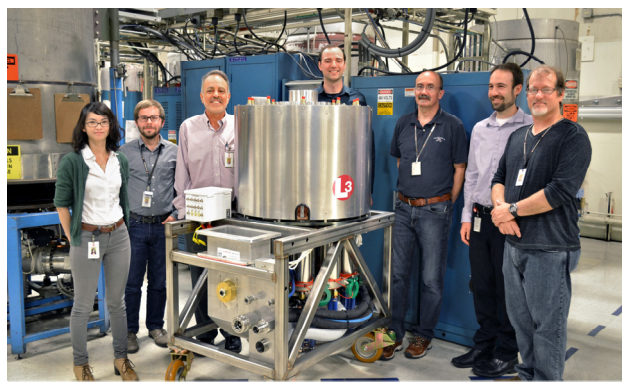

Figure 2: L-3 Communications Electron Devices' L6200 1.2 MW, 704 MHz multi-beam IOT for ESS.

OTHER RECENT DEVELOPMENTS

Development work has started on all the accelerator components that will be delivered as in-kind contributions. For the partners that joined the ESS project already in the design phase, this is true since a long time. Other partners joined more recently during the construction

ISBN 978-3-95450-185-4

phase, but also here progress is rapid. There are additional development activities taking place in Lund on modulators and LLRF. In total 30 PDRs (Preliminary Design Reviews) and CDRs (Critical Design Reviews) of accelerator systems or sub-systems have taken place in Lund or at partner laboratories during the last 12 months.

Many systems, especially complex ones with long lead times, have moved from design to prototyping, and in some cases even production. In Catania, the construction of the proton source [3], see Fig 3, recently had reached the point where the first plasma could be observed. The proton source will be the first piece of the linac to be delivered to Lund, and arrival is planned for the late autumn of 2017.

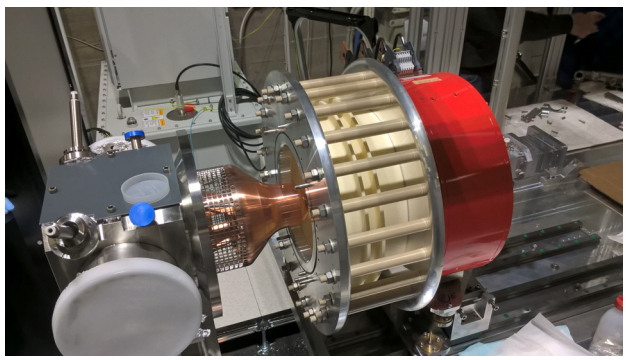

Figure 3: The microwave-discharge ion source designed and built by INFN in Catania.

Prototype spoke cavities [4] have been delivered to Orsay and tested since spring 2015. They have exceeded the ESS requirements of a gradient of 9 MV/m at a Q_0 of 1×10^9 with a good margin. A prototype spoke cryomodule is now being built up at Orsay.

Similarly, the first high-beta elliptical cavity prototype was delivered to Saclay already in 2014 and the first medium-beta cavity prototype was delivered at the end of 2015 [5]. Also these have exceeded the ESS requirements in vertical tests. Components of the first cryomodule, the Medium-beta Elliptical Cavity Cryomodule Demonstrator (M-ECCTD) are being assembled with the goal to start testing it in early 2017. The series cavities will be procured and tested by LASA for the medium betas and by Daresbury Laboratory for the high betas, and they will then be delivered to Saclay for assembly into cryomodules.

Further examples of existing prototypes include a MEBT buncher cavity in Bilbao, a LLRF system at Lund University, DTL permanent-magnet quadrupoles in Legnaro as well as an electro-magnetic quadrupole for the elliptical linac at Elettra. Furthermore, a non-ESS superconducting cavity has been successfully tested at the 352 MHz test stand at Uppsala University.

OUTLOOK

While linac components are being built at the partner laboratories, planning at ESS in Lund is now to a large extent focusing on the installation phase. Detailed installation plans have been worked out for the accelerator tunnel, for the klystron gallery which contains many more components than the tunnel, and for the stubs connecting the two.

Installation in the stubs will be a particularly challenging task. They will contain both waveguides and cables. They will have to be provided with cooling because of the power dissipation in waveguides and cables. And they must prevent neutron radiation from leaking from the tunnel into the gallery while still being, albeit with some effort, serviceable.

According to the current plans, full access to the accelerator tunnel will be given in March 2017, and the accelerator should be ready to produce a 571 MeV beam by June 2019 (the high-beta installation will continue until 2022). During this time, for instance around 600 km of cables need to be pulled and connectors need to be clamped to them, and more than 300 racks need to be filled with electronics up through the medium betas. This means that many teams will have to work in parallel with both installation and testing activities, and at the same time commissioning of parts of the accelerator will take place.

ACKNOWLEDGEMENT

This paper presents work performed by the entire Accelerator Division at ESS in Lund and by all the European in-kind collaboration partners to the ESS accelerator.

REFERENCES

[1] ESS Technical Design Report, Ed. S. Peggs, ESS–DOC–274 (2013).

[2] M. Eshraqi *et al.*, “ESS linac beam physics design update”, in *Proc. IPAC2016*, Busan, Korea, May 2016, paper MOPOY045, pp. 947–950.

[3] L. Celona *et al.*, “Preliminary commissioning results of the proton source for ESS at INFN-LNS”, in *Proc. IPAC2016*, Busan, Korea, May 2016, paper WEPMY035, pp. 2628–2631.

[4] P. Duchesne *et al.*, “Design of the 352 MHz, beta 0.50, double-spoke cavity for ESS”, in *Proc. SRF2013*, Paris, France, Sept. 2013, paper FRIOC01, pp. 1212–1217.

[5] F. Peauger *et al.*, “Progress in the elliptical cavities and cryomodule demonstrators for the ESS linac”, in *Proc. SRF2015*, Whistler, Canada, Sept. 2015, paper TUPB007, pp. 544–548.

ISBN 978-3-95450-185-4

A FIFTEEN YEAR PERSPECTIVE ON THE DESIGN AND PERFOMANCE OF THE SNS ACCELERATOR

S. M. Cousineau, Oak Ridge National Laboratory, Oak Ridge, TN

Abstract

Construction of the Spallation Neutron Source (SNS) accelerator began approximately fifteen years ago. Since this time, the accelerator has broken new technological ground with the operation of the world's first superconducting H^- linac, the first liquid mercury target, and 1.4 MW of beam power. This talk will reflect on the issues and concerns that drove key decisions during the design phase, and will consider those decisions in the context of the actual performance of the accelerator. Noteworthy successes will be highlighted and lessons-learned will be discussed. Finally, a look forward toward the challenges associated with a higher power future at SNS will be presented.

INTRODUCTION

The SNS accelerator was designed as a short pulse, high power proton driver for neutron production. The top levels goals of the accelerator are to provide 1.4 MW of proton beam power with 90% reliability. The final proton beam exiting the accelerator is composed of 1 us pulses of 1 GeV protons operating at a repetition rate of 60 Hz. A third goal, related to the reliability metric, is to maintain beam loss levels to the order of < 1 W/m, corresponding to approximately 100 mrem/hr residual radiation at 30 cm distance, throughout the accelerator in order to allow for routine, hands on maintenance of system components.

To obtain the short pulse structure of the beam, an H^- linac and accumulator ring combination was chosen. From there, the design decisions for the subsystems were driven by the high power, high reliability, low loss goals stated previously. These decisions and their impact on accelerator performance will be discussed in the forthcoming sections, following a brief summary of the accelerator performance to date.

PERFORMANCE METRICS

The accelerator was commissioned beginning in 2002, and the first neutrons were produced in 2006. The power ramp up to took longer than planned due to difficulties in the target systems [1]. The accelerator was operated in production mode with 1.4 MW of beam power for the first time in the fall of 2015. After this production cycle resulted in a premature target failure, the beam power power was reduced to 1.1 MW in a move to prioritize reliability for the neutron users. The power will be ramped back up in to 1.4 MW in a stepwise fashion over the course of the next few years in a controlled study of target cavitation damage versus beam power. Fig. 1 shows the beam power evolution of the SNS accelerator since the beginning of operations in 2006.

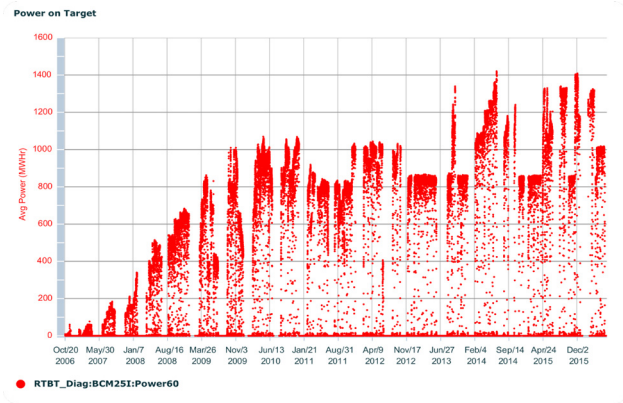

Figure 1: SNS beam power evolution.

The accelerator reliability metric is defined as the number of hours of delivered neutron production divided by the number of hours scheduled. Catastrophic equipment failures such as target failures that result in long downtimes have major impact on the reliability metric. The SNS has suffered seven premature target failures, as well as one equipment failure in the MEBT with comparable downtime. Target failures have progress from early life failures due to manufacturing details to failures due to cavitation damage at high power. Aside from these single event failures, the remainder of the accelerator systems are operating with very high reliability, as demonstrated in Fig. 2, which shows the historical reliability metric with and without the target and MEBT failures.

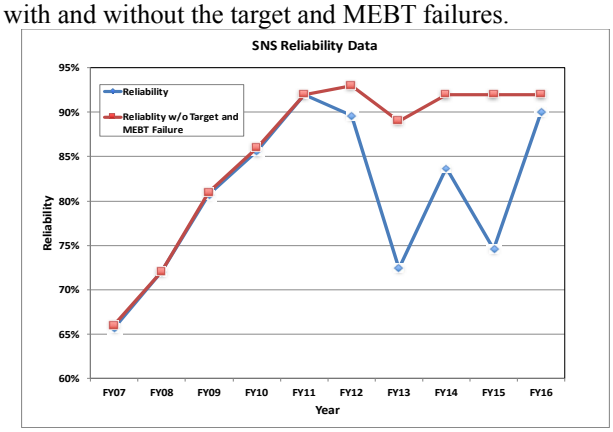

Figure 2: SNS accelerator reliability metric.

Finally, while reliability and beam power are the metrics relevant to the neutron user program, for the accelerator the level of residual radiation is top level consideration which determines how efficiently equipment maintenance can be performed. Table 1 below shows the activation levels throughout the accelerator following the 1.4 MW production run. With the exception of the ring injection area, which was always anticipated to be hot, the activation is well below the 1 W/m criterion.

ISBN 978-3-95450-185-4

Table 1: Activation 3-5 Hours after a 1.3 MW Production Beam Run

Region	Activation Level (mrem/hr @ 30 cm)
DTL	2 – 30
CCL	8 – 60
SCL	5 – 45
LEDP	90
HEBT General	< 5
HEBT DH25	90
Ring Injection	1000
Ring Extraction	80
Ring Collimation	90
Ring General	5-40

THE LINEAR ACCELERATOR

The linear accelerator is composed of a warm linac DTL and CCL combo to a beam energy 186 MeV , followed by a superconducting linac (SCL) with a medium beta section (β=0.61) and a high beta section ((β=0.61) to 1 GeV. The superconducting technology was chosen over the warm linac technology for a number of reasons, including reduced cost of construction and operation, higher availability compared to a warm linac, high vacuum to beam-gas scattering, and a large bore aperture to reduce beam loss. Since it was the world's first H^- SCL, the performance expectations were somewhat unknown, and the choice was considered both high risk and high potential. Although by now it is clear that the SCL has been a success, the first decade of operation has offered a number of surprises, both good and bad.

Expectations vs. Realities – SCL Cavities

The design gradients for the SCL cavities were 10.2 MV/m for the medium beta cavities, and 15.8 MV/m for the high beta cavities. When the cavities were first powered up at their design repetition rate of 60 Hz, the gradients for the medium beta cavities were generally above the design values, but the high beta cavities were well below expectations, with some cavities unable to run at all. The most majority of problems were associated with electron activity in the cavities, which limited the gradients to below design values for 51 cavities [2]. Due to these issues, the SNS linac has not yet been run in production with the design beam energy of 1 GeV. Much progress has been made toward repairing defective cavities and improving field gradients through mechanisms such as plasma processing, and the production beam energy is now 958 MeV. Fig. 3 shows the cavity gradients versus design early in the operational cycle in 2007, and during the 1.4 MW run in 2015.

One performance aspect that become apparent during the process of removal and repairs of cavities is the exceptional flexibility and adaptability of the SCL. This is due to the combination of a spare cavity to provide energy reserve, and individually powered cavities that allow for retuning an rephasing to obtain the same beam energy for the accumulator ring. The additional benefits of a digital LLRF system that allows beam blanking, a robust BPM system for time of flight measurements, and sophisticated applications software make it possible to tune up the entire SCL from scratch in a completely automated fashion in 40 minutes, and to retune after a cavity loss in only 20 seconds [3]. This level of expediency was never imagined during the design phase.

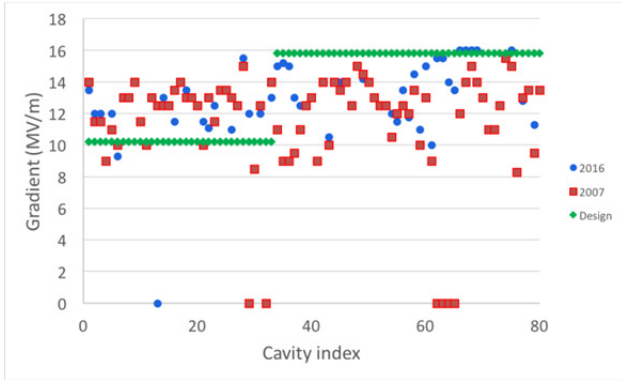

Figure 3: SCL cavity gradients in 2007 (red), in 2016 (blue), and for design (black).

Expectations vs Realities - Beam Dynamics in the Linac

Since the SNS SCL is the world's first superconducting H^- linac and there was not wisdom and experience to be garnered from elsewhere, simulations played a key role in setting the performance expectations [4]. From simulation work, it was initially thought that the SCL would be tuned up with design cavity phases to preserve the longitudinal match, and additionally to correlate the longitudinal and transverse phase advances. Finally, it was expected that the beam would be transversely matched throughout the entire linac, using matching algorithms and the intermittent dedicated matching sections in the linac. Between this model, and the very large bore in the SCL, simulations predicted a negligible amount of beam loss in the SCL region.

None of these expectations met reality. Regarding the cavity phases, the SCL was first configured to a constant focusing value (-18 degrees from the synchronous phase) and the the final configuration resulted from tuning the cavity phases on beam loss until the lowest beam loss state was reached.

In the transverse plane, a significant and unanticipated beam loss phenomenon has driven the lattice settings far away from the initial design value. H^- intrabeam stripping, which was not realized during the design stage, lead to significant beam loss in the SCL. The loss mechanism, which scales with beam density, and was confirmed through an experiment which compared beam loss levels for operating with protons and with H^- in the SCL [5]. To mitigate beam loss from this mechanism, the quadrupoles in the SCL have been reduced to approximately half of their design values. Any further reduction from these

ISBN 978-3-95450-185-4

values results in an increase in beam loss, which will be discussed shortly.

Prior to the reduction in transverse focusing, the activation in the SCL was increasing with beam power at an alarming rate. Fig. 4 shows the historic evolution of the activation in the SCL, and the reduction in slope after the defocusing was put in place. Clearly, if the design quadrupoles had been used for beam powers up to 1.4 MW, the average activation in the SCL would have been ~100 mrem/hr, which falls into the regime of a high radiation area that requires special work permit for maintenance.

It is worth noting that the original SNS linac design was a warm linac with approximately half the beam pipe aperture. If this design had been chosen instead of the large bore (76 mm diameter) SCL option, the SNS could not have been able to simultaneously achieve its high power goal while maintaining the < 1 W/m beam loss standard. Operation at high power would have resulted in high levels of residual radiation in the linac tunnel which would have complicated maintenance and cause degradation of system components.

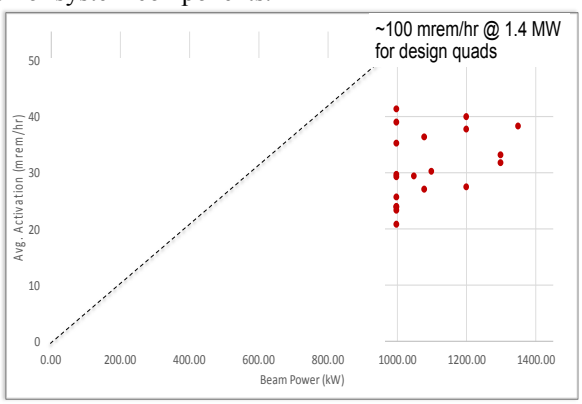

Figure 4: Average SCL activation versus beam power. The dashed line indicates the trend prior to reduced focusing.

Following along the trend of breaking from the design plans, the beam in the linear accelerator is not matched in any of the three planes, nor do the transverse phase advances match the longitudinal phase advances [3]. In practice, the beam envelope is arrived at through "monkey tuning" of the beam losses in the linac, and has significant beating in all planes.

Early efforts to transversely match the beam in the linac were thwarted hindered by an inability of the models to reproduced the measured RMS values. A multi-year campaign has now resulted in good agreement between model and measurement in an RMS sense in the SCL in both the longitudinal and transverse planes. The next steps in this effort are to achieve the same agreement in the warm linac, and then to apply control of the beam optics and matching using these tools.

Even after the defocusing of the optics to reduce intrabeam stripping, the transverse RMS beam size is still small compared to the diameter SCL bore aperture. In fact, the RMS is a factor of ~10 less than the bore size of 76 mm. Therefore, remaining beam loss in the SCL is likely due to extended beam halo. Presently, the source and character of the beam halo is not understood, but efforts are underway to resolve this problem.

Although the definition of "beam halo" is often disputed, SNS adopts the convention from the 2014 Workshop on Beam Halo Monitoring which defines beam halo as 10^{-4} – 10^{-6} of the beam intensity. Recently, a few diagnostics systems have been upgraded to detect beam at this level and efforts to utilize these diagnostics to understand and control beam halo in the SNS linac are underway [6].

Expectation vs. Realities – The MEBT Chopper System

One significant surprise which occurred outside of the SCL was the performance of the MEBT chopper system. The design of the SNS accelerator relied on two chopper systems – the LEBT chopper and the MEBT chopper – to provide the necessary microsecond beam structure for the accumulator ring. The LEBT performs the initial chopping, but leaves behind a 25 ns partially chopped beam tails. It was assumed during design that the partially chopped beam would fall outside of dynamic aperture and result in unacceptable beam loss in the linac and beam in gap in the ring. The fast MEBT chopper, with a rise time of 5 ns was designed remove most of these tails.

The inclusion of this fast chopper severely constrained the design of the MEBT. A MEBT without the fast chopper would have required four quadrupoles and one rebuncher to match the beam into the first DTL tank. On the other hand, the SNS MEBT required fourteen quadrupoles and four rebunchers to achieve the proper phase advance between chopper and antichopper.

While the MEBT chopper performed according to specifications, it did not have an appreciable impact on the beam loss in the linac. A small difference in the extraction region loss in the accumulator ring was observed with the MEBT chopper on, but since the losses were already low in this region, there was no significant benefit. In fall of 2014, the MEBT chopper target leaked and flooded the entire MEBT. The recovery resulted in a complete disassembly and reassembly of the MEBT, requiring four weeks of unscheduled downtime.

THE ACCUMULATOR RING

The SNS accumulator ring, which has accumulated up to 1.56e14 ppp is the most intense proton ring in the world on a charge per pulse basis. In order to meet the activation goals, beam loss must be kept on the order of 1e-4 of the beam intensity. The design of the ring was highly focused on controlling this beam loss and a variety of both large and small investments were made to assure that this goal was met. A detailed description of the design can be found in [7]. Overall, the ring has performed extremely well and in fact, and could accept a higher beam intensity while still maintaining reasonable loss levels. Nonetheless, ten years after the start of operations, it is interesting to the pose questions: What investments paid off? What investments didn't pay off? What was over-

ISBN 978-3-95450-185-4

looked during the design and what was the consequence? These are the questions that will be addressed in this discussion.

High Payoff Investments

Probably the largest pay off investment in the ring was the large beam aperture, which varies between 10 – 16 cm in the collimation region, to 20 – 30 cm for the beam pipes. The large aperture allows the beam to be injection painted into a large area which subsequently reduces the space charge tune shift and associated effects such as resonance crossing. In practice, the entire aperture is used during the accumulation cycle, which minimizes the foil traversals and resulting beam loss in the injection region. Another high payoff investment was the dual plane injection painting system, which allows independent painting in each plane according to an arbitrary user defined waveform. The aim of the injection painting is two-fold: First, to optimize the beam distribution for the target requirements, and second, to reduce the foil traversals and resulting injection beam loss. The impact of the latter goal can be easily demonstrating by accumulating nearly identical beam distributions with and without injection painting, and comparing the resulting beam loss, as shown in Fig. 5. The beam loss for the case with no injection painting is as much as five times more than the case with painting.

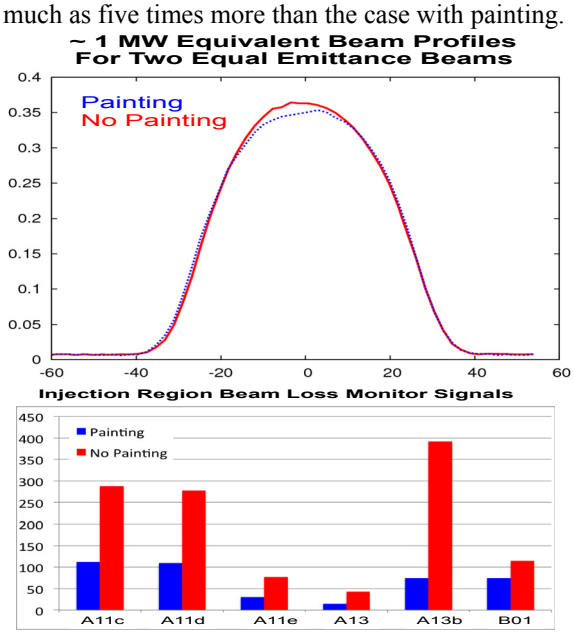

Figure 5: Top - Transverse profiles for painted (blue) and not painted (red) beams. Bottom - Injection area beam loss monitor signals for the above profiles.

The third and final large payoff investment is the ring collimation system. The collimation system is a two stage system with a set of primary scrapers and three secondary absorbers. The acceptance of the collimation system is ~300 pi mm mrad, significantly below the 480 pi acceptance of the remainder of the ring, ensuring that most particles far outside of the beam core intercept the collimation system instead of the beam pipe. While the primary scraper system has never been used during production, mainly because it is not needed, the secondary absorbers are critical and are considered to be the main reason that the remainder of the ring has very low activation.

Medium and Low Payoff Investments

Based on the experience of predecessor machines such as the Protons Storage Ring (PSR) at Los Alamos, one of the major concerns during the design of the SNS accumulator ring was beam loss due to collective effects such as space charge and instability. There was a significant concern over the possibility of an intensity-limiting electron proton (e-P) instability. As such, a number of pre-emptive measures were taken to prevent the instability for 1.4 MW operations. Most notably, the entire SNS vacuum chamber was TiN coated to reduce the secondary emission yield for electrons, and a 2nd harmonic RF stations was included in the baseline RF buncher design to allow control of the longitudinal beam distribution. In addition, both clearing electrodes and clearing solenoids were installed, and a instability feedback system was developed.

So far, there has not been any e-P instabilities during production style SNS beam operations. Trace levels of e-P activity are sometimes observed near the end of the beam accumulation, but it does not result in any observable beam loss. It is not possible to know if this success is due to the TiN coating or not. To date there has been no need for use of either the clearing electrodes or the suppression solenoids, and in fact the solenoids have never been powered up. The e-P instability has been observed during dedicated physics studies where the machine is configured specifically to excite the instability, and during these times the second harmonic has been shown to be a strong knob in extinguishing the instability. The feedback system, under development for the entire beam power ramp up, is now able to reliably damp the instability, as described in other works in these proceedings [8]. Along with the second harmonic RF, this represents a robust suite safety feature against the possibility of future e-P instabilities at higher beam powers.

While the e-P instability was the primary concern in the arena of collective effects, there was also significant attention dedicated to avoiding space charge induced beam resonances. The baseline lattice tunes of (6.23, 6.20) were carefully chosen to be in a resonance free zone, and another back up working point (6.4, 6.3) was carefully studied. In order to ensure that higher order resonances were avoided for all both tune sets, a set of four of sextupole families were installed in the ring to provide chromaticity correction and tune spread reduction, and two octupole corrector families for compensation of higher order resonances. Normal and skew sextupoles were also installed.

To date, neither the sextupoles nor the octupoles, nor any of the correctors of this order, have ever been used during a production beam run. While the main sextupoles are routinely used during beam physics studies, they have not been shown to reduce beam loss in the ring. Although it is possible that these magnets may become necessary for higher power beam operations in the future, for the time being, they are not nearly as critical as originally

ISBN 978-3-95450-185-4

anticipated and a significant cost savings could have been realized by excluding them from the baseline design.

Unanticipated Challenges

While the ring has operated mostly as planned from the beginning, a few unforeseen issues have arisen, mainly in the injection region.

The first issue results from a design change whose consequences were not fully appreciated, and a lack of sufficient modelling of the trajectories in the injection region. The result was that it was not possible to obtain good injection into the ring while simultaneously providing clean transport of the waste beam to the injection dump. Rectifying this problem required several modifications to the injection region in the first few years after turn on [9]. These modifications included, but were not limited to: A change in size and width of both the primary and secondary foil, and increase in the injection dump beamline aperture, an increase in the injection dump line septum magnet gap, and the installation of a new C-magnet in the injection dump line.

A final unexpected challenge in the injection region is associated with the convoy electrons, i.e., the electrons which are stripped from the H^-. For the SNS 1.4 MW beam power, these electrons constitute 1.6 kW of beam power and hence need to be properly handled. The foil is located in a magnetic field such that the electrons spiral downward along the field lines and intercept an electron catcher at the bottom of the vacuum chamber. The catcher is designed to capture the electrons and prevent reflection and out-scatter. However, due to a combination of fabrication errors and due to the modifications in the injection region, the electron catcher is not nor has ever been in the correct position. As a result, a significant number of electrons are reflected back toward the foil and intercept the foil mounting bracket and the surrounding beam pipe. This has caused damaged to the brackets leading to progressive changes in both the bracket geometry and material to mitigate the damage [10]. In addition, the catcher itself is suffering significant damage from the electrons and will need to be redesigned in the future.

FUTURE CHALLENGES

The SNS facility is planning for a beam power upgrade from the current baseline 1.4 MW to 2.8 MW to accommodate a second target station [11]. To achieve the new beam power, the beam energy will be increase from 1.0 GeV to 1.3 GeV, and the ion beam current will have to be increase from ~35 mA to ~50 mA, which is challenging. The new parameters result in approximately the same space charge tune shift in the accumulator ring, such that space charge effects are not a major concern. However, due to its highly nonlinear nature and notoriously unpredictable behaviour, the e-P instability could still be an issue. In addition, the beam power increase will result in a significant increase in the foil temperatures ~ 300 K [9]. Because the current foil temperature is not known, and because the sublimation rate versus temperature curve has a large error bar, there is some concern over the sublimation rate of foils at the higher power. An effort is underway to measure the current foil temperatures to more accurately predict the sublimation rate for 2.8 MW of beam power.

ACKNOWLEDGEMENT

ORNL is managed by UT-Battelle, LLC, under contract DE-AC05-00OR22725 for the U.S. Department of Energy. This research was supported by the DOE Office of Science, Basic Energy Science, Scientific User Facilities.

REFERENCES

[1] G. Dodson, “SNS Commissioning and Operations, the first 10 Years. An Overview of the Components Status after High Intensity Beam Operating Experience”, presented at HB2016, Malmö, Sweden, July 2016, paper THAM3X01, this conference.

[2] S. Kim, “SNS Superconducting Linac Operational Experience and Upgrade Path”, in *Proc. LINAC08*, Victoria, USA, 2008, paper MO103, pp. 11.

[3] A. Shishlo, “Model Benchmark With Experiment at the SNS Linac“, presented at HB2016, Malmö, Sweden, July 2016, paper WEPM2Y01, this conference.

[4] S. Nath *et al.*, “Longitudinal Beam-dynamics of the SNS SRF-Linac “, in *Proc EPAC02*, Paris, 2002, paper THPLE024, pp. 1031.

[5] A. Shishlo, A. Aleksandrov, V. Lebedev, and M. Plum, Phys. Rev Lett, 108, 114801 (2012).

[6] A. Aleksandrov, “Path to Beam Loss Reduction in the SNS Linac Using Measurements, Simulation and Collimation”, presented at HB2016, Malmö, Sweden, July 2016, paper THAM5Y01, this conference.

[7] S. Henderson et al, Nucl. Inst. and Methods, 763, 2014.

[8] N. Evans, “Broadband Feedback System for Instability Damping in the SNS Ring“, presented a HB2016, Malmö, Sweden, July 2016, paper TUPM1X01, this conference.

[9] M. Plum, “SNS Injection and Extraction Systems--Issues and Solutions”, in *Proc. HB2008*, Nashville, 2008, paper WGC04, pp. 268.

[10] M. Plum, “H- Charge Exchange Injection Issues at High Power”, presented at HB2016, Malmö, Sweden, July 2016, paper TUPM6X01, this conference.

[11] Technical Design Report Second Target Station, ORNL/TM-2015/24, 2015.

ISBN 978-3-95450-185-4

LHC RUN 2: RESULTS AND CHALLENGES

R. Bruce*, G. Arduini, H. Bartosik, R. de Maria, M. Giovannozzi, G. Iadarola, J.M. Jowett, K. Li, M. Lamont, A. Lechner, E. Metral, D. Mirarchi, T. Pieloni, S. Redaelli, G. Rumolo, B. Salvant, R. Tomas, J. Wenninger, CERN, Geneva, Switzerland

Abstract

The first proton run of the LHC was very successful and resulted in important physics discoveries. It was followed by a two-year shutdown where a large number of improvements were carried out. In 2015, the LHC was restarted and this second run aims at further exploring the physics of the standard model and beyond at an increased beam energy. This article gives a review of the performance achieved so far and the limitations encountered, as well as the future challenges for the CERN accelerators to maximize the data delivered to the LHC experiments in Run 2. Furthermore, the status of the 2016 LHC run and commissioning is discussed.

INTRODUCTION

The CERN Large Hadron Collider (LHC) [1,2] is built to collide 7 TeV protons or heavy ions of equivalent rigidity. Following the downtime after an incident in one of the main dipole circuits during the first commissioning in 2008 [3], the operation restarted at lower beam energy to minimize the risk. Therefore, the first proton run (2010-2013) [4–6] was carried out at 3.5 TeV–4 TeV. Furthermore, a bunch spacing of 50 ns was used instead of the nominal 25 ns. This implied fewer bunches with larger intensity and hence a high peak luminosity but larger than nominal pileup. Run 1 resulted in about 30 fb^{-1} of proton data and important physics results, most notably the discovery of the Higgs boson [7,8].

Run 1 was followed by a long shutdown (LS1, 2013–2014) with a large number of consolidation and upgrade activities [9]. The bus-bar splices between the superconducting magnets were improved, in order to make sure that the LHC could operate at higher energy without risk of repeating the 2008 incident. Run 2 started in 2015 and is planned to continue until the end of 2018. The main accelerator goals of Run 2 are to produce more than 100 fb^{-1} of data at a higher energy and using the nominal 25 ns bunch spacing, but with lower bunch charge for lower pileup.

The parameters achieved so far in Run 1 and Run 2, together with the design values, are shown in Table 1. At the time of writing in end of June 2016, the LHC has entered its production phase with a luminosity that has just reached nominal, a stored beam energy of around 250 MJ, and a good machine availability after a few initial technical issues. This article gives a review of the achievements so far, as well as the issues encountered and the challenges ahead for reaching the goals of the LHC.

BEAM FROM THE INJECTORS

The success of the LHC is highly dependent on the availability and the beam quality of the injector complex. Protons are injected at 450 GeV into the LHC, after passing through a chain of 4 accelerators: LINAC 2, PSB, PS, and SPS [10]. The present limitations on bunch intensity N_B and normalized emittance ϵ_n in the injector chain are summarized in Fig. 1 for the standard 25 ns LHC beam [11]. The brightness is limited by space charge effects in the PSB and the PS and the fact that, in the PSB, several injections are performed from LINAC 2 per PSB bunch. This means that in order to increase the intensity, more injections are needed, which occupy different phase-space areas and hence cause larger ϵ_n. In the SPS, longitudinal instabilities occur if $N_B \gtrsim 1.3\times10^{11}$ protons per bunch. The green dots in Fig. 1 show the actual achieved beams in 2015.

Figure 1 refers to the standard 25 ns LHC beams, which have been used so far in 2015–2016. Several different schemes exist [12], where the most interesting for LHC physics is the so-called BCMS beam (Batch compression, merging and splitting) [13, 14]. It has almost a factor 2 smaller ϵ_n, since lower-intensity bunches with smaller ϵ_n are taken from the PSB and merged in the PS to achieve about the same N_B as for the standard beam. However, fewer bunches per train can be achieved and hence a slightly smaller number of total bunches in the LHC.

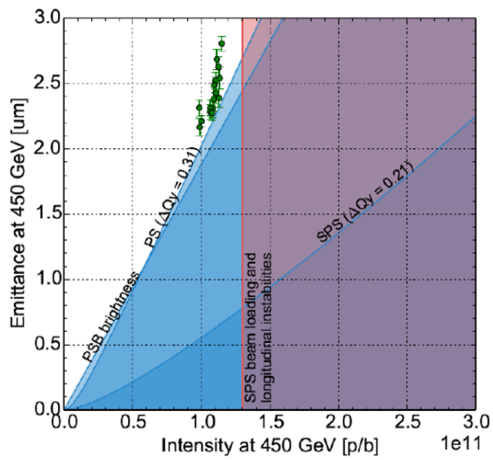

Figure 1: Limitations on the beam intensity and normalized emittance in the injector chain. The white area to the left represents the possible configuration space for the LHC beams and the green dots the beams used in 2015.

THE 2015 PROTON RUN

Because of the large number of changes applied in LS1, a significant recommissioning period was needed. Therefore 2015 was considered to be a commissioning year, with the main goal to reestablish high-intensity operation with the new running parameters. A beam energy of 6.5 TeV was

* roderik.bruce@cern.ch

ISBN 978-3-95450-185-4

Table 1: Typical proton running conditions in the LHC during operation so far in Run 1 (2010–2012) and Run 2 (2015–2016), shown together with the design parameters. The values of luminosity, crossing angle, beam-beam separation, geometric reduction factor, and number of colliding bunches, refer to the high-luminosity experiments in IR1 and IR5 only.

	Design	2010	2011	2012	2015	June 2016
Beam energy (TeV)	7.0	3.5	3.5	4.0	6.5	6.5
Protons/bunch (average at start of collisions)(10^{11} p)	1.15	1.0	1.3	1.5	1.1	1.1
Maximum number of bunches	2808	368	1380	1380	2244	2076
Maximum stored energy per beam (MJ)	362	23	112	143	277	266
Bunch spacing (ns)	25	150	50	50	25	25
Transverse normalized emittance ϵ_n, typical value in collision (μm)	3.75	2.6	2.4	2.4	3.5	3.4
half crossing angle (μrad)	143	100	120	146	145	185
Primary collimator cut (σ)	6.0	5.7	5.7	4.3	5.5	5.5
Secondary collimator cut (σ)	7.0	8.5	8.5	6.3	8.0	7.5
Tertiary collimator cut (σ)	8.3	15.0	11.8	9.0	13.7	9.0
Smallest allowed magnet aperture (σ)	8.4	17.5	14.1	10.5	15.5	9.9
β^* (m)	0.55	2.0–3.5	1.0–1.5	0.6	0.8	0.4
Maximum peak luminosity (10^{34} cm^{-2}s^{-1})	1.0	0.021	0.35	0.77	0.51	1.01
Total integrated luminosity (fb^{-1})		0.048	5.5	22.8	4.2	8.1

chosen as a compromise between energy reach and the time needed in terms of training quenches of the main dipole circuits to reach the nominal 7 TeV [15].

As shown in Table 1, a relaxed set of machine parameters were chosen for the 2015 operation, in order to ease the commissioning [16, 17]. The optical β-function at the collision point, β^*, was 80 cm, which is larger than the β^* =60 cm used in 2012, in spite of the higher energy and thus smaller beam size. This allowed a beam-beam separation of 11 σ, which gave room for a larger dynamic aperture than in 2012 [18]. Furthermore, the collimator settings used in 2015 were the 2012 settings kept in mm [17], in spite of the higher energy, which relaxed the impedance constraints compared to the alternative scenario of keeping the settings in σ. Furthermore, an additional 2 σ margin was introduced for machine protection. By relaxing these parameters, the risk that the operation would be perturbed by beam instabilities and sudden lifetime drops was kept small.

The hardware commissioning started in early 2015 and the first beams were circulating in April. The first operation took place with a small intensity, which was gradually ramped up, in order to give the opportunity to spot any machine protection issue early on. An initial physics run with 50 ns was performed, before the LHC moved to 25 ns operation in August and heavy ions in November. This was aimed at re-establishing operation at high stored energies before addressing limitations from electron cloud expected with the shorter bunch spacing.

The operation in 2015 was perturbed by several hardware issues. It was found that some electronic components of the quench protection system were not radiation hard, which caused single event upsets and spurious beam dumps [19]. This was fixed during a technical stop by replacing affected components.

The material of the movable absorbers for injection protection (TDI) showed non-conformities [20]. In order not to risk that the TDI would be damaged by miskicked beam, the maximum number of bunches per injection was limited to 144 as opposed to the nominal 288. High vacuum spikes were also observed during injection close to one of the two TDIs, and the level of the vacuum interlock had to be increased to avoid spurious beam dumps. It was later found that the TDI coating was damaged, and a possible link to the vacuum issues is studied. Both TDIs have been exchanged for the 2016 run with a new and improved design [20].

Other limits came from so-called UFOs (unidentified falling objects), which are believed to be dust particles falling into the beam [21–25]. The interactions of the the beam with UFOs induce particle showers on nearby elements, which caused 18 beam dumps and 3 quenches in 2015. Some conditioning of UFOs with time has been observed, and efforts have been done to optimize the beam loss monitor thresholds to minimize the downtime from dumps and quenches.

Furthermore, several beam dumps and quenches at the beginning of the 2015 run, always triggered by beam losses in the same dipole, were attributed to an unidentified lying object (ULO) [26]. Dedicated tests, where the beam was moved in steps around the aperture in this magnet, allowed to map out the shape of an aperture restriction, possibly a lying object, at the bottom of the vacuum chamber. The situation was solved by introducing an orbit bump to steer the beam with sufficient clearance past the ULO.

The main beam-physics related constraint that the LHC faced in 2015 was related to electron cloud (EC), which was since long foreseen to be a major performance limitation [27–29]. Free electrons may be accelerated by the beam towards the vacuum pipe. On impact, secondary electrons are produced, which in turn are accelerated and cause an avalanche effect. The consequences are an increased heat

ISBN 978-3-95450-185-4

load on the beam screens, increased vacuum pressure, and single or multi-bunch instabilities.

For the LHC, the main issue has been that the heat load to the cryogenic system limits the number of bunches that can be injected (2244 at the end of 2015) [30, 31]. The heat load was found to differ between machine sectors, which is not well understood. Because of a conditioning effect, special scrubbing runs were carried out, to condition the EC to a level where the beam quality is acceptable. Further conditioning was observed over the 2015 physics run. It should be noted, however, that due to the TDI limitation, longer trains of 288 bunches could not be injected, and hence the scrubbing was less efficient. Further limitations due to vacuum degradation at the injection kickers have also been encountered.

Some beam instabilities were encountered, driven mainly by EC, impedance, and an interplay between the two. The beams could, however, be stabilized through a high chromaticity, high octupole current and high damper gain [31,32], although the resulting increased tune spread, in combination with the tune spread from EC, made the tune footprint at 450 GeV reach the third order resonance. This was mitigated by a slight change in vertical tune. Efforts are also ongoing to improve the diagnostics and measurements of instability-related data [33].

Performance limitations due to beam-induced heating of various components, which were frequently encountered in Run 1, have been mitigated by a large effort to minimize the impedance and fix equipment non-conformities during LS1 [34, 35].

In spite of these issues, the LHC was in 2015 successfully commissioned at 6.5 TeV and 25 ns bunch spacing, and a total of 4.2 fb^{-1} of proton data was collected by the experiments.

THE 2015 HEAVY-ION RUN

The 2015 heavy-ion run with Pb-Pb collisions started in mid-November and lasted for about a month [36]. A commissioning period was followed by a reference proton run at the equivalent nucleon center-of-mass energy and the Pb-Pb run. The Pb beam energy was 6.37Z TeV, (Z is the nuclear charge), which provided a center-of-mass energy of over 1 PeV. This is a record for heavy-ion colliders.

A limitation to the achievable luminosity for heavy ions is bound-free pair production (BFPP), in which a colliding Pb ion captures an electron at the collision point and is subsequently lost locally in the dispersion suppressor, due to the change in charge [37]. These losses have been predicted to possibly induce quenches [38], which was shown also experimentally in 2015 [39, 40]. This effect was alleviated in 2015 by orbit bumps that moved the losses longitudinally to a harmless location in IR1 and IR5 [41].

The Pb run profited from an very good machine availability (around 80%), which was better than in the proton run, and about 40% of the time was spent in physics [42]. Because of excellent injector performance, an average of 1.6×10^8 ions per bunch was achieved at the start of collisions [36]. This largely surpassed the design value of 7×10^7 ions per bunch and was a key to achieving a peak luminosity of 3×10^{27} cm^{-2}s^{-1}, exceeding the peak design luminosity by a factor 3, as shown in Fig. 2.

At the end of 2016, there will be a p-Pb run, partly at the same energy as in 2013 [43,44], but mainly at the maximum available beam energy of 6.5 Z TeV. Another Pb-Pb run is scheduled in 2018.

2016 PROTON PARAMETERS

To explore further the LHC physics potential, a significantly higher integrated luminosity is needed than in 2015. The goal is to surpass 100 fb^{-1} in the whole Run 2 and 25 fb^{-1} in 2016, which is considered as a production year. Therefore, the parameters of the LHC have to be pushed to increase the peak luminosity, while at the same time the machine availability and the time spent in physics should be maximized. The parameters for 2016 are shown in Table 1 and we outline here how they were chosen.

The luminosity $\mathcal{L}$ for round beams and optics can be written as

$$\mathcal{L} = \frac{N_B^2 f_{\mathrm{rev}} k_B}{4\pi\beta^* \epsilon_{xy}} \times F, \tag{1}$$

where f_{rev} is the revolution frequency, k_B the number of bunches per beam, $\epsilon_{xy} = \epsilon_n/(\gamma_{\mathrm{rel}}\beta_{\mathrm{rel}})$ is the geometric emittance and F a geometric reduction factor. It can never be larger than 1 and is given by

$$F = \frac{1}{\sqrt{1 + \frac{(\sigma_s \tan\phi)^2}{\epsilon_{xy}\beta^*}}}. \tag{2}$$

Here σ_s is the bunch length and ϕ the half crossing angle.

As seen from Eq. (1), there are different ways to push the luminosity. Firstly, the intensity can be increased through k_B and N_B, where the latter gives a larger gain due to the square dependence in Eq. (1). There could be a possibility to push N_B towards the SPS limit of 1.3×10^{11} at the expense of slightly larger ϵ_n (see Fig. 1). This is more challenging for electron cloud and impedance effects. To stay within the stability boundaries, N_B can be increased incrementally to find the optimum. Similarly it is planned to gradually increase k_B while staying within the EC heat load limits, which was started already in 2015.

The transverse beam size can be decreased by acting on ϵ_n or β^*. The BCMS beams could be used to decrease ϵ_n, but it is desirable to finish all EC scrubbing studies with the standard beam before moving to BCMS, which risks also to be more prone to instabilities and worse lifetime due to the higher brightness [32, 35]. It is also still to be quantified how much ϵ_n of the brighter BCMS beam increases through the LHC cycle, before entering collisions.

Moreover, β^* can be decreased, independently of constraints on ϵ_n and intensity. In the LHC, β^* is limited mainly by the available aperture. When β^* is decreased, the β-function in the triplets of the final focusing system increases.

ISBN 978-3-95450-185-4

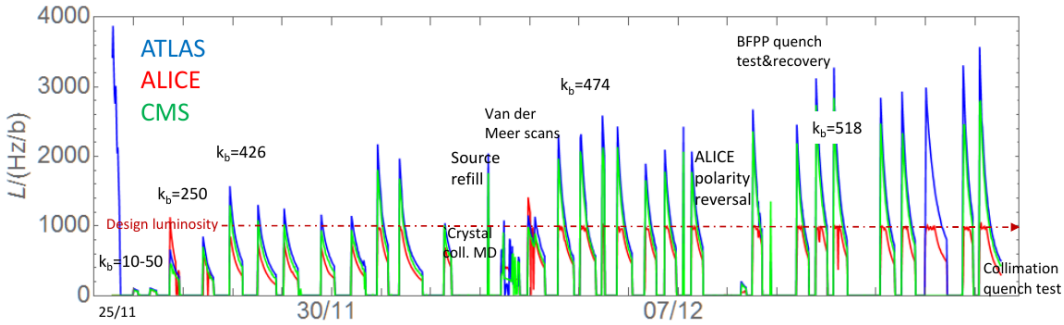

Figure 2: Luminosity for 3 of the 4 experiments, during the 2015 Pb-Pb run showing the progressive increase of number of bunches, k_b and the interruptions of regular data-taking. The dashed line shows the design luminosity [1]. The figure is taken from Ref. [36]. The ATLAS luminosity has recently been recalibrated and the peak corresponds to 3×10^{27} cm^{-2}s^{-1}.

The triplet aperture, normalized by the beam σ, therefore decreases, but it is only allowed to decrease so much that the collimation system still protects the aperture [45–47]. To reduce β^*, one can reduce ϕ in order to gain aperture margin or optimize the collimators to protect a smaller aperture.

Acceptable values of ϕ are given by what normalized beam-beam separation can be tolerated without degrading the dynamic aperture so much that the lifetime suffers. In 2015, a normalized beam-beam separation of 11 σ was used but a reduction to 10 σ has been shown to be possible [18, 48, 49], which has been implemented for the 2016 run.

An extensive machine development (MD) program on collimator settings, carried out in 2015, showed that the secondary collimators in IR7 could be moved in by 0.5 σ without jeopardizing the long-term stability of the cleaning or increasing the impedance too much [35,50]. Furthermore, tertiary collimators (TCTs) were previously kept rather open to minimize the risk that they, or the triplets behind them, could be damaged during an asynchronous beam dump [47]. These settings could now be significantly reduced, using a new optics in which the fractional phase advances between the dump kicker, TCTs and triplets are close to 0° or 180°, so that they can never be hit by primary beam during such an accident. This has resulted in a very important gain in protected aperture [51–53].

With the tighter collimation hierarchy and the smaller beam-beam separation, β^* =40 cm is the 2016 baseline, which was studied in detailed MDs [54]. This is well below the nominal value β^* =55 cm, and it relies also on a very well aligned triplet aperture [51].

The geometric factor F in Eq. (1) can be increased by decreasing ϕ (discussed above) or σ_z, which is limited by EC effects [31] and longitudinal instabilities [55]. In 2015, an RMS bunch length $\sigma_z \approx 10$ cm was deployed, which has been slightly decreased in steps in 2016, to approach the boundary of acceptable values. It should be noted that in the LHC, σ_z shrinks during the fills due to synchrotron radiation. Therefore, σ_z at the start of the fill should be large enough that no instabilities appear later in the fill. A longitudinal blowup during the fill is under study [55].

OPERATIONAL EXPERIENCE IN 2016

The recommissioning in 2016 with new parameters was smooth. The new β^* =40 cm optics could be corrected to a peak β-beat of less than 5% thanks to improved methods [56–58] and the absence of perturbing triplet movements as in 2015. The new collimator settings were successfully put into operation and showed excellent cleaning performance [59]. However, technical issues caused delays. About 6 days were lost due to interventions on the PS main power supply and its spare, and another 6 days due to a 66 kV transformer short circuit caused by an animal. Further delays were caused by water infiltration in IR3 that induced faults on contacts on collimator cables. This is summarized in Fig. 3, which shows the luminosity production since May 2016.

Another delay was caused by a vacuum leak the SPS beam dump, which still prevents trains longer than 96 bunches.Therefore, the plans of increasing k_B towards the maximum possible are, at the time of writing, put on hold due and k_B is temporarily limited to 2076 bunches, as seen in Table 1. With the shorter trains, the EC effects are less pronounced, and the intensity could quickly be ramped up to about 2000 bunches. The intensity rampup over time in 2016 is shown in the bottom plot of Fig. 4, where it can be compared to previous years of operation. It can be seen that the LHC now regularly stores about 250 MJ of energy per beam during the physics fills.

Apart from the mentioned faults, the recent availability has been excellent, as seen in Fig. 3, with systems such as cryogenics, power converters, RF, diagnostics and collimation working reliably. In one week, the LHC spent 75% of the time in physics. Many long fills of more than 20 h were possible, with a record of 0.74 fb^{-1} produced in one fill. After decreasing the bunch length in steps, the peak luminosity has now reached the nominal 10^{34} cm^{-2}s^{-1}. Compared to the nominal scenario, the bunch population in collision is about the same, but about 25% fewer bunches are used, and slightly larger beam-beam separation and bunch length. This is compensated by a 27% smaller β^* and slightly smaller emittance (see Eq. (1) and Table 1).

The progress of the production of integrated luminosity is shown in the top plot of Fig. 4, together with the data

ISBN 978-3-95450-185-4

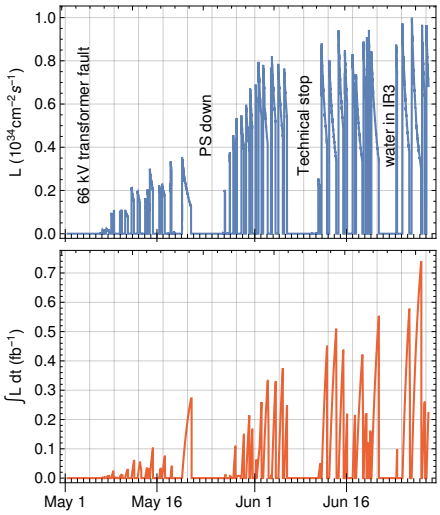

Figure 3: The instantaneous luminosity (top) and the integrated luminosity per fill (bottom) at the ATLAS experiment in May and June 2016.

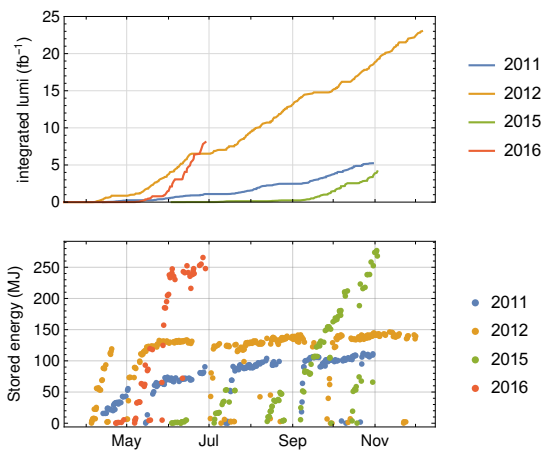

Figure 4: The accumulated luminosity at the ATLAS experiment (top) and the stored beam energy in each fill (bottom) over the years of LHC operation so far.

collection in previous years. The rate at which the LHC is gathering data is, since the end of May 2016, faster than any previous year, and more than 2 fb^{-1} per week could be produced. This is due to both the higher luminosity and the very good availability. So far, the LHC has on June 29 2016 collected 8.1 fb^{-1} for the high-luminosity experiments, which surpasses the 2015 run already by almost a factor 2.

CONCLUSION AND OUTLOOK

The LHC is presently (June 2016) on a good track of for reaching its 2016 goal of at least 25 fb^{-1}, thanks mainly to recent good availability, a very small β^*, and a good luminosity lifetime. The years 2017 and 2018 will also be focused on luminosity production, and it would be desirable to produce more than 40 fb^{-1} per year in order to exceed 100 fb^{-1} in Run 2. Therefore, further efforts to improve the performance are likely to be needed. It is also crucial for the success of the LHC that the recent good availability is maintained or even improved. Studies are performed to understand all causes of LHC downtime and how different faults depend on each other, so that efforts for improved reliability can be focused where they are needed the most [42]. In parallel, various means are studied in order to further increase the luminosity along the lines outlined above.

A main challenge for the LHC is to push the intensity limit from EC heat load. During the 2016 run, the conditioning effect has hardly been visible, however, only the shorter 72 and 96 bunch trains were used. To further understand and push the limits, tests should be done with longer trains of 288 bunches or the special doublet beam, which was developed for this purpose [60].

If the intensity cannot be further increased due to e.g. electron cloud, the high-brightness BCMS beams could be a good option. Moreover, further MD studies are planned to explore the long-range beam-beam effect and to find out whether the crossing angle can be further decreased without losing in luminosity lifetime. Preliminary studies have shown that a beam-beam separation even down to 8 σ could be feasible with BCMS beams [18]. The collimation hierarchy is also under study, where it might be possible to further reduce the openings. The limitations are given both by machine protection constraints, impedance, and stability of the cleaning hierarchy [47], in order to gain further in β^*. Combining these improvements, there is hope that the design luminosity could be exceeded by several tens of percent [61]. Further developments, such as flat optics, are also under study.

The LHC beam energy is presently 6.5 TeV, however, further tests could be envisaged to evaluate more precisely the number of additional training quenches that are required to reach 7 TeV, and thus how costly it is in terms of time [15].

Another long shutdown (LS2) is planned 2019–2020, in which major upgrades are foreseen in particular for the injector complex [62]. Tentatively, LS2 will be followed by Run 3 to 2023 and then LS3 (2024–2026), where major upgrades for high-luminosity LHC are to be installed [63]. With these improvements, the goal is to produce around 3000 fb^{-1} over the following 10 years.

ACKNOWLEDGMENTS

We would like to thank all involved colleagues for their contributions to the success of the LHC, as well as for specific input for this review.

REFERENCES

[1] O. S. Brüning *et al.* (editors). LHC design report v.1 : The LHC main ring. *CERN-2004-003-V1*, 2004.

[2] L. Evans and P. Bryant (editors). LHC machine. *JINST*, 3:S08001, 2008.

[3] P. Lebrun *et al.* Report of the Task Force on the incident of 19 September 2008 at the LHC. *CERN LHC Project Report 1168*, 2009.

ISBN 978-3-95450-185-4

[4] R. Alemany-Fernandez *et al*. Operation and Configuration of the LHC in Run 1. *CERN-ACC-NOTE-2013-0041*, 2014.

[5] Mike Lamont. Status of the LHC. *Journal of Physics: Conference Series*, 455(1):012001, 2013.

[6] S. Myers. The Large Hadron Collider 2008—2013. *Int. J. Mod. Phys. A*, 28:1330035, 2013.

[7] ATLAS collaboration. Observation of a new particle in the search for the standard model higgs boson with the ATLAS detector at the LHC. *Physics Letters B*, 716(1):1 – 29, 2012.

[8] CMS collaboration. Observation of a new boson at a mass of 125 GeV with the CMS experiment at the LHC. *Physics Letters B*, 716(1):30 – 61, 2012.

[9] F. Bordry *et al*. The First Long Shutdown (LS1) for the LHC. *Proceedings of the International Particle Accelerator Conference 2013, Shanghai, China*, page 44, 2013.

[10] M. Benedikt *et al*. LHC design report v.3 : The LHC injector chain. *CERN-2004-003-V3*, 2004.

[11] H. Bartosik *et al*. Can we ever reach the HL-LHC requirements with the injectors? *Proceedings of the Review of LHC & Injector Upgrade Plans Workshop (RLIUP)*, 2013.

[12] Y. Papaphilippou *et al*. Operational Beams for the LHC. *Proceedings of the LHC Performance Workshop (Chamonix 2014), Chamonix, France*, 2014.

[13] R. Garoby. New RF Exercises Envisaged in the CERN PS for the Antiprotons Production Beam of the ACOL Machine. *IEEE Transactions on Nuclear Science*, NS-32(5), 1985.

[14] H. Damerau *et al*. RF manipulations for higher beam brightness LHC-type beams. *Proceedings of IPAC13, Shanghai, China*, 2013.

[15] A. Verweij. Solved and remaining non-conformities in the superconducting circuits. *Proceedings of the LHC Performance Workshop (Chamonix 2014), Chamonix, France*, 2014.

[16] LHC Machine Committee, 2014.09.03, 2014.

[17] R. Bruce *et al*. Baseline LHC machine parameters and configuration of the 2015 proton run. *Proceedings of the LHC Performance Workshop (Chamonix 2014), Chamonix, France*, 2014.

[18] T. Pieloni *et al*. Beam-beam effects: long range and head-on. *Proceedings of the 6th Evian Workshop, Evian, France*, 2015.

[19] M. Pojer. QPS operational aspects. *Proceedings of the 6th Evian Workshop, Evian, France*, 2015.

[20] A. Lechner *et al*. TDI - past observations/limitations and improvements for 2016. *Proceedings of the 6th Evian Workshop, Evian, France*, 2015.

[21] T. Baer *et al*. UFOs in the LHC. *Proceedings of IPAC'11, San Sebastian, Spain*, page 1347, 2011.

[22] T. Baer. *Very fast losses of the circulating LHC beam, their mitigation and machine protection*. PhD thesis, Universität Hamburg, 2013.

[23] B. Auchmann *et al*. BLM Threshold Strategy (vs UFOs and Quenches). *Proceedings of the LHC Performance Workshop (Chamonix 2014), Chamonix, France*, 2014.

[24] B. Auchmann *et al*. How to survive a UFO attach. *Proceedings of the 6th Evian Workshop, Evian, France*, 2015.

[25] G. Papotti *et al*. Macroparticle-induced losses during 6.5 TeV LHC operation. *Proceedings of the International Particle Accelerator Conference 2016, Busan, Korea*, page 1481, 2016.

[26] D. Mirarchi *et al*. LHC aperture and ULO restrictions: are they a possible limitation in 2016? *Proceedings of the 6th Evian Workshop, Evian, France*, 2015.

[27] F. Zimmermann. A simulation study of electron-cloud instability and beam-induced multipacting in the lhc. *LHC Project Report 95, CERN*, 1997.

[28] G. Rumolo, F. Ruggiero and F. Zimmermann. Simulation of the electron-cloud build up and its consequences on heat load, beam stability, and diagnostics. *Phys. Rev. ST Accel. Beams*, 4:012801, 2001.

[29] G. Iadarola. *Electron cloud studies for CERN particle accelerators and simulation code development*. PhD thesis, University of Naples, 2014.

[30] G. Iadarola *et al*. Scrubbing: Expectations and Strategy, Long Range Perspective. *Proceedings of the LHC Performance Workshop (Chamonix 2014), Chamonix, France*, 2014.

[31] G. Iadarola *et al*. Electron cloud effects. *Proceedings of the 6th Evian Workshop, Evian, France*, 2015.

[32] K. Li *et al*. How to fight collective effect limitations. *Proceedings of the 6th Evian Workshop, Evian, France*, 2015.

[33] T. Levens *et al*. Instability diagnostics. *Proceedings of the 6th Evian Workshop, Evian, France*, 2015.

[34] B. Salvant *et al*. Expected impact of hardware changes on impedance and beam induced heating during run 2. *Proceedings of the LHC Performance Workshop (Chamonix 2014), Chamonix, France*, 2014.

[35] L. Carver *et al*. Instabilities and beam-induced heating in 2015. *Proceedings of the 6th Evian Workshop, Evian, France*, 2015.

[36] J.M. Jowett *et al*. The 2015 heavy-ion run of the LHC. *Proceedings of the International Particle Accelerator Conference 2016, Busan, Korea*, page 1493, 2016.

[37] J. M. Jowett, J. B. Jeanneret and K. Schindl. Heavy Ion Beams in the LHC. *Proc. of the Particle Accelerator Conf. 2003, Portland*, page 1682, 2003.

[38] R. Bruce *et al*. Beam losses from ultraperipheral nuclear collisions between Pb ions in the Large Hadron Collider and their alleviation. *Phys. Rev. ST Accel. Beams*, 12(7):071002, Jul 2009.

[39] M. Schaumann *et al*. LHC BFPP Quench Test with Ions (2015). *CERN-ACC-NOTE-2016-0024*, 2016.

[40] C. Bahamonde Castro *et al*. Power Deposition in LHC Magnets Due to Bound-Free Pair Production in the Experimental Insertions. *Proceedings of the International Particle Accelerator Conference 2016, Busan, Korea*, page 1418, 2016.

[41] J.M. Jowett *et al*. Bound-free pair production in LHC Pb-Pb operation at 6.37 Z TeV per beam. *Proceedings of the International Particle Accelerator Conference 2016, Busan, Korea*, page 1497, 2016.

[42] A. Apollonio *et al*. 2015 availability summary. *Proceedings of the 6th Evian Workshop, Evian, France*, 2015.

ISBN 978-3-95450-185-4

[43] J.M. Jowett *et al*. Proton-nucleus Collisions in the LHC. *Proceedings of IPAC13, Shanghai, China*, page 49, 2013.

[44] D. Manglunki *et al*. The First LHC p-Pb run: Performance of the Heavy Ion Production Complex. *Proceedings of IPAC13, Shanghai, China*, page 2648, 2013.

[45] R.W. Assmann. Collimators and Beam Absorbers for Cleaning and Machine Protection. *Proceedings of the LHC Project Workshop - 'Chamonix XIV', Chamonix, France*, page 261, 2005.

[46] R. Bruce *et al*. Simulations and measurements of beam loss patterns at the CERN Large Hadron Collider. *Phys. Rev. ST Accel. Beams*, 17:081004, Aug 2014.

[47] R. Bruce, R. W. Assmann and S. Redaelli. Calculations of safe collimator settings and β^* at the CERN Large Hadron Collider. *Phys. Rev. ST Accel. Beams*, 18:061001, Jun 2015.

[48] M. Crouch *et al*. Long range beam-beam interaction and the effect on the beam and luminosity lifetimes. *CERN-ACC-NOTE-2016-0019*, 2016.

[49] M.P. Crouch *et al*. Impact of Long Range Beam-Beam Effects on Intensity and Luminosity Lifetimes from the 2015 LHC Run. *Proceedings of the International Particle Accelerator Conference 2016, Busan, Korea*, page 1422, 2016.

[50] A. Mereghetti *et al*. β^*-reach – IR7 collimation hierarchy limit and impedance. *CERN-ACC-NOTE-2016-0007*, 2015.

[51] R. Bruce *et al*. IR aperture measurement at β^*=40 cm. *CERN-ACC-NOTE-2015-0037*, 2015.

[52] R. Bruce *et al*. Collimation with tighter TCTs at β^*=40 cm. *CERN-ACC-NOTE-2015-0036*, 2015.

[53] R. De Maria. Optics studies in view of 2016 LHC run. *presentation in the HSS section meeting, 2015.12.09*, 2015.

[54] A. Langner *et al*. LHC optics commissioning at β^*=40 cm and 60 cm. *CERN-ACC-NOTE-2015-0035*, 2015.

[55] H. Timko *et al*. Operational and beam dynamics aspects of the RF system in 2015. *Proceedings of the 6th Evian Workshop, Evian, France*, 2015.

[56] R. Tomás *et al*. Record low β beating in the LHC. *Phys. Rev. ST Accel. Beams*, 15:091001, Sep 2012.

[57] A. Langner and R. Tomás. Optics measurement algorithms and error analysis for the proton energy frontier. *Phys. Rev. ST Accel. Beams*, 18:031002, 2015.

[58] A. Langner *et al*. Optics model. *Proceedings of the 6th Evian Workshop, Evian, France*, 2015.

[59] D. Mirarchi. Status of loss maps and validation. *presentation in the LHC Collimation Working Group, 2016.04.25*, 2016.

[60] G. Iadarola and G. Rumolo. Electron cloud and scrubbing: perspective and requirements for 25 ns operation in 2015. *Proceedings of the 5th Evian Workshop, Evian, France*, 2014.

[61] R. Bruce and S. Redaelli. 2016 LHC configuration: can we get to β^* = 40 cm? *Proceedings of the 6th Evian Workshop, Evian, France*, 2015.

[62] J. Coupard *et al*. (editors). LHC Injectors Upgrade, Technical Design Report, Vol. I: Protons. *CERN-ACC-2014-0337*, 2014.

[63] G. Apollinari *et al*. (editors). High-Luminosity Large Hadron Collider (HL-LHC) : Preliminary Design Report. *CERN-2015-005*, 2015.

ISBN 978-3-95450-185-4

RECENT PROGRESS OF J-PARC MR BEAM COMMISSIONING AND OPERATION

S. Igarashi† for the J-PARC MR Beam Commissioning Group
KEK/J-PARC Center, Tsukuba, Ibaraki 305-0801 Japan

Abstract

The main ring (MR) of the Japan Proton Accelerator Research Complex (J-PARC) has been providing 30-GeV proton beams for elementary particle and nuclear physics experiments since 2009. The beam power of 415 kW has been recently achieved with 2.15×10^{14} protons per pulse and the cycle time of 2.48 s for the neutrino oscillation experiment. Main efforts in the beam tuning are to minimize beam losses and to localize the losses at the collimator section. Recent improvements include the 2nd harmonic rf operation to reduce the space charge effect with a larger bunching factor and corrections of resonances near the operation setting of the betatron tune. Because the beam bunches were longer with the 2nd harmonic rf operation, the injection kicker system was improved to accommodate the long bunches. We plan to achieve the target beam power of 750 kW in JFY 2018 by making the cycle time faster to 1.3 s with new power supplies of main magnets, rf upgrade and improvement of injection and extraction devices. The possibility of the beam power beyond 750 kW is being explored with new settings of the betatron tune.

INTRODUCTION

The Japan Proton Accelerator Research Complex (J-PARC) consists of the high intensity proton accelerators and the experimental facilities to make use of the proton beams [1]. It has three accelerators; a 400 MeV linear accelerator, 3 GeV rapid cycling synchrotron (RCS) and 30 GeV main ring (MR). MR is a synchrotron with the circumference of 1567.5 m and with three-fold symmetry as shown in Fig. 1. The first straight section is for injection devices and beam collimators. The proton beams from RCS are transported through a beam transport line (3-50BT) to MR. The second straight section is for slow extraction (SX) devices to deliver the beam to the hadron hall. The third straight section is for rf cavities and fast extraction (FX) devices to extract the beam to the neutrino beam-line or the beam abort line.

The cycle time is 2.48 s for the FX mode. The beam is extracted in one turn at the top energy to the neutrino oscillation experiment (T2K). For the SX mode the cycle time is 5.52 s with the flattop duration of 2.93 s. Beam spills of 2 s duration are then delivered to elementary particle and nuclear physics experiments in the hadron hall.

The T2K experiment observed the appearance of electron neutrinos from muon neutrinos made from the secondary particles of the high intensity protons [2]. High intensity proton beams are further demanded for the precise measurements of neutrino mixing parameters.

The beam power has been steadily increased as shown in Fig. 2 in the last six years. It was mostly about 390 kW in the operation of Jan. ~ May of 2016 for FX with 2×10^{14} protons per pulse (ppp). The plan to achieve the target beam power of 750 kW is to make the cycle faster from 2.48 s to 1.3 s with 2×10^{14} ppp. A milestone for the number of accelerated protons was therefore reached. Further efforts are being made for higher intensity. The user operation of 415 kW was successful during the last three days.

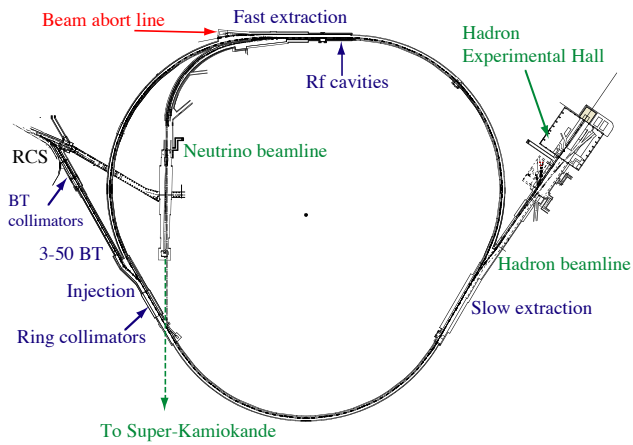

Figure 1: Layout of J-PARC MR.

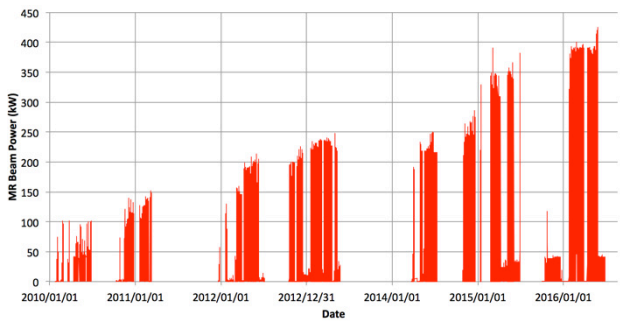

Figure 2: Beam Power Trend Graph.

OPERATION STATUS FOR THE FAST EXTRACTION

Eight bunches of beams are injected to MR in 4 times during the injection period of 0.13 s. The acceleration takes 1.4 s and the accelerated protons are extracted in one turn. The recovery for the magnet currents takes 0.94 s and the total cycle is 2.48 s. Figure 3 shows the beam

† susumu.igarashi@kek.jp

ISBN 978-3-95450-185-4

intensity measured with DCCT as a function of the cycle time for a shot of beam power of 416 kW. The number of protons per bunch (ppb) is 2.7×10^{13} at the injection and the number of accelerated protons is 2.15×10^{14} ppp. The beam loss is estimated to be 170 W during the injection period and 417 W during 0.12 s in the beginning of acceleration. The total beam loss is within the MR collimator capacity of 2 kW. The beam loss at 3-50BT is estimated to be 100 W. It is also within the 3-50BT collimator capacity of 2 kW.

The beam loss distribution in the circumference is shown in Fig. 4. The beam loss is measured with beam loss monitors [3] located at all 216 main quadrupole magnets. The gains of the 24 loss monitors (#1 ~ #20 and #213 ~ #216) including the collimator area are set to low, and the others (#21 ~ #212) have higher gain about 8 times. The beam loss is reasonably localized in the collimator area of (#6 ~ #11). Details of the collimator operation are described in Ref. [4].

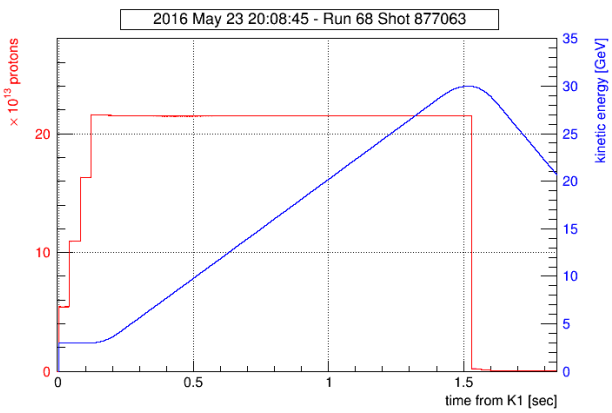

Figure 3: Beam intensity (shown in red) for a user-operation shot of the beam power of 416 kW as a function of the cycle time.

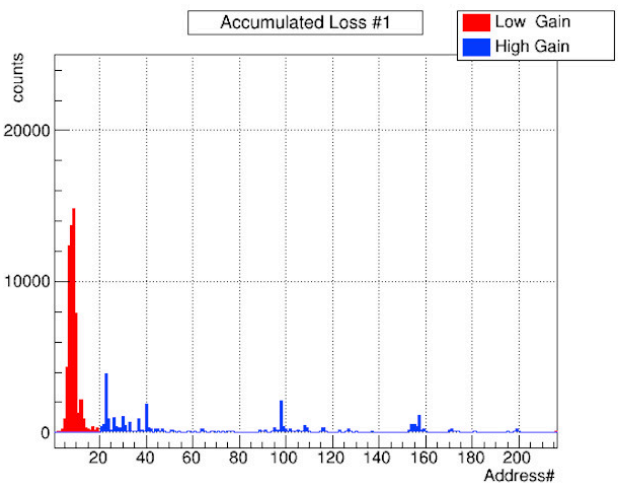

Figure 4: Beam loss distribution measured with beam loss monitors in the circumference as a function of MR address for a shot of the beam power of 416 kW.

RECENT IMPROVEMENTS

Injection Beam Distribution

RCS beam parameters such as painting and operation tune and chromaticity have been intensively explored for high intensity MR operation [5]. Profiles with a low peak should be preferable for reducing the space charge effects. Profiles with little tail should also be preferable for the beam loss reduction. By the RCS beam parameter optimization we managed to have the profiles with parabola distributions, even though the profiles used to be Gaussian distributions. The profile of injection beam is measured with an optical transition radiation monitor (OTR) [6] in 3-50BT (Figure 5).

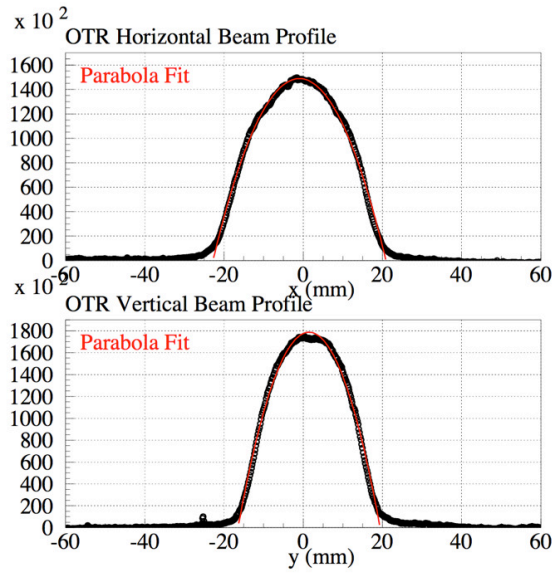

Figure 5: Horizontal beam profile (upper fig.) and vertical beam profile (lower fig.) measured with OTR in 3-50BT.

Rf Pattern

Beam studies with the 2nd harmonic rf indicated the improvement of the bunching factor and beam survival. When the 2nd harmonic rf was set to 0 kV with the fundamental rf of 100 kV, bunching factor was measured to be between 0.2 and 0.3 and the bunch length became about 200 ns. When the 2nd harmonic rf was set to 70 kV with the fundamental rf of 100 kV, bunching factor was improved to be between 0.3 and 0.4 and the bunch length was as long as about 400 ns.

For the recent user operation the fundamental rf of 160 kV and 2nd harmonic rf of 85 kV have been applied during injection period to improve the bunching factor and to reduce the space charge effects. The bunching factor was measured to be about 0.3 during injection period. In the beginning of acceleration the fundamental rf voltage turned up to 280 kV in 60 ms and turned down to 256 kV at 0.4 s after the acceleration start until the acceleration end. The 2nd harmonic rf lasts 0.1 s in the beginning of acceleration and turned off for the rest of acceleration.

ISBN 978-3-95450-185-4

Injection Kicker Improvements

The injection kicker system was improved to cope with long bunches for the 2nd harmonic rf operation. The rise time of the injection kicker were improved to be faster with the speed up circuit [7]. The tail was suppressed with the tail matching circuit. There is a reflection pulse that would make an extra kick to a circulating bunch. A compensation kicker was newly installed to cancel the extra kick [8]. It has been used in operation and reduced the beam losses at injections.

Instability Suppression

The chromaticity pattern in the cycle time was optimized to minimize the beam loss. To suppress instabilities, the chromaticity is kept to be negative, typically −6 during injection. If the chromaticity is too small in negative value, instabilities may be observed causing beam losses. If the chromaticity is too large in negative value, we may observe beam losses those are probably due to chromatic tune spread. The optimization is iterated after the change of the beam intensity and parameters of following feedback systems.

A bunch by bunch feedback system has been used to suppress coherent oscillation of each bunch effectively [9]. To suppress internal bunch oscillation, a more wideband feedback system named intra-bunch feedback system [10] is applied during injection and in the beginning of acceleration. The system consists of new stripline BPM's which have wide frequency response, a signal processing circuit and stripline kickers with the bandwidth of 100 kHz ~ 100 MHz. BPM signals are sampled at the rate of 64th harmonic of the RF frequency. The signal processing circuit extracts the betatron oscillation signals on each slice and feedbacks kick signals for each slice. The system has been applied effectively during injection and up to 0.12 s after the acceleration start.

Optics Measurement and Correction

We have recovered the effective physical aperture by corrections of the optics and closed orbit distortion (COD). The stripline kickers and the power amplifiers of the intra-bunch feedback system are used for beta measurement during injection and up to 0.37 s after the acceleration start. The kicker is to excite the betatron oscillation. The amplitudes of the oscillation are then measured with all the BPM's. The square root of beta should be scaled to the oscillation amplitude. The dispersion function is derived from the COD for the momentum deviation of $|\delta| < 1.3\%$. The betatron tune during injection and acceleration is measured from the frequency of the betatron oscillation that is induced by exciters. The results of beta, dispersion and tune are corrected to what we intend to set by adjusting the currents of 11 quadrupole magnet families. Figure 6 shows the horizontal and vertical tunes before and after the optics correction as a function of the cycle time. The tunes after the correction have less deviation from the setting tunes.

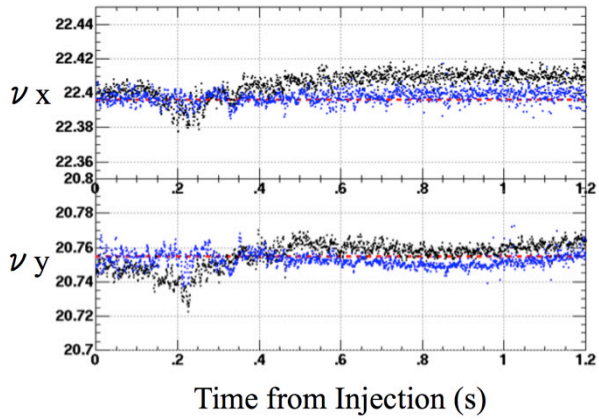

Figure 6: Horizontal tune (upper plot) and vertical tune (lower plot) as a function of the cycle time. Measurements before the optics correction are in black dots and results after the correction are in blue dots. The correction is done up to 0.5 s. The red dashed lines show the setting tunes.

Space Charge Tune Spread

The space charge tune spread was estimated for the beam power of 380 kW. The number of ppb was 2.5×10^{13} for the cycle time of 2.48 s. The transverse 2σ emittance was assumed to be 16π mm mrad and the bunching factor was set to 0.3 based on the measurements. Figure 7 shows the distribution of the tunes of macro particles with the particle tracking simulation program SCTR [11], which takes the space charge effects into account. The operation tune was set to (22.40, 20.75). The tune spread was estimated to be 0.3. There are some resonances of concern, such as a linear coupling resonance $\nu_x+\nu_y=43$, a half integer resonance $2\nu_y=41$ and third order resonances.

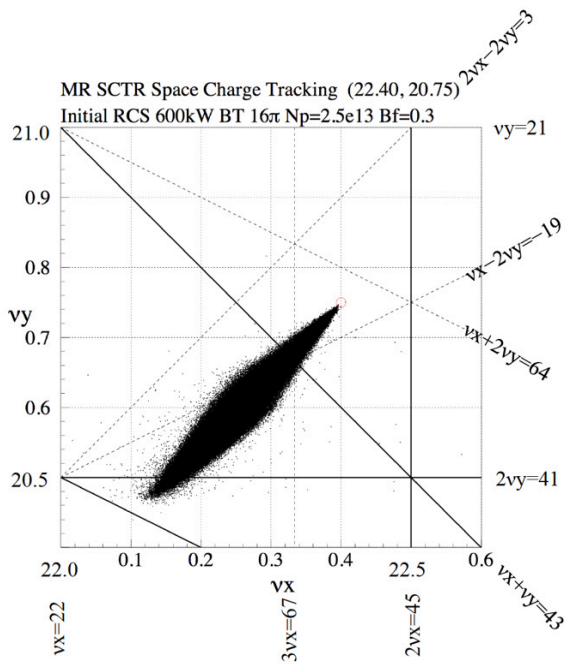

Figure 7: Space charge tune spread and resonances of concern.

ISBN 978-3-95450-185-4

Linear Coupling Resonance Correction with Skew Quadrupole Mangets

Rotation errors of the quadrupole magnets and vertical COD at the sextupole magnets cause the linear coupling resonance $\nu_x + \nu_y = 43$. Four skew quadrupole magnets (SQ's) have been used to correct the resonance. Current settings of the SQ's were optimized to recover the beam survival when the tune was set to be (22.28, 20.71) on the resonance for low intensity beams at first [12]. They were further optimized to minimize the beam loss for the high intensity operation. The beam survival has been improved for the beam power of 380 kW equivalent as shown in Fig. 8.

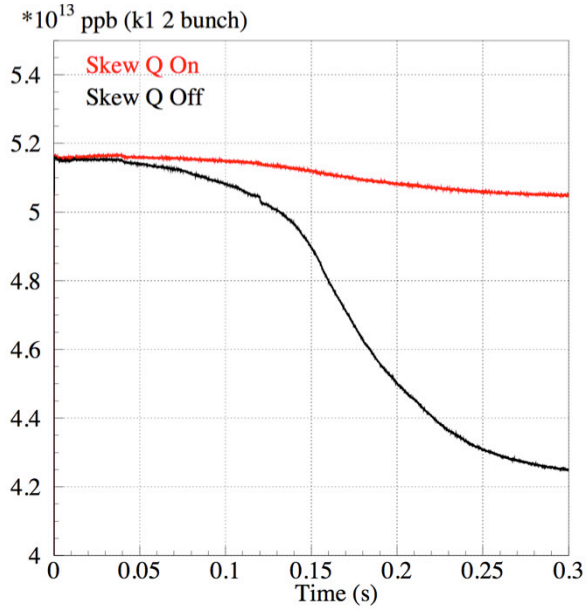

Figure 8: Beam intensity during injection and in the beginning of acceleration for 2-bunch beam for the beam power of 380 kW equivalent with SQ's on (red line) and off (black line).

Half Integer Resonance Correction with Trim Coil of Quadrupole Magnets

The FX septum magnets make undesirable quadrupole fields for circulating beams with the leak fields. They were measured for all 8 FX septum magnets. The sum of the strength K1 corresponded to 3 % of a main quadrupole magnet. Correction currents for the trim coils of three quadrupole magnets near the FX septum magnets were calculated. The correction has been applied and optics were measured at (22.19, 20.54) near the half integer resonance of $2\nu_y = 41$. Improvement of the beta modulation was then observed with the correction.

Third Order Resonance Corrections with Trim Coils of Sextupole Magnets

Third order resonances of $\nu_x + 2\nu_y = 64$ and $3\nu_x = 67$ have been corrected with trim coils of four sextupole magnets. The current setting of trim coils of two sextupole magnets was optimized to recover the beam survival for low intensity beams when the tune was set (22.42, 20.78) on the 3rd order resonance of $\nu_x + 2\nu_y = 64$. The resonance strength $G_{1,2,64}$ expressed by Eq. (1) was then derived from the measurement.

$$G_{1,2,64} = \frac{\sqrt{2}}{8\pi}\beta_x^{1/2}\beta_y k_2 \exp[i(\phi_x + 2\phi_y)] \quad (1)$$

The same procedure was repeated when the tune was set (22.34, 20.75) on the 3rd order resonance of $3\nu_x = 67$. The resonance strength $G_{3,0,67}$ expressed by Eq. (2) was also derived.

$$G_{3,0,67} = \frac{\sqrt{2}}{24\pi}\beta_x^{3/2} k_2 \exp[i(3\phi_x)] \quad (2)$$

Trim coils of four sextupole magnets were used to correct both of $\nu_x + 2\nu_y = 64$ and $3\nu_x = 67$. A solution was solved for a simultaneous equation to reproduce the two resonance strengths in the complex planes as shown in Fig. 9 and 10. It was applied for the high intensity operation and the beam loss was improved.

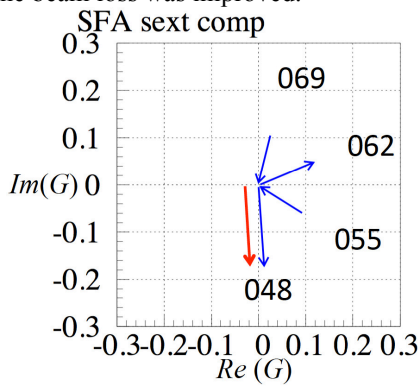

Figure 9: Each contribution of SFA magnets for resonance strength of $\nu_x + 2\nu_y = 64$ in the complex plane at the tune of (22.33, 20.83) with the trim coil correction of SFA048 of +1.1 A (red vector) and with the trim coil correction of four sextupole magnets; SFA048 +1.11 A, SFA055 −0.69 A, SFA062 +0.81 A, SFA069 −0.69 A (blue vectors).

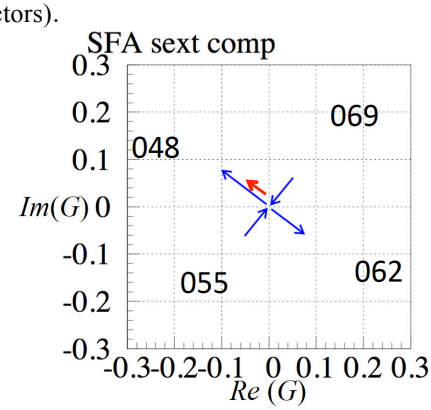

Figure 10: Each contribution of SFA magnets for resonance strength of $3\nu_x = 67$ in the complex plane at the tune of (22.33, 20.83) with the trim coil correction of SFA048 of +0.3 A (red vector) and with the trim coil correction of four sextupole magnets; SFA048 +1.11 A, SFA055 −0.69 A, SFA062 +0.81 A, SFA069 −0.69 A (blue vectors).

ISBN 978-3-95450-185-4

OPERATION WITH THE BETATRON TUNE OF (21.35, 21.43)

We have explored the possibility of operation with the other betatron tunes. So far the operation tune was (22.40, 20.75), where we observed a serious linear coupling sum resonance of $\nu_x + \nu_y = 43$ within the space charge tune spread. We have searched the area of 21.0 ~ 21.5 for both horizontal and vertical tunes, where there is no linear coupling sum resonance as shown in Fig. 11. Detail search was done and the tune setting of (21.35, 21.43) was the best for the beam survival. The quadrupole field of the FX septum magnets and the third order resonances of $\nu_x + 2\nu_y = 64$ and $3\nu_x = 64$ were corrected. The linear coupling difference resonance of $\nu_x - \nu_y = 0$ was corrected with the SQ's. Further the currents of two octupole magnets were optimized to minimize the beam loss. The rf voltage pattern was same as the operation of (22.40, 20.75) described in the preceding section. The parameters of the bunch by bunch and intra-bunch feedback systems were adjusted for the new tune. The chromaticity was set to be −7. We have tested shots of the beam power of 440 kW. The beam loss during injection was 443 W and loss in the beginning of acceleration was 795 W. The sum of the losses was within the MR collimator limit. But it was higher than the loss in the normal operation and should be reduced.

The compensation kicker was not ready to use, because the phase advance between the injection kicker and the compensation kicker was not appropriate for the new tune setting. Changing the polarity of the compensation kicker is a solution and the beam loss reduction is expected. It will be tested in the next available study time.

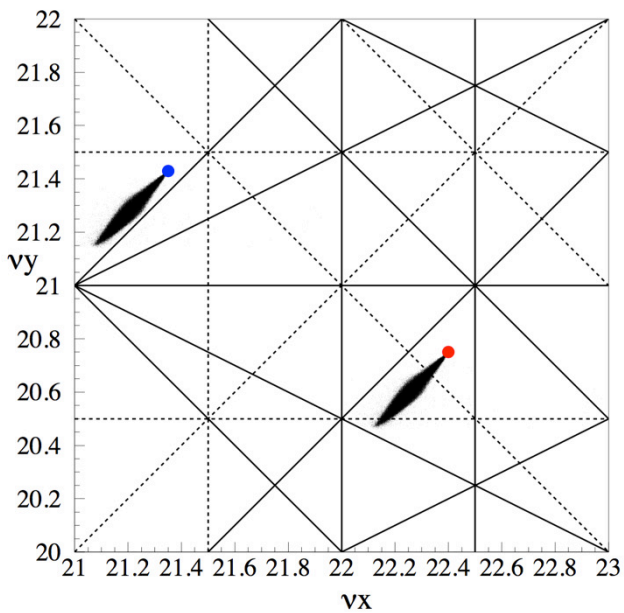

Figure 11: Structure resonances of up to 3rd order (solid lines) and non-structure resonances of half integer and linear coupling resonances (dashed lines). Space charge tune spread shown for the tune of (22.40, 20.75) and (21.35, 21.43) for the beam power of 380 kW.

UPGRADE PLAN FOR THE BEAM POWER OF 750 kW AND MORE

We plan to make the cycle time faster from 2.48 s to 1.3 s to achieve the beam power of 750 kW. The power supplies of main magnets are being upgraded by JFY 2018 [13]. The construction of three new buildings is planned for the power supplies. The rf cavities are also being upgraded for the faster cycling [14]. Additional collimators are being considered to upgrade for the total power capability of 3 kW [4]. The kicker magnets for injection and extraction are being improved and the septum magnets for injection [15] and extraction [16] are upgraded for the faster cycling.

SUMMARY

The beam power of 415 kW has been recently achieved from J-PARC MR with 2.15×10^{14} ppp and the cycle time of 2.48 s for the neutrino oscillation experiment. The beam loss was observed to be 600 W mostly localized at the collimator section. Recent improvements include the 2nd harmonic rf operation to reduce the space charge effect with a larger bunching factor and corrections of resonances near the operation setting of the betatron tune. We plan to achieve the target beam power of 750 kW in JFY 2018 by making the cycle time faster to 1.3 s with new power supplies of main magnets, rf upgrade and improvement of injection and extraction devices. The possibility of the beam power beyond 750 kW is being explored with new settings of the betatron tune.

REFERENCES

[1] Y. Yamazaki et al, "Accelerator Technical Design Report for J-PARC", http://hadron.kek.jp/~accelerator/TDA/tdr2003/index2.html.

[2] K. Abe et al (T2K collaboration), "Observation of Electron Neutrino Appearance in a Muon Neutrino Beam", *Phys. Rev. Lett.*, 112, 061802, Apr. 2014.

[3] T. Toyama et al, "Beam Diagnostics at the First Beam Commissioning of the J-PARC MR", in *Proc. PAC09*, Vancouver, BC, Canada, Nov. 2009, paper WE4GRC01, pp. 1964-1966.

[4] M. Shirakata et al, "New Arrangement of Collimators of J-PARC Main Ring", in *this conference*, paper THAM4Y01.

[5] H. Hotchi et al, "1-MW Beam Operation Scenario of the J-PARC 3-GeV Rapid Cycling Synchrotron", *JPS (The Physical Society of Japan) Conf. Proc.*, vol. 8, 012013, Sep. 2015.

[6] Y. Hashimoto et al, "Two-Dimensional and Wide Dynamic Range Profile Monitor Using OTR / Fluorescence Screens for Diagnosing Beam Halo of Intense Proton Beams", in *Proc. HB2014*, East Lansing, MI, USA, Nov. 2014, paper TUO2AB04, pp. 187-191.

[7] T. Sugimoto et al, "Upgrade of the Injection Kicker System for J-PARC Main Ring", in *Proc. IPAC2014*, Dresden, Germany, Jun. 2014, paper MOPME069, pp. 526-528.

[8] T. Sugimoto et al, "Performance of the Compensation Kicker Magnet for J-PARC Main Ring", in *Proc. IPAC2016*, Busan, Korea, May 2016, paper THPMW021, pp. 3588-3590.

ISBN 978-3-95450-185-4

[9] Y. Kurimoto et al, "The Bunch by Bunch Feedback System in the J-PARC Main Ring", in *Proc. DIPAC2011*, Hamburg, Germany, May 2011, paper TUPD74, pp. 482-484.

[10] K. Nakamura et al, "Intra-bunch Feedback System for the J-PARC Main Ring", in *Proc. IPAC2014*, Dresden, Germany, Nov. 2014, paper THOAA03, pp. 2786-2788.

[11] K. Ohmi, et al., "Study of Halo Formation in J-PARC MR", in *Proc. PAC07*, Albuquerque, NM, USA, Jun. 2007, paper THPAN040, pp. 3318-3320.

[12] J. Takano et al, "Linear Coupling Resonance Correction of the J-PARC Main Ring", *JPS Conf. Proc.*, vol. 8, 012022, Sep. 2015.

[13] Y. Morita et al, "Development of the J-PARC Main Magnets Power Supplies for High Repetition Operation", *JPS Conf. Proc.*, vol. 8, 012006, Sep. 2015.

[14] M. Yoshii et al, "Status of the J-PARC Ring Rf Systems", in *Proc. IPAC2014*, Dresden, Germany, Jun. 2014, paper THPME062, pp. 3376-3378.

[15] T. Shibata et al, "The Development of a New High Field Injection Septum Magnet System for Main Ring of J-PARC", in *Proc. IPAC2016*, Busan, Korea, May 2016, paper TUPMR039, pp. 1337-1339.

[16] T. Shibata et al, "The Development of a New Low Field Septum Magnet System for Fast Extraction of Main Ring of J-PARC", in *Proc. IPAC2016*, Busan, Korea, May 2016, paper TUPMR040, pp. 1340-1342.

ISBN 978-3-95450-185-4

ACCELERATOR PHYSICS CHALLENGES IN FRIB DRIVER LINAC*

M. Ikegami, K. Fukushima, Z. He, S. Lidia, Z. Liu, S. M. Lund, F. Marti, T. Maruta†, D. Maxwell, G. Shen, J. Wei, Y. Yamazaki, T. Yoshimoto, Q. Zhao
Facility for Rare Isotope Beams, Michigan State University, MI 48824, USA

Abstract

FRIB (Facility for Rare Isotope Beams) is a heavy ion linac facility to accelerate all stable ions to the energy of 200 MeV/u with the beam power of 400 kW, which is under construction at Michigan State University in USA. FRIB driver linac is a beam power frontier accelerator aiming to realize two orders of magnitude higher beam power than existing facilities. It consists of more than 300 low-beta superconducting cavities with unique folded layout to fit into the existing campus with innovative features including multi charge state acceleration. In this talk, we overview accelerator physics challenges in FRIB driver linac with highlight on recent progresses and activities preparing for the coming beam commissioning.

INTRODUCTION

The Facility for Rare Isotope Beams (FRIB) is a high-power heavy ion accelerator facility now under construction at Michigan State University under a cooperative agreement with the US DOE [1]. Its driver linac operates in CW (Continuous Wave) mode and accelerates all stable ions to kinetic energies above 200 MeV/u with the beam power on target up to 400 kW. This novel facility is designed to accelerate and control multiple ion species simultaneously to enhance beam power. The linac has a folded layout as shown in Fig. 1, which consists of a front-end, three Linac Segments (LSs) connected with two Folding Segments (FSs), and a Beam Delivery System (BDS) to deliver the accelerated beam to the production target. The front-end consists of two ECR (Electron Cyclotron Resonance) ion sources, a normal conducting CW RFQ (Radio Frequency Quadrupole), and beam transport lines to separate, collimate, and bunch the multiple ion charge states emerging from the ECR sources. Ion sources are located on the ground level and an extracted beam from one of two ion sources is delivered to the linac tunnel through a vertical beam drop. In the FRIB driver linac, superconducting RF cavities are extensively employed. After acceleration up to 0.5 MeV/u with a normal conducting RFQ, ions are accelerated with superconducting QWRs (Quarter Wave Resonators) and HWRs (Half Wave Resonators) to above 200 MeV/u. There are two types each of QWRs ($\beta = 0.041$ and 0.085) and HWRs ($\beta = 0.29$ and 0.53) with different geometrical beta. The frequency and aperture diameter for QWRs are 80.5 MHz and 36 mm respectively, and those for HWRs are 322 MHz and 40 mm respectively. We have three $\beta = 0.041$ cryomodules housing four cavities and 11 $\beta = 0.085$ cryomodules housing eight cavities in LS1 (Linac Segment 1). We have 12 $\beta = 0.29$ cryomodules housing six cavities and 12 $\beta = 0.53$ cryomodules housing eight cavities in LS2 (Linac Segment 2). There are 6 $\beta = 0.53$ cryomodules followed by a space to add cryomodules for future upgrade in LS3 (Linac Segment 3). The total number of superconducting RF cavities is 332 including those for longitudinal matching in the Folding Segments. Each superconducting RF cavity is driven by an independent solid state amplifier. Transverse focusing in the superconducting linac sections is provided by superconducting solenoids (8 Tesla, 20 mm bore radius). It is unique to have such large scale linac sections with low-β superconducting RF cavities together with multi charge state acceleration at high CW power. This poses accelerator physics challenges specific to the FRIB driver linac.

We reported beam physics challenges in FRIB at the previous series of this worksop [2]. Here, we don't repeat the challenges we identified at the previous workshop while we have been continuously pursuing those areas. As general accelerator challenges for high power linacs were summarized at the previous workshop [3], we try to focus in this paper on challenges specific to FRIB and/or those for

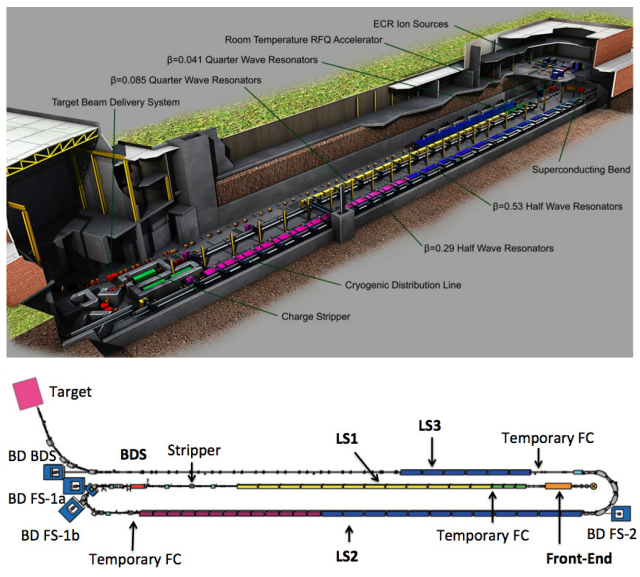

Figure 1: Layout of FRIB driver linac. Top: Cut view of FRIB driver linac building. Bottom: Schematic layout for the FRIB driver linac (top view).

* Work supported by the U.S. Department of Energy Office of Science under Cooperative Agreement DE-SC0000661

† On leave from KEK/J-PARC

ISBN 978-3-95450-185-4

which active studies are on-going in FRIB.

In the next section, we review accelerator physics challenges for FRIB with emphasis on beam dynamics related issues. Before summarizing the paper, we also show present construction status of FRIB and its commissioning schedule briefly.

ACCELERATOR PHYSICS CHALLENGES

As a high power frontier accelerator, mitigation of uncontrolled beam loss is one of its major challenges for FRIB. This is especially true for FRIB as it is more difficult to detect heavy ion beam loss than lighter ions with sufficient sensitivity. In addition, as a user facility to support nuclear physics experiments, high beam availability of larger than 90 % is required with yearly beam on target of 5,500 hours. One of major challenges regarding the beam availability is to achieve swift enough switch over of ion species. It is typically requested to change ion species once in a week or two, and regarding retuning should be completed in one day or shorter.

Development of Online Model

To achieve the availability goal and to mitigate the uncontrolled beam loss during tuning, it is indispensable to develop efficient tuning schemes based on online model. To this end, it is required to develop a robust online model and flexible environment to develop application software for tuning. To support online tuning, we need to have a simple and quick model with minimum accuracy to serve for the tuning. As FRIB driver linac involves specific features which are not covered by usual fast models, we decided to develop a dedicated envelope model in house. Those features include multi-charge state acceleration, non-axial symmetric field for quarter wave resonators, and charge stripping.

In addition, we decided to develop an online model based on IMPACT [4] as a back up to serve for advanced tuning which may not be covered by a simple model. IMPACT is a three-dimensional particle-in-cell code originally developed to study space charge effects. Space charge effect is negligible in most part of FRIB linac thanks to its low peak intensity. None the less, IMPACT has been adopted as the reference code to develop FRIB lattice after extending it to cover multi charge state acceleration to take advantage of its robust framework. As advanced tuning, we anticipate halo mitigation (or matching beyond rms matching) and second order acrhomat tuning at arc sections. We also utilize IMPACT as a modeling engine for virtual accelerator, which enable us to benchmark tuning algorithms. Although execution speed is a main concern for IMPACT as an online model, we have confirmed that it can be run with around 1 second with a standard server for the first linac segment by turning off the space charge calculation and optimizing simulation conditions.

As for a simple model, we have developed a envelope model named FLAME [5]. This model was originally prototyped with Java and extensively benchmarked against

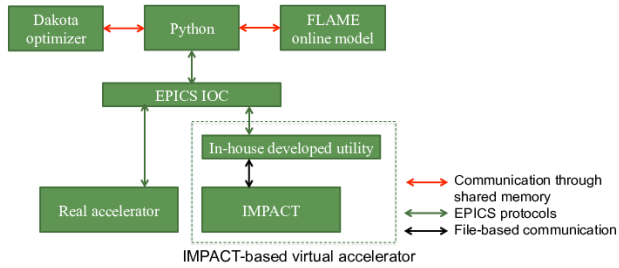

Figure 2: Schematic for commissioning application development environment.

IMPACT. After verifying its physics model, we converted it to a C++ code to further optimize the performance and to improve its interfaces. We expect that this model serves sufficiently for most of basic tunings such as orbit correction, rms matching, and phase/amplitude tuning.

We have developed an environment to develop commissioning applications with Python as a scripting language, FLAME as an online model, and Dakota as optimization tools as shown in Fig. 2. Both FLAME and Dakota have Python interfaces. We use IMPACT-based virtual accelerator to verify tuning algorithms. We have prototyped basic tuning applications with this environment. So far, Java prototype for FLAME is used for the prototyping and we are converting it to be FLAME-based.

Extended Error Studies and Model Enhancement

To achieve efficient tuning, we need deep understanding of the machine and a good model to represent it. To deepen our understanding of the accelerator, we are continuing error studies or case studies assuming realistic conditions, which will be our knowledge-base on possible responses of the machine to realistic errors [6]. Figure 3 shows an example of those extended error studies where longitudinal acceptance for LS1 assuming RF amplitudes ± 20 % off the nominal randomly. This study gives us a guidance to optimize operation parameters for RF cavities.

Accuracy of modeling for a linac is often determined by the modeling capability of its front-end. Space-charge effects are negligible for most part of FRIB due to relatively small peak current. However, an obvious exception is low energy beam transport immediately after ECR ion sources. In particular, existence of contaminant ion species and charge states make it complicated to model the dynamics in the charge selection process where unintended ion species and charge states are separated with a dipole magnet and eliminated with a slit. We are continuing efforts to improve the modeling of front-end using Warp code [7] with three dimensional field map [8].

Contaminant Ion Species Loss Study

We have identified a few mechanisms which could result in uncontrolled beam loss in FRIB linac, one of which is caused by contaminant ion species. In generating a heavy ion beam with an ECR ion source, other ion species but

ISBN 978-3-95450-185-4

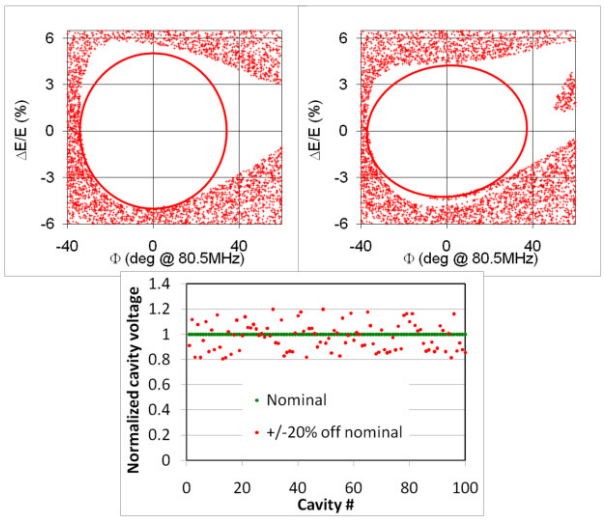

Figure 3: An example of extended error study with IMPACT. Longitudinal acceptance for LS1 with nominal RF amplitudes (top left) and that with RF amplitude ±20 % randomly off the nominal (top right). Bottom figure shows the RF amplitude distribution assumed in the case in top right.

with similar Q/A (or the charge to mass ratio) can contaminate the beam. In some cases contaminants come from supporting gasses, and in other cases from gasses introduced in previous experiments. Contaminants with similar Q/A can be accelerated with intended ions in the first linac segment. However, they could have very different Q/A after charge stripper as lighter ions are more easily stripped. Then, contaminant with very different Q/A has a mismatch to the optics, which can result in a beam loss after charge stripper. Those particles with different Q/A from intended are supposed to be eliminated at charge selector situated after the first dipole magnet in the arc section. However, Q/A of a contaminant could be too different to be delivered to the charge selector resulting uncontrolled beam losses between charge stripper and charge selector (See Fig. 4). One of examples for the contaminant is $^{14}N^{2+}$ for $^{238}U^{34+}$. They have exactly the same Q/A of 0.146 and hence they are both accelerated by LS1 being captured in an RF bucket. After the stripper, however, $^{14}N^{2+}$ may become $^{14}N^{7+}$ (Q/A=0.5) while typical charge state for uranium will be $^{238}U^{78+}$ (Q/A=0.328). Then, $^{14}N^{7+}$ will not reach the charge selector with optics tuned for $^{238}U^{78+}$ resulting a beam loss.

We are conducting a simulation study to find an optimum design of collimators to localize the losses from contaminants [9]. As we need to deliver various ion species for the experiment, the collimator system should accommodate a wide range of Q/A ratio between contaminant and intended ions. Figure 5 shows an example for the simulation where Q/A of contaminant is assumed to be 20 % larger than the intended beam.

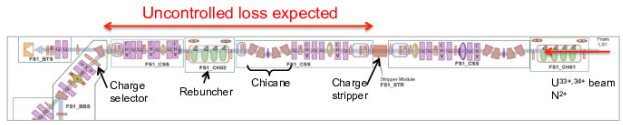

Figure 4: Schematic for lattice around charge stripper. Area with beam loss from contaminant anticipate is also shown.

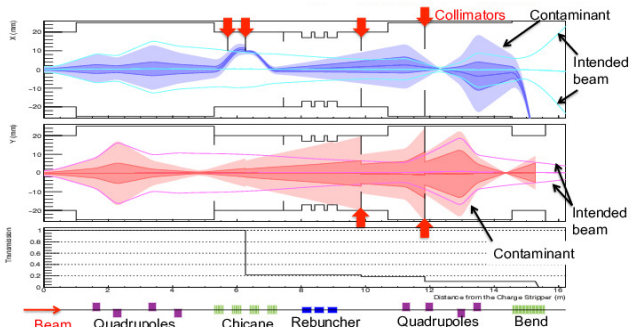

Figure 5: An example of IMPACT simulation for collimation of contaminant ion species. Assumed Q/A for contaminant is 20 % larger than the intended beam. Beam envelopes are simulated from charge stripper to charge selector. Top: horizontal envelope, middle: vertical envelope, and bottom: transmission efficiency of contaminant. Light blue and magenta solid lines show the envelopes of intended beam. Shaded areas in blue and red show the envelopes of contaminant. Locations of collimators under consideration are also shown with red arrows.

Residual Gas Stripping Loss Study

Another beam loss mechanism is residual gas stripping. Accelerated ions can lose electrons by scattering with residual gas molecules, and generated ions with irregular charge state can cause beam losses. The rate of residual gas stripping is determined by the vacuum pressure level and gas component, and single electron stripping is dominant where an ion lose an electron.

As the vacuum level is generally higher in room temperature sections than in superconducting sections, this loss mechanism is a concern in room temperature sections primarily. Residual gas stripping in dispersion section is a particular concern. If the single stripping occurs in non-dispersive segments, there is a large likelihood that the scattered particle stays in the acceptance. Meanwhile, if the stripping occurs in a dispersive area, generated ions with irregular charge state can have significantly different beam trajectory and result in a beam loss. It will be especially the case for vicinity of charge selector in the first 180 degree arc section, where we anticipate that beam absorber for charge selection can be a notable gas source. It led us to focus on residual gas stripping loss study for the first folding segment primarily.

We are conducting a simulation study to find an optimum design of collimators to localize the losses from residual

ISBN 978-3-95450-185-4

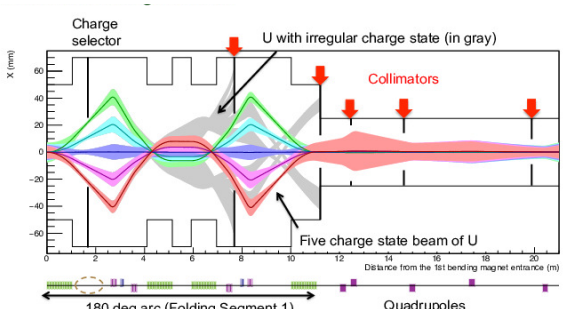

Figure 6: An example of IMPACT simulation for residual gas stripping. Shaded areas in green, light blue, violet, magenta, and red show the envelopes of five charge states of uranium which will be delivered to the second linac segment. Shaded areas in gray show the envelope of ions with irregular charges state generated at charge selector. Locations of collimators under consideration are also shown with red arrows.

gas stripping assuming the primary source of gas stripping is around charge selector [9]. Figure 6 shows an example for the simulation where ions with irregular charge state are generated at charge selector. The study will be extended to deal with residual gas stripping in other locations.

Other Technical Challenges

Although we emphasizes challenges in FRIB regarding beam dynamics in this section, we also have other challenges if we extend the scope to hardwares. We don't elaborate on this in this paper as it was summarized in a review paper in the previous workshop [3]. Representative examples of technical challenges for FRIB linac include charge stripper and MPS (Machine Protection System). As for charge stripper, we plan to adopt liquid lithium stripper to sustain the energy deposition [10]. In MPS, a particular challenge is to detect loss of heavy ions in low energy section with sufficient sensitivity where conventional ionization chamber is not sensitive enough. We are planning to adopt multiple detection methods with different sensitivity and response time to overcome this difficulty [11].

CONSTRUCTION STATUS AND SCHEDULE

As of July 2016, construction of FRIB building is progressing ahead of schedule especially for its front-end area. It allowed us to start to install technical equipment for front-end and transfer lines. We plan to start beam commissioning of ion source in September 2016 and beam commissioning of RFQ and MEBT (Medium Energy Beam Transport) in February 2017. It will be followed by start of beam commissioning of the first three cryomodules in LS1 in early 2018. The commissioning effort will be continued in a staged way until completion of the project in fiscal year 2021.

SUMMARY

FRIB is a high-power heavy ion accelerator facility presently under construction at Michigan State University to support nuclear physics experiments. FRIB consists of a driver linac and experimental facility, and its linac accelerates all stable ions including uranium to kinetic energies of more than 200 MeV/u and continuous wave beam power up to 400 kW. This beam power is more than two orders of magnitude higher than the existing heavy ion linac facilities, resulting in various accelerator physics challenges. In this paper, challenges for FRIB have been discussed with emphasis on beam dynamics issues avoiding the overlap with previous papers in this workshop series [2, 3]. We have reported recent activities on online model development, extended error simulations, and collimator design study to mitigate beam losses from contaminant ion species and residual gas stripping. The former two topics are preparations for beam commissioning and operation. The latter two are to finalize the design of collimators to localize the beam losses from anticipated beam loss mechanisms, which may eventually limit the reachable beam power.

We have also reported construction status of FRIB and updated schedule for its beam commissioning. The construction is progressing on track and we plan to start beam commissioning of one of two ion sources in September 2016.

REFERENCES

[1] J. Wei, et al., "FRIB accelerator status and challenges", LINAC'12, Tel Aviv, August 2012, p. 417.

[2] M. Ikegami, et al., "Beam dynamics studies for the Facility for Rare Isotope Beams driver linac", HB2014, East Lansing, November 2014, p. 231.

[3] J. Wei, et al., "Accelerator challenges of high intensity linacs and the facility for rare isotope beams", HB2014, East Lansing, November 2014, p. 12.

[4] J. Qiang, R. D. Ryne, S. Hbib, V. Decyk, J. Comput. Phys. 163 (2000) 434.

[5] Z. He, et al., "Development status of FRIB-Linear-Accelerator-Modeling-Engine based on-line beam commissioning application", to be submitted to LINAC2016.

[6] Q. Zhao, et al., "Beam simulation studies for FRIB", in these proceedings, TUAM5Y01.

[7] For info on the Warp code see: http://warp.lbl.gov.

[8] S. M. Lund and C. Y. J. Wong, "Efficient particle in cell simulations of beam collimation in the FRIB front-end", in these proceedings, WEPM3Y01.

[9] T. Maruta, et al., "Simulation study on the beam loss mitigation in the 1st arc section of FRIB linac", to be submitted to LINAC2016.

[10] F. Marti, et al., "Heavy ion charge stripping at FRIB", in these proceedings, TUPM2X01.

[11] Z. Liu, et al., "Collimation design and beam loss detection at FRIB", in these proceedings, WEPM8X01.

ISBN 978-3-95450-185-4

BEAM OPTICS SIMULATION STUDY ON THE PRE-STRIPPER LINAC FOR RARE ISOTOPE SCIENCE PROJECT*

J. W. Kim†, J. H. Jang, H. C. Jin, Institute for Basic Science, Daejeon, Korea
P. N. Ostroumov, B. Mustapha, J. A. Conway, Argonne National Laboratory, Argonne IL, USA

Abstract

The rare isotope science project (RISP) under development in Korea aims to provide various heavy-ion beams for nuclear and applied science users. A pre-stripper linac is the first superconducting section to be constructed for the acceleration of both stable and radioisotope beams to the energy of 18.5 Mev/u with a DC equivalent voltage of 160 MV. The current baseline design consists of an ECR ion source, an RFQ, cryomodules with QWR and HWR cavities and quadruple focusing magnets in the warm sections between cryomodules. Recently we have developed an alternative design in collaboration with Argonne's Linac Development Group to layout the linac based on state-of-the-art ANL's QWR operating at 81.25 MHz and multi-cavity cryomodules of the type used for the ATLAS upgrade and Fermilab PIP-II projects. End-to-end beam dynamics calculations have been performed to ensure an optimized design with no beam losses. The numbers of required cavities and cryomodules are significantly reduced in the alternative design. The results of beam optics simulations and error sensitivity studies are discussed.

INTRODUCTION

A next-generation rare isotope science facility using the in-flight fragment (IF) separation technique requires a high-current heavy-ion accelerator capable of delivering ^{238}U beam with a few hundred kW power to a thin production target [1]. First, high currents of highly charged ions are needed to efficiently produce such high-power heavy ion beams. An ECR ion source operating at 28 GHz [2] has been developed, but for the heaviest ions, the beam current in a single charge state is still lower than required for a next generation IF facility.

To fully utilize the available accelerating voltage of a heavy-ion linac, charge strippers are employed in the process of multi-step acceleration. To accelerate a uranium beam to 200 MeV/u, charge stripping at 18 MeV/u was determined to be optimal. A significant merit of a superconducting linac is that its longitudinal acceptance is large enough to simultaneously accelerate multiple charge states of uranium produced at the charge stripper. Therefore, a large fraction of the beam is accelerated after the stripper and beam losses in the charge state selection section are significantly reduced resulting in lower radiation levels in that region.

*Work supported by National Research Foundation Grant No. 20110018946 and the Rare Isotope Science Project.
†jwkim@ibs.re.kr

The layout of the pre-stripper linac of the Rare Isotope Science Project (RISP) ongoing in Korea [3] is shown in Fig 1. The linac is designed to accelerate either radioisotope beams from the ISOL target or stable beams from the ECR. In fact, a plan is to accelerate both radioisotope and stable beams simultaneously when their charge-to-mass ratios are within 2%. For instance, $^{132}Sn^{18+}$ can be accelerated together with $^{238}U^{33+}$. The isotope beam from ISOL is charge-bred before being injected into the pre-stripper linac. The charge breeding takes tens of ms in EBIS, which is under development at RISP [4], and stable ions can be accelerated during charge-breeding. Since the time duration for injection and extraction of isotope beams is much shorter than 1 ms and the breeding takes tens of ms, the fraction of stable beam can be over 90%. The simultaneous acceleration scheme of stable and radioisotope beams was devised for the proposed multi-user upgrade of the ATLAS linac at Argonne [5].

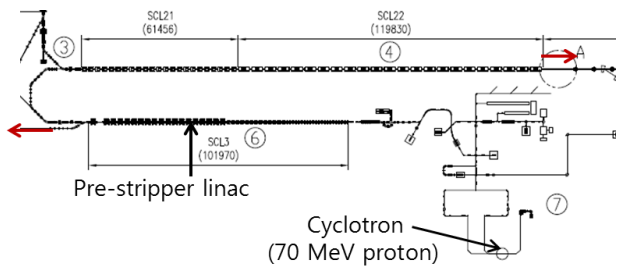

Figure 1: Layout of the pre-stripper linac of the RISP baseline design.

The injector includes an RFQ and the beam energy to the first cavity is 500 keV/u. The pulsing of stable ions according to the time structure of the charge-bred radioisotope beam is formed by an electric chopper. At the end of pre-stripper linac the two beams are switched by a kicker magnet either to low energy experimental area or to the achromatic 180° bending section after charge stripping.

CURRENT BEAM OPTICS DESIGN

The current design of the pre-stripper linac is based on the use of two kinds of superconducting cavities: QWR (β_{opt}=0.047) and HWR (β_{opt}=0.12) operating at 81.25 and 162.5 MHz, respectively [6]. Transverse focusing components were decided to be quadrupole doublets based on the thought that superconducting solenoids located inside cryomodule can affect the cavity

ISBN 978-3-95450-185-4

performance with leakage magnetic fields and also alignment of solenoids can be less accurate.

The numbers of sc-cavity and cryomodule of the current baseline design are listed in Table 1 in comparison with those of a new design proposal based on Argonne's cavities and cryomodules. In the baseline design, cryomodules of the first 22 units contain a single QWR cavity each, followed by cryomodules with two and four HWRs each. Both kinds of cavities are assumed to operate at a peak surface electric field (E_p) of 35 MV/m, while ANL's design assumes E_p to be 40 MV/m.

Table 1: Linac Parameters of the RISP Baseline Design in Comparison to the ANL Design Proposal

Parameters	RISP baseline	ANL proposal
Number of QWR (or QWR1)	22	15
Number of HWR (or QWR2)	102	49
Number of cryomodule	54	9
Total length	100 m	53.3 m

The main beam for the linac lattice design is ^{238}U, and TRACK [7] and TRACEWIN [8] have been used for the beam dynamics simulations. The beam phase spaces after RFQ acceleration were the input to the pre-stripper sc-linac. The RFQ is designed to have an adiabatic bunching section and a beam transmission higher than 98 %, which makes the longitudinal beam phase space at the end of the RFQ larger than for the design using an external multi-harmonic buncher (MHB).

The longitudinal acceptance of the linac and phase space of the U beam after the RFQ are shown in Fig. 2. They are carefully optimized for a proper matching and large margin, which requires slow ramping of acceleration voltages in the first few cavities and also for the cavities following the rf frequency jump from 81.25 MHz to 162.5 MHz.

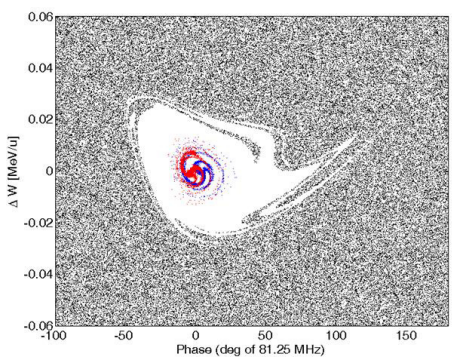

Figure 2: Longitudinal phase acceptance of the pre-stripper linac together with the phase space of a U beam.

A NEW DESIGN PROPOSAL

Considering the use of a large number of cavities and cryomodules in the current design and the risk in rf frequency jump in the middle of the linac, a new design using long cryomodules with superconducting solenoids based on realistic performance of ANL low-beta cavities has been proposed. This design study was performed in early 2016 utilizing two kinds of QWR cavities as mentioned in Table 1. Models of the QWR's with their electric field distributions are shown in Fig. 3 and their main parameters are listed in Table 2.

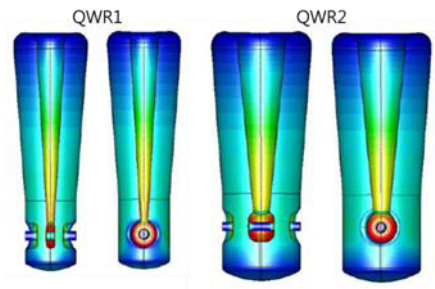

Figure 3: Electric field models of the two kinds of QWR's.

Table 2: Design Parameters of QWR1 and QWR2

Parameter	QWR1	QWR2
f (MHz)	81.25	81.25
β_{opt}	0.05	0.109
L_{eff} (cm)	18.5	40.2
E_{peak}/E_{acc}	5.6	5.6
B_{peak}/E_{acc} (mT/MeV/m)	7.7	7.3
R/Q (Ω)	493	552
G (Ω)	23	32
Aperture (mm)	40	40

The QWR cavities were designed to self-compensate the RF steering effects, therefore no active steering is needed in the linac when machine errors are not applied. The steering correction versus particle velocity for different tilt angles of the cavity's drift tube face was calculated. Figure 4 shows the beam steering in QWR1 for different steering correction angles including the uncorrected case (0°). It is clear that the 1° drift-tube face tilt is the closest to the zero line for the beam vertical angle (y'), which measures the steering effect. For QWR2 the beam steering effects can be similarly corrected with an angle of about 4°.

For the evaluation of the new linac lattice design, the goals of beam dynamics simulations were as follows: (1) to provide matching between the RFQ and the SC linac, (2) to define the value of the accelerating voltage and synchronous phase for each SC cavity and the solenoid field and (3) to demonstrate zero-loss beam acceleration in the pre-stripper linac.

ISBN 978-3-95450-185-4

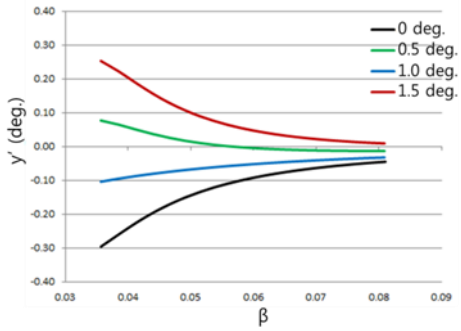

Figure 4: Steering correction for the QWR1. Vertical axis is the beam angle in the vertical plane which measures the steering due to the vertical asymmetry of the QWR geometry.

The simulation starts from a MHB with $U^{33+,34+}$. To define the parameters of the accelerating and focusing lattice, a relatively low number of particles is used, typically 10^4 for each charge state of uranium. The space charge effects for U beam are negligible after the RFQ, therefore we follow the dynamics of each charge state in the same accelerating bucket along the MEBT and pre-stripper linac. In realty each charge state occupies a separate bucket at the RFQ frequency.

The criteria for selection of the linac parameters is the proper matching in the transverse and longitudinal phase space for each focusing period along the linac. In particular, good matching must be provided in the transitions between cryomodules. Usually, a well-matched beam produces the lowest rms emittance growth. The available voltage from the SC resonators in the first two cryomodules exceeds the limit dictated by a smooth and adiabatic acceleration and can introduce significant non-linear motion in the longitudinal phase space if fully used. Therefore, we have applied ramping of both the accelerating voltage and synchronous phase in the first two cryomodules. Figure 5 shows a TRACK screenshot for the simulation of a U beam from the MHB to the end of the pre-stripper linac. The simulation starts with 5×10^5 particles in each charge state of 33+ and 34+, where 98.83 % particles are accepted by the RFQ and accelerated in the linac. It is important to note that there are no U beam losses along the SC linac.

To evaluate tolerances to misalignment and machine errors, beam simulations were performed for the linac including all sources of machine error. Three sets of errors with increasing amplitudes were simulated for $U^{33+,34+}$. Table 3 lists the error types and their values for every set of errors. It is important to note that for misalignment, the error given is the maximum absolute value used to generate a uniform error distribution, while for rf error, the sigma value is given for a Gaussian distribution truncated at 3σ. The Gaussian rf errors are to simulate jitter or dynamic errors that cannot be corrected for. Static rf errors are not included in these simulations because they are constant shifts in the cavity phase and amplitude that could, in principle, be measured and corrected.

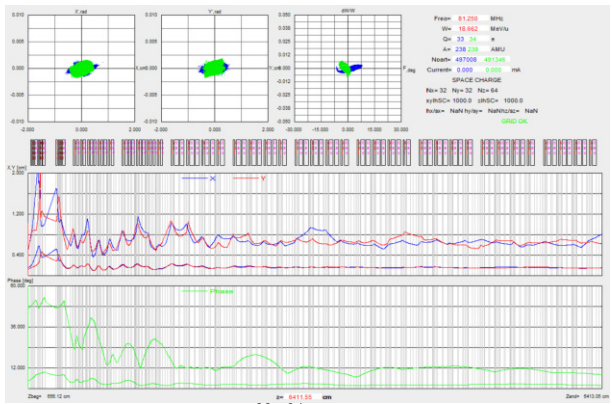

Figure 5: Evolution of $U^{33+,34+}$ beam envelopes (rms and full) along the MEBT and SC pre-stripper linac.

The first set of error in Table 3 represents the nominal error values and the rf errors were doubled in the second set, while the misalignment errors were doubled in the third one. For every error set, 100 randomly generated linac configurations (also known as seeds) were simulated, each with a total of 10^5 macro-particles starting from the LEBT ($5\text{x}10^5$ for each charge state). Both cases, before and after applying corrective steering, were simulated to study the effect of corrections and determine the required number, location and strengths of the steering coils.

Misalignment errors are uniformly generated within the given maximum values. RF errors are generated within a Gaussian truncated at the 3σ value given in table 3.

Table 3: Error Types and Amplitudes for Three Sets of Errors Used in the Simulations

Error set	Cavity & Solenoid misalignment (mm)	Cavity phase error (deg.)	Cavity amplitude error (%)
1	0.25	0.5	0.5
2	0.25	1.0	1.0
3	0.5	0.5	0.5

The transverse correction scheme used in the error simulations with corrective steering is shown in Fig. 6. In this scheme, every cryomodule is treated as a separate correction section. The general idea is to use the steering coils on the solenoids placed in the middle of the cryomodule and the beam position monitors attached to the solenoid placed at the cryomodule end and between cryomodules. For every correction section, at least two monitors are required in order to correct both the position and angle of the beam. Only two correctors and two monitors are used in this scheme. In the case where the combined strength of the two central correctors is not sufficient, a third corrector placed at the cryomodule entrance can be used. In these simulations, the corrector strength was limited to 5 mrad angular kick. The monitor precision and misalignment were set to 100 microns each. With increasing error amplitudes, the correction scheme

ISBN 978-3-95450-185-4

may fail at one point. In this case, we can include more correctors and monitors in every correction section and or increase the corrector strength.

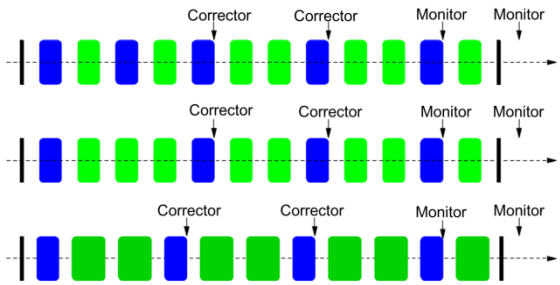

Figure 6: Correction scheme used in error simulations with corrective steering. The different strings correspond to the three different cryomodules of the linac, where every cryomodule is treated as a separate correction section.

The results of the error simulation with and without corrective steering are shown in Fig. 7 for the second error set. On the left, the figures show the beam centroids before (in red) and after correction (in blue). On the right, they show the distribution of angular kicks and the corresponding magnetic field strength required from the corrective steering coils. In comparison with the results of the other two error sets, we could see clearly that with increasing misalignment errors, the beam centroid spread after correction is wider and the required corrective field is stronger. It is important to note that the maximum required magnetic field integral for the corrective steering coils is 8000 G*cm, which would require a maximum magnetic field of 400 G for an effective coil length of 20 cm.

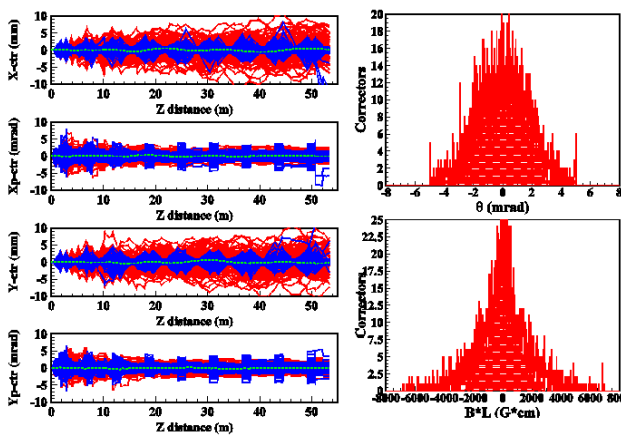

Figure 7: Error and correction simulation results for the second error set. On the left are beam centroids before and after correction. On the right are the corrector strength in mrad and the corresponding magnetic field integral in G*cm required.

The fractional beam losses before correction for the first two sets of errors were in the order of 5×10^{-7} and 5% for the third set. After correction, the loss becomes less than 1×10^{-7} for the second set, and almost zero for the other two sets. Based on the results of these error and correction simulations, we can conclude that the proposed design for the RISP pre-stripper linac is robust and offer a wide range of tolerance to errors and flexibility for beam tuning without any beam loss.

CRYOGENICS ASPECT

The operation temperature of the two kinds of QWR can be either 4.5 K or 2 K. It can be chosen considering the cryogenic budget depending on the operation temperature. In addition to the cryomodule thermal loads, heat loads on the cryogenic distribution system is included. The cryogenic distribution system for 2.0 K operation estimates is based upon supplying each cryomodule with 5 K helium gas where internal heat exchangers and J-T valves convert the 5 K supply to 2 K liquid/gas.

The result of cryogenic load estimation is summarized in Table 4. It is worthwhile to point out that the total required operating power at 2.0 K is double that for 4.4 K operation. This is because the static heat leak is large relative to the dynamic loads. Even though the dynamic thermal load decreases by almost a factor of 5 from 781 W at 4.4 K to 198 W at 2.0 K, the static loads do not follow the same trend.

The new design assumes to operate the two kinds of QWR at 4.5 K. The capacity of cryogenic plant considered is 2.5 kW at 4.4 K while it is 4.2 kW for the pre-stripper linac of the current baseline design.

Table 4: Cryogenic Heat Loads for 2.0 K and 4.4 K Operation for the ANL Design Study

T_{op}	Cryomodules	Distribution	Total at 4.4 K
2.0 K	435 W	355 W	2.64 kW
4.4 K	985 W	355 W	1.34 kW

SUMMARY

A new design of pre-stripper linac has been studied in comparison with the present baseline design of RISP. The new design uses much less number of cavities and cryomodules by adopting state-of the art cavities in operation at ANL [9, 10]. The lattice design includes 5.7 m long cryomodules and superconducting solenoid focusing magnets. Beam optics study including error analysis shows similar tolerances with that of present baseline design. A significant saving in cryogenic system and long-term operation costs is also expected.

REFERENCES

[1] J. A. Nolen, Nucl. Phys. A 787, 84 (2007).
[2] G. Machicoane et al., "Design Status of ECR ion source and LEBT for FRIB", Proc. of ECRIS 2012, Sydney, Australia (2012), p.172.

ISBN 978-3-95450-185-4

[3] S.C. Jeong, "Progress of the RAON heavy ion accelerator project in Korea", Proc. of IPAC 2016 Conf., Busan, Korea May, 2016, p.4261.
[4] S. Kondrashev, J. Kim, Y. Park, H. Son, Advanced EBIS charge breeder for Rare Isotope Science Project, Proc. of IPAC 2016 Conf., Busan, Korea May, 2016, p.1304.
[5] B. Mustapha et al, "Simultaneous acceleration of radioactive and stable Beams in the ATLAS Linac" Proc. of HB2014, East Lansing, Michigan, 2014, p334.
[6] D. Jeon et al, J. Korean Phys. Soc. 65, 1010 (2014).
[7] P.N. Ostroumov, V. Aseev and B. Mustapha, TRACK, ANL Technical Note, Updated for version 3.7.
[8] D. Uriot and N. Pichoff, "TraceWin", CEA Saclay, June 2014.
[9] P.N. Ostroumov et al., "Completion of efficiency and intensity upgrade of the ATLAS facility", Proc. of LINAC2014, Geneva, Switzerland, 2014, p.449.
[10] M.P. Kelly et al., "Commissioning of the 72 MHz quarter-wave cavity cryomodule at ATLAS", Proc. of LINAC2014, Geneva, Switzerland, 2014, p.440.

ISBN 978-3-95450-185-4

CHALLENGES AND PERFORMANCE OF THE C-ADS INJECTOR SYSTEM*

Y. Chi†, Institute of High Energy Phys, Beijing, China

Abstract

Along with the rapid development of nuclear power plants in China, treatment of the nuclear waste has become a crucial issue. Supported by the "Strategic Priority Research Program" of the Chinese Academy of Sciences (CAS), the Chinese Accelerator-Driven System (C-ADS) project is now on-going. The accelerator of C-ADS is a superconducting (SC) Continues Wave (CW) proton linear accelerator (linac) with 1.5GeV energy and 10mA beam current. In the injector part many challenges to developing technologies including Radio Frequency Quadrupole (RFQ) and low β SC cavities and related hardware's. This paper presents the progress of development of C-ADS injectors and related hardware.

ROADMAP OF C-ADS

In January 2011, a special program of nuclear energy promoted by the CAS - Advanced Fission Energy Program - was launched. This program is a strategic plan with its long-term planning until 2032 (see Figure 1). The R&D of the first phase has been funded by the "Strategic Priority Research Program" of CAS.

(i) Phase I (R&D Facility)

- Accelerator goal: 10 mA × 250 MeV
- Reactor goal: 10 MWth
- Schedule goal: Before the end of the decade
- Short term goals: 5 MeV by 2015; 25 MeV by 2016

(ii) Phase II (Experimental Facility)

- Accelerator goal: 10 mA × 1 GeV
- Reactor goal: 100 MWth
- Schedule goal: Approximately 2032

(iii) Phase III (Demonstration Facility)

- Accelerator goal: 10 mA × 1.5 GeV
- Reactor goal: 1000 MWth

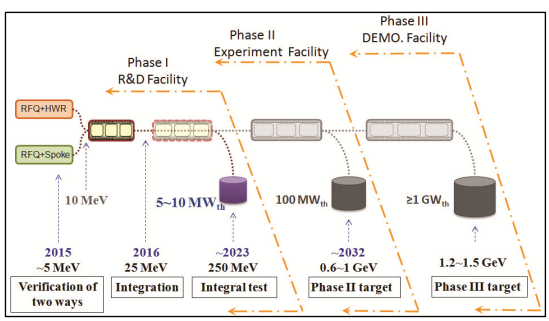

Figure 1: Road map of C-ADS project.

DESIGN OF C-ADS LINAC

Proton Beam Requirements for C-ADS

C-ADS are anticipated as a demonstration facility for transmutation of nuclear waste on an industrial scale, and would require a beam power of at least 10 MW. Besides the high beam power, the reliability of the machine should be very high. The design specification of the proton beam for C-ADS is shown in Table 1.

Table 1: Specifications of the Required Proton Beams of C-ADS

Parameters	Value	Unit
Particle	Proton	
Energy	1.5	GeV
Current	10	mA
Beam power	15	MW
RF frequency	162.5/325/650	MHz
Beam loss	<1	W/m
Duty factor	100%(CW)	
Beam trips per year	<2500*	1s<t<10s
	<2500	10s<t<5m
	<25	t>5m

Design Philosophy of the C-ADS Linac

The C-ADS linac is an extremely challenging accelerator, and there is no existing model in the world yet. The concept may share features in common with several other high power accelerators being developed in the U.S. and Europe, such as Project-X, MYRRHA, IFMIF and EURISOL.

With the approved SC Radio Frequency (RF) technology, especially the positive test results of low β Spoke resonators and Half Wave Resonators (HWR) at FNAL and ANL, and the success of the medium β Elliptical cavities at SNS, it is believed that an all superconducting proton linac except the RFQ is possible and favored due to the difficulty to deal with huge heat deposit in a CW room-temperature acceleration structure. Another advantage of using superconducting cavities is that one can use independently phased resonators to make local compensation when some cavities fail during operation. This is very important to achieve the very strict demands for the reliability of the ADS driving accelerator. So, C-ADS linac uses SC acceleration structures except the RFQs, and works in CW mode.

The RF frequencies for the main linac have been selected as 325 MHz for the Spoke cavity section and 650 MHz for the Elliptical cavity section. However, two different designs employing different RF frequencies are

* Work supported by Chinese Academy of Sciences (CAS)
† chiyl@ihep.ac.cn

ISBN 978-3-95450-185-4

pursued for the two injectors in the technical developing phase. One is 325 MHz for Injector-I at Institute of High Energy Physics (IHEP) and the other is 162.5 MHz for Injector-II at Institute of Modern Physics (IMP).

The most crucial requirement for developing and operating an ADS accelerator is the very high reliability, reflected by the different numbers of beam trips for different durations, as shown in Table 1. To achieve the goal, special design methods in the driver linac have to be adopted. The hardware will be designed and operated with conservative performance margins, and will incorporate fault-tolerant capabilities in the physics design. However, no matter how we improve the hardware's reliability performance, it should be expected to meet some failures of important devices with a much lower frequency. The accelerator design has to deal with these situations. Both global and local compensation methods have been proposed to tackle cavity failures in superconducting linacs, with the latter being considered suitable for meeting the very high reliability in ADS linacs. In C-ADS linac, the local compensation-rematch method has been further developed to deal with the failures of two kinds of major components: SCRF cavities and transverse focusing elements including SC solenoids and room-temperature quadrupoles.

For the very low energy part, it is difficult to apply the local compensation method, thus two parallel injectors will be employed. When one is in the online operation mode, the other is operated as a hot-spare and can be switched to the online mode quickly.

Another key issue in designing the linac is that beam losses should be kept as low as possible along the linac, with a usual acceptance of 1 W/m for all high-power proton accelerators. This is especially difficult for the C-ADS, since it has a beam power about 10 times higher than the most powerful existing linac such as the SNS linac. And, this means a beam loss rate of 7×10-8/m at the higher energy part for C-ADS linac, requiring very delicate error and beam loss studies.

Layout of C-ADS Accelerator

The accelerator layout is shown in Figure 2. It consists of four distinct regions:

- Injector (0-10 MeV): Two alternatives are being developed: one based on an ion source, 325 MHz Radio Frequency Quadrupole (RFQ), and 325 MHz low β single Spoke resonator named Spoke012; and the other on an ion source, 162.5 MHz RFQ, and 162.5 MHz low β HWR named HWR010.
- Low β acceleration (10-147 MeV): Two types of single Spoke resonators operating at 325MHz will be utilized - one at β=0.21 (Spoke021), the other at β=0.40 (Spoke040). A total of 96 cavities are required.
- High β accelerator (147-1500 MeV): Two types of Elliptical cavities operating at 650 MHz will be utilized - one at β=0.63 (Ellip063), the other at β=0.82 (Ellip082). A total of 142 cavities are required.
- MEBT2 and HEBT. The second Medium Energy Beam Transport line (MEBT2) transports and matches the beam from either of the two injectors to the main linac, while the High Energy Beam Transport (HEBT) delivers high energy beam to the neutron target.

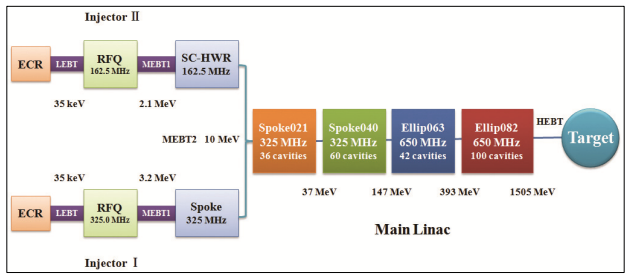

Figure 2: Layout of C-ADS linear accelerator.

R&D OF KEY ACCELERATOR TECHNOLOGIES

RFQ Accelerators

A RFQ accelerator is used to simultaneously bunch, focus and accelerate the very low energy (20-95 keV) beam from the proton source to energy in the range 2-7 MeV. For an ADS accelerator system, the RFQ is typically normal conducting and work in CW (100% duty cycle) mode, and it is one of the most challenging technical aspects of any ADS accelerator system. Although several RFQ accelerators capable of providing CW proton currents in the range 30 to 100 mA have been developed and demonstrated performance levels that meet the requirements for industrial-scale ADS systems, C-ADS paid much attention to the RFQ accelerator from the very beginning.

Two prototype RFQ accelerators have been designed, fabricated and commissioned (see Figure 3). One is a 325 MHz RFQ (named RFQ-I), responsible by IHEP and the other is 162.5 MHz RFQ (named RFQ-II) by IMP. The main parameters of these two RFQs are shown in Table 2.

Table 2: Main Parameters of Prototype RFQs for C-ADS

Parameters	RFQ-I	RFQ-II
RF frequency (MHz)	325.0	162.5
RF power (kW)	300	110
Beam current (mA)	10	10
Injection energy (keV)	35	35
Output energy (MeV)	3.2	2.1
Inter-vane voltage (kV)	55	65
Maximum modulation	2	2.3
Beam transition	98.7%	99.5%
εn.rms.t (πmmmrad)	0.2/0.2	0.3/0.3
εn.rms.l(πMeV-deg)	0.06	0.05
Accelerator length(cm)	467.0	420.8

ISBN 978-3-95450-185-4

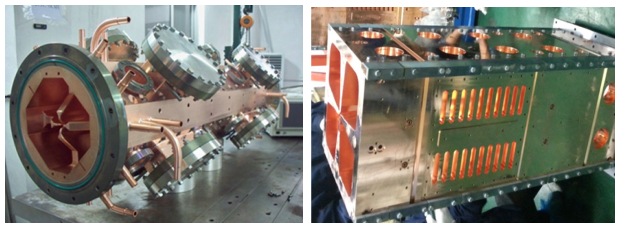

Figure 3: The RFQ-I and RFQ-II (1/4 part).

Superconducting RF Cavities

The SC RF technologies in the context of C-ADS linacs are of the following advantages and therefore selected for C-ADS project:

- High accelerating gradients (~20 MV/m) and therefore lower capital and operating costs,
- Low RF structure power dissipation which leads to efficient transfer of RF power to the beam,
- Large aperture to reduce interception of halo particles,
- Extremely low vacuum to minimize beam-gas interactions thereby reducing beam loss,
- Potential for high reliability with a linac architecture in which one SC cavity is powered by a single RF source and SC cavities are maintained as online spares.

Seven types of SC cavities have been designed and prototyped almost in parallel. They include HWR, Spoke and Elliptical cavities, and may meet the requirement to accelerate the proton beam from low energy (2-3 MeV) to the target 1.5 GeV. Their main parameters and typical vertical test (VT) results are summarized in Table 3.

Totally seventeen Spoke012 cavities, eight Spoke021 cavities, two Spoke040 cavities, two Elliptical082 and 12 HWR010 cavities were developed (see Figure 4 and Figure 5) and vertically tested and exceeded the operation specification, which is noted as the "target" in Figure 6 and Figure 7.

Figure 4: Spoke012, Spoke021, Spoke040 cavities.

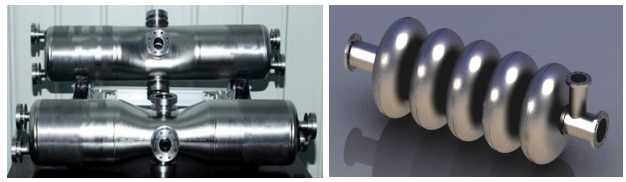

Figure 5: HWR010, Elliptical082 cavities.

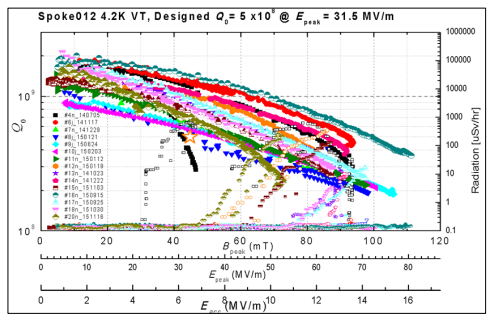

Figure 6: Vertical test results of Spoke012 cavities.

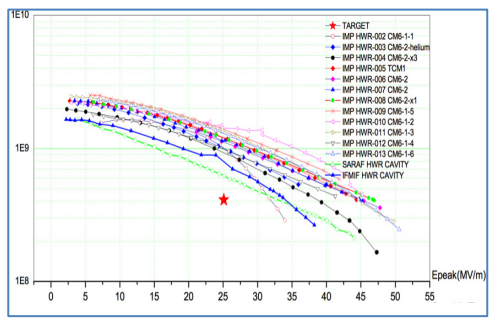

Figure 7: Vertical test results of HWR010 cavities.

Table 3: Design Specifications and Vertical Test Results of SC Cavities for C-ADS

	Spoke012	HWR010	HWR015	Spoke021	Spoke040	Ellip063	Ellip082	Unit
Frequency	325	162.5	162.5	325	325	650	650	MHz
β_0*	0.14	0.10	0.15	0.24	0.46	0.63	0.82	-
Aperture	35	40	40	50	50	100	100	mm
L_{eff}	0.129	0.185	0.277	0.221	0.424	0.757	0.985	mm
E_{acc} Max	6.5	4.5	6.5	7.5	6.8	13.5	16.0	MV
E_{peak}	32.5	25	32	24/31	25/32	29/38	28/36	MV/m
B_{peak}	46	50	40	50/65	50/65	50/65	50/65	mT
Temp	4	4	4	2	2	2	2	K
P_{loss}	<10	<10	<15.5	<16.8	<6.5	<21	<39	W
E_{acc} Max @VT,4K	13	8.5	12.5	11	11.5	N/A	9	MV/m
Q_0 Max @VT, 4K	1.8	3	3	2	2	N/A	1.7	$\times 10^9$

*β_0 is the optimum β for single Spoke cavities, while it is the geometrical β for Elliptical cavities

ISBN 978-3-95450-185-4

In parallel with the SC cavities development, the corresponding RF Solid State Amplifier (RF SSA), Low Level RF (LLRF) system, high power input couplers, tuners and Cryomodules (CM) for the two injectors have also been developed.

INTEGRATION AND COMMISSIONING OF INJECTORS

In order to develop the relevant techniques and the beam tuning method, the short term and principal goal of phase I for C-ADS is to construct two 10 MeV injectors with different schemes.

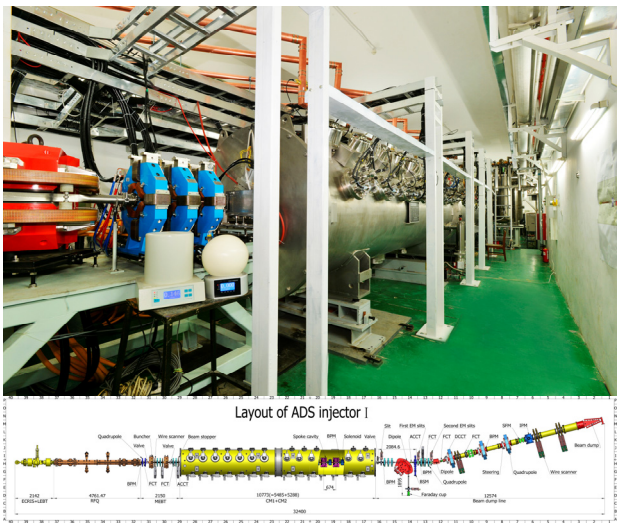

Figure 8: C-ADS Injector-I at IHEP

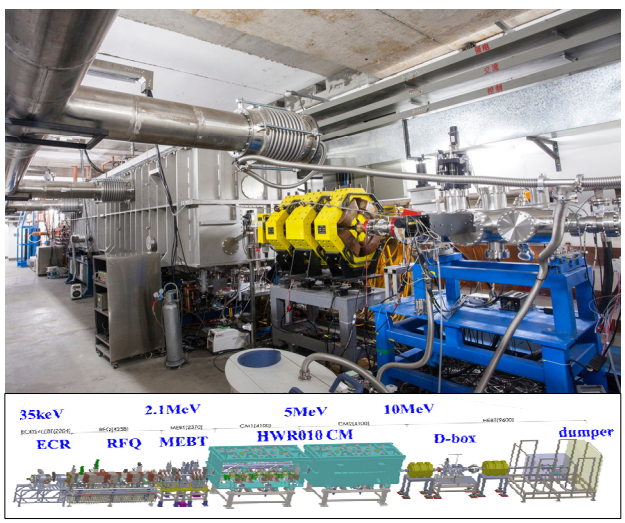

Figure 9: C-ADS Injector-II at IMP.

The Injector-I and Injector-II are integrated and commissioned by several stages during 2013-2016.

Finally, in May 2016, the Injector-I at IHEP (see Figure 12) and Injector-2 at IMP (see Figure 13) was integrated, consisting of the ECR ion source, LEBT, RFQ, SC Cavities, MEBT and beam stop. Injector-I consists of total 14 Spoke012 cavities in the CM1 and CM2, employ SSA and microTCA LLRF system and operating at 2K temperature (see Figure 8). Injector-II consists of total 12 HWR010 cavities in the CM1 and CM2, employ SSA and customized LLRF system and operating at 4 K temperature (see Figure 9).

Commissioning of Injector-I

On September 25th, 2014, the ECR Source + LEBT + RFQ have been commissioned with max. 90% duty factor beam, the beam power is 32.4 kW. Yet, the CW beam has not been achieved since RFQ-I encountered some troubles in RF conditioning at high power for CW operation. The highest CW RF power reached is only 200 kW.

On October 28th, 2015, the CM1 output reached 6 MeV with pulsed beam at 2 K temperature.

On June 15th, 2016, the CM2 output reached 10.1 MeV/10 mA with 20 μs pulsed beam at 2 K temperature. The transition rate of SC cavities is 100%. The measurement of beam energy and current and transition rate are shown in Figure 10 and Figure 11 and Figure 12.

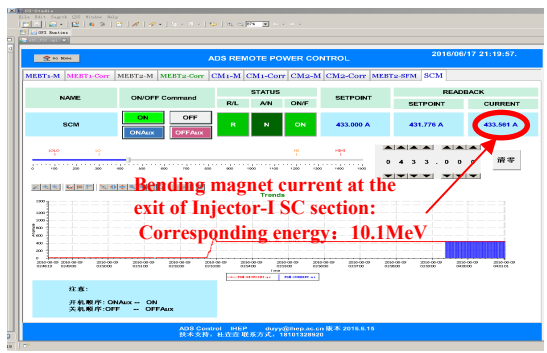

Figure 10: Beam energy measurement of Injector-I.

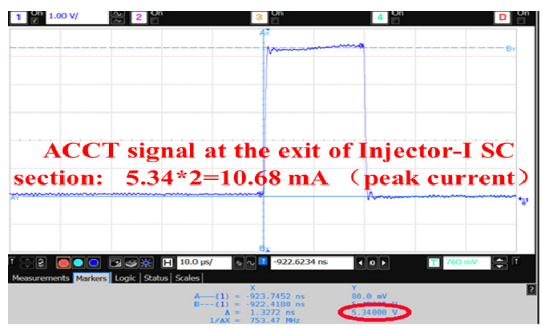

Figure 11: Beam current measurement of Injector-I.

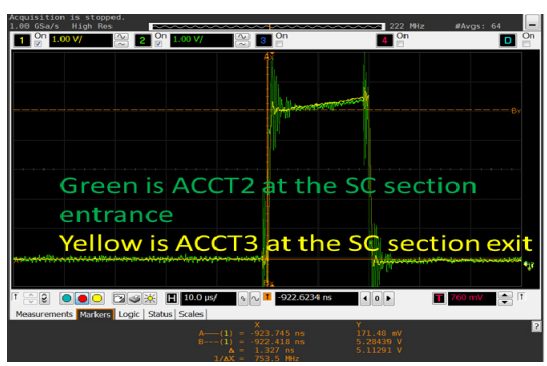

Figure 12: The transition rate of SC cavities.

ISBN 978-3-95450-185-4

At present continues beam commissioning and machine studies on going in order to get stable beam and understanding behavior of SC linac and proton beam. The final goal of beam commissioning is to get CW proton beam with 10 MeV/10 mA.

Commissioning of Injector-II

On June 6th, 2014, the ECR Source + LEBT + RFQ have been commissioned first beam with 2.16 MeV.

On June 30th, 2014, operated 4.5 hrs with 10 mA CW beam.

On June 6th, 2015, a low duty pulsed beam with current of 10.1 mA and energy of 5.2 MeV was achieved.

On January 2nd, 2016, operated 450 min with 4 MeV/1.7 mA CW beam, see history record in Figure 13.

At present Injector-II is under commissioning and expect to get 10 MeV proton beam soon.

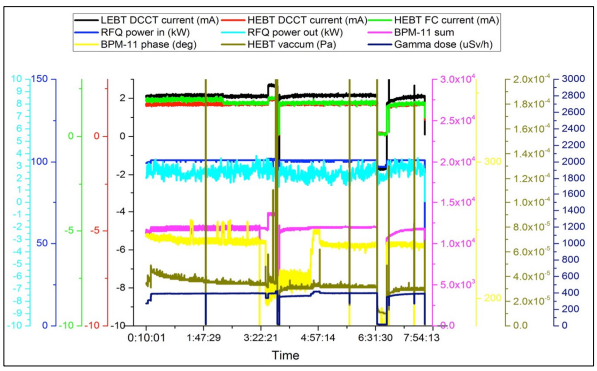

Figure 13: History record of 4MeV/1.7mA/CW/450min of injector-II.

CONCLUSION

There are active programs in many countries to develop, demonstrate and exploit accelerator-driven systems technology for nuclear waste transmutation and power generation. Among them, MYRRHA and C-ADS are the representative projects, already partly funded and expected to become operational in the near future.

For the tens of MW beam power required for industrial-scale ADS concepts, superconducting linear accelerator technology has the greatest potential to deliver the required performance.

Over the past five years of Phase I, C-ADS has made significant progress in the R&D of the SC linac. One of the exciting achievements concerning the SC linac is that a CW RFQ and several types of lowβSC cavities have been developed successfully.

In the end of year 2015, China Initiative ADS (CIADS) project is officially approved by Chinese government. The CIADS is a 6 year (2017-2022) project; the site is located in the Huizhou city region in Guangdong province south part of China.

ISBN 978-3-95450-185-4

FIGURE-8 STORAGE RING – INVESTIGATION OF THE SCALED DOWN INJECTION SYSTEM

H. Niebuhr*, A. Ates, M. Droba, O. Meusel, D. Noll, U. Ratzinger, J.F. Wagner
Institute for Applied Physics, Goethe-University, Frankfurt am Main, Germany

Abstract

To store high current ion beams up to 10 A, a superconducting storage ring (F8SR) is planned at Frankfurt university. For the realisation, a scaled down experimental setup with normalconducting magnets is being built. Investigations of beam transport in solenoidal and toroidal guiding fields are in progress. At the moment, a new kind of injection system consisting of a solenoidal injection coil and a special vacuum vessel is under development. It is used to inject a hydrogen beam sideways between two toroidal magnets. In parallel operation, a second hydrogen beam is transported through both magnets to represent the circulating beam. In a second stage, an ExB-Kicker will be used as a septum to combine both beams into one. The current status of the experimental setup will be shown. For the design of the experiments, computer simulations using the 3D simulation code bender were performed. Different input parameters were checked to find the optimal injection and transport channel for the experiment. The results will be presented.

F8SR – FIGURE-8 STORAGE RING

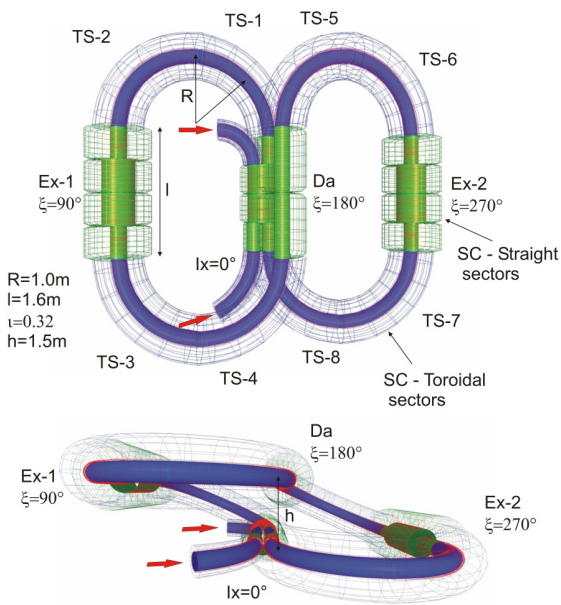

Figure 1: F8SR – Low-Energy Superconducting Magnetostatic Storage Ring.

The F8SR is a low-energy superconducting magnetostatic storage ring for high current beams, for example proton beams up to 10 A with an energy of up to 150 keV. Higher charged ion species can be stored with higher energies. In order to focus the high current beams, toroidal magnets (called toroids) and solenoids are used around the whole ring. The twisted Figure-8 geometry is necessary because of the RxB drift of beams transported through the toroidal magnetic fields. An additional advantage of this structure is the possibility to transport two different beams independently, one in each direction, and to perform interaction experiments at two areas of the ring where the beams cross. The F8SR is shown in Fig. 1.

SIMULATIONS USING THE PARTICLE-IN-CELL CODE BENDER

To investigate the dynamics of ion beams in solenoidal and toroidal magnetic field systems and for the development of the scaled down injection experiment, simulations using the Particle-in-Cell code bender [1] were performed. For this purpose, the external fields of the magnets used in the experiment were calculated using CST (M-Static Solver) on a mesh of 1x1x1 mm resolution and the beam tube geometry was included (required for losses calculations). Different geometries, injection coils and magnetic field strengths were used to investigate the beam behavior and to find a working and realizable injection system with a high acceptance and transmission.

To get a look on the beam path and behavior from different points of view, the tracking results of the ring beam and the injection beam are plotted together with the magnetic field strength B_z. One result is shown in Fig. 2. In this figure the upper picture shows a top view on the drift of the two beams, the ring beam moves from left to right and the injection beam from above to right. The lower picture shows the side view.

Using this view the basic idea of the injection system can be seen and how it works. The injected beam drifts from the injection channel to the transport channel and then gets transported trough the second toroid. Using the plotted parameters, the injected beam is matched perfectly, so no gyration occurs and the beam adjustment does not change. In this process, the beam also drifts down to the level of the ring beam. The possibility of using a kicker system to merge the two beams is available. In this simulation, the ring beam was not matched perfectly and so the beam adjustment – visible by the different gyration inside the first and the second toroid – changed. By using different parameters for the ring beam, this effect can be reduced.

For the characterization of an injection system, a set of simulations with different parameters were necessary. To compare the results, a method to figure out how large the

* niebuhr@iap.uni-frankfurt.de

ISBN 978-3-95450-185-4

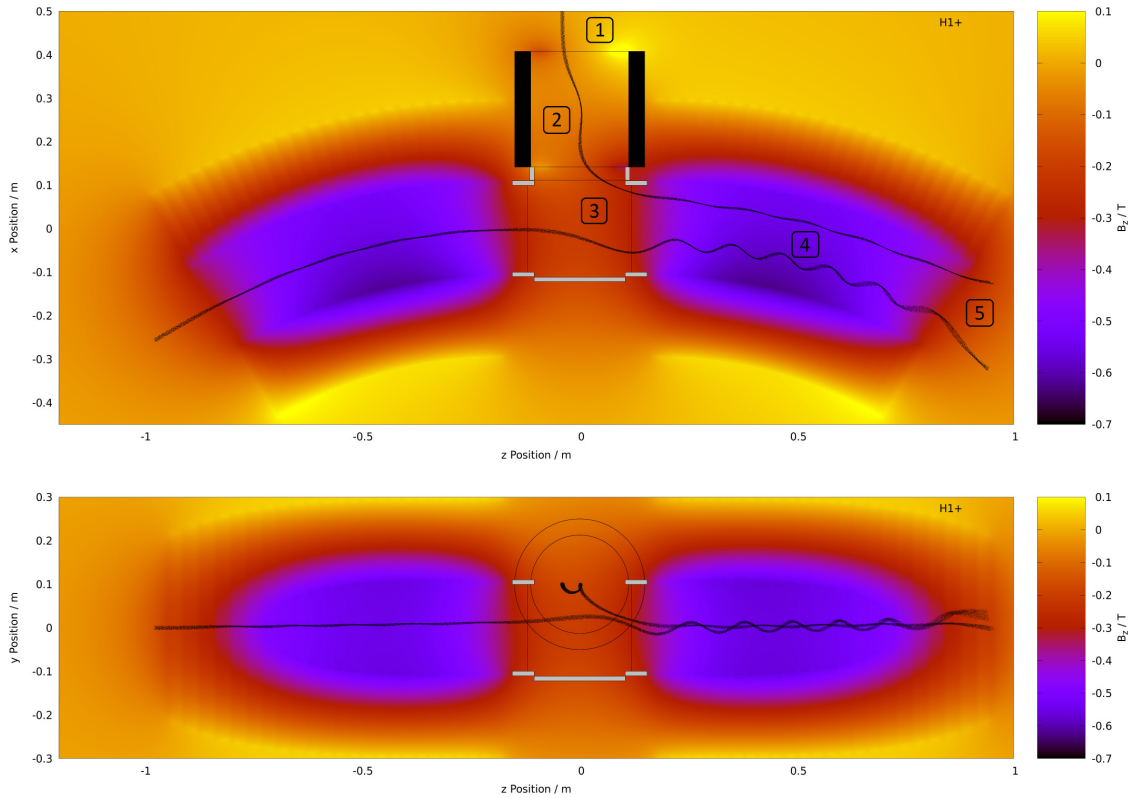

Figure 2: Looking on the beam path (upper picture from above / lower one from the side) of the ring beam and the injection beam. The magnetic field of the injection coil was B_{axis} = 0.326 T, the offset of the injection channel 100 mm and the injection position x=508 mm, y=100 mm and z=-40 mm.

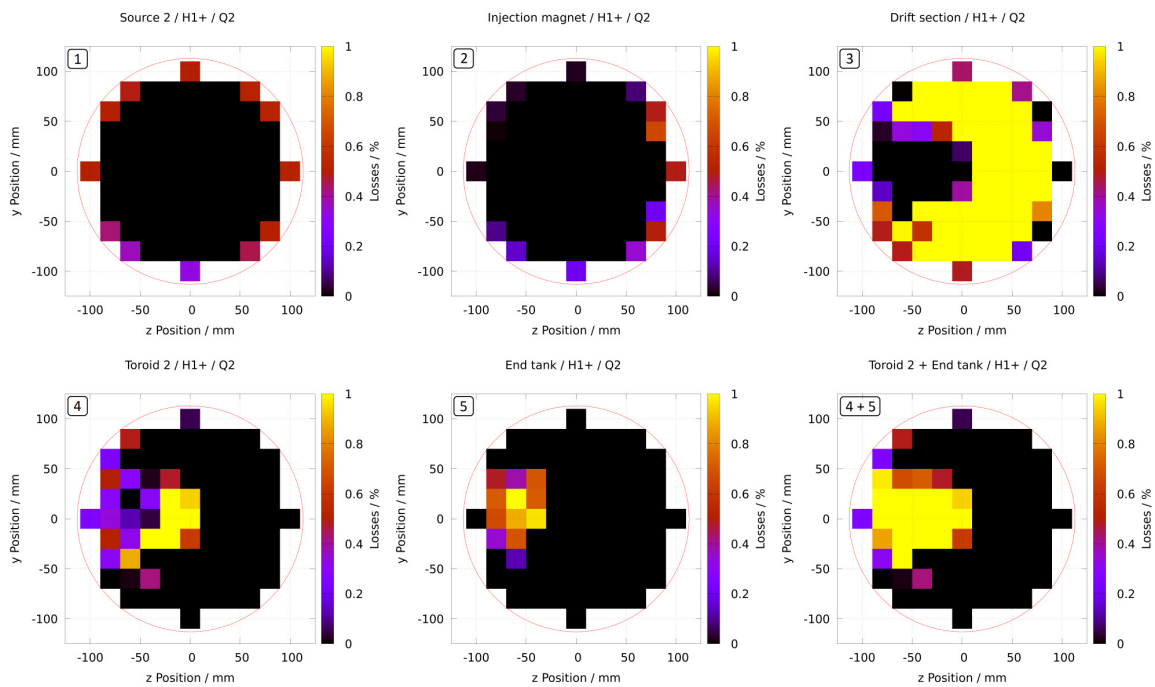

Figure 3: The picture shows the losses in each component of the transport and injection channel for 81 simulations with different starting positions in front of the injection magnet (z/y-coordinates). The magnetic field of the injection coil was B_{axis} = 0.326 T and the offset of the injection channel 100 mm.

ISBN 978-3-95450-185-4

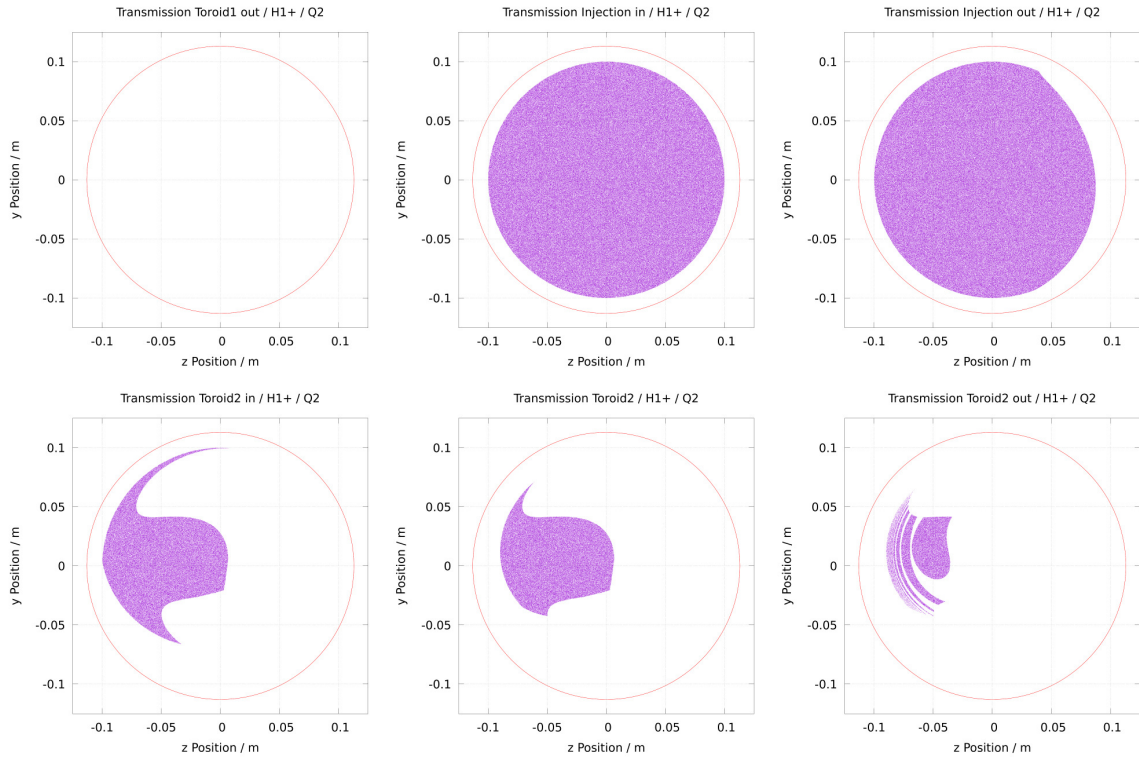

Figure 4: The picture shows the starting position in front of the injection magnet (z/y-coordinates) against the transmission until the entrance, center or exit of different components of the injection and transport channel. The magnetic field of the injection coil was B_{axis} = 0.326 T and the offset of the injection channel 100 mm.

injection channel, the transmission and the acceptance is had to be developed. Simulations with different magnetic field structures and strengths, geometries and injection parameters were performed to find the realizable injection system as described here.

To check one setup 81 simulations were done using the same geometry and magnetic field strength and structure and only the starting position of the beam in front of the injection channel varying across the whole zy-surface. The losses were tracked and assigned to the components in which they took place. A loss map was generated which shows at which position to start the beam in the zy-surface 100 mm in front of the injection coil to get beam losses in a specific component.

A result of this analysis method is shown in Fig. 3. By having the possibility to see where the beam gets lost if it starts at different transverse positions, it is possible to investigate how far the beam gets transported through the beam line. Here, the started beams mostly go through the injection coil and mainly get lost in the drift section (area between the three magnets). Only a bunch of started beams reaches the entrance of the second toroid. Still less of them get transported trough the toroid and reach the end tank behind the magnet.

Finally, the sum of the losses in the second toroid and the end tank is of interest (second row / third picture (Fig. 3)). Beams reaching one of these two components get transported through the injection system. It will be possible to kick these beams completely into the middle of the tube and then combine them with the ring beam by using a kicker system at the entrance of the second toroid. The yellow area of around 8x10 cm is the acceptance of the injection system. The transmission shown by color is mostly around 100 % in this area.

Another way to investigate the acceptance and transmission of an injection system is to use a homogeneous distribution (without starting angle) with the radius of the injection vacuum tube and transport this "beam" trough the whole experiment. In this kind of simulation, monitors are positioned at the entrance, center and exit surfaces of the components. A transmission map is generated which shows where to inject in front of the injection magnet (in the zy-surface) to get the beam transported until a monitor. This type of simulation runs faster and gives a more precise view on the acceptances and the injection planes. Another difference is that the transmission until a specific monitor is plotted and not the losses. So a direct view on the acceptance is possible. Disadvantages of this simulation type are that calculations with an actual beam distribution need more postprocessing and simulations with space charge are not possible.

In Fig. 4, results of this method are shown. The same simulation parameters were used than in the simulations shown before in Fig. 3.

ISBN 978-3-95450-185-4

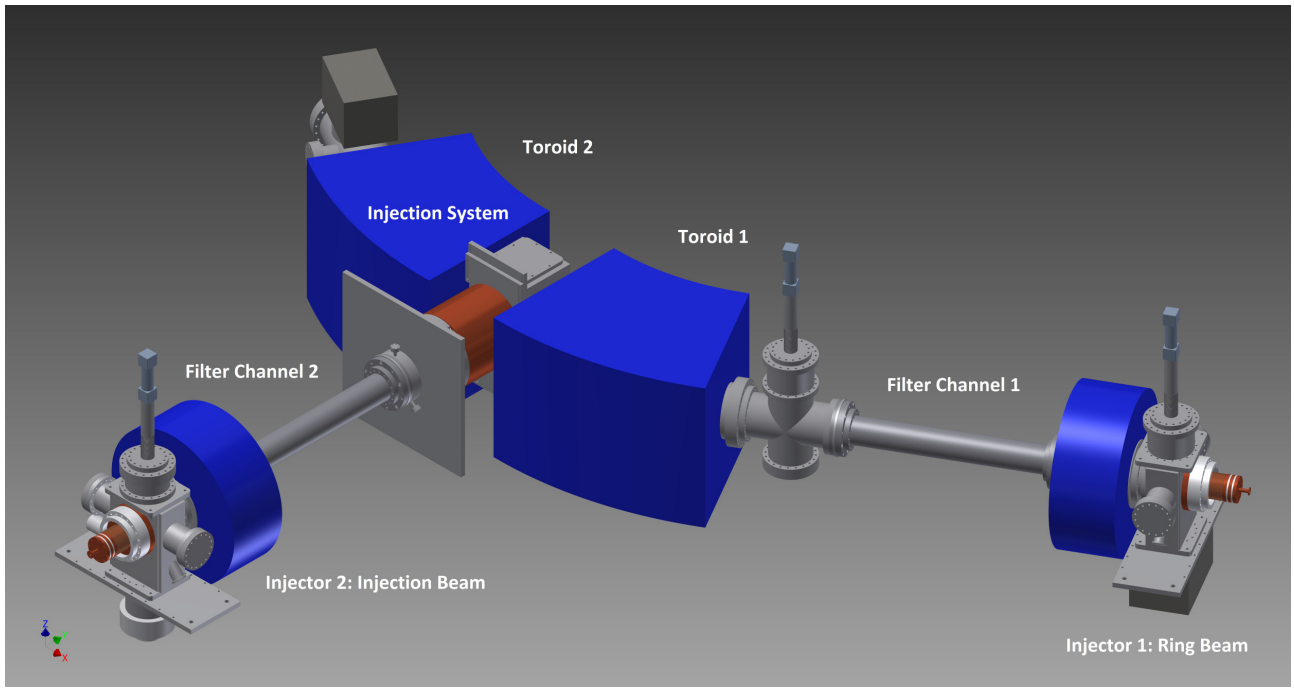

Figure 5: The complete layout of the experiment.

Here, the acceptance of the injection system can be seen very precisely. The results are comparable to the one shown before using the other simulation method. Using this method, it is possible to see the structure of the acceptance. Especially the acceptance at the exit of the second toroid shows an unexpected and rare structure. But for the development of the injection system the monitor at the entrance of the second toroid (second row, first picture (Fig. 4)) is the important one. By using a kicker system, all ions which come to this point will be injected. Additionally a monitor in the center of the second toroid was positioned in this simulations. This one shows the acceptance of the injection system without a kicker system. These results will be used during the first experiments. At this time, no kicker system is available and two independent beams will be monitored. Later the ExB kicker will be implemented to combine the beams to get one final beam.

Using bender and the different analysis methods, a final geometry for the injection system was found and the necessary parts were developed. This final geometry will be used in future simulations. It has nearly the same dimensions (few millimeters longer injection channel) than the geometry used in the shown simulations. The main difference is that the height-adjustability of the injection tank can be used now.

THE EXPERIMENT

The injection experiment is under construction at the moment. The two injectors, the two filter channels [2], the two toroids, the end tank and the whole periphery (power supplies, high voltage terminals, etc.) are ready for use now [3]. The height-adjustable vacuum tank is under construction and the injection magnet was ordered and will be delivered at the end of the year. The detectors were built and will be tested during the next months. The construction of the experiment will be finished at the beginning of next year. In Fig. 5 the final layout of the injection experiment is shown.

THE NEW DETECTORS

For the measurement of the positions and the dynamics of the two ion beams, two new detector systems were developed and built. Detector Number One is a non-destructive detector using phototransistors to detect the fluorescence generated by the reaction of the beams with the residual gas. The phototransistors are positioned around the beams at the tube walls and look at the beams radially. The 92 signals are measured using an electronic system connected to a PC. The PC is used to calculate the beam positions and diameters. This type of detector will be positioned at different spots in the experiment and will also be built moveable to detect the beams at different positions. By comparison of the different results at different positions, the beam dynamics can be investigated.

The disadvantage of this detector is that it is not possible to detect beams near the wall of the tube. Such beams will hit the detector structure and can not be measured. For this situation a second detector was developed and built.

Detector Number Two is a destructive detector and was designed to measure the beams at each position in the vacuum tube, for example in front of the other detector. It can be positioned in front of the first detector if a beam near the wall is expected. The detector consists of 64 single Faraday cups (FDCs) with a suppression for secondary electrons.

ISBN 978-3-95450-185-4

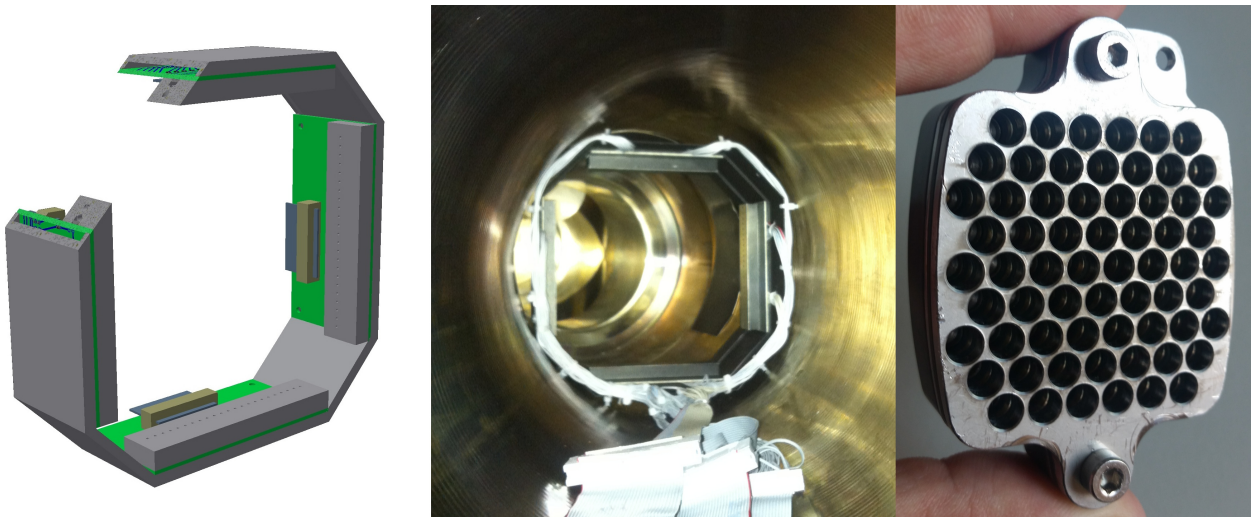

Figure 6: The left picture shows the layout of the non-destructive detector using phototransistors (Detector Number One). The middle one shows the non-destructive detector inside the first toroid. The right picture shows the destructive Faraday cup detector (Detector Number Two).

Each of the 64 signals will be measured independently by the same electronic system mentioned before.

Pictures of the detectors and the layout of the first one are shown in Fig. 6.

OUTLOOK

The scaled down injection experiment of the F8SR project is under construction at the moment. This step should be finished at the end of the year. After the setup of the injection system will be finished, the first experiments can take place. The offset of the injection channel, the magnetic fields of the magnets and the transverse positions at the beam injection are the main parameters which will be varied.

Future simulations will include the final geometry and the height-adjustablility of the injection system. Further analysis methods will be applied and different beam distributions will be used. Finally, a comparison with the measurements will be done.

REFERENCES

[1] D. Noll, M. Droba, O. Meusel, U. Ratzinger, K. Schulte and C. Wiesner, "The Particle-in-Cell Code Bender and Its Application to Non-Relativistic Beam Transport", in Proc. HB2014, East Lansing, USA, November 2014, paper WEO4LR02, pp. 304-308.

[2] M. Droba, A. Ates, O. Meusel, H. Niebuhr, D. Noll, U. Ratzinger, J. F. Wagner, "Simulation Studies on Beam Injection into a Figure-8 Type Storage Ring", in Proc. IPAC14, Dresden, Germany, June 2014, paper TUPRO045, pp. 1126-1128.

[3] J.F. Wagner, A. Ates, M. Droba, O. Meusel, H. Niebuhr, D. Noll, U. Ratzinger, "Status of Injection Studies into the Figure-8 Storage Ring", in Proc. IPAC15, Richmond, VA, USA, May 2015, paper MOPWA036, pp. 187-189.

ISBN 978-3-95450-185-4

STUDY ON THE MAGNETIC MEASUREMENT RESULTS OF THE INJECTION SYSTEM FOR CSNS/RCS*

M.Y. Huang[1,2#], S.N. Fu[1,2], N. Huang[1], L.H. Huo[1], H.F. Ji[1,2], W. Kang[1,2], Y.Q. Liu[1,2], J. Peng[1,2], J. Qiu[1,2], L. Shen[1,2], S. Wang[1,2], X. Wu[1,2], S.Y. Xu[1,2], J. Zhang[1,2], G.Z. Zhou[1,2]
1：Institute of High Energy Physics, Chinese Academy of Sciences, Beijing, China
2：Dongguan Institute of Neutron Science, Dongguan, China

Abstract

A combination of the H- stripping and phase space painting method is used to accumulate a high intensity beam in the Rapid Cycling Synchrotron (RCS) of the China Spallation Neutron Source (CSNS). The injection system for CSNS/RCS consists of three kinds of magnets: four direct current magnets (BC1-BC4), eight alternating current magnets (BH1-BH4 and BV1-BV4), two septum magnets (ISEP1 and ISEP2). In this paper, the magnetic measurements of the injection system were introduced and the data analysis was processed. The field uniformity and magnetizing curves of these magnets were given, and then the magnetizing fitting equations were obtained.

INTRODUCTION

The China Spallation Neutron Source (CSNS) is a high power proton accelerator-based facility [1]. It consists of an 80 MeV H- linac (upgradable to 250 MeV for CSNS-II), a 1.6 GeV Rapid Cycling Synchrotron (RCS), a solid tungsten target station, and some instruments for neutron applications [2]. With a repetition rate of 25 Hz, the RCS, which accumulates an 80 MeV injection beam, accelerates the beam to the designed energy of 1.6 GeV and extracts the high energy beam to the target. The design goal of beam power for CSNS is 100 kW and can be upgradable to 500 kW [3].

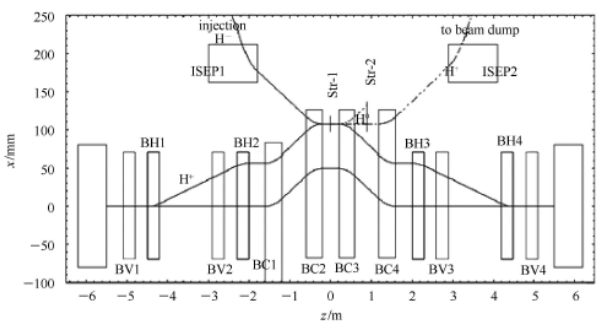

Figure 1: Layout of the RCS injection system.

For the high intensity proton accelerators, the injection with H- stripping and phase space painting is actually a practical method [4] which is used for CSNS/RCS. Figure 1 shows the layout of the RCS injection system. It consists of a fixed horizontal bump (four direct current (DC) dipole magnets, BC1-BC4), a horizontal painting bump (four alternating current (AC) dipole magnets, BH1-BH4), a vertical painting bump (four AC dipole magnets, BV1-BV4), two septum magnets (ISEP1, ISEP2), and two stripping foils (Str-1, Str-2) [5].

In order to obtain the field uniformity and magnetizing curves of different kinds of magnets in the injection system for CSNS/RCS, the magnetic measurements need to be done. By using some codes of numerical analysis, the measurement results can be processed. Then the field uniformity and magnetizing curves can be given and the magnetizing equations can be fitted.

MEASUREMENTS OF BC MAGNETS

For the injection system of CSNS/RCS, four DC dipole magnets, BC1-BC4, give a fixed horizontal bump in the middle for an additional closed-orbit shift of 60 mm. The physics design parameters of the four BC magnets are the same and they share only one power supply.

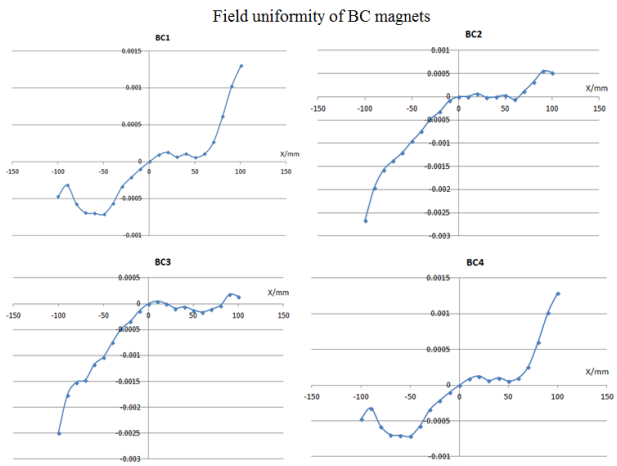

Figure 2: Field uniformity of the four BC magnets.

After the measurements of the four BC magnets, their field uniformity can be obtained, as shown in Fig. 2. It can be known that the field uniformity of any one BC magnet is smaller than ±0.3% which meets the physics design requirement (<±0.5%). In addition, it can be found that there are some differences between the four BC magnets although they are the same in the physics design.

The magnetizing curves of the four BC magnets and their auxiliary coils also can be given after the magnetic measurements. By using some codes of numerical analysis, the magnetizing curves can be fitted. After the analysis of fitting errors, it can be known that the linear of

*Work supported by National Natural Science Foundation of China (Project Nos. 11205185)
#huangmy@ihep.ac.cn

ISBN 978-3-95450-185-4

the magnetizing curves is very good. Then the linear fitting equations of the four BC magnets and their auxiliary coils can be given, as shown in Table 1.

Table 1: The Magnetizing Fitting Equations of the Four BC Magnets and their Auxiliary Coil

Magnet	BC	Equation (BL/T·mm, I/A)
Main	BC1	BL = 0.1821×I+0.06024
	BC2	BL = 0.1822×I+0.1789
	BC3	BL = 0.1823×I+0.182
	BC4	BL = 0.1824×I+0.1789
Auxiliary coil	BC1	BL = 0.08891×I+0.06674
	BC2	BL = 0.08899×I+0.007756
	BC3	BL = 0.08971×I+0.02102
	BC4	BL = 0.08911×I+0.01571

MEASUREMENTS OF BH MAGNETS

For CSNS/RCS, the transverse phase space painting method is used for injecting a small emittance beam from the linac into the large ring acceptance. Four AC dipole magnets, BH1-BH4, are used for horizontal painting and another four AC dipole magnets, BV1-BV2, are used for vertical painting.

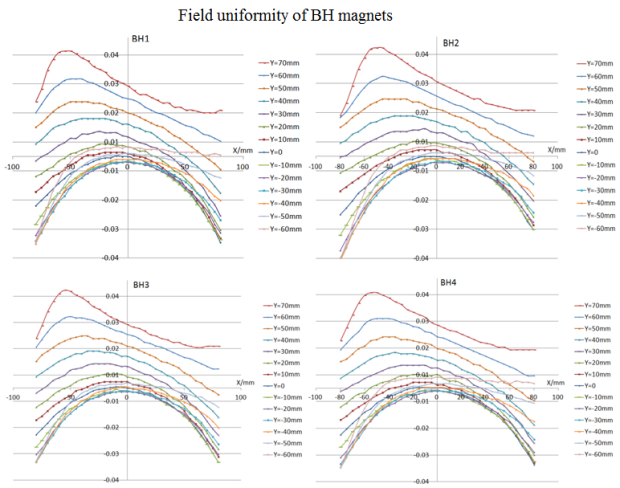

Figure 3: Field uniformity of the four BH magnets.

The physics design parameters of the four BH magnets are the same and they share only one power supply. The design requirement of the field uniformity for BH magnets is smaller than ±1.5%. After the magnetic measurements, the field uniformity of the four BH magnets can be obtained, as shown in Fig. 3. It can be found that, in some areas, the field uniformity of BH magnets is larger than ±1.5% which doesn't meet the physics design requirement. After multi-turn tracking simulation by the code ORBIT [6], the effects of bad field uniformity for the real particle distribution area can be studied [7] and it can be found that the anti-correlated painting method is more suitable.

As shown in Fig. 4 (left), the current curves of the power supply of the four BH magnets are given, and then the measurements of magnetizing curves can be done. In Fig. 4 (right), the magnetizing curves of BH magnets are given. It can be known that the rising rate and falling rate are very important factors to impact the magnetizing curves. In addition, the error becomes lager while the current smaller than 3000 A. Furthermore, by using some codes of numerical analysis, the magnetizing curves can be fitted and the fitting equations can be obtained.

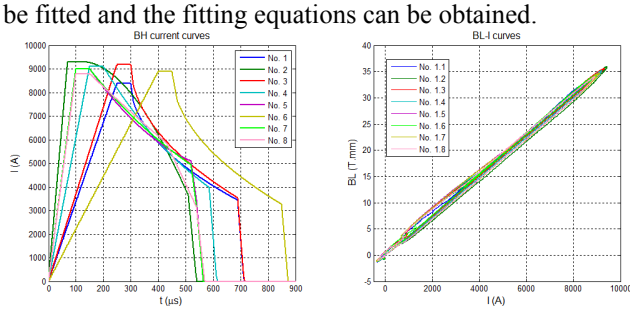

Figure 4: The current curves (left) and magnetizing curves (right) of BH magnets.

MEASUREMENTS OF BV MAGNETS

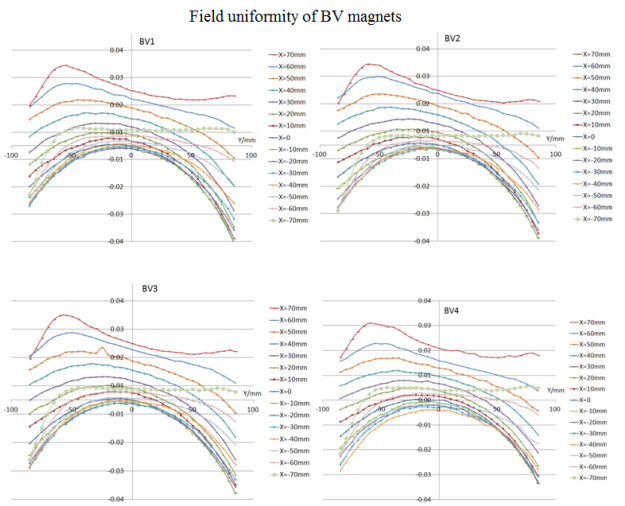

Figure 5: Field uniformity of the four BV magnets.

Similar to the four BH magnets, the physics design parameters of the four BV magnets are the same and they also share only one power supply. The design requirement of the field uniformity for BV magnets is smaller than ±1.5%. After the magnetic measurements, the field uniformity of the four BV magnets can be obtained, as shown in Fig. 5. It can be found that, in some areas, the field uniformity of BV magnets can achieve about ±4% which is larger than ±1.5% and doesn't meet the physics design requirement. After multi-turn tracking simulation by the code ORBIT, the effects of bad field uniformity for the real particle distribution area can be studied and it can be found that the effects can impact the injection painting process.

The current curves of the power supply of the four BV

ISBN 978-3-95450-185-4

magnets are given in Fig. 6 (left), and the measurements of magnetizing curves can be done. Figure 6 (right) shows the magnetizing curves of BV magnets. It can be known that the rising rate and falling rate are very important factors to impact the magnetizing curves. In addition, the error becomes larger while the current is small. Furthermore, by using some codes of numerical analysis, the magnetizing curves can be fitted and the fitting equations can be obtained.

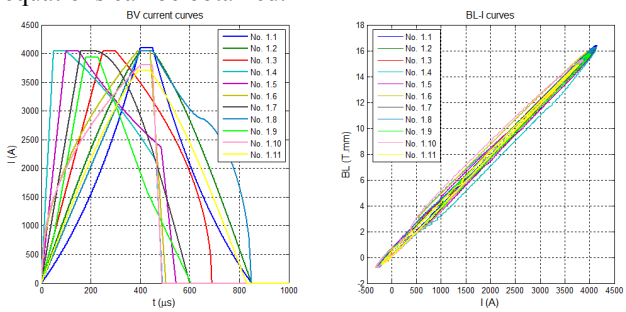

Figure 6: The current curves (left) and magnetizing curves (right) of BV magnets.

MEASUREMENTS OF SEPTUM MAGNETS

There are two septum magnets in the injection system. The physics design parameters of the two septum magnets are the same, but they don't share one power supply. After the magnetic measurements, the field uniformity of the two septum magnets can be obtained, as shown in Fig. 7. It can be known that the field uniformity of any one septum magnet is smaller than ±0.4% which meets the physics design requirement (<±0.5%).

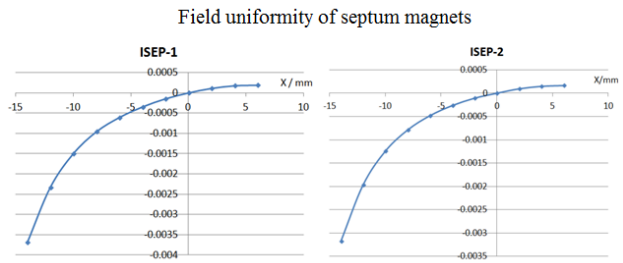

Figure 7: Field uniformity of the two septum magnets.

Table 2: The Magnetizing Fitting Equations of the Two Septum Magnets

Septum	Equation (BL/T·mm, I/A)
ISEP-1	BL = 0.1533×I+0.1647
ISEP-2	BL = 0.1531×I+0.2709

During the magnetic measurements, the magnetizing curves of the two septum magnets can be obtained. By using some codes of numerical analysis, the magnetizing curves can be fitted. Through the analysis of fitting errors, it can be known that the linear of the magnetizing curves is very good. Then the linear fitting equations of the two septum magnets can be given, as shown in Table 2.

CONCLUSIONS

In this paper, the measurements of different kinds of magnets in the injection system were introduced. The field uniformity and magnetizing curves of different magnets were given. It can be found that the field uniformity of BC magnets and septum magnets meets the physics design requirement. However, in some areas, the field uniformity of BH and BV magnets cannot meet the physics design requirement. By using some codes of numerical analysis, the magnetizing curves of different kinds of magnets can be fitted, and the magnetizing fitting equations were obtained.

ACKNOWLEDGMENT

The authors want to thank other CSNS colleagues for the discussions and consultations.

REFERENCES

[1] S. Wang et al., Chin. Phys C, 33, 1-3 (2009).
[2] CSNS Project Team, China Spallation Neutron Source Feasibility Research Report, Chinese Academy of Sciences, 2009 (in Chinese).
[3] J. Wei et al., Chin. Phys C, 33, 1033-1042 (2009).
[4] J.Y. Tang et al., Chin. Phys C, 30, 1184-1189 (2006).
[5] M.Y. Huang et al., Chin. Phys C, 37, 067001 (2013).
[6] J. Gabambos et al., ORBIT User's Manual, SNS/ORNL/AP Technical Note 011, 1999.
[7] M.Y. Huang et al., Study on the transverse painting during the injection process for CSNS/RCS, proceedings of IPAC2015, Richmond, VA, USA, pp. 2025-2027, 2015.

ISBN 978-3-95450-185-4

H- CHARGE EXCHANGE INJECTION FOR XiPAF SYNCHROTRON

H. J. Yao†, S. X. Zheng, G. R. Li, X. L. Guan, X. W. Wang, Q. Z. Xing , Key Laboratory of Particle & Radiation Imaging (Tsinghua University), Ministry of Education, Beijing 100084, China
also at Laboratory for Advanced Radiation Sources and Application, Tsinghua University, Beijing 100084, China
also at Department of Engineering Physics, Tsinghua University, Beijing 100084, China

Abstract

The physics design of the H- charge exchange injection system for Xi'an Proton Application Facility (XiPAF) synchrotron with the missing dipole lattice is discussed. The injection scheme is composed of one septum magnet, three chicane dipoles, two bump magnets and one carbon stripping foil. A 7 μg/cm^2 carbon foil is chosen for 7 MeV H- beam for high stripping efficiency and low coulomb scattering effect. The simulation results of the horizontal and vertical phase space painting finished by two bumper magnets and mismatching respectively are presented.

INTRODUCTION

Xi'an Proton Application Facility (XiPAF) is under construction in Xi'an, China, to fulfil the need of the experimental simulation of the space radiation environment, especially for the research of the single event effect (SEE). XiPAF is mainly composed of a 7 MeV linac injector, a synchrotron (60~230 MeV) and two experimental stations. The synchrotron [1] has a 6-fold "Missing-dipole" FODO lattice with its circumference of 30.9 m, the focusing structure consists of 6 dipoles and 12 quadrupoles, and six 2.21 m long drift space is left for accommodation of injection, extraction and acceleration system etc. The stripping injection method is chosen to achieve higher beam intensity of 2×10^{11} proton per pulse (PPP). And the phase space painting is chosen to control the space charge effect. The parameters from the linac injector are shown in Table 1.

Table 1: Injection Parameters for XiPAF Synchrotron

Parameter	Value	Unit
Injection ion type	H-	
Beam energy	7	MeV
Peak current	5	mA
Maximum repetition rate	0.5	Hz
Beam pulse width	10~40	μs
Normalized RMS emittance	~0.25	π mm·mrad
Injection period	0.85	μs
Number of particles	2×10^{11}	

INJECTION LAYOUT

The layout of injection system for XiPAF synchrotron is shown in Fig.1, a carbon strip foil near the center of the injection section and three DC chicane dipoles (CH1, CH2, CH3), are arranged in the injection section; and two bumper magnets (Bump1, Bump2) located in the two sections adjacent to the injection section.

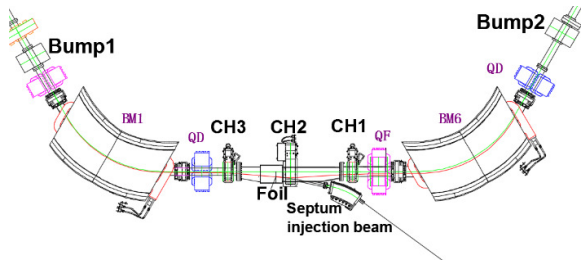

Figure 1: Injection Layout of XiPAF synchrotron.

In order to inject the beam properly, the closed orbit need to be bumped to the position of the strip foil during the beam injection. Three DC Chicane dipoles produce a fixed bump in the closed orbit near the strip foil. Then two bumpers are switched on to bend the closed orbit an additional 2.4 cm outward, and to make the closed orbit passing through the strip foil so that the injected beam and circulating beams overlap. The closed orbit bump produced by three chicane dipoles and two bumpers is shown in Fig.2.

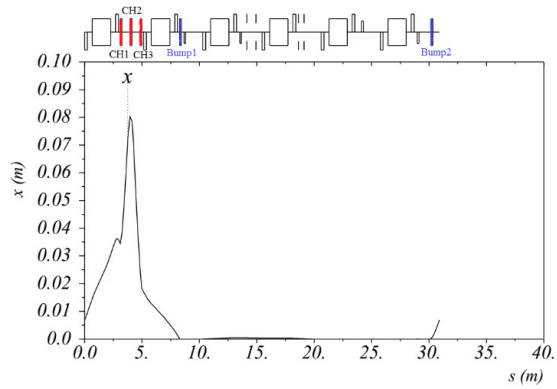

Figure 2: The closed orbit bump.

Table 2: Main Parameters of Chicanes and Bumpers

Parameter	CH1	CH2	Bump1	Bump2
Kick angle (mrad)	70	140	10	7
Magnetic field (T)	0.17	0.28	0.024	0.017
Effective length(mm)	150	200	160	160

The main parameters of three chicane dipoles and two bumpers are given in Table 2. The parameters of CH3 are same with the ones of CH1. During injection, 7 MeV H- beam is converted to protons by the strip foil. After the injection, the two bumpers are switched off to move the closed orbit off the strip foil completely.

† yaohongjuan@mail.tsinghua.edu.cn

ISBN 978-3-95450-185-4

STRIPPING FOIL

For XiPAF synchrotron, H^- charge exchange injection method is adopted to achieve high intensity. At end of the second chicane, there is a carbon stripping foil on the path of injection. H^- particles are stripped two electrons and converted to protons by the carbon strip foil in the injection. The thickness of carbon stripping foil is chosen from two aspects to consider, the foil should be thick enough to strip two electrons of H^- while the emittance growth caused by it is acceptable.

When H^- particles enter the foil, electrons of the particle can be stripped away or the particle can capture electrons from atoms in the foil. The fraction of H^-, H^0, H^+ can be calculated using the formula [2] as following:

$$\begin{aligned} N^- &= e^{-(\sigma_{-10}+\sigma_{-11})x} \\ N^0 &= \frac{\sigma_{-10}}{\sigma_{-10}+\sigma_{-11}-\sigma_{01}}[e^{-\sigma_{01}x}-e^{-(\sigma_{-10}+\sigma_{-11})x}] \\ N^+ &= 1-N^- -N^0 \end{aligned} \quad (1)$$

Where N-, N0, N+ are the three charge fractions, x is the number of target atoms per cm^2, σ_{-10}, σ_{01}, σ_{-11} are the electron loss cross sections. The measurements of these cross sections for H- in carbon have been obtained by Gulleyet al. [3] at 800MeV as

$$\begin{aligned} \sigma_{-10} &= (6.76 \pm 0.09) \times 10^{-19}\ cm^2 \\ \sigma_{01} &= (2.64 \pm 0.05) \times 10^{-19}\ cm^2 \\ \sigma_{-11} &= (0.12 \pm 0.06) \times 10^{-19}\ cm^2. \end{aligned} \quad (2)$$

Then we can evaluate three cross sections for 7 MeV H^- in carbon, and calculate the stripping efficiency, that is fraction of H^+ for several different thickness foils, the results are listed in Table 3. Where l is the thickness and η is stripping efficiency; $\Delta\varepsilon_{rmsx}$, $\Delta\varepsilon_{rmsz}$ and $\Delta\delta_{rms}$ are rms emittance growth in horizontal and vertical direction, and momentum spread increase respectively, the data in these three columns is multiplied by 10, which means passing through the foil 10 times.

Table 3: Results of stripping efficiency, emittance growth and momentum spread increase vary with foil thickness.

l (μg/cm²)	η (%)	10Δε$_{rmsx}$ (πmm·mrad)	10Δε$_{rmsz}$ (πmm·mrad)	10Δδ$_{rms}$ (%)
5	93.4	0.91	0.79	0.02
6	96.5	1.09	0.95	0.024
7	98.1	1.27	1.11	0.028
8	99.0	1.45	1.27	0.031

From the results in Table3 we can see that stripping efficiency increases with the foil thickness, but the foil cannot be too thicker, because when the beam passes through the foil, the coulomb scatterings cause the emittance and the momentum spread to increase, and thicker foil means larger emittance and momentum spread growth. The emittance growth and the momentum spread increase of passing through strip foil are given in formula (3) and (4) respectively [4]

$$\Delta\epsilon_y = 58.87\frac{\beta_y[m]}{\beta^2(pc[MeV])^2}\frac{l[\mu g/cm^2]}{X_0[g/cm^2]} \quad (3)$$

Where $\Delta\varepsilon_y$ denotes emittance growth for horizontal direction x or vertical direction z, β_y is β function value at the strip foil for horizontal direction x or vertical direction z, l is thickness in μg/cm², the radiation length X_0 is 42.97 g/cm² for carbon.

$$\Delta\delta = \frac{\Delta E}{\beta^2 E} = \frac{KZz^2}{A\beta^4 E}\left[ln\frac{2m_e c^2\beta^2\gamma^2}{I} - \beta^2\right]l \quad (4)$$

Where K=0.307 MeV/(g /cm²) is a constant, me is the rest mass of electron, Z and A are the atomic charge and mass number of the foil, $I=16Z^{0.9}$ is the effective ionization potential of the medium atom. The rms emittance increase and the momentum spread growth due to multiple coulomb scattering are calculated and shown in Table 3.

From the injection simulation results given at the next section we know the average hits number per proton is about 6, at Table3 we use 10 hits number with enough margin to do the calculation. From the linac injector with a debuncher the beam momentum spread is ±0.45% and the acceptance of the ring is ±0.7%, so the thickness of 5~8 μg/cm² can be acceptable.

The thickness of 5 μg/cm² foil is about 25 nm, even the 8 μg/cm² foil is only 40 nm, these foils cannot be self-supporting, they are made on glasses. The size of foil is 15 mm (width)×30 mm (height), the "U" shape frame with three supported edges and one free edge is used to support the foil. We did several experiments and now three thickness foil of 5 μg/cm², 7 μg/cm², 8 μg/cm² are successfully moved on to the "U" shape frame from the glasses, Fig.3 shows the picture of 5 μg/cm² and 8 μg/cm² foils.

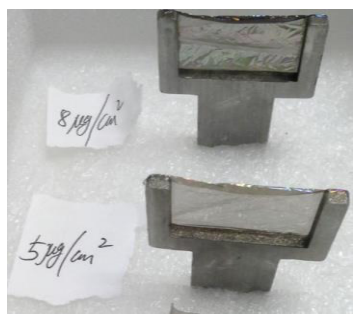

Figure 3: The "U" shape frame with foils.

From our experience, the foil is thicker and the success rate of the experiment is higher. Based on the above factors, the thickness of 7 μg/cm² is chosen, which provides more than 98% stripping efficiency while the emittance growth and momentum spread increase remain acceptable.

ISBN 978-3-95450-185-4

PHASE SPACE PAINTING

XiPAF synchrotron requires 2×10^{11} proton per pulse injected into the ring, so the phase space painting method is adopted. The injected beam is painted into the large transverse phase space to reduce the influence of space charge effects. As shown in Fig.1, two bumpers make a time dependent bump orbit for beam painting in horizontal plane. As for the vertical plane, the phase space painting is realized by phase space mismatching, at the same time an off-center coordinate at the injected point in vertical phase space is used for more uniform distribution after painting.

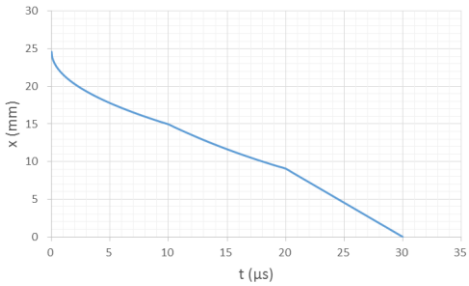

Figure 4: The orbit bump moving curve.

We have simulated the phase space painting using ORBIT [5] code and the space-charge effects have been taken into account. About the moving curve, we did a lot of calculations using square-root function, exponential function and linear function. After the optimization the orbit bump moving curve is given in Fig.4, which is a piecewise function and the falling down time is 30 μs. The injected beam is painted in two phase space to control the tune shift under 0.2. Two dimension plots in horizontal phase space (x, P_x), vertical phase space (z, P_z) and in real space (x, z) are given in Fig.5 at different turns.

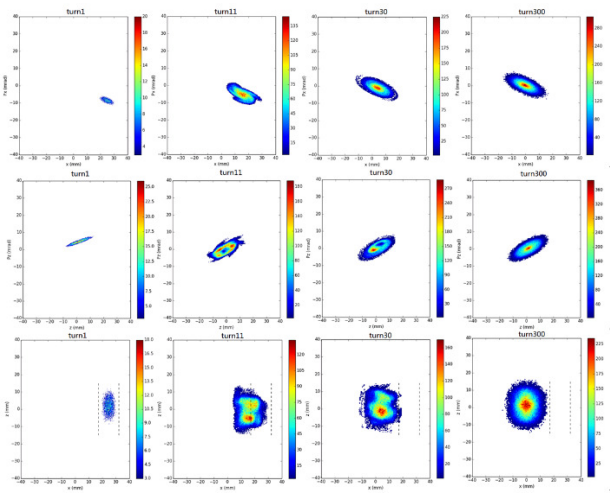

Figure 5: Phase space and real space distribution at different turns (the three rows are (x, P_x), (z, P_z), and (x, z) respectively; the four columns are turn 1, turn 11, turn 30 and turn 300 respectively).

The rms emittance of 7 MeV injected beam is 2 π mm·mrad, after the transvers phase painting the rms emittance is shown in Fig.6, 2×10^{11} proton can be obtained after 11 turns injection, and the average number of hits on the foil per proton is 6 before the circulating beam keep away from the foil.

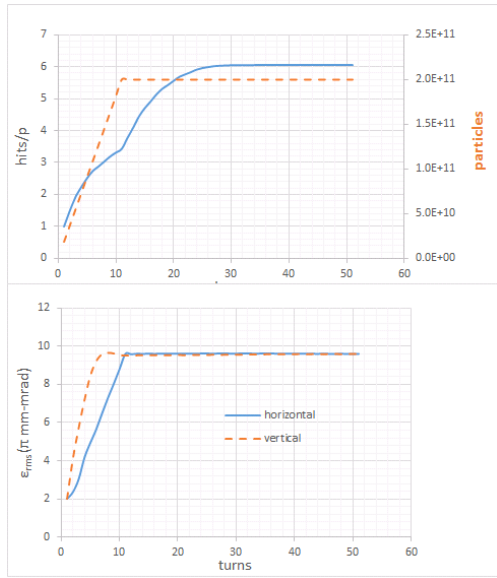

Figure 6: The hits number on the foil and the rms emittance after phase painting.

CONCLUSION

The 7 MeV H^- charge exchange injection system has been designed for Xi'an Proton Application Facility. The 15 mm (H)×30 mm (V), 7 μg/cm^2 foil is chosen to provide more than 98% stripping efficiency, the emittance growth and momentum spread increase are acceptable; the foil has been successfully moved to the "U" shape frame. 2×10^{11} particles per pulse are injected into the synchrotron using the phase painting method. At present the bumpers, chicane dipoles and stripping foil system are under construction.

ACKNOWLEDGEMENT

The authors would like to thank Dr. J. Qiu and X. Y. Zhang for the guidance of using ORBIT code.

REFERENCES

[1] S.X. Zheng *et al.*, "Design of the 230MeV proton accelerator for Xian Proton Application Facility", this conference, MOPR006, HB2016, Sweden.

[2] R. C. Webber, C. Hojvat, "Measurement of the electron loss cross sections for negative hydrogen ions on carbon at 200MeV", *IEEE Transactions on Nuclear Science*, Vol. NS-26, NO.3, 1979, pp. 4012-4014.

[3] M.S. Gulley *et al.*, "Measurement of H^-, H^0 and H^+ yields produced by foil stripping of 800 MeV H^- ions", *Physical Review A*, Vol. 53, NO.5, 1996, pp. 3201-3210.

[4] H.H. Liu, "Design of a compact medical synchrotron and 3D dose delivery of rapid cycling beam", Ph.D. thesis, Phys. Dept., Indiana University, USA, 2013.

[5] J. D. Galambos *et al.*, "ORBIT User Manual Version 1.10", July 1999.

ISBN 978-3-95450-185-4

RF-KNOCKOUT SLOW EXTRACTION DESIGN FOR XiPAF SYNCHROTRON

H. J. Yao, G. R. Li, Q. Zhang, S. X. Zheng†, X. L. Guan, X. W. Wang
Key Laboratory of Particle & Radiation Imaging (Tsinghua University), Ministry of Education, Beijing 100084, China
also at Laboratory For Advanced Radiation Sources and Application, Tsinghua University, Beijing 100084, China
also at Department of Engineering Physics, Tsinghua University, Beijing 100084, China

Abstract

The physics design of slow extraction for Xi'an Proton Application Facility (XiPAF) synchrotron is discussed. The extraction scheme is composed of two resonant sextupoles, one electrostatic septum (ES) and two septum magnets. The phase space diagram under the Hardt condition at the entrance of ES and the last three turn's trajectory before extraction are presented. A program is written with C++ to simulate slow extraction process by RF-knockout (RF-KO), the calculation results of dual frequency modulation (FM) and amplitude modulation (AM) are given, and the standard deviation of the fluctuation parameter R_1 can be limited 0.2 with optimum parameters under a sampling frequency of about 10 kHz.

INTRODUCTION

Xi'an Proton Application Facility (XiPAF) is under construction in Xi'an, China, to fulfil the need of the experimental simulation of the space radiation environment, especially for the research of the single event effect (SEE). XiPAF is mainly composed of a 7 MeV linac injector, a synchrotron (60~230 MeV) and two experimental stations. The synchrotron [1] has a 6-fold "Missing-dipole" FO-DO lattice with its circumference of 30.9 m. The irradiation experiments require 1~10 s proton beam, so the slow extraction system has been designed for XiPAF synchrotron. For this facility, the third-integer resonance and RF-KO (Radio Frequency Knock Out) technology are applied to accomplish slow extraction. The parameters of XiPAF synchrotron related to slow extraction system are listed in Table 1.

Table 1: The Parameters of XiPAF Synchrotron

Parameter	Value	Unit
Injection energy	7	MeV
Extraction energy	60~230	MeV
Circumference	30.9	m
Maximum repetition rate	0.5	Hz
Maximum β_x/β_y	5.8/6.0	
Extraction υ_x/υ_y	1.678/1.794	

EXTRACTION SYSTEM SCHEME

The scheme of extraction system for XiPAF synchrotron is shown in Fig.1, the extraction elements consist of four sextupoles (SR1, SR2, SC1, SC2), one electrostatic wire septum (ES), two septum magnets (MS1, MS2) and one RF-KO kicker. As showed in Fig. 1, one pair sextupole magnets SR1 and SR2 are used for resonance excitation. The phase advance between SR1 and SR2 is about $5\pi/3$, and they have same strength but opposite sign., which leads to the same function on resonance but cancellation of the chromaticity correction Another pair sextupole magnets SC1 and SC2 are used for chromaticity correction. The phase advance between SC1 and SC2 is also about $5\pi/3$, and they have same strength and same sign, which leads to the same function on chromaticity without affecting the resonance.

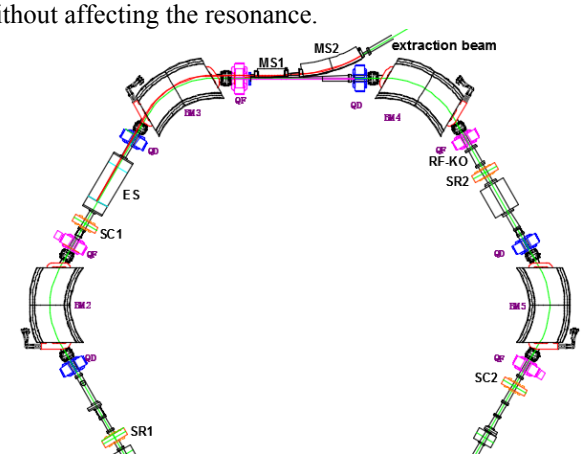

Figure 1: The extraction system scheme for XiPAF synchrotron.

The ES is used to give a kick to the particles entering the ES gap by the electrostatic field in order to separate from the circulating beam remaining inside the separatrix. In addition, two septum magnets MS1 and MS2 are used to deflected beam toward the beam transport line for extraction. The main parameters of ES, MS1 and MS2 are listed in Table 2.

Table 2: Main Parameters of ES, MS1 and MS2

Parameter	ES	MS1	MS2
Kick angle (mrad)	11	87.3	453.8
Max. magnetic field (T)	/	0.34	081
Max. electric field (MV/m)	5.7	/	/
Effective length (m)	0.8	0.6	1.3
Septum thickness (mm)	0.1	15	30

The ES is closed to the focusing quadrupole where the beta function has large value, and the phase advance between ES and MS1 is 92 degrees. Based on the formula (1), a large horizontal deflection will be obtained at the septum magnet MS1, which makes the design of MS1 easier.

† zhengsx@tsinghua.edu.cn

ISBN 978-3-95450-185-4

$$\Delta x = \theta\sqrt{\beta_{ES}\beta_{MS}}\,\sin\mu\,. \qquad (1)$$

Where θ is the kicker angle of ES, β_{ES} and β_{MS} are beta function values at ES and MS1 respectively, μ is the phase advance between ES and septum magnet MS1.

TRACKING SIMULATION

Computer simulations of third-integer resonance extraction has been performed using MAD-X [2] code, the horizontal tune is chosen at 5/3. Figure 2 shows the phase space distributions at the entrance of the ES (a), the exit of ES (c) and the entrance of the first septum magnet MS1 (d). The Fig.2 (b) is the local zoomed graph of (a). From this figure, we can see that only one separatrix is crossed with the septum of ES, the normalized sextupole strength is 35 $m^{-1/2}$, and the spiral step is 5 mm as shown in Fig.2 (b).

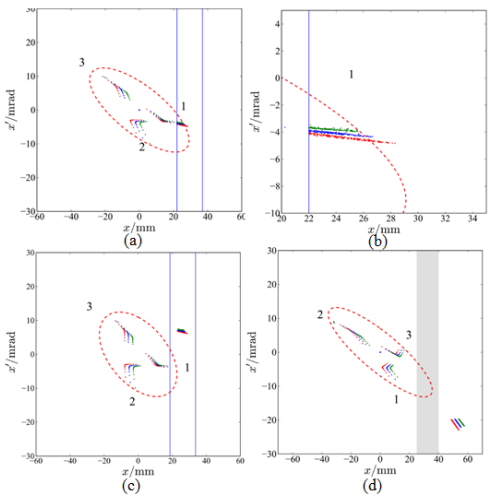

Figure 2: The phase space distributions at three different positions: the entrance of ES (a), the exit of ES (c), the entrance of MS1 (d), (b) is the local zoom of (a).

The ES is located in the descending part of the dispersion to fulfil the Hardt condition [3]. At the entrance of ES, $D_n \approx 1.2\ m^{0.5}$, $D_n' \approx 0.45\ m^{0.5}$, when the chromaticity value is -0.7, the Hardt condition is fulfilled. Figure 3 shows the separatrix at the entrance of ES under three different momentum spread -0.1% (red), 0 (blue), and 0.1% (green). It is apparent that the separatrix of extraction for three conditions are overlapping, which means the Hardt condition is fulfilled very well.

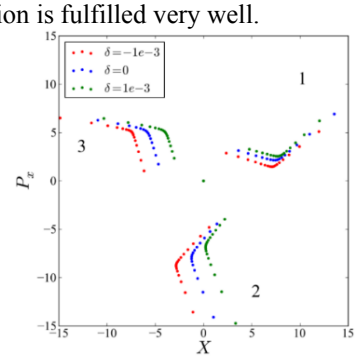

Figure 3: The separatrix under three momentum spread and with the Hardt condition fulfilled.

We calculated the trajectories of last three turns of the particle with the maximum spiral step before it enters the electrostatic septum, and the extraction trajectory together, which are shown in Fig.4. The original point of the trajectories is the entrance of ES. The maximum position of the extraction trajectory appears at the focusing quadrupole between ES and MS1, so a large bore quadrupole is used at this position.

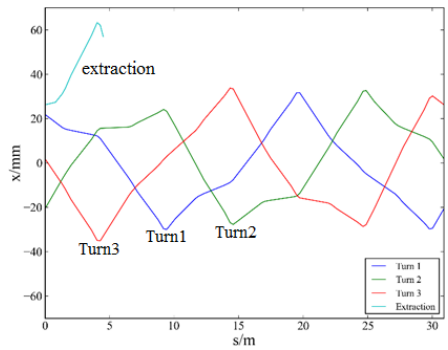

Figure 4: The last three turns before entering the electrostatic septum and the extraction trajectory.

RF-KNOCK OUT

For XiPAF, the RF-Knock Out slow extraction method is used to obtain the beam current for 1~10 s. The circulating particles continue to be extracted from the inside of the separatrix to its outside by using the constant separatrix and transverse RF field. To have a perturbation resonant with the particle, the frequency of the transverse RF field should be matched with that of the betatron oscillation.

A C++ code Li-Tracker is written to simulate the RF-KO slow extraction process, which including all kinds of elements in XiPAF synchrotron, and it's a multi-particles tracking program. Due to the limitation of calculation time, in our simulation the extraction time 0.01 s has been used for the calculation, it is about 60000 turns. The phase space distribution is shown in Fig.5, 18000 particles and 60000 turns are used in this simulation. From the turn 0 the sextupoles SR1 and SR2 are ramped linearly in 6000 turns; and then the RF-KO is turned on in the next 54000 turns while the magnetic elements keep constant.

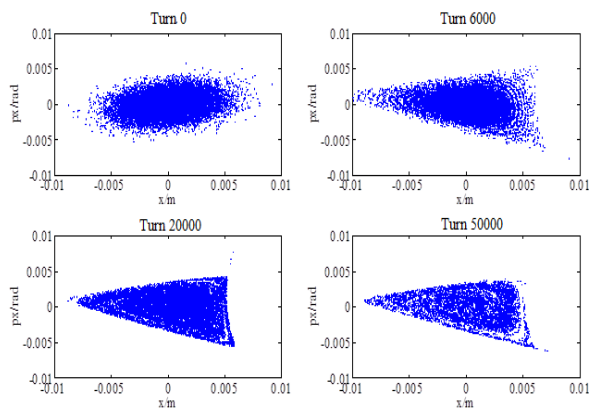

Figure 5: The phase distribution during extraction.

ISBN 978-3-95450-185-4

For the RF-KO slow extraction method, the parameters of frequency modulation (FM) and amplitude modulation (AM) are very important. In our calculations, the dual FM method as described in Ref [4] and AM function in Ref [5] are used in order to make the extraction spill more uniform. The optimized parameters including the center frequency, the bandwidth, the AM parameters and so on, have been obtained and listed in Table 3.

Table 3: The Optimized Parameters of Dual FM and AM

Parameter	Value	Vale
Extraction energy (MeV)	60	230
Center frequency (MHz)	2.24	3.91
Bandwidth (kHz)	22	37
Repetition frequency (kHz)	5	5
AM parameter r_0^2	50×10^{-6}	32×10^{-6}
AM parameter σ_0^2	32×10^{-6}	6×10^{-6}
τ_{prac}/τ_{ext}	1.25	1.25
R_1	±17%	±20%

The 230 MeV, 0.01 s extraction spill structure and the FFT result are shown in Fig.6 under a sampling frequency of about 10 kHz. From the FFT result, we can observe the peak due to the RF-KO. In our calculations the synchrotron oscillation has not considered. In order to characterize the spill structure and to compare it, one parameter R_1, the standard deviation of the fluctuation from the analytical estimation is defined in Ref [5]. The results of R_1 is also listed in Table 3. The value of R_1 is smaller, which means that the spill is more uniform.

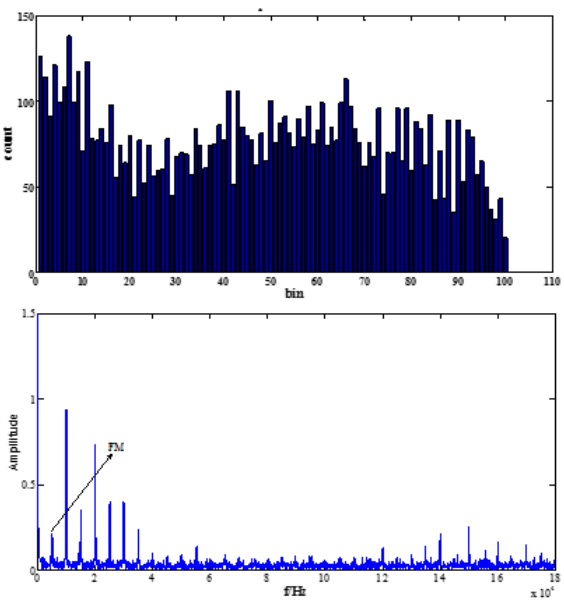

Figure 6: The extraction spill structure and FFT result.

The kick angle with the turn number is shown in Fig.7; from the figure we can see that the maximum kick angle is about 6 μrad for the extraction duration of 0.01 s and the extraction energy of 230MeV, then maximum kick angle needed for extraction time of 1 s and extraction energy of 60MeV can be derived, which is 1.1 μrad, and is 1.4 μrad for 7 MeV. With margin, 2 μrad is used for the kicker voltage calculation. A pair of plate electrodes is employed as the RF kicker, the electrodes gap is 0.11 m and the length is 0.3 m, the peak-peak voltage value is ±215 V.

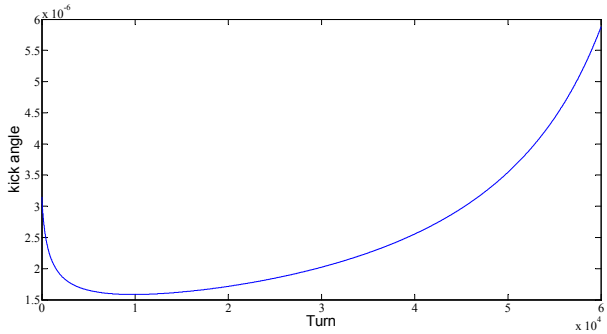

Figure 7: The kick angle vs turn number.

CONCLUSION

The third integer slow extraction with RF-KO method for XiPAF synchrotron has been described. The tracking simulation of the 3rd order resonance is done with MAD-X code, and the extraction process with RF-KO method is simulated with Li-Tracker code, and the main parameters of electrostatic septum, septum magnets, FM, AM and kicker electrodes have been listed in this paper. The parameter R_1 is ±20% for 60~230 MeV under a sampling frequency of about 10 kHz, which meets the requirement of the experimental stations.

At present, the block diagram of the RF-KO system with a complicated feedback system has been designed to keep the extracted beam current more stable, and the Code Li-Tracker is improving with the synchrotron oscillation and space charge effect are taken into account, we will report the new development in the future.

REFERENCES

[1] S.X. Zheng et al., "Design of the 230MeV proton accelerator for Xi'an Proton Application Facility", this conference, MOPR006, HB2016, Sweden.

[2] H. Grote, F. Schmidt, "The MAD-X program user's reference manual", Geneva, Switzerland, 2016.

[3] W. Hardt, "Ultraslow extraction out of LEAR (transverse aspects)", CERN Internal Note PS/DL/LEAR Note 81-6, 1981.

[4] K. Noda, T. Furukawa, et al., "Advanced RF-KO slow extraction method for the reduction of spill ripple", *Nucl. Instr. and Meth. in Physics Research A* 492, 2002, pp 253-263.

[5] T. Furukawa, K. Noda, et al., "Global spill control in RF-knockout slow extraction", *Nucl. Instr. and Meth. in Physics Research A* 522, 2004, pp 196-204.

ISBN 978-3-95450-185-4

DESIGN OF THE 230 MeV PROTON ACCELERATOR FOR XI'AN PROTON APPLICATION FACILITY

S.X. Zheng, Q.Z. Xing, X.L. Guan, H.J. Yao, C. Cheng, T.B. Du, H.Y. Zhang, G.R. Li, L. Du, R. Tang, M.W. Wang, L. Wu, Y. Yang, H.J. Zeng, Q. Zhang, Z. Yang, H.P. Jiang, C.T. Du, Q.Z. Zhang, W.H. Huang, C.X. Tang, H.B. Chen, D. Wang, X.W. Wang†, Key Laboratory of Particle & Radiation Imaging (Tsinghua University), Ministry of Education, Beijing 100084, China
also at Laboratory for Advanced Radiation Sources and Application, Tsinghua University, Beijing 100084, China
also at Department of Engineering Physics, Tsinghua University, Beijing 100084, China
Z.M. Wang, C. Zhao, B.C. Wang, Y.H. Yan, Y.P. Wang, H. Zhang, M.T. Qiu, W. Chen, State Key Laboratory of Intense Pulsed Radiation Simulation and Effect (Northwest Institute of Nuclear Technology), Xi'an, 710024, China
W.Q. Guan, Y. He, J. Li, NUCTECH Co. Ltd., Beijing 100084, China
S. Y. Lee, Indiana University, Bloomington, IN 47405 USA

Abstract

We report a design of the 230 MeV proton accelerator, the Xi'an Proton Application Facility (XiPAF), which will be located in Xi'an city, China. The facility will provide proton beam with the maximum energy of 230 MeV for the research of the single event effect. The facility, composed of a 230 MeV synchrotron, a 7 MeV H^- linac injector and two experimental stations, will provide a flux of 10^5~10^8 p/cm^2/s with the uniformity of better than 90% on the 10 cm×10 cm sample.

INTRODUCTION

To fulfil the need of the experimental simulation of the space radiation environment, especially the investigation of the single event effect, the project of Xi'an Proton Application Facility (XiPAF) is under construction in Xi'an City, China. The facility is mainly composed of a 230 MeV synchrotron and a 7 MeV H^- linac injector and two experimental stations. A proton flux of 10^5~10^8 p/cm^2/s with the uniformity of better than 90% on the 10 cm×10 cm sample is designed. Table 1 shows the parameters of the synchrotron and linac injector.

Table 1: Main Parameters of the XiPAF

Parameter	Injector	Synchrotron
Ion type	H^-	Proton
Output energy (MeV)	7	60~230
Peak current (mA)	5	
Repetition rate (Hz)	0.1~0.5	0.1~0.5
Beam pulse width	10~40 μs	1~10 s
Max. average current (nA)	100	30
Flux (p/cm^2/s) (10×10cm^2)		10^5~10^8

The schematic layout of the XiPAF Accelerator system is presented in Fig. 1. The H^- beam is produced at the ion source (IS), accelerated to 7 MeV in linac injector, and then transferred to synchrotron through Medium Energy Beam Transport (MEBT). This H^- beam is stripped into protons by carbon foil in synchrotron and it is accelerated up to 230 MeV. Then the beam is extracted to experimental station through High Energy Beam Transport (HEBT). The HEBT have two beamlines, where T2 is used for 60 to 230 MeV proton application extracted from synchrotron directly, and the T1 can degrade the proton energy from 60 MeV to 10 MeV for low energy application. The lowest extraction energy from the synchrotron is 60 MeV.

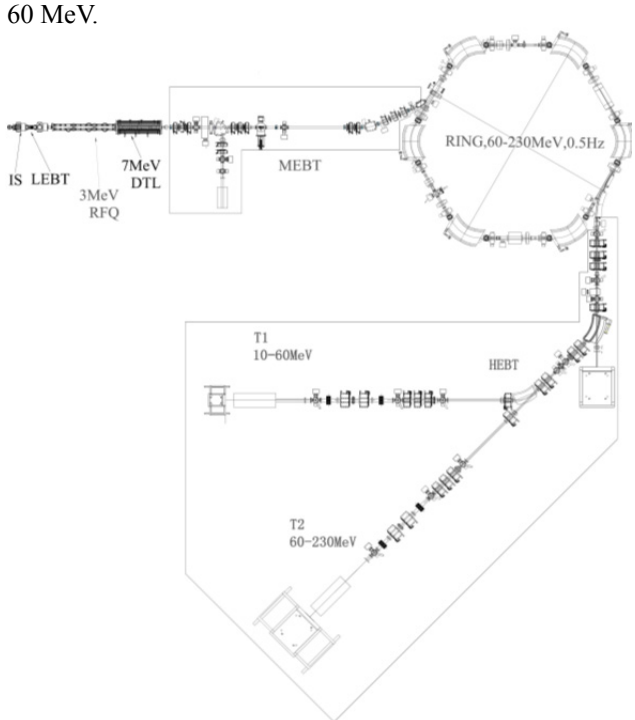

Figure 1: Layout of XiPAF accelerator system.

The main features of this accelerator are listed as follow:

- H^- injection enables transverse space painting flexibility in order to alleviate space charge effects at low energy.
- The 6-fold "Missing-dipole" FODO structure simplifies the lattice design and work point tuning.

† wangxuewu@tsinghua.edu.cn

ISBN 978-3-95450-185-4

- The magnet-alloy loaded cavity simplifies the accelerating system and provides wide beam frequency swing.
- Slow extraction with the 3rd integer resonance can provide stable, uniform and low current for proton irradiation requirement.

SYNCHROTRON

The H^- beam is striped into proton beam by carbon foil in injection system of synchrotron, then proton beam is adiabatically captured by RF bucket. The captured 7 MeV proton beam can be accelerated up-to 230 MeV in 0.5 second. The proton beam will be slow-extracted in 1 to 10 s.

Lattice Design

A 6-fold symmetric lattice is chosen for the synchrotron ring [1]. The basic lattice structure is called 'missing dipole' which is a FODO structure with one dipole is replaced by straight line. These straight line section can accommodate injection, extraction, accelerating elements. Table 2 presents the main parameters of the synchrotron lattice. The maximum magnetic field of dipole is 1.52 T at 230MeV.

Table 2: Main Parameters of the Synchrotron Lattice

Parameter	Value	Unit
Circumference	30.9	m
Dipole effective length	1.6	m
Dipole bending angle	60	degree
Dipole edge angle	30	degree
Maximum beta function(x/y)	5.7/6.0	m
Maximum dispersion	2.6	m
Tune at extraction(x/y)	1.68/1.79	
Chromaticity(x/y)	-0.2/-2.3	
Transition energy	1.64	

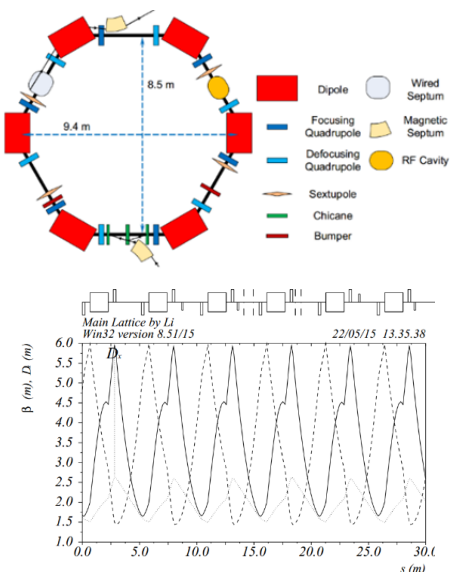

Figure 2: Layout (TOP) and twiss parameters (BOTTOM) of main ring elements.

Figure 2 shows the synchrotron layout and main parameters. The maximum beta functions are 5.9 and 6.0 meter for x and y direction separately. The base tunes are 1.68/1.79 which are chosen for the sake of 3rd integer resonated slow extraction.

Injection and Extraction System

The design intensity is 2×10^{11} proton per pulse (PPP) in synchrotron. We chose a strip injection and phase space painting method to reduce beam loss. The injection system is consisted of 3 chicane dipoles, 2 bumpers, one of injection septum magnet and one of carbon stripper. The 3 chicanes form a fixed bump closed orbit. In addition, an additional 2.4 cm bump orbit is created by 2 bumpers and restored in 30μs. The phase space painting process has been simulated, and the result shows the tune spread can be well controlled.

The 3rd integer resonance and RF-KO method are adopted for slow extraction. The extraction time can be varied from 1s to 10 s. The extraction elements consist of 4 sextupoles, 2 extraction magnet septum, an electrostatic wired septum and a RF-Knock-Out (RF-KO). The RF kicker signal is turned on to excite the 3rd integer resonate of circulating beam. A complicated feedback system will be used to keep extracted beam current stable. The detailed injection and extraction system design are reported in Ref [2] and [3] respectively.

Magnet Alloy Loaded Cavity

The magnet-alloy (MA) loaded broadband coaxial cavity system, shown in Fig. 3, is adopted due to its good frequency characteristics and high saturation flux density characteristics.

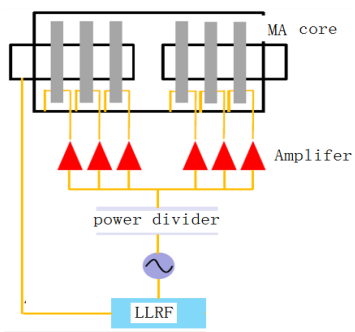

Figure 3: Layout of MA cavity system.

Table 3: Main design parameters of MA loaded cavity

Parameter	Value	Unit
Frequency	1~7	MHz
Maximum voltage	800	V
Number of ring	6	
Impedance of ring	50	Ω
Impedance of cavity	300	Ω
Size of ring	450×300×25	
Power consume	180	W/core
Length of cavity	<630	mm
Inner D of beam pipe	120	mm

ISBN 978-3-95450-185-4

There are 6 solid state amplifiers separately coupled to 6 MA rings, each ring can induce 100 V voltage with 50 Ω impedance. This topology structure uses the cavity as an RF combiner and it simplified the system structure. Table 3 presents the main parameters of the MA loaded cavity.

7 MeV H- LINAC INJECTOR

The 7 MeV linac injector [4] is composed of the 50 keV H- ion source, Low Energy Beam Transport line (LEBT), 3 MeV four-vane type Radio Frequency Quadrupole (RFQ) accelerator, 4MeV (from 3 to 7MeV) Alvarez-type Drift Tube Linac (DTL), and the corresponding RF power source system. The designed number of the accumulated protons in each pulse in the synchrotron is 2×10^{11}. We choose the injection energy of 7 MeV for both achievable particle intensity and the cost of the linac injector.

ECR Ion Source and LEBT

One 2.45GHz microwave-driven Cesium-free Electron Cyclotron Resonance (ECR) ion source has been manufactured and tested successfully for XiPAF facility by Peking University. The 12.4 mA of the H- beam current was measured by one Faraday cup after the analysing magnet with the RF power of 2.8 kW, beam pulse width of 1 ms, repetition rate of 100 Hz, extraction voltage of 50 kV. The measured normalized RMS emittance is 0.16 π mm mrad.

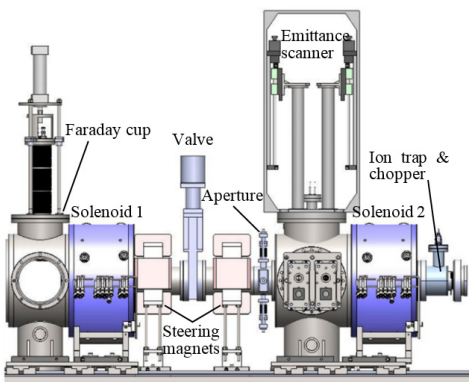

Figure 4: Layout of LEBT.

As shown in Fig.4, an adjustable aperture is exploited in the LEBT to obtain the designed current of 6 mA at the entrance of the RFQ accelerator. The matched Twiss parameters (α=1.05, β=4.94 cm/rad) can be achieved by two solenoids. The beam pulse can be shortened to 10~40 μs by one chopper between the solenoid-2 and the RFQ accelerator. The chopped particles will lose outside the RFQ cavity.

RFQ Accelerator

One 3-meter-long four-vane Radio Frequency Quadrupole (RFQ) will accelerate H- from 50 keV to 3 MeV The value of ρ/r_0 is kept to be 0.8 throughout the structure, where ρ is the transverse curvature of the vane tip and r_0 is the mean bore radius. The design result is shown in Fig. 5, with *B* is the focusing strength, *X* is the focusing parameter, *A is* the acceleration parameter, *W is* the synchronous energy, Φ_s is the synchronous phase, *m* is the modulation factor, and *a is* the minimum bore radius.

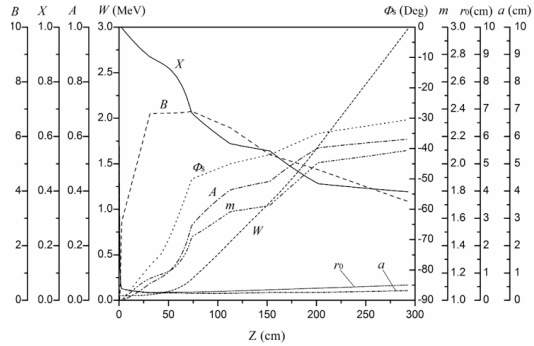

Figure 5: Parameters of RFQ vs. longitudinal position.

The length of the dipole-mode stabilizer rods is chosen to be 14.7 cm to maximize the frequency interval between the operating mode and its neighbouring dipole modes. The RF peak power of 406 kW is needed including the structure loss of 388 kW and beam power of 18 kW.

Drift Tube Linac

DTL will accelerate H- from 3 MeV to 7 MeV. Samarium-cobalt permanent magnets are adopted as the transverse focusing quadrupoles for the DTL. The field gradients are designed to be constant (84.6 T/m), except that the gradients of the first four quadrupoles are adjusted to match the RFQ output beam. The total length of the DTL is about 2.2 m and the number of the accelerating cells is 23. The RF peak power of 300 kW is needed including the structure loss of 276 kW and beam power of 24 kW.

CONCLUSIONS

A 230 MeV proton accelerator had been designed for XiPAF. The facility is suitable for wide energy proton irradiation with slow extraction from 60 to 230 MeV. The project is under construction. All accelerator sub-systems including main magnets, injection elements, extraction elements and the power supplies have completed their conceptual design and the final design is in progress. The beam commissioning will be expected at the end of 2018.

ACKNOWLEDGMENT

The authors would like to thank Prof. S.X. Peng for providing the design and experimental test result of the ECR H- source.

REFERENCES

[1] G. R. Li *et al.*, "Design of the key parameters in an advanced radiation proton synchrotron", Modern Applied Physics, 6, 2015.

[2] H. J. Yao *et al.*, "H charge exchange injection for XiPAF synchrotron", presented at HB2016, Malmo, Sweden, July 2016, paper MOPR004, this conference.

[3] H. J. Yao et al., "RF-Knockout Slow Extraction Design for XiPAF Synchrotron", presented at HB2016, Malmo, Sweden, July 2016, paper MOPR005, this conference.

ISBN 978-3-95450-185-4

[4] Q. Z. Xing et al., "Design of the 7MeV linac Injector for the 200MeV Synchrotron of the Xi'an Proton Application Facility", in *Proc. IPAC'16*, Busan, Korea, May 2016, paper MOPMW014, pp. 426-428.

ISBN 978-3-95450-185-4

COLD AND HIGH POWER TEST OF LARGE SIZE MAGNETIC ALLOY CORE FOR XiPAF'S SYNCHROTRON

G.R. Li, S.X. Zheng*, H.J. Zeng, Z. Yang, H.J. Yao, X.L. Guan, X.W. Wang, W.H. Huang,
Key Laboratory of Particle & Radiation Imaging (Tsinghua University),
Ministry of Education, Beijing 100084, China,
also at Laboratory for Advanced Radiation Sources and Application,
Tsinghua University, Beijing 100084, China,
also at Department of Engineering Physics, Tsinghua University, Beijing 100084, China

Abstract

A compact magnetic alloy (MA) loaded cavity is under development for XiPAF's synchrotron. The cavity contains 6 large size MA cores, each is independently coupled with solid state power amplifier. Two types of MA core are proposed for the project. We have developed a single core model cavity to verify the impedance model and to test the properties of MA cores under high power state. The high power test results are presented and discussed.

INTRODUCTION

Xi'an Proton Application Facility (XiPAF), under construction in Xi'an, China, is dedicated to radiation applications like proton therapy, single event effects (SEE) study [1]. XiPAF's accelerator complex is composed of a 7 MeV Linac, a compact synchrotron (7~230 MeV) and two application beam lines. The synchrotron works in slow cycling mode and can accelerate proton beam from 7 MeV to 230 MeV in 0.5 s.

We propose to use a compact MA loaded cavity for beam acceleration because: 1. MA material has the property of wide band, thus we can use a single cavity to cover the large frequency range of our machine. This property can also simplified the control system compared to ferrite loaded cavity; 2. For slow cycling operation of our machine, a voltage of several hundred volts is enough, so the cooling of MA loaded cavity would not cause serious problem.

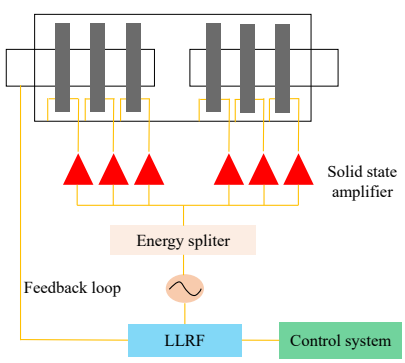

Figure 1: MA loaded RF system for XiPAF's synchroton.

The schematic design of our MA loaded cavity is shown in Fig. 1. The cavity contains 6 large size MA cores. The impedance of each core will be designed close to 50 Ω, so they can be independently coupled with solid state power amplifier without special impedance match. The main parameters of the cavity are listed in Table. 1.

Table 1: Parameters of the MA Loaded Cavity

Parameter	Value	Unit
Frequency range	1~7	MHz
Harmonic number	1	
Max. Voltage	800	V
Core number	6	
Shunt impedance per core	~80	Ω
Max. power dissipation per core	~110	W
Q value	~0.5	
Core outer diameter	450	mm
Core inner diameter	300	mm
Core thickness	25	mm

Two local company in China have provided two types of large size MA core (see Fig. 2):

- Type A: The material of ribbon is 1K107 produced by AT&M[1]. The thickness of ribbon is 18 µm. The core is solidified with epoxy resin.
- Type B: The material of ribbon is FT-3M, which is the most widely used material in this area. The thickness of ribbon is 18 µm. The core is solidified with silica gel.

We have carried out several experiments of both low power and high power to test the performance of large size MA cores.

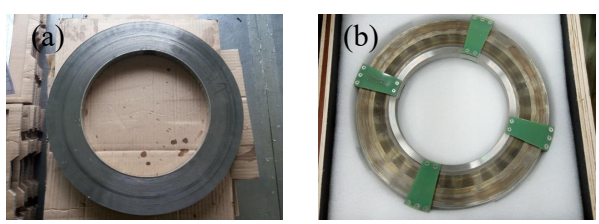

Figure 2: Large size MA cores, (a) Type A, (b) Type B.

* zhengsx@tsinghua.edu.cn

[1] http://www.atmcn.com/

ISBN 978-3-95450-185-4

RESULTS OF COLD TEST

The shunt impedance R_p of each core can be written as [2]

$$R_p = (\mu_p' Q f) t \ln\left(\frac{R_o}{R_i}\right) \quad (1)$$

$$\mu_p' = \mu_s' \left(1 + \frac{1}{Q^2}\right) \quad (2)$$

where R_o, R_i and t are the outer diameter, inner diameter and thickness of the core, Q is defined as μ_s'/μ_s'', $\mu_s' - j\mu_s''$ is the complex permeability of the material. The product $(\mu_p' Q f)$ is independent of the size of core and is used to evaluate magnetic material.

We have measured the complex impedance of the MA cores through a vector network analyzer and deduced their $(\mu_p' Q f)$ and Q. The measured results are shown in Fig. 3. Cold test results show that 1K107 and FT-3M material have similar performance. The cores made of FT-3M have better $(\mu_p' Q f)$ when the frequency reaches several MHz. Their $(\mu_p' Q f)$ ranges from 4 GHz to 9 GHz in the frequency range of 1~7 MHz. With the size of the core, the shunt impedance ranges from about 50 Ω to 120 Ω in the frequency range of 1~7 MHz. A single core model cavity is built to further

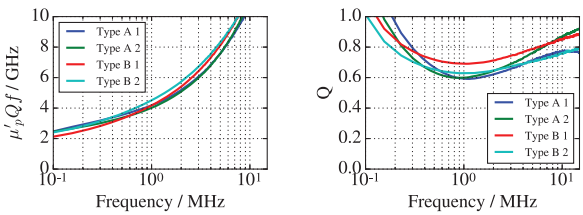

Figure 3: $(\mu_p' Q f)$ and Q value of large size MA core.

Figure 4: Single core test cavity.

test the MA cores (see Fig. 4). A tunable capacitance is installed on the cavity to adjust the resonant frequency. We measure the impedance through the couple loop as shown in Fig. 5. The measured results show the cavity has good wide band property, the standing wave ratio stays below 1.7 in the frequency range of 1~7 MHz. However, the measured result is not well consistent with the theory result. Here, the theory complex impedance is calculated as $Z_{\text{core}} // \frac{1}{j\omega C}$, where Z_{core} is the measured impedance of MA core without cavity. We infer that the distributed inductance is the main reason of the difference, because the image part of measured impedance grows much faster than the image part of theory impedance.

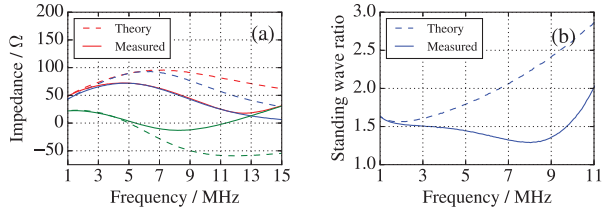

Figure 5: Imedance and standing wave ratio measured through the couple loop. In (a), the blue, green and red lines indicate the real part, image part and absolute value of complex impedance, the dashed lines stand for theory result, the solid lines stand for measured result.

RESULTS OF HIGH POWER TEST

We have carried some high power experiments to test the shunt impedance of MA core under strong field and high temperature. The shunt impedance of MA core is estimated by

$$R_p = \frac{V_C^2}{2P_{\text{in}}} \quad (3)$$

where V_C is the voltage across the capacitance, P_{in} is the input power from amplifier. A thermal camera is used to monitor the temperature distribution on the surface of MA core.

Instantaneous Experiment

The shunt impedance under strong field is evaluated through instantaneous experiment. The input power is ON only for a short time to avoid significant temperature rise. The test result is shown in Fig. 6. The maximum input power reaches about 2000 W, correspond to a average energy density of 1.4 W/cc. For both types of MA core, there is no sign shows the shunt impedance will decrease until this energy density.

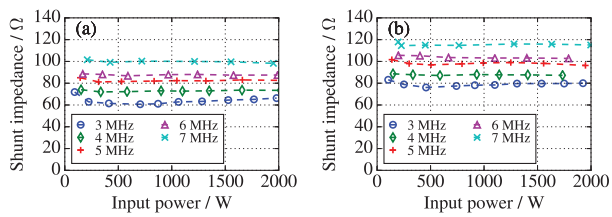

Figure 6: Shunt impedance of large size MA core under different input power, (a) Type A, (b) Type B.

Continuous Experiment

The MA cores are coupled with continuous 3 MHz RF power without special cooling to test their shunt impedance under high temperature.

For type A core, local damage happened when the input power is 800 W and the maximum surface temperature

ISBN 978-3-95450-185-4

reaches 240 °C. The measured shunt impedance decrease slightly as shown in Fig. 7. There is epoxy resin leaking outside the core in some spots (see Fig. 8). The spots locate at the splints used to support the core which have made the heat dissipation more difficult. The local temperature should be higher than 240 °C that can not be observed by thermal camera. After the damage happened, we conducted high power test with input power of 300 W and 500 W. The measured shunt impedance reaches a balanced value after the temperature is stable and does not behave significant decrease compared with instantaneous test result. Local epoxy resin leakage seems not causing serious problem for the shunt impedance.

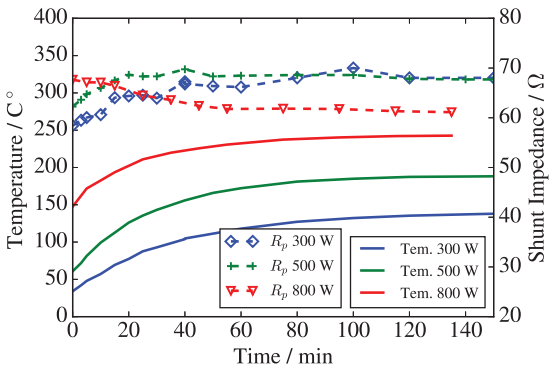

Figure 7: Long time high power test result of type A core. The 300 W and 500 W tests are conducted after 800 W test.

For type B core, there is also damage when input power reaches 800 W, but no shunt impedance decrease as shown in Fig. 9. The damage way is different from type A core. There is local swell under the splint (see Fig. 10). The swell disappears after the core gets cooled. Under same input power, type B core's maximum surface temperature is a little higher than type B core's. We think this is due to the worse thermal conductivity of silica gel than epoxy resin.

ACKNOWLEDGEMENT

We would like to acknowledge H. Sun, H. Shi of IHEP and Z. Xu of IMP for their help on the design of the MA loaded cavity and MA cores test.

SUMMARY

Two types of large size MA core have been tested for XiPAF's MA loaded cavity project. Cold test shows the performance of 1K107 and FT-3M material are similar. Instantaneous high power test shows both type of MA core can sustain a average energy density of about 1.4 W/cc. In long time high power experiment, high temperature has caused local epoxy resin leakage for type A core (~240 °C) and slight shunt impedance decrease. For type B core, there is local swell under temperature ~260 °C, but no significant shunt

Figure 8: Local damage of type A MA core.

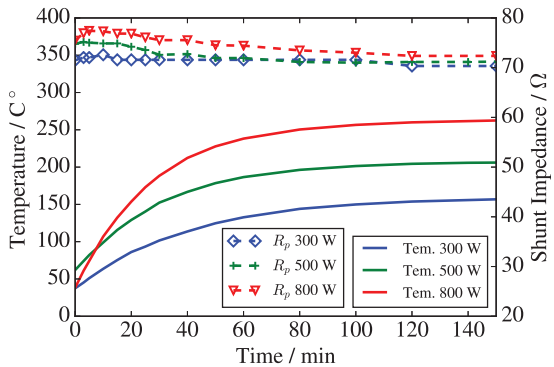

Figure 9: Long time high power test result of type B core.

Figure 10: Local damage of type B MA core.

impedance decrease. It seems that the difference comes from the material used for solidification.Silica gel has worse thermal conductivity, but it is more stable than epoxy resin under high temperature.

REFERENCES

[1] G.R. Li *et al.*, "Design of the key parameter in an advanced radiation proton synchrotron", *Modern Applied Physics* 6, 2015.

[2] H. Klingbeil, "Ferrite cavities", *arXiv:* 1201.1154v1, 5 Jan 2012.

ISBN 978-3-95450-185-4

PRESSURE PROFILES CALCULATION FOR THE CSRm AND BRing

P. Li†, J.C. Yang, Y.J. Yuan, J.C. Wang, J. Meng, C. Luo, Z. Chai, R.S. Mao, M. Li, W.L. Li, Z.Q. Dong, W.H. Zheng, X.C. Kang, S.P. Li, Institute of Modern Physics, Chinese Academy of Sciences, Lanzhou 730000, China

Abstract

A new large scale accelerator facility is being designed by Institute of Modern Physics (IMP) Lanzhou, which is named as the High Intensity heavy-ion Accelerator Facility (HIAF). This project consists of ion sources, Linac accelerator, synchrotrons (BRing) and several experimental terminals. During the operation of Bring, the heavy ion beams will be easily lost at the vacuum chamber along the BRing when it is used to accumulate intermediate charge state particles. The vacuum pressure bump due to the ion-induced desorption in turn leads to an increase in beam loss rate. In order to accumulate the beams to higher intensity to fulfil the requirements of physics experiments and for better understanding of the dynamic vacuum pressure caused by the beam loss, a dynamic vacuum pressure simulation program has been developed. Vacuum pressure profiles are calculated and compared with the measured data based on the current synchrotron (CSRm). Then the static vacuum pressure profiles of the BRing and one type of pump which will be used in the BRing are introduced in this paper.

INTRODUCTION

The HIAF project consists of ion sources, Linac accelerator, synchrotrons and several experimental terminals. The Superconducting Electron-Cyclotron-Resonance ion source (SECR) is used to provide highly charged ion beams, and the Lanzhou Intense Proton Source (LIPS) is used to provide H_2^+ beam. The superconducting ion Linac accelerator (iLinac) is designed to accelerate ions with the charge-mass ratio Z/A=1/7 (e.g. $^{238}U^{34+}$) to the energy of 17 MeV/u. Ions provided by iLinac will be cooled, accumulated and accelerated to the required intensity and energy (up to 1.4×10^{11} and 800 MeV/u of $^{238}U^{34+}$) in the Booster Ring (BRing), then fast extracted and transferred either to the external targets or the Spectrometer Ring (SRing). As a key part of the HIAF complex, SRing is designed as a multifunction experimental storage ring. A TOF detector system will be installed for nuclei mass measurements with isochronous mode. An electron target with ultra-low temperature electron beam will be built for Dielectronic Recombination (DR) experiments. Both stochastic cooling and electron cooling systems are considered to be equipped in order to provide high quality beams for experiments and compensate energy losses of internal target experiments. MRing is used for the ion-ion merging [1]. The layout of the HIAF project is shown in Fig. 1.

† LIPENG@IMPCAS.AC.CN

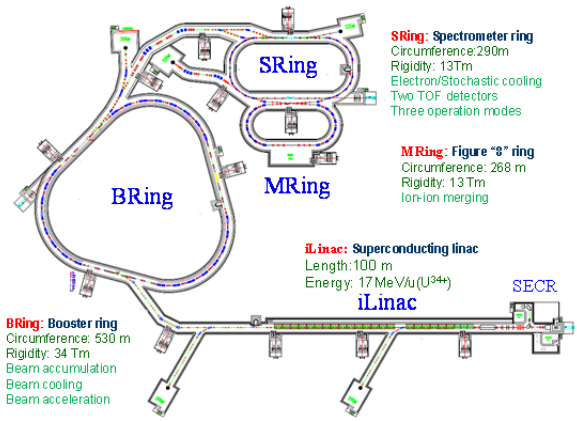

Figure 1: Layout of HIAF project.

CSRm VACUUM PRESSURE PROFILE

Static Pressure Profiles

The HIRFL-CSR complex consists of the main cooler storage ring (CSRm), Radioactive Ion Beam line (RIB) production and transfer line two (RIBLL2), experimental storage ring (CSRe), and experimental stations. The two existing cyclotrons, the Sector Focus Cyclotron and Separated Sector Cyclotron, at the Heavy Ion Research Facility in Lanzhou (HIRFL) are used as the injector system. The heavy ion beams from HIRFL are injected into the CSRm, then accumulated, electron cooled, and accelerated, before being extracted to the CSRe for internal target experiments and other physics experiments [2].

CSRm is a racetrack shape synchrotron that consists of four arc sections with the circumferences of 161.00 m. Each arc section is composed of four dipoles, five focusing quadrupoles, and three defocusing quadrupoles.

The total volume of the CSRm vacuum system is about 7200 L and the total inner surface is about 160 m^2 (not including the equipment inside the vacuum system). Sputter ion pumps (SIP) and titanium sublimation pumps (TSP) are selected as the main pumps, which are distributed in about 4 m along the rings according to the calculation. Sputter ion pumps with pumping speeds of 200~400 l/s remove non-getterable gases such as methane and argon. Titanium sublimation pumps have a high capacity for hydrogen at very low pressure, where the residual gas is mainly H_2 (90%). The pumps have an area of 5000 cm^2 of sublimated titanium and a pumping speed of approximately 2000 l/s for active gases [3].

The dynamic vacuum pressure calculation method which developed from the VAKDYN code [4] is implemented to calculate the equilibrium pressure profile for the CSRm. The newly developed simulation code is named as HIAF-DYSD. For the computation of the

ISBN 978-3-95450-185-4

CSRm pressure profiles, the following parameters are used:

1. Along the CSRm, the beam pipe temperature is T=293 K.
2. There are two types of SIP and TSP at the CSRm, with the pumping speed of SIP1=200 l/s, SIP2=300 l/s, TSP1=1000 l/s and TSP2=2000 l/s for the hydrogen.
3. Operational experiences of many particle accelerators in the world suggests that, after the pretreatment mentioned above, the outgassing rate of the materials should be lower than $5*10^{-13}$ mbar*l/(s*cm^2) [3]. In this paper, the outgassing rate for hydrogen is assumed to be $7*10^{-13}$ mbar*l/(s*cm^2).

According the parameters mentioned above, the vacuum pressure profile for the CSRm is calculated and shown in the Fig. 2. With 8 gauges installed in the CSRm, measured vacuum pressure data was recorded and compared with the calculation result.

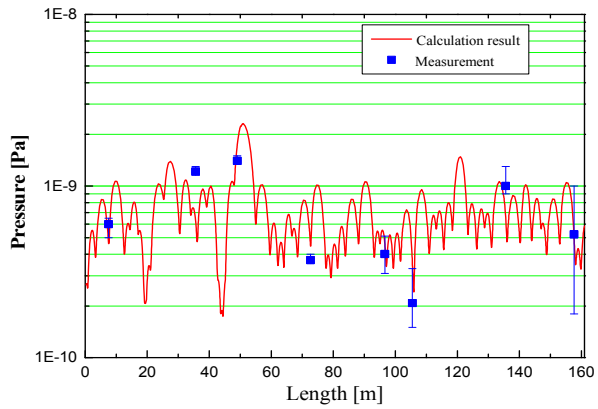

Figure 2: Static pressure profile for CSRm.

In the code VAKDYN and HIAF-DYSD, the Crank-Nicholson method is used to solve the differential equation that describes the pressure profile [4]. Another program (Bolide) which provided by Alexander Smirnov from Joint Institute for Nuclear Research (Dubna, Russia) is adopted to calculate the pressure profiles to do the comparison. The simulation result for the CSRm by using his code can be seen in Fig. 3.

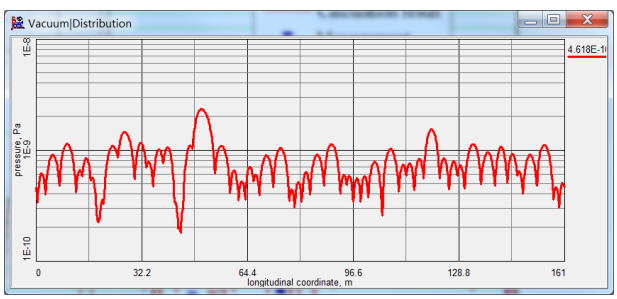

Figure 3: Static pressure profile for CSRm using Bolide.

According to the simulation result, the beam intensity is too low to make the vacuum pressure bump too much under the condition of high pump speed in the CSRm.

Dynamic Pressure Profiles

During the operation of heavy ion accelerator, the heavy ion beams are easily lost at the vacuum chamber along the ring when it is used to accumulate intermediate charge state particles. The vacuum pressure bump due to the ion-induced desorption in turn leads to an increase in beam loss rate [5]. The average dynamic pressure is calculated with the assumption that the heavy ion beams are lost continuously around the CSRm ring.

The uranium beam $^{238}U^{32+}$ that was accumulated in the CSRm in 2011 is chosen as the reference ion to simulate the beam loss distribution with the machine operation parameters. The desorption rate is assumed $2*10^4$ molec./ion as the input parameters for the ion-induced desorption part of the outgassing of the vacuum chamber walls coming from Lianc3 at CERN [6]. For the uranium beam, the number of the lost ions is $2*10^8$ ion/s. With the total surface 160 m^2, the total dynamic outgassing rate is estimated to be about $1*10^{-13}$ mbar*l/(s*cm^2). Dynamic pressure simulation for the hydrogen in the CSRm can be seen in Fig. 4.

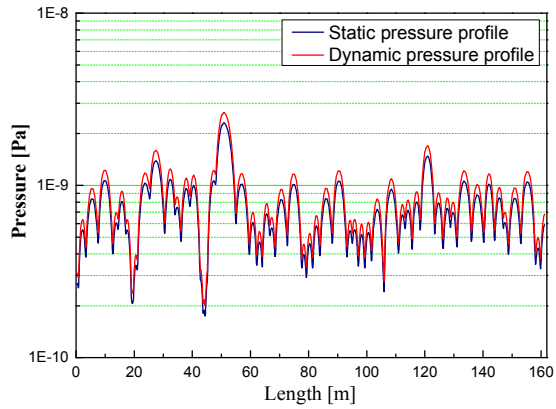

Figure 4: Dynamic pressure simulation for the CSRm.

BRing VACUUM PRESSURE PROFILE

Static Pressure Profiles

BRing is used to accumulate and accelerate ions provided by iLinac up to high intensities and energies. A two-plane painting injection system, which means that ions can be injected both in horizontal and vertical phase space simultaneously, is designed in order to get highly accumulation gain factor. Both fast extraction and slow extraction systems are equipped in BRing, in order to deliver ion beam to targets or experimental terminals.

The Booster Ring has a threefold- and mirror-symmetric lattice over its circumference of 530 m. Each super period consist of 8 DF structure arc and FODO straight sections. Sputter ion pumps (SIP) and titanium sublimation pumps (TSP) are also selected as the main pumps. The space between two dipoles is only 600 mm and not long enough to install normal TSP, therefore, a new type of pump NEXTorr will be installed in the limited space.

ISBN 978-3-95450-185-4

The NEXTorr D 2000-10 is an extremely compact pump which integrates sputter ion pump and NEG pump technologies with larger pumping speed (2000 L/s) and capacity to sorb gases. The getter cartridge is made of porous sintered getter disks stacked in a highly efficient gas trapping structure featuring pumping speed in excess of 2000 l/s (H2). The cartridge is integrated into a CF 100 flange containing heating elements for the getter activation [7].

With the defined pumping speed of TSP, SIP and NEXTorr, the static pressure profiles of BRing with 4 period sections can be seen in Fig. 5.

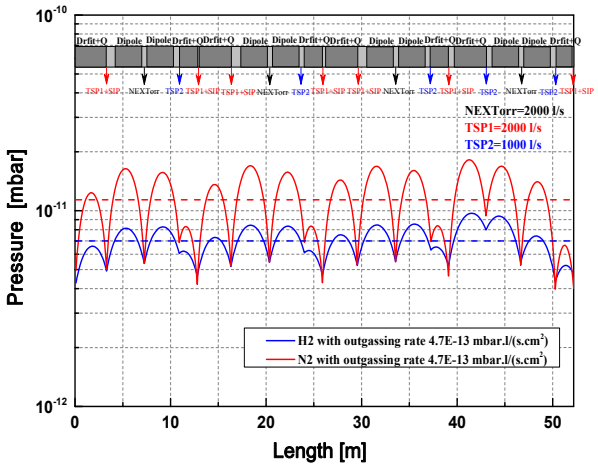

Figure 5: Static pressure profile for 50m part in BRing.

Setup to Measure Ion Induced Desorption Rate

The effect of ion-induced molecular desorption significantly influences the operation of low charge-state heavy ion accelerators and has an important impact on the design of future machines [8]. Therefore, an experimental setup to measure the ion induced desorption rate is designed and installed at the CSRm. Fig. 6 shows the layout of this setup.

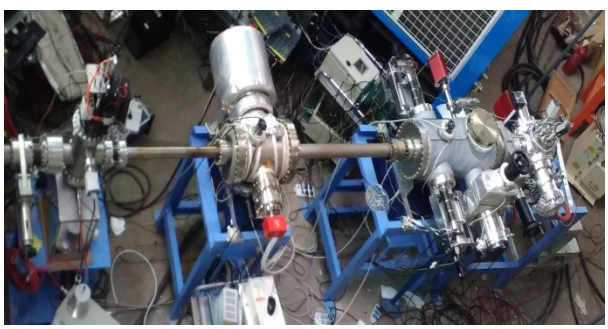

Figure 6: The layout of experimental setup.

This setup consists of three chambers: first chamber which installed an Integrating Current Transformer (ICT), Al_2O_3 fluorescence screen is used to measure the beam current and align the incoming beam; the second chamber which installed a TSP, SIP and NEXTorr is used to pump out the desorption gases; the experimental chamber is equipped with a pressure (extractor) gauge and a residual gas analyzer (RGA) to measure the total pressure increase and the partial pressure distribution during ion bombardment.

More beam test will be conducted in this setup to measure the ion induced desorption rate of different materials in the future.

CONCLUSION

The vacuum pressure profiles for the CSRm and BRing have been calculated by using the newly developed code. An experimental setup has been installed at the CSRm and will measure the ion beam induced desorption rate in the near future. Based on the simulation results and measurement data, the collimation system for the BRing is under designing.

ACKNOWLEDGEMENT

We thank Dr. Alexander Smirnov for providing the dynamic vacuum simulation code to verify the code HIAFDYSD.

We thank Dr. Peter Spiller (GSI) for providing P. L. an opportunity to work at GSI to learn the collimation. We also thank Dr. Lars Bozyk (GSI) and Dr. Carsten Omet (GSI) for giving P. L. much help on the beam simulation code. Special thanks to Dr. Lars Bozyk for his directions on collimator design and help during the prototype test experiment.

REFERENCES

[1] HIAF Conceptual Design Report, unpublished.

[2] Peng Li *et al.*, “Beam loss distribution calculation and collimation efficiency simulation of a cooler storage ring in a heavy ion research facility”, *Phys. Rev. ST Accel. Beams*, vol. 17, p. 084201, 2014.

[3] X.T. Yang *et al.*, “The ultra-high vacuum system of HIRFL-CSR”, *Vacuum*, vol. 61, p. 55, 2001.

[4] V. Ziemann., “Vakdyn, a program to calculate time dependent pressure profiles”, *Vacuum*, vol. 81, p. 886, 2007.

[5] P. Spiller et al, “Optimization of the SIS100 Lattice and a Dedicated Collimation System for Ionisation Losses”, in Proc. 33rd ICFA Advanced Beam Dynamics Workshop on High Intensity and High Brightness Hadron Beams, Bensheim, Germany, 2004 , pp. 40–44.

[6] E. Mahner *et al.*, “Ion-stimulated gas desorption yields of electropolished, chemically etched, and coated (Au, Ag, Pd, TiZrV) stainless steel vacuum chambers and St707 getter strips irradiated with 4.2 MeV/u lead ions”, *Phys. Rev. ST Accel. Beams*, vol. 8, p. 053201, 2005.

[7] NEXTorr User manual. https://www.saesgetters.com/products/nextorr-pumps

[8] E. Mahner et al., “Heavy-ion induced desorption yields of cryogenic surfaces bombarded with 4.2 MeV/u lead ions”, Phys. Rev. ST Accel. Beams, vol. 14, p. 050102, 2011.

ISBN 978-3-95450-185-4

TRANSVERSE BEAM SPLITTING MADE OPERATIONAL: RECENT PROGRESS OF THE MULTI-TURN EXTRACTION AT THE CERN PROTON SYNCHROTRON

A. Huschauer*, J. Borburgh, S. Damjanovic, S. S. Gilardoni, M. Giovannozzi, M. Hourican, K. Kahle, G. Le Godec, O. Michels, G. Sterbini, CERN, Geneva, Switzerland
C. Hernalsteens, Ion Beam Applications, Louvain-la-Neuve, Belgium

Abstract

Following a successful commissioning period, the Multi-Turn Extraction (MTE) at the CERN Proton Synchrotron (PS) has been applied for the fixed-target physics programme at the Super Proton Synchrotron (SPS) since September 2015. This exceptional extraction technique was proposed to replace the long-serving Continuous Transfer (CT) extraction, which has the drawback of inducing high activation in the ring. MTE exploits the principles of non-linear beam dynamics to perform loss-free beam splitting in the horizontal phase space. Over multiple turns, the resulting beamlets are then transferred to the downstream accelerator. The operational deployment of MTE was rendered possible by the full understanding and mitigation of different hardware limitations and by redesigning the extraction trajectories and non-linear optics, which was required due to the installation of a dummy septum to reduce the activation of the magnetic extraction septum. The results of the related experimental and simulation studies, a summary of the 2015 performance analysis, as well as more recent performance improvements are presented in this paper.

INTRODUCTION

To provide high-intensity beams for fixed target physics at the SPS, the longitudinal structure delivered by the PS has to comply with certain requirements. In order to reduce beam loading and to provide an almost continuous spill towards the experimental facilities, uniform filling of the SPS is desired. Considering that the length of the SPS is about eleven times the circumference of the PS, and that a gap for the rise time of the SPS kickers is needed, the non-resonant CT process was proposed in 1973 [1]. This extraction technique, which occurs over five turns at 14 GeV/c, allows to optimize the duty cycle as only two subsequent extractions from the PS are necessary. On the downside, the CT extraction comes with the major drawback of significant beam loss occurring at multiple locations around the ring [2], leading to high dose to personnel during accelerator repair and maintenance as well as to long cool down times.

Therefore, the MTE technique was proposed to replace the CT process in 2001 [3]. MTE is a resonant extraction mechanism, which exploits advanced concepts of non-linear beam dynamics and applies a fourth order stable resonance to perform beam splitting in the horizontal phase space. The resulting beamlets - one core and four islands - are then extracted over five turns.

Due to the complexity of the MTE scheme, its operational implementation has had to overcome many challenges. In 2010, about one month of operational experience could be gathered with this novel technique, and two major issues were identified [4]:

(1) significant fluctuations in the efficiency of the transverse splitting, the losses at extraction and the trajectories in the transfer lines, and
(2) unacceptably high radioactive activation of the magnetic extraction septum (SMH16).

In order to overcome the second problem, a so-called dummy septum (TPS15), i.e. a passive absorber to shield SMH16, was developed and installed in straight section (SS) 15 of the PS during the Long Shutdown 1 (LS1) between 2013 and 2014 [5]. A certain fraction of the losses during the extraction is intrinsic to the process itself and the debunched longitudinal structure of the beam: during the rise time of the fast kickers, the continuous beam is swept from the internal to the external side of SMH16, causing unavoidable beam loss. Using TPS15, the activation of SMH16 can be reduced by relocating these losses from SS16 to the well-shielded SS15. It was only after the installation of this device that the MTE commissioning could be resumed.

In this paper, several experimental and simulation studies are presented, which allowed to increase the understanding of the MTE process and eventually led to the implementation of appropriate measures to overcome the two aforementioned problems. As a result of these studies, the MTE process was operationally deployed and has been used to deliver high-intensity beams to the SPS as of September 2015. Since then, it has successfully replaced the CT extraction [6].

Furthermore, an analysis of the MTE performance in 2015 and recent operational improvements, which aim at increasing the robustness of this extraction technique, are discussed.

PERIODIC OSCILLATIONS OF THE SPLITTING EFFICIENCY

The efficiency of the transverse splitting is the natural figure-of-merit of the MTE performance and is defined as

$$\eta_{\mathrm{MTE}} = \frac{\langle I_{\mathrm{Island}} \rangle}{I_{\mathrm{Total}}}, \qquad (1)$$

where $\langle I_{\mathrm{Island}} \rangle$ and I_{Total} stand for the average intensity in each island and the total beam intensity, respectively. The

* alexander.huschauer@cern.ch

ISBN 978-3-95450-185-4

nominal efficiency is 20%, corresponding to an equal beam sharing between islands and core. One of the challenges of working with transversely split beams is the fact that it is difficult to directly measure the locations of the various beamlets in the phase space. Therefore, η_{MTE} is inferred from phase space projections, which are obtained by using horizontal wire scanners (WSs).

Figure 1 shows the time evolution of several measured horizontal profiles. Clear oscillations of the intensities captured in the various beamlets are observed, with oscillation periods in the order of tens of minutes. This phenomenon caused cycle-by-cycle variations of η_{MTE} and, therefore, significant deviations from the minimum acceptable value of 19% set by the SPS.

Based on an extensive measurement campaign and subsequent simulation studies, the splitting process was understood to be significantly perturbed by a low-frequency modulation of the tune. The observed oscillations were actually caused by a current ripple introduced by the switch-mode power converters used to power the different circuits of the Pole-Face Windings (PFW), which are special auxiliary windings used to control transverse tunes and linear chromaticities [7]. The current ripple at the intrinsic frequency of these power converters of 5 kHz was found to be larger than expected and, more importantly, the lack of synchronization of the clocks of the different power converters resulted in a modulation of the tune at 5 kHz with varying amplitude in time. Figure 2 shows the excellent agreement between the time evolution of the measured profile amplitude of the outermost island (see Fig. 1) and the amplitude of the 5 kHz component of the PFW current.

Following a hardware intervention to reduce the current ripple at 5 kHz, the fluctuation of η_{MTE} was significantly improved. This achievement, which was the prerequisite to again transfer MTE beams to the SPS, is also visualized in Fig. 2, where the intensity of the different beamlets measured with a WS is shown to be constant in time.

By means of time-dependent 6D simulations with the PyORBIT code [8] - using PTC [9] as underlying tracking code - the effect of a tune modulation at 5 kHz on the efficiency of the transverse splitting was investigated. Therefore, the multipole elements required to perform the horizontal splitting, i.e. dedicated sextupole and octupole magnets, were programmed according to the operationally used values and the horizontal tune was constantly increased over 50×10^3 turns to cross the resonance and perform the transverse splitting. In addition, a 5 kHz tune modulation corresponding to the maximum measured ripple amplitude of the PFW circuits was included in the simulations. In Fig. 3, the resulting topology of the horizontal phase space is compared to the case

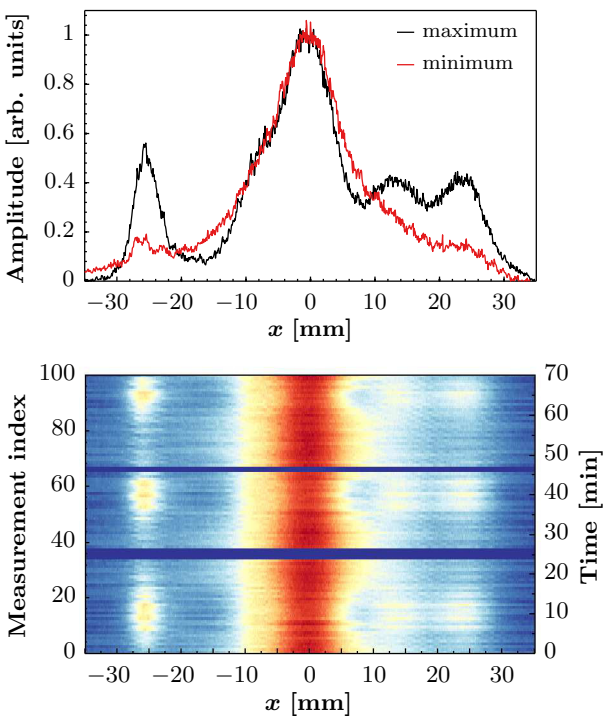

Figure 1: Top: Comparison between good and bad splitting efficiency based on measured horizontal profiles. Bottom: Waterfall representation of multiple measured horizontal profiles, with the colour scale corresponding to the amplitude of the data shown in the image at the top. Each measurement was recorded on a different cycle and clear oscillations of the beamlets' intensities are visible.

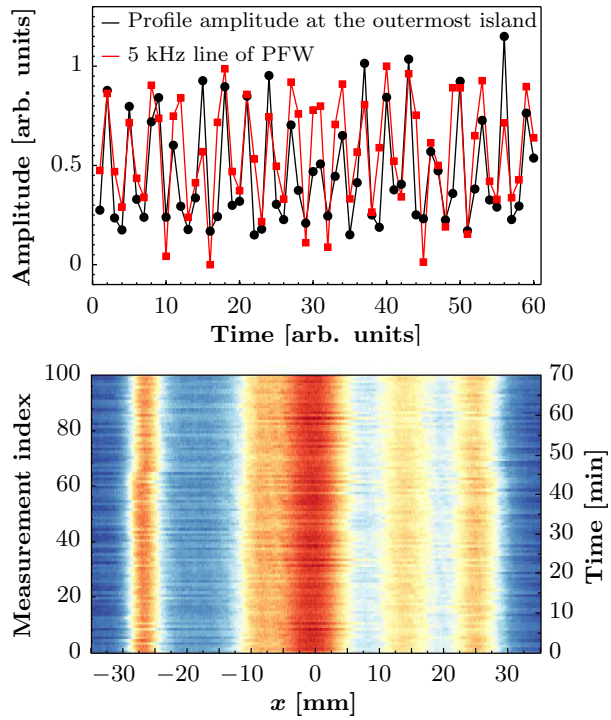

Figure 2: Top: Comparison between the time evolutions of the measured profile amplitude of the outermost island and the amplitude of the 5 kHz current ripple of the PFW. Bottom: Waterfall representation of multiple measured horizontal profiles after an intervention aimed at damping the PFW current ripple at 5 kHz. A significant improvement with respect to the measurements shown in Fig. 1 is clearly visible.

ISBN 978-3-95450-185-4

without any tune ripple. Due to the absence of the transverse damper, which is used to horizontally excite the beam for about 14×10^3 turns (the PS revolution period corresponds to 2.1 µs) after the crossing of the fourth order resonance at a frequency close to the resonant tune frequency to improve the trapping probability into the stable islands, simulations without any ripple show an efficiency of only 14%. However, similar experimental results of η_{MTE} were achieved without using the transverse damper, which highlights the very good capabilities of the non-linear model of the PS. Furthermore, a tune ripple was found to severely affect the splitting process, leading to a reduction of η_{MTE} by more than 1% for the chosen parameters.

Additional simulations, whose results are summarized in Fig. 4, revealed that the splitting efficiency is even more severely affected by frequencies lower than 5 kHz. For higher frequencies, however, the impact on the splitting was found to be less important. Furthermore, the secondary oscillation frequencies of the particles close to the stable fixed points (SFPs) inside the islands were understood to be in the low-kHz regime. Therefore, it was concluded that the depopulation of the islands in the presence of a low-frequency tune ripple occurs due to an overlap of the external excitation frequency with the particles' natural frequency of motion during the splitting process.

Based on the results of the presented studies, the feasibility of synchronizing the different power converters and of moving their switching frequencies to higher values are currently being investigated.

IMPROVED NON-LINEAR EXTRACTION OPTICS

Subsequent to the successful splitting in the horizontal phase space, the beamlets have to be rotated in order to correctly position them at SMH16. The results of the previously discussed time-dependent simulations revealed that the operationally used rotation process occurred very quickly and, therefore, non-adiabatically. Eventually, this results in filamentation and emittance blow-up, as the particles captured inside the islands are not able to follow the rapid motion of the SFPs (see Fig. 5).

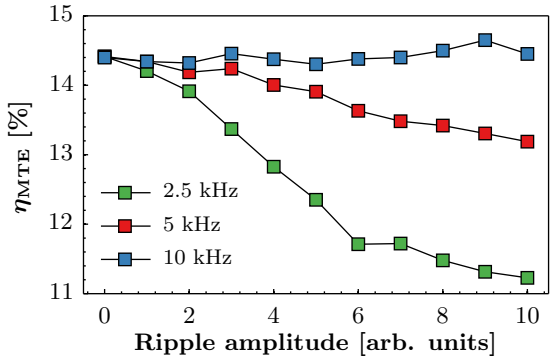

Figure 4: Dependency of the splitting efficiency on the frequency and amplitude of the external perturbation.

Further simulation studies with PTC led to the understanding that the surface of the islands can be reduced by properly choosing the multipolar configuration. Nevertheless, it has to be considered that any reduction of the surface is always accompanied by a certain probability of de-trapping [10]. This surface reduction in combination with the intended adiabatic rotation can eventually be achieved by acting either on the sextupolar or the octupolar component of the magnetic field. As acting on the octupolar component is accompanied by a significant change of the amplitude of the SFPs in the islands, it was decided to slowly adapt the sextupolar component to perform an appropriate rotation.

The results of simulations with an improved multipolar configuration are shown in Fig. 6. During the rotation, the islands follow the movement of the SFPs and slowly adapt to the new configuration. Thereby, they are elongated and the external one is reduced in horizontal size, which provides additional margin for the proper extraction process, as the clearance between the beam and the blade of the extraction

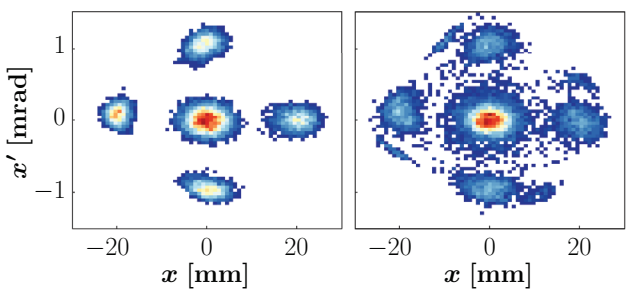

Figure 3: Simulated horizontal phase space portraits at the end of the splitting process in the absence of a tune ripple (left) and with a ripple amplitude corresponding to the maximum measured current ripple on the PFW circuits (right). The efficiency of the splitting process is clearly reduced in the latter case.

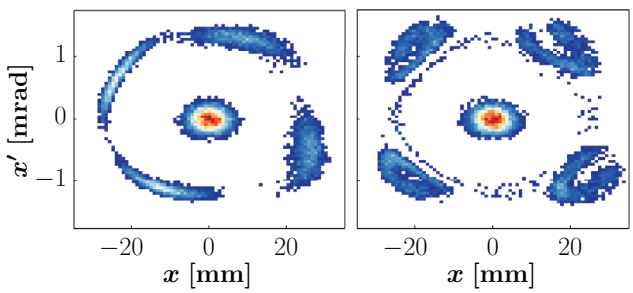

Figure 5: Simulated horizontal phase space portraits during a non-adiabatic final rotation. Once the beamlets are sufficiently separated (see Fig. 3), the rotation occurs within 2000 turns. An intermediate situation after 1000 turns is shown on the left and the phase space on the right corresponds to the end of the rotation process.

ISBN 978-3-95450-185-4

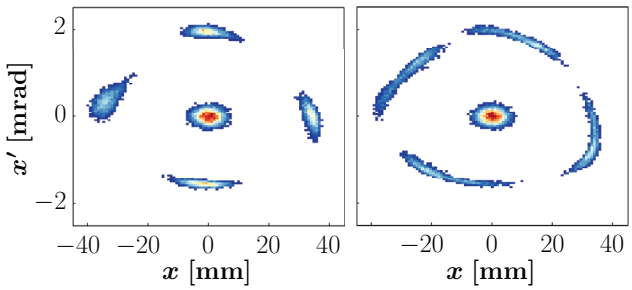

Figure 6: Simulated horizontal phase space portraits showing the evolution of an improved final rotation, which takes about six times longer than the one illustrated in Fig. 5. η_{MTE} is conserved during the process and the final surface of the islands is significantly reduced.

septum is increased and only particles in the tails of the island's distribution are likely to be absorbed.

The changes to the multipolar configuration were experimentally implemented and the extraction efficiency was indeed improved by about 4%. The final step pursued to further increase the extraction efficiency was to correctly position the dummy septum with respect to SMH16, i.e. to establish shadowing conditions. The corresponding experimental results are set out in the following section.

SHADOWING CONFIGURATION

TPS15 has been designed to absorb particles that would otherwise be lost at SMH16 during the rise time of the fast extraction kickers. As this device constitutes an additional aperture restriction in the extraction region, a complete redesign of the extraction bump was required to extract the MTE beam. Experimental studies showed the necessity to move TPS15 to its minimum position of 80.5 mm and an angle of 0 mrad in order to provide sufficient separation between the beam and the septum blade during the extraction process.

Therefore, the remaining degrees of freedom to position SMH16 in the shadow of TPS15 corresponded to the position and angle of SMH16 and a fine scan of these parameters was experimentally conducted to determine the settings, which minimize beam loss in SS16.

By means of a fast beam loss monitor (BLM) in SS16, which allows to resolve beam loss on a time scale shorter than one turn, losses occurring during the extraction of the islands can be distinguished from those created during the final turn. In Fig. 7, a typical beam loss pattern during the last five turns is shown. To evaluate the shadowing efficiency, the sum of the losses occurring for the core and the islands was considered as figure of merit and the dependency of this value on the position and angle of SMH16 was investigated. For an angle of 0 mrad, beam loss was observed to be a quadratic function of the position, with a minimum located at 58.65 mm (see Fig. 7 bottom). The losses measured at this position corresponded to a reduction by about a factor three compared to the value obtained for the settings of TPS15 and SMH16, which were considered operational at the time

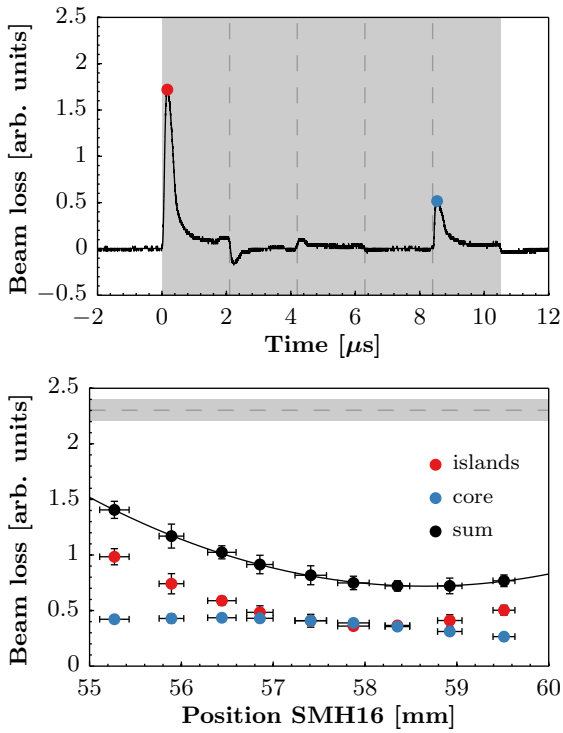

Figure 7: Top: Signal of the fast BLM16. The grey area indicates a duration of five turns, with the dashed lines being separated by one turn. The red and the blue circles correspond to the maximum beam loss occurring during the extraction of the islands and the core, respectively. Bottom: Dependency of beam loss on the position of SMH16 for an angle of 0 mrad. Red and blue circles correspond to the losses of the islands and the core, respectively, and the black circles represent their sum. Error bars describe the standard deviation obtained over 10 consecutive measurements. The dashed line and the grey band indicate mean value and standard deviation of losses for the nominal septa settings.

these measurements were conducted (82.5 mm / 0 mrad and 55.5 mm / 3 mrad, respectively). Based on these results, the following settings were chosen as new operational configuration: TPS15 at 80.5 mm / 0 mrad and SMH16 at 57.5 mm / 1 mrad. These values constitute an acceptable compromise for both MTE and the other operational users.

PERFORMANCE ANALYSIS OF THE 2015 RUN

Based on the increased understanding of the MTE process and the implemented mitigation measures to overcome the issues, which stopped the deployment of MTE in 2010, it became again possible to transfer MTE beams to the SPS at the end of 2015. From September 21$^{\mathrm{st}}$ until the end of the proton run on November 16$^{\mathrm{th}}$, MTE replaced the CT technique. Continuous beam optimisation was carried out, and intensities of up to 2.0×10^{13} p could be operationally extracted.

ISBN 978-3-95450-185-4

the proton run on November 16th, MTE replaced the CT technique. Continuous beam optimisation was carried out, and intensities of up to 2.0×10^{13} p could be operationally extracted.

The striking advantage of MTE over CT is visualized in Fig. 8, where measurements with slow BLMs, which are installed around the PS circumference in the 100 straight sections and integrate beam loss over 1 ms, are presented. Beam loss occurs mainly in the extraction region and activation of the rest of the machine is significantly reduced.

Figure 9 presents the time evolution of the extracted beam intensity and of the extraction efficiency η_{ext}. For MTE, η_{ext} is around 97-98%, whereas typical values for CT at similar beam intensity are around 95%. Hence, MTE reduces extraction losses with respect to CT by almost a factor of 2 and concentrates them in the well-shielded SS15.

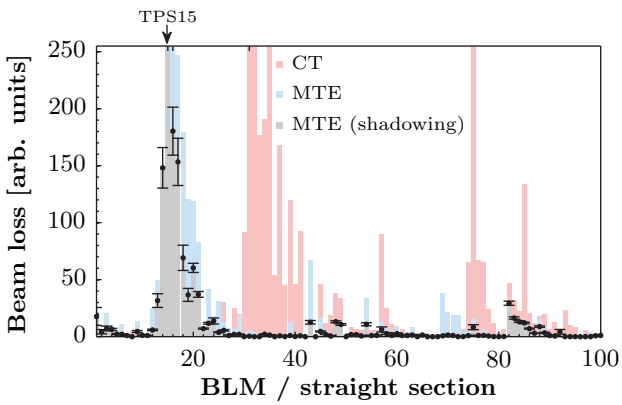

Figure 8: Integrated beam loss measured after extraction on the MTE cycle using TPS15 and SMH16 in shadowing configuration. Only BLM15 is saturated, and beam loss at the adjacent SMH16 is significantly reduced. For comparison, the MTE case without TPS15 and the CT case are shown. Error bars for the case of MTE with shadowing correspond to the standard deviation of 500 consecutive measurements.

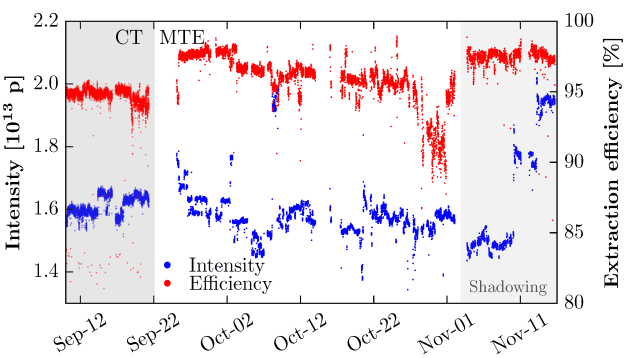

Figure 9: Evolution of the PS proton intensity measured prior to extraction and of η_{ext} during the 2015 MTE run. Operation with CT and the period using the shadowing configuration are highlighted in grey.

A summary of some statistical indicators describing the MTE performance for an intensity of 2.0×10^{13} p is listed in Table 1.

Table 1: Splitting and Extraction Efficiencies for the 2015 MTE Beam with an Intensity of 2.0×10^{13} p. Based on 15×10^3 different measurements, the mean (μ), median (Q_2), and standard deviation (σ) of the two quantities are quoted.

η_{MTE}			η_{ext}		
μ	Q_2	σ	μ	Q_2	σ
19.90	19.92	0.41	97.50	97.56	0.60

RECENT PERFORMANCE IMPROVEMENTS

As a result of the aforementioned performance improvements of the MTE technique and the operational experience gained during the MTE run in 2015, the decision was taken to adopt MTE as the operational extraction scheme throughout the 2016 run.

In parallel to the operational use of MTE, studies are being carried out to further improve the MTE reproducibility. This especially concerns the optimization of the applied multipole functions and of the settings of the wide band stripline kicker of the transverse damper system.

Figure 10 shows that an excitation of at least 20% of the maximum available excitation amplitude is required to properly populate the islands during the splitting process. The transverse splitting also crucially depends on the horizontal emittance before resonance crossing and the transverse damper was found to be efficient in reducing the dependency of η_{MTE} on the initial emittance.

Furthermore, scans of the excitation frequency confirmed that its fractional part is required to be close to 0.25, while η_{MTE} was found to be basically independent of the integer tune value of the excitation frequency.

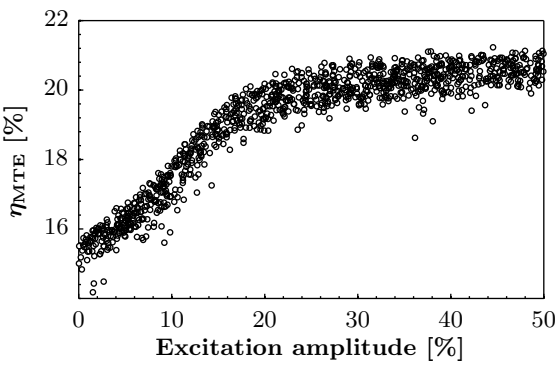

Figure 10: Dependency of the splitting efficiency on the excitation amplitude of the transverse damper (in % of the maximum amplitude). An amplitude of at least 20% is required to achieve proper splitting efficiency.

ISBN 978-3-95450-185-4

REFERENCES

[1] C. Bovet *et al.*, "The Fast Shaving Ejection for Beam Transfer from the CPS to the CERN 300 GeV Machine," IEEE Trans. Nucl. Sci. **20**, 438 (1973).

[2] J. Barranco García and S. Gilardoni, "Simulation and Optimization of Beam Losses During Continuous Transfer Extraction at the CERN Proton Synchrotron," Phys. Rev. ST Accel. Beams **14**, 030101 (2011).

[3] R. Cappi and M. Giovannozzi, "Novel Method for Multiturn Extraction: Trapping Charged Particles in Islands of Phase Space," Phys. Rev. Lett. **88**, 104801 (2002).

[4] M. Giovannozzi, "Status of MTE," Presentation at the LHC Injectors and Experimental Facilities Committee (IEFC) meeting, CERN, Geneva, Switzerland (12 May 2010).

[5] C. Bertone *et al.*, "Studies and Implementation of the PS Dummy Septum to Mitigate Irradiation of Magnetic Septum in Straight Section 16," CERN-ACC-2014-0043 (2014).

[6] J. Borburgh *et al.*, "First Implementation of Transversely Split Proton Beams in the CERN Proton Synchrotron for the Fixed-Target Physics Programme," EPL **113**, 34001 (2016).

[7] P. Freyermuth *et al.*, "CERN Proton Synchrotron Working Point Matrix for Extended Pole Face Winding Powering Scheme," in *Proc. of IPAC10*, Kyoto, Japan (2010).

[8] A.P. Shishlo, T.V. Gorlov, and J.A. Holmes, "The Python Shell for the ORBIT Code," *Proc. of ICAP09*, San Francisco, USA (2009).

[9] F. Schmidt, E. Forest, and E. McIntosh, "Introduction to the Polymorphic Tracking Code: Fibre Bundles, Polymorphic Taylor Types and "Exact Tracking"," CERN-SL-2002-044-AP. KEK-REPORT-2002-3 (2002).

[10] M. Giovannozzi *et al.*, "The CERN PS Multi-Turn Extraction Based on Beam Splittting in Stable Islands of Transverse Phase Space: Design Report," CERN-2006-011 (2006).

ISBN 978-3-95450-185-4

MACHINE ELEMENT CONTRIBUTION TO THE LONGITUDINAL IMPEDANCE MODEL OF THE CERN SPS

T. Kaltenbacher*, F. Caspers, C. Vollinger
CERN, Geneva, Switzerland

Abstract

This contribution describes the current longitudinal impedance model of the SPS and studies carried out in order to improve, extend and update it. Specifically, new sources of impedances have been identified, evaluated and included in the model. One finding are low Q and low-frequency (LF; here below 1 GHz) resonances which occur due to enamelled flanges in combination with external cabling e.g. ground loops. These resonances couple to the beam through the gap with enamel coating which creates an open resonator. Since this impedance is important for beam stability in the CERN Proton Synchrotron (PS), RF by-passes were installed on the enamelled flanges, and their significance for the SPS beam is currently under investigation. Simulations, bench and beam measurements were used to deduce model parameters for beam dynamic simulations.

INTRODUCTION

A significant SPS upgrade is mandatory in order to meet the expectations for the planned LHC upgrade scenarios [1] since there are still intensity limitations apparent for future high-intensity LHC beams [2, 3]. Beam measurements and the current longitudinal beam coupling impedance model of the SPS [4] have unveiled the main contributors to the resistive impedance which are vacuum flanges, and the 200 MHz cavities to name but a few. The main contributor to the high R/Q impedances are the kicker magnets and again the 200 MHz cavities [3].

Vacuum flanges in the SPS were found to be responsible for single- and multi-bunch longitudinal instabilities. Therefore, an impedance reduction campaign of these vacuum flanges (VF) during the Long Shutdown 2 (LS2 in 2019) is LIU baseline. However, it is not yet clear if the flange insulation has to be maintained or not. In order to answer this question, a campaign is planned during a technical stop in 2016 [5] to shortcircuit all insulated VF of the 109 QF (quadrupole focusing magnet) short straight sections (SSS) by so-called soft clamps. Detailed beam parameter measurements before and after the deployment of these soft clamps will provide the basis for the decision whether the VF can maintain their enamel insulation or not. Based on this decision, the current flange shield design for impedance reduction will have to be reviewed or can be kept. This is very important, since many of the positions that have to be shielded are equipped with enamelled flanges. In the PS [6], insulated vacuum flanges are used to avoid eddy currents induced by fast ramping (ramp rates $\approx$ 2.3 T/s) of C-shaped magnet , and to avoid that ground loops are closed via the beam pipe. From measurements, it could be shown that the flange capacitance and the connected CBN (ground loops) form a resonator with a resonant frequency of about 1.5 MHz which had to be dampened with by means of RF-bypasses. As before for the PS, also in the SPS, the enamelled flanges were introduced to avoid eddy current propagation along the beam pipe, and in addition to allow a sectorising of the vacuum system such that only *one* ground connection is installed at each half-cell (approx. every 32 m). In the SPS however, the ramping rates of H-window magnets are about 10 times slower than in the PS and induced net currents on the beam pipe are thus considerably smaller as well. From laboratory measurements, it could be shown that the induced current from focusing quadrupole magnets (QF) is below 1.5 A and from defocusing quadrupole magnets (QD) less than 200 mA. In addition, from measurements, it could be shown that in the SPS, a resonator which is formed by the flange capacitance and the ground loop, is resonating at about 2.5 MHz. The same measurements also indicated a number of resonances at higher frequencies, i.e. at about 20 MHz, about 60 MHz, and higher. It should be mentioned already here that these resonances show a spread around the indicated frequencies due to slight variations in the grounding loop lengths and topology, as is illustrated in Fig. 1. Consequently, the current impedance model has to be extended to include these low-frequency resonances occurring due to enamelled flanges.

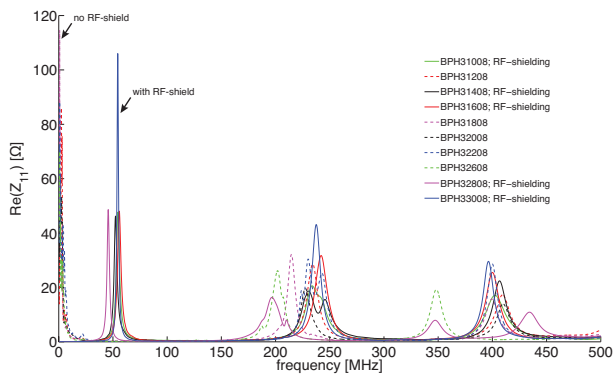

Figure 1: Differentially measured reflection coefficient S_{11} was used to calculated the real part of input impedance Z_i - $Re(Z_i)$ - of 10 QF SSS with and without RF-shield.

MEASUREMENTS

In order to evaluate these low frequency resonances, two different type of measurements were performed with a vector network analyser (VNA) in the SPS. Firstly, measurements of reflection S-parameters (S_{11}) were carried out to obtain

* Thomas.Kaltenbacher@cern.ch

ISBN 978-3-95450-185-4

the low-frequency input impedance of enamelled flanges, and secondly we performed measurements via a pick-up (PU) installation. The PU consisted of conducting loops that are connected to an inner and outer conductor of a coaxial cable and were put in place to the left and right side of the flanges. Via the PU installation, beam induced measurements from the surface were possible. Again, reflection S-parameters were taken as read-out signal to allow an evaluation in the same manner as for the first set of data. In order to rule out spurious signals caused by coupling effects due to the surrounding installation, independent *differential* RF measurements were performed for the very same positions. These single-ended and differential measurements, as well as the beam induced measurement set-ups are described in more detail below together with their results.

RF Measurements

For the single-ended (s.e.) RF measurement, the VNA was connected to the pick-up (PU) by means of a BNC-N adapter (see Fig. 2). During the measurements, we could determine that the upper signal frequency limit of the s.e. RF measurement to a value of about 30 MHz, caused by the coupling of the outer conductor of the cable to other electrical installations and equipment, i.e. the EM surrounding.

The differential (diff.) RF measurement method was applied using a hybrid junction (MACOM H-9-N; nominal bandwidth 2 to 2000 MHz) [7]. Two RF measurement cables with pins connected to them (see Fig. 3) and provided an independent measurement of the very same pick-up.

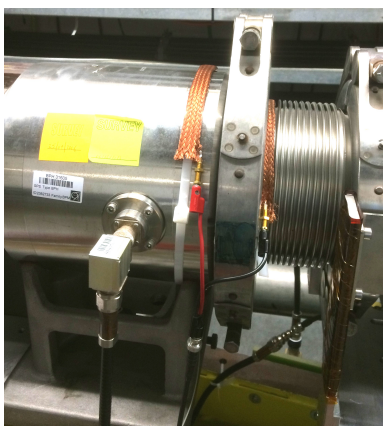

Figure 2: Pick-up (PU3) position in the short straight section of the focusing quadrupole magnet QF31610 in the SPS.

Via the hybrid, signals between the 0° and 180° phase shift port were taken. It is worthwhile to mention that both cables were calibrated simultaneously by means of a one-port calibration and that the differential characteristic impedance is 100 Ω. This characteristic impedance was used to convert the reflection coefficient S_{11} to the input impedance (Z_i). As expected, this set-up is limited towards low frequencies at about 1 MHz, when spurious signals caused by data interpolation as well as calibration effects of the VNA become visible. Also, operation of the hybrid junction below 2 MHz is difficult, so that we did not consider these very low frequency values. The upper frequency limit shows up at about 500 MHz and is caused by increased loss from contact resistance and signal interferences.

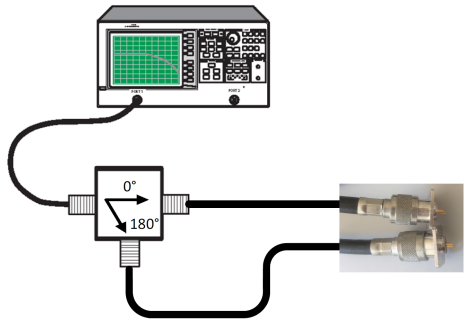

Figure 3: Schematic of differential RF measurement set-up.

Beam Induced Measurements

In order to show the coupling of the beam to the EM surrounding through enamelled flanges, beam induced measurements were performed. Three positions with enamelled flanges were chosen (PU1 to PU3) and fitted with to so-called soft clamps. These clamps are tailor-made from copper braids into which cable ties were slid similar to a sleeve. The cable ties allowed to strap the soft-clamp on the beam pipe to the left and right side of the flange. A socket was soldered on each of the clamps beforehand and the PU was completed by connecting the clamps with a banana-BNC adapter (see Fig. 2) which in turn was connected to a spare coaxial cable running from the tunnel to the surface. Such a pick-up represents a single-ended measurement of the (beam) induced signal across a VF. The signals were acquired one second after injection with a fast, high analogue band-width oscilloscope with 50 ps time sampling period and afterwards converted to frequency domain by means of fast Fourier transform (FFT). Although in the SPS, the single bunch beam (with bunch length $4\sigma_t \approx 3$ ns) had a nominal intensity of 1×10^{11} protons per bunch (ppb), all measured data traces except one were taken with 4×10^{10} pbb due to the availability of the cycle during our measurements. Figure 4 shows the spectra of beam induced signals for the three pick-ups (PU1 to PU3) in different locations. Note that for PU3, two traces taken with different intensities are shown and the magnitude scales accordingly ($\approx 10/4$).

SIMULATIONS

Macro-Particle Longitudinal Beam Dynamics

Longitudinal beam dynamics simulations with BLonD [8] were performed with the updated impedance model for the SPS including the scattered LF contribution (see Fig. 1). Two kind of simulations were performed. Firstly, a 72 bunch beam with 25 ns spacing during the ramp, and secondly a synchrotron frequency shift simulation from quadrupole

ISBN 978-3-95450-185-4

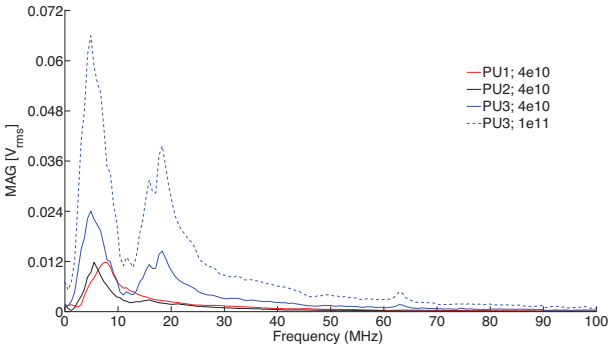

Figure 4: Single-ended spectrum of the beam induced measurements for pick-up PU1 to PU3. Note that the magnitude scales as expected for PU3 by about 2.75 (theoretically 10/4=2.5).

oscillations. Preliminary results have shown that there seems to be no significant effect on neither beam stability nor on the synchrotron frequency shift due to short bunch length [9].

EM Simulation

Figure 5 shows a simplified model of an MBA/MBA flange interface with 4-convolution bellows (undulation was not modelled). This model was used to show the coupling of a TEM signal excited on a wire (1 mm diameter) along the beam axis in order to mimic a wire measurement.

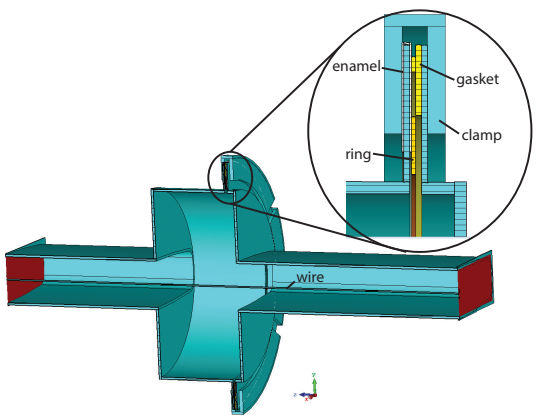

Figure 5: CST model of the simplified MBA/MBA flange structure with bellows and clamp. Note the wire along the beam axis is touching both microwave ports (red).

This special simulation approach was used since wake field simulations did not show any coupling to LF resonances. From our simulations, we see that the aspect ratio of enamel thickness (i.e. opening for coupling) and the VF object dimensions are so extreme that the VF opening remains undetected in the time domain solver. However, the HF solver of CST Microwave Studio [10], was used for S-parameter simulations (HF solver) of the simplified insulated flange structure. It is important to note that the object was embedded in vacuum so that the metal structure of the flange and beam pipe did no touch the perfect electric conducting (PEC) boundaries. This way modes from the inside are allowed to couple to the outside of the structure through the enamel layer (300 µm thick) via the clamp (see Fig. 6). In the Results and Conclusion section will be shown how the coupling takes place in the simulation.

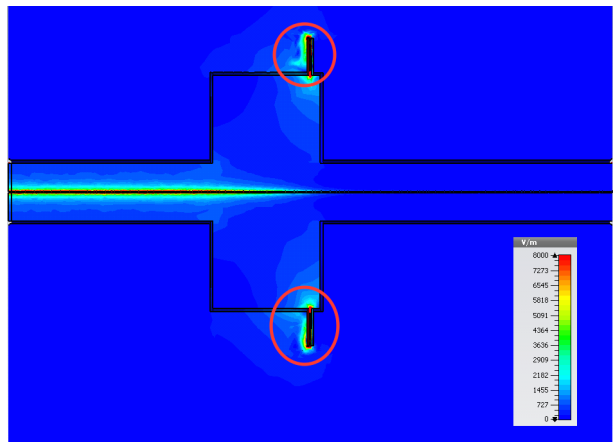

Figure 6: E-field magnitude of the mode at 13.8 MHz of the model shown in Fig. 5 with $\mu_r = 50$. Note the coupling to the surrounding through the VF including the gasket and enamel (red circles).

RESULTS

Beam Induced Measurement Results

The method of beam induced measurements was evaluated for the three pick-ups shown in Fig. 4. All three positions show a significant peak below 10 MHz which is most likely caused by resonance of the VF capacitance and the common bounding network (CBN). Furthermore, the spectrum of PU3 shows also significant peaks around 18 and 62 MHz which coincide with resonances measured differentially at the very same position.

RF Measurement Results

As explained in the introduction, RF-shields were installed in about 860 intermagnet pumping ports during the impedance reduction campaign in the year 2000 [11], however, detailed documentation is sometimes missing or unreliable for some positions. Thus, as a first exercise measurements of the input impedance from S-parameter on QF SSS at the beam monitor position were carried out in order to deduce whether an RF-shield is installed at a certain position or not. As expected, in locations known to be equipped with RF-shields, the first resonance appears at approx. 60 MHz whereas at locations known to be without RF-shields, the first resonance is measured at about 10 MHz (see Fig. 1).

As a next step, this method was used in the locations of the pick-ups in order to allow a comparison of input impedances measured by the s.e. and diff. methods as is shown in Fig. 7 for pick-up nr. 3. Note that pick-up nr. 3 is installed in the SSS of magnet QF31610 (see Fig. 2). For the s.e. measurement the two variations of the connections, the outer conductor

ISBN 978-3-95450-185-4

(GND) of the coaxial cable to the right or left of the VF, are shown. The data shows an increasing input impedance below 5 MHz which could be attributed to the independently evaluated flange capacitance of about 600 pF. From the measurement of input impedance with the s.e. method, we observe an increase above 20 MHz due to the capacitive coupling of the coaxial cable to the (EM) surrounding. Qualitatively both measurement methods agree very well with each other and the beam induced signal shows an excellent agreement with the differentially measured impedance.

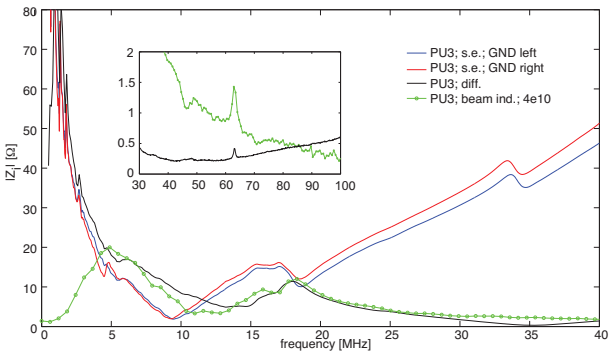

Figure 7: Measurement results for pick-up (PU3) including the impedance by single-ended (s.e.) and differential (diff.) method. GND left and right describes the configuration where the outer conductor of the coax. cable was connected to with respect to the VF. The beam induced (beam ind.) spectrum for a single bunch beam with an intensity of 4×10^{10} protons is scaled to match the impedance values. Inset: Zoom on resonance at 62 MHz from beam induced measurement (green) and diff. RF measurement (black).

EM Simulation Results

Figure 8 shows the transmission signal S_{21} from the simulated flange model presented in Fig. 5. From the simulations, we observe a significant dip at about 1.64 GHz which could be attributed to a strong coupling of the flange to the outside through the enamel layer, even if the fixation clamp is absent in the model. Adding the clamp in the model causes the dip to scatter due to a build-up of EM-fields that are leaking to the outside at the clamp position. A large variation of the EM surrounding exists in the SPS and causes a varying inductance of ground loops at the enamelled VF positions. In order to include this EM surroundings in our simulation model, an additional ring was inserted at the gasket location to mimic the EM environment, and different material properties were assigned to this ring. The simulation results show that the variation of material properties of the ring (relative permeability μ_r and permittivity ε_r) cause a shift of the resonance frequencies towards lower values, and thus provide a simulation model for the EM situation in the SPS at the VF positions. The successful description of measurement data by simulations is the base for further studies concerning the beam coupling to the shown LF resonances.

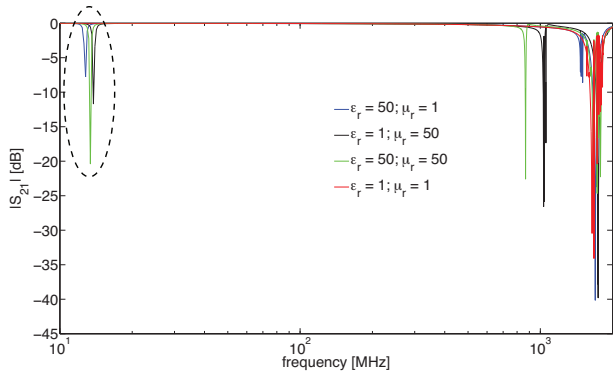

Figure 8: Simulated transmission S-parameter (S_{21}) for the simplified flange model shown in Fig. 5 with μ_r and ε_r variation assigned to a ring that was inserted next to the gasket (see Fig. 5). The shifted LF resonances are highlighted.

CONCLUSION

In this work we have introduced and evaluated LF resonances connected to enamelled vacuum flanges in the SPS. This allowed us to update the current SPS impedance model and to analyse the additional contribution in terms of beam coupling impedances. Furthermore, a simplified simulation model of the VF was proposed in order to describe and reproduce coupling from the flange inside to the outside EM surrounding. Beam dynamic simulations could not point out any significant effect neither on the stability threshold of a multi-bunch beam not on the synchrotron frequency shift. However, further studies will be carried out to qualify the significance of this coupling by performing further EM and beam dynamics simulations.

ACKNOWLEDGEMENT

We are grateful to our RF colleagues T. Bohl for his support during the beam induced measurements and the pick-up installation in the SPS, E. Shaposhnikova, and J. F. Esteban-Müller for their useful inputs and discussions. We would like to thank also A. Lasheen and J. Repond for their beam dynamics simulation and P. Kramer for his support during the measurements in the SPS.

REFERENCES

[1] J. Coupard *et al.*, "LHC Injectors Upgrade, Technical Design Report, Vol. I: Protons", Dec. 2014

[2] T. Argyropoulos *et al.*, "Identification of the SPS impedance at 1.4 GHz", in *Proc. 4th Int. Particle Accelerator Conf. (IPAC'13)*, Shanghai, China, May 2015, paper TUPWA039, pp. 1793–1795.

[3] E. Shaposhnikova *et al.*, "Identification of high-frequency resonant impedance in the CERN SPS", in *Proc. 5th Int. Particle Accelerator Conf. (IPAC'14)*, Dresden, Germany, June 2014, paper TUPME029, pp. 1416–1418.

[4] J. E. Varela *et al.*, "An extended SPS longitudinal impedance model", in *Proc. 6th Int. Particle Accelerator Conf. (IPAC'15)*, Richmond, USA, May 2015, paper MOPJE035, pp. 360–362.

ISBN 978-3-95450-185-4

[5] B. Goddard, presentation at 173rd IEFC meeting on 20th May 2014, https://indico.cern.ch/.

[6] H. Damerau *et al.*, "Evaluation of the broadband longitudinal impedance of the CERN PS", CERN, Geneva, Switzerland, CERN-ATS-Note-2012-064 MD, May 2012.

[7] MACOM Technology Solutions Inc., Lowell, USA, http://cdn.macom.com/datasheets/H-9.pdf.

[8] BLonD, Beam Longitudinal Dynamics code, http://blond.web.cern.ch.

[9] A. Lasheen and J. Repond, private communication

[10] CST AG, Darmstadt, Germany, http://www.cst.com

[11] P. Collier and A. Spinks, "Survey of the Short Straight Sections in the SPS for the Impedance Reduction Programme", CERN, Geneva, Switzerland, SL-Note-99-025 SLI, April 1999.

ISBN 978-3-95450-185-4

THE SPS 200 MHz TWC IMPEDANCE AFTER THE LIU UPGRADE

T. Roggen*†, R. Calaga, F. Caspers, T. Kaltenbacher, C. Vollinger,
CERN, Geneva, Switzerland

Abstract

As a part of the LHC Injectors Upgrade project (LIU) the 200 MHz Travelling Wave Cavities (TWC) of the Super Proton Synchrotron (SPS) will be upgraded. The two existing five-section cavities will be rearranged into four three-section cavities (using two existing spare sections), thereby increasing the total voltage from 7 MV (I_{RF} = 1.5 A, current LHC) to 10 MV (I_{RF} = 3.0 A, HL-LHC) [1, 2]. Projections of the HL-LHC (High Luminosity Large Hadron Collider) era are conceived by the macro-particle simulation code BLonD [3], that makes use of an impedance model of the SPS, developed from a thorough survey of machine elements [4]. This paper analyses the impedance contribution of the 200 MHz cavities in the two configurations, using electromagnetic simulations. Measurements of the existing cavities in the SPS and a single-section prototype are also presented.

INTRODUCTION

The 200 MHz TWC system of the SPS currently consist of two four-section cavities and two five-section cavities. To guarantee stability of the future HL-LHC beams in the SPS, the required controlled longitudinal emittance blow-up will have to be increased. This implies a larger bucket and voltage amplitude, but one must not forget that the increased intensity will also cause more beam loading in the cavities, which has to be compensated by the RF system as well. The existing two five-section cavities with the available 1 MW power plant will struggle with the future HL-LHC beams, and solutions were proposed in [1]. The two existing five-section cavities will be rearranged into four three-section cavities (using two existing spares), and two additional power plants of 1.4 MW/cavity are foreseen. The two four-section cavities will remain in their current configuration. This will not only be beneficial for the fundamental mode, but the total impedance will reduce by 20% in this new configuration [1].

For projections of the HL-LHC era requirements, the macro-particle simulation code BLonD [3] is used. It relies on an impedance model of the SPS, developed from a thorough survey of machine elements [4]. In this paper the impedance contribution of the 200 MHz cavities in the two configurations is assessed using measurements taken in situ in the tunnel, laboratory measurements of a single section on the surface and electromagnetic simulations (CST Studio Suite [5]). In particular, attention will go to the 628 MHz Higher Order Mode (HOM) couplers, since recent studies showed that the intensity threshold for beam stability can be improved when, amongst others, the impedance contribution of the longitudinal 628 MHz HOM is reduced at least by a factor of 2 [6, 7].

* Fellowship co-funded by the European Union as a Marie Curie action (Grant agreement PCOFUND-GA-2010-267194) within the Seventh Framework Programme for Research and Technological Development.
† toon.roggen@cern.ch

SINGLE SECTION CAVITY

General Description

The currently installed SPS 200 MHz TWC system, described in [8], consists of two four-section cavities and two five-section cavities. A single section of 11 cells is available on the surface as well for additional measurements. This 11-cell section is a spare section, which is closed, as in the tunnel, by two lids to allow measurements. No power couplers are installed on this section and as for the HOM couplers only the four 628 MHz HOM couplers with detachable 50 Ω loads are put into place (Fig. 1). The couplers for the longitudinal 938 MHz HOMs and the couplers for the transverse 460 MHz HOMs were not installed. This choice is motivated by two aspects: In the first place their effect on the 628 MHz HOM damping is considered minimal to non-existing. In the second place, and more importantly, the single-section cavity study was done to reassure that a known setup could be modelled and simulated correctly. The requirement for the model is that it represents exactly the laboratory setup, and as such a laboratory setup with as little (unnecessary) complexity as possible is an obvious choice. It should be noted that spare 938 MHz HOM couplers are available, in the event this would be desired. On the other hand, no spare 460 MHz HOM couplers were available. Typical transmission and reflection measurements were performed between two probes, mounted on the beam pipe axis, between different 628 MHz HOM couplers, or combinations of both. In addition, the RF voltage feedback pick-up loops, used to measure the Fundamental Pass Band (FPB) field flatness, served as a measurement interface with the cavity as well.

Table 1: Resonant measurements of the SPS 200 MHz single-section cavity around 628 MHz, with no loads on the 628 MHz HOM couplers.

Freq [MHz]	R/Q [Ω]	Q_0
624.3	0.5	18400
626.8	10	22300
628.8	56	18000
631.6	27	19500
634.3	4.6	17800

ISBN 978-3-95450-185-4

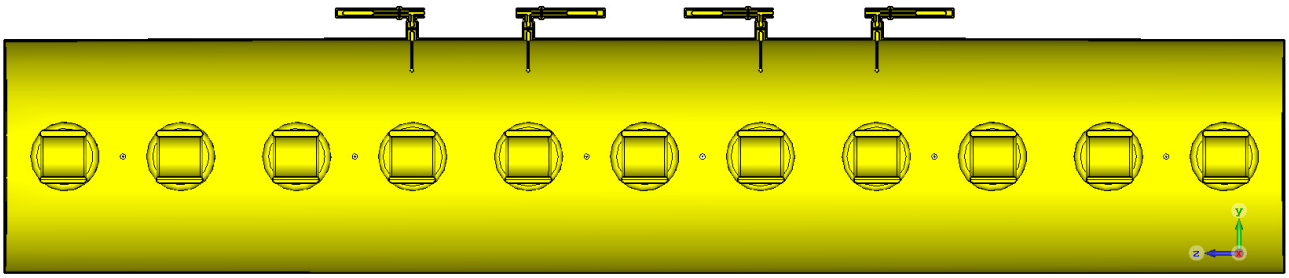

Figure 1: Simulation model of the 11-cell section of the SPS 200 MHz TWC with installed 628 MHz HOM couplers and RF voltage feedback pick-up loops.

Measurements

Figure 2 shows the cavity transmission characteristics around 628 MHz measured between two weakly coupled probes, installed on the beam pipe axis. The undamped cavity (50 Ω loads not mounted on the 628 MHz HOM couplers) has, as expected, several resonant peaks around 628 MHz. With the 50 Ω loads installed the input signal is considerably damped (-25 dB) and the Q is significantly reduced. The dip around 637 MHz for the loaded HOM couplers (blue curve) is assumed to be caused by destructive interference between the two probe's. This can be overcome by changing their relative positions. Table 1 shows R/Q and Q based on beadpull measurements for the unloaded section. The transmission measurements between a single probe and a HOM coupler allow to draw identical conclusions, though the data is more challenging to interpret.

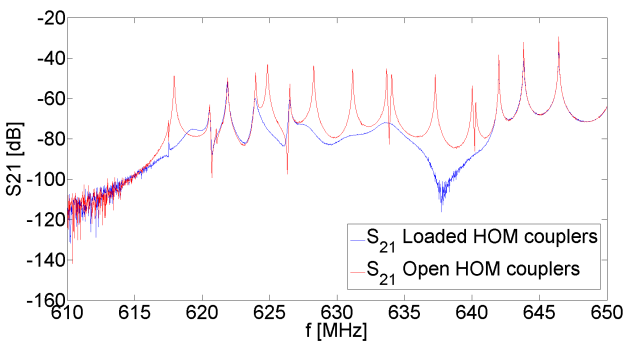

Figure 2: Measured transmission (S_{21}) characteristics around 628 MHz for two weakly coupled probes mounted in the centre of the beam pipe on each side of the single-section cavity.

Simulations

The position of the 628 MHz HOM couplers with respect to the drift tubes seems to be well optimised in the past. Simulations also show that certain modes preferably couple to one of the two HOM pairs (e.g. the 628 MHz mode couples stronger to the outer pair of HOM couplers, while the 632 MHz mode couples stronger to the inner pair of HOM couplers). This was confirmed by measurements as well. In order to get confirmation that the applied model represents the single section, actual measurement setups were simulated. Figure 3 shows the S_{21} for the single-section structure equipped with four 628 MHz HOM couplers. As an input interface the RF voltage feedback pick-up loop close to one lid was used to insert the signal (P1 on Fig. 3), the measurement was taken at the pick-up loop on the other side of the cavity section (P2 on Fig. 3). The frequency difference between measurements and simulations is within the uncertainty of the measurement, arising e.g. from a combination of tolerances and an expansion of the measured structure due to temperature differences. The seemingly strong resonance present at 629.6 MHz is in fact a transverse mode that manifests only in the single-section cavity with lids. Consequently, this transverse mode does not appear in the four- and five-section cavity simulations or measurements. The R/Q and Q_E (Q external) for a loaded single-section cavity were simulated as well (Tab. 2).

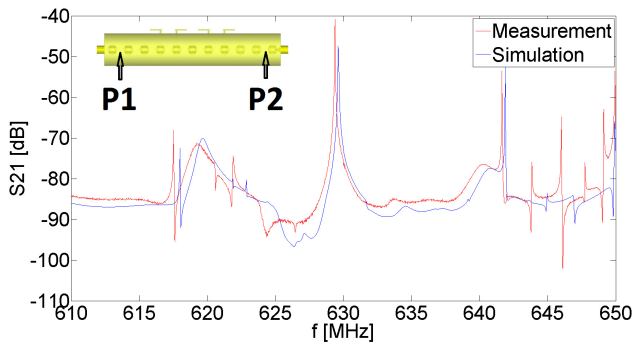

Figure 3: Comparison between simulation and measurement for an S_{21} between two RF voltage feedback pick-up loops (P1 and P2) in the single-section cavity.

IN SITU MEASUREMENTS

General Description

A large number of measurement data was taken during the technical stop in February 2016, most of it on cavity II, since this four-section configuration will remain in the machine after the upgrade. Fundamental power couplers, main load, all HOM couplers and all auxiliary equipment was connected, though no RF power nor beam was present. It is worth mentioning that the model size of a five-section cavity becomes cumbersome in the CST software due to its large

ISBN 978-3-95450-185-4

Table 2: Resonant simulations of the SPS 200 MHz single-section cavity around 628 MHz, with loads on the 628 MHz HOM couplers.

Freq [MHz]	R/Q [Ω]	Q_E
620.2	0.145	156
622.3	2.83	7162
622.9	1.97	3.93e+004
624.4	12.1	2.58e+004
625.2	15.0	517
626.9	34.5	8013
628.6	1.87	472
630.9	14.5	56
631.4	45.4	258
634.4	0.899	446
634.6	30.4	742
637.0	48.5	255
638.3	20.0	110

dimensions (20.603 m, excluding the fundamental power coupler lines). Not only the number of required mesh cells is huge (>100 million tetrahedrons), also the ratio of the structure length to smallest component dimension reaches values that compromise adequate handling by the mesher.

Measurements

Form the measurements clear differences are observed between the four- and five-section cavities but also between the two 4 section cavities in terms of transmission characteristics. The exact reason for this difference is currently not well understood and the significance on the impedance model has not yet been studied. It also became clear that a single-section measurement cannot be easily scaled up to a multi-section equivalent: different resonances shift differently both in frequency and amplitude (Fig. 4). As for the 460 MHz transverse HOM couplers, these do not seem to have any contribution to the damping of the 628 MHz HOMs, as was confirmed by removing the loads on those couplers. This did not have any additional damping effect on the S_{21} in Fig. 4. From a frequency perspective their presence in the cavity induces a small frequency shift. At 460 MHz on the other hand the 460 MHz HOM coupler damping works as foreseen.

Simulations

For cavity II a measurement setup was simulated too: The S_{21} was evaluated for the four-section cavity equipped with power couplers, loaded 460 MHz, 628 MHz and 938 MHz HOM couplers. The connected input and output RF voltage feedback pick-up loops are indicated on Fig. 5. The difference in frequency can again be explained by a combination of tolerances and an expansion of the measured structure due to temperature differences. The comparison shows that the simulation model represents quite well the cavity in the actual machine.

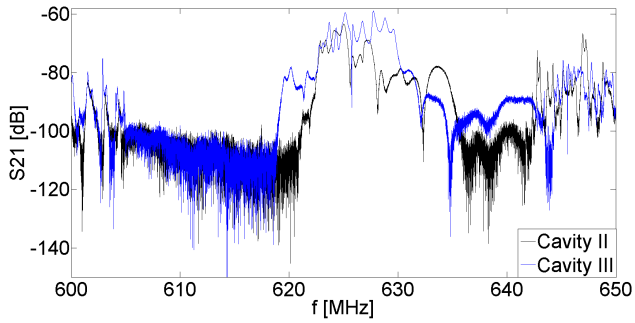

Figure 4: S_{21} characteristics around 628 MHz between the two most outer pickup loops for cavity II (four-section) and cavity III (five-section).

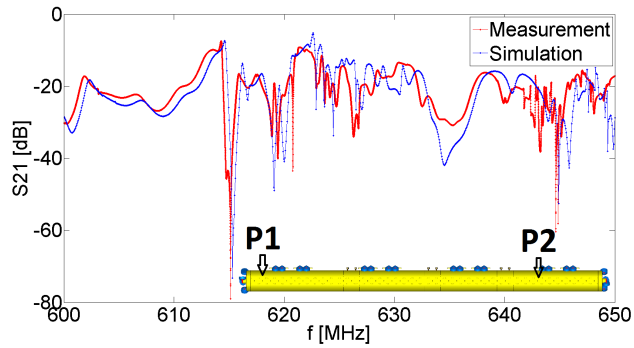

Figure 5: Comparison between simulation and measurement for an S_{21} between two RF voltage feedback pick-up loops (P1 and P2) in cavity II in the tunnel.

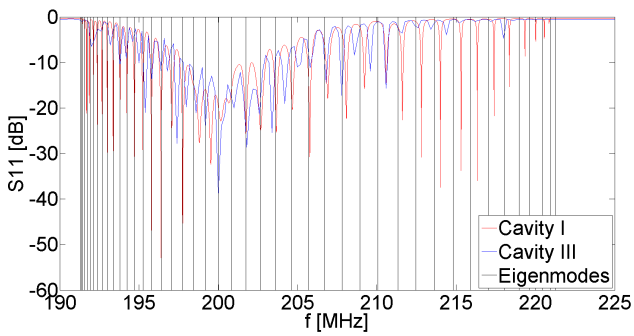

Figure 6: Fundamental passband reflections (S_{11}) for the feeder line measured into the cavity. Comparison between cavity I (four sections) and cavity III (five sections). In black the eigenmodes of a four-section cavity simulation are given.

FEEDER LINE

Reflections in the feeder line of cavity I (four sections) were investigated between 100 MHz–1000 MHz. The feeder line was disconnected from the (cold) generator on the surface at the last combiner and reflections were analysed both into the generator and into the cavity. Detailed measurements were taken in the fundamental passband region (190 MHz–225 MHz) and the HOMs at 460 MHz (400 MHz–500 MHz), 628 MHz (615 MHz–645 MHz) and 938 MHz (900 MHz–1000 MHz). Two cavity setups were measured:

ISBN 978-3-95450-185-4

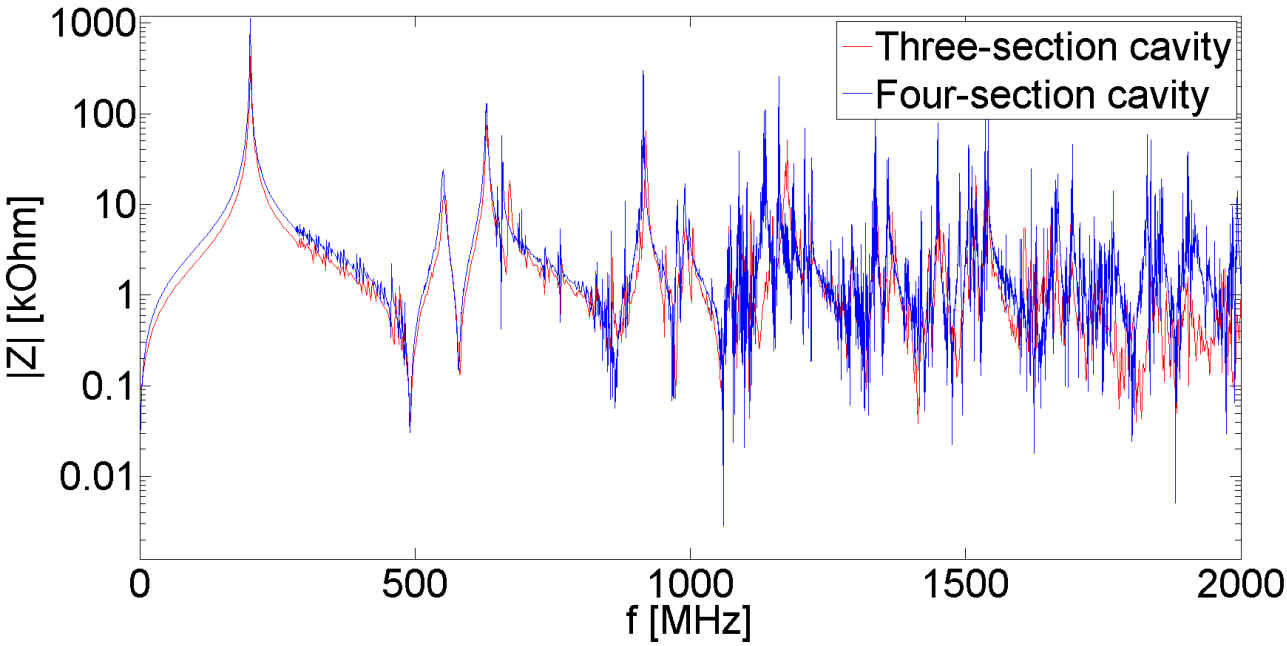

Figure 7: Impedance plots obtained from electromagnetic simulations with CST Studio Suite. Blue: Four-section cavity including 460 MHz, 628 MHz and 938 MHz HOM couplers, power couplers and RF voltage feedback pick-up loops. Red: Future three-section cavity, based on the layout of present four- and five-section configurations.

with and without the 50 Ω loads connected to the 628 MHz HOM coupler. The feeder line has an attenuation of about 0.2 dB/100 m and has a length of 90–180 m, depending on the generator distance from the cavity. Reflection measurements into the cavity show that the fundamental passband drops to -17 dB at 200 MHz (Fig. 6), which is comparable with the results found for cavity III, reported in [9]. Table 3 summarizes S_{11} near the HOM's, showing that the feeder line only provides a very limited amount of HOM damping and that the generator currently does not contribute to the damping of the 460 MHz or 628 MHz HOMs. When measuring the feeder line in the direction of the cavity, no change in S_{11} could be observed around 628 MHz if one removed the 50 Ω loads on the 628 MHz HOM couplers. Although not fully understood yet, this seems to imply that the excitation of 628 MHz through the feeder line does not reach the cavity, but is mainly reflected before.

Table 3: Average reflection measured on the feeder line of cavity I in the spectrum of 100 MHz–1000 MHz.

Freq [MHz]	Feeder line S_{11} [dB]	Generator S_{11} [dB]
460	0	0
628	-1 – -2	0
938	-4 – -5	-2 – -5

IMPEDANCE CONTRIBUTION OF THE 200 MHZ CAVITIES

Four-section Cavity

The above measurement-simulation comparisons give confidence that the models prepared for the impedance calculations are a proper representation of the actual cavities installed in the machine. The impedance result from wake-field simulations of the four-section cavity is shown in Fig. 7 and is used for BLonD simulations.

Three-section Cavity: Prognosis

Based on the experience with the existing cavities an impedance prognosis for the three-section cavities is simulated (Fig. 7). The used three-section model only differs from the existing model in its number of sections. All HOM couplers and power couplers are assumed to remain identical, since no upgraded designs are available yet. This impedance can now be included in the BLonD simulations to further predict future machine performance.

CONCLUSIONS

Confidence in the applied models was built up through comparison of electromagnetic simulations with measurements of both a spare section of the 200 MHz TWC and the actual cavities installed in the SPS. The transmission characteristic comparisons show a good agreement. The adequate damping of the 628 MHz HOM dampers of the cavities was assessed, and both the feeder line and 460 MHz HOM couplers do not appear to have a significant contribution to the damping in this frequency range. The good agreement

ISBN 978-3-95450-185-4

between measurement and simulation allowed to construct the impedance model of the four-section 200 MHz TWC. The three-section cavity impedance model is obtained by a reconfiguration of the modelled sections. The impedance models can now be included in the studies on the HL-LHC beam requirements.

ACKNOWLEDGEMENT

The authors would like to thank Eric Montesinos and his BE-RF-PM section for preparing the single-section cavity in the workshop according to different layouts and to facilitate the measurements done in the SPS tunnel. They also thank Alexej Grudiev, Yaroslav Shashkov and Patrick Kramer for their valuable ideas and input during discussions.

REFERENCES

[1] E.N. Shaposhnikova, E. Montesinos and E. Ciapala, "Upgrade of the 200 MHZ RF System in the CERN SPS", in *Proc. IPAC'11*, San Sebastian, Spain, September 2011, paper MOPC058, pp. 214–216.

[2] J. Coupard *et al.*, "LHC Injectors Upgrade, Technical Design Report, Vol. I: Protons", CERN-ACC-2014-0337, 2014, pp. 440–442.

[3] BLonD, Beam Longitudinal Dynamics code, `http://blond.web.cern.ch/`.

[4] J. Varela *et al.*, "An Extended SPS Longitudinal Impedance Model", in *Proc. IPAC'15*, Richmond, VA, USA, May 2015, paper MOPJE035, pp. 360—362.

[5] Computer Simulation Technology, Bad Nauheimer Str. 19 64289 Darmstadt Germany, `http://www.cst.com/`.

[6] A. Lasheen, T. Argyropoulos, J. Repond and E. Shaposhnikova, "Effect of the Various Impedances on Longitudinal Beam Stability in the CERN SPS", in *Proc. IPAC'16*, Busan, Korea, May 2016, paper TUPOR008, pp. 1666–1669.

[7] E. Shaposhnikova *et al.*, "Removing Known SPS Intensity Limitations for High Luminosity LHC Goals", in *Proc. IPAC'16*, Busan, Korea, May 2016, paper MOPOY058, pp. 989–991.

[8] G. Dôme, "The SPS Acceleration System Travelling Wave Drift-tube Structure for the CERN SPS", CERN-SPS-ARF-77-11, 1977, pp. 1–10.

[9] P. Kramer, F. Caspers, C. Vollinger, E. Montesinos, J. Varela, "In Situ Measurements of the SPS 200 MHz Accelerating Cavity III", CERN-ACC-2015-0021, 2015, pp. 1–10.

ISBN 978-3-95450-185-4

THE NEW HL-LHC INJECTION AND TRANSPORT PROTECTION SYSTEM

F. M. Velotti[1], W. Bartmann, C. Bracco, M. A. Fraser, B. Goddard, V. Kain,
A. Lechner, M. Meddahi, CERN, Geneva, Switzerland
[1] also at EPFL, Lausanne, Switzerland.

Abstract

The High-Luminosity LHC (HL-LHC) upgrade represents a challenge for the full chain of its injectors. The aim is to provide beams with a brightness a factor of two higher than the present maximum achieved. The 450 GeV beams injected into the LHC are directly provided by the Super Proton Synchrotron (SPS) via two transfer lines (TL), TI2 and TI8. Such transfer lines are both equipped with a passive protection system to protect the LHC aperture against ultra-fast failures of the extraction and transport systems. In the LHC instead, the injection protection system protects the cold apertures against possible failures of the injection kicker, MKI. Due to the increase of the beam brightness, these passive systems need to be upgraded. In this paper, the foreseen and ongoing modifications of the LHC injection protection system and the TL collimators are presented. Simulations of the protection guaranteed by the new systems in case of failures are described, together with benchmark with measurements for the current systems.

INTRODUCTION

The high brightness of the HL-LHC beams represent an unprecedented challenge for the full set of the passive protection devices of the LHC injection and transport system. An upgrade of the main injection absorber, TDI, is foreseen in order to maintain the necessary protection of the LHC cold aperture. Also, the SPS-to-LHC transfer line collimators will be replaced with more suitable devices for the aimed beam brightness.

The LHC injection system is composed by: injection septum MSI, injection kicker MKI, injection dump TDI and two auxiliary absorbers TCLIA and TCLIB; all acting on the vertical plane. The HL-LHC injection system will not be too different from the present one. The main modification is represented by the new TDI, i.e. the segmented TDI (TDI-S).

The TDI-S will be composed by three separated blocks: the first two blocks will be 1.425 m, made of Graphite (R4550 or similar), the last one instead will be made of higher Z material (60 cm of Aluminium and 70 cm of Copper). Every block will be separated from each other by 125 cm and the last block is also 2 mm further away from the circulating beam than the others to avoid direct impact of the beam. This is the design baseline at the moment of writing this paper.

Among the other modifications, it is worth to mention also the slightly different crossing and separation schemes as well as the upgrade of the transfer line collimators (TCDI). The TCDIs upgrade represents a key upgrade because the aperture of the LHC (especially the horizontal one) during the transport from the SPS is directly protected only by these collimators. They are designed to protect the LHC and the MSI from any kind of failures of the SPS extraction and TL elements.

The protection against fast losses relies on prompt detection of the change in field of the magnet under observation. The MSI (its time constant is about 1 s) is constantly monitored from different systems (Fast Extraction Interlock and Fast Magnet Current Monitor), which guarantee an adequate protection and redundancy. For ultrafast failures of the SPS extraction kickers, the TCDIs represent the last resort to protect the MSI and the LHC arc aperture.

In case of ultrafast failure of the LHC injection kicker instead, the LHC (HL-LHC) injection protection devices are the one responsible to for the protection of the vertical LHC aperture. The TDI (TDI-S) is the main protection against MKI failures - it is installed about 90° vertical phase-advance from the MKI to maximise the protection guaranteed. The TCLIA and TCLIB protect against possible phase-advance errors between MKI and TDI; they are placed at $\Delta\mu_y \approx 180° + 20°$ and $\Delta\mu_y \approx 360° - 20°$ from the TDI respectively.

In this paper the following notation will be used:

$$\sigma_{LHC} \equiv \sqrt{\beta(s)\ 3.5\,\text{mm mrad}/(\beta\gamma)} \quad (1)$$

$$\sigma_{HLLHC} \equiv \sqrt{\beta(s)\ 2.5\,\text{mm mrad}/(\beta\gamma)}, \quad (2)$$

where $\beta(s)$ is the beta-function at an s location and $(\beta\gamma)$ is the product of the relativistic factors.

TRANSFER LINE COLLIMATORS

The main aim of the TL collimators is to ensure adequate protection of the LHC cold apertures. From the LHC Design Report [1], the minimum available aperture in the arc is $7\,\sigma_{LHC}$, hence this represents the target protection for the TL collimation system.

In order to define the collimator jaws aperture needed to guarantee the above cited protection, all possible sources of error have to be taken into account. All the considered errors are listed in Table 1; summing these contributions linearly, considering a typical beam size of 0.5 mm, the total error is $\approx 1.4\,\sigma_{LHC}$ [2]. The maximum escaping amplitude in a "three-phase" collimation system is given by pure geometrical considerations, i.e. $A_{max} = A_{jaw}/\cos(\pi/6)$; where A_{jaw} is the required jaw position, including errors. For the

ISBN 978-3-95450-185-4

LHC $A_{max} = 7\,\sigma_{LHC}$, so the collimator half-gap should be $A_{jaw} = 4.5\,\sigma_{LHC}$. Due to the very conservative tolerances used in the definition of the LHC minimum aperture, the TL collimators have been operated at 5 σ during LHC Run 2. In view of the HL-LHC upgrade, such collimators will be updated in order to guarantee the required protection of the LHC arc aperture. As detailed described in [3], their active length will be increased to deal with the higher brightness. As a consequence, some of them had to be moved from their current location and hence a optics rematch was done to maintain $\beta_x \times \beta_y > 3600\,\mathrm{m}^2$, that is the brightness limitation. The phase-space coverage is unchanged, even if some mechanical tolerances are increased due to the longer jaws.

Table 1: Errors for the TL Collimator Jaws [2].

Error type	Unit	Value
Inter-jaw parallelism	μm	50
Jaw axis wrt tank	μm	100
Tank axis wrt beam size	μm	180
Surface flatness	μm	100
Knowledge of bema position	μm	44
Beam size errors	σ	0.5

MKI FAILURE MODE ANALYSIS

The beam coming from the SPS through the two transfer lines is horizontally deflected by the injection septum and vertically by the injection kicker, MKI. Once the injected beam trajectory is equal to the vertical closed orbit at the kicker longitudinal location, $y_{inj}(s_{MKI}) = y_{CO}(s_{MKI})$, the MKI provides the necessary deflection, $\theta_{MKI} \approx 850\,\mu$rad, to adjust the beam vertical transverse momentum.
The injection kicker is composed by four tanks per ring. To provide the required deflection, a total integrated field of 1.2 T m is needed. Such dipole field is required for a maximum of about 8 µs, which is the maximum possible beam length for LHC injection. Due to the LHC box stacking injection, the rise and fall time of the MKI magnetic field has to be very short, 0.9 µs and 3.0 µs respectively.The reason of such tight requirements on fall and rise time is because this defines the minimum possible space between LHC batches and hence the maximum number of bunches usable for LHC physics. To preserve the beam emittance during the injection process, the MKI flat top ripples amplitude must be below ±0.5 % the nominal field [1].
Each MKI tank is equipped with its own Pulse-Forming Network (PFN). Two resonant charging power supply (RCPS) per system are used to charge the PFNs and a main and dump switch are required at both ends of the PFN to be able to control the pulse duration. To satisfy the challenging requirements, a well matched high bandwidth system is required. This is achieved with a multi-cell PFN and a multi-cell travelling wave kicker magnet, both connected via a transmission line terminated by a matched resistor [4].

Assuming that the beam energy tracking system (BETS) and the re-triggering system always work, and that the MKI pulse length is 8.2 µs, in case of failure only a limited number of bunches can escape the injection region with a dangerous amplitude. This is true only for the following possible MKI failures: charging failure, erratic triggering of the kickers, missing triggering of one switch and timing error.
As a consequence of these failures, the circulating or the injected beam could be swept on the TDI front-face or completely dumped onto the TDI. This could happen any time during the PFN charging process, hence the resulting MKI waveform could have a shorter flat-top (4.1 µs) at any field value up to the maximum. This yields to a maximum of 186 bunches (considering 225 ns batch spacing) that can be deflected at any angle. The flashover inside a magnet needs also to be included among the possible failures. Depending on the longitudinal location of the breakdown, the field seen by the beam can be reduced or amplified. This can affect the whole injected beam (maximum of 288 bunches for 25 ns operation) as well as the circulating one. A short circuit is created and the pulse is reflected - if this happens right at the beginning of the magnet, the current in that magnet will be zero; if it happens at the end instead, the current is doubled and so the field. In case of flashover in more than one magnet simultaneously, the system can provide up to a maximum of twice the design field, 200 %. For both circulating and injected beam, a kick of about 20 % the nominal one corresponds to an impact parameter on the TDI larger than 5 σ.

TRACKING STUDIES OF THE MOST CRITICAL MKI FAILURE FOR HL-LHC INJECTION SYSTEM

A flashover into the MKI magnets can translate in an alteration of the MKI nominal kick, between 0 and 125 %, depending on its longitudinal position. Due to the nature of the LHC box stacking injection, the MKI is ready to kick an upcoming injected SPS batch while another is already circulating in the machine. In case of asynchronous triggering of the MKI, the circulating beam can be deflected by 0 to 0.85 mrad. Of course any combination of the just described failures has a non-zero probability, although very small, hence they are considered beyond design.
In these possible failures, the interesting part for machine protection is represented by the range of kicks $[-20, 20]$%. Above these, the impact parameter on to the TDI is above $5\,\sigma_{LHC}$ and hence almost the whole beam will be lost directly there. This situation can be seen equivalently for the injected and for the circulating beam, where these range of kicks can be originated by a flashover in the MKI at particular longitudinal position. In this range, the scenario that leads to the highest number of particle with the biggest amplitude is represented by the grazing impact on the TDI (i.e. when $y(s_{TDI}) = 8.1\,\sigma_{HLLHC}$). This is the case because the

ISBN 978-3-95450-185-4

TDI-S, due to its design, let only the 0.2 % of the particles that hit it survive, hence this scenario maximises the particles at high amplitudes. The highest number of bunches that can be deflected coherently is 288.
In order to evaluate the maximum amplitude with intensity above the safe beam flag, the survival function S:

$$S(x) \equiv 1 - F(x) = \int_x^{\infty} f(t)dt \tag{3}$$

normalised to the beam intensity (6.62×10^{13} p$^+$)) of the tracked particles, in the cases of the above described failures, has been calculated at the exit of the injection protection system.
The amplitude at the exit of the injection system is calculated taking into account also angles (normalising the vertical action to the betatron beam size), that is:

$$Y = \sqrt{y^2 + (\beta_y y' + \alpha_y y)^2}. \tag{4}$$

When $S(Y) = 5 \times 10^{11}$ p$^+$, represents the maximum amplitude above the safe beam flag. To be noticed, this is a quite pessimistic way of assessing the minimum protected aperture because the implicit assumption made is that all particles with a larger normalized amplitude will be lost at exactly the same longitudinal location.
The simulations of MKI failures, as just described, have been carried out for both B1 and B2 and for different protection device configurations : i) nominal settings, i.e. TDI-S, TCLIA and TCLIB at 8.0 σ_{HLLHC} half-gap; ii) TDI-S at 9.2 σ_{HLLHC} and TCLIA/B at 8.0 σ_{HLLHC}; iii) TDI-S and TCLIs at 9.2 σ_{HLLHC}; iv) TDI-S with maximum error, 2.5 σ_{HLLHC}, and nominal settings for TCLIs; v) injection protection maximum error, i.e. all injection protection devices misaligned of 2.5 σ_{HLLHC}. The maximum error on the injection protection devices takes into account injection precision delivery [5], local orbit, optics discrepancy with the nominal during setting-up and mechanical errors (Table 2). Other possible optics errors that could lead to a beta-beat of maximum 10 % [6], translates in a phase-advance error between the MKI and the TDI smaller than 10°, hence they can be neglected because of the design strategy of the injection protection system. The error on the local orbit is assumed to be maximum 1.1 σ_{HLLHC} due to the two sided collimator nature of the injection protection devices. A bigger error will translate in high losses and a consecutive trigger of the dump. The errors assumed to check the protection guaranteed by the LHC injection protection system have been added linearly and took the most extreme cases in order to be as conservative as possible.
The simulations are done for a 450 GeV beam with normalized emittance of $\epsilon^N_{x,y} = 1.37\,\pi$ mm mrad. The tracking inside active accelerator elements is performed with MAD-X and instead the tracking inside the collimator jaws is done with `pycollimate`. The simulated loss patterns for the three different protection device configurations are shown in Fig. 1 for B1 as example. The losses distribution for B2 is

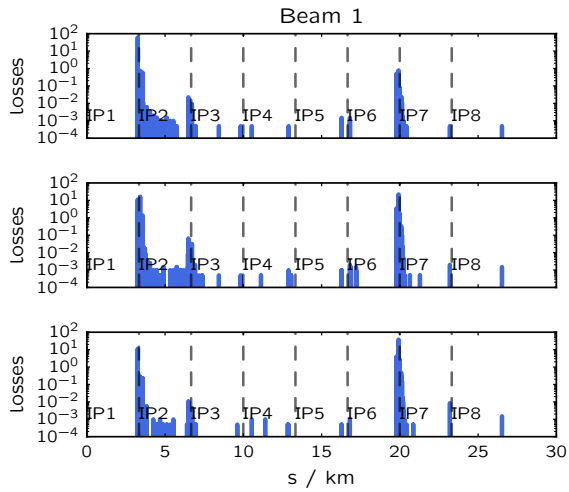

Figure 1: Losses distribution on the HL-LHC elements in case of failure of the MKI for three different protection devices configurations. Left, for Beam 1 and right for Beam 2.

equivalent. It is interesting to highlight the evolution of the losses in IR7 as function of the injection protection elements settings - the losses increase by about an order of magnitude for only 1.2 σ_{HLLHC} error at the TDI. Evaluating then the survival function at the exit of the injection protection system (Fig. 2), the worst case is represented by the scenario with all protection devices misaligned by 2.5 σ_{HLLHC} for B2. This gives the maximum amplitude of the halo with intensity equal to the setup beam flag, that is 10.3 σ_{HLLHC}, hence the maximum dangerous amplitude of the halo originated by SPS extraction, transport and injection process shall be considered to be 10.3 σ_{HLLHC}, which corresponds to 8.7 σ_{LHC}. These studies, and their implication, are discussed in details in [6].

Table 2: Maximum errors, at the TDI and TCLIs, assumed to evaluate the amplitude of the halo escaping the injection protection system, calculated assuming an emittance of 2.5 mm mrad.

Parameter set	**Value** ($\sigma_{\mathbf{HLLHC}}$)
Injection precision	0.35
Mechanical tolerances	0.35
Setting-up optics	0.71
Local orbit	1.1
Total	2.5

ISBN 978-3-95450-185-4

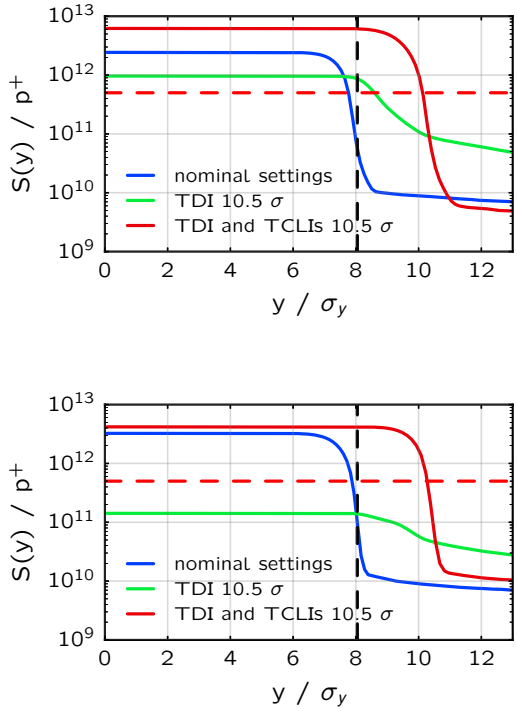

Figure 2: Survival function of the tracked particle distribution at the exit of the HL-LHC injection protection system for B1 (Top) and B2 (Bottom) for the cases: i, iv and v.

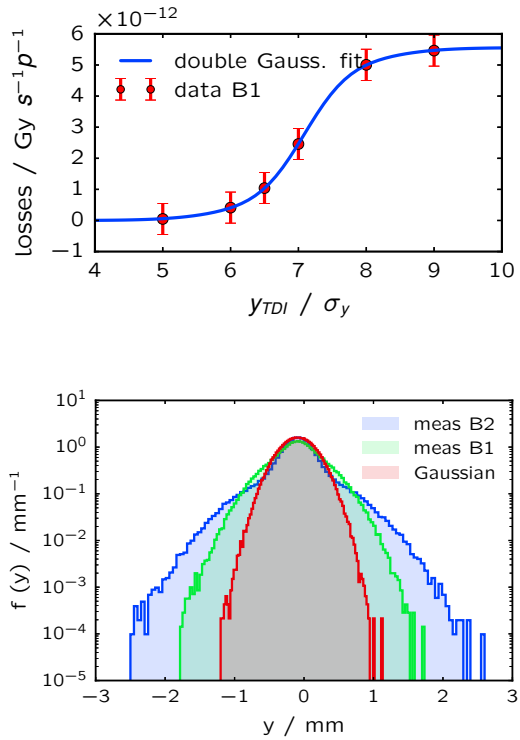

Figure 3: (Top) Measured normalised losses at the TDI in IP2 (red dots) as function of the theoretical beam displacement the the TDI. The solid blue line is a least square fit of the measurement point with a double Gaussian CDF. (Bottom) Reconstructed vertical beam profile distribution (for B1 and B2) with the data shown in Fig. 4 at the IP1. These are compared with the ideal Gaussian distribution (red) at the same location.

EXPERIMENTAL DATA FROM THE PRESENT LHC INJECTION PROTECTION SYSTEM

In order to benchmark the simulations presented in this paper, experimental data have been taken on the present LHC injection protection system. The aim of these measurements was to validate with beam the chosen settings of the TDI. All injection protection devices were set to $6.8\,\sigma_{LHC}$ and centred around the established machine closed-orbit. Pilot beams (one bunch of $\approx 1\times10^{10}$ protons) are then injected and sent directly to the dump without completing a full revolution. Two superconductive correctors, positioned between the MSI and the TDI, are used to steer the beam on to the TDI, simulating an MKI kick. Such correctors are set in a way that there is a direct control of the beam displacement at the TDI. Varying the corrector strengths and recording losses at the TDI, TCLIA and TCLIB, the actual aperture of the TDI can be retrieved. In Fig. 4, the measurements taken during Run 2 commissioning are plotted (blue dots). Here the closest BLM, and with the longest integration time, at each protection device was used. Their readings were normalised by the extracted intensity from the SPS. The losses trend, at the TCLIA and TCLIB, is reverted between 6.5 and $7\,\sigma_{LHC}$ (half nominal sigma was the resolution of the measurements), confirming the theoretical half-gap of the TDI of $6.8\,\sigma_{LHC}$.

From these data, the beam profile at the TDI can be also inferred. At the time of the measurements, the beam was not scraped in the SPS. As suggested in literature [7], the beam delivered in this way to the LHC is more likely to have a double Gaussian profile than being normally distributed. In fact, the TDI BLM data can be fitted with the function (Fig.3–top):

$$f(x) = c_1(1-c_2)\mathcal{N}[\mu_0,\sigma_1](x) + c_2c_1\mathcal{N}[\mu_0,\sigma_2](x), \quad (5)$$

where the same average, μ_0, is used for both Gaussian distributions due to the assumption of symmetric beam; c_1 and c_2 are scaling factors and σ_1, σ_2 the standard deviations of the two Gaussian distributions. The same procedure was repeated for both B1 and B2. The resulting distribution is plotted in Fig. 3–bottom and compared with the ideal Gaussian distribution at the chosen location. The observable difference between the fit results for B1 and B2 is thought to be originated from the impossibility to measure losses with high impact parameter in IP8 (B2). This was due the interlock triggering at the experiments and the consequent interruption of commissioning procedure.

ISBN 978-3-95450-185-4

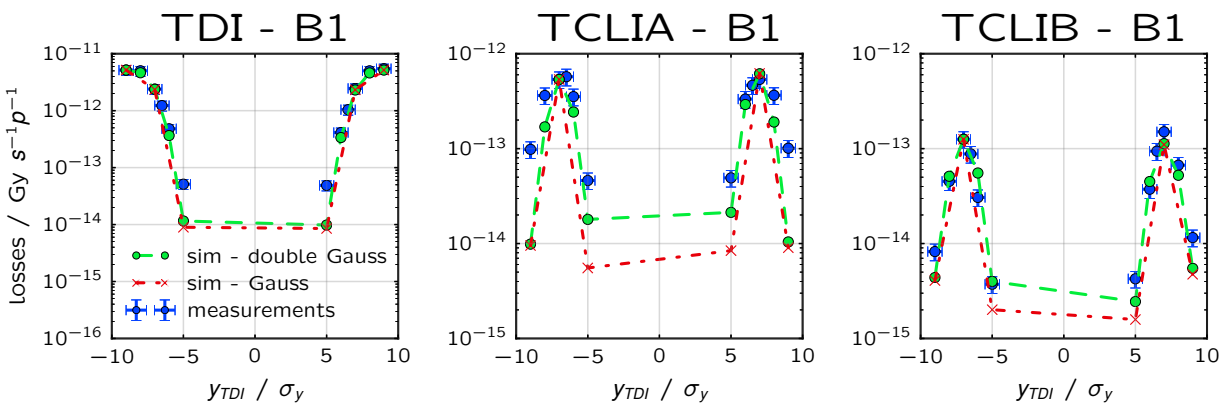

Figure 4: Comparison of measurements (blue dots) and simulations (dashed lines) of losses induced by different MKI kick at the three injection collimators. In red are plotted the results from particle tracking starting with a Gaussian transversally distributed beam, in green the same tracking has been performed but using the beam vertical profile obtained from Fig. 3.

To be able to compare simulations and measurements, a conversion from proton undergone inelastic scattering in the collimators and BLM signal has to be done. Previous studies [8] show the complexity in obtain reliable calibration factors for the injection collimator BLM data, hence the comparison done is based on the ratio among different BLMs. The proximity of the protection devices to each other makes the losses at the previous device interfere with the readings of the following one via particle shower development. In Fig. 4, the measurements form 2016 commissioning have been compared with two beam configurations: ideal Gaussian (red dashed line) and double Gaussian (green dashed line) distributed beam. As expected, the main difference between the types of transverse beam distribution is visible for small beam displacements at the TDI. At the TCLIA, the discrepancy with simulations reaches the maximum for $9\,\sigma_{LHC}$ deflection of about an order of magnitude. The main source of disagreement between BLM readings and simulations is originated from the fact that the simulations only account for primary and secondary protons lost at the different devices and not for any another kind of particles. Also, the simulations are done considering an ideal machine configuration, which is obviously not the case. The agreement at the TCLIB is smaller than a factor 2 overall. A better agreement could be achieved taking into account possible errors and particle shower developments, although for the propose of these studies this was not necessary. It can be concluded that the agreement between simulations and measurements is satisfactory, especially considering the uncertainty on beam position at the different devices and particle shower contribution.

CONCLUSIONS

Failures of the MKI are a serious machine protection concern. The increase in brightness will only translate in an increased danger if no countermeasures are put in place. The TDI upgrade will permit to properly protect the downstream elements (mainly the D1 and the triplet) and to survive a direct impact of the full SPS train.

A model for the HL-LHC injection system has been developed and possible failure cases studied in detail. An estimation of the maximum amplitude with intensity equal to the setup beam flag has been given.

A very good agreement between BLM readings and particle tracking has been shown. Due to the similarities with the model developed for HL-LHC and LHC, the prediction presented in this chapter for the new injection protection system can be considered validated.

ACKNOWLEDGEMENTS

The authors would like to thank all the people that have contributed with valuable comments and stimulating discussions, mainly M. Barnes, R. Bruce, M. Giovannozzi, S. Redaelli and J. Uythoven.

ISBN 978-3-95450-185-4

REFERENCES

[1] O. Brüning et al., "LHC Design Report", CERN, Geneva, 2004, http://cds.cern.ch/record/782076

[2] V. Kain et al., "The New Transfer Line Collimation System for the LHC High Luminosity Era," IPAC2014, June 2014, MOPRI096, p. 839.

[3] V. Kain et al., "Changes to the Transfer Line Collimation System for the High-Luminosity LHC Beams", FERMILAB-CONF-15-271-AD, IPAC15, Richmond, USA, pp.2124-2127.

[4] L. Ducimetière et al, "Design of the injection kicker magnet system for CERN's 14 TeV proton collider LHC", CERN-SL-95-80-BT, LHC-NOTE-337, TRI-PP-95-50, 1995.

[5] B. Goddard et al, "Aperture and Delivery Precision of the LHC Injection System", LHC-Project-Report-753, CERN-LHC-Project-Report-753, 2004.

[6] R. Bruce et al., "Parameters for aperture calculations at injection for HL-LHC", CERN note, manuscript in preparation.

[7] L. Drøsdal et al, "SPS Scraping and LHC Transverse Tails", IPAC13, Shanghai, China, pp. 957-959.

[8] C. Bracco, "Experiments on the margin of beam induced quenches a superconducting quadrupole magnet in the LHC", IPAC12, New Orleans, USA, pp. 124-126.

ISBN 978-3-95450-185-4

CORRECTOR MAGNETS FOR THE CBETA AND eRHIC PROJECTS AND OTHER HADRON FACILITIES*

N. Tsoupas†, S. Brooks, A. Jain, F. Meôt, V. Ptitsyn, and D. Trbojevic
Brookhaven National Laboratory, Upton, NY 11973, USA

Abstract

The CBETA project [1] is a prototype electron accelerator for the proposed eRHIC project [2]. The electron accelerator is based on the Energy Recovery Linac (ERL) and the Fixed Field Alternating Gradient (FFAG) principles. The FFAG arcs of the accelerator are comprised of one focusing and one defocusing quadrupoles which are designed as either, iron dominated or Halbach-type permanent magnet quadrupoles [3]. We present results from 2D and 3D electromagnetic calculations on corrector electromagnets for both the iron dominated, and Halbach type quadrupoles.

INTRODUCTION

The proposed eRHIC accelerator [2] will collide 20 GeV polarized electrons with 250 GeV polarized protons or 100 GeV/n polarized $^3He^{+2}$ ions or other non-polarized heavy ions. The electron accelerator of the eRHIC will be based on a 1.665 GeV Energy Recovery Linac (ERL) placed in the RHIC tunnel with two recirculating rings placed also in the RHIC tunnel alongside the hadron RHIC accelerator. Fig. 1 is a schematic diagram of the eRHIC accelerator showing the hadron accelerator (blue ring), and the electron accelerator (red ring).

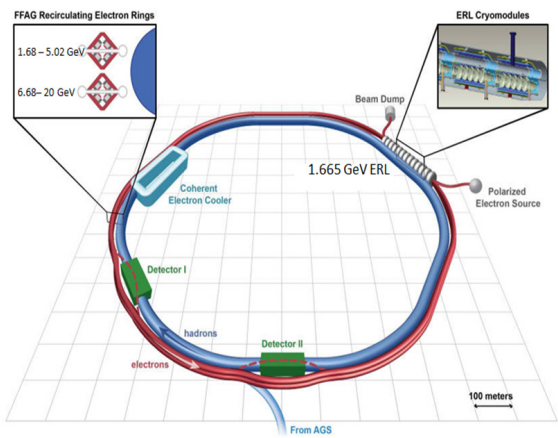

Figure 1: Schematic diagram of the eRHIC accelerator. The blue and red rings are the hadron and the electron accelerators respectively. The right insert is the ERL and the left insert is a cross section of the two FFAG rings of the electron accelerator. The green rectangles are the experimental areas for the electron-hadron collisions.

The 1.655 GeV ERL is shown as insert in the top right corner and the cross section of the two recirculating electron rings shows in the insert on the top left corner. The experimental areas of the electron-hadron collisions are the green rectangles. Two important concepts are involved in the electron accelerator, namely, the ERL and the FFAG concepts. The ERL concept provides 1.665 GeV of energy to the electron bunches each time they pass through the ERL for the electrons to achieve the top energy of the 20 GeV before the collision with the hadrons. Following the collision the electrons deliver back to the ERL the 20 GeV of energy by recirculating 12 times through the ERL, each time delivering to the ERL 1.665 GeV of energy. Since it takes 12 passes for the electrons to achieve the 20 GeV of energy, and also 12 passes to give back the energy to the ERL, the electron bunches circulating in the accelerator have 12 different energies, ranging from 1.685 to 20 GeV. The three electron bunches with the energies 1.685, 3.350 and 5.015 GeV are circulating in one FFAF arc and the rest of the bunches with energy range from 6.68 GeV to 12.0 GeV in the second FFAG arc. Thus this FFAG places electron bunches with large energy range in a small transverse distance of ~22 mm in each of the FFAG arcs. The CBETA which is the prototype of the eRHIC accelerator will employ both, the ERL and FFAG concepts and is under construction in Cornell University. Fig.2 is a layout of the accelerator showing the ERL (LA) the FFAG sections (FA, ZA, ZB, and FB) and the splitter/merger sections (TX, SX).

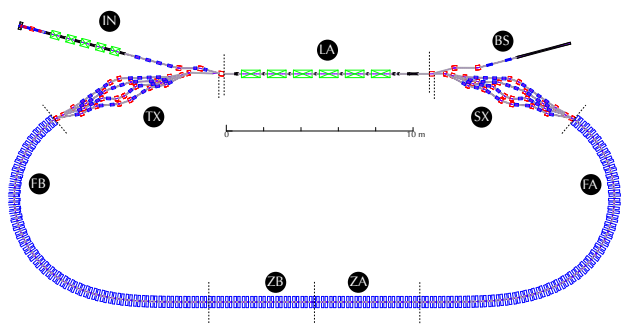

Figure 2: Layout of the CBETA accelerator. The section labeled (LA) is the ERL, The sections labeled (FA), (ZA), (ZB), and (FB) are the FFAG which will accommodate 4 energies of the recirculating electron bunches.

The FFAG arcs for either eRHIC or CBETA accelerators consists of FODO cells, each cell comprised of one focusing and one defocusing quadrupole. The top plot in Fig. 3 shows the orbits, the middle plot the $\beta_{x,y}$ functions, and the bottom the $\eta_{x,y}$ dispersion functions of the electron bunches with

* Work supported by the US DOE
† tsoupas@bnl.gov

ISBN 978-3-95450-185-4

the four different energies in one of the CBETA cells. The remarkable property of the FFAG is the accommodation of bunches with large energy range into a relatively small transverse space of the FODO cell.

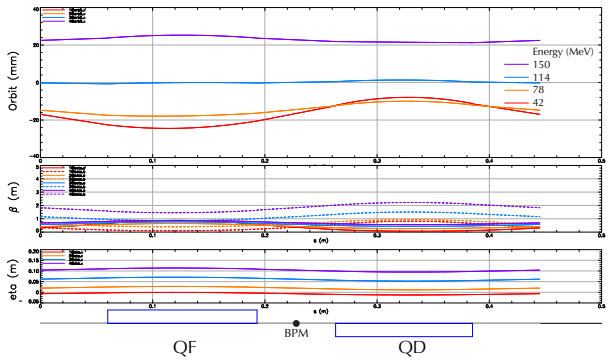

Figure 3: The orbits, the $\beta_{x,y}$ functions, and the $\eta_{x,y}$ dispersion functions of the electron bunches with the four different energies in one of the CBETA cells.

THE MAGNETS OF THE FFAG CELL

There are two possible designs for the magnets of the FODO cell. The iron dominated permanent magnets shown in the left picture of Fig. 4 and the Halbach type magnets shown in the right picture of the figure.

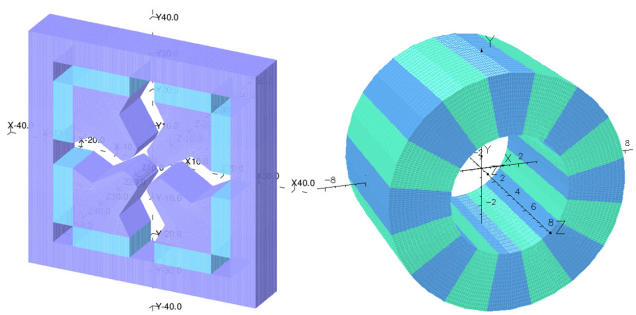

Figure 4: (Left) Isometric view of iron dominated magnet. (Right) Halbach type quadrupole.

The material shown as dark blue in the left picture of Fig. 4 is soft iron and the permanent magnet material is shown as the cyan color. The Halbach type of magnet shown in the right picture of Fig. 4 is made of permanent magnet wedges which are magnetized along a specified direction. Details on the design and measurements of these magnets are in Ref. [1].

THE CORRECTOR MAGNETS

In the following subsections we describe the corrector magnets for the iron dominated quadrupole and the Halbach quadrupole, and we provide results from the 2D and 3D electromagnetic design of the corrector magnets. The specifications of the corrector magnets call for electromagnets with air cooled conductors and an effective strength in the range of ±50 Gauss for the normal and skew dipole and ±0.4 T/m for the normal quadrupole. The field uniformity of the corrector should be $\sim \pm 10^{-2}$ in the range of ±3 cm. In all calculations the material of the permanent magnet was not included since it does not affect the field of the corrector due to the high saturation ($\mu \approx 1.0$) of the permanent magnet material. The insignificant effect of the permanent magnet on the corrector's field has been proven experimentally [4].

Correctors for the Iron Dominated Magnets

For the iron dominated magnets we have found three type of corrector magnets that comply with the specifications, the normal quadrupole and the normal and skew dipole.

The normal quadrupole corrector Figure 5 shows the isometric views of two different but equivalent coil arrangements which can generate a quadrupole field. The left picture in Fig. 5 shows the coils of the corrector wound on the poles of the magnet, and the right picture shows the coils on the return yoke. The field uniformity of the quadrupole corrector is $\sim \pm 10^{-4}$ and exceeds the specifications

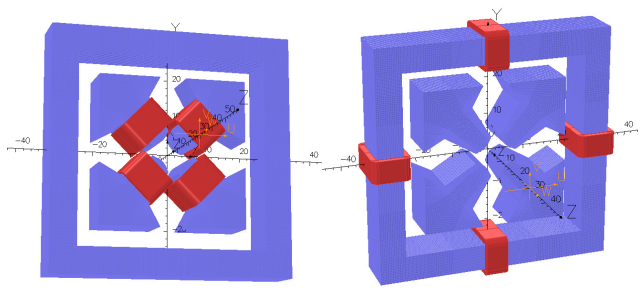

Figure 5: (Left) Isometric view of the magnet with the corrector coils on the poles . (Right) Isometric view of the magnet with the corrector coils on the return yoke.

The normal dipole corrector Figure 6 (Left) is an isometric view of the magnet with the coil of the normal dipole corrector. (Right) An expanded view of the cross section midway the length of the magnet. The corrector can provide a dipole field of 50 Gauss with current density of 1 A/mm^2. The conductor of the coil are arranged to provide an approximate cos(θ) current distribution.

The skew dipole corrector Figure 7 (Left) is an isometric view of the magnet with the coil of the normal dipole corrector. (Right) An expanded view of the cross section midway the length of the magnet. The corrector can provide a dipole field of 50 Gauss with current density of 1 A/mm^2. All the conductor of the coil above the median plane carry the same current density and those below the median plane the opposite current density.

Correctors for the Halbach Type Magnets

The Halbach magnets can accommodate almost any corrector multipole. Here we will present the normal and skew

ISBN 978-3-95450-185-4

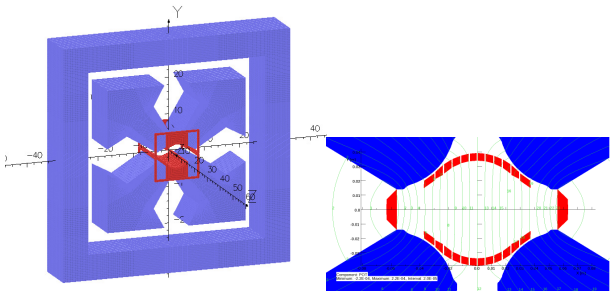

Figure 6: (Left) Isometric view of the magnet with the coil of the normal dipole corrector. (Right) Cross section of an expanded view midway of the magnet. The green lines are the equipotential magnetic lines.

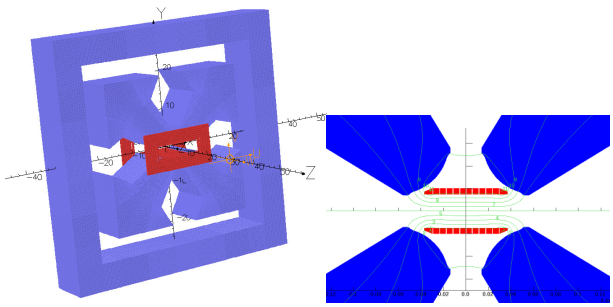

Figure 7: (Left) Isometric view of the magnet with the coil of the skew dipole corrector. (Right) Cross section of an expanded view midway of the magnet. The green lines are the equipotential magnetic lines.

dipole and quadrupole. A rectangular window frame magnet can accommodate all the correctors. For example the left picture in Fig. 8 shows a window frame magnet with a coil powered as a normal dipole is placed around a Halbach quadrupole magnet. It has been shown experimentally [4]

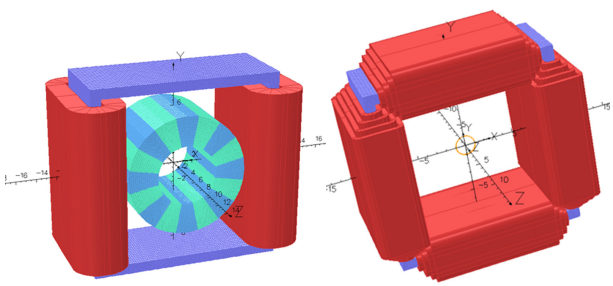

Figure 8: (Left) Isometric view of a window frame magnet as a normal dipole corrector placed around a Halbach magnet. (Right) A window frame magnet with coils in all its sides can be used as a normal dipole and quadrupole and skew dipole. By rotating the window frame magnet by 45^o the corrector can provide normal and skew dipole and skew quadrupole.

that the field of the window frame dipole corrector magnet is superimposed to the that of the Halbach magnet. The superposition is independent of the corrector's field direction (isotropic). The superposition is due to the saturated nature of the permanent magnet that makes the permeability of the permanent magnet material ($\mu \approx 1.0$). A skew dipole can be made by rotating the window frame magnet (left picture in Fig. 8) by 90^o or by placing an additional coil on the horizontal sides of the window frame as shown in the right picture in Fig. 8. The side coils are powered independently of the top-bottom coils. The normal quadrupole corrector is identical to the window frame magnet shown in the left picture of Fig. 8 but the coils are powered in such a way to generate a quadrupole field. A window frame magnet powered as a quadrupole is also known as a Panofsky quadrupole. By rotating a Panofky quadrupole by 45^o we generate a skew quadrupole field. In addition the four coils can also provide normal and skew dipoles simultaneously.

CONCLUSIONS

We designed dipole and quadrupole correctors for the iron dominated and the Halbach type of magnets which are two possibilities for the cells of CBETA or eRHIC projects . We found that the correctors for the Halbach magnets are easier to design and provide the required field with superior field uniformity.

REFERENCES

[1] http://arxiv.org/abs/1504.00588

[2] E.C. Aschenauer, et al., "eRHIC Design Study: An Electron-Ion Collider at BNL", arXiv:1409.1633, Chapter 3, (2014).

[3] K. Halbach, "Design of permanent multipole magnets with oriented rare earth cobalt material" , Nucl. Instrum. Meth. 169 (1980) pp. 1-10.

[4] private comunication Jain Animesh coauthor.

ISBN 978-3-95450-185-4

MITIGATION OF NUMERICAL NOISE FOR BEAM LOSS SIMULATIONS

F. Kesting*[1,2], G.Franchetti[2,1]
[1] Institute for Applied Physics (IAP), University of Frankfurt, Germany
[2] GSI, 64291 Darmstadt, Germany

Abstract

Numerical noise emerges in self-consistent simulations of charged particles, and its mitigation is investigated since the first numerical studies in plasma physics [1–3]. In accelerator physics, recent studies find an artificial diffusion of the particle beam due to numerical noise in particle-in-cell tracking [4], which is of particular importance for high intensity machines with a long storage time, as the SIS100 at FAIR [5] or in context of the LIU upgrade [6] at CERN. In beam loss simulations for these projects artificial effects must be distinguished from physical beam loss. Therefore, it is important to relate artificial diffusion to artificial beam loss, and to choose simulation parameters such that physical beam loss is well resolved. As a practical tool, we therefore suggest a scaling law to find optimal simulation parameters for a given maximum percentage of acceptable artificial beam loss.

HEAVY-ION BEAM LOSSES

The uncontrolled loss of charged particles is an important issue in high energy particle accelerators. For 1 GeV proton beams, it was found that 1 W/m is the maximum tolerable beam loss to allow hands-on-maintenance [7]. If more the energy is deposited, a worker would be exposed a too high dose during maintenance, and hence a health hazard.

However, this limit of energy deposition is only valid for 1 GeV proton operation. According estimates for heavy-ion machines were only found recently [8] by dedicated simulation studies in which a uniform beam loss along a beam pipe is considered. The pipe is irradiated for 100 days, while the effective dose rate was calculated four days after the radiation stopped. Then, the residual activity is compared to the residual activity caused by 1 GeV protons, in order to infer a scaling law for heavy ions. Using this scaling law, we estimate the maximum acceptable beam loss per run in the SIS100 for U^{+28} particle beams at different energies, see the Table 1.

Table 1: Maximum Acceptable Beam Loss

part. energy	energy dep.	# particles
200 MeV/u	75 W/m	$1.1 \cdot 10^{13}$
500 MeV/u	23 W/m	$1.3 \cdot 10^{12}$
1000 MeV/u	12 W/m	$3.4 \cdot 10^{11}$

The design goal of the SIS100 is a maximum of $5 \cdot 10^{11}$ particles of U^{+28} stored in the machine, such that only the loss of a full 1GeV/u Uranium beam depicts a hazard. For particle beams with less energy a complete, but uniform, beam loss can be tolerated.

Further, beam loss may cause a heating of superconducting structures, such that the material changes to the normal conducting phase. This may lead to a serious machine damage, or at least will require maintenance, and thus an interruption of beam time. It was found at the Large Hardron Collider (LHC) at CERN, that a nominal beam loss of the order of 10^{-6} corresponding to 10^6 protons can cause a magnet quench [9]. The limit on the nominal beam loss for the LHC is exceptionally small, because the beam energy and the and the intensity are very high compared to other machines. Simulation studies on the superconducting magnets of the SIS100 synchrotron at FAIR show that there is no risk of a magnet quench [10].

The lifetime of organic insulators and protection diodes in superconducting magnets is expected to give the most restrictive limit to beam loss for the SIS300 synchrotron. It was found in simulation studies that a maximum of 2 percent nominal beam loss can be tolerated for this machine [11].

In summary, the maximum acceptable beam loss varies greatly for various scenarios, such that different upper bounds are required for artificial beam loss in numerical simulations.

ARTIFICIAL BEAM LOSS

In the following chapter, we present an analytic model to predict artificial beam loss induced by numerical noise in particle-in-cell tracking. Beam loss occurs whenever the emittances of a single particle i are larger than the acceptance of the machine. A collimator allows controlled particle loss, as particles with large amplitudes can be removed without activating the accelerator structures. By adjusting the geometry of a collimator, the acceptance of a machine can be set to the required size. The rms emittance of a particle beam is given by

$$\epsilon_x = \sqrt{\langle x^2 \rangle \langle x'^2 \rangle - \langle x x' \rangle^2}, \tag{1}$$

and accordingly for the y-plane. Here, $\langle \cdot \rangle$ is the moment of the according coordinate, and

$$\langle x^2 \rangle = \sigma_x^2 \qquad \langle x'^2 \rangle = \sigma_{x'}^2 \tag{2}$$

are the variances of the phase space coordinates, which quantify the beam size.

The rms emittance of a beam growths linearly in the presence of numerical noise, as long as numerical noise is weak and not correlated. The average emittance growth per integration step of length Δs was derived from a single particle

* f.kesting@gsi.de

ISBN 978-3-95450-185-4

model as [4]:

$$\frac{\Delta\epsilon_x}{\Delta s} \simeq \Lambda \frac{\sigma_x^2}{2\epsilon_x} \left(\frac{q\delta E_x}{m_o c^2 \beta^2 \gamma^3} \right)^2 \Delta s. \quad (3)$$

Here, Λ accounts for the particle density of the distribution, with $\Lambda = 1$ for K-V beams and $\Lambda = 0.5$ for Gaussian beams. Further, m_0 is the mass of the particle, c is the speed of light, and β, γ are the relativistic factors. The factor δE_x accounts for the precision of the Poisson solver, and can be found by a simple numerical investigation. We randomly initialize the particle distribution, and calculate the electric field in the center of the beam. We repeat this procedure n times, and we identify the standard deviation of the n samples with δE_x. This analysis has a low computational load compared to a full tracking simulation, and can be used to efficiently find optimal simulation parameters for long-term tracking simulation, as shown in Ref. [4, 12].

As the particle beam diffuses due to numerical noise, the single particles may exceed the acceptance in long-term tracking simulations. We therefore expect to observe numerical noise induced particle loss. In the following, we derive estimates for such artificial beam loss, and find a scaling law on simulation parameters. These scalings can be used to find optimum simulation parameters in terms of computational load for a maximum tolarable amount of artificial beam loss.

The general form of a particle distribution function for a beam after injection is given by

$$f(\epsilon_{x,i}, \epsilon_{y_i})(s) = f\left(\frac{\epsilon_{x_i}}{\epsilon_x(s)} + \frac{\epsilon_{y_i}}{\epsilon_y(s)} \right), \quad (4)$$

where ϵ_{x_i} and ϵ_{y_i} are the single particle emittances. For an investigation on artificial beam loss, we have to consider that $f(\epsilon_x, \epsilon_y)(s)$ changes while tracking due to numerical noise. In the following we discuss artificial beam loss for the Gaussian distribution, and the Kapchinsky-Vladimirsky (K-V) distribution.

Gaussian Distribution

The Gaussian particle distribution is given by

$$f(\epsilon_{x,i}, \epsilon_{y_i})(s) = \frac{1}{4\epsilon_x \epsilon_y} e^{-\frac{1}{2}\left(\frac{\epsilon_{x,i}}{\epsilon_x(s)} + \frac{\epsilon_{y_i}}{\epsilon_y(s)} \right)}, \quad (5)$$

such that the single particle coordiantes follow a Gaussian distribution function. The mathematical condition for single particles to hit a collimator is given by the inequality

$$\frac{x^2}{(3\sigma_x)^2} + \frac{y^2}{(3\sigma_y)^2} > 1, \quad (6)$$

or, in terms of emittances,

$$\frac{\epsilon_{x_i}}{9\epsilon_x} + \frac{\epsilon_{y_i}}{9\epsilon_y} > 1. \quad (7)$$

For illustration, we plot a sample Gaussian distribution in Fig. 1 together with the condition given by Eq. 7. Most of the particles are initially not affected by the collimator. However, a grow of single particle emittance will slowly induce losses.

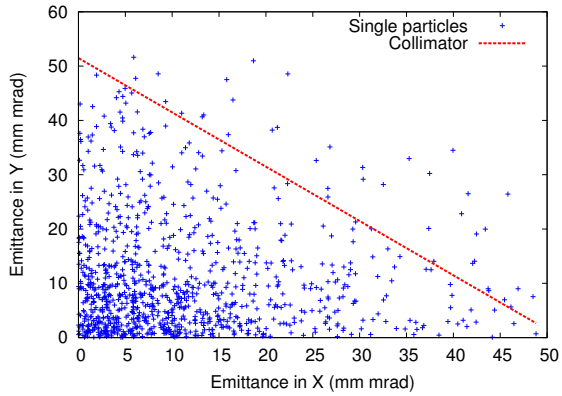

Figure 1: Distribution of single particle emittances (blue points) of a Gaussian beam, and the condition for collimation according to Eq. 7 (red line).

To estimate the amount of artificial particle loss, we develop a theoretical model where we consider beams with equal rms emittances, i.e. $\epsilon_x(s) = \epsilon_y(s) = \epsilon(s)$. We then find the condition for collimation as

$$\epsilon_{x_i}(s) + \epsilon_{y:i}(s) > 9\epsilon(s_0) \equiv A, \quad (8)$$

where A is the acceptance of the machine, set by the collimators. With this, we find the nominal beam loss as

$$\frac{\Delta N}{N} = 1 - \int_0^A d\epsilon_{x_i} \int_0^{A-\epsilon_x} d\epsilon_{y_i} f(\epsilon_{x_i}, \epsilon_{y_i})(s). \quad (9)$$

We use Eq. 5, to derive

$$\frac{\Delta N}{N} = \left(\frac{A}{2\epsilon_x(s)} + 1 \right) e^{-\frac{A}{2\epsilon_x(s)}}, \quad (10)$$

while the evolution of the rms emittance $\epsilon_x(s)$ is described by the scaling law Eq. 3. This model can be compared to previous models of beam loss [13, 14], where nominal beam loss was estimated by solving a diffusion equation via Bessel basis functions. For sufficiently large nominal emittance growth, it was found that

$$\frac{\Delta N}{N} = 1 - \exp\left(-\frac{\lambda_1}{4A} \left(\frac{\Delta\epsilon_x}{\Delta s} \right) s \right), \quad (11)$$

where λ_1 is the first zero of the Bessel function. We compare Eq. 10 and Eq. 11 in Fig 2, and find a significantly larger nominal beam loss for the model derived in this proceeding,. This discrepancy can be explained by the assumption of large emittance growth in Ref. [13], which refers to a beam shape given by the Bessel function J_0, while in our model a Gaussian distribution is assumed. Further, the self-consistent effect of the particle loss on numerical noise is not considered in our model. Therefore, our model is only valid for particle losses, where the distribution remains Gaussian, and the particle loss itself is not changing the strenght of numerical noise.

ISBN 978-3-95450-185-4

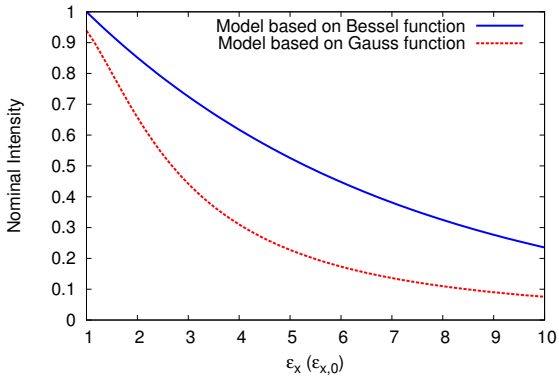

Figure 2: Comparision of models for beam loss caused by diffusion, where a Gaussian beam distribution is assumed (red line), or the distribution is approximated by the Bessel function J_0 (blue line).

K-V Distribution

The previously derived model for artificial beam loss is valid only for Gaussian beams. In the following, we investigate the artificial beam loss for particles beams described by the Kapchinsky-Vladimirsky (K-V) distribution [15], that is given by

$$f(\epsilon_{x_i}, \epsilon_{y_i})(s) \propto \delta\left(\frac{\epsilon_{x,i}}{2\epsilon(s)} + \frac{\epsilon_{y_i}}{2\epsilon(s)} - 1\right). \qquad (12)$$

such that solely a single line $\epsilon_{x,i} = 2\epsilon - \epsilon_{y,i}$ is populated, as shown in Fig. 3.

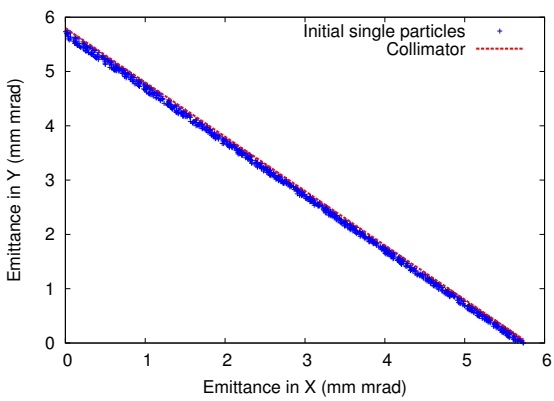

Figure 3: Distribution of single particle emittances (blue points) of a K-V beam, and the according condition for collimation (red line).

When placing the collimators at the edges of the beam, we find that even a weak numerical noise, and thus small artificial beam diffusion, may cause dramatic artificial beam loss in K-V beams

ESTIMATION OF OPTIMAL SIMULATION PARAMETERS

Previous results for Gaussian beams can be used to find optimal simulation parameters for beam loss studies. In the following, we discuss the case of beam loss simulations for the SIS100 at FAIR, but for simplicity assume a circular beam. The beam and simulation parameters are given as:

- beam size: $\sigma_x \simeq \sigma_y \simeq 7$ mm,
- tunes: $Q_x = 18.87$, and $Q_y = 18.74$,
- emittance: $\epsilon_x \simeq \epsilon_y \simeq 5.7$ mm mrad
- integration lenght: $\Delta s \simeq 5.703$ m
- ring length: $L = 1083.5$ m
- number of turn: $N_t = 2.0 \cdot 10^5$
- number of kicks: $N_s = 2 \cdot 10^5 \cdot 190$
- space charge tune shift: $Q_x \simeq Q_y \simeq -0.21$
- relativistic factors: $\beta = 0.56768$, $\gamma = 1.2147$
- particle: Uranium-238 in charge state 28

In the following, we consider an exemplary scenario, where the physics case requiers a maximum of 1 percent of artificial beam loss. We use Eq. 3 and Eq. 10, to find the condition for the minimum precision of our solver as

$$\langle \delta E_x \rangle \leq 28.9 \text{ Vm}^{-1}. \qquad (13)$$

In the following, we find optimal simulation parameters for the MICROMAP tracking library [16], that utilizes a two-dimensional spectral solver [17–19]. For the solver, we use as a first attempt $N_M = 1000$ macro-particles, and a mesh of $N_G \times N_G = 64 \times 64$ grid points. By analyzing $n = 1000$ samples of the electric field initializations, we find

$$\delta E_x \simeq 210 \text{ Vm}^{-1}. \qquad (14)$$

We thus have to increase the precision of the solver, by a factor of about 7 to limit the nominal beam loss to 1 percent, which requires $N_M \simeq 53.000$ macro-particles. If instead we consider a maximum of 0.1 percent of beam loss, our theory predicts an optimum number of macro-particles of $N_M \simeq 514.000$.

BEAM LOSS SIMULATIONS

In the following, we present beam loss simulations of coasting beams whose dynamics is distorted by strong numerical noise, and compare it to our analytical derivations. The tracking is performed with MICROMAP [16], while we use the beam and simulation parameters as listed in the previous chapter. The collimators are placed at $\pm 3\sigma_x$ and $\pm 3\sigma_y$, such that particles with larger amplitude are scraped within the first turns. As this effect is superposed with the artificial beam loss pattern, we normalize the beam intensity after 2000 turns. In order to resolve well the beam loss pattern, we repeated the simulation 15 times, and show the average loss pattern in Fig. 4.

We reach agreement on the model with the loss pattern for different number of macro-particles. In the following, we investating the beam loss pattern of a rms equivalent [20,21] K-V beam, for which the collimators are placed at positions slightly larger than the beam size. In Figure 5, we show the beam loss pattern for different number of macro-particles, and with the same beam and simulation parameters as for Gaussian beams.

ISBN 978-3-95450-185-4

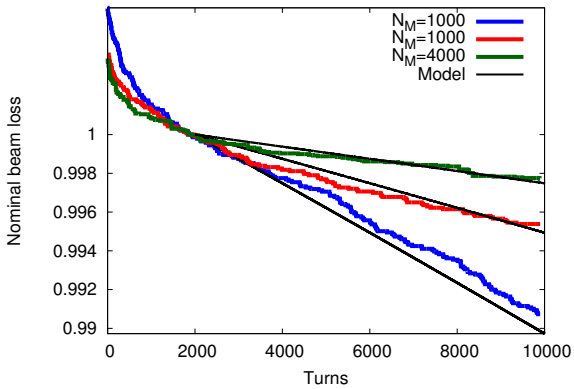

Figure 4: Beam loss pattern within the first 10,000 turns in a SIS100 scenario for a Gaussian beam with different number of macro-particles.

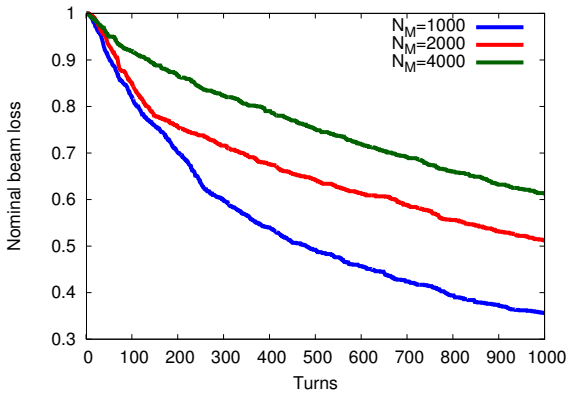

Figure 5: Beam loss pattern within the first 1000 turns in a SIS100 scenario for a K-V beam for different number of macro-particles.

The beam loss pattern for K-V beams shows an above-average beam loss during the very first turns. This is due to the fact, that the emittances of many particles are very close to the edge of acceptance, and even a small random fluctuation in the coordinate may induce beam loss. Later, the beam loss becomes more moderate, but is still much stronger compared to Gaussian beams.

SUMMARY

We developed a theory for estimating optimal simulation parameters for a maximum acceptable beam loss. The theory is based on previous investigation on the propagation and generation of numerical noise. We show with numerical simulation typical loss patterns for Gaussian and K-V beams, that are in agreement with analytical derivations.

ACKNOWLEDGEMENT

The research leading to these results has received funding from the European Commission under the FP7 Research Infrastructures project EuCARD-2, grant agreement no.312453.

REFERENCES

[1] Okuda, Hideo, and Charles K. Birdsall."Collisions in a Plasma of Finite-Size Particles." Physics of Fluids (1958-1988) 13.8 (1970): 2123-2134.

[2] Langdon, A. Bruce. "Effects of the spatial grid in simulation plasmas." Journal of Computational Physics 6.2 (1970): 247-267.

[3] Hockney, R. W. "Measurements of collision and heating times in a two-dimensional thermal computer plasma." Journal of Computational Physics 8.1 (1971): 19-44.

[4] Kesting, F., and G. Franchetti. "Propagation of numerical noise in particle-in-cell tracking." Physical Review Special Topics-Accelerators and Beams 18.11 (2015): 114201.

[5] Spiller, P., and G. Franchetti. "The FAIR accelerator project at GSI." Nuclear Instruments and Methods in Physics Research Section A: Accelerators, Spectrometers, Detectors and Associated Equipment 561.2 (2006): 305-309.

[6] J. Coupard et al., "LIU Technical Design Report (TDR)" No. CERN-ACC-2014-0337, 2014.

[7] Assmann, R. W. "Proceedings of the 46th ICFA Advanced Beam Dynamics Workshop on High-Intensity and High-Brightness Hadron Beams (HB2010), Morschach, Switzerland." PSI, 2010.

[8] Stražík, I., E. Mustafin, and M. Pavlovič. "Residual activity induced by heavy ions and beam-loss criteria for heavy-ion accelerators." Physical Review Special Topics-Accelerators and Beams 13.7 (2010): 071004.

[9] Bruce, R. E. A., et al. "Simulations and measurements of beam loss patterns at the CERN Large Hadron Collider." Physical Review Special Topics-Accelerators and Beams 17.8 (2014): 081004.

[10] FAIR baseline technical report. GSI, 2006.

[11] Mustafin, Edil, et al. "Radiation Damage to the Elements of the SIS300 Dipole." Particle Accelerator Conference, 2005. PAC 2005. Proceedings of the. IEEE, 2005.

[12] Kesting, F. and G. Franchetti, "Mitigation of particle-in-cell induced numerical noise for space charge simulation of SIS100" GSI Scientific Report 2015 (2016).

[13] Sorge, S., G. Franchetti, and A. Parfenova. "Measurement of the acceptance by means of transverse beam excitation with noise." Physical Review Special Topics-Accelerators and Beams 14.5 (2011): 052802.

[14] Edwards, Donald A., and Michael J. Syphers. "An introduction to the physics of high energy accelerators." John Wiley and Sons, 2008.

[15] Kapchinskij, I. M., and V. V. Vladimirskij. "Limitations of proton beam current in a strong focusing linear accelerator associated with the beam space charge." Proceedings of the International Conference on High Energy Accelerators and Instrumentation. 1959.

[16] See website of G. Franchetti.

[17] Turchetti, G., et al. "3D solutions of the Poisson-Vlasov equations for a charged plasma and particle-core model in a line of FODO cells." The European Physical Journal C-Particles and Fields 30.2 (2003): 279-290.

ISBN 978-3-95450-185-4

[18] Benedetti, C., A. Franchi, and S. Ranibaldi. "Accuracy analysis of a 2D Poisson-Vlasov PIC solver and estimates of the collisional effects in space charge dynamics." Computational Accelerator Physics 2003: Proceedings of the Seventh International Conference on Computational Accelerator Physics, Michigan, USA, 15-18 October 2003. Vol. 15. CRC Press, 2005.

[19] Rambaldi, S., et al. "Accuracy analysis of a spectral Poisson solver." Nuclear Instruments and Methods in Physics Research Section A: Accelerators, Spectrometers, Detectors and Associated Equipment 561.2 (2006): 223-229.

[20] Lapostolle, Pierre M. "Possible emittance increase through filamentation due to space charge in continuous beams." Nuclear Science, IEEE Transactions on 18.3 (1971): 1101-1104.

[21] Sacherer, Frank J. "RMS envelope equations with space charge." Nuclear Science, IEEE Transactions on 18.3 (1971): 1105-1107.

ISBN 978-3-95450-185-4

STATUS OF THE BEAM INSTRUMENTATION SYSTEM OF CSNS

J.L. Sun#, W.L. Huang, P. Li, F. Li, M. Meng, R.Y. Qiu, J.M. Tian, Z.H. Xu, T Yang, L. Zeng, T.G. Xu#, Institute of High Energy Physics, Chinese Academy of Sciences, China

Abstract

The beam instrumentation system has been developed to tune and investigate the high intensity proton beam in the China Spallation Neutron Source (CSNS) project. All the physical design of the monitors has been finished and start the system set up procedure. Many kinds of beam monitors are required to measure wide dynamic range of the beam parameters, e.g. intensity, energy. Construction and application of beam monitor system are described in this paper and the first test results during the RFQ and DTL1 commissioning will be introduced also.

INTRODUCTION

The CSNS is designed to accelerate proton beam pulses to 1.6 GeV kinetic energy at 25 Hz repetition rate, striking a solid metal target to produce spallation neutrons. The accelerator provides a beam power of 100 kW on the target in the first phase. It will be upgraded to 500 kW beam power at the same repetition rate and same output energy in the second phase. A schematic layout of CSNS phase-1 complex is shown in Figure 1. In the phase one, an ion source produces a peak current of 25 mA H- beam. RFQ linac bunches and accelerates it to 3 MeV. DTL linac raises the beam energy to 80 MeV. After H- beam is converted to proton beam via a stripping foil, RCS accumulates and accelerates the proton beam to 1.6 GeV before extracting it to the target [1, 2].

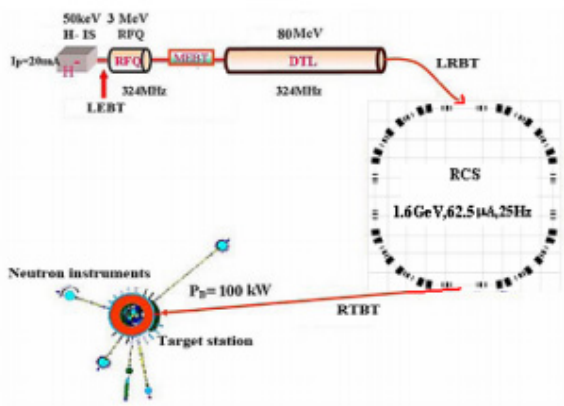

Figure 1: Schematics of the CSNS complex.

BEAM MONITORS

For the entire beam instrumentation system of CSNS, amounts of beam monitors are installed along the beam line, including beam position monitor (BPM), beam current monitor, beam profile monitor, beam loss monitor (BLM) and so on. Layout of the beam instrumentation system as shown in Figure 2.

#sunjl@ihep.ac.cn, xutg@ihep.ac.cn

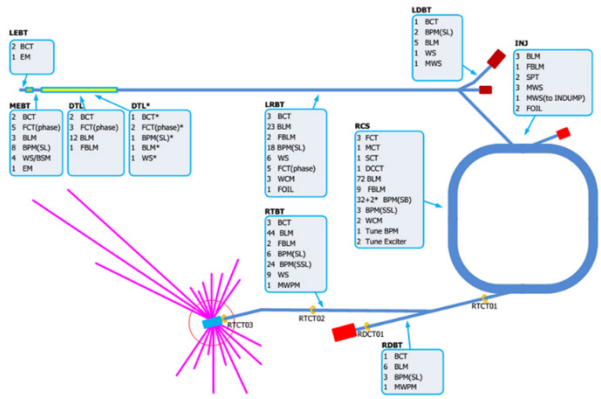

Figure 2: Layout of the beam instrumentation system of CSNS.

Beam Current Monitor

Two types of current transformers have been developed, the fast current transformer (FCT) and normal CT. FCT has a response time less than 300 ps, and used to measure the beam energy by using the TOF method, there are 5 FCT installed in the MEBT after the RFQ, and four of them were used to measure the beam energy during the RFQ commissioning, as shown in Figure 3. The measurement result is 3.1 MeV while the design energy is 3.0 MeV.

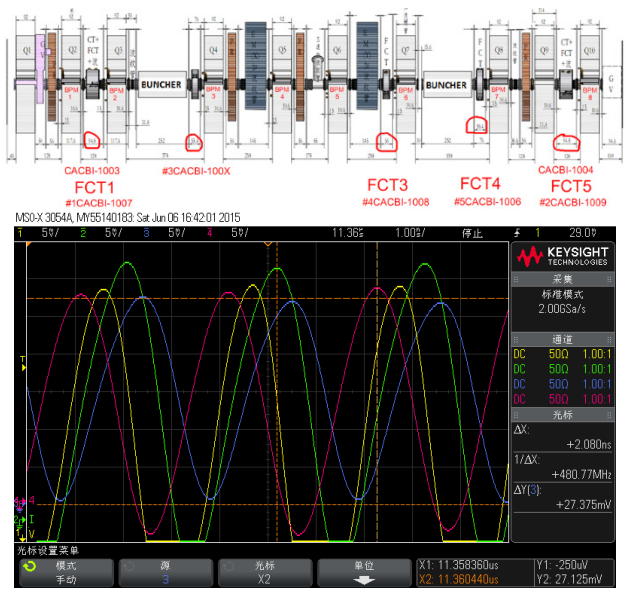

Figure 3: Layout of the MEBT, 5 FCT are labeled by red circle (up) and the beam phase measured by an oscilloscope (down).

Wall current monitor (WCM) is another way to measure the beam current. Two different design were finished based on different requirements. The WCM for LINAC as

ISBN 978-3-95450-185-4

shown in Figure 4, the band width is 16 kHz ~ 1.5 GHz, two types of magnetic material, MN60 and C2025, have been used to improve its performance. The band width of WCM for RCS ring is reduced to 5 kHz to 100 MHz by using different magnetic materials, which are Amorphous & Nano-crystalline.

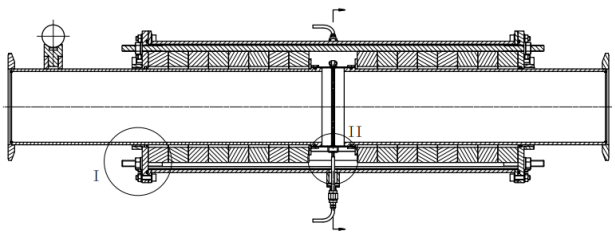

Figure 4: Schematic design of the WCM for LINAC.

Beam Position Monitor

Two type of BPM were designed for the accelerator, stripline for LINAC and shoe-box for the RCS ring and RTBT, as shown in Figure 5. 38 shoe-box BPM are installed in the RCS ring, 32 of them will be used to the orbit measurement, 3 of them will provide the beam position signal to the RF system, 1 for tune measurement, and the last 2 have lower capacitance will be used mainly during commissioning to measure lower signals.

Figure 5: Stripline BPM designed for LINAC (left) and shoe-box BPM for RTBT (right).

A BPM calibration system was designed to fit all size of monitor. One of the calibration results of stripline BPM as shown in Figure 6, the miss match between electric center and mechanical center is less than 0.15 mm.

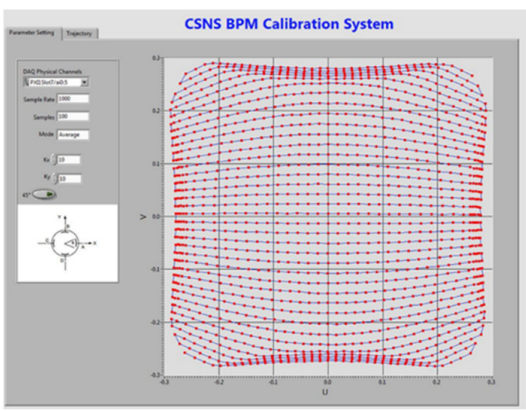

Figure 6: Calibration result of a stripline BPM.

Beam Profile Monitor

Stepper motor driven wire scanner and multi-wire scanner are the two devices chose for the beam profile measurement. Carbon wire with 50 μm diameter is used for MEBT wire scanner, as carbon wire has less energy deposition and can last longer than metal wires. Tungsten wire with 30 μm diameter is chose for the LINAC after DTL and RTBT section. The multi-wire scanner are mainly used in the injection area and in front of the beam dumps to have a faster profile measurement. The wire distribution of the wire scanners as shown in Figure 7.

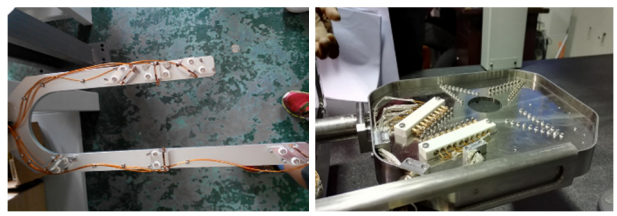

Figure 7: Three wires with 45° angle separating distributed on the frame of the wire scanner, only one wire exposed in the beam pipe at the same time (left); Wires distribution of the multi-wire scanner (right).

Glowing screen beam footprint monitor was set up at the LINAC to dump beam transport line (LDBT) as another way to measure the beam profile. A tungsten mesh is put into the middle of the beam pipe, it will be heated up by the proton beam because of the energy deposition, and start glowing. The glowing can be captured by a suitable camera, and the roughly beam profile can be measured then. Figure 8 shows the mechanical design of the beam footprint monitor, 100 meshes tungsten net is chose and the maximum temperature on the net is around 500 degrees Celsius through simulation. The wave length of the glowing is mainly between 7 μm to 10 μm, which belongs to the far infrared.

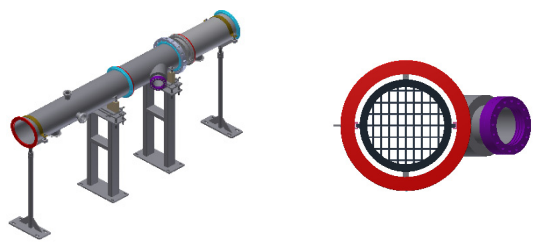

Figure 8: Mechanical design of the glowing screen beam footprint monitor, overall view (left) and the view from the beam entry side (right).

Beam Emittance Measurement System

Double slits system was set up for the low energy section beam emittance measurement, mainly for LEBT@50 keV, MEBT@3 MeV and DTL1@20 MeV. Graphite plate is welded in front of the copper plate of the first slit for the DTL1 set, in order to prevent the copper activation. The first slit of all 3 sets are with water cooling to protect the copper plate from the beam damage. One of the measurement results as shown in Figure 9, for the

ISBN 978-3-95450-185-4

beam after RFQ ε_x=0.16π mm·mrad, ε_y=0.265π mm·mrad when the beam intensity is 15mA.

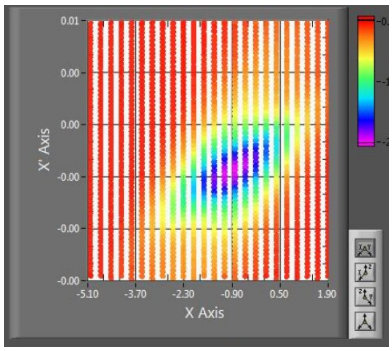

Figure 9: Emittance measurement result of the beam after RFQ (X plane).

Beam Loss Monitor

Different types of monitor were designed to measure the beam loss and to prevent the activation and heat load by intense beam loss. Ionization chamber with Ar+N2 filled, plastic scintillator together with photomultiplier and the neutron detector with BF3 filled are used to detect γ-ray and neutron induced by the lost particles. 162 ionization chambers in total distributed along the beam line as the main mean to measure the beam loss. Plastic scintillator used as the fast BLM for some key positions. The neutron detector focus on the low energy beam loss detection. Two types of BLMs were tested during the DTL1 commissioning as shown in Figure 10. Ionization chamber and Neutron detector located under the first slit of the emittance measurement system after DTL1, beam loss signal can be measured when the slit goes into the beam. The yellow line, which has 172 mV amplitude, is from ionization chamber and the green line, which has 3.31 V amplitude, is from Neutron detector.

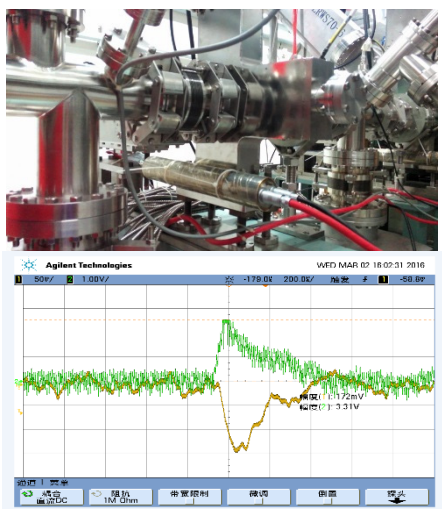

Figure 10: Ionization chamber and neutron detector were located under the first slit of the emittance measurement system of DTL1 (up); beam loss signal measured by these two BLM (down).

Mont Carlo simulation was carried out by FLUKA to validate the test result, as shown in Figure 11, which shows a kind of good agreement between simulation and experimentation. The x-coordinate shows the beam current loss measured by the CT just after the first slit, and the y-coordinate shows the beam loss signal measured by the ionization chamber and the simulated by FLUKA.

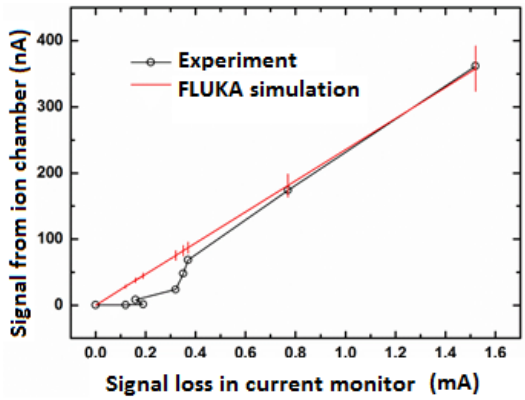

Figure 11: Simulate validation of the BLM test.

DATA ACQUISITION SYSTEM

Electronics are specific designed for all kinds of monitors, and tested during the RFQ and DTL1 commissioning. All signals are integrated into NI based system through ADC, AI or DI boards. The software for date analysis, motor control, and high voltage control are finished based on LabVIEW, and integrated into EPICS.

SUMMARY

RFQ, DTL1 commissioning have been finished March, 2016, lots of beam diagnostic elements have been tested, e.g. CT, FCT, stripline BPM, wire scanner, emittance measurement. All elements manufacturing will be finished July, 2016. LINAC commissioning will be started in September, 2016, the performance of all kinds of beam monitors will be checked this year.

REFERENCES

[1] Shinian Fu *et al.*, "Status and Challenges of the China Spallation Neutron Source", in *Proc of IPAC'11*, San Sebastián, Spain, paper TUXA01 (2011).

[2] Shinian Fu *et al.*, "Status of the China Spallation Neutron Source Project", in *Proc. of PAC'09*, Vancouver, Canada, paper TH1GRI02 (2009).

ISBN 978-3-95450-185-4

XAL APPLICATIONS DEVELOPMENT FOR CSNS TRANSPORT LINES

Yong Li, W.B Liu, Z.P Li, J. Peng
Dongguan Campus, Institute of High Energy Physics，Dongguan 523803, China

Abstract

XAL is an application programming framework initially developed at the Spallation Neutron Source (SNS). It has been employed as a part of control system via connection to EPICS to provide application programs for beam commissioning at the China Spallation Neutron Source (CSNS). Several XAL-based applications have been developed for Beam Transport line at CSNS and successfully applied in the MEBT and DTL-1 beam commissioning. These applications will be discussed in this paper.

INTRODUCTION

The CSNS, including of proton accelerator, target station and neutron spectrometers, is a large facility to produce neutron by 1.6 GeV protons colliding a target of heavy metal [1]. The accelerator is mainly composed of a linac with a modest but upgradable energy and a rapid cycling synchrotron (RCS) of the fixed energy at 1.6 GeV. The installation and beam commissioning of the front end of linac, medium energy beam transport line (MEBT) and first section of the drift tube linac (DTL-1) was finished. The beam commissioning of DTL2-4 and the linac to ring beam transport line (LRBT) is upcoming this September.

XAL [2] is a Java framework for developing accelerator physics applications for the commissioning and operation of the SNS. It was used and developed by many accelerator laboratories, e.g. SNS, SLAC, FRIB, LANL, etc. XAL was designed to be extensible and has evolved to support ongoing accelerator operations. CSNS and SNS have lots of similarities in both physics and hardware. Therefore, the XAL was selected as the tool for beam commissioning of CSNS accelerator.

Some of the applications in XAL can be directly used, such as general applications like SCNAD-1D, SCNAD-2D, some physical applications like orbit correction, MPX [3], etc. However, more XAL applications can only be transplanted after appropriate modifications for the reason of the differences of hardware devices or data formats. For example, The PASTA application [4], which is for the adjustment of the phase and amplitude of the cavity, has been changed a lot for CSNS. The reason is that the BPMs were used in SNS for the phase scanning while FCT were used in CSNS. Meanwhile, a number of new XAL-based applications have also been developed, some of which are described as below.

APPLICATIONS WITH DATABASE

Due to the advantages of data management and data query, database is used by more and more accelerator laboratories for the management of the data with large volume. According to their own consideration, different database management system was used in different laboratories. The Oracle is used in SNS, the J-PARC choose PostgreSQL, FRIB use MYSQL, and in our case we choose the MYSQL database.

Database related applications are widely used in the beam commissioning. Applications in XAL, like Score [5], PVlogger choose the database to logger signal and restore machine. Some examples of physical applications used database in CSNS will be presented.

Model Management

Model management is one of the most important applications in the beam commissioning, which is responsible for the management of the lattice model, model storage, lattice calculation, etc.

Based on the lattice and model service architecture diagram [6], the client application was developed to manage models. Fig 1 is the operation interface, which provides three model sources: database, local file, and the XML file. The models will be displayed according to the serial number, model name, date, energy, and comments when-connecting to the database. The model can be founded by filtering the letter in the model table or searching by time span. The device information including position, type, the magnet field and cavity field will be displayed in the table below when a model is chosen. We can put the stored values to control system for the selected magnets or certain types of magnets. The lattice calculation for the current model can be carried out and the results also can be displayed with graphics. This function has been embedded in the MPX application.

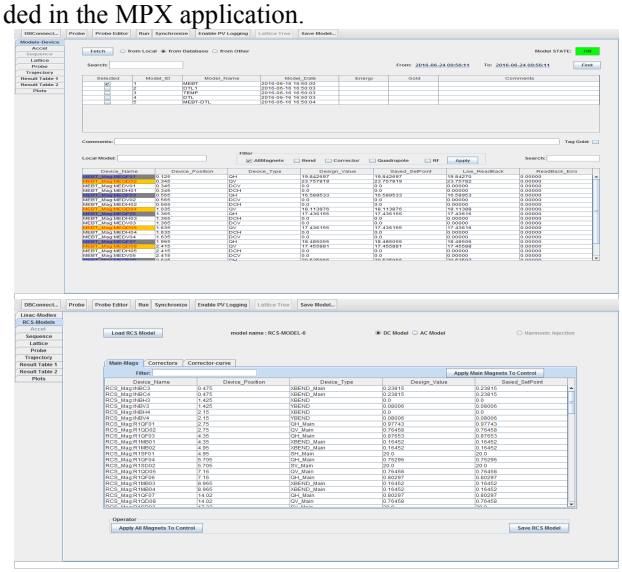

Figure 1: Model management application (The above is for Linac, the below is for RCS).

ISBN 978-3-95450-185-4

The design above only meets the requirements of the model management for linac. Due to the particularity and complexity of the RCS ring, the mode management for RCS ring was redesigned. Fig 1 (below) shows the design of RCS model management.

The information of a corrector in RCS is an array of 21 numbers which stand for 21 energy points. So the correctors should be separated from the other magnets. The DC mode and AC mode are also different when the stored values were applied to the control system. In addition, harmonic injection of the magnets' power supplies has also been considered.

Score Application

Accelerators are inherently complicated devices consisting of multiple systems, such as magnet, power supply, control, vacuum and so on. Efficiently managing the proper device settings is an important part of operations and beam study. We need one application to save machine settings, compare live values with save values and restore saved values. A program called SCORE (Save Compare and Restore) was developed at the SNS for this purpose. However, Oracle database management system was used in SNS, so we cannot use it directly. We modify the interface which is associated with the Oracle. The database schema also made some changes. Fig 2 is a test of the MEBT and DTL sequence with the information of magnets, power supplies, RF cavities and beam diagnostics instruments.

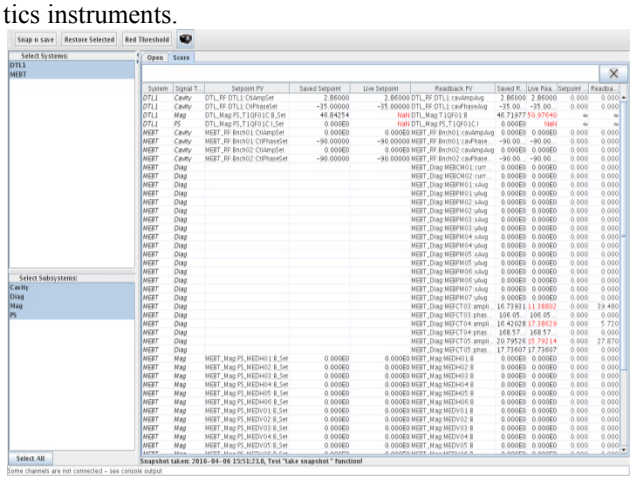

Figure 2: Score application.

Magnet Manager Application

CSNS linac and RCS contain more than 400 dipole, quadrupole, sextupole, octupole, corrector and kicker. We created magnet database to store magnet installation information, magnetization curve data and fit results [7]. This database also can be used by records creating application to create the records for the soft IOC database easily. A magnet database manage application was developed in JavaFX to upload and fit magnetization curves data. Fig 3 is one of the example shows one magnet measurement result.

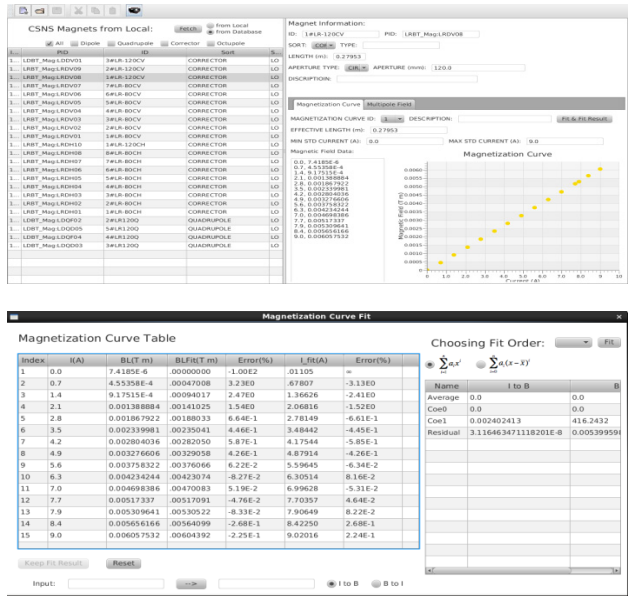

Figure 3: Magnet database manager interface and magnetization curve polynomial fitting interface.

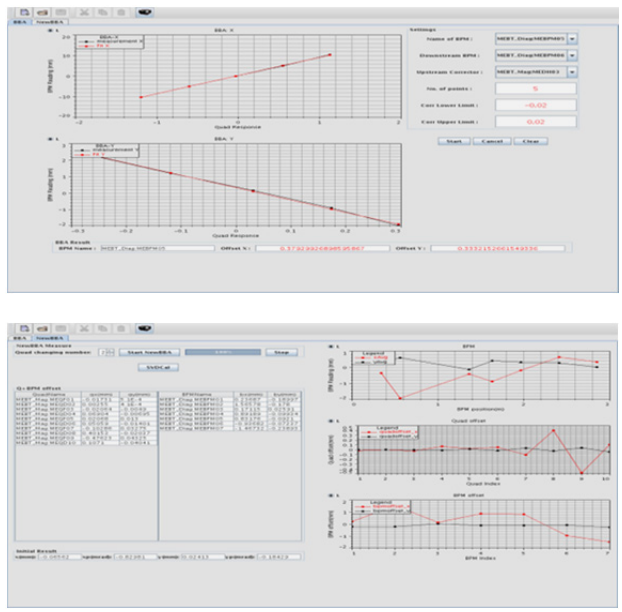

Figure 4: The operation interface of BBA application (he above is first method, the below is second method).

APPLICATIONS WITHOUT DATABASE

BBA Application

The control of beam loss is quite strict for the reason of high power proton. Orbit correction should be done first to decreasing the beam loss. Unfortunately, it can't reach the expected purpose with big errors. One of the strongest error sources of beam orbit distortion is random misalignments of quads and BPMs. The most advanced approach for distorted beam orbit fine correction is the BBA technique. Two kinds of BBA approaches were applied in CSNS. The first is a tradition approach, which can give the value of BPM offset conveniently and accurately. However, scanning over all BPMs is time consuming

ISBN 978-3-95450-185-4

procedure. The second modification BBA algorithm looked more promising, which can get the quad and BPM transverse misalignments simultaneously. This algorithm is based on difference orbit multiple measurements. Meanwhile, the liner optics between all beam line elements must be known. Fig 4 is the operation interface of BBA application, which gives the offsets of all quads and BPMs respectively.

Double Slit Emittance Analysis

The emittance is one of the most important transverse parameters in linear accelerators or transfer lines. Multiple wire scanners (WS) and double slit were installed in CSNS/MEBT to measure the emittance. The first method is based on wire scanner profile measurement at three or more locations along the beam line. The raw data of WS with modification format can be applied in xal wireanalysis program [8] to obtain the exact emittance. However the data format of double slit is more complicated. A new application is encoded, and embedded into the wireanalysis panel. The two small phase ellipse in Fig 5 is calculated by statistics and Gaussian fitting methods respectively. The data used in the calculations are experimentally measured and not processed, which are different from the data after fitting according to the color in SNS. In addition, the influence of the selection of threshold on the calculation results has also been considered [9].

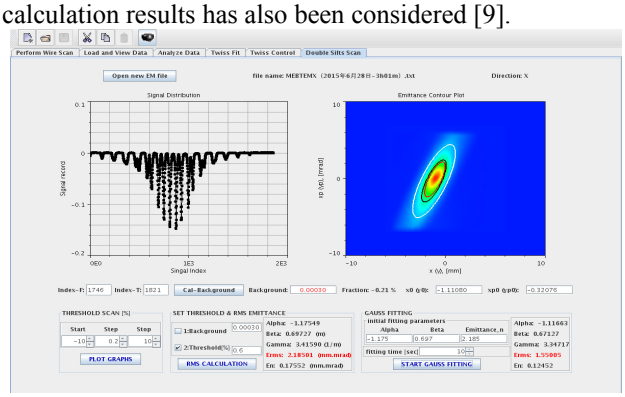

Figure 5: The emittance analysis application.

Fudge Factor Measurement Application

Due to all kinds of errors, the real optics will be different from the design one. The fudge factor measurement application was developed to deal with this issue and improve the optics of CSNS transport line. The fudge factor AF, used to describe the correction of quadrupole strength to restore the optics, which is calculated by fitting the measured response matrix to the model response matrix. An XAL optimization package was employed to do the fitting. Fig 6 is the GUI of the Fudge factor measurement tool which shows one example of one quad with given error.

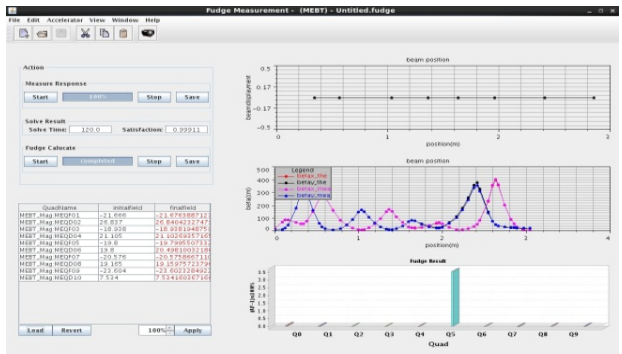

Figure 6: Fudge factor measurement application.

SUMMARY

Based on the XAL framework, some applications were modified or written for CSNS and has been successfully used in the beam commissioning of CSNS linac and transfer lines. This paper discussed some applications with and without database.

REFERENCES

[1] CSNS Feasibility Study Report, June, 2009, IHEP.
[2] T. Pelaia, et al., *in Proc. ICALEPCS'07*, pp. 34-36.
[3] J. Galambos, et al., in *Proc. PAC'05*, pp. 79-83.
[4] J. Galambos, et al., in *Proc. PAC'05*, pp. 1491-1493.
[5] J. Galambos, J. Patton, T. Pelaia., in *Proc. ICALEPCS'07*, pp. 656-658.
[6] P. Chu, et al., in *Proc. ICALEPCS'13*, pp. 464-466.
[7] W.B Liu, et al., "Development of Commissioning Software for CSNS", in *Proc. ICFA mini-workshop on Beam Commissioning for High Intensity Accelerators*, Guangdong, June. 2015.
[8] http://ics-web.sns.ornl.gov/TuningGuide/Twiss/Twiss.html.
[9] Z.P Li, Y. Li, J. Peng, in *Proc. IPAC'16*, pp. 916-918.

ISBN 978-3-95450-185-4

SPACE CHARGE EFFECTS OF HIGH INTENSITY BEAMS AT BRING*

J. Li#, J.C. Yang, IMP CAS, Lanzhou, 730000, China

Abstract

Space charge effects perform one of the main intensity limitations for low energy synchrotron. Large tune spread and crossing resonance stop-bands can hardly be avoided for intensive heavy ion beam at high intensity. Several subjects like Betatron and structure resonance, and tune spread are discussed. Simulations are carried out for $^{238}U^{34+}$ focusing on emittance and intensity change during RF capture at the injection energy at the booster ring of the High Intensity heavy ion Accelerator Facility (HIAF).

INTRODUCTION

The HIAF [1] is a new heavy ion accelerator complex under feasibility study for construction by Institute of Modern Physics (IMP). It consists of two accelerators: a linear accelerator – iLinac (17 MeV/u for $^{238}U^{34+}$, 48 MeV for proton) and a booster ring – BRing (0.2~0.8 GeV/u for $^{238}U^{34+}$, 9.3 GeV for proton). Schematic layout of the HIAF complex is illustrated in Fig. 1. The figure also shows a superconducting ECR ion source and an intense proton source LIPS, a high precision spectrometer ring – SRing (0.2~0.8 GeV/u for $^{238}U^{92+}$), a merging ring – MRing (0.2~0.8 GeV/u for $^{238}U^{92+}$), a radioactive beam transfer line – HFRS and five experimental terminals – T1~T5. Considering heavy-ion feature of the HIAF, we focus our study on $^{238}U^{34+}$ in this report.

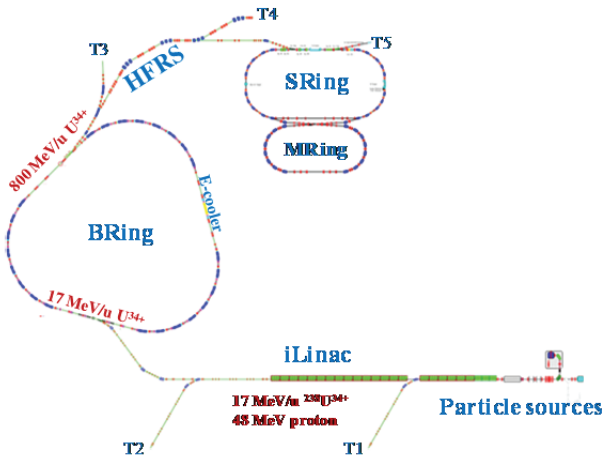

Figure 1: Layout of the HIAF complex.

OVERVIEW OF THE BRING

The BRing performs the step to increase beam intensity up to space charge limit at the injection energy and to accelerate storage beam to extraction energy, i.e. to accelerate $1{\cdot}10^{11}$ ions from 17 MeV/u to 0.2~0.8 GeV/u for $^{238}U^{34+}$. It operates under fast cycle mode with 1ms injection plateau for two-plane painting and slow mode with almost additional 10s reserved for electron cooling. Main parameters of the BRing are summarized in Table 1.

Table 1: Main parameters of the BRing

Circumference	492.53 m	
Super-periodicity	3	
Bunching factor	0.35~0.4	
Acceptance (x/y,δp/p)	200/100 πmmmrad, ±0.5%	
Particle type	proton	$^{238}U^{34+}$
Injection energy	48 MeV	17 MeV/u
Cycle mode	EX+PT (fast)	PT (fast) PT+EC (slow)
Betatron tune	(11.45,11.42)	(8.45,8.42)

*EX: Charge exchange, PT: painting, EC: electron cooling, fast: fast cycle mode, slow: slow cycle mode.

Lattice of the BRing is three-fold symmetrical with each super-period consists of an eight-FODO-like arc and an about 60 m long dispersion-free straight section featured with the length of 16 m drift reserved for either electron cooler, painting injection, or six RF acceleration cavities. Fig. 2 shows a layout of the BRing Twiss parameters and horizontal beam envelope for one super-period.

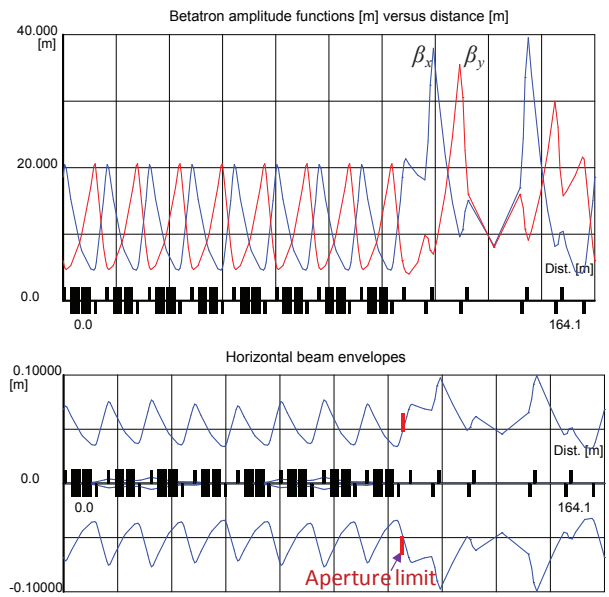

Figure 2: The BRing Twiss parameters and horizontal beam envelope for one super-period.

*Work supported by NSFC (Grant No. 11475235)
#lijie@impcas.ac.cn

ISBN 978-3-95450-185-4

RESONACES IN TUNE SPACE

The BRing is a three-fold symmetry synchrotron. Both Betatron resonance and structure or systematic resonance need to considere for high intensity operation, of which the later is more severe.

Structure Resonances

For the BRing operation of $^{238}U^{34+}$ at injection energy, we set working point as (8.45, 8.42) with safe distance from dangerous low order structure resonances indicated in the tune space of Fig. 3, e. g. the third-order structure resonances Q_x-$2Q_y$=9 and Q_y-$2Q_x$=9. The linear coupling resonance Q_x-Q_y=0, however, is next to the setting working point. For the BRing operation at high intensity, they should be compensated by skew quadruple field and sextuple fields. Considering experiences from other complex [2], it's suggested to adopt auxiliary winds on quadruples and sextuples. The fourth-order resonances shown as pink lines in Fig. 3 are weak and ignored.

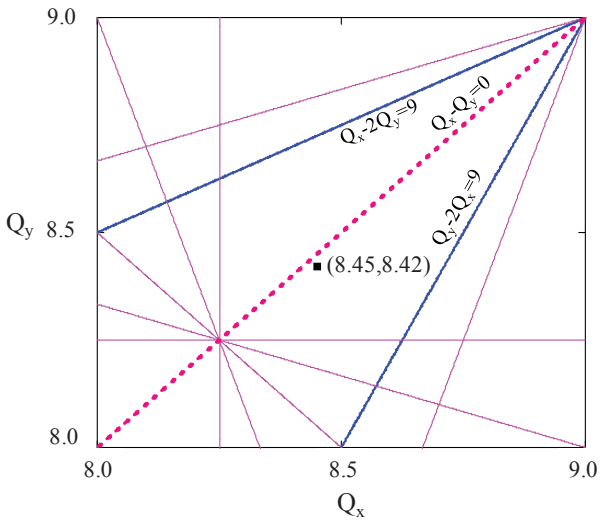

Figure 3: Structure resonances at BRing: 3rd order (blue solid), 4th order (pink solid); linear coupling (red dash).

Betatron Resonances

The nominal working point locates just next to two half-integer resonances referring the operation experience from JPARC [3]. Fig. 4 shows the Betatron resonances in tune diagram.

The charged particle beam produces repulsive force and resulting in depressed spread in tune space. The tune spread likely crosses the close-by low-order resonance stop-bands shown as dashed lines in Fig. 4 when the spread expands. Considering operation at high intensity, it seems necessary to compensate below second and third order of resonance stop-bands with multiple fields.

Second order (by skew quadruple fields):

Q_x-Q_y=0

Third order (by sextuple fields):

3Q_x=25, Q_x+2Q_y=25 2Q_y-Q_x=8

Third order (by skew sextuple fields):

3Q_y=25, 2Q_x+Q_y=25

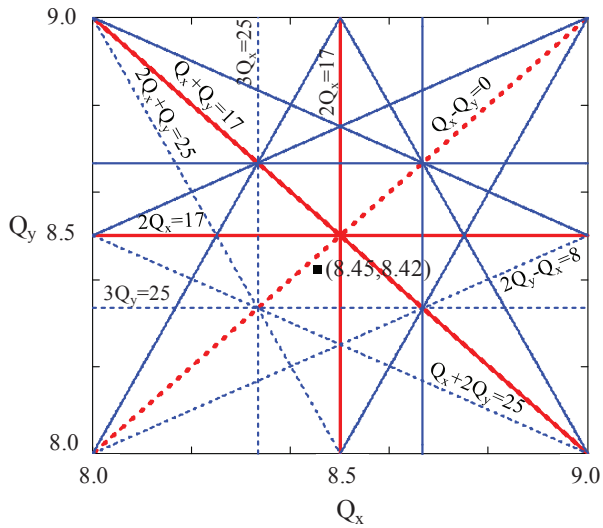

Figure 4: Betatron resonances in tune diagram at BRing: 2nd order (red solid line), 3rd order (blue solid line); resonance stop-bands to be compensated (dash line). The nominal working point ("■") for $^{238}U^{34+}$ operation is set as (8.45, 8.42) at injection energy.

CALCULATION OF TUNE SPREAD

Particles number or incoherent tune spread under space charge limit can be estimated roughly through formula (1) below,

$$N_i = \frac{\Delta Q_{y\_inc} \cdot \beta^2\gamma^3}{-r_i} \cdot \frac{B_f \cdot \varepsilon_y}{g_f \cdot \pi}\left(1+\sqrt{\frac{\varepsilon_x \cdot Q_y}{\varepsilon_y \cdot Q_x}}\right) \quad (1)$$

where, ΔQ_{y_inc} is incoherent tune shift, β and γ are relativistic factors, and r_i=7.5·10^{-18}m is classical radius of $^{238}U^{34+}$. $\varepsilon_{x,y}$ corresponds to full transverse beam emittance. g_f is transversal forming factor and equals to 1 for transverse K-V beam distribution. Longitudinal bunch factor B_f is 1 for coasting beam and can reach 0.35~0.4 when dual harmonic RF system is adopted.

Table 2: Tune Spread at Design Intensity for the BRing

Particle type	proton	$^{238}U^{34+}$	
Injection energy	48 MeV	17 MeV/u	
Design intensity	1.0·10^{12}	1.0·10^{11}	
$\varepsilon_x/\varepsilon_y$ (πmmmrad)	200/100	200/100	50/50
Beam distribution	K-V	K-V	K-V
$\Delta Q_{y\_inc\_coasting}$	-0.06	-0.08	-0.2
$\Delta Q_{y\_inc\_bunched}(B_f=0.35)$	-0.16	-0.24	-0.57
$\Delta Q_{y\_inc\_bunched}(B_f=0.4)$	-0.14	-0.21	-0.5
Time at inj. energy	~1 ms	~1 ms	10 s
Cycle mode	Fast	Fast	Slow

ISBN 978-3-95450-185-4

Either after two-plane painting injection at fast cycle mode or additional electron cooling at slow mode, the transversal distribution of stored beam in the BRing is approximate uniform. So we make a K-V distribution approximation in calculation and simulation. With design intensity at BRing, we derived the incoherent tune spreads by formula (1) with assuming transverse acceptance of the BRing is fully occupied after painting injection, and the beam is electron-cooled down to 50 πmmmrad at the two transverse planes. The calculation results listed in Table 2 shows an acceptable tune spread at design beam intensity for fast cycling mode, but a large spread of -0.5 for cooled beam.

SIMULATION OF TUNE SPREAD

BRing operates at two cycle modes. They feature time length difference at injection energy, e. g. about 1ms at slow mode for filling up the transverse acceptance by painting injection and 10 s for cooling. During the whole process of painting and cooling, the stored beam is coasting due to absence of RF voltage. Thereafter, the RF system is switched on and longitudinally captures the stored beam with a bunching factor of 0.35~0.4. In tune spread simulation below, we assume this factor is 0.35 and the initial beam distributions are K-V at transverse planes. Table 3 lists the main parameters in simulation.

Table 3: Main Parameters in Simulation for the BRing

Particle type	$^{238}U^{34+}$	
Injection energy	17 MeV/u	
Beam intensity	$1.0\cdot10^{11}$	
$\varepsilon_x/\varepsilon_y$ (πmmmrad)	200/100	50/50
Initial distribution	K-V	K-V
Time at injection energy	~1ms	10 s

Spread at Filling up Transverse Acceptance

After filling up transverse acceptance by painting within about 100 revolution periods, the horizontal and vertical beam emittances are 200 πmmmrad and 100πmmmrad respectively. RF capture condenses the circulating beam longitudinally and increase tune spread according to formula (1). Fig. 5 plots the simulation result at the situation.

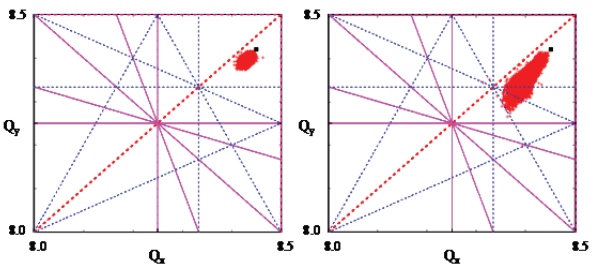

Figure 5: Tune spread of coasting (left) and bunched (right) U^{34+} beam after filling up the transverse acceptance. The dot "■" marks the nominal working point at the BRing.

Tune spread by simulation gives almost a half width of that by calculation in Table 2. It also shows that the spread of bunched beam crosses third-order Betatron resonances but not for coasting beam.

Spread of Cooled Beam at 50/50πmmmrad

The magnetization electron cooling is used at the BRing for intensive ion beam. In this operation mode, 10s is reserved for cooling down large emittance U^{34+} beam after the acceptance is occupied up by painting injection. The RF system is not applied in cooling process until acceleration. Fig. 6 plots the tune spread of coasting and bunched beam with 50 πmmmrad emittance at both transverse planes.

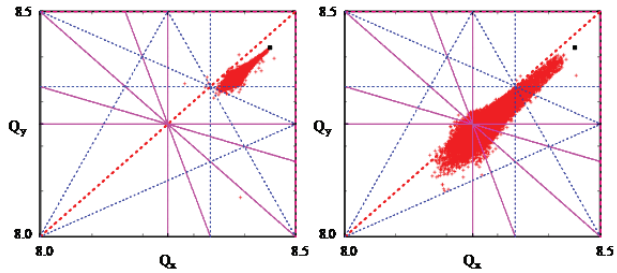

Figure 6: Tune spread of coasting (left) and bunched (right) U^{34+} beam with emittances of 50/50 πmmmrad.

The simulation result also indicates nearly a half width of tune spread comparing to calculation. Moreover, the spread touches the third-order resonance for coasting beam and crosses four third-order Betatron resonances and the linear coupling difference resonance for bunched beam. The compensation of coupling resonance is suggested for slow cycle mode. The fourth-order structure resonances are weak and ignored.

SIMULATION OF THE EMITTANCE

To observe the transverse beam emittance change and survival beam intensity at the designed intensity – $1.0\cdot10^{11}$ number of U^{34+} ions, ten thousands of macro particles is tracked 40000 turns or 0.35 s for study the RF bunching process from initial coasting beam,. We applied constant RF voltage of 4 kV with zero synchronous phase angles on two RF cavities at the second harmonic number. The simulation tracks the whole capturing process from coasting beam at the case of either filling up transverse acceptance or cooling down to 50 πmmmrad at fixed injection energy of 17 MeV/u.

The simulation is performed by pyORBIT code under 2.5D space charge model [4].We set aperture limit just after the last defocusing quadruple at the end of FODO-like arc section, which collects lost particles that oscillates out of transverse acceptance of the BRing. Its position is marked as "Aperture limit" in Fig. 2. The aperture is elliptical with 41 mm semi-minor-axis at the horizontal limit and 50 mm semi-major-axis at the vertical plane. The aperture limit records all the lost particles messages in simulation.

ISBN 978-3-95450-185-4

Emittance at Filling up Transverse Acceptance

After filling up transverse acceptance, the circulating beam is affected by both resonances and RF bunching. Fig. 7 shows the emittance change and survival intensity in simulation. The relative emittance in the figure is defined as the ratio of instant emittance to its initial value – 200 πmmmrad at horizontal and 100 πmmmrad at vertical. The normalized survival intensity is defined as the ratio of beam intensity to its initial value – 10000 macro particles or $1.0 \cdot 10^{11}$ $^{238}U^{34+}$. The horizontal axis marks the turn number where one revolution period is 8.7 μs at injection energy.

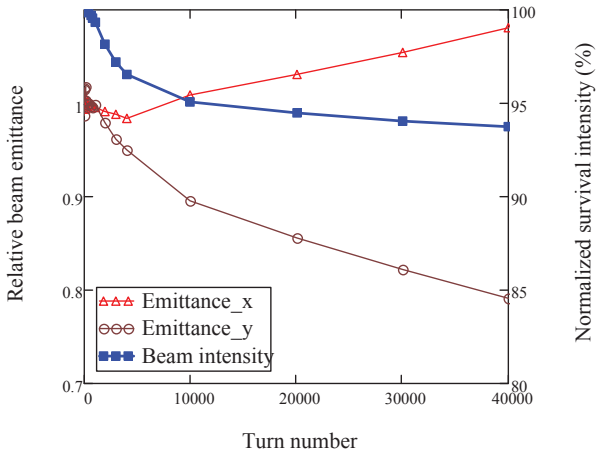

Figure 7: Simulation of relative emittance at horizontal (red "Δ") and vertical (brown "○") planes after filling up the transverse acceptance, and normalized survival beam intensity (blue "■") during RF capture process from initial coasting beam.

Simulation results in Figure 7 indicates that the vertical emittance starts growth from about 1000 turns or 8.7 ms while the horizontal one decreases simultaneously. The phenomenon means that the linear coupling resonance causes emittance exchange at the two transverse planes which then induced beam loss under the vertical aperture limit. The beam loss reaches 6% after 40000 turns. To reduce the loss, compensation of the linear coupling resonance is suggested.

Emittance of Cooled Beam at 50/50πmmmrad

The simulation begins from the time of storage beam being cooled down to 50/50 πmmmrad. In other words, the RF capturing simulation below proceeds without electron cooling. Fig. 8 shows the dependences of emittance and beam intensity on turn number in logarithmic coordinate. According to the simulation result, a fast emittance growth of 15% at horizontal and 25% at the vertical occurs within 100 turns during RF capturing. Similar phenomenon of emittance exchange through linear coupling also occurs but 15% slower than the case of filling up transverse acceptance of the BRing. The storage beam loss only 0.4% after 40000 turns of simulation. That's much less than the former case.

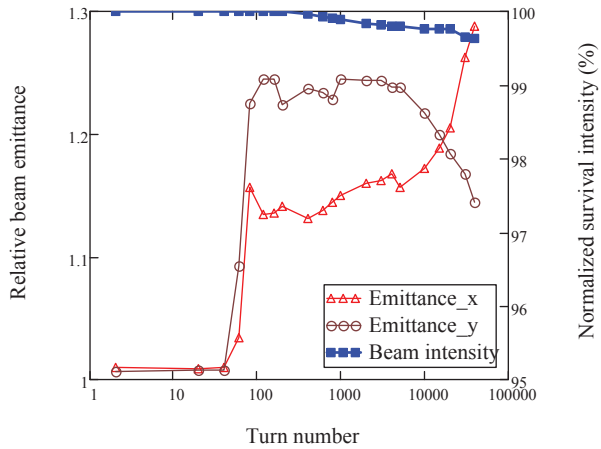

Figure 8: Simulation of relative emittance at horizontal (red "Δ") and vertical (brown "○") planes with 50/50 πmmmrad emittance, and normalized survival beam intensity (blue "■") during RF cavity capture process from initial coasting beam to bunch.

We attribute the beam loss larger at the former case to close proximity with emittance and acceptance, and less loss at 50/50 πmmmrad to shrinked transverse emittance under linear coupling.

CONCLUSION

The structure and Betatron resonances are discussed for the nominal working point at injection energy at the BRing. Tune spreads of two cases at the design intensity are evaluated by calculation but twice the width comparing to simulation. Transverse emittance exchange occurs from about turn 1000 in RF bunching tracking at the two operation cycle modes. Shrinkage of transverse emittance by electron cooling is helpful for reducing beam loss when linear coupling resonance is involved.

OUTLOOK

Further study is considered for the BRing with near actual transverse and longitudinal distribution, and field errors at the injection energy. Compensation of resonances is suggested but more details for technical design are required.

REFERENCES

[1] J.C. Yang *et al.*, "High Intensity heavy ion Accelerator Facility (HIAF) in China", NIM B, 317 (2013).
[2] C. Gardner, "Booster Stopband Corrections", Booster Technical Note No.217 (1993).
[3] H. Hotchi, "Space Charge Induced Beam Loss and Mitigation in the J-PARC RCS", Space-charge 2015 workshop, Oxford, United Kingdom (2015).
[4] A. Shishlo *et al.*, "The Particle Accelerator Simulation Code PyORBIT", Procedia Computer Science, 51 (2015).

ISBN 978-3-95450-185-4

OVERVIEW OF THE ESSnuSB ACCUMULATOR RING

M. Olvegård, T. Ekelöf, Uppsala University, Sweden
E. Benedetto, M. Cieslak-Kowalska, M. Martini, H. Schönauer, E. Wildner
CERN, Geneva, Switzerland

Abstract

The European Spallation Source (ESS) is a research center based on the world's most powerful proton driver, 2.0 GeV, 5 MW on target, currently under construction in Lund. With an increased pulse frequency, the ESS linac could deliver additional beam pulses to a neutrino target, thus giving an excellent opportunity to produce a high-performance ESS neutrino Super-Beam (ESSnuSB). The focusing system surrounding the neutrino target requires short pulses. An accumulator ring and acceleration of an H^- beam in the linac for charge-exchange injection into the accumulator could provide such short pulses. In this paper we present an overview of the work with optimizing the accumulator design and the challenges of injecting and storing $1.1 \cdot 10^{15}$ protons per pulse from the linac. In particular, particle tracking simulations with space charge will be described.

INTRODUCTION

Starting in a few years, the European Spallation Source (ESS) [1] in Lund, Sweden, will provide users with high-flux spallation neutrons for a large variety of experiments where neutrons are needed as a probe. The neutron production is based on a superconducting high-power proton linac which generates a 2 GeV proton beam with 5 MW average power on target. See Table 1 for a selection of the beam parameters at the end of the ESS linac. This impressively powerful proton driver has drawn the attention of particle physics. In particular, the ESS neutrino Super Beam (ESSnuSB) project plans to use a 5 MW beam from the ESS linac to produce an intense neutrino beam in a dedicated target station [2, 3]. The neutrino super beam will be sent in the direction of Garpenberg, Sweden, 540 km from Lund, where a 0.5 Megaton Water Cherenkov detector is located in an underground mine to detect them. Along the propagation to Garpenberg the neutrinos in the super beam, which consists purely of either muon neutrinos or muon antineutrinos, will oscillate to different flavor states and might thus be detected as muon or electron neutrinos in the Cherenkov detector. The flux of electron and muon neutrinos and antineutrinos will be detected with the aim of discovering and measuring leptonic charge-parity (CP) violation. Leptonic CP violation has been long foreseen and ESSnuSB has a high sensitivity to measure it due to the optimal positioning of the detector at the second oscillation maximum [3].

In order for the experiment to be completed within the planned 10 years of operation, ESSnuSB need the high beam intensity to be preserved all the way from the linac to the target. Firstly, the pulse repetition frequency of the linac must be increased such that the nominal duty factor of 4% is doubled. In this way 5 MW would be dedicated to the neutron production and another 5 MW to the neutrino generation. Furthermore, the neutrino target station is equipped with a magnetic focusing device, a van der Meer horn, which focuses the secondary pions that are generated as the protons from the ESS hits the target. The horn focuses pions of one sign and defocuses pions of the opposite sign. The sign of the pions to be focused is changed by reversing the direction of the current in the magnet coil. The pions decay predominantly into a muon and a muon neutrino. The former is absorbed before it has time to decay further whereas the latter continues to travel through the earth towards Garpenberg. The neutrino flux at the detector can be optimized by tuning the focusing of the secondary pions. The positively charge pions produce neutrinos and the negatively charged pions produce antineutrinos.

Table 1: Nominal Beam Parameters at the End of the ESS Linac

Beam energy	2.0	GeV
Pulse beam current	62.5	mA
Pulse duration	2.86	ms
Pulse repetition rate	14	Hz
Beam power	5	MW

The horn consists of a toroidal magnet where the particle must cross the current conductor to reach the magnetic field region. Roughly 350 kA is needed to generate the necessary field, a current which leads to ohmic heating of the surface [4]. This means that the horn cannot be powered during the 2.86 ms of the duration of the ESS linac pulse. The pulse must be reduced to a few microseconds, while preserving the total beam power delivered to the target. An accumulator ring placed at the end of the linac has been designed for this pulse compression. There, the long pulses from the ESS linac will be transformed into shorter pulses of 1.32 µs duration, with a correspondingly increased pulse current. A schematic of the implantation of the ESSnuSB accumulator ring and target station is shown in Fig. 1.

Each pulse from the ESS linac contains $1.1 \cdot 10^{15}$ protons. The filling of the ring with this very high charge can only be done through injection painting with charge exchange. That means that H^- ions are accelerated in the linac and transferred to the ring. At the injection point the ions are stripped off their two electrons using a foil, or possibly in the future with laser stripping. This implies that the linac will have to operate alternately with protons and H^-. The modifications to the linac required for neutrino production have been investigated thoroughly, see [5] for details.

There are several beam pulse configurations available for simultaneous production of neutrons and neutrinos, all of

ISBN 978-3-95450-185-4

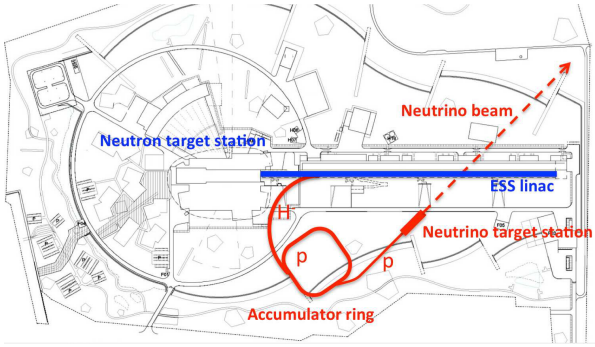

Figure 1: The ESSnuSB implantation at the ESS site.

them resulting in a doubling of the linac duty factor to 8 %. A first option is to simply double the pulse repetition rate from 14 Hz to 28 Hz, making every second pulse an H^- pulse intended for neutrino production. This option, which is depicted in upper half of Fig. 2, would require a ring with very large aperture or two to four rings stacked on top of each other, similarly to the Proton Synchrotron Booster (PSB) at CERN [6]. Alternatively, the 2.86 ms pulse could be split into two to four batches that would be accumulated separately. That would require pulsing the linac up to 70 Hz, as in the lower part of Fig. 2. Our current baseline option is to split the ESS linac pulse into four such batches, which implies that the accumulator will collect $2.75 \cdot 10^{14}$ protons for each batch. The simulations presented here assumes this beam intensity and configuration. Later on, other options will be considered.

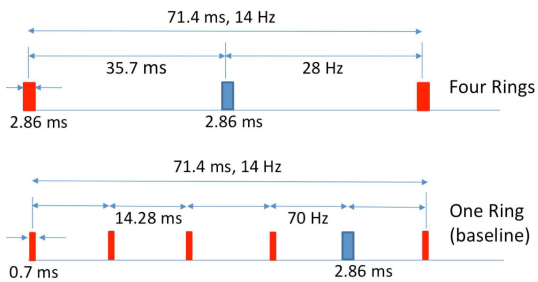

Figure 2: Sketch of the different accumulation scenarios. Protons pulses are in blue and H^- pulses are in red.

THE ACCUMULATOR RING

The first version of the lattice of the ESSnuSB accumulator ring was adopted from the similar Spallation Neutron Source (SNS) accumulator ring [7]. The ring was scaled in length to 376 m in order to better suit the higher beam energy of 2.0 GeV, and minor additional adjustments were made. The lattice has a four-fold symmetry with FODO cells in the arcs and four long dispersion-free straight sections for accommodating injection, extraction, RF cavities and instrumentation. The injection region contains a fixed orbit bump and a variable bump with fast kickers. The fast kickers are employed for transverse injection painting.

The high intensity beam from the ESS linac will suffer tune shifts due to direct space charge. The space charge forces are reduced by painting the transverse phase space in the ring with the linac beam. The 1σ normalized transverse emittance of 0.25 mm mrad from the linac will thus be transformed to the target normalized emittance of 100 mm mrad, here covering 86.5% of the beam particles. At the same time, the painting can be modeled to create the desired beam profile. In this case, the interest is to minimize space charge forces and subsequent tune shifts, wherefore it is ideal to have a beam distribution which is as close as possible to uniform in the transverse plane. On the contrary, a Gaussian profile gives rise to space charge forces that are very strong at the density peak, which in turn leads to large tune spreads. We assume a Gaussian beam distribution arriving at the injection point from the linac and aim at modeling the injection painting to produce a quasi square distribution. In addition, heating of the stripping foil due to multiple particle crossings from the circulating beam must be considered in the optimization.

RF cavities, both a first harmonic and a second harmonic cavity, are employed to preserve the extraction gap. The first harmonic is split up over three cavities with in total 5 kV and a second-harmonic cavity in anti-phase of 2.5 kV. Since the accumulation takes only 540 turns and the time between pulses is 14.3 ms the extraction gap cannot be created in the ring but must be generated already in the linac.

An early indication of emittance growth in the vertical plane due to space charge, induced a study of three different working points with a fixed bare tune in the horizontal plane. The working points are as follows:

a) $Q_x = 10.395, Q_y = 11.321$

b) $Q_x = 10.395, Q_y = 11.254$

c) $Q_x = 10.395, Q_y = 11.202$

They will later be referred to by the labels a, b and c.

SIMULATIONS

We have performed beam tracking simulations using the ESSnuSB accumulator lattice. The tracking has been done using the particle-in-cell code pyORBIT [8], with comparison tests in Accsim [9]. PyORBIT uses PTC [10] external libraries, which is particularly convenient when using time dependent elements, such as the fast kickers for the injection painting. Two sets of simulations were done to study the beam under the effect of space charge. The first set considers the full beam intensity, thus after the injection has been completed. The second includes the injection painting and simulates the full accumulations process. Part of the second set was also compared with an equivalent simulation done in Accsim. The details of these simulations will be described here.

Full Intensity

In the baseline design, the accumulator ring lattice will have to be able to store a total beam intensity of $2.75 \cdot 10^{14}$

ISBN 978-3-95450-185-4

protons during the time between injection and extraction, possibly for a few hundred turns. A first series of simulations were made to assess whether the current lattice design can do that without losses and with minimal emittance growth. To this end, we used the lattice with injection kickers turned off, i.e. without the fast orbit bump but with the fixed bump. We used the lattice in three configurations corresponding to the three working points a, b and c, always with RF cavities powered. Note that there is no ramping of the cavities since there is no acceleration.

As a worst-case scenario we have assumed a Gaussian beam distribution with a 1σ geometrical emittance of 8.5 mm mrad, which corresponds to the target emittance in the ring. In reality we hope to produce a more flat distribution with the injection painting. A Gaussian energy distribution with rms spread 0.02 % was chosen, in agreement with what is expected at the end of the ESS linac. The longitudinal distribution was set to uniform but with a 15 % gap for extraction.

The ring lattice was imported from a MADX file and a file was created which contains all the elements divided into slices. In each slice, or node, a space charge kick is applied. Roughly 500 space charge nodes were used. We include a 2D transverse space charge model with a grid of 128×128 bins, which is weighted slice by slice with the longitudinal beam density ("2.5D") calculated in 128 slices. In addition, we include longitudinal space charge forces with 128 bins. The number of bins in the space charge models, as well as the amount of 100'000 macro-particles used in the tracking, have been selected based on a series of simulations where the computation time is weighed against the accuracy of the convergence of the result.

Figures 3 and 4 show the emittance evolution in the horizontal and the vertical plane during the 500 turns the tracking was performed. The rms emittance growth is plotted relative to the initial value, which reveals the fact that working point a exhibits a clear growth in the vertical plane whereas the horizontal emittance has its smallest growth for the same working point. We see some remnant numerical noise, though, a higher number of macro-particles yields the same overall result.

A tune spread of approximately 0.2 is obtained both numerically with pyORBIT and analytically with the Laslett coefficients.

With Injection Painting

With a revolution period of 1.32 µs it takes 540 turns to accumulate one batch, corresponding to a fourth of a nominal proton pulse from the linac. This injection will be done through painting, where the injection point is fixed to 42.5 m in the horizontal direction and 46 mm in the vertical direction with respect to the closed orbit without injection bump. At the start of the injection the bump is at its maximum amplitude around 30 mm, see Fig. 5, and therefore closer to the injection point. During the time it takes to inject one batch, the amplitude is reduced. Only after the injection is complete, the bump amplitude is set to zero.

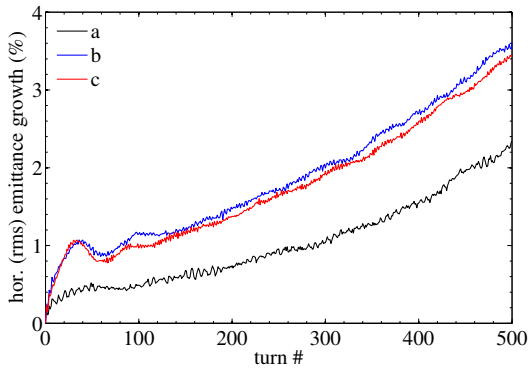

Figure 3: Worst-case scenario: Horizontal emittance growth relative to the initial emittance, plotted for the three working points.

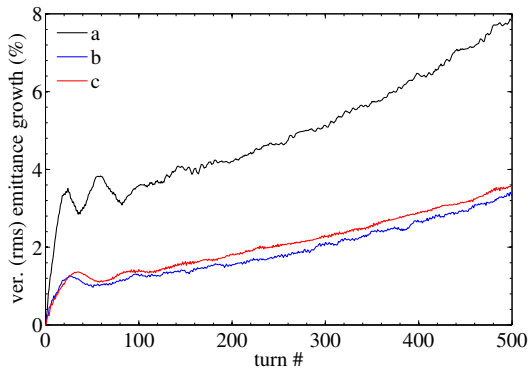

Figure 4: Worst-case scenario: Vertical emittance growth relative to the initial emittance, plotted for the three working points.

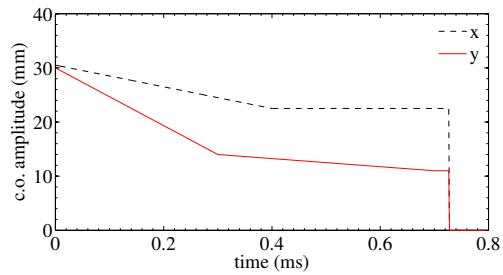

Figure 5: The closed orbit bump (c.o.) amplitude as a function of time. At the end of the injection, at $t = 0.73$ ms corresponding to 550 injected turns, the bump amplitude is set to zero for computational ease. In reality it takes some microseconds to completely remove the bump.

The same space charge models and binning as in the simulation set described above was used here. This time a beam with Gaussian transverse distribution with emittance corresponding to the ESS linac beam was used. As before, we chose a Gaussian energy distribution with rms spread 0.02 % and uniform longitudinal distribution with a 15 % gap for extraction. We inject one such bunch every turn, represented by 2000 macro-particles, and inject during 550

ISBN 978-3-95450-185-4

turns. After the injection is complete we track for another 50 turns and then extract the total particle distribution, now consisting of 1'100'000 macro-particles.

The emittance evolution during the injection is displayed in Fig. 6. Contrary to the first simulation set, these results indicate that working point c is not the best choice for our lattice. Although the emittance growth is small in the horizontal plane it is quite large in the vertical plane in comparison to working points a and b. By looking at the emittance growth that we would expect without space charge forces, shown in Fig. 7, we conclude that working point b seems best from the point of view where effects from space charge forces are minimized.

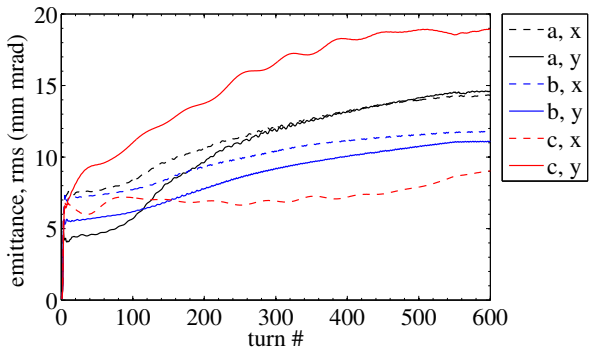

Figure 6: With painting: Horizontal and vertical emittance during injection, plotted for the three working points.

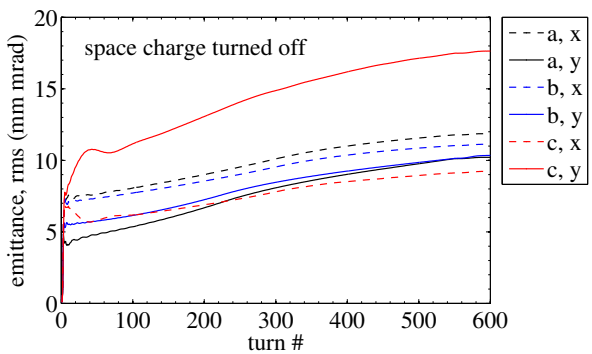

Figure 7: With painting: Emittance evolution for the three working points when space charge forces are ignored.

Taking a closer look at the beam after tracking in lattice in the configuration of working point b we see that there is room for further optimization. Figure 8 shows the horizontal and vertical profiles. The profiles are not flat but rather triangular with a hint of halo formation. There is also an asymmetry in the transverse phase space distributions, revealed in the density plots in Fig. 9. Both the asymmetry and the peaked profiles will have to be reduced by remodeling the injection kicker ramp that defines the painting procedure.

Lastly, we show the tune diagram in Fig. 10. The core of the beam hits the fifth order vertical resonance line and the third order horizontal resonance line. The classic neck-tie

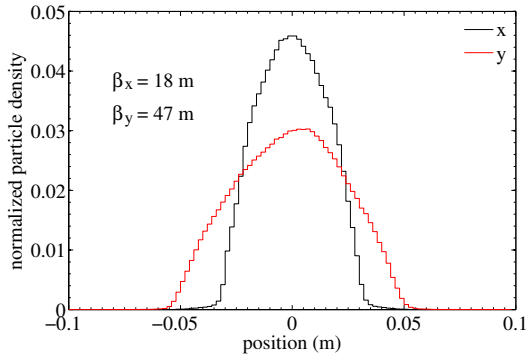

Figure 8: Projections onto the horizontal axis and the vertical axis, working point b.

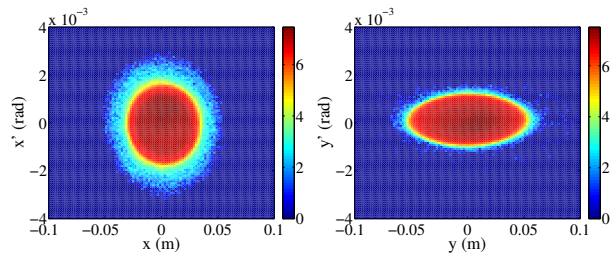

(a) horizontal (b) vertical

Figure 9: Density plots of the horizontal (a) and vertical (b) phase space. The colorbar marks the density in log scale.

shape is lost which makes it difficult to identify an overall tune shift, though it is below the 0.2 obtained in the simulation set at full intensity. The tune diagrams look similar for the three working points.

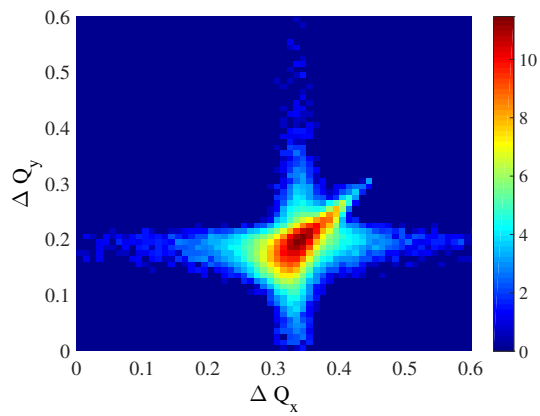

Figure 10: Tune density diagram where the color bar shows the density in log scale.

Comparison with Accsim

When modeling the injection procedure one must consider that the foil used for stripping the injected H^- ions cannot sustain unlimited particle crossings by the circulating beam. The simulation program Accsim was used to investigate the number of foil hits, from which the energy

ISBN 978-3-95450-185-4

deposition and temperature increase in the foil can be estimated. The thermal response of the foil to the beam has also been investigated analytically [11]. A simulation with Accsim, including the full painting procedure, was done with the lattice configuration *c* and similar parameter sets as described above. The result was compared with results from pyORBIT.

The horizontal and the vertical profiles obtained in the two simulations are shown in Fig. 11. While the horizontal profiles agree within the statistical uncertainty, in vertical the pyORBIT simulation result in a notably larger profile. Though the discrepancy is not yet fully understood it is worth mentioning that the number of macro-particles is limited to 99'000 in the case of Accsim. The limited statistics may at least partially account for the asymmetry in the profiles.

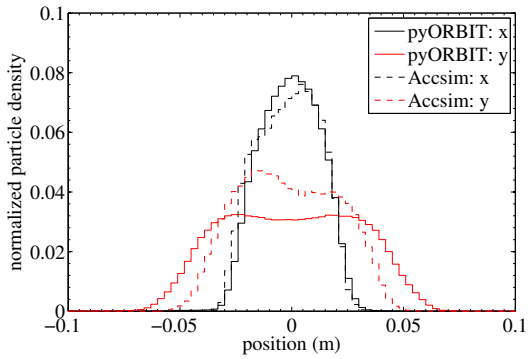

Figure 11: Projections onto the horizontal axis (black) and the vertical axis (red), working point *c*. A comparison between pyORBIT (solid line) and Accsim (dashed line).

In addition we present the evolution of the rms emittance obtained with Accsim in Fig. 12(a), with space charge turned on, and Fig. 12(b) with space charge turned off, to be compared with Figs. 6 and 7. Also from these plots it becomes apparent that there is a discrepancy in the vertical plane between the two programs. Note, however, that when the result obtained with and without space charge are compared, Accsim exhibits a strong emittance growth in both planes in the 95 % emittance. It is still to be confirmed whether the final emittances obtained in the Accsim and pyORBIT simulations are within the target of 100 mm mrad, normalized (86.5 %).

CONCLUSION AND OUTLOOK

We have performed beam tracking studies with space charge in order to evaluate the first design of the ESSnuSB accumulator ring. The study includes tracking at full intensity in order to assess the severity of the space charge effects and associated tune shifts that are to be expected. In addition, simulations including the phase space painting have been made. The result indicates that the painting procedure require further optimization. The next step is therefore to look into various transverse painting schemes. The lattice may be re-tuned to move away from dangerous resonances.

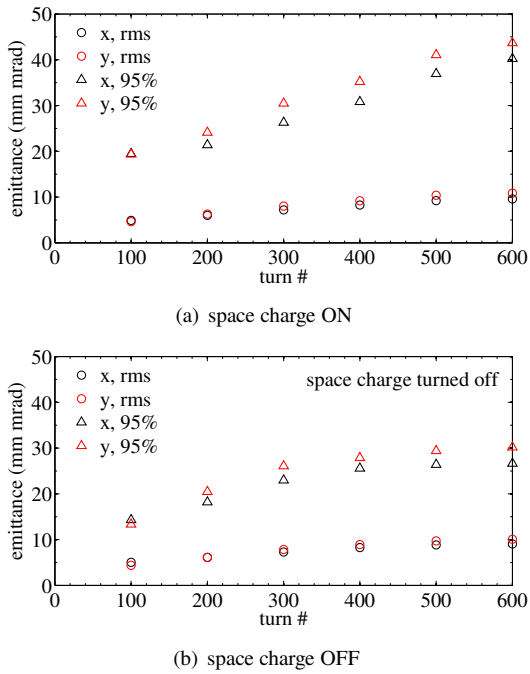

(a) space charge ON

(b) space charge OFF

Figure 12: Emittance evolution during injection obtained with Accsim when space charge is turned on (a) and off (b) in the simulation.

The beam arriving from the ESS linac will consist of trains of micro bunches. The bunches are 3 ps long and are bunched at 352 MHz. Future studies will investigate the effect of the micro-bunching on the beam behavior in the ring.

REFERENCES

[1] S. Peggs (Ed.), ESS Technical Design Report, 2013.

[2] E. Baussan *et al.*, *Nucl. Phys.* B, vol. 885, pp. 127-149, 2014.

[3] E. Wildner *et al.*, accepted for publication in *Advances in High Energy Physics*, Hindawi publishing, 2016. `http://arxiv.org/abs/1510.00493`

[4] N. Vassilopoulos, "The ESS neutrino super beam optimization design studies", NuFact workshop, Beijing, China, 2013.

[5] F. Gerigk and E. Montesinos, "Required modifications of the ESS accelerator architecture for ESSnuSB", CERN-ACC-NOTE-2016-0XXX (2016).

[6] K. Reich, "The CERN Proton Synchrotron Booster", in *Proc. of PAC'69*, pp. 959-961, 1969.

[7] W. T. Weng, BNL-65618, 1998.

[8] A. Shishlo *et al.*, *Procedia Computer Science* 51, pp. 1272, 2015.

[9] F. W. Jones *et al.*, *Part. Accel.* 31, pp. 199-204, 1990.

[10] E. Forest *et al.*, CERN-SL-2002-044 (AP), KEK-Report 2002-3, 2002.

[11] M. Martini, CERN-ACC-NOTE-2015-0005, 2015.

ISBN 978-3-95450-185-4

LONGITUDINAL PARTICLE TRACKING CODE FOR A HIGH INTENSITY PROTON SYNCHROTRON

M. Yamamoto*, Japan Atomic Energy Agency, Tokai, Ibaraki 319-1195, Japan

Abstract

We have been developing a longitudinal particle tracking code to design and investigate the beam behavior of the J-PARC proton synchrotrons. The code simulates the longitudinal particle motion with a wake voltage and a space charge effect. The code also calculates a longitudinal emittance and a momentum filling factor at an rf bucket under the multi-harmonic wake voltage and the space charge effect. The most different point from the other codes is that a revolution frequency of a synchronous particle is exactly calculated from a bending magnetic field pattern, and it is independent of an acceleration frequency pattern. This feature is useful to check an adiabaticity of the synchrotron. We will describe the specification of the code.

INTRODUCTION

The longitudinal particle tracking code is a powerful tool to investigate the beam behavior in the synchrotron. Although an analytic treatment can be applied for some simple conditions [1], it is very difficult to evaluate the accurate beam behavior under the complicated conditions such as a multi-turn injection, the beam loading effect, the space charge effect, and so on. Many codes has been developed so far and there are some publicly available codes such as ESME [2] and BLonD [3].

We have also been developing a longitudinal particle tracking code for the J-PARC since 1997 [4], and it is aimed at the high intensity proton synchrotron where an acceleration voltage is generated by a Magnetic Alloy (MA) loaded rf cavity [5]. Since the MA cavity has a broadband impedance, we have to pay attention of the beam loading not only for the fundamental acceleration harmonic but also the higher harmonics. The higher harmonics induce the rf bucket distortion, unwanted emittance growth, and they sometimes cause the beam loss.

The J-PARC synchrotrons utilize a multi-harmonic beam loading compensation system by a feedforward method [6, 7]. Our code has been originally developed to estimate how higher harmonics should be compensated. Thereafter, the calculation procedure of the beam emittance and the momentum filling factor under the multi-harmonic beam loading is adapted to check the tolerance of the rf bucket.

We will describe the some basic equations and approaches for simulating the high intensity proton beam. Although the descriptions are only mentioned for the J-PARC, they are also adapted for the other high intensity proton synchrotrons.

* masanobu.yamamoto@j-parc.jp

BASIC FEATURES

Our code uses a macro particles of around six thousands per bunch. This number comes from the multi-turn injection at the Rapid Cycling Synchrotron (RCS). The Linac beam is injected into the RCS during 306 turns, and 20 macro particles are injected on each turn. The total number of the macro particles per bunch becomes the multiplication of them.

Difference Equation of Motion

Our code is based on a difference equation of the longitudinal motion [8] as same as the other codes. Our code choose a time from the beginning of the acceleration as the longitudinal coordinate system although a phase of the sinusoidal wave for the fundamental acceleration voltage is sometimes chosen in the other codes. The basic simultaneous equations are:

$$(\Delta E)_{\mathrm{turn}} = eV_{\mathrm{t}}(t) - \Delta E_{\mathrm{s}} \quad (1)$$

$$(\Delta T_{\mathrm{rev}})_{\mathrm{turn}} = T_{\mathrm{revs}} \left(\frac{1 + \alpha \dfrac{\Delta p}{p_{\mathrm{s}}}}{1 + \dfrac{\Delta \beta}{\beta_{\mathrm{s}}}} - 1 \right) . \quad (2)$$

The variables in eqs. (1) and (2) are:

$(\Delta E)_{\mathrm{turn}}$	Difference of the energy gain per turn between the arbitrary particle and the synchronous one
$(\Delta T_{\mathrm{rev}})_{\mathrm{turn}}$	Difference of the revolution period per turn between the arbitrary particle and the synchronous one
$V_{\mathrm{t}}(t)$	Total voltage per turn for the arbitrary particle at a time t
ΔE_{s}	Energy gain per turn for the synchronous particle
T_{revs}	Revolution period for the synchronous particle
p_{s}	Momentum of the synchronous particle
Δp	Difference of the momentum between the arbitrary particle and the synchronous one
β_{s}	β of the synchronous particle
$\Delta \beta$	Difference of β between the arbitrary particle and the synchronous one
e	Elementary electric charge
α	Momentum compaction factor

The reason why we choose the time coordinate system is that it is useful to simulate the case that the frequency of the

ISBN 978-3-95450-185-4

fundamental acceleration voltage is different from $hf_{\rm revs}$ where h is a harmonic number and $f_{\rm revs}$ is a revolution frequency of the synchronous particle.

Synchronous Particle Tracking

Before tracking the arbitrary particles, we have to know the synchronous particle motion. The revolution period of the arbitrary particle is defined by the momentum compaction factor with the momentum difference between the arbitrary particles and the synchronous particle. Our code adopts a special technique to calculate the synchronous particle.

A popular method to calculate the synchronous particle uses a famous differential equation described by a ramping of a bending magnetic field pattern:

$$\Delta E_{\rm s} = 2\pi\rho R\frac{dB(t)}{dt} \ . \tag{3}$$

The variables in eq. (3) are:

ρ	Bending radius of the accelerator ring
R	Average radius of the accelerator ring
$B(t)$	Bending magnetic field at a time t

However, this is an indirect method to track the synchronous particle. Eq. (3) only suggests a instant gradient of the energy gain. If we want to know the energy gain per turn, we must know the revolution period to perform the integration and it is still unknown.

The revolution period of the synchronous particle can be obtained directly by a forward difference method [10] as

$$\begin{aligned} m_0c^2\sqrt{1+\left(\frac{B(t+T_{\rm revs})\rho}{m_0c}\right)^2} \\ = \ \frac{B(t+T_{\rm revs})c^2\rho}{C}T_{\rm revs} \ . \end{aligned} \tag{4}$$

The variables in eq. (4) are:

m_0	Rest mass of the particle
c	Speed of the light
C	Circumference of the accelerator ring

Since Eq. (4) is a nonlinear equation, it is solved numerically.

After the revolution period is obtained, we can calculate the energy gain as

$$\begin{aligned} \Delta E_{\rm s} \ = \ & m_0c^2\sqrt{1+\left(\frac{B(t+T_{\rm revs})\rho}{m_0c}\right)^2} \\ & -m_0c^2\sqrt{1+\left(\frac{B(t)\rho}{m_0c}\right)^2} \ . \end{aligned} \tag{5}$$

Acceleration Voltage Pattern

In our code, the acceleration voltage pattern is designed without any consideration for the high intensity beam issues. The fundamental acceleration voltage $V_{\rm rf}$ and the synchronous phase $\phi_{\rm s}$ are obtained by the relation as

$$\Delta E_{\rm s} = V_{\rm rf}\sin\phi_s \ . \tag{6}$$

These variables are finally defined independently under the requirement of the beam emittance and the momentum filling factor [9].

The beam emittance $\varepsilon_{\rm L}$ is calculated by

$$\begin{aligned} \varepsilon_{\rm L} = 2\sqrt{\frac{eV_{\rm rf}\beta_{\rm s}^2E_{\rm s}}{\pi h^3\omega_{\rm revs}^2\eta_{\rm s}}}\times \\ \int_{\phi_{\rm b1}}^{\phi_{\rm b2}}\sqrt{\cos\phi-\cos\phi_{\rm b2}+(\phi-\phi_{\rm b2})\sin\phi_s}\ d\phi \ . \end{aligned} \tag{7}$$

The variables in eq. (7) are:

$E_{\rm s}$	Total energy of the synchronous particle
$\omega_{\rm revs}$	Angular revolution frequency of the synchronous particle
$\eta_{\rm s}$	Slippage factor of the synchronous particle
$\phi_{\rm b2}$	Maximum phase of the beam emittance
$\phi_{\rm b1}$	Minimum phase of the beam emittance

Eq. (7) is integrated numerically by a simple trapezoidal rule in the code. The minimum phase $\phi_{\rm b1}$ is obtained under the given $\phi_{\rm b2}$ as

$$\cos\phi_{\rm b1}-\cos\phi_{\rm b2}+(\phi_{\rm b1}-\phi_{\rm b2})\sin\phi_{\rm s}=0 \ . \tag{8}$$

Furthermore, the momentum filling factor $P_{\rm f}$ with the given $\phi_{\rm b2}$ is calculated as follows:

$$P_{\rm f} = \frac{\sqrt{\cos\phi_{\rm s}-\cos\phi_{\rm b2}+\sin\phi_{\rm s}(\phi_{\rm s}-\phi_{\rm b2})}}{\sqrt{2\cos\phi_{\rm s}+\sin\phi_{\rm s}(2\phi_{\rm s}-\pi)}} \ . \tag{9}$$

Note that the filling factor does not depend on the amplitude of the acceleration voltage and it only depends on the injected bunch width. The design value of the filling factor is one of the issues for the longitudinal beam motion. From the experience of the simulation, it is set about 80-90 % for the J-PARC synchrotrons to prevent from the beam loss caused by the beam loading.

In order to make the simulation time shorter, the acceleration voltage pattern, the energy gain and the revolution period of the synchronous particle are prepared by another code previously and the tracking code reads them thereafter.

Voltage Tracking

Another special feature of our code is adapting a voltage wave length tracking. The code tracks not only the revolution period of the particles in eq. (2) but also the wave length of the acceleration voltage. The reason is already mentioned previously. We can simulate using the arbitrary frequency pattern which is different from $hf_{\rm revs}$.

Typical example is adding a momentum offset at the RCS injection to make a bunching factor larger [10]. In this case, the frequency offset with respect to the synchronous particle is added to the original acceleration frequency pattern.

ISBN 978-3-95450-185-4

Beam Current FFT

We have to know the beam harmonics to calculate the wake voltage and the space charge effect. First of all, the arbitrary particles are divided in N bins over one revolution period. The number of bins is 512 for the harmonic number of 2 (RCS) and it is 2048 for the harmonic number of 9 (MR). Since the binning is time consuming procedure, it is better to use a quotient function in stead of the separation by a conditional sentence. After binning, FFT procedure is performed based on the revolution frequency and then we can obtain the beam harmonics.

Wake Voltage

The calculation method of the wake voltage $V_{\rm b}$ caused by the cavity impedance is quite simple. The beam harmonics $I_{\rm b}$ obtained by FFT are multiplied by the cavity impedance $Z_{\rm cav}$ as

$$V_{\rm b}(n\omega_{\rm rev}) = Z_{\rm cav}(n\omega_{\rm rev}) \times I_{\rm b}(n\omega_{\rm rev}) \ , \qquad (10)$$

where n is an integer number. It does not matter whether $Z_{\rm cav}$ is an analytic impedance model or a real measurement result. Actually, we evaluate the effect by the parasitic resonance with the real measurement result.

The amplitude and the phase of the wake voltage on each harmonic are calculated on the frequency domain in eq. (10), and then they are reproduced on the time domain by an inverse FFT as

$$V_{\rm b}(t) = \sum_{n=1}^{N_{\rm b}} V_{{\rm b}n}(n\omega_{\rm rev}) \sin(n\omega_{\rm rev}t + \phi_{{\rm b}n}) \ , \qquad (11)$$

where $\phi_{{\rm b}n}$ is a phase difference of the wake voltage for each harmonic and $N_{\rm b}$ is the upper limit of the harmonics to be calculated. For example, $N_{\rm b} = 40$ is chosen for the RCS (∼33 MHz) and $N_{\rm b} = 70$ for the MR (∼13 MHz). Since $N_{\rm b}$ depends on the cavity band width and the bunch width, a heuristic approach is necessary.

Fig. 1 shows the calculation result for 1 MW-eq. beam acceleration in the RCS. The shaded histogram shows the bunch shape, the blue line indicates the fundamental acceleration voltage and the red line indicates the wake voltage. Since the beam intensity is very high, the wake voltage is larger than the fundamental acceleration one. This wake voltage is compensated by the feedforward system.

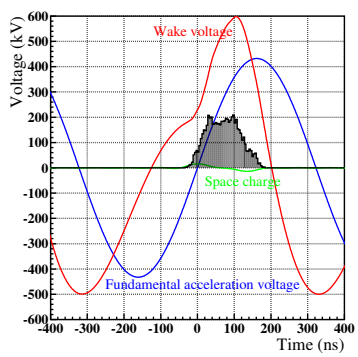

Figure 1: Calculation for the wake voltage (red) and the space charge effect (green) in the RCS.

Space Charge

The space charge effect in the longitudinal direction is calculated by the following formula:

$$V_{\rm sp}(n\omega_{\rm rev}) = -i \cdot nZ_0 \frac{g_0}{2\beta_{\rm s}\gamma_{\rm s}^2} \times I_{\rm b}(n\omega_{\rm rev}) \ , \qquad (12)$$

where g_0 is a geometrical factor and Z_0 is a characteristic vacuum impedance. The space charge effect in the time domain is obtained by the inverse FFT of eq. (12) as

$$V_{\rm sp}(t) = \sum_{n=1}^{N_{\rm sp}} V_{{\rm sp}n}(n\omega_{\rm rev}) \sin(n\omega_{\rm rev}t + \phi_{{\rm sp}n}) \ , \qquad (13)$$

where $\phi_{{\rm sp}n}$ is a phase difference for each harmonic of the space charge voltage and $N_{\rm sp}$ is the upper limit of the harmonics to be calculated.

Defining $N_{\rm sp}$ is an issue because the space charge voltage $V_{\rm sp}$ becomes somewhat noisy waveform if the inverse FFT is performed up to $N/2$. Fig. 2 shows the calculation result of the space charge voltage for the parabolic bunch shape in the RCS where $N_{\rm sp} = 256$ is used. Although the analytic solution should be straight line, the calculation result shows noisy aspect by the binning. From the experience of the simulation [11], we use following relation for $N_{\rm sp}$ as

$$N_{\rm sp} = \frac{2\pi}{\omega_{\rm revs}\sqrt{\sum_{i=1}^{N_{\rm p}} \Delta t_i^2}} \ , \qquad (14)$$

where $N_{\rm p}$ is the number of the macro particles and Δt_i is the time difference of each macro particles with respect to the center of the bunch. Fig. 3 shows the calculation result where $N_{\rm sp} = 10$ (red line), $N_{\rm sp} = 15$ (green line) and $N_{\rm sp} = 30$ (blue line). Eq.(14) suggests $N_{\rm sp} = 14$ is suitable in this case, and the calculation result also suggest $N \sim 15$ is almost enough.

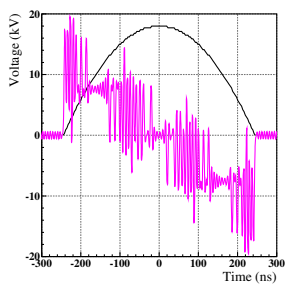

Figure 2: Calculation result of the space charge effect in the case of $N_{\rm sp} = 256$. Black line indicates the parabolic bunch shape.

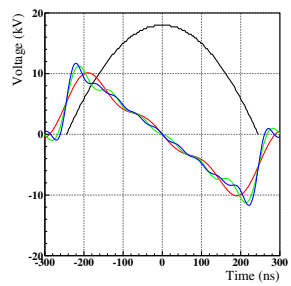

Figure 3: Calculation result of the space charge effect in the case of $N_{\rm sp} = 10$ (red), $N_{\rm sp} = 15$ (green) and $N_{\rm sp} = 30$ (blue).

Beam Emittance and Momentum Filling Factor

The beam emittance and the momentum filling factor mentioned in eq.(7) and (9) are calculated under the condition without the beam loading and the space charge effects.

ISBN 978-3-95450-185-4

On the other hand, our code can calculate them including the multi-harmonic beam loading and the space charge effects over whole acceleration period.

The voltage used in this calculation is the total one $V_{\rm t}$, and it consists of the fundamental acceleration voltage $V_{\rm rf}$, the second harmonic voltage $V_{\rm rf2}$ to make the bunch shape flat, the wake voltage $V_{\rm b}$ and the space charge voltage $V_{\rm sp}$, that is:

$$\begin{aligned} V_{\rm t}(\phi) &= V_{\rm rf}\sin\phi + V_{\rm rf2}\sin\{2(\phi-\phi_{\rm s})+\phi_2)\} \\ &+ \sum_{n=1}^{N_{\rm b}} V_{{\rm b}n}\sin\left(\frac{n}{h}\phi+\phi_{{\rm b}n}\right) \\ &+ \sum_{n=1}^{N_{\rm sp}} V_{{\rm sp}n}\sin\left(\frac{n}{h}\phi+\phi_{{\rm sp}n}\right) \ , \end{aligned} \tag{15}$$

where ϕ_2 is a phase offset for the second harmonic voltage to adjust the bunch shape.

In that case, the longitudinal beam emittance $\varepsilon_{\rm L}$ is obtained as follows:

$$\varepsilon_{\rm L} = 2\sqrt{\frac{e\beta_{\rm s}^2 E_{\rm s}}{\pi h^3 \omega_{\rm revs}^2 \eta_{\rm s}}} \times \int_{\phi_{\rm b1}}^{\phi_{\rm b2}} \left[\sqrt{\int_{\phi}^{\phi_{\rm b2}} \{V_t(\phi') - V_{\rm rf}\sin\phi_{\rm s}\}\, d\phi'}\right] d\phi \ . \tag{16}$$

Eq. (16) is also integrated numerically by the simple trapezoidal rule. In order to calculate the emittance precisely, we have to find a macro particle on an outermost trajectory under the beam loading and the space charge effect. If the macro particle has a value $(\phi_{\rm i}, \Delta p_{\rm i})$ in the phase space, the maximum phase $\phi_{\rm b2}$ is obtained from

$$\frac{e}{\pi h \eta_{\rm s} E_{\rm s} \beta_{\rm s}^2} \int_{\phi_{\rm i}}^{\phi_{\rm b2}} \{V_t(\phi') - V_{\rm rf}\sin\phi_{\rm s}\}\, d\phi' - \left(\frac{\Delta p_{\rm i}}{p_{\rm s}}\right)^2 = 0 \tag{17}$$

Once $\phi_{\rm b2}$ is found, the minimum phase $\phi_{\rm b1}$ is defined by

$$\int_{\phi_{\rm b1}}^{\phi_{\rm b2}} \{V_t(\phi') - V_{\rm rf}\sin\phi_{\rm s}\}\, d\phi' = 0 \ . \tag{18}$$

Furthermore, the momentum filling factor $P_{\rm f}$ is calculated as follows:

$$P_{\rm f}(\phi) = \frac{\sqrt{\int_{\phi}^{\phi_{\rm b2}} \{V_t(\phi') - V_{\rm rf}\sin\phi_{\rm s}\}\, d\phi'}}{\sqrt{\int_{\phi}^{\phi_{\rm bk2}} \{V_t(\phi') - V_{\rm rf}\sin\phi_{\rm s}\}\, d\phi'}} \ , \tag{19}$$

where $\phi_{\rm bk2}$ is the maximum phase of the rf bucket which is obtained from

$$V_{\rm t}(\phi_{\rm bk2}) - V_{\rm rf}\sin\phi_{\rm s} = 0 \ . \tag{20}$$

Fig. 4 shows the total voltage (upper graph) and the rf bucket (lower graph) with (red line) and without (blue line) the wake voltage at the RCS extraction. Fig. 5 shows the beam emittance and the momentum filling factor with (red line) and without (blue line) the wake voltage over whole acceleration period in the RCS. As can be seen, the higher harmonic beam loading causes the rf bucket distortion and the emittance gradually becomes larger.

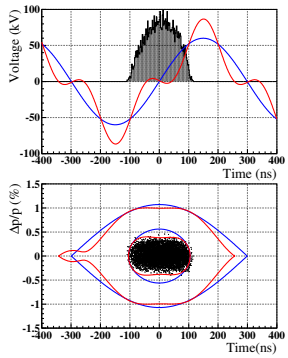

Figure 4: Calculation results for the rf bucket and the trajectory with the beam loading (red) and without the beam loading (blue) in the RCS.

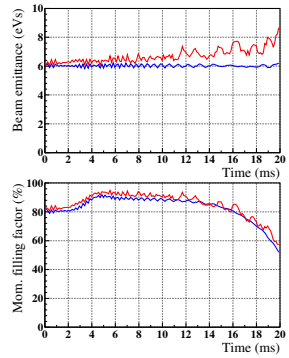

Figure 5: Calculation results for the beam emittance and the momentum filling factor with the beam loading (red) and without the beam loading (blue) in the RCS.

Adiabaticity

It is very important for the longitudinal motion to calculate an adiabaticity $\epsilon_{\rm a}$. It is defined by

$$\epsilon_{\rm a} = \frac{1}{\omega_{\rm s}^2}\left|\frac{d\omega_{\rm s}}{dt}\right| \ , \tag{21}$$

where $\omega_{\rm s}$ is the angular synchrotron frequency. When $\epsilon_{\rm a} \ll 1$, typically $\epsilon_{\rm a} < 0.1$, the change of the accelerating voltage is considered as enough adiabatic in comparison with the synchrotron motion [12]. Since the adiabaticity becomes larger near the extraction in the J-PARC synchrotrons, a frequency correction is necessary to keep the beam orbit center.

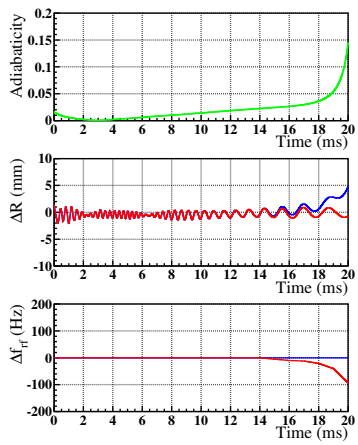

Figure 6: Calculation results for the adiabaticity, the beam orbit and the frequency correction in the RCS.

ISBN 978-3-95450-185-4

Fig. 6 shows the calculation results of the adiabaticity (upper graph), the beam orbit (middle graph), and the frequency correction for the acceleration pattern (lower graph) over whole acceleration period of the RCS. Since the adiabaticity reaches around 0.1 near the extraction, the orbit deviates from the center without the frequency correction (blue line). The orbit is corrected by the frequency adjustment (red line).

Phase Modulation

A controlled emittance blow-up is one of the method to solve some high intensity issues. Our code can calculate the controlled emittance blow-up by a phase modulation using Very High Frequency (VHF) cavity [13]. The voltage added by the VHF cavity $V_{\rm V}$ is expressed as

$$V_{\rm V} = V_{\rm pm} \sin(h_{\rm pm}\omega_{\rm revs}t + \psi(t) + \psi_{\rm pm}) \,, \qquad (22)$$

where $V_{\rm pm}$ and $h_{\rm pm}$ are an amplitude and a harmonic number of the VHF cavity, and $\psi_{\rm pm}$ is a phase offset value. $\psi(t)$ is a modulation term as follows:

$$\psi_{\rm pm}(t) = \Delta\phi_{\rm pm} \sin\omega_{\rm pm}t \,, \qquad (23)$$

where $\Delta\phi_{\rm pm}$ is an "amplitude" of the phase modulation and $\omega_{\rm pm}$ is an angular modulation frequency. The integer multiple of the synchrotron frequency is usually chosen for the modulation frequency. After all, the total voltage felt by the beam becomes the summation of eqs. (15) and (22). Since the code uses the time domain coordinate, the method of the voltage wave length tracking should be adapted for the VHF voltage. For that purpose, the phase modulation is translated in an instance VHF frequency $f_{\rm V}$ as

$$f_{\rm V}(t) = h_{\rm pm}f_{\rm revs} + \frac{\Delta\phi_{\rm pm}}{2\pi}\omega_{\rm pm}\cos\omega_{\rm pm}t \,. \qquad (24)$$

There is no special procedure to calculate the beam emittance and the momentum filling factor for the phase modulation because the blow-up by the phase modulation is a diffusion process and the trajectory of the particle does not change so much turn by turn.

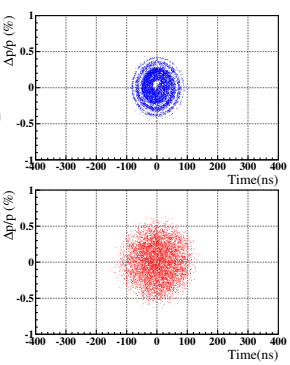

Figure 7: Calculation result of the longitudinal emittance in the MR with (red) and without the phase modulation (blue).

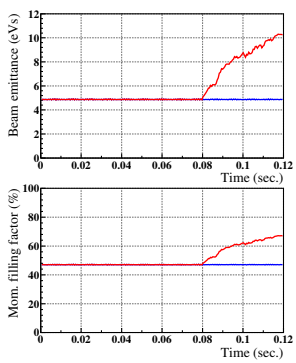

Figure 8: Calculation result of the beam emittance and the momentum filling factor with (red) and without (blue) the phase modulation.

Fig. 7 shows the beam distribution with (lower graph) and without (upper graph) the phase modulation in the MR injection. The VHF cavity parameters are $V_{\rm pm} = 100$ kV, $h_{\rm pm} = 635$, $\omega_{\rm pm} = 15\omega_{\rm s}$ and $\Delta\phi_{\rm pm} = \pi$. Fig. 8 shows the beam emittance and the momentum filling factor with (red line) and without (blue line) the phase modulation in the MR injection. As can be seen, the emittance gradually increases from 5 eVs to 10 eVs.

SUMMARY

We have been developing the longitudinal particle tracking code for the high intensity proton synchrotron. It has the special feature for tracking the synchronous particle and the voltage wave length, which is useful to check the adiabaticity. Since the code calculates the beam emittance and the momentum filling factor with the beam loading and the space charge effect, it is worth to evaluate the tolerance in the high intensity beam acceleration.

REFERENCES

[1] H. Moshammer, Nucl. Inst. Meth. Phys. Res. A, 323 (1992), p. 553

[2] J.A. MacLachlan and J.F. Ostiguy, User's Guide to ESME es2011 (2011)

[3] BLonD, Beam Longitudinal Dynamics code: http://blond.web.cern.ch/

[4] M. Yamamoto *et al.*, Proc. of the 11th Symp. on Accel. Sci. and Tech., SPring8 (1997)

[5] C. Ohmori *et al.*, Proc. of PAC 1999, p. 413

[6] F. Tamura *et al*, Phys. Rev. ST Accel. Beams 14 (2011), 051004

[7] F. Tamura *et al*, Phys. Rev. ST Accel. Beams 16 (2013), 051002

[8] J.A. MacLachlan, FN-529, 1989

[9] R. Baartman, TRI-DN-K226, 1993

[10] M. Yamamoto *et al.*, Nucl. Instr. and Meth. A 621 (2010), p.15

[11] Tom. Uesugi, Private communication.

[12] W.T. Weng, AIP Conf. Proc. 184, p. 242, 1989

[13] M. Yamamoto *et al.*, Proc. of IPAC 2012, WEPPR008 (2012), p. 2952

ISBN 978-3-95450-185-4

INTERPRETATION OF WIRE-SCANNER ASYMMETRIC PROFILES IN A LOW-ENERGY RING

M. Cieslak-Kowalska, CERN, Geneva, Switzerland and EPFL, Lausanne, Switzerland
E. Benedetto, CERN, Geneva, Switzerland

Abstract

In the CERN PS Booster, wire-scanner profile measurements performed at injection energy are affected by a strong asymmetry. The shape was reproduced with the code PyORBIT, assuming that the effect is due to the beam evolution during the scans, under the influence of space-charge forces and Multiple Coulomb Scattering at the wire itself. Reproducing the transverse profiles during beam evolution allows to use them reliably as input for simulation benchmarking.

INTRODUCTION

The PSB, the first circular accelerator in the CERN injector chain, is made of 4 rings stacked on top of each other. It operates on energy range from 50 MeV to 1.4 GeV. The acceleration cycle of the beam lasts 500 ms. PS Booster provides full beam range to various CERN users with beam intensities varying from 40e10 p+ to 800e10 p+ per ring and transverse normalized emittances between 1 mm.mrad and 15 mm.mrad.

One of the PSB goals is to provide to the LHC high quality beam in terms of high brightness, defined as the intensity divided by the transverse emittance.

Usually, emittance measurements are taken at the extraction energy flat top, however in order to perform some dedicated measurements explained later in the paper and benchmark them with simulations, we collected data at the beginning of the acceleration ramp. The beam profiles measured at the injection energy are asymmetric (Figure 1) and in this paper we try to explain this effect.

We assume that the asymmetry is due to two effects and their superposition.

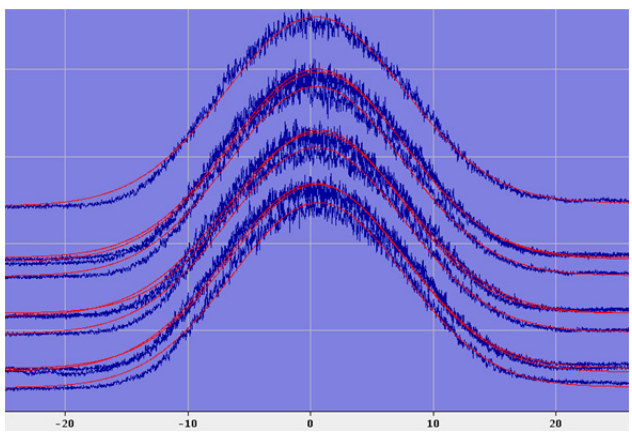

Figure 1: Example of an asymmetric measured vertical profile in PS Booster, at 60 MeV at C406.

The first effect is the Multiple Coulomb Scattering of the beam at the wire itself. Protons of the beam interacts with the atoms of the material of the wire scanner and due to electromagnetic interactions change theirs transverse momenta, which results in emittance growth. We measured this effect and we present the experimental results compared with the data from numerical simulations and analytical estimates. Thanks to this experiment, we defined an equivalent of the wire thickness used for further simulations.

The second effect is the space charge, which is very strong in the range of the PSB operation energies, and might induce emittance blow-up during the measurement time. Due to space-charge, the beam suffers from emittance blow up or losses, depending on the actual tune and the tune necktie which overlaps machine resonances. Moreover, for several beams like EAST-type beams and some special LHC beams, for which the final emittance is reached via transverse scraping [1], we observe tails repopulation due to the space charge itself.

An example of the reconstructed profile after transverse shaving is presented in this paper.

PS Booster Wire Scanners

The PSB is equipped with 8 independently operated, 25 µm-thick carbon wire scanners - one per plane for each of the 4 PSB rings. The user is able to measure the beam profile twice during one cycle: with the "IN" and the "OUT" scan indicating the direction of the wire move. The "IN" scan goes from negative values (-50 mm) to positive (+50 mm), according to the PSB convention, and the opposite for the "OUT" scan. Three speed of the wire are available: 10 m/s, 15 m/s and 20 m/s. Assuming 10 m/s wire speed, the measurement of a beam with an emittance of 2 mm mrad takes about 3 ms.

EMITTANCE BLOW UP DUE TO THE SCATTERING AT THE WIRE

The emittance blow up due to the scattering at the wire depends on the energy of the impacting beam which translates into a different scattering angle. We performed an experiment in which we swapped the wire scanner at low energy with a vertical "IN" scan in order to induce emittance blow up and then we measured the increase of emittance at extraction energy with a vertical "OUT" scan. As a reference, we considered measurements with the "OUT" scan, with the "IN" scan launched before injection, i.e. with no beam in the machine. The measured beam had a normalized emittance of ~ 2.2 mm mrad in both planes and an intensity of I = 160e10 p+. Data was

ISBN 978-3-95450-185-4

collected as a function of the beam energy at the time of the "IN" scan, for two speeds of the wire scanner: 10 m/s and 15 m/s. For each point, we considered the average over 20 measurements.

In the next paragraph we present the measured increase in the normalized emittance $\Delta\varepsilon_{norm}$ with respect to the energy when the IN scan was performed. The outcome of the experiment was then compared to the results of the numerical simulations and the expected values calculated with analytical formulae.

SIMULATION OF MULTIPLE COULOMB SCATTERING AT THE WIRE

The Multiple Coulomb Scattering at the wire has been simulated using the code PyORBIT [2] code (with PTC [3] tracking), which includes space charge calculations and a particle-matter interaction module. The wire moving through the beam has been modelled as a moving scattering foil. We profited from the fact that the Foil class in PyORBIT has a dedicated routine using a simple Multiple Coulomb Scattering implementation. The foil is defined by its transverse dimensions and its thickness (in $\mu m/cm^2$).

The moving wire was modelled as a foil of vertical size equal to the wire diameter and a time dependent transverse position. The initial position of $y_{min} = -0.025$ m (instead of the -0.050 m) was chosen in order to shorten the time needed for each simulation. The 3 sigma beam size is much smaller than 25 mm, so this assumption is valid.

Simulations were performed in order to find the equivalent foil thickness which will allow us to simulate a flying wire and reproduce the measured profiles. The initial foil thickness has been defined as:

$$thickness\ (foil) = \rho * d_{eq}$$

Where:

ρ – density of the Carbon, i.e. 2.26 g/cm3 [4]

d_{eq} – equivalent of the foil (wire) thickness. The real wire diameter is d = 25 μm [5]

We made a scan in the energy range of interest, i.e. from the current PS Booster injection energy of 50 MeV up to 260 MeV. For each energy, we launched the simulations of the wire going through the beam in the vertical plane and we measured the increase of normalized vertical r.m.s. emittance.

In the simulations the space charge module was switched off in order to separate the space charge related effects from the scattering at the wire. The simulated particle herd had an initial Gaussian distribution with the normalized reference emittance of 2.2 mm mrad, comparable to the one measured in the machine. In order to ensure that there was no additional blow up due to other factors, we launched in parallel a simulation without the moving wire scanner. In this case, we obtained the $\Delta\varepsilon_{norm} = 10^{-4}$ mm mrad, which proved that the interaction with the wire was the only source of emittance increase.

The data from simulations and from measurements were then compared to the analytical predictions based on the formulae [5]:

$$\Delta\varepsilon_n^{x,y} = \frac{\pi\, d\, f_r}{4\, v}\,\frac{1}{2}\,\beta_{x,y} < \Theta_{rms}^2 > (\beta\gamma)$$

Where:

πd/4 – wire diameter equivalent

fr – revolution frequency

v – wire speed

βx,y – beta function in x/y plane

βγ – relativistic factors

The average scattering angle has been calculated using the formula [6]:

$$< \Theta_{rms}^2 > = (\frac{13.6MeV}{pv})^2\ \frac{d}{L_{rad}}\ [1 + 0.038ln\frac{d}{L_{rad}}]^2$$

Where:

L_{rad} – radiation length of carbon = 18.9 cm [4]

p – momentum of the impacting particles

v – speed of the particles

Figures 2 and 3 present the comparison of the theoretical, simulated and measured data of the normalized r.m.s. emittance blow up as a function of the beam energy during the scan, for the two speeds of the wire scanner: 10 m/s and 15 m/s. In Fig. 2 and 3, we also included the points of a scan of the simulated emittance blow up as a function of the equivalent wire thickness, for the current and future PSB injection energy: 50 MeV (β = 0.314) and 160 MeV (β = 0.52). We tested a wire equivalent thickness d_{eq} of 1.0d, πd/4, 0.5d and 0.25d.

Based on the presented data we conclude that for purposes of further simulations, the wire thickness can be approximated with a thickness equivalent of 0.5d. This value seems to be a very good fit for both wire speeds, for the energy range above ~80 MeV (β = 0.39). We observe a difference between the measurements and the simulated values for the energies of 50 MeV to 80 MeV.

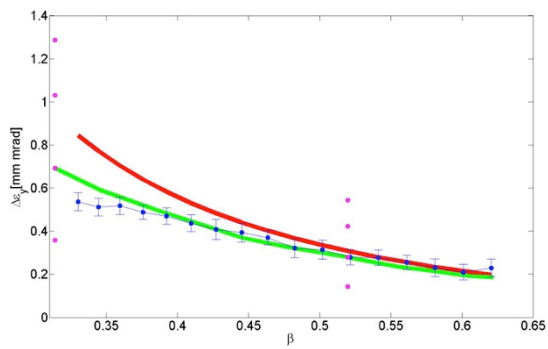

Figure 2: Theoretical (in red), simulated (in green) and measured (in blue) normalized rms emittance blow up as a function of the beam relativistic beta. Wire speed 10 m/s, assuming 99% confidence interval. The magenta points are a scan over the wire equivalent thickness.

ISBN 978-3-95450-185-4

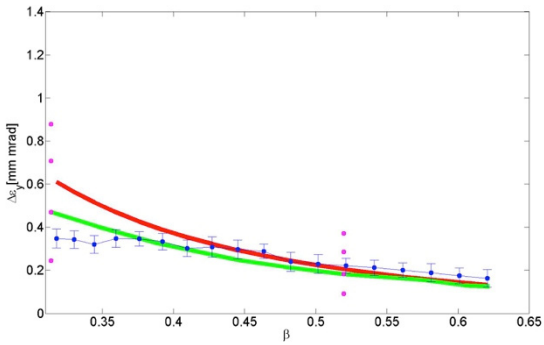

Figure 3: Theoretical (in red), simulated (in green) and measured (in blue) normalized rms emittance blow up as a function of the beam relativistic beta. Wire speed 15 m/s, assuming 99% confidence interval. The magenta points are a scan over the wire equivalent thickness.

EMITTANCE BLOW UP DUE TO SPACE CHARGE EFFECTS

The low intensity beams in the PSB are shaped with a process called "shaving" consisting in reducing the beam intensity and beam transverse emittances by scraping the beam on the PSB aperture restriction [1]. When the shaving is finished, we observe tail repopulation driven by space charge, which we suspected might be one reason of the asymmetry of the measured profile.

In the experiment, we set up a dedicated cycle in PSB with the flat top energy of 60 MeV, where we performed the shaving and we measured the profiles of the shaved beam every 1 ms to see its evolution in time. We observed rms emittance increase in time as well as changes in the shape of the measured profiles.

Figure 4 presents a profile taken with the wire scanner, measured right after shaving, while the beam experience tails repopulation. Our hypothesis here is that since the wire scan lasts a few ms, it captures the evolution of the tails, resulting in an asymmetric profile. The left side of the beam profile was registered much earlier that the right side. In other words the left tail of the beam had less time to evolve than the right side.

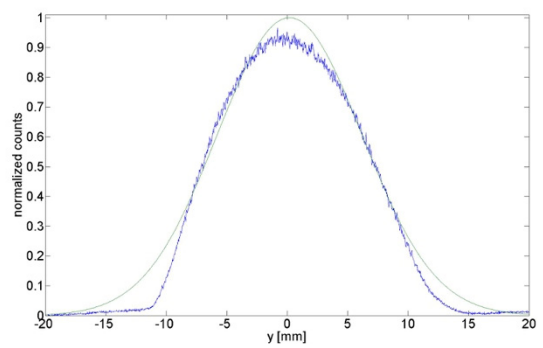

Figure 4: Measured profiles after the shaving process in PSB. Time C433.

SPACE CHARGE SIMULATIONS

We wanted to reproduce this measured beam profile numerically, so we simulated the vertical shaving in PyORBIT. After the shaving process is finished we let the beam evolve under space charge and we observed the tails repopulation. We added to the simulation also a moving wire, as described in the previous section, to combine the blow up due to the space charge with the blow up coming from the Multiple Coulomb Scattering.

Figure 5 shows the r.m.s. emittance evolution during the motion of the wire scanner, under space-charge forces and Multipole Coulomb Scattering. When the wire scanner starts interacting with the tail of the beam, the beam starts experiencing a strong emittance growth, much larger than the one associated with space-charge. For illustration, we also run a case with 1.5 times larger beam intensity (black, dashed curve on Fig.5), to see the effect of space charge. This was a purely academic exercise, the simulations are not self-consistent and one can notice a large mismatch.

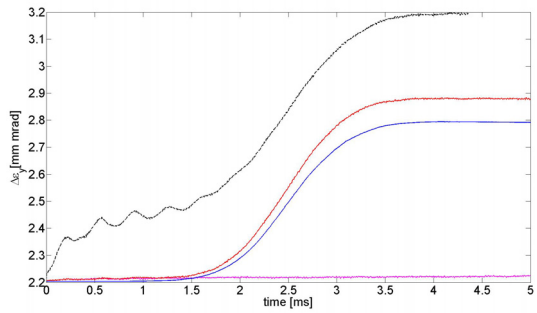

Figure 5: Simulated emittance increase versus time. In red: space charge and scattering, in blue: only scattering, in magenta: only space charge. The case with a 1.5 larger intensity is marked with a black dashed line.

RECONSTRUCTION OF THE ASYMMETRIC PROFILE

In order to reconstruct the measured beam profile we needed multiple samples of the beam at different time stamps. We dumped the beam profiles every 0.1 ms, simulating the sampling coming from the flying wire scanner. Assuming the wire moving with the speed of 10 m/s and measuring from -50 mm to +50 mm in vertical plane, the time needed to fly through the beam is 10 ms, corresponding to ~6600 turns of the simulation and 100 profiles in total.

The profile presented in Fig. 6 is therefore a reconstructed profile with the y-position correlated to the movement of the wire, such that the bins around a given position are taken from the profile dumped at the corresponding time. There is a strong, visible asymmetry in the reconstructed profile, to be compared with the experimental data of Fig. 4.

ISBN 978-3-95450-185-4

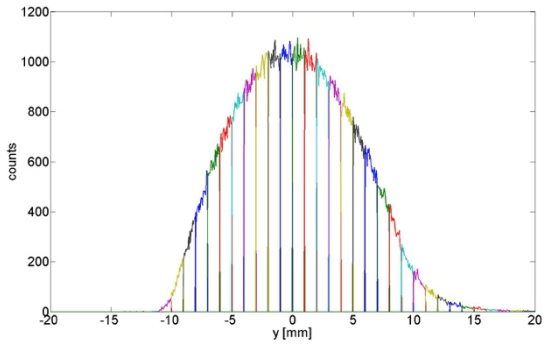

Figure 6: Reconstructed profile of the beam undergoing tails repopulation and multiple scattering at the wire scanner, to be compared with Fig.4. Time C433.

In order to identify the different contributions to the profile asymmetry, we simulated four different cases: with/without space charge and with/without Multipole Coulomb Scattering. The reconstructed profiles are reported in Fig. 7. The dominating phenomena is the scattering at the wire, however the space charge also contributes slightly to its asymmetry. We reconstructed the profile also for the artificial case where we increased the beam intensity by 50% to see whether a strong space charge also leads to the profile asymmetries. This case is marked with a black line in Fig. 7, but also in this case we observed little asymmetry coming from space charge. The reason is, as one can see from Fig. 5, that the simulated space-charge blow-up is occurring in a much shorter timescale as compared to the wire passage.

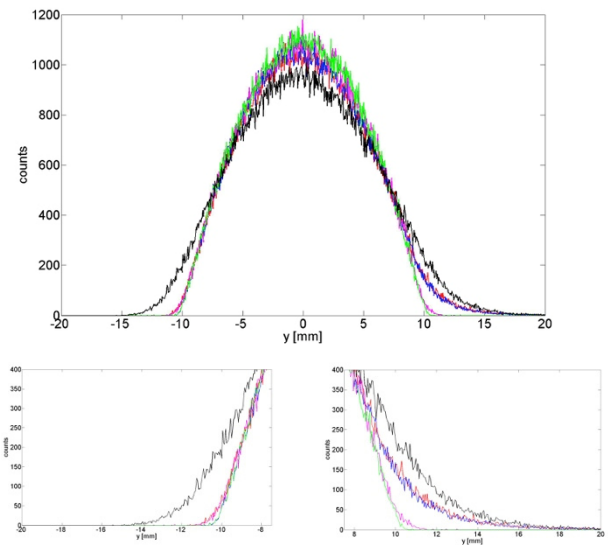

Figure 7: Reconstructed profile of the beam at C433. In red: space charge + the wire scanner, in blue: only wire scanner, in magenta: only space charge, in green: none of the effects. The case with an increased intensity is marked with a black line. The left and right tails are zoomed at the lower plot.

CONCLUSIONS

We have modelled in PyOrbit a wire scanner flying through the beam and we have developed a routine to post-process the data and reconstruct the profiles taking into account the time needed to perform a measurement, i.e. a few ms for a 2 mm mrad beam. With our recipe, we successfully managed to reproduce the asymmetry observed in the measured profiles at low energies in the CERN PS Booster.

First of all, we have measured the emittance blow-up due to Multiple Coulomb Scattering at the wire, as a function of the beam energy, we have compared it with analytical formula and simulations and we have obtained an equivalent thickness to be used in our further simulations.

We have focused our analysis on the profiles measured after beam scraping, during the "shaving" process in the PSB, occurring at around 60 MeV and after which we expect tail repopulation.

Our hypothesis was that the Multiple Coulomb Scattering together with the space charge are be two main sources of the emittance blow up, and that this increase of beam size is captured by the wire scanner while it is flying through the beam.

The conclusion, for this particular case, was that the Multipole Coulomb Scattering at the wire was the dominant phenomenon, while the tail repopulation driven by space charge had a negligible effect on the measured profile asymmetry. Improvements in the PSB optics model, which is presently ongoing [7], and/or different case study might put in evidence a larger contribution from space charge.

In any cases and for any mechanism driving beam blow-up or losses, the ability to reproduce the transverse profiles measured with the wire scanners while the beam is evolving, allows using them reliably as input for simulation benchmarking.

ACKNOWLEDGEMENT

The authors would like to thank Guido Sterbini, for suggesting the procedure to measure the beam blow-up due to scattering at wire, Ana Guerrero Ollacarizqueta and Emiliano Piselli for their advices and expertise while setting up the wire scanners measurements.

REFERENCES

[1] M. Kowalska, E. Benedetto, V. Forte, B. Mikulec, G. Rumolo "New Shaving Scheme for Low Intensity Beams in the CERN PS Booster and Feasibility at 160 MeV", in *Proc. IPAC'15*, paper THPF087.

[2] A. Shishlo, S. Cousineau, J. Holmes, T. Gorlov, "The Particle Accelerator Simulation Code PyORBIT", ICCS 2015, Volume 51, 2015, Pages 1272–1281.

[3] E. Forest, E. McIntosh, F. Schmidt, "Introduction to the Polymorphic Tracking Code", 2002.

ISBN 978-3-95450-185-4

[4] Atomic and Nuclear Properties of materials, Table 6.1 Abridged from pdg.lbl.gov/AtomicNuclearProperties by D. E. Groom (2007).
[5] F. Roncarolo, "Accuracy of the Transverse Emittance Measurements of the CERN Large Hadron Collider", PhD thesis, 2005.
[6] K. A. Olive *et al*., (Particle Data Group), "Passage of Particles through Matter", Chin. Phys. C, 38, 090001 (2014) and 2015 update.
[7] E. Benedetto *et al*., "Space Charge Effects and Mitigation in the CERN PS Booster, in View of the Upgrade", presented at HB2016, Malmö, Sweden, July 2016, paper THPM9X01, this conference.

ISBN 978-3-95450-185-4

GENERAL FORMULA TO DEDUCE THE SPACE CHARGE TUNE SPREAD FROM A QUADRUPOLAR PICK-UP MEASUREMENT

E. Métral†, CERN, Geneva, Switzerland

Abstract

In 1966, W. Hardt derived the oscillation frequencies obtained in the presence of space charge forces and gradients errors for elliptical beams. Since then, a simple formula is usually used to relate the shift of the quadrupolar mode (obtained from the quadrupolar pick-up) and the space charge tune spread, depending only on the ratio between the two transverse equilibrium beam sizes. However, this formula is not always valid, in particular for machines running close to the coupling resonance $Q_x = Q_y$ with almost round beams. A new general formula is presented, giving the space charge tune spread as a function of i) the measured shift of the quadrupolar mode, ii) the ratio between the two transverse equilibrium beam sizes and iii) the distance between the two transverse tunes.

INTRODUCTION

The incoherent direct space charge tune spread is a fundamental parameter in the beam dynamics of high-intensity high-brightness beams but most of the time it is only computed analytically or simulated. It would be good to be able to measure it in running machines, which is possible with quadrupolar pick-ups by looking at the shift of the quadrupolar mode with intensity (note that there is no shift of the dipole mode with intensity due to the direct space charge as the latter follows the evolution of the beam centre and does not modify its motion). Since the derivation from W. Hardt of the oscillation frequencies obtained in the presence of space charge forces and gradients errors for elliptical beams [1], a simple formula is usually used to relate the (horizontal) space charge tune spread to the (horizontal) shift of the quadrupolar mode due to intensity, which depends only on the ratio between the equilibrium rms vertical beam size σ_{y0} and the equilibrium rms horizontal beam size σ_{x0} [2,3,4]

$$\Delta Q^{SC}_{x,\text{spread}} = \frac{2Q_{x0} - Q_{2x}}{\frac{1}{2}\left(3 - \frac{1}{1+\frac{\sigma_{y0}}{\sigma_{x0}}}\right)} , \qquad (1)$$

where $2\,Q_{x0}$ is the low-intensity quadrupolar tune and Q_{2x} is the intensity-dependent quadrupolar tune.

However, Eq. (1) is not always valid and it corresponds to the case when the coupling between the two transverse planes, introduced by space charge, is neglected. This formula is in particular not valid for machines running close to the coupling resonance $Q_x = Q_y$ with almost round beams, which is the case of many machines (and in particular of the CERN LHC injectors where we plan to measure the space charge tune spread using quadrupolar pick-ups) and the purpose of this paper is to provide the more general formula which depends also on the distance between the two transverse tunes [5]. Note that the extreme cases of a small or large tune split were already discussed in Ref. [6] for the case of a round beam.

The (2D) transverse envelope equations are first reviewed in Section 1, as well as the coupled equations to be solved in the presence of small perturbations on top of equilibrium beam sizes. The usual Eq. (1) is then recovered in Section 2 in the uncoupled case. The new formula providing the space charge tune spread in the general case (i.e. also close to the coupling resonance) is finally derived and discussed in Section 4.

TRANSVERSE ENVELOPE EQUATIONS

The (2D) transverse envelope equations are now well-known and used [7,8] in particular since the work of Sacherer [9] who showed that the envelope equations derived by Kapchinsky and Vladimirsky (known as the KV equations) [10] for a continuous beam with uniform charge density and elliptical cross-section are also valid for general beam distributions if one considers the second moments only. Considering a particle in an ensemble of particles which obeys the single-particle equations, adding the space charge force to the external (linearized) force and averaging over the particle distribution, the equations of motion for the centre of mass can be obtained (note that due to Newton's third law the average of the space charge force is zero). Looking at the second moments and in particular at the position and momentum offsets of the particles from their respective averages, the 2D transverse envelope equations can finally be obtained [7,8]

$$a'' + K_x\, a - \frac{2K_{sc}}{a+b} - \frac{\varepsilon_x^2}{a^3} = 0 ,$$
$$b'' + K_y\, b - \frac{2K_{sc}}{a+b} - \frac{\varepsilon_y^2}{b^3} = 0 , \qquad (2)$$

with

$$a = 2\sigma_x , \qquad b = 2\sigma_y , \qquad (3)$$

$$\varepsilon_x = 4\varepsilon_{x,rms} , \qquad \varepsilon_y = 4\varepsilon_{y,rms} , \qquad (4)$$

where $'$ stands for the derivative with respect to the azimuthal coordinate s, $\sigma_{x,y}$ are the transverse rms beam sizes, $K_{x,y}$ describe the transverse external forces, $\varepsilon_{x,y,rms}$ are the transverse rms beam emittances and K_{sc} is a coef-

† Elias.Metral@cern.ch

ISBN 978-3-95450-185-4

ficient proportional to the horizontal space charge tune spread (considering that the space charge tune spread extends from the low intensity tune to the tune with maximum space charge tune shift) through (in the smooth approximation) [11]

$$\Delta Q^{SC}_{x,\,\mathrm{spread}} = -\,\Delta Q^{SC}_{x,\,\mathrm{linear\ shift}} = \frac{K_{sc}\,R^2}{Q_{x0}\,a_0\left(a_0+b_0\right)}\,, \qquad (5)$$

where R is the average machine radius, Q_{x0} is the low-intensity horizontal tune and a_0 and b_0 are the horizontal and vertical equilibrium beam sizes (obtained from Eq. (2) when the terms with the derivative are zero). Both transverse planes have thus to be treated jointly for high-intensity beams due to the space-charge coupling.

The beam may execute some collective motion on top of the equilibrium beam sizes

$$a(s) = a_0 - \Delta a(s) \quad \text{and} \quad b(s) = b_0 + \Delta b(s)\,, \qquad (6)$$

where the perturbations Δa and Δb are considered small with respect to the equilibrium beam sizes. Linearizing the equations yields

$$\begin{aligned} \Delta a'' + K_a\,\Delta a &= K\,\Delta b\,, \\ \Delta b'' + K_b\,\Delta b &= K\,\Delta a\,, \end{aligned} \qquad (7)$$

with

$$K_a = 4K_x - \frac{2K_{sc}\left(2a_0+3b_0\right)}{a_0\left(a_0+b_0\right)^2}\,, \qquad (8)$$

$$K_b = 4K_y - \frac{2K_{sc}\left(2b_0+3a_0\right)}{b_0\left(a_0+b_0\right)^2}\,, \qquad (9)$$

$$K = \frac{2K_{sc}}{\left(a_0+b_0\right)^2}\,. \qquad (10)$$

Using the smooth approximation

$$K_x = \left(Q_{x0}/R\right)^2\,, \qquad K_a = \left(Q_a/R\right)^2\,, \qquad (11)$$

$$K_y = \left(Q_{y0}/R\right)^2\,, \qquad K_b = \left(Q_b/R\right)^2\,, \qquad (12)$$

and assuming small tune shifts, yields

$$\begin{aligned} Q_a &= 2Q_{x0} + \Delta Q_a = 2Q_{x0} - \frac{K_{sc}R^2\left(2a_0+3b_0\right)}{2Q_{x0}\,a_0\left(a_0+b_0\right)^2}\,, \\ Q_b &= 2Q_{y0} + \Delta Q_b = 2Q_{y0} - \frac{K_{sc}R^2\left(2b_0+3a_0\right)}{2Q_{y0}\,b_0\left(a_0+b_0\right)^2}\,. \end{aligned} \qquad (13)$$

The coupled equations can finally be re-written

$$\begin{aligned} \frac{d^2\Delta a}{d\phi^2} + Q_a^2\,\Delta a &= K\,R^2\,\Delta b\,, \\ \frac{d^2\Delta b}{d\phi^2} + Q_b^2\,\Delta b &= K\,R^2\,\Delta a\,, \end{aligned} \qquad (14)$$

with $\phi = \Omega_0\,t$, where Ω_0 is the angular revolution frequency and t the time.

FAR FROM THE COUPLING RESONANCE INDUCED BY SPACE CHARGE

Far from the coupling resonance $Q_a = Q_b$, the two equations of Eq. (14) can be considered uncoupled and the solutions of the homogeneous equations are given by

$$\Delta a = \Delta a_0\,e^{jQ_a\phi} \quad \text{and} \quad \Delta b = \Delta b_0\,e^{jQ_b\phi}\,. \qquad (15)$$

Starting from the definition of Q_a in Eq. (13) and expressing K_{sc} with respect to the space charge tune spread (using Eq. (5)), Eq. (1) can be recovered, where Q_a is noted there Q_{2x}. Figure 1 shows how the relation between the space charge tune spread and the measured quadrupolar tune shift varies with the ratio of the transverse equilibrium beam sizes.

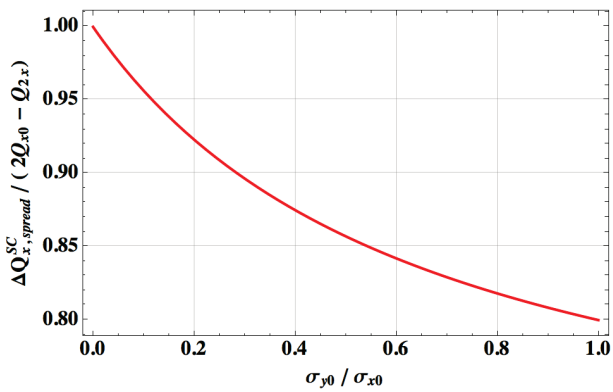

Figure 1: Ratio between the space charge tune spread and the measured quadrupolar tune shift with respect to the ratio of the transverse equilibrium beam sizes.

CLOSE TO THE COUPLING RESONANCE INDUCED BY SPACE CHARGE

Close to the coupling resonance $Q_a = Q_b$, the solutions of the coupled equations of Eq. (14) are a bit more involved. The coupled oscillations can be solved by searching the normal (i.e. decoupled) modes (u,v) linked by a simple rotation (see also Fig. 2)

ISBN 978-3-95450-185-4

$$\begin{pmatrix} \Delta a \\ \Delta b \end{pmatrix} = \begin{bmatrix} \cos\alpha & -\sin\alpha \\ \sin\alpha & \cos\alpha \end{bmatrix} \begin{pmatrix} u \\ v \end{pmatrix} , \quad (16)$$

where α is the coupling angle (equal to 0 in the absence if coupling and to ± 45 deg in the presence of full coupling).

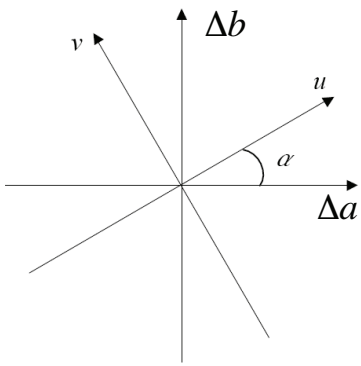

Figure 2: Tilted normal modes due to coupling.

The equations of the two normal modes are given by

$$\frac{d^2u}{d\phi^2} + Q_u^2 u = 0 , \qquad \frac{d^2v}{d\phi^2} + Q_v^2 v = 0 , \quad (17)$$

with

$$Q_u = Q_a - \frac{|C|}{2}\tan\alpha , \qquad Q_v = Q_b + \frac{|C|}{2}\tan\alpha , \quad (18)$$

$$\tan(2\alpha) = \frac{|C|}{\Delta} , \qquad |C| = \frac{R^2 K}{Q_0} , \quad (19)$$

$$\Delta = Q_b - Q_a , \qquad Q_0 = (Q_{x0} + Q_{y0})/2 . \quad (20)$$

Using the fact that

$$\tan(2\alpha) = \frac{2\tan\alpha}{1-\tan^2\alpha} , \quad (21)$$

$$\frac{|C|}{2}\tan\alpha = \frac{1}{2}\left(-\Delta \mp \sqrt{\Delta^2 + C^2}\right) , \quad (22)$$

and therefore Eq. (18) can be re-written

$$\begin{aligned} Q_u &= Q_a - \frac{1}{2}\left(-\Delta \mp \sqrt{\Delta^2 + C^2}\right) , \\ Q_v &= Q_b + \frac{1}{2}\left(-\Delta \mp \sqrt{\Delta^2 + C^2}\right) , \end{aligned} \quad (23)$$

where the ± sign depends on the sign of Δ (it should be the same sign as the one of Δ).

The new formula can then be deduced and it is given by

$$\Delta Q_{x,\mathrm{spread}}^{SC,new} = \frac{q}{\frac{1}{2}\left(3 - \frac{1}{1+x}\right)} - \frac{-\Delta \mp \sqrt{\Delta^2 + C^2}}{3 - \frac{1}{1+x}} , \quad (24)$$

with

$$q = 2Q_{x0} - Q_u , \quad x = \frac{\sigma_{y0}}{\sigma_{x0}} \quad \text{and} \quad y = Q_{y0} - Q_{x0} , \quad (25)$$

$$\Delta = 2y + \frac{3\,\Delta Q_{x,\mathrm{spread}}^{SC,new}}{2}\left(1 - \frac{1}{x}\right) , \quad (26)$$

$$|C| = \frac{2\,\Delta Q_{x,\mathrm{spread}}^{SC,new}}{1+x} . \quad (27)$$

The observable from the quadrupolar pick-up (the quadrupolar tune shift) is q and the first part of Eq. (24) is the usual formula (see Eq. (1)). Solving Eq. (24) yields the new general formula giving the horizontal space charge tune spread as a function of the ratio between the vertical and horizontal equilibrium beam sizes (x), the distance between the transverse tunes (y) and the measured quadrupolar tune shift (q) [5]

$$\Delta Q_{x,\mathrm{spread}}^{SC,new}(x,y,q) = \frac{1}{6+9x+6x^2}\Big[q\left(3+7x+7x^2+3x^3\right) + 4xy + 10x^2y + 6x^3y \mp (1+x)\sqrt{q^2\left(9-2x^2+9x^4\right) + 4qx\left(-6-x+6x^2+9x^3\right)y + 4x^2\left(2+3x\right)^2y^2}\Big] \quad (28)$$

with the – sign when Δ > 0 (and the + sign when Δ < 0). The ratio between the new formula from Eq. (28) and the usual formula from Eq. (1) is plotted in Fig. 3 for the example case q = 0.4, where it can be seen that the usual formula should not work for the machines running close to the coupling resonance with almost round beams, as the CERN LHC injectors. More detailed (2D) plots are shown in Fig. 4 for different parameters, revealing that a difference up to a factor ~ 1.5-2 can be reached in some cases.

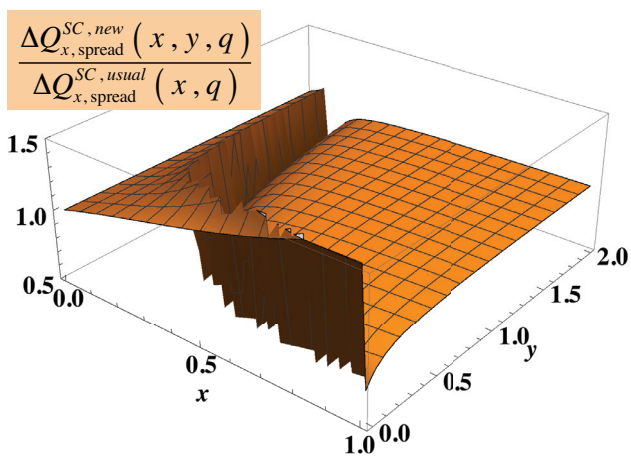

Figure 3: Ratio between the new formula from Eq. (28) and the usual formula from Eq. (1) as a function of x and y, for the example case q = 0.4 [5].

ISBN 978-3-95450-185-4

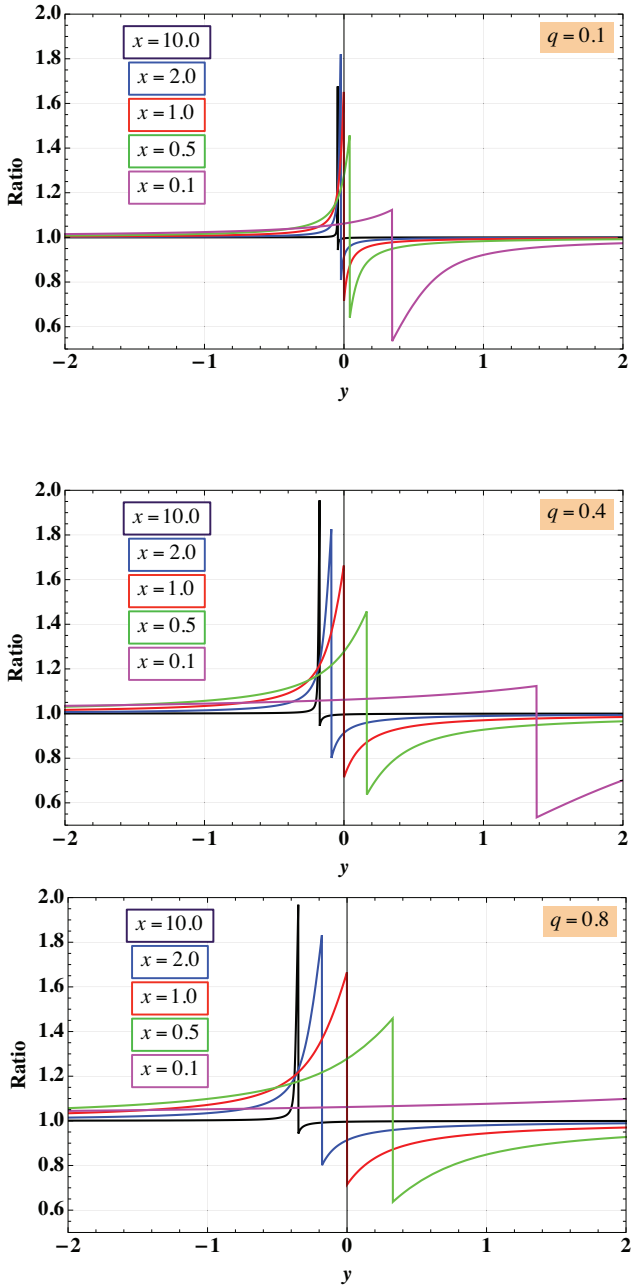

Figure 4: Ratio between the new formula from Eq. (28) and the usual formula from Eq. (1) as a function of y for different values of x: (a) for q = 0.1, (b) for q = 0.4 and (c) for q = 0.8.

CONCLUSION

A new general formula, giving the link between the incoherent direct space charge tune spread and the measured intensity-dependent shift of the quadrupolar mode, has been derived taking into the account the coupling between the transverse planes introduced by space charge and which is neglected in the usual formula (see Eq. (1)). This more involved formula is given in Eq. (28) and depends also on the tune distance between the low-intensity transverse tunes. The ratio between the new and the usual formula is plotted in Fig. 3 as a function of the ratio between the vertical and horizontal equilibrium beam sizes and the distance between the transverse tunes, for the example case of a measured quadrupolar tune shift of 0.4. Some example cases are also shown in Fig. 4 on 2D plots, where it can be seen that differences from the usual formula can be as large as a factor ~ 1.5-2. These results should be checked by simulations and beam-based measurements in the running machines.

REFERENCES

[1] W. Hardt, On the incoherent space charge limit for elliptic beams, CERN/ISR/Int. 300 GS/66.2, 1966.

[2] M. Chanel, Study of beam envelope oscillations by measuring the beam transfer function with quadrupolar pick-up and kicker, Proceedings of EPAC96, Sitges, Spain.

[3] O. Boine-Frankenheim, Space charge effects in rings (not only) at FAIR, ICFA mini-workshop on space charge, CERN, 2013.

[4] R. Singh et al., Observations of the quadrupolar oscillations at GSI SIS-18, Proceedings of IBIC2014, Monterey, CA, USA.

[5] E. Métral, Measurement of the space charge tune spread with a quadrupolar pick-up: new (general) formula vs. “usual” one, CERN-ACC-SLIDES-2015-0001, 2015.

[6] R. Baartman, Betatron resonances with space charge, AIP Conf. Proc. **448**, 56 (1998), Shelter Island, New York (USA).

[7] A.W. Chao, Physics of Collective Beam Instabilities in High Energy Accelerators, New York: Wiley, 371 p, 1993.

[8] K.Y. Ng, Physics of Intensity Dependent Beam Instabilities, World Scientific, 776 p, 2006.

[9] F. Sacherer, Rms envelope equations with space charge, CERN internal report, SI/DL/70-12.

[10] I.M. Kapchinsky and V.V. Vladimirsky, Proc. Int. Conf. on High-Energy Accelerators and Instrumentation, CERN 1959, p. 274-288.

[11] E. Métral and G. Rumolo, USPAS course on "*Collective Effects in Beam Dynamics*" in Albuquerque, New Mexico, USA, June 22-26, 2009.

ISBN 978-3-95450-185-4

SPACE CHARGE MODULES FOR PyHEADTAIL

A. Oeftiger*, CERN, Meyrin, Switzerland; S. Hegglin, ETH Zürich, Zürich, Switzerland

Abstract

PyHEADTAIL is a 6D tracking tool developed at CERN to simulate collective effects. We present recent developments of the direct space charge suite, which is available for both the CPU and GPU. A new 3D particle-in-cell solver with open boundary conditions has been implemented. For the transverse plane, there is a semi-analytical Bassetti-Erskine model as well as 2D self-consistent particle-in-cell solvers with both open and closed boundary conditions. For the longitudinal plane, PyHEADTAIL offers line density derivative models. Simulations with these models are benchmarked with experiments at the injection plateau of CERN's Super Proton Synchrotron.

INTRODUCTION

The self-fields of particle beams superpose the electromagnetic fields applied by magnets and radio frequency (RF) cavities in synchrotrons. The corresponding space charge effects lead to defocusing in the transverse plane and focusing (defocusing) in the longitudinal plane for operation above (below) transition energy. For non-linear beam distributions, space charge results in a tune spread which is an important factor e.g. when investigating betatron resonances or the influence of Landau damping during instabilities. We present the implemented space charge models of the collective effects simulation software PyHEADTAIL [1] which is developed in Python. PyHEADTAIL models beam dynamics by transversely tracking macro-particles linearly between interaction points around the circular accelerator. Longitudinal particle motion is modelled either by linear tracking or non-linear (sinusoidal) drift-kick integration. The forces from collective effect sources such as electron clouds, wake fields from impedances or space charge are integrated over the respective distance and applied as a momentum kick at the following interaction point [2]. Recently, large parts of PyHEADTAIL have been parallelised for NVIDIA graphics processing units (GPU) architectures [3]. Our particle-in-cell library PyPIC used for the self-consistent space charge models in PyHEADTAIL especially benefited from these efforts – the corresponding speed-ups are reported here.

This paper is structured as follows: we first address the implemented space charge models, which is followed by our GPU parallelisation strategies and achieved improvements, and, finally, we compare simulation results with measurements at CERN's Super Proton Synchrotron (SPS). Our developed software and libraries are available online [4].

SPACE CHARGE MODELS

A PyHEADTAIL macro-particle beam of intensity N, particle charge q and particle mass m_p is described by the 6D set of coordinates $(x, x', y, y', z, \delta)$, where x denotes the horizontal offset from the reference orbit, y the vertical offset, $x' = p_x/p_0$ and $y' = p_y/p_0$ the corresponding transverse normalised momenta for $p_0 = \gamma m_p \beta c$ the total beam momentum, z denotes the longitudinal offset from the synchronous particle in the laboratory frame and $\delta = (p_z - p_0)/p_0$ the relative momentum deviation. Most of the space charge models are based on "beam slices" which represent longitudinally binned subsets of the beam distribution. The density per slice is determined by nearest grid point (NGP) interpolation (i.e. lowest order).

Longitudinal Space Charge

For an emittance-dominated bunched beam, which is usually the case in a circular accelerator, the longitudinal electric field depends on the local line density $\lambda(z)$. Beams in CERN's circular accelerators typically have a very long bunch length in comparison to the vacuum tube diameter. Therefore, the non-linear image fields suppressing the longitudinal electric field have to be taken into account for the longitudinal space charge model. In PyHEADTAIL we provide such a so-called $\lambda'(z)$ model following the extensive analysis in [5, chapter 5]. The space charge forces are computed assuming a linear equivalent field

$$E_z^{\text{equiv}}(z) = -\frac{g}{4\pi\epsilon_0\gamma^2}\frac{d\lambda(z)}{dz} \quad , \tag{1}$$

where g denotes the geometry factor and ϵ_0 the vacuum permittivity. Conceptually, the real longitudinal profile is treated like a parabolic line density

$$\lambda(z) = \frac{3Nq}{4z_m}\left(1 - \frac{z^2}{z_m^2}\right) \tag{2}$$

with parabolic bunch half length z_m. In particular, this model identifies the mean value of the real electric field $\langle z E_z^{\text{real}}(z)\rangle_z$ (which includes the non-linear image effects) with the corresponding analytical expression for the parabolic distribution with the generalised geometry factor g, which then absorbs the image field contributions. Our implemented model is valid for bunches satisfying $z_m > 3r_p$ where $2r_p$ denotes the diameter of a perfectly conducting cylindrical vacuum tube. In this case, the geometry factor g becomes independent of the bunch length and can be averaged over the whole distribution yielding [5, Eq. (5.365b)]

$$g = 0.67 + 2\ln\left(\frac{r_p}{r_b}\right) \tag{3}$$

where r_b denotes the radial half width of a transversely round ellipsoidal beam with uniform charge distribution. As a further remark, [5, chapter 6] also discusses the case of two parallel conducting plates with distance $2r_p$, for which the

* adrian.oeftiger@cern.ch, also at EPFL, Lausanne, Switzerland

ISBN 978-3-95450-185-4

image term $2\ln(r_p/r_b)$ becomes $2\ln(4r_p/(\pi r_b))$. Figure 1 compares the longitudinal kicks for a round vacuum tube and the above model (for which $g = 5.25$, compare to $g_0 = 6.36$ in free space) with the real electric field kicks computed in free space by the particle-in-cell (PIC) algorithm described in subsection . Indeed, the $\lambda'(z)$ yields a lower E_z due to the image effects. The beam has been divided into only 32 slices which is few for the NGP interpolation, correspondingly the $\lambda'(z)$ model kicks appear step-like (the PIC algorithm in contrast uses one order higher interpolation).

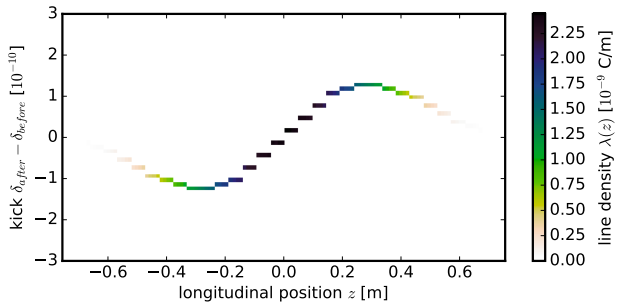

(a) $\lambda'(z)$ model (incl. an $r_p = 5$ cm round vacuum tube boundary).

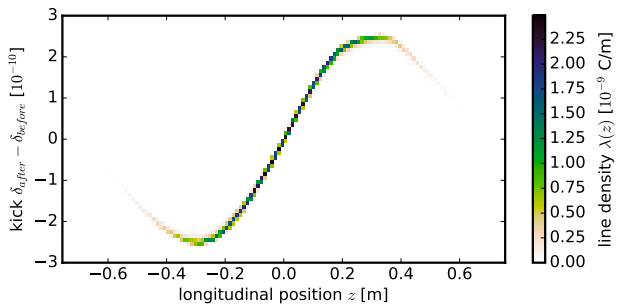

(b) 3D PIC model (free space).

Figure 1: Longitudinal kicks vs. position for 32 slices.

Transverse Gaussian Space Charge

A frequently employed 2D space charge model for the transverse plane has been established by M. Bassetti and G.A. Erskine in 1980 [6]. They derived a computationally optimised analytical expression (the "Bassetti-Erskine" or B.E. formula) for the electric field of a two-dimensional Gaussian charge density function

$$\rho(x,y) = \frac{Nq}{2\pi\sigma_x\sigma_y}\exp\left(-\left(\frac{x^2}{2\sigma_x^2}+\frac{y^2}{2\sigma_y^2}\right)\right) \qquad (4)$$

which generates the electric fields [7]

$$E_u = \frac{Q}{4\pi\epsilon_0}u\int_0^\infty dt\frac{\exp\left(-\frac{x^2}{2\sigma_x^2+t}-\frac{y^2}{2\sigma_y^2+t}\right)}{(\sigma_u^2+t)\sqrt{(\sigma_x^2+t)(\sigma_y^2+t)}} \qquad (5)$$

for $u = x, y$. For $\sigma_x > \sigma_y$, the B.E. formula reads

$$E_y + i\,E_x = \frac{Nq}{2\epsilon_0\sqrt{2\pi(\sigma_x^2-\sigma_y^2)}}\left[w\left(\frac{x+iy}{\sqrt{2(\sigma_x^2-\sigma_y^2)}}\right)-\exp\left(-\frac{x^2}{2\sigma_x^2}-\frac{y^2}{2\sigma_y^2}\right)w\left(\frac{x\frac{\sigma_y}{\sigma_x}+iy\frac{\sigma_x}{\sigma_y}}{\sqrt{2(\sigma_x^2-\sigma_y^2)}}\right)\right] \qquad (6)$$

involving the complex-valued Faddeeva function $w(x+iy)$. It belongs to the family of error functions and can be evaluated much faster than numerically solving the full integral (5) [8].

PyHEADTAIL applies this semi-analytic model slice by slice to the respective transverse distribution along the beam. If the actual distribution deviates from a Gaussian, the "Bassetti-Erskine" formula (6) only represents an approximation. This needs to be kept in mind especially in the presence of dispersion, when a non-Gaussian momentum distribution contributes to the transverse profile. Figure 2 depicts an $N = 2\times10^{11}$ SPS bunch with a very large longitudinal r.m.s. emittance of $\epsilon_z = 0.42$ eV s (at an RF bucket acceptance of 0.68 eV s) where the RF bucket non-linearities deform the matched momentum distribution. This reflects in the evidently non-Gaussian horizontal beam profile given a dispersion of $D_x = 7.96$ m and a horizontal normalised emittance of $\epsilon_x = 0.84$ mm mrad.

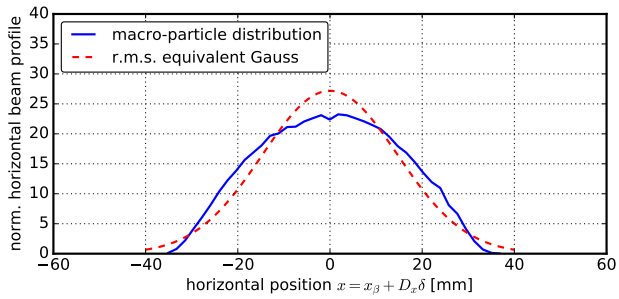

(a) Beam profile and Gaussian r.m.s. equivalent for central beam slice.

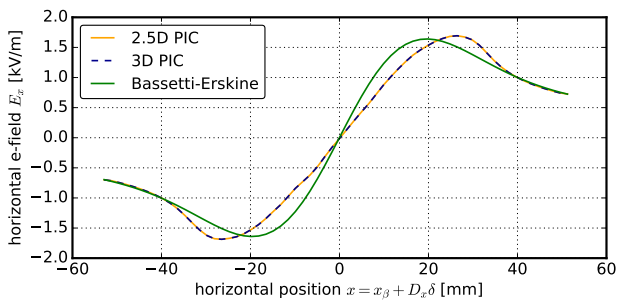

(b) Corresponding horizontal electric field from PIC and (Gaussian) Bassetti-Erskine models.

Figure 2: Large ϵ_z entail non-Gaussian momentum distributions which affect the horizontal distribution via dispersion.

Particle-in-cell Model

PIC algorithms model space charge self-consistently [9]. In order to compute the kicks, the macro-particle distribution is first interpolated to nodes of a regular mesh (particle-to-mesh or "P2M" step), then the charge distribution on the mesh is solved for the potential and consequently the force (solve step), and finally the force is interpolated back to

ISBN 978-3-95450-185-4

the particles (mesh-to-particles or "M2P" step). A separate library has been developed named PyPIC to encapsulate the PIC algorithm.

In synchrotrons, the relative momenta between the particles are usually much smaller than p_0. This can be exploited when solving the Maxwell equations by Lorentz boosting to the beam rest frame, where we neglect the relative particle motion and correspondingly only have to deal with an electrostatic problem. Before the P2M step, we Lorentz boost from the co-moving laboratory frame $(x, y, z)_{\text{lab}}$ to the beam rest frame

$$(\tilde{x}, \tilde{y}, \tilde{z})_{\text{beam}} = (x, y, \gamma z)_{\text{lab}} \quad . \tag{7}$$

Correspondingly, the bunch becomes much longer, the mesh is then constructed in the beam frame. In PyPIC we have implemented a linear spatial Cloud-In-Cell (CIC) interpolation, i.e. the shape function of the macro-particles is a constant Heaviside step function over the diameter of a cell. With the resulting mesh charge density ρ, we are ready to solve the discrete version of the 2D or 3D Poisson equation,

$$\Delta\phi = -\frac{\rho}{\epsilon_0} \quad , \tag{8}$$

on the mesh for the mesh potential ϕ.

To this end, we implemented several Poisson solvers in both 2.5D (i.e. slice-by-slice 2D transverse solving) and full 3D variants. The solvers cover finite difference (FD) approaches with direct matrix solving via QR or LU decomposition (with Dirichlet or arbitrary boundary conditions) and Green's function methods (free space or rectangular boundary conditions) exploiting the Fast Fourier Transform (FFT) algorithm.

The FD implementations construct a sparse Poisson matrix A with a first-order nearest-neighbour stencil. In case of the LU decomposition $A = LU$, the sparse lower and upper triangle matrices L, U are then precomputed at set-up. At each solve step, the linear matrix equation $LU\phi = -\rho/\epsilon_0$ is solved given the respective vector ρ containing the mesh charge density of all nodes. This approach is extremely efficient on the CPU in conjunction with the KLU algorithm [10] if the Poisson matrix remains constant over many solve steps [11]. Therefore, e.g. matrix element indices for the boundary conditions should not change due to a differently shaped boundary, otherwise the LU decomposition needs to be recomputed which is computationally expensive. The QR decomposition is slower than the LU decomposition (cf. e.g. [12]) but numerically more stable than the LU decomposition, hence it serves as a reference. Finite difference equations always require boundary conditions which can be advantageous if indirect space charge effects from the vacuum tube need to be taken into account. If the transverse beam sizes are rather small compared to the vacuum tube, the mesh can become prohibitively large though. In this case, the following method may be more appropriate.

Another approach to solve Eq. (8) is to use the free space D=2 (for $\mathbf{x} = (\tilde{x}, \tilde{y})_{\text{beam}}$) resp. D=3 (for $\mathbf{x} = (\tilde{x}, \tilde{y}, \tilde{z})_{\text{beam}}$) Green's functions G,

$$\phi(\mathbf{x}) = \frac{1}{2^{D-1}\pi\epsilon_0} \int d^D\widehat{\mathbf{x}} \quad G\left(\widehat{\mathbf{x}} - \mathbf{x}\right) \rho\left(\widehat{\mathbf{x}}\right) \quad . \tag{9}$$

We apply Hockney's trick where the domain of the Green's function is doubled by cyclical expansion in each dimension [9]. The potential in this expanded region will be incorrect and discarded but the periodicity allows to make use of the computationally very effective FFT algorithm for the convolution. In principle, the Green's function needs to be evaluated on a square (cuboid) mesh with equal distances in all directions. In the transverse plane, aspect ratios may be large due to the betatron function ratio and additional dispersion effects. At least in the 3D case, the aspect ratio of the transverse with respect to the longitudinal plane will certainly be large and will thus require many mesh points to cover the whole distribution which may become computationally heavy. Therefore, we make use of the integrated Green's functions (IGF) $\widehat{G}$ ([13, Eq. (56),(57)] for the 2D case and [14, Eq. (2)] for 3D), which conceptually include the aspect ratio into the discrete Green's function by integrating over each cell assuming ρ to be constant across the cell. This approximation has to be kept in mind when choosing the mesh size. The Fourier transform of the IGF is computed at set-up and stored until the mesh is changed. At each solve step, it is multiplied by the Fourier transformed mesh charge density ρ and the result inversely Fourier transformed to yield the potential,

$$\phi = \mathcal{F}^{-1}\left[\left(\mathcal{F}\widehat{G}\right) \cdot \left(\mathcal{F}\rho\right)\right] \quad . \tag{10}$$

The FFT convolution approach is much more efficient at a complexity of $O(n \log n)$ than computing the convolution integral in real space with $O(n^2)$, where n the total number of mesh nodes. Using this method with the FFTW [15] implementation on the CPU is found to take less than twice as long as the KLU direct solving approach mentioned before [11].

After the potential on the mesh ϕ has been determined, the electric mesh fields $\tilde{\mathbf{E}}$ in the beam frame are calculated as

$$\tilde{\mathbf{E}} = -\nabla\phi \tag{11}$$

via a numerical first-order finite difference gradient implementation. Finally, the electric fields are interpolated back to the macro-particles (M2P) and Lorentz boosted back to the laboratory frame,

$$(E_x, E_y, E_z)_{\text{lab}} = \left(\gamma\tilde{E}_x, \gamma\tilde{E}_y, \tilde{E}_z\right)_{\text{beam}} \quad . \tag{12}$$

The Lorentz forces for each macro-particle include the magnetic fields arising when transforming to the laboratory frame,

$$(B_x, B_y, B_z)_{\text{lab}} = \left(-\beta E_y/c, \beta E_x/c, 0\right)_{\text{lab}} \tag{13}$$

$$\implies (F_x, F_y, F_z)_{\text{lab}} = q\left(\frac{\tilde{E}_x}{\gamma}, \frac{\tilde{E}_y}{\gamma}, \tilde{E}_z\right)_{\text{beam}} \quad . \tag{14}$$

ISBN 978-3-95450-185-4

To conserve the total charge, the interpolation functions and order at both the P2M as well as the M2P step necessarily need to match [9]. As a side note, the usual straight-forward interpolation functions can be the source of noise and grid heating effects in the traditional PIC approach. Recently, symplectic algorithms have been derived to solve these issues [16], which can be interesting for long-term simulations over many turns since the symplectic nature implies a finite bound on the energy error.

Figure 3 shows the PIC computed electric field of a coasting beam with a Kapchinsky-Vladimirsky (KV) distribution in the transverse plane for the SPS. For $\lambda = 5.1\,\mathrm{C/m}$ and beam edges at $r_x = 2.5\,\mathrm{mm}$ and $r_y = 1.6\,\mathrm{mm}$, the maximal electric field at the beam edge analytically gives

$$E_x = \frac{\lambda}{\pi\epsilon_0}\frac{1}{r_x + r_y} = 15.2\,\mathrm{kV/m} \quad , \tag{15}$$

which matches the result from the PIC algorithm.

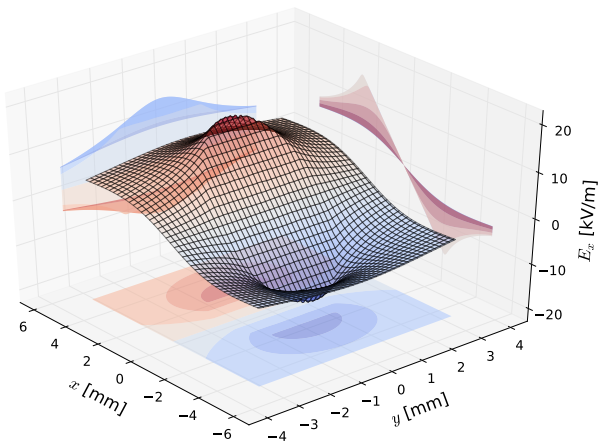

Figure 3: Horizontal electric field of a KV beam in the SPS.

GPU HIGH-PERFORMANCE COMPUTING

PyHEADTAIL has been made available for graphics processor unit (GPU) high-performance computing. The library PyCUDA [17] provides an interface for GPU memory stored arrays that adopts the API of the standard Python library for scientific computing, NumPy, hence making large portions of the code easily applicable to both NumPy arrays and GPUArrays. To make the GPU usage in PyHEADTAIL as transparent and flexible as possible for new GPU users, a context management system to switch between GPU and CPU contexts has been developed [18]. Algorithms for the GPU need to make use of the pronounced parallel hardware structures and therefore often differ from serial CPU algorithms. The context managers switch between implemented algorithms e.g. for the bunch distribution statistics. For the GPU implementations it is therefore of crucial importance to have access to the underlying CUDA [3] API from Python which is fully provided by PyCUDA. Implementing and calling custom CUDA kernels is flexible and straight forward from the Python top layer. Besides the NumPy array API and the CUDA access, the third important ingredient to PyHEADTAIL on the GPU is the incorporation of powerful GPU computing libraries such as cuFFT [19], cuSOLVER [20], cuSPARSE [21] and Thrust [22]. We achieve this partly via the Python binding library scikit-cuda [23] and partly via self-implemented interfaces using ctypes.

For the PyHEADTAIL space charge suite we have developed a GPU version of PyPIC. The performance bottlenecks appear very differently during the aforementioned three particle-in-cell steps P2M, solve and M2P when comparing runtime profiles between the CPU and GPU versions. Figure 4 shows the fraction of time spent on both architectures during each step for quadratically increasing transverse mesh sizes given a fixed number of macro-particles. Comparing the cuFFT 3D Fourier transform performance to FFTW on a mesh of size $(16, 32, 64)$ gives a speed-up of up to $S = 35.8$, comparing to the standard NumPy FFT extension even reaches $S = 65.5$. This explains why the solve step with the free space FFT-based Green's function Poisson solver does not have such a significant impact on the overall timing during the particle-in-cell algorithm on the GPU, while it essentially marks the bottleneck on the CPU.

Effectively, the particle deposition on the mesh is the most performance critical part in the GPU PIC algorithm. We have implemented an atomic deposition algorithm, in which a CUDA thread for each particle is launched which locks the memory location of the respective mesh node charge from access by other threads, reads the memory value, adds to it and then stores the updated value. With this approach, we observed a rather slow performance as memory bank conflicts and thread stalls can happen for both the software-emulated 64-bit and the hardware-accelerated 32-bit `atomicAdd` variants. This finding is especially pronounced in the 3D case where each particle updates eight surrounding mesh nodes (instead of four in the 2D case). The problem decreased when using less macro-particles for a given mesh size – however, to achieve a good resolution for the electric fields, at least 10 macro-particles per cell are required [9].

To address this issue, we implemented a sorted deposition particle-in-cell algorithm described in [24]. In this approach, the macro-particle coordinate arrays are first sorted by their cell IDs, for which we used the Thrust library with its `sort_by_key` functions. Subsequently, a thread is launched for each cell which loops through the particles within this cell to construct guard cell charge densities. In a third step, a kernel merges the four (2D) resp. eight (3D) guard meshes to the final mesh charge density ρ array. We achieved a speed-up of $S = 3.5$ for the mesh size $(64, 64, 32)$ and 1×10^6 macro-particles when comparing the sorted deposition to the double precision `atomicAdd` deposition. In addition, the M2P step profits from the sorted arrays since global GPU memory is accessed in a coalesced manner: the kernel call on unsorted arrays takes 25% longer than on sorted arrays. Further approaches to address the memory bank conflicts (such as using L1 caching) have been investigated e.g. for SYNERGIA in [25] and for ELEGANT in [26, 27].

ISBN 978-3-95450-185-4

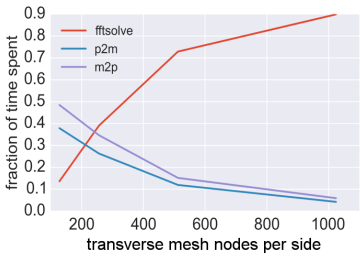

(a) CPU implementation.

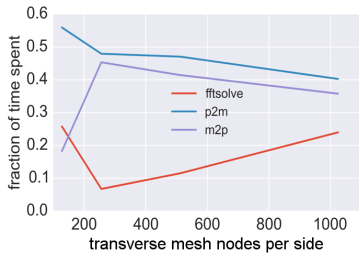

(b) GPU implementation.

Figure 4: Timing proportions between the P2M, solve and M2P step for the FFT-based Poisson solver vs. number of mesh nodes per transverse side. The number of macro-particles is fixed to 5×10^5.

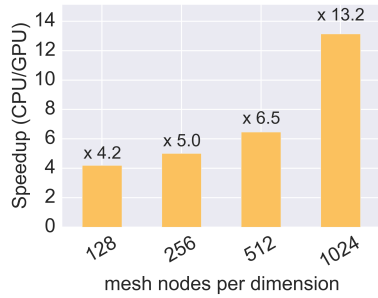

Figure 5: Overall 2.5D PIC speed-up achieved vs. number of mesh nodes per transverse side comparing a NVIDIA K40m GPU to a single 2.3GHz Intel Xeon E5-2630 (v1) CPU core.

For the 2.5D case, the transverse Poisson equations can be solved for all slices in parallel. Since the cuFFT calls for each slice work with small arrays compared to the GPU memory size, the cuFFT batch solving works very effectively. All in all, we achieved overall PIC speed-ups of up to $S = 13.2$ compared to the CPU. Figure 5 shows how the GPU usage becomes increasingly beneficial for larger mesh sizes at a fixed number of 5×10^5 macro-particles. Also increasing the number of macro-particles scales less than linearly for the relevant parameter range as opposed to the CPU. These results allow the GPU accelerated space charge simulations to access much higher resolutions and increase the validity of simulations (also over longer time scales).

SPS BENCHMARK

Since strong space charge leads to transverse detuning, the resonance condition especially in the centre of a Gaussian bunch is shifted to higher tunes. Large-scale static tune scans with high-brightness single bunch beams at the injection plateau of the SPS revealed a significant influence of the $4Q_x = 81$ octupolar resonance [28]. Here, we deliberately drive this resonance with a single extraction octupole (`LOE.10402`) at $k_3 = 25\,\mathrm{m}^{-4}$ acting as a localised octupolar field error. The $N = (2.05 \pm 0.1) \times 10^{11}$ single bunches arrive from the upstream Proton Synchrotron with normalised transverse emittances $\epsilon_x = (0.84 \pm 0.05)$ mm mrad and $\epsilon_y = (1.06 \pm 0.04)$ mm mrad at an r.m.s. bunch length of $\sigma_\tau = (0.93 \pm 0.01)$ ns. The incoherent space charge tune spread of these bunches amounts to $\left(\Delta Q_x^{\mathrm{SC}}, \Delta Q_y^{\mathrm{SC}}\right) = (-0.09, -0.16)$. While fixing the coherent vertical tune $Q_y = 20.31$, we measure the transverse averaged emittance growth for horizontal tunes between $20.16 \leq Q_x \leq 20.30$ over a time span of 3 s in a set-up equivalent to [28]. For each working point, three consecutive shots per transverse plane are wire scanned to obtain the beam profiles and extract the respective normalised emittance via a Gaussian fit (subtracting the dispersion contribution in the horizontal plane). The orange curve in figure 6 shows the dependence of the averaged transverse emittance blow-up on Q_x. The $4Q_x = 81$ resonance causes a shifted significant emittance growth peak with its maximum at $Q_x = 20.28$.

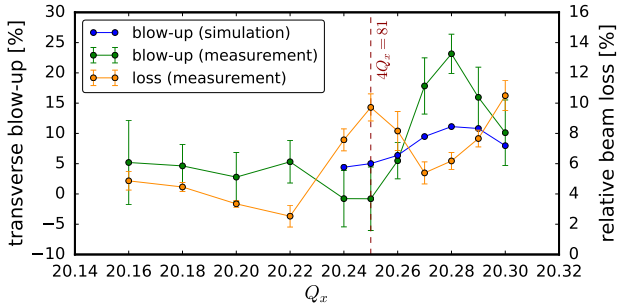

Figure 6: Transverse emittance growth vs. coherent horizontal tune for Bassetti-Erskine space charge simulations over 10×10^3 turns and measurements over 130×10^3 turns.

Corresponding simulations spanning 0.23 s cycle time with the PyHEADTAIL space charge models (including the non-linear model of the SPS [29]) have been set-up resolving the TWISS parameters and corresponding beam sizes around the SPS ring. The results plotted in blue also show the maximum blow-up at $Q_x = 20.28$. However, around $Q_x = 20.25$ itself we find emittance growth predicted by the simulations which is not observed in the measurements. Simulations for longer cycle times with a good loss model might recover this: the measurements show strong losses around $Q_x = 20.25$ as the beam halo is excited to large transverse amplitudes where the weaker beam self-fields lead to a resonance condition much closer to $Q_x = 20.25$. So far our simulations did not include the SPS impedance model which leads to significant vertical coherent detuning of $\Delta Q_y^{\mathrm{imped.}} = -0.03$ at $N = 2 \times 10^{11}$ [30].

CONCLUSION

We have described the space charge models implemented in PyHEADTAIL. The GPU parallelisation strategies and achieved speed-ups of up to $S = 13.2$ for our self-consistent particle-in-cell space charge algorithms have been reported. These will play a major role in the on-going developments of the SPS model for high-brightness beams, for which a first benchmark has been presented in the last section.

ISBN 978-3-95450-185-4

REFERENCES

[1] E. Metral *et al.*, "Beam Instabilities in Hadron Synchrotrons", in *IEEE Transactions on Nuclear Science*, vol. 63, no. 2, Apr. 2016, pp. 1001-1050.

[2] K.S.B. Li *et al.*, "Code development for Collective Effects", in *ICFA Advanced Beam Dynamics Workshop on High-Intensity and High-Brightness Hadron Beams (HB2016)*, Malmö, Sweden, July 2016, paper WEAM3X01, this conference.

[3] J. Nickolls, I. Buck, M. Garland and K. Skadron, "Scalable parallel programming with CUDA.", in *Queue*, vol. 6, no. 2, 2008, pp. 40-53.

[4] PyCOMPLETE, Python Collective Effects Library, Accelerator Beam Physics Group, CERN, Switzerland, 2016, `http://github.com/PyCOMPLETE/`.

[5] M. Reiser, "Theory and Design of Charged Particle Beams", John Wiley & Sons, Jun. 2008.

[6] M. Bassetti and G.A. Erskine, "Closed Expression for the Electrical Field of a Two-dimensional Gaussian Charge", in CERN-ISR-TH-80-06, CERN, Switzerland, 1980.

[7] H. Wiedemann, "Statistical and Collective Effects", in Particle Accelerator Physics, 3rd ed. New York: Springer, 2015, p. 644.

[8] A. Oeftiger *et al.*, "Review of CPU and GPU Faddeeva Implementations", in *Proc. 7th Int. Particle Accelerator Conf. (IPAC'16)*, Busan, Korea, May 2016, paper WEPOY044, pp. 3090-3093.

[9] R.W. Hockney and J.W. Eastwood, "Computer Simulation Using Particles", CRC Press, 1989.

[10] T.A. Davis and E. Palamadai Natarajan, "Algorithm 907: KLU, A Direct Sparse Solver for Circuit Simulation Problems", in *ACM Transactions on Mathematical Software*, vol. 37, no. 6, 2010, pp. 36:1-36:17.

[11] G. Iadarola, A. Axford, H. Bartosik, K. Li and G. Rumolo, "PyECLOUD for PyHEADTAIL: development work", presentation in Electron Cloud Meeting, May 14, 2015, `http://indico.cern.ch/event/394530/`.

[12] G.A. Geist and C.H. Romine, "LU Factorization Algorithms on Distributed-memory Multiprocessor Architectures", in *Siam. J. Scl. Stat. Comput.*, vol. 9, no. 4, 1988, pp. 639-649.

[13] J. Qiang, M.A. Furman and R.D. Ryne, "A Parallel Particle-in-cell Model for Beam–beam Interaction in High Energy Ring Colliders", in *Journal of Comp. Phys.*, vol. 198, no. 1, 2004, pp. 278-294.

[14] J. Qiang, S. Lidia, R.D. Ryne and C. Limborg-Deprey, "Erratum: Three-dimensional Quasistatic Model for High Brightness Beam Dynamics Simulation", in *Phys. Rev. ST Accel. Beams*, vol. 10, no. 12, Dec. 2007, p. 129901.

[15] M. Frigo and S.G. Johnson, "The Design and Implementation of FFTW3", in *Proceedings of the IEEE*, vol. 93, no. 2, 2005, pp. 216-231.

[16] H. Qin *et al.*, "Canonical Symplectic Particle-in-cell Method for Long-term Large-scale Simulations of the Vlasov-Maxwell System", arXiv:1503.08334v2 [physics.plasm-ph], 2015.

[17] A. Klöckner *et al.*, "PyCUDA and PyOpenCL: A Scripting-based Approach to GPU Run-time Code Generation", in *Parallel Computing*, vol. 38, no. 3, Mar. 2012, pp. 157-174. See also `http://documen.tician.de/pycuda/`.

[18] S. Hegglin, "Simulating Collective Effects on GPUs", MSc thesis, D-MATH/D-PHYS Dep., ETH Zürich, Zürich, Switzerland, 2016.

[19] cuFFT, Fast Fourier Transform library, CUDA Toolkit, NVIDIA, 2016, `https://developer.nvidia.com/cufft/`.

[20] cuSOLVER, collection of dense and sparse direct solvers, CUDA Toolkit, NVIDIA, 2016, `https://developer.nvidia.com/cusolver/`.

[21] cuSPARSE, Sparse Matrix library, CUDA Toolkit, NVIDIA, 2016, `https://developer.nvidia.com/cusparse/`.

[22] N. Bell and J. Hoberock, "Thrust: A productivity-oriented library for CUDA.", in *GPU computing gems Jade edition*, vol. 2, 2011, pp. 359-371.

[23] L. Givon, scikit-cuda, Python interface to CUDA device / runtime, cuBLAS, cuFFT and cuSOLVER, 2015, `http://scikit-cuda.readthedocs.io/`.

[24] K. Ahnert, D. Demidov and M. Mulansky, "Solving Ordinary Differential Equations on GPUs", in *Numerical Computations with GPUs*, Springer International Publishing, 2014, pp. 125-157.

[25] Q. Lu and J. Amundson, "Synergia CUDA: GPU-accelerated Accelerator Modeling Package", in Journal of Physics: Conference Series, vol. 513, no. 5, 2014, p. 052021.

[26] I.V. Pogorelov, K. Amyx, P. Messmer, "Accelerating Beam Dynamics Simulations with GPUs", in *Proc. Particle Accelerator Conf. (PAC 2011)*, New York, USA, May 2011, paper WEP164, pp. 1800-1802.

[27] K. Amyx *et al.*, "CUDA Kernel Design for GPU-based Beam Dynamics Simulations", in *Proc. 3th Int. Particle Accelerator Conf. (IPAC'12)*, New Orleans, USA, May 2012, paper MOPPC089, pp. 343-345.

[28] H. Bartosik, A. Oeftiger, F. Schmidt and M. Titze, "Space Charge Studies with High Intensity Single Bunch Beams in the CERN SPS", in *Proc. 7th Int. Particle Accelerator Conf. (IPAC'16)*, Busan, Korea, May 2016, paper MOPOR021, pp. 644-647.

[29] H. Bartosik, A. Oeftiger, M. Schenk, F. Schmidt and M. Titze, "Improved Methods for the Measurement and Simulation of the CERN SPS Non-linear Optics", in *Proc. 7th Int. Particle Accelerator Conf. (IPAC'16)*, Busan, Korea, May 2016, paper THPMR036, pp. 3464-3467.

[30] H. Bartosik *et al.*,"TMCI Thresholds for LHC Single Bunches in the CERN-SPS and Comparison with Simulations", in *Proc. 5th Int. Particle Accelerator Conf. (IPAC'14)*, Dresden, Germany, May 2014, paper TUPME026, pp. 1407-1409.

ISBN 978-3-95450-185-4

SPACE CHARGE MITIGATION WITH LONGITUDINALLY HOLLOW BUNCHES

A. Oeftiger*, S. Hancock, G. Rumolo, CERN, Meyrin, Switzerland

Abstract

Hollow longitudinal phase space distributions have a flat profile and hence reduce the impact of transverse space charge. Dipolar parametric excitation with the phase loop feedback systems provides such hollow distributions under reproducible conditions. We present a procedure to create hollow bunches during the acceleration ramp of CERN's PS Booster machine with minimal changes to the operational cycle. The improvements during the injection plateau of the downstream Proton Synchrotron are assessed in comparison to standard parabolic bunches.

INTRODUCTION

In the framework of the LHC Injectors Upgrade (LIU) project, the Large Hadron Collider (LHC) will have to be provided with beams of double intensity N but approximately the same transverse normalised emittances $\epsilon_{x,y}$ compared to present operation [1]. Each synchrotron of the LHC injector chain has been assigned an emittance blow-up and beam loss budget [2, Table 1]. In particular, the Proton Synchrotron (PS) is allowed a budget of $\Delta\epsilon/\epsilon_{\mathrm{ini}} \leq 5\%$ and $\Delta N/N_{\mathrm{ini}} \leq 5\%$. For the LIU beam parameters, the present pre-LIU machine conditions are found to exceed these values [3] which is why a series of machine upgrades are foreseen [4].

The most important limiting factor in the PS is direct space charge. Since the incoherent transverse space charge tune spread scales with the inverse energy,the 1.2 s long PS injection plateau during the standard double-batch (72-bunches) 25 ns LHC beam production is the most critical time. Therefore, the injection energy will be increased from the present $E_{\mathrm{kin}} = 1.4\,\mathrm{GeV}$ to 2 GeV.

Given the constraints on the normalised transverse emittances, intensity and bunch length, a further common strategy to mitigate space charge impact is to reshape the longitudinal beam profile of the usually Gaussian or even rather quasi-parabolic bunches. The canonical approach is to use a double RF harmonic in bunch lengthening mode (BLM) during the critical cycle times to diminish (or cancel) phase focusing around the RF bucket centre. This RF potential deformation results in both a larger RF bucket area (longitudinal acceptance) and flatter iso-Hamiltonian contours around the centre (and therefore bunch distributions with depressed line densities). An alternative to reshaping the longitudinal profile indirectly via a modified Hamiltonian is to alter the phase space distribution directly. This consideration leads us to the concept of "hollow" bunches. Figure 1 illustrates these two cases by plotting the longitudinal phase space (z, δ) with z the longitudinal bucket centre offset, $\delta = (p - p_0)/p_0$ the relative momentum deviation and p_0 the total momentum.

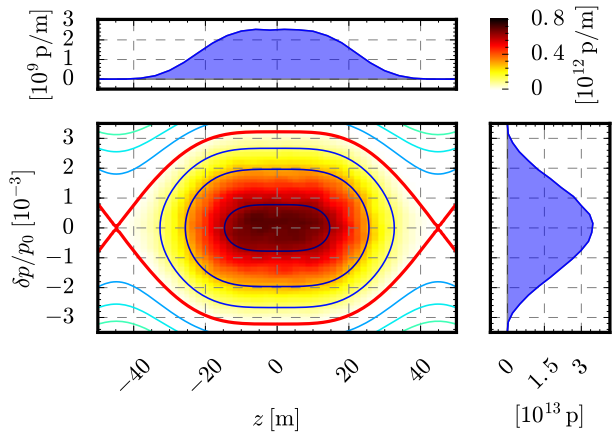

(a) Double-harmonic bucket in BLM (i.e. 180° relative phase and $V_{h=2} = V_{h=1}/2$) populated with a matched distribution (note the quasi-Gaussian distribution in the momentum projection).

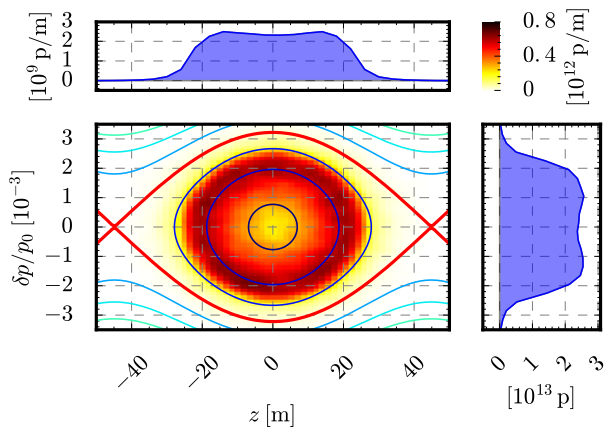

(b) Single-harmonic bucket at the same fundamental RF voltage populated with a hollow distribution. The spatial projection is flat equivalent to the second harmonic case, but additionally also the momentum projection becomes flat.

Figure 1: Longitudinal phase space plots (z, δ) from PyHEADTAIL simulations comparing between double-harmonic shaped and hollow bunches.

The lower left shows the momentum δ versus the coordinate z, the separatrix in red encloses the RF bucket. The density of the particle distribution is given by the heat map in the upper right corner. In addition, the iso-Hamiltonian contours indicate the momentary flow of particle trajectories. The upper plot shows the spatial projection and the plot to the right the momentum projection.

In this paper, we present hollow bunches as a viable additional tool to mitigate space charge and hence to reach the required LIU goals. This study has been tailored to the characteristics of LHC beams and involves minimal changes

* adrian.oeftiger@cern.ch, also at EPFL, Lausanne, Switzerland

ISBN 978-3-95450-185-4

to the currently PSB operational cycles. Nevertheless, the general applicability and potential of the concept become apparent. The idea is to create hollow bunches in the Proton Synchrotron Booster (PSB) and subsequently transfer them to the PS to overcome the brightness limits given by the affordable emittance blow-up during the PS injection plateau.

The structure of the following sections is laid out as follows: at first, we discuss the theoretical reasoning behind the idea. Then, we describe the procedure to reliably create hollow longitudinal distributions during the PSB acceleration ramp. Thirdly, the approach to extract the transverse emittances from the inherently non-Gaussian horizontal beam profiles (due to dispersion) is explained. Finally, we present the improvements measured for the hollow beams in comparison to the standard LHC-type beams. This paper is meant to complement and elaborate on our previously reported findings in [5]. Our efforts build on the experience from past hollow bunch experiments [6, 7].

THEORETICAL CONSIDERATIONS

For a transversely Gaussian normal distributed bunch of particles in a circular accelerator, the detuning effect of the beam self-fields can be quantified in terms of the transverse space charge tune spread [8],

$$\Delta Q_u(z) = -\frac{r_p \lambda(z)}{2\pi\beta^2\gamma^3} \oint ds \frac{\beta_u(s)}{\sigma_u(s)\left(\sigma_x(s)+\sigma_y(s)\right)} \quad (1)$$

with $u = x$ or $u = y$ for the horizontal resp. vertical plane, z denoting the longitudinal position with respect to the beam centre-of-gravity, $\lambda(z)$ the line charge density in C/m, r_p the classic particle radius, β the speed in units of speed of light, γ the Lorentz factor, $\beta_u(s)$ the betatron function depending on the longitudinal location s around the accelerator ring and $\sigma_u(s)$ the corresponding transverse beam sizes. In presence of dispersion $D_x(s)$, the momentum distribution contributes to the horizontal beam size. Assuming also the momentum distribution to be Gaussian normal distributed yields the well-known expression

$$\sigma_x(s) = \sqrt{\frac{\beta_x(s)\epsilon_x}{\beta\gamma} + D_x^2(s)\delta_{\text{rms}}^2} \quad , \quad (2)$$

where ϵ_x is the normalised beam emittance and δ_{rms} the root mean square of the relative momentum distribution. NB: Eq. (2) is no longer valid for beams with a momentum distribution that significantly deviates from a Gaussian.

From Eq. (1) it immediately follows that

1. space charge scales with the inverse energy, $\Delta Q_u \propto 1/(\beta\gamma^2)$, hence the most critical cycle time for an accelerator is around the injection;
2. reducing the peak line density λ_{max} decreases the maximum tune shift; and
3. a broader momentum distribution leads to larger horizontal beam sizes and hence a smaller tune spread (cf. Eq. (2) when increasing δ_{rms}).

Reducing the incoherent tune spread makes the beam less prone to betatron resonances located near the working point [9] – such as the integer resonance which causes the observed critical emittance growth in the PS [3].

Longitudinally hollow phase space distributions address the latter two aspects of Eq. (1) to reduce ΔQ_u^{max} compared to Gaussian or parabolic bunches. Figure 1b exhibits the intrinsically flattened $\lambda(z)$ as well as the increased δ_{rms}. The increased momentum spread is an evident advantage of hollow distributions over double-harmonics, which becomes apparent comparing the momentum projections between Fig. 1b and Fig. 1a.

HOW TO CREATE HOLLOW BUNCHES

Dipolar Parametric Resonances

The mechanism we exploit to create hollow bunches is based on driving a longitudinal parametric resonance by phase modulation [10]. To this end, we use the PSB phase loop system which aligns the RF reference phase ϕ_{rf} with the centre-of-gravity of the bunch. By modulating ϕ_{rf} around the synchronous phase ϕ_S,

$$\phi_{\text{rf}}(t) = \phi_S + \hat{\phi}_{\text{drive}} \sin(\omega_{\text{drive}} t) \quad , \quad (3)$$

we excite the dipole mode of the resonance. For this, the driving frequency ω_{drive} needs to satisfy the resonance condition

$$m\,\omega_{\text{drive}} \simeq n\,\omega_S \quad , \quad (4)$$

where ω_S denotes the angular synchrotron frequency. The integer numbers m and n characterise the m:n parametric resonance. The $m = n = 1$ resonance proves most useful for our purposes – higher harmonic resonances deplete the bunch centre less as they produce two or more filaments pointing outwards from the core (instead of just one). Figure 2 depicts such a measured phase space $(\phi, \Delta E)$ distribution (with $\phi = -hz/R$ and $\Delta E = \delta p_0 c/\beta$ for h the harmonic and R the radius) resulting from driving the 1:2 resonance.

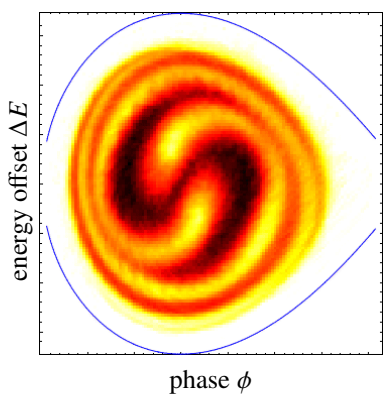

Figure 2: Longitudinal phase space $(\phi, \Delta E)$ for the 1:2 resonance via phase space tomography [11] in the PSB.

ISBN 978-3-95450-185-4

Two main factors suppress the linear synchrotron frequency [12, Eq. (3.16)]

$$\omega_{S,0} = \omega_{\mathrm{rev}} \sqrt{\frac{hqV_{\mathrm{RF}}|\eta\cos(\phi_S)|}{2\pi p_0 \beta c}} \quad , \tag{5}$$

where q denotes the particle charge, V_{RF} the RF voltage, $\eta \doteq \gamma_{\mathrm{tr}}^{-2} - \gamma^{-2}$ the slippage factor (with γ_{tr} the transition energy), and ω_{rev} the angular revolution frequency. The *RF bucket non-linearities* decrease the synchrotron tune for non-zero synchrotron amplitudes $\tilde{\phi}$ towards the separatrix by [12, Eq. (3.60)]

$$\omega_{S,\mathrm{nl}}(\tilde{\phi}) = \frac{\pi\omega_{S,0}}{2K(\sin(\tilde{\phi}/2))} \approx \left(1 - \frac{\tilde{\phi}^2}{16}\right)\omega_{S,0} \tag{6}$$

with $K(k)$ the complete elliptic integral of the first kind. Furthermore, since the PSB operates below transition, $\eta < 0$, *longitudinal space charge* additionally reduces ω_S. The linearised expression for a matched Gaussian-type bunch reads [13, Eq. (1.47)]

$$\omega_S^2(N,\tilde{\phi}) = \omega_{S,\mathrm{nl}}^2(\tilde{\phi}) + \frac{\omega_{\mathrm{rev}}^2}{\sqrt{2\pi}\sigma_z^3}\frac{Nr_p\eta R^2 g}{\beta^2\gamma^3} \quad , \tag{7}$$

with g the geometry factor taking into account the bunch aspect ratio as well as indirect space charge from a perfectly conducting vacuum tube [14].

PyHEADTAIL Simulations

We have carried out extensive studies of the bunch modulation with the collective effects simulation software PyHEADTAIL [15, 16]. Longitudinal space charge has been included via a line density derivative model [17]. By driving the 1:1 resonance at a frequency slightly below the linear synchrotron frequency, $\omega_{\mathrm{drive}} \approx 0.9\omega_{S,\mathrm{lin}}$ (accounting for the aforementioned detuning effects), the particles in the bunch core are excited to higher synchrotron amplitudes. Figure 3 shows the depletion process of the bunch centre within a few synchrotron periods during the acceleration ramp leading to hollow longitudinal phase space distributions. In this particular case, the Gaussian distributed bunch started from a longitudinal r.m.s. emittance of $\epsilon_z = 1.12\,\mathrm{eV\,s}$ at $E_{\mathrm{kin}} = 0.7\,\mathrm{GeV}$. The resonance has been excited at $\hat{\phi}_{\mathrm{drive}} = 18°$ for a frequency of $\omega_{\mathrm{drive}}/(2\pi) = 760\,\mathrm{Hz}$ during $T_S = 6$ synchrotron periods. We have used 512 fixed slices across the bucket and 2×10^6 macro-particles to fully resolve the dynamically changing space charge potential of the oscillating bunch.

The synchrotron frequency spread due to Eq. (6) between the inner- and outer-most particles leads to a filamentation-like angular spread. The modulation duration determines the azimuthal span to which the excited particles surround the depleted bucket centre. The optimal duration distributing the particles as evenly as possible depends in descending importance on the excitation amplitude $\hat{\phi}_{\mathrm{drive}}$, the ratio between longitudinal emittance ϵ_z and bucket acceptance, and finally the beam intensity. The latter dependency becomes apparent during intensity scans up until $N = 6.4\times10^{12}$, where we find the obtained depletion of the resulting phase space distribution to decrease with increasing N [18].

As laid out before, Eq. (7) predicts an additional detuning from space charge. To compare this with the effect from the bucket non-linearities, Eq. (6), we ran longitudinal simulations during $T_S = 100$ in the PSB ($\eta < 0$) for various intensities. All simulation runs start from the same initial Gaussian distribution with $\sigma_z = 15\,\mathrm{m}$ r.m.s. bunch length. We fix particles at synchrotron amplitudes across the whole bunch and extract their synchrotron tune by Fourier transforming their synchrotron motion. These values are plotted in Figure 4 versus the respective initial synchrotron amplitudes, which are expressed as the maximal spatial amplitude z_{max} of the particle's trajectory.

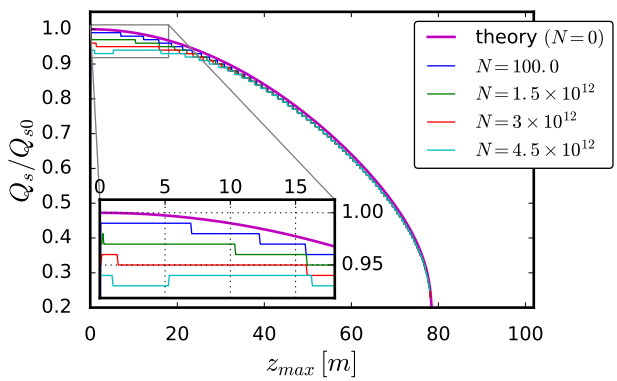

Figure 4: Normalised actual synchrotron frequency $Q_S/Q_{S,0} \equiv \omega_S/\omega_{S,0}$ vs. synchrotron amplitude expressed in $z_{\mathrm{max}} = \tilde{\phi}R/h$, the violet line corresponds to Eq. (6).

At $z_{max} = 0$ one can directly observe the tune depression given by Eq. (7). Then, for larger synchrotron amplitudes to-

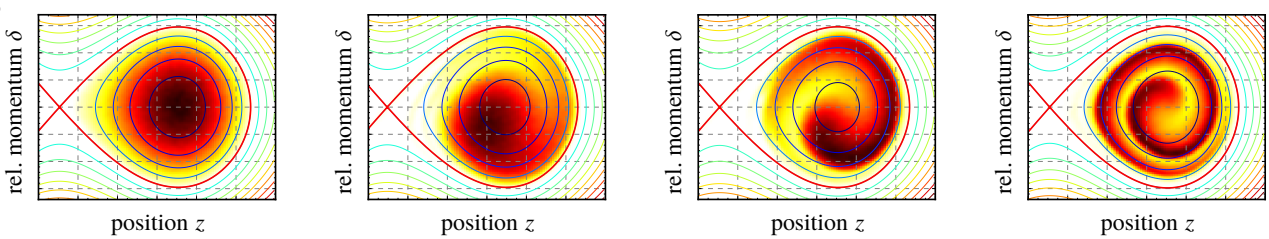

(a) PSB C575, Gaussian start. (b) PSB C579, after $3.5T_S$. (c) PSB C583, after $6T_S$. (d) PSB C591, filamenting.

Figure 3: Longitudinal phase space (z, δ) during the PyHEADTAIL simulation illustrating the dipolar parametric resonance.

ISBN 978-3-95450-185-4

wards the bucket separatrix, the non-linear sinusoidal bucket additionally reduces the linearised synchrotron tune.

Without space charge for $N = 0$, one obtains a certain tune spread across the bunch comparing the bucket centre $z_{max} = 0$ to the bunch ends at $z_{max} = 2\sigma_z = 30\,\mathrm{m}$. This effect becomes even more pronounced if one would move the bunch centre to non-zero z (which is the case for the parametric resonance). The closer we shift the bunch centre towards the separatrix, the larger the synchrotron tune spreads across the bunch. This is precisely the mechanism that leads to the angular spreading of the bunch in longitudinal phase space during the parametric resonance depletion procedure.

Now, adding the space charge effect, Fig. 4 reveals that at larger intensities N the tune spread across the bunch diminishes (compare again between $z_{max} = 0$ and $z_{max} = 30\,\mathrm{m}$). For $N = 4.5 \times 10^{12}$, the Gaussian bunch imprints a nearly constant plateau onto the nearly parabolically decreasing $N = 0$ synchrotron tune curve: space charge makes the bunch resist phase focusing. (At yet larger intensities or smaller σ_z the tune around the origin would even turn into a local dip.) This effect is known as suppression of decoherence by space charge [19].

The analysis in terms of frequency spread also provides a possible remedy: the absolute tune spread ΔQ_S per Δz due to the bucket non-linearities (i.e. the derivative of the magenta curve in Figure 4) evidently increases towards the separatrix. Therefore, exciting the particles to higher synchrotron amplitudes by means of a larger driving amplitude $\hat{\phi}_{\mathrm{drive}}$ may restore a sufficient synchrotron tune spread across the bunch in order to surround the bucket centre with particles.

To sum up, the final longitudinal emittance ϵ_z varies with the bunch intensity, modulation duration and amplitude. In order to reach a specific ϵ_z, modifying $\hat{\phi}_{\mathrm{drive}}$ turns out to be the most effective parameter, while the excitation duration is fixed beforehand by maximising the azimuthal phase space distribution.

Implementation in PSB

As reported in [5], based on the current operational LHC-type beam set-up, we introduced the phase modulation at cycle time C575 (corresponding to an intermediate energy of $E_{\mathrm{kin}} = 0.71\,\mathrm{GeV}$) in a single harmonic accelerating bucket. During 9 ms equivalent to 6 synchrotron periods the beam is driven onto the resonance starting from an initial matched longitudinal emittance of $\epsilon_{z,100\%} \approx 1.1\,\mathrm{eV\,s}$. With these settings, the resulting distributions appeared consistently and reproducibly depleted.

Varying the driving frequency for the parametric resonance revealed a broad resonance window. The beam turned out to be correctly excited for frequencies in the range

$$649\,\mathrm{Hz} \leq \frac{\omega_{\mathrm{drive}}}{2\pi} \leq 734\,\mathrm{Hz} \quad . \tag{8}$$

This resonance window is sharply defined up to 1 Hz.

Special attention had to be given to optimise the phase loop gain during the excitation process: for a too strong gain, the phase loop continuously realigns the phase of the main C02 cavities with the beam. This counteracts the excitation and leads to severely perturbed distributions. Our first experiment series using the radial loop instead of the phase loop for the phase modulation was in fact severely affected by this phase loop action [20].

Eventually, the long filament can be smoothed to a ring-like phase space distribution by high frequency phase modulation at harmonic $h = 9$ with the C16 cavities. Figure 5 shows tomographic reconstructions [11] of longitudinal phase space at important cycle times. The horizontal axis is reverted compared to Fig. 3, since $\phi = -hz/R$. Note the coincidence of the phase space distributions at cycle time C591 between simulation results in Fig. 3d and measurement in Fig. 5b.

SPACE CHARGE MITIGATION IN PS

To assess the impact of direct space charge during the 1.2 s PS injection plateau at $E_{\mathrm{kin}} = 1.4\,\mathrm{GeV}$ and $h = 7$, we compare single bunch beams of the usual LHC parabolic type with the modified hollow type by measuring transverse emittance blow-up and beam loss. For each shot, tomography and wire scans yield the z, δ, x, y distributions 15 ms after injection and again 20 ms before the second batch injection time. Table 1 lists the experiment parameters.

Emittance Determination with Dispersion Effects

Hollow bunches exhibit a non-Gaussian δ distribution by construction, therefore Eq. (2) does not apply. In principle,

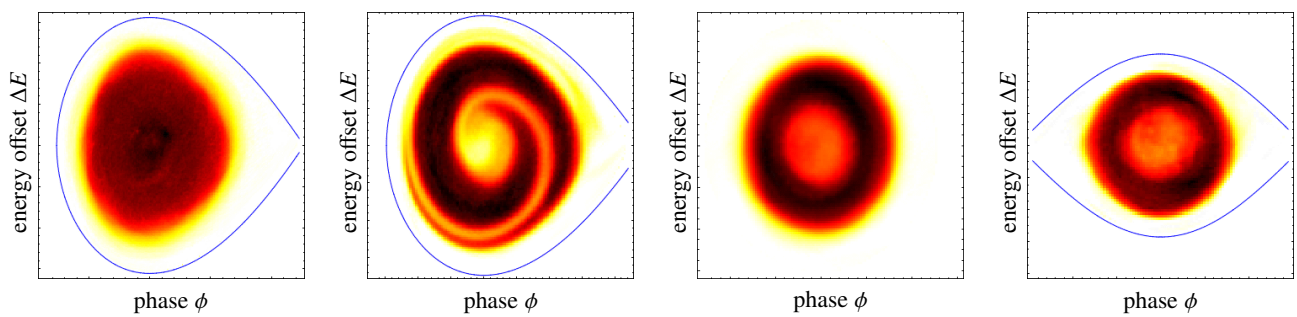

(a) PSB C573, before excitation. (b) PSB C591, after excitation. (c) PSB C800 (5 ms to extract.). (d) PS C171 (1 ms after inject.).

Figure 5: Longitudinal phase space $(\phi, \Delta E)$ reconstructed via tomography at different stages in the PSB (measurements) [5].

ISBN 978-3-95450-185-4

Table 1: Relevant Experiment Beam Parameters for PS

parameter	hollow value	parabolic value
N	$(1.66 \pm 0.05) \times 10^{12}$	$(1.84 \pm 0.03) \times 10^{12}$
$\epsilon_{z,100\%}$	1.43 ± 0.15 eV s	1.47 ± 0.11 eV s
$\epsilon_{z,\mathrm{rms}}$	0.32 ± 0.02 eV s	0.3 ± 0.01 eV s
Q_x, Q_y	(6.23, 6.22)	

each particle's horizontal position is a sum of two independent random variables, the f_β-distributed betatron motion x_β and the f_{disp}-distributed dispersion contribution $D_x\delta$,

$$x = x_\beta + D_x\delta \quad , \tag{9}$$

where $D_x = 2.3$ m at the wire scanner. Therefore, the horizontal distribution function is given by the convolution

$$p(x) = \int dx'\, f_\beta(x') f_{\mathrm{disp}}(x - x') \tag{10}$$

$$\text{with} \quad f_{\mathrm{disp}}(x) = f_\delta(D_x\delta)/|D_x| \quad . \tag{11}$$

Considering the beam as an ensemble, we have measured f_{disp} (via tomography) as well as p (the wire scanner profile). Assuming f_β to be Gaussian distributed, we can determine its variance σ_β^2 and hence the normalised emittance

$$\epsilon_x = \beta\gamma\sigma_\beta^2/\beta_x \tag{12}$$

via a least squares algorithm by comparing the convolution of the educated guess for f_β and the measured f_{disp} with the measured p, cf. Fig. 6. Applying this procedure to both beams, we find Eq. (2) to underestimate ϵ_x from 24.8% to 34.8% for both the parabolic as well as the hollow bunches.

Experimental Results

As discussed in [5], we prepare both beam types with varying bunch lengths by adiabatically ramping the total RF voltage during the initial 15 ms to values between the initial 25 kV and 80 kV. Due to varying shot-to-shot efficiency of the C16 blow-up, we achieve total bunch lengths over a range of $B_L = 130 \,..\, 220$ ns. Figure 7a depicts consistently depressed peak line densities by a factor 0.9 for the flattened

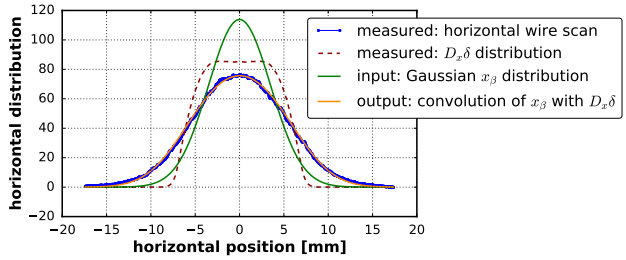

Figure 6: Wire scan comprising betatron and dispersive part.

profiles compared to the parabolic ones. A theoretically ideal rectangular profile of $4\sigma_z$ length would yield a $\sqrt{2\pi}/4 \approx 0.63$ depression factor compared to a perfect Gaussian. Both extrema are plotted in Fig. 7a for comparison.

We want to compare the impact of space charge for both beam types for fixed B_L, N and ϵ_u. To unify this set in one quantity, we choose to evaluate $\Delta Q_u^{\mathrm{max}}$ assuming a 6D Gaussian distributed beam in Eq. (1). Hence we apply (2) as well as using the Gaussian peak line density $\lambda_{\mathrm{max}} = N/(\sqrt{2\pi}\sigma_z)$ where we set $\sigma_z = B_L/4$. Figure 7b shows how hollow bunches provide statistically significantly lower vertical emittances for the same unified reference tune shift $\Delta Q_u^{\mathrm{max}}$. The real tune shift of the hollow bunches is a factor 0.88 lower due to their reduced λ_{max} and the larger σ_x. In contrast, the parabolic bunches are rather well represented by the Gaussian approach (factor 0.97 lower real tune shift).

Finally, keeping the maximum RF voltage 80 kV, we scan the intensity by varying the injected turns in the PSB. Figure 7c exhibits the emittance blow-up $\epsilon_y^{\mathrm{fin}}/\epsilon_y^{\mathrm{ini}}$ versus the brightness, which is again lower for the hollow bunches.

CONCLUSION

We have set up a reliable process to create hollow bunches with minimal changes to the operational PSB cycle. Due to the lower peak line density, the hollow bunches are shown to be less affected by space charge compared to the parabolic bunches during the PS injection plateau.

ACKNOWLEDGEMENT

The PSB feedback systems have been set up to create and transfer hollow bunches owing to the invaluable support by Maria-Elena Angoletta and Michael Jaussi.

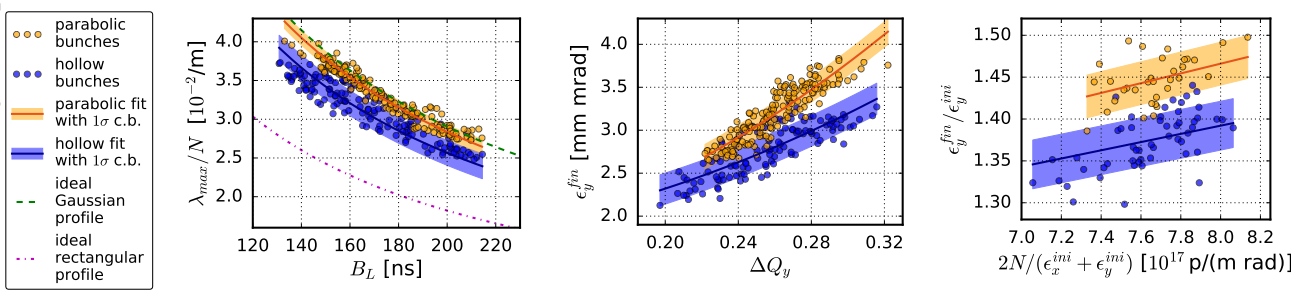

(a) Intensity normalised peak line charge density vs. total bunch length.

(b) Vertical emittances (end of inject. plateau) vs. space charge tune shift.

(c) Vertical emittance blow-up vs. brightness (at $V_{\mathrm{rf}} = 80$ kV).

Figure 7: Comparison of hollow and parabolic bunches. Fits include 1σ confidence bands [5].

ISBN 978-3-95450-185-4

REFERENCES

[1] H. Damerau *et al.*, "LHC Injectors Upgrade, Technical Design Report, Vol. I: Protons", CERN-ACC-2014-0337, Geneva, Switzerland, 2014.

[2] H. Bartosik *et al.*, "Can We Ever Reach the HL-LHC Requirements with the Injectors?", in *RLIUP: Review of LHC and Injector Upgrade Plans*, Archamps, France, Oct. 2013, pp. 95-104.

[3] R. Wasef *et al.*, "Space Charge Effects and Limitations in the CERN Proton Synchrotron", in *Proc. 4th Int. Particle Accelerator Conf. (IPAC'13)*, Shanghai, China, May 2013, paper WEPEA070, pp. 2669-2671.

[4] S. Gilardoni *et al.*, "LIU: Which Beams in the Injectors Fulfill HL-LHC Upgrade Scenario 1 Goals?", in *RLIUP: Review of LHC and Injector Upgrade Plans*, Archamps, France, Oct. 2013, pp. 69-73.

[5] A. Oeftiger, H. Bartosik, A. Findlay, S. Hancock and G. Rumolo, "Flat Bunches With a Hollow Distribution for Space Charge Mitigation", in *Proc. 7th Int. Particle Accelerator Conf. (IPAC'16)*, Busan, Korea, May 2016, paper MOPOR023, pp. 652-655.

[6] R. Cappi, R. Garoby, S. Hancock, M. Martini, J.P. Riunaud, "Measurement and Reduction of Transverse Emittance Blow-up Induced by Space Charge Effects", in *Proc. 15th IEEE Particle Accelerator Conf. (PAC'93)*, Washington, DC, USA, May 1993, pp. 3570-3572.

[7] R. Garoby and S. Hancock, "New Techniques for Tailoring Longitudinal Density in a Proton Synchrotron", in *Proc. 4th European Particle Accelerator Conf. (EPAC'94)*, London, UK, June 1994, pp. 282.

[8] K. Schindl, "Space Charge", CERN/PS 99-012(DI), Geneva, Switzerland, 1999.

[9] R. Baartman, "Betatron Resonances With Space Charge", in *AIP Conference Proceedings*, vol. 448, 1998, pp. 56-72.

[10] H. Huang *et al.*, "Experimental Determination of the Hamiltonian for Synchrotron Motion with RF Phase Modulation", in *Phys. Rev. E*, vol. 48, no. 6, Dec. 1993, pp. 4678-4688.

[11] S. Hancock, S.R. Koscielniak, M. Lindroos, "Longitudinal Phase Space Tomography with Space Charge", in *Proc. 7th European Particle Accelerator Conf. (EPAC 2000)*, Vienna, Austria, Jul. 2000, pp. 1726-1728.

[12] S.Y. Lee, "Accelerator Physics", World Scientific, 3rd edition, 2012.

[13] A.W. Chao, "Physics of Collective Beam Instabilities in High Energy Accelerators", Wiley, 1993.

[14] M. Reiser, "Theory and Design of Charged Particle Beams", John Wiley & Sons, Jun. 2008.

[15] E. Metral *et al.*, "Beam Instabilities in Hadron Synchrotrons", in *IEEE Transactions on Nuclear Science*, vol. 63, no. 2, Apr. 2016, pp. 1001-1050.

[16] K.S.B. Li *et al.*, "Code development for Collective Effects", presented at the ICFA Advanced Beam Dynamics Workshop on High-Intensity and High-Brightness Hadron Beams (HB2016), Malmö, Sweden, July 2016, paper WEAM3X01, this conference.

[17] A. Oeftiger and S. Hegglin, "Space Charge Modules for PyHEADTAIL", presented at the ICFA Advanced Beam Dynamics Workshop on High-Intensity and High-Brightness Hadron Beams (HB2016), Malmö, Sweden, July 2016, paper MOPR025, this conference.

[18] A. Oeftiger, "Space Charge Effects and Advanced Modelling for CERN Low Energy Machines", unpublished Ph.D. thesis, LPAP, EDPY, École Polytechnique Fédérale de Lausanne, Lausanne, Switzerland, 2016.

[19] G. Rumolo, O. Boine-Frankenheim, I. Hofmann, Y. Liu and A. Al-Khateeb, "Effects of Space Charge on Decoherence in Ion Beams", in *Proc. Particle Accelerator Conf. (PAC 2003)*, Portland, USA, May 2003, vol. 4, pp. 2607-2609.

[20] A. Oeftiger, H. Bartosik, A.J. Findlay, S. Hancock and G. Rumolo, "MD210 Note: Creation of Hollow Bunches in the PSB", CERN-ACC-NOTE-2016-0045, Geneva, Switzerland, Jun. 2016.

ISBN 978-3-95450-185-4

DYNAMIC BETA AND BETA-BEATING EFFECTS IN THE PRESENCE OF THE BEAM-BEAM INTERACTIONS

X. Buffat, L. Medina, T. Pieloni *, C. Tambasco, R. Tomás, CERN, Geneva, Switzerland,
J. Barranco and P. Gonçalves Jorge, EPFL, Lausanne, Switzerland.

Abstract

The Large Hadron Collider (LHC) has achieved correction of beta beat down to better than 5%. The beam-beam interactions at the four experiments result as extra quadrupole error in the lattice. This will produce a change of the beta* at the experiments and a beating along the arcs which for the High Luminosity LHC (HL-LHC) will be very large. Estimations of these effects will be given with the characterisation of the amplitude dependency. A first attempt to correct his beating is also discussed.

INTRODUCTION

Head-On (HO) Beam-Beam (BB) collisions as well as Long-Range (LR) interactions induce a force on the particles that depends on their amplitude. For small amplitude particles (i.e. below $\approx 1\sigma$), the force is approximately linear which means that the particles traveling see the beam coming from the opposite direction as a defocusing quadrupole when they are close enough to the beam center. Beam-beam interactions will induce a change in the β-function all along the accelerator [1]. In the simplest case for small amplitudes, one can derive analytically the change of the β-function coming from N small quadrupole errors (i.e. head-on collisions at small amplitudes) at positions s_i (i = 1,...,N) [2]:

$$\frac{\Delta\beta(s)}{\beta_0(s)} = \frac{2\pi\xi}{\sin(2\pi Q_0)} \sum_{i=0}^{N} \cos(2 \mid \mu_0(s) - \mu_0(s_i) \mid - 2\pi Q_0). \quad (1)$$

During the 2015 LHC Physics Run a study of possible impacts of the dynamic beta effects of beam-beam on the collider performances, modifying the β^* at the two high luminosity experiments. While the effect on the LHC performances has been shown to be of maximum 1% level the study has highlighted a much more relevant contribution to the beating along the circumference with possible implications to machine protections. The LHC β-beating from the lattice imperfections is measured and corrected in commissioning phase to a level beetween the 5-7% [5, 6]. The measurements and corrections are performed with single beams and beam-beam effects are not accounted for. Studies of the implications in β-beating for the LHC configuration of 2015 have shown that in collisions a beating of up to 8% is expected mainly due to the head-on collisions with a beam-beam parameter ξ of approximately 0.0037 per Interaction Point (IP) . The computed β-beating for the LHC set-up of 2015 are shown in Figure 1. The beating comes mainly from the head-on collisions at the IPs, two in the cases shown in this paper. The maximum beating expected is obtained when full head-on collision is established.

A similar effect is expected for the High Luminosity LHC (HL-LHC) case, where due to the much stronger head-on (ξ_{bb} ≈0.01 per IP), a maximum β-beating of approximately 15% and 24% is expected for the case of two and three head-on collisions, respectively. In Figure 2 the β-beating for the HL-LHC is shown for the baseline scenario defined in [3] with two head-on collisions in the ATLAS and CMS experiments. For the HL-LHC the effect is independent on the β^* as the beam-beam parameter is when no crossing angle is present at the IP as for the crab-crossing scenario.

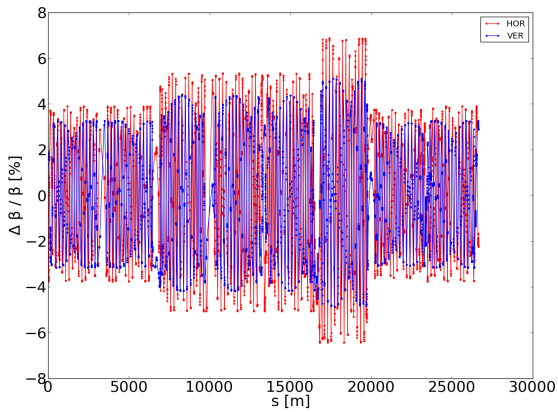

Figure 1: Beta-beating as a function of the longitudinal coordinate in the LHC for two head-on collisions at IP1 and IP5.

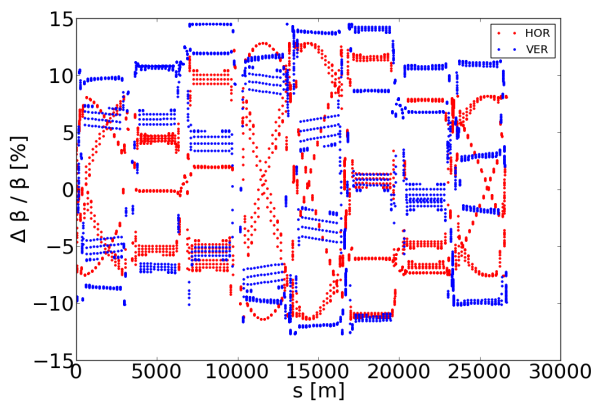

Figure 2: Beta-beating computed for the HL-LHC baseline scenario as a function of the longitudinal coordinate.

* tatiana.pieloni@cern.ch

ISBN 978-3-95450-185-4

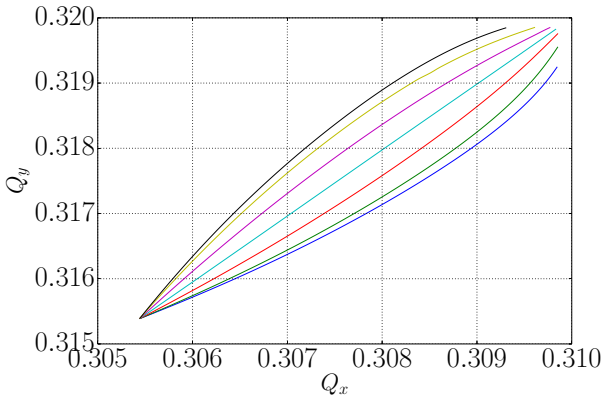

Figure 3: Particles detuning with amplitude due to two head-on collisions. The particle amplitudes go from 0 to 8 σ RMS beam size. The different curves show the behaviour for oscillations at different angles in the X-Y plane.

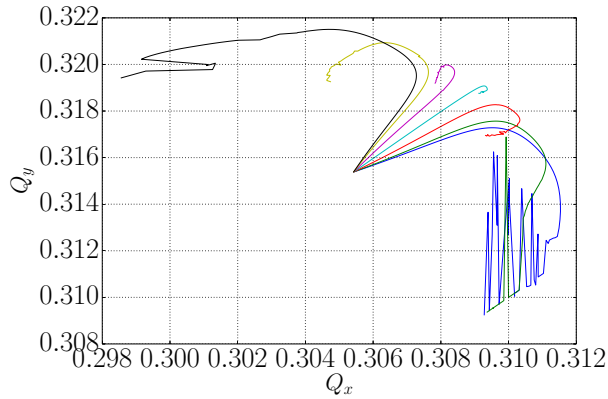

Figure 4: Particles detuning with amplitude due to two head-on collisions and long-range encounters. The particle amplitudes go from 0 to 8 σ RMS beam size. The different curves show the behaviour for oscillations at different angles in the X-Y plane.

There are two aspects to study one related to luminosity performances and one related to the impact to the collider protection systems. The first can profit of such an effect since by optimizing the phase advance between the beam-beam interactions and keeping the beating corrections and errors at minimum one can obtain a reduction of the β_* at the IPs as done for example in [4]. For the HL-LHC case reductions of the beta function at the IP of maximum 9% have been evaluated with the present optics. The possible effects to the protection system need a careful understanding of the dynamics since the different interactions HO and LR act differently on core and tail particles. Figures 3 and 4 show the detuning with amplitude of particles colliding head-on and with long range interactions, respectively. The different lines show the behaviour of the particles with different angle in the x-y plane.

NON-LINEAR β BEATING

Due to the non-linearity of the beam-beam forces, the motion of particles oscillating at different amplitudes will be affected differently. In order to evaluate the impact of beam-beam interactions in terms of optics function, we compute the effective β function at a given point in the lattice using single particle tracking simulations. A matrix containing the phase space coordinates at the Poincaré section of interest for 5000 consecutive turns is obtained using MAD-X. The singular value decomposition of this matrix provides the transformation matrix to normalised coordinates which, when compared to the Floquet transformation, determines the optics functions. Figures 5 and 6 show the results of such an analysis in the presence of head-on and long-range beam-beam interactions in the LHC, in a configuration similar to the regular operational conditions during the 2016 run. As expected the variations of the optics function at zero amplitude correspond to those obtained with the linear model.

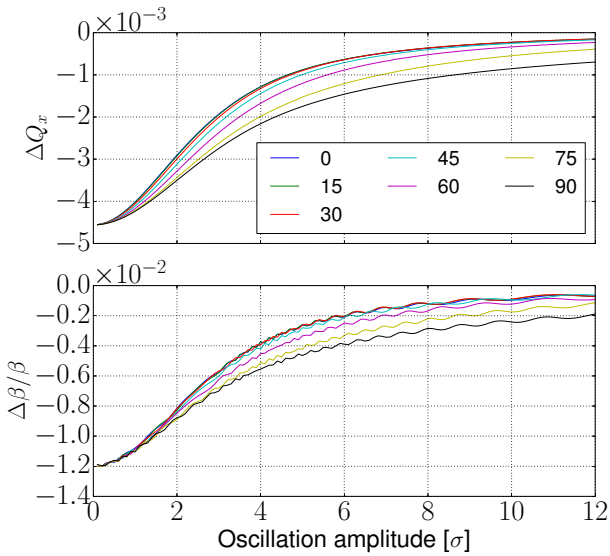

Figure 5: Horizontal tune shift and β beating at the interaction point 1 due to head-on beam-beam interactions in interaction points 1 and 5 in the LHC, for particles oscillating at different amplitudes. The different curves show the behaviour for oscillations at different angles in the X-Y plane.

In the presence of head-on beam-beam interactions only, the tune shift is maximum for particles oscillating at small amplitudes and vanishes asymptotically for large oscillation amplitudes. This behaviour of the tune shift is visible in Figure 5, the β-beating follows the same trend. While reasonably small in the case of the LHC, the head-on beam-beam tune shift considered for the HL-LHC as well as the FCC-hh is significantly larger. In such condition the maximum linear β beating induced by head-on beam-beam interaction could exceed the achieved correction of the bare optics and

ISBN 978-3-95450-185-4

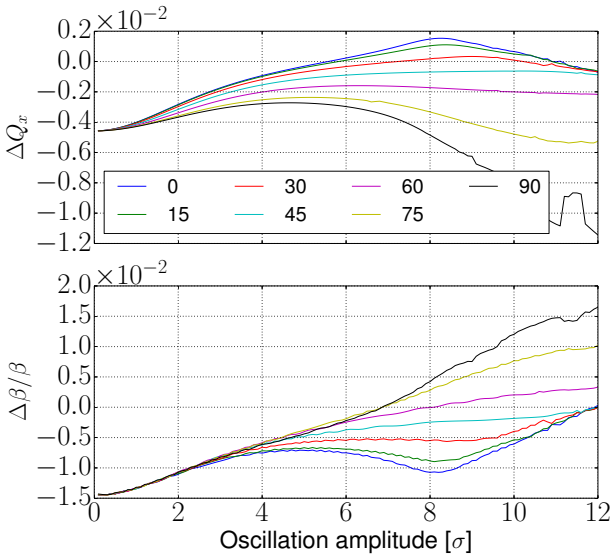

Figure 6: Horizontal tune shift and β beating at the interaction point 1 due to head-on and long-range beam-beam interactions in interaction points 1 and 5 in the LHC, for particles oscillating at different amplitudes. The different curves show the behaviour for oscillations at different angles in the X-Y plane.

possibly the tolerances imposed by the collimation system. Nevertheless, the effect on halo particles remains negligible. As opposed to head-on interactions, the forces due to long-range beam-beam interactions do not vanish for large amplitude particles. As a result, both the tune shift and the β-beating do not vanish at large amplitude. Figure 6 illustrates this behaviour, in the case of the LHC. While important optics distortions are visible for amplitudes above 6 σ, they will not affect the machine performance since particles with such an amplitude would be collimated. The efficiency of the cleaning could nevertheless be affected in case the β-beating below 6 σ approaches the tolerances.

The effect of the phase advance between the interaction points on the β-function has also a strong effect. Preliminary studies have showed that the maximum of the β-beating can be adjusted by varying the phase advance between the interaction points. The simulations also revealed that the maximum of the β-beating on a given plane could be very different from one side of the ring to the other which should be taken into account in the design phase, for example of the collimation system.

OPTICS CORRECTION

Beta-beating of up to 8 % and 6 % in the horizontal and vertical planes, respectively, is caused by head-on and long-range beam-beam effects in the four interaction points of the LHC at 7 TeV with a bunch population of 1.3×10^{11} particles and $\beta^* = 0.6$ m. The correction of the β-beating [7] is computed by rematching the interaction region (IR) with the closest quadrupole magnets to the IP, however using the triplet to perform the correction for LR BB is not possible because it would require opposite polarities in common magnets for the beams.

Table 1: Correction of the Peak β-beating due to LR BB at IP1 and IP5 (LHC Beam 1)

	ΔK_1	ΔK_2	Peak β-beating [%]	
	[10^{-6} m^{-2}]	[10^{-3} m^{-3}]	Horizontal	Vertical
IP1				
Uncorrected	-	-	1.81	1.87
Q4	+7	-	0.32	0.30
Q5	+15	-	0.52	0.54
MCSSX	-	9	0.08	0.20
IP5				
Uncorrected	-	-	1.81	1.86
Q4	−7	-	0.31	0.30
Q5	−15	-	0.52	0.49
MCSX	-	2	0.17	0.10

For the case of only LR-BB at IP1 (vertical crossing angle), the results on the variation of the strengths from their nominal values, $K + \Delta K$, of Q4, Q5, and MCSSX –at the left/right of the IP–, show a significant reduction of the peak β-beating (Table 1). The correction of the case of LR BB at IP5 by means of Q4 and Q5 is analogous to the former, resulting in ΔK of similar magnitude and opposite polarity due to the horizontal crossing angle. For the same reason, MCSX is used instead of MCSSX for the correction at IP5.

Rematching of the optics at the start/end of the interaction region (as well at the IP), where the HO BB effect is present, was the strategy adopted to correct the induced β-beating. Different configurations involving the quadrupole strengths of Q4 to Q7 were tested, and beams 1 and 2 were studied separately. As seen in Figure 7, the correction achieved

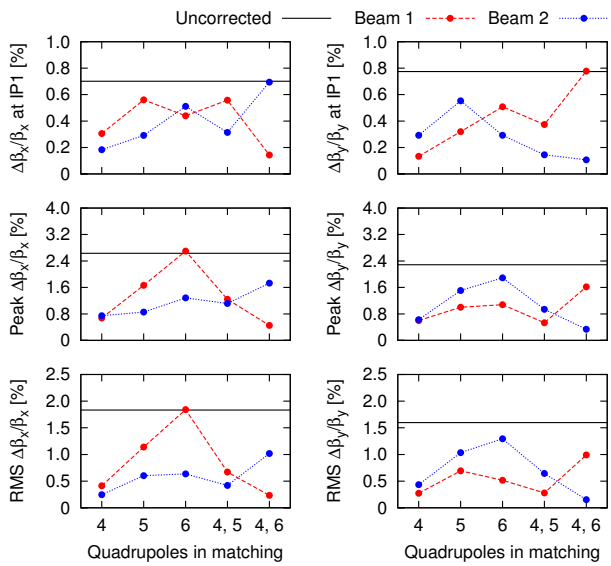

Figure 7: Correction of the beta-beating at IP1, peak beta-beating, and rms beta-beating, due to HO-BB at IP1.

ISBN 978-3-95450-185-4

by the adjustment of a single quadrupole, such as Q4 or Q5, proved to be the most efficient: the peak- and rms- β-beating are reduced by a factor of 4 for both planes, and the β-beating is decreased by a factor of 2.5 or more, depending on the plane and beam under consideration. Similarly, the correction by the pair Q4-Q5 is also noticeable, and the corresponding tune-shift is lower, i. e. $\Delta Q_x = -0.0068$ and $\Delta Q_y = -0.0064$ (beam 1), compared to -0.0086 horizontally and -0.0066 vertically, for the correction with Q4 exclusively. Matchings involving Q6 do not perform satisfactory due to its strength being very close, in the case of LHC, to its limit.

Refined matchings and further studies as a function of the bunch population and β^*, for the LHC and HL-LHC, are ongoing.

CONCLUSIONS

Beam-beam effects can lead to important beating of beta functions. The maximum beating for the LHC and its upgrade is of the order of 8% and up to 24%, respectively. This could lead to important consequences in terms of machine protection, collimation and performances. A preliminary study shows the amplitude dependent beating for the case with head-on and long-range interactions. The phase advance between the beam-beam interactions have also an important role changing the location of the maximum beating. This could be optimized in the lattice design of colliders in the design phase. The beam-beam induced beating is very different from normal single beam effect and needs further investigations to understand the impact on other systems (i.e. collimation). A first proposal to correct for the beam-beam induced beating has been explored and the procedure described. Preliminary results for the LHC case have been presented and shows the possibility to reduce the beating due to long-range interactions by a factor 2.5. Further studies and an experimental verification is foreseen to prove the correction proposal for the LHC.

REFERENCES

[1] W. Herr and T. Pieloni, "The Beam-Beam Effects", CERN Accelerator School: Advanced Accelerator Physics Course, pp.431-459, Trondheim, Norway, 18-29 Aug 2013.

[2] A. Wu Chao, M. Tigner, Handbook of Accelerator Physics and Engineering, World Scientific, 1999.

[3] E. Metral et al., "HL-LHC Operational Scenarios", CERN-ACC-NOTE-2015-0009, Geneva, 2015.

[4] D. Brandt, W. Herr, M. Meddahi and A. Verdier, IS LEP BEAM-BEAM LIMITED AT ITS HIGHEST ENERGY ?, Proceedings of the 1999 Particle Accelerator Conference, New York, 1999.

[5] R. Tomás et al., Phys. Rev. ST Accel. Beams **15**, 091001 (2012).

[6] A. Langner and R. Tomás, Phys. Rev. ST Accel. Beams **18**, 031002 (2015).

[7] R. Tomás et al., Phys. Rev. ST Accel. Beams **13**, 121004 (2010).

ISBN 978-3-95450-185-4

CERN PS BOOSTER LONGITUDINAL DYNAMICS SIMULATIONS FOR THE POST-LS2 SCENARIO

D. Quartullo*, CERN, Geneva, Switzerland - Università di Roma La Sapienza
S. Albright, E. Shapochnikova, H. Timko, CERN, Geneva, Switzerland

Abstract

The CERN PS Booster is the first synchrotron in the LHC proton injection chain, it currently accelerates particles from 50 MeV to 1.4 GeV kinetic energy. Several upgrades foreseen by the LHC Injectors Upgrade Program will allow the beam to be accelerated from 160 MeV to 2 GeV after Long Shutdown 2 in 2021. The present RF systems will be replaced by a new one, based on Finemet technology. These and other improvements will help to increase the LHC luminosity by a factor of ten. In order to study beam stability in the longitudinal plane simulations have been performed with the CERN BLonD code, using an accurate longitudinal impedance model and a reliable estimation of the longitudinal space charge. Particular attention has been dedicated to the three main features that currently let the beam go stably through the ramp: Double RF operation in bunch-lengthening mode to reduce the transverse space charge tune spread, exploitation of feedback loops to damp dipole oscillations, and controlled longitudinal emittance blow-up. RF phase noise injection has been considered to study if it could complement or substitute the currently used method based on sinusoidal phase modulation.

INTRODUCTION

In 2021, after Long Shutdown 2 (LS2), all the injectors of the LHC will be upgraded according to the LHC Injectors Upgrade (LIU) program [1]. These improvements will contribute to an increase of the LHC luminosity by a factor of ten, meeting the expectations of the HL-LHC project.

CERN's PS Booster (PSB) is the first synchrotron in the LHC proton injection chain, it currently receives particles from the linear accelerator Linac2 at 50 MeV kinetic energy and accelerates them up to 1.4 GeV before extraction to the Proton Syncrotron (PS). In the post LS2 scenario, following the specifics of the LIU PSB program, Linac2 will be replaced by the new Linac4 and the injection energy will be increased to 160 MeV, in addition nominal LHC-type beams will be extracted at 2 GeV.

The PSB currently has three RF systems. Acceleration is done at h=1, while the h=2 system is used at injection and during the ramp in bunch lengthening mode to reduce the peak line density and minimize the transverse space charge tune spread. A high harmonic cavity (h<=16) is used to blow up the longitudinal emittance of the beam in a controlled way, since high emittance bunches are needed in the PSB for stability and in the PS for space charge reduction before bunch splitting at flat bottom. In the post-LS2 scenario these three RF systems will be replaced by wide-band Finemet loaded cavities [2], which will be modular and will allow multi-harmonic operation. All the functionalities given by the current systems will be supplied by the new system as well.

In a future scenario where a lot of beam parameters will change, and where the momentum program and some impedance contributions (of RF systems and other ring components) will be different, it is vital to predict possible instabilities, which may lead to particle losses and deterioration of beam quality during the ramp and at extraction.

The most reasonable tool for this is reliable multi-particle longitudinal tracking, and the CERN BLonD code [3] has been adapted for this purpose. BLonD was conceived in 2014 and has been used extensively to simulate longitudinal dynamics of the various CERN rings (LEIR, PSB, PS, SPS and LHC) for both ions and protons. Several features are included: Acceleration, multiple RF systems, collective effects, multibunch operation, low level RF feedbacks, phase modulation or phase noise injection for controlled longitudinal emittance blow-up.

This paper describes features of the BLonD code together with obtained results. We start with an explanation of how the induced voltage is derived turn by turn, show how to numerically calculate an accurate phase shift program in double RF bunch-lengthening mode with a voltage ratio of 3/4 (currently used for LHC beams) with intensity effects and then we will briefly present the low level RF feedbacks used in the PSB and a result from their implementation in BLonD. Finally the theory behind controlled longitudinal emittance blow-up with RF phase noise injection will be introduced and the corresponding algorithm in the code will be explained. RF phase noise has never been tested in the PSB but simulations can reveal its usability in this particular case.

INDUCED VOLTAGE CALCULATION

Longitudinal Space Charge and Impedance Model

The longitudinal space charge effect is significant in non-relativistic machines so an accurate calculation of its contribution is very important. Let's call Z_{sc} the purely imaginary space charge impedance and $\lambda(t)$ the longitudinal bunch profile such that $\int_T dt\lambda(t) = N$, where N stands for the beam intensity; here t is the time longitudinal coordinate and $T = [0, T_{rev}]$ is the one-turn time interval. The space charge induced voltage can be calculated with good approximation using

$$V_{sc}(t) = \frac{e}{\omega_{rev}} \frac{|Z_{sc}|}{n} \frac{d}{dt} \lambda(t), \qquad (1)$$

* danilo.quartullo@cern.ch

ISBN 978-3-95450-185-4

where e is the proton charge, $\omega_{rev} = 2\pi f_{rev}$ is the design angular revolution frequency and $n = f/f_{rev}$, and f is a generic positive frequency value. Equation (1) shows that the problem of calculating the space charge induced voltage reduces to find the $|Z_{sc}|/n$ value for each beam energy through the ramp. The first point of this curve has been carefully estimated dividing the PSB into 211 sections and, for each of them, taking into account the beam pipe cross section and beam transverse standard deviation to estimate the space charge contribution in that portion of the ring. Finally an average on all the 211 sections was calculated [4]. The $|Z_{sc}|/n$ value found at 160 MeV (603 Ω) was then rescaled through the ramp with $\beta\gamma^2$ (85 Ω at 2 GeV).

The PSB impedance model contains contributions from 36 Finemet gaps, extraction kickers and cables, KSW kicker magnets, resistive wall and beam pipe step transitions [2, 5]. Figures 1 and 2 show the sum of all contributions at injection and extraction energy, for completeness Figure 2 takes into account the longitudinal space charge impedance. The 100 MHz limit derives from measurements and the visible notches in the plots correspond to Finemet impedance reduction at revolution frequency and its multiples up to 8 due to the action of Low Level electronics. We can see that the real part of the Finemet impedance without reduction dominates all the other components while the Finemet imaginary part is prevalent below 1 MHz and dominated by the space charge impedance above that frequency, mostly at low energies.

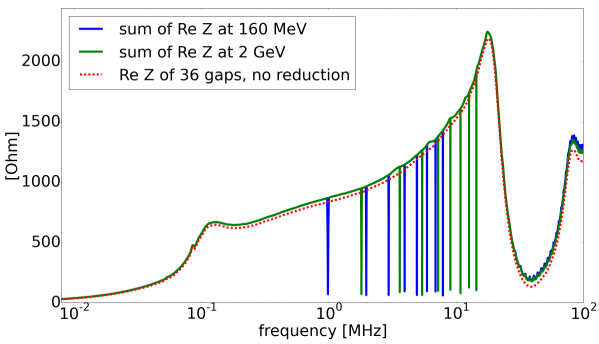

Figure 1: Sum of all the real parts of the impedances at 160 MeV and 2 GeV.

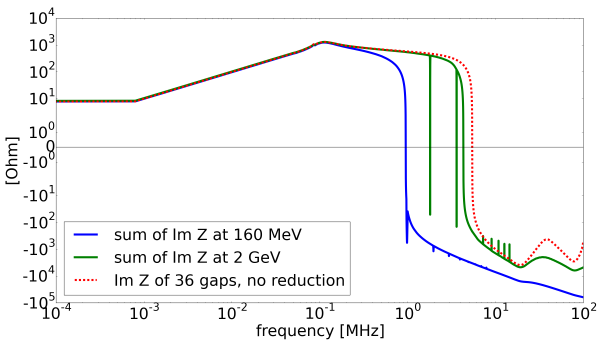

Figure 2: Sum of all the imaginary parts of the impedances at 160 MeV and 2 GeV.

Multi-turn Wake

The space charge induced voltage defined in Eq. (1) cannot be multi-turn in opposition to the one derived from the other PSB impedances that can be calculated numerically as:

$$V_{ind}(t) = -2ef_{max}IDFT(DFT(\lambda) \times Z), \qquad (2)$$

where the discrete Fourier transform and its inverse automatically suppose the signal is periodic in time domain, $f_{max} = 1/(2\Delta t)$ is the maximum frequency that one is interested in with Δt being the sample interval in time domain.

In an ideal case, without acceleration and with stationary line density, it would be reasonable to consider the profile as being periodic on the ring. The period would be T_{rev} and consequently only the points corresponding to f_{rev} and multiples would be considered when the spectrum is multiplied by the impedance in Eq. (2). In the PSB case, where the revolution period approximatively halves from injection to extraction, and the line density varies considerably along the ramp, it is instead more correct to consider an extended period for the profile, meaning that the signal is padded with zeros before performing the Fourier transform and consequently the impedance curve in frequency domain is resolved in detail. In addition, simulations show that even in the idealistic case without zero padding, the induced voltage does not decay in one turn, and so padding zeros is necessary in any case to correctly simulate intensity effects, see Fig. 3. Here and later the PSB convention for the cycle time is used, with injection at 275 ms (C275) and extraction at 775 ms (C775).

It would be ideal to calculate the induced voltage for a certain turn, save its continuation into memory for the next turns, track the particles, apply the saved voltage and so on. One problem is that, because of acceleration, T_{rev} varies and calculating the multi-turn wake in time domain would be computationally expensive since for every sum of two contributions, one from the past and the other from the present, an interpolation is needed. We therefore operate in frequency domain using the fact that a shift of the induced voltage in time domain corresponds to a multiplication by a complex exponential in frequency domain. As a consequence we were able to replace interpolations with multiplications and sums.

Finally we should mention the front wake. In a non-relativistic machine, such as the PSB, the bunch produces a front wake. Operating an inverse Fourier transform on the total impedance of our model the front wake is clearly visible. The one decaying in one turn is, by definition of circular convolution, already taken into account in simulations. However, the one decaying after one turn, although not negligible and comparable to the wake behind, has not yet been included in BLonD. The problem is not trivial since one should go back and forth between two or more consecutive turns to find the correct induced voltages to save into memory.

ISBN 978-3-95450-185-4

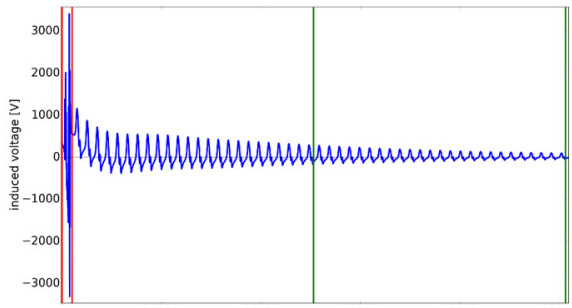

Figure 3: Multi-turn induced voltage at C285: the bunch sits between the red vertical lines while the green lines mark $25T_{rev}$ and $50T_{rev}$. Realistic simulation with intensity of 3.6×10^{12} and complete PSB impedance model.

DOUBLE RF OPERATION WITH INTENSITY EFFECTS

In the PSB the voltage of the h=2 RF system is currently summed to the accelerating voltage in anti-phase or bunch lengthening mode. This method is used to reduce the peak line density and increase the bunching factor, reducing transverse space charge. Constant peak voltages $V_1 = 8$ kV and $V_2 = 6$ kV are chosen for nominal LHC beams and the same configuration will likely be used in the post-LS2 scenario [6]. Figure 4 shows in simulation a typical profile related to this cavity setting, where the relative phase between the two RF systems is calibrated in such a way that the two peaks have the same height.

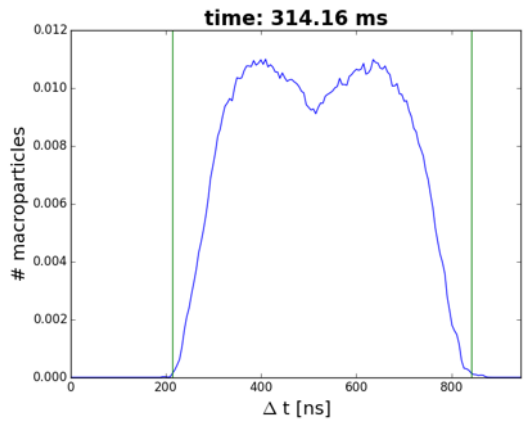

Figure 4: Example of profile using $V_1 = 8$ kV and $V_1 = 6$ kV in bunch lengthening mode.

In operation the correct phase for bunch lengthening is found empirically through beam measurements at different points during the ramp and a linear interpolation is used for intermediate points. Because of hardware reasons an additional complication is that the phase shift programmed does not correspond to the true value, therefore they cannot be used in simulations. It is essential to find a method to numerically calculate the correct phase shift if we want to reproduce the double RF dynamics in simulations.

In the following equation let $\Delta\phi_{12}$ be the relative phase between the two RF systems:

$$V_{rf}(\phi) = V_1 \sin(\phi) + V_2 \sin(2\phi + \Delta\phi_{12}) \qquad (3)$$

Without acceleration and intensity effects $\Delta\phi_{12} = \pi$ is the solution to our problem. With acceleration if ϕ_s is close to 0 the phase shift $\Delta\phi_{12} = \pi - 2\phi_s$ is a solution, where ϕ_s is the synchronous phase in single harmonic. Because of the strong acceleration during the second part of the PSB ramp this solution is not accurate, if we add intensity effects the discrepancy is worse.

An algorithm has been developed in BLonD to numerically calculate $\Delta\phi_{12}$, compensating for high ϕ_s and intensity effects. The idea of the algorithm is to integrate the total voltage to obtain the total potential and then numerically find $\Delta\phi_{12}$ in such a way that the two minima have the same depth, see Fig. 5. This procedure is done turn by turn while tracking, so that the phase found for turn n is used as the initial value inside the minimization algorithm for turn n+1. The result is that a potential with minima having the same depth leads to profiles with two peaks at the same height.

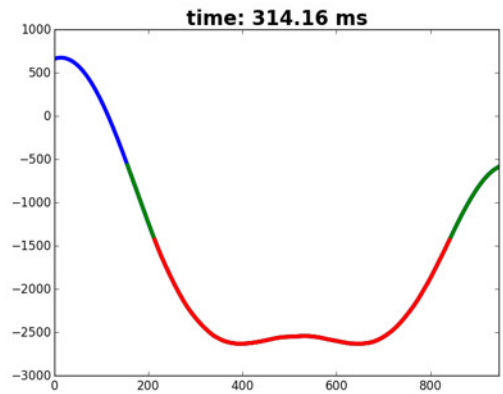

Figure 5: Example of total potential having the desired shape.

We obtained excellent results using this algorithm. Figure 6 shows the profile density evolution of a realistic simulation with intensity N=3.6×10^{12} and longitudinal emittance ϵ = 1.1 eVs.

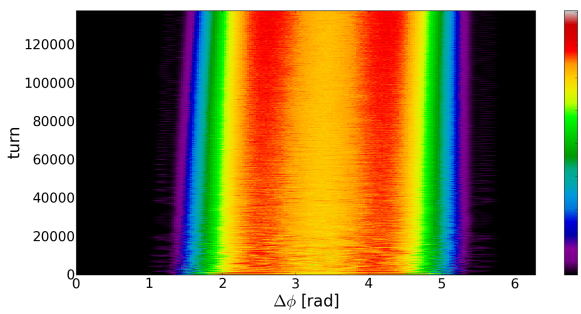

Figure 6: Density plot of the evolution of the bunch profile, from injection to time C400: the red stripes correspond to the two equal peaks.

ISBN 978-3-95450-185-4

Finally Fig. 7 shows the relative phase program used for that simulation (in red) together with the phase program without considering the multi-turn wake (in yellow). The difference is significant and shows the importance of memorizing the induced voltage for the following turns. For completeness the image shows the inaccurate solution $\Delta\phi_{1,2} = \pi - 2\phi_s$ as well (in blue) and the correct phase program in absence of intensity effects (in green).

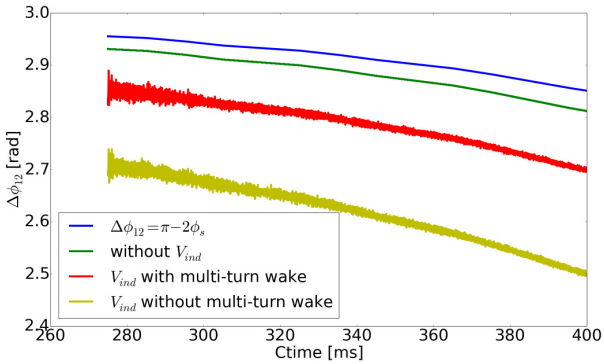

Figure 7: Phase shift programs between the two RF systems from injection to time C400.

PHASE AND RADIAL LOOPS

Phase and radial loops are fundamental to PSB operation, and it is impossible to smoothly accelerate high intensity beams without them. The phase loop is intended to shift the bucket onto the bunch trying to match the two of them, while the radial loop tries to keep the beam centred on the design orbit. The main result is to damp dipole oscillations of the beam.

This feedback mechanism has been implemeted in BLonD and tested on a realistic simulation for the post-LS2 scenario. We simulated a bunch with 0.37 eVs emittance in single RF with peak voltage V = 16 kV from C275 to C350. The collective effects were included with an intensity of 3.6×10^{12} protons. The small emittance and high peak voltage were chosen to have strong dipole oscillations in the absence of loops, see Fig. 8, the feedback routines significantly damp those oscillations.

RF PHASE NOISE FOR BLOW-UP

One of the requirements of LIU for the post LS2 scenario is to increase the longitudinal emittance to 3 eVs during the ramp, from an initial 1.4 eVs (this value is not definitive). With the present ramp, that is from 50 MeV to 1.4 GeV, an emittance of 1.4 eVs is currently achieved starting from 1 eVs using sinusoidal phase modulation of a high harmonic RF system. A separate cavity called C16, with high harmonic number h<=16, creates resonance islands inside the bunch, causing emittance blow up. While preliminary experiments and simulations show that the method based on phase modulation will be able to blow up the beam to the desired 3 eVs in the future, here we propose another approach

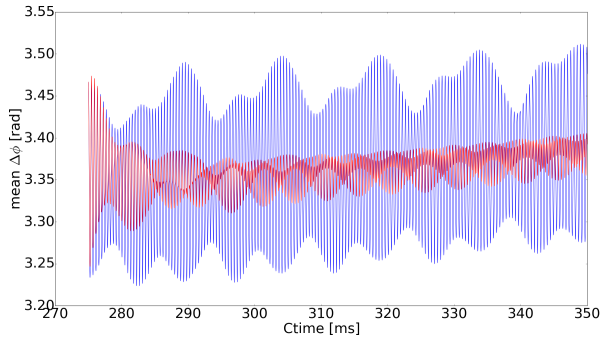

Figure 8: Dipole oscillations of the bunch from C275 to C350 with phase and radial loops on (red trace) and off (blue trace).

to increase the longitudinal emittance in a controlled way, with phase noise injection in the h=1 cavity. This method is currently used in CERN SPS and LHC [7] in the absence of dedicated high harmonic RF system. It has never been tested in the PSB, therefore simulations are a first step to understand if phase noise injection can be a valid alternative, or complement, to phase modulation.

The idea behind phase noise injection is simple. If we inject phase noise with a limited frequency band into a cavity, then all the particles inside the bunch having a synchrotron frequency inside that band will be excited and the amplitude of their oscillations will increase. Figure 9 explains the concept with an example. The red and green curves represent the synchrotron frequency distribution in single RF calculated in two different ways: The first tracks numerically macro-particles and counts how many times a certain particle crosses the axis dE = 0 in one second, the other calculates $f_s = dH/d\epsilon$ where $H(\Delta t)$ is the Hamiltonian passing through the point $(\Delta t, 0)$ and $\epsilon(\Delta t)$ is the area enclosed by it, that is the emittance (in blue). The yellow and black pairs of vertical lines define the bunch position according to two different conventions: The first pair derives from applying the foot tangent method to the bunch profile (PSB LIU current convention), the second discarding all the slices having fewer macro-particles than 5% of the profile peak. The two horizontal lines define the value of the bunch emittance according to the two conventions (around 1.2-1.3 eVs in the example) while the four dashed lines correspond to the frequency of the synchronous particle f_{s0} together with 0.9 f_{s0}, 0.8 f_{s0} and 0.7 f_{s0}. This plot shows for example that if we want to reach an emittance of 2 eVs we should apply a noise with band $[0.7f_{s0}, f_{s0}]$.

In simulation the noise is generated in the following way taking the LHC implementation as an example. We generate white noise in time domain sampling a standard normal distribution a finite number of times. By definition, its spectrum is flat along all the frequencies. The next step is to multiply it in frequency domain with our band limited spectrum S (usually constant inside the band and zero outside), obtaining the noise probability density $dPf = DFT(N) \times \sqrt{2f_{max}S}$;

ISBN 978-3-95450-185-4

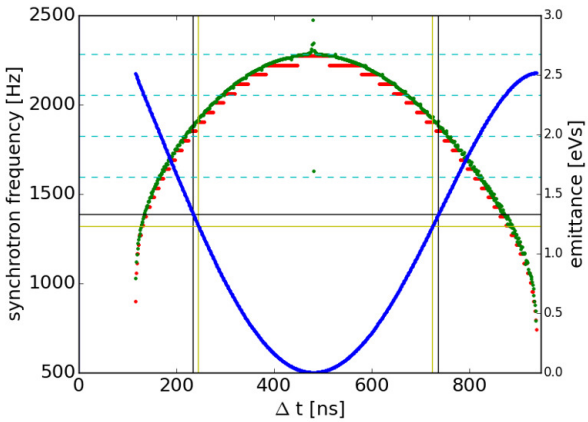

Figure 9: Example of synchrotron frequency distribution in single RF during acceleration; the emittance curve is in blue while the vertical lines define where the bunch position.

here $f_{max} = f_{rev}/2 = 1/(2T_{rev})$. Finally the desired phase noise in time domain is obtained calculating $IDFT(dPf)$.

All the simulations were done in single RF using the same momentum program. We made a first study choosing a constant peak voltage of 8 kV, this value is also currently used to accelerate the beam with the main harmonic C02 ferrite cavity. Figure 10 shows the bunch emittance along the cycle using the vertical cut convention discussed above. Starting from a realistic distribution from Linac4 having $\epsilon = 1.2$ eVs at injection time, the bunch loses 20 % of its particles in the interval [C600, C700]. From the plot we can see that the bucket area is not sufficient, even in an idealistic case without intensity effects (red curve) we would have little time to smoothly blow up the beam.

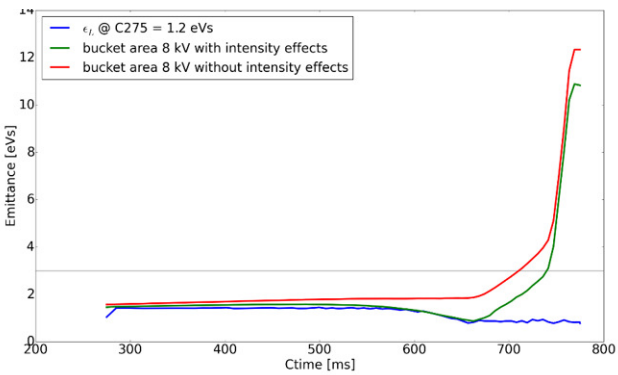

Figure 10: Emittance evolution with constant 8 kV (blue curve). Unacceptable number of losses in the second part of the ramp where the bucket area is not sufficient (green curve); the horizontal line is placed at 3 eVs to show the target.

We then examined the constant 16 kV peak voltage case, knowing that the Finemet cavities will be able to supply up to 24 kV. The result was quite different, enough time for blow up and sufficient bucket area made it possible to reach the target value of 3 eVs by injecting noise during the interval [C450, C600], see Fig. 11. The band of the spectrum was chosen as [0.8 f_{s0}, 1.1 f_{s0}], the lower margin was decided looking at the synchrotron frequency distributions between C450 and C600 and realising that the targeted emittance choosing 0.8 f_{s0} increased from 2 eVs to 3 eVs in that time interval, then we gradually rose the noise amplitude to a value leading to the desired blow up. Since f_{s0} decreases from about 1.75 kHz to 1 kHz in the interval [C450, C600], the phase noise was regenerated every 5000 turns to be able to follow the change. In addition, at every noise update, the amplitude of the spectrum was rescaled with f_{s0} to obtain the same noise strength $\sigma_{\phi_{noise}}$ during this time interval.

The profile at extraction had a bunch length lower than 205 ns, a $\delta p/p$ greater than 1.5×10^{-3} and the LIU specifications were fulfilled, in addition no particle losses were observed.

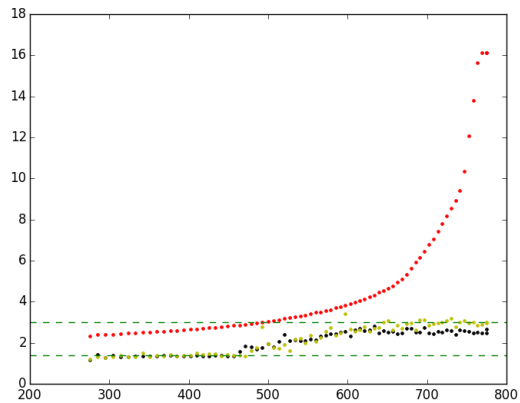

Figure 11: Emittance evolution with constant 16 kV starting from a 1.4 eVs bunch and injecting noise during the interval [C450-C600]. The foot tangent (yellow) and vertical cut (black) conventions are used to determine the corresponding emittances; the bucket area is in red.

CONCLUSION

Collective effects, as well as double RF operation in bunch-lengthening mode, phase loop and emittance blow-up are currently of fundamental importance in PSB operation, which will be the same in the post LS2 scenario. We showed that the BLonD code takes into account all these features and we gave examples of realistic simulations for the nominal LHC beam. We were able to blow up the emittance, as requested by LIU project, injecting phase noise in single RF. Further studies and simulations with intensity effects combining together blow-up, phase loop and double RF will complete the picture.

ACKNOWLEDGEMENT

We should thank the BLonD team at CERN. A special thank goes to A. Lasheen and J. E. Muller for valuable discussions on how to correctly implement intensity effects in low energy machines. Finally all the following people at CERN gave important help or support: M. E Angoletta, E. Benedetto, A. Blas, V. Forte, K. Hanke, M. Paoluzzi and G. Rumolo.

ISBN 978-3-95450-185-4

REFERENCES

[1] "LIU Technical Design Report - Volume I: Protons", edited by M. Meddahi and others, CERN-ACC-2014-0337, 2014

[2] M. M. Paoluzzi et al., "Design of the New Wideband RF System for the CERN PS Booster," IPAC'16, Busan (Korea), 2016, pp. 441-443.

[3] CERN BLonD code, `https://blond.web.cern.ch/`

[4] D. Quartullo and V. Forte, "Longitudinal Space Charge Simulations with BLonD at Injection in the CERN PS Booster," EuCARD2/XBeams Workshop on Space charge, Oxford, 2015.

[5] C. Zannini, private communications, CERN, 2014.

[6] V. Forte, E. Benedetto, A. Lombardi and D. Quartullo, "Longitudinal Injection Schemes for the CERN PS Booster at 160 MeV Including Space Charge Effects," IPAC'15, Richmond (USA), 2015, pp. 371-381.

[7] H. Timko, P. Baudrenghien and E. Shaposhnikova, "Studies on Controlled RF Noise for the LHC," HB2014, East-Lansing (USA), 2014, pp. 414-418.

ISBN 978-3-95450-185-4

ON THE IMPACT OF NON-SYMPLECTICITY OF SPACE CHARGE SOLVERS*

M. Titze†, CERN, Geneva, Switzerland
and Humboldt-University of Berlin, Germany

Abstract

To guarantee long-term reliability in the predictions of a numerical integrator, it is a well-known requirement that the underlying map has to be symplectic. It is therefore important to examine in detail the impact on emittance growth and noise generation in case this condition is violated. We present a strategy of how to tackle this question and some results obtained for particular PIC and frozen space charge models.

INTRODUCTION

A typical application of a space charge solver is to simulate the behaviour of a beam of charged particles over a reasonably long period of time inside a storage ring. In particular this is the case when studying emittance growth near resonance lines in a tune diagram [1].

On the one hand, it is a well-known fact that the simulation of a system admitting a Hamiltonian has to be symplectic in order to remain on the energy shell [2]. On the other hand, this basic condition is usually violated if one integrates the underlying equations of motion in a straightforward manner. Probably the most simplest example when this happens is the Explicit-Euler method. But also in the sophisticated case of a space charge solver, now acting on the set of bunches in a large dimensional phase space, symplecticity is not necessarily be fulfilled as we shall see.

In this article we present results in which we tested an analytic (Basetti-Erskine) solver, and a so-called (2 + 5)-D Particle-In-Cell (PIC) solver, which are both implemented inside the widely-used space charge tracking program PyORBIT, against the usual symplecticity condition. Both methods involve the addition of so-called space charge nodes at particular steps around the ring, which simulate the result of interaction between the charged particles. Our reference case will be the (uncoupled) plain tracking case obtained with PyORBIT and MAD-X.

The symplecticity checks were performed by using two different, but closely related, methods of numeric differentiation. These methods are straightforward and can basically be applied to any tracking code. We are mainly considering a test ring of 1km circumference with 416 space charge nodes, but also use a FODO map with just 4 nodes.

We will see that, as the reader probably might have expected, up to the precision of our methods the previously mentioned PIC solver violates the symplecticity condition, while the analytic solver is symplectic. We expect that the outcome of this violation might have an influence on long-term studies involving PIC solvers. One such effect which clearly distinguish both methods is the generation of noise in the transversal emittances in the PIC case [3]. The natural question thus arrises whether the symplecticity violation is the main driving term behind this behaviour.

In order to give an indication to the answer, we performed several tracking studies, using a low number of macroparticles, on a FODO cell and a small test ring. There are several reasons for choosing a low number: Firstly, due to the fact that we need at least to check the Jacobi-Matrix, we can not go much higher. Secondly, it turned out that a small ring with reasonable parameters can mimik a similar situation with a large phase-space. However, the outcome is also varing more, which has to be taken care off by simulating the same situation several times.

SYMPLECTICITY CHECKS

Before we are able to apply the numeric differentiation methods, let us remark that PyORBIT is not dumping the beam in canonical coordinates, a fact which must be taken into account.

Numeric Differentiation Method

A straightforward way of how to check the symplecticity of a numerical integrator at a given point x is to approximate its Jacobi-Matrix by 1D fits for every pair of directions. Namely, if $M\colon P \to P$ denotes the given map from $2k$-dimensional phase space $P \subset \mathbb{K}^{2k}$ to itself, we specify a step size[1] ϵ and approximate $\partial_j M_i(x)$ for a given point x by the slope of a linear fit of the values $M_i(x + k\epsilon b_j)$, $k \in \mathbb{Z}$, where the b_j denotes a basis and M_i the ith component with respect to that basis.

Then the symplecticity condition is checked by computing $R := (M')^{tr} J M' - J$, where $M' = (\partial_j M_i(x))_{ij}$ is the now determined Jacobi-Matrix of M at x and J the matrix representation of the given symplectic structure in the above basis. In the following we will understand by the (Frobenius) norm of R the distance of M at a given point $x \in P$ towards sympleciticity.

If we assume that in every direction b_j the amount of bunch configurations $x + k\epsilon b_j$ for variing k is the same number K, and if we denote the number of particles by N, we effectively have to track $36N^2K$ times through the ring to compute the entire Jacobi-Matrix. It is therefore not feasible to perform this computation for a large number of particles.

* Work supported by German Federal Ministry of Education and Research (BMBF)
† malte.titze@cern.ch

[1] In general this step size has to be choosen seperately for every direction and component.

ISBN 978-3-95450-185-4

Table 1: Symplecticity Error for Various Codes for a FODO Cell having 4 Space Charge Nodes

Code	$\|R\|_{2D}$
PyORBIT (pure tracking)	$1.4966 \cdot 10^{-5}$
Basetti-Erskine	$2.2518 \cdot 10^{-5}$
PIC	$3.5421 \cdot 10^{-3}$

But for a numeric confirmation of the non-symplecticity this is also not necessary.

2d Fit Method

An alternative way to check the symplecticity condition is based on the observation that around x we can write M in form of a Taylor series

$$M(x+a) = M(x) + M'(x)a + o(|a|^2).$$

Inserting for a the quantities ϵb_j and $\tilde{\epsilon} b_k$, in which ϵ and $\tilde{\epsilon}$ are sufficiently small, we obtain

$$\epsilon\tilde{\epsilon}\langle M'(x)b_j, M'(x)b_k\rangle = o(\epsilon\tilde{\epsilon}^2) + o(\epsilon^2\tilde{\epsilon}) + \langle M(x+\epsilon b_j) - M(x), M(x+\tilde{\epsilon}b_k) - M(x)\rangle.$$

M is then symplectic at x if, in the limit $\epsilon, \tilde{\epsilon} \to 0$, for every pair (j,k) of directions the coefficient in front of the $\epsilon\tilde{\epsilon}$-polynomial, given by the 2D-fit of the values

$$\langle M(x+\mu\epsilon b_j) - M(x), M(x+\nu\tilde{\epsilon}b_k) - M(x)\rangle, \qquad \mu,\nu \in \mathbb{Z},$$

equals $\langle b_j, b_k\rangle$. It is clear that this method works for any symplectic structure $\langle\cdot,\cdot\rangle$ and any basis.

BENCHMARKING RESULTS

Symplecticity Errors

Before we are going to benchmark the codes on our test ring, let us adress the question about which of the codes can we regard as 'symplectic', in the sense that its approximated derivative, given by one of the methods in the previous section, has an error which is so small, that the (uncoupled) drift case leads to a similar error.

To begin with, let us consider the case of a basic FODO cell having just 4 space charge nodes. Table 1 summarizes our findings: It shows that the symplecticity error with respect to the particle model (here 16 particles) is nearly the same for the Basetti-Erskin model and the plain tracking.

On the other hand, we see a rather significant error for the PIC case, which means that the code can hardly be symplectic.

Let us now turn to our model of a 1km ring with several space charge nodes. For the tracking around this ring (no space charge yet), it turns out that we basically require two different families of step sizes: one for the spatial directions and one for the momentum directions of the canonical coordinates (we used $\epsilon_q = 4 \cdot 10^{-4}$, $\epsilon_p = 1 \cdot 10^{-5}$).

Although the ring now contains all 416 space charge nodes and thus the sensitiveness is likely to be lower than the current step size, we can still ask how far the resulting map is away from a symplectic solution. In our case we found, for 16 macroparticles, a derivation of $|R|_{2D} = 8.9790 \cdot 10^{-5}$ and $|R|_{ND} = 3 \cdot 10^{-4}$ in case of the ND-method, so the 2D-fit method gives slightly better results. However, we found that in case of pure MAD-X tracking, we obtained for both modes $|R|_{\mathrm{2D}} = 2.4907 \cdot 10^{-6}$ and $|R|_{\mathrm{ND}} = 3.0440 \cdot 10^{-6}$ respectively, so the ND-method has almost the same precision here.

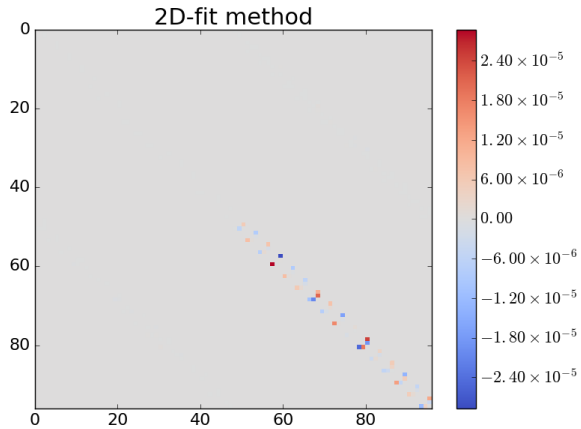

Figure 1: Typcial example of pure drift PIC error matrix R

Fig. 1 shows a typical example of the error matrix we obtained with the PIC solver, determined with the 2D-fit method. The entries in the error matrix usually do not drop below 10^{-6} and we take this scale as a rough lower limit of the precision of our methods.

Figs. 2 and 3 are showing the corresponding residuals of the fits for both methods, respectively, for a typical example of pairs of directions in which the residual were largest, by which we were able to check if the step sizes were choosen appropriately. Here we have used 16 macroparticles, the PIC space charge solver, 3rd order fits in every case and $K = 5$ different values to determine the slope at the midpoint.

The outcome of the corresponding symplecticty checks with space charge are shown respectively in Figs. 4 and 5 for the analytical- and the PIC solver.

Emittance Growth in the Sandbox Model

While starting some tracking simulations for 10k turns, we observed that our sandbox ring mimics roughly the behaviour of the 'large scale' scenario, if parameters are adjusted properly. This means that the growth in the mean of the horizontal and vertical emittances increases as in the large-scale case, and slows down when adding more particles.

However there is also a drawback: Namely the small number of macroparticles leads to a larger fluctuation of the outcome. This means that we have to perform tracking experiments repetitively to obtain results of better reliability.

ISBN 978-3-95450-185-4

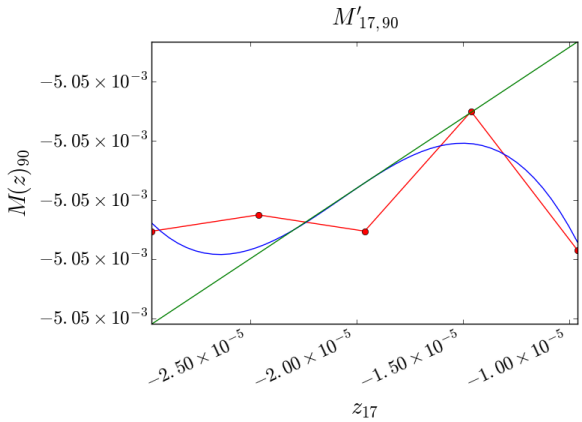

Figure 2: Slope fit of ND method.

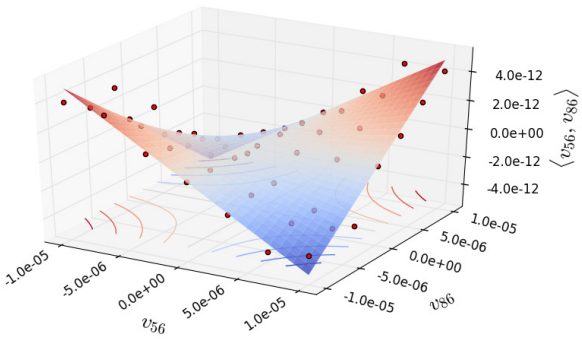

Figure 3: 2D-fit method.

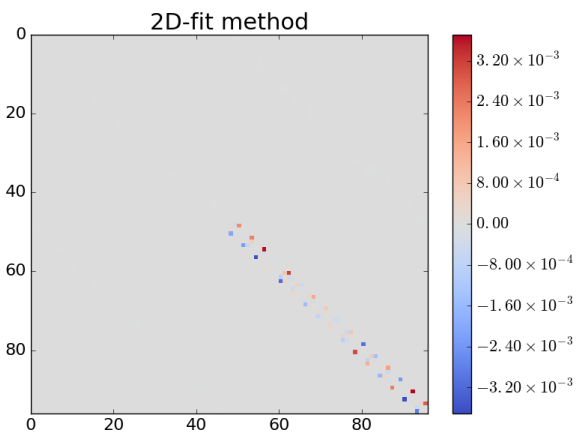

Figure 4: Basetti Erskine model with $|R|_{2D} = 0.0118$.

This was especially the case for particle numbers below approx. 25.

Our first goal was to determine, in dependency of the (random) initial coordinates, a possible correlation between the symplecticty error and the number of particles. The result can be found in Tab. 2.

As one can see from this table, the error reduces by adding more particles, which might be contrary to the picture that by adding more dimensions, one might add more space and thus be farther away.

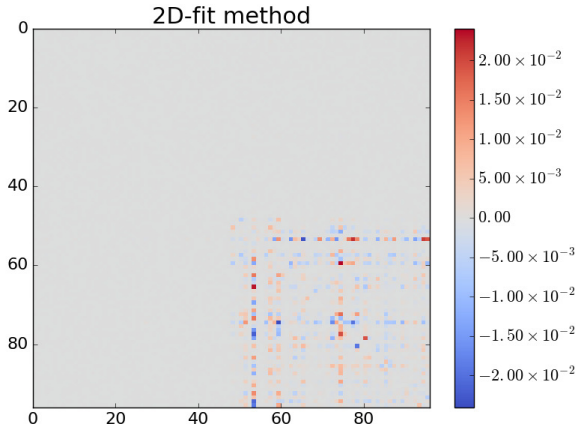

Figure 5: (2 + 5)-D PIC solver with $|R|_{2D} = 0.14461$

Table 2: Mean Values of Initial Error Matrices with Space Charge

Number of particles	$\|R\|_{ND}$	$\|R\|_{2D}$
8	3.1370	1.4629
12	0.8866	0.4711
16	0.3293	0.1950
20	0.2100	0.1063
24	0.1673	0.0877

Furthermore, we were looking at how the error in symplecticity evolves with the number of turns. Our results are summarized in the next four Figures 6 to 9 in which we were tracking a system of particles over 10k turns. The green curves shows the mean of the vertical and horizontal emittances. At every 500 turns we dumped the beam to a file and determined the error of the derivative of the one-turn map at that given point towards symplecticity (blue curves). The straight lines indicate regression fits of the green and blue data points respectively.

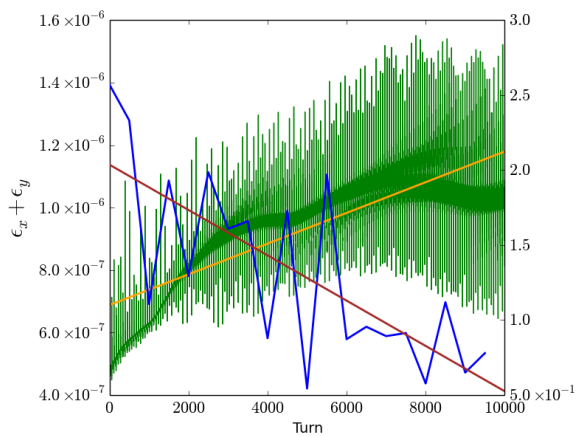

Figure 6: Mean emittance growth with 8 particles. Description: see text body.

ISBN 978-3-95450-185-4

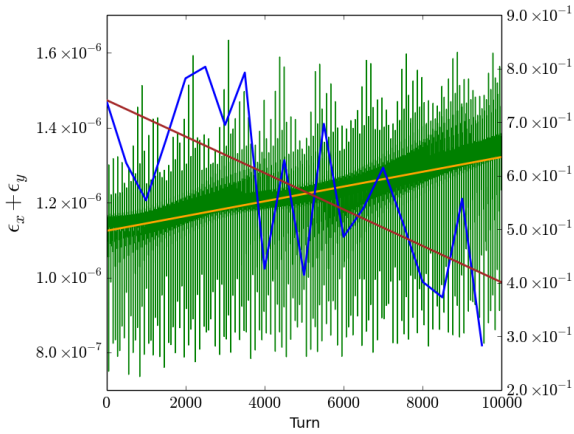

Figure 7: 12 particles.

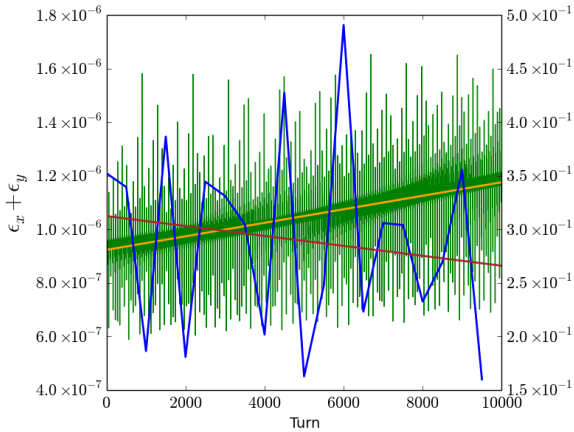

Figure 8: 16 particles.

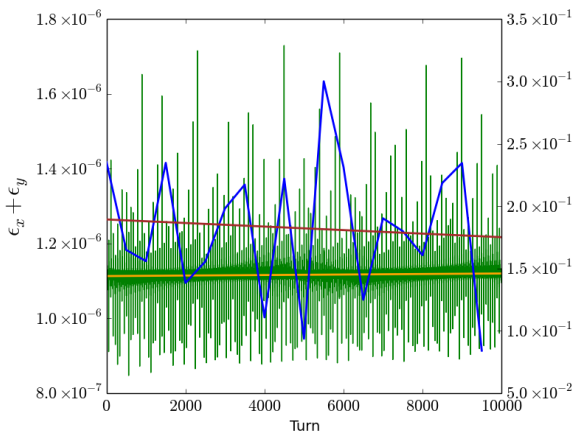

Figure 9: 20 particles.

These last benchmarkings indicate that there might be a correlation between the slopes of the emittance growth and the symplecticity errors. Our current explanation is that if the emittance increases, so does the phase space. If the particles are spread out more in phase space, there is less interaction between them, which means that we drop more and more into (symplectic) single particle tracking.

Of course, using regression lines may hide essential features and may not be appropriate here. But for a first try it should be good enough. In Fig. 10 we have plotted the slopes against each other, using 95% confidence intervals of the regression fits as error bars. It is clear that we require more data points to make further assertions, but a correlation is already been visible.

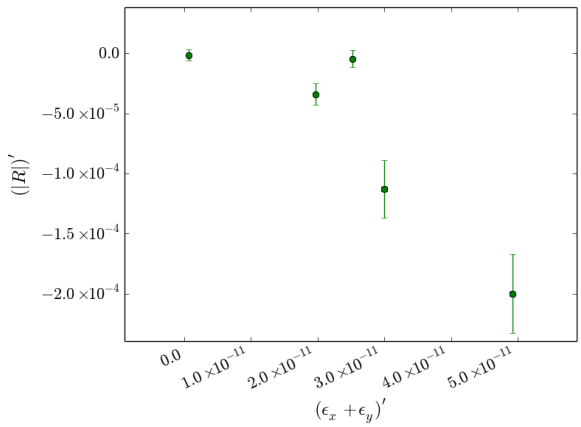

Figure 10: Slope of mean vert. and hor. emittances vs. slope of symplecticity error (2D-fit method here).

CONCLUSION

By using numeric differentiation methods we were able to determine the symplectic - respectively - non-symplectic nature of our space charge solvers. Furthermore we found certain correlations between the errors of symplecticity of the ring-map and the mean emittances growth of the beam.

We are currently gathering more data in oder to improve our picture and understanding.

ACKNOWLEDGEMENT

We would like to thank A. Oeftiger for many fruitful discussions and his essential help with certain coding issues. We also thank F. Schmidt, also for many fruitful discussions, H. Bartosik for his help with PyORBIT and last but not least we want to thank the sponsoring by the Wolfgang-Gentner-Program of the German Federal Ministry of Education and Research (BMBF).

REFERENCES

[1] H. Bartosik, Y. Papaphilippou, M. Benedikt, “Beam dynamics and optics studies for the LHC injectors upgrade”, in *CERN-THESIS-2013-257*, CERN, Geneva, Switzerland, Nov. 2013.

[2] H. Goldstein, "Klassische Mechanik", Akademische Verlagsgesellschaft, Frankfurt a.M., 1963.

[3] J. Struckmeier, “Concept of entropy in the realm of charged particle beams”, *Phy. Rev. E*, vol. 54, no. 1, p. 830 - 837, Jul. 1996.

ISBN 978-3-95450-185-4

SIMPLE MODELS FOR BEAM LOSS NEAR THE HALF INTEGER RESONANCE WITH SPACE CHARGE

C. M. Warsop, D. J. Adams, B. Jones, B. G. Pine, ISIS, Rutherford Appleton Laboratory, U.K.

Abstract

The half integer resonance is often used to define the high intensity limit of medium or low energy hadron rings where transverse space charge is significant. However, the mechanism leading to particle loss as beam approaches this resonance, which thus defines the limit, is not clearly understood. In this paper we explore simple models, based on single particle resonance ideas, to see if they describe useful aspects of motion as observed in simulations and experiments of 2D coasting beams on the ISIS synchrotron. Single particle behaviour is compared to 2D self-consistent models to assess when coherent motion begins to affect the single particle motion, and understand the relevance of coherent and incoherent resonance. Whilst the general problem of 2D resonant loss, with non-stationary distributions and nonlinear fields is potentially extremely complicated, here we suggest that for a well-designed machine (where higher order pathological loss effects are avoided) a relatively simple model may give valuable insights into beam behaviour and control.

INTRODUCTION

Background

The half integer resonance is often taken as defining the high intensity limit of hadron rings, where there is the expectation that lower order, quadrupole errors will drive the dominant loss. However, the details of mechanisms driving particle emittance growth and loss as beam approaches resonance are not well understood.

Whilst the well known intensity limit based on the incoherent tune shift gives a useful rule of thumb, it over estimates losses as it neglects coherent motion of the beam [1]. The coherent model, on the other hand, gives a fuller, self-consistent picture by taking into account the envelope modulation, and predicts resonance at the higher, coherent limit. However, coherent theory is based on Kapchinskij-Vladimirskij (KV) distributions and RMS equivalent models that are only valid as long as RMS emittances are conserved, i.e. when there is no emittance growth. Therefore, they cannot be used to understand particle motion and loss as beam approaches resonance. To derive models to explain such losses, a modified single particle model is required that includes the effect of the coherent response of the beam.

As a first step, this paper analyses single particle motion in the frozen space charge case for a representative waterbag beam. An initial comparison with coherent theory is also given. Future work will build on these results, exploring their limitations with detailed self-consistent simulations.

Building on Experimental Results from ISIS

The idea that single particle models should be useful for describing half integer resonance comes from experimental observations on the ISIS proton synchrotron [2]. Extensive experimental and simulation work studying the approach of half integer resonance in 2D coasting beams have characterized the evolution of transverse beam profiles in detail [2, 3]. Comparison of these results with comprehensive ORBIT models indicated that "lobe" features on profiles corresponded to half integer resonant islands. This suggests that a useful starting point for models is single particle theory, with the expectation that corrections for coherent effects will be required.

Below we calculate particle trajectories for resonant particle motion in a frozen space charge model, next we analyse the main dependencies this predicts for driving term strength, tune and intensity. Finally, we discuss and compare predictions with those from coherent theory, and outline future work.

FROZEN WATERBAG MODEL

This analysis considers the motion of a test particle, in a smooth focusing system, in the space charge field of a *frozen* waterbag beam distribution. This distribution is chosen as a representative case that includes key features a KV distribution does not: it has tune variation with amplitude and is non-stationary. It is the initial motion of this non-stationary distribution that we are interested in for studying the onset of resonance. This non-stationary waterbag beam would redistribute in any realistic *non-frozen* beam model, and this means the Hamiltonian derived below is certainly not an invariant over long time scales. Usually the type of analysis used here assumes resonance with long term invariance with KV beams, e.g. [4]. However, what is of interest here is the short term motion of a beam; its initial redistribution as it approaches resonance. Therefore, we use this *"short term invariant"* to predict the initial trajectories of particles, before the beam redistributes significantly. This should indicate how the beam behaves on approaching resonance.

The analysis of particle motion is made difficult by the piecewise definition required for the space charge potential inside and outside the waterbag beam. This complication is removed using the method of phase averaging, following work in [4]. This gives a smoothed action-angle approximation, from which we can extract particle motion.

Phase Averaged Hamiltonian

We analyse the motion of a test particle in the field of a 4D, axisymmetric waterbag beam with radius a of the form $n(r) = n_0(1 - \frac{r^2}{a^2})$, (for $r \leq a$, zero otherwise) with $r^2 =$

ISBN 978-3-95450-185-4

$x^2 + y^2$. We consider motion of particles in one plane only, e.g. the $y = 0$ plane, so $r = x$. The motion of the beam in one dimension is defined in canonical coordinates (x, P_x), with periodic "time" dependence s, via the quadrupole driving term $K_d(s)$, in a smooth focusing system with zero intensity tune $\omega = \frac{Q}{R}$. The periodic system corresponds to a ring of mean radius R with betatron tune Q. The Hamiltonian is:

$$H(x, P_x, s) = \tfrac{1}{2}P_x^2 + \tfrac{1}{2}\omega^2 x^2 + K_d(s)x^2 + V(x), \qquad (1)$$

where the space charge potential $V(x)$ is defined in a piecewise way as:

$$V(x) = \begin{cases} V_i = -k(\frac{x^2}{a^2} - \frac{x^4}{4a^4}), & \text{if } x \le a, \\ V_o = -k(\frac{3}{4} + \log\frac{|x|}{a}), & \text{if } x > a, \end{cases} \qquad (2)$$

with $k = \frac{q^2 N}{2\pi\epsilon_0 mc^2\beta^2\gamma^3}$ the perveance, q and m the particle charge and mass, N the number line density, c the speed of light and β and γ relativistic parameters.

To perform the phase averaging we now transform to action-angle variables (ϕ, J) defined by:

$$x = \sqrt{\frac{2J}{\omega}}\sin\phi; \quad P_x = \sqrt{2J\omega}\cos\phi, \qquad (3)$$

and then the aim is to determine $\overline{H} = \overline{H(\phi, J, s)} = \frac{1}{2\pi}\int_0^{2\pi} H(\phi, J, s)d\phi$, the Hamiltonian averaged over one betatron oscillation. The system is assumed to be near resonance. Equation (3) is substituted into (1) and (2), and the integrations completed.

It is convenient to split the Hamiltonian (1) into two parts, the simpler first three terms H_0 and the piecewise final term, that we average to find $\overline{V(J)}$. Phase averaging over H_0, with the assumption that the system is near a single half integer resonance, $2Q = l\theta$, with $\theta \equiv \theta(s) = \frac{s}{R}$, leads to the usual, well known result. The driving term is periodic with one dominant term: $K_d(s) = k_l \cos l\theta$, and we find

$$H_0 = \omega J + \frac{k_l J}{2\omega}\cos(2\phi - l\theta). \qquad (4)$$

The full Hamiltonian is now $\overline{H} = H_0 + \overline{V(J)}$, where the last term is the result of phase averaging over the piecewise potential (2). This, when expanded in action-angle coordinates, becomes

$$V_i = -\frac{k}{a^2}\Big[\frac{J}{\omega}\Big(1 - \cos 2\phi\Big) - \frac{J^2}{\omega^2 a^2}\Big(\frac{3}{8} - \frac{1}{2}\cos 2\phi + \frac{1}{8}\cos 4\phi\Big)\Big], \qquad (5)$$

$$V_o = -k\Big[\log\Big(\sqrt{\frac{2J}{\omega a^2}}|\sin\phi|\Big) + \tfrac{3}{4}\Big]. \qquad (6)$$

The phase averaging calculation depends on whether the test particle has an amplitude such that it is always within the beam (*core*), or one that exceeds the beam radius for some of the oscillation (*halo*). It is useful to define the normalised amplitude (as in [4]) given by $\sigma = x/a = \sqrt{2J/\omega a^2}$, where $\sigma = 1$ or $J = J_a = \omega a^2/2$, corresponds to the beam edge. For a particle always within the beam $J \le J_a$, $\sigma \le 1$ the phase averaging is just over the V_i term in (5).

$$\overline{V_c} = I_0 = \frac{1}{2\pi}\int_0^{2\pi} V_i d\phi. \qquad (7)$$

This gives a simple result, as oscillating terms average to zero (in the absence of driving terms, and in the incoherent approximation):

$$I_0 = k\Big[-\frac{1}{a^2\omega}J + \frac{3}{8}\frac{1}{a^4\omega^2}J^2\Big]. \qquad (8)$$

For a particle of an amplitude $J > J_a$, $\sigma > 1$, it is useful to define the angle ϕ_1 with $\sin\phi_1 = 1/\sigma$. This defines the phase at which the test particle crosses the beam boundary. To achieve the averaging we integrate over a representative part of the oscillation: the internal potential V_i is integrated from $\phi = 0 \to \phi_1$ and the external V_o from $\phi = \phi_1 \to \pi/2$:

$$\overline{V_h} = I_1 + I_2 = \frac{2}{\pi}\Big[\int_0^{\phi_1} V_i d\phi + \int_{\phi_1}^{\frac{\pi}{2}} V_o d\phi\Big]. \qquad (9)$$

The results of these integrations are

$$I_1 = -\frac{k}{a^2}\Big[\frac{J}{\omega}\Big(\phi_1 - \frac{1}{2}\sin 2\phi_1\Big) - \frac{J^2}{w^2 a^2}\Big(\frac{3}{8}\phi_1 - \frac{1}{4}\sin 2\phi_1 + \frac{1}{32}\sin 4\phi_1\Big)\Big], \qquad (10)$$

and

$$I_2 = -k\Big[\frac{3}{4}\Big(\frac{\pi}{2} - \phi_1\Big) + F(\sigma)\Big]. \qquad (11)$$

where the integral $F(\sigma) = \int_{\phi_1}^{\pi/2}\log(\sigma|\sin\phi|)d\phi$, $(\phi_1 > 0)$ is not defined in terms of normal functions, but in the domain relevant here is simple in form and easily tabulated, see Fig. 1.

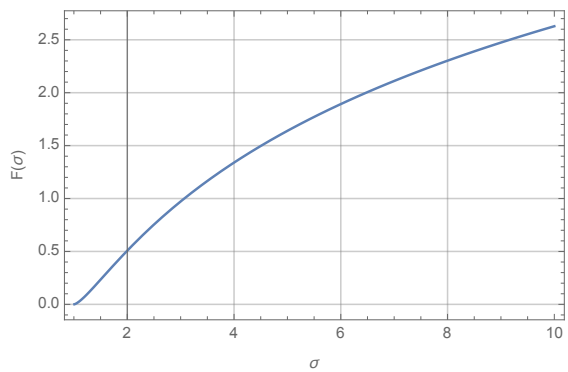

Figure 1: The function $F(\sigma)$.

The s dependence due to resonance in H_0 (4) is removed via a canonical transformation with an F_2 generating function and associated equations:

$$F_2 = \bar{J}(\phi - \frac{l}{2}\frac{s}{R}); \quad J = \bar{J}; \quad \bar{\phi} = \phi - \frac{l}{2}\frac{s}{R}; \quad \bar{H} = H - \frac{l}{2R}J. \qquad (12)$$

ISBN 978-3-95450-185-4

The result is

$$\overline{H} = \overline{H(J,\bar{\phi})} = \delta J + SJ\cos 2\bar{\phi} + \overline{V(J)}, \qquad (13)$$

where $\delta = (\omega - \frac{l}{2R}) = \frac{1}{R}(Q - \frac{l}{2})$, $S = \frac{k_l}{2\omega}$ and,

$$\overline{V(J)} = \begin{cases} V_c = I_0 & \text{if } J \le J_a \quad (core). \\ V_h = I_1 + I_2 & \text{if } J > J_a \quad (halo). \end{cases} \qquad (14)$$

Essentials of Particle Motion

We now look at the predictions of this model, using the example of a nominal coasting beam in the ISIS ring. Resonance in just one plane is considered, $2Q_y = 7$ (particles are assumed to have zero amplitude in the orthogonal plane). The relevant parameters are: $Q_y = 3.60$, R =26 m, a =0.05 m, $l = 7$, $\Delta k_7 = 0.005$ ($\Delta k_7 = k_7/k = 2k_7/\omega^2$), and $N_p = 4.4 \times 10^{13}$ ppp (protons per pulse, where $N = N_p/(2\pi R)$). By setting the driving strength $\Delta k_7 = 0$ and using numerical solutions for $F(\sigma)$ and its derivative we can calculate the frequency variation with J, i.e. $w(J) = Q(J)/R = \frac{\partial H(J)}{\partial J}$. This is shown in Fig. 2.

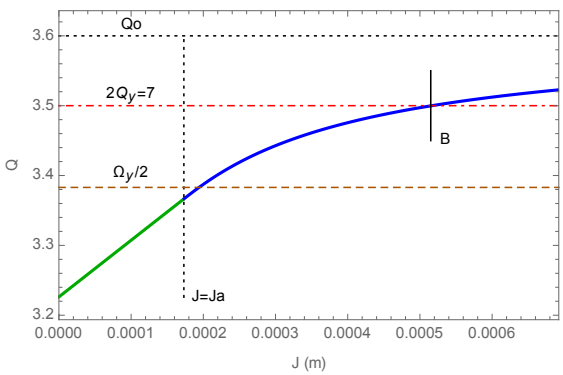

Figure 2: Example of $Q(J)$ for waterbag beam (see text).

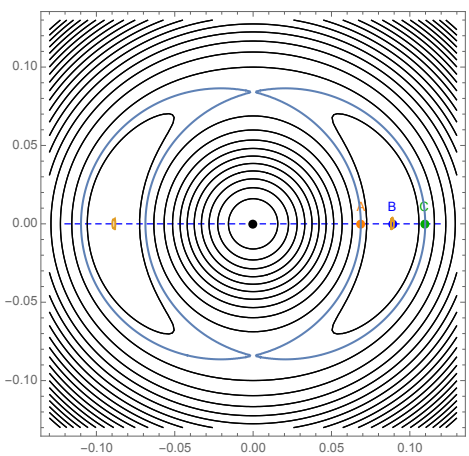

Figure 3: Example of $\overline{H}$ for waterbag beam, normalized coordinates $(x, P_x/\omega)$ in metres (see text).

The system is a non-linear oscillator with a frequency characterized by the $Q(J)$ dependence above. Single particle resonance, i.e. the stable fixed point, coincides with the intercept of the $Q(J)$ curve with the $Q_y = 3.5$ line in Fig. 2 (point "B"). Contours of the *"short term invariant"* surface $\overline{H}$, equation (13) are shown in Fig. 3. The contours of this surface give an indication of the initial trajectories of particles, of the nominally matched beam, here of radius 0.05 m. Of particular interest is the stable fixed point ("B" in Fig. 3), and also the inner and outer limits of the separatrix and their intercepts with the x-axis (points "A" and "C" in Fig. 3). The fixed points are calculated in the normal way, using $\dot{\phi} = 0$, $\dot{J} = 0$ with Hamilton's equations, and the separatrix being the contour that passes through the unstable fixed point. Particles drawn along trajectories corresponding to the contours shown will either be confined in the central core region, drawn outward to oscillate about the the fixed points at the centre of the two resonant islands, or else make larger oscillations around both islands. The two resonant islands are expected to correspond to "lobes" observed in transverse profile measurements on ISIS. This model now allows us to predict the variation of the location and extent of these lobes with respect to beam parameters.

Comparison with Simple Tracking Results

The results presented here, $Q(J)$ and $\overline{H}$, have been compared with tunes and Poincaré maps from simple 1D particle tracking results, where motion was integrated directly and piecewise potentials explicitly included. Results show good agreement within the expected approximations.

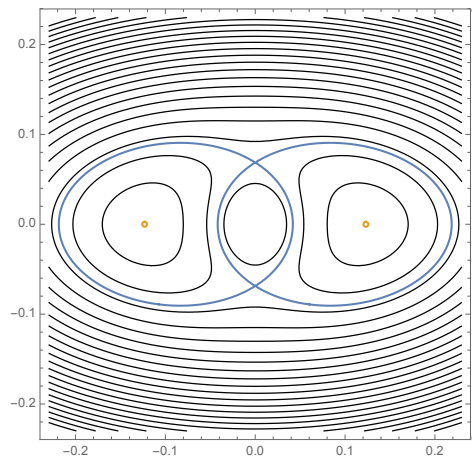

Figure 4: $\overline{H}$ with increased driving term strength Δk_7, note change in scale (see text).

PREDICTIONS OF MODEL

Continuing with the simplified example of ISIS, the dependence of $Q(J)$, $\overline{H}$ on beam parameters is now investigated.

Effect of Driving Term Strength

Beam parameters assumed are $Q_y = 3.60$, $R = 26$ m, $a = 0.05$ m, $l = 7$, $N_p = 4.4 \times 10^{13}$ ppp and various values of Δk_7. Results for $\Delta k_7 = 0.005$ are shown in Fig. 3. When $k_7 = 0$ the lobes disappear and contours become circular. Setting $\Delta k_7 = 0.05$ gives the result in Fig. 4. The

ISBN 978-3-95450-185-4

results show that the effect of increasing driving strength is to increase asymmetry and enlarge the extent of the two resonant lobes, whilst reducing the size of the central core region. In Fig. 5 we show in detail the variation of the stable fixed point and inner and outer limits of the separatrices (points "A", "B" and "C" defined in Fig. 3) with driving strength.

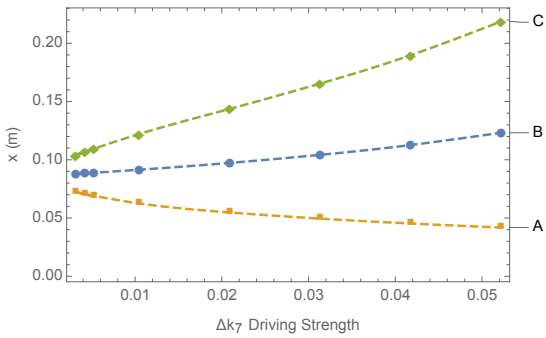

Figure 5: Dependence of island location and size on driving term strength.

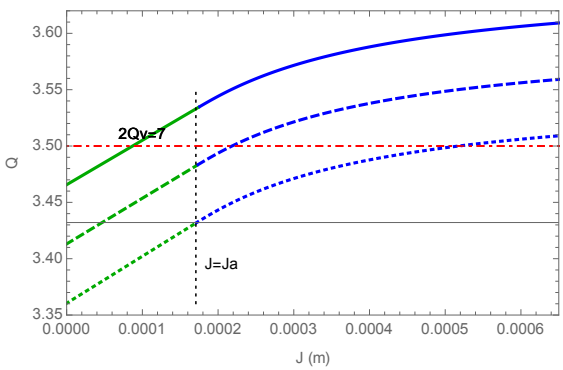

Figure 6: $Q(J)$ as a function of lattice Q (see text).

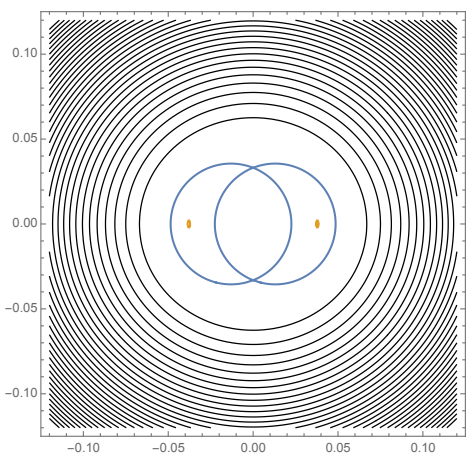

Figure 7: $\overline{H}$ with raised $Q = 3.65$ (see text).

Effect of Q

The effect of varying lattice tune $Q = \omega/R$ is now examined. Beam parameters are $R = 26\,\mathrm{m}$, $a = 0.05\,\mathrm{m}$, $l = 7$, $N_p = 2.2 \times 10^{13}$ ppp. In Fig. 6, the dependence $Q(J)$ is shown for $Q = 3.65,\ 3.60,\ 3.55$ (top to bottom), $\Delta k_7 = 0$. The results show that as the lattice tune moves down, so the $Q(J)$ intercept with $Q_y = 3.5$, the stable fixed point and islands, move outward through the beam. In Fig. 7 the surface of $\overline{H}$ is shown for $Q = 3.65$, $\Delta k_7 = 0.005$: the stable fixed points are near the core of the beam as expected. This suggests that higher Q values may perturb the core a little, but generate smaller halo than lower tunes, where location of the stable fixed point suggests particles (and profile lobes) would be pulled further out from the core.

Effect of Intensity

The dependence of $Q(J)$ for three different intensities $N_p = 1.1,\ 2.2,\ 4.4 \times 10^{13}$ ppp, (top to bottom), is shown in Fig. 8, with parameters: $Q = 3.60$, $R = 26\,\mathrm{m}$, $a = 0.05\,\mathrm{m}$, $l = 7$, and $\Delta k_7 = 0$. In this case the effect is to move the stable fixed point from the core to the outside of the beam as intensity increases, with a corresponding movement of the resonant islands and profile lobes.

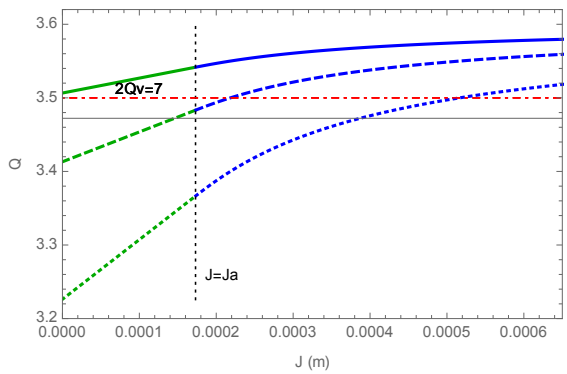

Figure 8: $Q(J)$ as a function of intensity (see text).

Effect of Dynamic Intensity and Q Ramps

In a situation with a real beam, often the parameters above will change with time. For example, during multi-turn injection, intensity will ramp over 100s of turns. One might expect the situation in Fig. 8 to be descriptive, with the tunes in the beam pushing down with intensity and the separatrices moving correspondingly outward. Similarly, ramping the tune by changing quadrupoles in the lattice may give a dynamic situation related to Fig. 6. This simple picture ignores many complications, as discussed below.

LIMITATIONS OF THE MODEL

Non-Stationary Distribution, Mismatch

The fact that the waterbag distribution is non-stationary means that over long time scales the above analysis will not predict particle trajectories. If, in addition, beams are strongly mismatched, then redistribution may be faster and correspondence to the above analysis weaker. However, it may be that once the beam has redistributed and "grown",

ISBN 978-3-95450-185-4

the above model, with a modified beam radius, will give a first estimate of behaviour.

Coherent Motion

As noted, the above model is not self-consistent, and thus *ignores any coherent response* of the beam. Coherent effects will, in general, modify space charge fields and particle motion. Near coherent resonance effects on the beam are expected to be strong and a frozen single particle model to have limited value. However, further away from resonance effects will be weaker, and single particle models would be expected to explain main features of the motion, perhaps with some smaller modifications.

The dependence of coherent frequency of the beam envelope on space charge can be estimated using the concept of equivalent beams [1]. We expect the RMS parameters and resonant frequencies of our waterbag beam to behave in the same way as a KV beam with the same RMS emittance (ϵ_{RMS}). The edge of the 4D waterbag beam is at $6\epsilon_{\mathrm{RMS}}$. Assuming a circular beam and the large tune split approximation valid for ISIS (nominal tunes $(Q_x, Q_y) = (4.31, 3.83)$), we find coherent frequencies using (in the notation of [1]):

$$\Omega_y = \sqrt{4Q_y^2 - 5Q_x\Delta Q_x} \tag{15}$$

with $\Delta Q_x = r_p N_p/(2\pi\beta^2\gamma^3 4\epsilon_{\mathrm{RMS}})$, r_p is the proton radius. This theory is two dimensional and provides coherent frequencies in both planes, but for this 1D model only one plane is relevant.

An example is shown in Fig. 2, where $\frac{\Omega_y}{2}$ is shown as the horizontal dashed line. This is expected to sit above the peak incoherent shift (as the coherent intensity limit is higher than the incoherent) [1], and its relative position will scale proportionately with intensity. When the driving frequency ($2Q_y = 7$ line) approaches the coherent frequency $\frac{\Omega_y}{2}$, then coherent resonance is expected with large coherent envelope oscillations and associated beam redistribution. Otherwise, coherent effects will be less pronounced and predictions of the single particle model will be more useful (with modification).

In Fig. 2, the system is away from coherent resonance: lowering the intensity would move the coherent tune upward towards resonance. This gives a first indication of when coherent effects will dominate: future work will make more use of predictions of RMS envelope motion to modify the above model, and test the results in detail with simulations.

2D Motion, Higher Order Effects

The work above ignores the motion of particles with finite emittance in the plane orthogonal to resonance. Assuming no additional resonance or coupling, one may expect the average effect to be a reduced average tune shift for larger amplitude particles, as they spend less time in the core of the beam. Future work will investigate this in more detail. The possibility of other resonances and space charge (particularly octupole) terms also need to be considered.

SIMULATIONS AND EXPERIMENTS

Comparison with Simulations

Work is presently underway comparing the results above with output from 2D self-consistent simulations (using the ISIS SET code). Initial results show reasonable agreement of incoherent frequency distributions and coherent frequencies between the above model and a simulated waterbag beam. There is also some correspondence between phase space distributions and phase space structure predicted above, but more detailed analysis is required.

Comparison with Experiments

ISIS experiments, where coasting high intensity beams are pushed onto the half integer resonance are described in [2, 3]. In these experiments profiles were observed to form a lobe on each side of the central beam distribution, corresponding to the resonant islands discussed above. The size and distance of these with respect to the central beam core has been measured as a function of driving strength and tune. The lobes were observed to move outward with increasing driving term strength and also outward as the tune was lowered. This is in *qualitative* agreement with the predictions above. However, more work is required to address the approximations in the model and thus allow a more useful *quantitative* comparison.

SUMMARY

The *"short term invariant"* Hamiltonian for a frozen waterbag beam has been calculated using the method of phase averaging. This has been used to give predictions of the dependence of halo structure on parameters of driving strength, tune and intensity. The limitations in the model have been discussed and the influence of coherent effects briefly assessed. Predictions show qualitative agreement with experimental observations. However, further developments of calculations and detailed comparisons with self-consistent simulations are required to facilitate a more quantitatively predictive model.

REFERENCES

[1] R. Baartman, "Betatron Resonances with Space Charge", in *Proc. Workshop on Space Charge Physics in High Intensity Hadron Rings*, Shelter Island, NY, 1998 *AIP Conf. Proc.*, CP448, pp.56–71.

[2] C. Warsop *et al.*, "Studies of Loss Mechanisms Associated with the Half Integer Limit on the ISIS Ring", in *Proc. HB2014*, East-Lansing, MI, USA, November 2014, paper MOPAB40, pp. 123–127.

[3] C. Warsop *et al.*, "Simulation and Measurement of Half Integer Resonance in Coasting Beams in the ISIS Ring", in *Proc. HB2012*, Beijing, China, November 2012, paper WEO1C02, pp. 434–438.

[4] M. Venturini *et al.*, "Resonance analysis for a space charge dominated beam in a circular lattice", *Phys. Rev. ST Accel. Beams*, vol. 3, p. 034203, Mar. 2000.

ISBN 978-3-95450-185-4

DEVELOPMENT OF PHYSICS MODELS OF THE ISIS HEAD-TAIL INSTABILITY

R.E. Williamson, B. Jones, C.M. Warsop, ISIS, Rutherford Appleton Laboratory, STFC, UK

Abstract

ISIS is the pulsed spallation neutron and muon source at the Rutherford Appleton Laboratory in the UK. Operation centres on a rapid cycling proton synchrotron which accelerates 3×10^{13} protons per pulse from 70 MeV to 800 MeV at 50 Hz, delivering a mean beam power of 0.2 MW.

As a high intensity, loss-limited machine, research and development at ISIS is focused on understanding loss mechanisms with a view to improving operational performance and guiding possible upgrade routes. The head-tail instability observed on ISIS is of particular interest as it is currently a main limitation on beam intensity.

Good models of impedance are essential for understanding instabilities and to this end, recent beam-based measurements of the effective transverse impedance of the ISIS synchrotron are presented. This paper also presents developments of a new, in-house code to simulate the head-tail instability and includes benchmarks against theory and comparisons with experimental results.

INTRODUCTION

The transverse head-tail instability is a main concern for high intensity operation in many hadron synchrotrons including ISIS and its proposed upgrades. The instability imposes a limit on beam intensity through associated beam loss and the subsequent undesired machine activation. However classical theories, such as the model of Sacherer [1], do not include space charge and associated tune spreads which are required for accurately modelling high intensity beams.

Recent work [2 – 4] has put forward limited theoretical models to treat head-tail motion in the presence of space charge. However, currently there is no comprehensive model of head-tail with space charge. Testing of these models against observations is required to ascertain fully their usefulness and limits. As such, numerical simulations have been employed [5] to analyse collective effects and link experimental results to theory. Ultimately, understanding head-tail in high intensity beams may allow improved operations avoiding the instability, with lower beam losses and the possibility of higher beam intensities.

The ISIS Synchrotron

ISIS operation centres on a rapid cycling synchrotron (RCS) with a 163 m circumference composed of 10 superperiods. It accelerates 3×10^{13} protons per pulse (ppp) from 70 – 800 MeV on the 10 ms rising edge of a sinusoidal main magnet field. The repetition rate of 50 Hz results in an average beam power on target of 0.2 MW.

Injection is via charge exchange of a 70 MeV, 25 mA H^- beam over ~130 turns with painting over both transverse acceptances, collimated at 300 π mm mrad. The unchopped, injected beam is non-adiabatically bunched and accelerated by the ring dual harmonic RF system (h = 2 and 4). Nominal betatron tunes are $(Q_x, Q_y) = (4.31, 3.83)$ with peak incoherent tune shifts exceeding ~ -0.5. The beam intensity is loss limited with the main driving mechanisms being foil losses, longitudinal trapping, transverse space charge and the head-tail instability [6].

Measurements on ISIS have consistently shown that the two proton bunches exhibit vertical head-tail motion over 1 – 2.5 ms into the 10 ms acceleration cycle [7, 8]. The instability is suppressed by ramping the vertical tune down, away from the integer ($Q_y = 4$) during the time of the instability. However, with rising operating intensities, beam losses associated with head-tail increase and lowering the tune further tends to induce beam loss associated with the half integer resonance [9, 10].

Recent studies have shown that the instability is present with dual harmonic RF acceleration as well as with single harmonic RF [10, 11], and possibly worse with the second harmonic. Work is ongoing to develop a feedback system to damp the instability [12] alongside studies modelling and understanding the instability mechanism.

This study presents initial developments in building impedance and instability simulation models of the ISIS synchrotron. Beam-based measurements of the effective transverse impedance are presented. These allow for a better understanding of the driving force behind the head-tail instability.

A new in-house macro-particle simulation code, currently in development to simulate the head-tail instability as observed on ISIS, is also introduced. Convergence tests of the code are presented together with benchmarks against theory. Simulations are compared to experimental data from ISIS with single harmonic RF acceleration. Plans for future experimental studies, simulation and theory work are outlined.

Head-Tail Observations

ISIS operates at the natural machine chromaticities ($\xi_x = \xi_y$ = -1.4 [13]), without sextupole correction. As mentioned above, the impedance acting on the beam leads to a coherent vertical instability early in the acceleration cycle. Measurements have been made using a vertical beam position monitor (BPM) over 0 – 5 ms during acceleration in the case of lower intensity beams (5×10^{12} ppp) and single harmonic RF. Measurements at this intensity minimise the effect of space charge and allow direct comparison with Sacherer theory. Further measurements at high intensity and with dual harmonic

ISBN 978-3-95450-185-4

RF were also taken [10, 11] but are not discussed in this paper.

Figure 1 shows a typical vertical BPM sum and difference signal over several turns during the instability, with single harmonic RF, indicating clear head-tail motion with mode $m = 1$. Using the vertical tune at 1 ms ($Q_y = 3.83$), and the chromaticity given above, the accumulated phase shift $\chi = 11.25$ rad. From Sacherer's theory the growth rate of each head-tail mode may be calculated. However, as found in previous studies [7, 8], this value of χ results in a higher growth rate for head-tail mode $m = 2$ than $m = 1$. A modified theory that could explain this is given in the same reference.

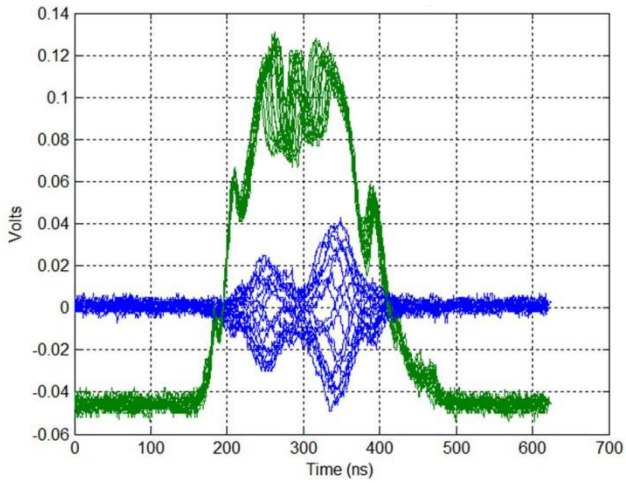

Figure 1: Sum (green) and difference (blue) vertical BPM signals over several turns around 1 ms through the acceleration cycle.

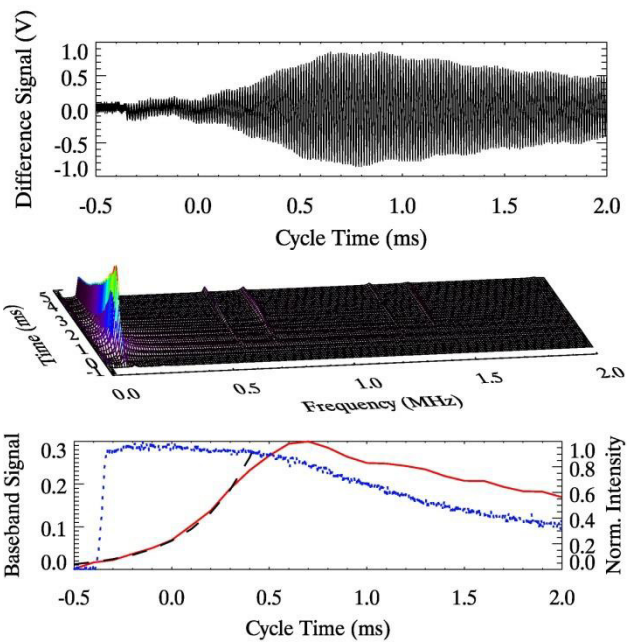

Figure 2: Vertical BPM difference signal, top; its Fourier transform as a function of time, middle; baseband (red), exponential fit (dashed black) and beam intensity (dotted blue) as a function of time, bottom. Peak intensity = 4.6×10^{12} ppp.

BEAM-BASED IMPEDANCE MEASUREMENTS

Operating with the RF off and a DC main magnet field, observations of steady-state coasting beams provide important measurements related to instabilities and the effect of space charge. Central to these is an understanding of the impedance of the machine and the identification of their source(s).

Operating at nominal Q values, beam loss associated with vertical beam growth is observed at intensities $> 3\times10^{12}$ ppp. Measurements of the vertical growth rate of this coasting beam instability can be made using BPMs [14]. An example, shown in figure 2, clearly exhibits strong coherent motion associated with the lowest betatron sideband frequency (baseband), $(Q_y - 4)\omega_0 = q\omega_0$. Growth times increase rapidly with intensity and as Q_y approaches 4.

Growth Rate Versus Intensity

Coasting beam theory [1] predicts the transverse frequency shift due to an applied impedance $Z_\perp$ to be,

$$\Delta\omega = i\frac{ec}{4\pi Q\gamma E_0}Z_\perp I\,. \qquad (1)$$

Assuming a time dependence, $e^{i\omega t}$, the associated growth rate is $\tau^{-1} = -\mathrm{Im}(\Delta\omega)$ so instability corresponds to a real negative impedance. Equation 1 also implies that for a given tune (Q) and beam energy (γE_0) the growth rate is linear with intensity (I).

An example measurement of vertical growth rate as a function of intensity, for $Q_y = 3.83$ is shown in figure 3, where the growth rate is given by an exponential fit to the baseband signal. Error bars on growth rate are one sigma uncertainty estimates from the exponential fit. The linear fit of growth rate against intensity may be compared to equation 1 to find an effective impedance for the frequency of that sideband. Similar results are found at different tune values.

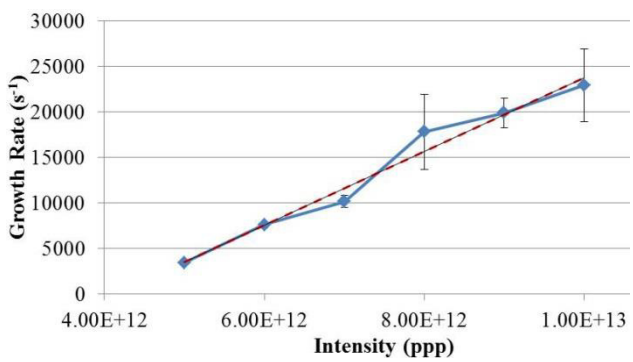

Figure 3: Growth rate versus beam intensity ($Q_y = 3.83$). Effective impedance at this tune is 5.76 ± 0.5 MΩ/m.

Growth Rate Versus Tune

Changing the vertical tune moves the baseband frequency $(Q_y - 4)\omega_0$ and, as such, probes the

ISBN 978-3-95450-185-4

impedance at a different frequency. It also alters the growth rate directly, as seen in equation 1. Figure 4 shows the growth rate as a function of vertical tune at a fixed beam intensity. The growth rate is measured as in the previous section. The error on measured Q_y ($\pm$ 0.0022) stems from the resolution of the Fourier transform.

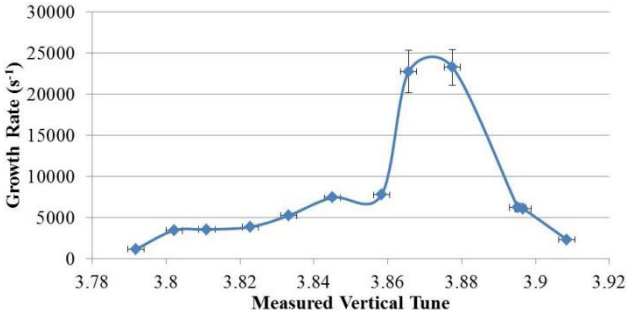

Figure 4: Growth rate versus measured vertical tune. Intensity = 1×10^{13} ppp.

With this data and equation 1 the effective impedance can be calculated as a function of frequency (measured baseband frequency), figure 5. The error on the measured effective impedance is combined from the exponential fit required for each data point and the error on the measured betatron tune. It is clear from figure 5 that there is a sharp narrowband impedance around 85 kHz with a full width of ~25 kHz, peaking at 3.71 ± 0.35 MΩ/m. The position of the narrowband impedance, its width and height, are consistent between measurement campaigns.

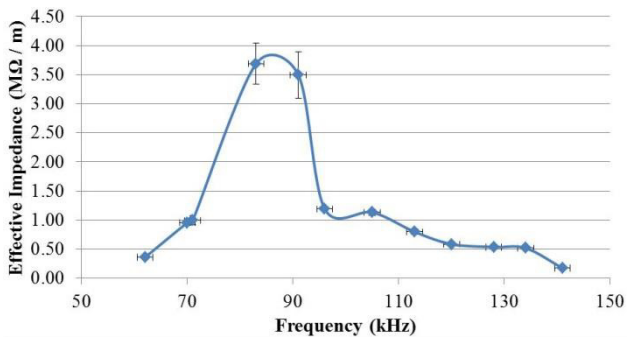

Figure 5: Effective impedance versus baseband frequency. Intensity = 1×10^{13} ppp.

Measurements Summary

Measurements of coasting beam growth rates have been made and compare favourably with the theoretical model of Sacherer with growth rates increasing linearly with intensity. Data were also taken at different painted beam emittances with similar results as a function of intensity.

Experimental observations show that head-tail growth rates increase rapidly as Q_y increases toward 4 which has led to the resistive wall being cited as the driving impedance [7, 8, 11]. However, crude calculations of the resistive wall impedance, from the thick-wall formula, result in lower growth rates than those observed.

It is clear from the growth rate as a function of tune, and the interpreted effective impedance versus frequency, that there is a vertical narrowband impedance at ~85 kHz. This could be the driver for head-tail motion seen in ISIS RCS operation. The origin of the narrowband impedance, and its relevance to head-tail is currently under investigation.

NEW SIMULATION MODEL

A new, stand-alone macro-particle simulation code has been written to study head-tail behaviour on ISIS. The code is based on an existing in-house longitudinal code [15] with the addition of a simple smooth focusing model for transverse motion and wakefield kicks to simulate the interaction between the beam and its environment.

Wakefield Model

Wakefield kicks are implemented in the code on a turn-by-turn basis by default, but can be more frequent. As with similar codes [16, 17] the beam is segmented longitudinally and the wake calculated at each slice due to the effect of each upstream slice. This may be from particles within the same bunch or from preceding bunches.

Most theoretical wakefield models assume ultra-relativistic beams ($\beta\sim1$). This means that, in order not to violate the principle of causality, wakes can only propagate backwards and influence subsequent particles. However, head-tail behaviour on ISIS is observed at β values much lower than this (~0.4). The importance of this in instability modelling is not fully understood.

For initial convergence tests and benchmarks ISIS parameters have been assumed. A thick resistive wall wakefield has been modelled with the wake function [5],

$$W_{RW}(z) = -\frac{cL_{RW}}{b^3}\left(\frac{\beta}{\pi}\right)^{3/2}\sqrt{\frac{Z_0}{\sigma z}} \qquad (2)$$

where L_{RW} is the length of the resistive wall, b is the beam pipe radius, $\beta = v/c$ the relativistic parameter, Z_0 is the impedance of free space and σ is the beam pipe conductivity. As noted above the β dependence is important in the case of ISIS beams.

Convergence Tests

To ascertain whether the particle tracking code is accurately modelling the relevant physics a number of convergence tests have been performed. In these tests simulations were run without RF, with a DC main magnet field, resistive wall wake and a high beam pipe conductivity of 100 $\Omega^{-1}m^{-1}$. A constant beam pipe radius was assumed with uniform impedance around the ring.

Investigations were made of the number of simulated turns, number of longitudinal slices, number of macro-particles, random number seed and the number of time points for the growth rate fit. Convergence was considered attained when the change in growth rate between parameters was smaller than the error on the calculated growth rate, ~1% error. The error on the

ISBN 978-3-95450-185-4

growth rate arises from the finite length of simulation, the number of macro-particles and longitudinal slices. No space charge was included in these tests.

Coasting Beam Benchmarks

With the converged simulation parameters a number of benchmarks were performed to evaluate the code against theory. Similar to the beam-based impedance measurements, equation 1 was tested by varying the beam intensity and tune. As in the experimental case, the growth rate was calculated from an exponential fit to the lowest betatron sideband from the Fourier transform of a simulated vertical BPM difference signal.

To simulate a BPM the average transverse displacement (Δy_i) and the macro-particle population (I_i) was calculated for each longitudinal slice (i) and for each simulated turn of the machine. The BPM difference signal was then interpreted as the product of these ($\Delta y_i I_i$) i.e. the first moment of the beam.

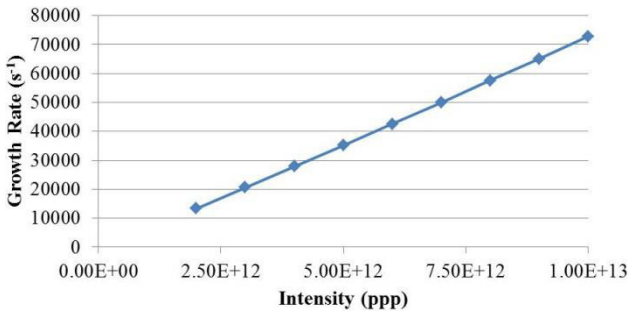

Figure 6: Simulated growth rate versus beam intensity (Q_y = 3.83, σ = 100 $\Omega^{-1}m^{-1}$).

Figure 6 shows the simulated growth rate as a function of beam intensity whilst keeping all other parameters constant. As previously, error bars on growth rate are one sigma uncertainty estimates from the exponential fit to the baseband signal. As expected from equation 1 the growth rate is linear with intensity and agrees reasonably well with growth rate estimates from theory.

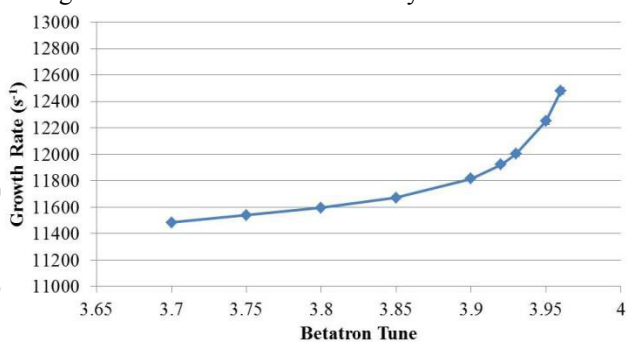

Figure 7: Simulated growth rate versus vertical tune. Intensity = 2×10^{12} ppp.

Figure 7 shows the simulated growth rate as a function of tune. As in the beam-based impedance measurements, equation 1 can be used to obtain the effective impedance as a function of frequency, figure 8. As expected, the simulated effective impedance has a similar functional form to the thick resistive wall model ($Z_{RW} \propto \omega^{-1/2}$).

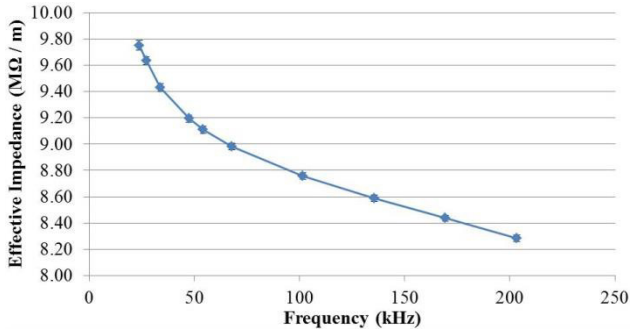

Figure 8: Simulated effective impedance versus baseband frequency. Intensity = 2×10^{12} ppp.

ISIS Simulation

The thick resistive wall approximation underestimates the measured impedance at the lowest betatron sideband. While research is still ongoing into the beam-based impedance measurements, for these initial simulations the beam pipe conductivity in the resistive wall impedance model has been modified to match artificially the measured impedance at the dominant, lowest sideband.

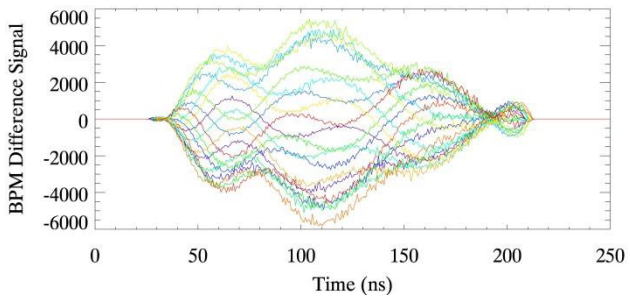

Figure 9: Simulated vertical BPM difference signal over 20 turns of the simulation around 1 ms with nominal tune.

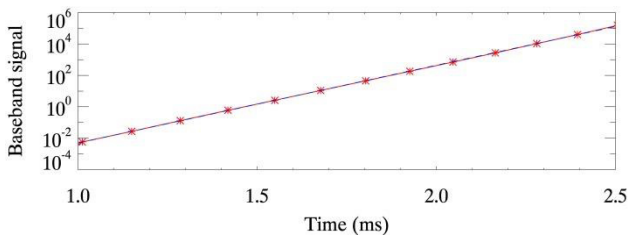

Figure 10: Simulated baseband as a function of time (red) on a logarithmic scale, exponential fit (blue dash).

Figures 9 and 10 show the simulated vertical BPM difference signal over several turns and time dependence of the baseband. The mode structure shows a mixture of m = 2 and m = 3 which is consistent with theory given the chromatic phase shift along the bunch. However, as with previous simulations [8], this does not match experimental observations (figure 1) where an m = 1 mode is persistent over many hundreds of turns. The simulated growth rate is much faster than theory predicts (11,400 s^{-1} compared to 446 s^{-1}) and much closer to observed growth times of order 10,000 s^{-1}.

ISBN 978-3-95450-185-4

SUMMARY

The head-tail instability has been identified as a key intensity limit for operation of the ISIS synchrotron. Work building impedance and instability simulation models of the synchrotron has been presented together with initial results simulating head-tail behaviour on ISIS. Combined with these studies work is underway on developing a prototype beam feedback system to damp instabilities [6, 12], due for installation in 2017.

Beam-based measurements have been made of the effective transverse impedance of the ISIS synchrotron using a coasting beam at 70 MeV (ISIS injection energy). Results indicate the presence of a narrowband impedance, the source of which is currently being investigated alongside whether it is the driver for the observed head-tail instability.

An in-house macro-particle simulation code is under development to aid understanding of the head-tail instability as observed at ISIS. Convergence tests have been performed with the code for coasting beams and zero space charge. Coasting beam code benchmarks against established theory [1] have been met with initial results looking promising. As with previous studies [7, 8] preliminary simulations of ISIS with a thick resistive wall impedance predict a head-tail mode $m = 2$ whereas a persistent $m = 1$ mode is observed in operations.

FUTURE WORK

Experiments are planned to establish the source of the narrowband impedance observed in the beam-based impedance measurements. Investigations are focused on the beam extraction kicker magnets and the vertical betatron exciter as these are expected to interact strongly with the vertical motion of the beam. Tests will also be performed on whether the narrowband impedance is the driver of the observed head-tail motion early in the ISIS acceleration cycle. More precise knowledge of head-tail, the current machine impedance model and its effect on the beam will inform future machine upgrades.

Developments of the in-house simulation code are planned to benchmark fully the results against Sacherer theory. Simulation results of the ISIS synchrotron will then be compared to theory and experiment for resistive wall impedance only, and the measured impedance model as it develops. It is planned to analyse the experimental and simulation data with reference to the theory of Rees [7].

Once the observations of low intensity, single harmonic RF head-tail motion at ISIS are understood studies will progress to high intensity beams. Previous experiments have shown space charge has a strong effect on the head-tail instability [11]. Simulations at high intensity will require the additional modelling for transverse space charge. Finally, work will move to investigating head-tail motion with dual harmonic RF where there is currently no theoretical model to describe observations.

REFERENCES

[1] F. Sacherer, "Transverse bunched beam instabilities", Proc. First Course of the International School of Particle Accelerators of the 'Ettore Majorana' Centre for Scientific Culture, Rep. CERN 77-13, Jul. 1977, pp. 198 – 218.

[2] M. Blaskiewicz, "Fast head-tail instability with space charge", *Phys. Rev. ST Accel. Beams*, vol. 1, p. 044201, Aug. 1998.

[3] A. Burov, "Head-tail modes for strong space charge", *Phys. Rev. ST Accel. Beams*, vol. 12, p. 044202, Apr. 2009.

[4] V. Balbekov, "Transverse modes of a bunched beam with space charge dominated impedance", *Phys. Rev. ST Accel. Beams*, vol. 12, p. 124402, Dec. 2009.

[5] V. Kornilov, O. Boine-Frankenheim, "Head-tail instability and Landau damping in bunches with space charge", *Phys. Rev. ST Accel. Beams*, vol. 13, p. 114201, Nov. 2010.

[6] D.J. Adams *et al*., "Operational experience and future plans at ISIS", presented at HB'16, Malmö, Sweden, Jul. 2016, paper TUPM3Y01.

[7] G.H. Rees, "Interpretation of the higher mode, head tail motion observed on ISIS", *Particle Accelerators*, Vol. 39, pp. 159 – 167, May 1992.

[8] R.E. Williamson, D.J. Adams, B. Jones, V. Kornilov, and C.M. Warsop, "Simulation of the head-tail instability on the ISIS Synchrotron", in *Proc. HB'14*, East Lansing, MI, USA, Nov. 2014, pp. 113 – 117.

[9] C.M. Warsop, D.J. Adams, B. Jones, and B.G. Pine, "Simple models for beam loss near the half integer resonance with space charge", presented at HB'16, Malmö, Sweden, Jul. 2016, paper MOPR030.

[10] C.M. Warsop *et al*., "High intensity loss mechanisms on the ISIS rapid cycling synchrotron", *Proc. HB'14*, East Lansing, MI, USA, Nov. 2014, pp. 203 – 207.

[11] V. Kornilov *et al*., "Thresholds of the head-tail instability in bunches with space charge", in *Proc. HB'14*, East Lansing, MI, USA, Nov. 2014, pp. 240 – 244.

[12] S.J. Payne, "Strip line monitor design for the ISIS proton synchrotron using the FEA program HFSS", in *Proc. IBIC'13*, Oxford, UK, Sep. 2013, pp. 435 – 437.

[13] C.M. Warsop, "Special diagnostic methods and beam loss control on high intensity proton synchrotrons and storage rings", Ph.D. thesis, Phys. Dept., Sheffield University, UK, Jan. 2002, pp. 86 – 90.

[14] C.M. Warsop et al., "High intensity studies on the ISIS synchrotron, including key factors for upgrades and the effects of half integer resonance", in Proc. HB'10, Morschach, Switzerland, Sep. 2010, pp. 619 – 623.

[15] R.E. Williamson, D.J. Adams, and C.M. Warsop, "High intensity longitudinal dynamics studies for an ISIS injection upgrade", in *Proc. HB'12*, Beijing, China, Sep. 2012, pp. 492 – 496.

[16] G. Rumolo, F. Zimmermann, "Electron cloud simulations: beam instabilities and wakefields", *Phys. Rev. ST Accel. Beams*, vol. 5, p. 121002, Dec. 2010.

[17] M. Blaskiewicz, "The TRANFT User's Manual", BNL, Upton, NY, USA, Rep. BNL-77074-2006-IR, Aug. 2006.

ISBN 978-3-95450-185-4

BEAM ACCELERATION AND TRANSITION CROSSING IN THE FERMILAB BOOSTER*

V. A. Lebedev†, J.-F. Ostiguy, C.M. Bhat
Fermilab, Batavia, IL, USA

Abstract

To suppress eddy currents, the Fermilab rapid cycling Booster synchrotron has no beam pipe; rather, its combined function dipoles are evacuated, exposing the beam directly to the magnet laminations. This arrangement significantly increases the resistive wall impedance of the dipoles and, in combination with the space charge impedance, substantially complicates longitudinal dynamics at transition. Voltage and accelerating phase profiles in the vicinity of transition are typically empirically optimized to minimize beam loss and emittance growth. In this contribution, we present results of experimental studies of beam acceleration near transition. Using comparisons between observed beam parameters and simulations, we obtain accurate calibrations for the rf program and extract quantitative information about parameters of relevance to the Booster laminated magnets longitudinal impedance model. The results are used to analyse transition crossing in the context of a future 50% increase in beam intensity planned for PIP-II, an upgrade of the Fermilab accelerating complex.

INTRODUCTION

Over the 40 years existence of Fermilab Booster the beam intensity has increased steadily to respond to the demands of the experimental program. In recent years this pace has increased to accommodate a succession of neutrino experiments. To meet the needs of the LBNF/DUNE experimental program, the next planned upgrade of the Fermilab accelerating complex referred to as PIP-II, calls for an additional 50% increase in beam intensity.

Early on, transition crossing has been identified as a machine performance bottleneck. Although transition crossing has evolved into a sophisticated and well-tuned operational procedure, an increase in intensity beyond the current level requires quantitative understanding of all effects driving the process. In this paper we present results of studies aimed at understanding the dynamics of beam acceleration and transition crossing in sufficient details to construct a model with predictive ability. The model aims not only at investigating the impact of an intensity increase on performance, but also at investigating ways to minimize beam loss and emittance growth due to transition crossing.

It is well-known that a jump in accelerating phase from ϕ_{acc} to $\pi-\phi_{acc}$ is required to preserve longitudinal motion stability. In the absence of beam induced forces and motion non-linearity the dynamics below and above transition is symmetric resulting in no emittance growth at transition. In practice the beam induced forces, break this symmetry as well as motion linearity. The result is an intensity dependent focussing mismatch and non-linear distortions of the bunch phase space. The subsequent synchrotron oscillations lead to filamentation and emittance growth.

In contrast to other fast cycling proton synchrotrons, the Fermilab Booster has no dedicated vacuum chamber inside its dipoles; rather, the entire volume between the magnet poles is evacuated. While this arrangement eliminates the issues associated with eddy currents induced by the time-varying bend field in a conventional chamber, having the beam directly exposed to the pole laminations substantially increases the wall impedance. The bunch length achieves its minimum at transition. The corresponding increase in peak current causes an increase in beam induced voltage. The very low synchrotron frequency enhances the non-linearity contribution to emittance growth.

Table 1 presents Booster parameters relevant to beam acceleration and transition crossing.

Table 1: Major Booster Parameters

Injection energy	0.4 GeV
Extraction energy	8 GeV
Ramp rate	15 Hz
Harmonic number	84
Circumference	474.2 m
Momentum compaction	0.03346
Maximum rf voltage	1.2 MeV
RF frequency swing	37.9-52.8 MHz
Number of bunches	82
Nominal beam intensity	$4.2\cdot10^{12}$

MEASUREMENTS

To minimize problems with possible signal distortion in electronics and data acquisition as well as possible miscalibrations, raw signals were acquired from a resistive wall monitor (RWM) and from the circuit presenting the analog sum of rf voltages for all cavities (RFSUM). In addition, the signal from a beam position monitor used by the radial position feedback system (RPOS) was recorded. The data were acquired with a multi-channel digital oscilloscope. A sampling rate of 1.2 GHz was selected so as to measure both voltage waveform and the longitudinal density distribution with sufficient resolution. The RWM and RFSUM signals completely characterize the beam behaviour in the longitudinal plane including the amplitude and phase of the accelerating voltage. As will be seen below, the RPOS signal provides accurate calibrations of the rf voltage and phase. Because of the oscilloscope memory limit of $4.5\cdot10^6$ samples, the duration of each measurement was set to 3.6 ms. Since this interval is much shorter than the complete 33.3 ms accelerating cycle, data were acquired only during

* Work performed for Fermi Research Alliance, LLC under Contract No. DE-AC02-07CH11359 with the United States Department of Energy
† val@fnal.gov

ISBN 978-3-95450-185-4

two time intervals of interest: (1) immediately after injection, when adiabatic bunching occurs and (2) at transition. Beam intensities ranged from $1.2\cdot10^{12}$ to $4.8\cdot10^{12}$ particles and two sets of data were acquired for each intensity value. Good reproducibility at each intensity was observed in spite of a time jitter ranging from 0 to 18 turns observed in the course of these measurements.

Data analysis was performed into two phases. First, at each turn the arrival time, rms width and peak amplitude of individual bunches were determined from the RWM signal, while the zero-crossing time and amplitude for each period of rf voltage were determined from the RFSUM signal. Accounting for instrumentation offsets, individual bunch profiles were fitted to a truncated Gaussian while each rf period was fitted to a sinusoid. The difference between the bunch arrival time and the zero crossing time for rf (Figure 1) was used to extract the accelerating phase. After verifying that all bunches - including bunches near a two-bunch gap used for extraction - behaved similarly, the data was averaged over all bunches on a turn-by-turn basis. This significantly improved the accuracy while reducing the data to a more manageable size.

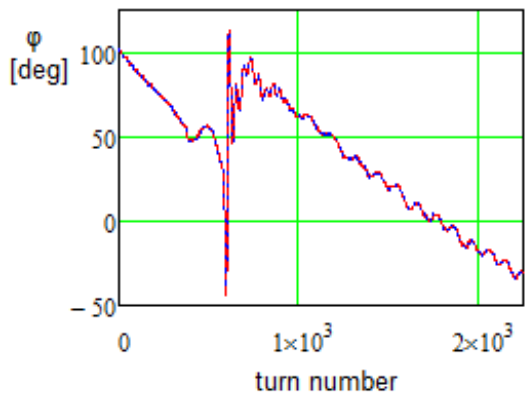

Figure 1: Phase difference between the bunch arrival time and rf zero crossing in vicinity of transition crossing; blue and red lines present two independent measurements with beam intensity of $4.82\cdot10^{12}$ particles.

The second phase of the analysis aimed at obtaining accurate calibrations for the rf voltage, rf phase and momentum offset. The measured phase difference between the bunch and rf voltage includes a shift due to a cable propagation delay. While the cable lengths for the RWM and RFSUM signals (10 mm/deg) are not known with sufficient accuracy to determine this delay directly, it may be determined by correction of the associated phase shift which is linearly dependent on the rf frequency: $\Delta\phi=2\pi f_{RF}\Delta T$. Here ΔT is the difference in cable length expressed as a signal propagation delay. The linear dependence is clearly seen in Figure 1.

Using the RPOS signal, ΔT as well as an accurate calibration for RFSUM may be obtained by a procedure that will be now described. Knowing the accelerating phase (ϕ_{accn}) the rf voltage (V_n), and the beam deceleration due to resistive part of impedance (V_{bn}) one obtains the dependence of the beam energy (and consequently the momentum deviation on turn n+1,

$$\mathrm{E}_{n+1} = \mathrm{E}_n + e\left(V_n \sin\left(\varphi_{acc_n}\right) - V_{b_n}\right), \quad V_{b_n} = A_V N_p / \tau_{b_n}, \tag{1}$$

Here τ_{bn} is the measured rms bunch length, N_p is the number of particles in the beam and A_V is a constant directly related to the effective longitudinal impedance. The assumed dependence of V_{bn} on τ_{bn} implies that the resistive part of the impedance has a weak dependence on frequency over a wide frequency range. This assertion is supported both by impedance measurements [1] and by analytical theory [2]. By combining the predictions of Eq. (1) to the measurements, one can extract ΔT, A_V, and the scaling factors for the RFSUM and RPOS signals. Note that since the revolution frequency changes mostly at low energy, the data collected at injection is much more sensitive to variations in ΔT.

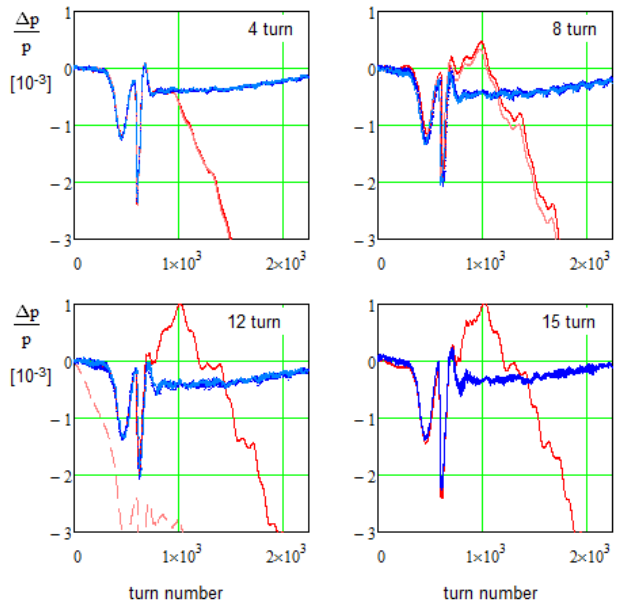

Figure 2: Predicted (red) and measured (blue) momentum offsets in vicinity of transition crossing for different beam intensity measured in number of injection turns; 4,8,12 and 15 turns correspond to $[1.17, 2.48, 3.78, 4.82]\cdot10^{12}$ particles. For each intensity two measurements are shown.

Results of the fitting procedure for all measured data are presented in Figure 2. Good agreement between measurements and predictions is achieved below transition. Above transition, the poorer fit is caused by small systematic errors in the accelerating phase: the observed discrepancy corresponds to approximately 0.5 degree of error in accelerating phase. A probable source for this error is the difference between the accelerating phase determined as the center of rf bucket and the measured synchronous phase determined as a bunch centroid. The sign of this difference changes at transition due to changed symmetry of accelerating bucket. The difference is estimated to be on the order of 0.25 deg. Because the bucket left-right symmetry is inverted at transition, the error is effectively doubled. The error amounts to 2% of the ~12 deg rms bunch length near transition. The procedures outlined below provided calibrations for the rf voltage and rf phase well within 1% and

ISBN 978-3-95450-185-4

1 deg, respectively. This accuracy is sufficient for reliable simulations of transition crossing [2].

The left pane in Figure 3 shows the accelerating phase variation in the vicinity of transition for different intensities. The beam deceleration arising from the resistive part of the impedance causes a shift of the accelerating phase toward on-crest acceleration as the beam intensity increases. Averaged values of this shift, referenced to the rf voltage for a beam intensity of $1.17 \cdot 10^{12}$ are presented in the right pane of Figure 3. As expected, the phase shift exhibits a linear dependence on intensity; furthermore, the slope is consistent with the measured and predicted values of the real part of the wall impedance. It should be mentioned that Figure 3 incorporates rf voltage corrections to account for minor changes in accelerating voltage due to incomplete beam loading compensation by local cavity feedbacks. Without these corrections, the linear dependence of the phase shift on intensity is not nearly as clear.

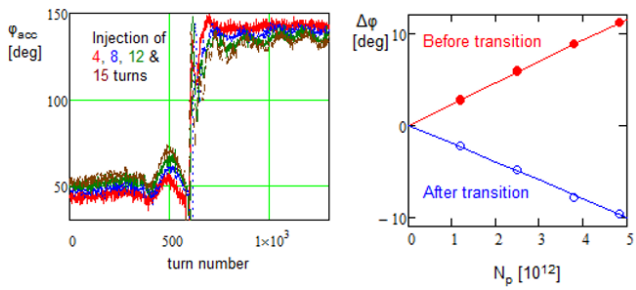

Figure 3: Accelerating phase variations in vicinity of transition crossing for different beam intensities (left) and corresponding shift of accelerating phase before and after transition crossing with beam intensity.

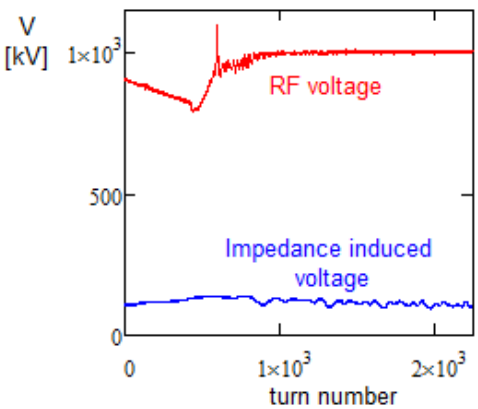

Figure 4: Dependence of rf voltage amplitude and impedance induced decelerating voltage averaged over bunch on the turn number in vicinity of transition crossing for beam intensity of $4.82 \cdot 10^{12}$ particles.

The large swing in accelerating phase well visible in Figure 1 is out of scale on Figure 3. This phase swing originates from the abrupt change in beam loading associated with the transition phase jump which is faster than the response time of the cavity feedback. As shown in Fig. 4, a corresponding spike in the rf voltage amplitude is clearly visible. The impedance induced voltage represents about 15% of the rf voltage amplitude.

SIMULATIONS

The rf voltage and accelerating phase extracted from measurements were used as input for the simulations described in Ref. [2]. However, two important parameters could not be directly measured.

The first one is the exact timing of the transition crossing. Simulations show that altering the transition crossing timing relative to the rf waveform by 10-20 turns has a significant effect on the rms bunch length above transition. Experimental data indicates that the transition jump timing jitter is on that order. From a simulation point of view, this prevents a precise determination of the exact moment at which transition occurs. It also suggests that reduction of the jitter would be beneficial.

The second parameter is the second order slip factor, η', defined by the following equation:

$$\Delta T / T = \eta \left(\Delta p / p \right) + \eta' \left(\Delta p / p \right)^2 + \ldots .$$

Presently, no reliable procedure is available to accurately determine the second order slip factor at transition. Direct measurements would be very challenging. Potentially, the second order slip factor could be obtained using modern map based techniques but there is considerable uncertainty in the non-linearity of Booster magnets. Note that a change in η' on the order of ~0.05 significantly affects the rms bunch length variations above transition.

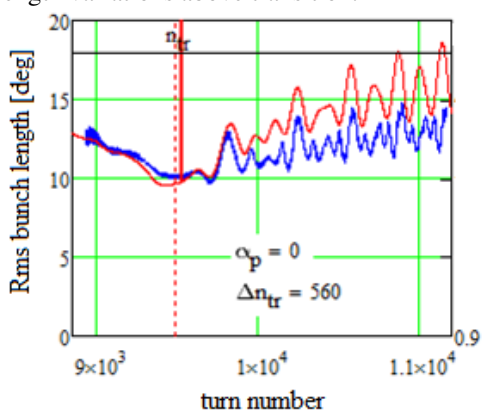

Figure 5: Dependence of rms bunch length on turn number in vicinity of transition crossing: blue – measurements, red – simulations; beam intensity of $4.82 \cdot 10^{12}$ particles.

With manual adjustment of the transition timing and second order compaction factor, simulations yield good agreement with the measurements. Figure 5 compares the measured to simulated rms beam sizes. The rms size extracted from the measurement data is systematically smaller after transition because the Gaussian fit algorithm used to extract the rms size excludes the long tails that develop in the longitudinal profile after transition. Figure 6 shows the computed profile and the decelerating voltage due to impedance before and after transition. The tail elongation after transition crossing is obvious. The decelerating voltage at transition reaches 30% of the accelerating voltage; this implies that any further intensity increase would require additional cavity voltage.

At PIP-II design intensity of $6.5 \cdot 10^{12}$, simulations at this stage suggest that with minor improvements it should be

ISBN 978-3-95450-185-4

possible to cross transition with a relative emittance increase comparable to the one observed under present operational conditions. That said, an issue that has been omitted from our simulations is the possibility of a microwave instability developing shortly after transition. While simple formulas provide estimates for intensity thresholds and growth rates, credible simulations require special attention to distinguish an actual instability from the intra-bunch motion excited by numerical noise.

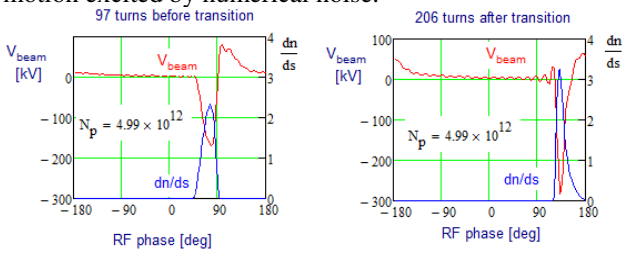

Figure 6: Longitudinal bunch density and beam induced voltage shortly before (left) and shortly after (right) transition crossing.

ACKNOWLEDGMENT

The authors wish to thank the Booster Department and the Operations Group for their support in acquiring machine data.

REFERENCES

[1] J. Crisp, http://beamdocs.fnal.gov/AD-public/DocDB/ShowDocument?docid=408

[2] J.-F. Ostiguy, *et.al.* "Modeling longitudinal dynamics in the Fermilab Booster Synchrotron", proc. IPAC 2016, pp. 874-876

ISBN 978-3-95450-185-4

SUPPRESSION OF HALF-INTEGER RESONANCE IN FERMILAB BOOSTER*

A. Valishev†, V. Lebedev, Fermilab, Batavia, IL, USA

Abstract

The particle losses at injection in the FNAL Booster are one of the major factors limiting the machine performance. The losses are caused by motion nonlinearity due to direct space charge and due to nonlinearity introduced by large values of chromaticity sextupoles required to suppress transverse instabilities. The report aims to address the former - the suppression of incoherent space charge effects by reducing deviations from the perfect periodicity of linear optics functions. It should be achieved by high accuracy optics measurements with subsequent optics correction and by removing known sources of optics perturbations. The study shows significant impact of optics correction on the half-integer stop band with subsequent reduction of particle loss. We use realistic Booster lattice model to understand the present limitations, and investigate the possible improvements which would allow high intensity operation with PIP-II parameters.

INTRODUCTION

The Booster has been the workhorse of the Fermilab accelerator complex for several decades and continues to deliver high-intensity high-repetition rate proton beams for the physics program. Recent improvements allowed to obtain beam acceleration at each Booster cycle. It increased the effective ramp rate from 7 to 15 Hz and played a significant role in attaining the 700 kW operation for NOvA experiment [1]. The Booster intensity is limited by particle losses throughout the injection, acceleration, and extraction cycle, which lead to the radio-activation of the accelerator components and enclosure. Consequently, the examination of the loss sources and development of ways to mitigate them are the continued focus of efforts. It becomes especially important in view of the upgrade plans for the PIP-II project [2]. The area of interest for the present report is the particle losses induced by direct space charge interaction at injection energy.

The studies of space charge effect in FNAL Booster have a long history. A massive campaign to simulate and mitigate the losses at injection was undertaken during the Tevatron collider Run II [3-7]. In particular, it was determined that the extraction dogleg that disturbs the 24-fold lattice symmetry of the Booster and thus enhances the half-integer stop band can have a significant impact on the single-particle dynamics [4]. The importance of half-integer resonance has been realized by Sacherer [8] and later research confirmed and enhanced the aspects of interplay between space-charge and lattice resonances [9-13]. Also, significant progress has been made in the accurate measurement and reconstruction of the Booster optics model owing to the implementation of the LOCO algorithm [13]. This makes it possible to model the beam dynamics with the actual machine configuration in operations and then perform predictable adjustments.

The present work aims at i) revisiting the space-charge dynamics in the FNAL Booster making use of the recent improvements in the lattice model and understanding the main limiting factors; ii) proposing operational improvements to reduce particle losses; iii) making projections towards operation with PIP-II parameters or even higher intensity.

APPROACH AND TOOLS

In the present study we concentrate solely on the incoherent single-particle effects arising through the time-modulation of nonlinear transverse self-field within the bunch and the betatron and synchro-betatron resonances leading to the beam emittance growth and particle losses. We also limit the time period of interest to a few hundred turns right after the beam injection and bunching and before the energy ramp. Such approach allows to use relatively simple tools for the modelling of space-charge effects – the so-called frozen space-charge model that implies Gaussian beam density profile. We also approximate the smooth azimuthal distribution of space-charge action by a number of thin kicks along the orbit. The advantage of such approach is the fast calculation time and the availability of reasonable well developed and tested tracking codes. In the future the simulations will be augmented by the true self-consistent PIC tools.

We use the simplified and realistic Booster lattice models [13] to quantify the requirements on optics control that would help mitigating particle losses at injection. The simplified representation is a 24-cell symmetric lattice with some artificially introduced gradient errors, which emulate the beta-beating of the realistic lattice.

The code used in this study was Lifetrac [14], a particle tracking code developed for modelling beam-beam interactions. The machine lattice was modelled using the element-by-element drift-kick approximation. The lattice data are imported from MAD-X [15] model files where the element slicing is performed using the methods available internally in MAD-X. For the purpose of this work the slicing was done with the so-called Teapot algorithm [16]. The thin lens tracking is implemented following [17], and makes use of the paraxial approximation for the multipole elements and properly treats non-paraxial effects in the drifts. This method proved to be accurate for the LHC and DAΦNE tracking studies [18].

We used 120 thin beam-beam elements (17 per betatron period) to model the action of space-charge. The simplifications limiting the physics model in the study were: i)

* Fermilab is operated by Fermi Research Alliance, LLC under Contract No. DE-AC02-07CH11359 with the United States Department of Energy.
† valishev@fnal.gov

ISBN 978-3-95450-185-4

non-adaptive space-charge algorithm (i.e. the beam emittance was considered frozen) and ii) no modulation of space-charge kick by the longitudinal particle position within the bunch (which overestimates the space-charge effect but neglects synchro-betatron resonances).

The beam parameters used in the studies for the present Booster operation and for the PIP-II scenario are listed in Tables 1 and 2, respectively. The lattice functions of the idealized 24-period model and the actual reconstructed Booster model are shown in Figs. 1 and 2.

Table 1: Booster Nominal Parameters in Simulation

Beam energy	400 MeV (β=0.713, γ=1.426)
RF Voltage	0.7 MV
Synchrotron tune	0.078 (35 kHz)
Bucket size	4.2×10^{-3}
Energy spread	2.1×10^{-3}
Bunch length	σ_z=1.26 m
Transverse emittance	15 mm×mrad (95% normalized)
Aperture	2.86 cm in H, 2.08 cm in V
Betatron tunes	Q_x=6.70, Q_y=6.80
Chromaticity	C_x=-20, C_y=-14
Number of particles	0.42×10^{13} in 84 bunches
Space-charge tune shift	ΔQ_x=-0.197, ΔQ_y=-0.307

Table 2: Beam Parameters for PIP-II scenario

Number of particles	0.66×10^{13} in 84 bunches
Space-charge tune shift	ΔQ_x=-0.31, ΔQ_y=-0.4

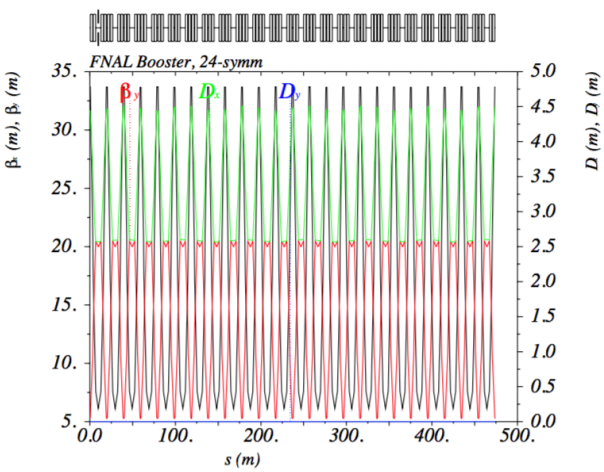

Figure 1: Lattice functions of idealized 24-period model.

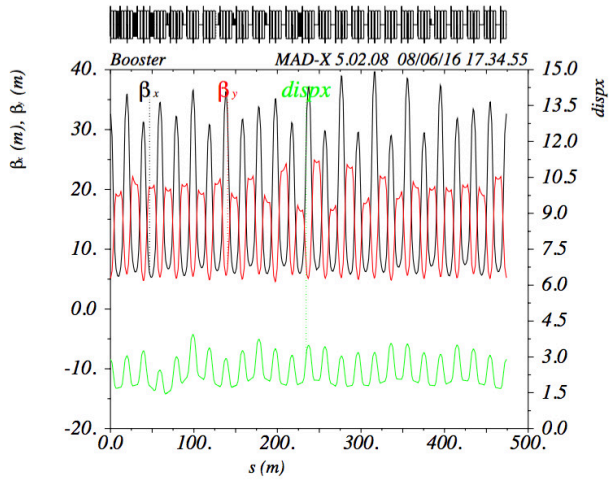

Figure 2: Lattice functions of LOCO measured model.

RESULTS AND DISCUSSION

We perform macro-particle bunch simulations to evaluate the evolution of beam emittance and particle losses. Figures 3-5 show the beam intensity and emittance over 10,000 tracking turns for the nominal and PIP-II scenarios. It is clear that for the PIP-II parameters even a minor distortion of the ideal 24-fold symmetry leads to significant losses. One should remember, however, that the employed model overestimates the space-charge effect and the final conclusions could be less restrictive.

We also rely on the Frequency Map Analysis [19] for better understanding of the beam dynamics. Figures 6-17 present the frequency maps for the three cases of lattice (ideal 24-fold symmetry, 10% beta-beat, and 20% beta-beat) for two values of the beam intensity – nominal and PIP-II. The color in plots represents the betatron tune variation along the particle trajectory over 1000 turns (blue – 10^{-7}, red – 10^{-3}). The axes in the amplitude space are labelled in units of beam sigma.

One observes that in the ideal 24-periodic lattice the half-integer stop band is not present and the dynamics is well-behaved. The particle losses can probably be attributed to the action of nonlinear coupling resonance $2Q_x$-$2Q_y$=n. As the perfect periodicity is ruined, the width of ½ resonance increases and it also starts to overlap with the coupling resonance, considerably shrinking the stable motion area.

The dynamics of particles with energy offset (not shown) exhibits a more pronounced effect of the half-integer resonance due to the impact of chromaticity. However, in the present model the transverse space-charge kick was not modulated by the longitudinal position in the bunch and drawing conclusions from the off-momentum particle results would be premature.

ISBN 978-3-95450-185-4

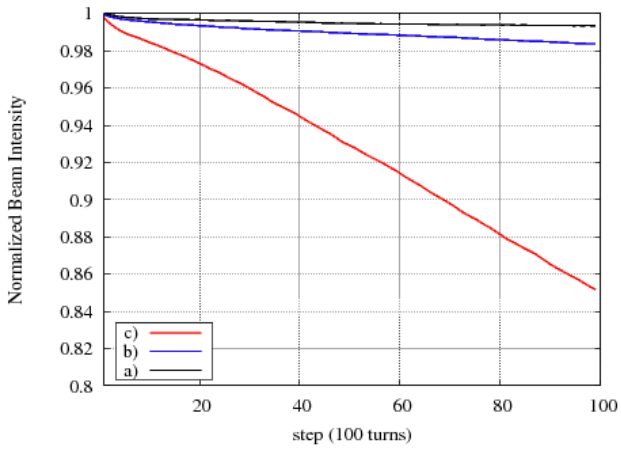

Figure 3: Simulated evolution of normalized bunch intensity over 10,000 turns for the nominal Booster parameters. a) idealized 24-period lattice; b) 10% beta-beat lattice; c) 20% beta-beat lattice.

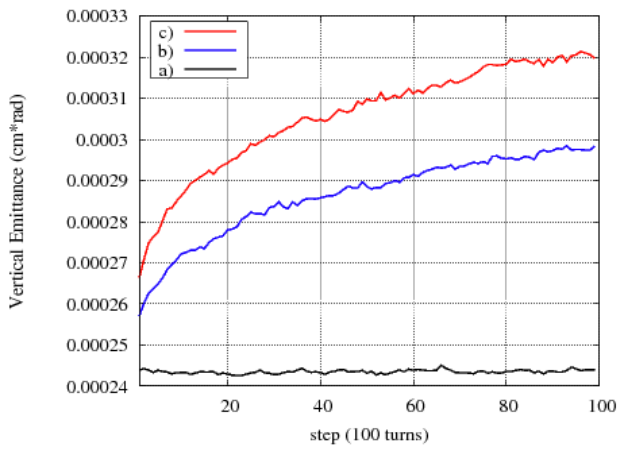

Figure 4: Simulated evolution of beam emittance over 10,000 turns for the nominal Booster parameters. a) idealized 24-period lattice; b) 10% beta-beat lattice; c) 20% beta-beat lattice.

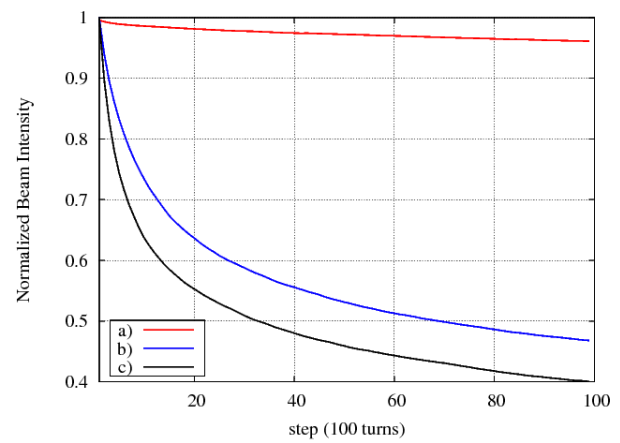

Figure 5: Simulated evolution of normalized bunch intensity over 10,000 turns for the PIP-II scenario parameters. a) idealized 24-period lattice; b) 10% beta-beat lattice; c) 20% beta-beat lattice.

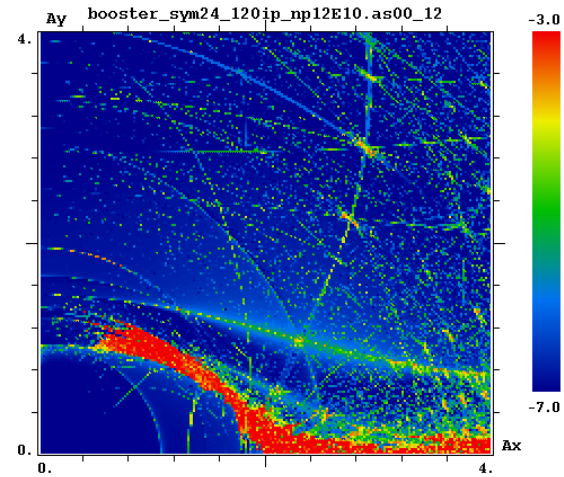

Figure 6: FMA in the amplitude space for the nominal parameters in idealized 24-period lattice.

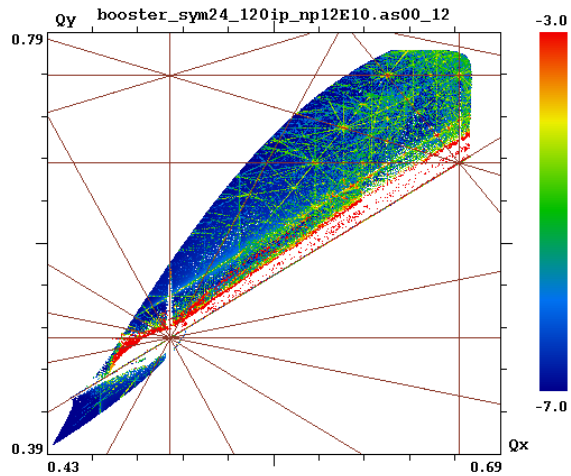

Figure 7: FMA in the tune space for the nominal parameters in idealized 24-period lattice.

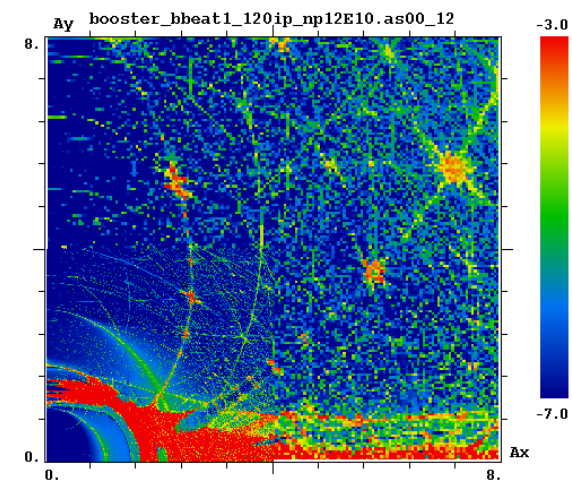

Figure 8: FMA in the amplitude space for the nominal parameters in 10% beta-beat lattice.

ISBN 978-3-95450-185-4

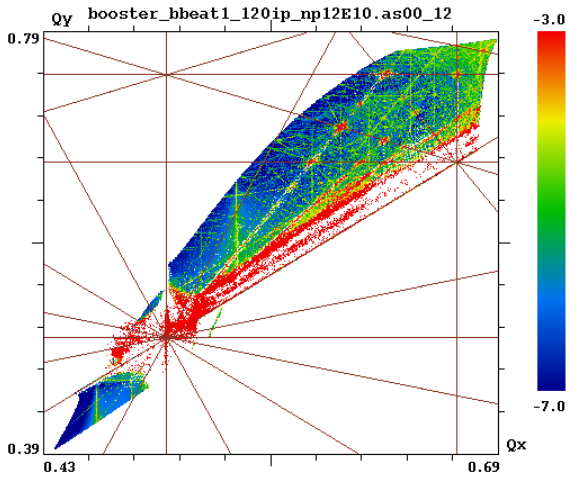

Figure 9: FMA in the amplitude tune space for the nominal parameters in 10% beta-beat lattice.

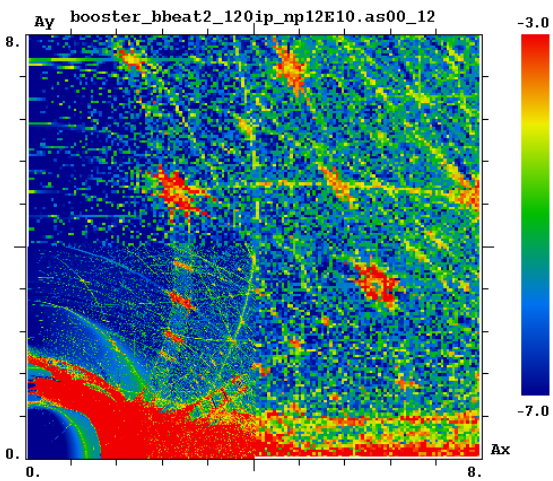

Figure 10: FMA in the amplitude space for the nominal parameters in 20% beta-beat lattice.

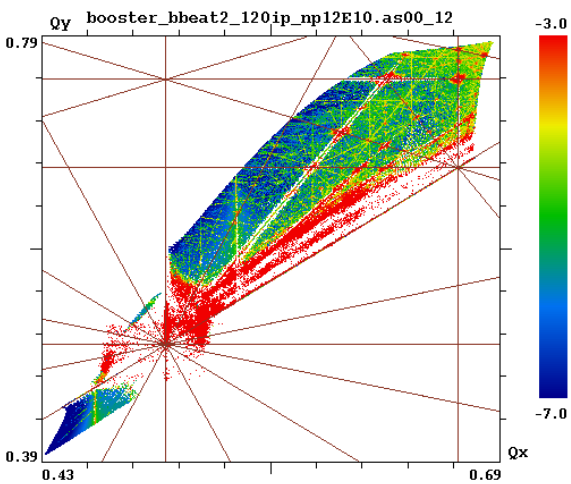

Figure 11: FMA in the tune space for the nominal parameters in 20% beta-beat lattice.

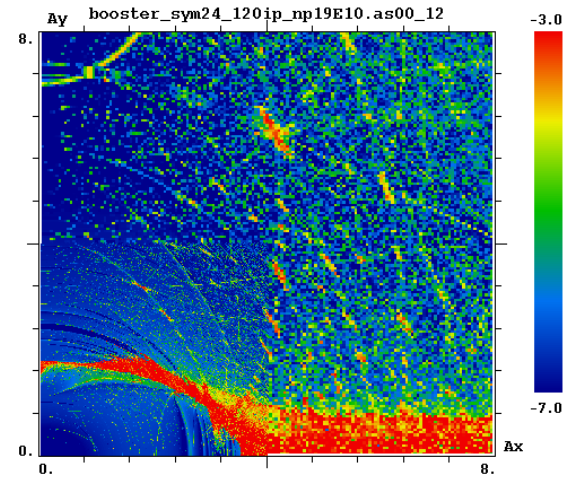

Figure 12: FMA in the amplitude space for the PIP-II scenario parameters in idealized 24-period lattice.

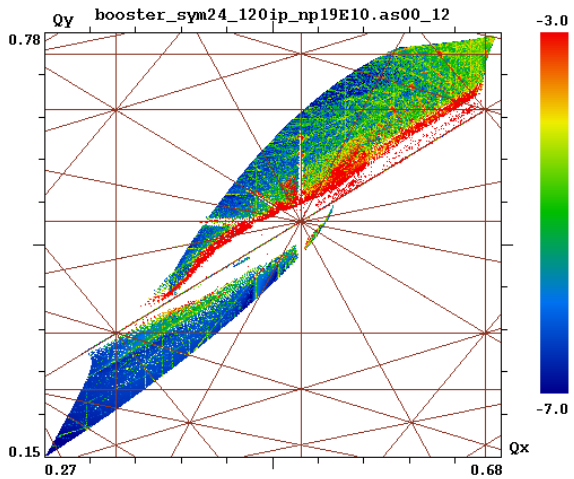

Figure 13: FMA in the tune space for the PIP-II scenario parameters in idealized 24-period lattice.

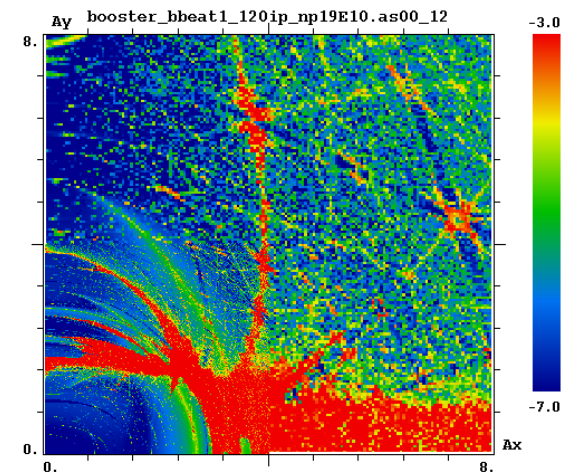

Figure 14: FMA in the amplitude space for the PIP-II scenario parameters in 10% beta-beat lattice.

ISBN 978-3-95450-185-4

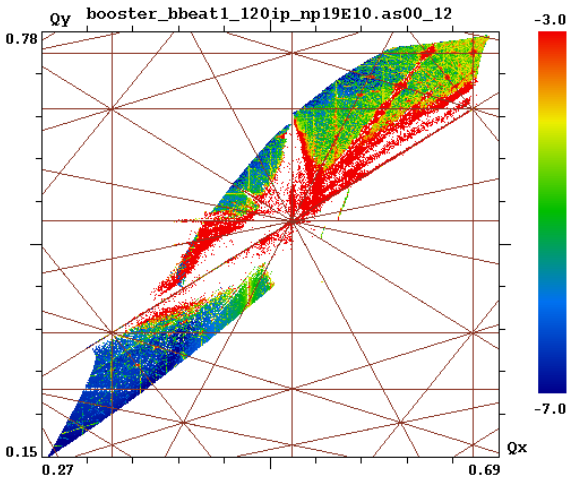

Figure 15: FMA in the tune space for the PIP-II scenario parameters in 10% beta-beat lattice.

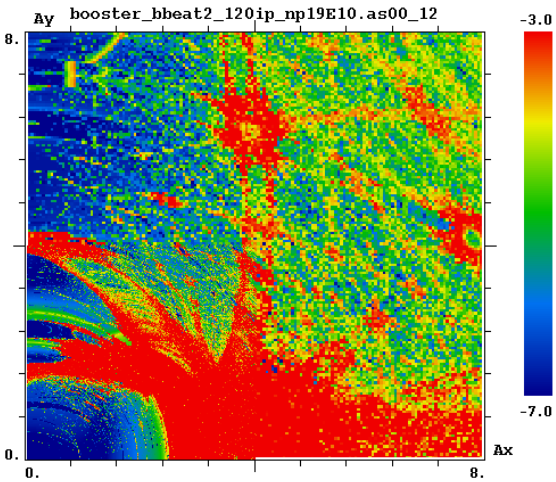

Figure 16: FMA in the amplitude space for the PIP-II scenario parameters in 20% beta-beat lattice.

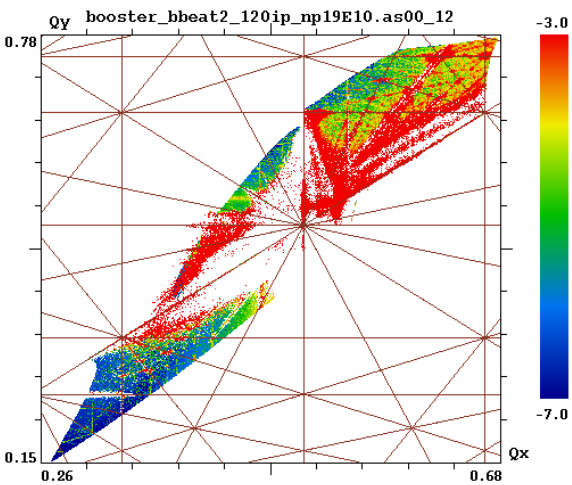

Figure 17: FMA in the tune space for the PIP-II scenario parameters in 20% beta-beat lattice.

SUMMARY

The employed model allows for very fast evaluation of machine tuning options with known limitations (non-adaptive space-charge and the absence of synchrotron modulation). The implementation of these features in Lifetrac is in progress. In parallel, the MAD-X space-charge module is being tested on the test cases discussed in this report.

The preliminary results indicate the importance of the half-integer resonance as a limiting factor: at the beam intensities exceeding 0.4×10^{13} the core particles cross the half-integer line, also the perfectly symmetrical 24-period lattice allows for operation with the intensity of 0.66×10^{13}.

ACKNOWLEDGMENT

We thank the entire Booster team and in particular W. Pellico and C.Y. Tan for useful discussions and machine data.

REFERENCES

[1] W.Pellico, "Status of current Booster with refurbished cavities", Workshop on Booster Performance and Enhancements, Fermilab 23-24 November 2015. https://indico.fnal.gov/conferenceOtherViews.py?view=standard&confId=10547

[2] PIP-II Reference Design Report, FNAL PIP-II-doc-1 http://pip2-docdb.fnal.gov/cgi-bin/DocumentDatabase/

[3] E.Prebys *et al.*, "Increasing the intensity of the Fermilab Booster", PAC'03, 12-16 May, 2003, Portland, OR, http://accelconf.web.cern.ch/AccelConf/p03/PAPERS/RPAG022.PDF

[4] W.Chou *et al.*, "Fermilab Booster Modeling and Space Charge Study", PAC'03, 12-16 May, 2003, Portland, OR, http://accelconf.web.cern.ch/AccelConf/p03/PAPERS/RPAG017.PDF

[5] J.Amundson P.Spentzouris, "Space Charge Experiments And Simulation In The Fermilab Booster", PAC'05, May 16-20, 2005, Knoxville, TN, http://accelconf.web.cern.ch/AccelConf/p05/PAPERS/TPAT059.PDF

[6] Y.Alexahin *et al.*, "Effects of Space Charge and Magnet Nonlinearities on Beam Dynamics in the Fermilab Booster", PAC'07, 25-29 June, 2007, Albuquerque, NM, http://accelconf.web.cern.ch/AccelConf/p07/PAPERS/THPAN105.PDF

[7] X.Huang *et al.*, "Emittance measurement and modeling for the Fermilab Booster", PRSTAB 9, 014202 (2006).

[8] F.J.Sacherer, Ph.D Thesis, University of. California, Berkeley, UCRL-18454 (1968).

[9] A.Fedotov, I.Hofmann, "Half-integer resonance crossing in high-intensity rings", PRSTAB 5, 024202 (2002).

[10] S.Cousineau *et al.*, "Resonant beam behavior studies in the Proton Storage Ring", PRSTAB 6, 074202 (2003).

[11] S.Bernal *et al.*, "RMS envelope matching of electron beams from ''zero'' current to extreme space charge in a fixed lattice of short magnets", PRSTAB 9, 064202 (2006).

ISBN 978-3-95450-185-4

[12] M.Fitterer *et al.,* "Systematic studies on the effect of linear lattice optics for space-charge limited beams", PRSTAB 2015.

[13] C.Y. Tan, "Optics corrections in Booster", FNAL Beams-doc-4566-v3, http://beamdocs.fnal.gov/AD-public/DocDB/ShowDocument?docid=4566

[14] D. Shatilov, Particle Accelerators, vol. 52, 1996, pp. 65-93.

[15] MADX Program, http://cern.ch/madx

[16] H. Burkhardt *et al.,* "Improved TEAPOT method and tracking with thick quadrupoles for the LHC and its upgrade", IPAC2013, Shanghai, China, 2013, paper MOPWO027, pp. 945-947.

[17] G. Ripken, F.Schmidt, "A symplectic six-dimensional thin-lens formalism for tracking", CERN-SL-95-12, 1995.

[18] M.Zobov *et al.,* "Simulation of Crab Waist Collisions in DANE with KLOE-2 Interaction Region", EEE Trans. Nucl. Sci., Vol. 63, No. 2, pp. 818-822, 2016.

[19] D. Shatilov *et al.*, "Application of frequency map analysis to beam-beam effects study in crab waist collision scheme", Phys. Rev. ST Accel. Beams, vol. 14, 2011, 014001.

ISBN 978-3-95450-185-4

ELECTRON LENS FOR THE FERMILAB INTEGRABLE OPTICS TEST ACCELERATOR*

G. Stancari†, A. Burov, K. Carlson, D. Crawford, V. Lebedev, J. Leibfritz, M. McGee, S. Nagaitsev, L. Nobrega, C. S. Park, E. Prebys, A. Romanov, J. Ruan, V. Shiltsev, Y.-M. Shin[1], C. Thangaraj, A. Valishev, Fermilab, Batavia IL, USA, and D. Noll, IAP Frankfurt, Germany
[1]also at Northern Illinois University, DeKalb IL, USA

Abstract

The Integrable Optics Test Accelerator (IOTA) is a research machine currently being designed and built at Fermilab. The research program includes the study of nonlinear integrable lattices, beam dynamics with self fields, and optical stochastic cooling. One section of the ring will contain an electron lens, a low-energy magnetized electron beam overlapping with the circulating beam. The electron lens can work as a nonlinear element, as an electron cooler, or as a space-charge compensator. We describe the physical principles, experiment design, and hardware implementation plans for the IOTA electron lens.

INTRODUCTION

High-power accelerators and high-brightness beams are needed in many areas of particle physics, such as the study of neutrinos and of rare processes. The performance of these accelerators is limited by tolerable losses, beam halo, space-charge effects, instabilities, and other factors. Nonlinear integrable optics, self-consistent or compensated dynamics with self fields, and beam cooling beyond the present state of the art are being studied to address these issues. Moreover, nonlinearity, chaos, and the quest for integrability under controlled experimental conditions sheds light on the behavior of dynamical systems in general.

The Integrable Optics Test Accelerator (IOTA) is a research storage ring with a circumference of 40 m being built at Fermilab [1, 2]. Its main purposes are the practical implementation of nonlinear integrable lattices in a real machine, the study of space-charge compensation in rings, and a demonstration of optical stochastic cooling. IOTA is designed to study single-particle linear and nonlinear dynamics with pencil beams of 150-MeV electrons. For experiments on space-charge dynamics, 2.5-MeV protons will be injected.

In accelerator physics, nonlinear integrable optics involves a small number of special nonlinear focusing elements added to the lattice of a conventional machine in order to generate large tune spreads while preserving dynamic aperture [3]. This provides improved stability to perturbations and mitigation of collective instabilities through decoherence and Landau damping.

One way to generate a nonlinear integrable lattice is with specially segmented multipole magnets [3]. There are also two concepts based on electron lenses [4]: (a) axially symmetric thin kicks with a specific amplitude dependence [5–7]; and (b) axially symmetric kicks in a thick lens at constant amplitude function [8, 9]. These concepts use the electromagnetic field generated by the electron beam distribution to provide the desired nonlinear transverse kicks to the circulating beam. In IOTA operations with protons, the electron lens can also be used as an electron cooler [10] and as a space-charge compensator [11–13].

In this paper, we summarize the functions of the electron lens in IOTA and discuss current plans to build and test the experimental apparatus.

ELECTRON LENS IN IOTA

In an electron lens, the electromagnetic field generated by a pulsed, magnetically confined, low-energy electron beam is used to actively manipulate the dynamics of the circulating beam [14–16]. Electron lenses have a wide range of applications [17–26]. In particular, they can be used as nonlinear elements with tunable shape as a function of betatron amplitude.

Nonlinear Integrable Optics

The goal of the nonlinear integrable optics experiments, including the ones with electron lenses, is to achieve a large tune spread, of the order of 0.25 or more, while preserving the dynamic aperture and lifetime of the circulating beam. Experimentally, this will be observed by recording the lifetime and turn-by-turn position of a low-intensity, low-emittance 150-MeV circulating electron bunch, injected and kicked to different betatron amplitudes, for different settings of the nonlinear elements (magnets or electron lenses).

There are two concepts of electron lenses for nonlinear integrable optics: thin radial kick of McMillan type and thick axially-symmetric nonlinear lens in constant amplitude function.

Thin Radial Kick of McMillan Type The integrability of axially symmetric thin-lens kicks was studied in 1 dimension by McMillan [5, 6]. It was then extended to 2 dimensions [7] and used to improve the performance of colliders [27]. To implement this concept, the electron lens has to have a specific current-density distribution: $j(r) = j_0 a^4/(r^2 + a^2)^2$, where j_0 is the current density on axis and a is a constant parameter (effective radius). Moreover, the betatron phase advance in the rest of the ring must be near an odd multiple of $\pi/2$. In this scenario, the electron

* Fermilab is operated by Fermi Research Alliance, LLC under Contract No. DE-AC02-07CH11359 with the United States Department of Energy. Report number: FERMILAB-CONF-16-244-AD-APC.
† Email: ⟨stancari@fnal.gov⟩.

ISBN 978-3-95450-185-4

gun and magnetic transport system must be able to achieve and preserve the desired current-density profile.

Axially Symmetric Kick in Constant Beta Function The concept of axially symmetric thick-lens kicks relies on a section of the ring with constant and equal amplitude functions. This can be achieved with a solenoid. The same solenoid magnetically confines the low-energy beam in the electron lens. In this case, any axially symmetric electron-lens current distribution generates two conserved quantities, as long as the betatron phase advance in the rest of the ring is an integer multiple of π. At large electron beam currents in the electron lens, the focusing of the electron beam itself dominates over the solenoid focusing and can be the source of the constant amplitude functions. This scenario favors long solenoids, low beta functions, and it is insensitive to the current-density distribution in the electron lens. Although in IOTA the achievable tune spread is smaller in this case than it is in the McMillan case, this scenario is more robust and will probably be the first one to be studied experimentally, using existing Gaussian or similar electron guns.

Electron Cooling

Electron cooling in IOTA would extend the range of available brightnesses for proton experiments with large self fields. It would also provide a flow of neutral hydrogen atoms through spontaneous recombination for beam diagnostics downstream of the electron lens. There are also scientific questions related to nonlinearities and cooling that can be investigated in IOTA, such as whether nonlinear integrable optics allows cooled beams to exceed the limitations of space-charge tune spreads and instabilities. Some of these aspects were discussed in Ref. [10]. Electron cooling poses strict requirements on the field quality in the main solenoid.

Space-Charge Compensation

Although space-charge compensation is commonly used in linacs, its implementation in rings is still an active field of research. Charge neutralization over the circumference of the ring is usually not practical. Local compensation schemes require high charge densities, which in turn can cause beam scattering, distortions of the lattice, and beam-plasma instabilities. Because an electron lens is based upon magnetically confined electron beams, some of these effects can be mitigated.

There are two ways an electron lens can be used as a space-charge compensator. One relies on an electron gun that generates the required charge distribution in transverse space and in time, to reproduce the bunch shape of the circulating beam [11]. In the other scheme, the so-called 'electron column', the electrons are generated by ionization of the residual gas and trapped axially by electrodes and transversely by the solenoidal field, in a configuration similar to a Penning-Malmberg trap [12]. The electron gun and collector are not necessary.

The physics of the interaction between circulating bunches and electron plasma is still a very open field of research [28]. However, the required gun, solenoid, and electrode parameters are similar to those of an electron lens, and therefore theory and experiment can be studied in IOTA.

APPARATUS

Construction of IOTA is planned for 2016–2018, and the electron lens should be ready for experiments at the time of commissioning of the ring.

Several Tevatron components can be reused. The gun and collector assemblies of the two Tevatron electron lenses (TEL-1 and TEL-2) were removed from the accelerator tunnel and tested for ultra-high vacuum. Gun and collector solenoid will be re-measured before final installation. Some existing magnet and high-voltage power supplies from the Tevatron are also available.

Convex thermionic dispenser cathodes for generating Gaussian beams have been purchased. They will be used for the thick nonlinear lens experiments. The design of the McMillan electron gun is still in progress.

Whereas the existing gun and collector solenoids from the Tevatron are adequate for IOTA, the toroidal bends and the main solenoid need to be redesigned because of cost and infrastructure (resistive solenoid in IOTA vs. superconducting solenoid in Tevatron) and because of the tight spaces for components in the small ring.

Girders and supports for the electron lens and adjacent components were designed. Manufacturing is almost complete.

In the next few months, we plan to set up a test installation in straight configuration (gun assembly, diagnostics, collector assembly) to check out the subsystems and test electron beam diagnostics.

The total beam current will be measured at the collector. A diagnostic cube with retractable devices will be installed upstream of the collector to measure the current profile.

The beam tube inside the main solenoid will be instrumented with beam-position monitors and cylindrical pickup electrodes, which can also be used for ion clearing and for electrostatic confinement.

A recent overview of the apparatus was given in Ref. [29].

CONCLUSIONS

In the Fermilab Integrable Optics Test Accelerator, nonlinear lenses, based on magnetically confined electron beams, will be used for experimental tests of integrable transfer maps, for electron cooling of protons, and for studies of space-charge compensation.

The combination of these three functions and the limited physical space make the design of the apparatus challenging, but no major obstacles have been encountered so far. The hardware (in part reused from previous experiments, in part redesigned) will be assembled first in a straight test setup and successively incorporated in the IOTA ring.

Several aspects are under study, such as the design of the new McMillan electron gun and the development of experi-

ISBN 978-3-95450-185-4

mental configurations, including the sensitivity of integrable dynamics to imperfections.

Research on electron lenses is linked to several applications (collimation, beam-beam compensation, tune-spread generation, ...) and it provides a flexible way to contribute to the physics program of the Fermilab Accelerator Science and Technology (FAST) facility.

ACKNOWLEDGMENTS

The authors would like to acknowledge the contributions of D. Broemmelsiek, W. Johnson, H. Piekarz, R. Thurman-Keup, T. Zolkin (Fermilab), and S. Antipov (University of Chicago and Fermilab) in developing theoretical concepts and technical solutions for the Fermilab Integrable Optics Test Accelerator.

REFERENCES

[1] S. Nagaitsev et al., in *Proceedings of the 2012 International Particle Accelerator Conference* (IPAC12), New Orleans, LA, USA, May 2012, edited by J. Corbett, C. Eyberger, K. Morris, C. Petit-Jean-Genaz, T. Satogata, and V. R. W. Schaa (IPAC'12 / IEEE, 2012), p. 16; FERMILAB-CONF-12-247-AD (2012).

[2] A. Valishev et al., in *Proceedings of the 2012 International Particle Accelerator Conference* (IPAC12), New Orleans, LA, USA, May 2012, edited by J. Corbett, C. Eyberger, K. Morris, C. Petit-Jean-Genaz, T. Satogata, and V. R. W. Schaa (IPAC'12 / IEEE, 2012), p. 1371; FERMILAB-CONF-12-209-AD-APC (2012).

[3] V. Danilov and S. Nagaitsev, Phys. Rev. ST Accel. Beams **13**, 084002 (2010).

[4] G. Stancari et al., in *Proceedings of the 2015 International Particle Accelerator Conference* (IPAC15), Richmond, VA, USA, May 2015, edited by S. Henderson, E. Ayers, T. Satogata, V. R. W. Schaa (JACoW, 2015), p. 46; FERMILAB-CONF-15-136-AD-APC (2015).

[5] E. M. McMillan, University of California Report UCRL-17795 (1967).

[6] E. M. McMillan, in *Topics in Modern Physics*, edited by W. E. Brittin and H. Odabasi (Colorado Associated University Press, Boulder, Colorado, 1971), p. 219.

[7] V. Danilov and E. A. Perevedentsev, in *Proceedings of the 1997 Particle Accelerator Conference* (PAC97), Vancouver, Canada, May 1997, edited by M. K. Craddock and M. Reiser (IEEE, 1998), p. 1759.

[8] S. Nagaitsev and A. Valishev (private communication, 2013).

[9] G. Stancari, in *Proceedings of the 16th Advanced Accelerator Concepts Workshop* (AAC 2014), San Jose, CA, USA, July 2014, edited by M. Hogan (AIP Conf. Proc., submitted), FERMILAB-CONF-14-314-APC, arXiv:1409.3615 [physics.acc-ph] (2014).

[10] G. Stancari et al., in *Proceedings of the International Workshop on Beam Cooling and Related Topics* (COOL15), Newport News, VA, USA, September 2015 (submitted for publication), FERMILAB-CONF-15-446-AD-APC.

[11] A. V. Burov, G. W. Foster, V. D. Shiltsev, Space-Charge Compensation in High-Intensity Proton Rings, FERMILAB-TM-2125 (2000).

[12] V. Shiltsev, in *Proceedings of the 2007 Particle Accelerator Conference* (PAC07), Albuquerque, NM, USA, June 2007, edited by C. Petit-Jean-Genaz (IEEE, 2007), p. 1159.

[13] C.-S. Park et al., Results of the Electron Column Space-Charge Compensation Simulations, talk presented at the *FAST/IOTA Scientific Program Meeting*, Batavia, Illinois, June 2016, ⟨https://indico.fnal.gov/event/11852⟩.

[14] V. Shiltsev et al., Phys. Rev. ST Accel. Beams **11**, 103501 (2008).

[15] V. Shiltsev, in *Handbook of Accelerator Physics and Engineering*, edited by A. W. Chao, K. H. Mess, M. Tigner, and F. Zimmermann (2nd ed., World Scientific, 2013), p. 641.

[16] V. D. Shiltsev, Electron Lenses for Super-Colliders (Springer, 2016).

[17] V. Shiltsev et al., Phys. Rev. ST Accel. Beams **2**, 071001 (1999); New J. Phys. **10**, 043042 (2008).

[18] V. Shiltsev et al., Phys. Rev. Lett. **99**, 244801 (2007).

[19] X. Zhang et al. Phys. Rev. ST Accel. Beams **11**, 051002 (2008).

[20] G. Stancari and A. Valishev, in *Proceedings of the ICFA Mini-Workshop on Beam-Beam Effects in Hadron Colliders* (BB2013), CERN, Geneva, Switzerland, March 2013, edited by W. Herr and G. Papotti, CERN-2014-004 (CERN, Geneva, 2014), p. 121; FERMILAB-CONF-13-046-APC (2013).

[21] G. Stancari et al., Phys. Rev. Lett. **107**, 084802 (2011).

[22] G. Stancari, in *Proceedings of the Meeting of the Division of Particles and Fields of the American Physical Society*, Providence, RI, USA, August 2011, edited by T. Speer (SLAC eConf C110809); preprint arXiv:1110.0144 [physics.acc-ph] (2011); FERMILAB-CONF-11-506-AD-APC (2011).

[23] W. Fischer et al., Phys. Rev. Lett. **115**, 264801 (2015).

[24] G. Stancari et al., Conceptual design of hollow electron lenses for beam halo control in the Large Hadron Collider, CERN-ACC-2014-0248, FERMILAB-TM-2572-APC, arXiv:1405.2033 [physics.acc-ph] (2014).

[25] A. Valishev and G. Stancari, Electron lens as beam-beam wire compensator in HL-LHC, FERMILAB-TM-2571-APC, arXiv:1312.1660 [physics.acc-ph] (2013).

[26] S. Fartoukh et al., Phys. Rev. ST Accel. Beams **18**, 121001 (2015).

[27] D. Shwartz et al., in *Proceedings of the ICFA Mini-Workshop on Beam-Beam Effects in Hadron Colliders* (BB2013), CERN, Geneva, Switzerland, March 2013, edited by W. Herr and G. Papotti, CERN-2014-004 (CERN, Geneva, 2014), p. 43.

[28] V. N. Litvinenko and G. Wang, Phys. Rev. ST Accel. Beams **17**, 114401 (2014).

[29] M. W. McGee et al, in *Proceedings of the 2016 International Particle Accelerator Conference* (IPAC16), Busan, Korea, May 2016, edited by C. Petit-Jean-Genaz, D. E. Kim, K. S. Kim, I. S. Ko, K. R. Kim, V. R. W. Schaa (JACoW, 2016), p. 2271.

ISBN 978-3-95450-185-4

SPIN TRACKING OF POLARIZED PROTONS IN THE MAIN INJECTOR AT FERMILAB*

M. Xiao†, Fermilab, Batavia, IL 60565, USA
W. Lorenzon and C. Aldred, University of Michigan, Ann Arbor, MI 48109-1040,USA

Abstract

The Main Injector (MI) at Fermilab currently produces high-intensity beams of protons at energies of 120 GeV for a variety of physics experiments. Acceleration of polarized protons in the MI would provide opportunities for a rich spin physics program at Fermilab. To achieve polarized proton beams in the Fermilab accelerator complex, shown in Fig.1, detailed spin tracking simulations with realistic parameters based on the existing facility are required. This report presents studies at the MI using a single 4-twist Siberian snake to determine the depolarizing spin resonances for the relevant synchrotrons. Results will be presented first for a perfect MI lattice, followed by a lattice that includes the real MI imperfections, such as the measured magnet field errors and quadrupole misalignments. The tolerances of each of these factors in maintaining polarization in the Main Injector will be discussed.

INTRODUCTION

The Main Injector is a multi-purpose synchrotron [1] which ramps up the proton beam from a kinetic energy of 8 GeV to 120 GeV. It provides neutrino beams for the MINOS, MINERvA and NOvA experiments, as well as the future Long-Baseline Neutrino Facility and Deep Underground Neutrino Experiment. It will also provide muon beams for Fermilab's Muon g-2 and Mu2e experiments. It delivers beam to the SeaQuest fixed-target experiment and to a dedicated facility for testing of detector technologies.

The acceleration of polarized protons in the MI was initially studied with the use of two superconducting helical dipole Siberian snakes. However, in 2012 it was discovered that there was no longer sufficient space in the MI to place two Siberian snakes at opposite sides of the ring [2]. A solution using one 4-twist Helical Snake in the MI [3] was found that seemed promising to provide polarized proton beams to the experiments. Spin tracking studies in the MI became necessary to reveal if it was possible or not in practice to produce and maintain a polarized proton beam in the Fermilab accelerators using single Siberian snakes in the larger synchrotrons. This report presents studies to determine the intrinsic spin resonance strengths for the relevant synchrotrons using a perfect lattice. This is followed by the implementation of various realistic imperfections, such as magnet field errors and quadrupole misalignments, into the MI lattice to study the tolerances of closed orbit corrections in maintaining polarization. All results presented here assume that the Siberian snake is a point-like spin flipper. The simulation using a single 4-twist helical dipole and its imperfection will be discussed at a later stage.

* Work supported by U.S.Department of Energy under the contract No. DE-AC02-76CH03000 and the National Science Foundation under Grant 1505458
†meiqin@fnal.gov

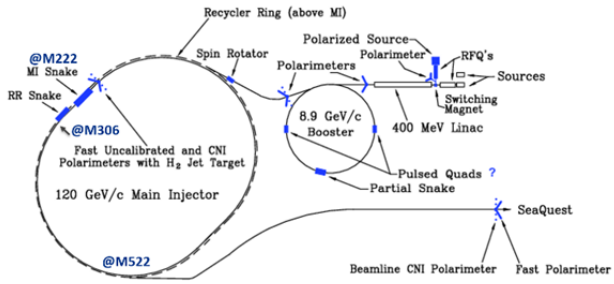

Figure 1: Main Injector accelerator complex conceptual layout showing equipment needed for polarized proton beam (in blue).

SPIN DYNAMICS OF THE POLARIZED PROTON

For a beam of particles, the polarization vector is defined as the ensemble average of spin vectors. The evolution of the spin vector of a beam of polarized protons in external magnetic fields is governed by the Thomas-BMT equation [4]

$$\frac{d\vec{S}}{dt}=\frac{e}{\gamma m}\vec{S}\times\left[(1+G\gamma)\vec{B}_{\perp}+(1+G)\vec{B}_{//}+(G\gamma+\frac{\gamma}{\gamma+1})\frac{\vec{E}\times\vec{\beta}}{c}\right], \quad (2.1)$$

where the polarization vector $\vec{S}$ is expressed in the frame that moves with the particle. $\vec{B}_{\perp}$ and $\vec{B}_{//}$ are the transverse and longitudinal components of the magnetic fields in the laboratory frame with respect to the velocity $\vec{\beta}c$ of the particle. The vector $\vec{E}$ stands for the electric field, G is the anomalous gyromagnetic g-factor, and γmc^2 is the energy of the moving particle. In a pure magnetic field, $\vec{E}$ =0.

In the SU(2) representation, the spin vector can be expressed with two-component spinor $\psi=(\psi_1,\psi_2)^T$ where ψ_1,ψ_2 are complex numbers. The conversion between SU(2) and SO(3) is

$$\vec{S}=\psi^{+}\vec{\sigma}\psi \quad (2.2)$$

where $\vec{\sigma}=(\sigma_1,\sigma_2,\sigma_3)$ are Pauli matrices. Due to the unitarity of the spin vector, $P=|\psi_1|^2+|\psi_2|^2$, P is the polarization. $P=1$ for a single particle. In spinor notation, the T-BMT equation can be written as

$$\frac{d}{dt}\psi=-\frac{i}{2}(\vec{\sigma}\cdot\vec{\omega})\psi \quad (2.3)$$

ISBN 978-3-95450-185-4

The rotation from θ_i to θ_f is expressed by a unitary matrix M as

$$\psi_f = M\psi_i = e^{-i(\vec{n}\cdot\sigma)\phi/2}\psi_i \qquad (2.4)$$

where $\vec{n}$ is the rotation axis, ϕ is the spin rotation angle. ψ_i is the initial spin state, ψ_f is the final spin state.

SPIN TRACKING USING PTC

Tracking Code PTC

The Polymorphic Tracking Code (PTC) [5] written by Étienne Forest is a library of Fortran90 data structures and subroutines for integrating the equations of orbital and spin motion for particles in modern accelerators and storage rings. PTC implements the high energy physics lattices and uses the "Fully Polymorphic Package", FPP, as the engine to do the Lie algebraic calculations. FPP implements Taylor maps (aka Truncated Power Series Algebra or TPSA) and Lie algebraic operations, which allows it to extract a Poincaré map from PTC. FPP also provides the tools to analyze the resulting map. The most common and important tool is the **normal form**: with this at hand, one can compute tunes, lattice functions, and nonlinear extensions of these and all other standard quantities of accelerator theory. Indeed, the combination of PTC and FPP gives access to all of standard perturbation theory on complicated accelerator lattice designs.

Normal Form for Spin on the Closed Orbit: $\vec{n}_0$

In PTC, spin is considered as a spectator, the closed orbit does not depend on spin. A map: $T = (m, S)$, where ***m*** is an orbital map and ***S*** is a spin matrix that depends on the orbit. This map acts on a ray $\vec{z}$ and a spin vector $\vec{s}$ as

$$T(\vec{z},\vec{s}) = (m(\vec{z}), S(\vec{z})\vec{s}) \qquad (3.1)$$

The matrix for the spin is evaluated at $\vec{z}$ and multiplies onto the vector $\vec{s}$. If a beam line #1 is followed by beam line #2, the spin map for the full beam line is then given by

$$\begin{aligned} T_2 \circ T_1 &= (m_2, S_2)\circ(m_1, S_1) \\ &= (m_2 \circ m_1, S_2 \circ m_1 S_1) \end{aligned} \qquad (3.2)$$

The matrix $S_2 \circ m_1 S_1$ is simply the product of $S_2 S_1$ where $S_2(\vec{z})$ is evaluated at $\vec{z} = m_1(\vec{z})$ with $\vec{z} = (x, p_x, y, p_y, z_5, z_6)$. If the map is a one-turn map around the closed orbit at some position s whose coordinates will be $\vec{0} = (0,0,\cdots,0)$, without loss of generality, it is straight forward to raise T_s to a power $T_s^k(\vec{0},\vec{s}) = (\vec{0}, S_s^k(\vec{0})\vec{s})$. This simply reflects the fact that on the closed orbit, the matrix S for the spin is a constant matrix turn after turn. This matrix is a rotation and thus contains an invariant direction denoted as $\vec{n}_0$. We have $S_s^k(\vec{0})\vec{n}_0 = \vec{n}_0$. Now at some arbitrary position s, the matrix $S(\vec{0})$ can be expressed in terms of $\vec{n}_0$ and its rotation angle θ_0 around $\vec{n}_0$:

$$S_s^k(\vec{0}) = \exp(k\theta_0\vec{n}_0\cdot\vec{L}) \qquad (3.3)$$

The matrices L_i are the usual generator of rotations obeying the commutation relations of the rotation group:

$$[L_i, L_j] = \varepsilon_{ijk} L_k \qquad (3.4)$$

They are

$$L_1 = \begin{pmatrix} 0 & 0 & 0 \\ 0 & 0 & -1 \\ 0 & 1 & 0 \end{pmatrix} \quad L_2 = \begin{pmatrix} 0 & 0 & 1 \\ 0 & 0 & 0 \\ -1 & 0 & 0 \end{pmatrix} \quad L_3 = \begin{pmatrix} 0 & -1 & 0 \\ 1 & 0 & 0 \\ 0 & 0 & 0 \end{pmatrix} \qquad (3.5)$$

where ε = -1 is chosen in the FPP package. $L_{1,2,3}$ are referred to as $L_{x,y,z}$ most of the time. Fig. 2 gives a pictorial view of the algorithms of PTC. The red dot represents a ray moving in the "real world." The blue dots represent the spin.

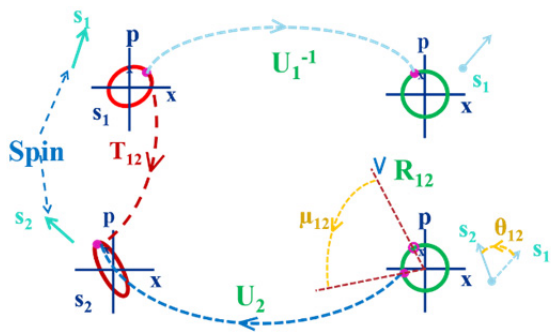

Figure 2: Pictorial view of the algorithms of PTC.

The Nonlinear Normal Form for the Invariant Spin Field (ISF): $\vec{n}(z)$

The invariant spin field (ISF) [6] was introduced by Barber and his collaborator as follows: there exists a vector $\vec{n}(\vec{z},s)$, a 3–vector *field* of unit length obeying the T–BMT equation along particle orbits $(\vec{z}(s);s)$ and fulfilling the periodicity condition $\vec{n}(\vec{z},s+C) = \vec{n}(\vec{z},s)$, where C is the circumference. Thus

$$\begin{aligned} &\vec{n}(\vec{m}(\vec{z},s);s+C) = \vec{n}(\vec{m}(\vec{z},s);s) \\ &= S_{3\times3}(\vec{z};s)\vec{n}(\vec{z};s) \qquad or \quad S\vec{n} = \vec{n}\circ\vec{m} \end{aligned} \qquad (3.6)$$

where $\vec{m}(\vec{z};s)$ is the new phase space vector after one turn starting at $\vec{z}$ and s and $S_{3\times3}(\vec{z};s)$ is the corresponding spin transfer matrix. This equation states that a vector $\vec{n}(z)$ whose transformation is under the spin matrix $S(\vec{z})$ is the same as its transformation under the map $\vec{m}(\vec{z};s)$. This equation can be easily applied to $\vec{n}_0$ since it is a constant under the application of $S(\vec{0})$ and the closed orbit is by the definition a constant, i.e. $\vec{m}(\vec{0}) = \vec{0}$. For an arbi-

ISBN 978-3-95450-185-4

trary $\vec{z}$, Eq. (3.6) implies that if we follow $\vec{n}(\vec{z},s)$ after k turns, the answer is simply $\vec{n} \circ m^k$. Thus the Fourier spectrum of $\vec{n} \circ m^k$ will not contain the spin frequency. This object behaves as if spin motion did not exist. If viewed as a vector field, the entire three dimensional field $\vec{n}(\vec{z},s)$ is left invariant under the action of the full spin-orbital map T. Obviously, if a particle at coordinate $\vec{z} = (x, p_x, y, p_y, z_5, z_6)$ starts with a spin slightly different from $\vec{n}(\vec{z},s)$, the actual spin will move around the axis $\vec{n}(\vec{z},s)$ and its spectrum will contain the spin tune as well as the orbital tunes. The chief aspects of the ISF are that: 1) For a turn–to–turn invariant particle distribution in phase space, a distribution of spins initially aligned along the ISF remains invariant (in equilibrium) from turn–to–turn, 2) For integrable orbital motion and away from orbital resonances, the ISF determines the maximum attainable time averaged polarization

$$P_{\lim} = \left|\langle \vec{n}(\vec{z},s) \rangle\right| \tag{3.7}$$

on a phase space torus at each s, where $\langle\ \rangle$ denotes the average over the orbital phases, 3) Under appropriate conditions, $J_s = \vec{n} \cdot \vec{S}$ is an adiabatic invariant while system parameters such as the reference energy are slowly varied.

SPIN TRACKING IN THE MI

The beam in the MI is injected at M306 (see Fig. 1) from the Recycler Ring at an energy of 8 GeV, and accelerated to 120 GeV from 0.413 seconds to 1.08 seconds, then slow spilled for another 0.5 seconds to the extraction Septum at M522 to the fixed target experiment. The Siberian snake would be placed at M222, a straight section with a more than 10 m long drift space, opposite of the ring to M522. For the purpose of spin tracking in the MI, a special module called z_fnal_meiqin.f90 was written and added into the PTC library. It handles the acceleration of the proton beam through the γ-transition from a kinetic energy of 8 GeV at injection to the flat-top of 120 GeV (γ=9.528 to 128.93). Based on the MI ideal lattice, the transition energy γ is 21.619 at a time of 0.568 seconds after injection, as calculated by PTC. Furthermore, the real 21Cycle tables of the acceleration rate, the tunes and the chromaticity changes during the ramp, were also implemented in the module. There are 20 RF cavities in the MI for acceleration. They altogether are treated as one thin element at the end of the cavity section in PTC. The RF phase is 23.189° before the transition and (π-23.189°) right after the transition. The beam can be assigned by 95% of normalized emittance in the transverse planes and momentum deviations (Δp/p) in the longitudinal plane. Longitudinal emittance will then be calculated in the module.

With the help of Étienne Forest, a code in Fortran90, named fnal_injector_accelerate.f90, was written to do the orbit-spin tracking in the MI. We started with the flat output file of the latest MAD lattice of the Main Injector ring. The input file of the MAD lattice file was translated with Bmad [7] developed by David Sagan, Cornell University. Dave Sagan implemented the PTC/FPP library of Étienne Forest into his Bmad code. Therefore, they built up an interface between Bmad and PTC. MAD, Bmad and PTC agree to within machine precision.

After the orbit and spin were tracked for the first turn, the One-Turn-Map for both orbital and spin was obtained. Then the normal form for spin on the closed orbit: $\vec{n}_0$, was calculated, which actually is the Invariant Spin Field (ISF) on the closed orbit. Then, the spin polarizations of all particles at injection are chosen to be aligned with $\vec{n}_0$. A numerical computation of the ISF by stroboscopic average is compared with an evaluation of the normal form ISF of a single particle, and was found that there is very little difference between these two results.

Tracking with an Ideal Lattice

Multi-particle tracking was done first by sending 128 particles uniformly distributed (called "flat distribution" here) in vertical and longitudinal phase space, as seen in Fig. 3. These 128 particles represent the beam. Using these results, the average polarization for different beam distributions can be calculated by integration as follows:

$$P_{ave} = \frac{1}{\sigma_1 \sigma_2} \sum_{i=1}^{128} \rho(\varepsilon_1, \varepsilon_2) \vec{S}_i \Delta\varepsilon_1 \Delta\varepsilon_2 \tag{4.1}$$

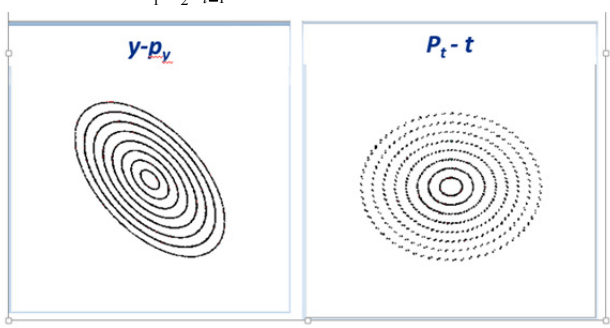

Figure 3: Particles distributed in the phase space.

For a Gaussian distribution,

$$\rho(\varepsilon_1, \varepsilon_2) = \frac{1}{\varepsilon_1 \varepsilon_2} e^{-\varepsilon_1/o_1} e^{-\varepsilon_2/o_2} \tag{4.2}$$

Then,

$$P_{ave} = \frac{1}{\sigma_1 \sigma_2} \sum_{i=1}^{128} e^{-\varepsilon_1/o_1} e^{-\varepsilon_2/o_2} \vec{S}_i \Delta\varepsilon_1 \Delta\varepsilon_2 \tag{4.3}$$

First, the particles were tracked with no snake. Fig. 4 presents the results of the average polarization. The *x-axis* is $\gamma = E/E_o$, $E_o = 0.938 GeV$, and *y-axis* is the Polarization, "1" represents 100% polarization aligned with $\vec{n}_0$, the Invariant Spin Field on the closed orbit. The black line is the result of the initial beam with uniform distribution (Flat), and the red line represents the result of the initial beam with Gaussian distribution (cut at 6σ). Both cases show that polarization will be lost soon after the beginning of the acceleration.

ISBN 978-3-95450-185-4

The particles were then tracked with a single snake placed in the ring. The snake is represented by a point-like spin flipper. Fig. 5 presents the average polarization of particles with 14 πmm·mrad (top panel) and 20 πmm·mrad (bottom panel) in vertical phase space, respectively. The momentum spread in both simulations is 1.25E-3. Polarization can be preserved at more than 90% at the end of the acceleration for most phase space distributions, except for the "Flat" distribution, which ends up at 88.8%. Similar results of average polarization were obtained for particles with 20 πmm·mrad in vertical phase space and momentum spread of 1.25E-3. The simulations show that the strongest resonance happens at γ=119.69 (Gγ=215), resulting in a big loss of polarization at the resonance, which however recovers in most cases. All the resonances here refer to the intrinsic spin resonances.

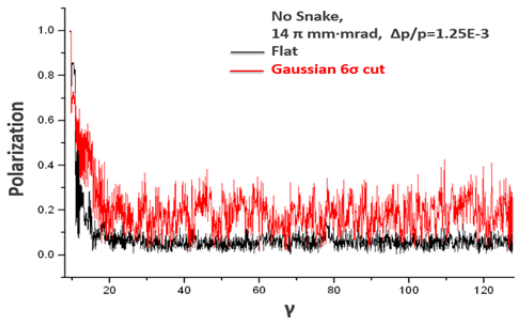

Figure 4: Spin tracking with no snake in the ring for beams with different distributions in phase space.

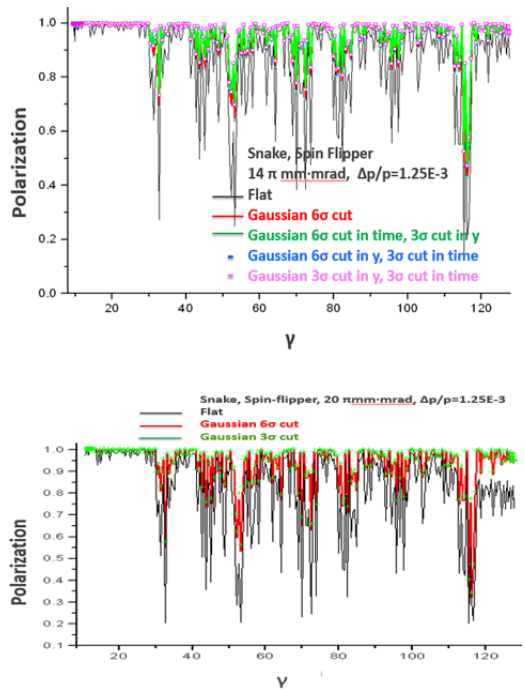

Figure 5: Spin tracking in an ideal MI lattice, using a point-like snake to flip the spin. Top panel: the emittance of the beam is 14 πmm.mrad. Bottom panel: the emittance of the beam is 20 πmm.mrad. The distributions in phase space are flat, Gaussian with 3σ or 6σ cut in y (vertical plane) and in time (longitudinal plane).

Tracking with a Realistic Lattice

The measured field errors [8] and the misalignment data of all the magnets in the MI ring have been implemented into the MI lattice. PTC reads the survey coordinates and uses its pointer and patch functions to place each magnet into its actual position in the ring. This includes all the misalignment information, such as the shifts in x, y and z, as well as the roll and pitch angles.

The closed orbit of the MI at injection before correction due to the magnetic field errors and misalignment is shown in Fig.6

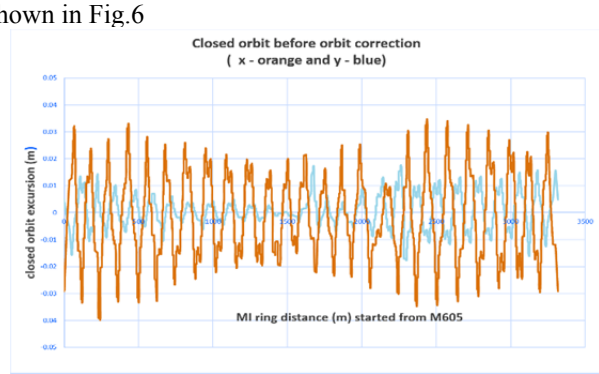

Figure 6: Closed orbit before correction.

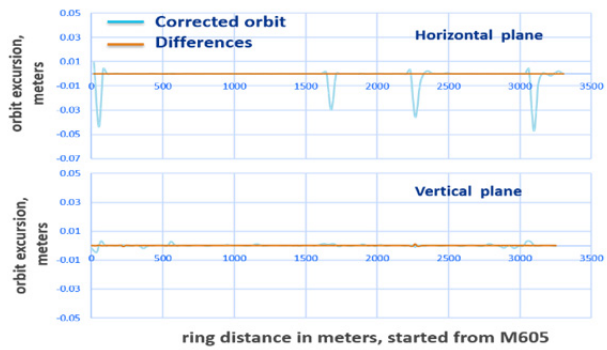

Figure 7: Closed orbit after correction.

The orbit correction program for MI operation is able to correct the orbit to its desired orbit in RMS differences of 0.18 mm and 0.15 mm in the horizontal and vertical planes, respectively. PTC takes the beam position monitor (BPM) readings of the machine corrected orbit as the desired orbit, and corrects the closed orbit to it with almost no difference, seen in Fig. 7.

Spin tracking in PTC was performed after various orbit corrections have been applied. Just as in tracking with an idea lattice, PTC adjusts the tunes and chromaticities after the orbit corrections, and also during the ramp according to the ramp table of the MI operation 21 Cycler, the event for beams to SeaQuest experiment. 256 particles uniformly distributed on the vertical phase space with an emittance of 20 πmm·mrad and on the longitudinal phase space with a momentum spread $\Delta p/p = 1.25 \times 10^{-3}$ were tracked. Fig. 8 presents the results. The *x-axis* is Gγ, with G=1.793 for protons, and γ the energy. The blue line represents the polarization for a beam with a flat particle distribution, while the orange line for a beam with a Gaussian distribution 6σ Cut. The final average polariza-

ISBN 978-3-95450-185-4

tion remains at 85.2% for the flat distribution, and at 88.1% for the Gaussian distribution 6σ Cut. This presents the best results that the MI can achieve for closed orbit corrections.

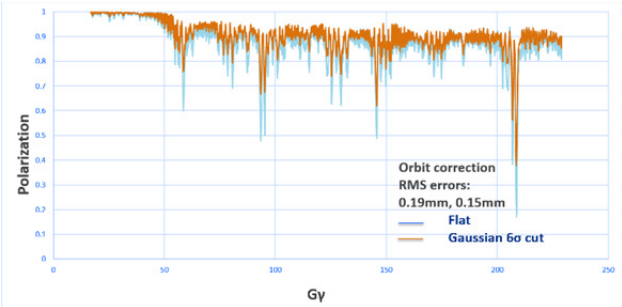

Figure 8: Average polarization after PTC corrected the closed orbit to the BPM readings. The RMS values of the differences are almost zero. Note that the RMS values of the difference between the BPM readings and the MI desired positions are 0.19 mm in the horizontal and 0.15 mm in the vertical plane. Final polarization is 85.2% for the flat distribution and 88.1% for the Gaussian distribution 6σ cut.

The base tune of the MI is 26.425 in the horizontal plane and the 25.415 in the vertical plane. The spin depolarizing resonances occur when $G\gamma = mP \pm \upsilon_y$, where P is the periodicity of the lattice, and υ_y is the vertical tune with υ_y=25.415. In the presence of magnetic field errors, periodicity is broken, P=1. Therefore, the most imperfect resonances occur for integers closest to $\pm\upsilon_y$. The tracking results show that the most imperfect resonances happen at Gγ=59, 94, 95, 146, 206, 209, which is near to M υ_y, , M=2, 4, 6, 8. The strongest resonance in this case is at Gγ= 209.

To see the effect of vertical orbit errors on the polarizations, we let PTC correct the closed orbit to the MI desired orbit with slightly larger RMS errors. Fig. 9 presents the results for three different cases. In the top panel, the correction of the RMS error is 0.19 mm in the horizontal and 0.21 mm in the vertical planes. Not only do the depolarization resonances shown in Fig. 8 get stronger, but the two moderate resonances near Gγ=125 combined into one stronger resonance. Similarly, this also happened for resonance near Gγ=150 and 175. In the middle panel, the polarization is lost completely at Gγ=90 when PTC corrected the closed orbit to the MI desired orbit for RMS errors of 0.27 mm in the horizontal plane and 0.28 mm in the vertical plane. At Gγ=89.6, the average polarization drops below 70%. In the bottom panel, RMS errors of 0.43 mm in the horizontal plane and 0.45 mm in the vertical plane lead to strong imperfect resonance near Gγ=59 and 58.4, resulting in complete loss of polarization.

CONCLUSIONS

Spin tracking of polarized protons in the Main Injector has been carried out for a "realistic" lattice that includes measured magnet field errors and misalignment survey

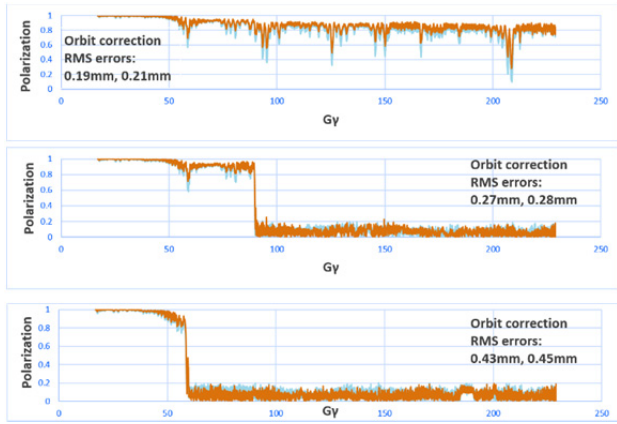

Figure 9: Average polarization for PTC closed orbit corrections to the desired orbit for various RMS values.

data, as well as various degrees of orbit corrections that demonstrate the requirements that are needed to preserve significant polarization in the Main Injector. The simulations have shown that the polarization in the Main Injector is very sensitive to the excursions of the closed orbit. RMS deviations between the corrected orbit and the desired orbit should not be larger than 0.2 mm in both the horizontal and the vertical planes. The present MI orbit correction program can get closed orbit corrected to the desired orbit with RMS excursions of 0.18mm in the horizontal plane and 0.15mm in vertical plane. The final polarizations in the MI after ramping the energy up to 120 GeV can be kept at 85.2% for a flat beam distribution and 88.1% for a Gaussian beam distribution a 6σ cut using a point-like snake (flip-spin).

Implementation of a full-size 4-twist helical dipole instead of a point-like snake has started. PTC has successfully performed Symplectic integration through a specific 4-twist helical dipole configuration at various energies. Spin tracking studies of polarized protons in the Booster, as well as in the transfer lines are underway. This will allow to confirm whether polarized protons can be produced and maintained in the Fermilab accelerator complex using single Siberian snakes in the larger synchrotrons.

ACKNOWLEDGEMENT

We would like to express appreciation to the Fermilab Accelerator Division, in particular to Sergei Nagaitsev and Ioanis Kourbanis, for their support. We would like to thank Étienne Forest (aka Patrice Nishikawa, KEK) for allowing us to use his remarkable PTC/FPP library and for his patience in explaining it to us in detail. We would also like to thank David Sagan (Cornell University) for use of his Bmad code to convert the MAD lattice format to a PTC readable format.

ISBN 978-3-95450-185-4

REFERENCES

[1] I. Kourbanis, *et al.*, "Current and Future High Power Operation of Fermilab Main Injector". FERMILAB-CONF-09-151-AD, 2009.

[2] W. Lorenzon, *et al.,* "Polarized Drell-Yan Measurements with the Fermilab Main Injector", Fermilab proposal P-1027, May 20, 2012.

[3] F. Antoulinakis*, et al.,* "One 4-Twist Helix Snake to Maintain Polarization in 8-120 GeV Proton Rings", JLAB-ACP-13-1722, Sep 4, 2013.

[4] V. Bargmann, Louis Michel and V. L. Telegdi, "Precession of the Polarization of Particles Moving in a Homogeneous Electromagnetic Field", Physical Review Letters, Vol, 2, No.10, P.435 (1959).

[5] É. Forest, "From Tracking Code to Analysis-Generalised Courant-Snyder theory for any accelerator models", Springer, August 2015.

[6 D.P.Barber *et al.*, "Spin Tune in the single Resonance model with a pair of Siberian Snakes", 15th Int. Spin Physics Symposium, BNL, Long Island, USA September 2002, AIP proceedings 675 (2003).

[7] D. Sagan, http://www.lepp.cornell.edu/~dcs/bmad/

[8] The Main Injector Project magnet data, http://www-ap.fnal.gov/MagnetData/

ISBN 978-3-95450-185-4

THE DESIR FACILITY AT GANIL-SPIRAL2: THE TRANSFER BEAM LINES

L. Perrot†, P. Blache, S. Rousselot, Université Paris-Saclay, Université Paris Sud, CNRS-IN2P3-IPN, Orsay, France

Abstract

The new ISOL facility SPIRAL2 is currently being built at GANIL, Caen France. The commissioning of the accelerator is in progress since 2015. SPIRAL2 will produce a large number of new radioactive ion beams (RIB) at high intensities. In 2019, the DESIR facility will receive beams from the upgraded SPIRAL1 facility of GANIL (stable beam and target fragmentation), from the S3 Low Energy Branch (fusion-evaporation and deep-inelastic reactions). In order to deliver the RIB to the experimental set-ups installed in the DESIR hall; 110 meters of beam line are studied since 2014. This paper will focus on the recent studies which have been done on these transfer lines: beam optics and errors calculations, quadrupoles, diagnostics and mechanical designs.

THE DESIR FACILITY WITHIN THE SPIRAL2 PROJECT

SPIRAL2 is a major extension project of the GANIL facility in Caen, France dedicated to the production of heavy ion beams at high intensities and of very exotic nuclides. With SPIRAL2, the French and International communities will make decisive steps in the understanding of the atomic nucleus and of the nucleosynthesis processes occurring in astrophysics. The collection of nuclear data will help preparing the next generation of nuclear reactors and the production of new isotopes suitable to nuclear medicine will be investigated. In addition, a high intensity fast neutron source will open new research domains in material science [1]. The SPIRAL2 facility will produce a large number of new radioactive ion beams (RIB) at high intensity. These beams will be produced using a new linear accelerator that will deliver deuterons up to 40MeV at 5mA intensity, protons up to 33MeV at 5mA and ions with A/Q=3 up to 14.5MeV/u at 1mA (see Fig. 1) [2].

* Work supported by the French research agency (ANR), through the program "Investissements d'Avenir", EQUIPEX Contract number ANR-11-EQPX-0012

† perrot@ipno.in2p3.fr

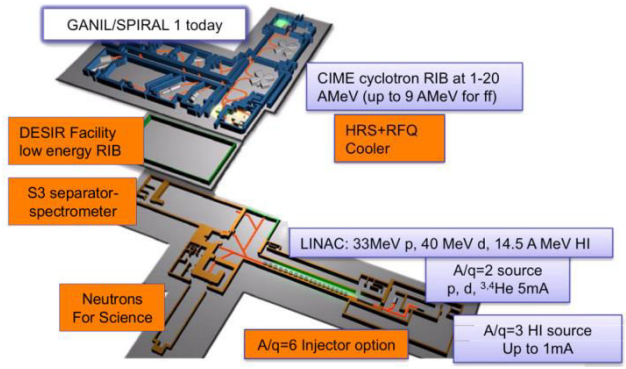

Figure 1: Scheme of the SPIRAL2 facility.

The DESIR (Decay, Excitation and Storage of Radioactive Ions) facility will receive beams delivered by the S3-LEB (Low Energy Branch of the new Super Separator Spectrometer) of SPIRAL2 [3]. Nuclides will be produced in fusion-evaporation, transfer and deep-inelastic reactions, and will notably consist in refractory elements. Finally, RIB produced in the fragmentation of high-intensity heavy ions and/or thick targets at the upgraded SPIRAL1 facility will also be available at DESIR [4]. The Steering comity of the SPIRAL2 project promote the phase 1+ witch include the DESIR facility with its transfer beam line coming from S3 and SPIRAL1.

Nuclear physics as well as fundamental weak-interaction physics and astrophysics questions will be addressed by means of laser spectroscopy, decay studies, mass spectrometry and complementary trap-assisted measurements. Experience at other ISOL facilities evidences that ion beams with a high degree of purity are required to push experiments towards the limits of nuclear stability [5, 6, 7].

GENERAL PRINCIPLES FOR DESIGN

The DESIR facility consists to a 1500 m2 experimental hall and 97m of upstream and interconnected beam lines. Along these lines, a RFQ-Cooler [8] and a High Resolution Separator (HRS) [9] will be in charge to provide a reduction of the emittance and high purification of the beams coming from S3-LEB and SPIRAL1 (see Fig. 2). The RFQ-Cooler will be located just before the HRS. Beam coming from S3-LEB or SPIRAL1 will can be injected in this branch or by-passed for direct injection up to the DESIR hall according physics experimental requirements. Experimental set-ups will be located in the large hall (see Fig. 2).

ISBN 978-3-95450-185-4

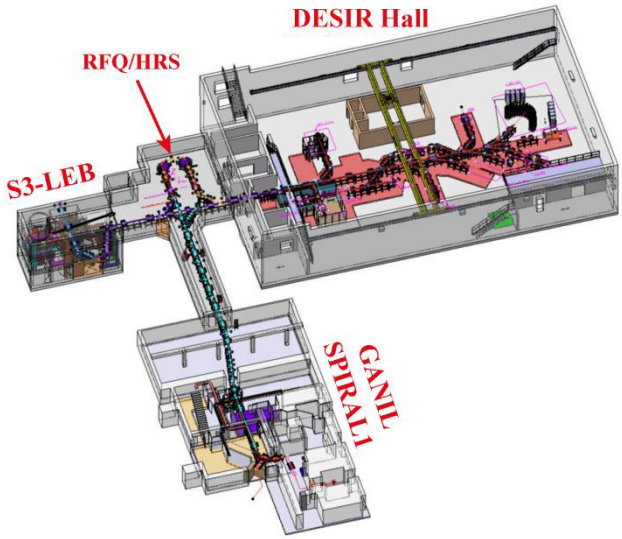

Figure 2: Scheme of the transfer beam line, S3-LEB and SPIRAL1 up to DESIR experimental hall. Designs of the building are not yet fully fixed.

Beam lines in DESIR experimental area, RFQ/HRS and SPIRAL1 lines will be at -1.75m underground. Beam line coming from S3-LEB will be at -8.5m ground. 3 various types of deviation must be designed: vertical (90°), and 2 in the horizontal plane (45° and 10°).

The building studies are actually under way. The final and optimal solution taking into account of all aspects will be delivered soon. The public enquiry will start in 2017, then building before making available for installation in 2019.

OPTIC CONCEPTION OF THE TRANSFER LINES

Nominal Beam Dynamic

Lines have been design in order to accept maximum beam energy to 60 keV and transverse geometric emittance to 80 π.mm.mrad. Only singly-charged ions will be transported, for which electrostatic optical devices are better suited [10, 11].

Careful studies of the beam dynamics were performed using the CEA TraceWin code [12]. This code allows to run large and close to real condition simulations, to use field maps of optical elements, to perform diagnostics location optimizations, errors studies, corrections and feed-backs [13].

Making use of the knowledge and long experience on electrostatic devices [14, 15], we have studied and designed all optics elements with respect to the maximum beam emittance and energy. Electrostatics devices like quadrupoles, steerers and deflectors have been studied using the Opera-3D simulation tool [16]. Then, calculated field maps were used and compared directly in the TraceWin simulations of the entire transfer beam line.

Figure 3 shows the RMS transverse beam envelops along the transfer line linking the S3-LEB to the entrance of DESIR experimental hall. We can observe a good agreement between the two calculations using pure and field maps for the optical elements.

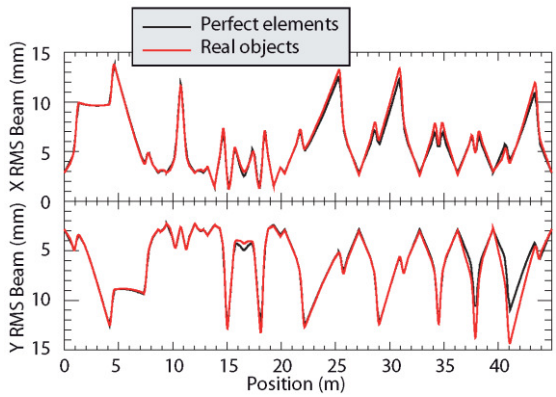

Figure 3: RMS transverse beam envelops along the 45m long transfer line linking the S3-LEB to the entrance of DESIR experimental hall. Black curves calculation using pure optical elements, red curves calculation using real field maps for optical elements.

Figure 4 shows the transverse beam distributions at the end of the line (the entrance of DESIR experimental hall). Calculated emittance growth is lower than 10% and transmission is better than 99.9%.

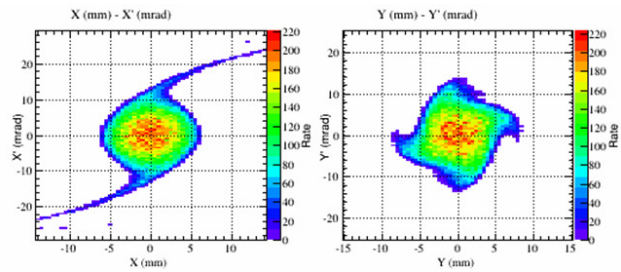

Figure 4: Calculated transverse beam emittances at the end of the line (the entrance of DESIR experimental hall) using field-maps for the optical elements.

Same calculations and methodology were taken for each beam lines. Nominal parameters are already defined. For a 60keV mono-energetic beam, maximum potential in the quadrupoles will be 3200V and 7880V in deflectors. We will use quadrupoles with aperture to D=100mm, length to 175mm with a circular shaping with R=57.5mm (reduce cost compare to hyperbolic shape). Two grounded rings will be 2mm thick, 100mm in aperture located at 27.5mm to the electrodes. Deflector radius will be ρ=400mm, aperture a=50mm, electrode height h=100mm, Pole face will be toroidal shape with radius to 335mm in order to have an optimized focus. 45° bending is obtained with 37° angular aperture and 90° bending is obtained with 83° angular aperture. Horizontal and vertical orbit correctors will be located at the same longitudinal position. Electrodes will be set at maximum potential to ±300Volts (see next section for explanation). Electrodes gap will be 100mm, Length to 100mm and width to 80mm with additional longitudinal shimming.

ISBN 978-3-95450-185-4

Errors Calculation

Quadrupoles, steerers and deflectors alignments have to be better than 0.1mm, field stability precision better to 1%, rotation better to ±0.1°. Diagnostics position must be better than ±0.5mm and beam sizes measurements precision must be lower than ±0.5mm.

With these real conditions, we make errors calculations on beam lines in order to ensure that our structures are stables and adjustable. It can be also use to define working range and precisions of the electric alimentation for optical elements.

For each line, we made 500 errors calculation by apply random and homogeneous errors to each element and primary beam. New lines parameters are recalculated for each case. Therefore, we obtain value set for each individual optical elements (see Figs. 5 and 6).

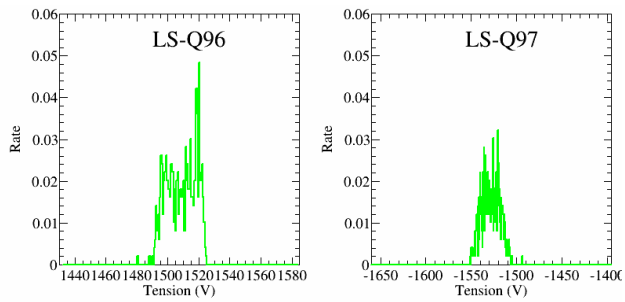

Figure 5: Examples of potentials distribution obtain for two quadrupoles for the 500 calculations.

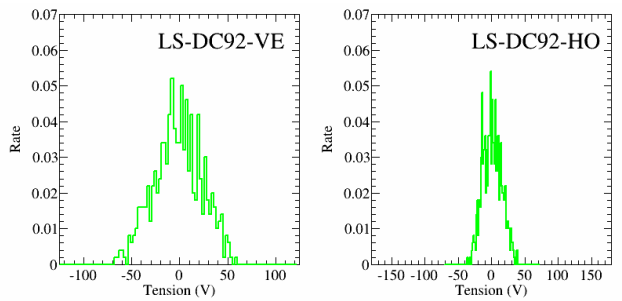

Figure 6: Examples of potentials distribution obtain for two steerers for the 500 calculations.

For each optical element, we determine the mean, the RMS, maximum and minimum values. A general criterion of the beam optic correction scheme can be the mean of the difference between the maximum and the minimum value divided by the average value for each quadruple. More this mean is small; more the beam line is stable. In our case, this value is close to 15%. For the beam alignment, our criterion is the mean of the difference between the maximum and minimum steerer by steerer. In our case, this value is close or lower than 150V. Therefore, we see that we have sufficient margin for the ±300Volts steerer alimentations.

We have also study the beam characteristics at the end of the lines. For each errors calculations, transverses positions and sizes are known and can be compared with the nominal properties. As an example we give in Table 1 the characteristics obtained at the end of the 45m long transfer line between S3-LEB and the DESIR hall.

Table 1: Calculated errors of the positions and sizes for the 60keV mono-energetic beam at the end of the 45m long transfer line from S3-LEB up to DESIR hall.

		Mean	RMS
Orbits or Positions	X (mm)	0.0	0.2
	X' (mrad)	0.0	0.3
	Y (mm)	0.0	0.3
	Y' (mrad)	0.0	0.3
RMS Sizes	X (mm)	2.9	0.7
	X' (mrad)	4.7	0.2
	Y (mm)	2.9	0.1
	Y' (mrad)	4.7	0.2

Using these errors conditions, the beam stability in the lines is estimated to be less than 1mm at 3RMS (orbit and size) and 2.1mrad for the transverses divergences sizes which is satisfying for our case.

MECHANICAL CONCEPTION

According beam process specifications we have already done the full transfer beam line integration. Coordination system and mechanical standards definition is done by the SPIRAL2 Phase1+ system group. IPN Orsay is in charge to make the complete mechanical conception up to 2D detail drawings of optics devices, diagnostics boxes, bellows, pipes, supports, frames.

Figure 7 shows the mechanical design of the electrostatic quadrupole, steerer vertical and horizontal.

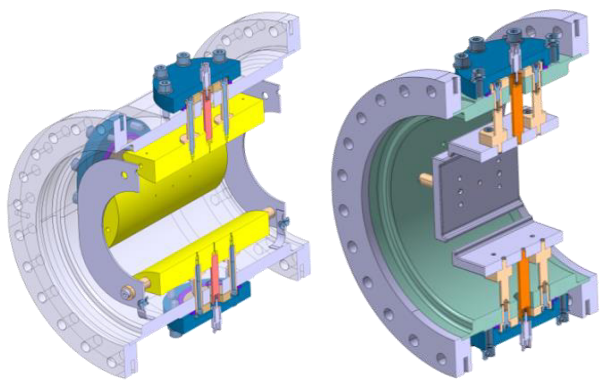

Figure 7: 3D design of the electrostatic quadrupole (left picture) and steerer (right picture) inside the vacuum chambers.

Vacuum chamber of quadrupole and steerer will be identical and machining with the same technic. Blocks will be assembling in order to form quadrupole doublet or triplet with a vertical and horizontal steerer. The mounting procedure has already been validated in through a prototype made in 2014. The prototype is in operation at CEN Bordeaux-Gradignan laboratory and connect to a R&D experimental device dedicated to DESIR.

ISBN 978-3-95450-185-4

Figure 8 shows the mechanical design of the electrostatic beam deflectors to 45° and 90° bending angles.

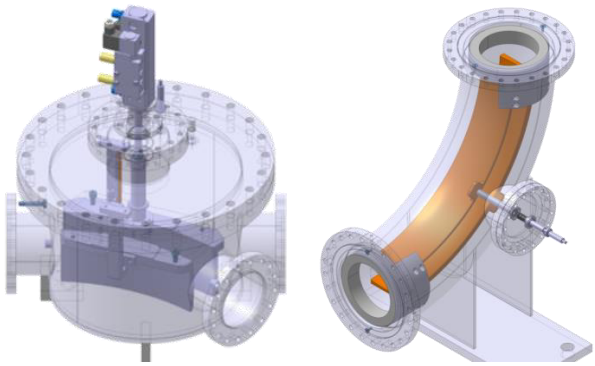

Figure 8: 3D design of the electrostatic beam deflectors 45° (left picture) and 90° (right picture) bending angles.

According the various paths of the beam in the transfer lines, we have design the 45° deflector in order to have the possibility to remove the electrodes to the line. Design is carefully study in order to obtain an excellent reproducibility of positioning.

Figure 9 shows example of a diagnostic box conception with 3 diagnostics which can be inserted in the beam line.

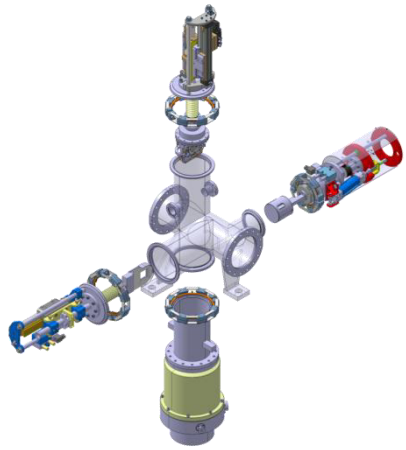

Figure 9: Diagnostic box conception with 3 diagnostics insertion (secondary emission profiler, low intensity profiler, faraday cup) and turbo-molecular pump.

The full integration takes into account of various parameters like building constraints, implantation of crate and electronics in the frame, GANIL mechanical standards, vacuum systems, installation and maintenance methodology, free space under the line, safety and security rules (see Fig. 10).

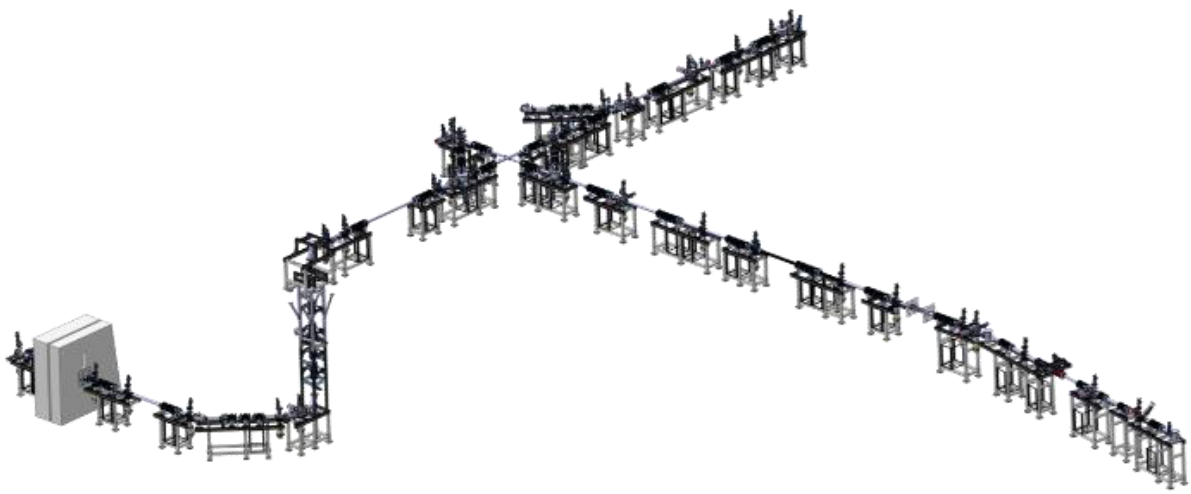

Figure 10: 3D view of the transfer line for the DESIR project.

CONCLUSION

We have presented here an introduction of the DESIR project. DESIR will be a new and extended experimental area dedicated to the study of the fundamental properties of new exotic radioactive nuclides to be produced at SPIRAL2-GANIL. This paper is focused on the long beam transfer lines which will connect the different production sites to the DESIR experimental hall. Low energy beams will be delivered by the Low Energy Branch of the new Super Separator Spectrometer (S3-LEB) and the upgraded SPIRAL1 facility.

Special care must be taken about focalization devices, deflectors, kicker benders and orbit correctors in combination with beam diagnostic measurements in order to minimize the overall cost of the beam lines and to optimize their tuning. This process has started in 2013. A prototype quadrupole structure has been manufactured. The set-up already operates properly at CENBG since 2015. It will offer the possibility to validate the machining choices and to have feed-backs with the beam dynamic calculations. We have already done some modifications which have been illustrated. All systems of the lines are integrated in the transfer line. The preliminary design review points few small modifications. Details studies are under way. According the collaboration between GANIL

ISBN 978-3-95450-185-4

and FAIR, building of series will start at the beginning of 2017.

Same methodology of studies will be taken in the DESIR experimental hall. Physics requirements for each experimental set-ups are not yet well defined. Installation of the sub-section beam line up to experimental set-ups will be phase in time.

ACKNOWLEDGMENT

This work is supported by the French research agency (ANR), through the program "Investissements d'Avenir", EQUIPEX Contract number ANR-11-EQPX-0012.

REFERENCES

[1] M.-G. Saint Laurent et al., SPIRAL PHASE-II, European RTT, Final report, Contract number ERBFMGECT980100, http://pro.ganil-spiral2.eu/spiral2, September (2001).

[2] E. Petit, on behalf of the SPIRAL2 collaboration, Progress of the SPIRAL2 project, in proceedings of the IPAC conference, San Sebastian, Spain (2011), http://www.jacow.org/

[3] B. Blank, The DESIR facility at SPIRAL2, Pramana – J. Phys 75 (2010) 343.

[4] B. Blank for the DESIR collaboration, The DESIR Facility, Letter of Intent for SPIRAL2 (2006), GANIL Caen-France, http://www.cenbg.in2p3.fr/desir/

[5] F. Azaiez, S. Essabaa, F. Ibrahim and D. Verney, The ALTO facility at Orsay, NPN, 23, Issue 2 (2013).

[6] The ISOLDE Facility, A Tool for Understanding the Strong Interaction, NPN, 20, Issue 4, (2010), http://www.scholarpedia.org/article/The_ISOLDE_facility

[7] M. Trinczek, Beam Delivery And Future Initiatives at The ISAC Radioactive Ion Beam Facility, in proceedings of the PAC conference, Vancouver, BC, Canada, (2009), http://www.jacow.org/

[8] R. Boussaid et al. Simulations of high intensity ion beam RFQ Cooler for DESIR/SPIRAL2: SHIRaC, Journal of Instrumentation, Vol. 9, July 2014.

[9] T. Kurtukian-Nieto, SPIRAL2/DESIR high resolution mass separator, Vol. 317, Part B, December 2013, 284-289.

[10] H. Wollnik, Optics of Charged Particles, (Academic Press, INC. 1987).

[11] F. Hinterberger, Ion Optics with Electrostatic Lenses, (CAS on Small Accelerators, CERN-2006-012, 2006)

[12] TraceWin code: http://irfu.cea.fr/Sacm/logiciels/index.php

[13] R. Duperrier and D. Uriot, Application of the extreme value theory to beam loss estimates in the SPIRAL2 linac based on large scale Monte Carlo computations, Phys. Rev. Spe. Topics – Acce and Beams 9, 044202 (2006).

[14] A. Septier and J. Van Acker, Les Lentilles Quadrupolaires Electrostatique, NIM 13 335 (1961)

[15] R. Baartman and D. Kaltchev, Short Quadrupole Parametrization, in proceeding of the PAC conference, Albuquerque, New Mexico, USA, (2007).

[16] Opera-3d - electromagnetic design in three dimensions, http://www.cobham.com/about-cobham/aerospace-and-security/about-us/antenna-systems/kidlington/products/opera-3d.aspx

ISBN 978-3-95450-185-4

STATUS OF THE BEAM DYNAMICS DESIGN OF THE NEW POST-STRIPPER DTL FOR GSI - FAIR

A.Rubin†, D. Daehn, X. Du, L. Groening, M.S. Kaiser, S. Mickat, GSI, Darmstadt, Germany

Abstract

The GSI UNILAC has served as injector for all ion species since 40 years. Its 108 MHz Alvarez DTL providing acceleration from 1.4 MeV/u to 11.4 MeV/u has suffered from material fatigue and has to be replaced by a new section [1]. The design of the new post-stripper DTL is now under development in GSI. An optimized drift tube shape increases the shunt impedance and varying stem orientations mitigate parasitic rf-modes [2]. This contribution is on the beam dynamics layout.

INTRODUCTION

The existing UNIversal Linear ACcelerator UNILAC at GSI (Fig. 1) serves as injector for the Facility for Antiproton and Ion Research (FAIR), which is under constructing now at GSI [3]. The UNILAC will provide all primary ions but protons.

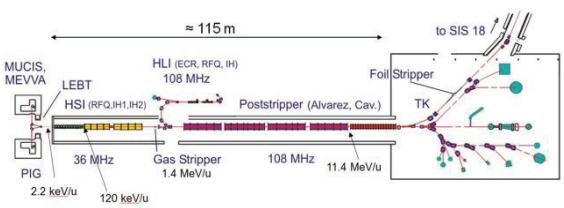

Figure 1: The UNIversal Linear ACcelerator (UNILAC) at GSI.

Due to the FAIR [4] requirements the UNILAC needs a considerable upgrade in nearest future. The existing post-stripper DTL suffered considerably from material fatigue during the last four decades and the amount of resources required for its maintenance increases continuously [5]. Replacement by a completely new DTL is due. The beam design parameters of the upgraded UNILAC are listed in Tab. 1.

Table 1: Parameters of the Upgraded UNILAC

Ion A/q	≤ 8.5
Beam Current	1.76 A/q mA
Input Beam Energy	1.4 MeV/u
Output Beam Energy	3-11.7 MeV/u
Beam Pulse Length	200µs
Beam Repetition Rate	10 Hz
Rf Frequency	108.408 MHz

BEAM DYNAMICS SIMULATIONS FOR THE 1ST ALVAREZ TANK

Beam dynamics simulations for the new post-stripper DTL were done for $^{238}U^{28+}$ using the TraceWin code [6]. The behaviour of the beam in the proposed structure was investigated for different zero current phase advances, as without current, as for the current of 15 mA. Input rms emittances were chosen as $E_x=E_y=0.175$mm·mrad (norm.), $E_z=16.57$deg·MeV. Periodic solutions were found for each case. The smallest transverse emittance growth along the 1st tank A1 (15mA) was obtained for a zero current phase advance k_0 of 55°-90°. It confirms results of the measurements in frame of the HIPPI experiments [7,8]. The initial zero current phase advances k_0 of 65°-90° also correspond to the stability areas of the Hofmann stability chart (Fig. 2).

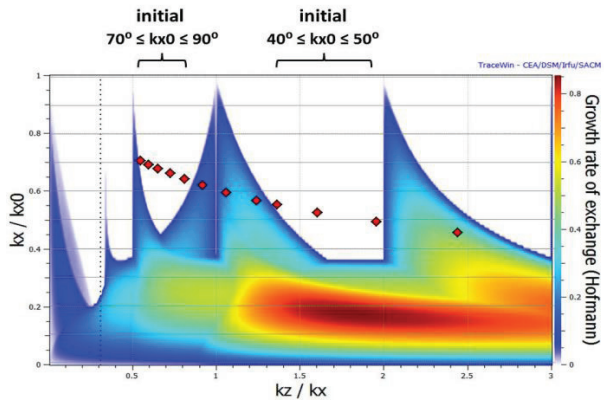

Figure 2: Initial zero current phase advances at Hofmann stability chart for the 1st tank of the new Alvarez-DTL.

Concerning the electric and magnetic field models the following cases for tank A1 were studied:

- "hard edge" model for E-field and B-field with identical quadrupoles in each drift tube (effective length of 96mm);
- 3D field maps for E-field, analytical field model for B-field with identical quadrupoles;
- 3D field maps for E-field and B-field with identical quadrupoles;
- "hard edge" model for E-field and B-field with three groups of quadrupoles (effective lengths 96 mm, 122 mm and 140 mm);
- 3D field maps for E-field, analytical field model for B-field with three groups of quadrupoles as above.

† a.rubin@gsi.de

ISBN 978-3-95450-185-4

Beam dynamics simulations were done for k_0= 65° and for I=15 mA. The results of simulations of all cases are basically identical (Fig. 3-4). The transverse rms emittance growth for A1 is up to 3%, longitudinally it is about 2% (Fig. 5).

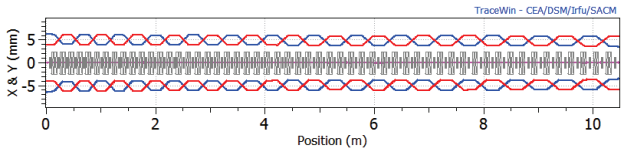

Figure 3: Transverse envelopes along A1.

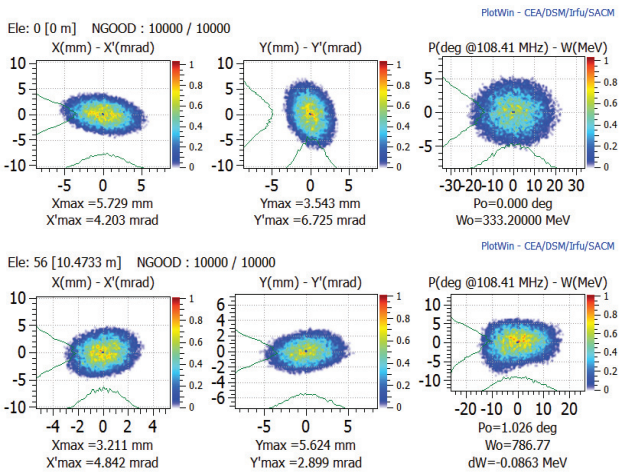

Figure 4: Input (top) and output (bottom) particle distributions for A1.

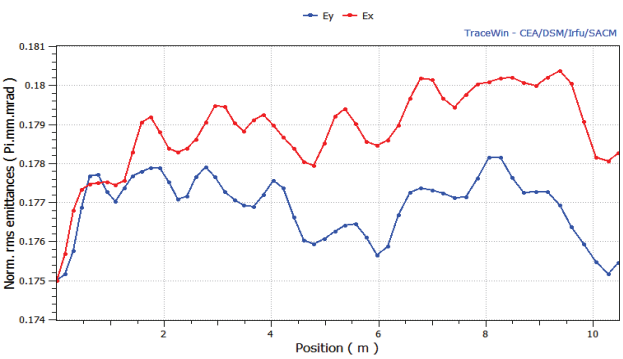

Figure 5: Transverse rms emittance along new tank A1.

GENERAL MODEL OF THE INTERTANK SECTION

The intertank sections for the presented design consist of quadrupoles, a phase probe, a current transformer, a valve, a profile grid, and a buncher. The layout is not finalized yet but the installation length is close to 1m. The recent design is shown in Fig. 6. The three quadrupoles, two of an effective length of 96 mm are assigned to the half drift tubes (Q1,3), are positioned to keep strict periodicity. The middle one (Q2) should have approximatelly 25% more of effective length. The distances between the quadrupole centers are about 50 cm. A re-buncher with 0.4-0.7MV is placed behind the 2nd quadrupole.

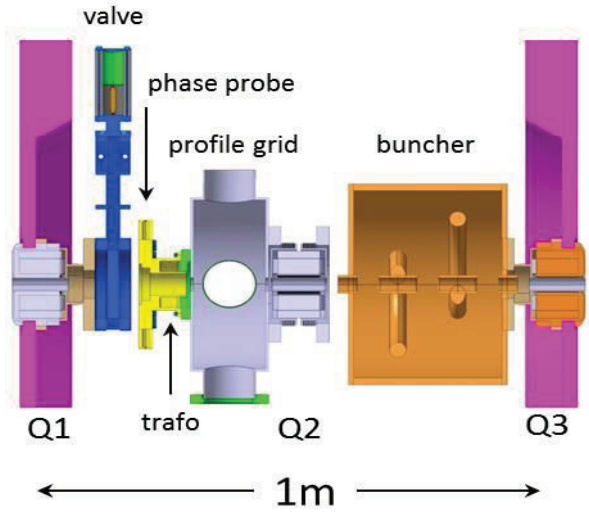

Figure 6: Design of the 1st intertank section.

BEAM DYNAMICS SIMULATIONS FOR THE COMPLETE ALVAREZ DTL

Beam dynamics simulation along the complete Alvarez DTL was done for the transverse zero current phase advance k_0 of 65° for each tank. The intertank sections allow for a matched transition. The layout is basically the same for all intertank sections, except the total length.

Regarding the periodic solution the following settings are proposed for the DTL: A1 - 55 cells, A2 - 45 cells, A3 - 37 cells, A4 - 33 cells, A5 - 18 cells. The rebuncher voltage is fixed at 0.5 MV for all intertank sections. The intertank quadrupole gradients were found separately. The gradients of the 1st and the 3rd quadrupole-in each intertank section vary from 31 T/m to 45 T/m, the 2nd ones are about 65 T/m. The transverse and longitudinal envelopes along the whole Alvarez DTL are shown on Fig. 7.

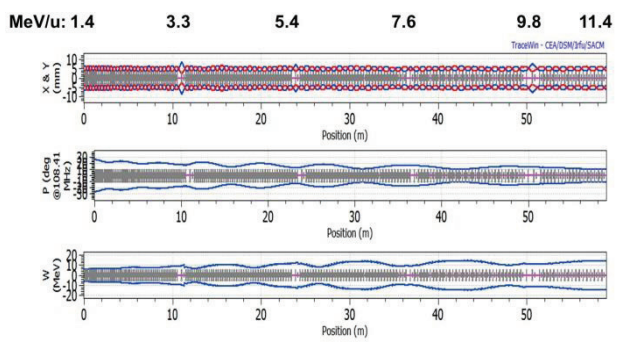

Figure 7: Transverse and longitudinal envelopes along the complete Alvarez DTL.

ISBN 978-3-95450-185-4

Output particle distributions are compact (Fig. 8) and can be easily matched to the following structures. The tranverse emittance growth is about 4%, longitudinal - it is about 1.5% along the whole DTL (Fig. 9).

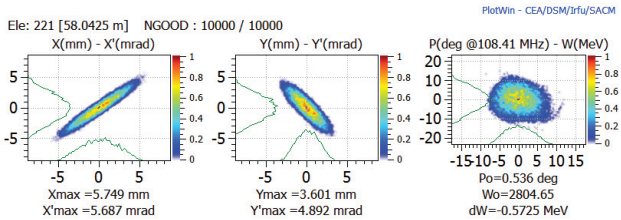

Figure 8: Output particle distribution behind the complete DTL.

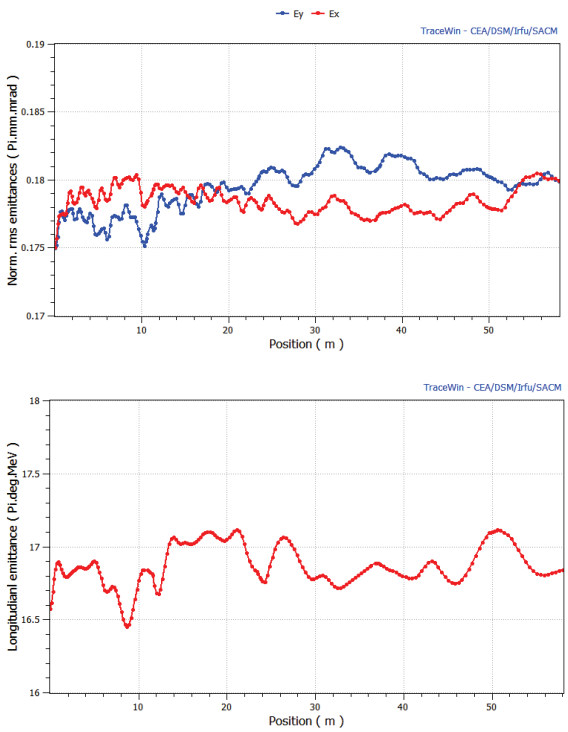

Figure 9: Transverse (top) and longitudinal (bottom) emittance along the new Alvarez DTL.

ALVAREZ DTL FOR TRANSPORT OF LOW ENERGY BEAMS

Simultaneously to the FAIR injector function, the UNILAC serves established GSI experiments requiring beam energies (nuclear-, biophxsics, material research) close to the Coulomb barrier, i.e. it provides energies in the range from about 3.0 MeV/u up to 11.7 MeV/u. For the low energy operation the rf-power of the downstream tanks is switched off starting from behind. The intertank bunchers are used then to maintain a reasonable bunch length up to the DTL exit. In comparison to the FAIR requirements the established UNILAC experiments require lower beam current but higher duty cycles.

Figure 10 illustrates the scenario with rf-power off for A2-A5. Low energy / low current beams are delivered to the exit of the DTL preserving short bunch length. Only 2.5% of the particles are outside ±45° behind the DTL. Shortening the 2nd tank will reduce this amount to zero. The bunchers' voltage range from 0.4 MV to 0.7 MV.

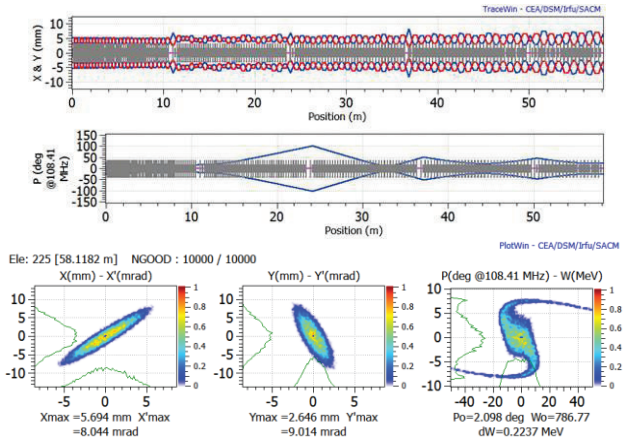

Figure 10: Transverse and longitudinal envelopes along the whole Alvarez DTL (top) and output particle distribution (bottom); rf-power is off for A2 - A5.

With the switched-off rf-power for A3-A5 the beam reaches the energy of 5.4 MeV/u. There are no particles outside ±15° behind the DTL (Fig. 11).

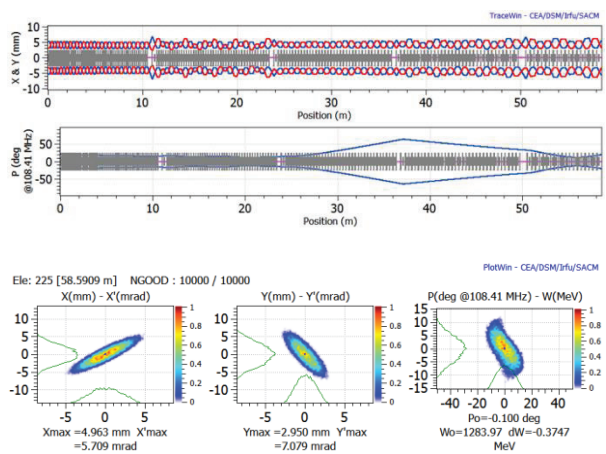

Figure 11: Transverse and longitudinal envelopes along the whole Alvarez DTL (top) and output particle distribution (bottom); rf-power is off for A3 - A5.

OUTLOOK

A conceptual beam dynamics design of the whole DTL was worked out and promising with respect to FAIR requirements in intensity and quality. Also the design considers the established UNILAC experiments. For the next iteration the optimization of the longitudinal beam parameters concerning lowest beam energies is planned. In parallel the mechanical design is detailed.

ISBN 978-3-95450-185-4

REFERENCES

[1] L. Groening et al., "Upgrade of the UNILAC for FAIR", in *Proc. HIAT'15*, Yokohama, Japan, Sept. 2015, paper TUA1I02, pp. 141-143.

[2] X. Du et al., "Alvarez DTL Cavity Design for the UNILAC Upgrade", in *Proc. IPAC'15*, Richmond, USA, May 2015, paper WEPMA017, pp. 2786-2788.

[3] "FAIR Baseline Technical Report", Vol. 2, GSI, Darmstadt, Germany, 2006, p. 335.

[4] S. Appel, "SIS18 Injection: Parameter Studies on MTI with space charge and longitudinal aspects", talk, Uranium Accelerator Chain Review, GSI, Darmstadt, Germany, Nov. 2013.

[5] S. Mickat et al, "Die UNILAC Post-Stripper-Sektion – Zustandsaufnahme und Betriebsrisiko", interner Report, GSI, Darmstadt, Germany, April 2013.

[6] TraceWin, http://irfu.cea.fr/Sacm/logiciels/index3.php

[7] L. Groening et al., Phys. Rev. Lett. 102, 234801, Jun. 2009.

[8] L. Groening et al., Phys. Rev. Lett. 103, 224801, Nov. 2009.

ISBN 978-3-95450-185-4

BEAM DYNAMICS SIMULATIONS AND CODE COMPARISON FOR A NEW CW RFQ DESIGN

Sergey Polozov [1,2], Winfried Barth [1,3,4], Timur Kulevoy [1,2], Stepan Yaramyshev* [1,3]
[1] National Research Nuclear University - Moscow Engineering Physics Institute, Moscow, Russia
[2] Institute for Theoretical and Experimental Physics of NRC Kurchatov Institute, Moscow, Russia
[3] GSI Helmholtzzentrum fuer Schwerionenforschung, Darmstadt, Germany
[4] Helmholtz-Institut Mainz, Germany

Abstract

Research and development of CW applications is an important step in RFQ design. The RF potential should be limited by 1.3-1.5 of Kilpatrick criterion for the CW mode. A 2 MeV RFQ is under development for the compact CW research proton accelerator, as well as for planned driver linac in Russia. The maximum beam current is fixed to 10 mA; the operating frequency has been set to 162 MHz. The new RFQ linac design will be presented and beam dynamics simulation results will be discussed. Calculations of the beam dynamics are provided using the codes BEAMDULAC (developed at MEPhI for linac design) and DYNAMION. A comparison of the software performance is presented.

INTRODUCTION

The development of CW high-power proton linacs with 1.0-2.0 GeV beam energy is a very actual aim of crucial accelerator technology. Such linac is useful for large scale research complexes as spallation neutron sources or accelerator driven systems. Low or medium-energy linacs can be used for several applications as boron-neutron capture therapy (BNCT), high productivity isotopes generation and material science [1-4]. Also compact research facilities, for example SARAF at Soreq Centre [5], are the modern trend for high intensity CW proton and deuteron linac development.

In 2013 the Russian accelerator-driver concept has been developed by the collaboration of researchers from MEPhI, ITEP and Kurchatov Institute [6-9]. The proposed linac layout is close to the conventional scheme: an RFQ and an RF focusing section up to 30 MeV as normal conducting part [10] and independently phased SC cavities for medium and high beam energies. Three different RF focusing methods were discussed: RF crossed lenses [11], radio-frequency quadrupoles with modified profile of electrodes [12] and axi-symmetrical RF focusing (ARF) [13]. Three branches of experimental beam lines, delivering beam energy of 3, 30 and 100 MeV for dedicated experiments, are foreseen as the main feature of the proposed concept.

A preliminary design of a CW RFQ linac has been already started at MEPhI and ITEP [14, 15]. The recent detailed layout of the presented 2 MeV CW RFQ is based on a preliminary concept, exploiting long-term experience for proton and heavy ion linac development at MEPhI [16], ITEP [17,18], as well as decades of GSI expertise in construction, optimization and routine operation of linac facilities [19-24]. Most recently, the prototype for a heavy ion CW linac with a SC main part is under construction at GSI and HIM in frame of a collaboration with IAP (University Frankfurt) [25].

The beam dynamics simulations for the new RFQ accelerating-focusing channel, as well as an analysis of the RFQ characteristics, have been performed by means of different software to provide for a cross-check of the design features and the calculated results. The main RFQ parameters are summarized in Tab.1.

Table 1: Main Parameters of the CW RFQ

Ions	protons
Input energy	46 keV
Output energy	2.0 MeV
Frequency	162 MHz
Voltage	90 kV
Length	345 cm
Average radius	0.530 cm
Vanes half-width	0.412 cm
Modulation	1.000 - 2.250
Synchr. phase	-90° - -33°
Max. input beam current	10 mA
Max. input beam emittance	6 cm·mrad
Particle transmission	> 99%

DESCRIPTION OF THE CODES

The presented RFQ accelerating-focusing channel has been designed at MEPhI by means of the BEAMDULAC code [26]. A cross-check, including calculations of RFQ characteristics and beam dynamics simulation, was performed by use of the DYNAMION software [27].

The BEAMDULAC code has been developed at MEPhI for self-consistent beam dynamics investigations in RF linacs and transport channels. The motion equation for each particle is solved under implementation of the external electromagnetic fields and the inter-particle Coulomb field simultaneously. The BEAMDULAC code utilizes the cloud-in-cell (CIC) method for accurate treatment of the space charge effects. It allows consideration of the shielding effect, which is sufficiently important for transverse focusing in the narrow channel. The fast Fourier transform (FFT) algorithm is used to solve the Poisson equation on a 3D grid. The obtained Fourier series for the space charge potential can be analytically differentiated, and thus each component of the Coulomb electrical field can be found as a series with known coefficients. The dedicated version of the

* s.yaramyshev@gsi.de

ISBN 978-3-95450-185-4

BEAMDULAC code was created for fast RFQ channel design and beam dynamics simulations.

The multiparticle code DYNAMION calculates beam dynamics in linear accelerators and transport lines under space charge conditions with high accuracy and reliability. A detailed description of the external and internal fields is provided by the DYNAMION package. Also the use of measured data or electromagnetic fields, calculated by external codes, is possible. Generally, the particle motion in the whole linac, potentially comprising RFQ(s), DTL(s) and transport lines, can be calculated in one run. Simulations of high intensity beam dynamics are performed taking space charge forces into account (by different dedicated routines).

All geometrical data, available from the external calculations, measurements, specifications and tables for the machining, can be used: cell length, aperture, width and rounding of the electrodes for an RFQ; tube and gap length, aperture, and tube rounding for a DTL. Dedicated subroutines of the DYNAMION package precisely calculate the 3D electrical field mapping, solving the Laplace equation for the potential:

RFQ Input/Output Radial Matcher: the area for the grid is formed by the surface of electrodes / flange of the tank.

RFQ cells: the area for the grid for each cell is formed by the surface of modulated electrodes; the potential is approximated with a classical 8-term series assuming the quadrupole symmetry; 3D electrical fields are calculated as corresponding derivatives of the potential.

DTL gaps: the area for the grid is formed by the surface of tubes; the potential and the 3D electrical fields for each gap, including the slack of the field into tubes, are approximated with 30-term series assuming axial symmetry; coefficients of the series are introduced into calculations as input data.

The transport line elements (quadrupole lenses, bending magnets, solenoids, etc.) are described inside the code or can be represented by measured or calculated field mapping. Several additional features are developed for more reliable simulations: slits, strippers, apertures, beam shift and rotation, breeding of particles, etc.

The assumed or measured misalignments of the linac elements can be defined for the simulations.

Input particle distribution of several types (KV, truncated Gaussian, uniform, etc.) are available inside the code. The data of an emittance measurement can be used for generating of the input particle distribution which includes non-uniformities of a real beam.

A multiparticle distribution, which represents *the mixture of ions* with a different charge, mass and energy can be carried out under space charge conditions.

ANALYSIS OF RFQ CHARACTERISTICS

The maximum electrical field strength on the vane surface along the channel strongly influences on all RFQ parameters. For the presented CW RFQ design the field strength has been limited by the 1.5 Kilpatrick criterion E_{kp} = 148 kV/cm.

The average radius of 0.530 cm and the vanes half-width/rounding of 0.412 cm have been defined together with the RFQ voltage of 90 kV (Tab. 1). The maximum electrical field on the vane surface, calculated for the real topology of each RFQ cell, is shown in Fig. 1.

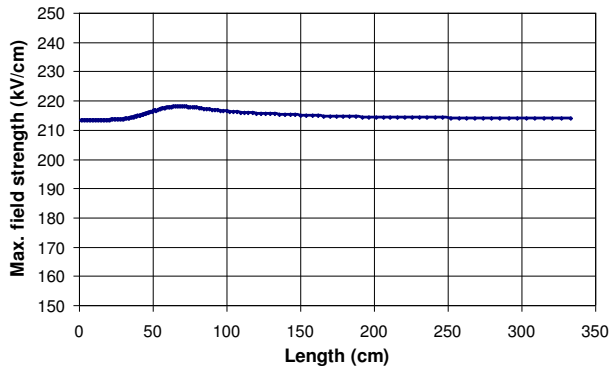

Figure 1: Maximum strength of electrical field strength on the vane surface, calculated along the RFQ channel (for each cell separately).

Almost constant electrical field strength along the channel provides for effective focusing and acceleration, especially as RF voltage and RF power are strongly limited due to the CW regime.

Assuming a low beam current and a smooth approximation, the phase advance μ (Fig. 2) and the normalized local acceptance V_k (Fig. 3) for each RFQ cell can be calculated from a stable solution of the Mathieu-Hill equation for particle motion, using the Floquet functions:

$$V_k = \nu_f \frac{a^2}{\lambda}$$

where ρ is a module of the Floquet function, $\nu_f = 1/\rho^2$, a - aperture radius of the cell, λ - wave length of the operating frequency; ν_f can be treated as a minimum of the phase advance μ on the focusing period.

Additionally a tune depression can be semi-analytically calculated for each RFQ cell, assuming a given current phase density (beam brilliance) for a uniformly charged beam (KV distribution).

The Coulomb parameter h combines parameters of the beam and the accelerating channel:

$$h = j \cdot \frac{B\lambda}{\mu_0 \beta I_0},$$

where $j = I / V_p$ - beam brilliance, I - beam current, V_p - normalized beam emittance, B - ratio of the peak current to the pulse current, $I_0 = 3.13 \cdot 10^7 \cdot A/Z$ - characteristic current, A, Z - mass and charge numbers, μ_0 - phase advance for "zero" current, β - relative velocity of

ISBN 978-3-95450-185-4

particle. The phase advance and acceptance of the channel under tune depression could be evaluated as

$$\mu = \mu_0\left(\sqrt{1+h^2} - h\right),$$

$$V_k = V_{k0}\left(\sqrt{1+h^2} - h\right).$$

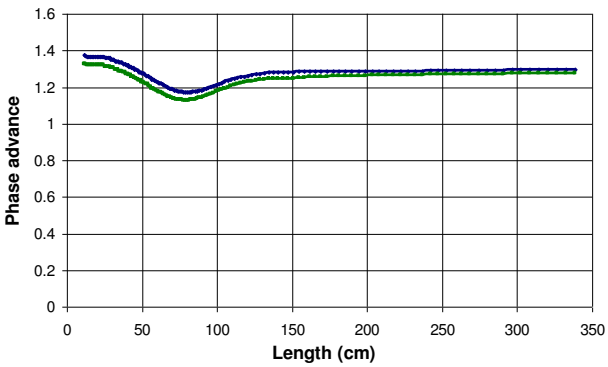

Figure 2: Phase advance for low beam current (blue) and under space charge conditions (green), calculated along the RFQ channel (for each cell separately).

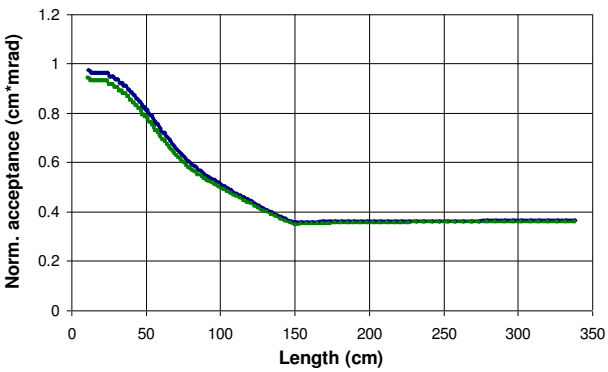

Figure 3: Normalized local acceptance for low beam current (blue) and under space charge conditions (green), calculated along the RFQ channel (for each cell separately).

As follows from Figures 2 and 3, under design space charge conditions (beam current 10 mA, total unnorm. beam emittance 6 cm·mrad), the decrease of the RFQ phase advance and acceptance is only a few percent, thus an influence of the space charge effects is neglectable.

In particular, this is ensured by the chosen relatively high input particle energy of 46 keV. A lower input RFQ energy might lead to a slightly compacter RFQ, but results in much stronger space charge effects, especially inside the gentlebuncher. Obviously this would lead to nonlinear effects, emittance growth and a degradation of the beam quality.

BEAM DYNAMICS SIMULATIONS

Assuming low tune depression, the results of beam dynamics simulations are recently presented only for low beam current, demonstrating the coincidence between the used codes. A set of simulations under space charge conditions is now under consideration, in parallel to the final optimization of the modulation along the RFQ.

A profile of the RFQ input radial matcher has been defined in the way to provide for a smooth matching of the beam emittance to the RFQ acceptance. The matched Twiss-parameters have been obtained from the results of dedicated beam dynamics simulations for the RFQ acceptance. The same 6D phase space input macroparticle distribution, continuous in longitudinal phase plane, has been introduced into both codes (Fig. 4).

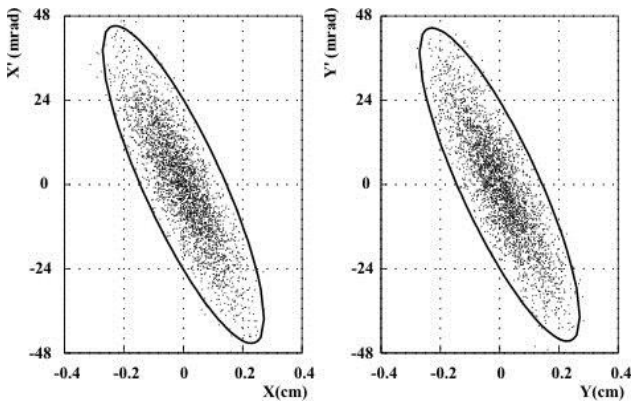

Figure 4: The transverse beam phase portraits at the RFQ entrance; ellipses represent 99% of the particles.

The resulted particle distributions behind the RFQ (Fig. 5) illustrate good similarity. Possible sources of minor discrepancy are recently under investigations.

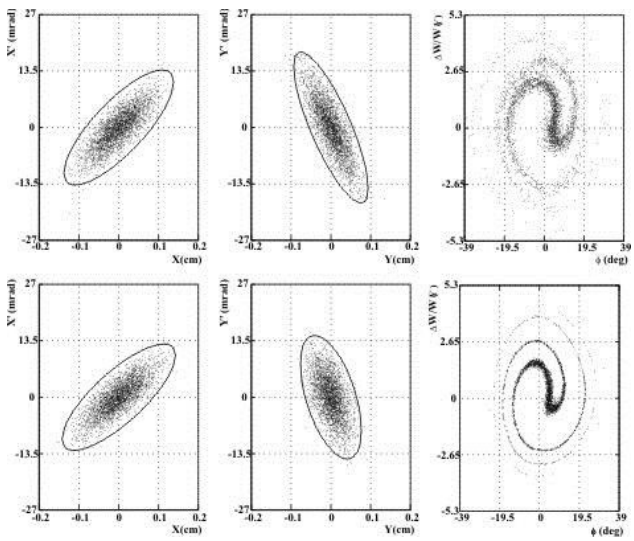

Figure 5: The beam phase portraits behind RFQ for transverse and longitudinal phase planes, simulated by the BEAMDULAC-RFQ (top) and the DYNAMION (bottom) codes; ellipses represent 99% of the particles.

ISBN 978-3-95450-185-4

CONCLUSION

A new CW 2 MeV RFQ linac design is proposed. The maximum field strength is limited by the 1.5 Kilpatrick criterion. The machine can accelerate a 10 mA proton beam with a particle transmission close to 100%. Beam dynamics simulations were performed by means of the codes BEAMDULAC and DYNAMION. A preliminary design of an RFQ modulation can be efficiently performed by the BEAMDULAC-RFQ code. The DYNAMION code, which uses an accurate treatment of the external electrical field, is useful for the detailed beam dynamics simulations. The results of the codes are in good agreement. The electrodynamics simulations, as well as mechanical layout for a new CW RFQ cavity are in progress. Final optimization of the RFQ channel has been already started.

REFERENCES

[1] C. Prior, Proc. of HB'10, 6–10 (2010).
[2] S.M. Polozov, A. D. Fertman, Atomic Energy, 113, Issue 3, 155–162 (2012).
[3] P.N. Ostroumov, Proc. of IPAC'15, 4085-4090 (2015).
[4] N. Solyak, S. Nagaitsev, V. Lebedev et al., Proc. of IPAC'10, 654-656 (2010).
[5] L. Weissman, D. Berkovits, A. Arenshtam et al., Journal of Instrumentation, 10, T1004 (2015).
[6] A.E. Aksentyev, P.N. Alekseev, K.A. Aliev et al., Atomic Energy, 117, Issue 4, 270-277 (2015).
[7] A.E. Aksentyev, et al., Atomic Energy, 117, Issue 5, 347-356 (2015).
[8] V.A. Nevinitsa, A.A. Dudnikov, A.A. Frolov et al., Atomic Energy, 117, Issue 1, 14-18 (2014).
[9] Y.E. Titarenko, V.F. Batyaev, K.V. Pavlov, et al., Atomic Energy, 117, Issue 1, 19-28 (2014).
[10] A.Ye. Aksentyev et al., Proc. of RuPAC'14, 324-326 (2014).
[11] A.I. Balabin, G.N. Kropachev, NIM A, 459, 87-92 (2001).
[12] A.S. Plastun, A.A. Kolomiets, Proc. of LINAC'12, 41 – 43 (2012).
[13] E.S. Masunov, N.E. Vinogradov, Physical Review ST AB, 4, 070101 (2001).
[14] A.E. Aksentyev, T. Kulevoy, S.M. Polozov, Proc. of IPAC'14, 3286-3288 (2014).
[15] A.Ye. Aksentyev, A.A. Kalashnikova, T.V. Kulevoy et al., Proc. of RuPAC'14, 319-321 (2014).
[16] S.M. Polozov, Prob. of Atomic Sci. and Tech., 3 (79), 131-136 (2012).
[17] D. Kashinsky, A. Kolomiets, T. Kulevoy et al., Proc. of EPAC'04, 854-856 (2004).
[18] V.A. Andreev, A.I. Balabin, A.V. Butenko at al., Prob. of Atomic Sci. and Tech., 6 (88), 8-12 (2013).
[19] W. Barth, W. Bayer, L. Dahl et al., NIM A, 577, Issues 1–2, 211-214 (2007).
[20] S. Yaramyshev, W. Barth, L. Dahl et al., Proc. of LINAC'14, 3217-3219 (2014).
[21] W. Barth et al., Physical Review ST AB 18(4),·050102 (2015).
[22] F. Herfurth et al., Physica Scripta, T166 (T166):014065 (2015).
[23] S. Yaramyshev et al., Physical Review ST AB, 18 (5)·(2015).
[24] W. Barth et al, Physical Review ST AB 18(5), (2015).
[25] M. Miski-Oglu et al., Proc. of SRF'15, MOPB067, (2015).
[26] S.M. Polozov, Prob. of Atomic Sci. and Tech., 3 (79), pp. 131-136 (2012).
[27] S. Yaramyshev et al., NIM A, 558/1 (2006).

ISBN 978-3-95450-185-4

THE SIMULATION STUDY OF BEAM DYNAMICS FOR CSNS LINAC DURING BEAM COMMISSIONING

Y. Yuan[†,1,2], H. Ji[1,2], S. Wang[1,2], J. Peng[1,2]
[1] China Spallation Neutron Source, Institute of High Energy Physics, Chinese Academy of Sciences, Dongguan, China
[2] Dongguan Institute of Neutron Science, Dongguan, China

Abstract

China Spallation Neutron Source (CSNS) is a high intensity accelerator based facility. Its accelerator consists of an H- injector and a proton Rapid Cycling Synchrotron. The injector includes the front end and linac. The RFQ accelerates the beam to 3MeV, and then the Drift Tube Linac (DTL) accelerates it to 80MeV[1]. An Medium Energy Beam Transport (MEBT) matches RFQ and DTL, and the DTL consists of four tanks. Commissioning of the MEBT and the first DTL tank (DTL1) have been accomplished in the last run. Due to the difference of actual effective length and theoretical effective length of magnets in MEBT and DTL1, in order to compare its impact of beam transport, this paper takes a beam dynamics simulation on beam transport in MEBT and DTL1 with IMPACT-Z code[2]. Meanwhile, the transport of beam with different emittance in MEBT and DTL1 is studied because of the large emittance at RFQ exit. All the simulation includes magnet error and RF error.

INTRODUCTION

Before the magnet measurement , the magnet effective length of lattice is theoretical value, so the commissioning software and the beam dynamics simulation both take this value. After the magnet measurement, the magnet effective length closer to the actual situation is given. In order to compare its effects on beam transport in MEBT and DTL1, under circumstance of match, the three-dimensional code IMPACT-Z is taken to study. Due to the large emittance at the exit of RFQ in the beginning, some steps had been taken to decrease emittance in order to avoid more beam loss. Before these steps, the transport of beam with different emittance at the exit of RFQ needs to be considered. All the simulation includes magnet error and RF error.

SIMULATION STUDY OF BEAM DYNAMICS ON MEBT AND DTL1

CSNS/DTL consists of four accelerating cavities, the length among the cavities is designed to maintain longitudinal continuity. Figure 1 shows the layout of the front end and linac, inside the red box is MEBT and DTL. The last beam commissioning includes MEBT and DTL1. Correspondingly, in this paper, the simulation study have been taken on MEBT and DTL1. Beam is matched from RFQ exit to DTL1 entry by MEBT. Corresponding to the theoretical effective length and actual effective length of magnets, there are two lattices for MEBT and DTL1 which are both matched. Through comparing beam emittance growth of two lattices, the difference between them can be gotten.

Through giving different beam emittance from small to large at RFQ exit, the simulation can get the influence of initial emittance on the beam transportation in DTL1, and get the results how much emittance does RFQ exit achieved when beam loss occurs.

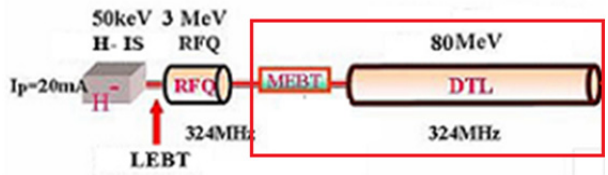

Figure 1: Layout of the front end and linac.

Emittance Growth with Different Magnet Effective Length

In the simulation, the initial distribution of particles is 6D water bag, the number of macro particles is 100,000, the currents of beams is 15mA, the normalized RMS emittance of beam at RFQ exit is 0.2 π mm.mrad. Table 1 shows all the theoretical statics errors about magnet and RF. In this simulation, assumed errors just include quadruple magnet alignment error and RF amplitude error. Figure 2 is a comparison of the horizontal emittance evolution of beam along linac. Figure 3 is a comparison of the vertical emittance evolution of beam along linac.

Table 1: Theoretical Static Errors

Errors	Range
Quad alignment error (transverse displacement)	±0.1mm
Quad alignment error (roll error)	±3mrad
Quad gradient error	±1%
RF amplitude error	±1%
RF phase error	±1degree

[†]yuanyue@ihep.ac.cn

ISBN 978-3-95450-185-4

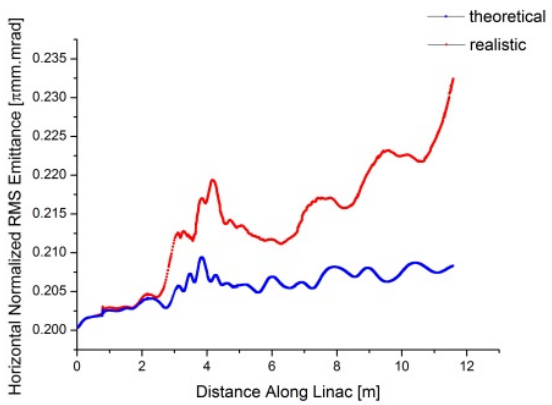

Figure 2: Beam horizontal RMS emittance growth along linac.

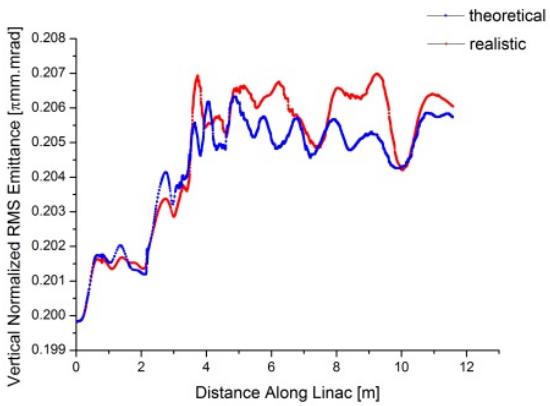

Figure 3: Beam vertical RMS emittance growth along linac.

As can be seen from the Figure 2, beam's horizontal RMS emittance growth is very small with theoretical effective length of magnets , but the emittance growth with actual effective length is significantly enlarge. However, Figure 3 shows that the difference of beam's vertical emittance is quite small. It seems beam's horizontal emittance is more sensitive to mismatch than vertical. Through comparing Figure 2 to Figure 3, a conclusion can be gotten that differences between two lattices is quite large, and the later simulation study must take the lattice with actual effective length of magnets in order to close with the actual situation.

Simulation Study of Different Emittance at RFQ Exit

In the simulation, the initial distribution of particles is also 6D water bag, the number of macro particles is still 100,000, the currents of beams is 15mA, the normalized RMS emittance of beam at RFQ exit is from 0.2 π mm.mrad to 0.32 π mm.mrad which are respectively 0.2, 0.22, 0.24, 0.26, 0.28, 0.30, 0.32. In this simulation, assumed errors include quadruple magnet alignment error, gradient error and RF amplitude error. Table 2 is the beam loss number of beam with different initial emittance. Figure 4 is a comparison of the horizontal emittance evolution of beam along linac. Figure 5 is a comparison of the vertical emittance evolution of beam along linac.

Table 2: Beam Loss Number

Emittance	0.20~0.28	0.30	0.32
Beam loss	*0*	*1*	*8*

As can be seen from the Table 2, it starts to appear beam loss when the initial emittance of beam at RFQ exit increases to 0.3. Also with the increase of initial emittance, beam loss corresponding enlarge. However, during the actual commissioning, beam loss may be more than this. Figure 4 shows that the horizontal emittance growth enlarge with the initial emittance increasing. However, Figure 5 shows that the vertical emittance growth is not obvious. It also seems beam's horizontal emittance is more sensitive to mismatch than vertical. As a result, the normalized RMS emittance of beam at RFQ exit is better limited to below 0.3.

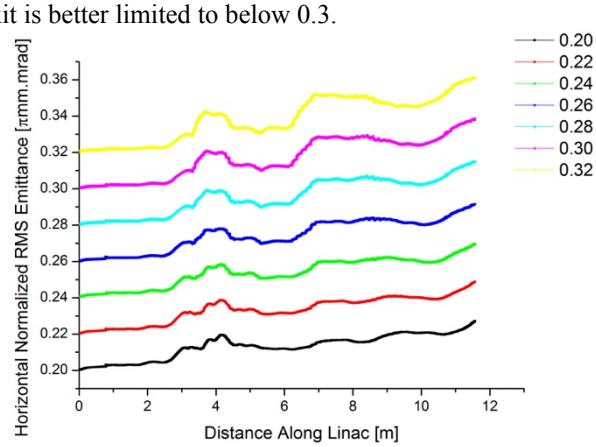

Figure 4: Beam horizontal RMS emittance growth along linac.

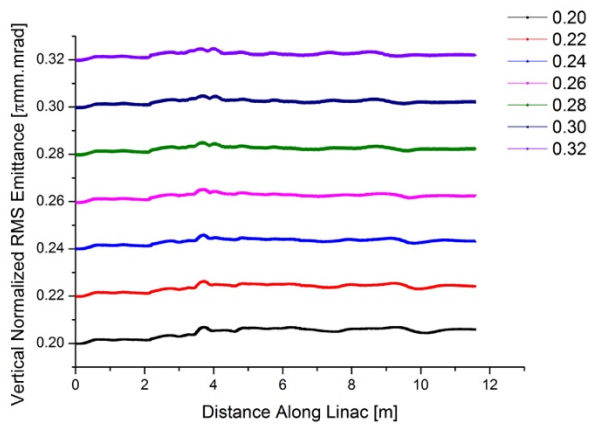

Figure 5: Beam vertical RMS emittance growth along linac.

CONCLUSION

In this paper, three-dimensional space-charge code IMPACT-Z is taken to study the impact of beam transport with theoretical magnet effective length and actual

ISBN 978-3-95450-185-4

effective length in MEBT and DTL1 during beam commissioning, a conclusion can be gotten that the later simulation study must take the lattice with actual effective length of magnets in order to close with the actual situation. Beam transport in MEBT and DTL1 is also studied under circumstance of different initial emittance at RFQ exit, it turns out the normalized RMS emittance of beam at RFQ exit is better limited to below 0.3πmm.mrad.

ACKNOWLEDGEMENTS

The author would like to thank colleagues in AP group at CSNS for some meaningful discussing.

REFERENCES

[1] WANG Sheng, FANG Shou-Xian, FU Shi-Nian, et al. Introduction to the overall physics design of CSNS accelerators[J]. Chinese Physics C, 2009, 33(S2): 1-3.

[2] J. Qiang, R. Ryne, S. Habib, V. Decyk. An Object-Oriented Parallel Particle-in-Cell Code for Beam Dynamics Simulation in Linear Accelerators[J]. Journal of Computational Physics, 2001, 163: 434.

ISBN 978-3-95450-185-4

BEAM DYNAMICS STUDY OF C-ADS INJECTOR-I WITH DEVELOPING P-TOPO CODE*

Zhicong Liu[1, 2], Chao Li[1†], Qing Qin[1†], Yaliang Zhao[1], Fang Yan[1],

[1]Key Laboratory of Particle Acceleration Physics and Technology, Institute of High Energy Physics, Chinese Academy of Sciences, Beijing, China
[2]University of Chinese Academy of Sciences, 100049, Beijing, China

Abstract

A parallelized, time-dependent 3D particle simulation code is under developing to study the high-intensity beam dynamics in linear accelerators. The self-consistent space charge effect is taken into account with the Particle-In-Cell (PIC) method. In this paper, the structure of program and the parallel strategy are demonstrated. Then, we show the results of code verification and benchmarking. It is proved that the solvers in P-TOPO code and parallel strategy are reliable and efficient. Finally, the beam dynamics simulation of C-ADS Injector-I at IHEP are launched with P-TOPO and other codes. The possible reasons for the differences between results given by separated codes are also proposed.

INTRODUCTION

A new particle simulation code Parallelized-Trace of Particle Orbits (P-TOPO) is now under development to study space charge effect at high intensity linacs [1-5]. The motivation is to improve the efficiency and calculation capability, based on the OpenMP techniques, of the TOPO code [6]. In the P-TOPO code, the basic elements, which supply external field to particles in linear accelerator, such as multi-pole, solenoid, RFQ, superconducting cavities, are modelled analytically or represented by field map obtained from CST. The internal interactive space charge filed between particles is solved with the classic PIC method [7].

The Injector-I of Chinese Accelerator Driven Sub-Critical System (C-ADS) project is composed of ECRIS, LEBT, RFQ, MEBT1, SC section and MEBT2, which is under beam commissioning in IHEP. In recent experiment, a 10.1 MeV, 10.03 mA pulse beam is successfully achieved [8]. In this paper we will give a brief introduction of Injector-I and show the beam simulation results in detail with P-TOPO code. In section 2, the brief structure and parallelization strategy of P-TOPO are introduced. In section 3, code verification and benchmarking are given. In section 4, simulation results of C-ADS Injector-I are given by P-TOPO code and other widely used codes. Several reasons are proposed to interpret the difference among results given by P-TOPO and other codes. Conclusion and summary are given in section 5.

* Supported by the Ministry of Science and Technology of China under Grant no.2014CB845501.
† Email address: lichao@ihep.ac.cn; qinq@ihep.ac.cn;

P-TOPO

P-TOPO is developed with C++ language and parallelized based on the OpenMP techniques to achieve a high beam processing. Now, it can be run at PC with any number of cores. The structure of this program is as Fig. 1.

1) The MAIN class is in charge of getting the electric-magnetic field from external elements or inner space charge field, and particle updating under the effect of these obtained fields.

2) The Lattice class composed of elements class could be used to establish accelerator lattice with great flexibility. The external field supplied by certain element could be represented by a field map from CST or by analytical approximation.

3) The Beam class saves the beam information and calculates the beam parameters, like twiss parameters, emittance, beam size, et.

4) The Distribution class serves as initial particle distribution generator for specific type.

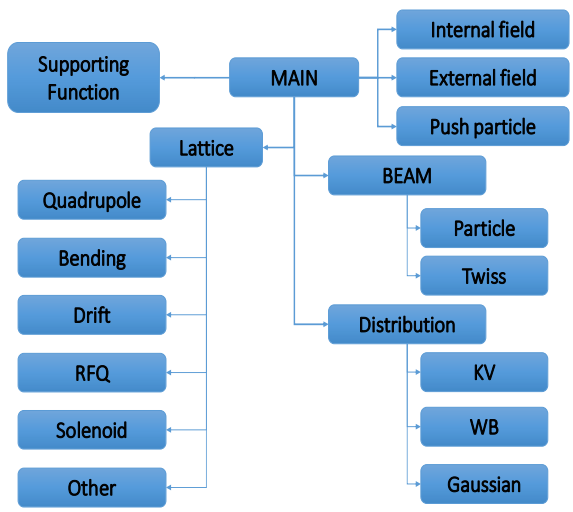

Figure 1: Layout of P-TOPO.

The parallelization occurs mainly in getting internal field, external field and particle pusher, where no interaction exists between different processing. Take the PIC module for example, it requires 4 separated steps to get the internal space charge field.

Step1, Weighting particles to grids;

Step2, Solving potential on the grids by FFT;

Step3, Obtaining the electric field on grid by the difference of the electric potential field;

ISBN 978-3-95450-185-4

Step4, Getting electric field particles feel.

In step 1 and step 4, the grid parallelization is taken and each thread handles different grids. The reason is the potential confliction that different threads may process a grid at the same time when they operate on different particle. It would be inefficient if we take strategy to avoid the conflict. In step 2 and step 3, the main part of solving field on grids is the Fast Fourier Transform. The fftw library is used in the solver and the inner parallelization strategy of fftw is also taken combined with OpenMP.

A performance test with space charge is taken at a common PC with 4 cores. With all the parallelization strategy, when the code runs in 4 threads, the speed is 3.6 times as fast as the single thread.

CODE VERIFICATION AND BENCHMARKING

Internal Field

The potential of a point charge state is used to verify the result of PIC solver. The grid number is 128*128*64. Dirichlet boundary condition is used in transverse direction and periodic boundary condition is used in longitudinal direction. Fig. 2 shows the comparison of P-TOPO result and theory expectation in transverse and longitudinal direction. The electric potential field from code agrees well with theory result. The slight deviation comes from the numerical noise of discretization.

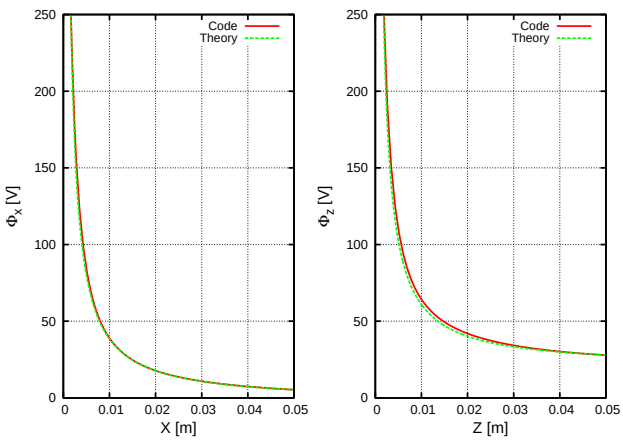

Figure 2: Comparison of the potential of point charge between P-TOPO and theory prediction.

Beam Evolution in FD Structure

The beam evolution along the periodic focusing channel could be expressed in the form of 2.5D rms envelope equation. The amplitude of the beam size oscillation is related to mismatch, and the phase advance and is related to the space charge force [9, 10]. Fig. 3 shows the evolution of beam rms size given by P-TOPO and theory expectation from rms envelope equation with 0mA and 15mA beam current in a FD structure. In the condition of zero beam current, the red solid curve is beam rms size from theory expectation and the green dashed curve is from P-TOPO. In the condition of 15mA beam current, the results form P-TOPO and theory expectation are represented by the blue dashed and purple solid curves. The turquoise solid line represents the external quadrupole field strength variation. It could be seen that these results agree well in both 0 and 15 mA cases. The slight differences between P-TOPO result and rms envelope equation is induced by numerical randomness and the evolution of emittance in P-TOPO simulation, which is supposed to be constant in rms envelope equations model.

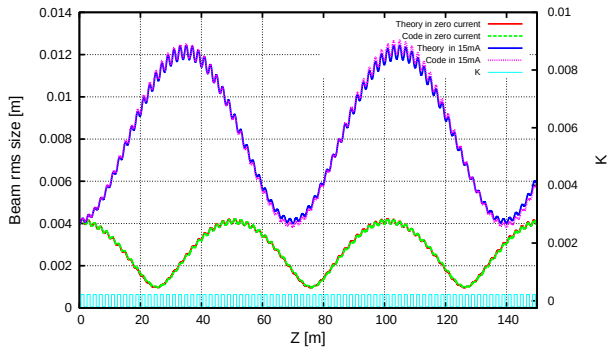

Figure 3: RMS size of the beam by P-TOPO and theory expectation in zero current and in 15mA.

BEAM DYNAMICS STUDY OF INJECTOR-I.

Injector-I of C−ADS is made of RFQ, MEBT1, CM1, CM2, and MEBT2 as shown in Fig. 4. In the following, we show the P-TOPO simulation separately with KV initial beam. The mesh number for space charge calculation is 64*64*32.

RFQ

The RFQ is designed with PARMTEQM at a frequency of 325MHz, and proposed to deliver proton beam from 35KeV to 3.2 MeV with a beam current of 15mA. In P-TOPO simulation, started with rms matched beam condition, the KV beam composed of 10K marcoparticles is used to show the beam evolution along the RFQ. The field of RFQ is obtained with 8 terms expansion in form of Fourier Bessel function. Fig. 5 shows the transverse and longitudinal emittance evolution of P-TOPO and TRACK in the condition of 0mA and15mA beam current.

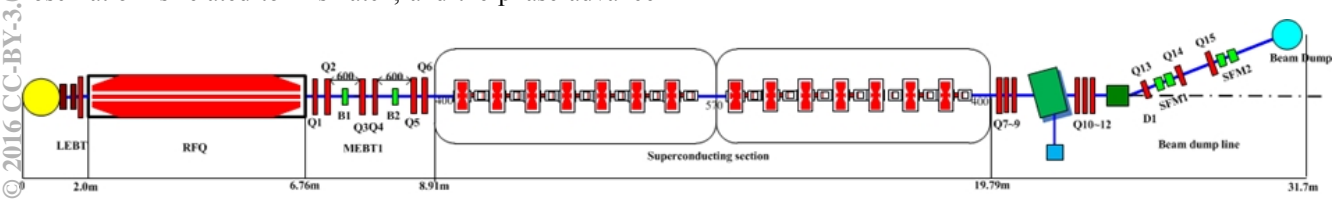

Figure 4: Layout of the ADS Injector-I testing facility

ISBN 978-3-95450-185-4

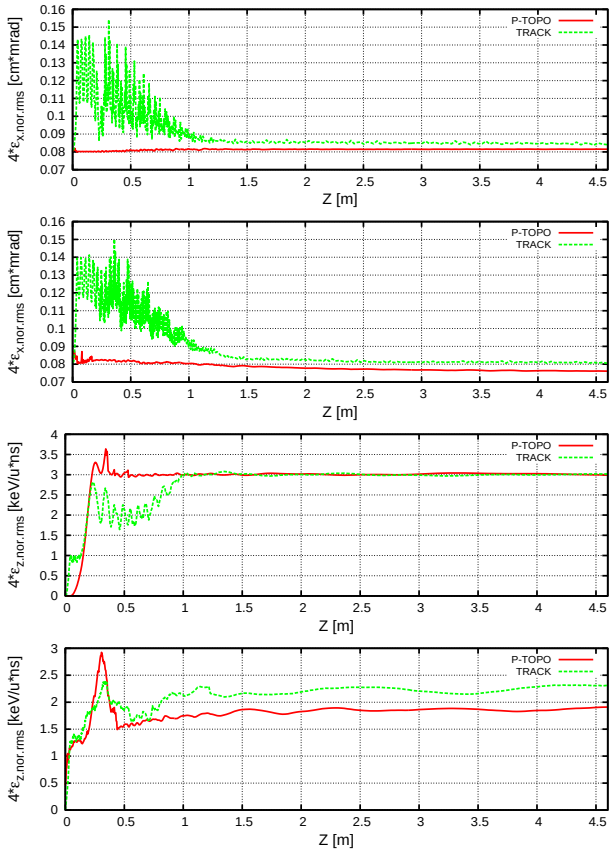

Figure 5: Transverse and Longitudinal emittance given by P-TOPO and TRACK in the condition of 0mA and 15mA.

In both of the transverse and longitudinal directions, the P-TOPO code shows much smoother emittance variation, especially in the front of the RFQ, where beam filamentation takes place and fierce bunch rotate. The deviation of final beam emittance and transmission given by TRACK and P-TOPO is in the reasonable region.

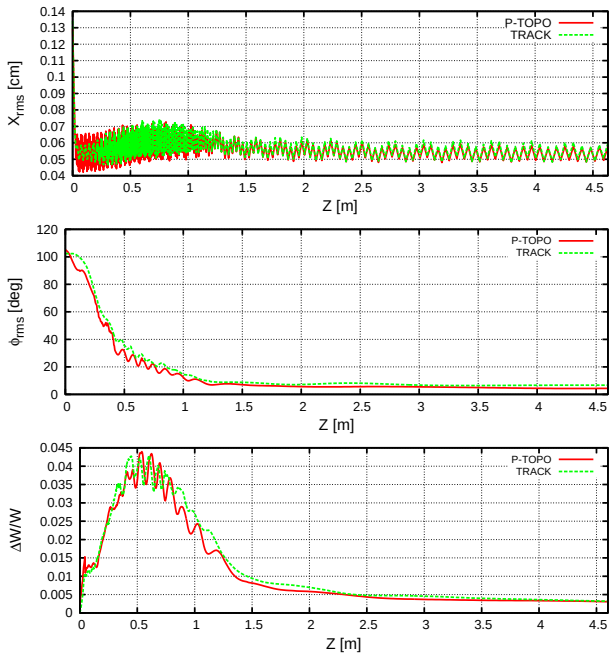

Figure 6: RMS beam size and energy spread.

Figure 6 shows the evolution of transverse and longitudinal rms beam size and energy spread. The rms size got from the P-TOPO and TEACK consist with each other. Still, slight discrepancy exists as the amplitude of envelop got from P-TOPO is a little larger than that from TRACK at the beginning of RFQ cells. At the end of the RFQ, longitudinal phase given by TRACK is a little advanced than that given by P-TOPO,

SC Section

In the SC section, the field in bunchers and SC cavities are represented by the field map. As said, the numerical interpolation is used to obtain the field that single particle feels. With the designed 15mA beam current, the 3.2 MeV proton beam at the exit of RFQ are bunched and transported to the entrance of SC section by the MEBT, where the beam are supposed to be rms matched. The SC section sustainably accelerates the beam into 10MeV. The TraceWin code is used for benchmarking. The output result from P-TOPO is 10.01 MeV, and the result from TraceWin is 10.06 MeV.

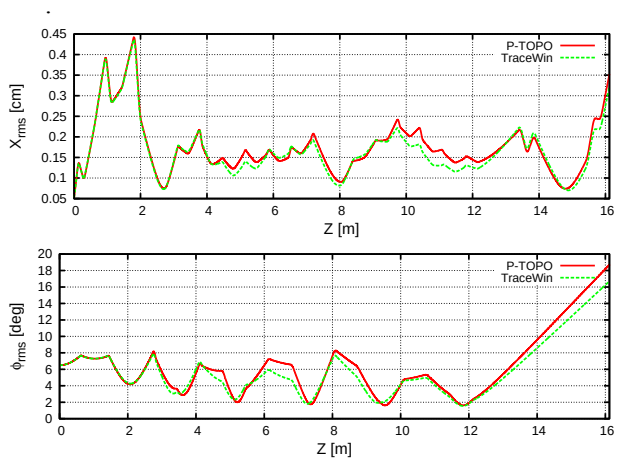

Figure 7: RMS beam size and phase envelop.

Figure 7 shows the rms beam sizes evolution in the transverse and longitudinal directions. The red solid curve is from P-TOPO and the green dashed curve is from TraceWin. The rms envelop is consist well with each other. Little deviation exists because of the different methods of the synchronous phase calculation.

Through P-TOPO simulation, the beam size and beam loss is effectively controlled and the emittance basically keeps constant along the Injector-I of C-ADS.

In the above study, besides the differences lied on initial beam distribution used, discrepancies among different codes are due to the differences of date processing and methods used in detail. Generally, one is the differences between T-code (P-TOPO) and Z-code (TRACK and TraceWin), which results in the differences of particle information collection and parameter calculation. The other is the criteria for beam loss, which actually happens only when particle touches the beam pipe.

ISBN 978-3-95450-185-4

CONCLUSIONS

The P-TOPO code has been verified. The method used to get space charge force has been tested with point charge and is proved to be fast and accuracy. The result of FD structure simulation and its comparison with theory expectation illustrate that the code is reliable. Parallelized with OpenMP, the performance of the whole program is obviously better than single thread program. In the future, P-TOPO would be transplanted to the cluster in IHEP.

The P-TOPO code has been employed at the study of Injector-I of C-ADS. The RFQ and the other part is simulated separately. The P-TOPO simulation proves the current design is in control. No sufficient beam loss and emittance growth appear. In future study, efforts will be focused on comparison between simulation and experiments.

ACKNOWLEDGMENTS

This work was supported by the Ministry of Science and Technology of China under Grant no.2014CB845501.

REFERENCES

[1] Chao Li, Zhicong Liu and Q. Qin, *Nucl. Instr. Meth. A,* 813(2016)13–18.
[2] Chao. Li and Y. L. Zhao, *Phys. Rev. ST Accel. Beams* 17, 124202 (2014).
[3] Chao Li, Invited talk in HB 2016.
[4] Chao Li, R. A. Jameson, Qing. Qin *et al.*, "Collective Beam Instability Modes in High Intensity Beam", unpublished.
[5] Chao. Li and Q. Qin, *Physics of Plasmas* 22, 023108 (2015).
[6] Chao Li, "The development of TOPOPIC code and halo suppresion study in FODO channel," Ph.D. thesis, University of Chinese Academy of Sciences, Beijing, China, 2013.
[7] R. W. Hockney and J. W. Eastwood, "The Particle-Mesh force calculation" in Computer Simulation Using Particles, Adam Hilger, Bristol and New York, NY, USA, 1989, pp. 120-165.
[8] Fang Yan, "Instability investigation of China ADS Injector-I," presented at the 57th ICFA Advanced Beam Dynamics Workshop on High-Intensity and High-Brightness Hadron Beams (HB2016), Malmö, Sweden, July 2016, paper TYAM4Y01, this conference.
[9] T. P. Wangler *et al.*, "Particle-core model for transverse dynamics of beam halo," *Phys. Rev. ST Accel. Beams*, vol. 1, p. 084201, 1998.
[10] Chiping Chen and R. C. Davidson, "Nonlinear properties of the Kapchinskij-Vladimirskij equilibrium and envelope equation for an intense charged-particle beam in a periodic focusing field," *Phys. Rev. E*, vol. 49, no. 6, pp. 5679-5687, Jun. 1994.

ISBN 978-3-95450-185-4

BEAM STEERING STUDIES FOR THE SUPERCONDUCTING LINAC OF THE RAON ACCELERATOR

Hyunchang Jin*, Ji-Ho Jang, Dong-O Jeon
Institute for Basic Science, Yuseong-daero 1689-gil, Yuseong-gu, Daejeon, Korea

Abstract

The RAON accelerator of Rare Isotope Science Project (RISP) has been developed to accelerate various kinds of stable ion beams and rare isotope beams for a wide range of science experiments. In the RAON accelerator, the superconducting linac (SCL) will be installed for the acceleration of the beams and it is composed of tens of cryomodules which include superconducting radio frequency cavities. Between two cryomodules, there is a warm section and two quadrupoles are located in the warm section with a beam diagnostics box in between. Also, in this warm section, one horizontal corrector and one beam position monitor (BPM) are mounted inside of first quadrupole, and one vertical corrector is located inside of second quadrupole for the beam steering. With these correctors and BPMs, the beam steering studies are carried out as varying the number of correctors and BPMs in the SCL of the RAON accelerator and the results are presented.

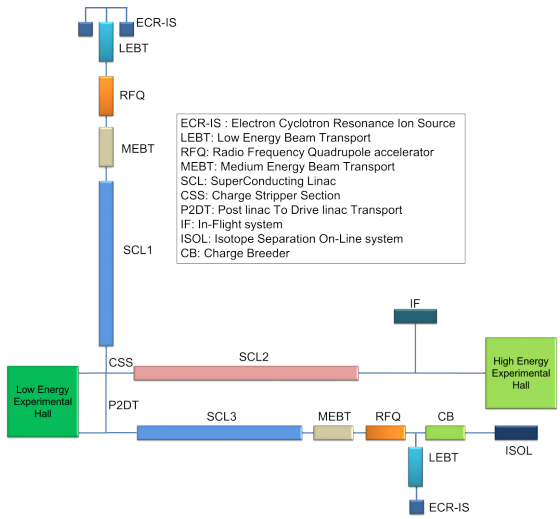

Figure 1: Layout of the RAON accelerator.

INTRODUCTION

The RAON accelerator [1] has been developed by the Rare Isotope Science Project (RISP) to accelerate and transport the rare isotope and stable ion beams from proton to uranium for a various kind of science experiments. The beams created by an electron cyclotron resonance ion source (ECR-IS) or an isotope separation on line (ISOL) system are transported to the radio frequency quadrupole (RFQ) after the low energy beam transport (LEBT) [2] and re-accelerated by the low energy superconducting linac (SCL1 or SCL3). These beams can be used for the low energy experiments or accelerated again by the high energy superconducting linac (SCL2) after passing through the charge stripping section [3] for the high energy experiments. Figure 1 shows the layout of the RAON accelerator.

The superconducting linacs of the RAON accelerator are divided into three sections, which are named SCL1, SCL2, and SCL3, depending on the type and number of superconducting cavities and the purpose of the beam acceleration. The SCL1 and SCL3 include two types of cavities, quarter-wave resonator (QWR) and half-wave resonator (HWR) and accelerate mainly the stable ion beams and the rare isotope beams, respectively. On the other hand, the SCL2 consists of two types of single spoke cavities (SSR1 and SSR2) and accelerates again the beams accelerated by the SCL1 or SCL3. The reference frequency of each section is also different depending on the type of cavity and it is 81.25 MHz for QWR cavities, 162.5 MHz for HWR cavities, and 325 MHz for SSR cavities, respectively. For the beam focusing and diagnostics at the superconducting linac, there is a warm section, which includes two quadrupoles, between cryomodules. At each warm section, a horizontal and a vertical correctors are mounted inside of first and second quadrupoles, respectively, and a beam-position monitor (BPM) is installed at first quadrupole for the beam steering. The schematic view of the SCL1 is shown in Fig. 2. In order to steer the distorted beam orbit to the reference orbit at the RAON accelerator, the beam steering studies has been carried out from the low energy section to the high energy section by using the singular value decomposition (SVD) [4] method and a graphical user interface (GUI) has also been developed with a beam optics code, DYNAC [5] and a computing program, MATLAB [6]. In this paper, the results of the beam steering simulations at the SCL1 will be presented and we will describe the simulation results for the cases with different number and location of correctors and BPMs.

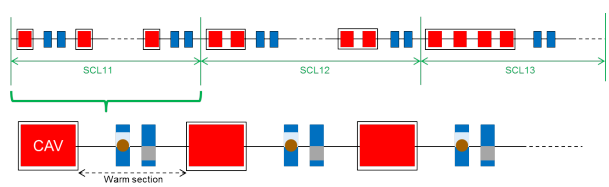

Figure 2: Schematic view of the SCL1. At each warm section, one horizontal corrector and one BPM are mounted at first quadrupole, and one vertical corrector is located at second quadrupole for the beam steering.

* hcjin@ibs.re.kr

ISBN 978-3-95450-185-4

BEAM STEERING PROCEDURE

For the steering of the beam orbit at the RAON accelerator, the SVD method based on the response matrix is used. The response matrix between correctors and BPMs are obtained by the DYNAC code and the corrector kick angle to steer the distorted beam orbit is calculated by the SVD method. The procedure of the beam steering with the DYNAC code and the MATLAB program is shown in Fig. 3. Also, the GUI for the beam steering has been developed [7]. Figure 4 shows the GUI which is recently updated to be used at the superconducting linac of the RAON accelerator. At the GUI, the magnet misalignment and the calculated kick angle of each corrector are shown at the upper window, the beam orbits before and after the steering are shown at the middle window, and the lattice information is shown at the lower window, respectively.

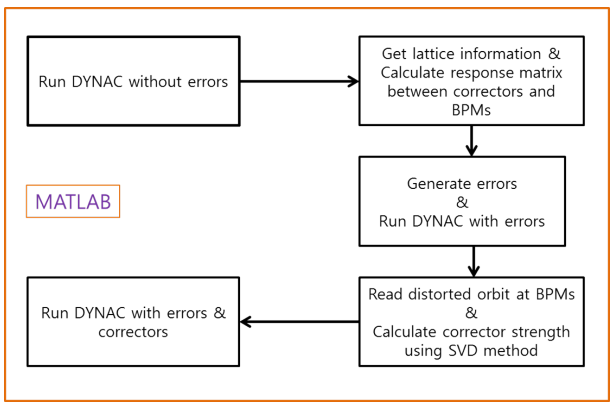

Figure 3: Procedure of the beam steering simulation.

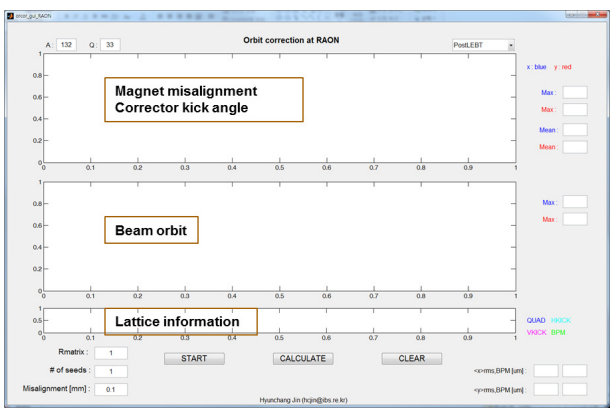

Figure 4: Initial screen of the recent beam steering GUI at the RAON accelerator.

SIMULATION RESULTS

For the beam steering studies at the SCL1, three cases with different number and location of correctors and BPMs are used. The first case (case 1) corresponds to the baseline lattice design which includes one horizontal corrector, one BPM, and one vertical corrector at each warm section. On the other hand, the case 2 and 3 represent the lattices which include two correctors and one BPM at every two and three warm sections, respectively. Figure 5 shows the schematic view of each case for the beam steering studies. The distortion of the beam orbit at the SCL1 is induced by the misalignments of equipments, launch errors, and so on. The errors used at the following simulations are listed at Table 1. Among these errors, the quadrupole root-mean-square (rms.) transverse misalignment which gives a dominant dipole kick to the beam orbit is varied from 100 μm to 500 μm, and other errors are given as default values. In addition, the reference uranium beam, $^{238}U^{33.5+}$, is used at the following simulations and the errors with 200 random seeds are applied for the statistics.

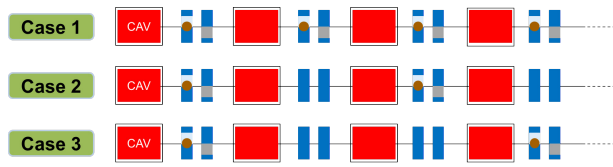

Figure 5: Three cases of the beam steering studies as varying the number of correctors and BPMs at the SCL1.

Table 1: Errors Used at the Beam Steering Simulations

Parameter	Value	Unit
Rms. $x(y)_0$	10	[μm]
Rms. $xp(yp)_0$	10	[μrad]
Quad. rms. misalign. x,y	300 (100 – 500)	[μm]
Cavity rms. misalign. x,y	10	[μm]

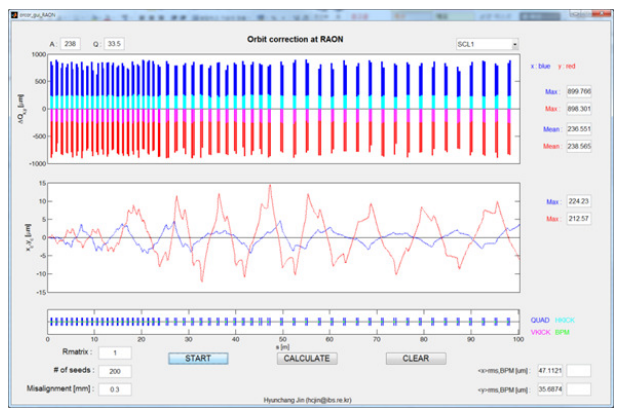

Figure 6: GUI for the case 1 before the beam steering with quadrupole rms. misalignment 300 μm.

Figure 6 shows the distortion of the beam orbit with a quadrupole rms. misalignment 300 μm for the case 1. Before the beam steering, the horizontal and vertical rms. orbit sizes are about 47.1 μm and 35.7 μm, respectively. After the beam steering, these values decrease to 3.9 μm and 2.8 μm, respectively. In order to steer the distorted beam orbit, the calculated average kick angles of horizontal and vertical correctors are about 0.37 mrad and 0.29 mrad, respectively,

ISBN 978-3-95450-185-4

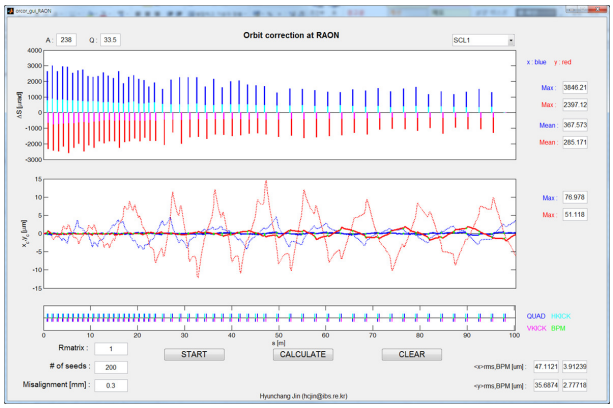

Figure 7: GUI for the case 1 after the beam steering with quadrupole rms. misalignment 300 μm.

which are much less than the mechanical maximum kick angle, about 2.0 mrad. The corrector kick angle and the beam orbit after the beam steering are shown in Fig. 7.

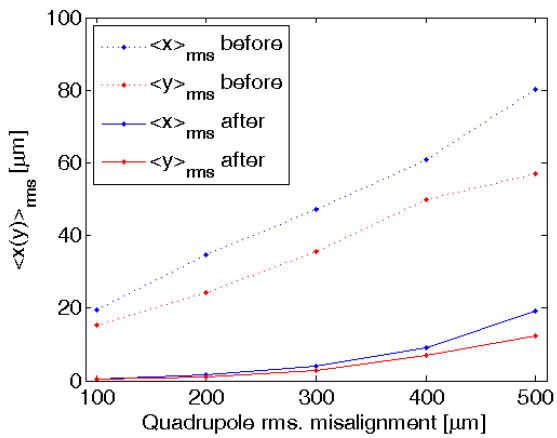

Figure 8: Rms. beam orbit sizes before and after the beam steering with quadrupole rms. misalignment 100 – 500 μm for the case 1.

Figure 8 shows the rms. beam orbit sizes before and after the beam steering as varying the quadrupole rms. misalignment from 100 μm to 500 μm for the case 1. The beam steering is carried out successfully up to 500 μm quadrupole rms. misalignment and the average kick angles of horizontal and vertical correctors for the beam steering are less than the mechanical maximum value as shown in Fig. 9.

Figure 10 shows the result of the beam steering simulation with the quadrupole rms. misalignment 300 μm for the case 2. At this case, the horizontal (vertical) rms. orbit size decreases from 45.9 (36.8) μm to 26.1 (27.5) μm, respectively. The orbit size after the beam steering does not decrease drastically at this case and the calculated kick angles of some correctors are also much larger than the mechanical maximum value.

The simulation result for the case 3 with quadrupole rms. misalignment 300 μm is shown in Fig. 11. After the beam steering, the orbit size decreases to about 7 μm which is

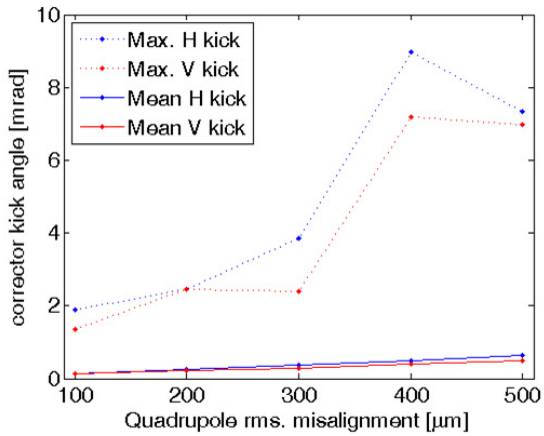

Figure 9: Maximum and average corrector kick angles for the beam steering with quadrupole rms. misalignment 100 – 500 μm for the case 1.

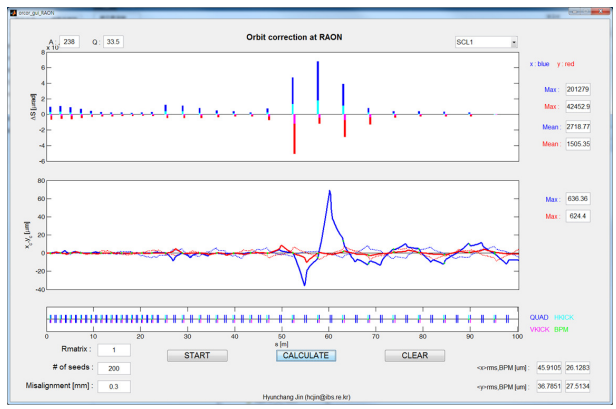

Figure 10: GUI for the case 2 after the beam steering with quadrupole rms. misalignment 300 μm.

smaller than result of the case 2. The difference of the case 2 and 3 comes from the transverse phase advance for the beam focusing and the locations of correctors and BPMs.

Figure 12 shows the comparison of beam orbit sizes after the beam steering for cases 1, 2, and 3 with the quadrupole rms. misalignment from 100 μm to 500 μm. As a result, the rms. orbit size after the beam steering for the case 3 is smaller than the one of the case 2 and close to the one of the case 1. For that reason, in order to reduce the number of correctors and BPMs, the case 3 is better than the case 2 for the current SCL1 lattice. To find the proper number of correctors and BPMs for the economical benefit, more studies with various number and location of correctors and BPMs will be continued at the superconducting linac of the RAON accelerator.

SUMMARY

We had presented the simulation results of the beam steering at the low energy superconducting linac, SCL1, of the RAON accelerator. The beam steering studies based on the SVD method were carried out with the correctors and BPMs

ISBN 978-3-95450-185-4

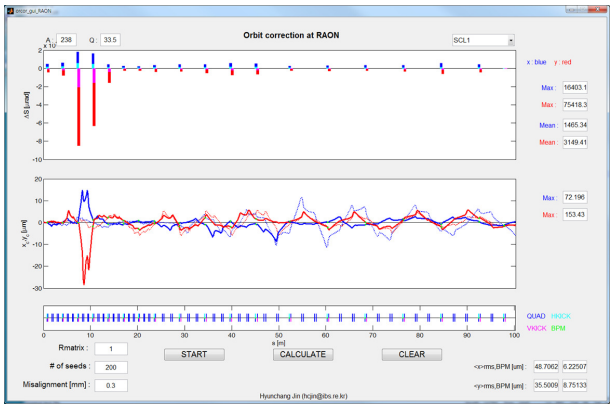

Figure 11: GUI for the case 3 after the beam steering with quadrupole rms. misalignment 300 μm.

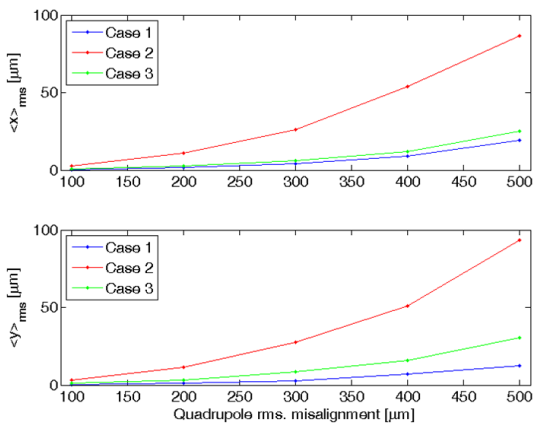

Figure 12: Comparison of rms. beam orbit sizes for cases 1, 2, and 3 with quadrupole rms. misalignment 100 – 500 μm.

located at the warm section of the SCL1. For the simulation, three cases with different number and location of correctors and BPMs were investigated and the orbit size was calculated before and after the beam steering for each case. As a result, the beam steering was performed successfully for the baseline lattice design within the mechanical maximum kick angle of the correctors. Additionally, for the beam steering at the SCL1, the result of the case including two correctors and one BPM at every three warm section was better than the one of the other case including two correctors and one BPM at every two warm section. For the economical benefit, more studies with various cases will be continued at the superconducting linac of the RAON accelerator.

ACKNOWLEDGMENTS

This work was supported by the Rare Isotope Science Project of Institute for Basic Science funded by Ministry of Science, ICT and Future Planning and National Research Foundation of Korea (2013M7A1A1075764).

REFERENCES

[1] D. Jeon, et al., "Design of the RAON accelerator systems", Journal of the Korean Physical Society 65.7 (2014).

[2] H. Jin and J. Jang, "Beam dynamics at the main LEBT of RAON accelerator", Journal of the Korean Physical Society 67.8 (2015).

[3] H. Jin, et al., "Achromatic and isochronous lattice design of P2DT bending section in RAON accelerator", Nuclear Instruments and Methods in Physics Research A 795 (2015).

[4] G. Golub and C. Reinsch. "Singular value decomposition and least squares solutions", Numerische mathematik 14.5 (1970).

[5] E. Tanke, "DYNAC: A multi-particle beam dynamics code for leptons and hadrons", Proceeding of LINAC02, Gyeongju, TH429 (2002), pp. 665-667.

[6] P. Marchand, "Graphics and GUIs with MATLAB", CRC Press, Inc., 1995.

[7] H. Jin and J. Jang, "Error analysis and correction at the main LEBT of RAON heavy ion accelerator", Proceeding of IPAC15, Richmond, MOPJE017 (2015), pp. 314-316.

ISBN 978-3-95450-185-4

ANALYTICAL APPROACH FOR ACHROMATIC STRUCTURE STUDY AND DESIGN

H. Y. Barminova, NRNU MEPhI, Moscow, Russia
A. S. Chikhachev, SSC VEI, Moscow, Russia

Abstract

The analytical approach is proposed to study the achromatic structures. The fully kinetic self-consistent time-dependent models are implemented in the approach. The method allows to predict the beam phase portrait behavior in magnetic fields of the structure with easy scaling and wide physical generality. The preliminary results of the method application for the bending magnets and the quadrupoles are presented.

INTRODUCTION

Achromatic structures are the important elements of the modern accelerator facilities [1-3]. The choice of suitable achromatic structures for the specific accelerator facility is a significant part of the facility research and development. The beam dynamic simulation with the help of numerous program codes (as example, [4-6]) is usually applied for this aims. In the case of multi-parameter task of charged particle beam formation with high intensity and high brightness the analytical approach is an attractive tool to describe the beam dynamics because it allows the task scalability and predicts the beam behavior with the most physical generality. Such an approach becomes possible, for instance, while using the self-consistent time-dependent models [7-9]. These models are the modifications of well-known Kapchinsky-Vladimirsky model (K-V model), which describes quasistationary continuous beam. In the paper presented the 2D and 3D models are used for the analysis of the beam phase portrait behavior in the dipole and quadrupole magnets, involved into the achromatic structure. These models are fully kinetic and time-dependent and correspond to uniformly charged intense beam both continuous and bunched. The models consider the continuous beam with elliptical cross-section and the bunched beam shaped as an ellipsoid with various relations between the semiaxes.

MOTION IN BENDING MAGNET

To describe analytically the motion of the beam with elliptical cross-section in the bending magnet the model is developed, corresponding to the uniformly charged beam. Some idealization of the task geometry is applied, namely, the bunch should have the most size in the coordinate direction corresponding to the direction of the magnetic force lines (2D approximation), and the magnetic field has a sharp edge, i.e. at this step the fringe fields of the dipole magnet are not taken into account. In addition, we assume the simple beam structure when it consists of one kind of the particle with the same values of both the charge and the mass.

Let us begin from the case of non-relativistic and non-intense or emittance-dominant beam. The approximation of uniformly charged beam moving in the uniform external field allow to write the invariant I for the linear equations of the beam particle motion:

$$I = \frac{(u\dot{x} - \dot{u}x)^2}{\varepsilon_x^2} + \frac{(v\dot{y} - \dot{v}y)^2}{\varepsilon_y^2} + \frac{x^2}{u^2} + \frac{y^2}{v^2} + C_0(x\dot{y} - \dot{x}y) \quad (1)$$

where x,y – the coordinate axes, connected with the beam mass center and rotating with the mass center in the laboratory coordinate system, u,v – the auxiliary time-dependent functions, C_0 – the mean angular momentum of the particle, the dot means the differentiation with respect to the time.

The kinetic distribution function f corresponding to the particle oscillations in the plane of the turn may be written as

$$f = \kappa\delta(I - 1), \quad (2)$$

where κ – the normalization constant, δ – the delta function. Such function automatically satisfies to Vlasov equation and really describes the beam with elliptical cross-section in the plane of the turn:

$$n = \int f(I)dxdy = \frac{\pi\kappa}{uv}\varepsilon_1\varepsilon_2\sigma(1 - Ax^2 - By^2 - Cxy) \quad (3)$$

where

$$A = \frac{1}{u^2} - \frac{C_0^2\varepsilon_2^2}{4v^2}, B = \frac{1}{v^2} - \frac{C_0^2\varepsilon_1^2}{4u^2}, C = C_0\left(\frac{\dot{u}}{u} - \frac{\dot{v}}{v}\right).$$

Here σ is Heaviside function, ε_1 , ε_2 – the values, which characterize the partial emittances of the beam in the cross-section, corresponding to the plane of the turn.

Using the equations (1) and (2), one can obtain for the beam rms values:

$$\frac{1}{R_x^2} = \left(A + B + ((A - B)^2 + C^{2)^{1/2}}\right)/2$$
$$\frac{1}{R_y^2} = \left(A + B - ((A - B)^2 + C^{2)^{1/2}}\right)/2 \quad (4)$$

ISBN 978-3-95450-185-4

where R_x and R_y – the rms values of the semiaxes of the elliptical beam cross-section, corresponding to the coordinate plane, connected with the plane of the turn.

The equations obtained above give the possibility to estimate the effect of the emittance transformation in the plane of the turn and to determine the general factors affecting the phenomenon.

Analytically estimated maximum value of the emittance transfer is $k = \varepsilon_2 / \varepsilon_1$, which corresponds to the turn of the beam center of the mass at the angle 180º.

It is evident, that initial relations between the beam phase characteristics (at the inlet into the magnetic field area) as well as the initial beam angular momentum affect strongly the beam phase transformation followed. For the quanitative estimate of the emittance transformation during the beam turn at the arbitrary angle the system of the ODE should be solved representing the particle motion in the magnet.

Note here, that first the effect of the emittance transfer for the simple geometry of the bunch was studied in [10,11].

MOTION IN QUADRUPOLE MAGNET

Here the phase portrait behavior of intense charged particle bunch moving in the magnetic field of the stationary quadrupole is studied. We assume that the beam mass center moves in the symmetry plane of the magnet. To study this case the approximation of strong linear dependence of the forces acting on the particles is supposed for both the external field of the magnet and the own bunch fields arisen due to the own space charge. Let us consider only non-relativistic beam motion again.

In the coordinate system (x,y,z), connected with the bunch center of mass, particle motion equations may be written as

$$\begin{aligned} x'' &= \omega' x_0 y' + \omega' x y_0' + \frac{e}{m}\frac{\partial \Phi}{\partial x}, \\ y'' &= -\omega' x_0' x - \omega' x_0 x' + \frac{e}{m}\frac{\partial \Phi}{\partial y}, \\ z'' &= -\omega' y_0' z + \frac{e}{m}\frac{\partial \Phi}{\partial z}. \end{aligned} \tag{5}$$

Here $x_0(t)$, $y_0(t)$ are the coordinates of the ellipsoidal bunch center in laboratory coordinate system, $\Phi(x,y,z)$ – the potential of the self-consistent bunch field, ω' is the gradient of the cyclotron frequency corresponding to the field of the quadrupole, e and m are the charge and the mass of the beam particle respectively.

The motion of the bunch center is described by the equations

$$\begin{aligned} x_0'' &= \omega' x_0 y_0', \\ y_0'' &= -\omega' x_0 x_0', \end{aligned}$$

with initial conditions

$$x_0\big|_{t=0} = y_0\big|_{t=0} = 0, x_0'\big|_{t=0} = v, y_0'\big|_{t=0} = 0.$$

Here v is the bunch velocity. So the equation for the motion of the bunch mass center may be rewritten as

$$x_0' = \pm\sqrt{v^2 - \omega'^2 x_0^4 / 4}.$$

The potential of the uniformly charged ellipsoid we may represent as [12]:

$$\frac{e\Phi}{m} = \frac{e\Phi_0}{m} + \frac{3q}{2}(K_x x_1^2 + K_y y_1^2 + K_z z_1^2),$$

where Φ_0 – the potential in the center of the ellipsoid, (x_1,y_1,z_1) – the coordinate system, connected with the main axes of the bunch, K_x, K_y, and K_z are determined by the following equations:

$$\begin{aligned} K_x &= 2(K - E)/\varepsilon^2 R_x^3, \\ K_y &= 2(E - K(1-\varepsilon^2))/R_x R_y^2, \\ K_z &= 2(1 - R_z E / R_x (1-\varepsilon^2)^{1/2})/R_x R_y R_z \end{aligned}$$

Here K and E are the full elliptical integrals of 1st and 2nd type respectively, $\varepsilon = (1 - R_y^2/R_x^2)^{1/2}$ is the argument of the integrals K and E, $q = e^2 N / m$, N – the value of the particles per the bunch, e and m are the charge and the mass of the particle respectively.

Taking into account the equations (5), one can write the following invariants for the case of the strong bunch center motion in the symmetry plane of the magnet:

$$\begin{aligned} I_{xy} &= A_1 x'^2 + 2A_2 x x' + A_3 x^2 + B_1 y'^2 + \\ &+ 2B_2 y y' + B_3 y^2 + C_1 x' y' + C_2 y x' + C_3 x y' + C_4 \end{aligned} \tag{6}$$

$$I_z = L z' - L' z,$$

where L(t) is the solution of the equation

$$L'' - (\omega' y_0' - 3qK_z)L = 0. \tag{7}$$

From the condition $dI/dt \equiv 0$ we can obtain the system of the ODE of 1st order, which fully determines the bunch phase portrait behavior in the magnetic field of the quadrupole:

ISBN 978-3-95450-185-4

$$
\begin{aligned}
A_1' &= -2A_2 + \omega_H C_1 \\
A_2' &= -A_3 - A_1 M_1 + (\omega_H C_3 - C_1(M_2 - \omega' x_0'))/2 \\
A_3' &= -2A_2 M_1 - C_3(M_2 - \omega' x_0') - 2A_2 \omega' y_0' \\
B_1' &= -2B_2 + \omega_H C_1 \\
B_2' &= -B_3 - B_1 M_3 - (\omega_H C_2 + C_1 M_2)/2 \\
B_3' &= -2B_2 M_3 - C_2 M_2 \qquad (8) \\
C_1' &= -C_2 - C_3 + 2\omega_H (B_1 - A_1) \\
C_2' &= -C_4 - C_1 M_3 - 2(A_1 M_2 - \omega_H B_2) \\
C_3' &= -C_4 - C_1 M_1 - 2(A_2 \omega_H - B_1 M_2) - C_1 \omega' x_0' \\
C_4' &= -C_2 M_1 - C_3 M_3 - 2(A_2 + B_2) M_2 - \\
&- C_2 \omega' y_0' + 2B_2 \omega' x_0'
\end{aligned}
$$

Here

$$
\omega_H = \omega' x_0, M_1 = 3q(K_y + \cos^2\theta(K_x - K_y)),
$$
$$
M_2 = 3q \sin 2\theta (K_x - K_y)/2,
$$
$$
M_3 = 3q(K_x - \cos^2\theta(K_x - K_y)
$$

The angle θ characterizes the position of the coordinate system, connected with the main axes of the elliptical cross-section of the hipper-ellipsoid in 4D phase spase, corresponding to the usual space, with respect to the axes of the coordinate plane (x,y). The angle α corresponds to the angle between the axes (x,y) and the main axes of the elliptical cross-section of the hipper-ellipsoid in 4D phase space, corresponding to the velocity space.

Using the invariants, let us write the distribution function as

$$
f = \kappa\delta(I_{xy} + I_z^{(1)2} - 1)\delta(I_z^{(2)2}), \qquad (9)
$$

where $I_z^{(1)}$ and $I_z^{(2)}$ are the linear invariants, corresponding to both independent solutions of the equation (7).

The direct calculation of the density with the distribution function (9) confirms the self-consistency of the model.

The equations (8) should be solved numerically. Some results of such calculations by means of the Runge-Kutta method of the 4th order are shown in Figure 1 and Figure 2.

In Figure 1 the effect of the emmitance transfer is shown dependent on the cyclotron frequency. Figure 2 illustrates the time-dependent behavior of the specific angles of the bunch cross-section in the coordinate space (θ) and in the velocity space (α) with respect to the initial position of the main axes of the phase ellipses.

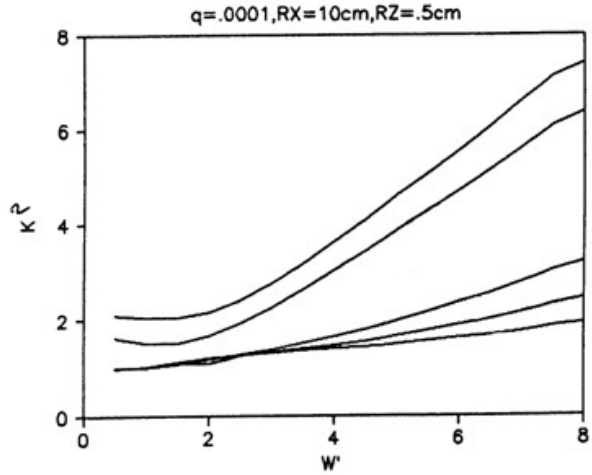

Figure 1: The dependence of the coefficient of the emittance transfer on the gradient of the cyclotron frequency.

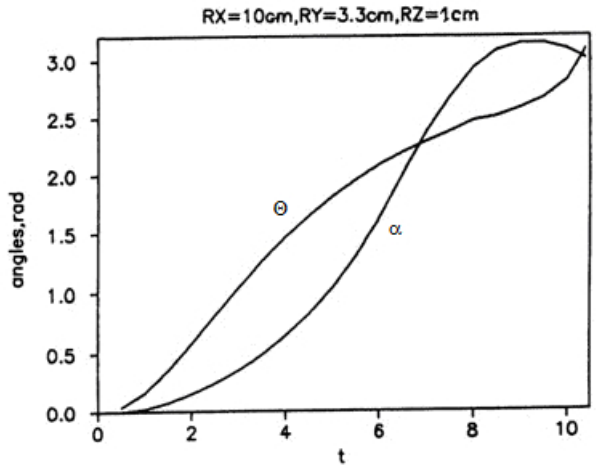

Figure 2: Time-dependence of the turn angles of the phase ellipses with respect to their initial position.

CONCLUSIONS

The self-consistent models are the basis of the proposed analytical approach to study and develop the achromatic structures involving the dipole and quadrupole magnets. The approach allows to determine the general physical factors which affect the properties of the achromatic structure, particularly its possibility to change all the beam phase characteristics, both desired and undesired. The preliminary study shows the significant influence of the initial beam phase characteristics on the phase portrait transformation during the beam motion in the dipole and quadrupole magnets. The dependence of the emittance transfer on the quadrupole field gradient, the affect of the initial beam angular momentum and other peculiarities of the task geometry on the phase portrait behavior are found.

ISBN 978-3-95450-185-4

REFERENCES

[1] "ATF, Accelerator Test Facility, Design and Study Report", KEK 1995.

[2] A. Anoshin, E. Fomin, V. Korchuganov *et al.*, "Modernization and Development of Kurchatov Center of Synchrotron Radiation and Nanotechnology", in *Proc. RuPAC'08*, Zvenigorod, Russia, pp. 197-200.

[3] A.Wrulich, "Overview of 3rd Generation Light Sources", Sincrotrone Trieste, ST/M-92/3, March 1992.

[4] S. Webb, D. Bruhwiler, D. Abell, K. Danilov, S. Nagaitsev, A. Valishev, V. Danilov and A. Shishlo, "Simulating High-Intensity Proton Beams in Nonlinear Lattices with PyORBIT", in *Proc. IPAC'12,* New Orleans, Louisiana, USA, May 2012, paper WEPPR012, pp. 2961-2963.

[5] http://www.phy.anl.gov/atlas/TRACK/.

[6] K. R. Crandall and D. P. Rusthoi, TRACE-3D Documentation, 3rd Edition, May 1997, LANL, Los Alamos, New Mexico 87545, USA.

[7] E. E. Barminova, A. S. Chikhachev, Radiophys. and Quant. Electron., 34, № 9, 1041 (1991).

[8] E. E. Barminova, PhD Thesis, MEPhI, Moscow, Russia, 2001.

[9] H. Y. Barminova, A. S. Chikhachev, Phys. Rev. ST Accel. Beams 16, 050402 (2013).

[10] V. V. Kushin, B. P. Murin, E. V. Gromov, Proc. RTI RAS USSR, 16 (1973).

[11] V. V. Kushin, Techn. Phys. 54, № 1, 103 (1984).

[12] R. Z. Muratov, "Ellipsoid Potentials", (Moscow: Atomizdat, 1966 (in Russian)).

ISBN 978-3-95450-185-4

ESSnuSB PROJECT TO PRODUCE INTENSE BEAMS OF NEUTRINOS AND MUONS

E. Bouquerel* on the behalf of the ESSnuSB project,
IPHC, UNISTRA, CNRS, 23 rue du Loess, 67200, Strasbourg, France

Abstract

A new project for the production of a very intense neutrino beam has arisen to enable the discovery of a leptonic CP violation. This facility will use the world's most intense pulsed spallation neutron source, the European Spallation Source (ESS) under construction in Lund. Its linac is expected to be fully operational at 5 MW power by 2023, using 2 GeV protons. In addition to the neutrinos, the ESSnuSB proposed facility will produce a copious number of muons at the same time. These muons also could be used by a future Neutrino Factory to study a possible CP violation in the leptonic sector and neutrino cross-sections. They could be used as well by a muon collider or a low energy nuSTORM. The layout of such a facility, consisting in the upgrade of the linac, the use of an accumulator ring, a target/horn system and a megaton Water Cherenkov neutrino detector, is presented. The physics potential is also described.

ESSνSB PROJECT

The ESSνSB (standing for European Spallation Source Neutrino Super Beam) project proposes to study a Super Beam which uses the high power linac of the ESS facility [1] based at Lund in Sweden as a proton driver and a MEMPHYS type detector [2, 3] located in a deep mine at a distance of about 500 km, near the second neutrino oscillation maximum (Fig. 1).

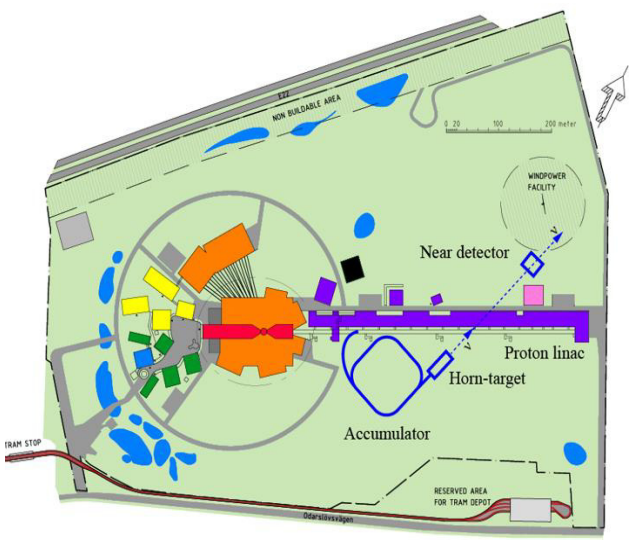

Figure 1: ESSνSB layout on top of the ESS facility.

* Elian.Bouquerel@iphc.cnrs.fr

The ESS Linac

ESS will deliver a first proton beam for neutron production at reduced energy and power by 2019. A proton beam of the full design power 5 MW and energy 2.0 GeV will be delivered by 2023. There will be 14 pulses of 62.5 mA current and 2.86 ms length per second (Table 1). In order for the ESS to be used to generate a neutrino beam in parallel with the spallation neutrons, some modifications of the proton linac are necessary. A preliminary study of these modifications that are required to allow simultaneous acceleration of H^+ (for neutron production) and H^- (for neutrinos) ions at an average power of 5 + 5 MW has been made [4].

Table 1μ Main ESS Facility Parameters [1]

Parameter	Value
Average beam power	5 MW
Proton kinetic energy	2.0 GeV
Average macro-pulse current	62.5 mA
Macro-pulse length	2.86 ms
Pulse repetition rate	14 Hz
Max. acc. cavity surface field	45 MV/m
Max. linac length	352.5 m
Annual operating period	5000 h
Reliability	95%

The Accumulator Ring and Beam Switchyard

An accumulator ring to compress the pulses to few μs is mandatory to avoid overheating issues of the neutrino targets. A first estimation gives a ring having a circumference of 376 m [5] (Table 2). Each pulse from the ESS linac will contain 1.1×10^{15} protons, which for a normalized beam emittance of 200 π mm mrad in the ring by multi-turn injection (the emittance from the linac should be in the order of a few mm-mrad) will lead to the space-charge tune shift of about 0.75.

Table 2: Accumulator Parameters [5]

Parameter	Value
Circumference	376 m
Number of dipoles	64
Number of quadrupoles	84
Bending radius	14.6 m
Injection region	12.5 m
Revolution time	1.32 μs

The H^- ions will be fully stripped during the injection into the accumulator using either stripping foils or a laser-stripping device [5, 6]. The extraction of the beam from the ring needs a group of kickers that should have a rise time of not more than 100 ns.

ISBN 978-3-95450-185-4

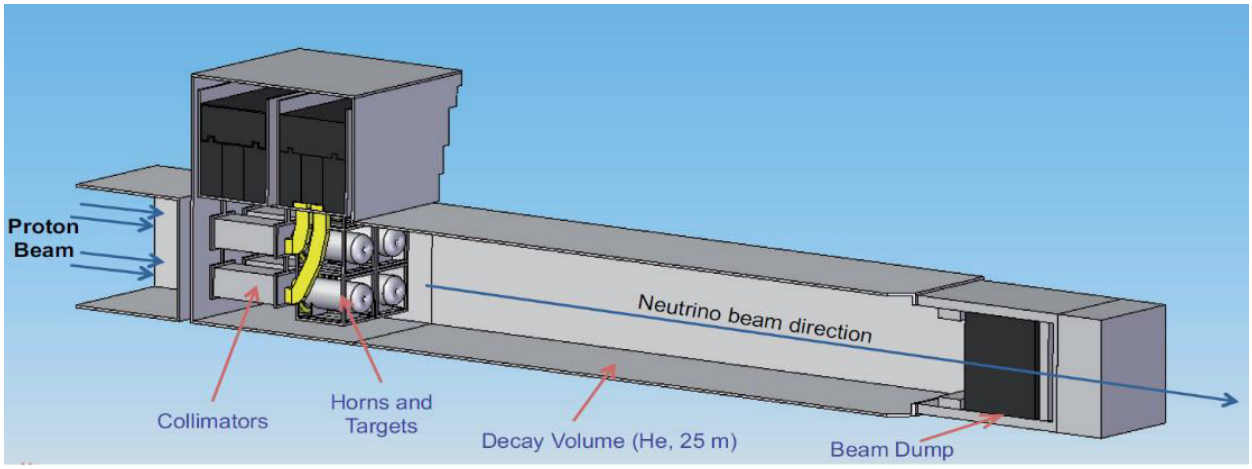

Figure 2: Schematic view of the target/horn station [7].

Four separate targets are needed in order to mitigate the high power dissipation in the target material. A beam switchyard system downstream the accumulator ring will distribute the protons onto the targets [8] (Figs. 2,3).

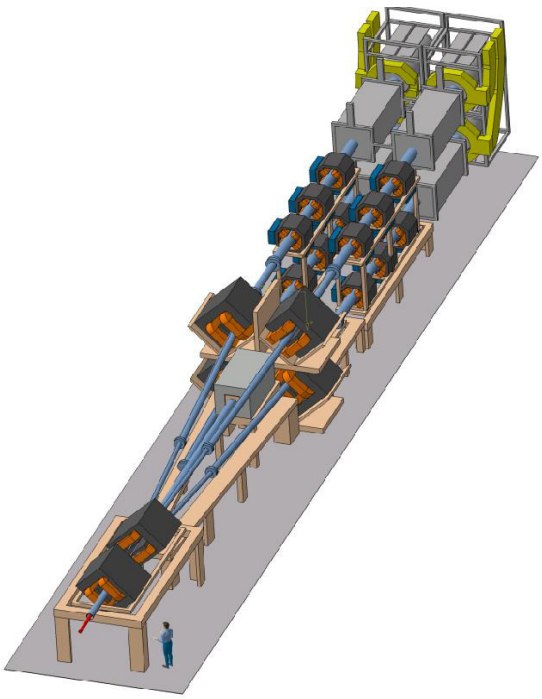

Figure 3: Beam switchyard.

The Horn/Target Station

The target station includes the target itself that is hit by the protons leading to the production of short-lived mesons, mainly pions, which decay produce muons and muon neutrinos. A packed bed of titanium spheres cooled with pressurized helium gas has become the baseline target design for a Super Beam based on a 2-5 GeV proton beam with a power of up to 1.2 MW per target. The packed bed concept has been studied using Computation Fluid Dynamics (CFD) software tools [7].

Other main components of the target station are the hadron collectors called magnetic horns (Fig. 4), which focuses the hadrons towards the decay tunnel (long enough to allow the mesons to decay, but not as long as to allow for a significant amount of the muons to decay).

In order to mitigate the detrimental effects of the very high power of the proton beam hitting the target, EUROv [7] has proposed a system with four targets and horns, sharing the full beam power between the four. This system will be adopted here.

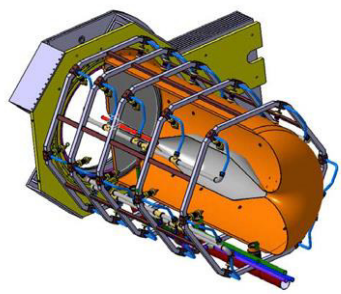

Figure 4: Horn layout (the target is inside).

Underground Detector Site

The Northern Garpenberg mine, located at 540 km NW of the ESS site in Lund in Sweden, is one of the candidate mines that could host the large underground Water Cherenkov detector. This mine is being studied in detail collecting geological and rock mechanics information at potential detector locations, situated at 1000 m depth (3000 m water equivalent) and at least 500 m from locations with active mining operations, by making core drillings, core logging, rock strength testing and rock stress measurements of the surrounding rock.

Once a suitable location for the neutrino detector underground halls has been determined (total volume of 6×10^5 m^3), a design of the geometry and construction methods for the underground halls will be made based on the measured strength and stress parameters of the rock.

ISBN 978-3-95450-185-4

PHYSICS POTENTIAL

According to first evaluations [9], for which 5% systematic error on the signal and 10% systematic error on the background were assumed, leptonic CP violation could be discovered at 5 σ confidence level within at least 50% of the CP phase range for baselines in the range 300-550 km with an optimum of about 58% of the phase range at a baseline of about 420 km, already a very competitive physics performance [10]. According to the same first evaluations, the neutrino mass hierarchy can be determined at more than 3 σ confidence level for baselines in the range 300–500 km depending on the proton beam energy. In addition, inclusion of data from atmospheric neutrino oscillations in the mass hierarchy determination will certainly improve the physics reach of this project.

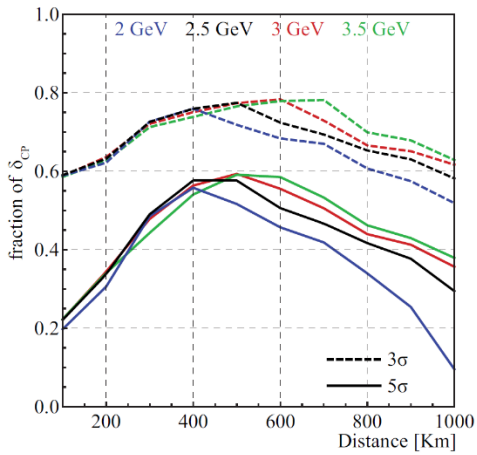

Figure 5: The fraction of the full CP range as function of the baseline. The lower (upper) curves are for CP violation discovery at 5 σ (3 σ) significance.

Figure 5 presents the CP fraction coverage versus the distance to the far detector for 3 σ and 5 σ confidence level. To estimate this performance several proton energies have been used on top of the default one of 2 GeV since it is possible to upgrade the linac to deliver higher energy protons.

MUON PRODUCTION

In addition to the neutrinos, the ESSnuSB proposed facility will produce a copious number of muons at the same time. 2.7×10^{23} protons are foreseen to hit the targets within one-year operation. Preliminary studies show that 3.5×10^{20} pions and 4.2×10^{22} muons, per m^2 and per year will be available at the level of the beam dump which is located 25 m after the horn-target system [11, 12]. Figure 6 presents the impacts of remaining pions and produced muons at the surface of the beam dump.

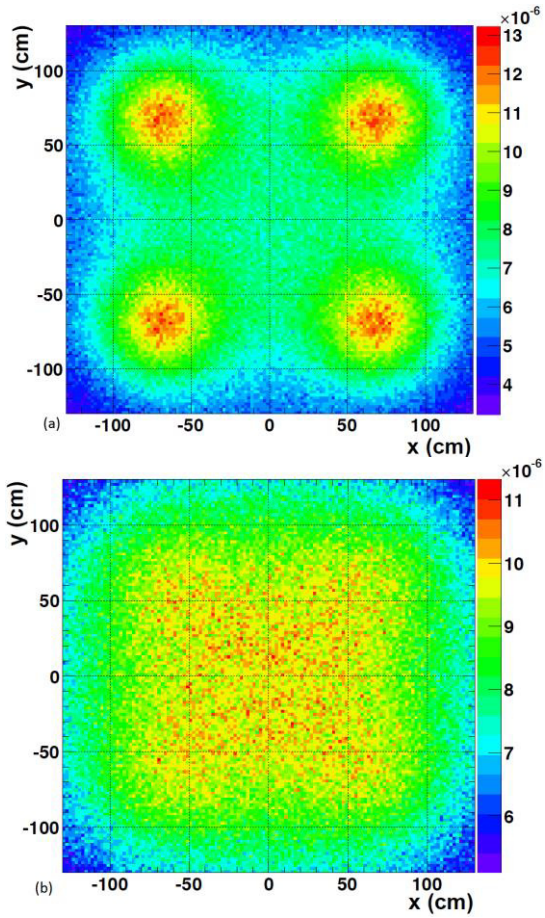

Figure 6: Pions (a) and muons (b) at the surface of the beam dump (normalized by proton).

The produced muons could be used by a low energy nuSTORM [13] facility to measure neutrino cross-sections at the energies where this neutrino facility will be operated. They could also be useful for 6D muon cooling experiments and in an ultimate stage they could be used to operate a Neutrino Facility or a muon collider.

The mean value of the momentum of pions and muons is 0.7 GeV and 0.46 GeV, respectively (Fig. 7). For these energies, the mean free path of pions is of the order of 40 m after which they will decay to give some more muons. The mean free path for the muons is 2.9 km which is enough to send them in a ring, as the one foreseen for nuSTORM, where they can decay in straight sections to produce muon and electron neutrinos to be used to measure cross-sections.

Table 3: Magnetic Rigidity for Protons, Pions and Muons

Particle	<Ek> (GeV)	Bσ (T.m)
Protons	2.0	9.28
Pions π^+, π^-	0.7	2.76
Muons μ^+, μ^-	0.46	1.85

ISBN 978-3-95450-185-4

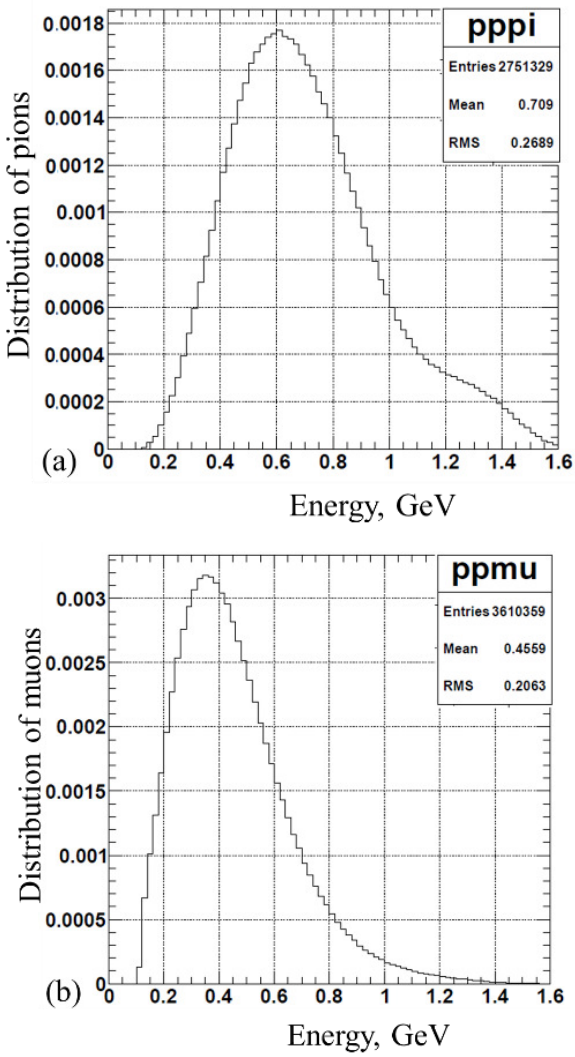

Figure 7: Momentum distribution: pions (a); muons (b).

While for nuSTORM muon beam an iron absorber is needed to lower the muon momentum to a mean value of 400 MeV in order to perform 6D muon cooling experiments (of which success could lead to the construction of a Neutrino Factory and of a muon collider), for ESSnuSB the muon momentum is directly around the required values. nuSTORM plans to collect in the region between 200 MeV/c and 500 MeV/c about 4.3×10^{17} muons per year while the ESSnuSB facility could provide more than 2.5×10^{20} muons per year for the same momentum range.

MUON EXTRACTION

As shown previously in Fig. 6, four spots induced by the four targets and horns are visible for the pion distribution while for the muons coming from the pion decays these spots are more diluted. The majority of these particles is concentrated over a surface of 2x2 m^2 which constitutes a difficulty for their extraction and injection in a beam pipe.

Several configurations are currently under studies to extract these particles. One of them consists in moving further back in the tunnel the beam dump and placing absorbers with the aim of absorbing the protons and some of the remaining pions. The muons would be then collimated, with some remaining pions, and deflected using bending magnets (Fig. 8).

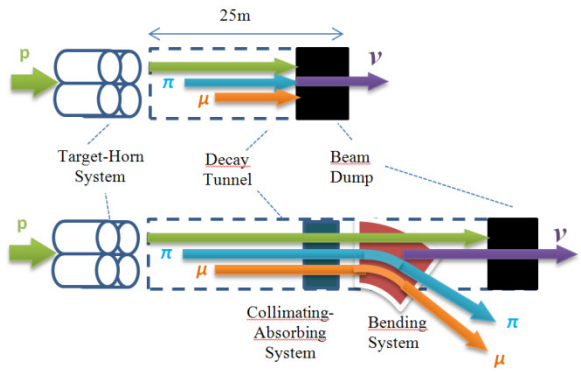

Figure 8: Principle of muon extraction.

From the particle kinetic energies, the magnetic rigidity is estimated to be 2.76 T.m and 1.85 T.m for the pions and the muons respectively (Table 3). As an example, the deflection of the muons of an angle of 175 mrad (10°) with respect to the proton beam axis would need an induced magnetic field of 0.25 T. In the meanwhile, the remaining pions would also be deflected by 117 mrad. The angle of divergence of the pions and muons, which mainly depends on their kinetic energy, is needed to properly design the absorbers. The characteristics of these secondary beams have to be carefully defined in order to estimate the impact on the bending system.

Moreover, such a system is supposed to be protected from any particle interactions to avoid radiation issues and also it has to be accessible for any maintenance operation in case of failure.

Estimations of the losses during the absorption process will also help in determining if the deflection of the particles produced by a single horn-target (instead of the 4) would be sufficient for the facilities which are located downstream. The focussing of these particles will be done out of the tunnel once the deflection process is achieved.

ACKNOWLEDGMENT

This project is now supported by the COST Action CA15139 "Combining forces for a novel European facility for neutrino-antineutrino symmetry-violation discovery" (EuroNuNet).

REFERENCES

[1] The European Spallation Source, http://europeanspallationsource.se/, "ESS Technical Design Report", Release 1.0, Nov. 2012.

[2] A. de Bellefon et al., hep-ex/0607026.

[3] L. Agostino et al. [MEMPHYS Coll.], JCAP 1301 (2013) 024 [arXiv:1206.6665 [hep-ex]].

ISBN 978-3-95450-185-4

[4] F. Gerigk and E. Montesinos, Tech. Rep. CERN-ACC-NOTE-2015-0040, CERN, Geneva, Switzerland, http://cds.cern.ch/record/2110681.

[5] E. Wildner et al., THPF100, Proceedings of IPAC2015, Richmond, VA, USA.

[6] M. Martini, "Modelling accumulator stripper foil heating for ESSNUSB facility," Tech. Rep. CERN-ACC-NOTE-2015-0005, CERN.

[7] T. R. Edgecock et al., "High intensity neutrino oscillation facilities in Europe," Physical Review Accelerators and Beams, vol. 16, no. 2, Article ID 021002, 2013.

[8] E. Bouquerel, MOPWA017, Proceedings of IPAC2015, Richmond, VA, USA.

[9] E. Baussan et al. arXiv:1212.5048 [hep-ex].

[10] P. Coloma and E. Fernandez-Martinez, JHEP 1204 (2012) 089 [arXiv:1110.4583 [hep-ph]].

[11] M. Dracos, "The European Spallation Source Neutrino Super Beam for CP Violation discovery", NuFact15 Proceedings, August 2015.

[12] N. Vassilopoulos,' ESSνSB: Update on secondary beam studies', PoS(NUFACT2014)078.

[13] P. Kyberd et al. [nuSTORM Collaboration], arXiv:1206.0294 [hep-ex].

ISBN 978-3-95450-185-4

LASER STRIPPING H- CHARGE EXCHANGE INJECTION BY FEMTOSECOND LASERS

T. Gorlov, SNS Project, Oak Ridge National Laboratory, Oak Ridge, Tennessee 37831

Abstract

A new method of H- laser assistant charge exchange injection using femtosecond laser pulses is considered. The existing method uses a divergent laser beam that allows compensation for the angular and momentum spread of the stripped beam. The femtosecond laser pulse has a similar property that can cover the spread and yield efficient laser stripping. Results of simulations with realistic femtosecond laser and H- beam parameters are discussed. The proposed method may have some benefits for particular technical conditions over other methods.

INTRODUCTION

Femtosecond lasers may be applied for H- charge exchange injection method or laser stripping. Laser stripping has been actively developed at the SNS project over the past decade. Theoretical investigation began in [1]. Practical application has been proven for stripping of short (6 ps) pulses [2] and for long (10 us) pulses of H- [3]. The second step of the three-step laser stripping scheme [1] considers resonant excitation of the H^0 beam by laser at the incidence angle α:

$$\omega_0 = \gamma_p(1 + \beta_p \cos(\alpha))\omega \qquad (1)$$

where β_p and γ_p are relativistic factors of the H^0 beam with longitudinal momentum p. Equation (1) represents a precise resonant condition for monochromatic laser frequency ω and discrete atomic excitation frequency ω_0. Longitudinal momentum spread δp of a realistic beam spreads out particles from resonance particle with design momentum p. As a result, most particles are not excited and stripped. In this way, longitudinal momentum spread complicates laser stripping and presents a challenging practical problem. This section presents a qualitative review of the methods of compensating δp in terms of (1), skipping the complicated mathematical mechanism of laser-bunch interaction.

Paper [1] proposed the use of a divergent laser beam with at an angle of δα to cover the spread δγ(δp), δβ(δp). A laser beam with angle of about 0.5 mrad provides good resonance conditions for all the particles of the bunch. This method has been tested experimentally [2, 3].

Another method of δp compensation has been proposed in [4] and developed in [5]. It involves broadening the discrete atomic resonance frequency ω_0 by applying an electric field in the particle's rest frame or a magnetic field in the laboratory frame. All off-resonance particles can be excited by using wide continuum atomic resonance $\delta\omega_0$ when a high energy atom is emerged into a strong magnetic field in the laboratory frame.

This paper discusses another method of momentum beam compensation which involves broadening the laser frequency ω in terms of (1). The picosecond laser pulse that has been considered in [2] or [3] has a narrow band frequency ω which may be broadened by using femtosecond laser pulses. The spectrum *f(ω')* of finite laser pulse

$$E(t) = E_0 e^{-\frac{t^2}{4\sigma^2}} \cos(\omega t) = \int_{-\infty}^{\infty} f(\omega')\cos(\omega' t)d\omega' \qquad (2)$$

with pulse length σ (in terms of energy) can be calculated by Fourier transform

$$f(\omega') = \frac{E_0 \sigma e^{-\sigma^2(\omega'+\omega)^2}(1+e^{4\sigma^2\omega\omega'})}{2\sqrt{\pi}} \qquad (3)$$

The RMS width σ_ω of the function is estimated to be

$$\sigma_\omega \approx \frac{1}{\sigma}\sqrt{\frac{1}{2} - \frac{1}{\pi}} = \frac{0.42}{\sigma} \qquad (4)$$

A shorter pulse has a wider spectrum. The required laser pulse width σ_t may be estimated by differentiating ω over momentum p and equating dω to σ_ω. The SNS accelerator has a relative longitudinal momentum spread ($\Delta p/p \approx 10^{-4}$) and the laser pulse width σ_t is estimated to be about 1 ps. This rough estimate indicates that a sub-picosecond or femtosecond laser pulse is required to compensate the longitudinal momentum spread for high efficiency excitation.

All three methods have their relative advantages and disadvantages and each method can become more convenient for accelerator with particular parameters. The divergent laser beam method allows for adjustment of the incidence angle α for beam energy in a wide range; however, it requires precise laser optics tuning. The atomic broad shape resonance method does not require tuning the laser beam optics but may require a more complicated (or simplified) magnet system for stripping the H- beam. It also requires more beam energy [5]. The third method differs from the others by using femtosecond lasers. The H- bunch usually has a multi-picosecond width that requires about the same longitudinal width as the laser to achieve adequate interaction overlap. For this reason, a femtosecond laser pulse is difficult to use for stripping the H- bunch at a nonzero incidence angle of α. Adequate overlap with femtosecond pulse is only achieved by using head-on interaction or setting the angle at 0. As existing

This work has been supported by Oak Ridge National Laboratory, managed by UT-Battelle, LLC, under contract DE-AC05-00OR22725 for the U.S. Department of Energy.

ISBN 978-3-95450-185-4

powerful femtosecond lasers have only one or two wavelengths, laser stripping is only possible for fixed H^- energy defined by (1) where $\alpha = 0$. Another disadvantage to this method is the more complicated scheme of stripping with head-on interaction.

MODEL OF INTERACTION

This section presents a more detailed physical model for the interaction of a femtosecond laser pulse with a H^0 beam. A H^0 atom interacting with the femtosecond laser pulse can be characterised by the time-dependant, quantum-mechanical wave function $\Psi(t) = C_1(t)\psi_1 + C_2(t)\psi_2$. The atom is excited from the ground state ψ_1 to an excited state ψ_2. The coefficients $|C_1|^2$ and $|C_2|^2$ represent the probability of the atom to be in the corresponding states.

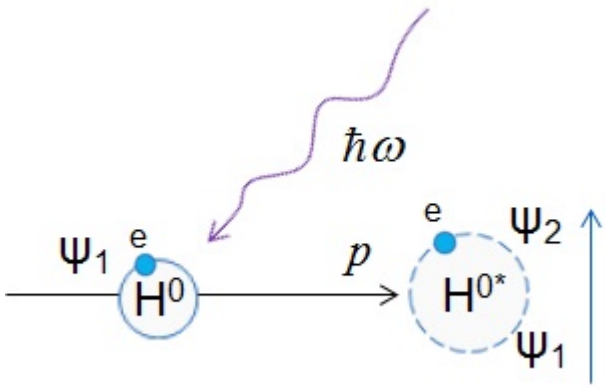

Figure 1: Interaction of atomic hydrogen with laser beam in general case for $\alpha \neq 0$ in (1).

As found in all previous studies, the wave-function and the excitation (or stripping) efficiency $|C_2|^2$ can be found by solving the time-dependant Schrodinger equation:

$$i\hbar\dot{\Psi} = (\hat{H}_0 + \hat{V}_{laser})\Psi \qquad (5)$$

This equation represents the dynamic of an electron in a proton field H_0 with an external laser field V_{laser}.

For the sake of simplicity, using atomic units and eliminating derivations, the main equations for laser-H^0 interaction in the particle's rest frame are expressed thusly:

$$\begin{aligned} \dot{C_1} &= i\mu\frac{E(t)}{2}e^{-i\omega_0 t}C_2 \\ \dot{C_2} &= i\mu\frac{E(t)}{2}e^{+i\omega_0 t}C_1 \end{aligned} \qquad (6)$$

The electric component of the femtosecond laser pulse is written in a complex form with the Gaussian profile:

$$E(t) = E_0 e^{-\frac{t^2}{4\sigma^2}+i\omega t} \qquad (7)$$

The parameters of the laser electric field component E_0, its frequency ω, and the pulse width σ must be transformed from the laboratory frame to the particle's rest frame using relativistic transformations. This section discusses equation (6) in detail and presents a quantitative explanation of how the short laser pulse would achieve high efficiency excitation of the whole bunch.

The H^0 particle remains in the ground (non-excited) state before interaction $C_1(-\infty) = 1$, $C_2(-\infty) = 0$ and transitions to the atomic state $C_2(\infty)$ after interaction with the laser. Consequently, it is convenient to reassign the time variable, as it is not needed for $C_2(\infty)$:

$$\begin{aligned} \dot{C_1} &= i\mu\sigma\frac{E_0}{2}e^{-i\sigma\Delta\omega t-\frac{t^2}{4}}C_2 \\ \dot{C_2} &= i\mu\sigma\frac{E_0}{2}e^{+i\sigma\Delta\omega t-\frac{t^2}{4}}C_1 \end{aligned} \qquad (8)$$

where $\Delta\omega = \omega_0 - \omega$ is an off-resonant term. The equation (8) may be solved analytically for the particle with the exact resonance condition $\omega_0 = \omega$ and the excitation probability may be written as:

$$|C_2(\infty)|^2 = \sin(\sqrt{\pi}\mu\sigma E_0)^2 \qquad (9)$$

The particle may be excited to 100% only by particular laser peak power: $\sqrt{\pi}\mu\sigma E_0 = \pi/2$. The excitation condition (9) used in this study is a nonlinear, relatively high laser power and cannot be obtained by a cross section method. The laser peak power with amplitude of its electric component $E_0 = \sqrt{\pi}/(2\mu\sigma)$ is the nominal power for excitation of a design particle and will be used throughout this paper. Equation (8) is difficult to solve analytically for $\Delta\omega \neq 0$; however, it may be solved approximately for small $\Delta\omega$, similar to the perturbation method in quantum mechanics. Equation (8) may be written as

$$\begin{pmatrix} \dot{C_1} \\ \dot{C_2} \end{pmatrix} = A(t,\Delta\omega)\begin{pmatrix} C_1 \\ C_2 \end{pmatrix} \qquad (10)$$

and may be solved exactly for $\Delta\omega=0$, which may be considered as zero approximation $C_{10}(t)$, $C_{20}(t)$. First-order approximation may be found from the equation:

$$\begin{pmatrix} \dot{C_1} \\ \dot{C_2} \end{pmatrix} = A(t,\Delta\omega)\begin{pmatrix} C_{10}(t) \\ C_{20}(t) \end{pmatrix} \qquad (11)$$

where the excitation probability $|C_2|^2$ may be expressed in the following way:

$$|C_2|^2 = \left| i\mu\sigma\frac{E_0}{2}\int_{-\infty}^{\infty} e^{+i\sigma\Delta\omega t-\frac{t^2}{4}}C_{10}(t)\,dt \right|^2 \qquad (12)$$

Solution of (12) is beyond the scope of this paper.

Equation (8) visually demonstrates (without solving) that a short laser pulse may compensate off-resonant particles. An increased longitudinal momentum spread δp results in an increased resonant spread $\delta\omega_0$, which can be compensated by a smaller laser pulse width σ to make the excitation probability close to 1. The power of the laser pulse Q, which is proportional to $P_0\sigma$ where P_0 is a peak

ISBN 978-3-95450-185-4

power, may be represented as a function of laser pulse width σ and $\delta\omega_0$, taking into account condition (9):

$$Q \sim \sigma P_0 \sim \sigma E_0^2 \sim \frac{1}{\sigma} \sim \delta\omega_0 \sim \delta p_z \qquad (13)$$

This relation shows that increased momentum spread requires increased laser power.

THREE PARTICLES CALCULATION

This section presents an example of the interaction of a femtosecond laser pulse with three H^0 particles of different parameters of longitudinal momentum: p, p+Δp, and p+2Δp. Parameter $\Delta p=10^{-4}p$ corresponds to a realistic parameter of longitudinal momentum spread taken from the SNS accelerator. The laser pulse is considered as a round Gaussian beam with a transverse RMS size of 1 mm and wavelength of 1064 nm. The energy of the design particle is calculated to be 3.22GeV for excitation to the second excited state. Figures 2, 3, and 4 represent the dynamics of excited states $|C_2|^2$ in the particle's rest frame for various laser pulse widths.

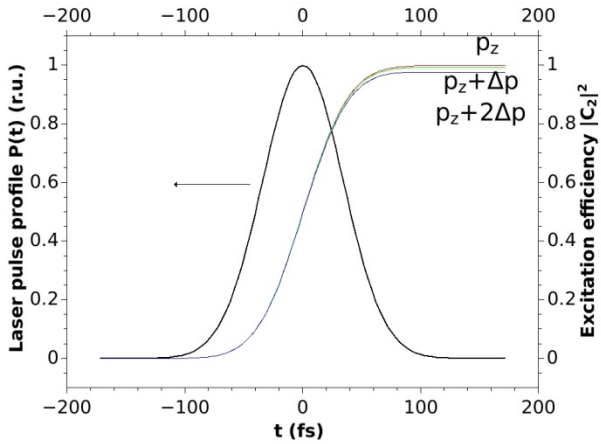

Figure 2: Excitation of three particles by the 300fs and 10 μJ laser pulse in the particle's rest frame. All particles with momentum p, p+Δp, and p+2Δp are excited.

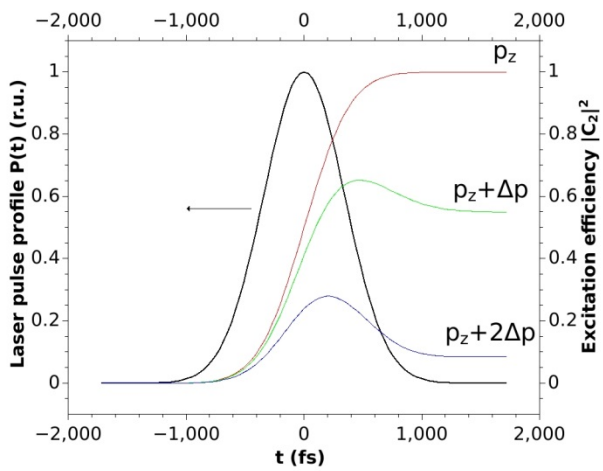

Figure 3: Excitation of three particles by the 3000fs (or 3ps) and 1.0 μJ laser pulse in the particle's rest frame.

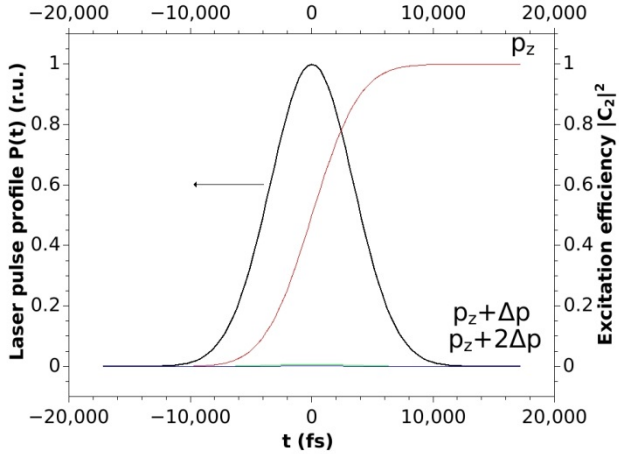

Figure 4: Excitation of three particles by the 30000fs (or 30ps) and 0.1 μJ laser pulse in the particle's rest frame. Off-resonance particles with momentum p+Δp, and p+2Δp are not excited.

The laser pulse energy is calculated for 100% excitation of the design particle with momentum p. It should be noted that the laser pulse width in the particle's rest frame shown in the figures is smaller than nominal width in the laboratory frame by factor of γ(1+β). The figures demonstrate that a femtosecond laser pulse of about 300fs can excite all particles within the given longitudinal momentum spread. Realistic beam excitation efficiency may be calculated by integration over beam distribution *f(p,r)*:

$$\int_{-\infty}^{\infty} |C_2(p_z,r)|^2 f(p_z,r) 2\pi r dr dp_z \qquad (14)$$

however, the result will be close to the three particle estimate.

Table 1 shows possible variants of laser wavelength, laser power, H^0 excitation state, and H^0 beam energy. The laser pulse width is 300fs.

Table 1. Parameters of H^0 and Laser Pulse

Laser wavelength	Laser pulse energy	H^0 beam energy	H^0 excitation state
1064 nm	10 μJ	3.22 GeV	2
1064 nm	61 μJ	3.97 GeV	3
1064 nm	175 μJ	4.24 GeV	4
800 nm	10 μJ	2.22 GeV	2
800 nm	61 μJ	2.78 GeV	3
800 nm	175 μJ	2.98 GeV	4

This table shows an estimate of the minimum laser pulse energy 10 μJ required for stripping the second excited state. The second excited state with a beam energy of 3.22 GeV may be easily stripped by a regular (non-superconducting) magnet. The estimated femtosecond

ISBN 978-3-95450-185-4

laser pulse width and energy may be achieved with existing femtosecond laser technology [6].

The experimental scheme of this method appears complicated due to the head-on interaction of the femtosecond laser and the H^- beam. This is not discussed in this paper and requires further investigation.

SUMMARY

- A femtosecond laser pulse may be used for high efficiency stripping of a realistic beam with longitudinal momentum spread.
- An increased longitudinal beam spread would require more average laser beam power.
- Femtosecond laser stripping may be applied only to a few discrete H^- beam energies.
- Estimated required laser parameters appear achievable with current femtosecond laser technology.
- Femtosecond laser stripping scheme for real accelerator is not developed and requires additional investigation.

ACKNOWLEDGMENTS

The author acknowledges H. Kapteyn for his valuable and educational communication about existing femtosecond laser technology.

This work has been supported by Oak Ridge National Laboratory, managed by UT-Battelle, LLC, under contract DE-AC05-00OR22725 for the U.S. Department of Energy.

REFERENCES

[1] V. Danilov et al., "Three step H^- charge exchange injection with a narrow-band laser", *Phys. Rev. ST. Accel. Beams*, vol. 6, p. 094202, May 6, 2003.

[2] V. Danilov et al., "Proof-of-principle demonstration of high-efficiency laser-assisted H^- beam conversion to protons", *Phys. Rev. ST. Accel. Beams*, vol. 10, p. 053501, May 2, 2006.

[3] S. Cousineau et al., "First results of laser-assisted H^- stripping of a 10us, 1 GeV beam at the SNS accelerator", presented at the 57th ICFA beam dynamics workshop on high-intensity and high-brightness hadron beams (HB2016), Malmo, Sweden, July 2016, paper TUP8MX01, *this conference*.

[4] I. Yamane, T. Suzuki, and T. Takayama, "Laser stripping via a broad Stark state for a high intensity proton ring", cern, Geneva, KEK Report, No. 2002-76, 2002.

[5] T. Gorlov, V. Danilov, and A. Shishlo, "Effective calculation of laser stripping via a broad shape resonance", *Phys. Rev. ST. Accel. Beams*, vol. 13, p. 050101, July 23, 2010.

[6] H. Kapteyn et al. "Ultrafast lasers for demanding applications: State of the art and ongoing prospects", 3rd mini workshop on H^- laser stripping and accelerator applications, Fermilab, IL, September 2013.

ISBN 978-3-95450-185-4

EFFECT OF BEAM LOSSES ON WIRE SCANNER SCINTILLATOR READOUT, HYPOTHESIS AND PRELIMINARY RESULTS

B. Cheymol*, European Spallation Source, Lund, Sweden

Abstract

In an hadron accelerator, the characterization of the beam transverse halo can lead to a better understanding of the beam dynamics and a reduction of the beam losses. Unfortunately the effect of losses on beam instrumentation implies a reduction of the instrument sensitivity due to the background noise.

In this paper, we will discuss the effect of losses on the wire scanner scintillator foreseen for the ESS linac, in particular the different hypothesis for the input will be describes and preliminary results will be present.

INTRODUCTION

In the elliptical sections of the ESS linac [1] the Wire Scanner (WS) station will be equipped with scintillators to measure the hadronic shower created by a thin tungsten wire [2]. One of the main reasons is that above 200 MeV the secondary emission signal is not strong enough to measure directly the current produced in the wire, the signal from a scintillator will be stronger and also cleaner, but this detector will be also sensitive to radiation induced by beam losses. Preliminary simulations have been performed to check this effect and define beam loss limits for the WS operation.

Several beam losses scenario have been simulated with the Monte Carlo (MC) code FLUKA [3] in order to estimate the influence of losses on the beam profile measurement. Note that all the particles distributions presented in this paper are not the results of beam dynamic simulations.

HYPOTHESIS AND INPUT PARAMETERS

Hypothesis

To simplify the problem, we propose to study the effect of various beam losses scenario in a single elliptical period (one elliptical cryomodule followed by one quadrupole doublet). It was assumed, in a first approximation, that the contribution from upstream or downstream losses will be either too low to be detected or easily removed in the data analysis.

A simplified geometry of an elliptical cryomodule has been implemented in the MC code, only the main components have been simulated, all the cryogenic pipe, cable, RF guide have not been implemented in the simulated geometry. Despite the fact that the Medium and High β cavities are slightly different, the geometry is independent of the beam energy, a 5 cells cavity has been chosen for this study, which the one foreseen to be installed in the High β section for beam energy above 570 MeV, the length of the cryomodule is about 6.5 meters. The quadruples consists in a single volume of copper. The author would like to emphasis that no electromagnetic field has been implemented in the simulations.

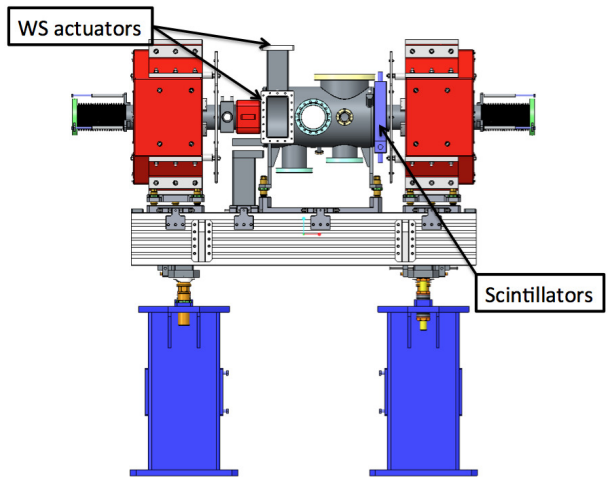

Figure 1: Preliminary design of the elliptical LWU, the length flange to flange is 1920 mm (courtesy of STFC Daresbury Laboratory).

The Linac Warm Unit (LWU) chamber has been simulated (see Fig. 1), the scintillator are attached to this chamber, the detector assembly is shown in Fig. 2. The minimum aperture in the LWU is 100 mm.

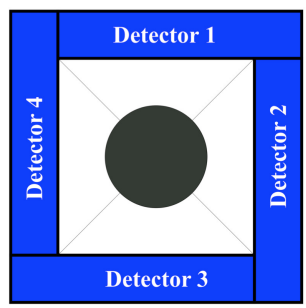

Figure 2: Detector assembly for the ESS WS system.

The scintillator material in these simulations are not the one foreseen to be used for the ESS WS system, in preliminary design phase of the WS detector BGO crystal was the primary candidate for the scintillator and all the simulations presented in this paper have been performed with this type of scintillator. nevertheless, since the geometry is identical, the signal to noise ratio shall be comparable for both versions of the detector.

For this simulations and in a first approximation, the beam sizes of the core were assumed to be constant in the cold linac with $\sigma_x = \sigma_y = 2$ mm. The beam has no energy spread.

* benjamin.cheymol@esss.se

ISBN 978-3-95450-185-4

Beam Distributions for the Simulations

Full beam loss In order to get a overall vision of beam loss effect on scintillators, a series of simulations have been performed with a pencil beam interacting with the beam pipe in the middles of quadrupoles. Simulations have been performed at 2 positions, in the middle of the upstream quadrupole and in the middle of the downstream quadrupole with respect of the detector position (see Fig. 1). The angle of impact was varying from 1 to 250 mrad and the beam energy from 200 to 2000 MeV.

A second series of simulations were done in order to check the effect of unwanted steering of the beam. The beams were created at the beginning of the cell at the center of beam pipe, an angular kick of 6 mrad and 10 mrad was given to the particles in order to have the interaction point of the beam center with the beam pipe in the center of the quadrupole and in the center of the cryomodule. the beam energy was varying from 200 to 2000 MeV. For this cases, only the beam core has been simulated

For all the losses simulated, the beam impacts on the upper quadrant of the beam pipe.

Halo During the operation of the WS system, the background noise will be mainly generated by losses due to particles lost from the beam halo (only the transverse halo has been considered in this study). In order to decrease the time of the MC simulations and have a good statistic, hollow beams have been simulated with a minimum radius of 10 mm. The origin of the beam is set at 100 mm upstream to the cryomodule entrance.

The beam halo distributions are difficult to predict, several distributions have been considered in order to explore a large range of possibilities from a fully unmatched beam to almost perfect matching of the beam to the lattice. The distributions are identical in both planes.

In the worst case scenario, the particles will fill all the geometrical acceptance the cold linac, in a first approximation, the influence of the beam energy on the particle distribution in the phase space has been neglected. In real space, the particles were generated in ring with a minimum radius of 10 mm and a maximum radius of 45 mm with a uniform density , the particles divergence was set to ± 7.5 mrad and to $\sigma_{x'}$=6 mrad, these values corresponds to twice the geometrical acceptance of an elliptical section period, beam energy was scan form 200 MeV to 2000 MeV.

Similar simulations have been performed with different cut in the real space (15 σ and 10 σ of the beam core), with a distribution of the particle divergence equal to ± 6 mrad and ± 4mrad, all distributions have been considered uniform.

Based on the work presented in [4], several beam distributions were generated to simulate intermediate cases between a "fully filamented" beam presented above and an ideal beam "matched" to the structure. Beam sizes were assumed to be independent of the beam energy, as well as the distribution of the halo in the real space, while, in order to simulate the effect of the acceleration, the divergence of the particles decreases with the beam energy. Uniform and gaussian distributions have been simulated, for gaussian distribution we assumed that the halo has an rms of 4 times the rms of the beam core (i.e 8 mm). Several cute has been simulated (20 σ,15 σ and 10 σ of the beam core), and i In the simulations. The beam halo divergence is increased by at least a factor 2 compare to the ideal beam in case of a gaussian distribution, for the flat distribution, the maximum divergence is ≈ 6 times the rms value of the ideal beam divergence. In addition, a smaller divergence has been simulated with an increase of few tens of percent compare to the distributions presented in [4], to simulate an optimal case with reduces losses. The evolutions of the divergence as function of the beam energy is shown in Fig. 3.

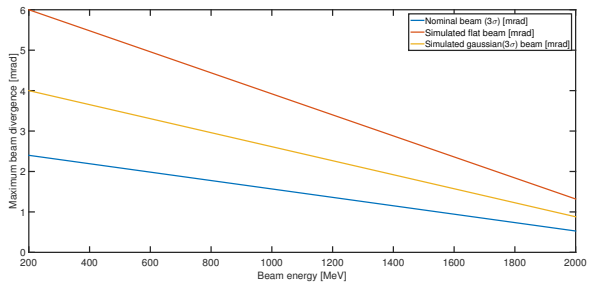

Figure 3: Maximum simulated divergence as function of the beam energy. In the document, the red curve is refereed to "flat", the yellow curve to "gauss high" and the blue one to "gauss low".

The parameters of the various simulated distribution are summarized in Tab. 1 and Tab. 2, in the next sections of this paper, the distribution will be referenced by the name presented in the table.

Table 1: Summary of the beam distribution simulated when they are independent of the beam energy. Extension in real space are given in term of σ of the beam core

	Extension	
Name	real space	divergence
"fil. uniform"	22.5σ uniform	± 7.5 mrad uniform
"fil. gauss"	22.5σ uniform	$\sigma_{x'}$ (1 rms) = 6 mrad
"15 6"	15σ uniform	± 6 mrad uniform
"15 4"	15σ uniform	± 4mrad uniform
"10 6"	10σ uniform	± 6 mrad uniform
"10 4"	10σ uniform	± 4mrad uniform

As example, the particles distribution in the phase space for two the extreme cases are shown in Figs. 4 and 5.

PRELIMINARY RESULTS

Full Beam Loss

As shown in Fig. 6 to Fig. 8, the energy deposited in the detector 1 is strongly dependent of the losses angle, and less on the beam energy. Compare to the scintillator signal (less

ISBN 978-3-95450-185-4

Table 2: Summary of the beam distribution simulated, extension in real space are given in term of σ of the beam core type, the divergence can be seen in Fig. 3

	Extension	
Name	real space	divergence
"20sig."	20σ uniform	flat
"15sig. flat"	15σ uniform	flat
"15sig. gauss"	15σ gauss	gauss high
"10sig. flat"	10σ uniform	flat
"10sig. gauss"	10σ uniform	gauss high
"Nominal"	10σ flat	gauss low

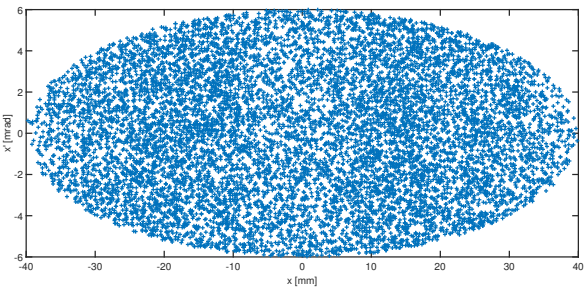

Figure 4: Distribution of the particles in the phase space for the "20sig." case (beam energy is 200 MeV) .

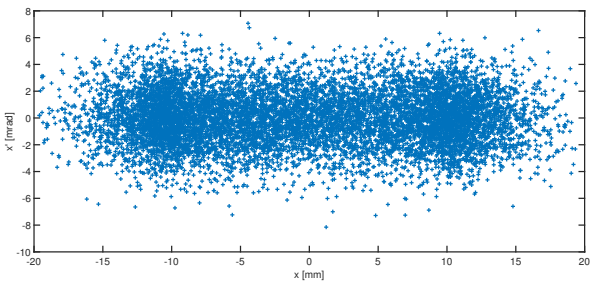

Figure 5: Distribution of the particles in the phase space for the "10sig. gauss" case (beam energy is 200 MeV).

than 1 keV per primary), in all the cases the beam loss signal on the detector will be much higher than the expected signal during a profile measurement.

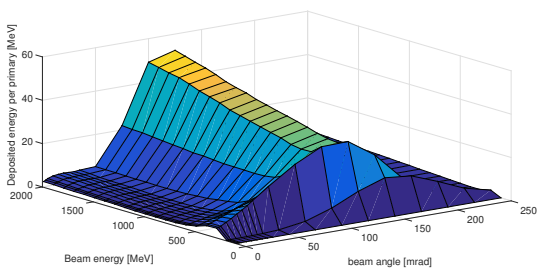

Figure 6: Estimated energy deposited in detector 1 as function of the beam energy and angle of impact. The loss is in middle of the upstream quadrupole.

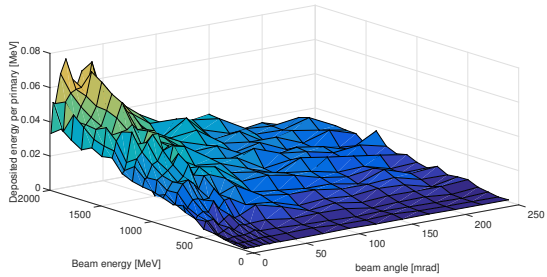

Figure 7: Estimated energy deposited in detector 1 as function of the beam energy and angle of impact. The loss is in middle of the downstream quadrupole.

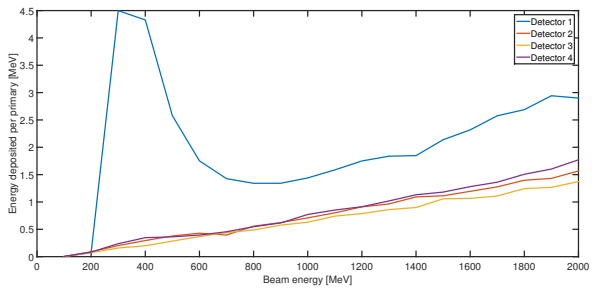

Figure 8: Evolution of the deposited energy as function of the beam energy on the 4 detectors, the beam impacts in the upstream quadrupole with an angle of 3 mrad.

From these results, it seems possible to detect the position of a losses, also detect the direction of the loss, a clear difference on the signal of each detector can be detected (see Fig. 8).

For the cases of unwanted beam steering, like the previous results, the WS acquisition will be fully saturated as shown in Figs. 9 and 10.

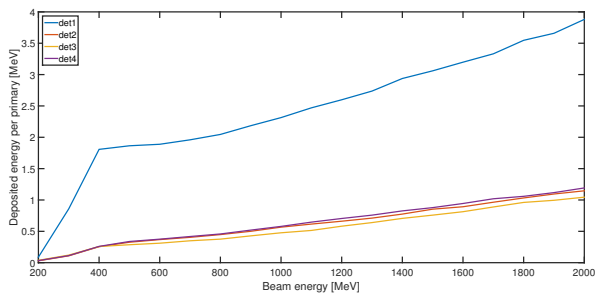

Figure 9: Evolution of the energy deposited in each scintillator as function of the beam energy, the impact is in the middle of the upstream quadrupole corresponding to an angular kick of 6 mrad.

For the 6 mrad case, it is interesting to note that the loss direction can be detected and the signal on the detector 1 increase rapidly below 400 MeV and slowly above and up to 2 GeV. This can be explain by the cinematic of the reaction ad the detector geometry, the signal on the scintillator is dominated by the energy deposition induced by protons.

ISBN 978-3-95450-185-4

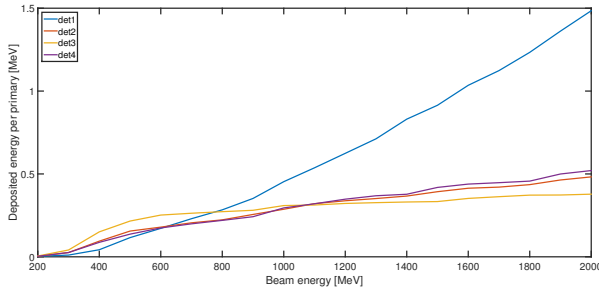

Figure 10: Evolution of the energy deposited in each scintillator as function of the beam energy, the impact is in the middle of the upstream cryomodule corresponding to an angular kick of 10 mrad.

Below 400 MeV, more than 80 % of the signal is generated by protons, above this energy, the protons are emitted in a cone which becomes smaller when the beam energy increases, as consequence a smaller portion of this particle interacts with the scintillator and their contribution to the signal decreases. Nevertheless, the production of secondaries particles increases with the energy and therefor increase the signal, at 2 GeV, 50 % of the signal is induced by the secondaries particles.

The signal on the other detectors increase almost linearly with the beam energy.

For a beam impacts in the middle of the cryomodule, at low energy the signal on all the detectors are more or less equal, the direction of the loss can be detected only at high energy. In this case, the beam and the product of the induced shower interact with more matter than in the previous case, due to this interaction, at low energy the flux of particles will be almost uniform at the scintillator location, while as the energy increases, the beam interacts less an less with the matter leading to a rapid increase of signal of the detector positioned in the same quadrant of the loss.

Halo

For a given distribution and a given beam energy, as shown in Fig. 11 the signal on the 4 detectors is almost identical, thus all the following results are presented for a single detector.

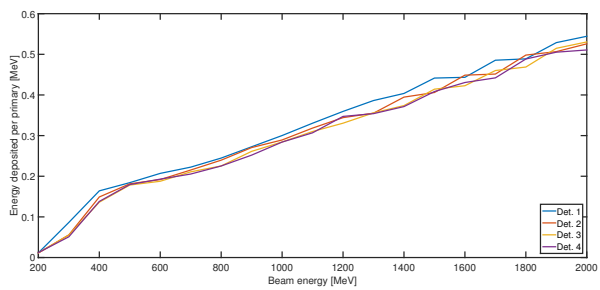

Figure 11: Evolution of the energy deposited in each scintillator as function of the beam energy, for the beam distribution "fil. uniform"

Energy deposition With the same particle distribution for the energies considered, the energy deposited in the detector increases with the beam energy (see Fig. 12). it also appears clearly that the beam divergence has a strong impact on the losses, more important than the extension in the real space.

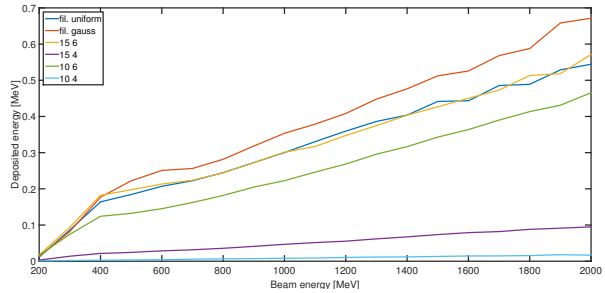

Figure 12: Evolution of the energy deposited in one scintillator as function of the beam energy, the distributions in this figure are independent of the beam energy.

The same influence of the beam halo divergence can be seen when the influence of the acceleration has been simulated (see Fig. 13).

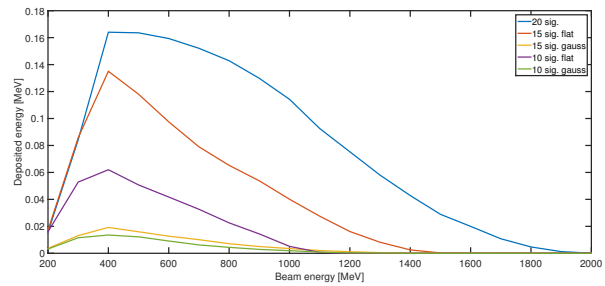

Figure 13: Evolution of the energy deposited in one scintillator as function of the beam energy, beam halo divergence is decreasing with the energy .

In all the cases, the peak energy deposition is around 400 MeV. Above this energy, the signal decreases with the beam energy, due to the smaller divergence, at the exception of the biggest beam the signal is almost zero above 1500 MeV, nevertheless due to the small statistic in the MC simulations and of the cut in the particle distribution, some losses are expected in the high energy range of the ESS linac, It appears that the losses might be an issue between 200 and 600 MeV, which corresponds to the ESS medium β section energy range. The influence of the beam divergence is important, with a lower divergence ("nominal" beam in Fig. 3) the energy deposited is almost null above 300 MeV.

Due to the simplified geometry and the low statistic present in the simulation, the peak at 400 MeV might be artifact of the MC simulations, depending on the amount of matter that the loss particles will see this peak might slightly move. These data are certainly not a representative of the losses expected in the ESS linac, nevertheless, they can be used to set the operating domain of the WS.

ISBN 978-3-95450-185-4

Signal The previous results were uses to estimate the Signal to Noise Ration (SNR) expected during a beam profile measurement. The expected peak signal from the WS as been simulated with the same geometry and assuming a 40 μm tungsten wire. The minimum signal is expected for a beam energy of 400 MeV, the maximum signal at 2000 MEV. In post processing and with the date presented in the previous section, the background signal has been estimated for various proportion of particles in the halo and the expected Signal to Noise Ration (SNR) during a beam profile measurement has been calculated for the lowest expected signal (400 MeV). The results are summarized in Figs. 14 and 15.

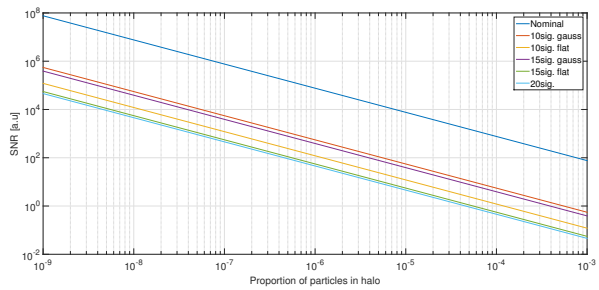

Figure 14: Expected SNR at 400 MeV for beam halo distribution independent of the beam energy.

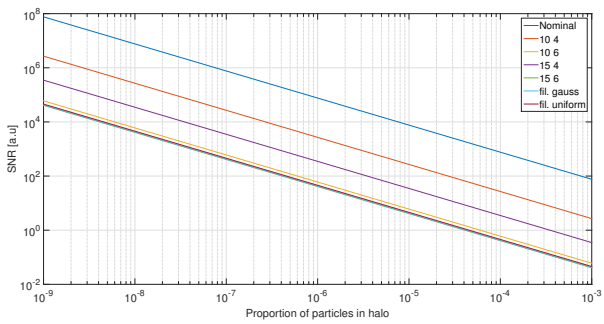

Figure 15: Expected SNR at 400 MeV for beam halo distribution dependent of the beam energy.

In all cases, if the 10^{-9} of the particles are in the halo as simulated in the MC code, the SNR is better than 10^4, if this proportion increase to 10^{-6} the SNR will be $\approx$ 100 in the worst case and up to 10^{-5} in the best case simulated. At High energy, for the cases with a divergence decreasing with the beam energy, the SNR increases. The reconstruction of the beam profile might be compromised if the losses in the ESS superconducting linac is too high.

CONCLUSION AND PERSPECTIVE

The studies presented in this paper might be far from what will be observed in the ESS linac, the low statistic in the MC simulations as well as the arbitrary beam distributions induced certainly large uncertainty on the results. Nevertheless, the two extreme cases presented in Figs. 14 and 15 are setting the limits for the expected beam losses.

These preliminary studies show that the WS detectors are quite sensitive to beam losses, the performance of the WS might suffer if the losses exceed 10^{-6} and if the halo is not mitigate.The detector concept proposed for the ESS wire scanner shows an interesting sensitivity to the beam halo parameters. In high power hadron linac, matching the halo seems a better alternative to the classical core matching in order to reduce the beam losses toe an acceptable level [5], the detector part of the WS system might be used not only to measure the beam core profile but also, together with other monitors like the Beam Loss Monitor [6], to match the beam halo.

In order to confirm the ability of the WS system to be used for the halo matching, the particles distributions used for the simulation must be refined with dedicated beam dynamic simulations. More accurate MC simulations are as well needed, in particular, the effect of losses over few period need to be simulated. The electromagnetic field of the quadrupoles and the cavities might affect the beam loss pattern, and therefore must be studied.

REFERENCES

[1] M. Eshraqi et al.,"The ESS linac", in *Proc. IPAC '14*, Dresden, Germany, THPME043.

[2] B. Cheymol, "Scintillator detectors for the ESS high energy wire scanner" in *Proc. HB'16*, Malmo, Sweden.

[3] A. Ferrari, P.R. Sala, A. Fasso, and J. Ranft, "FLUKA: a multi-particle transport code" CERN-2005-10 (2005), INFN/TC_05/11, SLAC-R-773.

[4] R. Miyamoto., "An ESS linac collimation study", in *Proc. HB'14*, East-Lansing, MI, USA.

[5] N. Chauvin et al., "Halo Matching for High Intensity Linacs and Dedicated Diagnostics", in *Proc. HB'14*, East-Lansing, MI, USA.

[6] I. Dolenc Kittelmann, "Simulations and Detector Technologies for the Beam Loss Monitoring System at the ESS Linac" in *Proc. HB'16*, Malmo, Sweden.

ISBN 978-3-95450-185-4

EFFECTS OF ENERGY DEPOSITION MODELS AND CONDUCTIVE COOLING ON WIRE SCANNER THERMAL LOAD, ANALYTICAL AND FINITE ELEMENT ANALYSIS APPROACH

B. Cheymol*, European Spallation Source, Lund, Sweden

INTRODUCTION

A number of wire scanners will be installed in the ESS linac [1] to measure beam profile and perform emittance measurement with a 3-gradients type method. The ESS wire scanner will be equipped with 33 µm for carbon wire in the warm linac and a 40 µm for tungsten wire in the cold linac.

Due to the high power on the beam, the duty cycle has to be reduced to allow the insertion of interceptive devices, preliminary estimations of the wire thermal load [2] show that the wire can withstand the 2 dedicated modes:

- A slow tuning mode (i.e. 50 µs, up to 62.5 mA, 1 Hz).
- A fast tuning mode (i.e. 10 µs, up to 62.5 mA, 14 Hz).

The temperatures have been estimated with a simple analytical model assuming no conductivity effect, the energy deposited in the wire has been estimated with the stopping power extracted from table and assuming a constant thickness of the wire equal to its diameter, this paper proposes to update the estimation of the wire temperature with different model for the energy deposition and to compare the results of the analytical model to the results of a Finite Element (FE) analysis. In all the document, the beam intensity is equal to 65 mA.

ANALYTICAL MODEL PARAMETERS

The thermal load on wire induced by the beam could in the worst case damage the wire. Given a linac pulse, populated by N_{part} particles with RMS transverse beam sizes σ_x and σ_y, traversing a wire, the induced temperature can be calculated as:

$$\Delta T = \frac{N_{part}}{\rho Cp(T)V}\frac{\Delta E}{2\pi\sigma_x\sigma_y}e^{-(\frac{x^2}{2\sigma_x^2}+\frac{y^2}{2\sigma_y^2})} \quad (1)$$

Where $Cp(T)$ is the specific heat capacity of the material of the wire, ρ is the wire material density and V volume of the wire and ΔE the energy deposited in the wire per particle.

Wire Material Properties

An analytical model of the specific heat capacity of the carbon and of the tungsten has been used for the estimation of the temperature, data can be found in [3] and [4]. The density of the materials (respectively 1.8 g·cm^{-3} for carbon and 19.25 g·cm^{-3} for tungsten) as well as the emissivity (0.8 for carbon and 0.1 for tungsten) a were assumed to be independent of the temperature in a first approximation.

* benjamin.cheymol@esss.se

Cooling Process

In first approximation, the conductive cooling is negligible, thus it is assumed that the wire cooling is dominated by black body radiation, described by Stefan-Boltzmann law. The heat radiated from the wire surface is proportional to the fourth power of the temperature. The difference from the ideal black-body radiation is described by a factor called emissivity and the radiated power is given by :

$$P = \sigma\varepsilon A(T^4 - T_0^4) \quad (2)$$

Where σ is the Stefan-Boltzmann constant, ε the emissivity, A the area of the body, T its temperature and T_0 the ambient temperature (set in all the studies presented in the document at 298 K). After a linac pulse the temperature variation can be calculated as:

$$\frac{dT}{dt} = \frac{\sigma\varepsilon A(T^4 - T_0^4)}{\rho Cp(T)V} \quad (3)$$

Other processes like thermoionic emission or wire sublimation are more efficient at high temperature, nevertheless for the ESS wire scanners and in general for wire scanners (or SEM grid) use at low energy beam, the thermoionic emission will perturb the signal from secondary emission. The wire temperature shall be kept below 2000 K to avoid this effect, thus these processes are neglected in this note.

Energy Deposition Models

IThe energy deposited per particle has been estimated with the stopping power extracted from tables and the length of interaction assuming a constant stopping power across the wire diameter. For low beam energy, the stopping power increases when the particles move into the wire material. Assuming a constant stopping power, calculated for the incident beam energy leads to underestimation of the deposited energy.

For simplification, in the analytical model, the energy deposited by each particle crossing the wire is identical. This assumption leads to error due to the cylindrical geometry of the wire if the wire diameter is taken as interaction length. To reduce this error, an equivalent thickness of the wire can be calculated as:

$$e_{equ.} = \frac{\pi d}{4} \quad , \quad (4)$$

where d is the wire diameter.

The equivalent thickness of the wire is reduced by ≈ 25 % compared to the wire diameter, the energy deposition is

ISBN 978-3-95450-185-4

reduced by the same fraction, both calculations of the deposited energy have been used for the estimation of the wire temperature.

The energy deposited per particle in the wire has been also estimated with the Monte Carlo code FLUKA [5], for beam energies from few MeVs to 2 GeV. The results is normalized by primary in the simulations and allows a direct comparison with the previous method.

The comparisons between the models are shown in Fig. 1 and Fig. 2 for both wire considered in the ESS linac, the energy deposited calculated for interaction length equal to the wire diameter is taken as a reference.

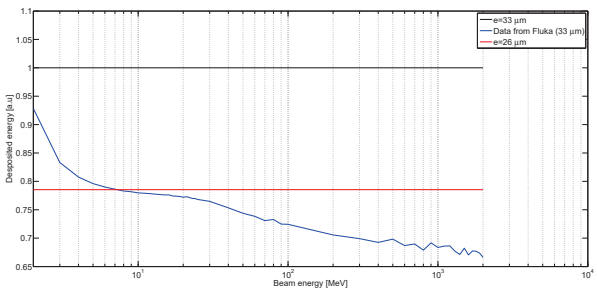

Figure 1: Normalized energy deposition on a 33 µm carbon wire as function of the beam energy estimated with stopping power table (black and red curve) and by a Monte Carlo code (blue curve).

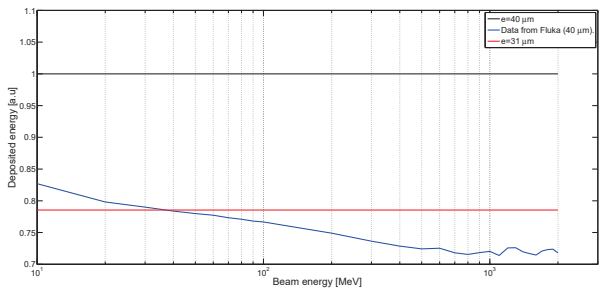

Figure 2: Normalized energy deposition on a 40 µm tungsten wire as function of the beam energy estimated with stopping power table (black and red curve) and by a Monte Carlo code (blue curve).

Compared to the reference, the estimation of the energy deposited with an equivalent thickness is almost 25 % lower. At low energy, the results form the Monte Carlo code is higher than the results of estimation with the tables, this is mainly due to the assumption of a constant stopping power. For the high energies, the results from the Monte Carlo simulations show a reduction of the deposited energy of almost 35 % for a carbon wire and almost 30 % for a tungsten wire compare to the reference. Due to the limitations of the code, the energy deposited might be even lower. FLUKA is not able to track electrons below 1 keV, thus, a the low energy tail of $\delta-rays$ spectra might be counted in the energy deposition while in reality some of them will escape the wire and not contribute to the thermal load.

ESTIMATION OF THE TEMPERATURE WITH THE ANALYTICAL MODEL

The wire temperature has been estimated using an analytical model and for the 3 energy deposition models for the higher thermal load in the ESS linac, for carbon wire, the worst case is the first wire scanner in MEBT (E_{beam} = 3.63 MeV, σ_x = 1.85 mm, σ_y = 1.45 mm) and for tungsten wire, the worst case is the WS installed in the LEDP (E_{beam} = 90 MeV, σ_x = 2.6 mm, σ_y = 1.8 mm).

All simulations have been performed assuming a pulse length of 100 µs at a repetition rate of 1 Hz. The temperature on the wire has been calculated for 10 consecutive pulses, with the wire centered in the beam. The results are presented in Fig. 3 to Fig. 4.

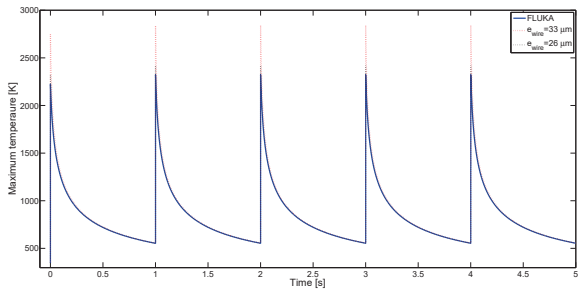

Figure 3: Peak temperature evolution as function of the energy deposited for a wire scanner in the MEBT, beam pulse is 100 µs (33 µm carbon wire).

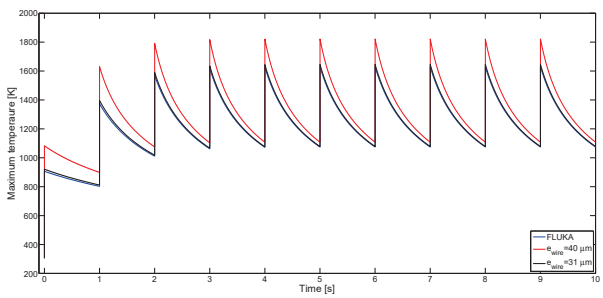

Figure 4: Peak temperature evolution as function of the energy deposited for a wire scanner installed in the LEDP, beam energy is 90 MeV (40 µm tungsten wire).

Up to 90 MeV beam, for all wire considered, the difference between the results given by the Monte Carlo code and the analytical model using an equivalent thickness are negligible. At higher energy the difference between the models appears more clearly, the difference is about 50 K between FLUKA and the equivalent thickness. Considering the full wire diameter lead to an error about 500 K in the worst case and about 100 K for the 2 GeV case (see Fig. 5).

COMPARISON WITH FINITE ELEMENT ANALYSIS

In the analytical model, the conduction is neglected, this might be a good assumption for a carbon wire due to the

ISBN 978-3-95450-185-4

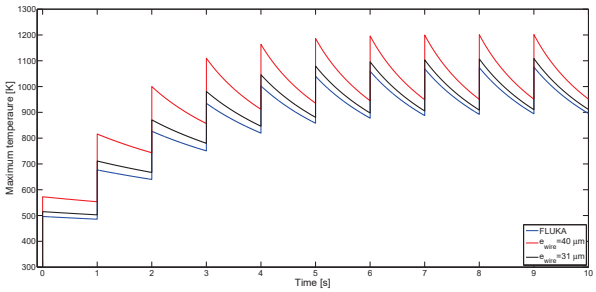

Figure 5: Peak temperature evolution as function of the energy deposited for a wire scanner installed at the linac end, beam energy is 2000 MeV, beam sizes are equal to 2 mm in both planes (20 µm tungsten wire)

high emissivity of the material, but for a tungsten wire, the emissivity is almost an order magnitude lower and its thermal conductivity is higher, the conduction might not be negligible and can be the main contributor of the cooling process.

In order to estimate the influence of thermal conductivity on the wire temperature, it has been decided to perform a series of simulation with the Finite Element code ANSYS®.

Finite Element Model

From the energy deposition estimated with the Monte Carlo code FLUKA, a 3D map of the heat generation (in $W \cdot m^{-3}$) has been generated for different beam energies, beam sizes and wire type. Then, these maps have used as an input in ANSYS to calculate the wire temperature. The exact wire properties are not know, the ANSYS model has been fed with the properties of pure tungsten (data can be found at [4]) and the properties of the R4550 graphite. The emissivity of these two material was assumed to be constant. The temperature at the wire ends has been fixed in the model to 298 K, the ambient temperature is set at the same value.

Carbon Wire

The beam parameters used to generate the 3D maps are shown in Table 1, the parameters have been chosen in order to have a case with a maximum temperature around 2000 K and one case with a maximum temperature equal to approximately 700 K without stopping power gradient along the beam path. The maximum temperature evolutions for both cases and for the analytical and FE models are shown in Fig. 6 and Fig. 7.

Table 1: Beam Parameters Used to Generate the 3D Heat Generation Maps for the 33 µm Carbon Wire.

Energy [MeV]	σ_x [mm]	σ_y [mm]
20	1	1
200	1	1

For the 20 MeV case, the agreement between the 2 models is good, the temperature after the first pulse is approximately the same (1695 K for the analytical model and 1665 K for the

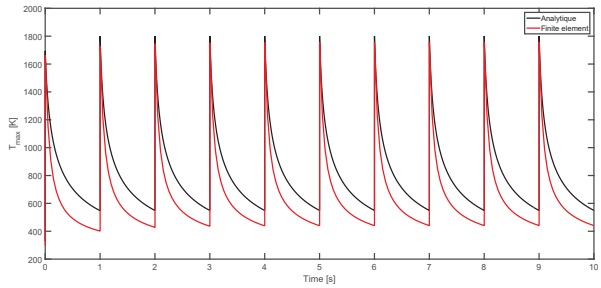

Figure 6: Evolution of the peak temperature estimated with an analytical model (blue curve) and a FE model (red curve), the beam energy is 20 MeV (33 µm carbon wire).

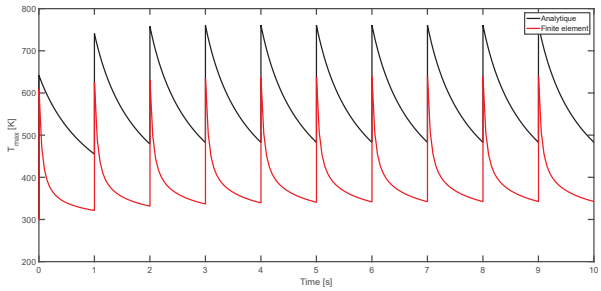

Figure 7: Evolution of the peak temperature estimated with an analytical model (black curve) and a FE model (red curve), the beam energy is 200 MeV (33 µm carbon wire).

FE model). The cooling is more efficient in the FE model, after the first period of cooling, the temperature is 547 K in the analytical model and 401 K in the FE model. The maximum temperature over the 10 pulses are also similar (1801 K in the analytical model and 1756 K in the FE model), the error between the models is approximately 3 %.

For the 200 MeV case, if the temperature after the first pulse is similar for both models (≈ 620 K), the difference after the first cooling period is around 150 K and the maximum temperature over the 10 pulses shows a difference of 33 % (760 K in the analytical model and 638 K in the FE model). The analytical model over estimate the temperature, this is might due to the small radiation cooling efficiency for temperature below 800 K. In order to check the effect of the different cooling processes, the radiation and conductivity have been alternatively which off in the FE code [1]. The results of the 20 MeV case are shown in Fig 8 and Tab 2.

Table 2: Temperature on 33 µm Carbon Wire for a 20 MeV Beam With $\sigma_x = \sigma_y = 1$ mm Estimated With different Models.

	Analytical	FE model		
Radiation	on	on	on	off
Conductivity	off	on	off	on
T_m 1 pulse [K]	1695	1665	1665	1665
T_m [K]	1801	1756	1938	2623

[1] For this, the material thermal conductivity has been reduce by 6 orders of magnitude in the material properties

ISBN 978-3-95450-185-4

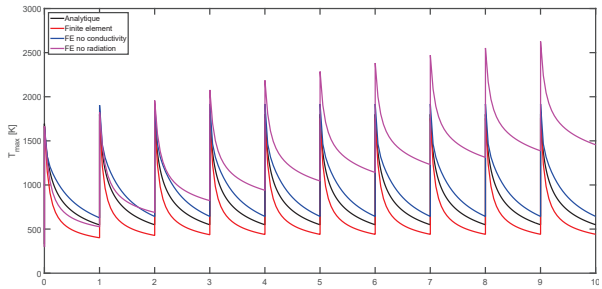

Figure 8: Comparison of different FE models for a 20 MeV beam and a 33 µm carbon wire.

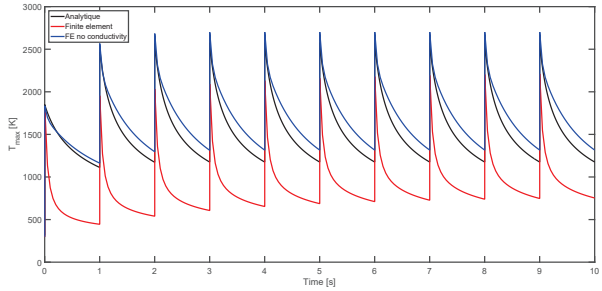

Figure 9: Evolution of the peak temperature for different FE models and on a 40 µm tungsten wire for a 200 MeV beam.

The temperature after the first pulse is similar in all the cases (error ≈ 2 %) and identical in all the FE models. without radiation cooling activated, the temperature is not stabilized after 10 pulses, the difference is above 800 K compare to full FE model. If the conductive cooling is not activated int the FE model, the equilibrium is reached after couple of pulses, a similar evolution as the analytical mode. From the results it seems that the analytical model overestimated the radiation cooling, the estimated maximum temperature in this case is 9 % lower.

Similar conclusions can be made for the low temperature case, the analytical model overestimated the radiation cooling, without conduction, the 2 models (FE and analytical) are in good agreement, nevertheless in this range of temperature, thermal conductivity can not be neglected.

For all results presented in this subsection, it is interesting to note that the temperature close to wire ends is still at 298 K after 10 seconds.

Tungsten Wire

Similar studies has been performed for a 40 µm tungsten wire, the beam parameters used for the 3D maps generation are presented in Table 3, these parameters have been chosen in order to be in the same temperature range as the carbon wire example.

Table 3: Beam Parameters Used to Generate the 3D Heat Generation Maps for the 40 µm Tungsten Wire

Energy [MeV]	σ_x [mm]	σ_y [mm]
200	1	1
2000	2	2

As shown in Fig. 9 and in Table 4 for the high temperature case, the FE model without thermal conduction activated and the analytical model show similar behavior as what was seen for the carbon wire case in particular an overestimation of the radiative cooling in the analytical model.

With conduction activated, the cooling is more efficient, the maximum temperature is 700 K lower after the first cooling period. The maximum temperature over 10 seconds is almost 20 % lower compare to the analytical model, in this model the equilibrium is reach faster than the FE model.

Table 4: Temperature on 40 µm Tungsten Wire for a 200 MeV Beam With $\sigma_x = \sigma_y = 1$ mm Estimated With Different Models.

	Analytical	FE model	
Radiation	on	on	on
Conductivity	off	on	off
T_{max} [K]	2573	2210	2701
T_{max} at 1 second [K]	1112	445	1162

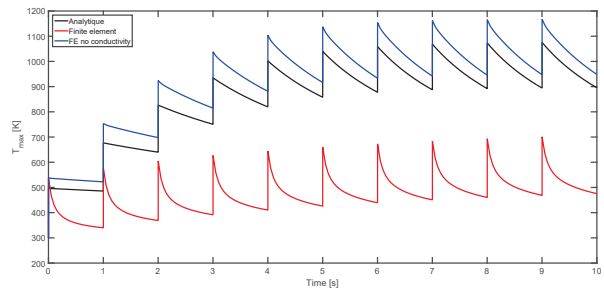

Figure 10: Evolution of the peak temperature for different FE models and on a 40 µm tungsten wire for a 2000 MeV beam.

For a lower thermal load on the wire (i.e. the 2000 MeV case), these discrepancies between the models are higher as shown in Fig. 10. With lower temperature after the first pulse, the radiation cooling is not efficient and there is almost no cooling process, this clearly appears in the analytical model and in the FE model with conductivity non activated. The models are not converging and the difference on the peak temperature between the full FE model and the analytical model is up to a factor 2 at the equilibrium,

The analytical model for a tungsten wire does not seem to be accurate for low duty cycle and low thermal load. To confirm the behavior of a tungsten wire, another series of simulations with the fast mode scan parameters (i.e. 14 Hz, 10 µs) have been performed with the same e beam parameters (see Table 3).

As shown in Fig. 11 for the 200 MeV, the temperature is stabilizes only if the conduction is not activated in the models, for the full FE model, after 29 pulse, the equilibrium is not reached, the maximum temperature for the models are summarized in Table 5. The radiation cooling seems

ISBN 978-3-95450-185-4

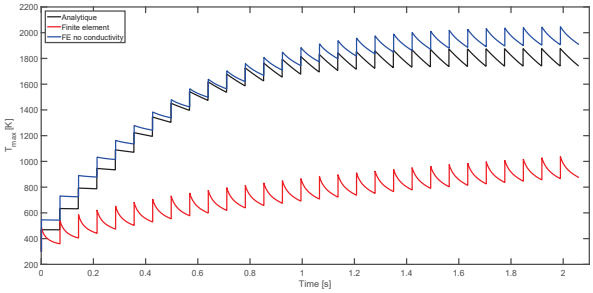

Figure 11: Evolution of the peak temperature for different FE models and on a 40 µm tungsten wire for a 200 MeV beam, during a fast mode scan.

to be efficient if the temperature is above 500 K. The peak temperature is reduce by a factor 2 in the full FE model compare to the analytical model, this is similar to what was seen in the previous set of simulations.

Table 5: Temperature on 40 µm Tungsten Wire for a 200 MeV Beam With $\sigma_x = \sigma_y = 1$ mm in Fast Mode.

	Analytical	FE model	
Radiation	on	on	on
Conductivity	off	on	off
T_{max} [K]	1878	1038	2048

At 2000 MeV, with lower thermal load, a similar behavior of the different models can be seen in Fig. 12. The equilibrium is not reach for all models, and it appears clearly that the analytical model overestimates the radiation cooling at low temperature, but the estimated temperature is at least a factor 2.5 higher than the full FE model.

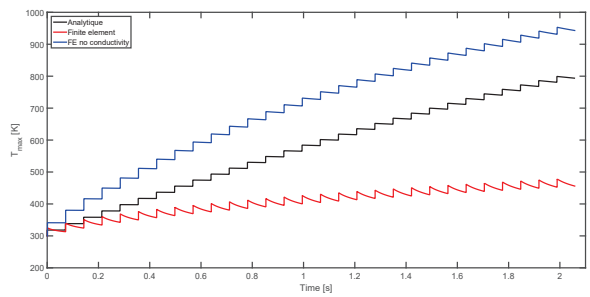

Figure 12: Evolution of the peak temperature for different FE models and on a 40 µm tungsten wire for a 2000 MeV beam, during a fast mode scan.

Like the carbon wire case, the temperature close to the wire end remains at 298 K after the last pulse.

CONCLUSION

It is often written in the literature that the conductivity can be neglected to estimate the thermal load on a thin wire. From the simulations performed for this note, it can be concluded that this statement is true only for a thin carbon wire operating at high temperature. For tungsten wire and operation at low temperature, the simple analytical model without conductivity is valid only to estimate with enough accuracy the temperature rise after a single shot.

The analytical model seems valid for high emissivity material and high temperature operation, domain where the radiation cooling is the most effective. Outside this domain, using a simple analytical model can lead to an overestimation to the wire temperature by 33 % for a carbon wire and by up to a factor 2.5 for tungsten wire compare to a full treatment of the cooling processes. Nevertheless, it must be noted that the thermal properties of the wire material are not well known, the results presented in this note might a best case scenario. Some discrepancy between the material thermal properties used in the FE model and the "real" wire properties might occur.

It would be interesting to perform a series of tests with a tungsten wire to validate the results of the FE model or update the thermal properties of a tungsten filament.

Assuming a best case scenario from the FE model, if the difference for carbon wire can be neglected during a design phase, the difference for a tungsten wire might induce some over constraints on machines parameters during operation of the interceptive devices.

For an accelerator like ESS, with a very high beam power density, the machine operation is not constraint by this overestimation of the wire temperature, the temperature after a single shot is high enough to neglect the thermal conductivity, in most of the case simulated for the ESS wire scanner, the temperature is above 1200 K after a single shot.

For accelerators with lower beam power density, the temperature after a single shot might below few hundred of Kelvins, and thus be outside the domain of validity of the analytical mode, for these cases a full FE model is be mandatory to estimate the maximum duty cycle which the wire can withstand.

REFERENCES

[1] M. Eshraqi *et al.*, "The ESS Linac", in *Proc. IPAC'14*, Dresden, Germany, THPME043.

[2] B. Cheymol, "Thermal load and signal level of the ESS wire scanner" in *Proc. LINAC'14*, Geneva, Switzerland, MOPP036,

[3] M. Plum, "Wire scanner and harp signal levels in the SNS", SNS Technical Note SNS 104050200-TD0023 - R00.

[4] `http://aries.ucsd.edu/LIB/PROPS/PANOS/`

[5] A. Ferrari, P.R. Sala, A. Fasso, and J. Ranft, "FLUKA: a multi-particle transport code" CERN-2005-10 (2005), INFN/TC_05/11, SLAC-R-773.

ISBN 978-3-95450-185-4

HIGH POWER AND HIGH DUTY CYCLE SLIT AND GRID SYSTEM FOR HADRON ACCELERATOR COMMISSIONING

B.Cheymol*, A. Ponton, European Spallation Source, Lund, Sweden

INTRODUCTION

Transverse emittance is one of the key measurements to be performed during the commissioning of the low energy sections of an hadron linac. The good knowledge of the beam transverse phase space allows a safe and efficient operation of the machines by using the results of the measurement for beam dynamic simulations.

In this paper we will discuss the accuracy and the limits of the transverse emittance measurement performed with the slit-grid method based on the ESS beam parameters at the RFQ (beam energy equal to 3.62 MeV) and DTL tank 1 (beam energy equal to 21 MeV) output [1]. The goal of this paper is to set the limits of the operating domain of the slit and grid system in machine similar to ESS, in particular to achieve emittance measurement with a beam pulse length up to 1 ms. The authors assume that the emittance will be measured on a diagnostic test bench with a matching sections.

In the following the emittance is referred to the RMS normalized emittance, the slit geometrical parameters are summarized in Fig. 1 for reference, the angle of the slit is the angle between one slit blade and the z-axis of the beam.

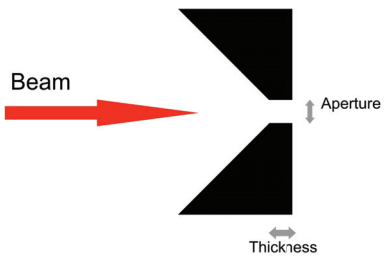

Figure 1: Schematic diagram of the slit used in the simulations (dimensions are not on scale).

BEAM DISTRIBUTIONS

At the exit of the RFQ and the DTL, beam sizes are too small to use interceptive devices with pulses longer than 20-50 μs. In order to reach relatively high duty cycle, the beam sizes at the slit location must be increased to reduce the thermal load, in addition the beam divergence has to be kept small enough to avoid angular cut in the transverse phase space during the emittance measurement, in a ideal case, the beam shall be parallel in both transverse planes, thus to expand the beam with small emittance increase and keep the divergence small enough a triplet of quadrupoles is mandatory.

Based on these specifications and similar quadrupoles characteristics from other facilities, preliminary simulations were performed with the TraceWin code [2] in order to generate beam sources which can be used as input for all the studies presented in this paper. Without a full optimization of the beam dynamics, these inputs have been considered as test cases for the design of an emittance meter. The Fig. 2 and Fig. 3 show the transverse phase spaces for the RFQ and DTL at the output to the triplet, the Twiss parameters are summarized in Table 1.

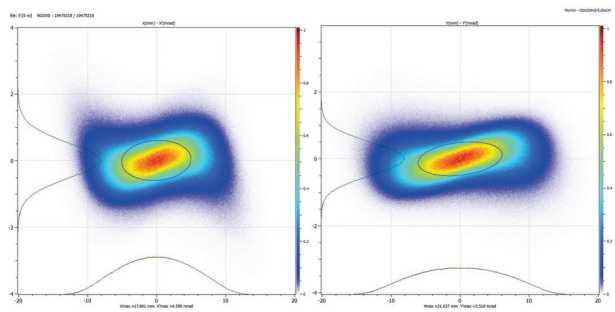

Figure 2: Transverse phase space distributions at the end RFQ matching section.

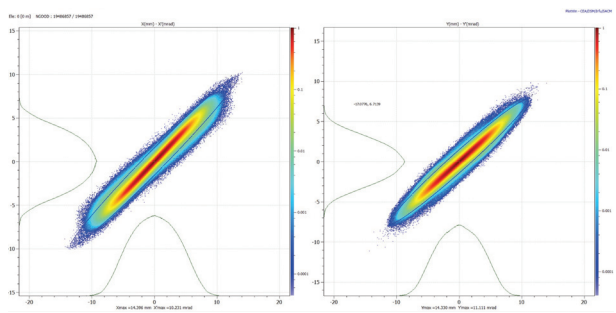

Figure 3: Transverse phase space distributions at the end DTL matching section.

Table 1: Beam Parameter Expected at 150 mm Upstream The Theoretical Slit Position For The RFQ and DTL Cases

Location	RFQ		DTL	
Plane	H	V	H	V
α	-0.076	-0.216	-6.19	-5.25
β [mm/πrad]	8.41	12.52	8.58	7.64
$\varepsilon_{norm.}$	0.2633	0.2601	0.3303	0.3103

In both cases, the beams have been transported form the RFQ entrance to the end of the matching section, The particles distributions are taken at 150 mm upstream the theoretical slit position in order to reserve space for mechanical integration.

* benjamin.cheymol@esss.se

ISBN 978-3-95450-185-4

PRELIMINARY ESTIMATION OF THE THERMAL LOAD

Thermal load on the slit is one of the most critical point of the design of an emittance meter. Based on experience learn from LINAC4 slit and grid system, graphite or more generally low density materials are the best options for the slit material, the slit can be tilted to decrease the beam power density and thus reduce the thermal load [3].

For this study, slit and grid system will be mainly derived from the LINAC4 design, an optimization of the slit is nevertheless mandatory to cop with the higher beam power of the ESS linac. In this preliminary estimation of the temperature, only R4550 graphite has been simulated, the angle of the slit w.r.t the beam axis is set to 15 degrees. A 3D energy deposition map has been generated with the Monte Carlo (MC) code FLUKA [4] and then use as an input a Finite Element (FE) analysis with the ANSYS applications. Based on the LINAC4 experience, the temperature shall not exceed 1300 K to insure mechanical integrity of the slit.

3.62 MeV Beam

For a 1 ms pulse length, the peak temperature is$\approx$ 1000 K, in this case it might be possible to increase even more the duty cycle without approaching the mechanical limits of the R4550 graphite. It is interesting to note that the results from FE analysis presents a big discrepancy compare the temperature estimation with an analytical model without conduction, and that the temperature gradient in the slit decreases with time even during the pulse.

In order to check the influence of thermal conduction on the results, a new set of FE simulations have been performed. In a first step, the thermal conduction of the slit material was reduced by 6 order of magnitude in FE models, as consequence, the results of this simulations and the the results of the analytical model show a difference at a percent level, which can be explain by some difference in the specific heat capacity model. Unlike the previous FE model, the temperature gradient is clearly visible at all time step on the temperature map, showing that the coupling between ANSYS and FLUKA is correctly done, conductive cooling for this beam energy seems efficient even at small time scale. A similar behavior has been reported for the LINAC4 slit design in [5] , other authors reports a high efficiency of the thermal conductivity for low energy protons beam.

21.3 MeV Beam

The thermal conductivity is less efficient in this case, the difference between the analytical model and FE model is less than 20 %. With a higher beam density compare to the RFQ case ($\approx$ 3.5 mm) the slit can not withstand a pulse length of 1 ms, the temperature is slightly above the limit after 500 μs (T_{max} = 1570 K). Increasing the beam sizes to 6 mm allows the slit to withstand a higher duty cycle, the peak temperature is around 1150 K at the end of a 1 ms beam pulse, nevertheless, the α parameters of such beam are over the acceptance of the slit and grid system, as consequence this case is not considered in this paper, more detail can be found in [6].

ERROR ON THE EMITTANCE RECONSTRUCTION WITH A SLIT AND GRID SYSTEM

The slit and grid method for measuring the beam transverse phase space might induced some errors in the emittance reconstruction, in this paper, we propose to discuss the influence of the error on the slit/grid position and the influence of Multiple scattering on the slit edges.

Error on Slit and Grid Positioning

The positions of the slits and the grids have to be measured with a good accuracy to reduce the error on the emittance reconstruction.

Vertical and horizontal emittance scans have been simulated for different distance between the slit and the grid (from 600 mm to 4000 mm in step of 100 mm), the transverse beam position is sampled in step of 0.5 mm. The monitor consists in a grid equipped with 100 μm diameter wires and a pitch equal to 500 μm. The signal is assumed to be equal to be the number of particles crossing each wire. The slit aperture was set from 100 μm to 500 μm in step of 100 μm.

Random error has been applied to each couple: slit position-wire position (i.e. angle). The errors are assumed to be gaussian with an RMS value from 0 to 100 μm. in step of 10 μm for the grid and in step of 50 μm for the slit. For each slit-grid distance, 50 virtual emittance scans have been performed, the average ϵ_{RMS} over these 50 scans has been be compared to the reference emittance given in Table 1.

RFQ A first estimation of the emittance has been done without error on the slit/grid position for the different slit aperture and wire diameter in both transverse planes. As shown in Fig. 4 the error is independent of the slit aperture, small variation can be explain by statistical error. It can be observed that the error seems to be more or less constant for distance between the slit and the grid longer than 1000 mm, the error in this case is less than ± 0.2 %. Similar results can be observed in the vertical plane.

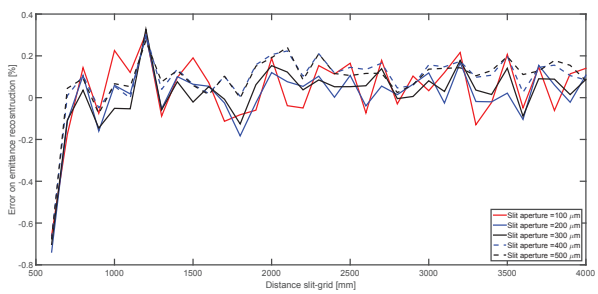

Figure 4: Error on horizontal emittance reconstruction as function of the slit and grid distance for different slit aperture. the wire diameter is 100 μm

ISBN 978-3-95450-185-4

With an α close to 0, the influence of the slit aperture on the emittance reconstruction can be neglected, to improve the statistics of the simulations, all the results presented in the following have been estimated with a slit aperture of 500 μm and a wire diameter equal to 100 μm.

As shown in Fig. 5, with error on the grid and slit position the distance between the slit and the grid has to be increase to reduce the error on the reconstructed emittance below an acceptable level.

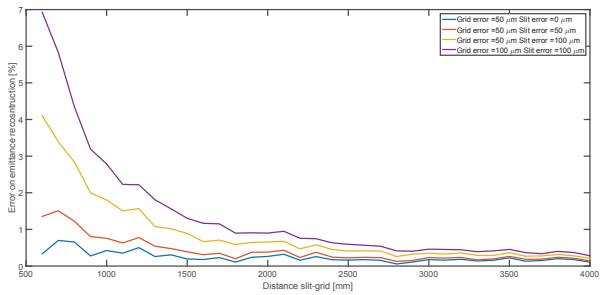

Figure 5: Error on horizontal emittance reconstruction as function of the slit and grid distance for different couple of errors on grid position and slit position, the slit aperture is 500 μm and the wire diameter is 100 μm.

With an error on grid and slit position equal to 100 μm, the error on emittance reconstruction is less than 1 % if the distance between these tow elements is above 2.5 meters. Increasing the slit and grid position accuracy to 50 μm will improve the accuracy of the whole system.

A distance of 3000 mm between the slit and the grid has been taken as reference fro the Monte Carlo simulations presented in the next sections. It has to be noted that during the commissioning the beam might not be Gaussian, with 3 meters between the slit and the grid, the beamlet can be sample with 3-4 wires per sigmas (in a single shot measurement), which allow a sufficient angular resolution.

DTL As shown in Fig. 6, in the DTL case the silt aperture has a higher influence on the emittance reconstruction, if the distance between the slit and the grid is above 2500 mm, the error is less than 4 % and down to ≈ 1 % for the thinner slit aperture. As for the RFQ case, the wire diameter is not influencing the emittance reconstruction, the same distance between the slit and the grid has been also chosen for the next simulations (3000 mm).

Multiple Scattering Effect

Multiple scattering on the slit edges can affect the measurement accuracy and lead to over estimated the beam transverse emittance, the Monte Carlo simulation package FLUKA has been used to study this effect.

The sources generated by the TraceWin code have been used as input for the simulations, in order to simplify the post processing, the beam is considered as mono energetic. The aperture and the thickness of the slit are free parameters the angle of the slit is set at 15 degrees, the SEM grid is

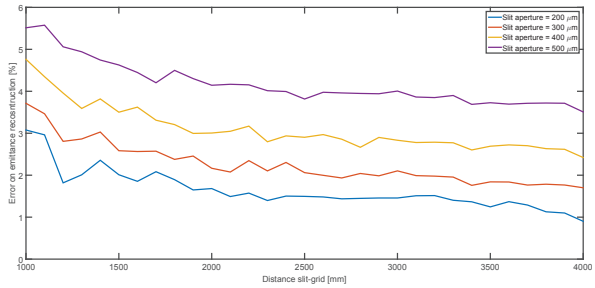

Figure 6: Error on horizontal emittance reconstruction as function of the slit and grid distance for different slit aperture, the wire diameter is 100 μm. Error on grid position and slit position is set to 50 μm, the sampled distribution is shown in Fig. 3.

simulated as a screen positioned 3 meters downstream the slit, the position and the energy of each particle crossing the screen are measured, all particles with an energy smaller than the input energy are considered scattered. The results of the Monte Carlo code have been then used to estimate, in post processing, the beamlet profile sampled on a SEM grid with a pitch of 500 μm and a wire diameter of 100 μm. In a first step, a single slit position has been simulated, to reduce statistical errors, the slit is centered at 0, then full emittance scans have been simulated.

The influence of Multiple scattering on emittance reconstruction increases with the beam energy, thus the slit has to be design to reduce the error for a 21 MeV beam.

DTL The slit aperture varied from 100 μm to 500 μm and the slit thickness from 1 to 3.5 mm. As shown in Fig. 7 for a slit aperture equal to 100 μm, the proportion of scattered particles is strongly dependent of the slit thickness [1]. With a 2 mm thick slit the ratio is at the percent level, there is almost no difference between 3 and 3.5 mm, with a ratio close to 10^{-3}.

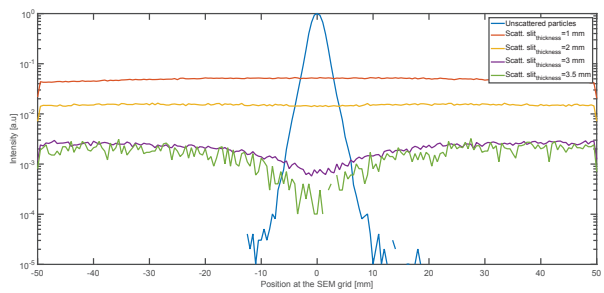

Figure 7: Scattered and un scattered particle distributions at the SEM grid location, for the slit in position x=0 for different slit thicknesses and a slit aperture equal to 100 μm (beam energy is 21.3 MeV).

The influence of the slit aperture has been also simulated with a slit thickness equal to 3 mm, the results are presented

[1] if this parameter is below 1 mm, the ratio of scattered particles can be up to 25 %

ISBN 978-3-95450-185-4

in Fig. 8. Up to an aperture equal to 400 μm, the ratio of scattered particles decrease almost linearly as the slit aperture increases. The difference between 400 μm and 500 μm is relatively small, mainly due to lack of statistic. For a given slit thickness, the number of scattered particles is almost independent of the slit aperture, thus the ratio scattered/unscattered decreases as function of the slit aperture.

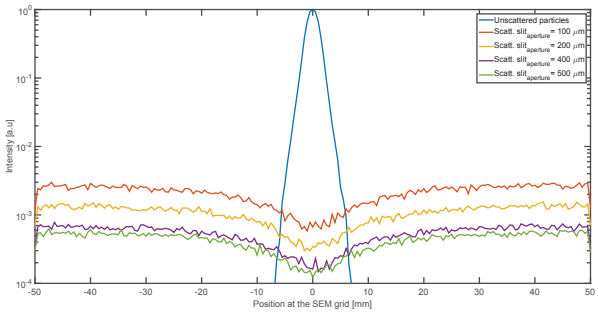

Figure 8: Scattered and un scattered particle distributions at the SEM grid location, for the slit in position x=0 for different slit apertures, the slit thickness is equal to 3 mm and the beam energy to 21.3 MeV.

The source of scattered particles has two origins, a first one is dominant when the slit thickness is below the penetration range of proton in the slit material, some particles have enough energy to cross the slit material and reach the SEM grid. The second origin is particles scattered on the slit edges, with a perfect slit (i.e no thickness) and neglecting the first source mentioned, all particles selected by the aperture shall not be scattered, in reality, a small fraction of these particles interact with the slit due to their divergences. The effect is relatively small but increases with the slit thickness and becomes dominant for slit thickness larger that the particle penetration depth in the slit material.

Reducing the slit aperture will improve the accuracy of emittance reconstruction and but to avoid angular cut the slit thickness shall be also reduced at the same time, it will be beneficial to use a higher density material for the slit.

Unfortunately, few materials have similar thermal properties as the R4550 graphite. One option is to use a composite of carbon fiber and molybdenum (MoGr), recently developed for the LHC collimator upgrade, this novel material shows thermal properties close to graphite with a higher thermal conductivity, moreover with a density almost 2 times higher than the graphite (2.8 $g.cm^{-3}$ compare to 1.7 $g.cm^{-3}$), the slit thickness can be reduced [7].

3.63 MeV Beam For the lower energy beam and a 3 mm slit thickness in graphite, the ratio is almost one order of magnitude lower (10^{-4}) compare to the DTL case, the design is not driven by this case (see and Fig. 9).

Emittance Reconstruction In the MC simulations the SEM grid is fixed and the slit moved by 0.5 mm steps to cover all the horizontal plane, different slit parameters have been simulated, as well as different scattered particles weight (in post processing). The normalized rms emittances have been estimated statistically, the results are shown in Table 2 and Table 3 for different slit parameters. Only the simulations performed in for the horizontal plane are presented, similar results are observed in the vertical plane.

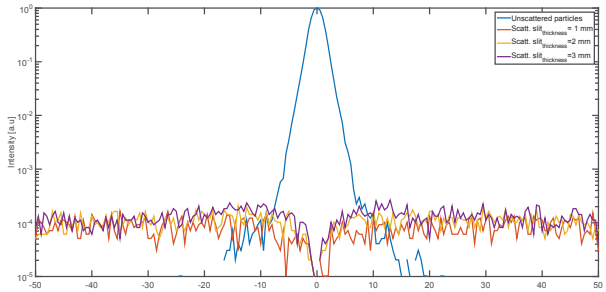

Figure 9: Scattered and un scattered particle distributions at the SEM grid location, for the slit in position x=0 for different slit thicknesses, the slit aperture is equal to 400 μm (beam energy is 3.63 MeV).

Table 2: Error on Reconstructed Emittance With and Without Scattering Activated for the RFQ Case

Simulations parameters			Error on emittance [%]	
Slit ap.	slit th.	Grid pitch	Scattering	
[μm]	[mm]	[μm]	off	on
400	0	500	0.6	220
400	1	500	0.2	12.3
400	3	500	0.19	18

Table 3: Error on Reconstructed Emittance With and Without Scattering Activated for the DTL Case

Simulations parameters			Error on emittance [%]	
Slit ap.	slit th.	Grid pitch	Scattering	
[μm]	[mm]	[μm]	off	on
200	2	500	1.4	1295
400	2	500	2.7	990
400	3	500	2.8	862
400	3.5	500	2.7	385
200	3	500	-4.2	576

As show in Table 2 and Table 3, the statistical calculation of the rms emittance induce an important error if data is not treated, in particular for the DTL cases, particles far from the ellipse axis have a large impact on the rms emittance, alternative methods are needed to analysis the data. It has to be noted that the area of the transverse phase space sampled in the MC is much larger than what is need for a proper measurement ,as example, the sampling area of the beamlet is $\pm 15\sigma$ times the rms profile of the beamlet As consequence, since the scattered particles are spread in all

ISBN 978-3-95450-185-4

the phase space samples in the MC simulations, the value on the reconstructed emittance is dominated by this effect .

It is interesting to note, that in the case of the thicker slit (3mm) with the smallest aperture, the emittance without scattering activated is underestimated, particles with high divergence angles are not properly measured, the rms beamlet profile is well reconstructed, but the beamlet "intensity" is reduced, leading to underestimate the contribution of these fraction of phase space on the rms emittance. Using a material with higher density like MoGr, will allow the reduction of the slit thickness to 2 mm, and used a thinner slit aperture. In this case, the error due to the reconstruction shall be less than 2 % with a limited contribution from multiple scattering.

DATA ANALYSIS

Several methods are available to analyze the data from an emittance scan, this section is describing few simple methods to remove the contribution of scattered particles and their application on the Monte Carlo simulations results, more complex algorithms can be applied to the data.

Data Thresholding

The most common and most simple method for emittance analysis is to apply a cut on the data. All the values below a given threshold will be excluded from the calculation, in general this threshold is a fraction of the peak signal obtain after the scan. For all the case presented in Table 2 and Table 3 the threshold need to match the reconstructed emittance without scattering activated is less than 0.5 % of the peak value.

Background Subtraction

A shown in Fig. 7 and Fig. 9, the distribution of scattered particles on the SEM grid is more or less flat. Since only few wires in the center of the SEM gird are needed to reconstruct the wire, the outer wire can be used to estimate the amount of signal generated by the scattered particles at the SEM grid location, them this signal can be subtracted to the data. Using this method will allow also to reduced the effect of the electronic noise on emittance reconstruction.

Phase Space Cut

The last method considered in this paper is refereed as "phase space cut", the goal of the method is to remove the data far form the emittance ellipse axis. A Gaussian fit is apply to each beamlet profile, then the data above 6 times above the sigma of distribution found with the fitting are excluded from the estimation of the emittance.

This 3 methods can be combined to improve the data analysis, some example are shown in Fig. 10 and Fig. 11.

For both energy cases, using a background subtraction together with a phase space cut allow to find the same value for the emittance as the one the one found with Monte Carlo Data when scattering is off without any threshold, error

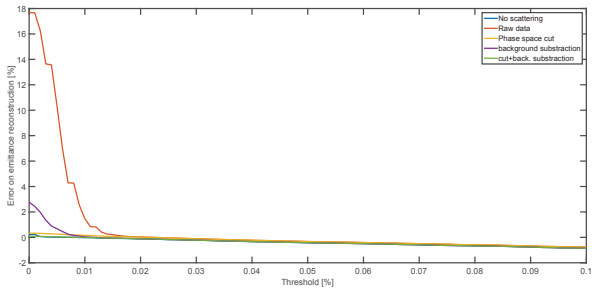

Figure 10: Emittance reconstruction as function of data threshold for different method of analysis. The beam energy is 3.63 MeV.

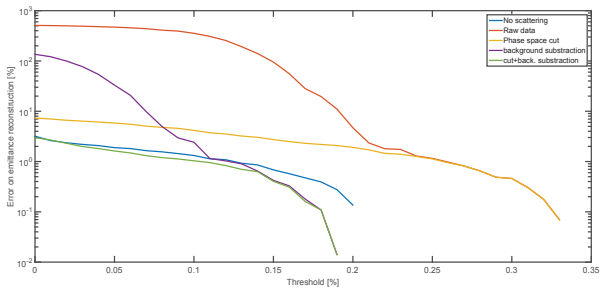

Figure 11: Emittance reconstruction as function of data threshold for different method of analysis. The beam energy is 21MeV.

compare to the "real" emittance (i.e. the one defined by the Tracewin distributions) is less than 2 %.

For the lower energy case, a threshold equal to ≈ 0.02 % on the data is needed to match the reference emittance for all the methods considered, at higher energy, a threshold equal to ≈ 0.1 % is needed to reach the matching point, but only for the background subtraction method and a combination of background subtraction and phase space cut. The other methods need a higher threshold and match the reference data only when the analysis gives a smaller emittance than the Tracewin values. With the proper method an error equal to ≈ 3 % is expected.

CONCLUSION

In high power hadron machine, the thermal load on interceptive instrument is one of the limiting factor for an increase of duty cycle during commissioning. After the preliminary studies presented in this paper, with an optimized slit design and an optimized beam dynamic, we can conclude that the emittance can be measured with pulse length longer than 400 μs and up to 1 ms at the exit of the RFQ with an error less than 5 % on the emittance reconstruction in machine with similar beam as ESS. Nevertheless to complete and confirm this preliminary study, it will be interesting to simulate the influence of the space charge on the emittance reconstruction. As final conclusion, the authors would like to emphasis that the best performance is achieved when the α parameter close to zero, in this case, the slit geometry has a small influence on the emittance reconstruction.

ISBN 978-3-95450-185-4

REFERENCES

[1] M. Eshraqi et al.,"The ESS linac", in *Proc. IPAC'14*, Dresden, Germany, THPME043.

[2] R.Duperrier et al. in *Proc. of ICCS'02*, p.411.

[3] B. Cheymol et al., "Design of the Emittance Meter for the 3 and 12 MeV LINAC4 H^- Beam", CERN-BE-2010-013.

[4] A. Ferrari, P.R. Sala, A. Fasso, and J. Ranft, "FLUKA: a multi-particle transport code", CERN-2005-10 (2005), INFN/TC_05/11, SLAC-R-773.

[5] F. Carra et al. "LINAC4 3MeV test stand: Thermo-mechanical analysis of the Slit", CERN technical report EDMS-1102149.

[6] B. Cheymol, "High power and high duty cycle emittance meter for the ESS warm linac commissioning", ESS technical note, ESS-0038060.

[7] A. Bertarelli et al. "Novel materials for collimators at LHC and its upgrades" in *Proc. HB'14*, East-Lansing, MI, USA, THO4AB03.

ISBN 978-3-95450-185-4

SCINTILLATOR DETECTORS FOR THE ESS HIGH ENERGY WIRE SCANNER

B. Cheymol*, European Spallation Source, Lund, Sweden

Abstract

In the ESS linac [1], during commissioning and restart phase, wire scanner (WS) will be used intensively to characterize the transverse beam profiles. At low energy, the mode of detection is based on Secondary Emission (SE), while at energies above 200 MeV, the primary mode of detection will be the measurement of the hadronic shower created in the thin wire.

In this paper we will present the design and the output signal estimation of the shower detector, based of inorganic crystal and silicon photodetector

INTRODUCTION

In the ESS superconducting linac and downstream, 8 WS stations will be installed alone the beam line. Each station will be equipped with two linear actuator to sample the separately the transverse planes and the last 5 stations, in the elliptical sections and in the transfer line to the target, will be used in shower detection mode in addition of the SE signal from the wire. The actuator fork will be equipped with a 40 μm tungsten wire, for the ones to be used in the shower mode, the detectors will be positioned 400 mm downstream the wire [2].

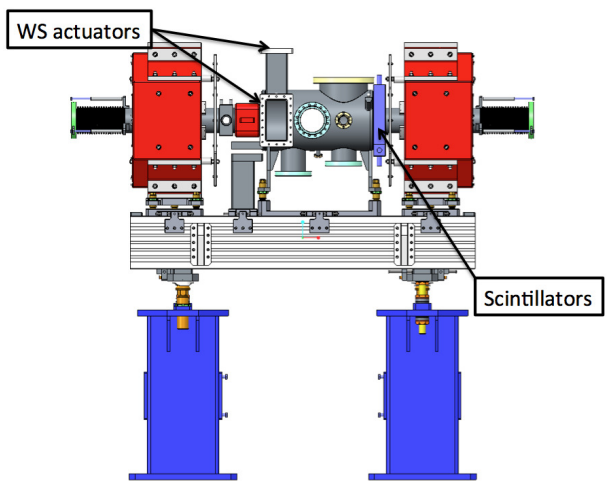

Figure 1: Preliminary design of the elliptical LWU, the total length flange to flange is ≈ 1932 mm, WS actuators are not shown (courtesy of STFC Daresbury Laboratory).

As shown in Fig. 1, due to the low energy of beam compared to proton synchrotron, the full system will be installed in a Linac Warm Unit (LWU), between two quadrupoles. This geometry has been chosen in order to avoid perturbation of the hadronic shower if the detectors would have been installed downstream the quadruple.

* benjamin.cheymol@esss.se

DETECTOR CONCEPT

In high energy physics experiment, wavelength shifting (WLS) fibers are often used to collect the light from scintillator in order to reduce calorimeter geometry complexity [3]. The same approach can be use for the ESS wire scanner, not to simplify the geometry but to protect the photodetector from radiation.

The light generated in the scintillator can be collected through a fiber. which can transport the light to the photodetector installed in an area with less radiation compare to the accelerator tunnel. In an ideal case, the photodetector can be installed in the klystron gallery in the same electronic cabinet as its front end electronic and its digitizer card.

Detector Architecture

The acquisition electronic of the ESS WS is currently under development at Synchrotrone Elettra Trieste. For the SEM mode, it is foreseen to use two separated channels per wire, one with high gain and low bandwidth the other with a low gain and high bandwidth. With this setup it will possible to get a high dynamic range for the profile in a single scan. The same concept will be used for the scintillator readout.

Previous simulations show that 4 separated detector are needed to insure good homogeneity of the signal across the beam pipe [2], each detector will be connected to 2 Front-End (FE) electronic as for the SEM mode. The assembly geometry of the detector is shown in Fig. 2.

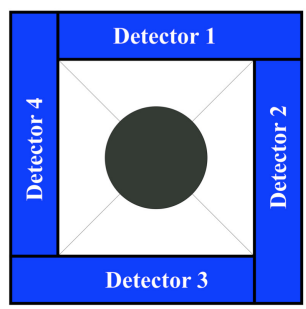

Figure 2: Detector assembly for the ESS WS system.

A combination of WLS fibber and clear fiber will be used to transport the light from the detector to a radiation free area, the detector architecture is shown in Fig. 3.

The scintillation light will be collected by two WLS fiber on each detector assembly, since the attenuation length of this fiber is high (few meters), their lengths have to be kept as short as possible. Silica fiber have a low attenuations, and are better candidates to transport the light over a long distance, for the ESS application the length from the WS station in the tunnel to the electronic rack in the klystron gallery is about 60 meters.

ISBN 978-3-95450-185-4

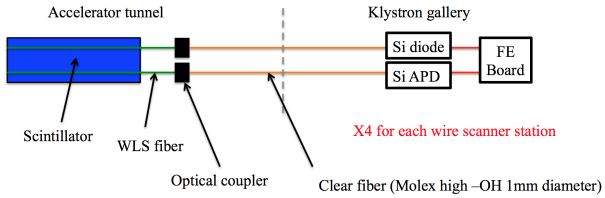

Figure 3: Conceptual design of the ESS wire scanner shower detector.

The light will be converted to current by a photodiode and an avalanche photodiode, in order to increase the dynamic range of the measurement. Each photodetector will be connected to its own FE end electronic.

Scintillator and WLS Choice

Most of the plastic and crystal scintillator have their peak emission in the visible range of the light, more precisely in the blue-green region. WLS can be used to shift the blue light to green light, their absorption peak shall match the peak emission of the scintillator, the BCF-91a from Saint Gobain and the Y-11 from Kuraray have a peak absorption close to 420 nm, which corresponds to the peak emission of the majority of plastic scintillator. Unfortunately, the radiation dose in the accelerator tunnel might be too high for organic scintillator, crystals are less sensitive to radiation and seems a better option.

One alternative to plastic scintillator is to use the LSO scintillator, which had a peak emission at 420 nm, a fast decay time (40 ns) and a high photon yield ($\approx 30\ \gamma\ .\text{keV}^{-1}$), in addition, the LSO is not hydroscopic unlike the NaI crystal. The LSO has been study extensively for calorimetry application for high energy physics and is available from different supplier [4].

As show in Fig. 4 and Fig. 5, its spectra matches the two WLS fibers considered, 80 % of the spectra are absorbed, only the high wavelengths are outside the absorption spectra of the fibers.

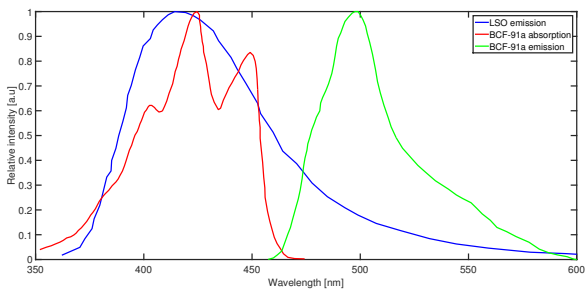

Figure 4: Optical spectra of the Saint Gobain BCF-91A wavelength shifter.

WLS fibers are available on different sizes with single or double cladding, in this study, a 1 mm diameter single clad fiber has been considered in order to match the numerical aperture (NA) of a silica fiber and its diameter. The decay time of such fibers is few ns.

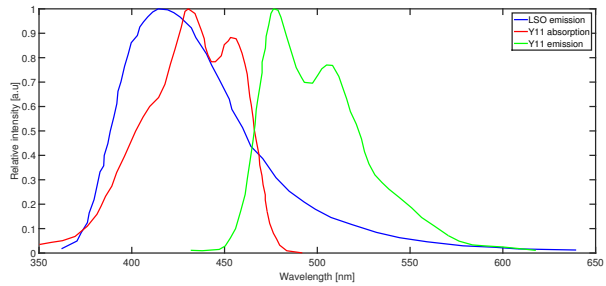

Figure 5: Optical spectra of the Kuraray Y11 wavelength shifter.

SIMULATIONS OF THE DETECTOR

The light production and collection have been simulated by the Monte Carlo (MC) code FLUKA [5], the shifting process, the light transport have been treated analytically in post processing.

The detector assembly geometry used in the MC simulations is shown in Fig 6.

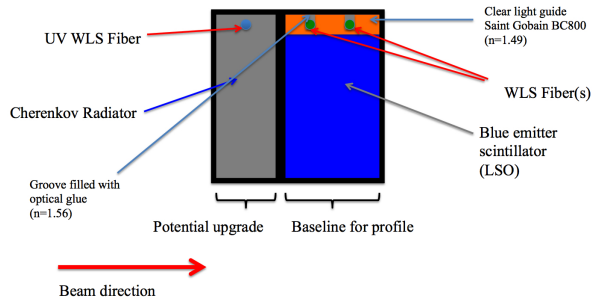

Figure 6: Cross section of the detector assembly used in the MC simulations.

The crystal might be difficult to machine, therefore, a plastic light guide (Saint Gobain BC-800, $n = 1.49$) will be used to installed the WLS fiber in groove filled with optical glue ($n = 1.56$), the detector size is $250 \times 45 \times 30 mm^3$, the light guide dimension is $250 \times 5 \times 30 mm^3$. All the assembly in surrounded by reflecting material, with a reflexion varying index from 0.94 to 0.99 and encapsulated in an aluminum box with a thickness of 2 mm. The WLS fiber has been simulated as a cylinder of 1 mm diameter for the core surrounding with a 20 μm thick clad, materials are polystyrene for the core and PMMA for the clad.

In addition, for an upgrade phase of the WS system, a Cherenkov radiator (in quartz) will be installed in front of the scintillator assembly. Bremsstrahlung background from the cavities might perturb the profile measurement, a Cherenkov detector is insensitive to this radiation and should allow beam profile measurement when the cavities are at their peak accelerating gradient. A similar detector architecture is foreseen for the Cherenkov detector with an UV WLS fiber, simulations is on going at the time this paper is written [6]. Nevertheless, the quartz plate has been implemented

ISBN 978-3-95450-185-4

in the MC simulations in order to simulate the complete hadronic shower generated by the beam interaction with all the material before the scintillator assembly.

Light Collection and Transport

The light production and the absorption by the WLS fiber have been simulated with a simplified geometry. In the MC code, only one scintillator assembly has been simulated with a beam interacting directly with the detector. The number of photons generated in the crystal and the number of photons absorbed in the WLS fiber core have been measured for different reflective material index and separately on both fibers. The results show that light collection yield per fiber varies from 9 % to 14 % as function of the reflective index. The number of photon absorbed in the WLS fiber cores identical for the 2 fibers, thus no effect of detector inhomogeneity is expected.

The conversion in the WLS fiber and the light transport has been calculated in post processing. In the MC code, the scintillation light is monochromatic, a coefficient equal 0.8 has been applied to simulate the non absorption of the high energy wavelength of the LSO spectrum. In addition a the WLS quantum efficiency of the WLS fiber is set at 0.85, and the light trapping efficiency to 0.03.

The last parameter might be increased if the fiber end is wrapped by a reflecting material, in the simulation presented in this paper, it is assumed that the light is not reflected and thus lost. Note that the trapping efficiency can go up to $\approx 0.06 - 0.07$ if the light is fully reflected on the fiber end.

As mentioned previously, the WLS fibers have a short attenuation length, clear plastic fiber have also a short length for our application and are radiation sensitive. Silica fibers have long attenuation length and are less sensitive to radiation, two options have been estimated:

- A pure Silica fiber ($NA \approx 0.22$)
- A silica fiber with hard polymer cladding (SPC) ($NA \approx 0.48$)

Both have attenuation equal to ≈ 25 dB.km^{-1} at the peak emission of the WLS fiber (500 nm). The pure silica fiber has a higher resistance to radiation, but a low NA compare to the WLS fiber ($NA \approx 0.5$), only 40 % of the light from the WLS fiver can be trapped in the silica fiber, in addition the optical connector has an efficiency of 80-90 %, in total the full efficiency of this system is about 30 %.

Due to the higher NA of the SPC fiber, up to 90 % of the light coming from the WLS fiber can be trapped and transport. Nevertheless the radiation resistance of this fiber is less, one possible mitigation is to split the clear fiber path in two. The first one from the detector to the tunnel penetration will allow easy maintenance and replacement of the exposed part of the fiber, the other, from the penetration to the klystron gallery. In this case the fiber will not exposed to high radiation dose and will be installed permanently in the cable tray. Two optical connectors are needed for the solution, assuming he same efficiency of ≈ 85 %, the proportion of the light transported is up to 60 %.

The two options have been considered for the signal estimation.

Signal Estimation

For this simulation, a simplified geometry of the LWU has been modeled in the MC code, the wire consists in a foil with a thickness equal to 32 μm to take in account the round shape of the wire, the energy deposited in each scintillator has been measured and then use as input for post processing. In the first step, the number of photons generated per proton crossing the wire (in the center of the beam pipe) has been estimated for beam energy from 100 MeV to 2100 MeV by converting the deposited energy in photon (see Fig. 7).

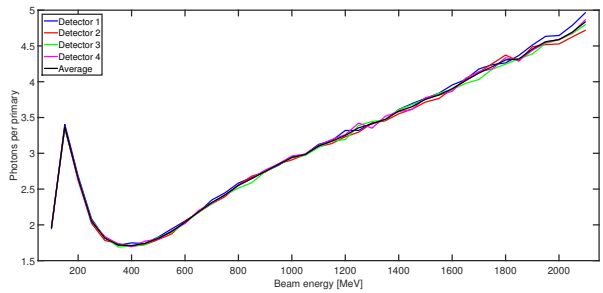

Figure 7: Number of photons generated in the LSO crystals per proton crossing the wire as function of the beam energy.

The response of the 4 scintillators is almost equal, an average value has bee taken for the next steps of the study. The minimum signal is expected for a beam energy equal to 400 MeV, above this energy, the signal increase almost linearly with the beam energy. A peak can be seen at 150 MeV, corresponding to a full energy deposition of scattered proton in the detector.

These data have been then used to estimate the peak light power at 400 and 2000 MeV as function of a clear fiber length for the two options presented in the previous section. In this estimation, the light collection efficiency of the WLS fiber is set to 11 % which correspond to a reflective index of the material equal to 0.96, the emission of the WLS is assumed to be monochromatic with a peak at 500 nm. The beam sizes are assumed to be equal to 2 mm in both transverse planes and the beam intensity is set to 62.5 mA.

As shown in Fig. 8, the light power varies by a factor 5 depending on the beam energy and on the efficiency of the clear fiber. At the ESS facility, it expected to have a fiber length no longer than 60 meters, in this case the peak light power has a range from ≈ 4 W at 400 MeV with lowest fiber efficiency to $\approx$19 W at 2000 MeV and the highest fiber efficiency.

The light power has been converted to current at the exit of a photodiode and of an APD, for this, a preliminary choice of the detector has been done. The photodetectors shall have a high sensitivity at 500 nm, a surface larger than the section of the fiber to insure good optical coupling and a

ISBN 978-3-95450-185-4

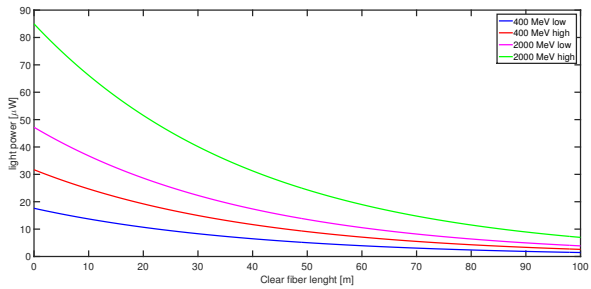

Figure 8: Peak light power as function of the clear fiber length for a beam energy equal to 400 and 2000 MeV. *low* corresponds to the efficiency of a pure silica fiber, *high* corresponds to the efficiency of a SPC fiber.

low noise, the Si diode S1227-33BR and the APD S5344 from Hamamatsu fit these requirements and their sensitivity (0.3 $A.W^{-1}$ for the diode and 20 $A.W^{-1}$ for the APD) have use to estimate the signal, note that the gain of the APD is set at 50 in the estimation and might be too high in some cases, saturation of the detector might perturb the measurement.

The expected signals as function of the wire position for both type of detectors are shown in Fig. 9 and Fig. 10

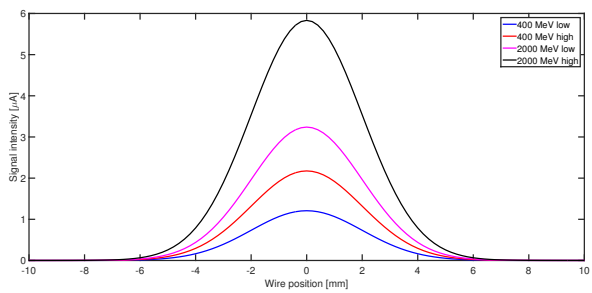

Figure 9: Expected signal at the output of the Si diode after 60 m of clear fiber.

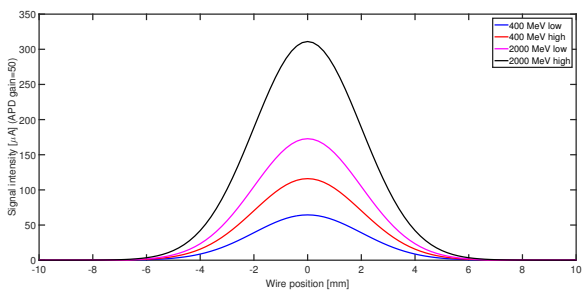

Figure 10: Expected signal at the output of the Si APD after 60 m of clear fiber.

The gain of the APD can be tuned, and at high energy a lower gain might be enough. At the time this paper is written, all these inputs are used has inputs for the FE specifications, after the preliminary design phase, the choice of the photodetector will be frozen.

Time Dependency of the Signal

A bunch by bunch measurement of the profile like in the synchrotron is not mandatory for a linac application, a time resolution of 0.5-1 μs is requested for the ESS WS system. The decay time of the detector assembly is long compare to the bunch frequency of the ESS linac (2.86 ns), the bunch structure will be vanished but some artifact might appear, simulations have been performed to cheek this effect.

In a first approximation, it was assumed that the bunch length (up to 20 ps) is null compare to the LSO crystal decay time, the charge per bunch is identical and the wire is not moving. The arrival time of the scintillation photon on the WLS fibber has been measured with the MC code, the decay time of the fiber and the different optical path of the shifted photon have been simulated in post processing for a single bunch. The time distribution obtained has been used to generate the time structure of the signal at the exit of the WLS fiber, by shifting the original distribution by 2.86 ns and adding the the new distribution to the previous distribution.

As shown in Fig. 11 for a beam pulse equal to 5 μs, the expected signal will have a rise and decay time equal to ≈300 ns, on the flat top on the signal the signal is almost constant (< 1 % peak to peak) and shows a time structure with a frequency equal to 352 MHz.

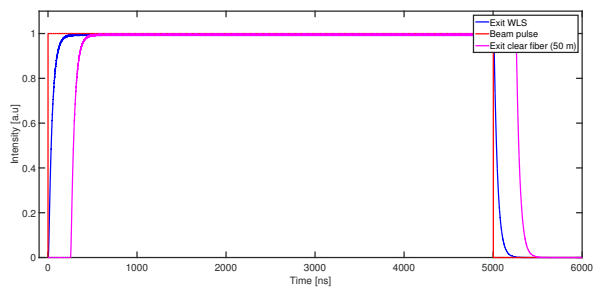

Figure 11: Expected rise/fall time signal for (i.e light) a single wire position, beam pulse is 5 μs.

After 50 meters of clear fiber, the signal will be shifted by 250 ns, it was assumed that the silica fibers are inducing time dispersion.

Detector Homogeneity

The homogeneity response of the detectors has been checked with same MC code, a pencil beam is moved across the beam pipe aperture form -25 mm to 25 mm in step of 5 mm, and then interacts with the tungsten foil, the energy deposited in each scintillators has been measured, it is assumed that the signal will be proportional to this quantity.

As shown in Fig. 12 , the signal can vary increase by almost 50 % across the beam pipe aperture if a single detector is installed. 4 detectors are needed to insure a good homogeneity. At 2000 MeV by summing the signal from the 4 detectors the absolute error is less than 2 % over the range considered in the study (see Fig. 13) , it has to be noted that the error is close to the statistical error of the MC code. At

ISBN 978-3-95450-185-4

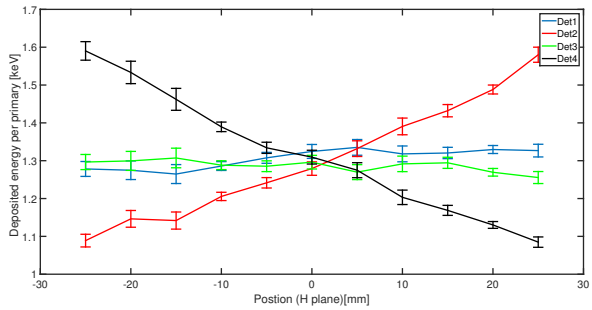

Figure 12: Energy deposited in each of the detectors at y=0 when the horizontal plane is scanned. Similar results are observed in the vertical plane with an inversion of the detector curves (i.e the flat curves are obtained with detector 2 and 4).

lower beam energy, the effect on the border will be higher, simulations are on going.

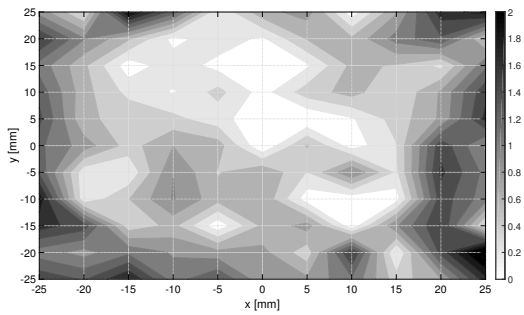

Figure 13: Absolute error map as function of the wire position, the beam energy is equal to 2000 MeV.

CONCLUSION AND OUTLOOK

The detector concept proposed in this paper seems interesting for the ESS application, in particular the absence of sensitive electronic in the tunnel area. The signal is expected to be less perturb by the interference of a high power accelerator environment (in particular the RF system), the conversion from light to current in the electronic cabinet will allow a cleaner signal.

Nevertheless, some assumptions taken during the study shall be confirmed, as mentioned in this paper the optical interfaces are almost perfect and the light trapping efficiency in the silica fiber to be evaluated, for this it is excepted to develop a small set-up in our laboratory. Prototypes might be down in order to asses this issues, in an ideal scenario, a beam test of few variants of the detector assembly shall be tested with beam, the goal will be to calibrate the MC simulations. In particular few reflective materials can be tested as well as different options for the optical coupling of the various part of the detector assembly. This phase will allow also to finalize the choice of the WLS fiber.

A full study of the Cherenkov detector will be also performed in the coming months.

REFERENCES

[1] M. Eshraqi et al., "The ESS linac", in *Proc. IPAC'14*, Dresden, Germany, THPME043, pp. 3320-3323.

[2] B. Cheymol, "ESS wire scanner conceptual design" ESS Technical note ESS-0020237.

[3] S. Filippov et al."Experimental Performance of SPD/PS Detector Prototypes" CERN-LHCb-2000-031.

[4] L. Zhang et al. "LSO/LYSO Crystals for Calorimeters in Future HEP Experiments" in *J. Phys.: Conf. Ser. 293 012004* 2011.

[5] A. Ferrari, P.R. Sala, A. Fasso, and J. Ranft, "FLUKA: a multi-particle transport code" CERN-2005-10 (2005), INFN/TC_05/11, SLAC-R-773.

[6] F. Duru et al."CMS Hadronic EndCap Calorimeter Upgrade studies for SLHC Cherenkov light collection from quartz plate" CMS note 2007/019 May 2007.

ISBN 978-3-95450-185-4

ONLINE MEASUREMENT OF THE ENERGY SPREAD OF MULTI-TURN BEAM IN THE FERMILAB BOOSTER AT INJECTION*

J. Nelson, Brown University, Providence, RI, U.S. A.
C.M. Bhat† and B. S. Hendricks, Fermilab, Batavia IL, U.S.A.,

Abstract

We have developed a computer program interfaced with the ACNET environment of Fermilab accelerators to measure energy spread of the proton beam from the LINAC at an injection into the Booster. It uses a digitizing oscilloscope and provides users an ability to configure the scope settings for optimal data acquisition from a resistive wall current monitor. When the program is launched, a) a *one shot timeline* is generated to initiate beam injection into the Booster, b) a gap of about 40 ns is produced in the injected beam using a set of fast kickers, c) collects line charge distribution data from the wall current monitor for the first 200 μs from the injection and d) performs complete data analysis to extract full beam energy spread of the beam. The program also gives the option to store the data for off-line analyses. We illustrate a case with an example. We also present results on beam energy spread as a function of beam intensity from recent measurements.

OVERVIEW

In recent years Fermilab has undertaken significant improvements to the existing accelerators to meet its high intensity proton demands for accelerator based HEP experiments onsite as well as long baseline neutrino experiments. One of the important aspects of this program is "Proton Improvement Plan" [1] with a baseline goal to extract the beam at 15 Hz rate from the Booster all the time with about 4.6E12 p/Booster cycle. With PIP -II [2], it is foreseen to increase the Booster beam delivery cycle rate from 15 Hz to 20 Hz, replace the existing normal conducting LINAC by superconducting RF LINAC and increase beam intensity by 50%. Hence, the current Booster plays a very significant role at least the next one and half decades in the Fermilab HEP program.

In support of the proposed upgrades to the Booster, a thorough understanding of the properties of the beam at injection is crucial; in particular, monitoring energy spread of the beam from the LINAC after the completion of injection. In the past, many attempts have been made to measure beam energy spread (e.g., ref. [3]) in bits and pieces using up dedicated beam time; often such measurements are carried out only soon after a major maintenance period. Furthermore, all the past measurements were on partial turn beam in the Booster. During 2013-2014, we developed a very robust method [4] to measure the beam energy spread on the multi-turn beam after creating a notch of width ≈ 40 nsec in the injected beam. These attempts lead us to develop an application software to automatize beam energy spread measurement at injection on request. In this paper we explain the general principle, various functionalities of the software and illustrate with recent measurements.

* Work supported by Fermi Research Alliance, LLC under Contract No. De-AC02-07CH11359 with the United States Department of Energy
† cbhat@fnal.gov

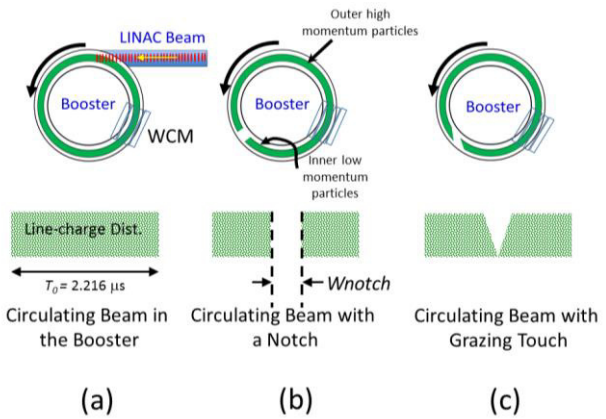

Figure 1: Schematic of newly injected multi-turn beam from the LINAC with a notch and notch filling due to slippage of the particles.

APPLICATION SOFTWARE

Physics Behind the Program

Particle beam that exits a pre-accelerator will always be having an energy spread ΔE(full) about its mean (synchronous) energy E_s. When such a beam is injected into a synchrotron and accumulates, the higher and lower momentum particles slip differently relative to the synchronous particle while they circulate in the synchrotron. A schematic view of particle distribution of such a beam injected from the LINAC into the Booster is shown in Fig. 1(a). However, to differentiate between fast moving particles from the slow moving particles, one can create a notch (Fig. 1(b)) of width "*Wnotch*" in a fully debunched beam using a fast beam kicker and monitor the slippage of particles relative to particles with synchronous energy (see Fig. 1(c)). Evolution of line-charge distribution measured using a wall current monitor (WCM) for each case is shown in Fig 1 for clarity. By measuring the notch width and the time required for the highest momentum particles to cross (or touch in WCM data) the lowest momentum particles, "*Tgraze*", we can extract the beam energy spread using,

$$\Delta E = \frac{\beta^2 E_s}{|\eta|}\frac{Wnotch}{Tgraze}$$

Where, β is the relativistic speed and η is the slip factor of the Booster lattice (≈-0.4582).

ISBN 978-3-95450-185-4

Program Overview and Measurement

The Fermilab Booster is a 15 Hz rapid cycling synchrotron built using combined function dipole magnets. The Booster receives beam from the 400 MeV LINAC with 200 MHz bunch structure and operates between an injection kinetic energy of 400 MeV and extraction kinetic energy of 8000 MeV for protons. The beam revolution period at injection in the Booster is $T_0 \approx 2.216\ \mu s$. A single beam pulse from the LINAC is up to about 60 μs, capable of providing > 25 Booster turn beam at a beam delivery rate of 25 mA. However, currently the maximum number of Booster turn is set to be about 18 for operational safety. Generally the 200 MHz bunches from the LINAC do exhibit variation in the intensity and possibly a small variation in the beam energy spread through the pulse. Figure 2 depicts typical LINAC pulses for 4, 13, 14 Booster turn beam. Hence, after the completion of the injection it may be required to allow a few revolutions to settle down and to give a constant line charge density DC beam before the notch is produced. In addition to this, there is an additional complication from bunch formation due to a small amount of left-over RF voltage from the main accelerating RF cavity of the Booster, unless the power amplifiers are turned off completely.

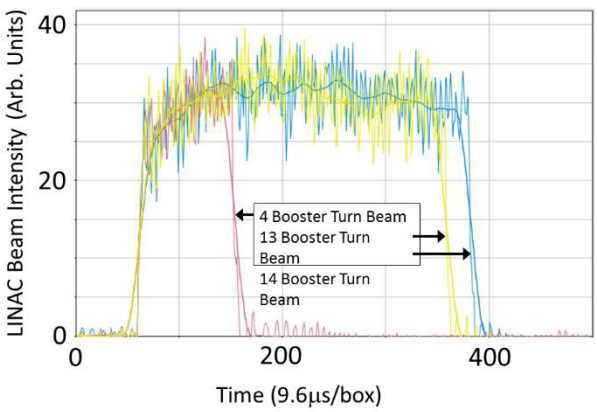

Figure 2: Typical LINAC beam pulses jest before injection into the Booster.

To measure the longitudinal properties of the circulating beam in the Booster one uses a 6 GHz bandwidth wall current monitor (WCM) [5] (see Figure 3). A fully debunched beam cannot be detected using the WCM; for such a beam the WCM signal looks like the one shown in Figure 1(a). As soon as a notch is produced using a set of fast kickers [6], one can see distinctly the region without beam and one with beam; an integration of the WCM signal for period T_0 scales as the beam intensity. By taking the WCM data for several revolutions one can study the time evolution of the notch. A Tektronix, TDS7154B Digital Phosphor Oscilloscope of type 1.5GHz 20GS/s is used in the Booster to record the WCM data.

The application program was designed to be used in Fermilab ACNET Console Environment. A schematic view of the flow chart representing the structure of the soft-ware

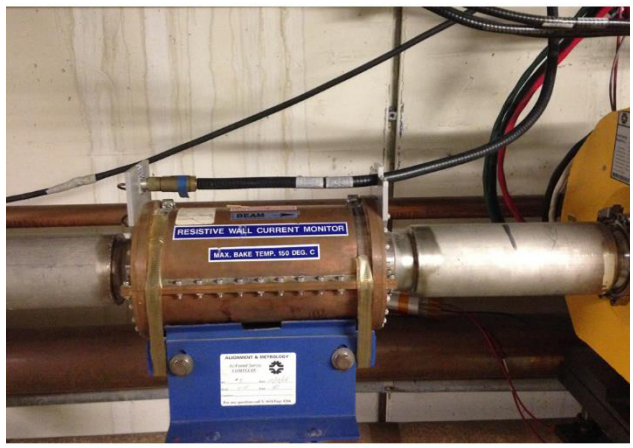

Figure 3: Wall Current Monitor in the Booster ring.

program is shown in Fig. 4. This program controls various types of hardware that are necessary to measure the energy spread of the beam. The program works as follows:

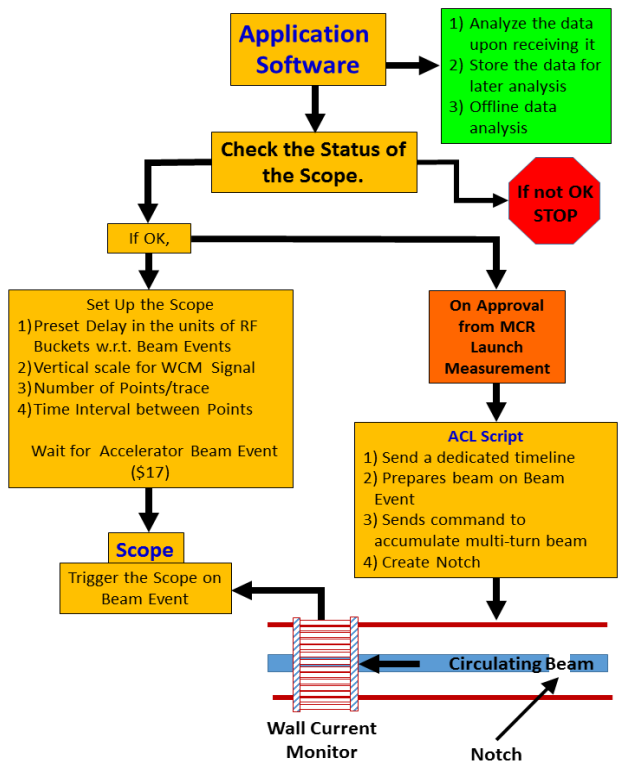

Figure 4: The flow chart of the application software.

1) Check if the executing the program is safe (all necessary instruments are available to measure the Booster energy spread) and warns if another user is using the same devices. If so, one cannot proceed.

ISBN 978-3-95450-185-4

2) If it is ok, then user can send scope set up. Then the program sets necessary parameters on the Tektronix scope *viz.*, a) a window for receiving WCM data with upper and lower amplitude levels (default values are 1 V and -.04 V, respectively, if WCM signal saturates than user need to set properly), b) number of data points (default is 50000 for "Record length"), c) space between the data points ("interval" 0.4 ns), d) beam event of interest and e) a constant delay with respect to beam event to start collecting the data.
3) If the scope is available, then program executes another software written in *accelerator command language* (ACL) upon permission from the Main Control Room (MCR) crew chief which enables a) a "*1-shot timeline*. (A timeline is a user requested sequence of different types of accelerator system *clock* events, with and without beam, put in certain order to make accelerator operation smooth. This is specific to Fermilab ACNET environment), b) moves all timers related to RF paraphrase, beam feedback to later settings predetermined by the user, c) moves notch timer to soon after the injection. Number of Booster turns is set ahead of issuing the ACL script. Once the ACL command is issued the rest of the beam operation is automatic.
4) Scope collects the WCM data.
5) Analysis the data to extract the beam energy spread.
6) Gives a graphical output on a separate window for the user's perusal.

Some highlights of this programs functionality is, it is the first application program developed for the Fermilab Booster that can measure the beam energy spread of a multi-turn beam in the Booster at injection. This program gives an ability to measure the beam energy spread with minimum interruption on the operation and would help to improve the overall Booster performance.

Analysis of the Data

The online analysis of the WCM data is one of the critical task of this application program. Once the data is collected the data can be can be analysed online or offline after saving it. As far as this software is concerned the analysis of the data online or offline is identical. In both cases, the program has to make several decisions. For example, a) search for the first notch and the subsequent appearance of the notch on each revolution, b) determine notch width (95%), c) time required for grazing touch and d) average revolution period, etc.,

Before developing this application program two packages, one using MATLAB environment and another using Python platform [7] were developed for off-line data analysis. These two packages helped us to benchmark the newly developed program and make it very robust.

Search for the 1st Notch

An example of the data received from the WCM for ≈100 revolution in the Booster around injection is shown in Fig. 5. The icicle type structure develops soon after the first notch is produced in the beam and as the same notch arrives at the WCM once per revolution. Electronics used in the WCM before the data arrives at the scope is a DC coupled system. Consequently, as the multi-turn beam is injected into the Booster the beam amplitude increases initially above the background level and then slowly starts to decline as beam settles down. Hence one sees formation of a structure that resembles horse *mandible* and *cervical vertebrae* shape to the line charge distribution. The increase in the amplitudes of WCM data after about 150 μs is due to increasing RF voltage.

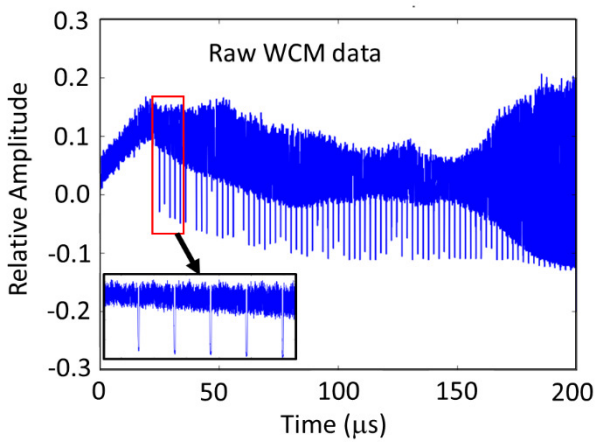

Figure 5: WCM data for the first 200 microsecond around injection. Zooming in it is possible to see a few of these notches, each is about 2.2 microseconds from each other (as shown in inset).

Over time the notch depth starts to decrease as the particles with different momenta drift toward its center and the notch begins to fade away. Until the grazing touch (for example see, picture "c" in Fig. 1), the notch depth or integrated area between two successive notches in the WCM data remains constant. Beyond the point of the grazing touch, the depth of the notch start decreasing. Therefore, by following the evolution of the notch and measuring the integrated area of WCM data for every revolution we should be able to measure the time required for grazing touch.

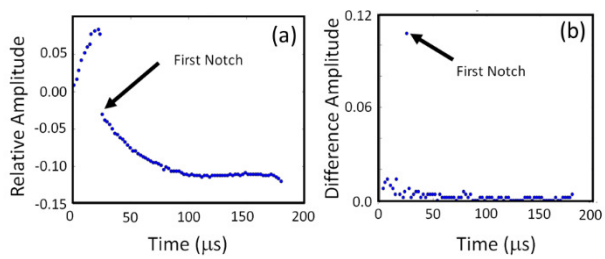

Figure 6 (a) Plot of all the minimum for every 2.2115μs. The first notch appears immediately after a large jump. (b) The absolute difference of the next point and its "left neighbour".

ISBN 978-3-95450-185-4

First the program scans the entire WCM profile shown in Fig. 5 and then it uses a guess period of 2.2115 μs to make "approximate cuts". The program then searches for the minimum in each piece and saves those amplitude values and their corresponding time coordinate. Since we are interested in knowing when the notch appeared in the WCM data for the first time and in knowing its width accurately, the program compares all minima and looks for where a sudden large jump occurs in the amplitude of the minimum. The time associated with first large excursion point in the searched set of amplitudes of minima in WCM data represents occurrence of the first notch. The program infers that the subsequent minimum from the first notch are the notch at subsequent revolutions. Figure 6 depicts result of the algorithm for a typical data set where the location of the notch is identified. To make identification of the first appearance of the notch more robust we take differential in minimum amplitude between cuts as shown in Fig. 6(b). This gives unambiguous time stamp for the first notch.

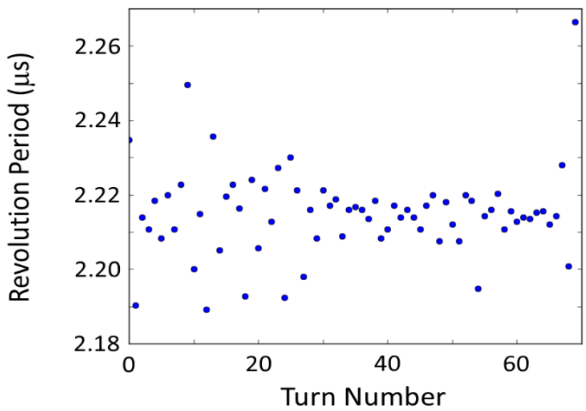

Figure 7: Revolution period versus index of appearance of the notch.

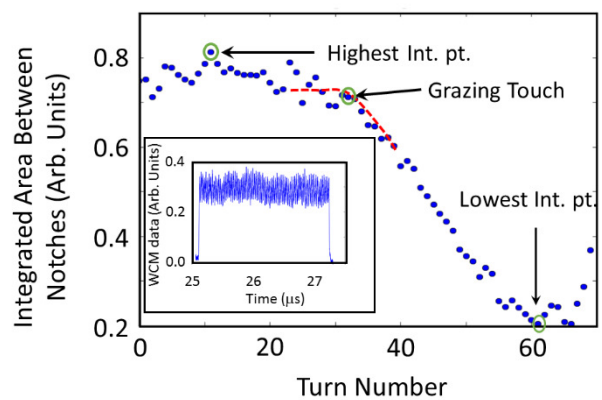

Figure 8: Revolution period versus turn number (index of appearance of the notch) from first notch. The inset shows typical beam WCM data between two successive appearances of a notch.

Figure 7 shows the time difference between the successive notch appearance and the index number of the notch (turn number). The revolution period is calculated taking an average of the first few points from Fig.7. Using newly calculated revolution period we can obtain better cuts on the data. The large scatter observed in the measured revolution period arises from the uncertainty in the location of the minimum in the notch region.

Figure 8 shows the integrated area between two successive minima established as in Fig. 6 (a) as a function of turn number. The base line for each revolution is calculated as an average of the minimum amplitude at notch region. Knowing the calibration factor between image current and the signal area as measured by the scope one can measure the beam intensity at injection soon after the notch is formed.

Data in Fig. 8 show that after the grazing touch the area starts falling down. This happens because the background level at the notch starts raising up due to the slipping off momentum particles in the ring. Measuring the number of revolutions required for the grazing touch is crucial. The program makes a decision based on an algorithm. It first calculates the approximate area of the *Tgraze* (which is the "Top notch"-("Top notch"-"Bottom notch")*0.15) and then starting from the lowest intensity point (see Fig. 8) comparing each point to this approximate area of the Tgraze. When it reaches a value greater than or equal to this approximated value the program has found the inflection point and stops. The corresponding turn number multiplied by revolution period gives *Tgraze*.

Finding the Notch Width

The shape of the notch even when it is formed will not be a nice rectangular well; in reality, its shape depends on the kicker pulse shape that produces the notch. Furthermore, non-zero voltage on the accelerating RF cavities, Vrf , gives rise to some level of bunching as shown in Fig. 9. (As long as the bucket height due to the Vrf is much smaller than beam energy spread, this method works very well).

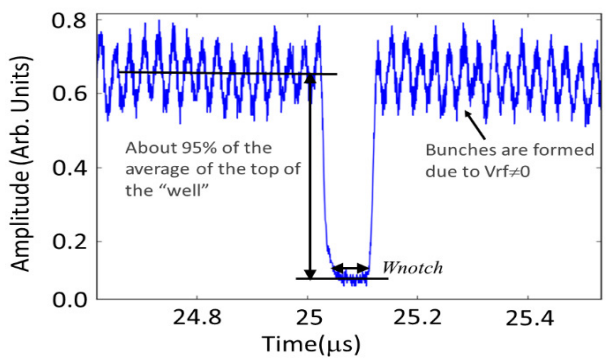

Figure 9: Width of the first notch.

Consequently, the error in measured notch width will contribute a large uncertainty in the final energy spread. The average of the baseline inside the notch where there is no beam and average of the bunch signal where there is beam,

ISBN 978-3-95450-185-4

were both calculated (see Fig. 9). The difference between these two averages gives the depth of the notch. Then we determine the width of the notch by searching for 95% drop on both sides of the notch. Such search is performed on the trace of the 1st notch as it appears in the WCM data.

Data Analysis and Results

Typical results from the data analysis are shown in Figure 10. The raw data for first 200 μs is displayed on the top. 1st notch in the beam, and an apparent beam intensity used to determine the grazing touch are shown in the middle row. The values of the measured full momentum spread "dP/P", measured number of revolutions needed for grazing touch "Graze Touch", momentum of the synchronous particles "P", the measured revolution period "Trev", and the measured notch width "NW" are displayed at the bottom for Fig. 10. The middle two figures can also be used to examine the displayed measured values qualitatively.

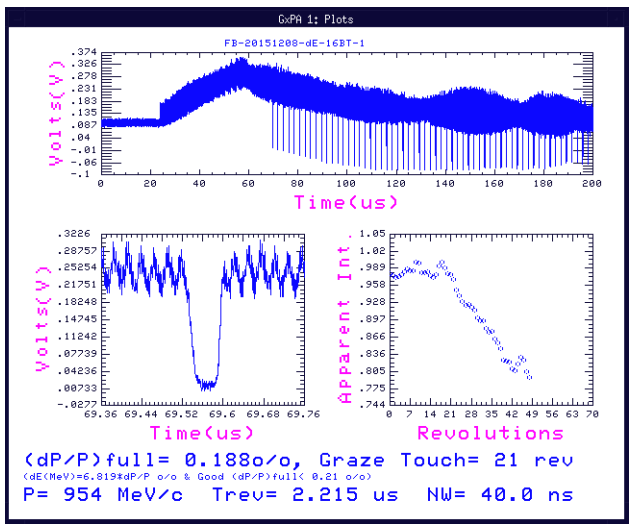

Figure 10: Result display from the program.

Figure 11 displays the measured values of the energy spread for different Booster beam intensities using the application program for the past six months. For example, the blue circles representing the measurements from March 24, 2016 for intensity in range of 1E12-6E12 p/Booster cycle did not show intensity dependence. The average energy spread from these measurement is ΔE (full) = 1.25 ±0.20 MeV.

There are multiple sources of uncertainties in the measured energy spread arising from systematics (which are not taken into account in the quoted values above)−1) the uncertainty in slip factor η would introduce about 1%, 2) the uncertainty in the beam energy give about 0.5%, 3) error in decision on *Tgraze* expected to be about 10% and 4) error on *Wnotch* expected to be about 5%. The errors from "3" and "4" can be reduced significantly by turning off the Vrf amplifier. These sort of measurements need dedicated beam time. We expect an overall error on the measured value of ΔE (full) is about 20%.

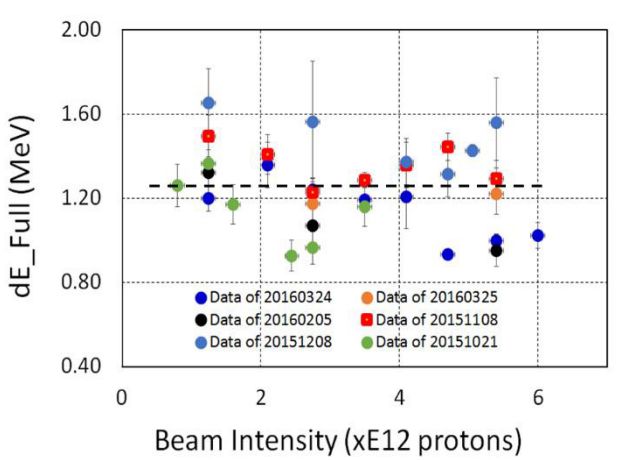

Figure 11: Measured full beam energy spread in the Booster at injection for different beam intensities over the past 7 months. The error bars are the maximum deviation from the mean values.

ACKNOWLEDGEMENT

Special thanks to Ming-jen Yang for many useful discussions and his help regarding data taking from the Tektronix scope. Thanks are also due to K. A. Triplett for his help in beam studies, cooperation from the MCR crew during the development of this software, and Demetrius Andrews for editing the manuscript. One of the authors J. Nelson would like to thank Fermilab 2015 SIST Summer intern program for financial support.

REFERENCES

[1] W. Pellico, et al., IPAC2014 (2014) p 3409; R. Webber et al., Beams Document 3781-v2 (2011).
[2] "The PIP-II Reference Design Report," V1 March 2015, http://www-bdnew.fnal.gov/pxie/PIP-II_RDR/ PIP-II_RDR.pdf.
[3] M. Popovic, (private communications, 2014).
[4] C. M. Bhat, et al., IPAC2015 (2015), THPF113, pp.3979-3981
[5] R. C. Webber, *AIP Conference Proceedings 212*, "Accelerator Instrumentation" 1989, p 85.
[6] "Booster Beam Notching," Salah Chaurize, *Workshop on Booster Performance and Enhancement*, November 23-24, 2015, Fermilab Beams Document 5013-V2; J. Lackey (private communications).
[7] C. M. Bhat, "MATLAB program for offline data analysis to measure beam energy spread" (2013-2015), also see IPAC2015 (2015), THPF113; J.J. Nelson and C. M. Bhat (Python package 2015, unpublished).

ISBN 978-3-95450-185-4

FERMILAB BOOSTER TRANSITION CROSSING SIMULATIONS AND BEAM STUDIES *

C.M. Bhat† and C.Y. Tan, Fermilab, Batavia, IL 60510, USA

Abstract

The Fermilab Booster accelerates beam from 400 MeV to 8 GeV at 15 Hz. In the PIP (Proton Improvement Plan) era, it is required that Booster deliver 4.2×10^{12} protons per pulse to extraction. One of the obstacles for providing quality beam to the users is the longitudinal quadrupole oscillation that the beam suffers from right after transition. Although this oscillation is well taken care of with quadrupole dampers, it is important to understand the source of these oscillations in light of the PIP II requirements that require 6.5×10^{12} protons per pulse at extraction. This paper explores the results from machine studies, computer simulations and solutions to prevent the quadrupole oscillations after transition.

INTRODUCTION

The Fermilab Booster was built in the 1970s [1] and will remain the workhorse for the PIP (Proton Improvement Plan) II era for many years until it is replaced. From the start of its operational life to the present (2016), the beam flux per hour through it has increased by an order of magnitude. See Fig. 1. The goal of PIP is to provide 4.2×10^{12} protons per pulse at extraction. And in the PIP II era, Booster is required to provide 6.5×10^{12} protons per pulse at extraction. There can be many show stoppers that prevent us from achieving the PIP II goals. [2] One obstacle that we have identified is transition crossing.

The traditional belief at Fermilab is that transition crossing in Booster is dominated by space charge effects or other beam intensity effects. [3–5] Many simulations have been done to reproduce measurements and to suggest methods to help the beam cross transition properly. However, from what we can see, these simulations only use a select few Booster beam pulses for comparison which we have found to be very naïve. In our experience, there is sufficient pulse to pulse variation in any measurement that we need to have a large enough sample set to actually be able to have any insight into the problem.

Therefore, in order to avoid the pitfall of using too few data sets, we have collected sufficient Booster transition crossing data for our analysis. We will use this data to generate a hypothesis as to what causes the beam to suffer from quadrupole oscillations after it crosses transition. We will then test our hypothesis with computer simulations. And finally, we will suggest methods for mitigating this problem.

* Operated by Fermi Research Alliance, LLC under Contract No. DE-AC02-07CH11359 with the United States Department of Energy.

† cbhat@fnal.gov

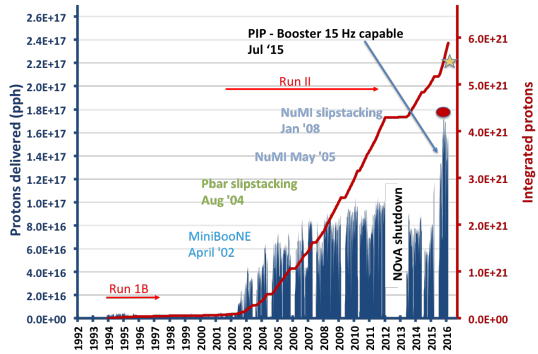

Figure 1: The proton flux per hour in Booster increased from $< 10^{16}$ to $> 10^{17}$ over a decade.

MOTIVATION

One of the recent striking observations that led to suspect the traditional lore mentioned earlier was that the amplitude of the longitudinal quadrupole oscillations measured with a wall current monitor (Fig. 2) did not scale at least as a quadratic w.r.t. beam current, I_b. (Note: it is quadratic because we are using a wall current monitor to measure the quadrupole oscillations and thus the measured amplitude contains a factor of I_b. For example, the emittance growth from space charge effects has another factor of I_b. [6]). In fact, it looked like the amplitude of the quadrupole oscillations was independent of I_b after normalizing the measured amplitude w.r.t. I_b. An example of what we saw is shown in Fig. 3 for 4.5×10^{12} and 2.5×10^{12} protons per Booster batch where the quadrupole dampers have been set to a very low gain value (0.1 units). These plots trace the evolution of the I_b normalized 2× synchrotron peak during the ramp. We noticed that the maximum amplitude of the quadrupole peak is ∼0.5 units in both cases and is independent of I_b.

These observations motivated us to investigate whether the source of quadrupole oscillations is, in fact, a bucket mismatch rather than from space charge or other beam intensity effects.

DATA COLLECTION AND ANALYSIS

The wall current data clearly exhibits quadrupole oscillations after transition. In order to clearly see these oscillations, the data has to be processed to reveal the amplitude modulation. This is easily done by peak detecting the data. Two examples of the wall current data after peak detection and filtering is shown in Fig. 4.

The plots shown in Fig. 4 were taken with the quadrupole dampers on and with $\sim 4.5 \times 10^{12}$ protons. Under these

ISBN 978-3-95450-185-4

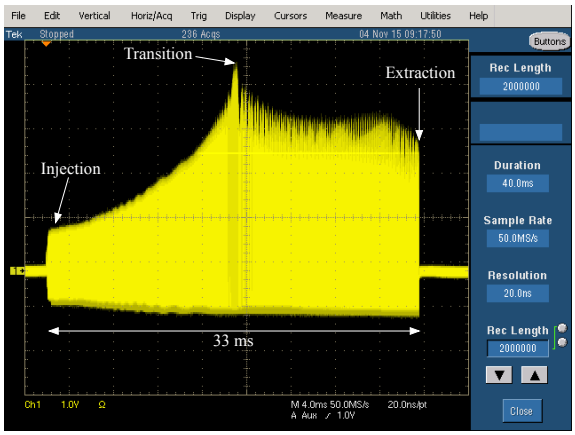

Figure 2: The wall current signal for the entire ramp as seen on an oscilloscope. There is clearly a quadrupole oscillation after transition.

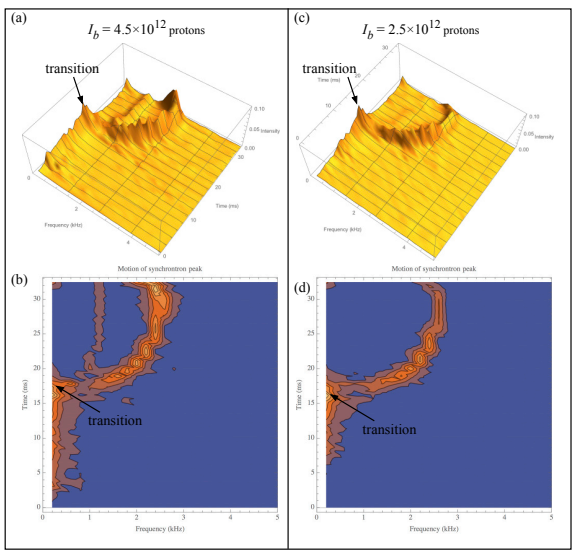

Figure 3: The motion of the intensity normalized 2× synchrotron peak during the ramp. The quadrupole dampers have been set to a very low gain value (0.1) in these plots.

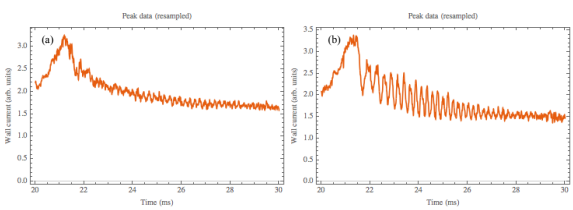

Figure 4: These plots show the envelope of the beam current after processing. Both (a) and (b) were taken with the quadrupole dampers on and beam current $\sim 4.5 \times 10^{12}$ protons.

supposed same conditions, it is obvious, that their behaviors are quite different at transition crossing. These two plots demonstrate that it is important to take multiple data sets rather than just rely on a few. The variations in their behavior can be traced back to the capture process and to the jitter of the Booster dipole ramp. The former is less likely because we have made the capture more adiabatic recently [7].

Jitter in the Booster Dipole Ramp

The Booster dipole ramp comes from a 15 Hz resonant circuit. The Booster RF is not a function of the dipole ramp. Instead its frequency ramp is triggered with an event called TCLK. Since these two systems are not tied together, there is a difference between the true transition time, which is determined by the energy of the ramp, and where the RF thinks it should execute its transition phase jump. Thus, there is a jitter between TCLK and the zero crossing of the Booster ramp. Its distribution is shown in Fig. 5.

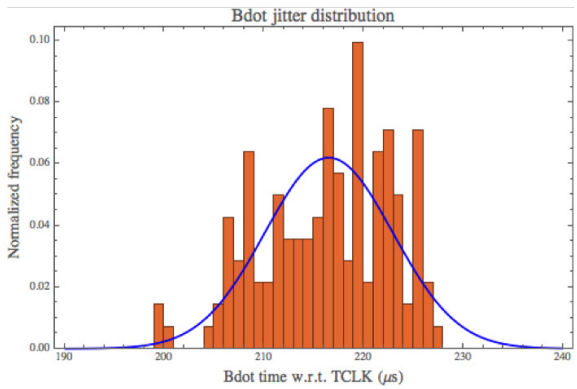

Figure 5: This shows the jitter between the zero crossing of the magnet ramp (Bdot) and the TCLK event.

From the measured data, we found that the base spread of the zero crossing of the Booster ramp (Bdot) and the TCLK event is about 30 μs with a mean value $\pm 6.4\mu$s. However, this jitter can introduce an error as much as ±10 Booster turns at transition!

Quantifying the Mismatch

We will parameterize the mismatch by taking the ratio of the first quadrupole peak to the transition peak. The advantages of doing this are that the strength of the wall current signal is normalized and any later bunch evolution effects do not affect it. An example of how we get the ratio is shown in Fig. 6.

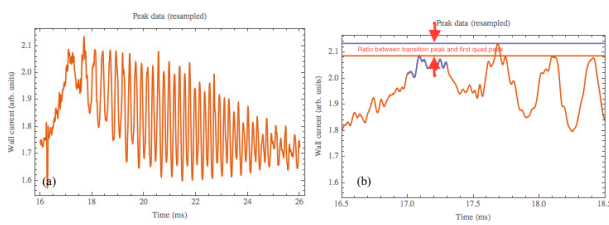

Figure 6: (a) This is an example of the envelope of the modulation with the quadrupole dampers turned off (b) The quantification of the mismatch is the ratio between the first quadrupole peak and the transition peak.

ISBN 978-3-95450-185-4

Measurement Results

We took data at two different intensities 2.5×10^{12} protons (8 Booster turns) and 5.2×10^{12} protons (16 Booster turns) as a function of RF transition time setting. This time, we turned off the quad damper on all measurements to avoid any bias arising from the dampers. More than 10 data sets were collected for each RF transition time setting. All the data were then processed to get the ratio between the first quadrupole peak and the transition peak. The results are shown in Fig. 7. It is clear from this figure that both data sets have the same minimum value but shifted, irrespective of the beam intensities. We interpret that this shift comes from beam loading of the cavities. Next, we can also see that the spread of the data at each RF transition time setting tells us that we have to collect enough data before performing any analysis. Insufficient data can lead us to the wrong conclusions if we are not careful.

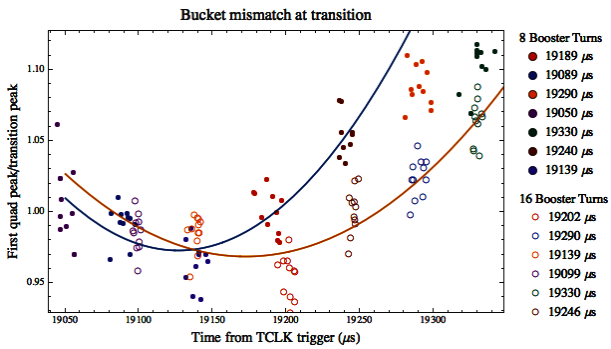

Figure 7: The ratio the transition peak to the first quadrupole peak of 8 BT and 16 BT are plotted here. The quadratic curves are used for guiding the eyes only.

Finally, we can form a hypothesis from the data. Our interpretation of these measurements is that space charge or beam intensity effects are not the dominant source of the quadrupole oscillations because there are no obvious I_b dependent effects. Therefore, our hypothesis is that bucket mismatch is the culprit.

SIMULATIONS

We have carried out 2D longitudinal beam dynamics simulations using ESME [8] to study the variation of peak current by taking into account the longitudinal space charge effects in our simulation model. The self-impedance per revolution harmonic n arising from space charge in a beam traveling in a perfectly conducting beam pipe is modeled as,

$$\frac{Z}{n} = -\frac{Z_0[1 + 2ln\left(\frac{b}{a}\right)]}{2\beta\gamma^2} \qquad (1)$$

and by relating the Fourier coefficient of the space charge energy increment with that from the beam current. Where Z_0, a and b are impedance of free space (=377 Ω), beam pipe radius and average beam radius, respectively. We do not include any other impedances like impedances from resistive wall or RF cavities/bellows etc. It is important to notice that the Booster does not have any beampipes in the region of the dipoles. So, we have to take extra precautions when specifying the radius of the beampipe. We use $\gamma_T = 5.4782$ for the transition gamma for the Booster lattice. We assume that the beam and beam pipe radius to be 1.0 cm and 2.86 cm, respectively. The simulations were carried out as follows: (1) Inject LINAC beam pulses with 200 MHz structure. Each bunch is populated with parabolic distribution with $\Delta E \approx$ 1.4 MeV [9]. (2) Assume beam intensities of 3×10^{12} and 6×10^{12} protons/Booster batch. (3) Capture the beam iso-adiabatically. The observed emittance growth was about 20% during capture. (4) The beam is accelerated on a sinusoidal magnetic ramp up to about 6.8 GeV, which is well beyond the transition crossing. (5) Assumed one-turn RF phase jump near transition. These simulations were repeated at various values of slip factor, η, around the transition energy which are indicated in Fig. 8.

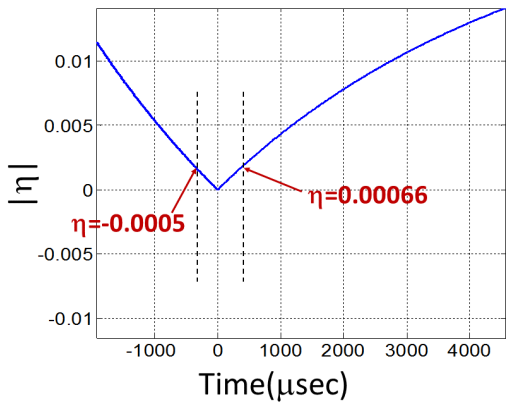

Figure 8: Absolute values of η versus time around transition. The minimum value on the curve corresponds to$|\eta| = 0$. The range of η used for the simulations are indicated by the dashed lines.

Figure 9 shows the simulated peak currents and its oscillations after transition crossing. The predicted oscillations of the peak current (which comes from bunch length oscillations) is certainly due to bucket mis-match. Simulations also show beam particle losses if the phase jump is forced to be far away from $\eta = 0.0$, this is consistent with measurements though we do not know exactly when $\eta = 0.0$. In any case, simulations show that if we go up in intensity from 3×10^{12} protons/Booster batch to 6×10^{12} protons/Booster batch we do not see the change in the amplitude of the oscillations which would scale with intensity if the space charge force plays a dominant role. This feature is very similar to the measurement that we have shown in Fig. 10.

Finally, we compare measurement data with predictions. The comparison shows oscillations that have similar features both in amplitude and phase despite our lack of knowledge about when $\eta = 0.0$ exactly occurs in our measurements. In this presentation, we have aligned the first two peaks where

ISBN 978-3-95450-185-4

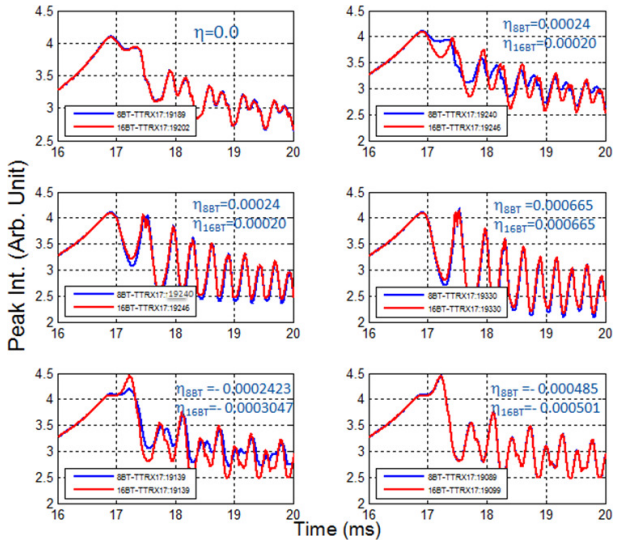

Figure 9: Simulated peak currents as a function of acceleration time for various slip factors around the transition energy. The blue curve is 3×10^{12} and the red curve is 6×10^{12} protons per Booster batch.

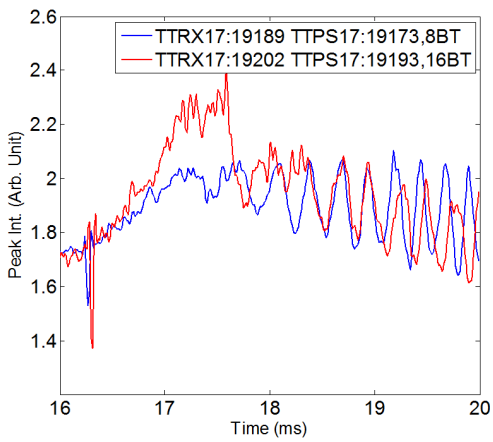

Figure 10: Measured peak intensity oscillations for the optimal settings of transition phase jumps with quad-dampers off for 2.7×10^{12} protons/Booster batch (blue) and 5.2×10^{12} protons/Booster batch (red).

the bunch length is minimum. Our comparisons for 2.7×10^{12} protons/Booster batch and 5.2×10^{12} protons/Booster batch are shown in Fig. 11. In both cases, the measured frequency of the oscillations are higher than what we have predicted. This needs further investigations.

MITIGATION

From our measurements, the cause of the oscillations after transition crossing in the Booster comes from multiple sources. The dominant sources are: (1) Bdot jitter. See for example Fig. 7 and (2) phase mismatch (see for Fig. 9). The source of the Bdot jitter can be traced to the variation in the magnetic ramp due to changes in the ComEd power line

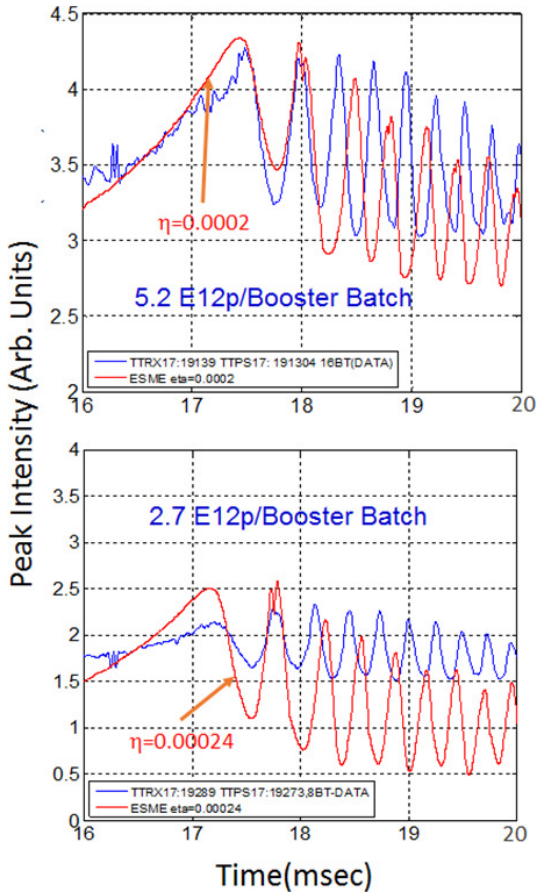

Figure 11: Measurement data compared with simulations. In the absence of information on measurement data on $\eta = 0.0$, we compare data with simulation in a rather random way based on similar features on oscillations. Exact comparison needs further information on measurements on timings of$\eta = 0.0$

frequency which is of the order of 100 mHz out of 60 Hz. Since the Booster magnets have a 15 Hz sinusoidal ramp that is derived from ComEd, the power line frequency errors introduce both time and amplitude jitters of the order of 50 μsec in the minimum magnetic field, $B_{\min}$, (as well as at the maximum magnetic field, $B_{\max}$) relative to the beam injection time. This in turn introduces time jitter to the transition RF phase jump leading to the oscillations. Our observations clearly show a cycle dependent factor in the bunch length oscillation amplitudes which is much larger than any other effects, in particular beam intensity. Currently, R&D for mitigating the Bdot jitter is being carried out. To correct for the phase mismatch, we are making improvements to the LLRF (low level RF) to incorporate transition phase jumps based on RF frequency rather than on the "start of cycle" event from the clock system (TCLK). Since our measurement data shows longitudinal space charge is not an issue at beam intensities of the order of 5.5×10^{12} (supported by simulations), we have extended our simulations to higher beam intensities. From these simulations, we have found that we

ISBN 978-3-95450-185-4

can increase beam intensities by more than 50% from the current maximum operational beam intensities without any quadrupole oscillation problems due to space charge. The higher intensity simulations are above the baseline beam intensity limits set by the PIP-II design [2].

CONCLUSION

Our measurements and simulations show that the leading cause of the quadrupole oscillations after transition come from bucket mismatch and not from space charge or beam intensity effects. In addition, because of Bdot jitter there is significant variation in the bucket mismatch from cycle to cycle. To mitigate these oscillations we have proposed two solutions — not any one by itself can solve the problems; both of them need to be in place for better performance of the Booster and intensity upgrades.

ACKNOWLEDGMENTS

We wish to thank W. Pellico for helpful discussions.

REFERENCES

[1] "Fermilab History and Archives Project", http://history.fnal.gov/booster.html

[2] "The PIP-II Reference Design Report," V1 March 2015, http://www-bdnew.fnal.gov/pxie/PIP-II_RDR/PIP-II_RDR.pdf.

[3] X. Yang *et al*, "Reducing the Longitudinal Emittance of the 8-GeV Beam via the RF Manipulation in a Booster Cycle", Fermilab Notes, FN-0770-AD, 2005.

[4] X. Yang *et al*, "Transition Crossing Simulation at the Fermilab Booster", TUPAS042, PAC'07, Albuquerque, New Mexico, USA, 2007, pp. 1739-1741.

[5] V. Lebedev, "Acceleration and transition crossing in Booster", Beams-doc-5146-v2, http://beamdocs.fnal.gov/AD-public/DocDB/ShowDocument?docid=5146, 2016.

[6] J. Wei, "Transition Crossing", Handbook of Accelerator Physics and Engineering (3rd Ed), pg. 314–316, World Scientific, 2006. 27–36.

[7] C. M. Bhat, IPAC2015 (2015) p 3976; DPF2015,http://arxiv.org/ftp/arxiv/papers/1510/1510.08427.pdf; and proceedings of this conference.

[8] J. MacLachlan, ESME,http://www-ap.fnal.gov/ESME.

[9] C. M. Bhat *et al*, IPAC2015 (2015) p 3979.

ISBN 978-3-95450-185-4

STUDY OF MAGNETS SORTING OF THE CSNS/RCS DIPOLES AND QUADRUPOLES*

Y. An[1, 2, #], S. Xu[1, 2], S. Wang[1, 2], Y. Li[1, 2], J. Peng[1, 2], H. Ji[1, 2]
[1]Institute of High Energy Physics, Chinese Academy of Sciences(CAS), Beijing 100049, China
[2]Dongguan Neutron Science Center, Dongguan 523803, China.

Abstract

The Rapid Cycling Synchrotron plays an important role in the China Spallation Neutron Source. RCS accumulates and accelerates the proton beams from 80MeV to 1.6GeV for striking the target with the repetition rate of 25Hz. RCS demands low uncontrolled loss for hands on maintenance, and one needs a tight tolerance on magnet field accuracy. Magnet sorting can be done to minimize linear effects of beam dynamics. Using closed-orbit distortion (COD) and beta-beating independently as the merit function, and considering maintaining the symmetry of the lattice, a code based on traversal algorithm is developed to get the dipoles and quadrupoles sorting for CSNS/RCS. The comparison of beam distribution, collimation efficiency and beam loss are also investigated according to beam injection and beam accelerating.

INTRODUCTION

The CSNS accelerator consists of a low energy H^- Linac and high energy RCS. H^- beam with energy of 80MeV is scraped and transformed into proton beam by the carbon foil located in the injection region. After around two hundred turn accumulation, the proton beam is accelerated to 1.6GeV and then extracted to strike the target with the design power of 100KW. For the convenience of maintenance and high power requirements, the uncontrolled beam loss should be less than 1 Watt/m. In order to achieve this goal, the expected magnet errors are designed to be in the order of 10^{-3} for main dipoles and quadrupoles. Table 1 shows the main parameters of RCS [1].

Table 1: Main Parameters of RCS

Parameters	Units	Values
Circumference	m	227.92
Repetition Rate	Hz	25
Average current	μA	62.5
Inj. Energy	MeV	80
Ext. Energy	GeV	1.6
Beam Power	kW	100
Quad		48
Dipole		24
Corrector		16/16
BPM		32/32
Nominal Tunes(H/V)	1	4.86/4.78

As a key component of CSNS, RCS consists of 4-fold symmetric structure, and each of which is constructed by a triplet cell. Figure 1 shows the twiss parameters of RCS [2]. The long drift is reversed for the installation of cavities, collimator, injection elements and extraction elements, and the dispersion function in this area is designed to be zero. The short drift in the arc of the accelerator is reserved for installation of BPMs, correctors, sextupoles, and so on.

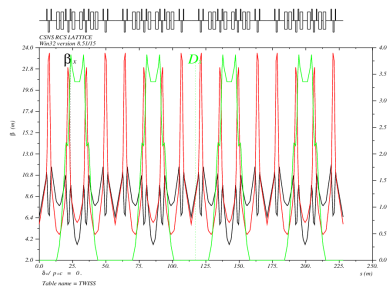

Figure 1: Twiss parameters of CSNS/RCS.

In section 2 we present in detail the sorting strategies. In section 3 we apply them to the CSNS/RCS model. In section 4 we investigate the sorting effects according to beam injection and beam accumulation. Conclusion is drawn in section 5.

SORTING STRATEGIES

Algorithm Description

Supposing there is M magnets should be arranged in M locations, the problems seems to be settled to find the solution of permutation of the M magnets. Now the steps of solving the problem are described as follows:

i) If there are two magnets, and the magnets indexes are A and B, the solution can be descripted as the order $\{A, B\}$ or $\{B, A\}$;

ii) If there are three magnets, and the magnets indexes are A, B and C. Firstly, the C magnet is fixed in the third location, and then the other two magnets can be sorted

*Work supported by National Natural Science Foundation of China (11405189)
#anyw@ihep.ac.cn

ISBN 978-3-95450-185-4

according to step one. Secondly, the *C* magnet is fixed in the second location, and then the other two magnets can also be sorted according to step one. Lastly, the *C* magnet is fixed in the first location, and then the other two magnets can also be sorted according to step one.

iii) If there are four magnets, and the magnets indexes are *A*, *B*, *C* and *D*. Firstly, the *D* magnet is fixed in the fourth location, and the other three magnets can be sorted according to step two. Secondly, the *D* magnet is fixed in the third location, and the other three magnets can also be sorted according to step two. Thirdly, the *D* magnet is fixed in the second location, and the other three magnets can also be sorted according to step two. Lastly, the *D* magnet is fixed in the first location, and the other three magnets can also be sorted according to step two.

iv) If there are *M* magnets, the magnet sorting can be done by repeating the above steps.

The above algorithm was developed with MATLAB, and then embedded in Accelerator Toolbox [3]. The above algorithm has advantage for its high efficiency on seeking the solutions and especially for a high memory tolerance compared with the code integrated in MATLAB such as *perms*.

Dipole and Quadrupole Sorting Strategies

There are 24 dipoles located along the azimuth of the ring, and can be divided into type-A and type-B dipoles. Type-A and type-B dipoles are powered by one power supply system but with different water cooling system. As shown in figure 2, the yellow column depicts type-A dipoles while the green column depicts type-B dipoles. In order to get a good arrangement of the dipoles, one needs to compare the closed orbit distortion (COD) caused by dipoles field errors and pick up the smallest closed orbit distortion. The process of the dipole sorting was to be done in two steps. Firstly, type-B dipoles were arranged for its corresponding smallest COD. And then, after the order of type-B dipoles were fixed, and the arrangement for type-A dipoles was figured for the evaluation of the COD. The dipoles field measurement was done in DC mode and AC mode, however, the DC dipoles field error was not conformed to AC dipoles field error very closely, and the most important that, the repeatability of field measurement in DC mode is about 2E-4 while that in AC mode is about 5E-4. So the arrangement of the dipoles was determined by DC field measurement.

There are 48 quadrupoles located along the ring, and powered by 5 group power supplies as follows: two strings of eight Q206 (diameter 206mm) quadrupoles, one string of sixteen Q272 (diameter 272mm) quadrupoles, one string of eight Q222 (diameter 222mm) quadrupoles, and one string of eight Q253 (diameter 253mm) quadrupoles. The quadruple distribution along the CSNS/RCS ring is also shown in figure 2. The red column depicts quadrupole Q206 with two power supplies, the blue column depicts quadrupole Q272, the pink column depicts quadrupole Q222, and the cyan column depicts quadrupole Q253.

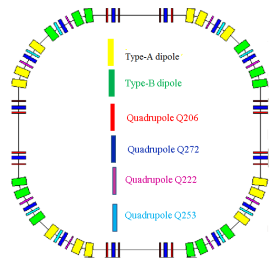

Figure 2: Magnet distribution along the CSNS/RCS ring.

DIPOLES AND QUADRUPOLES SORTING RESULTS

The field errors of dipoles can cause large closed orbit distortion, and that will make the central of beam oscillate close to the vacuum chamber. On the one hand, scattering along the vacuum chamber can make beam loss. On the other hand, the quantity of the magnet field off the center is a little worse than that in the centre of the magnet. So the dipoles should be sorted carefully. Firstly, one of the type-B dipoles was installed in the tunnel. Secondly, the left eleven type-B dipoles were carefully sorted by founding the smallest closed orbit distortion. Lastly, after the positions of the type-B dipoles fixed, the left twelve type-A dipoles were carefully sorted again by founding the smallest closed orbit distortion.

The field errors of the quadrupoles can cause beta beating, destroy symmetry of the lattice structure, and make beam emmittance growth. On the one hand, the lattice symmetry should be well restored. On the other hand, beta beating caused by quadrupoles should be well compensated by quadrupoles itself. When doing the sorting of the quadrupoles Q272, the sixteen magnet are divided into two groups according to their absolute non-uniformity field errors, and one group with larger non-uniformity field errors while the other group with smaller non-uniformity field errors. Firstly, the eight quadrupoes in the larger non-uniformity field errors group are carefully arranged. One thousand of the quadrupoles sorting patterns with small beta beating are saved, and then according to the symmetry of lattice structure, a reasonable sorting pattern is adopted. Secondly, the left eight quadrupole Q272 are carefully sorted, not considering the lattice symmetry. After the quadrupole Q272 arrangement is fixed, the quadrupole Q222, quadrupole Q206, and Q253 are carefully sorted. Figure 3 in left shows the closed orbit distortion comparison after 24 dipoles sorting. The red line indicates the closed orbit distortion caused by random arrangement of the dipoles, and the dark line indicates the closed orbit distortion caused by carefully sorting arrangement of the dipoles, and the closed orbit distortion decreased from 8mm to 1.5mm. Figure 3 in middle and right show the comparison of the horizontal beta beating from quadrupoles sorting, and the red line depicts the beta beating with random quadrupole arrangement while the dark line depicts the beta beating with sorting quadrupole arrangement.

ISBN 978-3-95450-185-4

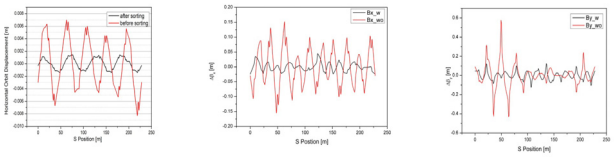

Figure 3: Left: The comparison of the horizontal closed orbit distortion after dipoles sorting. Mid: the comparison of the horizontal beta beating after quadrupoles sorting. Right: the comparison of the vertical beta beating after quadrupoles sorting.

THE EFFECTS OF MAGNETS SORTING TO BEAM DYNAMICS

Beam Distribution

In the present numerical simulation, 2e5 macro particles were used. Figure 4 shows the comparison of beam distribution after dipoles and quadrupoles sorting. Because of the strong space charge effects, the effects of sorting magnet are not very obvious. And that can also be proved in Figure 5, which shows the comparison of the emittance at the end of anti-correlated injection.

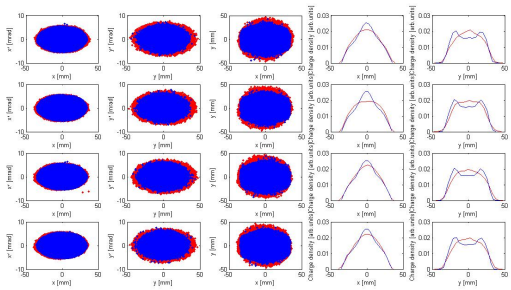

Figure 4: Beam distribution after the dipoles and quadrupoles sorting. From the top to bottom, the distribution corresponds to random dipoles, sorting dipole, random quadrupoles and sorting quadrupoles respectively.

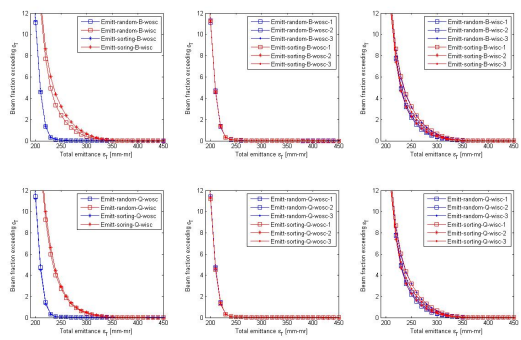

Figure 5: The emittance comparison of due to different cases.

Collimation Efficiency and Beam Loss

The collimator efficiency is defined as the ratio of particles lost in collimator than that lost in the ring. Figure 6 shows the comparison of collimator efficiency and beam lose after magnet sorting. From left to right, the first two groups correspond to dipole errors neglecting space charge effects in beam injection and accelerating respectively. The second two groups correspond to dipole errors considering space charge effects in beam injection and accelerating respectively. The third two groups correspond to quadrupoles errors neglecting space charge effects in beam injection and accelerating respectively. The fourth two groups correspond to quadrupoles errors considering space charge effects in beam injection and accelerating respectively.

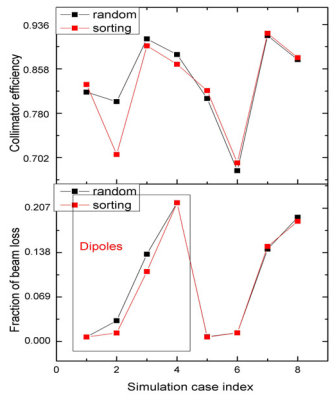

Figure 6: The comparison of collimation efficiency and beam loss.

CONCLUSIONS

For the requirements of the high power, the main dipoles and quadrupoles of CSNS/RCS should be carefully arranged along the azimuth of the accelerator. A code based on traverse algorithm is well developed to get all permutation results of sorting and to pick the best result according to lattice symmetry, small beta beating and small closed orbit distortion. After dipoles and quadrupoles sorting, the beta beating and closed orbit distortion are decreased, and the lattice symmetry are restored. The effects of magnet sorting are carefully investigated according to beam distribution, collimator efficiency and beam loss. Due to strong space charge effects, magnets sorting effects to beam dynamics are not very obvious in our simulation.

REFERENCES

[1] S. Wang, Y. W. An, S. X. Fang *et al.*, "An overview of design for CSNS/RCS and beam transport", SCIENCE CHINA Physics, Mechanics & Astronomy 54 (Suppl 2): s239-s244, 2011
[2] URL http://mad.home.cern.ch/mad/.
[3] URL http://www.slac.stanford.edu/~terebilo/at/.

ISBN 978-3-95450-185-4

TRANSIENT BEAM LOADING BASED CALIBRATION FOR CAVITY PHASE AND AMPLITUDE SETTING

Rihua Zeng*, European Spallation Source ERIC, Lund, Sweden
Olof Troeng†, Lund University, Sweden

Abstract

Traditional phase scan method for cavity phase and amplitude setting is offline and hard to track the variations of environment and operation points. An alternative beam loading based calibration method is investigated in this paper, which might become useful online/real time calibration method.

INTRODUCTION

Setting correctly phase and amplitude for accelerating cavity is crucial in beam commissioning and beam operation. The phase refers here the synchronous phase which is defined as, for a given particle traversing the cavity, the phase shift from RF phase at which it obtain the maximum energy gain. It is equivalent to the phase angle between beam and accelerating voltage in vector diagram. The amplitude refers here the cavity voltage, which is defined as the absolute value of the line integral of the electric field seen by the beam along the accelerating axis, which reflects the maximum achievable energy gain for beam acceleration.

This paper introduce some general methods used for phase and amplitude setting in different accelerators, analyse the advantage and disadvantage of theses methods, and then discuss an online beam based calibration method which seems promising and very suitable to be employed at ESS.

PHASE SCAN

Phase scan methods are referring here to the way of calibrating setting point for RF cavities by scanning RF phase and amplitude, measuring beam arrival times at down-stream locations, comparing measured phase to model predicted data, and identifying the best-matched data for calibration.

ΔT-method

The ΔT-method is a classical phase scan method and used widely in normal conducting linac such as in LAMPF, Fermilab, JPARC and SNS. Linear system response is assumed in ΔT-method and it is only valid in the vicinity of design phase and amplitude. ΔT-method is a cavity-by cavity operation, assuming that the cavities upstream to the one being adjusted are "on", and the cavities downstream are "off". Beam phases (or beam arrival time) are provided by two downstream BPMs. The two BPMs can be neighbouring each other, or separated by several cryo-modules, which depends on the specific location of cavity (the sensitivity of beam velocity to energy gain becomes low as beam energy goes high) being adjusted. The cavities between two BPMs are usually detuned more than 10 cavity bandwidth.

The general procedures of the ΔT-method are listed below [1, 2]:

- Find approximate phase and amplitude set point, by observing BPM signals and beam loading effect, and doing RF based calibration.
- Cavity being adjusted is off. Record two downstream BPMs phases $\phi_{\text{bpm1-0}}$ and $\phi_{\text{bpm2-0}}$.
- Ramp the cavity being adjusted to nominal field calibrated by RF power based measurement (amplitude accuracy in RF based calibration is around 10%).
- Turn on beam with low repetition rate, low beam intensity and low beam pulse length.
- Record two downstream BPMs phases ϕ_{bpm1} and ϕ_{bpm2}.
- Calculate relative changes of BPMs phases between cavity "on" and "off" $\Delta\phi_{\text{bpm1}} = \phi_{\text{bpm1-0}} - \phi_{\text{bpm1}}$ and $\Delta\phi_{\text{bpm2}} = \phi_{\text{bpm2-0}} - \phi_{\text{bpm2}}$. Plot $\Delta\phi_{\text{bpm1}}$ and $\Delta\phi_{\text{bpm2}}$.
- Scan the cavity RF phase with certain phase step (for example 0.5°) over the certain range (for example, ±5°) of design phase, and repeat above procedures at each phase step, to generate a constant-amplitude, variable-phase curve in $(\Delta\phi_{\text{bpm1}}, \Delta\phi_{\text{bpm1}})$ plane.
- Calculate the slope of the curve, which depends on cavity amplitude, and compare it with the slope values of model predict curves at different amplitude. These predicted curves have a common point of intersection.
- Use some fitting algorithm to determine best-fit amplitude.
- Having determined proper amplitude, it is now possible in model to calculate the transfer function relating $\Delta\phi_{\text{bpm1}}$ and $\Delta\phi_{\text{bpm2}}$ to phase deviation $\Delta\phi$ and energy deviation ΔW at the entrance of cavity with respect to nominal value. $\Delta\phi$ and ΔW can then be determined.
- Correct the phase set point, and if necessary, correct as well the input energy at cavity entrance according to the result in last step.

Signature Matching

Unlike the ΔT-method having a linear system response and small input energy displacement restriction, signature matching method can work at large displacement of initial conditions. In high energy part, signature matching methods can easily scan the phase over 360° at different amplitude, and make good match with model predict curve. However, at low energy linac, cavity phase scan can only be several ten degrees where beam stay sufficiently bunched to produce good signals at downstream BPMs, and the accuracy indicated at SNS for low energy part is not good enough. ΔT-method is probably necessary to get a good setting ac-

* rihua.zeng@esss.se
† oloft@control.lth.se

ISBN 978-3-95450-185-4

curacy for ESS spoke cavities. The general procedures for signature matching are listed below [3]:

- Ramp the cavity being adjusted to nominal field calibrated by RF power based measurement (amplitude accuracy in RF based calibration is around 10
- Detune the downstream cavities by more than 10 cavity bandwidth to bypass the beam, which locate between two downstream BPMs.
- Turn on beam with low repetition rate, low beam intensity and low beam pulse length Record two downstream BPMs phases ϕ_{bpm2} and ϕ_{bpm2}.
- Record two downstream BPMs phases ϕ_{bpm1} and ϕ_{bpm2}.
- Scan the cavity RF phase with certain phase step (for example, 0.5°) over the full range 360°, and repeat last step at each phase step, to generate a constant-amplitude, variable-phase curve in ($\Delta\phi_{\mathrm{bpm1}}$, $\Delta\phi_{\mathrm{bpm2}}$) plane.
- Predict the values in model for BPM phases ($\Delta\phi_{\mathrm{bpm1\text{-}calc}}$ and $\Delta\phi_{\mathrm{bpm2\text{-}calc}}$) as a function of synchronous phase.
- Spline fit the measured phase difference ($\phi_{\mathrm{bpm1}} - \phi_{\mathrm{bpm2}}$).
- Match the model predict values with measured ones, by minimizing the difference between ($\phi_{\mathrm{bpm1}} - \phi_{\mathrm{bpm2}}$) and ($\phi_{\mathrm{bpm2\text{-}calc}} - \phi_{\mathrm{bpm1\text{-}calc}}$) over the range of scanned phase. Phase deviation $\Delta\phi$, input beam energy deviation at entrance of cavity ΔW, and cavity amplitude deviation ΔV are adjusted in this matching procedure.
- Correct the phase and amplitude set points according to the result in last step.

TRANSIENT BEAM LOADING METHOD

Drift Beam Method

The drifting beam technique is based on very strong beam-cavity interactions in the SC cavity for high current beams. It was proposed several years ago and recently realized at SNS. It uses measured beam currents and pulse shapes with a beam current monitor (BCM), and beam induced signals in the SC cavity with the cavity control circuit. Using the measured beam current in a beam-cavity model that simulates the beam-loading in the cavity, by comparing model simulation results with the actual measurement of the cavity, cavity phase and the field amplitude are determined precisely. The general procedures are listed below [4]:

- Measure the beam current and beam pulse shape by BCMs.
- Tune the cavity as close ass possible to resonance.
- Turn off RF. Turn on beam with low repetition rate 1Hz, low beam intensity 10mA, and low beam pulse length.
- Measure the phase and amplitude of beam-induced signal.
- Measure the phase and amplitude of noise signal before next beam pulse coming. Subtract noise signal from beam-induced signal.
- Repeat the measurement in last step for ~10 beam pulses and average the results.
- Predict the beam-induced signal in model by measured beam current and beam pulse shape.
- Determine the phase offset and amplitude calibration coefficient by comparing measured result with model calculations.
- Set amplitude and phase.

COMPARISON BETWEEN PHASE SCAN AND DRIFT BEAM METHOD

By reviewing the literature of different method at SNS for phase and amplitude setting and collecting all parameters used for such setting, it is worthwhile to compare the different between different methods. To make it consistent, only the results from the same facility (SNS) are used for comparison. As this paper is focusing on superconducting cavities, only the methods used in superconducting cavities such as signature matching and drift beam method are chosen. However, it should be noted that, due to superconducting linac at ESS covers also low energy part, the method used for normal-conducting cavities at SNS like ΔT-method might be necessary for ESS.

Table 1: Key Performance and Parameter Comparison Between Phase Scan and Transient Beam Method

Accuracy and parameter used	Phase scan – signature matching	Transient beam loading – drift beam
Amplitude	±2.4%	±4%
Phase	±1°	±1°
Pulse length	<20 µs	>50 µs
Beam current	<20 mA	<20 mA
Rep. Rate	1 Hz	1 Hz

As shown in Table 1, both phase scan and transient beam loading methods can achieve good phase accuracy up to ±1°. To achieve a good accuracy, phase scan method requires as low beam loading as possible to not disturb the cavity field, while drift beam method requires a relatively stronger beam loading in cavity to get a strong beam induced voltage to suppress noise. The signal to noise ratio is often low in drift beam method at SNS, due to short beam pulsed length and low beam current, which is usually the case in early stage of beam commissioning to avoid damage to other hardware or beam dump.

IMPROVED TRANSIENT BEAM LOADING METHOD AT DESY

One of the main problem of drift beam method is poor signal to noise ratio (SNR) due to limited beam loading in beam commissioning. SNR is sometime less than 10, indicated by some measurement at SNS, which is probably one of the limitations to achieve higher and stable accuracy.

Suffering less from poor SNR like drift beam method at SNS, the transient beam loading based method for phase and amplitude setting used at DESY tried to improve SNR a lot with benefit from high performance hardware and works well now for FLASH and will most probably used in XFEL.

ISBN 978-3-95450-185-4

The main difference in method used at DESY from drift beam method is, instead of un-powering the cavity before beam drifting through, a constant driving power is first fed into the cavity to build up the cavity field up to operating gradient [5], and then the beam goes through the cavity, as shown in Figure 1. The drop of cavity voltage caused by beam loading is calculated by comparing two measured cavity voltage, one measured before beam coming, and the other one measured after beam coming. Higher SNR is ensured and high resolution of beam transient loading can be observed, thereby giving high quality information to calibrate the phase and amplitude of cavity field.

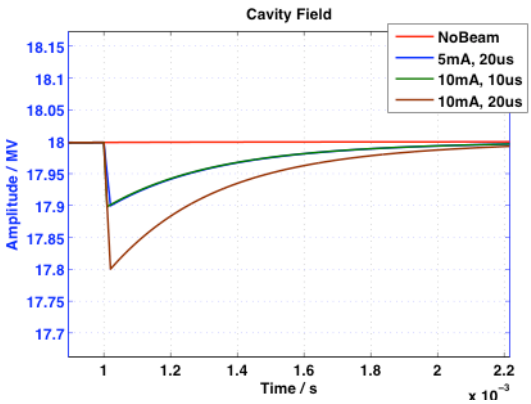

Figure 1: Schematic view of transient beam loading method used at DESY (ESS cavity parameters are used).

AN ALTERNATIVE ONLINE BEAM BASED CALIBRATION METHOD

The procedures for phase and amplitude setting used at DESY requires special operating conditions (open loop, two separated measurement, etc) and cannot thus be used in normal operation when the cavity is running in feedback mode and adaptive feed-forward mode with heavy beam loading. Considering big advantages at ESS for such online beam based calibration: heavy beam loading (62.5mA compared with 9mA in FLASH or XFEL) and 1 power amplifier per cavity (1 power amplify for 8 cavities in FLASH, and for 32 cavities in XFEL), an online beam transient based calibration method is thus investigated at ESS.

Our starting point is the equation [6]

$$\dot{\mathbf{V}}(t) = \left(-\omega_{1/2} + i\Delta\omega(t)\right)\mathbf{V}(t) + \kappa_g \mathbf{I_g}(t) + \kappa_b \mathbf{I_b}(t) \quad (1)$$

which describes the time evolution of the cavity voltage in the baseband[1] (we only consider the dynamics of the fundamental mode). Bold symbols denote complex quantities.

The measured cavity voltage is given by

$$\mathbf{V}_\mathrm{m}(t) = \mathbf{V}(t) + v(t) + \sum_k \mathbf{V}_k(t),$$

where $v(t)$ is measurement noise and the sum corresponds to interference from parasitic modes.

Also, the generator current $\mathbf{I_g}$ is not directly measured, but rather a quantity $\breve{\mathbf{I}}_\mathrm{g}$ proportional to it is measured by the directional coupler downstream the amplifier, i.e., $\breve{\mathbf{I}}_\mathrm{g} = \mathbf{k}\mathbf{I_g}$ for some complex $\mathbf{k}$.

Least Squares Estimation

From measurements of $\mathbf{V}_\mathrm{m}(t)$ and $\breve{\mathbf{I}}_\mathrm{g}(t)$, as well as the timing of the beam pulse, we can formulate a linear least squares problem for estimation of the beam phase.

Let the time-derivative of $\mathbf{V}_\mathrm{m}$ (computed as a first order difference), be the response variable

$$\mathbf{y} = \begin{bmatrix}\dot{\mathbf{V}}_\mathrm{m}(t_1) & \dot{\mathbf{V}}_\mathrm{m}(t_2) & \dots & \dot{\mathbf{V}}_\mathrm{m}(t_N)\end{bmatrix}$$

and let the measured terms in the time derivative of $\mathbf{V}_\mathrm{m}$ form the regressor matrix,

$$\mathbf{X} = \begin{bmatrix} \mathbf{V}_\mathrm{m}(t_1) & t_1\mathbf{V}_\mathrm{m}(t_1) & \breve{\mathbf{I}}_\mathrm{g}(t_1) & \Gamma(t_1) \\ \mathbf{V}_\mathrm{m}(t_2) & t_2\mathbf{V}_\mathrm{m}(t_2) & \breve{\mathbf{I}}_\mathrm{g}(t_2) & \Gamma(t_2) \\ \vdots & \vdots & \vdots & \vdots \\ \mathbf{V}_\mathrm{m}(t_N) & t_N\mathbf{V}_\mathrm{m}(t_N) & \breve{\mathbf{I}}_\mathrm{g}(t_N) & \Gamma(t_N) \end{bmatrix}$$

where

$$\Gamma(t_k) = \begin{cases} 0 & t_k \text{ before beam start} \\ 1 & t_k \text{ after beam start} \end{cases}.$$

Then the relation

$$\mathbf{y} = \mathbf{X}\boldsymbol{\theta}$$

is approximately satisfied for some parameter vector

$$\boldsymbol{\theta} = \begin{bmatrix}\theta_1 & \theta_2 & \theta_3 & \theta_4\end{bmatrix}^T,$$

where $\angle\theta_4$ is the beam phase that we are looking for.

The least squares estimate of $\boldsymbol{\theta}$ is given by

$$\boldsymbol{\theta}_\mathrm{LS} = (\mathbf{X}^*\mathbf{X})^{-1}\mathbf{X}^*\mathbf{y}.$$

Note that time-variation of the detuning is handled by the term θ_2, which corresponds to $\mathrm{d}(\omega_{1/2} + i\Delta\omega)/\,\mathrm{d}t$.

If there is significant interference from passband modes, their effect will be greatly amplified in $\dot{\mathbf{V}}_\mathrm{m}$, degrading estimation performance. This issue is well mitigated by filtering the observed data, including $\Gamma(t)$, through a lowpass filter with sufficient rejection the passband modes.

We have only given an overview of a possible improved beam phase estimation procedure. Some possible modifications for an actual implementation are mentioned below.

- If there is some uncertainty about the start of the beam pulse, the corresponding samples can be left out of the estimation problem.
- If some parameters in (1) are known with high accuracy, this information is easily incorporated into the estimation problem.
- If it is certain that the $\omega_{1/2}$ does not change during the pulse, the problem can be formulated so that the estimated parameter θ_2 is purely imaginary.

[1] In [6] expressions are given for κ_g and κ_b, however these are not important in this context.

ISBN 978-3-95450-185-4

Numerical simulations show the proposed model to be quite robust. Note that measurements must be taken both with and without beam. Also the interval $[t_1, t_N]$ should be sufficiently short that the detuning can be considered linear.

REFERENCES

[1] A. Feschenko, S. Bragin, Y. Kiselev, L. Kravchuk, O. Volodkevich, A. Aleksandrov, J. Galambos, S. Henderson, and A. Shishlo, "Development and implementation of δ t procedure for the sns linac," in *Proceedings of the 2005 Particle Accelerator Conference*. IEEE, 2005, pp. 3064–3066.

[2] K. Crandall, "The at tuneup procedure for the lampf 805-MHz linac," *Los Alamos Laboratory Report LA-6374-MS, June*, vol. 9176, 1976.

[3] J. Galambos, A. Aleksandrov, C. Deibele, and S. Henderson, "Pasta-an rf phase scan and tuning application," in *Proceedings of the 2005 Particle Accelerator Conference*. IEEE, 2005, pp. 1491–1493.

[4] Y. Zhang, I. Campisi, P. Chu, J. Galambos, and S. D. Henderson, "Determination of field amplitude and synchronous phase using the beam-induced signal in an unpowered superconducting cavity," *Nuclear Instruments and Methods in Physics Research Section A: Accelerators, Spectrometers, Detectors and Associated Equipment*, vol. 571, no. 3, pp. 574–582, 2007.

[5] M. Grecki and S. Pfeiffer, "Resonance Control of Superconducting Cavities at Heavy Beam Loading Conditions," in *Proc. of International Particle Accelerator Conference (IPAC'12)*. JACoW, paper THPPC077, pp. 3467–3469. [Online]. Available: http://jacow.org/ipac2012/papers/thppc077.pdf

[6] T. Schilcher, "Vector sum control of pulsed accelerating fields in lorentz force detuned superconducting cavities," Ph.D. dissertation, 1998.

ISBN 978-3-95450-185-4

MEASUREMENT AND INTERPRETATION OF TRANSVERSE BEAM INSTABILITIES IN THE CERN LARGE HADRON COLLIDER (LHC) AND EXTRAPOLATIONS TO HL-LHC

E. Métral†, G. Arduini, J. Barranco, N. Biancacci, X. Buffat, L.R. Carver, G. Iadarola, K. Li, T. Pieloni, A. Romano, G. Rumolo, B. Salvant, M. Schenk, C. Tambasco,
CERN, Geneva, Switzerland

Abstract

Since the first transverse instability observed in 2010, many studies have been performed on both measurement and simulation sides and several lessons have been learned. In a machine like the LHC, not only all the mechanisms have to be understood separately, but the possible interplays between the different phenomena need to be analyzed in detail, including the beam-coupling impedance (with in particular all the necessary collimators to protect the machine but also new equipment such as crab cavities for HL-LHC), linear and nonlinear chromaticity, Landau octupoles (and other intrinsic nonlinearities), transverse damper, space charge, beam-beam (long-range and head-on), electron cloud, linear coupling strength, tune separation between the transverse planes, tune split between the two beams, transverse beam separation between the two beams, etc. This paper reviews all the transverse beam instabilities observed and simulated so far, the mitigation measures which have been put in place, the remaining questions and challenges and some recommendations for the future.

INTRODUCTION

The first transverse instability in the LHC was observed during the first ramp tried with a single bunch of ~ 10^{11} p/b (on both beams B1 and B2) on 15/05/2010, with neither Landau octupoles (dedicated magnets used to provide transverse Landau damping and whose maximum absolute current is 550 A) nor transverse damper [1]. A dedicated study was then performed on 17/05/10 at 3.5 TeV starting with a Landau octupole current of – 200 A (the minus sign refers to the focusing octupole family, which corresponds to a negative amplitude detuning) and reducing it in steps until the bunch became unstable between ~ – 20 A and – 10 A. Figure 1(left) shows the measurement of the instability rise-time (~ 10 s) in the time domain while Fig. 1(right) reveals the behaviour in the frequency domain, where the similar rise-time, from the (azimuthal) mode – 1, could also be deduced [1]). This instability has been found to be in good agreement with prediction from the impedance model (within a factor ~ 2 or less), requiring a modest amount of Landau octupole current. Further measurements were performed in 2010 and 2011 in multi-bunch (with trains of bunches), revealing also a relatively good agreement with the impedance model (within a factor ~ 2) [2].

† Elias.Metral@cern.ch

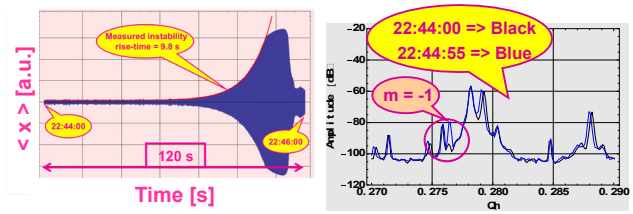

Figure 1: Dedicated single-bunch instability measurement at 3.5 TeV, two days after the first LHC transverse instability observed in 2010: (left) in the time domain and (right) in the frequency domain.

Things started to become more involved when we tried to push the performance of the LHC in 2011, and in particular in 2012. Several instabilities were observed at different stages of the LHC cycle, which perturbed the intensity ramp-up. All these instabilities could be cured by increasing the current of the Landau octupoles, the chromaticities and/or the gain of the transverse damper, except one transverse instability which remained at the end of the betatron squeeze [3,4]. Since then, transverse instabilities have been a worry for the future operation of the LHC and for HL-LHC [5].

The instability observations, the actions taken and the lessons learned are reviewed in Section 1 for the Run 1 (2010 to 2012), in Sections 2 and 3 for 2015 and 2016 respectively, while the future is discussed in Section 4.

RUN 1 (2010-2012)

The operation during Run 1 was performed with the 50 ns bunch spacing beam and with a lower energy (3.5 TeV first and then 4 TeV in 2012), and three types (in fact two after careful analysis) of instabilities perturbed the intensity ramp-up, which are discussed below.

In Collision: "snowflakes"

These instabilities happened always in the horizontal plane only and for both beams (see an example in Fig. 2). It concerned initially only the IP8 private bunches, i.e. the bunches colliding only at the Interaction Point 8. This was rapidly identified and these instabilities disappeared once the filling scheme was modified. The interpretation of this mechanism is that it happens on selected bunches with insufficient tune spread (and thus Landau damping) due to no head-on collisions, or transverse offsets [3,4].

ISBN 978-3-95450-185-4

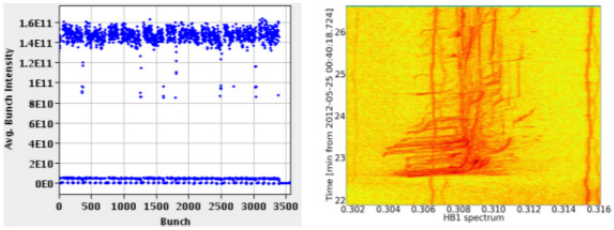

Figure 2: Example of "snowflakes" instability: (left) bunch intensity vs. number of the bunch (25 ns slot) and (right) horizontal frequency spectrum vs. time [3].

Putting the Beams Into Collision

A second type of instabilities happened at the end of the collision process, with the separation bumps collapsed, when ending with residual separations of ~ 2.1 σ in IP1 and ~ 1.2 σ in IP5 (values estimated from luminosities at the moment of the dump). These instabilities happened also in the horizontal plane. However, after careful analysis, it appeared that this type of instabilities happened only once or twice during the intensity ramp-up and it was never observed later in operational conditions.

During or at the End of the Squeeze Process

A third type of instabilities happened during or at the end of the squeeze, called EOSI (End Of Squeeze Instability), also in the horizontal plane. A characteristic picture is shown in Fig. 3(left), where 3 lines spaced by the (small-amplitude) synchrotron tune can be observed.

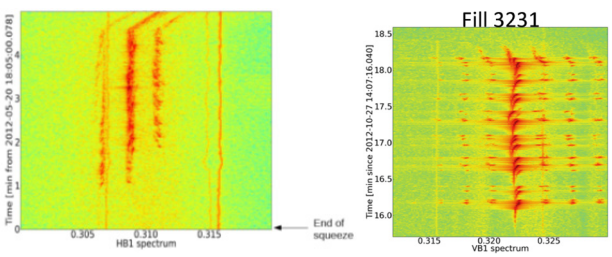

Figure 3: (Left) example of instability observed at the end of the squeeze: horizontal frequency spectrum vs. time after the end of the squeeze; (right) similar as in the left but after the "Middle of the Year Changes" [3,4].

Actions Taken

Based on the past work [6,7,1,2], the initial recommendations at the beginning of Run 1 were to try and keep the chromaticities as low as possible (~ 1-2) and to try and reduce the transverse damper gain as much as we could (to minimize the possible noise introduced and the associated transverse emittance growth). However, the issues discussed above rapidly appeared during spring and several actions were taken to continue and push the performance: (i) to avoid the beam dumps triggered during the collision process, it was proposed to change the sign of the Landau octupoles such that the tune spreads from beam-beam and octupoles do not fight against each other [8]; (ii) new values for the gain of the transverse damper, chromaticities and Landau octupole current were then suggested after a new analytical approach [9,10]. Indeed, it was found that if the transverse damper is not fully bunch-by-bunch, and if the chromaticity is not very well controlled (as it was the case during Run 1) then it is preferable to operate at relatively large chromaticity (~ 10-15) where a plateau is reached for the required stabilising octupole current. The first and second types of instabilities disappeared with the change of the Landau octupole polarity on August 7th (fill #2926) and the following increase of both the chromaticities and the gain of the transverse damper (which was then also used fully bunch-by-bunch during the squeeze): these changes are referred to as the "Middle of the Year Changes". Unfortunately three parameters were modified almost at the same time and it was not possible to identify the main beneficial effect(s). The third type of instabilities could not be cured [3,4] (see Fig. 3(right)).

Lessons Learned

After detailed analysis, it seems that the main reason for which the situation improved after the "Middle of the Year Changes" was the increase of the chromaticity, which was not well controlled during Run 1, and running at high chromaticity prevented to reach negative values. Furthermore, as the transverse damper was not initially fully bunch-by-bunch, more octupole current was required for low chromaticities [10]. The change in the octupole sign was finally found not to be helpful from both measurements and simulations (as can be seen from Fig. 4, where the same stability diagram is predicted for the most critical bunch and in the region of interest, i.e. for the negative real tune shifts which are expected from the impedance model) [11]. However, a positive sign is predicted to be much better for the case of the nominal configurations (see Fig. 4), and this is why the positive sign of the octupoles is used during Run 2.

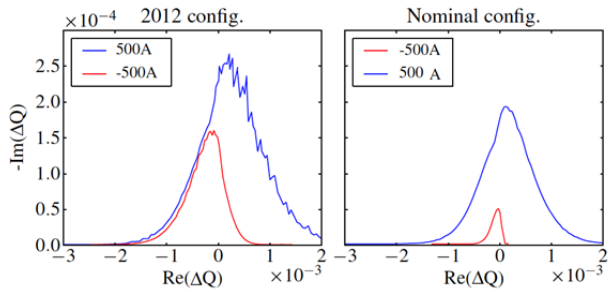

Figure 4: Comparison of the stability diagrams for the worst bunch at the end of the squeeze for each polarity of the octupoles, in 2012 and nominal configurations [11].

The main lesson learnt for the future was to better study the interplays between (all) the different mechanisms in a machine like the LHC. A lot of work has been done over the last few years (see for instance Ref. [12]) with in particular the proposed mechanism of the three-beam instability (both beams with an electron (e-)cloud) [13], the detailed analysis of the transverse mode coupling instability of colliding bunches [14] and the proposed mechanism of a modification of the stability diagram by

ISBN 978-3-95450-185-4

some beam-induced noise [15]. To be able to learn more on stability diagrams from beam-based measurements, Beam Transfer Measurements (BTF) should be performed.

2015

In 2015, we restarted the LHC at 6.5 TeV (instead of 4 TeV in 2012) and the goal of this first commissioning/exploratory year of Run 2 was to established operation with the nominal 25 ns bunch spacing beam, anticipating difficulties with the beam-induced e-cloud.

Impedance-Induced Transverse Beam Instability

After the experience of Run 1 it was decided to start with the positive sign of the Landau octupoles and to study in detail the effect of chromaticity on the transverse beam instabilities, starting first with a single bunch. A summary of these measurements, compared to the predictions from the DELPHI code [16,12], is depicted in Fig. 5(upper) [17]. Three regions can be identified. In the region of interest for the operation, Q' > ~ 2, a good agreement was reached between predictions and measurements. In particular it can be seen that an octupole current of ~ 100 A was always sufficient to stabilise the bunch. The other regimes are discussed in Ref. [17].

Destabilising Effect of E-cloud

After having performed the study with a single bunch we decided to perform the same study with a train of 72 bunches, for a chromaticity of Q' ~ 7, knowing that the beam stability predictions from simulation are the same for a multi-bunch beam for a perfect damper with a sufficiently high gain. Two series of measurements were performed and the results are shown in Fig. 5(lower). During the first measurements a much higher octupole current than predicted from impedance (by a factor ~ 5) was required to stabilise the beam, while during the second measurements, a current compatible with the predicted value was measured. After detailed analysis, it was found that the first instability was certainly due to e-cloud (or at least due to the interplay with e-cloud) as the synchronous phase shift along the batch was quite high (~ 0.8 deg), revealing that a significant amount of e-cloud was still present in the machine [18], while during the second instability, the synchronous phase shift along the batch was much lower (~ 0.3 deg) [17].

Destabilising Effect of Linear Coupling

Due to e-cloud and the significant values of both chromaticities and octupole current which are required to stabilise the beam at injection, incoherent losses were observed and the working point at injection needed to be optimized [18]: it was moved from (0.28,0.31) to (0.275,0.295), essentially to move away from the third integer (0.33) resonance. This worked well but the distance between the two tunes reduced from 0.03 to 0.02 and when the Laslett tune shifts were not corrected during the injection process, the two tunes got even much closer (~ 0.009), which led to instabilities, which are believed to be due to linear coupling [19].

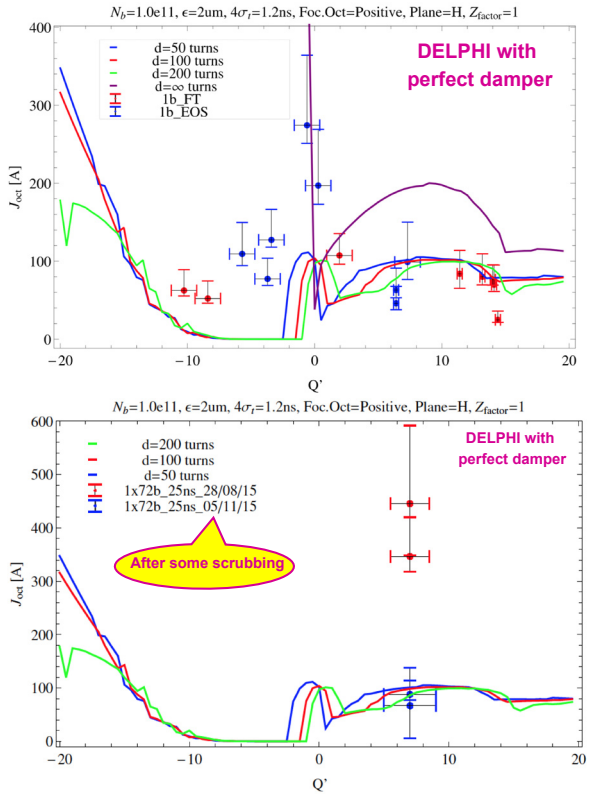

Figure 5: Stabilising octupole current vs. chromaticity: (upper) comparison between single-bunch measurements (dots: in red on the high energy flat-top and in blue at the end of the squeeze) and simulations (several curves depending on the transverse damper gain, assuming a perfect fully bunch-by-bunch damper); (lower) same as upper but with a train of 72 bunches spaced by 25 ns [17].

Beam Transfer Function (BTF) Measurements

A first stability diagram has been deduced from BTF measurements at injection [20]. The next step will be to fully understand the calibration factor as well as other interesting observations already reproduced by simulation but not yet fully understood [20].

Actions Taken

High chromaticities (~ 15) and about maximum octupole current were needed to keep the beam stable. As it was found that e-cloud can lead to instabilities also at high energy, a detailed simulation campaign was started to study the effects of the electrons from the arc dipoles and quadrupoles but also from the interaction regions. A detailed analysis of the effect of linear coupling on transverse beam instabilities was also started with a single bunch at high energy. With the new injection working point, both the Laslett tune shifts and the closest tune approach (called $|C^-|$) should be always corrected to avoid possible instabilities induced by linear coupling. The measurement of the $|C^-|$ at injection during the second half of 2012 revealed quite some high values [21]. Finally, the BTF measurements started to be benchmarked. This work

ISBN 978-3-95450-185-4

should continue as it opens the possibility to study the stability diagram and its evolution with time to detect possible deformations, which could explain a loss of transverse Landau damping.

Lessons Learned

While in 2012 the machine was operating at 4 TeV with the 50 ns beam and in 2015 it was operating at 6.5 TeV with the 25 ns beam, in both cases high chromaticities (~ 15) and almost maximum octupole current were needed to stabilise the beam. While in 2012 it is still not completely clear why such high values were needed, it was clear in 2015 that an important e-cloud was still present at high energy and that it could drive the beam unstable. Furthermore, linear coupling should be studied in more detail during all the LHC cycle.

2016

2016 is a year of production and we applied the lessons learned during 2015: (i) the injection working point has been further optimized to (0.27,0.295); (ii) the Laslett tune shifts at injection have been corrected automatically; (iii) high chromaticties (~ 15) have been used during all the cycle; (iv) almost the maximum octupole current has been used at high energy and (v) linear coupling has been corrected during the cycle.

Destabilising Effect of Linear Coupling

Linear coupling can be a problem for beam stability because it can lead to a loss of transverse Landau damping. A simple model was used in Ref. [22], using an externally given elliptical spectrum, no transverse damper, etc. A detailed simulation campaign was performed for the LHC at 6.5 TeV with the pyHEADTAIL code [12], including the impedance model, the transverse damper, chromaticity and octupoles [19]. As the simulations were very time consuming, they were performed for a single bunch of 3 10^{11} p/b (still below the Transverse Mode Coupling Instability threshold). It can be seen from Fig. 6 that as the (decimal) tune separation Q_{sep} approaches the value of the closest tune approach, the required octupole current to stabilise the bunch becomes as large as ~ 4 times the required octupole current without linear coupling.

After the detailed simulation campaign, a dedicated measurement was performed in the LHC at 6.5 TeV, where two instabilities due to linear coupling could be observed. The first one revealed a remaining bump in the closest tune approach during the betatron squeeze around ~ 2 m, which led to a stabilising octupole current ~ 4 times higher than the uncoupled threshold [19]. A second measurement was then performed at flat top before the betatron squeeze, with the nominal injection tune, increasing the closest tune approach to $|C^-|$ ~ 0.01 and reducing the tune separation in steps. Here again, a much larger octupole current (by a factor ~ 4.4) was found to be necessary to stabilise the bunch in the coupled case. Renormalising the beam parameters, this case corresponds to the red star in Fig. 6.

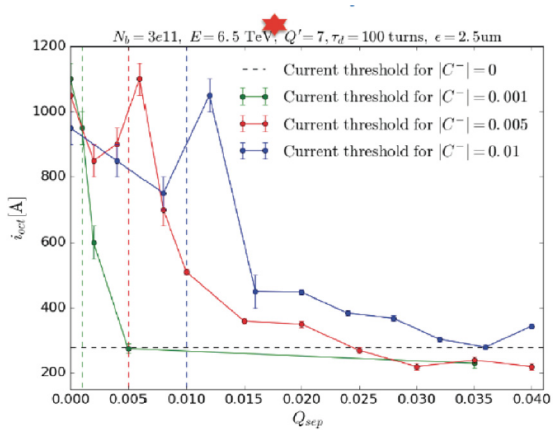

Figure 6: pyHEADTAIL [12] simulations of the stabilising octupole current vs. the (decimal) tune separation for a single bunch of 3 10^{11} p/b within 2.5 μm normalized rms transverse emittance interacting with the LHC impedance at 6.5 TeV with a chromaticity Q' = 7 and a transverse damper with a damping time of 100 turns [19].

In Collision: "pop corn" Instability

The LHC is currently operating with slightly more than 2000 bunches with a beam-induced heat load (due to e-cloud) close to the limit from the cryogenics capacity (160 W per half cell), meaning that a lot of electrons are still present in the machine [18]. And since the number of bunches reached ~ 600 bunches, the maximum octupole current and chromaticities of ~ 15 were not enough to stabilise the beam. Indeed, an instability has been observed in stable beam after few hours (see Fig. 7), which does not lead to beam losses but to transverse emittance blow-up (up to a factor ~ 2), only in the vertical plane of both beams and at the end of the trains of 72 bunches (where the bunch intensity is in fact the smallest due to some losses mainly at injection).

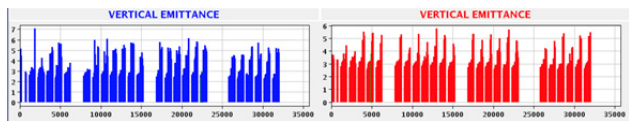

Figure 7: "Pop corn" instability observed in stable beam after few hours, despite the maximum octupole current and the high chromaticities (~ 15).

This instability clearly exhibits some signs of e-cloud and a possible mechanism was proposed [18]: when the intensity decreases a central stripe of electrons develops (between the two usual stripes observed in dipoles) where the density can become sufficiently high (in the order of 10^{12} e^-/m^3) to drive the beam unstable, without changing the total heat load [23]. Indeed, some past simulations, performed at 3.5 TeV, revealed that for an e-cloud density of 6 10^{11} e^-/m^3, the amplitude detuning from the octupoles was not sufficient to damp this vertical single-bunch instability [24] and that the effective knob was the chromaticity (more than ~ 15 units were needed), as already observed in the past at injection [25].

ISBN 978-3-95450-185-4

Actions Taken

Linear coupling was corrected all along the cycle and in particular during the betatron squeeze. The Laslett tune shifts are now corrected automatically at injection. The vertical chromaticities have been increased by ~ 7 units in stable beam (to reach values of ~ 20-25), which almost completely suppressed the vertical emittance blow-up.

Lessons Learned

Linear coupling has to be well corrected all along the LHC cycle to avoid using too much octupole current. Even in the presence of a large tune spread in stable beam (due to head-on) the beam can become unstable. Fortunately the beam could be stabilised by increasing considerably the vertical chromaticities (to values as high as ~ 20-25), which still leads however to sufficiently good lifetimes: a high chromaticity does not seem to be an issue for the current LHC.

FUTURE

The LHC just reached the design peak luminosity of 10^{34} cm^{-2} s^{-1} [26] at 6.5 TeV and with about 25% less bunches than nominal. In HL-LHC, the bunch brightness should be increased by a factor almost 3 and transverse beam stability might become a limitation in the future: (i) will we have enough octupole current to stabilise the beam (an RF quadrupole was proposed to enhance the beam stability if needed [27])?; (ii) will we be able to use these high chromaticities in the future and how will this impact the beam lifetime and the minimum crossing angle which can be used (even if very encouraging results were recently obtained [28])?

Impedance-Induced Transverse Beam Instability

A detailed HL-LHC impedance model has been developed, and the related single-beam stability predictions are shown in Fig. 8 (for the most critical case of a transverse profile cut at ~ 3.2 σ [19]), where it can be seen that even if the impedance is a factor ~ 2 higher than the model, there should be enough octupole current. However, linear coupling should be well corrected all along the cycle, and all the sources of stability diagram deformation should be identified and the deformations minimized.

Beam-Beam

During the collision process, the stability diagram is reduced at two locations, at ~ 6 σ and ~ 1.5 σ, as can be seen in Fig. 9. It is worth reminding that no instability was observed at the minimum of the stability diagram during the regular operational fills. However, the recommendation has been made to go from 2 σ to 1 σ in less than 1 s (i.e. faster than the predicted instabilities) [19].

E-cloud

The main issue for the current LHC operation and for the future seems to be the e-cloud. Will we succeed to remove all the electrons from the dipoles? What is / will be the effect on beam stability? What about the remaining electrons in the quadrupoles? These questions are currently being addressed.

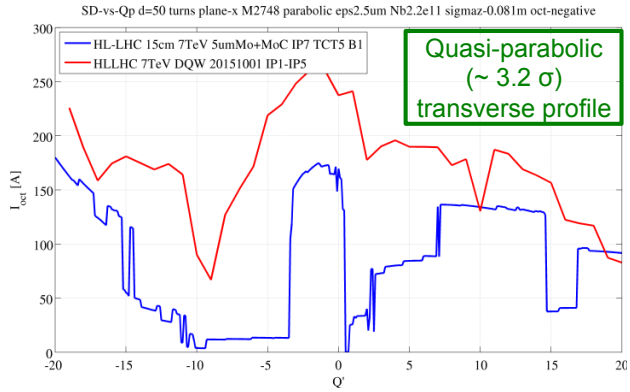

Figure 8: Single-beam stability predictions for HL-LHC at high energy (with, as foreseen, negative amplitude detuning from the Landau octupoles): without crab cavities (in blue) and with crab cavities (in red) [19].

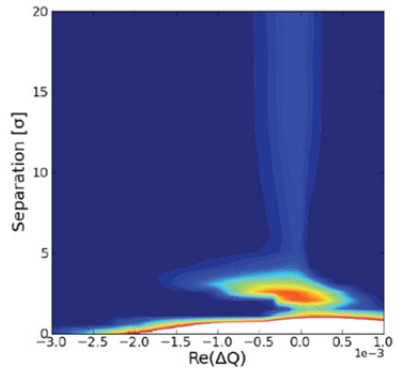

Figure 9: Evolution of the stability diagram during the collision process for the baseline scenario but with crab crossing off (similar picture with crab crossing on) [19].

CONCLUSION

The LHC is running very well, recently reaching the design peak luminosity [26]. However, transverse instabilities are a concern to push the performance further and despite the lot of progress made over the last years we still need to (fully) understand all the reasons for which, since 2012, we need to use at high energy the maximum octupole current and high chromaticities (~ 20-25 in 2016). Linear coupling between the transverse planes has been identified as a possible detrimental mechanism, which can considerably increase the required stabilising octupole current. E-cloud has also been clearly identified as a possible detrimental mechanism (also) at high energy, which can considerably increase both the required stabilising octupole current and the chromaticities. A simulation campaign has been started to try and better understand the mechanisms involved.

ACKNOWLEDGEMENT

Many thanks to the many LHC colleagues, in particular the operation crew for all the studies performed together and all the colleagues from the instrumentation and transverse damper teams, helping us to better observe and understand the beam instabilities.

ISBN 978-3-95450-185-4

REFERENCES

[1] E. Métral et al., Stabilization of the LHC single-bunch transverse instability at high energy by Landau octupoles, Proceedings of IPAC2011, San Sebastián, Spain.

[2] N. Mounet, The LHC transverse coupled-bunch instability, Ph.D. dissertation, EPFL, 2012, thesis No 5305.

[3] E. Métral et al., Review of the instability observed during the 2012 Run and actions taken, Proceedings of the LHC Beam Operation workshop, Evian, France, December 2012.

[4] E. Métral et al., Summary of the 2-day internal review of LHC performance limitations (linked to transverse collective effects) during Run I (CERN, 25-26/09/2013), CERN-ACC-NOTE-2014-0006, 2014.

[5] G. Apollinari, I. Béjar Alonso, O. Brüning, M. Lamont, and L. Rossi, High-Luminosity Large Hadron Collider (HL-LHC): Preliminary Design Report (CERN, Geneva, 2015).

[6] (Ed.) O. Brüning et al., LHC Design Report, CERN-2004-003 (Vol. I), 4 June 2004.

[7] E. Métral, Single-Bunch and Coupled-Bunch Instability at LHC Top Energy vs. Chromaticity, CERN RLC meeting, 21/04/2006.

[8] S. Fartoukh, …The Sign of the LHC Octupoles, CERN LMC meeting, 11/07/2012.

[9] E. Métral, Impedances, Instabilities and Implications for the Future, CMAC meeting #6, CERN, 16-17/08/2012.

[10] A. Burov, Nested Head Tail Vlasov Solver : Impedance, Damper, Radial Modes, Coupled Bunches, Beam-Beam and More…, CERN AP forum, 04/12/2012.

[11] X. Buffat, W. Herr, N. Mounet, T. Pieloni, and S. White, Stability diagrams of colliding beams in the large hadron collider, Phys. Rev. ST Accel. Beams, vol. 17, p. 111002, Nov 2014.

[12] E. Métral et al., Beam Instabilities in Hadron Synchrotrons, IEEE Trans. on Nucl. Sci., Vol. 63, NO. 2, April 2016 (invited contribution for the 50th anniversary of the PAC conference).

[13] A. Burov, Three-beam instability in the LHC, FERMILAB-PUB-13-005-AD (2013).

[14] S. White, X. Buffat, N. Mounet, and T. Pieloni, Transverse mode coupling instability of colliding beams, Phys. Rev. ST Accel. Beams, vol. 17, p. 041002, 2014.

[15] X. Buffat, Transverse beams stability studies at the large hadron collider, Ph.D. dissertation, EPFL, 2015.

[16] N. Mounet, DELPHI: an analytic Vlasov solver for impedance-driven modes, CERN HSC meeting, 07/05/2014.

[17] L.R. Carver et al., Current status of instability threshold measurements in the LHC at 6.5 TeV, Proceedings of IPAC2016, Busan, Korea.

[18] G. Rumolo et al., Electron cloud effects in the CERN accelerator complex, these proceedings.

[19] E. Métral, Update of the stability limits including the effect of electron cloud, implications for machine and HW parameters (e.g. ramp rates), Joint LARP CM26/Hi-Lumi Meeting, SLAC, CA, USA, 19/05/2016.

[20] C. Tambasco et al., BTF observations and simulations for LHC: an update for discussions, CERN internal HSC meeting, 27/06/2016.

[21] T. Persson et al., Improved control of the betatron coupling in the Large Hadron Collider, Phys. Rev. ST Accel. Beams, vol 17, p. 051004, 2014.

[22] E. Métral et al., Destabilising effect of linear coupling in the HERA proton ring, Proceedings of IPAC2002, Paris, France.

[23] G. Iadarola, Electron cloud studies for CERN particle accelerators and simulation code development, CERN-THESIS-2014-047 - 203 p.

[24] K. Li et al., Mitigation of electron cloud instabilities in the LHC using sectupoles and octupoles, Proceedings of IPAC2012, New Orleans, Louisiana, USA.

[25] E. Benedetto, Emittance growth induced by electron cloud in proton storage rings, Ph.D. dissertation, Politecnico di Torino, 2006, CERN-THESIS-2008-096.

[26] R. Bruce et al., LHC Run 2: results and challenges, these proceedings

[27] M. Schenk et al., Use of RF quadrupole structures to enhance stability in accelerator rings, these proceedings.

[28] T. Pieloni et al., Octupoles and long-range beam-beam effects for the HLLHC: can they compensate each other?, CERN internal HSC meeting, 27/06/2016.

ISBN 978-3-95450-185-4

IDENTIFICATION AND REDUCTION OF THE CERN SPS IMPEDANCE

E. Shaposhnikova, T. Argyropoulos, T. Bohl, A. Lasheen, J. Repond, H. Timko
CERN, Geneva, Switzerland

Abstract

The first SPS impedance reduction programme has been completed in 2001, preparing the ring for its role as an injector of the LHC. This action has eliminated microwave instability on the SPS flat bottom and later nominal beam could be delivered to the LHC. The High Luminosity (HL-) LHC project is based on beam with twice higher intensity than the nominal one. One of the important SPS intensity limitations are longitudinal instabilities with minimum threshold reached on the 450 GeV flat top. In this paper the work which was carried on to identify the impedance sources driving these instabilities is described together with the results expected from the next campaign of the SPS impedance reduction planned by the LHC Injector Upgrade (LIU) project.

INTRODUCTION

The LHC beam with 4 batches of 72 bunches with nominal intensity of 1.2×10^{11} p/b and spaced at 25 ns is operational in the SPS and was used by the LHC. During special machine development (MD) sessions the SPS has been able to deliver at top energy (450 GeV) up to four batches with bunch intensity of 1.4×10^{11}. This beam had nominal longitudinal and smaller than nominal transverse emittances.

The baseline LHC upgrade (HL-LHC) scenario is based on the SPS beam with 288 bunches of 2.3×10^{11} p/b spaced at 25 ns or 144 bunches of 3.6×10^{11} p/b at 50 ns [1].

Presently the intensity of the LHC beam is limited by beam loading in the 200 MHz Travelling Wave cavities. In the frame of the LIU (LHC Injectors Upgrade) project [2] the 200 MHz RF system will be significantly upgraded. The plan includes the shortening of the existing long cavities from 5 to 4 sections together with doubling of the total RF power [3]. These modifications should allow the beam intensity of 2.4×10^{11} p/b to be accelerated to the top energy, but without any margin due to longitudinal instabilities which lead to emittance blow-up. This beam should be injected into the 400 MHz RF system of the LHC. To avoid increase of relative particle losses in the LHC, the average bunch length at the SPS extraction should not exceed the present value of 1.65 ns achieved with available voltage of 7 MV.

Longitudinal beam instabilities observed during acceleration ramp have extremely low threshold (6 times below the nominal intensity). Even recently the impedance sources driving this instability were not exactly known [4]. In the present operation the LHC beam is stabilised by the 4th harmonic (Landau) RF system operating in bunch-shortening (BS) mode and controlled longitudinal emittance blow-up, however for the HL-LHC beam the longitudinal emittance needed for beam stability could be too large for acceleration and extraction to the LHC. So during the last few years significant efforts went in identification of the impedance sources driving longitudinal instabilities and building the reliable impedance model of the SPS. The results of these studies are presented below.

LONGITUDINAL INSTABILITIES

Single-bunch Instability

A strong dependence of bunch length on intensity is observed on the SPS 450 GeV/c flat top for single bunches with intensities similar to that required for the LHC upgrade scenarios. This bunch lengthening exists in both single and double RF operation and could not be explained by the potential well distortion from the defocusing voltage due to the SPS reactive impedance with ImZ/n=3.5 Ohm [5]. The results of measurements imply that the threshold of microwave instability is hit during the acceleration cycle. The threshold depends on voltage program used for acceleration [6] and on the flat top is higher for the larger RF voltage. For bunches with longitudinal emittance (2σ) of 0.27 eVs the threshold of fast instability is around 1.8×10^{11}, see Fig.1.

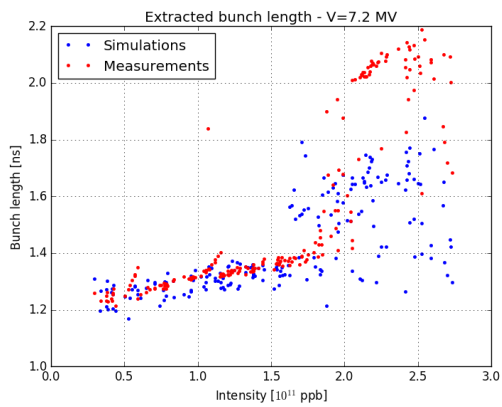

bunch intensity

Figure 1: Measured (red) and simulated (including ramp, blue symbols) bunch length at 450 GeV/c as a function of intensity for a single bunch in a single 200 MHz RF system with 7.2 MV. Voltage program with 7 MV during the 2nd part of the ramp.

Taking into account slow-developing instability during the ramp, for bunches with injected emittance around 0.25 eVs the threshold on the flat top is close to 1.0×10^{11} in a single 200 MHz RF system and to 1.2×10^{11} in a double RF operation with voltage ratio around 0.1 [6].

ISBN 978-3-95450-185-4

Multi-bunch Instability

The longitudinal multi-bunch instability observed in the SPS during acceleration has a very low intensity threshold: one batch of 12 bunches at 25 ns spacing with 4×10^{10} p/b and nominal injected longitudinal emittance (0.35 eVs) is unstable on the SPS flat top. Higher intensities become unstable during acceleration ramp (see Fig. 2).

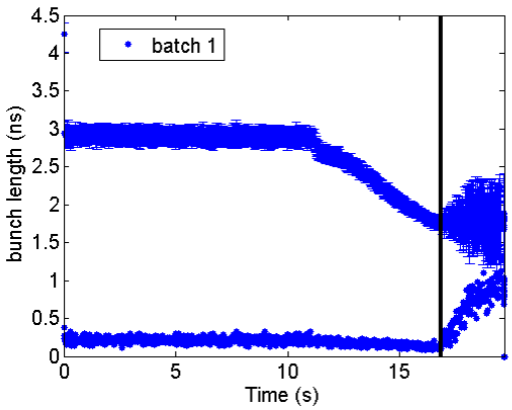

Figure 2: Longitudinal instability of 12 bunches spaced at 25 ns during the SPS ramp (from 26 to 450 GeV/c) in a single RF. Top trace: average bunch length, bottom: maximum bunch length deviation in the batch. Beam with average $N_b = 1.2 \times 10^{11}$ becomes unstable at 265 GeV/c.

Extensive beam measurements were performed recently with the goal to gain more information about possible impedance sources driving multi-bunch instability by studying dependence of its threshold on different machine and beam parameters, and in particular on the number of bunches in the batch and the length of the gap between the batches. The studies were conducted in a single RF system to minimise uncertainties related to the parameters of the 800 MHz RF system.

All measurements presented below were done in the new SPS optics Q20, in operation since 2012, having lower transition gamma γ_t (18 instead of previous 22.8) [7]. In this optics the gain in stability for a given longitudinal emittance is a factor of 2.8 at flat bottom and 1.8 at flat top (proportional to $\eta = 1/\gamma_t^2 - 1/\gamma^2$). Indeed significant increase in both transverse and longitudinal beam stability was obtained on the flat bottom. However for stability of the LHC beams on the flat top, a controlled emittance blow-up during ramp is still required in addition to operation of the higher harmonic RF system.

As can be seen from Fig. 3, 12 bunches with average bunch intensity N_b in the range $(0.5 - 2.0) \times 10^{11}$ and emittance ~ 0.32 eVs became unstable over a wide energy range during acceleration in a single RF system.

Bunches used for measurements in different MD (Machine Development) sessions had very different intensities (a factor 4 variation) and slightly different bunch length (2.8 ns ±5% variation on the flat bottom), but during

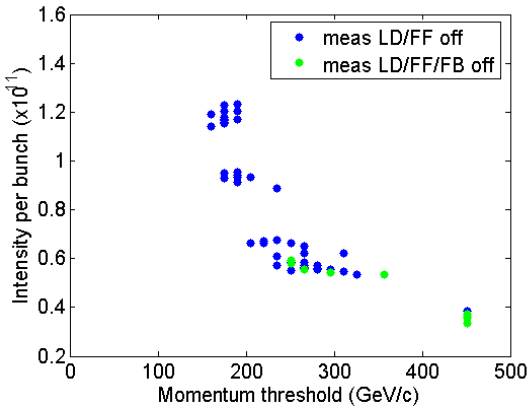

Figure 3: Threshold bunch intensity for 12 bunches as a function of beam energy during the SPS acceleration ramp in a single 200 MHz RF system. Measurements with longitudinal damper and feed-forward system off (blue dots), and without feedback in addition (green dots).

acceleration they all became unstable in the range (150-300) GeV/c. As expected from the calculated threshold for the coupled-bunch instability [8], the instability threshold clearly depends on beam energy E: more dense bunches become unstable earlier in the cycle. Far from transition energy the instability threshold scales roughly as $N_b \sim 1/E_{th}$, see Fig. 4, with minimum reached at the flat top energy.

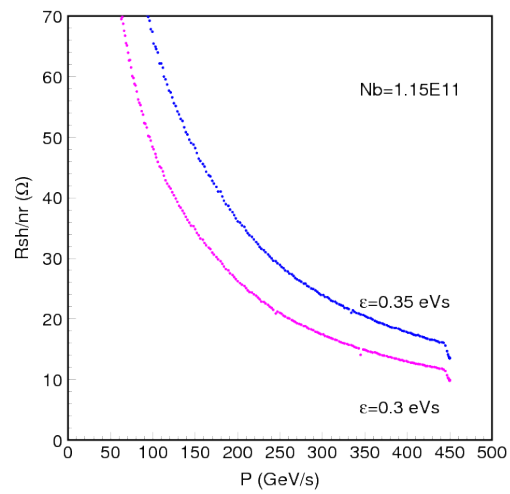

Figure 4: Coupled-bunch instability threshold R_{sh}/n_r ($n_r = f_r/f_0$ with $f_{r,0}$ being resonant and revolution frequencies) as a function of beam energy for bunch emittances of 0.3 and 0.35 eVs in a single 200 MHz RF system with a constant voltage of 6.5 MV above 100 GeV/c.

It was observed previously [4], that the instability threshold doesn't depend on the number of batches in the ring, at least for 50 ns spaced bunches with 250 ns batch gaps. A comparison of instability threshold $N_b E_{th}$ for batches with different number of bunches is shown in Fig. 5. Due to

ISBN 978-3-95450-185-4

sharp reduction of threshold during ramp batches with different bunch intensity appear unstable roughly at the same energy during ramp. This threshold was also measured for two batches of 12 bunches spaced at different distance, see Fig. 6, and no significant variation in threshold could be recorded. The short-range wake is compatible with the main and HOM (630 MHz) impedances of the 200 MHz RF system which have, correspondingly, quality factors of 150 and 500. The impedance of the fundamental mode is significantly reduced by feed-back and feedforward systems and impedance of this HOM is already well damped by dedicated damping loops installed in all cavities. Nevertheless, as confirmed by particle simulations performed at the SPS flat top with 72 bunches using code BLonD [9], the total impedance of 300 kOhm of the HOM at 630 MHz is one of the main sources of multi-bunch instability in the SPS. The measured sharp dependence of intensity threshold on energy can be also reproduced in simulations with realistic model of the main 200 MHz impedance. The simulations show also that for 24 bunches the instability threshold is 30% higher than for 72 bunches [10].

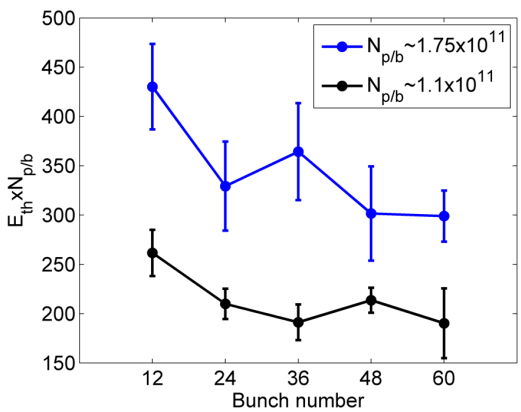

Figure 5: Instability threshold $E_{th}N_b$ for two different values of average bunch intensities N_b as a function of number of bunches spaced at 25 ns.

Measurements with Long Bunches

To identify possible sources of microwave instability various beam measurements were performed in the SPS. Microwave instability leads to an uncontrolled emittance blow-up and was one of the main intensity limitations for the SPS as an injector of the LHC. At that time the inter-magnet pumping ports were identified as a source of this instability by measuring the spectrum of long ($\sim$ 25 ns) single bunches injected into the SPS with RF off and intensity $\sim 2 \times 10^{10}$, above the instability threshold [11]. After shielding of 1000 pumping ports the microwave instability with RF on was not seen anymore on the 26 GeV/c SPS flat bottom for the LHC bunches up to an intensity of 2.0×10^{11}. The threshold has been also increased due to the Q20 optics.

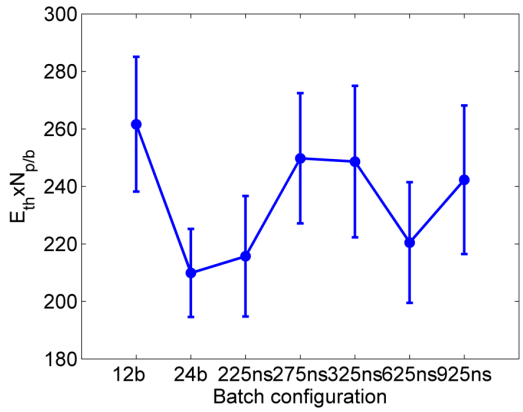

Figure 6: Instability threshold $E_{th}N_b$ for 12 bunches and different gaps between the two batches of 12 bunches (0, 225, 275, 325, 625 and 925 ns).

During developing of instability with RF off, unstable mode spectrum has a center frequency close to the resonant frequency of the impedance $\omega_r = 2\pi f_r$ and a width given by either the impedance width $\omega_r/(2Q)$ or by the bunch length τ (if $1/\tau \gg \omega_r/(2Q)$) [11]; hence longer bunches allow better resolution of resonant peaks, see Figs. 7, 8. In 2001, when the majority of pumping ports were shielded, practically no high frequency peaks were seen for intensity below 8×10^{10}. However, for higher intensities, bunch modulation at 1.4 GHz appeared.

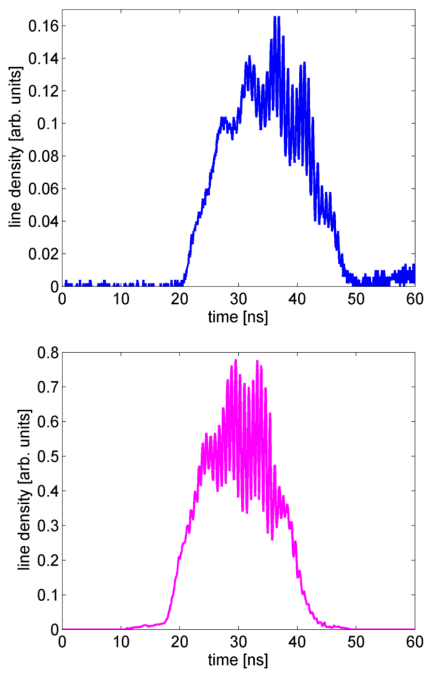

Figure 7: Line density modulation of long bunches $\sim$ 400 turns after injection into the SPS with RF off in measurements (top) and simulations using full SPS impedance model (bottom). Bunch intensity $\sim 1 \times 10^{11}$.

ISBN 978-3-95450-185-4

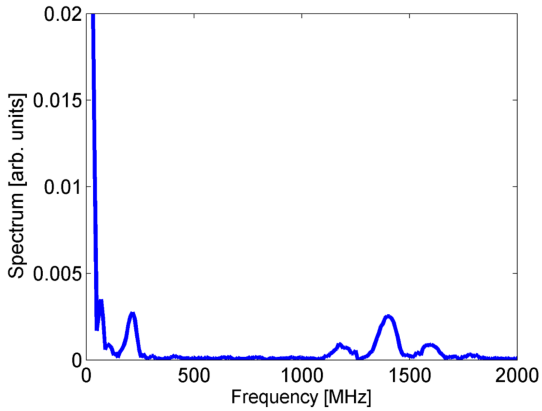

Figure 8: Fourier spectrum during developing of bunch instability shown in Fig. 7 (top).

Since microwave instability was again observed in the SPS, this time during acceleration of high intensity single bunches, measurements with long bunches injected into SPS with RF off were carried out to get more information about possible impedance sources [12], [13]. It was suspected that microwave instability is most probably driven by a resonant impedance at 1.4 GHz with peak in unstable bunch spectrum observed already in 2001. These measurements were repeated at intensities above 8×10^{11}. The possible parameter range of impedance (R_{sh} and Q) was narrowed down using a comparison of particle simulations with beam measurements [12], however the source of this impedance was not known till 2014, when it had been identified as an impedance of the SPS vacuum flanges. A layout survey of the whole SPS ring has been carried out to determine the total number and type of various vacuum flanges and to estimate their impedance contribution [14]. Most of these accidental cavities are damped by ceramic resistors to reduce the Q-factor and risk of coupled-bunch instabilities. Nevertheless the main impedance source responsible for longitudinal multi-bunch instabilities was identified to be vacuum flanges (VF) [10, 15].

Table 1 shows the most significant resonances found in the vacuum flanges [14]. The first two and the last rows of the Table show resonances in the cases where vertical and horizontal Beam Position Monitors (BPV and BPH, respectively) nearby are involved. Radiation losses are dominant for all enameled flanges having relatively low Q values (< 400). Higher Q values have been found for the non-enameled flanges. The resonances can also be divided in three groups: around 1.25 GHz, 1.4 GHz and 1.6 GHz, all visible in Fig. 8, however peaks around 1.4 GHz give the biggest contribution to the SPS impedance.

In the present SPS impedance model shown in Fig. 9, the vacuum flanges together with the 200 MHz and 800 MHz cavities are the three dominant contributors to the resistive impedance. The main contributions to the impedances with high R/Q are from the kicker magnets and again the 200 MHz cavities. The particle simulations performed

Table 1: The total impedance R_{sh} and quality factor Q of the dominant resonances of the SPS vacuum flanges with n identical elements in the ring. All these flange have enamel coating (except both “QF-QF" types) and attached bellows (except “QF-QF-nb"). Short or long damping resistor is placed inside bellows (except “BPV-QD” and “QF-QF-nb").

	Flange type	n	f_r [GHz]	R_{sh} [Ohm]	Q
1	BPV-QD	90	1.21	630	315
2	BPH-QF	39	1.28	1030	400
3	QF-MBA	83	1.41	1600	268
4	MBA-MBA	14	1.41	300	285
5	QF-QF	26	1.41	3765	1820
6	QF-QF-nb	20	1.61	590	980
7	BPH-QF	39	1.62	120	120

using this model can reproduced most of observed features (see e.g. Fig. 1), but there are also indications that some inductive impedance with $\mathrm{Im}Z/n \sim 1$ Ohm is still missing in the present model [6].

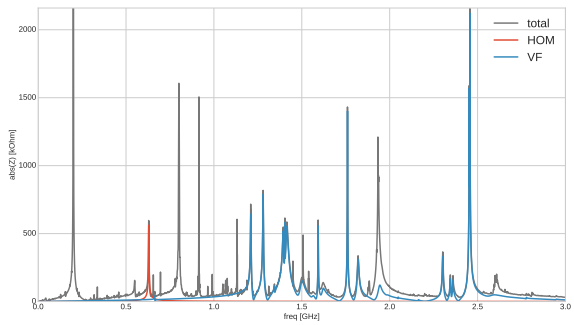

Figure 9: Present SPS longitudinal impedance model. Blue trace: contribution from the vacuum flanges (VF).

IMPEDANCE REDUCTION

The instability thresholds found from macroparticle simulations using code BLonD [9] at the SPS flat top for 72 bunches and a realistic SPS impedance model are shown in Fig. 10. The threshold found for one batch of 24 bunches is 30% higher [10].

As one can see, even with increased longitudinal emittance, possible due to RF upgrade, stability cannot be guaranteed for all bunches in the batch, mainly due to large bunch length spread along the SPS batch coming from controlled longitudinal emittance blow-up in presence of the beam loading in the 200 MHz TW RF system [16].

There are nine main types of flanges in the SPS and they can be divided into two large groups (with approximately 400 and 240 flanges each) by the shape of the main adjacent vacuum chambers (QD or QF), see Table 1. The present baseline of the LIU project [2] is to shield 240 QF-type vacuum flanges which have resonant impedances with the highest R/Q. The implementation will start during

ISBN 978-3-95450-185-4

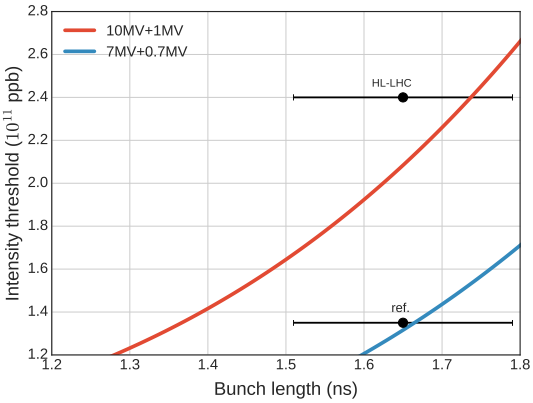

Figure 10: Instability threshold on the SPS flat top as a function of bunch length from particle simulations (code BLonD) with 72 bunches in a double RF (BS mode) for voltages of 10 MV (red line) and 7 MV (blue line) at 200 MHz and 10% value at 800 MHz. Black dots: beam parameters required by HL-LHC and those achieved in the SPS and used as a reference.

the end-of-year stops and will be completed in the long shutdown 2 (2019-2020). Since the majority of SPS flanges are insulating (enamel coating) with adjacent bellows, the shielding options depend on necessity to preserve isolation (gaps) or possibility to short circuit at least some of them (for details of ongoing investigation see [17]).

The instability thresholds found from particle simulations for the present SPS impedance model with realistic impedance reduction are shown in Fig. 11 for the situation after the RF upgrade (with 10 MV at 200 MHz). For main resonant peaks of ~ 130 insulating QF-flanges a reduction of R/Q by at least a factor 20 was assumed. After shielding, the impedance of non-insulating flanges and of un-shielded pumping ports was assumed to be zero. Reducing the quality factor Q of the 630 MHz HOM in the 200 MHz RF system by a factor of 3 could further increase the instability threshold. However their damping is already very good and it is difficult to improve it significantly [18].

Additional ways of reaching longitudinal beam parameters required by the HL-LHC at extraction from the SPS were also studied [15] and include increased RF voltage in the 800 MHz RF system, bunch rotation on the SPS flat top and new SPS optics with intermediate γ_t.

Other potential intensity limitations in SPS (as e.g. from interception devices and e-cloud effect) also exist and are under studies. They were not discussed here.

SUMMARY

The SPS impedance was significantly reduced in the past in preparation of the SPS as an LHC injector. A new SPS impedance reduction campaign is planned now for the HL-LHC project, which requires bunch intensities twice as high as the nominal one. One of the known intensity limitations is a longitudinal multi-bunch instability. The

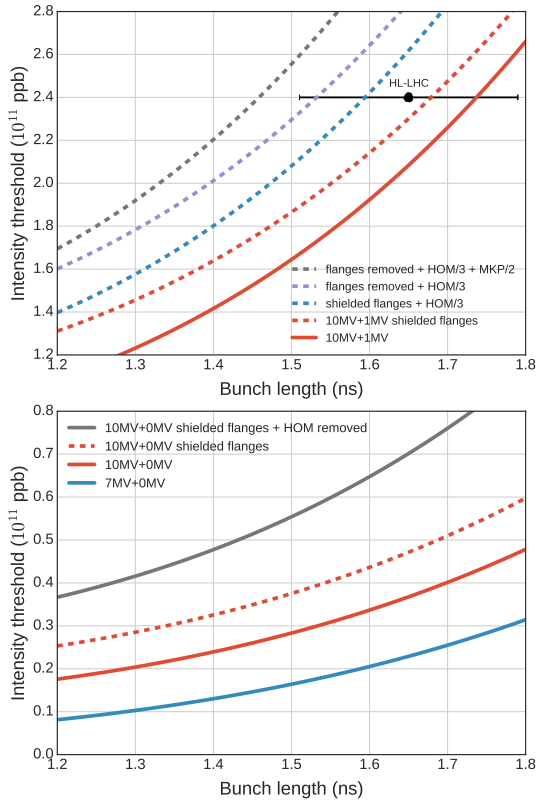

Figure 11: Top: instability threshold on the SPS flat top as a function of bunch length from particle simulations with 72 bunches in a double RF (BS mode) for voltages of 10 MV at 200 MHz and 1 MV at 800 MHz after RF upgrade (red). Dashed lines: different options of impedance reduction. Bottom: similar cases in a single RF system.

instability is presently cured using the 4th harmonic RF system and controlled emittance blow-up and its threshold will be increased after the foreseen upgrade of the 200 MHz RF system, but reaching the HL-LHC parameters cannot be assured without improving the machine impedance. The impedance sources responsible for this instability were identified using beam-based impedance measurements and implementation of their shielding and damping is foreseen during the next long shutdown.

ACKNOWLEDGMENTS

The work on impedance reduction involves many people and is coordinated by the LIU-SPS coordination team. The installation of shielding will be performed by CERN Vacuum Group. We are grateful to members of the LIU-SPS Coordination team and BD Working Group for useful discussions. We would like to thank R. Calaga, F. Caspers, A. Grudiev, T. Kaltenbacher, E. Montesinos, T. Roggen, B. Salvant, Y. Shashkov, J. Varela, C. Vollinger and C. Zannini for their contributions to SPS impedance measurements and calculations. We are grateful to H. Bartosik, H. Damerau and J. E. Muller for help in beam measurements. Special thanks go to the BLonD developers.

ISBN 978-3-95450-185-4

REFERENCES

[1] High-Luminosity Large Hadron Collider (HL-LHC): Preliminary Design Report edited by G. Apollinari *et al.*, Geneva, CERN (2015).

[2] "LHC Injectors Upgrade", Technical Design Report, Vol.I: Protons, edited by J. Coupard *et al.*, CERN-ACC-2014-0337 (2014).

[3] E. Shaposhnikova, E. Ciapala, E. Montesinos, "Upgrade of the 200 MHz RF system in the CERN SPS", *in Proc.* IPAC'11, San Sebastian, Spain (2011).

[4] E. Shaposhnikova *et al.*, "Longitudinal instabilities in the SPS and beam dynamics issues with high harmonic RF systems", *in Proc.* HB2012, Beijing, China (2012).

[5] T. Argyropoulos, "Longitudinal microwave instability in a multi-RF system", *Proc. HB2014*, East-Lansing, MI, USA (2014).

[6] A. Lasheen *et al.*, "Single bunch longitudinal instability in the CERN SPS", *in Proc.* IPAC'16, Busan, Korea (2016).

[7] H. Bartosik *et al.*, "Low gamma transition optics for the SPS: simulation and experimental results for high brightness beams", *in Proc.* HB2012, Beijing, China (2012).

[8] E. Shaposhnikova, "Longitudinal stability of the LHC beam in the SPS", CERN SL-Note-2001-031 HRF (2001).

[9] BLonD, Beam Longitudinal Dynamics code: http://blond.web.cern.ch/

[10] A. Lasheen *et al.*, "Effect of the various impedances on longitudinal beam stability in the CERN SPS", *in Proc.* IPAC'16, Busan, Korea (2016).

[11] T. Bohl, T. Linnecar and E. Shaposhnikova, Measuring the resonant structure of accelerator impedance with single bunches, PRL, v.78, N16 (1997).

[12] T. Argyropoulos *et al.*, "Identification of the SPS impedance at 1.4 GHz", *in Proc.* IPAC'13 (2013).

[13] E.Shaposhnikova *et al.*, "Identification of high-frequency resonant impedance in the CERN SPS", *in Proc.* IPAC'14, Dresden, Germany (2014).

[14] J. E. Varela, "Longitudinal impedance characterization of the CERN vacuum flanges", *in Proc.* IPAC'15, Richmond, VA, USA (2015).

[15] E. Shaposhnikova *et al.*, "Removing known SPS intensity limitations for high luminosity LHC goals", *in Proc.* IPAC'16, Busan, Korea (2016).

[16] T. Argyropoulos *et al.*, Controlled longitudinal emittance blow-up in a double harmonic RF system at CERN SPS, *in Proc.* HB2010, Morschach, Switzerland (2010).

[17] T. Kaltenbacher, F. Caspers, C. Vollinger, Machine element contribution to the longitudinal impedance model of the CERN SPS, *in this Proc.* (2016).

[18] T. Rogen *et al.*, The SPS 200 MHz TWC impedance after the LIU upgrade, *in this Proc.* (2016).

ISBN 978-3-95450-185-4

ELECTRON CLOUD IN THE CERN ACCELERATOR COMPLEX

G. Rumolo, H. Bartosik, E. Belli, G. Iadarola, K. Li, L. Mether, A. Romano, M. Schenk
CERN, Geneva, Switzerland

Abstract

Operation with closely spaced bunched beams causes the build-up of an Electron Cloud (EC) in both the LHC and the two last synchrotrons of its injector chain (PS and SPS). Pressure rise and beam instabilities are observed at the PS during the last stage of preparation of the LHC beams. The SPS was affected by coherent and incoherent emittance growth along the LHC bunch train over many years, before scrubbing has finally suppressed the EC in a large fraction of the machine. When the LHC started regular operation with 50 ns beams in 2011, EC phenomena appeared in the arcs during the early phases, and in the interaction regions with two beams all along the run. Operation with 25 ns beams (late 2012 and 2015), which is nominal for LHC, has been hampered by EC induced high heat load in the cold arcs, bunch dependent emittance growth and degraded beam lifetime. Dedicated and parasitic machine scrubbing is presently the weapon used at the LHC to combat EC in this mode of operation. This talk summarises the EC experience in the CERN machines (PS, SPS, LHC) and highlights the dangers for future operation with more intense beams as well as the strategies to mitigate or suppress the effect.

AN OVERVIEW OF ELECTRON CLOUD IN THE CERN ACCELERATORS

The Proton Synchrotron (PS)

In the PS, the electron cloud (EC) was first observed in 2001 during the last part of the cycle for the production of the the so-called LHC-type beams, i.e. the beams of the type needed for the LHC filling. The production scheme of these beams in the PS is based on two or three steps of bunch splitting in order to obtain at the exit of the PS bunch trains with 50 ns or 25 ns spacing, respectively. In either case, the final stage of bunch splitting takes place at the top energy (26 GeV/c) and is followed by adiabatic bunch shortening and fast bunch rotation shortly before extraction [1]. These two processes are meant to shorten the bunches from their 15 ns length after the last splitting to 12 and then 4 ns, respectively, and make them suitable to be injected into the SPS. Therefore, these beams only circulate in the PS for few tens of msec with a structure prone to EC formation (beam parameters are summarized in Table 1).

During this short time before extraction, an EC was initially revealed in 2001 by the presence of a baseline drift in the signal from the pick up as well as beam transverse instabilities [2]. In March 2007, an experiment for dedicated EC measurements was set up at the PS to be able to directly measure the electron signal by using a shielded biased pick up [3] and confirm its presence in the machine in the last phase of the LHC beams production. These studies confirmed that the EC develops during the last 40 to 50 ms before ejection, i.e. when the bunches are shortened by the RF gymnastics.

Table 1: Relevant beam parameters in the PS during the flat top RF gymnastics for the two bunch spacings of 50 and 25 ns

	50 ns	**25 ns**
Beam energy (GeV)	26	
Bunch intensity ($\times 10^{11}$ ppb)	1.3-2.0	1.3-1.6
Bunch length (ns)	15 → 12 → 4	
Number of bunches	36	72
Transv. norm. emittances (μm)	1-2	2-3

In the years 2011-2014, new systematic measurements of EC and effects on the beam have been performed at the CERN-PS with the goals of:

- Studying the dependence of the EC build-up evolution on some controllable beam parameters (bunch spacing, bunch intensity, bunch length);
- Collecting time resolved experimental data of EC build-up in some desired sets of beam conditions;
- Characterising the EC instability at 26 GeV.

These sets of data can serve two purposes. First, comparing them with build-up and instability simulations will allow us to validate (or improve) the simulation model on which our tools are based. Second, by matching the simulations to the experimental data in all the different beam conditions, we can pin down the secondary electron yield, SEY or δ_{max}, of the beam chamber and extrapolate then how much EC we can expect in the PS with the higher intensity beams foreseen in the frame of the LHC Injector Upgrade (LIU) project [4], and whether that can be detrimental to the beam.

The Super Proton Synchrotron (SPS)

The SPS has been suffering from EC formation since it first began to take and accelerate 25 ns beams produced in the PS with the scheme explained above. Observations of pressure rise, beam instability, emittance growth were first made in the early 2000 and all these effects strongly limited the capability of this accelerator of handling LHC-type beams [5]. While the coherent instabilities could be suppressed by the use of the transverse damper (against the horizontal coupled bunch oscillations) and running with sufficiently high chromaticity (against the strong single bunch effect in the vertical plane), emittance growth and positive tune shift along the bunch train could still be measured, pointing to the continuing presence of a strong EC inside the beam chamber. All

ISBN 978-3-95450-185-4

this led to the decision to have in 2002 the first dedicated scrubbing run, in which the SPS was operated exclusively with 25 ns beams for one full week. The goal was to use the bombardment from the EC itself to clean the beam chamber inner surface, and therefore lower its Secondary Electron Yield (SEY) and reduce, in turn, the amount of EC build-up. The strategy proved successful [6] and the week of scrubbing run was then repeated at the beginning of the 2003, 2004, 2006 and 2007 runs to provide the necessary machine cleaning. During these years, dedicated experiments were conducted in the SPS to study in detail the EC formation in cold regions (COLDEX) or in NEG coated chambers [7], or to benchmark simulation codes with machine observations [8]. From 2006 on, EC studies in the SPS acquired new momentum in the framework of the SPS upgrade studies [9] and the experimental activity over the following years was mainly focused to find the scaling law of the EC instability with beam energy [10] and to validate the efficiency of amorphous carbon (a-C) coating of the beam chamber [11]. From 2011 onwards, the nominal 25 and 50 ns LHC beams in the SPS appeared to be undegraded with no signs of the strong EC effect that was present during the first years of SPS operation. The achievable parameters are summarized in Table 2. The three values of bunch length quoted in this table correspond to injection into 2 MV buckets, after shortening at flat bottom by increase of the RF voltage to 3 MV, and at flat top after controlled longitudinal emittance blow up during the accelerating ramp.

All the EC machine development activity of the last few years at the SPS has been devoted to defining the status of the 25 ns beams in this machine and use the direct EC measurements in chambers equipped with strip monitors to understand beam induced scrubbing in different chamber geometries and with different materials. A comprehensive report of all observations in terms of beam behaviour, pressure rise and dedicated EC measurements during the 2012 scrubbing studies was published [12].

Table 2: Relevant Beam Parameters of the SPS 50 and 25 ns Beams

	50 ns	**25 ns**
Beam energy (GeV)	26 → 450	
Bunch intensity ($\times 10^{11}$ ppb)	1.2-1.8	1.1-1.3
Bunch length (ns)	4 → 2.8 → 1.5	
Number of bunches	144	288
Transv. norm. emittances (μm)	1-2	2-3

After the Long Shutdown 1 (2013-14), during which the whole SPS was exposed to air and the surfaces of the beam chambers were expected to return to high values of SEY, the two main questions to answer were:

- How long it would take to recover the previous SPS performance through beam induced scrubbing;
- Up to which beam intensity the SPS could be successfully scrubbed in view of future operation with higher intensity/higher brightness beams.

Seven days were dedicated to scrubbing run and scrubbing studies in the late 2014, during which the SPS performance with 25 ns beams was successfully recovered and first tests of injection of high intensity 25 ns beams were conducted. At the beginning, these beams caused large pressure rises and were hampered by violent instabilities and emittance blow up at the tails of the trains. Further studies with high intensity were conducted over 10 days of SPS scrubbing in 2015. Over these days, the beam could be successfully stabilised and losses decreased. The scrubbing campaign in 2015 with high intensity beams was so successful that scrubbing became the baseline for the upgrade of the SPS to higher intensity and higher brightness beams [13].

The Large Hadron Collider (LHC)

Several studies conducted in the past predicted that also the LHC would suffer from heat load, pressure rise and beam instabilities due to EC, when operating with trains made of closely spaced proton bunches (e.g. [14]). Since mid 2010 LHC entered this mode of operation. In the first phase, beams with 150 ns bunch spacing were injected, accelerated and brought to collision. During this period of operation, the only possible signature of EC build-up was a pressure rise observed in the common vacuum chamber, close to the Interaction Regions. Subsequently, at the end of October 2010, machine studies with tighter bunch spacings were initiated with the goal to characterize the EC build-up in the LHC, its effects and possible cures. The study of the 75 ns and 50 ns beams took place in dedicated MD sessions, during which the strong EC effects seen initially gradually decreased. Since the EC effects with 75 ns appeared significantly less pronounced than with 50 ns beams, this bunch spacing could be regarded as a relatively safe option for the 2011 run [15].

The LHC operation was therefore resumed in 2011 directly with 75 ns beams. However, at the beginning of April, 10 days were devoted to scrubbing of the LHC with 50 ns beams. The goal was to prepare the machine to switch to 50 ns beams and thus extend the luminosity reach for the 2011 run. During the scrubbing run, up to 1020 bunches per beam were injected into the LHC in batches of 36 and stored at injection energy. The quality of the beam significantly increased over this period. The success of the scrubbing run was proved by the subsequent smooth LHC physics operation with 50 ns spaced beams. Between mid April and end June the number of bunches collided in the LHC was increased up to its maximum value of 1380 per beam, while the intensity per bunch and the transverse emittances remained constant at their nominal values (i.e., 1.15×10^{11} ppb and 2.5 μm). The switch to 50 ns beams with lower transverse emittances (1.5 μm) and the adiabatic increase of the bunch current to 1.5×10^{11} ppb did not cause any significant recrudescence of the EC effects. Beams with 25 ns spacing were injected

ISBN 978-3-95450-185-4

into the LHC only during five MD sessions of the 2011 run. They appeared to suffer from strong instabilities at injection (damped with high chromaticity) and exhibited poor lifetime and blown up emittances even by the end of these study periods. However, the heat loads measured in the arcs with this type of beams could be used for extrapolating the evolution of the SEY on the beam screen in the arcs, which was estimated to decrease from an initial value above 2.0 to about 1.5 [16]. The year 2012 was a physics production year and the LHC mainly ran with high intensity 50 ns beams (1.7×10^{11} ppb). At the end of the run, in preparation for the high energy run of the LHC after the upcoming Long Shutdown 1 (LS1) with 25 ns beams, a dedicated scrubbing run took place with this type of beams, followed by test ramps and a pilot physics run to provide data for the experiments with the new spacing. The SEY of the beam screens did not seem to decrease much more than it had already (it remained between 1.4 and 1.5, beyond resolution with our method for estimating its value), as the scrubbing seemed to have entered its slow phase in which increasingly larger electron fluxes are needed to lower even slightly the SEY [17]. The main conclusion from the 2012 experience was that LHC operation with 25 ns would be possible in the post-LS1 operation, although it would be probably hampered by EC to a large extent and for a long time. In this scenario, the following two options were envisaged [18]:

1. Proceed with the standard 25 ns beams and hope to progress with the slow scrubbing while in parallel providing data to the experiments (scrubbing with physics)

2. Switch to low EC filling schemes still based on 25 ns bunch spacing - allowing for more bunches and higher bunch intensity with respect to the 50 ns beams (e.g. the 8b+4e [19])

After machine recommissioning with low intensity bunches, LHC multi-bunch operation was therefore resumed in 2015 with a first extended scrubbing run to allow a brief physics run with 50 ns beams. It immediately became apparent that the SEY of the beam screens in the arcs had been reset to the high values they had back in 2010. The first 10 days of scrubbing served the purpose to lower again the SEY to values between 1.4 and 1.5. A second scrubbing run over two weeks improved the LHC performance with 25 ns beams and ended with the demonstration that filling schemes at least up to 1200 bunches per beam could be successfully employed for physics. At this point, LHC entered the phase of intensity ramp-up and the option of possible scrubbing with physics was chosen. The technique seemed to work to some extent: by October 2015, 2242 bunches per beam were successfully put in collision, although several cycles of deconditioning/reconditioning were observed to occur and the achievement was only made possible by a gradual relaxing of the filling pattern in order to alleviate the EC heat load and not exceed the capacity of the cryogenic system, which ran very close to the limit. In particular, operation switched from trains of 144 bunches to trains of 72, and eventually to trains of 36 bunches to keep the heat load in the beam screen of the arcs below the limit of 135 W per half cell (W/hc) for one of the sectors.

In 2016, only a short scrubbing run took place, during which trains of 144 and 216 bunches were successfully injected and kept stable in the LHC at 450 GeV. The machine performance showed that conditioning had not been lost from the previous year and an intensity ramp-up could be safely carried out. However, due this time to limitations in the SPS, only filling patterns with trains of 72 bunches could be used for filling the LHC. Within about one month of the beginning of the intensity ramp-up, the LHC was filled with 2040 bunches per beam and LHC reached its nominal peak luminosity of 10^{34} cm^{-2} s^{-1}. The heat load in the beam screen of the arcs ran constantly close to the limit (160 W/hc), allowing potentially only for marginal increase now in either bunch intensity or number of bunches (or marginal decrease of bunch length). The final step has been for now to switch to trains of 2x48 bunches, which allows for a small decrease of the heat load for a slightly higher number of bunches (2076) and paves the way to switching to low transverse emittance variants of the LHC beams for the near future.

The LHC beam parameters are summarised in Table 3.

Table 3: Relevant beam parameters of the LHC 50 and 25 ns beams

	50 ns	**25 ns**
Beam energy (TeV)	0.45 → 3.5/4 → 6.5	
Bunch intensity ($\times 10^{11}$ ppb)	1.1-1.7	1.1
Bunch length (ns)	1.0-1.5	
Number of bunches	1400	2800
Transv. norm. emittances (μm)	1-2	2-3

SOME HIGHLIGHTS OF STUDIES IN THE DIFFERENT MACHINES

PS Measurements

Between 2011 and 2014, several EC studies took place in the PS in order to cover build-up in different sets of beam parameters or different locations (specifically, a straight section and a main magnet unit), as well as the instabilities at 26 GeV. EC build-up data were recorded for 25 ns and 50 ns beams and the bunch intensities were scanned in a wide range from well below nominal values to slightly above. The direct EC signals were recorded shortly before extraction, when in normal conditions each bunch of the beam has been already fully rotated (4 ns bunch length). However, specifically for these measurements, the bunch length at this time for a fixed bunch intensity was also targeted to 6.5 or 15 ns by simply adjusting or fully removing, respectively, the final step of the fast bunch rotation. This allowed studying the dependence of the EC build-up not only on the bunch intensity but also on the bunch length. The measurements

ISBN 978-3-95450-185-4

taken in the straight section 98 (SS84) were very successful and could be successfully benchmarked against simulations with the PyECLOUD code [20]. Measurements in the main magnet unit 98 (MU98), which had been also equipped with a shielded pick up fully specified through detailed build-up simulations, were unfortunately not successful because, due to a design flaw, the recorded signal turned out to be dominated by the electromagnetic signal induced by the beam passage. Instability measurements were carried out by removing the bunch rotation at the end of the LHC magnetic cycle and extending the cycle by few milliseconds before extraction and after adiabatic bunch shortening to 10 ns. The instability, which appeared mainly in the horizontal plane, could be recorded with a wideband pick up all along the beam over several turns, revealing a clear coupled-bunch pattern extended from the tail of the train towards the head (see Fig. 1). Although this instability can be potentially a problem for higher intensity 25 ns beams for the future LIU program, it has been proven that the transverse feedback system is able to delay its occurrence by few tens of milliseconds. This is deemed to be sufficient to preserve the beam stability for the future LHC-type beams with double intensity and double brightness.

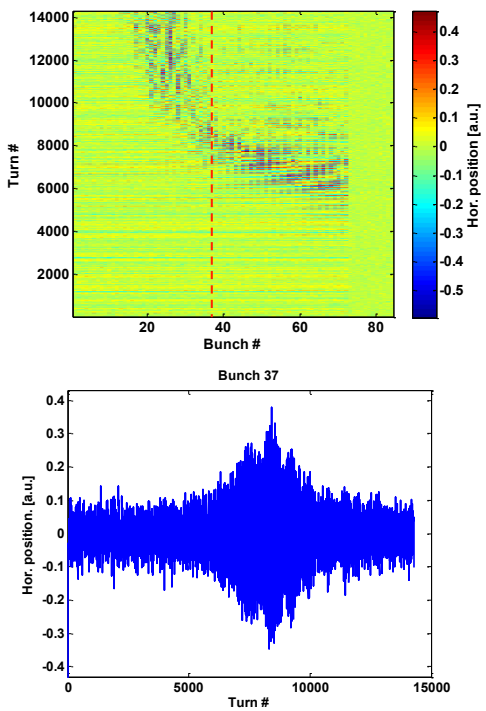

Figure 1: Bunch-by-bunch and turn-by-turn horizontal position along a train of 72 bunches in the PS at 26 GeV. The top plot shows the full 2D data set, with the cut highlighted by a dashed line displayed separately in the bottom plot. The instability is revealed by the exponentially growing signal.

SPS Studies

One of the key points to be addressed to understand the EC in the SPS is to determine the values of SEY thresholds for its formation in the different beam chambers and try to deduce what parts are critical for both present and future LHC beams. Figure 2 shows the electron flux to the chamber wall as a function of the SEY for four different values of bunch current and for four typical SPS chambers, i.e. MBA and MBB-type for dipoles plus QD and QF for quadrupoles (shapes and sizes of these chambers can be found in [20]). The following interesting features can be observed:

- The EC build-up is fairly insensitive to bunch intensity for dipoles, while thresholds tend to become slightly lower for lower currents in quadrupoles (or the behaviour is non-monotonic).
- Above the SEY threshold, the electron flux always becomes quickly larger for larger bunch currents.
- MBA-type chambers have higher SEY threshold value and therefore are the easiest to scrub, while MBB-type and quadrupole chambers have lower SEY threshold (comparable or lower values than those to which StSt potentially scrubs) and might be expected to suffer from large EC build-up even after extensive scrubbing.

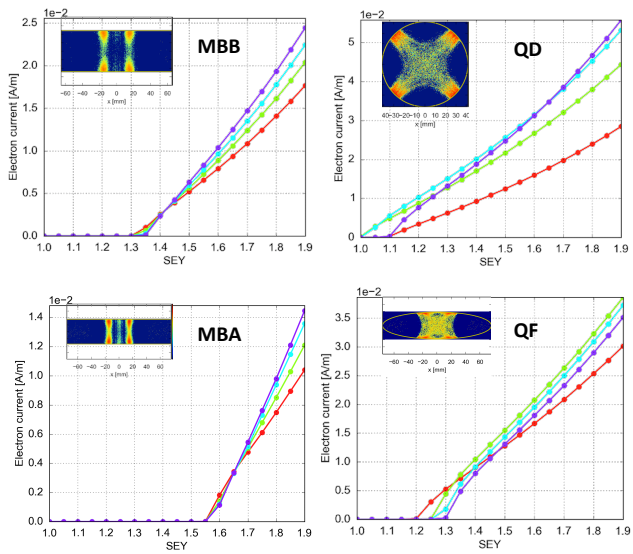

Figure 2: SEY curves for EC formation in the four types of SPS chambers (dipoles on the left and quadrupoles on the right side) and for four different bunch intensities (red 1.0×10^{11} p/b, green 1.5×10^{11} p/b, turquoise 2.0×10^{11} p/b, purple 2.5×10^{11} p/b).

Considering all the results of the above study as well as the results from the scrubbing campaigns in 2014 and 2015 with larger bunch currents than nominal (2.0×10^{11} p/b), it was decided to apply a-C coating [21] to the quadrupole chambers and some of the drift chambers during the Long Shutdown 2 (LS2), while relying in general on scrubbing for longer term operation of the SPS with LIU-type beam intensities. However, the MBB chambers along a full arc will also be coated in LS2, so that everything will be ready for full machine coating during the next shutdown if scrubbing will turn out not to be sufficient to guarantee the desired beam quality during Run 3.

ISBN 978-3-95450-185-4

LHC Observations

The main EC indicators in LHC are the heat load in the arcs as well as the beam stability and lifetime (which can be guaranteed only with machine settings in certain ranges). The heat load data from the cryogenic system give the total power dissipated (in W/half-cell) on the beam screens of both beams 1 and 2. Using the measured heat load it is possible to estimate the SEY of the arc chamber walls and monitor the progress of scrubbing. The exact procedure is based on the comparison of the heat load data with PyECLOUD simulations, run with realistic bunch-by-bunch intensities and lengths [16]. In high EC operation, i.e. with 25 ns beams, the beam stability can be only preserved with large chromaticity values. However, due to the tune footprint in presence of large chromaticity and strong EC, this also implies that the tunes must be kept far away from any dangerous resonance line in order not to trigger incoherent losses. Figure 3 shows the estimated tune footprint at LHC injection with large chromaticity and EC in all the cold arcs (dipoles and quadrupoles). Incoherent losses were observed when the vertical tune of the LHC was 0.31 at injection because of the proximity to the third order resonance. This could be easily avoided by lowering the vertical tune at injection to values around 0.29 (and consequently lowering the horizontal tune to keep the safety margin between the two that would avoid the onset of instabilities from coupling [22]).

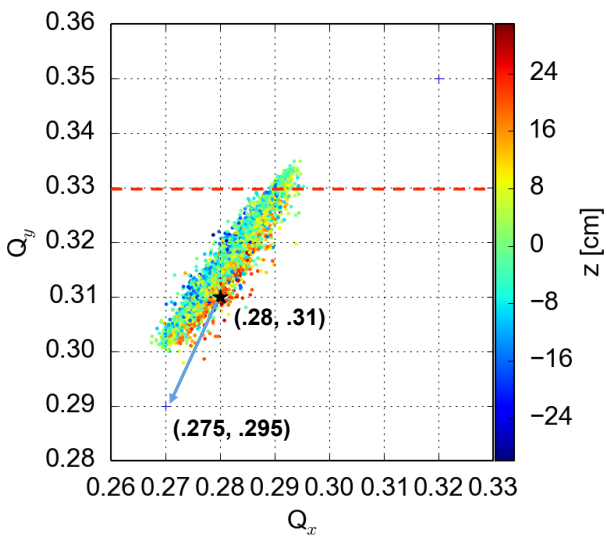

Figure 3: Tune footprint of the beam in LHC with octupoles powered to -20 A, chromaticities $Q'_{x,y}$ set to 15/20, and assuming an EC density of 5×10^{11} e/m^3 uniformly distributed along the whole ring.

The present strategy to run LHC with 25 ns beams is to use scrubbing runs just long enough as to gain enough margin for a smooth intensity ramp-up for physics, and then accumulate additional parasitic scrubbing while providing the beam to the experiments. Though this allows for a clear optimisation of the use of the LHC machine time, it has been observed that the machine in advanced state of scrubbing undergoes cycles of deconditioning/reconditioning. Scrubbing appears to be reasonably well preserved during Technical Stops and Machine Development sessions with low intensity/low energy beams, while deconditioning mainly occurs when running with low e-cloud/high synchrotron radiation schemes. The reason could be that synchrotron radiation can clean other parts of the beam chamber but it pollutes the previously scrubbed ones. However, this phenomenon is not worrisome, as recovery can then be achieved rather quickly. Scrubbing with physics has been pursued in 2015 and 2016. Lately, the time scale of the improvement appears to have become significantly longer, as no clear trend can be observed in the normalised heat load data, if we remove the uncertainty due to changing beam parameters and recalbrations of the measurements. Further scrubbing might be achieved in future by means of the use of longer trains or electron cloud enhancing schemes (e.g. the doublets [23]), or by attempting scrubbing at higher beam screen temperature if this is demonstrated to be effective. A few aspects of the EC effects in the LHC are presently still under investigation, like the different heat loads measured in different sectors (spread of about a factor three) and their different evolutions, the behaviour of EC with energy in dipoles and quadrupoles, and the EC driven instabilities at 6.5 TeV.

CONCLUSIONS AND OUTLOOK

Thanks to intensive measurements and highly improved simulation tools, we have reached a deep knowledge and understanding of EC phenomena in the different CERN accelerators. For the present beam parameters (25 ns beams), PS and SPS can deliver the required beams well within their original specs, while LHC still suffers from electron cloud, but is now operating thanks to scrubbing with physics.
For future beam parameters (double intensity, double brightness), the SPS will again rely on scrubbing, while being prepared to full a-C coating of the most EC prone chambers if that will not be sufficient during Run 3. HL-LHC operation will depend on the evolution of scrubbing during Run 2 and the experimental dependence of EC on bunch intensity. It may use EC free filling patterns like the 8b+4e, if needed. In general, anti-EC coatings inside the beam chambers are strongly recommended to be included in the baselines of all future projects.

ACKNOWLEDGMENTS

The authors would like to thank G. Arduini, V. Baglin, B. Bradu, G. Bregliozzi, K. Brodzinski, X. Buffat, R. Cappi, L. Carver, F. Caspers, P. Chiggiato, S. Claudet, P. Costa-Pinto, J. Esteban-Müller, S. Gilardoni, M. Giovannozzi, B. Goddard, M. Hostettler, M. Jimenez, V. Kain, E. Mahner, E. Métral, H. Neupert, A. Oeftiger, Y. Papaphilippou, G. Papotti, T. Pieloni, M. Pivi, S. Rioja-Funetelsaz, E. Rogez, B. Salvant, E. Shaposhnikova, G. Sterbini, M. Taborelli, L. Tavian, C. Yin-Vallgren, M. Van Gompel, C. Zannini, F. Zimmermann for their contributions.

ISBN 978-3-95450-185-4

REFERENCES

[1] R. Garoby, “Status of the Nominal Proton Beam for LHC in the PS”, CERN/PS 99-13 (RF).

[2] R. Cappi, *et al.*, Phys. Rev. ST Accel. Beams **5**, 094401 (2002).

[3] E. Mahner, T. Kroyer and F. Caspers, Phys. Rev. ST Accel. Beams **11**, 094401 (2008).

[4] "LIU Technical Design Report - Volume I: Protons", edited by M. Meddahi *et al.*, CERN-ACC-2014-0337 (2015).

[5] G. Arduini, K. Cornelis, W. Hoefle, G. Rumolo, and F. Zimmermann, in Proceedings of PAC 2001, 18-23 June 2001, Chicago, USA, CERN-SL-2001-0050 (2001).

[6] J.M. Jimenez *et al.*, LHC-Project-Report-632 (2003).

[7] V. Baglin, A. Rossi, *et al.* in Proceedings of ECLOUD04, 19-23 April 2004, Napa California, USA (2004).

[8] D. Schulte, G. Arduini, V. Baglin, J.M. Jimenez, F. Ruggiero, and F. Zimmermann , in Proceedings of PAC2005, 16-20 May 2005, Knoxville Tennessee, USA, LHC Project Report 847 (2005).

[9] G. Rumolo, E. Métral and E. Shaposhnikova, in Proceedings of LHC LUMI 2006, 16-20 October, Valencia, Spain (2006).

[10] G. Rumolo et al., Phys. Rev. Letters **100** (2008) 144801.

[11] C. Yin Vallgren *et al.*, Phys. Rev. ST Accel. Beams **14**, 071001.

[12] H. Bartosik *et al.*, CERN-ATS-Note-2013-019 (2013).

[13] "LIU-SPS Scrubbing Review: Conclusions and Recommendations", W. Fischer (BNL), Y. Suetsugu (KEK), K. Cornelis, J.M. Jimenez, M. Meddahi and F. Zimmermann, CERN, 8-9 September 2015, EDMS LIU-PM-RPT-0023 (2015).

[14] F. Zimmermann, in Proceedings of Chamonix X & XI, CERN-SL-2000-001 DI (2000) and. CERN-SL-2001-003 DI (2001).

[15] G. Arduini *et al.*, CERN-ATS-Note-2011-046 MD (2011).

[16] G. Rumolo *et al.*, in Proceedings of the LHC Beam Operation Workshop - Evian 2011, 12-14 December, 2011, Evian, France, CERN-ATS-2012-083 (2011).

[17] G. Iadarola, G. Arduini, H. Bartosik and G. Rumolo, in Proceedings of the LHC Beam Operation Workshop - Evian 2012, 17-20 December, 2012, Evian, France, CERN-ATS-2013-045 (2012).

[18] G. Iadarola and G. Rumolo, in Proceedings of the LHC Beam Operation Workshop - Evian 2014, 2-4 June, 2014, Evian, France, CERN-ACC-2014-0319 (2014).

[19] H. Bartosik and G. Rumolo, in in Proceedings of the LHC Beam Operation Workshop - Evian 2014, 2-4 June, 2014, Evian, France , CERN-ACC-2014-0319 (2014).

[20] G Iadarola and G. Rumolo, in Proceedings of ECLOUD’12, 5-9 June, 2012, Isola d’Elba, Italy, CERN-2013-002 (2012).

[21] C. Yin Vallgren, Ph.D. thesis, CERN-THESIS-2011-063 (2011).

[22] E. Métral, *et al.*, elsewhere in these proceedings.

[23] G. Iadarola *et al.*, in Proceedings of IPAC13, 12-17 May, Shanghai, China (2013).

ISBN 978-3-95450-185-4

SPACE CHARGE DRIVEN BEAM LOSS FOR COOLED BEAMS AND MITIGATION MEASURES IN THE CERN LOW ENERGY ION RING

H. Bartosik, S. Hancock, A. Huschauer, V. Kain, CERN, Geneva, Switzerland

Abstract

The performance of the CERN Low Energy Ion Ring (LEIR) with electron cooled lead ion beams is presently limited by losses, which occur during RF capture and the first part of acceleration. Extensive experimental studies performed in 2015 indicate that the losses are caused by the interplay of betatron resonances and the direct space charge detuning, which is significantly enhanced during bunching. Mitigation measures have already been identified and successfully tested, such as reducing the peak line charge density after RF capture, i.e. increasing the rms longitudinal emittance, and compensating third order resonances using existing harmonic sextupole correctors. New record intensities at extraction have been achieved. This talk describes the main experimental results from the 2015 measurement campaign including already implemented mitigation measures and the proposed strategy for even further increasing the LEIR intensity reach in the future.

INTRODUCTION

The Low Energy Ion Ring (LEIR) is the first synchrotron of the Large Hadron Collider (LHC) heavy ion injector chain at CERN. LEIR has accumulated, cooled and stacked ion beams of oxygen (O^{4+}), lead (Pb^{54+}) and argon (Ar^{11+}). During several machine development studies (MDs) with lead ions in late 2012 and early 2013, total intensities of up to 9.5×10^{10} charges could be achieved during the coasting beam phase. However, significant beam loss during and after RF-capture limited the available intensity at extraction to about 6.3×10^{10} charges [1,2]. In the framework of the LHC Injectors Upgrade (LIU) project, this intensity limitation for lead ion beams in LEIR has been identified as one of the main performance bottle-necks of the LHC ion injector chain [3]. In view of achieving the beam parameters required for the future LHC operation with lead ions in the High Luminosity LHC (HL-LHC) era [4], an intense machine development program was started at the end of 2015, with the aim of understanding and mitigating the particle loss in LEIR. The main outcomes of these studies will be presented in this paper.

The LEIR cycle presently used for filling the LHC with lead ion beams has a length of 3.6 s. In this scheme, seven injection pulses from Linac3, which are spaced by 200 ms (5 Hz injection rate), are accommodated on the injection plateau at a kinetic energy of 4.2 MeV/u. LEIR features a multi-turn injection with simultaneous stacking in momentum and in both transverse phase spaces. The nominal machine optics with the working point (Q_x, Q_y) = (1.82, 2.72) was tuned to optimize the injection efficiency [5]. Injection efficiencies of 50-70% are achieved in routine operation, which is close to the maximum efficiency predicted by simulations [6]. Figure 1 shows the optics functions with their quasi-twofold periodicity around the 78 m machine circumference of LEIR.

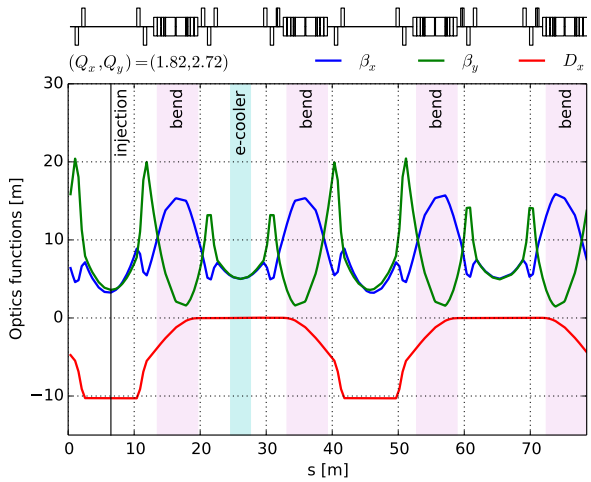

Figure 1: Optics functions along the LEIR circumference. The solenoid of the electron cooler slightly perturbs the lattice symmetry.

The phase space volume of the injected and accumulated beam is reduced by electron cooling. Subsequently, the coasting beam is captured into two bunches using a double harmonic RF system (h=2+4) in bunch lengthening mode, accelerated to a kinetic energy of 72.2 MeV/u and extracted towards the Proton Synchrotron (PS). The basic machine and beam parameters for Pb^{54+} ions are summarized in Table 1.

Table 1: LEIR Parameters for Pb^{54+} Ions

	Injection	Extraction
kinetic energy	4.2 MeV/u	72.2 MeV/u
relativistic β	0.095	0.392
relativistic γ	1.0045	1.087
circumference	25 πm	
transition γ_t	2.84	
working point Q_x/Q_y	1.82 / 2.72	

Figure 2 shows the intensity evolution along the LEIR magnetic cycle for different Linac3 beam current levels with typical loss patterns. Injection efficiencies of 50-70% and low beam loss rates during the electron cooling on the injection plateau are achieved even with the presently maximum available Linac3 pulse current of about 30 μA. At the moment, the accumulation of seven Linac3 pulses does not

ISBN 978-3-95450-185-4

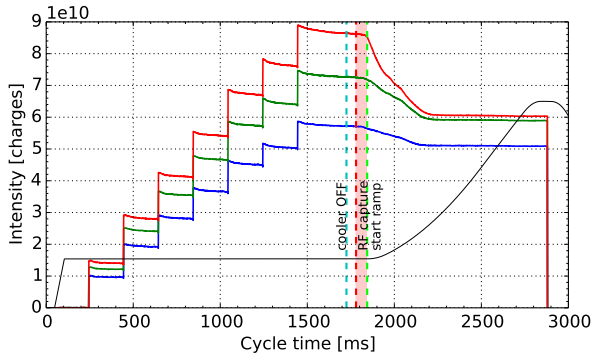

Figure 2: Intensity evolution along the LEIR cycle for different Linac3 current levels. The vertical lines indicate the cycle times where the electron cooler is switched off (cyan), and where the RF capture (red) and the acceleration (green) start. RF capture takes 60 ms as indicated by the red area. The magnetic field of the LEIR main bending magnets in arbitrary units is illustrated by the grey line.

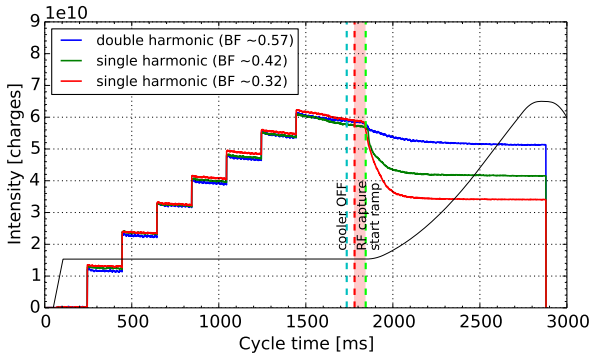

Figure 3: Comparison of losses for different line densities. The bunching factor is indicated in the legend.

constitute an intensity limitation in LEIR, but the achievable maximum intensity at the end of the injection plateau is determined by the Linac3 performance. However, losses after RF capture and during the early part of the acceleration critically depend on the accumulated beam current, and the maximum reachable intensity at the extraction plateau appears to saturate. Until recently, the underlying mechanism causing these losses was not understood. Among others, transverse space charge, transverse instabilities induced by the beam coupling impedance, electron cloud effects, and hardware issues have been suspected. As discussed in detail below, the experimental studies performed at the end of 2015, and the few weeks of beam operation in 2016, indicate that the losses are induced by the interplay of betatron resonances and the direct space charge detuning, which is significantly enhanced during bunching. No indication for coherent instabilities could be identified so far.

CHARACTERIZATION OF THE LEIR PERFORMANCE LIMITATION

Dependence of Losses on Line Charge Density

Figure 3 shows a comparison of the intensity evolution along the LEIR cycle for three different longitudinal phase space distributions. In all three cases the RF voltage functions were programmed such as to perform an iso-adiabatic capture of the coasting beam. The momentum spread of the coasting beam just before RF capture was adjusted using a periodic modulation of the electron gun voltage [5]. This allowed to tailor the longitudinal emittance of the two bunches after capture. In two cases the beam was captured in single harmonic. The losses clearly decrease when the bunching factor (BF), i.e. the average line density divided by peak line density, becomes larger. In other words, enhanced losses are observed in case the peak line charge density is too big. Note that the incoherent tune spread due to direct space charge is directly proportional to the peak line charge density, or inversely proportional to the bunching factor.

Transverse Emittance and Space Charge Tune Shift

The Beam Ionization Profile Monitors installed in LEIR allow to measure the transverse beam sizes along the cycle. The normalized emittances can be reconstructed using the optics functions of the MAD-X model and the rms momentum spread measured with the longitudinal Schottky monitor (typically around 1×10^{-3} after cooling). Figure 4 shows the measured normalized transverse emittances, the intensity along the cycle, and the calculated transverse direct space charge tune spread relative to the nominal bare machine working point in the tune diagram together with resonances up to third order: at the moment when the electron cooler is switched off, the beam is still coasting and the space charge induced tune spread is concentrated in the lower half between the bare working point and the maximum tune shift. The tune footprint is on top of the skew sextupole resonance $3Q_y = 8$ and the vertical emittance starts to grow (partially also due to intra beam scattering). This emittance growth is enhanced during the RF capture process and for the bunched beam. Once the beam is fully bunched, the direct space charge tune spread reaches its maximum value, and significant losses are observed. At that point, the tune footprint covers several betatron resonances (skew and normal) of third (and fourth) order.

A special configuration of the LEIR cycle was used in order to check the behaviour of the bunched beam after RF capture on the injection plateau. Thanks to the improved current from Linac3 in 2016, intensities of almost 8×10^{10} charges could be accumulated with only four injections. Figure 5 shows the intensity evolution along the cycle in this configuration, together with the space charge tune spread at the moment when the electron cooler is switched off (600 ms earlier compared to the standard settings) and after RF capture is completed (advanced by 200 ms).

Vertical emittance growth is observed as soon as the cooling is switched off; however, this does not lead to a change

ISBN 978-3-95450-185-4

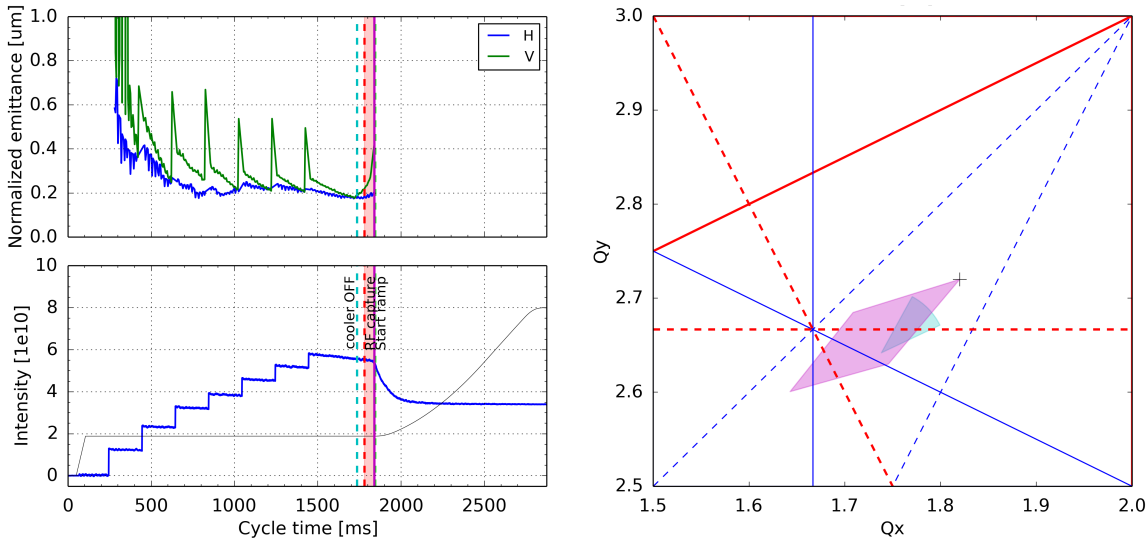

Figure 4: Normalized transverse emittances and intensity along the LEIR cycle in the operational configuration (left). The vertical cyan and magenta lines indicate the cycle times where the electron cooler is switched off and the capture process is completed, respectively. The corresponding calculated space charge tune spreads relative to the bare working point are illustrated in the tune diagram with the same colours (right).

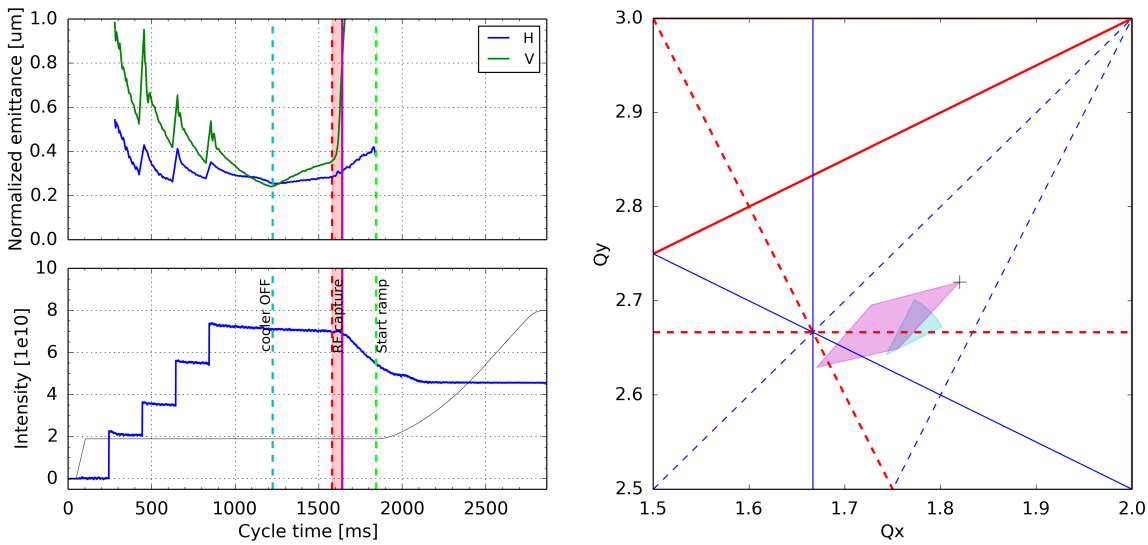

Figure 5: Normalized transverse emittances and intensity along the LEIR cycle in a special configuration, where the electron cooler is switched off after four injections and the RF capture is advanced by 200 ms (left). The calculated tune footprints are shown in the tune diagram (right) at the moment when the e-cooler is switched off (cyan) and after RF capture (magenta).

of the loss rate. Only for a significantly enhanced space charge tune spread during bunching the vertical emittance grows excessively. This growth is accompanied by beam loss at the vertical aperture bottlenecks of LEIR, which are the locations of large vertical β-function in the four bending magnets (see Fig. 1), where the height of the vacuum chambers is only 55 mm. Experimentally, this was demonstrated by creating small closed orbit bumps in these locations of the ring, which had a clear impact on the loss rate.

Therefore, it can be concluded that the loss mechanism is not related to the acceleration process itself, but rather to the changing particle density when the beam is bunched. It is also interesting that the loss rate for the bunched beam does not change significantly between the injection plateau and the first part of the ramp.

Tune Scan - Beam Survival

In order to identify the betatron resonances, which contribute to the observed emittance growth and losses, a tune scan was performed. For this measurement, a special LEIR cycle with five injections on the nominal working point was prepared. After the last injection, but still on the injection plateau with active electron cooling, the betatron tunes were moved to a new working point, the cooling was switched off,

ISBN 978-3-95450-185-4

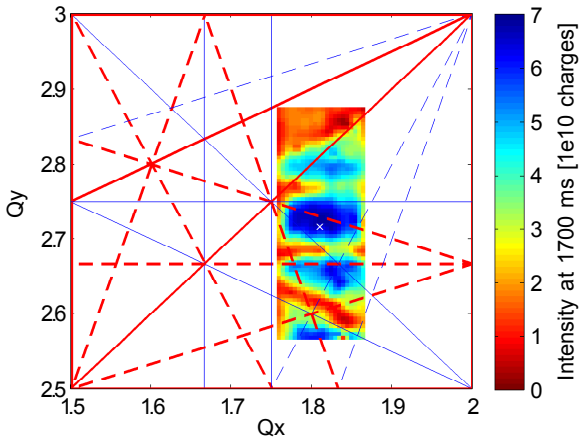

Figure 6: Beam survival after 400 ms storage of the bunched beam as function of the measured coherent tunes. Linear Chromaticity was corrected to $Q' \approx -1$. The nominal working point is marked by the white cross.

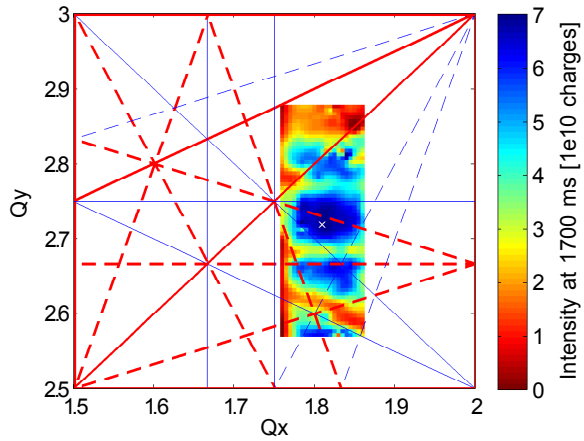

Figure 8: Beam survival after 400 ms storage of the bunched beam as function of the measured coherent tunes for reduced current in the chromatic sextupoles. The nominal working point is marked by the white cross.

and the beam was captured. Figure 6 shows the surviving intensity at 1700 ms cycle time after storing the captured beam on the injection plateau for about 400 ms for various measured coherent tunes in the tune diagram (about 300 working points). Enhanced losses are clearly observed above the skew $3Q_y = 8$ and the normal $Q_x + 2Q_y = 7$ third order resonances. These two resonances seem to be the most critical for driving the emittance growth described above. It is not yet understood why the skew sextupole resonance is so strongly excited. Notable losses are also observed above the $4Q_y = 11$ and the $4Q_x = 7$ fourth order resonances.

MITIGATION MEASURES

MaximizinG Bunching Factor

As described above, the space charge tune spread, and consequently the emittance blow-up and losses, can be reduced by maximizing the bunching factor. In LEIR, this can be achieved by programming an offset between the capture frequency and the central energy where the cooler deposits the beam. With the capture process suitably off-center, the core of the coasting beam distribution ends up surrounding the inner separatrices in the h=2+4 bucket. This results in a "hollow" distribution with an extremely flat longitudinal bunch profile as shown by the phase space tomography [7] in Fig. 7. This distribution can be preserved to some extent up the early part of the ramp by maintaining both the inner and outer acceptances constant. Bunching factors of up to 0.62 could be experimentally reached with this technique.

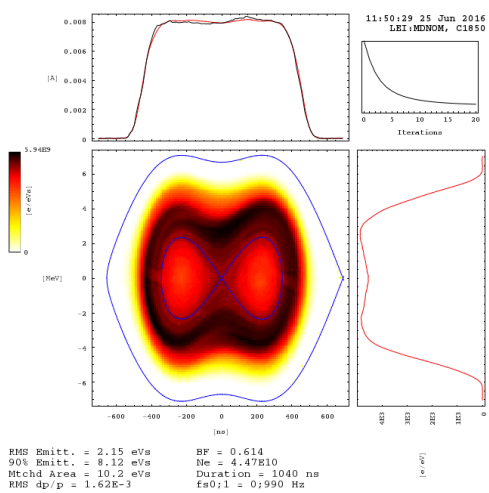

Figure 7: Measured longitudinal phase space distribution resulting from iso-adiabatic capture with RF frequency offset.

Reduction of Sextupole Resonance Excitation

Following the observations of strong losses close to sextupolar resonances with low beam intensity, a first attempt was made to use the two independently powered normal sextupole correctors and two independently powered skew sextupole correctors of LEIR to compensate resonances. It was not possible to measure resonance driving terms so far and therefore a systematic scan of sextupole currents was performed. Some improvement of the losses could be achieved [3].

In 2016 it was found that the chromatic sextupoles used for controlling chromaticity contribute to the resonance excitation and the beam loss encountered after RF capture. Reducing the current in the chromatic sextupoles makes the chromaticity more negative (closer to the natural chromaticity of the machine) and hence increases the tune spread due to the momentum spread of the beam. It should be mentioned that with active transverse feedback, the beam is stable throughout the cycle almost independent of the chromaticity setting.

With the best sextupole settings found so far, the chromatic tune spread is in the order of 10^{-2} only, which is still small compared to the space charge induced tune spread.

ISBN 978-3-95450-185-4

Using these sextupole settings, the losses close to the resonances are somewhat reduced as shown in Fig. 8, where the chromaticity was reduced by about 2 units in both planes. Interestingly, also the region just above the $3Q_y = 8$ resonance is improved, even though it is a skew resonance. This needs to be investigated in more detail in future studies, e.g. by measuring resonance driving terms. This could also help in understanding the source of this strongly excited resonance.

Implementation

Figure 9 illustrates the effect of the two mitigation measures described above on the achievable intensity at LEIR extraction when accumulating around 10×10^{10} charges. With deregulated RF capture frequency, which generates a hollow distribution with a BF of about 0.6, and reduced current in the chromaticity sextupoles, 9×10^{10} charges could be reached at extraction, which constitutes a new record for LEIR.

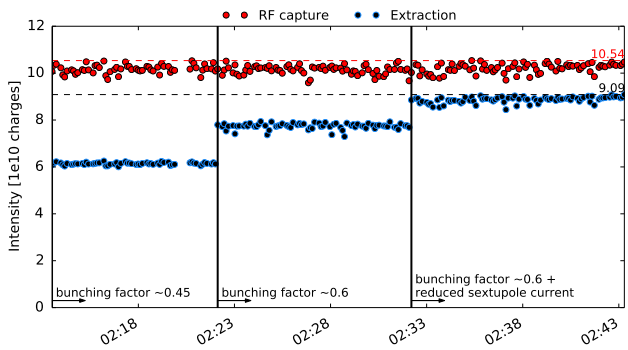

Figure 9: LEIR intensity with progressive implementation of the mitigation measures described in the text. The red and black dashed lines indicate the maximum achieved intensity at RF capture and extraction, respectively.

OUTLOOK

Following the hardware upgrades in the Linac3 complex during the last winter stop [3], it is possible to operate with 10 Hz injection rate by spacing the Linac3 injections by 100 ms. Experimental studies in the near future will therefore concentrate on exploring possible intensity limitations for the accumulation of up to 13 Linac3 pulses on the LEIR injection plateau with an increased electron current in the cooler. In case the accumulated intensity can be significantly increased, losses after RF capture are expected to remain a limitation. The following options for further mitigation will be considered:

- Ideally, the machine optics can be modified to obtain a working point in the lower quadrant of the tune diagram, e.g. fractional tunes of $q_x = 0.15$ and $q_y = 0.25$, which is far from low order resonances. However, the optics functions have to meet several constraints in the location of the electron cooler and in the injection region, while providing sufficient vertical acceptance [5].
- Further studies on the betatron resonances, e.g. resonance driving term measurements, should allow to better understand the main drivers for the excitation of the sextupole resonances, in particular the skew resonance below the nominal working point. Eventually, it should be possible to compensate these resonances (at least partially) using the existing chromatic and harmonic sextupole correctors. Therefore, hardware upgrades are currently ongoing to make this type of measurements possible.
- Further increasing the longitudinal emittance and thereby reducing the space charge tune spread. Additional RF voltage will be required in order to maintain a high bucket area throughout the acceleration cycle. This will become available by operating both existing RF cavities at the same time with the new digital low level RF.

In the long term, detailed simulation studies will be instrumental for fully characterizing and optimizing the LEIR beam performance, such as the development of a machine magnetic model including the nonlinearities (e.g. induced by the electron cooler guide fields), and space charge simulations. Furthermore, it should be mentioned that the LEIR impedance model is presently under development in the context of studying coherent effects.

SUMMARY AND CONCLUSIONS

The main intensity limitation of LEIR is beam loss during and after RF capture. The experimental studies presented here indicate that these losses are caused by the interplay of betatron resonances and the large direct space charge detuning. Maximizing the bunching factor and reducing the sextupole excitation allowed to mitigate the losses and reach record intensities with Pb^{54+} ions out of LEIR. In case significantly more intensity can be accumulated with the increased injection rate from Linac3, losses after RF capture are expected to remain a limitation and will be addressed with additional mitigation measures (e.g. a new machine optics if feasible). The improved performance of LEIR opens the possibility for further optimizing the lead ion beam production schemes for the HL-LHC era.

ACKNOWLEDGEMENTS

The authors would like to thank ME. Angoletta, G. Arduini, J. Axensalva, A. Blas, C. Carli, S. Gilardoni, S. Jensen, D. Küchler, D. Manglunki, M. Meddahi, Y. Papaphilippou, S. Pasinelli, G. Rumolo, R. Scrivens and G. Sterbini for their ideas and input in fruitful discussions and help during the experimental studies.

REFERENCES

[1] D. Manglunki, "Performance of the Injectors with Ions after LS1", Review of LHC and Injector Upgrade Plans Workshop (RLIUP), Archamps, France (2013).

ISBN 978-3-95450-185-4

[2] M. Bodendorfer *et al.*, "Beam Loss in the Low Energy Ion Ring (LEIR) in the Light of the LHC Injector Upgrade for Ions (LIU-IONS)", in *Proc. of HIAT'15*, Yokohama, Japan (2015).

[3] LHC Injectors Upgrade Technical Design Report, Volume 2: Ions, EDMS 1626950, CERN, Geneva, Switzerland (2016).

[4] J. Jowett *et al.*, "HL-LHC heavy-ion beam parameters at LHC injection", EDMS 1525065, CERN, Geneva, Switzerland (2015).

[5] LHC Design Report, Volume III, Chapter 34, CERN, Geneva, Switzerland (2004).

[6] C. Carli *et al.*, "Combined Longitudinal and Transverse Multiturn Injection in a Heavy Ion Accumulator", in *Proc. of PAC'97*, Vancouver, Canada (1997).

[7] S. Hancock, S.R. Koscielniak, M. Lindroos, "Longitudinal Phase Space Tomography with Space Charge", in *Proc. of EPAC'00*, Vienna, Austria (2000).

ISBN 978-3-95450-185-4

FIRST ANALYSIS OF THE SPACE CHARGE EFFECTS ON A THIRD ORDER COUPLED RESONANCE

G. Franchetti, GSI, Darmstadt, Germany
S. Gilardoni, A. Huschauer, F. Schmidt, R. Wasef, CERN, Geneva, Switzerland

Abstract

The effect of space charge on bunches stored for long term in a nonlinear lattice can be severe for beam survival. This may be the case in projects as SIS100 at GSI or LIU at CERN. In 2012, for the first time, the effect of space charge on a normal third order coupled resonance was investigated at the CERN-PS. The experimental results have highlighted an unprecedented asymmetric beam response: in the vertical plane the beam exhibits a thick halo, while the horizontal profile has only core growth. The quest for explaining these results requires a journey through the 4 dimensional dynamics of the coupled resonance investigating the fixed-lines, and requires a detailed code-experiment benchmarking also including beam profile benchmarking. This proceeding gives a short summary of the experimental results of the 2012 PS measurements, and address an interpretation based on the dynamics the fixed-lines.

INTRODUCTION

Space charge induced emittance growth and beam loss can be divided into two big classes. The beam loss deriving from the incoherent effects of space charge on lattice nonlinearities (this proceeding), and the beam loss that may arise from the growth of the coherent modes self-consistently excited by the space charge [1].

The incoherent effects of space charge in coasting beams create an emittance growth when the space charge detuning overlaps a machine resonance. However, the incoherent space charge tune-shift also stabilizes the emittance growth by bringing particles out of the resonance as they grow in transverse amplitude. The space charge induced beam loss in a nonlinear machine becomes dramatic for bunched beams when the synchrotron motion and space charge induce a periodic crossing of a machine resonance. A single resonance crossing in a conventional RF bucket with synchrotron tune of $Q_s \sim 10^{-2}$ produces a small emittance growth because of the relatively fast resonance crossing, but the cumulative effect arising from repeated resonance crossing, more than 300-400 crossing, makes large impact creating a beam diffusion to large transverse amplitudes, hence may lead to a steady beam loss over all the storage time.

For one dimensional resonances the mechanism leading to emittance growth and beam loss is explained in terms of instantaneous stable islands in the two-dimensional phase space and their crossing the particle orbits because of the combined effect of space charge and synchrotron motion Ref. [2]. This mechanism requires a long term storage, which typically corresponds to a number of turns equivalent to 100 or more synchrotron oscillations. Experimental and numerical studies on beam survival and emittance growth in this regime have investigated the one dimensional resonance $4Q_x = 25$ in Ref. [3], and $3Q_x = 13$ in Ref. [4]. The relevance of these studies is significant for SIS100 [5], and for LIU [6] at CERN, as well as for all accelerators operating with high intensity beams in regimes of long term storage.

RESULTS AND DISCUSSION

Coupled nonlinear resonances, of which the simpler class is the $Q_x + 2Q_y = N$, leads to significant difficulties in presence of space charge, and experimental studies are mandatory to unravel the complex dynamics. The effect of space charge on these type of resonances was studied in the CERN-PS in 2012 for the resonance $Q_x + 2Q_y = 19$. In this proceeding we present a short summary of the full experiment analysis. A more comprehensive presentation of the experimental results and discussion is part of a future publication.

In the experiment, in a resonance-free region of the tune diagram the third order resonance $Q_x+2Q_y = 19$ was excited with sextupoles with strength of $K_3 \simeq 0.015$ m^{-2}. The experimental campaign used a beam with 55×10^{10} proton per bunch, which produced an incoherent space charge tune-shift of $\Delta Q_x \simeq -0.05, \Delta Q_y \simeq -0.07$. The beam was stored for $\sim 0.5 \times 10^6$ turns, i.e. 1.1 seconds at an energy of 2 GeV, and beam profile measurements where taken at the beginning and at the end of the storage time. For several machine tunes, initial and final beam profiles where compared with the finding of an unexpected beam response to the distance from the resonance. When the space charge tune-spread overlaps the third order resonance and the machine tune is close to the resonance without beam loss, the beam profiles evolves differently in the transverse planes: in horizontal plane the beam exhibits core growth, whereas in the other plane a large halo is formed. This is shown in Fig. 1a,b for the tunes $Q_{x0} = 6.104, Q_{y0} = 6.476$. The asymmetry of the beam profile is quite evident and shows that a new and more complex dynamics is driving the beam halo formation. In the picture are also shown the profiles from computer simulation as obtained from MADX, and MICROMAP (see Ref. [7] for a general code benchmarking discussion). Figure 1c shows the overall beam response in the experiment. The profiles in Fig. 1a,b correspond to the largest emittance growth.

The explanation of the halo-core finding can be approached starting with a detuning analysis. The theory of the resonances (see Ref. [8,9]) shows that the more convenient quantity to measure the distance from the third order resonance is

$$\Delta_{r0} = Q_{x0} + 2Q_{y0} - 19.$$

ISBN 978-3-95450-185-4

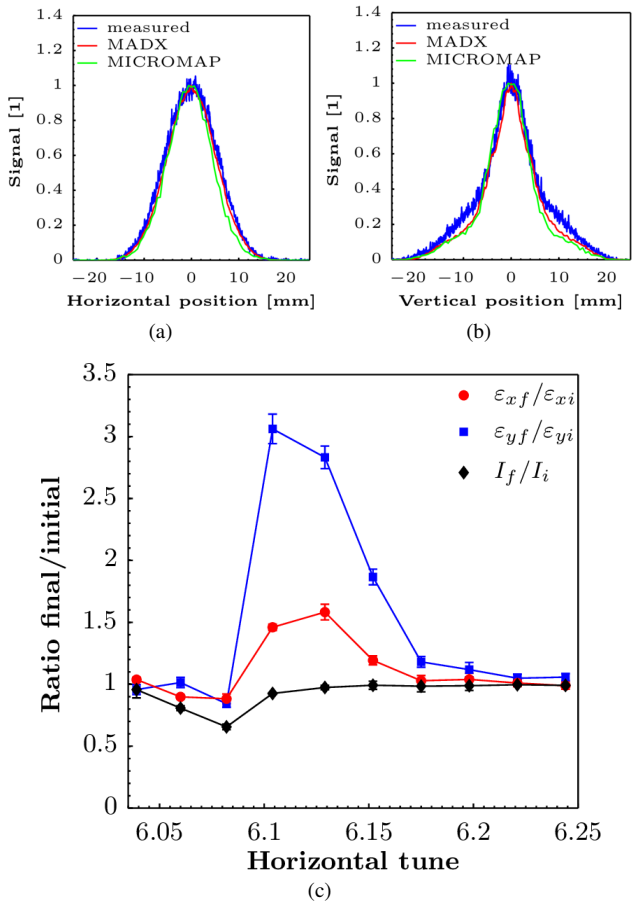

Figure 1: Part a, and b: horizontal and vertical beam profiles after 1.1 second storage of the beam in the CERN-PS. The asymmetry of the beam response is evident. In part c is shown the full beam response to all working points investigated.

When $\Delta_{r0} = 0$ the machine tunes sit on the resonance. This definition valid for the machine tunes can be extended to any arbitrary particle, hence it becomes $\Delta_r = Q_x + 2Q_y - 19$, where now the tunes Q_x, Q_y are the effective tunes experienced by a test particle, which is affected by space charge, chromaticity, and any other effects. If we call $\Delta Q_{sc,x}(X,Y), \Delta Q_{sc,y}(X,Y)$ the amplitude dependent detuning created by space charge for a particle with amplitudes X, Y, the distance from the resonance reads

$$\Delta_r = \Delta_{r0} + \Delta Q_{sc,x}(X,Y) + 2\Delta Q_{sc,y}(X,Y). \quad (1)$$

Therefore one can use this relation for a first order search of the amplitudes of the resonant particles.

Given the machine tunes Q_{x0}, Q_{y0} we find Δ_{r0}, and the resonant transverse amplitudes are found as the X, Y which satisfy the equation $\Delta_r = 0$.

The quantity Δ_r becomes therefore dependent from X, Y and can be regarded as a resonance detuning that incorporates the coupled character of the resonance $Q_x + 2Q_y = 19$. In Fig. 2 the two curves show the dependence of Δ_r for two types of particle amplitudes. The red curve is obtained for amplitudes type $(X, 0)$, while the black curve is obtained for amplitudes $(0, Y)$. The horizontal line of height $\Delta_r = 0$ intercepts the two curves at the resonant amplitudes, which in our case are $X \sim 5\sigma_x$, and $Y \sim 4\sigma_y$.

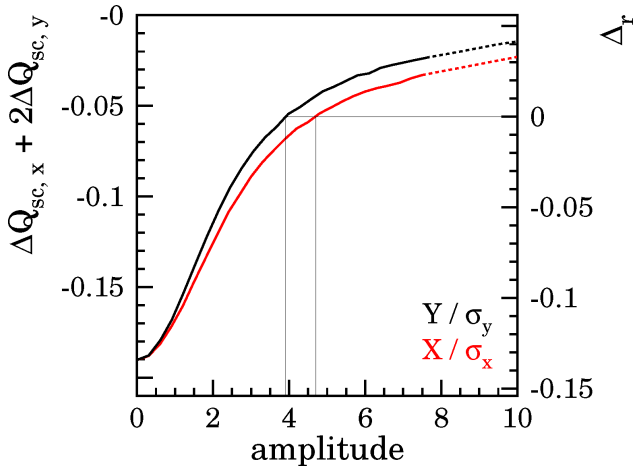

Figure 2: Resonance detuning Δ_r as function of the particle amplitude.

From the phenomena of periodic resonance crossing we expect that particle diffusion is not exceeding the outer position of the "resonant particles", which is $X \sim 5\sigma_x$, and $Y \sim 4\sigma_y$. However, a comparison with a multi-particle simulation in absence of chromaticity, shows that no halo with amplitude $X \sim 5\sigma_x$ is found.

By adding the chromaticity to Eq. (1) we can investigate the role of the chromaticity on the resonant amplitudes, for example for particles with maximum $\delta p/p$, and construct an equivalent graphic of Fig. 2. Adopting the same procedure as previously described, we can search for the resonant particles at largest amplitudes (condition $\Delta_r = 0$). We find that the halo predicted by this analysis is $X > 9\sigma_x$, and $Y \sim 9\sigma_y$. Once more, this result contradicts the experimental findings, in which the halo is found at $Y \simeq 5.5\sigma_y$.

INTERPRETATION WITH THE FIXED LINES

The explanation of the beam profile observed and retrieved from simulations in Fig. 1 goes beyond the detuning analysis, and have to be searched into the effects created by the 4D coupled dynamics. The analogous of the fixed-points is now the fix-lines [9–11]. The analytic form of these lines (or resonant tori) is parameterized as

$$x = \sqrt{\beta_x a_x}\cos(-2t - \alpha + \pi M), y = \sqrt{\beta_y a_y}\cos(t). \quad (2)$$

The coordinates x', y' are readily derived from Eq. (2). The fixed-line emittances a_x, a_y are determined by the distance to the resonance Δ_{r0}. The variable t parameterizes the fixed-line. In absence of space charge and of nonlinear detuning, the fixed-line has the largest extension in the y direction, and in particular the ratio of the fixed-line invariants takes the

ISBN 978-3-95450-185-4

value of $a_y/a_x = 8$ when a_y is maximum (see Ref. [10]). The coefficient M is 0, or 1 according to the condition of existence of the fixed line. In Fig. 3 we shows an example of

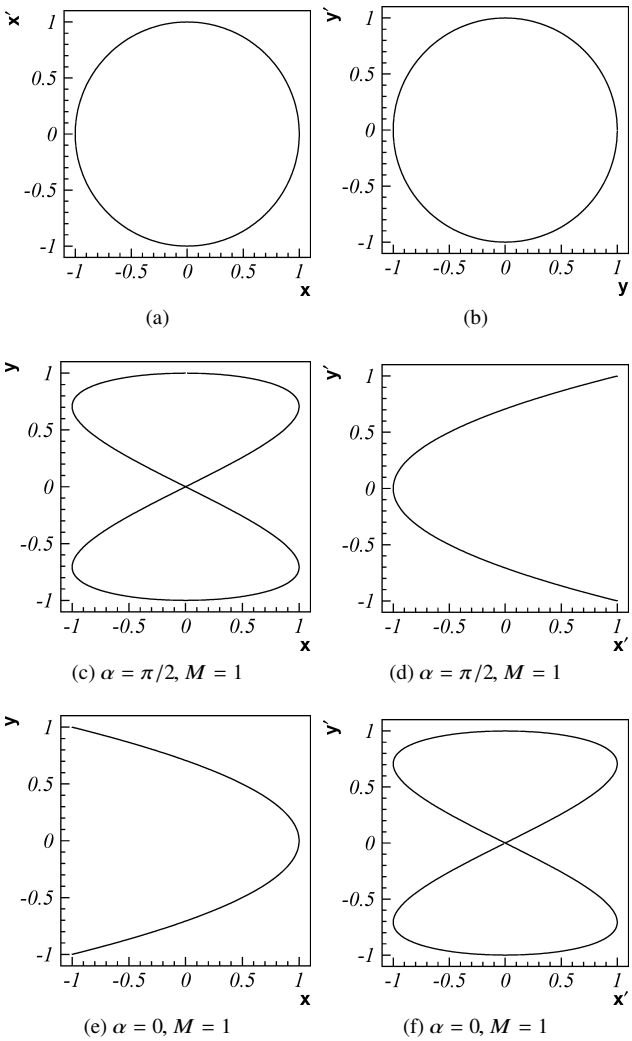

Figure 3: Fixed-line projections in normalized coordinates. The parameters in Eq. (2) are indicated in each picture. Note that the topology of the $x - y$ projection of a fixed-line depends substantially on the angle α.

the shape of these lines plotted in normalized coordinates. It is visible that the $x - y$ projection of the resonant particle on the fixed-line have a special form which can be easily identified. The dependence of α makes the shape "C" and the shape "8" exchangeable. Practically the parameter α is the phase of the driving term of the third order resonance, and in our case it depends on the location of the sextupoles used to excite the resonance with respect to the observation point along the machine (the flying wire position). Also on the interplay of space charge with the resonant dynamics is relevant, but the theory of fixed-lines with space charge is not available, hence only a numerical investigation can be presented.

The investigation of the role of the fixed-lines in the bunched beam is first carried out by freezing artificially the longitudinal motion in the simulation modeling the experimental beam profiles of Fig. 1, and by constructing a tune footprint of a set of test particles. The resonant particles are easily identified as the FFT method used to retrieve the single particle nonlinear tunes Q_x, Q_y, locks the single particle tunes of resonant particles to the line $Q_x + 2Q_y - 19 = 0$. We then plot the $x - y$ projection of the resonant orbits and compare it with the $x - y$ projections in Fig. 3 searching for indications of a fixed-lines dynamics. In part a of Fig. 4 we

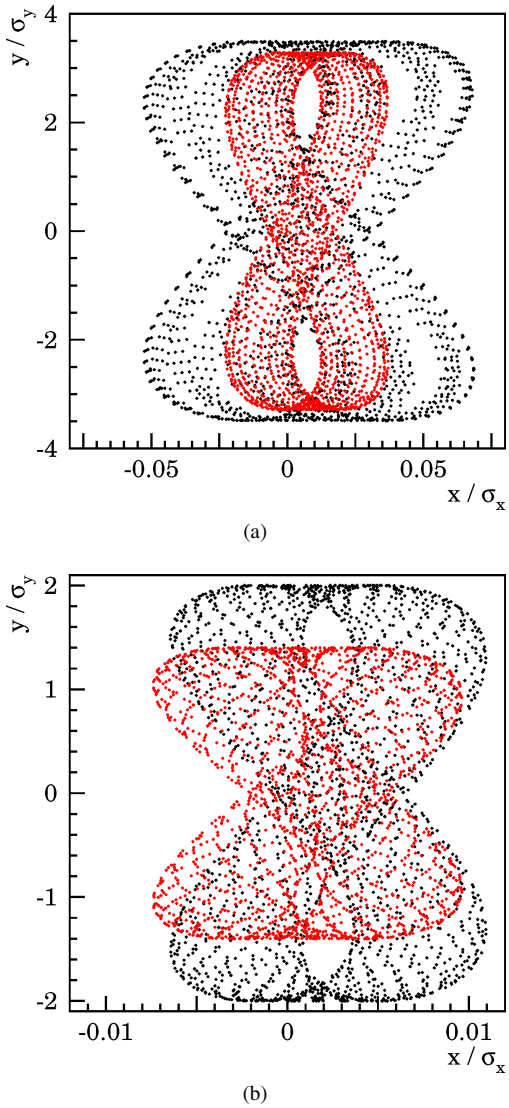

Figure 4: Part a). $x - y$ projection of the two largest resonant orbits at $z = 0\sigma_z$; Part b). The two largest resonant orbits now at $z = 1.5\sigma_z$.

show two resonant orbits for test particles located at $z = 0\sigma_z$. The topology of the orbit projection leaves no doubt that we see two particles locked to two distinct fixed lines having the "8" shape in $x - y$ projection. The asymmetric form of the orbits is remarkable although the resonant particle is not sitting exactly on the fixed-line. This result simply shows that the presence of the beam space charge detuning does not destroy the dynamics that creates the fixed-lines.

ISBN 978-3-95450-185-4

By repeating the analysis for particles at $z = 1.5\sigma_z$ we can visualize the resonant orbits at a location of the bunch with smaller transverse space charge. These resonant orbits are shown in part b of Fig. 4. Even in this case we clearly distinguish in the resonant orbits the pattern of the fixed-lines. The aspect ratio is now different, and the extension of the orbits is smaller.

This pattern of the extension of the fixed-lines along the bunch is consistent with the studies on one dimensional resonances. In Ref. [2] it is shown that the frozen transverse islands have the maximum size and their fixed-points have maximum amplitudes at longitudinal positions $z = 0$. For other longitudinal position within the bunch the fixed-points are found at smaller amplitudes. Eventually at locations enough far away from the bunch center, the fixed-points merge to the transverse origin and disappear. This pattern is at the base of the periodic resonance crossing mechanism. Figure 4a,b convey the same information as they show that instantaneous fixed-lines have amplitude function of the longitudinal particle coordinate z in the bunch reference frame. This pattern which exhibits the largest fixed-lines at $z = 0\sigma_z$, with amplitude decreasing for increasing the longitudinal amplitude, will create phenomena of periodic crossing of the fixed-lines. This can be seen in Fig. 5 where the evolution of the single particle emittance is shown during one synchrotron oscillation. The scattering of the invariant is clearly visible with 4 kicks per synchrotron oscillation.

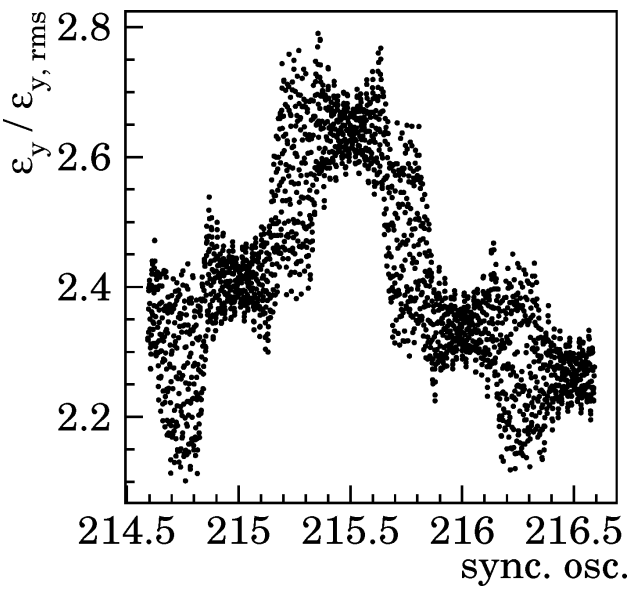

Figure 5: Emittance of one test particle during storage. The picture reveals the 4 kicks exerted by the fixed-lines during one synchrotron oscillation.

CONCLUSION AND OUTLOOK

In this proceeding we shortly summarize the main findings of the PS experiment performed in 2012. We find a simulation evidence that the dynamics creating the halo is determined by the fixed-lines. We find that the fixed-lines change amplitude according to the strength of the instantaneous space charge tune-spread, which depends on the particle longitudinal position within the bunch. This induces a phenomena of periodic crossing of the fixed-lines with the particle orbit. Scattering phenomena are found in the simulation as a clear trace of this fundamental mechanism. The asymmetry of the measured beam response is a result of the asymmetric shape of the instantaneous fixed-lines.

It remains open and is not discussed in this proceeding the influence of the many fixed-lines on the particle motion, and the explanation of why the halo in the experiment extends only up to $5.5\sigma_y$ although simulations clearly show the existence of many fixed-lines which extends on a larger surface, reaching up to $9\sigma_y$ when the effect of the chromaticity is included. If it is possible to identify which is the fixed-line of relevance for the scattering mechanism, it will be possible to predict the extension of the halo without actually running the very demanding multi-particle simulations. The understanding of this mechanism is also of relevance on the issue of the resonance compensation, which attempt was already presented in HB2014 in Ref. [12].

The discussion of all these aspects as well as of the open question here presented is left to a future publication.

ACKNOWLEDGMENT

"The research leading to these results has received funding from the European Commission under the FP7 Research Infrastructures project EuCARD-2, grant agreement no.312453".

REFERENCES

[1] I. Hofmann, in *Proc. HB'16*, Malmo, Sweden, July 2016, paper THPM1X01, this conference. .

[2] G. Franchetti and I. Hofmann, *Nucl. Instr. and Meth.* A **561**, (2006), pp.195-202.

[3] G. Franchetti, I. Hofmann, M. Giovannozzi, M. Martini, E. Métral, *Phys. Rev. ST Accel. Beams* **6**, 124201 (2003); E. Métral, G. Franchetti, M. Giovannozzi, I. Hofmann, M. Martini, and R. Steerenberg, *Nucl. Instr. and Meth.* A 561, (2006), 257-265.

[4] G. Franchetti, O. Chorniy, I. Hofmann, W. Bayer, F. Becker, P. Forck,T. Giacomini, M. Kirk, T. Mohite, C. Omet, A. Parfenova, and P. Schuett, *Phys. Rev. ST Accel. Beams* **13**, 114203 (2010).

[5] P. Spiller and G. Franchetti, *Nucl. Instrum. Methods Phys. Res., Sect.* A **561**, 305 (2006).

[6] J. Coupard *et al.*, "LHC Injectors Upgrade, Technical Design Report, Vol. I: Protons", LIU Technical Design Report (TDR), CERN-ACC-2014-0337.

[7] F. Schmidt *et al.*, "Code Bench-Marking for Long-Term Tracking and Adaptive Algorithms", in *Proc. HB'16*, Malmo, Sweden, July 2016, paper WEAM1X01, this conference.

[8] A. Schoch, "Theory of Linear and Non-Linear Perturbations of Betatron Oscillations in Alternating Gradient Synchrotrons", CERN 57-21 (Proton Synchrotron Division), Section 14 (1958).

ISBN 978-3-95450-185-4

[9] G. Franchetti and F. Schmidt, "Extending the Nonlinear-Beam-Dynamics Concept of 1D Fixed Points to 2D Fixed Lines", *Phys. Rev. Lett.* **114**, 234801 (2015).

[10] G. Franchetti and F. Schmidt, "Fix-lines and stability domain in the vicinity of the coupled third order resonance", http://arxiv.org/abs/1504.04389

[11] F. Schmidt, "Untersuchungen zur dynamischen Akzeptanz von Protonenbeschleunigern und ihre Begrenzung durch chaotische Bewegung", PhD thesis, DESY HERA 88-02 (1988).

[12] G. Franchetti, S. Aumon, F. Kesting, H. Liebermann, C. Omet, D. Ondreka, and R. Singh, GSI, S. Gilardoni, A. Huschauer, F. Schmidt, and R. Wasef, CERN in *Proc. of HB'14*, East Lansing, USA. paper THO1LR03. p. 330.

ISBN 978-3-95450-185-4

INTENSITY EFFECTS IN THE FORMATION OF STABLE ISLANDS IN PHASE SPACE DURING THE MULTI-TURN EXTRACTION PROCESS AT THE CERN PS

S. Machida*, C.R. Prior, STFC Rutherford Appleton Laboratory, Didcot, UK
S. Gilardoni, M. Giovannozzi, S. Hirlander[1], A. Huschauer[1], CERN, Geneva, Switzerland
[1]also at Vienna University of Technology, Vienna, Austria

Abstract

The CERN PS utilises a Multi-Turn Extraction (MTE) scheme to stretch the beam pulse length to optimise the filling process of the SPS. MTE is a novel technique to split a beam in transverse phase space into nonlinear stable islands. The recent experimental results indicate that the positions of the islands depend on the total beam intensity. Particle simulations have been performed to understand the detailed mechanism of the intensity dependence. The analysis carried out so far suggests space charge effects through image charges and image currents on the vacuum chamber and the magnets iron cores dominate the observed behaviour. In this talk, the latest analysis with realistic modelling of the beam environment is discussed and it is shown how this further improves the understanding of intensity effects in MTE.

INTRODUCTION

The Multi-Turn Extraction (MTE) scheme at cERN was conceived as method of beam transfer from the PS to the SPS to minimise beam loss [1]. It has been demonstrated experimentally several times [2] and is now in daily operation. It has also been suggested that an inverse process could be utilised for Multi-Turn Injection (MTI).

The mechanism of beam splitting and preservation of the separated beamlets can be identified as a nonlinear resonant driving term (octupole in this study) and amplitude dependent tune shift. In other words, the essential ingredients are the non-zero harmonic component of the multipole potential and zero-th component of the multipole potential (this can be the same multipole as the other). It is, however, not clear how the beam intensity affects the dynamics.

Experimental observation shows that the beamlets move outward as the beam intensity increases [3]. We have included a simple model of space charge effects in the MTE simulation that starts after the process of beam splitting to see how the beam intensity changes the beamlets' position in the phase space.

MODEL

Generally speaking, when space charge effects are included in particle tracking simulation, the charge distribution of each beamlet as well as its position in the transverse phase space should be updated self-consistently. The distributions are no longer determined only by the lattice elements. On the other hand, the beamlets are reasonably separated in the configuration space. Therefore we assume that only the position of each beamlet is modified by the interaction between the charge centres of the beamlets and is insensitive to the details of the charge distribution. This justifies the introduction of a frozen space charge model. The charge distribution is fixed at the start of the simulation and not updated after each integration step. However, one significant difference from the ordinary frozen model for a single beam is that the beamlet positions are calculated iteratively. When there is only a single beam, it always sits at the centre of phase space, which may be slightly shifted by closed orbit distortion. When there are multiple beamlets, contributions to the space charge potential from other beamlets produce dipole kicks which we take into account to solve for the beamlet positions self-consistently.

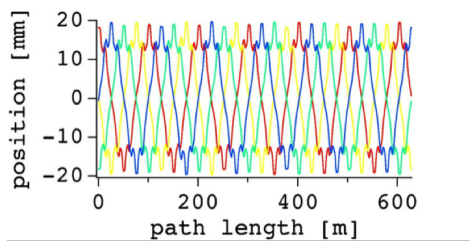

Figure 1: Position of the stable fixed points around the ring. They are all connected to make a closed orbit returning to the initial point after 4 turns.

In practice, to include space charge effects among the beamlets, the position of stable fixed points without space charge is first calculated everywhere in the ring, along an orbit that returns to the initial phase space point after 4 turns. This closed orbit is in addition to the normal orbit around the centre which comes back to the initial point on every turn. The position around the ring is shown in Fig. 1. Different colours indicate the evolution of each fixed point, but they are all connected making one single closed orbit. Once the fixed point positions are identified, space charge effects can be included by centring the space charge potential at that position. With a small time step, typically 10 ns, a particle is tracked taking into account the external magnetic lattice as well as the space charge potential.

Obviously, the closed orbit coming back after 4 turns under space charge is different from the orbit without space charge. That means that the position of the beamlets has to be adjusted to the new position and then the closed orbit has to be calculated again. This iteration repeats until the closed orbit found by the particle tracking agrees with the position

* email address: shinji.machida@stfc.ac.uk

ISBN 978-3-95450-185-4

of the beamlets identified before the tracking. About 10 iterations are enough to obtain adequate convergence provided such a closed orbit exists. In some cases, for example with extremely strong space charge, there is no fixed point and no convergence after many iterations.

So far only direct space charge potential has been considered. There are also image charges (electric) and image currents (magnetic) on the vacuum chamber and magnet pole faces, respectively. As we assume horizontal parallel plates for both the electric and magnetic boundary, there is an infinite number of image charges and current layers. In simulation, a sufficient number of layers of the image charges and currents is determined by looking at the convergence of the fixed point position as a function of the layers. The deviation of the fixed point position is within 1% when more than 10 layers (for image changes and image currents separately) are included.

In the case of parallel boundary conditions, we can construct an analytical model on the direct as well as image charge and image current contributions. For purposes of illustration, we first discuss the model with one beamlet at the centre and two beamlets at a distance from the centre. The outer two beamlets oscillate around the central beamlets in phase space. This model is not expected to lose the generality of the full multi beamlets situation as far as space charge interaction is concerned.

Let us first consider the contributions from the direct space charge and current for completeness. A repulsive electric force between particles with charges of the same sign weakens the restoring force so the betatron tune shift is negative. This is true for particles in the outer beamlets as well. As in a single beam, moving charges create a magnetic field that produces a force in the opposite direction to the electric repulsive force with a factor of -β^2, where β is the speed of particles normalised with the speed of light c. We consider only the horizontal direction.

$$F_{\text{direct, elec+magn}} = (1-\beta^2)\frac{3e\lambda}{4\pi\varepsilon_0}\frac{1}{x},$$

where e is the electric charge, λ is the line density, ε_0 is the permittivity of free space. The sum of electric and magnetic forces with a factor of (1-β^2) is still repulsive, but it becomes less when the beam momentum is high, e.g. at the extraction energy.

When there is a metallic boundary made up of parallel plates with half height h, image charges appear on the other side of the plates. Individual particles feel an attractive force, which strengthens the restoring force in the horizontal direction and weakens the restoring force in the vertical direction.

$$F_{\text{image, elec, s1}} = -\frac{e\lambda}{\pi\varepsilon_0}\frac{x}{(2h)^2+x^2}.$$

We can extend this model to the multiple beamlets case. Having the image charge of other beamlets on the other side of vacuum chamber plates, the restoring force of the outer beamlets with respect to the oscillation centre becomes stronger as you can see in Fig. 2.

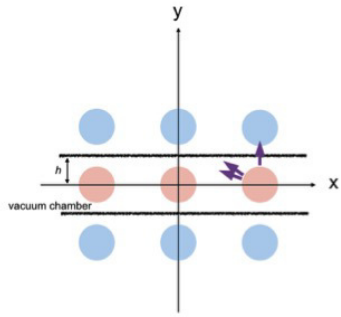

Figure 2: In addition to the force between the beamlet on the mid plane and its image, there is another force between the beamlet and the image charge of other beamlets indicated as two arrows pointing left. There should be force between the beamlets and the images below the vacuum chamber plate as well. As a result, restoring force to the outer beamlets with respect to the centre increases.

$$F_{\text{image, elec, m1}} = -\frac{e\lambda}{\pi\varepsilon_0}\left[\frac{x}{(2h)^2+x^2}+\frac{2x}{(2h)^2+(2x)^2}\right].$$

Of course, there is infinite layer of image charges with alternating signs. The image charge in the second layer acts to cancel the force of the first one, but not completely because the distance of the interaction is greater.

$$F_{\text{image, elec, ms}} = -\frac{e\lambda}{\pi\varepsilon_0}\Big[\frac{x}{(2h)^2+x^2}+\frac{2x}{(2h)^2+(2x)^2} -\frac{x}{(4h)^2+x^2}-\frac{2x}{(4h)^2+(2x)^2}+\dots\Big].$$

Notice that there is no image current at the same place of the image charge. Although the orbit of the beamlets oscillates around the ring, it does not move in time. Only a DC component of magnetic field is created, which can penetrate the metallic vacuum chamber wall. On the other hand, the DC component of the magnetic fields makes an image current on the magnet pole face. Let us assume the half gap of the magnet pole face is g.

$$F_{\text{image, magn, ms}} = \beta^2\frac{e\lambda}{\pi\varepsilon_0}\Big[\frac{x}{(2g)^2+x^2}+\frac{2x}{(2g)^2+(2x)^2} -\frac{x}{(4g)^2+x^2}-\frac{2x}{(4g)^2+(2x)^2}+\dots\Big].$$

This simple analytical model helps us understand how the direct and image space charge forces act, at least whether the overall effect is repulsive or attractive.

RESULTS

Two octupoles in the straight sections 39 and 55 (IOCT39 and IOCT55) and two sextupoles next to the octupoles in the same straight sections IXCT39 and IXCT55 are excited.

ISBN 978-3-95450-185-4

The pole face winding has a set current close to the machine operation condition. The magnet packing factor, defined as the fraction of the total magnet length over the circumference, is 0.8. The tunes without space charge are (6.255, 6.230).

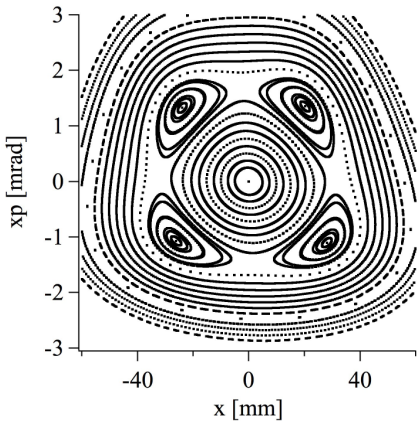

Figure 3: Horizontal phase space with islands when no space charge potential is included.

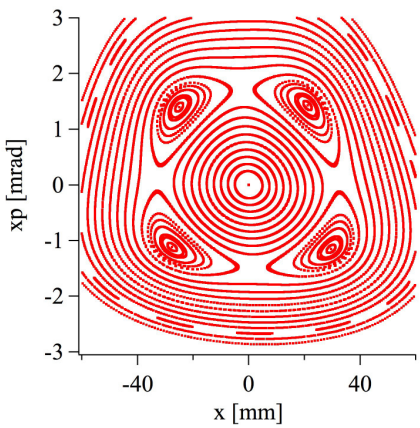

Figure 4: Phase space when the space charge from a total beam intensity of 3.27×10^{13} is included. The beam intensity of each beamlet is equal, namely 1/5 of the total beam intensity.

Figures 3 and 4 show the horizontal phase space without and with space charge effects from a total 3.27×10^{13} protons (shared equally across 5 beamlets). Figure 5 is the close-up view of the lower right island.

Figure 6 shows the intensity dependence of the fixed point locations with different boundary conditions. When only direct space charge is included, the islands move inwards (blue), but the change is small at the high beam momentum of 14 GeV/c. Image charges induce a large shift outwards (green). Image currents cause inward displacement that tends to cancel the image charge contributions.

In the simulation above, we assumed that all the five beamlets including at the centre have equal intensity. In order to see how an imbalance in beam intensity changes the behaviour, an *intensity imbalance factor* f is introduced between the core and the outer beamlets as follows,

$$I_{\text{core}} = (1 + 4f) \times I_{\text{eq}},$$
$$I_{\text{outer}} = (1 - f) \times I_{\text{eq}}$$

where I_{core} is the intensity in the core beamlet and I_{outer} is the intensity in each outer beamlet. When f is zero, all five beamlets have equal intensity I_{eq}. When $f = -0.25$, there is no beam in the centre and the whole intensity is shared by the outer beamlets equally. When $f = 1.0$, there are no

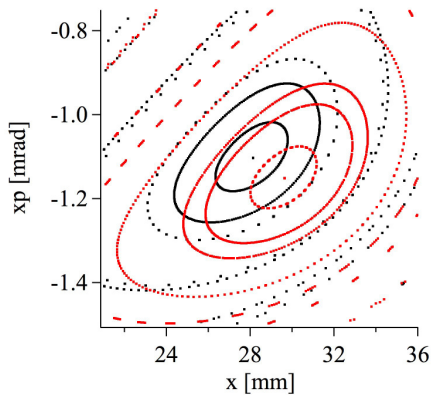

Figure 5: Close view of the lower right island. Black dots show the zero intensity case of Fig. 3 and red dots show the effect of space charge from Fig. 4. Single dots of black and red around the centre of each coloured ellipse indicate the fixed points.

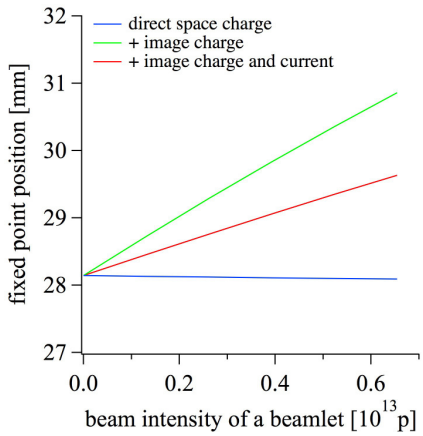

Figure 6: Location of the lower right island in Fig. 4 *v.* total beam intensity. Direct space charge produces a slightly negative tune shift and the island moves inwards with intensity. Image charge only gives a positive tune shift and the island moves outwards. Image current partially cancels the tune shift, and the slope of the line is less than the case with image charge only. The beam momentum is 14 GeV/c, the vacuum chamber half-height is h=35 mm, and the magnet pole face half-height is g=50 mm. We assume parallel plates to model the vacuum chamber and magnet pole faces. The packing factor of the magnets is 0.8. The total beam intensity is five times the beamlet intensity.

ISBN 978-3-95450-185-4

outer beamlets and only the central beamlet exists. The total beam intensity is kept constant.

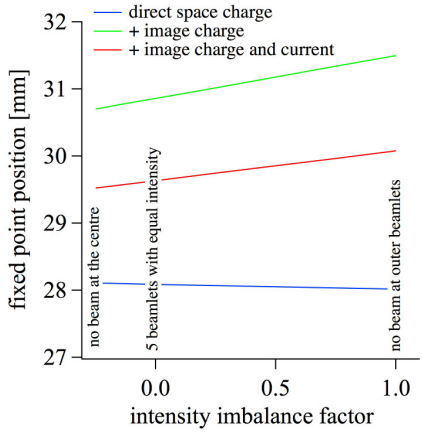

Figure 7: Fixed point position as a function of the intensity imbalance factor (see text).

Figure 7 shows how the fixed points move as a function of the intensity imbalance factor. The total beam intensity is fixed at 3.27×10^{13} and the horizontal tune used is the nominal tune, 6.255. The fixed point at zero current is positioned at 28.143 mm. The shift due to an imbalance in the beam intensity is rather small.

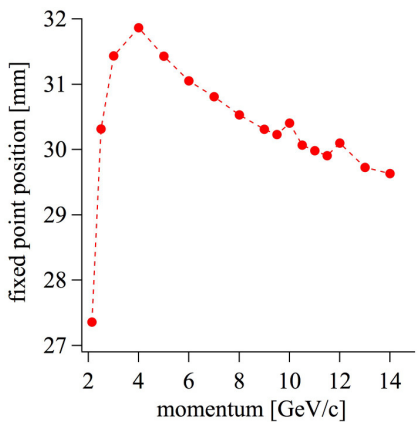

Figure 8: Fixed point position as a function of beam momentum.

Finally, the position of the fixed points as a function of beam momentum is shown in Fig. 8. Although there are some fine structures at momenta around 10 and 12 GeV/c whose reason is unknown, at the lower momentum, direct space charge effects are dominant. As the beam momentum increases, the contribution from the image charge/current becomes large and overcomes the direct space charge. As the beam momentum becomes even higher, the image charge/current space charge effects decrease due to the relativistic Lorentz factor.

COMPARISON WITH EXPERIMENT

So far, we have used parallel plates models for both the electric boundary image charges and the magnetic boundary image currents. However, more realistic boundary conditions have to be implemented in order to compare results from the simulation and experiment quantitatively. As a first step, a rectangular boundary has been introduced to treat the electric boundary.

We use the model in [4]. here Poisson's equation is solved by invoking a conformal Schwarz-Christoffel transformation.

$$G\left(u,v,u_0,v_0\right) = \frac{1}{4\pi}\ln\frac{\left(u-u_0\right)^2+\left(v+v_0\right)^2}{\left(u-u_0\right)^2+\left(v-v_0\right)^2},$$

where $G\left(u,v,u_0,v_0\right)$ is a Green's function and (u,v) and (u_0,v_0) are the transformed coordinates of the observation and source points, respectively. The mapping relations between coordinates before transformation (x,y) and after (u,v) are,

$$\begin{aligned} u &= \frac{\mathrm{sn}\left(2Kx/a,k\right)\mathrm{dn}\left(2Ky/a,k'\right)}{1-\mathrm{dn}^2\left(2Kx/a,k\right)\mathrm{sn}^2\left(2Ky/a,k'\right)}, \\ v &= \mathrm{cn}\left(2Kx/a,k\right)\mathrm{dn}\left(2Kx/a,k\right) \\ &\quad\times\frac{\mathrm{sn}\left(2Ky/a,k'\right)\mathrm{cn}\left(2Ky/a,k'\right)}{1-\mathrm{dn}^2\left(2Kx/a,k\right)\mathrm{sn}^2\left(2Ky/a,k'\right)}, \end{aligned}$$

where K is the complete elliptic integral of the first kind with module k and residual module k'. sn, cn and dn are the Jacobi elliptic functions. a and b are the horizontal and vertical aperture, respectively.

The electric field is the derivative of the potential. In order to calculate electric fields numerically, a circular cross-section beam of 2 mm radius with a uniform charge distribution is assumed. With this assumption, the electric fields at the beam edge are calculated numerically as

$$\begin{aligned} E_x &= -\frac{G\left(x+dx,y,x_0,y_0\right)-G\left(x-dx,y,x_0,y_0\right)}{2dx}, \\ E_y &= -\frac{G\left(x,y+dy,x_0,y_0\right)-G\left(x,y-dy,x_0,y_0\right)}{2dy}, \end{aligned}$$

where dx and dy are set to 0.1 mm. Electric fields inside the beam are a linear function of the coordinates (x,y) and zero at the centre.

Ignoring image currents on the magnet pole face for the moment, the force acting on the beam particles in the rest frame has two components,

$$F_{\mathrm{total}} = \left(1-\beta^2\right)F_{\mathrm{direct,\,elec}} + F_{\mathrm{image,\,elec}}.$$

The field obtained with the boundary conditions is the sum of the direct electric field and the image charge electric field. In order to calculate the direct magnetic field, we need the direct electric field without boundary. This has been done by assuming a vacuum chamber 100 times larger (the results are almost the same with 10 times larger). Finally, the force

ISBN 978-3-95450-185-4

is the combination of the following terms,

$$F_{\text{total}} = \left(1 - \beta^2\right) F_{\text{direct, elec}} + F_{\text{direct+image, elec}} - F_{\text{direct, elec}} .$$

The second term on the right hand side is the field obtained by solving for the potential with rectangular boundary conditions.

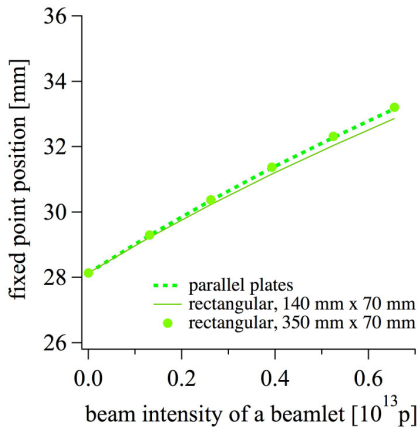

Figure 9: Fixed point position as a function of horizontal tune. The bare tunes are (6.255, 6.300). There is a slight difference between the results from parallel plates and a rectangular vacuum chamber.

We have compared the fixed point position as a function of beamlet intensity with different boundary conditions. Figure 9 shows that the parallel plates model and the rectangular vacuum chamber model give a slightly different intensity dependence. In order to check the consistency of two models, the results for a wider rectangular aperture are also shown in each case as solid circles. It is confirmed that the rectangular vacuum chamber gives similar results to those from parallel plates.

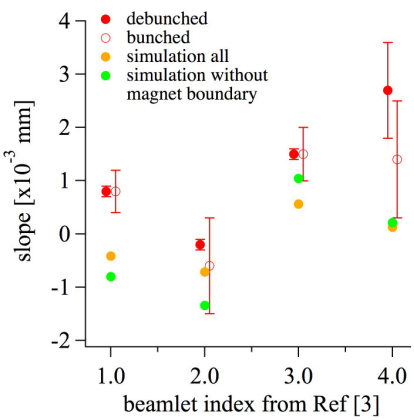

Figure 10: Slope of the beamlet position as a function of total beam intensity observed experimentally and by simulation. the slope is defined as a function of the total beam intensity of 10^{10} as in [3].

In reference [3] Fig. 13 and Table IV, the beamlet position as a function of the total beam intensity is shown and tabulated. These can now be compared with the corresponding simulation results. Figure 10 shows the slope of each beamlet. There are two simulation results: the first includes everything: direct space charge, image charges on the vacuum chamber and image currents on magnets; the second excludes image currents on magnets. Overall, experimental and simulation results look similar but there are two obvious discrepancies. First, the simulation results are equally distributed below and above zero whereas three experimental results have a positive slope and one has a negative slope. Secondly the difference between the maximum and the minimum slopes seems slightly different between simulation and experiment. We are investigating sources of the discrepancies.

One of the experimental findings - that there is no difference between debunched and bunched beams in terms of intensity dependence of beamlet position - can be understood if the main space charge contribution is from image charges and image currents. Each depends only on the total intensity and not on the bunching factor. This excludes the dependence of a longitudinal model in the simulation.

REFERENCES

[1] R. Cappi and M. Giovannozzi, Phys. Rev. Lett. **88**, 104801 (2002).

[2] S. Gilardoni, M. Giovannozzi, M. Martini, E. Metral, P. Scaramuzzi, R. Steerenberg and A.-S. Muller, Phys. Rev. ST Accel. and Beams **9**, 104001 (2006).

[3] Simone Gilardoni, Massimo Giovannozzi and Cedric Hernalsteens, Phys. Rev. ST Accel. and Beams **16**, 051001 (2013).

[4] Q. Shou, Q Jiang and Q Guo, J. Phys. A: Math. Theor. **42** (2009) 205202.

ISBN 978-3-95450-185-4

BROADBAND FEEDBACK SYSTEM FOR INSTABILITY DAMPING IN THE SNS RING*

N. J. Evans†, Oak Ridge National Laboratory, Oak Ridge, TN, USA

Abstract

The transverse feedback system in the Accumulator Ring of the Spallation Neutron Source (SNS) is intended to damp broadband (≈40-120 MHz), coherent betatron motion due to e-p interaction. The SNS feedback system is based on an analog delay-line model with some signal conditioning and tuning parameters implemented digitally. This system provides a simple setup with two primary knobs, phase and gain, as well as an equalizer. This simplicity comes at the cost of some flexibility normally found in a standard mode-by-mode design, namely mode-by-mode phase, and gain control. In this paper we discuss the design, tuning, evaluation, and operation of the SNS feedback damper, and discuss the tradeoffs implicit in the design of the system.

INTRODUCTION

Table 1 lists parameters of the SNS ring running in 1.4 MW neutron production operation. The purpose of the ring is to accumulate ≈ 10^{14} protons over 1 ms, about 1000 turns, to deliver a short intense pulse of protons to the neutron production target. This millisecond long cycle is repeated at 60 Hz. Since the early days of the design of the SNS ring, e-p instability due to the interaction of electrons in the vacuum vessel with the proton beam has been a serious concern necessitating the inclusion of many mitigation measures [1].

Table 1: SNS Ring Parameters for 1.4 MW Operation

Parameter	Value
Energy	939.5 MeV
Revolution Period	955 ns
RF 1st (2nd) harm	6.5(3.5) kV
Circumference	248 m
Bunch Length(FW)	650 ns
Charge	25μC
δ p/p Inj(Ext)	$10^{-4}(10^{-3})$
Pipe Radius	≥ 10cm
η	-0.2173
$\nu_{H,V}$	6.205, 6.165

The nature of e-p interaction leads to a broadband spectrum of coherent transverse betatron oscillation, in the case of SNS this spectrum has been observed in the range ≈≈40-120 MHz [2, 3]. The frequency spectrum evolves throughout a cycle, typically broadening toward higher frequencies as accumulation progresses. During dedicated study cycles in 2008, the e-p instability was induced in 8.5,10 and 20 μC/pulse beam at low repetition rate by changing various parameters such as storage time and 2nd harmonic RF cavity voltage. During these studies experimenters observed beam loss, and high frequency beam oscillation of several cm [3], but only in configurations specially tuned to produce the instability.

Broadband motion attributed to e-p has been seen in the SNS ring during normal operation, high frequency oscillation has only produced peak amplitudes < 1.5 mm during normal operation. This motion has not limited high intensity operation, up to the design power of 1.4 MW (24 μC/pulse), achieved in the Fall of 2015. The broadband transverse damper system in the SNS Accumulator ring was designed to address broadband betatron oscillation due to e-p interaction spanning the range from ≈40-120 MHz. Despite the fact e-p has not lead to operation limiting losses, the damper system has been used to suppress motion due to e-p interaction.

The state-of-the-art in broadband transverse damping typically makes use of a separate processing channel for each mode, or equivalently each time-slice of the bunch within the resolution of the system, e.g. JPARC, CERN SPS, among others [4, 5]. Each channel consists of a separate FIR filter used to tune the phase and gain of the feedback signal based on the history of that mode, or slice, over several turns.

The SNS system forgoes the complexity associated with such a design, instead using a delay-line model with certain digital signal processing elements to ease system setup. The feedback system is tuned for all modes simultaneously using a single gain, and phase knob. This simplicity comes at the cost of decreased flexibility with respect to tuning the phase and gain of each mode independently.

DAMPER SYSTEM

Figure 1 shows a schematic of the SNS damper system including: the stripline pickup and kicker, Low-level RF(LLRF), ADC, FPGA with processing blocks, DAC and power amplifiers.

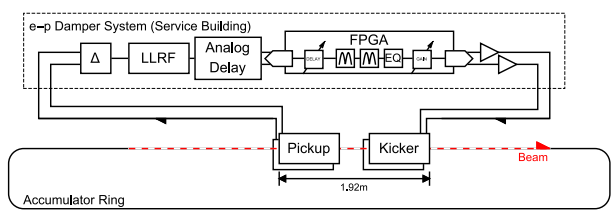

Figure 1: Schematic layout of the damper system.

* ORNL is managed by UT-Battelle, LLC, under contract DE-AC05-00OR22725 for the U.S. Department of Energy.

† evansnj@ornl.gov

ISBN 978-3-95450-185-4

The pickup and kicker are both 0.49 m long stripline pickups [6]. The pickup and kicker are 1.92 m apart, a betatron phase advance of about 0.3 rad. The response of the combined pickup-kicker configuration extends from about 25-180 MHz, with a peak response at 105 MHz, corresponding to the range of observed e-p activity in the SNS ring. Electronics in the ring service building are connected to the electrodes by 70 m of cabling in each direction, which contributes a total of 560.1 ns of delay to the system.

LLRF comprises a 300 MHz low-pass filter, amplification, and a 180° hybrid for each plane. Variable attenuators on the input to the difference hybrids provides a way to tune out the signal due to the closed orbit from the difference signal. Also included in the LLRF is a a cascaded set of binary delay lines to add upto 15.75 ns of additional delay with a precision of 250 ps, and several amplification stages as needed.

The digitizer comprises a 10-bit ADC, and a 12-bit DAC with up to 2 GSPS driven by a dedicated clock synched to the ring RF 10 MHz reference line. The digitizer clocks are driven at frequency such that each revolution contains an integer number of samples.

The FPGA provides several DSP functions: two notch filters at the revolution frequency implemented as two-tap FIRs (the second filter is used to reverse the effect of the first filter on the signal phase), an EQ which equalizes the magnitude response and corrects for phase dispersion in the cabling, and a coarse ≈8 ns digital delay necessary to tune the system.

After equalization, the addition of signal delay, and scaling by a gain multiplier, the difference signal is finally amplified and returned to the kicker. The horizontal and vertical planes have two and four 100W Intertronic/Eltac amplifiers [8, 9] dedicated to each electrode, respectively, for hardware details see [6].

Feedback Signal The difference signal used to damp beam motion is the product of the position and the beam current in the time domain. The inclusion of the beam current in the feedback signal has some consequences for the operation of the system during the accumulation cycle increasing the effective gain as the beam current increases.

The proper phase relative to the beam is attained primarily through delay. As the signal traverses the feedback system, including operator added delay, the betatron phase of the beam advances by the $\Psi_{p-k} \approx 0.3$ rad (there is a small difference between the two planes because of the two tune values) between the pickup and kicker and by an additional 2π Q radians per turn. By waiting N turns such that $\Psi_{p-k} + 2\pi NQ = (2j+1)\pi/2$, where j is any integer, the angular feedback kick can be applied when the measured betatron amplitude has rotated in the phase space to an angular deflection. The integer number of turns, N, delay must necessarily be larger than the total minimum delay in the system, which is dominated by the cabling, and the two turns of delay introduced by the notch filters. Table 2 shows the delay budget. Based on these numbers and the revolution period of 955 ns, we must have $N \geq 3$ in the SNS ring.

Table 2: Main Contributions to Delay

Source	Delay (ns)
2 × 70 m Cable	560.1
Electronics Pipeline	631.1
Comb Filters	955.0
Total	2146.2

Damping Production Beam

The data presented in this section was taken parasitically during normal 1 MW operation. Oscillation amplitude is on the order of 1 mm, and does not cause any measurable beam loss. However the broadband spectral content, which increases in frequency and amplitude as accumulation proceeds is unambiguous.

Figure 2 shows the power spectrum of difference signal of several modes of horizontal betatron motion in the lower sideband for both damped and undamped cases. The undamped beam shows clear activity at the fractional tune of ≈ 0.2, which is suppressed to within the background, about 25 dB, for the most active modes. The reference value for the log scale on each pane of Fig. 2 is the maximum power for that pane. Plotting the power in the damped difference signal at the betatron peak relative to the undamped reference value at each mode, Fig. 3 shows the effectiveness of the damper on the lower sideband across modes 10-120 at turns 600, and 900 of the accumulation cycle. Taken by itself, Fig. 3 can be easy to misinterpret. For instance, the decreased damping at higher modes at turn 600 is not due to the damper, but rather the lack of betatron motion at these modes when the damper is off. (A positive value on this figure would indicate the damper was driving certain modes.)

Figure 4 complements Fig. 3 showing the same information as Fig.2 but integrated over each sideband (upper sidebands are also included in this image), using a sliding window of 32 turns throughout the accumulation cycle to produce a spectrogram. It is more difficult to determine exactly how well the damping is working, but it is more obvious that the betatron motion due to e-p is suppressed over the entire band.

Tuning the System

The plots presented in the previous section illustrate the operation of the damper, but are difficult to evaluate in real time for the purpose of tuning the beam. Typically the preceding plots are produced after the system has been tuned. To tune the system we typically integrate the power contained in the difference signal in the entire band from 10-300 MHz, as shown in Fig 5.

As previously mentioned, both the gain and delay are set for all modes simultaneously. To set the working values for phase and gain we minimize the total power contained

ISBN 978-3-95450-185-4

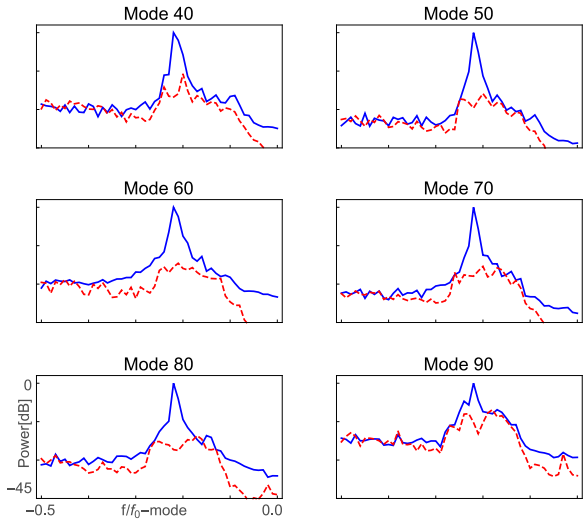

Figure 2: Power spectrum of several modes with damper off(blue, solid), and on(red, dashed) at turn 600 during the accumulation cycle during 1MW operation.

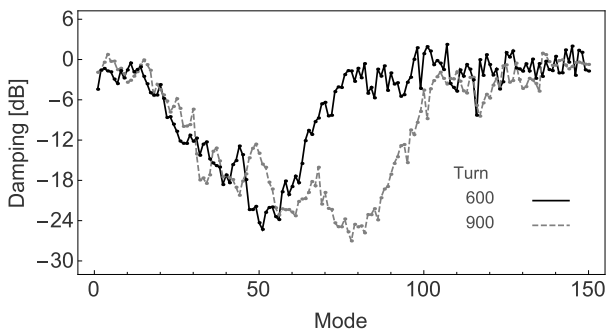

Figure 3: Ratio of damped to undamped power in the horizontal difference signal at the betatron peak for many modes at turns 600, and 900 of the accumulation cycle.

in the difference signal in the band from 10-300 MHz at extraction, in practice the oscillation power tends to grow monotonically throughout the cycle so this metric is effective at minimizing oscillation throughout the cycle. Figures 6, and 7 show the total oscillation power at extraction in the band 10-300 MHz as a function of digital gain multiplier, and ns of delay respectively. Detail regarding the activity in each mode is lost in this view, but it is clear that the damper improves the overall oscillation as gain is increased, but eventually begins to cause growth. Small delays, δ, from the optimal delay likewise cause growth in oscillation at extraction.

Design Limitations

Because each mode oscillates at the same tune, it is not necessary in principle to independently adjust the phase for each mode, the betatron motion itself provides the phase advance needed to properly apply the negative feedback. The downside to this method is that one must wait several complete revolutions for a phase advance near an odd multiple of

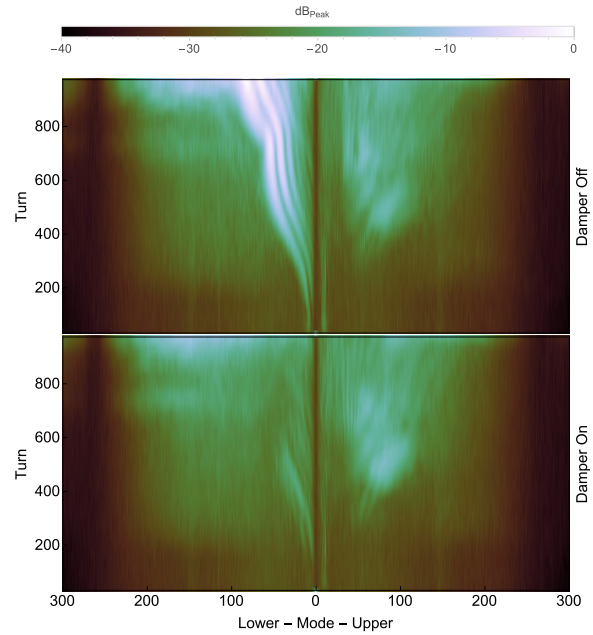

Figure 4: Power spectrum of several modes with damper off(blue), and on(red) at turn 600 during the accumulation cycle during 1MW operation.

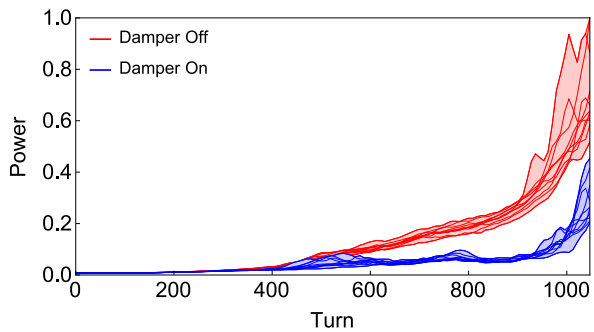

Figure 5: Total power in the horizontal difference signal in the frequency range 10-300 MHz throughout the accumulation cycle.

$\pi/2$, this delay between sensing and affecting beam motion reduces the effectiveness of the damper by, among other things, decreasing the maximum gain that can be applied before the system is driven. This delay can be reduced by reducing the minimum delay due to cabling and system latency to less than a single turn, or by changing the tune such the timing condition is satisfied in the smallest number of turns possible. Because the comb filters add a full turn of delay to the system, even if additional delay is kept to less than a single turn, the minimum delay in the current design is two turns.

The lack of mode-by-mode gain control is also a concern. In reality, for some gain multiplier in the signal processing chain, the effective gain depends on the magnitude of the transfer function of the entire system across all relevant frequencies.

ISBN 978-3-95450-185-4

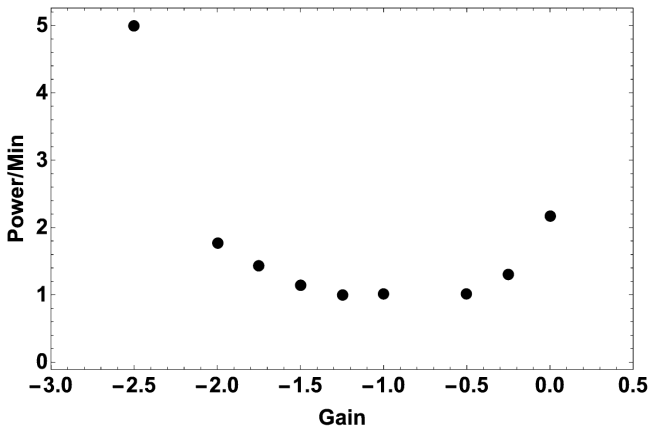

Figure 6: Total power in the horizontal difference signal at extraction from 10-300 MHz as a function of gain.

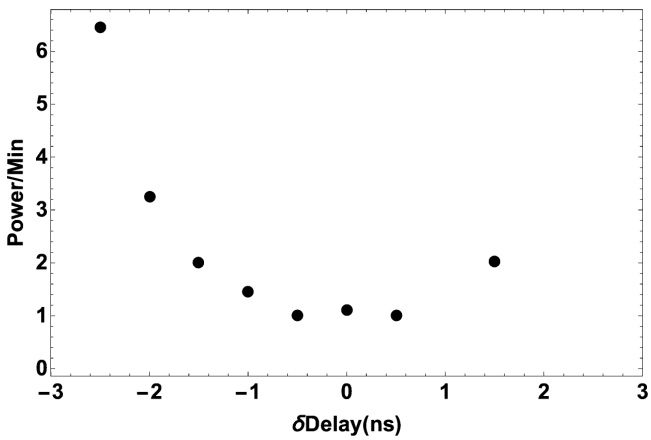

Figure 7: Total power in the horizontal difference signal at extraction from 10-300 MHz as a function of delay.

For a system which acts on n frequencies ω_n, the effective gain on the signal at each frequency is given by the response function of the system $|H(\omega)|$ multiplied by the digital gain multiplier, which is a constant, g. (I am assuming that the phase response is perfect for the sake of argument.) If the maximum gain that can applied to any frequency is some constant value g_{max}, then for each frequency we must have $g \times |H(\omega_n)| \leq g_{max}$. This means that some modes may be limited by the gain needed to maintain this condition for all modes simultaneously, a fact exacerbated if g_{max} is not independent of mode.

This is partially compensated by the fact that our system is designed with a peak response that coincides with the peak of e-p activity as seen in the SNS ring, and an equalizer that allows some tuning of the response function. Still, independent gain control remains the major advantage of mode-by-mode systems. A similar argument can be applied to independent mode-by-mode phase control.

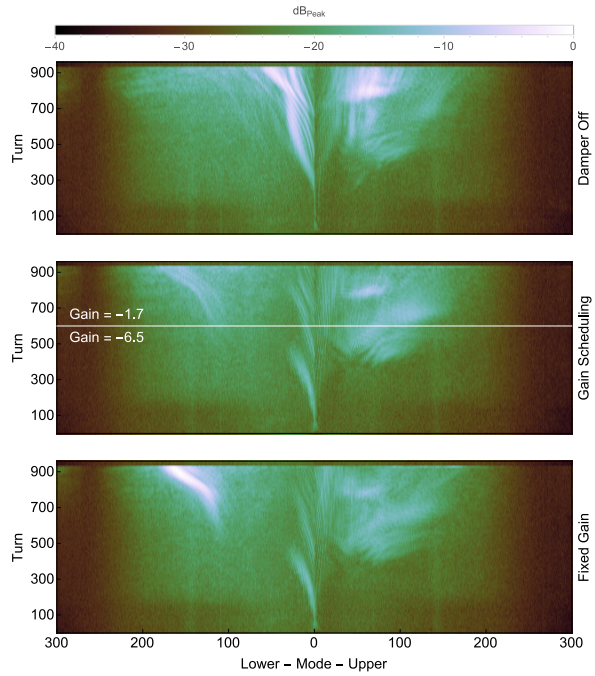

Figure 8: Power spectra for three cases to show the benefit of gain scheduling in the horizontal plane. For the damper on configurations gain is initially set about three times higher than the optimal value determined by minimizing oscillation power at extraction.

The consequences of this design decision can be seen in Fig. 8, which shows three cases: damper off, damper on but with a gain set too high, and damper on with gain scheduling to reduce the gain by 6 dB at turn 600. In the case where the damper is on with no gain scheduling, some of the higher modes, modes not even noticeable with the damper off, are driven by the system late in the cycle. A generalized gain schedule is easy to implement digitally, but this feature was not initially included in the SNS damper design so this experiment was performed using a TTL switch and a delay generator.

DISCUSSION

Because no losses due to e-p have been observed during normal operation, the damper system is not currently used during neutron production. In the future there are several circumstances which may necessitate the use of the damper system. Venting the ring for maintenance can affect contamination of the beam pipe, increasing the secondary electron yield. Though normal operation should eventually scrub the contamination from the beam pipe to at least the levels observed now, a swift return to full power could see losses due to e-p interaction, which the damper system could suppress.

Additionally, future plans for the SNS call for a doubling of the average power from 1.4 MW to 2.8 MW, through a combination of an increase in beam energy from 1.0 GeV to 1.3 GeV, and an increase in beam current while maintaining

ISBN 978-3-95450-185-4

the same accumulation time of ≈1000 1 μs machine turns. Alone, this increase in beam intensity could lead to increased broadband e-p activity, but part of this plan includes so-called 'smart chopping'.

Smart chopping involves reducing the injected pulse length throughout accumulation. This allows pulses long enough to occupy more of the extraction gap to be injected early in the cycle, as long as the resulting synchrotron motion before extraction is enough to compress the tails in time to within the allowed pulse length. The late injected pulses must be short enough to accommodate the extraction gap without the help of synchrotron rotation. Since longitudinal shape is one of the parameters that strongly affects e-p, it is possible that the addition of smart chopping may also increase e-p activity [7].

As a final possibility, note that to-date the damper has not been included as part of the neutron production setup tuning, additionally, all studies shown here have been done with production beam. It is possible that including the damper in this tuning procedure could allow for previously unusable regions of the parameter space to be explored, e.g. lower 2^{nd} harmonic RF cavity settings lead to a longitudinal distribution that increases e-p activity, but may also lower the momentum spread enough to reduce losses in dispersive regions, if the coherent oscillations could be controlled. This has not yet been explored for the SNS.

The hybrid approach presented here solves some of the problems inherent in a strictly analog system with respect to ease of tuning, but forgoes the complexity of other state-of-the-art, mode-by-mode dampers, and as a result suffers with respect to control of independent modes. Despite these limitations, this delay-line based system has proven effective in reducing broadband oscillation in the SNS ring.

ACKNOWLEDGEMENTS

The author would like to thank Sasha Aleksandrov for many fruitful discussions, as well as Jeff Bryan, Sarah Cousineau, Craig Deibele, Richard Dickson, Charles Peters, Mike Plum, and Zaipeng Xie for all their help.

REFERENCES

[1] J. Wei *et al.*, PRST-AB 3, 080101 (2000).

[2] S. Cousineau "Status of high intensity effects in the Spallation Neutron Source accumulator ring" in *Proc IPAC'11*, New York, 2011, paper MOOBS2, p. 17-21, https://jacow.org/HB2008/papers/wga16.pdf

[3] S. Cousineau, V. Danilov, M. Plum, C. Deibele, "Instability observations in the Spallation Neutron Source accumulator ring" in *Proc. HB'08*, Nashville, 2008, paper WGA16, p. 92-96, https://jacow.org/HB2008/papers/wga16.pdf

[4] K. Nakamura *et al.*, "Intra-bunch reedback system for the J-PARC main ring" in *Proc. IPAC'14*, Dresden, 2014, paper THOAA03, p. 2786-2788, http://jacow.org/IPAC2014/papers/thoaa03.pdf

[5] C. Rivettai *et al.*, "Broad-band transverse feedback against e-cloud or TMCI: plan and status" in *Proc. HB'12*, Beijing, 2012, paper THO1B05, p. 527-531, http://jacow.org/HB2012/papers/tho1b05.pdf

[6] C. Deibele, S. Assadi, M. Schulte, Z. Xie "Status and implementation of a wideband feedback system for e-p instabilities in the SNS" in *Proc. HB'08*, Nashville, 2008, paper WGF09, p. 462-465, https://jacow.org/HB2008/papers/wgf09.pdf

[7] Z. Liu "Linear Optics Correction and Observation of Electron Proton Instability in the SNS Accumulator Ring" Ph.D. thesis, Dpet. of Phys. Indiana University, Bloomington, Indiana, USA, 2011

[8] http://www.intertronicsolutions.com/

[9] http://eltac.co.uk

ISBN 978-3-95450-185-4

R&D ON BEAM INJECTION AND BUNCHING SCHEMES IN THE FERMILAB BOOSTER *

C. M. Bhat#
Fermilab, Batavia, IL 60510, USA

Abstract

Fermilab is committed to upgrade its accelerator complex to support HEP experiments at the intensity frontier. The ongoing Proton Improvement Plan (PIP) enables us to reach 700 kW beam power on the NuMI neutrino targets. By the end of the next decade, the current 400 MeV normal conducting LINAC will be replaced by an 800 MeV superconducting LINAC (PIP-II) with an increased beam power >50% of the PIP design goal. Both in PIP and PIP-II era, the existing Booster is going to play a very significant role, at least for next two decades. In the meanwhile, we have recently developed an innovative beam injection and bunching scheme for the Booster called "early injection scheme" that continues to use the existing 400 MeV LINAC and implemented into operation. This scheme has the potential to increase the Booster beam intensity by >40% from the PIP design goal. Some benefits from the scheme have already been seen. In this paper, I will describe the basic principle of the scheme, results from recent beam experiments, our experience with the new scheme in operation, current status, issues and future plans. This scheme fits well with the current and future intensity upgrade programs at Fermilab.

INTRODUCTION

Nearly one and a half decades ago, Fermilab started focusing on upgrades to its accelerator complex towards the intensity frontier that would substantially increase the average beam power delivered to the fixed target HEP experiments (as well as support then ongoing ppbar collider program) thereby transforming the facility into a world class accelerator based neutrino facility.

Currently, the chain of accelerators in the complex consists of an RFQ, 400 MeV normal conducting RF LINAC, 0.4-8 GeV rapid cycling Booster, 8 GeV permanent magnet Recycler Ring and 8-120 GeV (or 150 GeV) Main Injector. The last three machines in this chain are synchrotrons. The primary goal of the upgrades was delivering 700 kW of beam power at 120 GeV on the NuMI/NOvA target (a high energy neutrino experiment), and simultaneously provide proton beams to the low energy neutrino and fixed target experiments.

In 2010, after two and a half decades of successful operation of the Tevatron ppbar collider, the energy frontier HEP programs moved to the LHC at CERN. Since then many new developments have taken place at Fermilab. The Recycler, originally used as the primary anti-proton storage ring during the Tevatron collider era, has been upgraded to a high intensity proton storage ring that can be used as an injector to the Main Injector. This increased the Main Injector duty factor by nearly 30%. Though the Fermilab Booster is one of the oldest rapid cycling proton synchrotron in the world [1, 2] that cycles at 15 Hz and is in operation since 1971, until 2002 it delivered the beam on average at a rate of ≈1 Hz or less with a maximum beam intensity of ~3.5E12 p per Booster cycle (ppBc). During 2002-15 the beam delivery rate from the Booster has been increased to about seven cycles per sec as MiniBooNE and MINOS came online. The PIP was established around 2010 [3] to support the newly proposed NOvA, g-2, Mu2e, and short-baseline neutrino experiments which demanded doubling the Booster beam repetition rate from 7.5 Hz to 15 Hz with about 4.6E12ppBc. The foreseen Proton Improvement Plan-II [4, 5] supports the long-term physics research programs by providing MW type beam power to LBNE while sending beam to the on-going HEP experiments and forms a platform for the future of the Fermilab. The main components of the PIP-II are a new 800 MeV superconducting LINAC as an injector to the Booster and increase the Booster beam delivery repetition rate to 20 Hz with about 6.7E12 ppBc. In any case, the Booster is going to play a very important role at least for the next two decades and will remain the workhorse in the Fermilab accelerator complex.

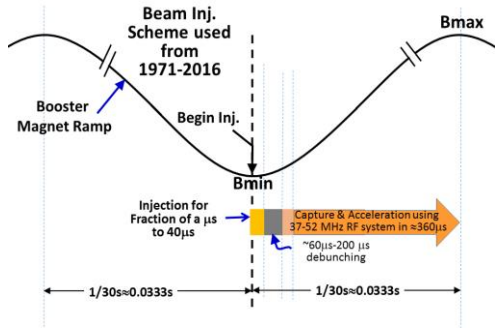

Figure 1: Schematic of the beam injection scheme in operation for the past forty five years of the Booster.

Booster uses sinusoidal magnetic ramp for beam acceleration. Its cycle rate is locked to 60 Hz ComEd power distribution system. The Booster has a circumference of 473.8 m with 96 combined function magnets distributed on a FOFDOOD (DOODFOF) 24 symmetric lattice period with independently controllable power supplies to its correctors to control its transverse dynamics. The fundamental accelerating RF system operates with a harmonic number h=84 and sweeps its

* Work supported by Fermi Research Alliance, LLC under Contract No. De-AC02-07CH11359 with the United States Department of Energy
# cbhat@fnal.gov

ISBN 978-3-95450-185-4

frequency in the range of 37.8 to 52.8 MHz in 1/30th of a second during the beam acceleration. The beam from the LINAC arrives at the Booster with a 200 MHz bunch structure. At the beginning the Booster was operated with single turn proton injection [6] and since 1978 Booster has adopted H^- multi-turn charge exchange injection technique [7].

Until the end of 2015 the Booster received the beam at the minimum of its magnetic field, B_{min} as shown in Fig. 1. Irrespective of the length of the LINAC beam pulse (< 40 μsec) the injected beam was allowed to debunch for a period of about 60-200 μsec and captured subsequently. Since the magnetic field was continuously increasing the beam was captured as quickly as possible with considerably large RF buckets. In addition to this, the fluctuation of the ComEd power line frequency which is of the order of 100 mHz out of 60 Hz introduced both time jitter (~50 μsec) and amplitude jitter in B_{min} (leading to ~0.5 MeV fluctuation). Also, as shown in Fig. 1, the beam capture and acceleration found to partly overlap during this part of the cycle. A combination of all these effects led to undesirable beam filamentation in the RF buckets leading to longitudinal emittance dilution, decreased beam capture efficiency and possibly transverse emittance growth at injection which might mimic space charge related issues. This also puts sever limits on achievable beam intensity. Over the years many improvements have been added to make the beam operation more efficient. Yet, the best efficiency observed so far was <95% with the scheme shown in Fig. 1 and a substantial longitudinal emittance dilution.

In 2014, we proposed a new injection scheme [8] called *Early Beam Injection scheme* (EIS), which fits well between PIP and PIP-II eras and has high potential to increase the beam power significantly. This scheme involves beam injection on the deceleration part of the magnet ramp in the Booster. At the end of 2015 we have implemented the new scheme in operation. Here, we explain briefly the general principle of the scheme, the results from beam dynamics simulations and beam studies, the current status of the scheme in operation, and future prospects.

EARLY INJECTION SCHEME

A schematic view of the newly proposed injection scheme is shown in Fig. 2. The basic idea of this scheme is to inject and capture the beam on a *pseudo front porch* created by imposing *dP/dt* = 0 in a changing magnetic field. Conventional wisdom was that this is not possible unless there is a front porch with a constant magnetic field. We noticed that around the minimum (and maximum) of an ideal sinusoidal dipole magnetic ramp the field changes slowly and symmetrically. Therefore, one can start injecting the beam relatively earlier than *Bmin*. In a decreasing magnetic field the injected beam with a fixed energy starts moving towards the outside of the ring (injection energy is below the transition energy of the Booster). In the case studied here, the beam injection is

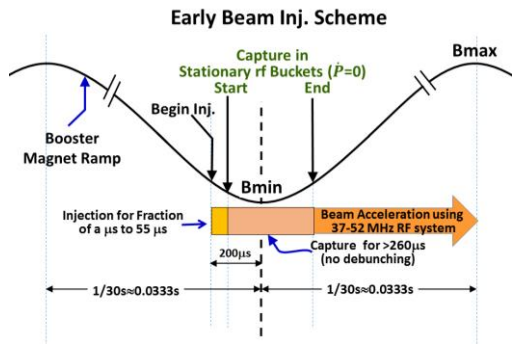

Figure 2: A schematic view of the new injection scheme in the Fermilab Booster.

carried out at ≈ 200 μsec prior to *Bmin*. For the Booster parameters (shown in Table 1) the maximum radial displacement of the beam centroid is ≈1 mm due to change in magnetic field, which is << 57.2 mm, the limiting physical aperture (the diameter of the RF cavity iris opening). The injection process itself takes as much time as the length of a LINAC pulse. Immediately after the completion of the injection, the Booster RF system is turned-on at a frequency matched to the beam revolution frequency. Debunching of the beam prior to the start of beam capture is eliminated. *dP/dt* = 0 is imposed by keeping radial feed-back turned off till the end of capture. Changing *B* field at a constant momentum still introduces varying revolution frequency in accordance with $\Delta B/B = \gamma_T^2 \Delta f/f$, where γ_T =5.478 is transition gamma for the Booster. The corresponding change in the RF frequency is ≈15.1 kHz. Thus, on the deceleration ramp the required RF frequency decreases initially and reaches its minimum at *Bmin* and increases symmetrically. This RF frequency variation should be taken in to account during the beam capture though the beam radially swings outside and inside. The beam is captured by increasing the RF voltage from about 20 kV to 400 kV in about 240 μsec. At the same time the beam synchrotron frequency changes from about 6 kHz to 27 kHz. In an ideal case, one demands much longer capture time. Since, the magnetic field is changing continuously and also the beam is moving radially during the capture, the time required to capture the beam cannot be increased much further.

The energy spread, Δ*E* (full), of the incoming multi-turn beam is about 1.25 ±0.20 MeV [9]. On the other hand, the bucket height from the residual RF voltage of nearly 20 kV is 0.9 MeV which is smaller than the energy spread of the injected beam. Hence, though the bunching starts immediately after the beam arrives into the Booster, the emittance dilution due to non-zero RF voltage is very small. (If the initial bucket height is comparable or larger than the energy spread of the incoming beam then one expects noticeable emittance dilution at capture.) By the completion of the capture the beam energy spread goes up to 3.6 MeV and the beam bunches will be on the increasing part of the magnetic field ramp. This beam energy spread

ISBN 978-3-95450-185-4

Table 1: Booster Parameters Used in the Simulations

Parameters	
Booster circumference (2πR) [m]	473.8
Injection KE [MeV]	400
Extraction KE [MeV]	8000
Cycle Time[sec]	1/15
Beam injection w.r.t. $\dot{B} = 0$ [μsec]	-200
Harmonic Number	84
Transition Gamma γ_T	5.478
RF Frequency [MHz]	37.8-52.8
Beam Structure at Injection	201MHz
LINAC Pulse length [μsec]	36-50
Number of Booster Turns	16-22
ΔE at Injection [MeV]	1.25 [9]
ε_L at injection/84 bunches [eV sec]	2.77
ε_L/bunch [eV sec]	0.033
Bunch Intensity [protons/bunch]	2E10-15E10
Beam transverse radius [cm]	1.2
Beam pipe (RF) radius [cm]	2.86

is still smaller than the Booster energy acceptance at injection which is ~5.4 MeV [10], hence, we do not anticipate any beam losses during the beam capture. RF feedback is turned-on for beam acceleration on the fully bunched beam.

We have demonstrated the feasibility of the EIS in the Booster using 2D- particle tracking simulation code ESME [11] including the longitudinal space charge effects. Table 1 lists the machine and the beam parameters used in the simulations. Figures 3-6 display the results from simulations for 9E10 p/Booster bunch which is about 70% larger than the PIP design intensity.

Simulations showed that there is a small longitudinal emittance dilution during the beam capture and that emittance is preserved till the transition energy. The dilution mainly comes from the non-zero RF voltage at injection. The transition crossing adds further emittance dilution; the full emittance increases by 70% from 0.048 eVs to 0.083 eVs. Majority of this arises from RF bucket mismatch as shown in Fig. 5. Interestingly, the simulations showed that the 95% emittance did not change much.

The Recycler Ring uses a multi-batch slip stacking technique [12] to increase the proton flux and it demands full beam energy spread from the Booster to be <13 MeV. The beam energy spread at the end of acceleration is about 20 MeV as shown in Fig. 6(a). To reduce the energy spread to an acceptable value by the Recycler Ring we adopt snap bunch rotation rather than currently used quadrupole RF voltage modulation [13]. The results from the simulations on snap bunch rotation are shown in Fig. 6(b). One can minimize any observed distortion in the rotated phase space distribution of the beam particles by adding 16% of 2nd harmonic RF component to the fundamental 53 MHz waveform to linearize the effective waveform during the bunch rotation.

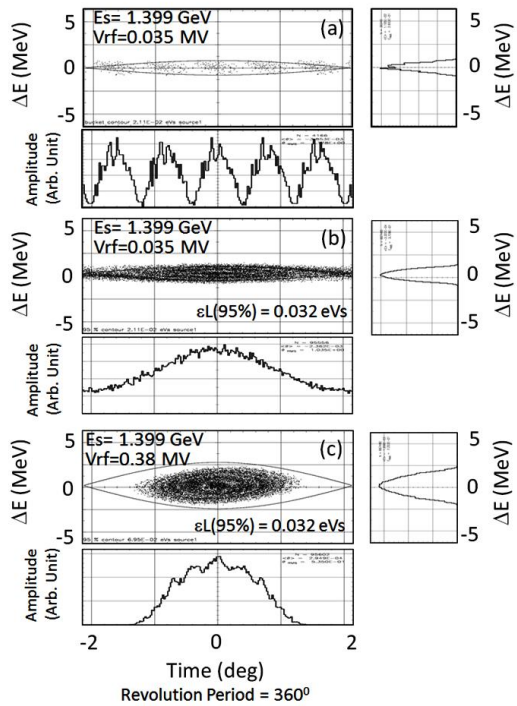

Figure 3: Simulated phase space distributions for the first 260 μsec, a) LINAC beam on the first turn in the Booster, b) at completion of 22 Booster turn injection, c) completion of beam capture in 37 MHz Booster RF bucket. The line-charge distribution and the predicted energy distributions are also shown on the right hand side.

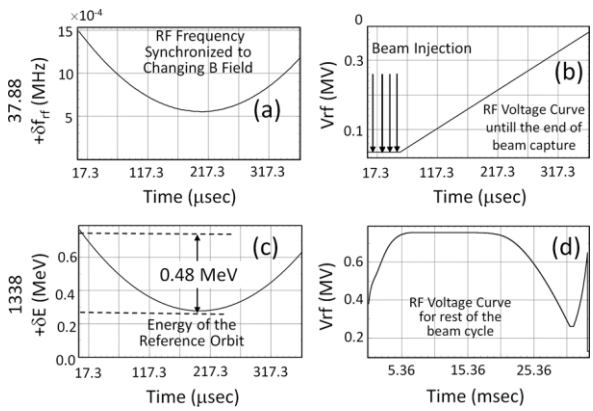

Figure 4: (a) Predicted variation of the RF frequency, (b) required RF voltage curve and (c) energy of the reference orbit, which represents the radial motion of the beam particles in the dipole field for the first 350 μsec. (d) predicted RF voltage curve for the entire acceleration cycle.

ISBN 978-3-95450-185-4

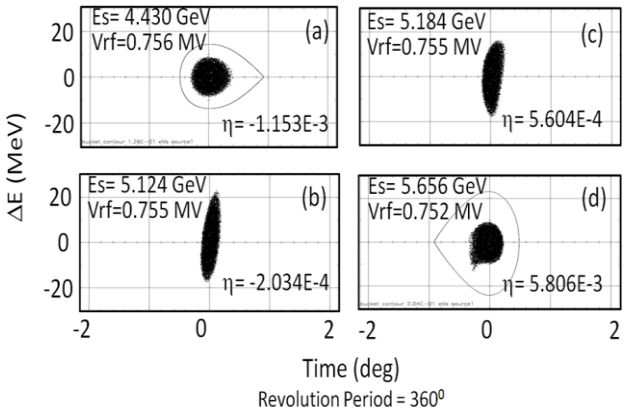

Figure 5: Simulations for the transition crossing. Distributions (a) before transition crossing, (b) and (c) very close to transition energy, (d) away from transition energy. We can see bucket mismatch.

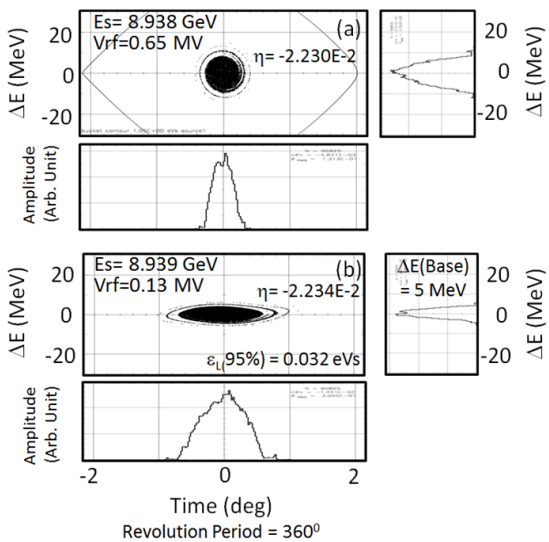

Figure 6: Simulation for snap bunch rotation: (a) before rotation commences and (b) at the end of rotation.

EXPERIMENTS

Proof of principle experiments have been carried out along the lines of simulations on the EIS. The top picture of Fig. 7(a) displays the measured data for the first 1 msec for beam injection, capture and the early part of the acceleration for ≈5.6E12 ppBc. Zero crossing of the Bdot curve (same as the *Bmin*) occurring at ≈ 200 μsec after the beam injection is also shown for clarity. We also show an approximate timing of the acceleration turn on in this figure. The beam transmission efficiency for the first 1 msec is found to be about 97%.

The data on various beam intensities under similar conditions but, for the entire cycle are shown in Fig. 7 (b). The observed sudden step loss at the beginning of each case is due to a notch created soon after the beam capture. (This notch keeps rise time of extraction kicker cleared from any beam.) This apparent decrease in efficiency is

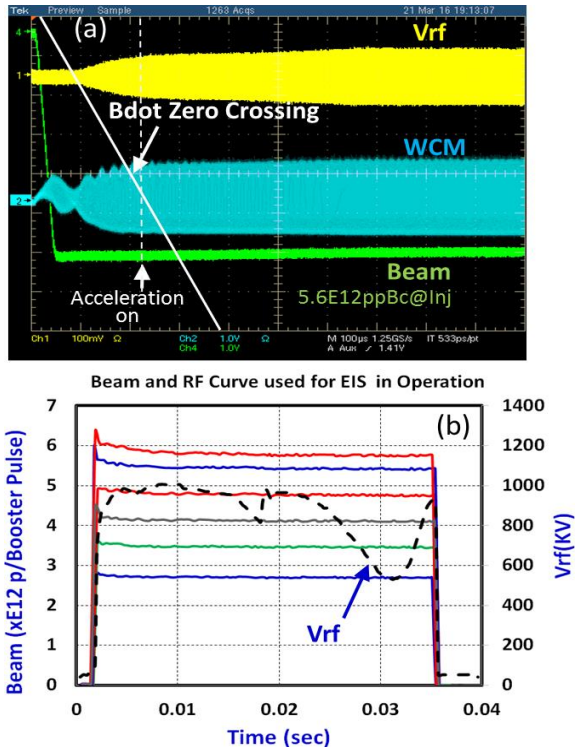

Figure 7: (a) Measurement data on first 1 msec at injection. (b) The beam through the acceleration cycle for different beam intensities. RF voltage curve is also shown here (dashed curve).

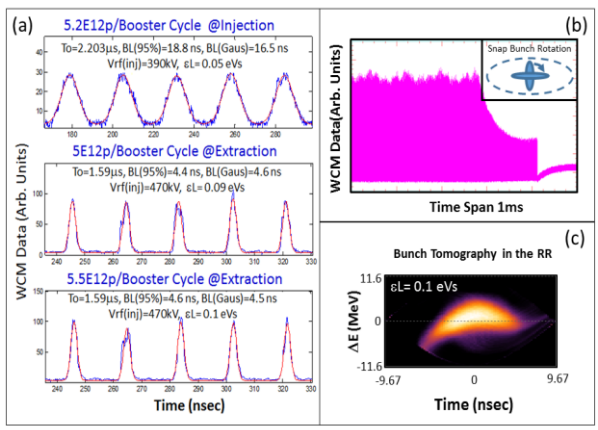

Figure 8: Measured wall current monitor (WCM) data on (a) five bunches at the end of beam capture and extraction for two intensities, (b) during the snap bunch rotation (schematic of bunch rotation shown in inset) and (c) the measured bunch tomography in the Recycler Ring for the beam coming from the Booster after bunch rotation.

~3.5%. These data show an average acceleration efficiency ~ 95% even for higher beam intensities.

Figure 8 (a) displays the bunch profiles and the measured longitudinal emittances at the end of the capture and also just before the extraction. The top two bunch traces are obtained on the same injected beam while the bottom trace

ISBN 978-3-95450-185-4

is for a case with higher beam intensity. Soon after the end of the beam capture the 95% emittance was found to be ≈ 0.05 (±15%) eVs which is about 50% larger than that expected from the simulations. About 400 μs before the extraction the 95% longitudinal emittance ≈ 0.1 (±15%) eVs per bunch for both intensities. Figure 8(b) shows the wall current monitor data taken during the snap bunch rotation on a beam with 5.5E12 ppBc. The decreasing amplitude of the wall current monitor signal is the result of increasing bunch length. We do not see any particle falling out of the buckets during this time. A tomoscope reconstruction of the phase space distribution of the beam particles transferred from the Booster to the Recycler 53 MHz RF bucket is shown in Fig. 8(c). The measured 95% emittance and the 1σ energy spread are about 0.1 eVs and 2.83 MeV, respectively. This emittance is consistent with that measured in the Booster at extraction. This energy spread is about 10% less than that generally obtained in the current operation (notice that operationally we use about 20% less beam particles per bunch than the one illustrated here).

As of December of 2015, we have replaced the old injection scheme in the Booster with the early injection scheme and gaining operational experience. Even with partial implementation of the EIS in operation we have seen a few advantages, *e.g.*, i) the beam longitudinal emittance delivered from the Booster to the Recycler or the Main Injector has improved by >10%, ii) the average RF power per Booster cycle has also gone down by 10-15% as compared with the old scheme and iii) we were able to send higher intensity beam to the down-stream facilities. Since the implementation of the EIS a number of other improvements were also added as part of the PIP plans. The Booster beam delivery rep-rate has been increased from 7.5 to 15 Hz. We were able to deliver up to 701 kW beam power on the NuMI/NOvA target, recently.

ISSUES, MITIGATION AND FUTURE PROSPECTS

There are a number of issues yet to be solved to take full advantages of the EIS in operation. Some of these are: 1) As mentioned earlier, the jitter in the *Bmin* relative to the beam injection clock event is quite large. This jitter arising from ComEd power line frequency is random and introduces large uncertainty during the start of adiabatic beam capture, there by emittance dilution in the early part of the cycle. Furthermore, this jitter also introduces uncertainty during transition crossing leading to RF phase mismatch and large quadrupole oscillation after transition crossing [14]. 2) The RF frequency does not follow the Booster dipole magnetic field ramp. (3) A better RF voltage regulation is needed at injection. Any unwanted imbalances in the RF voltage vectors introduces emittance dilution. As a consequence of these issues, we see longitudinal emittance dilution of about 50% during the beam capture. Transition crossing introduces another factor of two emittance increase. Currently R&D is in progress to mitigate every one of the above mentioned problems.

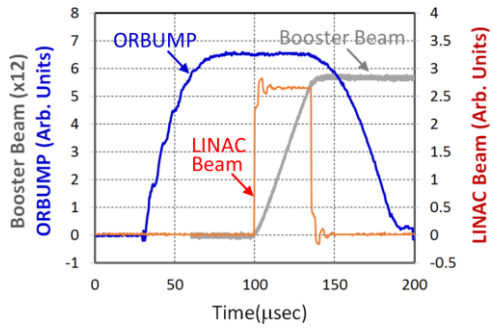

Figure 9: Current ORBUMP in the Booster at injection, LINAC pulse and injected and circulating beam with 5.8E12ppBc.

Table 2 summarizes the PIP and PIP-II performance goals. It also shows our expectation with full implementation of the EIS in operation after addressing the issues described earlier (which is important even for the PIP-II success). We find that the EIS fits well between PIP and PIP-II plans. With 6.4E12 ppBc at injection one can achieve ≈950 kW beam power on the NOvA target.

Table 2: PIP, PII-II Parameters and Expected from EIS

Parameters	PIP (**EIS***)	PIP-II
Inj. Energy (K.E.)	0.4 (**0.4**)GeV	0.8 GeV
Energy at Exit (K.E.)	8 (**8**) GeV	8 GeV
Booster Rep-Rate	15 (**15**)Hz	20 Hz
LINAC Pulse Length	≈30 (**45**) μsec	600 μsec
Intensity@Inj (ppBc)	4.52(**6.4**) E12	6.63E12
Inj. to Exit Efficiency	95% (**>97%**)	97%
Beam Power@Exit	94 (**≈135**) kW	184kW
Power@NOvA Target	700(**≈950**)kW	1.2 MW

*PIP with EIS.

The EIS in principle can accommodate 60% longer H^- pulses than the currently being used. The current LINAC can provide stable beam of about 50 μsec long pulses at 25 mA [15]. As shown in Fig. 9, the injection ORBUMP is wide enough to allow such a long beam pulse into the Booster. Thus, by using a longer LINAC beam pulses one should be able to increase the beam intensity beyond that mentioned above. We also do not anticipate any significant transverse emittance dilution due to multiple passage of the circulating beam through the stripping carbon foil [16]. In conclusion, EIS in the Booster has a high potential for increasing the beam intensity output by >40% than the PIP design with no/minimum beam loss.

ACKNOWLEDGMENT

I would like to thank W. Pellico, C. Drennan, K. Triplett, S. Chaurize, K. Seiya, B. Hendricks, T. Sullivan, F. Garcia, and A.Waller for many useful discussions and their help in the beam studies. Special thanks are due to Fermilab Accelerator Division MCR crew.

ISBN 978-3-95450-185-4

REFERENCES

[1] R. R. Wilson, Proc. of the 8th Int. Conf. on High Energy Accel. 1971, Geneva, Switzerland, p3; R. Billinge et al, IEEE Trans. Nuc. Sci. 1969 Particle Acce1. Conf. p. 969.

[2] "Fermilab History and Archives Project", http://history.fnal.gov/booster.html.

[3] "The Proton Plan," edited by B. Baller et al., Beams Doc. 1441-V1, 2004.

[4] W. Pellico, et al., Proc. IPAC14, www.jacow.org/IPAC2014/papers/thpme075.pdf; R. Webber et al., Beams Document 3781-v2 (2011).

[5] "The PIP-II Reference Design Report," V1 March 2015, http://www-bdnew.fnal.gov/pxie/PIP-II_RDR/PIP-II_RDR.pdf.

[6] D. F. Cosgrove, et. al., IEEE Transaction on Nucl. Sci. Vol. NS-24, No. 3, (1977) p 1423.

[7] C. Hojvat, et al., IEEE Transaction on Nucl. Sci. Vol. NS-26, No. 3, (1979) p 3149.

[8] C. M. Bhat, Proc. IPAC15, www.jacow.org/IPAC2015/papers/THPF112.PDF; C. M. Bhat, DPF2015, arXiv: 1510.08427 [physics.acc-ph].

[9] C. M. Bhat, et al., Proc. IPAC15, www.jacow.org/IPAC2015/papers/THPF113.PDF; J. Nelson, et al., MOPL020, these proceedings, HB2016, Malmö, Sweden (2016).

[10] C. M. Bhat, Beams Document 5014-v1 (2015).

[11] J. MacLachlan, http://www-ap.fnal.gov/ESME/.

[12] K Seiya et al., Proc. PAC2007, www.jacow.org/p07/PAPERS/TUODKI03.PDF.

[13] W. Pellico (private communications).

[14] C. M. Bhat and C. Y. Tan, MOPL021, these proceedings, HB2016, Malmö, Sweden (2016).

[15] F. Garcia (private communications).

[16] M. –J. Yang, (private communications) and Fermilab Booster Elog entry of Feb. 22, 2016.

ISBN 978-3-95450-185-4

INJECTION PAINTING IMPROVEMENTS IN THE J-PARC RCS

S. Kato†, H. Harada, K. Horino, H. Hotchi, M. Kinsho, K. Okabe, P. K. Saha, Y. Shobuda,
T. Takayanagi, N. Tobita, and T. Ueno
J-PARC center, Japan Atomic Energy Agency, Ibaraki, Japan

Abstract

In the J-PARC 3GeV RCS, the injection painting is essential method for the reduction of the space charge force. In the transverse painting, the H^- beam from Linac is distributed on the large phase-space area of the ring orbit during multiple turns. To implement this method, painting magnets form the time variable beam orbit. Therefore, the precise output current control of the magnet power supply was required. Because the power supply was controlled by mainly feedforward signal, we developed the iterative tuning method for the optimum feedforward parameter determination. As a result, we could reduce the tracking error of the current compared to before. In addition, we improved the measurement method of the footprint of the painting process. In the adjustment of the painting, we adopted the additional correction of the current tracking based on the measured footprint. As a result, the intended painting process and area were achieved accurately. Thus we established the precise control technique of the injection painting.

INTRODUCTION

The 3 GeV rapid cycling synchrotron (RCS) of the Japan Proton Accelerator Research Complex (J-PARC) serves as a high intensity proton driver aiming to achieve a 1 MW beam power. The 400 MeV H^- beam from Linac is converted to proton at the injection point by the charge-exchange foil and stored during injection period of 0.5 ms repeatedly using the multi-turn charge-exchange injection method. The RCS accelerates protons up to 3 GeV with a repetition rate of 25 Hz. The beam is provided as the neutron source for the Materials & Life Science Experimental Facility (MLF) and as the injection beam for the 50 GeV main ring (MR). The current progress of the hardware and commissioning is described in the reference [1] in detail.

The RCS is adopted the transverse injection painting in order to distribute the injection beam on the large phase-space area intentionally and mitigate the space-charge force which can become the beam loss source. The scheme of that is as follows [2]. The schematic view of the injection area and the variation of the horizontal orbit during the painting are shown in Fig. 1. In the horizontal plane, during the 0.5 ms injection period, four shift-bump magnets (SB1-4) shape the fixed bump orbit. In addition, four paint-bump magnets (PB1-4) shape the time dependent bump orbit. Fig. 1a(A) shows the bump orbit at the injection start timing (t = 0). The injection track is matched to this bump orbit at the injection point. During multi-turn injection, the track of H^- beam is fixed and the ring orbit is shifted slightly from the charge-exchange foil by decreasing the time dependent bump orbit height as shown in Fig. 1b(A) and Fig. 1c(A). Therefore, the injection beam changes its position and angle with respect to time along major axis in the phase-space ellipse of the ring orbit as shown in Fig. 1(B). As a result, the circulating beam becomes so broader compared with the Linac beam and the space-charge force is mitigated. In addition, the number of the charge-exchange foil hits by the circulating beams is decreased because the circulating beam is shifted from the foil.

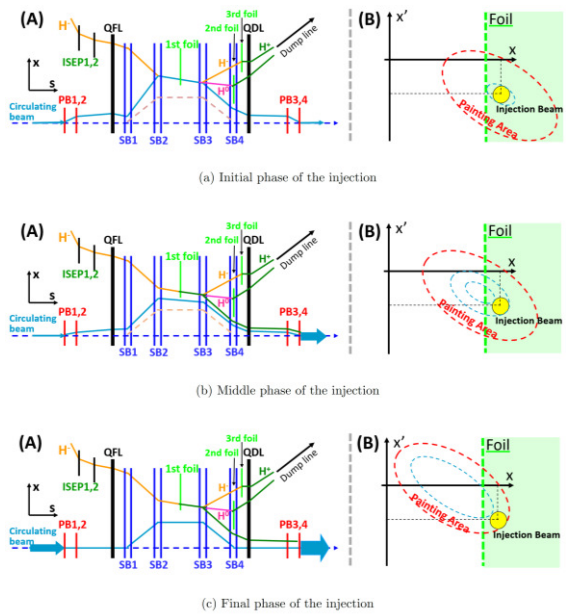

(a) Initial phase of the injection

(b) Middle phase of the injection

(c) Final phase of the injection

Figure 1: The horizontal orbit variation around the injection point during the injection period. Figure (A) indicates the orbits of the injection and the circulating beam. Figure (B) indicates the phase-space of the position and angle at the injection point.

In the vertical plane, two vertical paint magnets installed at the injection line change the injection beam angle at the injection point. The injection beam is brought closer to the central orbit from the edge of the painting area or vice versa in the phase-space ellipse of the ring orbit along angular axis. In the RCS, painting from the center to the outside in both horizontal and vertical phase-space is called Correlated Painting. On the other hand, painting from the outside to the center in vertical phase-space different from the horizontal painting is called Anti-Correlated Painting. When the injection beam position and angle are changed along the radial direction in proportion to the square root of the time, the beam is uniformly distributed on the phase-space area. Therefore, for

† skato@post.j-parc.jp

ISBN 978-3-95450-185-4

an elapsed injection time t, the horizontal time function is described by $x\ and\ x' \propto \sqrt{t/500\ \mu s}$.

For the precise beam tuning and the beam loss control, it is required that the injection beam is painted correctly in the expected phase-space area. The accuracy of the injection painting depends on the precision of the output current adjustment of the magnet power supplies because the time variation of the orbit is generated by the PBs whose power supply are separated. Hence, the improvement of the current adjustment is essential. In addition, the closed orbit distortion (COD) caused by the unbalance of the PBs output during the injection period occurred up to ±5 mm in the horizontal plane. Therefore, the improvement of the PBs output balance and the reduction of the COD should be also achieved by the precise current adjustment. To achieve the precise injection painting, the measurement technique for the time variable orbit height and the footprint of the painting process should be also developed to confirm the painted phase-space area. In terms of the efficiency of the beam tuning, the required time of the adjustment scheme including the current adjustment and the paining process observation should be short as much as possible.

In the RCS, the series of the injection painting adjustment has been improved to achieve these requirements and precise injection painting. In this paper, we present recent improvements focusing on the horizontal painting.

PRECISE CURRENT ADJUSTMENT OF THE POWER SUPPLY

Construction of the PB Magnet Power Supply

The basic construction of the PB magnet power supply is the four quadrant chopper circuit using IGBT switch. Actually, the power supply is operated as the two quadrant chopper circuit by cutting off two IGBT to avoid the reverse current flow in the magnet. As the chopper assemblies in front and back of the load, 18 sets of switch assembly are connected in parallel respectively. The switching frequency of IGBT is 50 kHz and the combined switching frequency is 600 kHz because 3 sets of switch share same switching pulse. The detail is described in the reference [3]. The rated maximum output current and the voltage is 29 kA and ±1.2 kV, respectively.

For this power supply, the appropriate IGBT control signal should be generated in order to output intended current. The IGBT control signal is generated by mixing the analog feedback and feedforward signals in the control unit. To generate these two signals, we input the Set Current Waveform (SCW) and the Set Voltage Waveform (SVW). These two waveforms, the output current and the output current deviation from the SCW corresponding to the tracking error are shown in Fig. 2. The SCW is the target time variation pattern. The time decay waveform of the SCW follows the function $\sqrt{1-(t/500\ \mu s)}$ from t = 0 though the function is proportional between t = 0 and t = 88 μs to suppress the rate of change of the current within permissive voltage level. The control unit compares the SCW and the output current and generates the analog feedback signal to reduce the tracking error. For this feedback, the significant current deviation is prevented even if the SCW is changed immediately and the power supply is protected. However, the tracking error cannot be obliterated completely when the output current changes largely during short time such as 500 μs because the response time constant of the feedback is approximately 20 μs. Therefore, the SVW is also input as the analog feedforward signal. The value of the feedforward signal corresponds to the opening and closing times of the IGBT directly. Namely, the SVW corresponds to the target output voltage pattern. The value of the SVW is approximately scaled to the actual output voltage.

For the adjustment of the output current, we optimize the SVW. First, the initial SVW is calculated by the SCW (i), the inductance (L_m) and the resistance (R_m) of entire load circuit following the basic function $V=L_m(di/dt)+iR_m$. After that, we obtain the output current and modify the SVW repeatedly to minimize the tracking error.

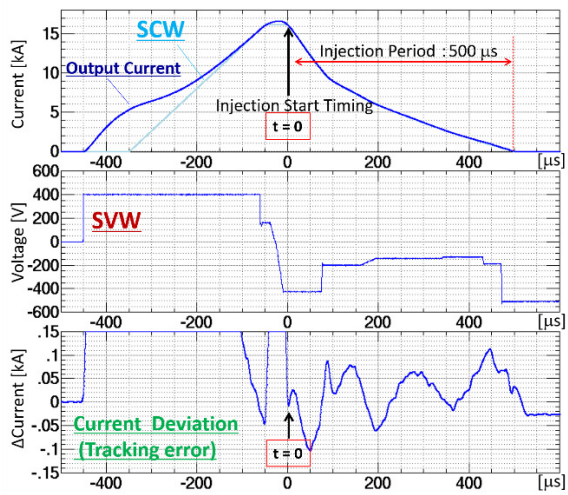

Figure 2: The typical waveforms of the SCW and output current (top), the SVW (center) and the current deviation (bottom) in the case of the PB1.

Improvement of the Adjustment Process

Previously, the accurate response of the output current to the change of the SVW was not comprehended. Therefore, each power supply had the tracking error which was more than ±100 A even after adjustment. By the accumulation of the tracking errors of four power supplies, the COD was up to ±5 mm because the error of 100 A generated the COD of 1 mm. In addition, the adjustment time was too long such as 1 hour per one power supply. Therefore, we comprehended the response and established the high accuracy automatic adjustment technique [4].

First, the response of the output current to the change of the SVW was measured. The measurement method is shown in Fig. 3. We prepared the trapezoidal waveforms of SCW shown in Fig. 3(a) and adjusted the SVW and the output current. The tracking error was ±100 A or less. These adjusted waveforms were used as the reference waveforms. For the response measurement, the SVW

ISBN 978-3-95450-185-4

variation of the ΔV was added during ΔT_V shown in Fig. 3(b). Then, the current deviation from the reference waveform was measured. This was defined using two parameters of ΔI and ΔT_I as shown in Fig. 3(c). The ΔI and ΔT_I are the peak value of the current deviation and the required time, respectively. This measurement was performed for each magnet because the shapes of the magnet yoke and the internal constitutions of the power supply were different slightly. In the following, the results of the PB1 is shown on behalf of the other. For the relation between ΔT_I and ΔT_V, it was confirmed that the ΔT_I is larger than ΔT_V. The difference is larger than the dead time of the reaction to ΔV which is 10 μs because the feedback effect is gradual. For the relation between ΔI and ΔV for the several ΔTv, the results are shown in Fig. 4(a). As shown, the ΔI is proportional to ΔV when the ΔTv is fixed. The relation of ΔI/ΔV and ΔTv is shown in Fig. 4(b). The ΔI/ΔV corresponds to the factor of proportionality. As shown, the rate of increase of the ΔI/ΔV is less than that of the ΔTv because the feedback effect suppresses the ΔI in the long ΔTv condition. Although the relation of the ΔI/ΔV and ΔTv were not proportional, it became possible to obtain the ΔI/ΔV for any ΔTv conditions using the approximated quadratic function shown in Fig. 4(b).

These responses were also measured using some trapezoidal waveforms whose flat top current were different and the decay type waveforms as shown in Fig. 2. As a result, it was confirmed that these responses were same regardless of the current and the shape of the waveform.

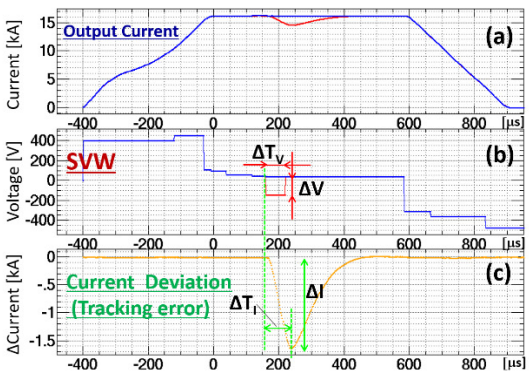

Figure 3: The reference waveform and the parameter definitions for the measurement of the output current response. The blue lines show the reference wave forms. The red lines show the modified wave forms. (a), (b), (c) show the output current, set voltage and current difference, respectively.

Second, the L_m and the R_m of the entire load circuit were measured in order to obtain the initial SVW which close to the final one. We prepared the trapezoidal waveforms of the SCW in the range of 4 to 16 kA and measured some relations between the SVW values as the voltage and the *dI/dt* of the current deviation. After that, the L_m and R_m were calculated using the simultaneous equations. In other words, the L_m and R_m related to the SVW rather than real output voltage were measured.

Third, the new waveform of the SCW which had smooth curve at the both side of the flat top was adopted in order to minimize the tracking error before t = 0.

Finally, we developed the high accuracy adjustment tool using measured responses. For the first step, the *dI/dt* of the current deviation was obtained with minimum time step of 2 μs. After that, the ΔV which suppresses the *dI/dt* was calculated using the results of the response measurement and applied to the SVW. These processes were repeated automatically.

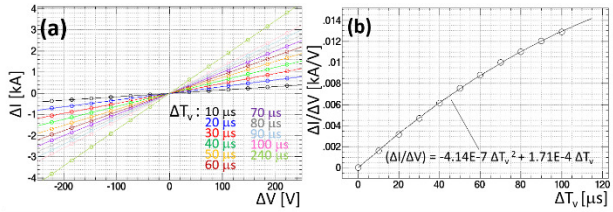

Figure 4: The relations between ΔI and ΔV for the several ΔT_V.

The adjustment results of the tracking error are shown in Fig. 5. The SVW calculated using new L_m and R_m was adopted as initial one. The number of adjustment iteration was 12. In Fig. 5, the previous adjustment results are also shown for comparison. As shown, the tracking error of the current could be reduced from the rising region of the SCW because of the new SCW and the iterative adjustment. As a result, the tracking error could be suppressed under ±50 A. Because this remained value corresponded to the value of fluctuation of each output pulse, the high accuracy adjustment was achieved. Moreover, the adjustment time was reduced to be under 20 minutes per one power supply for the automatic tool.

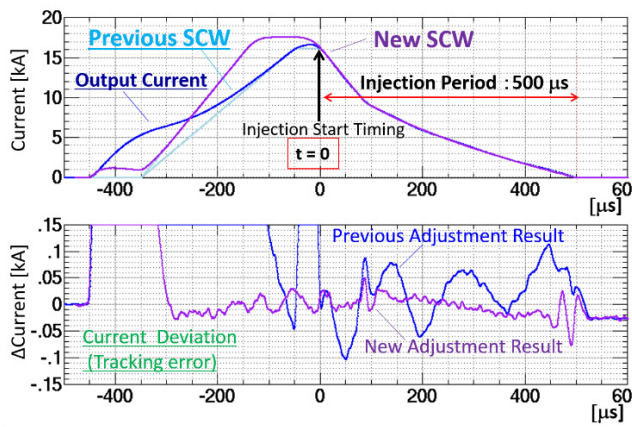

Figure 5: The results of the current adjustment. The blue lines show the previous pattern and the adjustment result. The purple lines show the developed pattern and the adjustment result.

MEASUREMENT METHOD OF THE PAINTING AREA

For the precise adjustment of the injection painting, it is required that the footprint of the painting process on the phase-space is measured continuously. For the horizontal

ISBN 978-3-95450-185-4

painting, the footprint and the final painted area can be obtained by measuring the time variation of the bump orbit height at injection point. Therefore, the measurement method which combines the online simulation model calculation and the COD measurement was established.

First, the COD was measured during injection period continuously. The multi-turn injection time was 100 μs. In order to obtain the COD from t = 0, the injection was completed until t = 0 by shifting just before the injection start timing specially. We obtained the COD by analyzing the signal of each BPM which had 4 electrodes [5]. The fourier transform (FT) was applied to the waveform of each electrode with time width of 51.2 μs. For the obtained spectrums, the peak value around the integer times of the revolution frequency of 614.25 kHz was regarded as the amplitude of the picked up signal. From the balance of these amplitudes of 4 electrodes, the orbit position at each BPM was determined. By repeating this manipulation from t = 0 with time step of 1 μs, we could obtain the time variable COD during injection period. As described above, the measurement of the COD during injection period required only 1 shot and shot time. The measurement was performed with and without the bump orbit of PBs and the COD caused by only PBs was extracted by subtracting these results.

Second, the kick angles of PBs expressed by K0 were estimated using the online simulation model fitting for the obtained COD. In the RCS, the model was constructed using SAD code. Its accuracy was confirmed by comparison with the measurement results of the various optical parameters in the beam commissioning up to now. For the fitting, only four K0 values of PBs were set as free parameter. Although the fitting target was the COD caused by only PBs, the fixed bump orbit formed by SBs was included in the fitting because this bump orbit closed between two BPMs located before and after of the injection point and did not relate that COD. The results are shown in Fig. 6. As a result, not only each K0 value but also the time variation of the bump orbit height at the injection point could be obtained continuously. Thus the footprint of the painting process could be measured.

PRECISE PAINTING ADJUSTMENT

Adjustment Process

For the precise painting adjustment, the methods of the current adjustment of the power supply and the measurement of the painting process were developed as described above section. In the RCS, the precise painting adjustment was established using these methods as follows.

First, the position and angle of the initial bump orbit at injection point was determined using the online simulation model and the measured beam parameter. The initial bump orbit is same with the fixed injection beam orbit. Therefore, the injection beam coordinate on the phase-space was determined to match the arbitrary painting area size at the end of injection period. Second, the initial K0 values of the four PBs which form the initial bump orbit was estimated by model fitting. And those values were converted to the output current of the PB. The conversion factor was measured using the trapezoidal waveform of the PB whose output current was fixed during injection period. Specifically, the COD and K0 measurement was performed for the trapezoidal waveform. After that, the factor was derived from the analyzed K0 and the value of the output current monitor. It was confirmed that the relation between the K0 and the value of the current monitor was proportional by the various current measurements. Third, the output current of the PB power supply was adjusted. The SCW of decay waveform was constructed based on the obtained initial current value. And the tacking error was reduced by the automatic adjustment technique. Finally, the footprint of the painting process and the painting area were measured to confirm whether the painted area size and the footprint was correct or not.

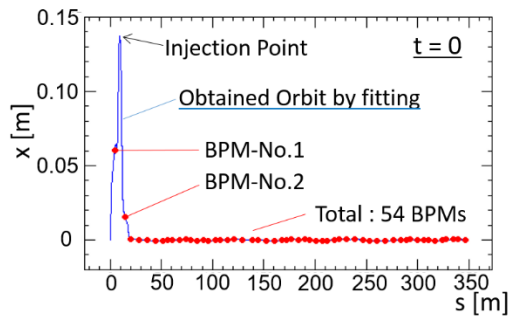

Figure 6: The obtained horizontal ring orbit by the COD fitting at t = 0. The red points are COD values measured by BPSs.

Results and Discussion

The result of the measured footprint of the painting process after adjustment is shown in Fig. 7 with red line. The target painting area was 150 π mm mrad. The line from center indicates the footprint of the painting process on the phase-space. As shown, the moving distance of the injection beam was insufficient. This result is equivalent to that the bump orbit height at t = 0 was insufficient. In other word, the output of the magnetic field was insufficient. The shortage was several hundred A at t = 0 for the decay waveform. This value was too large compared with the accuracy of the current adjustment. On the other hand, the bump height formed by the trapezoidal waveform whose current monitor value was same with that of decay waveform at t = 0 was sufficient. Therefore, this shortage of the magnetic field was caused by the existence of the decay region rather than the error of the conversion factor between K0 and the current.

By the investigation, it was found that the reason for this problem was the time delay of the current monitor value of the power supply in the decay region. For the PB power supply, the current monitor consisted of several Current Transformers (CT). Because the several CT were connected in parallel and these signals were synthesized, the generated current delayed in the synthesis circuit when the current changed quickly. In the decay region, the monitor value became bigger than the real output

ISBN 978-3-95450-185-4

current due to the time delay. Therefore, we were deceived into accepting the current as big. As a result, we set the current to be smaller.

Of course, the time delay of the magnetic field caused by the eddy current could be considered as the reason for the difference between the case of the trapezoidal and the decay waveform. However, the output of the magnetic field become bigger than the target value in the decay region in this case. Therefore, the magnetic field delay was not main reason though this effect was also contained.

In order to correct this issue, we regenerated the new SCW considering the shortage of the magnetic field and readjusted the output current. The shortage was converted to the current value and added to the original SCW. Some excessive current was also added. This correction was performed for the PB1 and PB2 which had larger output. Because the correction was based on the measured K0 value, it could potentially consider both time delay effects of the current monitor and the magnetic field.

The readjustment result is shown in Fig. 7 with blue line. The moving distance of the injection beam was enough improved by only one correction. In addition, the footprint followed the radial direction on the phase-space more accurate compared with before correction case because of the improvement of the output balance between PB1 and PB2.

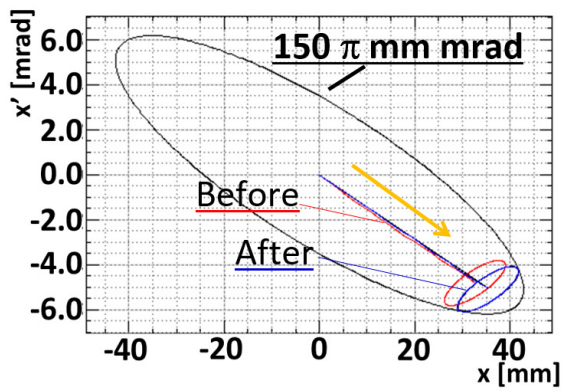

Figure 7: The measurement results of the footprint of the painting process on the horizontal phase-space of the ring orbit. The black ellipse indicates the target painting area. The orange arrow indicates the painting direction. The red and blue lines indicate the footprint of the painting process before and after readjustment, respectively. The red and blue ellipses indicate the injection beam of 4 π mm mrad.

The COD caused by the unbalance of the PB output during injection period is shown in Fig. 8. The amplitude of that could be reduce compared with previous one by the developed current adjustment technique and the correction. The amplitude became under ±2 mm during injection period. From these results, the precise painting adjustment method including the correction based on the measured K0 was established and the precise injection painting was achieved.

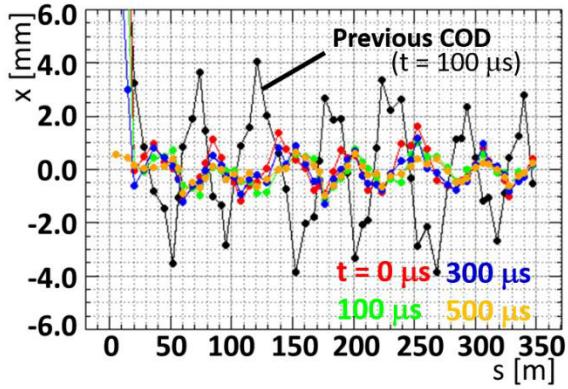

Figure 8: The CODs measured after painting adjustment. The black line is the previous result. The other lines indicate that of each time shown in the figure.

SUMMARY

In the RCS, the control of the injection painting was improved. To reduce the tracking error of the output current of the PB which directly relates the painting accuracy, the response of the output current to the feedforward signal which was control knob was examined. In addition, the automatic adjustment technique was developed using this result in order to reduce the current adjustment time of the PB power supply which occupies a lot of the beam turning session could be reduce. As a result, the required time and the accuracy became 1/3 and 2 times compared with previous one, respectively. To obtain the footprint of the painting process on the phase-space and the painted area size, the measurement method which combined the model calculation and the COD measurement was also established. The paining adjustment was performed using these developed methods. During the adjustment, it was found that the gap between the monitor current value of PB power supply and the outputted kick angle occurred. Therefore, the correction based on the measured kick angle was adopted to solve this issue. Finally, it became possible to distribute the injection beam on the target paint area correctly because of these improvements. In addition, the COD caused by the unbalance of the PB current also reduced. Therefore, we established the precise control of the injection painting.

REFERENCES

[1] H. Hotchi et al., "THE PATH TO 1 MW -BEAM LOSS CONTROL IN THE J-PARC 3-GeV RCS-", in this conference.

[2] H. Harada, KEK Report No. 2009-7.

[3] T. Takayanagi et al., "Development of a large-current high-precision pulse power supply", Electrical Engineering in Japan, vol. 166, Issue 3, 2009, pp.62-72.

[4] S. Kato et al., in Proc. of the 12th Annual Meeting of Particle Accelerator Society of Japan, Tsuruga, Japan, 2015, pp.1180–1184.

[5] N. Hayashi et al., in Proc. Of the EPAC08, Genoa, Italy, 2008, pp. 1128-1130.

ISBN 978-3-95450-185-4

H^- CHARGE EXCHANGE INJECTION ISSUES AT HIGH POWER*

M.A. Plum, Oak Ridge Spallation Neutron Source,
Oak Ridge National Laboratory, Oak Ridge, TN, USA

Abstract

At low beam powers H^- charge exchange injection into a storage ring or synchrotron is relatively simple. A thin stripper foil removes the two "convoy" electrons from the H^- particle and the newly-created proton begins to circulate around the ring. At high beam powers there are complications due to the heat created in the stripper foil, the power in the H^0 excited states, and the power in the convoy electrons. The H^- injected beam power at the Oak Ridge Spallation Neutron Source is the highest in the world. Although the SNS ring was carefully designed to operate at this level there have been surprises, primarily involving the convoy electrons. Examples include damage to the foil brackets due to reflected convoy electrons and damage to the electron collector due to the primary convoy electrons. The SNS Second Target Station project calls for doubling the beam power and thus placing even more stress on the charge-exchange-injection beam-line components. In this presentation we will compare charge-exchange-injection designs at high-power facilities around the world, discuss lessons learned, and describe the future plans at SNS.

INTRODUCTION

Charge exchange injection (CEI) is important because it is the only way to achieve low-beam-loss multi-turn injection into a storage ring or synchrotron. Accelerators that do not use CEI for multi-turn injection lose about 10% of the beam due to injection inefficiency. This may not be a problem for low injected beam powers, but for today's high-power storage rings and synchrotrons it makes anything other than CEI infeasible. Additionally CEI allows the newly injected beam to be deposited inside the phase space of the circulating beam, thus reducing the final emittance. Without CEI, $\varepsilon_{TOTAL} > N * \varepsilon_{INJECTED}$, where N is the number of turns injected. With CEI, $\varepsilon_{TOTAL} << N * \varepsilon_{INJECTED}$.

The only practical way today to achieve CEI is by using stripper foils. Alternative technologies such as a flowing sheet of mercury, or gas jets, are only applicable in special cases. Laser stripping is a promising technology but it is not ready yet.

At the Oak Ridge Spallation Neutron Source the injected H^- beam power is 1.5 MW – more than a factor of 10 higher than any other H^- injection system. The SNS has a unique arrangement of stripper foils and bending magnets to mitigate the inevitable complications of high power injection. Overall the SNS CEI system works well, but we have encountered some surprises as we have been working to increase the beam power to the design value of 1.4 MW on target.

*ORNL is managed by UT-Battelle, LLC, under contract DE-AC05-00OR22725 for the U.S. Department of Energy. This research was supported by the DOE Office of Science, Basic Energy Science, Scientific User Facilities.

BRIEF HISTORY OF CEI

Multi-turn CEI was invented and first demonstrated at BINP in Novosibirsk in 1966 [1]. A 1 MeV H^- ion beam was first stripped to H^0 by a CO_2 gas jet, then drifted through one of the ring dipole magnets, then stripped to H^+ by a hydrogen gas jet. The first experiments with this technique were amazingly productive and innovative, and produced results that impacted both proton beam injection and high intensity proton beam dynamics for many years.

The first use of a stripper foil for CEI was at the ZGS Booster project at ANL in Argonne in 1972. The stripper foils were 36 x 100 mm^2 pieces of 35 μm-thick poly-paraxylene mounted to a disk rotating at 1800 rpm, with the rotation synched to the booster injection cycle such that the foil was only in the path of the beam during injection. It is ironic that the world's first stripper foil mechanism was also the most complicated – but it worked very well. The expected lifetime of these foils was just two hours – so even from the very first use of stripper foils lifetime was an issue. A graphical history of CEI beam powers around the world is shown in Fig. 1. The three highest H^- injected beam powers are for the Los Alamos PSR (80 – 100 kW), J-PARC RCS (133 MW design), and SNS (1.5 MW design).

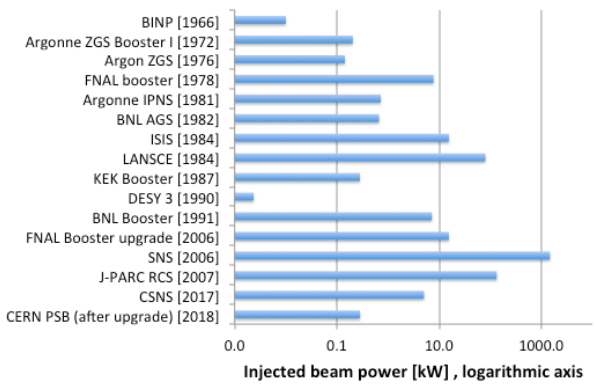

Figure 1: Summary of H^- beam powers used for CEI, from the first use of CEI to future facilities.

COMPLICATIONS OF CEI

Complications of CEI include 1) beam loss caused by foil scattering, 2) stripper foil lifetime, 3) control and disposal of un-stripped and partially stripped beam, 4) beam loss caused by H^0 excited states, 5) control of the stripped (convoy) electrons. The first three complications have been well addressed by other authors and so they will be only briefly mentioned here.

ISBN 978-3-95450-185-4

Beam Loss Caused by H^0 Excited States

When the H^- beam passes through the stripper foil, some of the beam emerging from the foil will be only partially stripped to H^0 particles if the foil is not thick enough to achieve 100% stripping efficiency. It is usually desirable to not have 100% efficiency because the foil would have to be so thick that it would cause excessive beam loss due to foil scattering, and because the foil might become too hot. Some of the H^0 particles will be in excited states (H^{0*}), with the electrons more loosely bound to the nucleus. The problem is that when these particles enter the magnetic fields of the storage ring or synchrotron the field is Lorentz-transformed to an electric field ($E = \gamma\beta B$) in the rest frame of the H^{0*} particles, and this E-field can cause the electrons to be stripped off. If this process occurs more than a few millimeters away from the stripper foil, the newly-created protons are likely to be outside the dynamic aperture of the ring, and they will be subsequently lost. If the beam power lost is more than a few Watts it can damage beam line components and cause excessive residual radiation. The excited state populations are distributed according to $n^{-2.8}$, where n is the principle quantum number of the H^0 state [2]. Figure 2 illustrates this process, and Fig. 3 shows the lifetimes of the excited states as a function of the electric field.

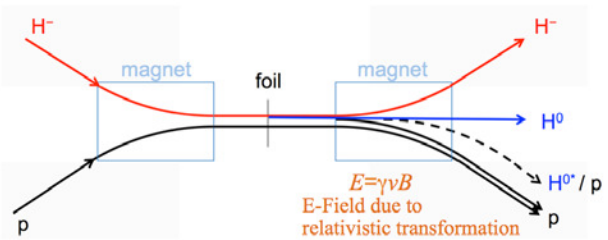

Figure 2: Illustration of H^{0*} states being created and then causing beam loss.

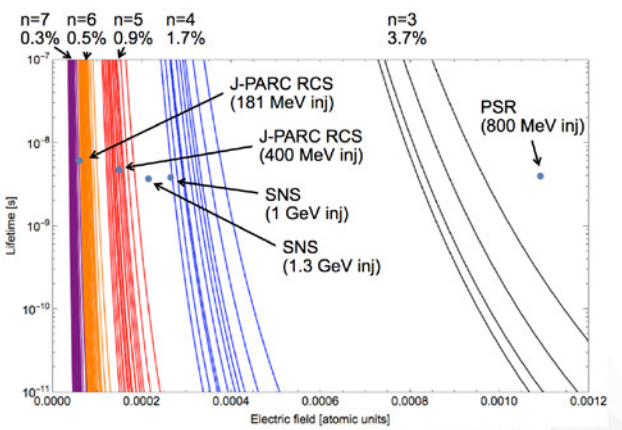

Figure 3: The H^0 excited state lifetimes vs. electric field, colored according to the principle quantum number n, with the relative populations also indicated. The operating points of today's highest power CEI injection systems are also indicated.

Beam loss caused by H^{0*} states was first discovered at the Los Alamos Proton Storage Ring [3]. Even after redesigning the PSR injection system beam loss due to H^{0*} states today still contributes 15 - 20% of the total beam loss (i.e. it causes 23 – 40 W beam loss), which is high enough to be barely tolerable. If the SNS did not take special measures to mitigate the H^{0*} beam loss we could expect about 2,300 W of loss, which is clearly intolerable.

Figure 3 illustrates the advantage of CEI at low beam energy. The J-PARC RCS is a nice example. Before the J-PARC linac was upgraded from 181 to 400 MeV, the only concern was H^{0*} states with $n > 6$, and after the upgrade the only concern is $n > 4$. Therefore only a small fraction of the H^{0*} states are susceptible to stripping. Low injection beam energy is a triple win because 1) the lower beam velocity leads to a smaller Lorentz transformation factor, 2) the B-fields are lower because the beam is less stiff, and 3) there is less power in the H^0 beam to start with. At J-PARC, even after the 400 MeV upgrade, the H^{0*} states cause less than 8 W of beam loss [4].

The SNS injection system was carefully designed to mitigate beam loss caused by H^{0*} states [5]. The key innovation [6] was to place the stripper foil inside one of the injection chicane magnets, as shown in Fig. 4. The field at the foil Lorentz transforms to an E-field high enough to immediately strip all the $n > 4$ states, and the following magnetic fields are, by design, too low to strip the $n < 5$ states. The net result is H^{0*} beam loss that is too low to accurately measure.

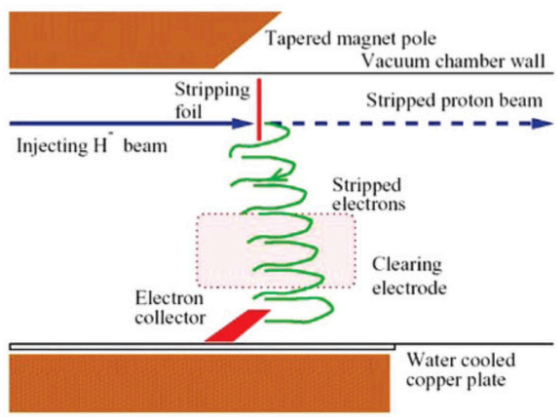

Figure 4: The SNS stripper foil inside one of the injection chicane magnets. Reproduced from ref [7].

Convoy Electrons

There are, however, some unintended consequences of placing the foil in a B-field. The most important one involves the convoy electrons stripped off the incoming H^- beam. At the design proton beam power of 1.4 MW on target, the convoy electrons carry 1.6 kW, and must therefore be carefully controlled. By design a water-cooled electron collector at the bottom of the vacuum chamber intercepts and traps these electrons, but in practice, due to a combination of fabrication errors and modifications to the injection point [8], the convoy electrons do not strike the electron collector at the optimum point. This results in

ISBN 978-3-95450-185-4

reflected convoy electrons (RCE), which are trapped by the magnetic field and can travel back up to strike the stripper foil, the stripper foil bracket, and the vacuum chamber [9]. The initial consequences of this were not realized [9,10] until the SNS beam power was increased to about 840 kW. At that time the solution was to redesign the stripper foil bracket, with the biggest modifications being a material change from Aluminum to titanium, and moving the foil 1 cm further out on the bracket arm.

This solution worked well until the beam power was increased to more than 1.2 MW proton power on target, when new issues were discovered with the electron collector and the stripper foil brackets. Figure 5 shows a stripper foil and bracket removed in July 2014, after being used for three months at beam powers of 1.1 to 1.4 MW, including ~20 days at 1.3 to 1.4 MW. The reflected convoy electrons heated the titanium enough to cause it to soften and sag, and there is also evidence of the titanium material being sputtered off.

Figure 5: An SNS stripper foil bracket showing damage due to reflected convoy electrons. Photo by Chris Luck.

The long term solution involves replacing the electron catcher and the associated vacuum vessel, but until this can be done we are testing a new type of bracket made of TZM (an alloy of 0.50% Titanium, 0.08% Zirconium and 0.02% Carbon with the balance Molybdenum). We chose this material after expanding our requirements to include 1) high sublimation temperature, 2) high sputtering threshold, and 3) low sputtering yield. The high sublimation temperature means the material can withstand higher operating temperatures. The high sputtering threshold means that the electrons striking the bracket must be very high energy before they can cause any sputtering, and the low sputtering yield means that in the event any sputtering does occur there will not be very much of it.

Of course there are also some drawbacks. TZM has a high density (10.2 g/cm^3) and high atomic numbers. It is therefore relatively heavy, which presents some difficulties for our stripper foil changer. The residual radioactivity will also be greater than for our light-weight, low-atomic-number titanium brackets.

Figure 6 shows a photograph of the TZM bracket that has seen our highest beam powers to date. It was used for about 16 days at 1.3 to 1.4 MW proton beam powers on target. There is almost zero damage to the bracket. We are now in the process of expanding our use of this bracket type, and we plan to install four of them this summer.

Figure 6: A TZM bracket used at 1.3 to 1.4 MW for about 16 days. Photograph by Chris Luck.

The electron catcher is also showing signs of damage due to convoy electron impact. It is made of carbon-carbon, and it showed very little signs of damage until we increased our beam powers to above about 1 MW on target. Figure 7 shows a photograph of the electron collector in 2012 (highest beam power before this photo was 1.08 MW). The electron collector comprises five undercut wedges. By design the convoy electrons should strike the undercut face of the middle wedge, such that any reflected electrons will be directed down on to another wedge, and also such that the low-energy secondary electrons will have very small gyro-radii and will consequently be trapped underneath the wedge.

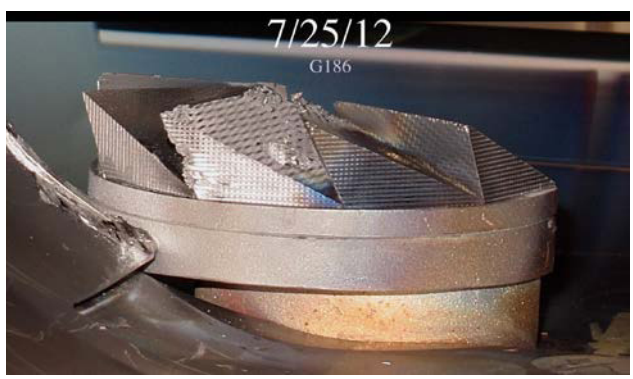

Figure 7: A photograph of the electron collector in 2012. Photograph by Chris Luck.

As we alluded earlier, due to a combination of fabrication errors and modifications to the injection point, the convoy electrons tend to strike center wedge on the top rather than the undercut face. This increases the probabil-

ISBN 978-3-95450-185-4

ity that reflected convoy electrons will travel back up into the vacuum chamber to cause problems.

Figures 8 and 9 show two more photographs of the electron collector taken in July 2015 and January 2016 2016. From these photographs it is evident that substantial damage occurred in just six months. During those months the beam power on target was typically in the 1.3 to 1.4 MW range.

Figure 8: The electron collector in July 2015. Photograph by Chris Luck.

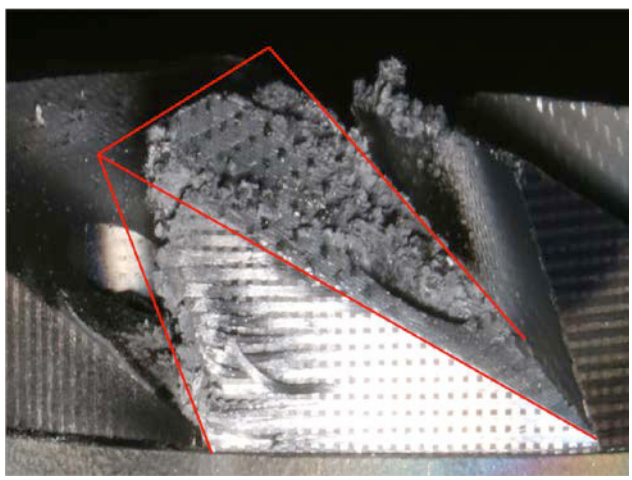

Figure 9: The electron collector in January 2016. The red lines show the approximate outline of the original undamaged wedge. Photograph by Chris Luck.

We are now in the process of redesigning the electron collector and the vacuum chamber that it sits in. The new vacuum chamber will have an additional view port to illuminate the stripper foil, and there will be provisions to allow the relative positions of the foil and the collector to be adjusted for optimum efficiency. The electron collector itself may also be redesigned to accommodate a wider range of convoy electron trajectories and to function with a higher electron power.

The SNS is the only accelerator that suffers from high convoy electron power. At the Los Alamos PSR the electron power at the primary stripper foil is 90 W, and no special accommodation was made for them during the design process. The electrons happen to strike the side of the vacuum chamber a short distance downstream of the foil, near the midline of the beam pipe, and they have created some discoloration in the pipe but there does not seem to be any other bad consequences. At the J-PARC RCS the convoy electrons carry a design power of about 145 W, they are directed to a water cooled block of graphite by the fringe field of the dipole magnet just upstream of the stripper foil, and this is working well.

Of course there are also the electrons stripped off by the secondary stripper foil (and tertiary foil at J-PARC). These foils strip any H^- beam that misses the primary foil, and any H^0 beam that does not get Lorentz-stripped as H^{0*} states. At PSR there is typically only ~2 W in these electrons, and at J-PARC there is just ~0.2 W. Their powers are too low to be of much concern. At SNS the power in the convoy electrons at the secondary stripper foil is about 64 W, which is high enough to be of concern. However, no special measures are taken to dump these electrons in a controlled location, and they have not caused any obvious problems to date. They probably strike the beam pipe a short distance downstream of the secondary foil after being deflected in the weak fringe field of the downstream chicane magnet.

SECOND TARGET STATION UPGRADE

The Second Target Station (STS) upgrade calls for increasing the beam energy to 1.3 GeV and increasing the beam power at the exit of the ring to 2.8 MW (the beam current also increases). These parameters will place additional demands on the ring injection section. The modifications for the injection section magnets are discussed in [11]. The convoy electron power will increase to ~3.2 kW at the primary stripper foil and ~130 W at the secondary stripper foil. This further increases the urgency of redesigning the primary electron collector to function with greater efficiency and also to be able to withstand higher power.

The STS design calls for carefully placing the secondary foil in the fringe field of the downstream chicane magnet. The field at the foil must be weak enough that the convoy electrons do not circle back and repeatedly pass through the foil. This could cause overheating of the foil in a manner similar to the charge-exchange extraction issues at TRIUMF [12]. Due to the limited space available for the chicane magnets in the upgraded design there is magnetic field overlap at the location of the secondary foil. Hence a few centimeters either upstream or downstream is enough to have a significant impact on the convoy electron trajectories at the secondary stripper foil.

The STS primary foil will have to be about 8% thicker to strip with the same efficiency at the higher beam energy. The optimum thickness of the nanocrystalline diamond foils in use today is ~0.38 mg/cm^2, so the new foils will be ~0.41 mg/cm^2. The operating temperature will therefore increase for two reasons – the higher beam current and the thicker foil. The higher beam energy is

ISBN 978-3-95450-185-4

actually a mitigating factor since the proton stopping power is about 5% less at 1.3 GeV compared to 1.0 GeV.

Based on finite element analysis simulations [13] we expect the maximum temperature of the hottest place on the stripper foil to increase by ~300 K. It is an open question about the impact of this temperature increase because absolute temperature simulations contain so many uncertainties (e.g. the effect of knock-on electrons, emissivity and specific heat at very high temperatures, the thermal parameters of nanocrystalline diamond vs. natural diamond, etc.). The relative temperatures are however more reliable. Figure 10 shows a plot of the sublimation rate for carbon as a function of temperature. Sublimation is the most important limiting factor for the SNS stripper foil lifetime. If the foil becomes too hot its thickness will decrease until it is too thin to achieve high stripping efficiency. The nominal STS stripper foil has an areal density of 0.41 mg/cm^2, corresponding to a physical thickness of ~1.3 μm. After a thickness decrease of about 10%, or ~0.13 μm, the stripping efficiency will drop off enough that the foil will need to be replaced. Our best estimates today predict a maximum foil temperature of ~1850 K, and the corresponding sublimation rate is ~0.001 μm/h, so the predicted lifetime is about 130 hours if the foil temperature is constant in time. However due to the 60 Hz pulse structure of the beam the temperature of the foil at the hottest location fluctuates by hundreds of degrees K.

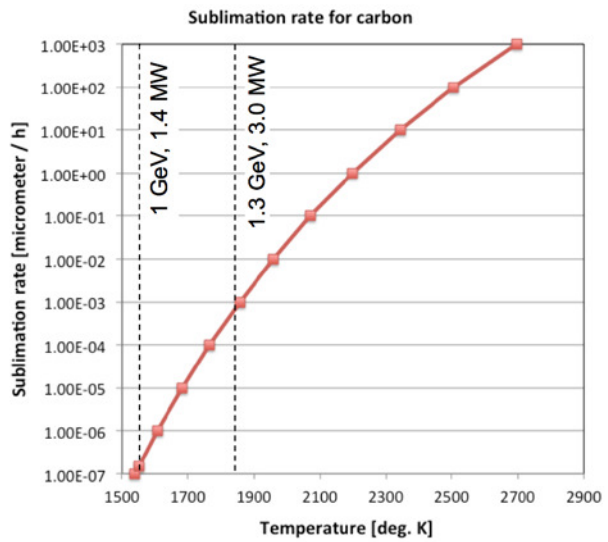

Figure 10: Sublimation rate for carbon as a function of temperature. Also indicated are the approximate expected foil temperatures at 1.0 GeV, 1.4 MW and 1.3 GeV, 3.0 MW beam parameters.

As shown in Fig. 10 the sublimation rate is a sharp function of temperature. A 100 K temperature change causes the sublimation rate to change by about one order of magnitude. We therefore expect that our STS stripper foils will last much longer than 130 hours. However we must keep in mind that this estimate has a large error bar.

To improve the accuracy of our simulations we are working to make an absolute temperature measurement of the stripper foils in use today, and then use the results to benchmark our simulations. Once this is done we will be able to confidently predict what the SNS-STS foil temperature will be.

SUMMARY

Multi-turn charge-exchange injection is a necessary and important component in today's storage rings and synchrotrons. CEI at high power has challenges with beam loss, stripper foil survival, and convoy electron damage. Today's accelerators have addressed these challenges, but complications continue to arise as beam powers are increased. The Second Target Station project at SNS will provide further interesting challenges.

REFERENCES

[1] G. I. Budker, G. I. Dimov, and V. G. Dudnikov, "Experiments on Producing Intensive Proton Beams by Means of the Method of Charge-Exchange Injection, Atomnaya Energiya, Vol. 22, No. 5, pp. 348-356, May 1967.

[2] M.S. Gulley et al., "Measurement of H^-, H^0, and H^+ yields produced by foil stripping of 800-MeV H^- ions," Phys. Rev. A53, pp. 3201-3210, May 1966.

[3] R. Hutson and R. Macek, "First Turn Losses in the LAMPF Proton Storage Ring (PSR)", Proceedings of PAC1993, Washington D.C., pp. 363-365.

[4] P.K. Saha et al., "Present Design and Calculation for the Injection-Dump Line of the RCS at J-PARC," Proceedings of 2005 Particle Accelerator Conference, Knoxville, Tennessee, pp. 3739 – 3741.

[5] J. Galambos, "Status of the SNS Injection System," Proceedings of EPAC98, Stockholm, pp. 341-343.

[6] A. Jason, B. Blind, P.J. Channel, and T-S.F. Wang, "Minimization of First-Turn Losses by Excited Neutrals in Charge-Changing Injection of Accumulator Rings," Proceedings of EPAC94, London, England, pp. 1219-1221.

[7] L. Wang et al., "Stripped electron collection at the Spallation Neutron Source," Phys. Rev. Accel. Beams 8, 094201 (2005).

[8] M. Plum, "SNS Injection and Extraction Systems - Issues and Solutions," Proceedings of HB2008, Nashville, TN, pp. 268-274.

[9] S. Cousineau, J. A. Holmes, M. A. Plum, and W. Lu, "Dynamics of uncaught foil-stripped electrons in the Oak Ridge Spallation Neutron Source accumulator ring," Phys. Rev. Accel. Beams 14, 064001 (2011).

[10] M. Plum et al., "Stripper foil failure modes and cures at the Oak Ridge Spallation Neutron Source," Phys. Rev. Accel. Beams 14, 030102 (2011).

[11] M.A. Plum et al., "Challenges for the SNS Ring Energy Upgrade," in Proceedings of IPAC2012, New Orleans, Louisiana, USA, pp. 520-522.

ISBN 978-3-95450-185-4

[12] Y.-N. Rao, R. Baartman, I. Bylinskii, V. Verzilov, "TRIUMF Extraction Foil Developments and Contamination Reduction," Proceedings of Cyclotrons2013, Vancouver, BC, Canada, pp. 269-271.

[13] Y. Takeda, private communication, "Thermal Simulations of Charge-Exchange Stripper Foils for High-Melting-Point Materials," Proceedings of IPAC2013, Shanghai, pp. 3312-3314.

ISBN 978-3-95450-185-4

AN EXPERIMENTAL PLAN FOR 400 MeV H⁻ STRIPPING TO PROTON BY USING ONLY LASERS IN THE J-PARC RCS

P.K. Saha*, H. Harada, S. Kato, M. Kinsho, J-PARC Center, KEK & JAEA, Japan
Y. Irie, I. Yamane, High Energy Accelerator Research Organization, KEK, Japan

Abstract

In the 3-GeV Rapid Cycling Synchrotron of Japan Proton Accelerator Research Complex, we are planning for a proof-of-principle experiment to demonstrate 400 MeV H⁻ stripping to proton by using only laser system. In order to avoid high magnetic field required in the process of laser-assisted H⁻ stripping, especially for lower H⁻ energies, we are studying the possibilities of using only laser system. The method is a three step process, same as the laser-assisted H⁻ stripping at the Spallation Neutron Source in Oak Ridge but lasers are used instead of high field magnets in the 1st step for an H⁻ conversion to H^0 and in the 3rd step for an excited H^0 (H^{0*}) conversion to a proton. A Nd:YAG laser, wavelength of 1064 nm can be properly used for both 1st and 3rd steps, where commercially available the most powerful excimer laser will be used for H^0 excitation (n=3) in the 2nd step. Although detail R&D studies are necessary to reach to the ultimate goal and needs to proceed step by step. A tentative schedule to carry out the experiment is set to be at the end of 2017. A detail of the present method and the expected outcome are presented in this paper.

INTRODUCTION

A stripper foil plays an important role for multi-turn H⁻ stripping injection in order to increase the beam current in the circular accelerators. Recently, beam power of 1 MW and above have successfully been achieved by such a conventional injection method [1, 2]. Although continuous efforts on durable foil production made remarkable progress on the foil lifetime [3], it is still unclear how to deal with multi-MW beam power. It may be hard to maintain a reliable and longer lifetime due to overheating of the foil and may be it is the most serious concern and a practical limitation to realize a multi-MW beam power. Other than foil lifetime, the residual activation near the stripper foil due to the foil scattering beam loss during multi-turn injection is also another uncontrollable factor and a serious issue for facility maintenance.

Figure 1 shows pictures of stripper foil before and after only 0.3 MW operation at 3-GeV RCS (Rapid Cycling Synchrotron) of J-PARC (Japan Proton Accelerator Research Organization). Although the foil was continuously used for nearly 5 months operation but the beam power was less than one third of the designed 1 MW. The total injected charge on the foil was nearly 1300 C and by taking into account the calculated average foil hits (10) of each injected proton, the total charge via foil was estimated to be 13000 C. Figure 2 shows a trend of the unstripped (missing) H⁻ due to the stripper foil deformation as shown in Fig. 1. Those missing H⁻ was further stripped to protons by one of the secondary foil but directed to the waste beam dump. The missing H⁻ was measured to be increased nearly 3 times higher than those in the beginning of the operation. Ideally the waste beam should be only 0.3%, which are all the single electron stripped H^0 but almost no missing H⁻. However, due the uncontrolled beam halos in the H⁻ beam, small vertical size of foil as well as beam positioning as close as to the horizontal edge of the foil in order to minimize circulating beam hitting the foil during multi-turn injection, there was about 0.2% missing H⁻ in the beginning. The missing H⁻ were reduced to about 0.1% by further tuning the H⁻ beam and adjusting the foil position as well. The operation of the machine even with such a foil deformation and missing H⁻

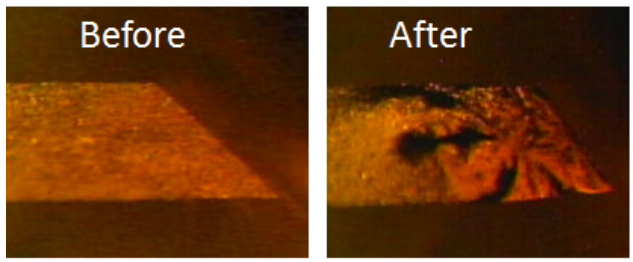

Figure 1: Stripper foil before and after operation with 0.3 MW beam power for about 5 months in the 3-GeV RCS of J-PARC. Deformation of the foil due to beam irradiation can easily be seen.

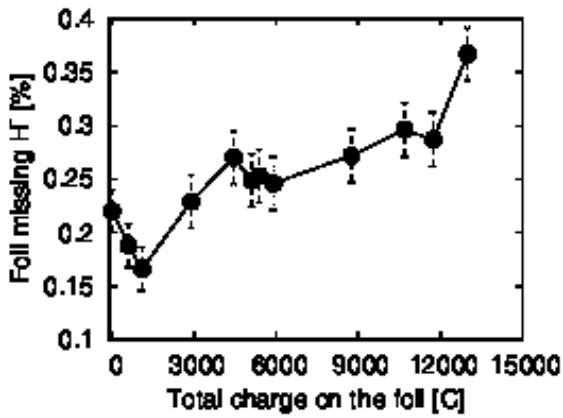

Figure 2: A trend of the stripper foil missing H⁻ measured at the waste beam dump. The missing H⁻ was increased nearly 3 times higher as compared to that in the beginning of the operation. At the designed operation even if a foil does not brake, the practical limitation of the foil lifetime may comes from the foil degradation.

* E-mail address: saha.pranab@j-parc.jp

ISBN 978-3-95450-185-4

was able continued because the beam power for the operation was less than one third of the designed 1 MW. It is thus highly concerned that at the designed operation even if a foil does not fail, the practical limitation of the foil lifetime may comes from the foil degradation due to such an increase of the H^- in the waste beam dump against the limited capacity of the beam dump.

A foil-less H^- charge exchange injection is thus very essential in order to ensure a stable operation of high intensity accelerators as well as to realize multi-MW beam power. As an alternate method other than using solid stripper foil, laser-assisted H^- stripping are studying for 1 GeV H^- beam at the SNS (Spallation Neutron Source) in Oak Ridge [4]. However, the method has a difficulty, especially at lower H^- energies due to extremely high magnetic fields are needed in addition to the laser. In order to overcome that difficulty, we are studying H^- stripping to protons by using only lasers. We are also planning for a proof-of-principle (POP) demonstration for the 400 MeV H^- beam in the 3-GeV RCS of J-PARC. A detail of the present method, experimental strategy, tentative schedule as well as an expected outcome are presented.

DIFFICULTIES OF LASER-ASSISTED H^- STRIPPING TO PROTON AT LOWER H^- ENERGIES

The laser-assisted H^- stripping to protons was originally proposed nearly two decades ago [5]. The method is a three-step process of magnetic stripping, laser excitation and magnetic stripping. The H^- is first converted to a neutral hydrogen atom (H^0) first by using Lorentz stripping in a strong magnetic field, the H^0 is excited (H^{0*}) by using laser from its ground state (n=1) to upper excited states (n≥3) and finally H^{0*} is converted proton by using Lorentz stripping in a strong magnetic field again. A little modified approach to reduce Doppler broadening in the second process of laser excitation was later proposed and also successfully demonstrated by a proof-of-principle (POP) experiment at the SNS, achieved 90% stripping efficiency for a short pulse of 6 ns, 900 MeV H^- [6, 7]. A more dedicated experiment was carried out recently to demonstrate 3 orders of magnitude improvement by increasing the H^- pulse length 5~10 μs [4, 8, 9].

In order to apply laser-assisted H^- stripping for the 400 MeV H^- beam in the RCS of J-PARC, we have also briefly studied the method recently [10]. We may achieve similar excitation probability of the H^0 by using nearly same laser beam power but the main difficulty is to achieve an extremely high magnetic field of more than 2 T required to utilize Lorentz stripping of the H^- and H^{0*} in the 1st and 3rd steps because of much lower H^- beam energy as compared to that of SNS. For 1 GeV SNS beam energy, the required magnetic field of 1.2 T and it was achieved for the test experimental purpose by using permanent magnets with an extremely smaller inner radius of only 1.5 cm [11]. In reality the circulating beam size is much bigger, where a typical beam size just after the injection process in the RCS as obtained in the simulation with no transverse painting injection but with full longitudinal painting to reduced the space charge effect is shown in Fig. 3. One needs a beam duct radius of nearly 6 cm at the injection point in order to avoid any uncontrolled beam losses at the injection region.

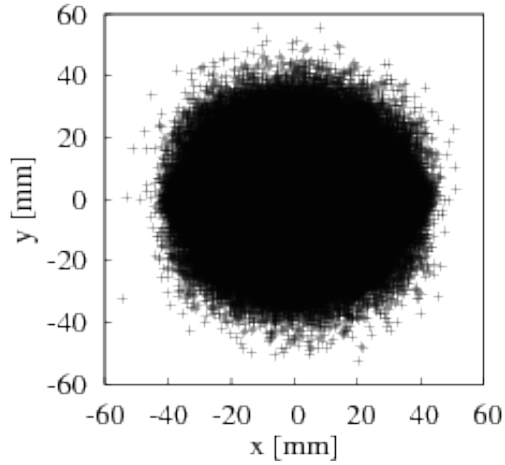

Figure 3: Circulating beam size at the end of injection period as obtained in the simulation for 1 MW beam power in the RCS of J-PARC. It may be very hard to achieve high magnetic field with an inner radius of the magnet nearly 6 cm in order to utilize needed Lorentz stripping of the H^- and H^{0*} for the 400 MeV H^- MeV in the process of laser-assisted H^- stripping.

NEW METHOD FOR H^- STRIPPING TO PROTONS BY USING ONLY LASERS

In order to overcome the difficulties of achieving high magnetic field required for the laser-assisted H^- stripping to protons, especially for H^- energy lower than 1 GeV, we proposed a new method where lasers can be used instead of any magnets. Figure 4 shows a schematic view of our newly proposed method for the H^- stripping to proton by using only lasers. The method in principle a three step process, similar to the previous one but magnetic stripping of H^- to H^0 and H^{0*} to proton in the 1st and 3rd steps, respectively are replaced by lasers. The widely available high power Nd:YAG lasers can be used for those purposes in order to utilized large photo-detachment and photoionization cross sections, in the former and later process, respectively. The principle in the middle or the 2nd step is exactly same as the previous method, where an H^0 atom from its ground state (1S) has to be excited to higher states up to n=3 (3p). The excited H^0 atom is denoted by H^{0*}. The excimer laser is one of the good choice for our case as the required laser wavelength has to be about 200 nm.

Optimum Laser Type and Their Wavelengths

We have to carefully choose the laser type and their parameters in order to obtain expected efficiency at each step. Due to the Doppler effect, laser wavelength, λ in particle laboratory frame (PLF) is shifted to λ_0 of the H^0 atom in

ISBN 978-3-95450-185-4

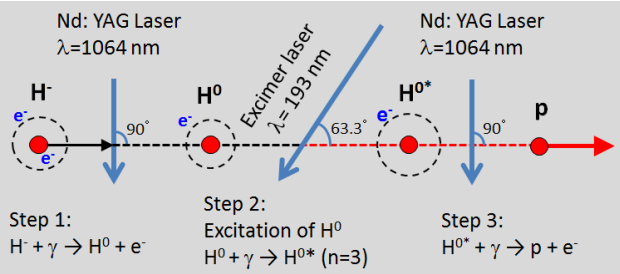

Figure 4: Schematic view of laser H^- stripping to proton by using only lasers. Noted parameters are typical ones for an H^- beam energy of 400 MeV.

the particle rest frame (PRF), given by

$$\lambda = \lambda_0(1 + \beta cos\alpha)\gamma \qquad (1)$$

where β and γ are relativistic parameters (0.713 and 1.4263, respectively for the 400 MeV H^-), α is the collision angle between laser and the beam in the laboratory frame. The advantage of using Nd:YAG lasers for the 1st and 3rd steps is that the direct high power IR (Infra red) laser beams can be used for those purposes. The laser beam angle to both H^- and H^{0*} are set to be 90 degrees in order to utilize the maximum photodetachment and photoionization cross sections given to around 750 nm of the laser wavelength in PRF [12]. The λ_0 by using Eqn. 1 is calculated to be 743 nm. The photon energy (E_{ph}) at this wavelength is calculated to be 1.67 eV, which is much higher than the binding energy (0.75 eV) of the loosely bound electron in the H^- as well as the ionization energy (1.5 eV) of and H^{0*} (n=3). However, the most difficult part is a sufficient excitation of the H^0 atom. The E_{ph} is as high as 12.1 eV for two level excitation of an H^0 atom, corresponds to a laser wavelength, λ_0 = 102 nm. The ArF excimer laser of 193 nm in the PLF can be a good choice for this purpose with an angle of 63.3 degree to the H^{0*} atom. A summary of the laser wavelengths and the corresponding laser types are given in Table 1.

Table 1: Required Laser Wavelengths and the Corresponding Laser Types

Process	E_{ph} (eV)	λ (nm)	α (deg.)	λ_0 (nm)	Laser
$H^- \rightarrow H^0$	1.67	1064	90	743	Nd:YAG
$H^0 \rightarrow H^{0*}$	12.1	193	63	102	ArF Excimer
$H^{0*} \rightarrow p$	1.67	1064	90	743	Nd:YAG

Required Laser Power for H⁻ Stripping

In this section we briefly described required laser power at each step for H^- stripping to protons. The H^- beam parameters for both longitudinal and transverse directions are very important in order to obtained higher stripping efficiency for a given laser beam power. The photodetachment cross sections, σ at 743 nm is about $4\times10^{-17}cm^2$ [12]. The saturation density, Φ^s in PRF given by E_{PH}/σ is calculated to be 6.7×10^{-3} J/cm^2. We consider relatively smaller H^- beam size in both longitudinal and transverse directions. For example, rms bunch length σ_L is 30 psec, while transverse beam radius is about 1 mm. The collision time, τ_i is then calculated to be about 10 psec. The laser pulse length, τ_l should be 40 psec at minimum. The laser energy then calculated by the expression given by

$$E_{laser} = (\Phi^s/\gamma(1 + \beta cos\alpha)) \times (\pi r^2) \times (\tau_l/\tau_i) \qquad (2)$$

where, laser pulse angle α to the H^- beam is 90 degree. The required laser energy E_{laser} is estimated to 0.6 mJ, corresponding to a laser peak power of about 15 MW. As the ionization cross section of H^{0*} to proton is nearly half of that photodetachment of H^- to H^0, the laser pulse energy in the 3rd step is thus required to be about 1.2 mJ.

The required peak power of the laser for an H^0 excitation up to n=3 state is given to be 1 MW in Danilov's paper for 1 GeV H^- beam [6, 7]. The same estimation for our 400 MeV H^- beam requires nearly twice higher laser peak power due to difference of the relativistic parameters, β and γ have to be taken into account in the estimation. The ArF excimer lasers commercially available these days by GAM LASER INC can provide 150 mJ energy with a typical pulse length 20 ns [13]. As long as we consider very short H^- pulse of 30 psec, such a laser can be a good choice for sufficient excitation of the H^0.

SCHEDULE AND SETUP FOR POP H⁻ LASER STRIPPING EXPERIMENT

Although a detail schedule for the POP experiment has not yet been fixed, the earliest chance is considered to be at the end of 2017. All equipment for the experiment are planned to installed by the end of 3 months long facility maintenance period starting from July, 2017.

We will use 400 MeV H^- beam from J-PARC Linac [1], where H^- beam and laser interaction point (IP) is fixed to be at the end of the straight section in the L-3BT (Linac to 3-GeV beam transport). Figure 5 shows a schematic view of the end section of J-PARC Linac and the place of the POP experiment is shown by a red rectangular box. Downstream of the IP, there are 3 branches of beam transports, where three charge fractions can be simultaneously measured as depicted in the figure. Any remaining H^0 we have to strip further to protons in order to measure it at the 90 degree beam dump.

Figure 6 shows a schematic view of the experimental setup. In stead of 3 lasers as shown in Fig. 4, we may use 2 lasers in this setup. The radius of H^- beam pipe should be smaller in that case in order to confirm the overlap of the laser pulse guided by mirrors to the 3rd step. The allowed path length of the laser pulse is 1.4 times longer than the H^0 one due their velocity difference. The beam pipe radius at IP is comparatively large and may not satisfy the above setup but we can construct an appropriate beam pipe and temporarily connect for the experiment.

ISBN 978-3-95450-185-4

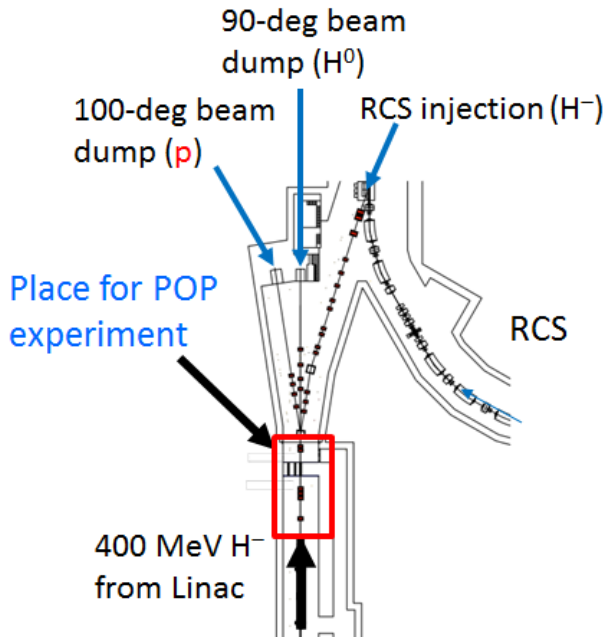

Figure 5: A schematic view of the end section of J-PARC Linac named L-3BT. The H^- laser stripping POP experimental setup has to be placed in the region indicated by the red rectangular box. We can simultaneously measure all three charge fractions in the downstream. Namely, fully stripped protons, neutral H^0 (by further stripping) and the unstripped H^- can be measured in the 100-degree, 90-degree and the RCS injection point, respectively.

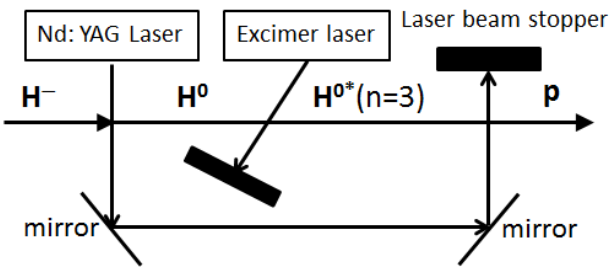

Figure 6: A schematic view of the setup for the POP experiment. One Nd:YAG laser can be efficiently used for an H^- stripping to H^0 and H^{0*} to proton through laser beam transportation by optical mirrors. The excimer laser will be used for the H^0 excitation.

Optimization of H^- Beam Parameters

Optimization of the H^- beam parameters are very important in order to achieve efficient overlapping with the laser pulse. Figures 7 and 8 show simulation results of the longitudinal bunch length and the dispersion function along the Linac. The bunch length at the IP with a lower peak current can be achieved less then 30 psec as compared to that 5 times longer in the normal operation. The dispersion derivative (D') plays an important role in order to minimize the laser

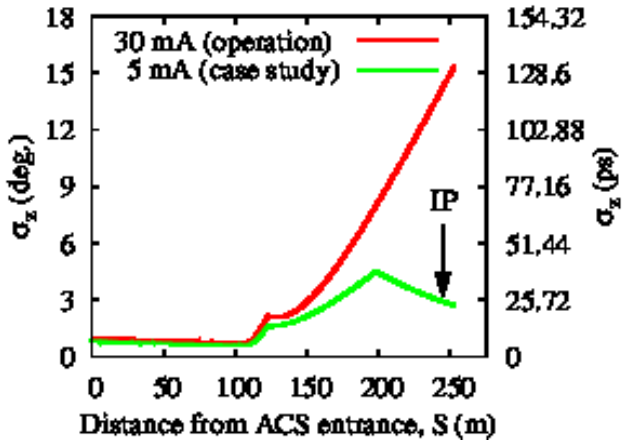

Figure 7: Simulation results of 400 MeV longitudinal H^- beam size in the J-PARC Linac. The longitudinal bunch length can be reduced to less than 30 psec as desired for the POP experiment.

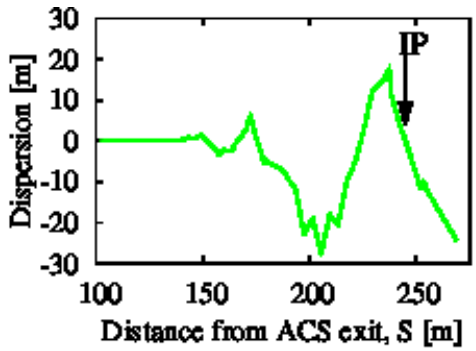

Figure 8: Calculated dispersion function as a function of the distance in the Linac starting from the end of ACS section. A dispersion derivative of required -1.3 can be achieved at the IP.

power [6, 7], where D' has to satisfy the condition given by

$$D' = -(\beta + cos\alpha)/sin\alpha \quad (3)$$

The D' has to be -1.3 for the 400 MeV H^- beam, which can be easily achieveable as shown in Fig. 8.

AVAILABLE LASERS FOR THE POP EXPERIMENT AND EXPECTED RESULTS

The primary motivation of the POP experiment is to demonstrate the feasibility of the present method for an H^- stripping to proton by using only lasers. We focus only a single micro pulse of the 400 MeV H^- beam which has a frequency of 324 MHz having a typical pulse length of 30 psec. The Nd:YAG laser used for 400 MeV H^- photodetachment studies in J-PARC has an energy as high as 1.6 J with a pulse length of around 20 ns [14, 15]. We can efficiently use that laser for the 1st and 3rd steps as demonstrated in Fig. 6. We will use 193 nm ArF excimer laser of the EX350A type with a specification as mentioned earlier. As for the measurement, we have several types of CTs (current transformers) and also

ISBN 978-3-95450-185-4

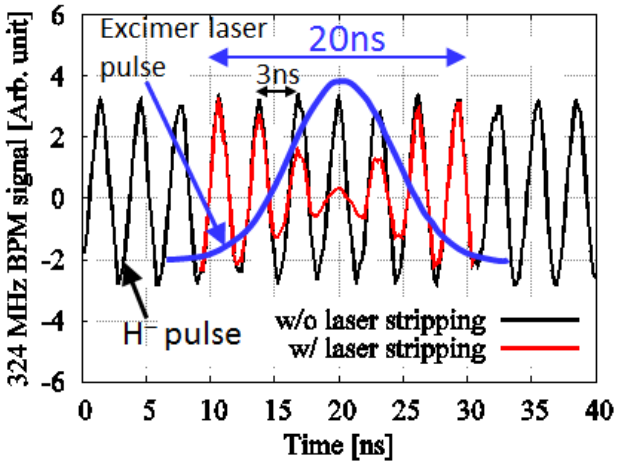

Figure 9: A typical 324 MHz H⁻ micro pulse structure measured by BPM pickup (black). The blue curve is a given laser pulse by which the H⁻ is expected to to protons as shown by the red curve.

BPMs (beam position monitors) capable of measuring each 324 MHz micro pulse. Figure 9 shows such a typical signal of a BPM pickup (black) measured for the H⁻ beam. If we assume a Gaussian laser pulse like the blue curve, we expect the original H⁻ will be stripped protons as shown by the red curve. Here we assume a 90% overlapping efficiency at the peak of the laser pulse.

The reason why we focus only on a single micro pulse in the POP experiment is that in the practical application we can utilize a laser optical resonator ring [6] which we called laser storage ring in order to cover all micro pulses during 0.5 ms injection time. The seed lasers should at least be capable of running at least 25 Hz. The laser pulse will be injected into the laser storage ring of 324 MHz, where laser pumping has to be done in order to recover the laser energy loss during multiple transmissions through optical devices in the ring. We have also already started detail R&D studies of the laser storage ring, which is may be the most difficult part in order to realize practical application H⁻ laser stripping to protons.

SUMMARY

In order to realize laser stripping of H⁻ to proton at lower energies, we proposed a method by using only laser system in order to overcome the difficulty with high magnetic fields which utilize Lorentz stripping of H⁻ to H^0 at the 1st step and H^{0*} to proton at the 3rd step. Instead, we will utilize large photodetachment and photoionization cross sections for the same purposes in the 1st and 3rd steps, respectively.

We plan a proof-of-principle demonstration experiment at the end of 2017 for a 400 MeV H⁻ beam in J-PARC. We will efficiently use one Nd:YAG laser for both 1st and 3rd steps, while an excimer laser for H^0 excitation up to n=3 state in the 2nd step. We expect a 90% stripping efficiency for at least a single micro pulse of the H⁻ beam of about 30 psec, which has a frequency of 324 MHz. The practical application of H⁻ laser stripping for the total injection period of 0.5 ms depends on the successful utilization of the laser storage ring.

ACKNOWLEDGEMENT

The authors would like to acknowledge many of our J-PARC colleagues for continuous support and cooperation on the present studies as well as concerning our future plan. It is also our opportunity to acknowledge Dr. S. Cousineau, T. Gorlov and Y. Liu of SNS for many fruitful discussion, suggestions and sharing ideas on this challenging topic.

REFERENCES

[1] High-intensity Proton Accelerator Project Team, "Accelerator Technical Design Report for J-PARC", JAERI-Tech 2003-044 and KEK Report 2002-13.

[2] J. Wei *et al.*, *Phys. Rev. ST Accel. Beams* 3, 080101 (2000).

[3] I. Sugai *et al.*, *Nucl. Ins. and Meth.* A 590, 16 (2006).

[4] S. Cousineau *et al.*, "Status of Preparations for a 10 μs H⁻ Laser-Assisted Stripping Experiment", in *Proc. of HB'14*, East-Lansing, MI, USA, 299, paper WEO3AB02, p.209.

[5] Isao. Yamane, *Phys. Rev. ST Accel. Beams* 1, 053501 (1998).

[6] V. Danilov *et al.*, *Phys. Rev. ST Accel. Beams* 6, 053501 (2003).

[7] V. Danilov *et al.*, *Phys. Rev. ST Accel. Beams* 10, 053501 (2007).

[8] T. Gorlov *et al.*, "H⁻ Beam Optics for the Laser Stripping Project", in *Proc. of HB'14*, East-Lansing, MI, USA, paper THO2LR01, p.350.

[9] S. Cousineau *et al.*, presented at HB'16, Malmö, Sweden, paper MOAM4P40, this conference.

[10] P.K. Saha *et al.*, "Preliminary Studies of Laser-assisted H⁻ Stripping at 400 MeV", in *Proc. of IPAC'15*, Richmond, VA, USA, paper THPF043, p. 3795 (2015).

[11] A. Aleksandrov *et al.*, "Magnet Design for the SNS Laser Stripping Experiment", in *Proc. of IPAC'14*, Dresden, Germany, paper TUPRO117, p. 1328 (2014).

[12] L. M. BRANSCOMB, "Physics of the One-And-Two-Electron Atoms", edited by F. Bopp and H. Kleinpoppen, North-Holland, (1968).

[13] GAM LASER INC. `http://www.gamlaser.com/EX350laser.htm`

[14] S. Meigo, *J. of Nucl. Mat.*, 450, 8, (2014).

[15] H. Takei, Private communication.

ISBN 978-3-95450-185-4

BEAM DYNAMICS CHALLENGES IN THE ESS LINAC

Yngve Inntjore Levinsen, M. Eshraqi, R. Miyamoto, M. Munoz, A. Ponton, R. De Prisco
European Spallation Source (ESS), Lund, Sweden

Abstract

The European Spallation Source (ESS) will be the world's brightest neutron source. It will be driven by a 5 MW proton linac that delivers a 2.86 ms pulse at 14 Hz, which means the peak beam power is 125 MW. This requires a careful design of the lattice structures, in order to allow for safe and reliable operation of the accelerator. We will discuss some of the design choices and some of the particular challenges that were faced during the design of the ESS lattice.

INTRODUCTION

The European Spallation Source ERIC project is already well into the construction phase [1], with an expected first beam on target in mid 2019. The long pulse spallation source is the first of its kind. The linear accelerator (linac) will provide an unprecedented proton beam power of 5 MW, with a proton beam current of 62.5 mA and a 2 GeV beam energy on target with a duty factor of 4 %. The linac is superconducting which allows for the long pulse length of 2.86 ms, and a 14 Hz pulse repetition rate.

The different sections of the ESS linac are listed in Table 1, and shown in Fig. 1. The normal conducting front-end consists of a ~2.5 m long LEBT after the ion source, followed by a ~4.55 m long 4-vane RFQ, a ~3.8 m long MEBT and 5 DTL tanks totalling ~39 m in length. There are three superconducting sections, first 13 spoke modules at the same radiofrequency as the normal conducting front-end of 352.21 MHz, then elliptical cavities at double the frequency. The two elliptical sections are called medium-β and high-β. A contingency space of 15 periods is left in for future upgrades. The total length of the accelerator including the transfer line is about 600 m.

Table 1: The Overview of the Different Sections of the ESS Linac

	Energy [MeV]	# modules	cav./mod. (Cells)	Length [m]
Source	0.075	-	0	-
LEBT	0.075	-	0	2.4
RFQ	3.65	1	1	4.6
MEBT	3.65	-	3	3.8
DTL	90.0	5	-	39
Spokes	216	13	2	56
Med.-β	571	9	4(6C)	77
High-β	2000	21	4(5C)	179
HEBT	2000	-	-	241

From a beam dynamics perspective, the main challenges associated with building such a high power linac are resulting from the high beam current. The result is strong space-charge forces which is challenging to accurately model and design for, and the low loss requirement of only 1 W/m means that an excellent control of the beam halo is required. Further, there is a high number of RF components that needs phase and amplitude corrections with beam. Due to the tight loss tolerances and need for high availability and reliability, there are tight requirements for dynamic errors of the RF phase and amplitude (with respect to the beam).

The design of the ESS lattice has been discussed in several earlier papers [1–6], including studies of the beam dynamics in individual sections as well as integrated studies [7, 8]. The design has undergone several changes since the TDR was released in 2012 [9]. The most significant change is that the beam energy has been reduced from 2.5 GeV to 2.0 GeV, while the beam current has been increased from 50 mA to 62.5 mA to keep the same 5 MW proton beam power at the target. The reduced space for accelerating structures has been converted to contingency space, so that the full upgrade to 3.5 GeV is still possible.

NORMAL CONDUCTING LINAC FRONT-END

The ion source is a microwave discharge ion source [10]. The source is designed to be able to provide a maximum of about 80 mA of proton beam current, with a pulse length flattop of up to 3 ms. The source voltage is 75 kV. The design choice is based on having a reliable high-current source with a long mean time between failures (MTBF). This is essential given the high reliability demands of a facility like ESS. The reliability of the ion source is expected to be very close to 100 %.

The low energy beam transport (LEBT) following the ion source consists of two solenoids of 330 mm length to focus the DC beam pulse, as well as a chopper and diagnostics to characterise the beam. The chopped beam is dumped on a cone aperture just before the RFQ entrance. A space-charge compensation of around 95 % is needed in order to meet the nominal performance.

The radio-frequency quadrupole (RFQ) is a 4-vane type with a length of 4.55 m. The RFQ is shown in simulations to have a very good beam capture, providing above 95 % of beam transmission through the structure under the assumption of a good space-charge compensation in the LEBT. The requirement is that at least 90 % of the beam should be transmitted through the RFQ. At the RFQ exit the beam energy has reached 3.62 MeV.

Between the RFQ and the drift tube linac (DTL), a matching is needed. This is done by the medium energy beam transport (MEBT), consisting of 11 quadrupoles and 3 RF buncher cavities. Additionally the head of the pulse coming from the LEBT will be degraded because there is a time

ISBN 978-3-95450-185-4

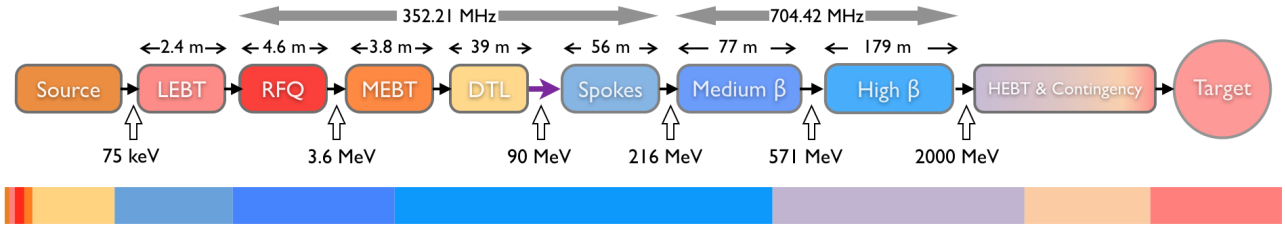

Figure 1: The layout of the ESS accelerator complex. The relative length of the sections are shown in the colour graph below. Superconducting sections are shown in shades of blue.

delay before the space-charge stabilises, so a chopper is installed in the MEBT to chop off the head and also the tail of the bunch with a faster rise time than the LEBT chopper. One steerer per quadrupole is available to correct the beam trajectory, and finally there is a selection of beam instrumentation to sufficiently characterise the beam coming out of the RFQ and assure we can do a proper matching into the DTL.

The ESS DTL consists of 5 tanks, accelerating the beam from 3.62 MeV to around 90 MeV. Permanent magnet quadrupoles (PMQ) in every second drift tube provide the transverse focusing. Steerers and BPMs are spread out in some of the empty drift tubes to correct and measure the trajectory. The BPMs are also used to measure the timing/phase of the beam, in order to correct the acceleration through the tanks. In between each tank there is a beam current monitor (BCT), and a Faraday cup is currently planned after tank 2 and 4. The first and foremost challenge in the DTL is to get a good beam transmission through the tanks, in particular in tank 1 where there is close to 0 transmission for non-ideal RF phases and amplitudes. Secondly it is important to steer the beam properly and provide a good quality beam towards the superconducting linac that follows.

SUPERCONDUCTING SECTIONS

The ESS linac consists of three families of superconducting cavities. The first are the double-spoke cavities, of which there are 13 pairs. The DTL and the spokes are separated by a low energy differential pumping section (LEDP). These cavities do not have as high accelerating gradient as the elliptical cavities, but allow for greater flexibility as the cavities can be retuned for different energies. That means we can retune the machine when a cavity is down with more ease, increasing reliability and availability of the machine.

In the rest of the ESS linac, the beam is accelerated by superconducting elliptical cavities. These cavities have a larger radial aperture and allow for a higher accelerating gradient, which is essential to reach the final target beam energy of 2 GeV within the approximately 350 m of acceleration structures. There are two families of elliptical accelerating cavities planned, with a contingency area following. The first structures are called medium-β, accelerating the beam from 216 MeV to about 571 MeV through 9 cryomodules of 4 six-cell cavities. After we have the high-β cavities which brings the energy to the nominal beam energy. The five-cell high-β cavities are almost the same length as the six-cell medium-β cavities, which allows the cryomodule to be the same length for both cavity types. We have 21 high-β cryomodules of 4 five-cell cavities in the ESS linac.

Each cryomodule houses a string of 2 (4) cavities in spoke (elliptical) sections. Each two ESS cryomodules are separated by what is called a linac warm unit (LWU). The LWU is composed of a quadrupole pair providing transversal focusing, a dual plane corrector, a dual plane BPM, as well as a central slot where there is space for beam diagnostics. The beam diagnostics in the linac is described in more detail in [11].

There is a trade off between lowering and increasing the RF frequency in superconducting structures. Lower frequencies are favoured due to looser tolerances in manufacturing cavity components. Lower frequencies also have the advantage of reducing RF losses in superconducting cavities, and ameliorating higher order mode (HOM) effects from the high-current beams. Higher frequencies are encouraged by the desire to keep the size of the superconducting cavities small, making them easier to handle and reducing manufacturing costs. The cryogenic envelope and power consumption are also reduced at higher frequencies [9].

The elliptical cavities run at twice the frequency of the upstream linac, 704.42 MHz. This frequency jump unfortunately provides a longitudinally unstable cross-over between the spoke cavities and the medium-β cavities, as will be shown later in this paper. The losses from this frequency jump are visible in the downstream linac until the dogleg.

In Fig. 2 we show the accelerating fields of the three families of superconducting RF cavities. The spoke cavity modules are shorter and provide lower accelerating gradient. We also see that the medium-β modules consist of 6 cells while the high-β modules consist of 5 cells at almost the same length.

LOSS DISTRIBUTIONS

For the ESS lattice it is important to have excellent knowledge of the expected loss levels in the machine. The machine will deliver 5 MW proton beam power, while the losses are required to stay below 1 W/m for the entire linac. That means that the relative amount of losses that can be accepted are on the order of 10^{-4}-10^{-7} per metre, depending on the beam energy where the losses happen.

Losses are seldom distributed evenly. Certain weaknesses in the lattice might produce more losses, or the misalign-

ISBN 978-3-95450-185-4

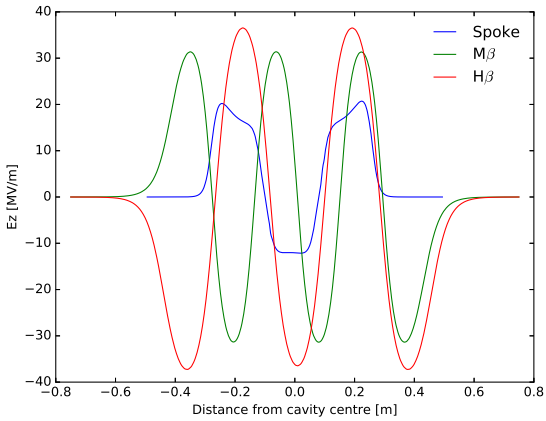

Figure 2: Comparison of the accelerating field in the three families of superconducting cavities. The double-spoke cavities shown in blue are followed by medium- and high-β cavities shown in green and red respectively.

ments are more unfavourable in certain regions. It is somewhat easier to predict loss distributions from a lattice than it is to predict the quantitative levels. There are also usually measures that may be taken until quantitative levels are mitigated, such as e.g. reducing the beam current.

We are here presenting a study of 20 000 machines with 600 000 macro-particles in each machine. For each machine we have applied the nominal tolerances for static and dynamic imperfections as have been defined earlier [7, 8]. In this study we have doubled the dynamic RF amplitude and phase jitters, in order to provoke more losses for the beam loss and activation studies. In the simulation we are therefore quoting the loss levels in arbitrary units, as a normalisation would represent losses that are significantly higher than what is actually expected in the machine. The increased dynamic error used does not change the distribution of losses significantly which makes this a useful way to improve statistics. Simulations are done from the exit of the RFQ until the beam reaches the target.

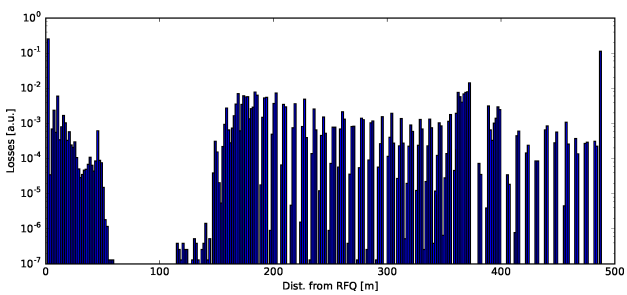

Figure 3: The distribution of losses along the ESS linac. The loss count is proportional to the number of particles lost. The last peak is in the dogleg. Losses in the last 10 m before target is excluded from the figure.

In Fig. 3 we show the losses along the linac, where the count is equal to the number of particles lost (i.e. no weight on the energy of the lost particles). We see a dense distribution of losses in the warm linac, a very clean spoke region and then losses from the medium-β onwards. The last peak at around 480 m is the beginning of the dogleg, where the off momentum particles are over steered into beam pipe.

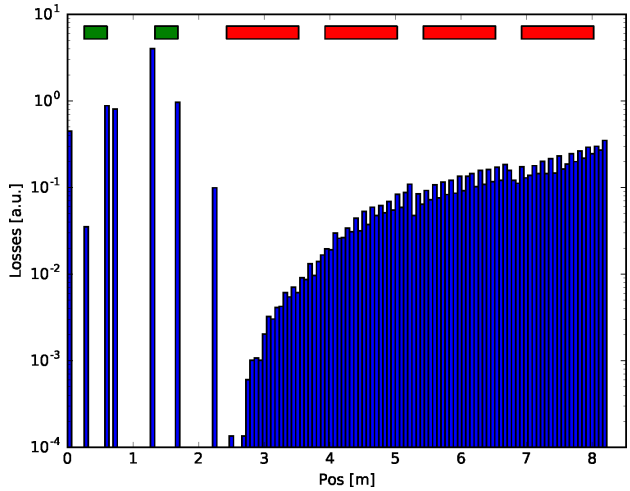

Figure 4: The distribution of the losses in a medium-β period. The LWU is contained in the first two metres, and the cryomodule in the next 6.5 m. The simulation has used a simplified aperture model where the LWU has 50 mm aperture and the cryomodule 60 mm aperture. Quadrupoles are marked in green, and cavities in red boxes.

There is an interesting regularity in the losses in the superconducting region which is shown better in Fig. 4. Here we show the loss distributions in each period of the medium-β overlapped. We see that the majority of the losses are in the warm linac (first 2 m of the figure), but there is a non-negligible amount of losses also inside the cryomodule. The relative amount of losses in the cryomodule may reduce with a more realistic aperture model, and would then be expected to be lost in the beginning of the downstream LWU.

In Fig. 5 the energy distribution of the losses in the medium-β and start of high-β is shown. We see here that there are very few losses being initiated from the normal conducting linac and the spoke section. The majority of losses have an energy equal to the medium-β input energy of 216 MeV or more. This is expected to originate from the challenging frequency jump between the spoke and medium-β section. We further note that there are almost no losses from the second half of the region these data are taken from, indicating that these are slow (longitudinal) losses.

In Fig. 6 the similar distribution is shown for the dogleg. Here the beam energy is 2 GeV, and we see that the dispersive region of the dogleg is cleaning some of the halo which is far from the reference beam energy. Also here we see losses from the frequency jump, with a logarithmically decaying number of particle lost as a function of particle energy.

ISBN 978-3-95450-185-4

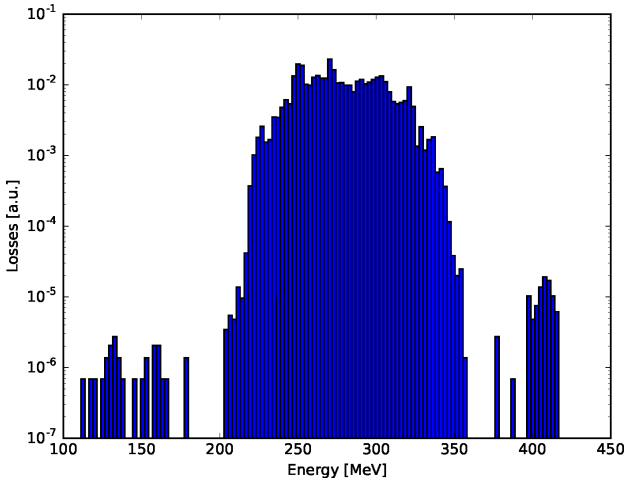

Figure 5: The energy distribution of the particles lost from the start of the medium-β and a few periods into the high-β section. Almost no losses from the upstream linac are seen.

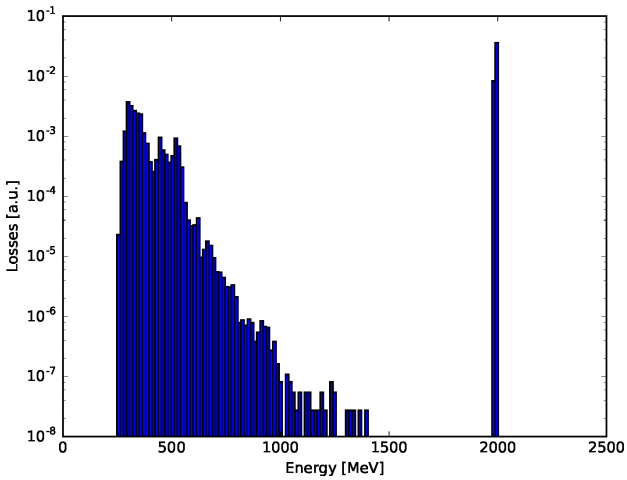

Figure 6: The energy distribution of losses in the dogleg region.

SUMMARY

The primary beam dynamics challenges of the ESS linac are following from the requirements of very low halo production and low fractional losses, in combination with a high current beam that produce strong space-charge forces in particular in the low energy front-end. Each section has been carefully designed and optimised with this in mind. In this paper we have discussed in more details the challenging frequency jump between the spokes and the medium-β sections, and shown that a significant part of the remaining simulated losses in the high energy part of the linac originates from this location.

REFERENCES

[1] M. Lindroos et al. 'ESS Progressing into Construction'. In: *IPAC'16, Busan, South Korea*. June 2016. DOI: 10.18429/JACoW-IPAC2016-FRYAA02.

[2] M. Lindroos et al. 'The European Spallation Source'. In: *Nuclear Instruments and Methods in Physics Research Section B: Beam Interactions with Materials and Atoms* 269.24 (Dec. 2011), pp. 3258–3260. ISSN: 0168583X. DOI: 10.1016/j.nimb.2011.04.012.

[3] R. Miyamoto et al. 'Beam Physics Design of the ESS Medium Energy Beam Transport'. In: *IPAC'14 Dresden, Germany*. 2014. DOI: 10.18429/JACoW-IPAC2014-THPME045.

[4] A. Ponton et al. 'ESS Normal Conducting Linac Status and Plans'. In: *LINAC'14, Switzerland*. 2014. http://jacow.org/linac2014/papers/thpp044.pdf

[5] Y. I. Levinsen et al. 'European Spallation Source Lattice Design Status'. In: *IPAC'15, Richmond, USA*. June 2015. DOI: 10.18429/JACoW-IPAC2015-THPF092.

[6] M. Eshraqi et al. 'ESS Linac Beam Physics Design Update'. In: *IPAC'16, Busan, South Korea*. 2016. DOI: 10.18429/JACoW-IPAC2016-MOPOY045.

[7] M. Eshraqi et al. *End to End Beam Dynamics of the ESS Linac*. 2012. https://cds.cern.ch/record/1558345

[8] M. Eshraqi et al. 'Statistical Error Studies in the ESS Linac'. In: *IPAC'14 Dresden, Germany*. 2014. DOI: 10.18429/JACoW-IPAC2014-THPME044.

[9] *ESS Technical Design Report*. 27th June 2013. http://docdb01.esss.lu.se/cgi-bin/public/DocDB/ShowDocument?docid=274

[10] L. Neri et al. 'Improved design of proton source and low energy beam transport line for European Spallation Source'. In: *Review of Scientific Instruments* 85.2 (1st Feb. 2014), 02A723. ISSN: 0034-6748, 1089-7623. DOI: 10.1063/1.4832135.

[11] A. Jansson, M. Eshraqi and S. Molloy. 'Beam Diagnostics for ESS Commissioning and Early Operation'. In: *IPAC'16, Busan, South Korea*. June 2016. DOI: 10.18429/JACoW-IPAC2016-MOPMR020.

ISBN 978-3-95450-185-4

HIGH CURRENT URANIUM BEAM MEASUREMENTS AT GSI-UNILAC FOR FAIR

W. Barth[1,2], A. Adonin[1], Ch. E. Düllmann[1,2,3], M. Heilmann[1], R. Hollinger[1], E. Jäger[1], O. Kester[1], J. Khuyagbaatar[1,2], J. Krier[1], E. Plechov[1], P. Scharrer[1,2,3], W. Vinzenz[1], H. Vormann[1], A. Yakushev[1,2], S. Yaramyshev[1]

[1] GSI Helmholtzzentrum für Schwerionenforschung, Darmstadt, Germany
[2] Helmholtz Institut Mainz, Germany
[3] Johannes Gutenberg-Universität Mainz, Germany

Abstract

In the context of an advanced machine investigation program supporting the ongoing UNILAC (Universal Linear Accelerator) upgrade program, a new uranium beam intensity record (≈10 emA, U^{29+}) at very high beam brilliance was achieved last year in a machine experiment campaign at GSI. The UNILAC as well as the heavy ion synchrotron SIS18 will serve as a high current heavy ion injector for the new FAIR (Facility for Antiproton and Ion Research) synchrotron SIS100. Results of the accomplished high current uranium beam measurements applying a newly developed pulsed hydrogen gas stripper (at 1.4 MeV/u) will be presented. The paper will focus on the evaluation and analysis of the measured beam brilliance and further implications to fulfil the FAIR heavy ion high intensity beam requirements.

INTRODUCTION

Meeting the FAIR science requirements [1] higher beam intensities have to be achieved in the present GSI-accelerator complex, through faster cycling and, for heavy ions, lower charge state which enters quadratically into the space charge limit (SCL). The desired beam energy of up to 1.5 GeV/u for radioactive beam production will be delivered by the synchrotron SIS100. Recently GSI put effort into increasing the uranium beam intensity delivered to the SIS18. An advanced machine investigation program for the UNILAC is aimed at meeting the FAIR requirements. For uranium (FAIR reference ion) the UNILAC has to deliver at least 3.3×10^{11} U^{28+}-particles during 100 µs.

In the High Current Injector (HSI) comprising an IH-RFQ and an IH-DTL, the beam is accelerated up to 1.4 MeV/u. In the gas stripper section the initial charge state (4+) is increased; an uranium beam (28+ or higher charge state) is matched to the Alvarez DTL. After acceleration up to the final UNILAC-beam energy of 11.4 MeV/u the transfer line (TK) to the SIS18 provides optionally foil stripping and a charge state separator (Fig. 1).

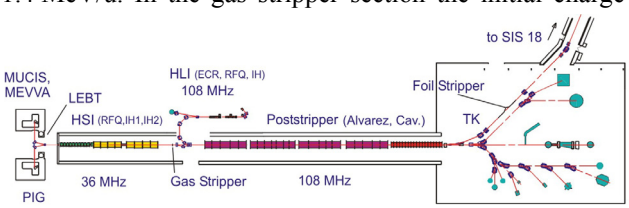

Figure 1: Schematic overview of the GSI UNILAC and experimental area. [1]

High current uranium beam machine experiments at HSI and the gas stripper section were conducted in November 2015. A multi-aperture extraction system for extracting a high brilliant ion beam from the VARIS ion source [2] was used. The RFQ-cavity underwent a dedicated conditioning and development program, providing for reliable rf-operation. These measures facilitated an extensive beam optimizing program and thus the success of this measurement campaign. The pulsed hydrogen stripping target [3,4] was further optimized aiming for operation at the maximum achievable average charge state. The high current measurements were therefore carried out for charge state 29+. The measured beam brilliance before the Alvarez-DTL was evaluated in detail. Due to an upgrade program, which renews the rf-amplifier system of the UNILAC post stripper (Alvarez) only three of the five Alvarez tanks were in operation. Thus, the achievable high current beam brilliance at injection into the SIS18 is currently estimated by using front-to-end high-current measurements [5] with a proton beam (with the same space charge capability as for the uranium beam) performed in 2014. Supplemented by extensive beam simulations [6] that were carried out recently for injection of a high-intensity uranium beam into the SIS18, the beam intensity, achievable from the FAIR injector chain, could be estimated.

HIGH CURRENT PROTON BEAM EMITTANCE MEASUREMENTS

The horizontal beam emittance is one of the crucial quantities at a fixed beam intensity to characterize the high-current capability of a synchrotron injector. The high current proton beam emittance growth inside the Alvarez was measured to be 17% (rms) [5] (Fig. 2). Considering the overall beam transmission of 90%, the loss of beam brilliance inside the Alvarez is 23%; the subsequent transport into the transfer line was accomplished without particle loss. However, due to a vertical bottle neck in the transfer line an additional loss of 15% was measured. The

ISBN 978-3-95450-185-4

transversal emittance remains the same until injection into the SIS18. The overall horizontal proton beam brilliance is diminished by 25% under high current conditions.

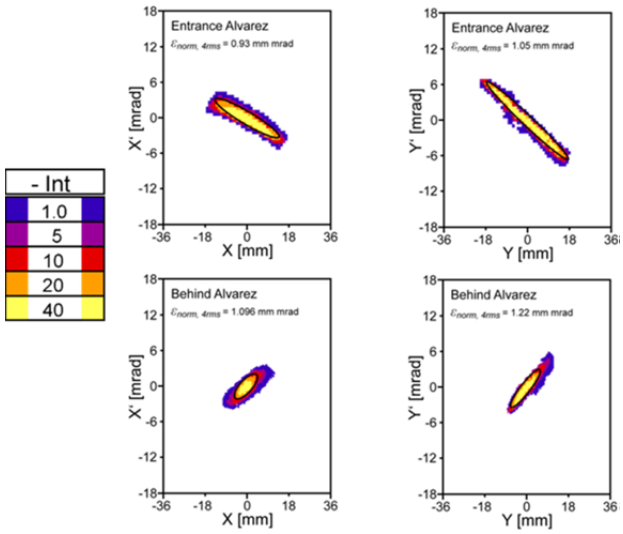

Figure 2: High-current proton beam emittance measurements at GSI-UNILAC poststripper accelerator. [5]

As shown in Fig. 3, the core of the high current phase space distribution remains constant during acceleration up to the final beam energy of 11.4 MeV/u and the adjacent beam transport in the transfer line to the SIS18. The fringe area blows up, while the beam envelope increases until particles get lost at the limiting beam aperture.

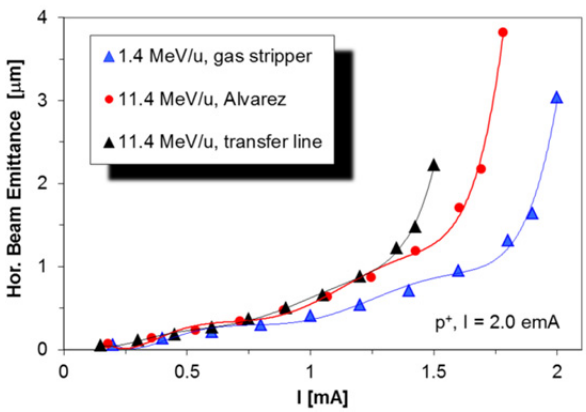

Figure 3: Analysis of high-current proton beam emittance measurements at Alvarez DTL (see Fig. 2) and transfer line to the SIS18; the beam transmission is 75%.

HIGH CURRENT ELECTRON STRIPPING IN A PULSED H_2-GAS CELL

Characterizing the stripping performance, the absolute stripping efficiency into the desired charge state is a key indicator. A sufficient charge state resolution is required to enable highest intensities in the desired charge state. As shown in Fig. 4, the stripping efficiency into the desired charge state could be improved (with the H_2 gas stripper cell). Applying a high density H_2-target (instead of a N_2-target) the yield is 50% higher, the maximum of the charge state distribution increases by 3 units.

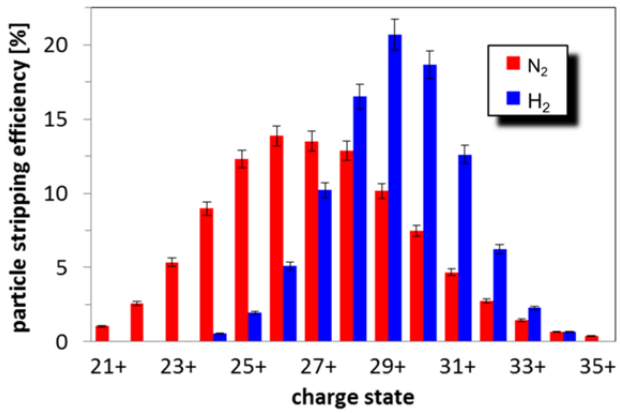

Figure 4: Charge state distribution after stripping of uranium projectiles in a H_2 gas target and a N_2 gas target.

With a pulse particle current of 0.345 pmA a new intensity record at 1.4 MeV/u was achieved. With further increase of the loading gas inside the H_2-gas cell an equilibrated regime was reached. For this equilibrium charge state (29+) the transversal beam emittance at 1.4 MeV/u (Fig. 5 at the top) was measured at the maximum electrical beam pulse intensity of 9.97 emA. Due to the lower efficiency for stripping at a N_2-target, the pulse intensity is reduced as well. The related beam emittance measured at 4.5 emA corresponding to charge state 28+, where the stripping efficiency is almost the highest, is shown in Figure 5 at the bottom.

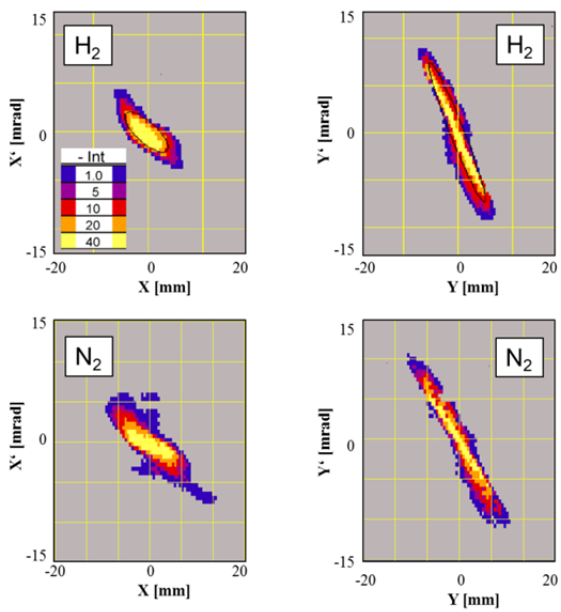

Figure 5: Measured horizontal (left) and vertical (right) high current uranium beam emittance after stripping to the equilibrium and charge separation at 1.4 MeV/u; at H_2- (top) [7] and at N_2-target (bottom) [8].

The main beam parameters achieved with H_2 and N_2 stripping targets are summarized in Tab. 1.

ISBN 978-3-95450-185-4

Table 1: Measured Beam Parameters [7]

	N_2-gas jet [8]	H_2- gas cell (pulsed)
Back-pressure	0.4 MPa	5.5 MPa
U^{4+}-current (HSI)	6.0 emA	6.6 emA
Stripping charge state	28+	29+
Stripping efficiency	12.7±0.5%	21.0±0.8%
Energy loss	14±5 keV/u	27±5 keV/u
Max. current	4.5 emA	9.97 emA
ε_x (90%, tot.) norm.	0.76 µm	0.66 µm
ε_y (90%, tot.) norm.	0.84 µm	1.15 µm
Hor. brilliance (90%)	5.32 mA/µm	13.60 mA/µm
FAIR requirements:		
ε_x (tot.) norm.	1 µm	
U^{28+}-Intensity	15 mA	
Hor. beam brilliance	15 mA/µm	

URANIUM BEAM OPTIMIZATION

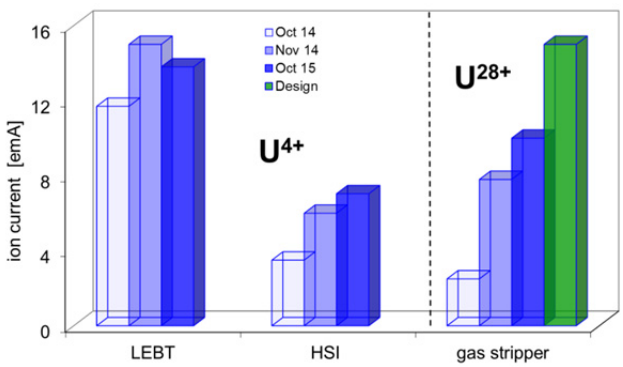

Figure 6: Measured uranium beam transmission at GSI-HSI and stripper section.

The U^{4+}-beam current and brilliance was improved by applying a 7 hole-aperture extraction system [8] at the VARIS ion source [2]. By optimization of the low energy beam transport and improved RFQ matching an RFQ transmission of 70% (9.70 emA) was achieved. After advanced rf optimization and rf conditioning the HSI RFQ tank yields for reliable high-current uranium beam operation. Optimizing the MEBT (Medium Energy Beam Transport) between RFQ and IH DTL by increasing the transverse and longitudinal focusing the previously disturbing beam losses could be minimized significantly, resulting in a stable overall high current operation. Beam matching to the gas stripper by adapting the quadrupole channel resulted in a beam transmission of 90% in this section. For the first time an U^{4+} beam current of 6.6 emA was available for heavy ion stripping. Applying the stripper gas cell at an optimal H_2 target thickness (≈14 µg/cm^2) and after re-optimization of the charge separation procedure under high current conditions, an increased stripping efficiency of about 21% was achieved.

Finally the uranium beam intensity at injection into the poststripper accelerator was increased by almost a factor of 4 accomplished in a 12 months lasting machine optimizing program (see Fig. 6).

BEAM BRILLIANCE ANALYSIS

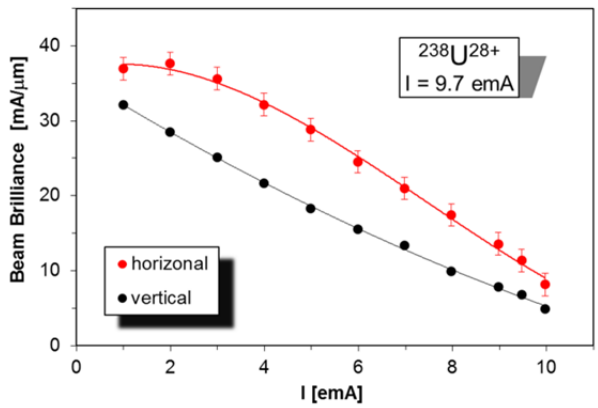

Figure 7: Horizontal and vertical brilliance (at 1.4 MeV/u) for uranium beam on H_2-target (9.7 emA, U^{28+}). [7]

For a wide range of different current densities and for the H_2 as well as for the N_2 target the fractional horizontal phase space distributions differ slightly in the peripheral region. The vertical beam emittance for uranium beam on a H_2-target (9.97 mA, U^{29+}) is significantly increased, while the horizontal emittance remains the same at higher beam current.

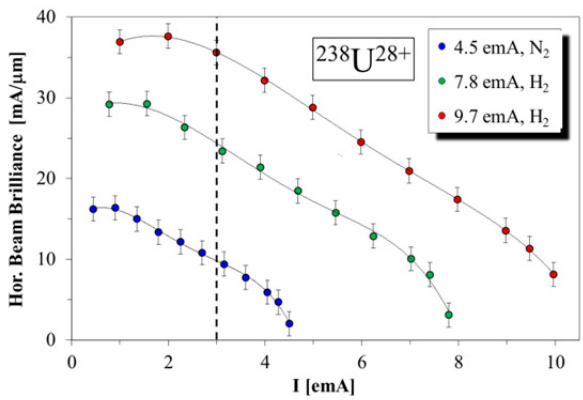

Figure 8: Beam brilliance for different beam intensities applying two different H_2 target thickness and equilibrium at the N_2 target.

For the high current beam dynamics layout of the gas stripper section, an enlarged vertical beam envelope in the interaction zone is foreseen, resulting also in an enhanced beam emittance growth due to strong particle straggling. Regardless of the ion current, the horizontal phase space distribution is nearly identical. Thus horizontal beam brilliance (Fig. 7) at 1.4 MeV/u is significantly higher. As shown in Fig. 8 the horizontal beam brilliance simply scales with the pulse current, independently on the used

ISBN 978-3-95450-185-4

target and/or the applied target thickness. For instance, the increase of the beam intensity by 1 emA leads to a four times higher horizontal beam brilliance (for a fractional current of 3 emA as indicated with a dashed line in Fig. 8). For the determination of the U^{28+}-beam brilliance, achievable at SIS18 injection, the front-to-end high-current proton beam measurements were used. Basically the UNILAC parameters scale with the mass-to-charge ratio m/q:

$$\frac{m}{q}(scal) = \frac{m/q\,(U^{28+})}{m/q\,(p^{+})} = \frac{8.5}{1}$$

Proton beam transmission TM_{fin} until SIS18-injection was measured as: $TM_{fin}(p^{+}) = 75\%$, while the measured proton rms emittance growth $EW_{fin}(p^{+})$ is negative: $EW_{fin}(p^{+}) = -3\%$. The resulting proton beam brilliance loss $BL(p^{+})$ could be evaluated for:

$$BL(p^{+}) = 100\% - \frac{TM_{fin}(p^{+})}{100\% + EW_{fin}(p^{+})} \cdot 100\% \approx 23\% \cdot$$

Assuming the brilliance loss scales with ion current density, the expected brilliance loss $BL(U^{28+})$ for the measured maximum uranium beam current (for charge state 28+) of 9.70 emA is:

$$BL(U^{28+}) = \frac{9.70 emA}{2 emA \cdot \frac{m}{q}(scal)} \cdot BL(p^{+}) \approx 0.6 \cdot 23\% \approx 15\%.$$

SUMMARY AND OUTLOOK

For operation with high intensity intermediate charge state heavy ion beams loss-free injection into the SIS18 is an essential condition. By horizontal collimation of the uranium beam emittance in the transfer line, the SIS18 space charge limit could be reached at significantly lower pulse currents, but accordingly longer injection times. The conducted high current proton beam emittance measurement throughout the UNILAC shows a loss of horizontal beam brilliance of 23%. The high current uranium beam brilliance (measured at 1.4 MeV/u) decreases accordingly until SIS18 injection. Besides the measured proton beam brilliance of the core stays constant during acceleration and transport to the SIS18. Through horizontal beam collimation (≤ 2 mm·mrad), the number of uranium particles in this phase space area is sufficient to fill the SIS18 up to the space charge limit (Fig. 9). Within a normalized emittance of 0.31 mm·mrad (tot. emittance = 2 mm·mrad) an available uranium beam current of 6 emA from the UNILAC corresponds to a normalized beam brilliance of 19.35 mA/mm·mrad, while 30 turns have to be injected in the SIS 18 [6,9]. The necessary pulse length is approximately 140 µs, available at UNILAC without any performance limitations. For further confirmation, it is evident to perform high intensity uranium beam measurements at full UNILAC energy.

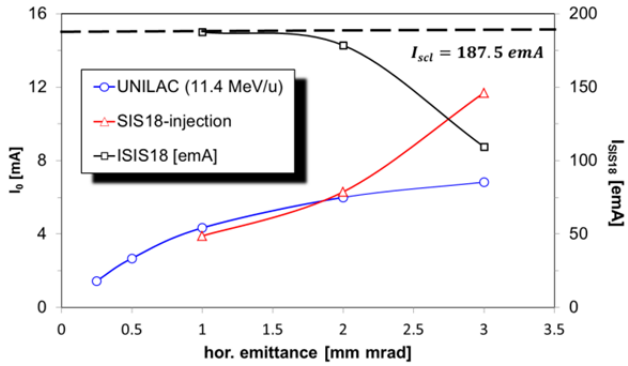

Figure 9: Injection current to reach SIS18-space charge limit (red), UNILAC-beam current (blue) and total current (black) as a function of U^{28+} horizontal input emittance at SIS18-injection.

ACKNOWLEDGEMENT

The authors are grateful for the support of the GSI linac, ion source, linac-rf, technical infrastructure and accelerator operation departments and colleagues from other GSI departments.

REFERENCES

[1] W. Barth *et al.*, "Future Heavy Ion Linac at GSI", in *Proc. IPAC'11*, San Sebastián, Spain, p. 2250-2252 (2011).
[2] R. Hollinger *et al.*, Nucl. Instrum. Meth., B 239 (2005) 227.
[3] P. Scharrer *et al.*, J Radioanal. Nucl. Chem. (2015) 305:837-842.
[4] P. Scharrer *et al.*, "An Upgrade for the 1.4 MeV/u Gas Stripper at the GSI UNILAC", in *Proc. 7th Int. Part. Acc. Conf. (IPAC'16)*, Busan, Korea, May 2016, paper TUPMR058, pp. 1394-1396.
[5] W. Barth *et al.*, Phys. Rev. ST Accel. & Beams 18, 050102 (2015).
[6] S. Appel, private communication (2016).
[7] W. Barth *et al.*, "High Brilliance Uranium Beams for FAIR", in *Proc. 7th Int. Part. Acc. Conf. (IPAC'16)*, Busan, Korea, May 2016, paper WEOBA03, pp. 2052-2054.
[8] W. Barth *et al.*, Phys. Rev. ST Accel. & Beams 18 040101 (2015).
[9] S. Appel, SIS18 – Parameter Studies on MTI Efficiency with Space Charge and Longitudinal Aspects, talk presented at the "GSI FAIR Injector Review", (2013).

ISBN 978-3-95450-185-4

ADVANCES IN THE DEVELOPMENT OF THE ESS-BILBAO PROTON INJECTOR

Z. Izaola*, I. Bustinduy, J. Corres, D. de Cos, C. de la Cruz, G. Harper, R. Miracoli, J. L. Muñoz, I. Rueda, A. Vizcaino, and A. Zugazaga, ESS-Bilbao, Spain

Abstract

We present the last advances in the operation and construction of the ESS-Bilbao 3 MeV proton beam injector. The proton ECR source allows to change the distance between the plasma chamber and the first extraction electrode, acceleration gap. The beam has been characterised at different acceleration gaps by current transformers, wire scanners and photographs of 2d profiles. In addition, we present the status of the construction of the RFQ; which is at its beginning.

INTRODUCTION

ESS-Bilbao aims to develop an accelerator components for ESS.One of the main contribution is the Medium Energy Beam Transport (MEBT). If project schedule allows we plan to test the MEBT with a proton beam. To achieve this goal, we are building an injector composed of a proton Ion Source (ISHP) [1], Low Energy Beam Transport (LEBT) [2] and a Radio-Frequency Quadrupole (RFQ) [3].

The injector is expected to produce a proton beam with an energy of 45 keV and high intensity with a rms emittance around 0.25 π mm mrad in order to fulfil the requirements of the RFQ. One innovative feature of ISHP is the possibility to vary the gap between the plasma chamber and the extraction electrodes; the so called acceleration gap.

This paper, firstly, discuss the general layout of the LEBT. Secondly, it shows the result of various measurement campaign aiming to optimise and understand the beam. Finally, it discuss briefly the design of the RFQ and the current status of its construction.

* zunbeltz.izaola@essbilbao.org

THE LOW ENERGY BEAM TRANSPORT

The Bilbao Accelerator LEBT (Figure 1) is composed of two solenoids placed at fixed positions, producing tunable magnetic fields. The solenoids have a smaller internal radius (involving more turns) at their ends than in their centres [4]. This way, the magnetic field profile along the axis is flatter than the one achieved with an uniformly shaped solenoid; which would present a typical bell-shaped magnetic field profile. Besides, the variable radius approach creates a magnetic field that remains confined within the solenoid limits, avoiding perturbations on any nearby elements (e.g. other solenoids and the vacuum pump).

In order to save beam-line space, each solenoid includes a set of two crossed (x/y) dipoles of the $\cos\theta$ type. The dipoles are capable of steering the beam to correct for misalignment of the beam line components, reaching a deflection up to ±4° of the protons. The presence of the dipoles limits the aperture to 100 mm [2].

Although the complete LEBT is equipped with three diagnostic boxes; one before the first solenoid, one between solenoids and one after the second solenoid; at this first stage we use only one solenoid and two boxes (Figure 2). The first box is equipped with an AC Current Transformer (ACCT1), a double-wire Wire Scanner (WS1) and a retractile beam collimator (BC) with a 5 mm radius hole to create a pencil beam. The second box contains a second ACCT2, a second WS (WS2), a quartz window for fluorescence measurements and a retractile beam shutter that protects the quartz. The two wires of the WS are at 45° from the horizontal and vertical directions. A Princeton Instrument CCD camera

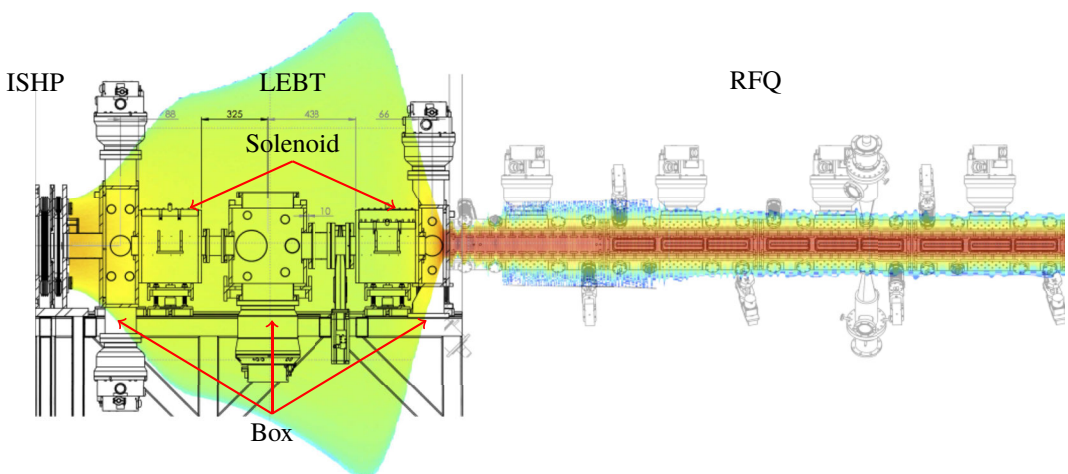

Figure 1: Schematic layout of the ESS-Bilbao injector from the H^+ Ion Source (left), through the LEBT (middle), to the RFQ (right). The coloured shadow represents the beam beam density along the injector.

ISBN 978-3-95450-185-4

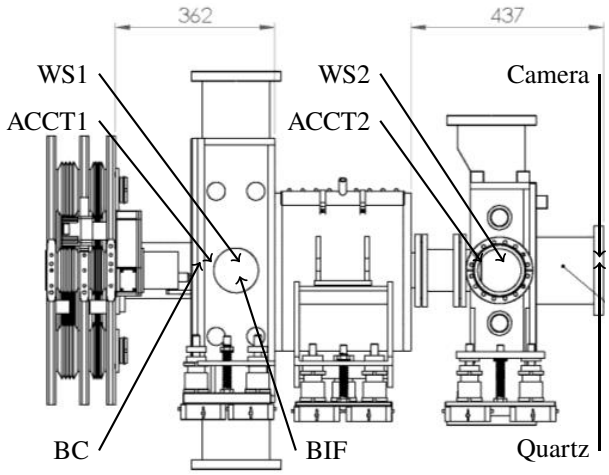

Figure 2: LEBT setup for the first stage of the beam commissioning.

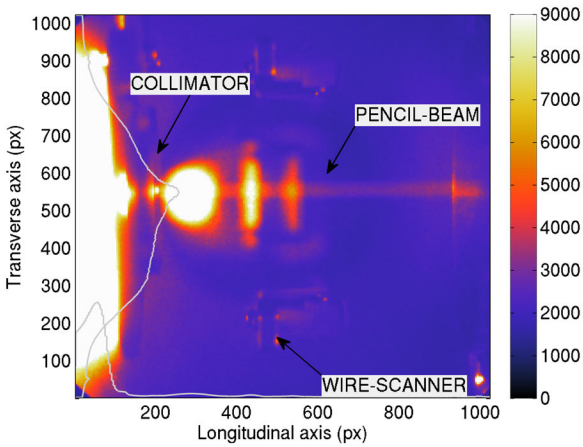

Figure 3: Image produced by the fluorescence induced by the collimated beam on the residual gas in the first diagnostics vessel of LEBT.

complements the quartz window in the exit port of the diagnostic box, for 2D profile photographs and pepper-pot measurements [5]. We used the camera also to record the Beam Induced Fluorescence (BIF) by mounting it in the side port of the first box (see Figure 3).

UNDERSTANDING THE BEAM

Our first goal was to find the acceleration gap with the highest transmission along the LEBT. Then, we studied 2D profiles of the beam; and this work lead to the investigation of different ion species in the beam.

Beam Current and Gap Optimisation

First we measured the effect of the solenoid strength in the transmitted beam current. The measurement was done with a 11 mm gap. Figure 4 shows that above 10 A on the

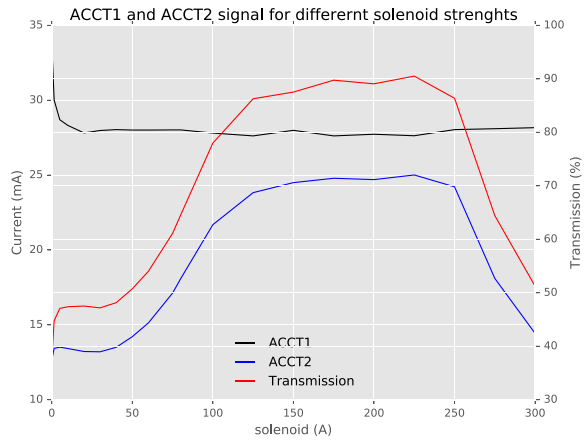

Figure 4: Beam current, before (ACCT1) and after (ACCT2) the solenoid, and transmission for different solenoid strengths.

solenoid power supply,[1] the beam current in the ACCT1 is stable. The elimination of the back-scattered electrons by the solenoid's fringe field may be the reason of beam current reduction at 10 A. Therefore, we will use 10 A as the baseline solenoid configuration to compare with. The transmitted beam current start increasing at ~150 A; reaching a plateau between 150 A to 180 A and reducing later, due to over-focusing of the beam.

The next step in the way of understanding the beam was to optimise the extraction gap. We measure 95 different beam profiles with extraction gaps between 8 mm and 14 mm, and solenoid currents between 10 A and 300 A.

Different ways were employed to characterise the beam concentration in the rms area. A graphic one was to study the collimated beam in the first diagnostic box, and measuring the Gaussian height and widths (Figure 3). The results agree with the ones presented in Figure 5. This Figure shows the transmission of the LEBT without the solenoid focalisation effect (10 A to avoid measuring secondary electrons). Although the higher current is achieved for the smallest gaps as foreseen, the best transmission is somewhere between 9 mm and 10 mm. When solenoid is energised transmission values are improved up-to 80 % for all different gaps.

The WS1 (see Figure 6 show that the beam profiles is far from being Gaussian. The fringe fields of the solenoid at 300 A reduce the background measured by the WS1. Even thought, the central part of the beam shows a quite flat top with two small peaks. The effect of the fringe fields is more pronounced for the horizontal signal than the vertical; causing a less symmetric beam. At shorter gaps the beam seems a bit more focused and therefore, less sensitive to the small effects of the fringe fields.

In summary; we get the highest beam intensity for the shortest gap, where the maximum transmission is for the

[1] The relation between power supply current and magnetic field is $B(\mathrm{T}) = 0.0013 \times I(\mathrm{A})$. So 10 A corresponds to 0.013 T, 100 A to 0.13 T, 150 A to 0.2 T, 180 A to 0.25 T and 300 A to 0.4 T.

ISBN 978-3-95450-185-4

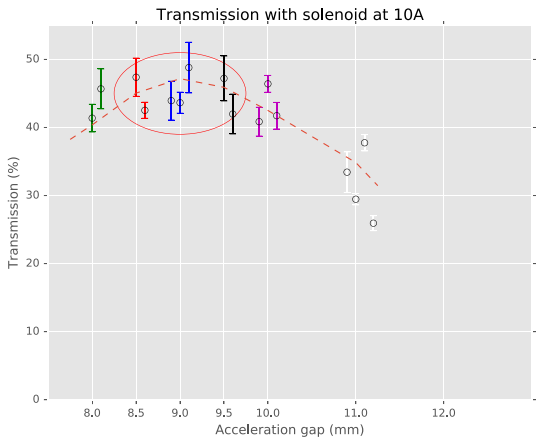

Figure 5: Transmission with the solenoid at 10 A for different acceleration gaps. Measurement at equal gaps have the same colour and some data have been displaced from the corresponding gap in the abscissa direction for a better display.

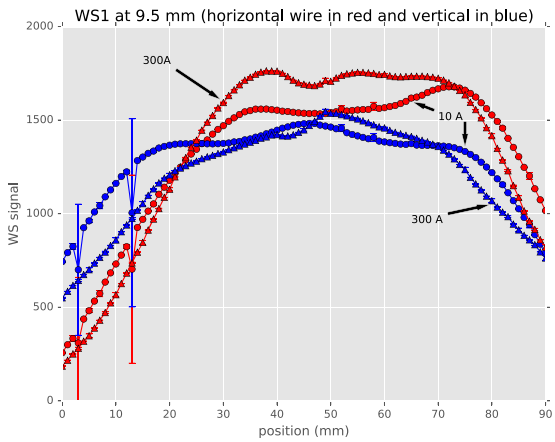

Figure 6: Beam profile measured by WS1 at 9.5 mm gap.

9 mm gap. With this data in mind, we select the region around 8.5 mm and 9.5 mm as the optimum acceleration gap from the point of view of beam intensity. Most importantly, the effect of the gap in the beam profile is smaller that we expected initially.

Beam 2D Distribution

The measured beam profiles incite us to make photographs of the beam to understand better the shape of the beam. The beam impacted a quartz windows whose upstream face is coated with a 50 Å aluminium layer. The luminescence produced in the quartz was recorded by a CCD camera. The aluminium layer prevented the direct light of the ion source to reach the camera. All the images where done with the solenoid at 10 A, without focusing the beam.

We found repeatedly, different distributions of the beam intensity on the quartz screen. Figures 7 and 8 show only two

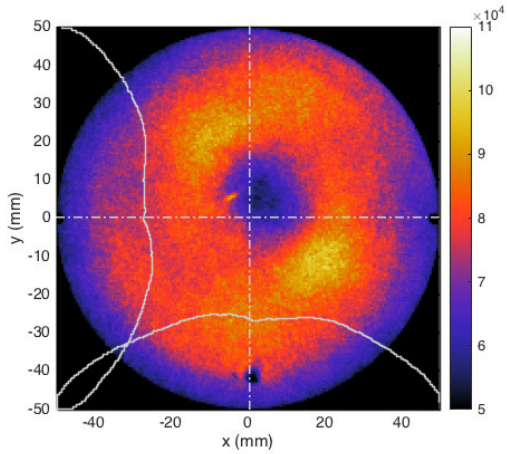

Figure 7: Photo of extracted beam for configuration family5.

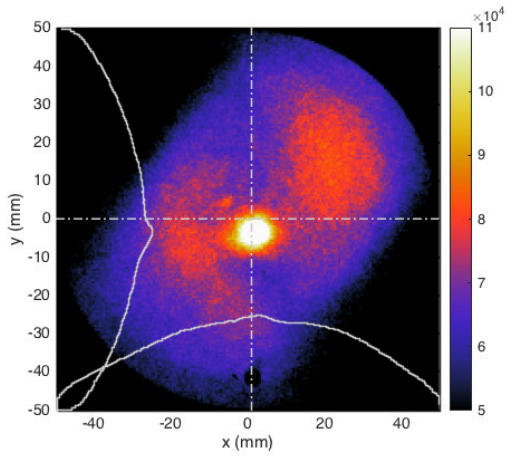

Figure 8: Photo of extracted beam for configuration family7.

examples of different identified *beam shapes*. We classified all recorded shapes in 5 *families*.

This families are reproducible with certain values of the confinement-magnetic-field coils and the input H_2 flow (see Table 1) of the ion source.

Previous research with a similar ion source at ESS-Bilbao [6], found plasma distributions that resembled the beam distribution shown in Figures 7 and 8. Different relative compositions of H^+, H_2^+ and H_3^+ were found. It shall be stressed that the imaged reported here are of *extracted beam,*

Table 1: Plasma Parameters of the Different "families"

Family	3	4	5	7	10
H_2 (%) flow	42	42	42	23	44
Coil#1 (A)	2	2	2	2	2
Coil#2 (A)	5.1	2	3.5	3.9	7.1
Coil#3 (A)	10	10	10	10	7.5
Coil#4 (A)	3.5	5.8	4.5	3.5	4.4

ISBN 978-3-95450-185-4

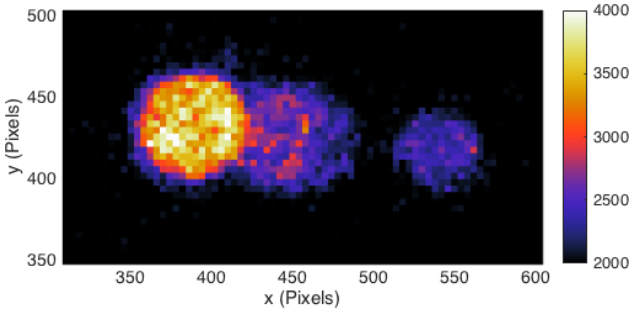

Figure 9: 2D beam profile with second steerer at 12 V for family5.

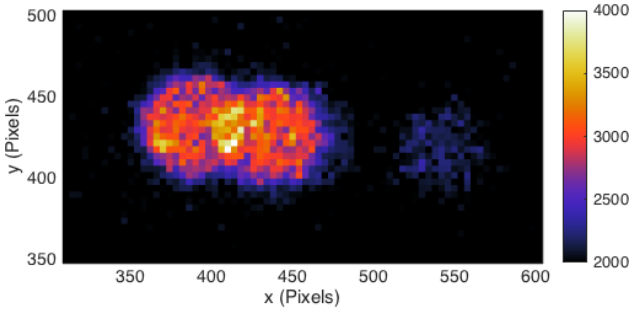

Figure 10: 2D beam profile with second steerer at 12 V for family7.

rather that of the plasma itself as in the cited paper, and were measured at 734 mm distance from the plasma meniscus.

Ion Specimens Present in the Beam

With this in mind, we intended to correlate each family with the specimen concentration. Although WS2 profiles were also used to identify different specimen peaks [7], we set up the following experiment: 2D beam profiles of the collimated beam where recorded with the camera for different values of the steering magnet; while the solenoid was off. Figures 9 and 10 show how the steerer splits the collimated beam into different specimens for the family5 and family7 configurations.

The photograph showed three spots separated horizontally. Profiles by integration of the vertical axis are shown for family5 is in Figure 11 and for family7 in Figure 12. The profiles of the other families are very similar to the profile of family5, and, therefore, only the results of this family are presented. Fitting the data to 3 Gaussian peaks and using a conversion factor of 0.19 mm px^{-1} provided by a calibration image, the distance between peaks can be calculated (see Table 2).

To test the initial hypothesis that the 3 peaks represent H^+, H_2^+ and H_3^+, we performed two TraceWin simulations. The initial beam has 0.5 π mm mrad emittance in both x and y planes. The energy is 45 keV and the current is 80 mA; 50 % of H^+ and 50 % of H_2^+ in the first simulation and 50 % of H^+ and 50 percent of H_3^+ on the second.[2] The aim of the

[2] At the time of the doing the simulations, it was not possible to use more than two particle specimen in TraceWin.

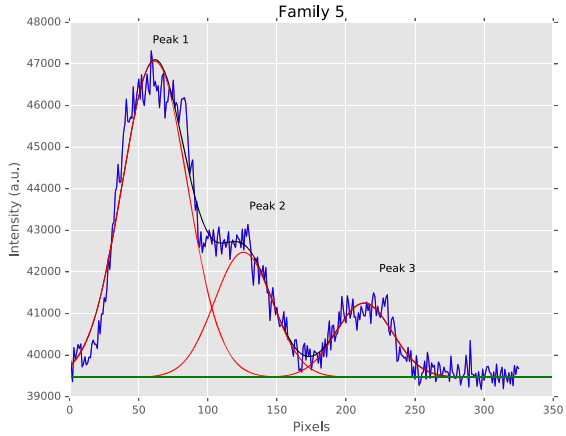

Figure 11: Horizontal profile with second steerer at 12 V for family5.

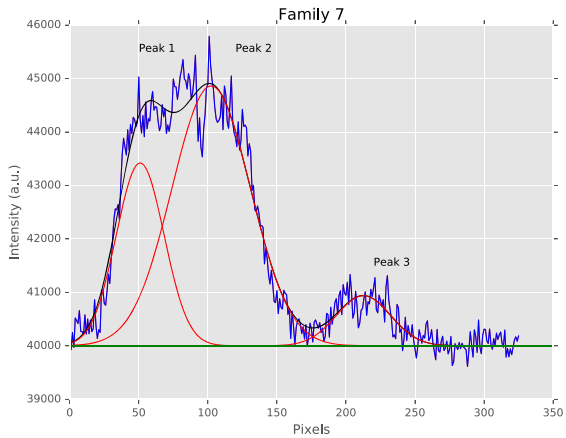

Figure 12: Horizontal profile with second steerer at 12 V for family7.

simulation is not to match the height of the peaks but their relative position; therefore the exact current of each beam is not important. Furthermore, to obtain a good statistic after the hole in the beam collimator, a initial high current is needed. The space-charge compensation is 90 %. The distance between the exit of the steerer and the scintillator screen is 252 mm. In order to accurately represent the experimental setup, measured field maps [8] were used for both solenoid and steerer components. A 60 000 point grid was gathered for each magnetic component (B_x, B_y, B_z) and was latter superimposed in TraceWin.

The simulations show that the H^+ peak shifted from the centre 30.9 mm; the H_2^+ 21.4 mm and the H_3^+ 17.1 mm. Table 2 compare this results with the ones from the experiments. From these values, we can assign peak #1 to H^+ with great confidence. Peak #3 seems to be due to particles heavier than H_3^+ because they are not displaced so much. It is still unclear what is the nature of those particles; they may be heavier ions coming out the plasma (impurities). Peak #2 is

ISBN 978-3-95450-185-4

Table 2: Position (Relative to the Collimator Centre) and Composition for families 5 and 7 and Simulated Positions of Peaks Relative to Beam Pipe Centre

	Position [mm]			Composition (%)		
Peak	#1 H^+	#2 H_2^+	#3 $H_3^+(?)$	#1 H^+	#2 H_2^+	#3 $H_3^+(?)$
Family5	30.2	18.1	1.4	64	23	13
Family7	32.1	22.4	1.3	24	67	9
Simulation	30.9	21.4	17.1			

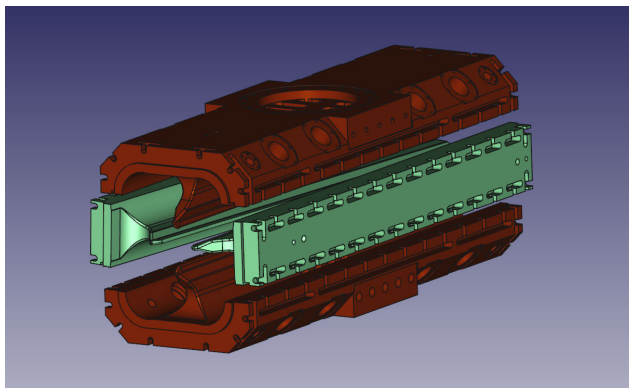

Figure 13: CAD image of the RFQ's first segments.

between the peaks of H_2^+ and H_3^+, so it maybe be due to the H_2^+ and other ion with a similar q/m ratio.

Integrating the fitted Gaussian allows to calculate the relative composition of the beam. Table 2 shows that the composition of H^+ and H_2^+ is very different in families 5 and 7. Furthermore, in the best of the cases, only 2/3 of the beam current is due to H^+ ions.

Measurements with the WS2 in the same conditions showed qualitatively similar results. Because the steerers move the peaks in the horizontal direction (as seen in the photographs), and the WS measures on a 45° angle, the peaks are seen on both wires of the WS.

RADIO-FREQUENCY QUADRUPOLE

The ESS-Bilbao Radio-Frequency Quadrupole (RFQ) [3] is designed to accelerate the proton beam from 45 keV to 3 MeV. It is a pulsed machine (duty cycle 4 %), operating at a frequency of 352.21 MHz. Design has finished and public procurement has started on June 2015.

The RFQ has total length of 3.12 m (3.86 λ) and will be assembled from four segments (see Figure 13) using Polymeric vacuum gaskets. The modulation of ESS-Bilbao RFQ is the result of an optimisation process based on a 2-term expansion (with a uniform 85 kV inter-vane voltage) using a modified version of RFQSIM code. The modulation has been verified using different codes: Toutatis, GPT+COMSOL and PARMTEQ/RFQGen. The overall transmission is between 87 % and 94 %.

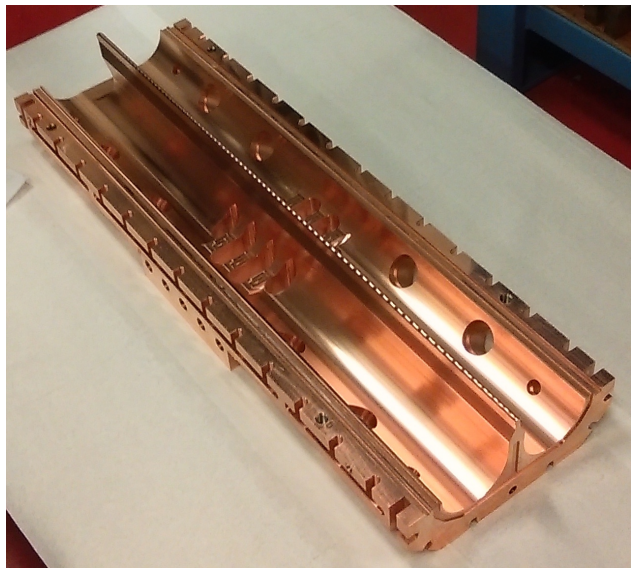

Figure 14: Major vane of the first section after fine machining.

The first segment of the RFQ is currently under fabrication (Figure 14). The first major vane is already finished and metrology is expected for June. When the four vanes are machined, they will be assembled and measured, and a final machining of the vacuum gaskets in the end faces will be done. This is expected for the last quarter of 2016. Mechanical and RF tests will be carried out with the first segment of the RFQ before the machining of the remaining three segments can start. Final assembly and tests with the whole RFQ are planned for late 2017.

CONCLUSIONS

The effect of the plasma parameters on the extracted beam profiles (Figures 10 and 9) is greater than we expected, if compared to the effect of the acceleration gap in these profile (Figure 6). Different ion source configurations show unlike profiles, not only in the plasma but also in the extracted beam, that are far from being "ideal Gaussian beam."

FUTURE WORK

The most important step in the following months is to measure the emittance of the beam. Other measurements include to search plasma parameters with a higher H^+ concentration. After this first characterisation of the beam is done, the whole LEBT will be installed. The final goal of the LEBT commissioning is to create a "map" of the emittance of the beam at the RFQ position for different configurations of the LEBT solenoids and steerers.

ACKNOWLEDGEMENT

The authors will like to acknowledge the work of all the staff at ESS-Bilbao in the design, building and running of the different parts of the injector.

ISBN 978-3-95450-185-4

REFERENCES

[1] J. Feuchtwanger et al. "Status of the Ion Sources at ESS-Bilbao." In: *Proceedings of IPAC2012*. TUPPC030. New Orleans, Louisiana, (USA), 2012.

[2] I Bustinduy et al. "First LEBT simulations for the Bilbao accelerator ion source test stand." In: *Procedings of HB2010*. 2010.

[3] Ibon Bustinduy and J. L. Muñoz, eds. *Technical Design Report: ESS-Bilbao RFQ*. 2nd ed. 2015. ESS-Bilbao Consortium Report Series ESSB-Rep-2015-010. Feb. 12, 2015. 330 pp. ISBN: 978-84-616-5445-1.

[4] J. Pozimsk et al. "Particle Dynamics Calculations and Emittance Measurements at the FETS." In: *Proceedings of LINAC 2006*. TUP066. Knoxville, Tennessee (USA), 2006.

[5] S. Jolly et al. "Data Acquisition and Error Analysis for Pepperpot Emittance Measurements." In: *DIPAC09 Conference Proceedings*. 2000.

[6] O. D. Cortázar et al. "Correlations between density distributions, optical spectra, and ion species in a hydrogen plasma (invited)." In: *Review of Scientific Instruments* 87.2 (2016). DOI: http://dx.doi.org/10.1063/1.4931720. http://scitation.aip.org/content/aip/journal/rsi/87/2/10.1063/1.4931720

[7] Zunbeltz Izaola et al. *Spectroscopy study of the beam for different plasma parameters*. Tech. rep. LEBT-BP-M006-FV. ESS-Bilbao, 2015.

[8] I. Bustinduy et al. *LEBT Solenoid Review*. LEBT-LD-IR15-V1-SOL-IBustinduy. ESS-Bilbao.

ISBN 978-3-95450-185-4

BEAM COMMISSIONING RESULTS FOR THE CSNS MEBT AND DTL-1

J. Peng†,Y.W An, M.Y Huang, L.S Huang, Y. Li, M.T Li, Z.P Li, Y.D Liu, X.H Lu, S.Y Xu
Y. Yuan, S. Wang, S.N Fu
Dongguan Campus, Institute of High Energy Physics, Dongguan 523803 China

Abstract

The China Spallation Neutron Source (CSNS) is designed to deliver a 1.6GeV proton beam to a solid metal target for neutron scattering research. It will be constructed in two phases. In the 1st phase, the beam power is designed to be 100kW. In the 2nd phase, the beam power will be upgraded to 500kW by doubling the linac output energy and beam current. The accelerator complex consists of a 50keV H^- ion source, a 3MeV radio frequency quadrupole (RFQ), an 80MeV drift tube linac (DTL), and a 1.6GeV rapid-cycling synchrotron (RCS). Until March 2016, the front end and the first tank of DTL have been fully commissioned. The primary design goals of peak current, transverse emittance and beam energy have been achieved. This paper reports on the methods and the results of the commissioning.

INTRODUCTION

The China Spallation Neutron Source (CSNS) is located in southeast China. The accelerator complex consists of a 50keV H^- ion source, a 3MeV radio frequency quadrupole (RFQ), an 80MeV drift tube linac (DTL), a 1.6GeV rapid-cycling synchrotron (RCS) and several beam lines [1]. The RF frequency for both RFQ and DTL is 324MHz. Until March 2016, two runs of beam commissioning have been completed. In the 1st run, the front-end has been commissioned and the primary goal is realized [2]. Beam with 15mA peak current, 500μs pulse length and 50% beam-on duty factor has successfully transported through the MEBT into a temporary dump. In the 2nd run, the DTL tank1 has been commissioned with a temporary beam line. Due to the limited capacity of the temporary dump, the pulse length was shortened to 400μs (chopped) and the repetition rate was reduced to 5Hz. The other parameters like beam peak current and energy have reached the design values. A summary of baseline design parameters and beam commissioning results is shown in Table 1.

MEBT COMMISSIONING RESULTS

The MEBT is used for matching beam output from the RFQ into the following DTL transversely and longitudinally. It consists of 10 quadrupoles, 6 steering magnets and two 324MHz bunchers. The schematic layout of the MEBT is shown in Fig. 1. Besides optic elements, there is a suit of diagnostics to monitor beam.

† pengjun@ihep.ac.cn

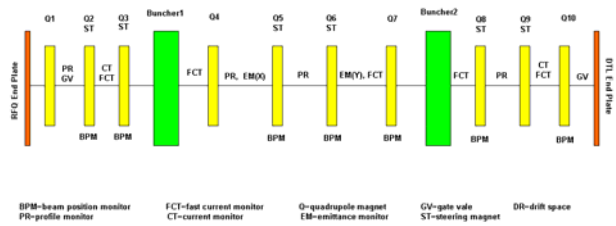

Figure 1: Layout of the CSNS MEBT.

Table 1: CSNS design vs. achieved beam parameters

	Baseline Design or Goal	Achieved
MEBT beam pulse length [μs]	420	500
MEBT pulse repetition rate [Hz]	25	25
Chopping rate [%]	50	50
LEBT peak current [mA]	20	31
MEBT peak current [mA]	15	18
DTL1 peak current [mA]	15	18
MEBT horiz emittance [π mm mrad (rms, norm)]	0.22	0.21
MEBT vertical emittance [π mm mrad (rms, norm)]	0.22	0.20
MEBT Beam Energy [MeV]	3.026	3.02±0.015
DTL1 output energy [MeV]	21.67	21.7±0.022

Transverse Twiss Parameters

For estimation of Twiss parameters at the beginning of the MEBT, beam profiles were measured with four wire scanners in the MEBT. If the wire scanner data is Gaussian and of high quality the easiest way to compute the beam sizes is fitting the profile with a Gaussian distribution. However, Guassian fit may not accurately represent the beam profile with halo. To calculate the RMS radius of this kind of profile, direct statistical calculation may be more suitable. Fig. 2 shows an example of the beam profile. The horizontal profile looks like Gaussian distribution while the vertical profile has significant halo "shoulders" [3].

After processing wire scanner data, estimation of the Twiss parameters was performed using beam sizes in conjunction with a beam propagation model. Table 2 lists the obtained Twiss parameters at the beginning of the MEBT.

ISBN 978-3-95450-185-4

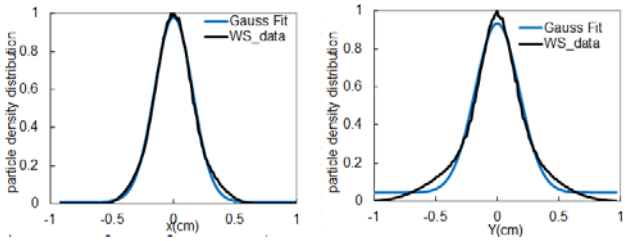

Figure 2: Beam profile measured with WS01 located after Q1.

Table 2: Twiss Parameters at the MEBT Entrance (I=15mA)

	α	β mm/mrad	Emittance rms, normalized mm mrad
Horizontal	-1.82	0.30	0.21
Vertical	1.32	0.10	0.20

A transverse emittance monitor is installed in the middle of the MEBT. It is double-slit type, and its first slit is located 1244mm downstream from the entrance of the MEBT.

We performed an experiment to test the accuracy of estimated Twiss parameters. First of all, we used the Twiss parameters in Table 2 as the initial beam parameters at the entrance of the MEBT. Secondly, we simulated the beam transporting through the MEBT with PARMILA [4]. Thirdly, at the location of the emittance monitor, we compared the simulated beam phase-space distributions with the measured ones from the emittance monitor. The results are shown in Fig. 3 and Table 3.

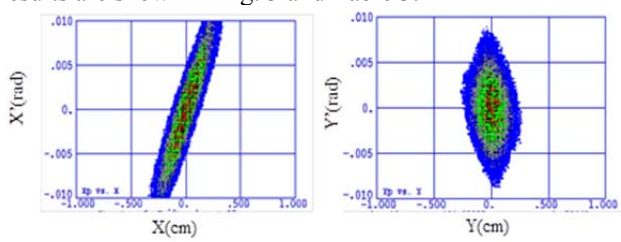

(a) Simulated phase-space distribution

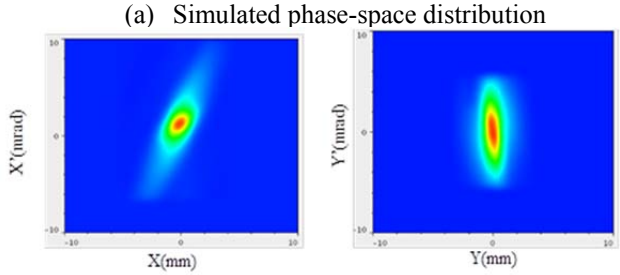

(b) Measured phase-space distribution

Figure 3: Phase-space distribution at the emittance monitor.

Theoretically the two groups of parameters should be equal. However, due to measurement errors, errors in the beam size calculation, and errors in the model, the values have a little variation, which is considered acceptable.

Energy Measurement

Five FCTs are placed in the MEBT for energy measurement and RF tuning of buncher cavities. Fig. 4 shows the FCT layout. The drift length for the Time-of-Flight (TOF) measurement of the RFQ output energy is 2.29m (about 30βλ). The measured RFQ output energy is 3.02±0.015MeV, compared with 3.026MeV nominal design value.

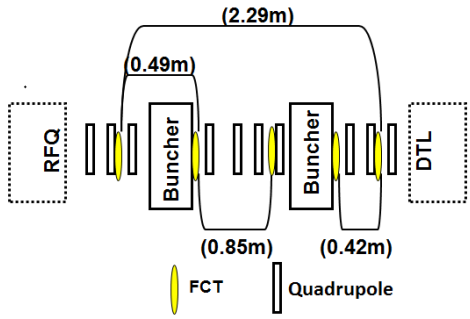

Figure 4: Schematic of FCT layout.

Table 3: Twiss Parameters at the Emittance Monitor (I=15mA)

	α	β mm/mrad	Emittance rms, normalized mm mrad
Horizontal			
Simulated	-2.46	0.69	0.21
Measured	-1.14	0.62	0.21
Vertical			
Simulated	0.16	0.30	0.20
Measured	0.02	0.37	0.18

RF Tuning of Buncher

At the beginning, the FCTs' electronic was unavailable, so we had to use BPMs downstream of bunchers to provide beam phase information. The basic procedure for determining the bunchering phase relies on the phase scan method. Fig. 5 shows an example of the buncher02, for which four phase scans at different amplitude were performed. The bunchering phase is located at the intersection of phase scan curves, which is -30degree.

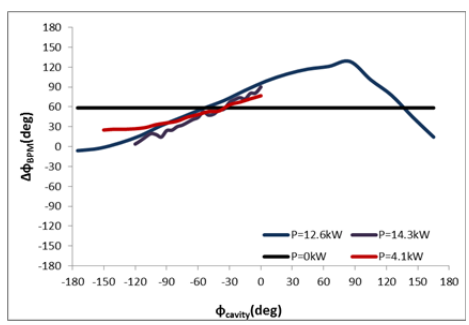

Figure 5: Measured phase differences (degrees) between two BPMs as functions of the buncher02 cavity phase.

ISBN 978-3-95450-185-4

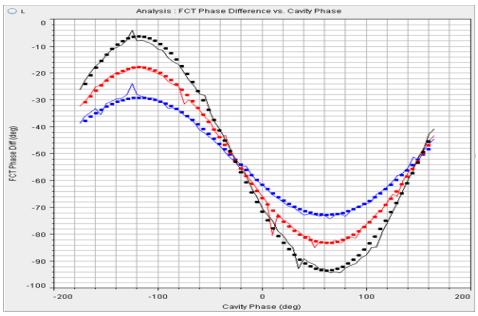

Figure 6: Measured phase differences (degrees) between two FCTs as functions of the buncher02 cavity phase. Plotted are experimental data (solid lines) and simulation results (solid circles) for three different RF amplitudes.

After the FCTs' electronic was available, a second technique was explored, which would also be used for tuning of the DTL tank 1. An application call PASTA was applied for phase scan and analysis [5]. It is based on the "phase-scan signature matching" approach [6]. In this method, the phase differences between two FCTs downstream of a cavity are measured as a function of the cavity phase. And then cavity amplitude, beam-cavity phase offset, input beam energy and FCTs' difference fudge of an online-model are varied to best fit those measured signatures.

As shown in Fig. 6, three sets of measured phase differences vs. cavity phase were recorded. The black curve was taken at nominal RF amplitude, the red one at 25% below nominal and the blue one at 50% below nominal. The bunchering phase of -27.9degree, measured in this way, agrees well with that measured by the first method. The bunchering phases of the buncher01 obtained by these two methods were -55degree and -60degree respectively. Besides, we found that the input energy, which is obtained along with the bunchering phase, is consistent with that measured by TOF in the MEBT. Table 4 summarizes these results.

Table 4: Measured RFQ Output Energy

	TOF	Buncer01 Scan	Buncher02 Scan	Design
W_{RFQ} (MeV)	3.02± 0.015	3.015	3.026	3.026

DTL COMISSIONING RESULTS

The drift tube linac consists of four accelerating tanks with final output energy of 80MeV. The transverse focusing is arranged in a FFDD lattice utilizing electric-magnet quadrupoles.

The first DTL tank has been commissioning with a temporary beam line. It contained a CT, a BPM, a wire scanner, an emittance monitor and two FCTs. The DTL1 commissioning results are summarized in Table 1. The design peak current of 15mA was readily achieved with 100% beam transmission. The goals of the DTL1 commissioning have been to demonstrate full system functionality, demonstrate beam acceleration with design beam parameters, test transverse focusing strategy, check the alignment accuracy and commission the diagnostic devices.

As mentioned before, the method of "phase scan signature matching" was applied for determining DTL tank RF setpoints too. A pair of FCTs in the temporary beam line was used to provide beam phase information. Fig. 7 shows the measured phase differences between two FCTs as functions of DTL1 RF phase. The blue curve was taken at nominal RF amplitude, the red one at 1% below nominal and the black one at 2% below nominal. It can be seen that the scan taken in the vicinity of the nominal amplitude fit better. The measured beam energy at the DTL1 exit is 21.722MeV, about 0.2% more than the design value of 21.677MeV.

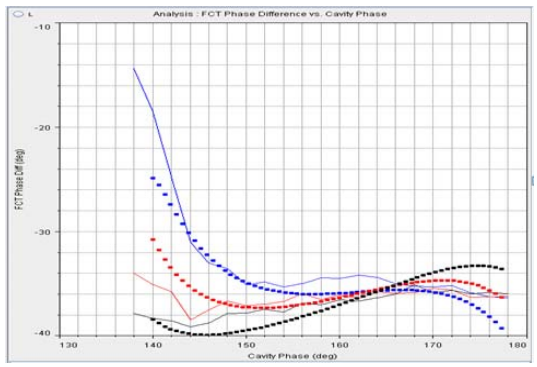

Figure 7: Plots of the DTL tank1 phase scan. Plotted are experimental data (solid lines) and simulation results (solid circles) for three different RF amplitudes.

CONCLUSION

The CSNS MEBT and DTL1 have been fully commissioned, the primary design goals of peak current, transverse emittance and beam energy have been achieved. The RFQ output energy, measured by phase scan method, agrees well with that measured by time-of-flight method. The remaining DTL tanks 2-4 have been installed in the tunnel. They will be commissioned in winter this year.

ACKNOWLEDGMENT

The beam commissioning of CSNS MEBT and DTL1 has been performed with the efforts of all the members of CSNS accelerator division. We would also like to acknowledge the help from the conventional facility division.

REFERENCES

[1] S. Fu *et al.*, "Linac Construction for China Spallation Neutron Source", Proceedings of Linac2012, Tel-Aviv, Israel, THPLB01.

[2] J. Peng *et al.*, "Commissioning Plan for the CSNS Linac", Proceedings of IPAC2013, Shanghai, China.

[3] Wangler T P, Allen C K, Chan K C D et al 2001 Experimental Study of Proton-beam Halo Induced by Beam Mismatch in LEDA Proc. 2001 PAC. Chicago p 2923–2925.

ISBN 978-3-95450-185-4

[4] Takeda Harunori. PARMILA, LA-UR-98-4478, 1998, Revised July 26, 2005.
[5] J. Galambos *et al.,* "PASTA-An RF Phase Scan and Tuning Application", Proceedings of PAC2005, Knoxville, Tennessee .
[6] T.L Owens *et al.,* "Phase Scan Signature Matching for Linac Tuning", Particle Accelerators, 1994, Vol98, p.169.

ISBN 978-3-95450-185-4

OPERATIONAL EXPERIENCE AND FUTURE PLANS AT ISIS

D.J. Adams, C.M. Warsop, B. Jones, B. Pine, H. Smith, R. Williamson, A. Seville, R. Mathieson, I.S.K. Gardner, D. Wright, A.H. Kershaw, A. Pertica, A. Letchford, STFC, Oxford, UK

Abstract

The ISIS spallation neutron and muon source has been in operation since 1984. The accelerator complex consists of an H^- ion source, 665 keV RFQ, 70 MeV linac, 800 MeV proton synchrotron and associated beam transfer lines. The facility currently delivers ~2.8×10^{13} protons per pulse (ppp) at 50 Hz, which is shared between two target stations. High intensity performance and operation are dominated by the need to minimise and control beam loss, which is key to sustainable machine operation, allowing essential hands-on maintenance. The facility has had several upgrades including an RFQ, Second Harmonic RF system, beam diagnostic DAQ improving beam control and a Second Target station. Future upgrades include a ring damping system and MEBT injection chopper. Operational experience of ISIS and its upgrades are discussed as well as current and future R&D projects.

INTRODUCTION

The ISIS neutron facility has been in operation since 1984 providing neutron and muon beams to the user community for a wide spectrum of materials research [1]. The facility originally consisted of an H^- ion source, 665 kV pre-injector, 70 MeV four tank drift tube linac injecting into a 163 m circumference, proton synchrotron. Un-chopped beam injected into the ring using H^- charge exchange accumulates 2.75×10^{13} protons over 130 turns, non-adiabatically trapped, and fast extracted at 50 Hz delivering a 160 kW beam to a depleted uranium target.

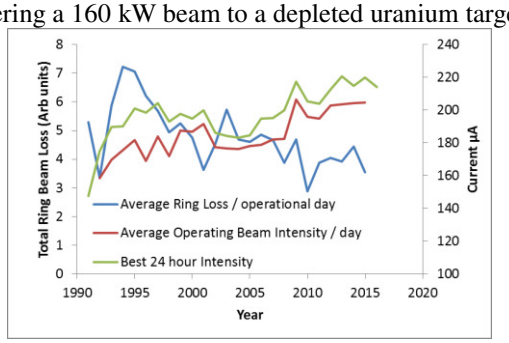

Figure 1: Operating ring beam loss and intensity since 1992.

As with any accelerator facility, post commissioning, there have been many incremental developments to increase operating intensity and improve beam loss control. The main upgrades have been Straight 1 (2002), Pre-Injector (2004), Ring Dual Harmonic RF (DHRF) cavities (2006-2012), Second Target Station (2007), Downstream Extracted Proton Beam line (EPB) refurbishments (2007-2015), with continued machine physics R&D improvements throughout the whole period.

The main challenge for high intensity operation of the facility is minimising and controlling beam losses, especially in the ring, which activate machine components restricting hands on maintenance. Fig. 1 shows yearly average total ring beam loss, operating intensity and best 24 hour operating intensity since 1992. The trend is for decreasing beam loss and increasing operating intensity to the point where we now routinely operate in excess of 220 µA, 176 kW. Whilst upgraded hardware has improved machine reliability this paper concentrates on upgrades and operational experience which have aided beam control.

MAIN ACCELERATOR UPGRADES

Pre-Injector Upgrade

The original pre-injector section of the accelerator consisted of a 665 kV Cockcroft Walton accelerator, Fig. 2 left, followed by a quadrupole and RF buncher matching section delivering a 19 mA, H^- beam to linac tank 1. As part of an intensity upgrade, to meet the demands of increased beams for the second target station, this section was replaced by 3 solenoids and an RFQ in 2004 [2], Fig. 2 right. After 18 months commissioning and soak testing in a dedicated test facility the new components were installed in the accelerator and have been very successful and reliable. The main commissioning issues were surface cleaning inside the RFQ, required to meet high RF field levels.

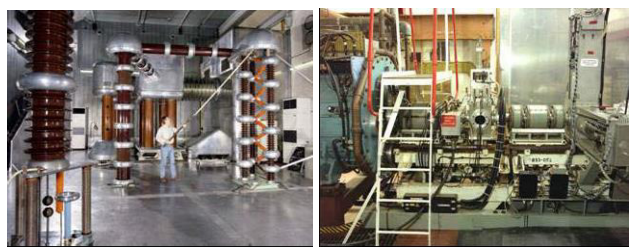

Figure 2: CockCroft Walton set (left) and new RFQ (right).

Typical operation now delivers 35 mA beams to tank 1 with 95 % transmission efficiency. Transverse mis-match into tank 1 reduces the beam current to 26 mA which is then maintained through the remaining linac tanks for injection into the ring [3].

Dual Harmonic RF Upgrade

The ring RF system was originally composed of six, h=2, ferrite loaded cavities delivering up to 160 kV/turn. Ring injection accumulated a DC beam which was then trapped into two bunches non-adiabatically and accelerated up to 800 MeV in 10 ms. Beam losses of 10 % limited operation to ~200 µA. The dual harmonic upgrade [4,5], saw the addition of four, h=4, cavities with 80 kV/turn total peak. Increased bucket acceptance and

ISBN 978-3-95450-185-4

bunching factors reduced trapping and acceleration losses and allowed higher intensity beam of up to 230 µA with equivalent losses. Fig. 3 shows beam loss (left) and intensity (right) during the cycle with and without the additional cavities.

Beam loading on the h=4 RF cavities is the main control issue. Compensation systems, based on existing h=2 hardware, and digital frequency control of both systems are in development [6].

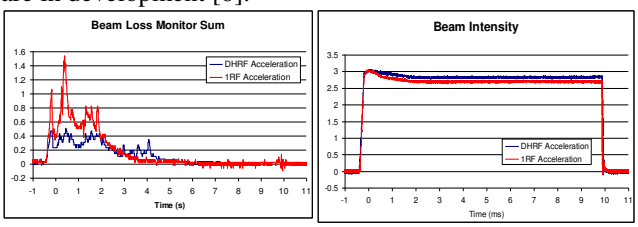

Figure 3: Beam loss (left) and intensity (right) with (blue) and without (red) DHRF cavity operation.

Straight 1 Upgrade

In 2002 the most active straight section in the ring, where collimation and vertical fast extract systems are situated, was redesigned and replaced. The vertical acceptance of the extraction channel was increased, including a new septum magnet, to allow lower beam loss operation. The collimation system was also replaced, including additional, optimised copper and graphite jaws. The increased jaw length was designed to allow for higher energy losses expected with dual harmonic operation. The upgraded system with energy deposition measurements also provides enhanced protection for machine error conditions.

Downstream EPB1 Upgrades

The Muon Facility at ISIS uses a graphite target inserted in an 800 MeV proton beam line ~20 m upstream of Target Station 1. In addition to producing muons this target scatters the incident proton beam causing downstream machine activation. TURTLE simulations suggest for a 10 mm thick target 1.4 % of incident beam is scattered and controlled on downstream collimators but 0.47 % is uncontrolled and deposited on downstream lattice components. A three phase upgrade (2007-2015), across long shutdowns, included: reducing collimator clearance to the primary proton beam from 17 mm to 9 mm, replacing all old quadrupoles with larger aperture versions, adding two extra to improve optic flexibility and adding quadrupole steering elements to allow independent muon and neutron target beam position control. TURTLE studies show proton losses are now localised to the collimators. This has allowed continued operation with tolerable dose levels.

ACCELERATOR PHYSICS AND R&D

High Intensity Limit of the Facility

The main challenge for high intensity operation of the facility is optimising beam loss in the ring. The main loss mechanisms are: injection foil stripping efficiency and scattering, non-adiabatic longitudinal trapping, a vertical head-tail instability driving emittance growth, halo generation associated with high space charge and resonance crossing.

As is the case on many high intensity machines, much operational optimisation is empirical. However, there is an on-going R&D programme to advance measurement, and develop experiments and models that improve understanding of the main loss mechanisms. This is as important for future machines and upgrades as it is for improvement of present performance. Experimental results from machines like ISIS (with particularly high space charge levels) are a valuable benchmark for future designs.

High Intensity Setup

Beam losses in the ring, Fig. 3, can be separated into three main time intervals: injection (-0.4–0.0 ms), trapping (0.0–2.5 ms) and acceleration (2.5–10.0 ms).

Injection loss (1%) is mostly generated by unstripped beam at the foil. Circulating beam losses are derived from emittance growth, mainly through space charge and foil scattering. Painting emittance amplitudes, tune and transverse optics are the effective tuning handles.

Longitudinal trapping loss (3%) results from the non-adiabatic capture process and is strongly affected by the injected beam distributions and the evolution of the RF bucket structure in the ring. The injection energy distribution is managed using linac and debuncher, whilst ring buckets are manipulated using, RF frequency, volts and phase between the h=2 and h=4 systems.

Transverse trapping losses, that are associated with the high incoherent tune depression peaking at >0.5 at 0.4 ms, are managed by ramping tunes, varying injection painting amplitudes and optimising RF parameters. Significant loss due to the head-tail instability is discussed below.

The other critical aspect of tuning is localising beam loss on the collimator systems. This is achieved using closed orbit (13 dipoles) and envelope control (20 trim quadrupoles). Each element is powered independently and controlled in 0.5 ms steps. A typical ring loss distribution is shown in Fig. 4. Peak loss is confined to super period 1 (collimators) with a little out-scatter into super period 2.

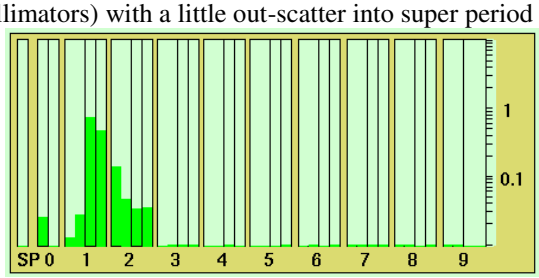

Figure 4: Beam loss around the 10 ring superperiods integrated over the acceleration cycle, 0-10 ms.

High Intensity Capability of the Ring

In its current configuration the ring has accelerated 3.15×10^{13} ppp at low repetition rate, equivalent to a 250 µA beam. Beam losses were at 9 % and well

ISBN 978-3-95450-185-4

controlled, just within the limit of acceptable operation. Increasing intensity further is feasible, but would require use of more machine aperture (via improved alignment) and reduction in head-tail instability losses. Both are actively under study.

Beam Measurements and DAQ Developments

The essential ISIS diagnostics are: intensity toroids, ionisation beam loss monitors (BLMs), position monitors and profile monitors [7]. Intensity monitors and BLMs are used for machine protection, via fast trip systems, as well as determining loss levels and distributions. Diagnostics are used to routinely measure basic parameters such as: transverse position and width and bunch length. In addition they are used, via suitable processing, analysis and modelling, to provide more advanced parameters: injected betatron amplitudes, tunes, closed orbits, beta functions and longitudinal distributions. These measurements are used to correct machine errors, characterise low beam loss operation and are essential for accelerator R&D.

Advances in digitisation speed, acquisition depth and cost have enabled more signals to be acquired at higher resolutions. Increases in computing power allow more detailed analyses and visualisation of acquired data in an operational environment. Two such measurements, longitudinal waterfall and BLM distribution, Fig. 5, are now available, updating at ~2 Hz. Migration to FPGA environments should allow full ring repetition rate, 50 Hz, measurements to be obtained. Such automated fast systems will advance machine operation and tuning from raw signal optimisations to machine parameter tuning.

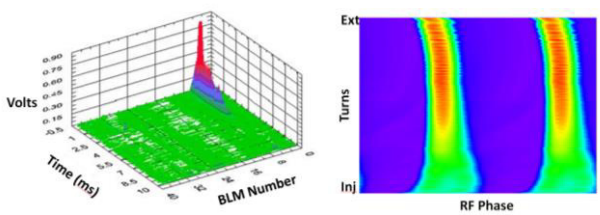

Figure 5: Spatial Beam loss distribution through the cycle (left), longitudinal waterfall plot, (right).

Scintillator Beam Loss Monitors

Beam operational levels were lowered between 2002 and 2006, Fig. 1, to manage a beam loss causing damage to an RF screen inside a main dipole, downstream of the collimator section in straight 1. Investigations concluded that uncontrolled loss escaping the collimators was the cause and conventional BLMs external to the dipole were shielded by the yoke. A non-metallic scintillator based BLM suitable for use in a fast cycling magnet was developed, and placed inside the yoke adjacent to the vacuum vessel.

Fig. 6, shows a scintillator (left) and loss traces (inverted) for the scintillator and BLM at the same lattice location. The scintillators show an equivalent signal thus validating those inside the dipole. These scintillators allowed detailed setup of the collimators and machine optimisations to minimise this loss mechanism [7]. Operational experience shows they do suffer signal degradation in high radiation fields. A study of these effects is in progress. A program to add scintillators to all 10 main ring dipoles will be completed by 2017.

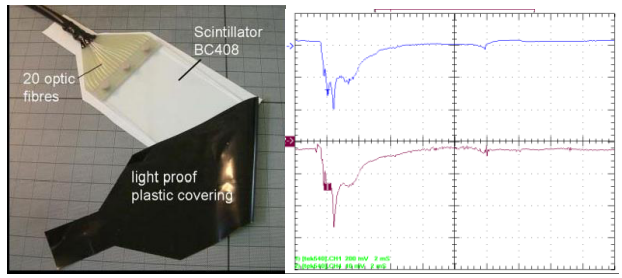

Figure 6: Scintillator (left), scope trace of scintillator and BLM (right) over the operational 10 ms cycle.

Transverse Profile Monitors

Accurate, non-destructive measurement of transverse profiles in the ring is essential for operation, modelling and high intensity R&D. Upgrades to the residual gas ionisation monitors allow beam profile measurements over thousands of turns in each machine pulse using an array of 40 channeltron detectors. Detailed studies of errors caused by ion drift field non-linearities and beam space charge have provided correction schemes and are an important area of development [8]. The detailed evolution of beam distributions these monitors provide are essential for more detailed understanding of beam loss mechanisms.

Head-Tail Instability and Beam Damper

The vertical head-tail instability has been observed in the ring since initial machine operations and typically causes loss at ~2 ms into the acceleration cycle [9]. This instability became more problematic after the DHRF upgrade, probably due to increases in intensity and bunch length: this is now one of the main loss mechanisms limiting operational beam intensity. Losses are minimised by decreasing vertical tune and by setting the bunch line density into an asymmetric shape using the phase difference between the h=2 and h=4 RF cavities.

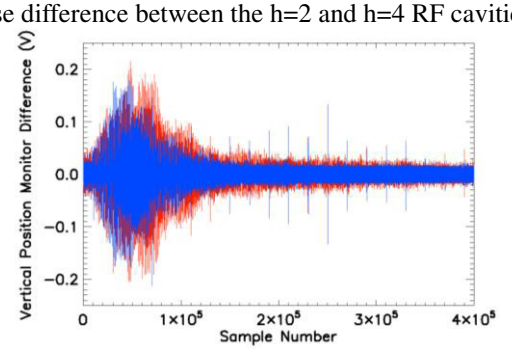

Figure 7: Vertical position monitor difference signal, 2-4 ms. Un-damped (red), damped (blue).

A damper system is now in development to counter this instability. A prototype system, with limited bandwidth

ISBN 978-3-95450-185-4

and power has demonstrated damping operation in recent tests. Preliminary results, Fig. 7, show vertical position with the damper system on (blue) and off (red) from 2-4 ms in the acceleration cycle. A more powerful and wider bandwidth system with stripline pick-up and kicker has been designed and is due for installation in 2017 [10].

Detailed R&D work is also underway to model and understand the complicated head-tail motion, which is significantly modified by space charge. A new simulation code is being developed and detailed investigations of beam impedances have started. Initial measurements using a coasting, 70 MeV, beam show a clear narrowband impedance centred at 85 kHz, Fig. 8 [11].

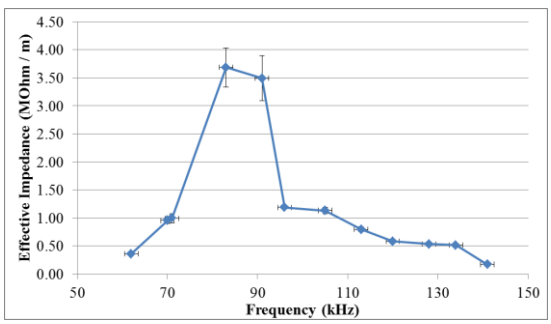

Figure 8: Beam-based measurement of effective impedance versus baseband frequency. Intensity = 1 × 10^{13} ppp.

Development of Ring Models and Simulations

Ring beam dynamics have been simulated in a variety of codes with the ultimate aim to understand and minimise beam loss. These inform tuning strategies during machine operation and contribute to accelerator R&D topics.

2D and 3D beam dynamics simulations with ORBIT [12] have allowed detailed studies of ring beam loss. These used linear lattice models to simulate injection and acceleration with dynamic tune, space charge, apertures and foil scattering. The model predicts 2.7 % loss compared with a measured 7 % loss [13].

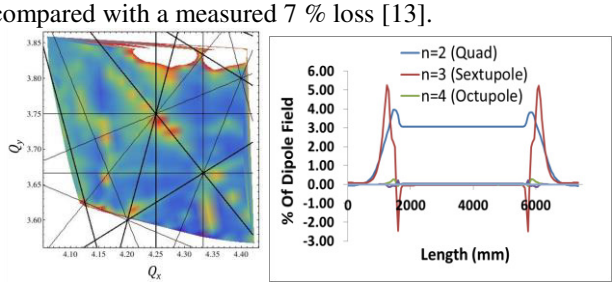

Figure 9: Ring Tune plane scan (left) and Main ring dipole multipole field distributions from OPERA model

New measurements of the tune plane, Fig. 9 left, show many higher order resonance lines not currently in the model. Non-linear magnet strengths, Fig. 9 right, derived from OPERA models and field measurements of magnets are being added to provide a more comprehensive and accurate lattice model for future studies.

Longitudinal dynamics have been simulated in ORBIT and an in-house code [13,14]. These models have been useful in achieving shorter extracted pulse lengths on ISIS for improved muon instrument performance, Fig. 10. Bunch length is compressed by ~50% FWHM with a combination of an adiabatic voltage ramp, switching the bunch length loop off during the final phase rotation and introducing a step function in the RF frequency. In other work, studies of longitudinal stability show the Keil-Schnell-Boussard (KSB) criteria is exceeded under normal ISIS operation. Understanding this effect is important as it is a key parameter for future machine designs.

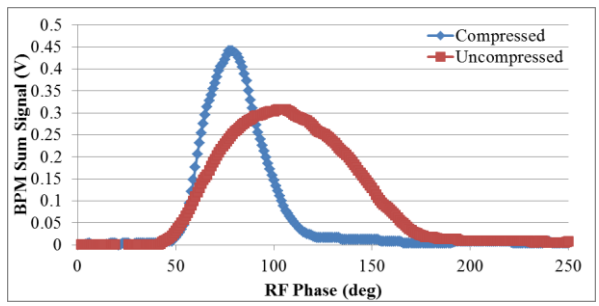

Figure 10: Position monitor line density vs RF phase for compression (blue) and normal operation (red).

FLUKA models are providing essential information on operation of the collimator system, factors determining activation levels, foil losses, operation of beam loss monitors as well as insight into machine damage. In particular, ORBIT beam loss simulation results have been used in FLUKA models of the injection and collimation straights to calculate machine activation, an important metric for current and future machine operations.

Studies of Loss Mechanisms

In addition to the work above, dedicated studies are looking at particular loss mechanisms, specifically half integer and image field losses.

Half integer resonance is often a main loss mechanism in high intensity proton rings, and is believed to contribute to trapping losses on ISIS. Detailed experiments have characterised beam redistributions during resonance crossing at high space charge levels and have been replicated well with comprehensive ORBIT simulations. Present work is concentrating on building simple theoretical models to explain the experimental results [15].

The effects of space charge and image forces in the unusual rectangular, conformal vacuum vessels in the ISIS ring are being studied in detail with the in house code SET3D [16]. Results indicate that closed orbit errors can lead to numerous extra driving terms from image forces, potentially resulting in additional beam loss.

FUTURE PROJECTS

MEBT Upgrade

Transverse beam loss in tank 1 due to optical mismatch from the RFQ can be reduced by installing an upstream MEBT matching section. This consists of quads and

ISBN 978-3-95450-185-4

re-buncher cavities Fig. 11. Simulations predict transmission efficiencies of 96 % through the new section and zero losses in Tank 1 [17] potentially increasing linac beam currents from 26 mA to 35 mA. Beam loading on the linac RF systems may be an issue at the highest currents.

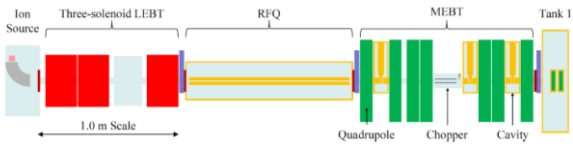

Figure 11: Arrangement of LEBT and MEBT.

The addition of a fast chopper in the MEBT allows direct injection into ring RF buckets. Beam simulations using the ORBIT code, for a 26 mA injection current chopped, with 60 % duty factor, and un-chopped, are shown in Fig. 12. Injection losses increase due to higher space charge levels of the chopped beam and also the increased injection interval, 200 µs to 300 µs, which increases loss due to foil scattering. However losses during acceleration currently associated with trapping at ~0.4 ms are much reduced. Overall beam losses are similar but at lower energy producing lower machine activation. Longitudinal optimisations for a 35 mA injection current case, which should have reduced foil losses is under study. MEBT designs and ancillary installations are in progress with full installation and commissioning due in 2019

Research for ISIS Upgrades

A number of ISIS upgrade options are under study. These range from staged upgrades of the present facility to 'green field' designs. A detailed consultation is also underway with expert teams on instruments, neutronics and targets to determine the optimal configuration for the next generation spallation source.

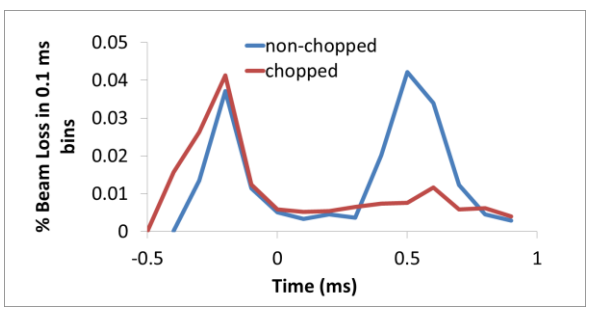

Figure 12: ORBIT simulations of injection and trapping loss, under normal operation and with an injection chopper.

Current ideas include upgrading the injector to 180 MeV, allowing beam powers of 0.5 MW from the existing ring [18], possibly followed by staged upgrades with rings in the existing hall - RCS or FFAG - which could feed multiple targets and be developed well into the multi MW regime. Detailed studies of optimal RCS and FFAG ring designs for these ideas are in progress [19].

The Front End Test Stand (FETS) currently under construction at RAL is a technology demonstrator for use on a high power linac [20]. Designed to deliver 60 mA, H^- beam, at 3 MeV with 10 % duty factor, possible applications include a linac upgrade. First beam through the RFQ is expected by the end of 2016. One exciting possible application for FETS is as an injector for a new "proof of principle" low energy FFAG ring. This would demonstrate the key aspects of performance for a future ISIS upgrade which could exploit all the advantages of a high intensity FFAG ring [19].

CONCLUSIONS

Since first commissioning in 1984, the ISIS facility has undergone a series of upgrades to improve machine performance. Developments to accelerator R&D and diagnostics have aided understanding of how to operate a machine close to the intensity limit in a controlled and sustainable manner. Experience and knowledge gained will be essential to develop ISIS, and design future upgrades.

REFERENCES

[1] D. Findlay,ISIS-Pulsed Neutron And Muon Source,PAC07.
[2] A.Letchford, PAC05, Testing, Installation, Commissioning and first operation of the ISIS RFQ pre-injector upgrade.
[3] C. Plostinar, IPAC12, Modelling the ISIS 70 MeV Linac.
[4] C R Prior, A-11, ICANS-XII, RAL Report 94-025, "Studies of Dual Harmonic Acceleration in ISIS".
[5] A. Seville, EPAC08, Progress on Dual Harmonic Acceleration on the ISIS Synchrotron.
[6] A. Seville, IPAC13, Progress on the ISIS Synchrotron low power RF system upgrade.
[7] S. Payne, HB2008, Beam Diagnostics at ISIS.
[8] R. Williamson, IPM Simulation and Correction with Strong Space Charge, Proc IPM Simulation Workshop, CERN (2016).
[9] G.H.Rees, Interpretation of the Higher Mode Head-Tail Motion Observed on ISIS, Particle Accelerators, Part Accel V39, 1992.
[10] S. Payne IBIC13, "Stripline monitor design for the ISIS proton synchrotron using the FEA program HFSS".
[11] R. Williamson, HB2016, Developments of Physics Models of the ISIS Head-Tail Instability.
[12] J.A. Holmes et al., ORBIT User Manual, ORNL Tech. Note SNS/ORNL/AP/011.
[13] D. Adams, PAC12, "Beam loss studies on the ISIS synchrotron using ORBIT".
[14] R.E. Williamson, HB2012, "High Intensity Longitudinal Dynamics Studies for an ISIS Injection Upgrade".
[15] C. Warsop, HB2016, "Simple Model for Beam Loss Near the Half Integer Resonance with Space Charge".
[16] B. Pine, Image Fields in the Rectangular Vacuum Vessels of the ISIS Synchrotron, HB2014.
[17] T Wood, "The ISIS pre-injector reconfiguration", Review of Scientific Instruments 87, 02B121(2016).
[18] D. Adams, HB2014, "Ring Simulations and Beam dynamics studies for ISIS upgrades 0.5 to 10 MW".
[19] C Prior, HB2016, "Studies of High Intensity Proton FFAGs at RAL".
[20] A. Letchford, Linac2014, "Status of the FETS Project".

ISBN 978-3-95450-185-4

IFMIF-EVEDA RFQ, MEASUREMENT OF BEAM INPUT CONDITIONS AND PREPARATION TO BEAM COMMISSIONING

M. Comunian†, L. Bellan[1], E. Fagotti, A. Pisent, Istituto Nazionale di Fisica Nucleare Laboratori Nazionali di Legnaro, Legnaro, Italy
[1]also at Univ. degli Studi di Padova, Padova, Italy

Abstract

The commissioning phase of the IFMIF-EVEDA RFQ requires a complete beam characterization with simulations and measurements of the beam input from the IFMIF-EVEDA ion source and LEBT, in order to reach the RFQ input beam parameters. In this article, the simulations of source LEBT RFQ will be reported with the corresponding set of measurements done on the Ion source and LEBT.

THE IFMIF-EVEDA PROJECT

The Linear IFMIF Prototype Accelerator (LIPAc) is an high intensity deuteron linear accelerator [1]; it is the demonstrator of the International Fusion Material Irradiation Facility (IFMIF) machine within the Engineering Validation Engineering Design Activities (EVEDA) scope. It is presently in an advanced installation phase at Rokkasho under the Fusion Energy Research and Development Directorate National Institutes for Quantum and Radiological Science and Technology (QST), in the prefecture of Aomori, Japan. LIPAc has been designed and constructed mainly in European labs with participation of JAEA in the RFQ couplers. It is composed of an injector delivered by CEA-Saclay [2], a RFQ [3] designed made and delivered by INFN on April 2016, a superconducting Linac designed by CEA-Saclay [4], RF power, Medium and High Energy Beam Transfer lines and a beam dump designed by CIEMAT [5].

THE IFMIF-EVEDA RFQ

The Radio Frequency Quadrupole (RFQ) 0.1 - 5 MeV, 130 mA, is an Italian in-kind contribution to the IFMIF-EVEDA project, under the INFN responsibility.

The RFQ design method has been aimed to the optimization of the voltage and R0 law along the RFQ, the accurate tuning of the maximum surface field and the enlargement of the acceptance in the final part of the structure. As a result, a length shorter than in all previous design characterizes this RFQ; very low losses (especially at higher energy) and small RF power dissipation [6].

In Table 1 and Fig. 1 are reported the main RFQ parameters along its length.

LAYOUT OF INSTALLED SOURCE AND LEBT

The injector is composed of a 2.45 GHz ECR ion source based on the CEA-Saclay SILHI source design and a LEBT line that will transport and match the beam into the RFQ thanks to a dual solenoid focusing system with integrated H/V steerers.

† Michele.comunian@lnl.infn.it

Table 1: RFQ Main Parameters

Length	9.814	m (5.7λ)
Total Cell number	489	
Voltage Min/Max	79.29/132	kV
Max modulation m	1.8	
Min aperture "a"	3.476	mm
R0 min/Max	5.476/7.102	mm
Ratio ρ/R0 (constant)	0.75	
Final Synch. phase	-35.5	Deg
Max Surf. Field (1.76 Kp)	24.7	MV/m

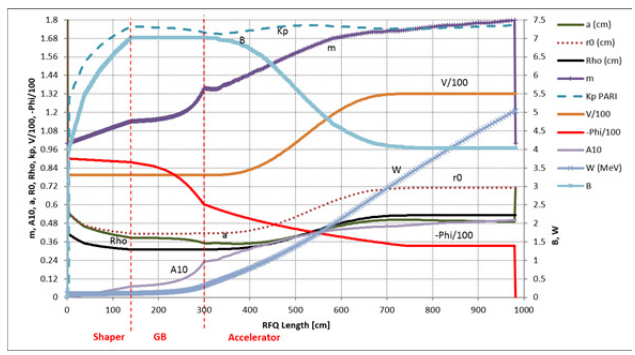

Figure 1: Parameters evolution along the RFQ.

The components of the LEBT are:

- Two solenoids with integrated steeres.
- Injection cone with repeller electrode after the two solenoids.
- Middle solenoids diagnostic box equipped with Doppler Shift Spectrometer instrumentation, Farady cup, Four Grid Analyser and Residual Gas Analyser.
- End diagnostic box after the solenoids, with an Allison scanner and self-polarised beam stop.

The commissioning is started in 2015 and will continue in 2016 interleaved with the RFQ installation in order to optimize the project schedule.

Design simulations show that to have less than 10% losses in the RFQ, the injected D+ beam must be 140 mA/100 keV CW with a normalized RMS emittance of 0.25 mm·mrad.

Commissioning activities use an equal generalised perveance H+ beam at RFQ injection, which consists of half current and half energy compare to deuterons at nominal conditions. This is done to allow hands-on maintenance activities since the activation power of 50 keV protons is negligible. Moreover, an electrostatic chopper has been implemented in between the two solenoids to provide sharp beam pulses of short length (~ 50-100 μs) for machine protection system in view of the RFQ com-

ISBN 978-3-95450-185-4

missioning. Typically commissioning activities are done at 10% of duty cycle.

BEAM DYNAMICS SIMULATION AND MEASUREMENT OF SOURCE AND LEBT

The simulation was divided in two parts.

The first one deals with the extraction system and the plasma meniscus estimation (AXCEL-INP [7] program was used). The AXCEL simulation gave first estimation of the Twiss parameters and the emittance. Then, the input beam parameter was fine-match to an emittance measurement, via the neutralisation level given by FGA.

The second part deals with the LEBT: the software used was TraceWin[8]. Field map of the solenoids and of the repeller electrode in the RFQ injection cone were used. The input beam studied [9] is an H+ beam at 50 keV and 55 mA (Q = 3.23×10^{-3} generalised perveance) with a ratio of 75% compared to H2+ and H3+. The simulated input beam follows an uniform transverse 4D distribution with 5 eV as energy spread and with the input parameters found with the procedure defined above.

The TraceWin simulation starts 200 mm from the source extraction hole after the electrodes.

The distribution at the output of the source is not generally in an equilibrium state and the few betatrone oscillations along the LEBT are not enough in order to relax it. It will relax along the 9 meters' length; therefore, the main critical part is at the RFQ injection.

The matched beam follows the Eq. 1, where the ε_x is the total emittance given from ε_x=a $\varepsilon_{x,rms}$ (a is an arbitrary costant) which is not normally constant along the line. The generalised perveance term is not constant also because the space-charge defocusing term depends on the neutralisation level.

$$r_x''(s) + k_x(s)r_x(s) - \frac{2Q(s)}{r_x(s)+r_y(s)} - \frac{\varepsilon_x^2(s)}{r_x^3(s)} = 0. \qquad (1)$$

The key parameters are the space charge defocusing term and the emittance defocusing term. In particular, the ratio between these two terms can help us to determine if the LEBT is emittance or space-charge dominated.

In simulations, static neutralisation was used in order to speed up calculations during the commissioning and its limitations were explored (see table 3).

From indirect calculation the exit of the extraction source seems to produce a too divergence beam at the first solenoid. Thus, the emittance growth is given mainly by the coupling from the solenoid nonlinearities and space charges.

The emittance trend was confirmed experimentally and by simulations during the March 2016 campaign, as in Fig.2 and Fig. 3 can be seen.

In fact, the neutralisation level of more than 95% between the solenoids implies an emittance-dominated beam (comparing the space-charge defocusing and thermal term from Eq. 1).

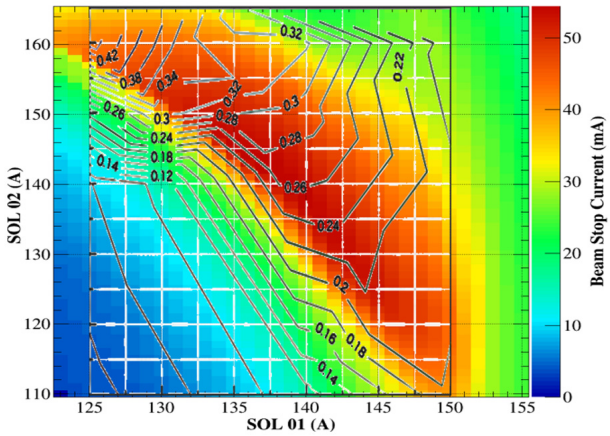

Figure 2: Beam stop current scan plot and rms norm. iso-emittance areas (black lines), measured at March work point. It is possible to identify the almost monotonic emittance trend from lower right corner to left upper corner.

Another degree of freedom found in the simulation was the neutralisation after the beam cone: the vacuum level is normally about 10^{-7} torr. Therefore, the contribution of the generated electrons from the residual gas is lower compared to the emitted electrons from the tungsten shield of the emittance meter.

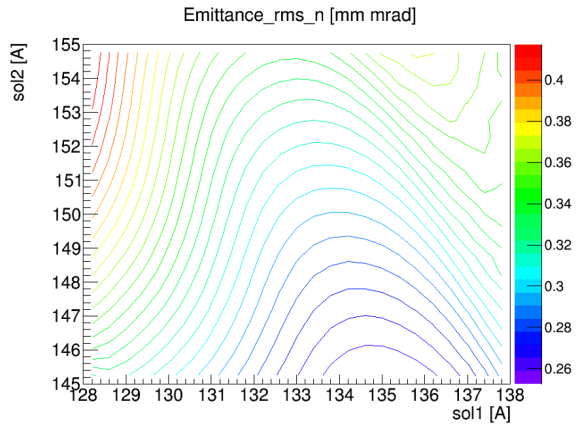

Figure 3: Particular of simulated rms norm. emittance gradient in the strong focusing zone (i.e. Sol1 from 120 A to 140 A, and Sol2 from 140 A to 165 A).

The electron cloud is attracted from the positive potential of the beam and neutralises. The overall effect of this neutralisation was estimated comparing with the BS (which is self-polarised) transmission and the emittance measurement.

As shown in the following table 2, there are two different regimes of neutralisation, which determine the current read by the BS and the emittance measurement, which needs to be taken into account.

The electron cloud dynamics is fairly complex and it is under study with another code (Warp[10]).

Another evidence seen by the measurement, foreseen by the simulation studies [11] and the theory is the dependence of the neutralisation level from the beam envelope.

ISBN 978-3-95450-185-4

Table 2: Example of Parameter Changes in the Neutralisation after the Cone for the Solenoid Point (128 A, 158 A)

EMU in/out	Sim. neut. after the cone	Meas.	Simulation
in	87%	0.38 mm mrad	0.36 mm mrad
in	0%	0.38 mm mrad	0.43 mm mrad
out	0%	49 mA	46 mA
out	87%	49 mA	55 mA

This fact limits the approximation of the same level of neutralisation in confined zones of the scan plot, which was also a part of the study.

Table 3: Neutralisation Results and Input for the Three Zones

Scan plot zone limit approximation zone	N. before the cone	N. after the cone
134-145 A sol1 135-145 A sol2	96%	80%
127-138 A sol1 145-155 A sol2	99% (from measurement)	80%
125-135 A sol1 155-165 A sol2	99%	87%

This approximate but almost complete description of the LEBT dynamics allows us to estimate the mismatch at the RFQ input, which stays 300 mm before the emittance meter. See Fig. 4 as an example.

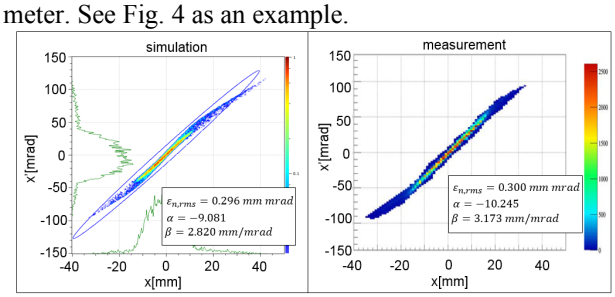

Figure 4: Simulated vs measured phase space at emittance meter for the point (130 A, 150 A).

From previous studies [12] the 30% mismatch zone[13] should be found in the upper left quadrant of Fig. 2. This fact was confirmed by the post analysis of the March campaign, as shown in Fig. 5. Once the 30% zone was identifying with an emittance around 0.3 mm mrad, it was possible to test the RFQ transmission and its output beam parameters.

RFQ SIMULATIONS

The RFQ is matched to the superconductive cavities with a MEBT line. The current of the accelerated particle can be seen at the low power beam dump position, at the end of the matching line. Before that the quadropoles and bunchers must be set in order to maximise transmission

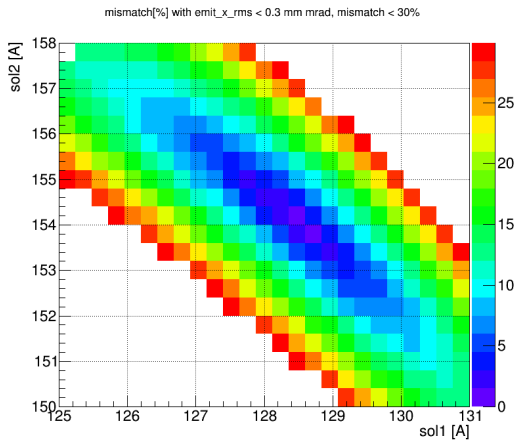

Figure 5: 30% mismatch zone located within the upper left quadrant of the scan plot (165-140 A sol2 and 124-140 A sol1).

In order to decuple the effect of bad MEBT quadrupole settings, the effect of not accelerated particles, injector problems and RFQ issues, it is important to estimate the output beam parameters (without the not accelerated particles) at the exit of the RFQ, respect to the LEBT solenoid values in the minimum mismatch zone (Fig. 5).

The Fig. 6 shows the current transmitted by the RFQ, without the not accelerated particles.

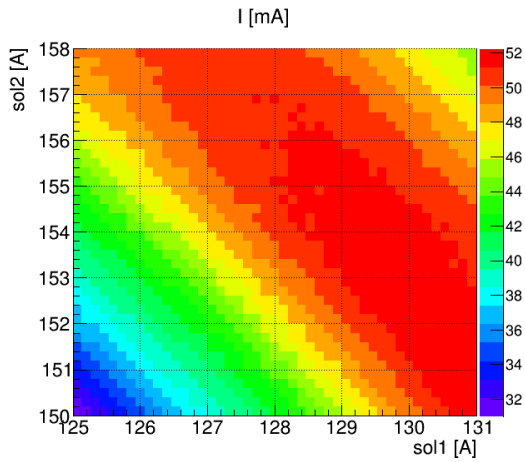

Figure 6: Current plot without the not accelerated particles in the scan plot zone with smaller mismatch.

The maximum transmission results to be 93%. We can define the mismatch compared to the output Twiss parameters for the point with maximum transmission.

The results can be seen in terms of output transverse beam emittance and mismatch in Fig. 7.

Within the maximum transmission area, the rfq output beam does not show significant changes in terms of Twiss parameters. The emittance may change of about 10% depending on the solenoid value.

On the contrary, if we move far away from the minimum mismatch zone, we may find zones with more than 16% of mismatch that couples with a smaller transmission to the RFQ.

ISBN 978-3-95450-185-4

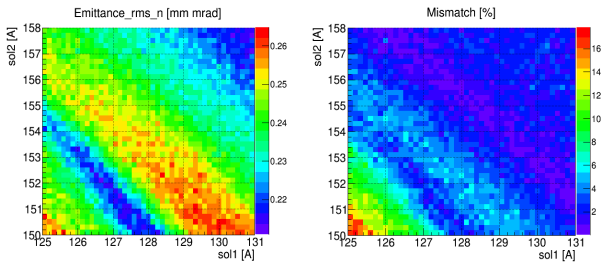

Figure 7: RFQ output beam parameters (mismatch and emittance) with the change of the lebt solenoids.

However, it would be useless to maximise the MEBT transmission in this zone, due to the fact that the rfq transmission would not be optimised. The simulation results shown by Fig. 6 and Fig. 7 evidence this fact.

Therefore, the MEBT quadrupole values should not affect the beam losses while moving the LEBT solenoid in the matching zone, but they need to be set with the simulation foreseen maximum transmission point of the accelerated particles.

SOURCE AND LEBT COMMISSIONING STATUS

At the state of the art the source is under commissioning at Rokkasho site, where the parameters still to be achieved are 65 mA H+ at 50 keV and 130 mA D+ at 100 keV with 0.25 mm mrad emittance in the equivalents strong focusing areas.

The LEBT behaviour is almost well understood and simulated, while the source needs a deeper beam dynamics studies and measurements for matching the QA requirements.

Some minor effects, which deal with secondary electrons, need to be fully understood but will require a different software to be managed.

CONCLUSION

The March campaign shows how strong can be the support given by the simulation even in such complex systems.

The results of the simulation and measurement from March 2016 are well in agreement, while they could effectively predict the area for matching the RFQ parameters. The prerequisites needed are:

- Measurements should be linked to all set of parameters of the LEBT, like gas pressure, solenoid settings extracted current, proton fraction. In this way it is possible to have under control all the observables of the many physical phenomena undergoing.
- the simulations must be performed taking into account their limit and their prerequisites.

On the contrary, the source presents many difficulties from the physics-modelling point.

Therefore, the extraction system simulation needs some extra caution: as an example, the presence of contaminants can affect the plasma state and deflect the beam from the expected trajectories.

Much effort should be put to this topic in order to start the RFQ commissioning.

REFERENCES

[1] P. Cara *et al.*, in *Proc. IPAC'16*, paper MOPOY057, Busan, Korea.
[2] R. Gobin *et al.*, in *Proc. IPAC*'13, paper THPWO003, Shanghai, China.
[3] M. Comunian and A. Pisent, in *Proc. IPAC'11*, paper MOPS031, San Sebastian, Spain.
[4] H. Dziko *et al.*, in *Proc. IPAC'13*, paper THPF006, Richmond, Virginia.
[5] J. Marcos *et al.* in *Proc. IPAC'16,* paper TUPMB019, Busan, Korea.
[6] A. Pisent *et al.*, in *Proc. EPAC'08*, paper THPP078, Genoa, Italy.
[7] INP, P. Spädke, Junkernst. 99, 65205 Wiesbaden, Germany, e-mail: p.spaedtke@inp-dme.com.
[8] http://irfu.cea.fr/Scam/logiciels/index.php
[9] B. Bolzon *et al.*., in *Proc. IPAC'16*, paper WEPMY033, Busan, Korea.
[10] WARP, http:// http://warp.lbl.gov
[11] N. Chauvin *et al.*, in *Proc. LINAC'10*, paper TH302, Tsukuba, Japan.
[12] Private communication, COB meeting, March 2016.
[13] T. P. Wangler, "RF Linear Accelerators", Wiley-Vch.

ISBN 978-3-95450-185-4

ESS LINAC PLANS FOR COMMISSIONING AND INITIAL OPERATIONS

R. Miyamoto*, M. Eshraqi, M. Muños, ESS, Lund, Sweden

Abstract

Beam commissioning of the proton linac of the European Spallation Source (ESS) is planned to be conducted in 2018 and 2019. At this stage, the last 21 cryomodules are not yet installed and the maximum beam energy and power are 570 MeV and 1.4 MW, with respect to the nominal 2 GeV and 5 MW. The linac will be operated in this condition until the remaining cyromodules are installed in two stages in 2021 and 2022. On top of the common challenges of beam dynamics and machine protection, commissioning of a large scale machine, such as the ESS linac within a relatively short integrated time of less than 40 weeks imposes an additional challenge to the scheduling and planning. This paper lays out the current plans of the ESS linac for its beam commissioning as well as the initial operation.

INTRODUCTION

European Spallation Source (ESS), currently under construction in Lund, Sweden, is a neutron source driven by a proton linac. When the linac reaches its unprecedented design average power of 5 MW, the ESS will the brightest neutron source in the world [1, 2]. It is planned that installation and commissioning of the ESS linac starts in 2017 and the first proton beam is delivered to the target by the end of 2019. The plan as the ESS facility is to start the user program in 2023 and gradually increase the neutron production and operation time towards the design specifications. Commissioning of a large-scale machine, such as the ESS linac, within a relatively short time imposes challenges on many areas including planning and preparations for the beam commissioning (BC). Many efforts have already made for planning of the commissioning from the point of view of the installation [3,4], radiation permit [5], beam diagnostics devices [6, 7], and control software [8]. In this paper, we review the procedures of the beam commissioning from the point of view of beam physics so that necessary types of lattice tuning and their methods are clarified and prepared prior to the beam commissioning.

ESS LINAC OVERVIEW

High Level Parameters

Table 1 lists the high level parameters of the ESS linac during the nominal operation. The 2 GeV energy, 62.5 mA current, and 4% duty cycle make average power of 5 MW. The long pulse length of 2.86 ms is a requirement from the users and thus fixed during any phase of operation. If the power is needed to be reduced during initial phases of operation, the peak current or and repetition rate is reduced. A high availability of 95% is also a requirement from the users due to the nature of the user program [9].

Table 1: High Level Parameters of the ESS Linac

Parameter	Unit	Value
Average beam power	MW	5
Maximum beam energy	GeV	2
Peak beam current	mA	62.5
Beam pulse length	ms	2.86
Beam pulse repetition rate	Hz	14
Duty cycle	%	4
RF frequency	MHz	352.21/704.42
Availability	%	95

Linac Structure

Figure 1 shows a schematic layout of the ESS linac. The initial part of the linac is consist of an ion source (IS); two normal conducting accelerating structures, a radio frequency quadrupole (RFQ) and drift tube linac (DTL); and two beam transports, a low energy beam transport (LEBT) and medium energy beam transport (MEBT). These are referred to as the normal conducting linac (NCL) as a whole. In addition to provide acceleration, functionalities of the NCL includes bunching in the RFQ and manipulations of the beam parameters. Once the beam exits the MEBT, there is no controlled change in the current and pulse length in the downstream section.

Following the NCL, there are three sections with different types of superconducting cavities, spoke cavities, medium-β elliptical cavities, and high-β elliptical cavities. These sections are referred to as SPK, MBL, and HBL for each and Superconducting Linac (SCL) as a whole. As seen in the figure, most of the energy gain is provided by the superconducting cavities in the SCL.

Another beam transport, a high energy beam transport (HEBT), follows the SCL. The HEBT has the same lattice structure as the HBL except the empty slots for the cryomodules, which allow to install additional cryomodules later in cases of contingencies or for an energy upgrade. At the end of the HEBT, there is a dipole for the upward bend and the linac is split into two from this point. When the dipole is off, the beam enters the dump line (DMPL) and is stopped by a tuning dump at the end. When the dipole is on the beam enters the dogleg and is bent back towards the target by another dipole after a 4.5 m elevation. After the second dipole is the final section of the linac and another beam transport, the accelerator-to-target (A2T) section. In the A2T, each pulse is sprayed over a rectangular region on the target surface by fast oscillating (~29 kHz in horizontal plane and ~40 kHz in vertical plane) dipole magnets to reduce the intensity (*rastering* process).

Further details of each section are provided later during the discussion of the commissioning plan for each section.

* ryoichi.miyamoto@esss.se

ISBN 978-3-95450-185-4

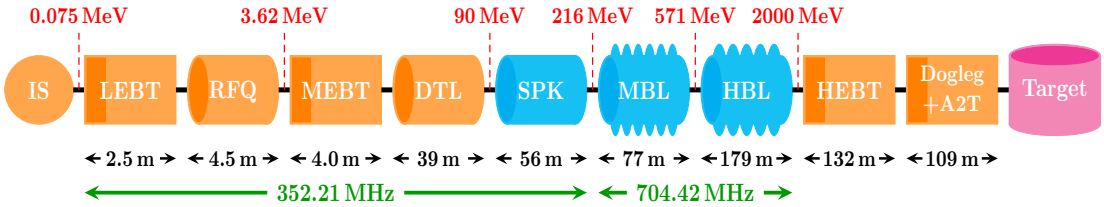

Figure 1: ESS linac schematic layout. Normal conducting structures and beam transports are in orange and superconducting structures are in blue.

BEAM COMMISSIONING OVERVIEW

Plan of the Initial Phase

The installation and commissioning of the ESS linac will be done in stages. On the first stage, starting in 2017, all the components except the cryomodules for the HBL will be installed. The linac will be commissioned at this state, where the maximum energy and average power are 571 MeV and 1.4 MW for each, and operated until the end of 2020. In 2021 and 2022, the cryomodules for the HBL will be installed in two stages, completing installation of all the components. From 2023, performance of the linac will be gradually raised, aiming to achieve the design specifications summarized in Table 1 in around 2025. The focus of this paper is on the initial stage until 2020. The following discusses the schedule and steps of this stage with more details [3–5, 10].

The commissioning of the IS and LEBT has been already started in the lab of the in-kind partner INFN-LNS in Catania, Italy and will be completed, including the beam commissioning, prior to the delivery to the ESS site scheduled in 2017. It is planned to fully test both again in the tunnel before the RFQ is installed.

In late 2018, the RFQ and MEBT will be installed and commissioned together. This means that the beam out of the RFQ must be characterized with diagnostics devices in the MEBT. For some hadron linacs, for instance the CERN LINAC4, the IS, LEBT, and RFQ were commissioned by itself without the following sections and the output beam of each section was characterized with a common movable test bench [11]. The movable bench was also considered for the beam commissioning of the ESS NCL [12] but is not currently in the plan due to the limitations in budget and schedule. By the end of 2018, the first DTL tank out of five will be also installed and commissioned.

In early 2019, DTL tanks 2-4 will be installed and commissioned. Up to this point, the beam will be stopped with a temporary beam stop and temporary shield walls will be placed after the DTL tank 4 to separate the sections under the beam commissioning and the rest and to allow the beam commissioning and other installation works in parallel. The installation of the rest of the sections is scheduled to be completed in mid-2019 and the beam commissioning will be resumed afterward. At this point, the available beam stops are the target, tuning dump, or one of Faraday cups (FCs) used as beam stops, located in the LEBT, MEBT, DTL, SPK, and MBL [6, 7]. Please note that only the target and the FC in the LEBT can stop the beam with the nominal current and pulse length. The beam commissioning will continue with a low power beam until the beam is safely delivered first to the tuning dump and then to the target. It is aimed to deliver the first beam to the target by the end of 2019 and the the power will be gradually increased towards 1.4 MW afterward.

Beam Modes

In addition to the nominal beam parameters in Table 1, several sets of beam parameters, *beam modes*, are defined to be used during the beam commissioning and general linac tuning [13, 14] (Table 2). The *probe* mode is the lowest power beam, mainly for the very first check of the system and hardware and the beam threading, the process to correct the trajectory and deliver the beam to the designated beam stop. The *fast tuning* and *slow tuning* modes are used to characterized the beam and achieve the desired beam parameters and thus the main types of modes during the beam commissioning. The fast tuning mode is mainly for setting the phases and amplitudes of cavity fields. The slow tuning mode could have a pulse length up 50 µs and this is meant to provide a good quality signal to invasive diagnostics devices, such as FCs and wire scanner (WS) profile monitors. The slow tuning mode will be also used to set the low-level RF (LLRF) feed-backs and feed-forwards for the cavities. The fast and slow tuning beams can be stopped with any of the beam stops.

Once the tuning with low power beams are completed, the next step is to gradually extend the pulse length and verify the beam losses are within the limit. The *long pulse* mode is for this purpose. After the LEBT, this beam can be stopped only with the tuning dump or target. Due to its 12 kW limitation, the tuning dump can stop the long pulse beam with the full current and full pulse length roughly only once per minute. This indicates that verification for high power beams, particularly beams with repetition rate higher than 1 Hz, must be conducted by sending the beam to the target. In addition to the modes listed in the table, another mode to verify the radiation shielding is also under discussion and to be added. Please also note that, to minimize the radiation, further limitations will be applied during the initial phase of the beam commissioning up to the DTL tank 4 [5].

COMMISSIONING OF EACH SECTION

This section provides an overview of the structure and functionalities of each section and discusses its beam com-

ISBN 978-3-95450-185-4

Table 2: List of Beam Modes

Type	Destinations	Main usages	Peak current [mA]	Pulse length [μs]	Repetition rate [Hz]
Probe	Any beam stop	Initial check Beam threading	6 - 62.5	≤ 5	≤ 1
Fast tuning	Any beam stop	RF setting	6 - 62.5	≤ 5	≤ 14
Slow tuning	Any beam stop	Invasive measurement LLRF setting	6 - 62.5	≤ 50	≤ 1
Long pulse	Tuning dump Target	Beam loss check Lorentz detuning check	6 - 62.5	≤ 2860	≤ 1/30
Production	Target	Neutron production	6 - 62.5	2860	≤ 14

missioning, focusing on the types of tuning needed for the considered section.

General Strategy

Before going into details of each section, we discuss a general strategy applied to any section. The first step of the beam commissioning is to thread the lowest ~6 mA current probe beam to the designated dump. Polarities of the BPMs, dipole correctors, and quadrupoles should be also checked at this point by producing multiple trajectories and observing the differences (*difference trajectory* method). If the commissioned section includes the RF cavities, the next step is to set the phases and amplitudes of the cavity fields with the phase scan technique, one by one from the first cavity of the section towards the downstream. This process is also done with the probe or fast tuning beam with the lowest current of ~6 mA. The centroid positions in all three planes should have been adjusted at this point but the transverse positions may have to be fine-tuned or readjusted after the transverse matching.

Following the adjustment of the centroid positions is measurement and matching of the Courant-Snyder parameters. The RMS sizes and profiles of the beam are measured with interceptive profile monitors during the beam commissioning and thus the slow tuning beam mode is used for this step. For the sections with a periodic structure (the sections providing acceleration, HEBT, and dogleg), the matching at the interface of two sections is desired. In the MEBT and A2T, adjustments of beam sizes are also required at some locations. Because the Courant-Snyder parameters of the beam depend on the beam current, this step has to be repeated when the current is changed.

After the centroid positions are adjusted and the matching is achieved, we gradually increase the pulse length (long pulse beam mode) and verify the beam losses are within the limit. As the case of the matching, this step also has to be repeated when the current is changed.

IS and LEBT

As already mentioned during the discussion of the plan, the IS and LEBT will be beam commissioned prior to the delivery to the ESS site and thus the work after the installation will be verifications of the measurements before the delivery. Nonetheless, as seen in the proposed beam commissioning plan [15], the LEBT has many functionalities and there are a lot of beam parameters to verify. Figure 2 shows a schematic layout of the LEBT. The main components of the LEBT are the two solenoids, chopper, iris, and diagnostics devices.

The diverging beam out of the IS is focused and matched to the RFQ entrance with the two solenoids. In the LEBT, there is a process referred to as *space-charge compensation* (SCC), where the electrons from the ionization of the residual gas, induced by the incoming pulse itself, are trapped within the pulse and reduce the space-charge force. The anticipated level of the SCC is around 95% for the ESS LEBT and thus it has a large impact for the beam focusing. The beam focusing can be verified with measurements of the Courant-Snyder parameters and emittances from the emittance measurement unit (EMU), located between two solenoids. The other commonly used method to optimize the focusing in the LEBT, after the installation of the RFQ, is to scan the solenoids and determine the settings based on the transmission out of the RFQ [16, 17]. The beam parameters out of the LEBT are sensitive to the level of the SCC [17]. If needed, the level of the SCC can be indirectly controlled by adjusting the vacuum level. Each solenoid includes the windings to produce dipole fields of both plane, allowing to correct the transverse centroid positions of the beam. The two non-invasive profile monitors (NPMs) seen in Fig 2 are in fact mainly for measurement of the transverse centroid positions.

During the production of each pulse, the IS is estimated to take a few ms to get stabilized and the beam from this transient period is likely to have wrong parameters. The

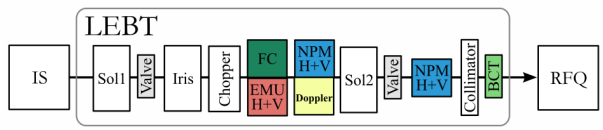

Figure 2: LEBT schematic layout (courtesy of B. Cheymol).

ISBN 978-3-95450-185-4

chopper, located between the solenoids, deflects and removes this part of the pulse. This means that, for example when producing a 2.86 ms pulse, the IS outputs a pulse of ~6 ms and approximately the initial half is removed so that the desired 2.86 ms is left. The deflected part of the beam is stopped by the RFQ entrance cone, denoted as "collimator" in Fig 2. Please note that the SCC is induced by the pulse itself and estimated to takes up to ~20 µs to reach to a stable state, meaning that the initial ~20 µs part of the pulse is still likely to have wrong parameters even after using the chopper. This ~20 µs part is removed with the chopper in the MEBT. The function of the chopper can be verified with the beam current transformer (BCT), housed inside the RFQ cone.

The current out of the IS is almost a fixed value. Thus, when producing a lower current beam, the beam is scraped with the iris with a hexagonal shape cross-section, located between the solenoids. The ideal Courant-Snyder parameters at the RFQ entrance are dependent, in fact nonlinear functions, of the peak current [13]. Thus, when the current is reduced with the iris, the solenoids have to be also adjusted accordingly and a well-defined procedure for this process has to be prepared. The reduction of the current is verified also with the BCT inside the RFQ cone.

The beam out of the IS contains not only protons but also other positively charged ions. The design specification is the fraction of the protons is larger than 75%. The Doppler detector allows to verify this fraction based on the difference in the Doppler shifts for different species.

RFQ and MEBT

After the IS and LEBT, the RFQ and MEBT will be beam commissioned together. For the RFQ, the only parameter to adjust is the amplitude of the field to achieve the desired output energy of 3.62 MeV. The output energy is reconstructed from time-of-flight (TOF) measurements with beam position monitors (BPMs) in the MEBT. After setting the amplitude of the field, the transmission should be verified. The efficiency of any RFQ is never perfect and the output beam includes particles not properly accelerated. Figure 3 shows a schematic layout of the MEBT. There is one BCT at the entrance and the other around the middle, behind the chopper dump. These two BCTs are to distinguish the transmissions of the particles with the right energy and the rest. This is based on the result of a study that, for the ESS RFQ, most of the particles with wrong energies have the IS output energy of 75 keV and they do not reach beyond the third quadrupole.

As seen in Figure 3, the MEBT lattice is consist of three buncher cavities, eleven quadrupoles, chopper, and chopper dump. Each quadrupole has additional windings to produce dipole fields of both transverse plane. The beam threading

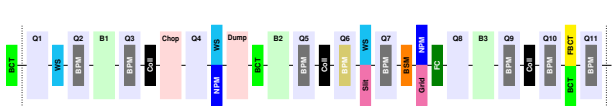

Figure 3: MEBT schematic layout.

is done with these dipoles and the BPMs installed inside the selected seven quadrupoles. The buncher cavities only provide the focusing in the longitudinal plane and do not change the energy by design. However, in case the output energy of the RFQ is slightly off and cannot be adjusted with the RFQ itself, they are capable of making a small adjustment of energy (the order of tens of keV) as well.

Out of the eleven quadrupoles, the first four are used to adjust the optics of the region with the chopper and it dump. The beam is expanded in both transverse plane at the exit of the chopper dump and the remaining seven quadrupoles are used to refocus the beam and match to the DTL. The MEBT houses three WSs and one EMU, consisting of a slit and grid, for each transverse plane. The measurements from these devices provide enough information to set the transverse optics but a further study should be performed to establish a well-defined process for the real machine. For the longitudinal plane, there is only one profile monitor, *bunch shape monitor* (BSM). Thus, to reconstruct the Courant-Snyder parameters and emittance and achieve the longitudinal matching, measurements with different settings of a buncher cavities are needed.

The function of the chopper will be checked in a later part the MEBT beam commissioning, after the centroid positions and the optics is adjusted. The rise and fall times of the MEBT chopper are on the order of 10 ns. The BPM with a special electronics in the sixth quadrupole and a fast beam current transformer (FBCT) towards the end are capable of measuring currents of single bunches around the leading and trailing edges of a pulse and verifying the function of the chopper. The MEBT includes dual-plane collimators at three locations to remove the halo in the transverse plane. Adjustment of the jaw positions of these collimators is also a process for the later part of the MEBT commissioning. Because the distribution is dependent on the current, this process is also has to be repeated every time when the current and the optics is changed.

DTL

The ESS DTL consists of five tanks. Every other drift tube houses a permanent quadrupole magnet (PMQ), forming a FODO channel, and some of the drift tubes without a PMQ houses a BPM or single plane dipole corrector. Because the transverse focusing is provided by the PMQs, the only parameters to adjust are the phase and amplitude of the field of each tank and dipole correctors.

SCL and HEBT

The three sections of the SCL have a similar lattice structure. One lattice period is consist of one quadrupole doublet and one cryomodule. In-between the doublet quadrupoles, there are a dual-plane dipole corrector, BPM, and space for other types of diagnostics devices (mainly profile monitors). The doublet and these devices in-between form a unit referred to as *linac warm unit* (LWU). Each cryomodule in the SPK houses two spoke cavities and each cryomodule in MBL and HBL houses four elliptical cavities. For each

ISBN 978-3-95450-185-4

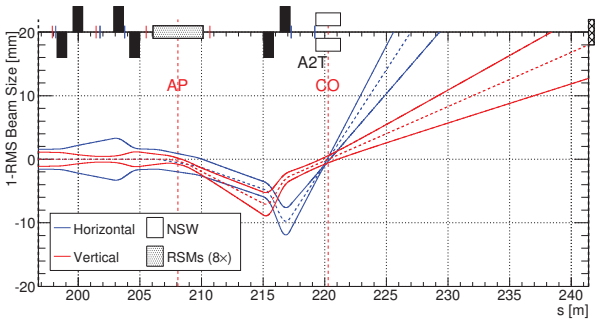

Figure 4: A2T schematic layout and RMS beam envelopes inside (courtesy of H. D. Thomsen).

section, the numbers of the lattice periods are 13, 9, and 21, making 62 superconducting cavities in SPK and MBL and 146 in total. Because of this many number of cavities, the major part of the SCL beam commissioning is to set the phases and amplitudes of the fields of all these cavities.

The second, fourth, and fifth LWUs in the SPK and MBL house a WS. These three WSs are to measure the transverse Courant-Snyder parameters and emittances at the initial part of each section and to perform the matching if necessary. The lengths of the LWUs and cryomodules in the MBL and HBL are identical, making the lattice periods of these sections identical. Because of no change in the lattice structure, the transverse matching is not considered at the MBL-HBL interface. The first LWUs in the SPK and MBL house a BSM to measure the longitudinal size and profile of the beam. The reason for the smaller number than the WSs is the difference in cost. As the case of the MEBT, to determine the Courant-Snyder parameters and emittance and and perform the longitudinal matching, multiple measurements have to be made for different settings of upstream cavities.

The HEBT is consist of 16 lattice periods, identical to those in the MBL and HBL. As described in the following, the beam optics of the A2T requires a careful adjustment to meet the requirements from the target. Hence, to provide a properly matched beam to the A2T, the HEBT houses three WSs towards the end. Even if the installation will have been completed through the target, the beam will not be sent to the target until the beam parameters are properly adjusted up to the end of the HEBT. Until then, the will be sent to the tuning dump.

Dogleg and A2T

Similar to the SCL and HEBT, the dogleg is also a focusing channel with quadrupole doublets but with a different period length. It consists of six periods with a vertical phase advance per period of 60 degrees, making it achromatic on the first order [18]. The achromatic condition can be verified by monitoring the vertical position at the first BPM in the A2T while modulating the energy out of the SCL by adjusting the last available cavity.

The target of sets boundaries on the beam parameters on its surface: the intensity has to be within 56 μA/cm^2 but at the same 99% of the particles have to be inside a rectangular region of 160 $\times$ 60 cm^2. The main function of the A2T is to manipulate the beam to meet these requirements. This is achieved by expanding the beam sizes with the optics and also sweeping the centroid position with the raster system. Details on the optics of the A2T and the raster system can be found elsewhere, e.g., [18], but we briefly discuss how to tune the lattice during the beam commissioning in the following. Figure 4 shows a schematic layout of the A2T together with RMS beam sizes of two transverse planes (for the case of the full amplitude of the raster system). The lattice is consist of six quadrupoles (black boxes) and the raster system, consisting of four fast dipole magnets per plane, sitting between the fourth and fifth quadrupoles. The Action Point (AP) is the center of the raster system and the Crossover (CO) is the location of the neutron shield wall, blocking the backscattered particles from the target and thus having an aperture radius of 20 mm, tighter than 60 mm for the upstream part, over a length of ~2 m. The last two quadrupoles between the raster system and CO set the phase advances of the two transverse planes 180 degrees, making the CO a fixed pivot point of the raster motion. There are dual plane corrector dipoles right before and right after the raster system so that the trajectory of the raster motion can be reproduced. By monitoring the position with the BPM at the CO while scanning these two dipole correctors, we can verify the 180 degrees phase advance between the AP and CO. The initial four quadrupoles are setting the beam sizes on the target surface and at the CO. It is planned to have one WS at AP and two imaging systems between the CO and the target. The measurements from these three devices should allow to reconstruct the Courant-Snyder parameters and emittances and thus to achieve the desired beam sizes with the initial four quadrupoles. Once the optics is adjusted, the anticipated maximum extent of the raster system can be verified again with the dipole correctors on the sides of the raster system. The next step is to actually use the raster system and check its function. The two imaging systems between the CO and the target can be used for this.

CONCLUSIONS

Start of the beam commissioning of the ESS linac being approaching, its plan was reviewed from the point of view of beam physics and types of required tuning. It has been identified which lattice components have to be adjusted to achieve the desired value of a given beam parameter. The necessary diagnostics devices for each type of verification and tuning are also checked to be in the plan. For all the types of the tuning, further detailed studies will be conducted to establish well-defined procedures and to understand the limitations.

ACKNOWLEDGMENTS

The authors would like to thank to B. Cheymol, R. de Prisco, Y. I. Levinsen, O. Midttun, A. Ponton, H. D. Thomsen for useful discussions.

ISBN 978-3-95450-185-4

REFERENCES

[1] M. Lindroos et al., in Proc. of IPAC'16, FRYAA02.

[2] H. Danared, in Proc. of HB'16, MOAM3P30.

[3] E. Tanke and D. McGinnis, "Accelerator Installaon Sequence", ESS Document No. ESS-0037305, 2015.

[4] E. Sargsyan and L. Lari, "Accelerator Installation Plan", ESS Document No. ESS-0055889, 2016.

[5] A. Jansson, "ESS Accelerator First Stage Beam Commissioning Plan", ESS Document No. ESS-0054490, 2016.

[6] S. Molloy, "PBI Taskforce Report", ESS Document No. ESS-0037620, 2015.

[7] A. Jansson et al., in Proc. of IPAC'16, MOPMR020.

[8] Y. I. Levinsen et al., in Proc. of IPAC'16, WEPOY043.

[9] E. Bargalló et al., in Proc. of IPAC'15, MOPTY045.

[10] M. Muñoz, "Warm Linac Beam Commissioning Sequence", ESS Document No. ESS-0043907, 2016.

[11] A. Lombardi et al., in Proc. of LINAC'14, MOIOA02.

[12] B. Cheymol, "Potential Beam Diagnostics for a Movable Test Bench", ESS Document No. ESS-0020683, 2015.

[13] E. Sargsyan and R. Miyamoto, "ESS Linac Beam Modes", ESS Document No. ESS-0037801, 2014.

[14] M. Muñoz, "Description of Modes for ESS Accelerator Operation", ESS Document No. ESS-0038258, 2016.

[15] A. Ponton and B. Cheymod, "Proposal for Off-site Beam Commissioning Sequence of the ESS Proton Source and LEBT", ESS Document No. ESS-0049241, 2016.

[16] Y. I. Levinsen et al., in Proc. of IPAC'15, THPF092.

[17] Y. I. Levinsen et al., in Proc. of IPAC'16, TUPMR020.

[18] H.D. Thomsen and S.P. Møller, in Proc. of IPAC'14, WEPRO073.

ISBN 978-3-95450-185-4

COMMISSIONING OF C-ADS INJECTOR I*

Jianshe Cao†, FangYan, Cai Meng, Huiping Geng, Rong Liu, Yanfeng Sui, Qiang Ye
Institute of High Energy Physics, Beijing, China

Abstract

As a test facility, the design goal of C-ADS Injector I is a 10mA, 10MeV CW proton linac, which uses a 3.2MeV normal conducting RFQ and superconducting single-spoke cavities for accelerating. The RF frequency of C-ADS Injector I accelerator is 325 MHz. In accordance to the progress of construction and considering the technical difficulties, the beam commissioning of C-ADS Injector I is carried out in several phases. This paper will summarize the beam commissioning in every phases and focusing on the final phase.

INTRODUCTION

"The China Accelerator Driven Sub-critical System (C-ADS)" is one of the "Strategic Priority Research Program" of CAS. Its main task is to cope with nuclear waste material and produce clean nuclear power. It have two injectors, C-ADS injector I is a 10MeV proton linac with 10mA continuous current made by IHEP. It consists of an ECR (Electron Cyclotron Resonance) ion source, a LEBT (Low Energy Beam Transport), a 3MeV RFQ (Radio-frequency Quadruple) with 325MHz frequency and a superconductivity linac accelerator with 3~10MeV [1]. The schematic diagram of C-ADS injector I is shown in Fig.1, and the specifications of the injector I are also listed in table 1.

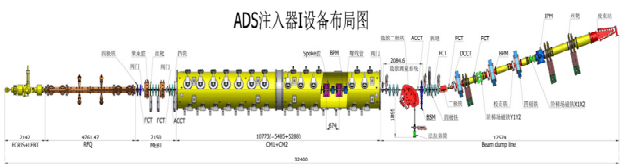

Figure 1: The Schematic diagram of C-ADS injector I.

Table 1: ADS Injector-I Test Facility Specifications

ADS Injector-I test facility specifications	
Particle	Proton
Output Energy (MeV)	10
Average Current (mA)	10
Beam power (kW)	100
Duty factor (%)	100
RF frequency (MHz)	325

COMMISSIONING PHASE AND RESULTS

As shown in Figure 1, the Injector-I testing facility is composed of an ECR ion source, a LEBT, a RFQ, a MEBT, a superconducting (SC) section, an energy Analysis Magnet (AM) and a beam dump line. The designed output energy of the RFQ is 3.2MeV. The SC section includes two cryomodules (CM1&CM2) with 14 β=0.12 SC spoke cavities, 14 solenoids and 14 cold BPMs, which is used to boost the proton beam energy up to 10 MeV [2]. At present, the commissioning of CM1 & CM2 with narrow pulse beam (duty cycle: 0.04 ‰, 2Hz/20us) is completed.

LEBT, RFQ, MEBT Commissioning

The LEBT connect the ECR source to the RFQ and provides the matching between the ECR and RFQ. The ion source provides 35keV CW or pulsed proton beam with average current over 10mA [2]. The Figure 2 shows the LEBT layout. The total length of the LEBT is 1.67m. It includes 2 solenoid, 1 DCCT, 1 ACCT and a chopping system. The chopper can provide short or long pulsed beam. Beam width can be adjusted start from 40 ns with repetition frequency of 1Hz up to 50Hz. The rise and down time is smaller than 20ns.

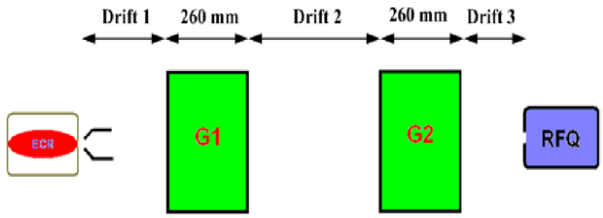

Figure 2: The layout of LEBT.

The emittance at the exit of the LEBT are measured by using Alison detector. The measurement result and the simulation result are shown in the Figure 3. The left on the Figure 3 is the simulated phase space 8.8cm downstream of the LEBT, and the right figure is the measured results. The both shape of the beam phase space looks very similar. Table 2 shows the designed twiss parameters and the measured results at the RFQ entrance. The twiss parameters are sensitive to the LEBT solenoid settings and we chose the one closet to the simulated parameters of the RFQ entrance in order to get matched beam [3].

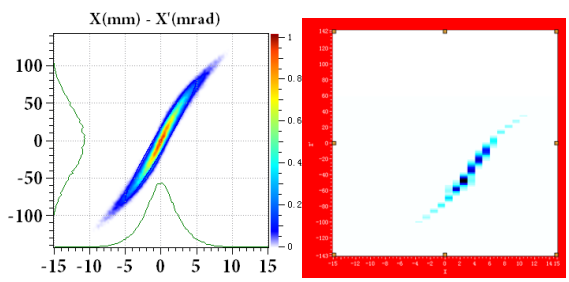

Figure 3: The simulation result (left) and the measurement result (right) of emittance at LEBT exit.

*Work supported by CAS Strategic Priority Research Program-Future Advanced Nuclear Fission Energy (Accelerator-Driven Sub-critical System).
† caojs@ihep.ac.cn

ISBN 978-3-95450-185-4

Table 2: Beam Parameters at the LEBT Exit

Parameters	I (mA)	α	β	E (π mm.mrad)
Design goal	10	2.41	0.0771	<0.20
Measurement	11.5	2.18	0.0774	0.14

The RFQ is composed of two resonantly coupled physical segments and each segment includes two technical modules connected together with flanges. Totally four couplers are mounted on the RFQ and two couplers on one physical segment. The output energy is 3.2MeV with the inter vane voltage of 55kV. The total accelerator length is 4.7m. The longitudinal normalized rms emittance is designed to be smaller than transverse emittance for better cavity efficiency [3].

The RFQ conditioning began on May 15th 2014. 71% duty factor was achieved in less than one month conditioning with short pulse, but stopped by vacuum leakage of the RFQ entrance plate, and the reason was the cooling water valve of the plate was closed by mistake. To prompt the conditioning process, an aluminum plate was installed instead of the original temporarily. Then 80% duty factor was achieved with short pulse after one week conditioning, but was interrupted again by the vacuum leakage of the RFQ coupling plate due to the welding it is not tight enough. On Aug. 21st 2014, the commissioning of 99.97% RF duty factor has reached. In the meanwhile CW conditioning was processed alternately. But on Sep. 27th, CW conditioning has to stopped for the MEBT&TCM installation according to the project schedule.

Though the beam duty factor is very close to CW, but it is really that the CW have not been reached. The reasons are as follows:

Early problems is lack of experience, such as the master oscillator can't be switched from pulse mode to CW mode directly, conditioning mode is inefficient (with pulse generator and switch gradually from pulsed to "CW"), as well as the coupler is damaged.

Later, the problems is that we have to catch up the project schedule. Once the CM2 commissioning with narrow pulse beam is completed, we will plan to restart the RFQ conditioning by CW mode and 3 mA beam commissioning.

The RFQ performance was checked by the beam with different duty factors. Over 95% transmission efficiency were achieved with the duty cycle greater than 90%, and the beam lasted over one hour stably, and then was stopped artificially for protecting the beam dump target [4]. The highest average beam power is greater than 31kW with output beam current of 11mA and 3.2MeV beam energy. The RFQ energy was measured with the time of flight method by using two FCTs downstream of the RFQ.

MEBT is composed of 6 Quadruples, 6 Steering magnets and 2 bunchers [5]. The beam based alignments were carried out for the MEBT BPMs, all the offsets of the BPM were less than 0.5mm. The beam center drift measured on all the BPMS are under the range of ±0.15mm with input cavity power of 280kW. Direct Root Mean Square formula was used in our case for the RMS beam size calculation to eliminate the calculate method error causing by the fitting formula [6].

The Table 3 shows the beam performance of twiss parameters and emittance comparison between the measurement and the simulations at the MEBT entrance.

Table 3: Beam Parameters at the MEBT Entrance

Parameters		αx/αy	βx/βy (mm/mrad)	Ex/y (π mm.mrad)
Simulation		-1.3/1.46	0.12/0.13	0.21/0.20
RFQ exit	Quad. scan	-1.8/0.72	0.17/0.09	0.16/0.21
	Double slits	-1.78/0.65	0.46/1.85	0.14/0.14

Beam diagnostic devices located in the MEBT include 6 Beam Position Monitors, 2 Fast Current Transformers (FCT), one AC current transformer (ACCT) and 3 Wire Scanners. The two FCT are used for the energy measurement. The space between the two FCTs is 1.67m. Two downstream BPMs were used for the phase scanning to determin the buncher settings. Figure 4 shows the phase scanning results of two bunchers.

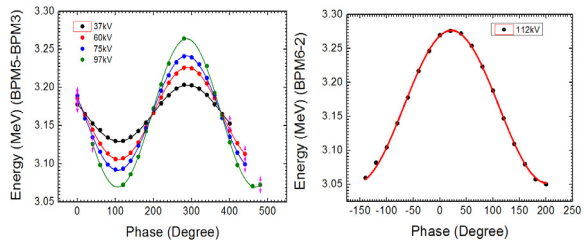

Figure 4: The phase scanning results of two bunchers, buncher 1 phase scan results V.S. different cavity voltage (left), buncher 2 (right).

TCM Commissioning

The testing cryomodule (TCM) includes two β=0.12 spoke cavities, two solenoids and two cold BPMs. The TCM is used to verify the performance of superconducting cavity, the cryogenic system, beam dynamic design, beam diagnostic system, superconducting solenoid and so on. The commissioning results of TCM is shown below:

- Beam duty factor: 1.5 ‰
- TCM transmission：98%
- Output current: 10.1mA
- Gradient achieved: Eacc=3.1MV/m

The maximum cavity gradient can only achieve 3.1MV/m (the specification is 7MV/m), that is because of field emission caused by cavity contamination which preventing the accelerating gradient from increasing. The improved technologies and methods have been adopted for the succeeding cryomodules of CM1 and CM2.

ISBN 978-3-95450-185-4

CM1 & CM2 Commissioning

The Figure 5 shows the schematic layout (on the top) of the injector I SC section and one period of accelerating (on the lower), respectively. Totally 14 periods are assembled in two cryomodules. The spacing between two cryomodules is 570mm. One standard period includes one β=0.12 spoke cavity, one SC solenoid and one cold BPM. The designed accelerating gradient was 6.08MV/m on basis of the first prototype testing results.

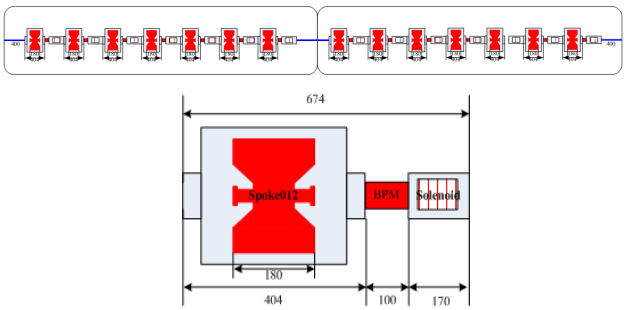

Figure 5: The SC section layout and periodical structure.

The CM1 was installed in the tunnel after the TCM commissioning and dismantled. The cavity phases are scanned 360 degree around to determine the designed sync and amplitude of all the cavities with two BPMs. The stably operating cavity gradient achieved was around 5.5MV/m during the CM1 commissioning. The output energy at the exit of CM1 reached 6.05MeV with 7 SC cavities, one cavity among them achieved accelerating gradient of 7.75MV/m, and the beam transmission for RFQ + CM1 and CM1 are 88.4% and 100%, respectively. The beam current of CM1 exit is 10.6mA. Figure 6 shows the emittance measurement results by two slits located at the exit of CM1.

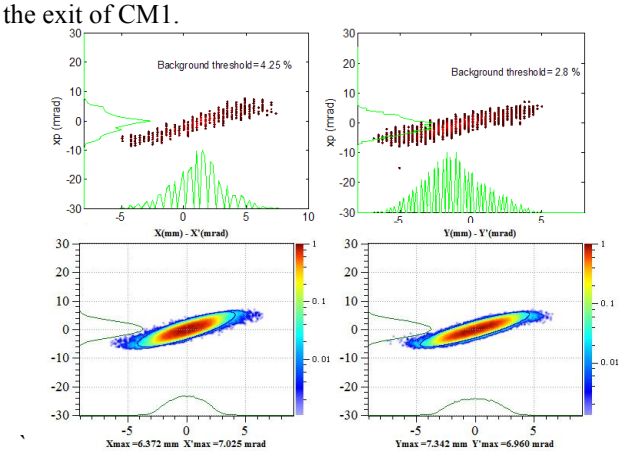

Figure 6: emittance measurement results (upper) by two slits at the exit of CM1 comparing with the simulation results (lower).

For the commissioning of CM2, it is similar with CM1. On June 17th, 2016, the injector I was successfully commissioned up to 10.1MeV at pulse beam current of 10.03mA with thirteen low-beta superconducting (SC) spoke cavities (#1 cavity is turn off). The energy was measured by using energy Analysis Magnet and two BPMs with time of flight method, respectively. After two days later, the beam energy reached 10.25 MeV with fourteen cavities. Figure 7 shows the 10.03 mA peak current at the exit of the SC (CM1&CM2) section.

The issues during the commissioning of CM1&CM2 is that we have to warmup the SC two times for adjusting the SC frequency, and it is hard to keep running stablely for a long time with multiple SC and cavities with high ACC simultaneously.

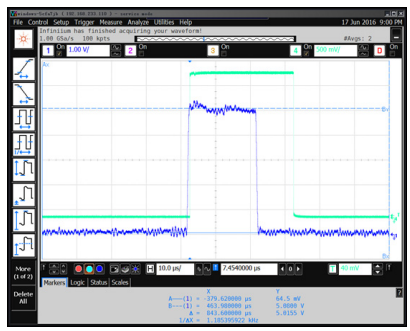

Figure 7: The peak current at the exit of the SC (CM1 & CM2) section is 10.03 mA.

SUMMARY AND ACKNOWLEDGEMENT

The ion source+LEBT+RFQ+MEBT+CM1+CM2 were successfully commissioned with pulsed beam. Next we plan to do long pulsed beam or CW commissioning for injector I with low beam current. Also, the RFQ is still on the way to CW operation, new conditioning method will be tried later. More experiments is needed to be done to further understanding the beam performance. Investigation of the machine reliability and stability will be done in the future.

Sincere acknowledgement to the commissioning group of C-ADS Injector-I for the great efforts during the commissioning.

REFERENCES

[1] J.H. Yue, J. Hu et al., “Phase and energy measurement system for C-ADS injector I”, Proceedings of IBIC2015, Melbourne, Australia.

[2] Y. Yang, H. P. Geng et al., “Commissioning of the China-ADS injector-I testing facility”, Proceedings of IPAC2016, Busan, Korea.

[3] F. Yan, S. L. Pei et al., “Physics design of a 10MeV injector test stand for an accelerator-driven subcritical system, Phys. Rev. ST Accel. Beams 18, 054201 (2015).

[4] Cai Meng et al., “Beam commissioning of C-ADS injecttor-I RFQ accelerator”, proceedings of IPAC2015, USA, 2015.

[5] H. Geng et al., “The MEBT Design for the China Accelerator Driven system”, proceedings of IPAC2011, San Sebastian, Spain, 2011.

[6] Y. Zhao, H. Geng et al., “Beam twiss measurement with WS including space charge effect”, Proceedings of IPAC2016, Busan, Korea.

ISBN 978-3-95450-185-4

OBSERVATIONS OF COUPLING DURING ACCUMULATION USING A NON-DESTRUCTIVE ELECTRON SCANNER IN THE SPALLATION NEUTRON SOURCE ACCUMULATOR RING*

R. Potts†[1], W. Blokland, S. Cousineau, J.A. Holmes, ORNL, Oak Ridge, TN, 37831, USA
[1]also at The University of Tennessee, Knoxville, 37996, USA

Abstract

An electron scanner has been installed in the accumulator ring of the Spallation Neutron Source (SNS). The non-destructive device permits turn-by-turn measurements of the horizontal and vertical profiles of the proton beam during accumulation with fine longitudinal resolution. In this study the device is used to investigate the source of transverse coupling in the SNS ring and to understand the impact of space charge on the evolution of the coupled beam. We present experimental observations of coupling dependent on tune, injected intensity, and accumulated intensity for a simplified accumulation scenario with no RF and no injection painting. We also investigate the effects of varying the skew quadrupoles and tune for beams with the SNS production-style ring injection and ring RF patterns.

INTRODUCTION

The SNS Accumulator Ring compresses up to 1050 turns of injected beam into a short 1 μs pulse containing up to 1.5×10^{14} protons. Once accumulated, this pulse is delivered to a liquid mercury target for neutron spallation by way of the Ring-to-Target Beam Transport (RTBT). The target has specific requirements for beam size and profile uniformity in both transverse planes. One primary requirement is that the peak on-target density remain less than 2.6×10^{16} protons/m^2 for a 1.5 MW beam. In order to achieve the on-target requirements, independent control of the transverse beam distributions is necessary. Previous studies have shown a loss of independent control between the planes. Initially this effect was only intermittently observed by accelerator operators during production shifts. In 2011 and 2012, it was shown that at high beam intensities the final accumulated beam distribution in each plane depended on the initial distribution in the alternate plane [1, 2]. Initially, the primary hypothesis was that the loss of control was due to space charge and could be related to the Montague Resonance [3] due to the small tune split of the coupled beam configurations. In 2015, it was shown that at low beam intensities the beam emittances could be caused to couple and fully exchange between the transverse planes by configuring a small tune split [4]. In this paper we present results of additional experiments from continuing efforts to understand the transverse coupling in the SNS Accumulator Ring. In previous studies, we have used traditional wire scanners to collect transverse beam profiles. This has proven to be a time prohibitive method to study beam oscillations. In this experiment we will use the Electron Scanner (ES), a novel diagnostic device recently developed in the SNS Accumulator Ring.

*ORNL is managed by UT-Battelle, LLC, under contract DE-AC05-00OR22725 for the U.S. Department of Energy. This research was supported by the DOE Office of Science, Basic Energy Science, Scientific User Facilities.
†pottsre@ornl.gov

ELECTRON SCANNER

The Electron Scanner obtains profiles by first passing an electron beam diagonally across the path of the accumulating proton beam. The electron beam is deflected in the presence of the electromagnetic field of the proton beam. The deflected path is then projected onto a fluorescent screen and an image is captured. The transverse profile is derived from the amount of the deflection along the projection [5]. The analysis, which can be run offline, slices through the center of the image and fits a gaussian peak to the pixel intensities along each slice to find the full set of (x, y) points. A spline curve is then fitted through the set of (x, y) points to calculate a smoother set of curve points so that a derivative can be taken to obtain a less noisy profile. The spline fit technique also allows the projection of the beam to be traced through the cutouts made by the electron scanner beam markers, which are used to provide a scale for the profile width. A derivative with respect to position is calculated from the difference of the spline curve with respect to the path of an undeflected electron beam.

The electron scanner has several advantages over traditional wire scanners. The first advantage is the non-destructive nature of the electron scanner, which allows us to collect data parasitically to regular production operations. This means that the electron scanner could become a useful diagnostics tool for regular use during operations in the future. Second, the electron scanner has the ability to capture 20 ns slices of the accumulating proton beam. When examining many slices together, this can provide a detailed longitudinal profile. This differs from the wire scanners which sum along the longitudinal profile of the beam. Additionally, a short scan time means that the transverse profiles can be studied across the length of the beam bunch. Finally, Fig. 1 shows the locations of the electron scanner compared to the wire scanners. Its position in the accumulator ring and a 1 Hz scan rate allow the electron scanner to collect large data sets quickly and without requiring operator interruption. It should be noted that each electron scanner profile represents the profile from within a certain point of a single proton beam, while a wire scanner profile represents

ISBN 978-3-95450-185-4

numerous data points each from separate single proton beams. This can allow the electron scanner to more easily detect pulse-to-pulse variations, e.g. centroid jitter or profile variations. The main limiting factors of the electron scanner are the HV transformer, which arcs around 60 kV limiting the peak proton beam intensity that can be scanned, and the aperture sizes, which limit the maximum size of the proton beam that can be scanned [6].

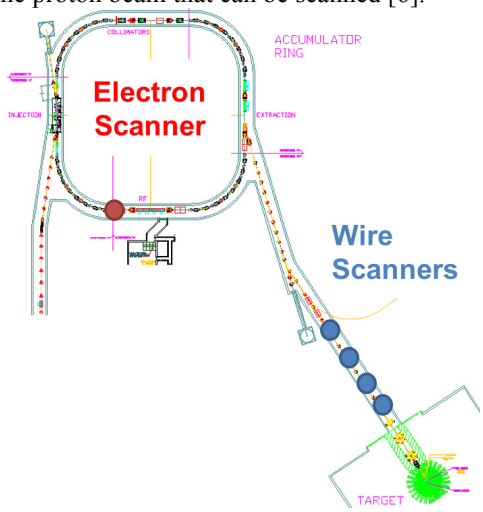

Figure 1: The Electron Scanner, red dot, is located in the SNS Accumulator Ring. The four wire scanners used in previous studies are located in the Ring-to-Target Beam Transport (RTBT), blue dots.

The electron scanner is capable of collecting 40 profiles within the longitudinal period of the accumulator ring. Figure 2 shows an example of how these can be combined to create a 3-dimensional profile of the beam. This 3D profile allows us to quickly see the consistency in transverse profile throughout the bunch. Additionally, the intentionally beamless gap in the ring can be seen as the pink-purple floor. We are able to quickly determine whether the beam has spread longitudinally with respect to other 3D profiles. Prior to examining our main results, an important part of our experiment was to reconfirm that the electron scanner would reasonably reproduce the wire scanner profiles. Figure 3 shows the electron scanner sum profile (left) and wire scanner profile (right) for the same data as shown in Fig. 2. The electron scanner sum profile is produced by summing the beam longitudinally. In this comparison, the profiles are of reasonable similarity in shape and some of the differences may be attributable to the differences in the rotation of the phase space. The horizontal Twiss parameters at the electron scanner are (α_x = 0.78, βx = 3.23) and at the wire scanner shown they are (α_x = 0.83, β_x =6.57). It should be noted that none of the wire scanners have vertical Twiss parameters similar to the electron scanner.

We will use these electron scanner sum profiles for two additional purposes. First, we will use this sum profile to calculate the RMS size. Second, we will assemble an evolution of the transverse beam profile over the duration of the experiment. Thus, each profile evolution will display the change in profile during both the accumulation and storage of the beam. However, the profile evolution will only present the sum of the bunch and will not show any longitudinal dynamics.

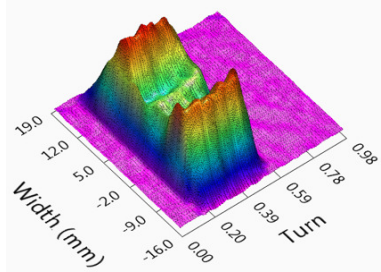

Figure 2: A 3-dimensional profile created from 40 separate horizontal profiles taken using the electron scanner. The horizontal profile width is shown in millimeters along the left axis, while the longitudinal position of the profile within a single turn is shown on the right axis.

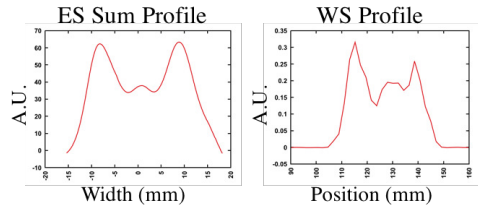

Figure 3: Comparison of an electron scanner sum profile (left) and wire scanner profile (right). The difference in profile could be attributed to the minor difference in Twiss parameters between the two diagnostics.

SIMPLIFIED ACCUMULATION EXPERIMENT

Our motivation is to create an experiment with a simplified accumulation and beam dynamics that will allow us to explore the effects of tune and intensity on coupling while using of the benefits of the Electron Scanner.

To simplify the beam dynamics, we make the following changes to the normal SNS configuration. First, we flattop the injection kickers to remove the effects of injection painting. Next, we manually short the ring RF to remove any longitudinal effects. In order to make sure the beam remained clear of the extraction gap, the beam was injected to fill only 25/64ths of the ring, which is approximate half the production size. Next, we use the ring sextupoles to zero the chromaticity and better isolate the effects of space charge tune shift. Then, we use the skew quadrupoles located throughout the ring to eliminate any signs of transverse lattice coupling seen by monitoring the turn-by-turn centroid motion of a single bunch injected with offset. Finally, extending the storage period allows us to observe the beam evolution without the complication of added accumulation. Therefore, we set the beam accumulation to 100 turns and allow for 300 turns of storage. This provides us with the opportunity to see any effects during the early evolution of the beam and also study the beam without adding additional charge.

The nominal betatron tunes of the SNS Accumulator Ring are ν_x = 6.23 and ν_y = 6.20. The tune for the first

ISBN 978-3-95450-185-4

configuration was ν = (6.2091, 6.1687), where $\Delta Q \approx 0.0404$. We refer to this configuration as the "split tune" configuration. The tune for the second configuration was ν = (6.1994, 6.1978), where $\Delta Q \approx 0.0016$. We refer to this configuration as the "equal tune" configuration.

During SNS production cycles, the size of the beam painted into the ring is optimized to reduce losses throughout the ring while matching the on-target beam requirements. During our experiment, we required a smaller beam size than the normal production size in order to fit the entire beam into the apertures of the electron scanner. The vertical aperture has tighter size limitations than the horizontal beam due to misalignment of the vacuum beam pipe and a larger betatron function, therefore we configured a smaller vertical beam size. The injection size for the split tune configuration was (17.3mm, 6.5mm). The injection size for the equal tune configuration was (17.9mm, 8.5mm). The MAD beta values at the injection spot are (β_x = 10.29, β_y = 11.06). The measured Twiss parameters at the electron scanner are (α_x = 0.78, β_x = 3.23, α_y = -0.72, β_y = 10.21).

The nominal beam energy during our experiment was 939.5 MeV. Due to the configuration of our experiments, our beam intensity is 7.5×10^{12} protons per pulse (ppp) or 1.2 μC. For the equal tune configuration, we also collected data for two lower intensities. In order to preserve the other configuration settings, we lowered the intensity by limiting the output from the H^- source. The two additional intensities are: "medium" intensity of 4.4×10^{12} ppp or 0.70μC, and "low" intensity of 2.5×10^{12} ppp or 0.35μC.

Effect of Tune

The top plot in Fig. 4 shows the evolution of the horizontal and vertical RMS beam sizes for the split tune configuration. Excluding the initial period of accumulation, the RMS sizes remain constant during beam storage from turn 100 to 400. When comparing the RMS sizes, it is important to remember that the betatron values at the location of the horizontal and vertical ES apertures are not equal, and the horizontal emittance of the beam is designed to be larger than the vertical emittance, as noted in the general experiment description. The left column of Fig. 5 shows the profile evolution for the same dataset.

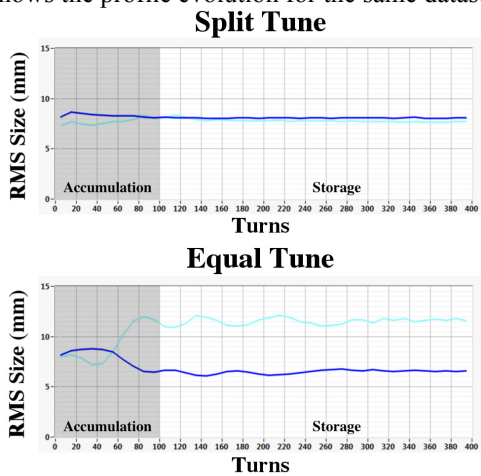

Figure 4: RMS size evolutions for the split tune (top) and equal tune (bottom) configurations for the simplified accumulation experiment. The horizontal RMS size is shown in dark blue and the vertical is shown in light blue.

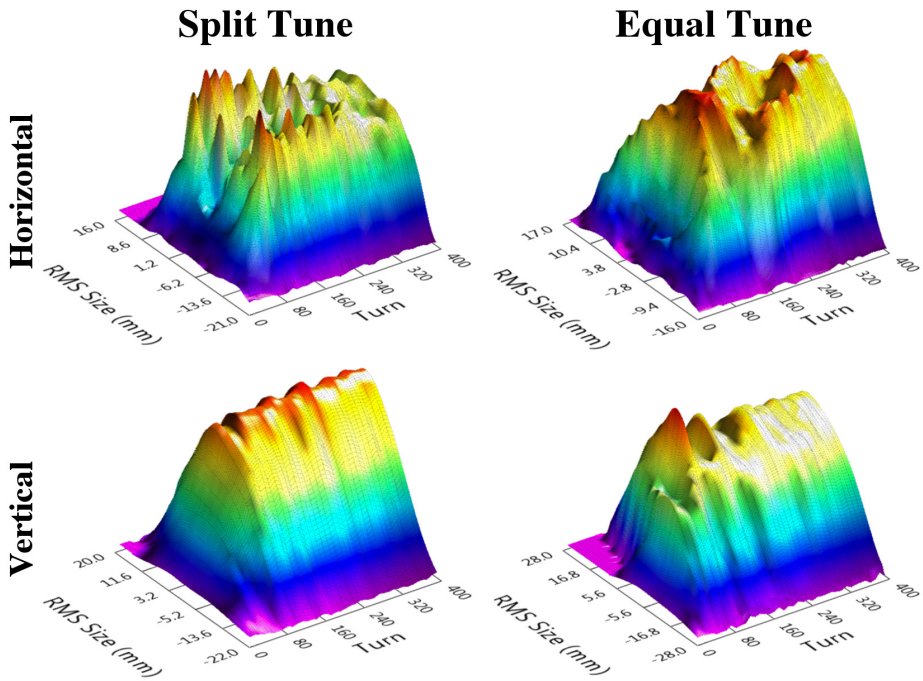

Figure 5: Profile evolutions constructed from electron scanner sum profiles for the simplified accumulation experiment. The horizontal evolutions are shown in the top row and the vertical evolutions are shown in the bottom row. The split tune configuration (left column) follows the expected evolution, while the evolution of the equal tune configuration (right column) displays coupling of the beam size and shape.

ISBN 978-3-95450-185-4

During accumulation, the horizontal profile is hollow due to the injection pattern defined by the flat-topped injection kickers and the choice of betatron tune. While the beam is stored, space charge forces cause the horizontal profile to dilute and the profile becomes rounded. This overall behavior follows our understanding of a beam without coupling and provides a reference for our experiment.

The bottom plot in Fig. 4 shows the evolution of the horizontal and vertical RMS beam sizes for the equal tune configuration. We see an exchange between the two planes within the first 50 turns. By the time the beam accumulation has stopped at turn 100, we see a coupled oscillation between the planes. This oscillation dampens as the storage continues. The right column of Fig. 5 shows the profile evolution for the same dataset. These profiles show that the beam shape oscillates along with the beam RMS size. The horizontal profile becomes peaked midway through accumulation and proceeds to oscillate between peaked and hollow. The vertical profile, to a lesser extent due in part to its limited size, also oscillates. This evolution indicates beam dynamics that are significantly different from the split tune configuration. As mentioned before, the tune of the SNS beam is often changed during production setup to minimize losses in the ring while optimizing the beam size and shape on the target. These dynamics mean: 1) the beam no longer responds as expected to systematic changes in the injection kickers, and 2) the beam size and shape can change significantly if the extraction point is altered.

Effect of Intensity

Figure 6 shows the RMS size evolutions for the three equal tune configurations described in the general experiment description. The full intensity figure (bottom) represents the same case presented in the previous section. An exponentially-damped sinusoid has been fitted starting at turn 105, which is the first data point in the storage period. The profile evolutions, not shown, display oscillations in both planes matching those seen in the RMS size evolutions. The oscillation period for these fits decreases with increasing proton beam. This result shows that space charge forces damp the oscillation in the beam, contrary to our previous expectation.

SNS PRODUCTION-STYLE EXPERIMENT

Our motivation is to study the effects of tune and skew quadrupoles on beams configured with the same settings as the last nominal SNS production cycle. This is an important continuation of our research as the original motivation of our research was the understanding and reduction of coupling effects seen during the regular production operations. In this configuration, we will use the nominal SNS dual-plane injection painting. We will use a dual harmonic ring RF. We will have a natural beam chromaticity. Several of the skew quadrupoles have been turned on. As mentioned before, the skew quadrupoles are designed to allow the reduction of any lattice coupling that might be present and may have been used to reduce nominal beam losses. Finally, we will not store the beam.

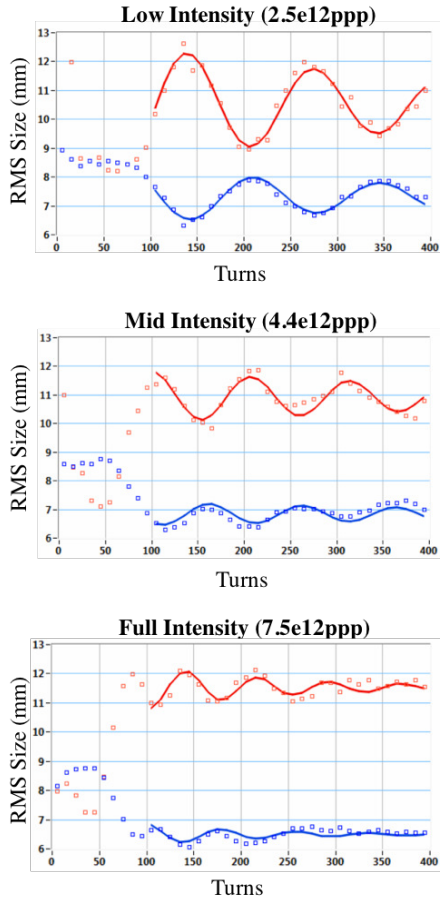

Figure 6: RMS size evolutions for the three equal tune cases of the simplified accumulation experiment: low intensity (top), mid intensity (middle), and full intensity (bottom). The electron scanner data is represented by points and the damped sinusoidal fit is represented by the solid lines. The horizontal RMS sizes are shown in blue and the vertical RMS sizes are shown in red.

The last production settings were for a betatron tune of ν = (6.2043, 6.1623), where $\Delta Q \approx 0.0420$. We refer to this configuration as the "production tune" configuration. The tune for the second configuration was selected to be ν = (6.1640, 6.1667), where $\Delta Q \approx 0.0027$. We refer to this configuration as the "equal tune" configuration. The last production settings were for an injection size of (17.5mm, 8.8mm). We expected the beam size to be symmetric and larger, however we continued with our original intention of using the last production configuration. The nominal beam energy during our experiment was 939.5 MeV. We used 878 turns of injected beam with 98 turns of beam ramping, which equates to a beam intensity of 9.0×10^{13} ppp or 14μC. Due to the larger beam size and intensity, and the restriction in the vertical aperture of the electron profile monitor device, the vertical electron scanner had trouble viewing the entire beam, especially in the last 100 turns. Therefore, only the horizontal data will be presented. However, any coupling effects seen in the horizontal

ISBN 978-3-95450-185-4

RMS size and profile evolutions would be mirrored in the vertical data.

Effect of Tune

Figure 7 shows the RMS size evolution for the two tune configurations for the production style experiment. Both cases show an expected slow increase in RMS size during continued accumulation. Figure 8 shows the horizontal profile evolutions for the production and equal tune configurations, top and middle figures respectively. We can see that while the RMS size evolutions followed similar trends, the profile evolutions are not similar. The production tune profiles maintain some amount of hollowness even at the end of the evolution, however the equal tune profiles quickly become diluted.

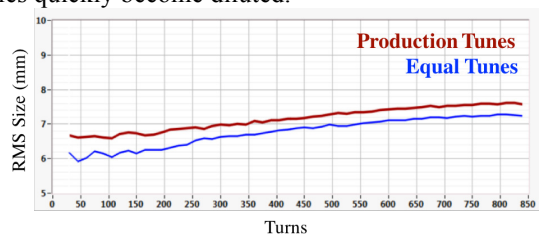

Figure 7: RMS beam sizes for the production tune (red) and equal tune (blue) configurations for the production style experiment.

Effect of Skew Quadrupoles

The skew quadrupoles are used in the production configuration in order to reduce any coupling present in the beam. This correction is done by monitoring the turn-by-turn oscillations of a single injected pulse and adjusting the skew quadrupole strengths. It was our expectation that using the skew quadrupoles would reduce the effects of coupling seen in the final distribution of the beam.

Figure 9 shows the RMS size evolution for the equal tune configurations with and without skew quadrupoles. While the general evolution of the RMS size is similar, the configuration with skew quadrupoles displays an additional level of coupling. By comparing the middle and bottom figures in Fig. 8, we can see that this additional coupling clearly appears as a rapid change in the shape and peak intensities of the profile evolution. Contrary to our expectations, the skew quadrupoles did not eliminate coupling and had a small effect on the beam evolution compared to the impact of the tune change.

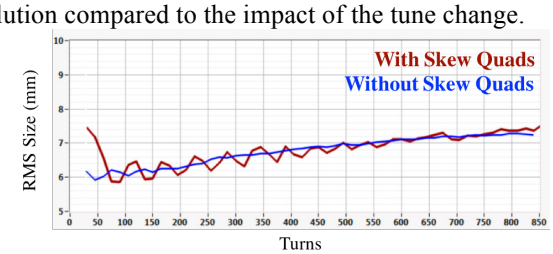

Figure 9: RMS beam sizes for the equal tune configuration with skew quadrupoles (red) and without skew quadrupoles (blue) for the production style experiment.

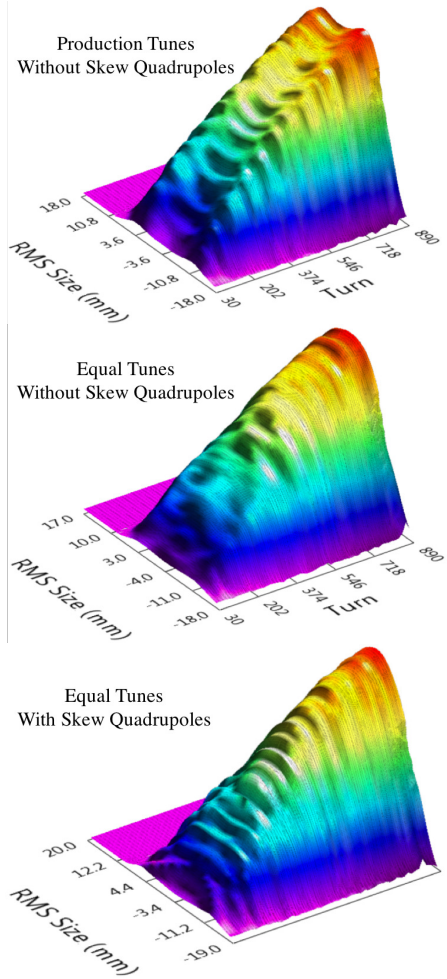

Figure 8: Horizontal profile evolutions are shown for the production style experiment.

CONCLUSION

We have presented the results of the first major physics study using the SNS Electron Scanner. We have demonstrated the following. First, an equal tune beam configuration produces coupling in RMS size and beam shape. Second, increased beam intensity dampened oscillations, instead of amplifying them as we expected. Finally, skew quadrupoles have been used to agitate the coupling, whereas we expected the effect to be the reduction of the coupling. Originally, we thought this was a Montague Resonance however these results imply an alternative source of coupling in the SNS Accumulator Ring, most likely linear lattice coupling.

REFERENCES

[1] S. Cousineau, in *Proc. IPAC'11,* pp. 17–21.
[2] R. Potts, S. Cousineau, and J. A. Holmes, in *Proc. HB'12*, pp. 223–225.
[3] B. W. Montague, "Fourth-Order Coupling Resonance Excited By Space-Charge Forces in a Synchrotron," CERN--68-38. European Organization for Nuclear Research, Geneva (Switzerland),1968.

ISBN 978-3-95450-185-4

[4] R. Potts, S. Cousineau, and J. A. Holmes, “Studies of the Montague Resonance in the SNS Accumulator Ring,” EuCARD2/XBeams Workshop on Space Charge 2015.
[5] A. Aleksandrov, *et al*., in *Proc. PAC'05,* pp. 2586–2588.
[6] W. Blokland, and S. Cousineau, in *Proc. IPAC'11,* pp. 1438–1442.

ISBN 978-3-95450-185-4

CODE BENCH-MARKING FOR LONG-TERM TRACKING AND ADAPTIVE ALGORITHMS

H. Bartosik, A. Huschauer, A. Oeftiger, F. Schmidt, M. Titze, CERN, Geneva, Switzerland
G. Franchetti, GSI, Darmstadt, Germany
J. Holmes, SNS, Oak Ridge, USA
Y. Alexahin, J. Amundson, V. Kapin, E. Stern, FERMILAB, Batavia, USA

Abstract

At CERN we have ramped up a program to investigate space charge effects in the LHC pre-injectors with high brightness beams and long storage times. This is in view of the LIU upgrade project [1] for these accelerators.

These studies require massive simulation over large number of turns. To this end we have been looking at all available codes and started collaborations on code development with several laboratories: MAD-X frozen & adaptive mode [2] and integration into the main branch of the MAD-X in-house development [3] code, PyORBIT [4] from SNS, SYNERGIA [5] from Fermilab, MICROMAP [6] from GSI .

We have agreed with our collaborators to bench-mark all these codes in the framework of the GSI bench-marking suite [7], in particular the main types of frozen space charge and PIC codes are being tested.

We also include a study on the subclass of purely frozen and the adaptive frozen modes both part of MAD-X in comparison with the purely frozen MICROMAP code.

Last, we will report on CERN's code development effort to understand and eventually overcome the noise issue in PIC codes.

INTRODUCTION

The aim of this study is threefold. On the one hand we would like to present the completion or near-completion of the GSI Bench-Marking Suite [7] of 2 PIC codes and the comparison with the results from 3 participating frozen SC codes. The second task is to report about the on-going study to understand how SC experiments compare with the various SC codes. To this end we are studying both the PS [8] and the SPS [9] at the integer resonance. This study of SC at the integer resonance in view of evaluating which tools are most suited to understand the dynamics is part of the mandate of a PhD [10] at CERN. Here we can just present a snapshot of what could be achieved up to this conference. Lastly, we would like to remind the community about the effect of grid noise on individual particles in the distribution. Techniques to overcoming this issue or at least minimizing its fake impact on the emittance evolution and particle loss will be crucial to see if PIC codes can be taken to use for long-term SC simulations or not. In fact, at this conference new concepts will be discussed that might do the trick. At CERN Malte Titze's [10] second part of his thesis is dedicated to such techniques.

GSI BENCH-MARKING SUITE

With the upcoming Fair [11] and LIU [1] projects at GSI and CERN respectively, a new sequence of SC workshop has been started to review how our codes can be used to predict long-term SC effects on the dynamics of storage rings in the regime of high intensity. During this first joint GSI-CERN Space Charge Workshop [12] held at CERN in 2013, with a follow-up collaboration meeting in 2014 [13] it had been decided to start a collective effort to bench-mark several PIC codes with the GSI bench-marking suite that has been used for code bench-marking of a number of frozen SC codes in previous years. In particular, the teams of PyORBIT [4] from SNS, the latest incarnation of ORBIT, and the SYNERGIA [5] team of FERMILAB have made the effort to go through all the nine steps of this GSI bench-marking suite.

Figure 1 shows the 9th step of a long-term simulation over 100'000 turns of the SIS18 GSI ring. It is quite interesting to note that for some 10^6 macro-particles the SYNERGIA (2.5D solver) reproduces the results of the frozen SC codes. What is remarkable about this finding is the fact that also SYNERGIA as a PIC code is suffering from grid noise as shown below.

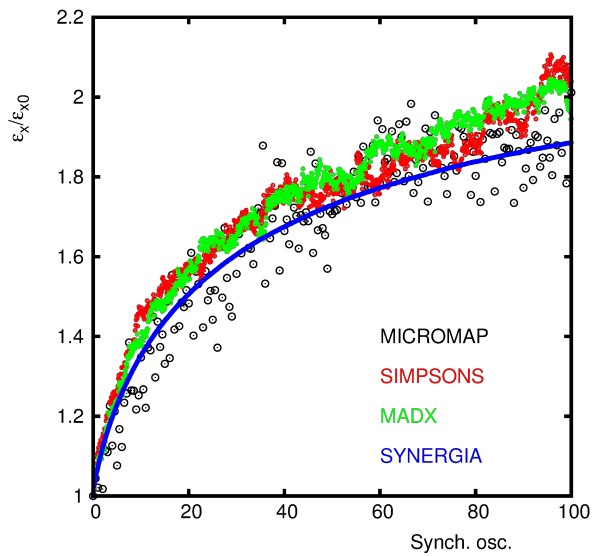

Figure 1: Emittance Evolution of the GSI SIS18 ring simulated with the 3 frozen SC Codes: MICROMAP, SIMPSONS, MAD-X and the PIC code SYNERGIA (1M macro-particles).

The complete results for both codes will now be introduced into the GSI bench-marking web site [7].

ISBN 978-3-95450-185-4

CODES IN COMPARISON WITH MACHINE EXPERIMENTS

Adaptive Mode

At first sight it seems astounding that a purely frozen code should be sufficient to describe the long-term evolution of the particle dynamics under the influence of SC and an ever changing particle distribution. On the other hand, a self consistent treatment is very slow in comparison and also burdened by grid noise. It seems therefore like an ideal approach to search for an intermediate solution that remains fast but also adapts the frozen distribution turn by turn closer to the actual distribution. To this end a very fast iterative algorithm [14] has been developed and implemented [15] into MAD-X that fits a Gaussian to whatever the actual distribution might be and thereby ignoring tails that might not be significant for the dynamics anyway. On top of this emittance recalculation, MAD-X allows to also recalculate the optics, so that even the beam sigmas are re-normalized occasionally. It goes without saying that this is indeed quite time consuming and therefore done only every 1000 turns in the case of the PS simulations.

However this approach is not really cost-free:

Pros: If a bench-marking as attempted in this study is successful one might have a unique manner to capture at least partially the self-consistent nature of the SC force. Moreover, the algorithm does degrade the speed only slightly. In fact, there has been a considerable effort with our collaborators at BNL [16] to optimize the speed of MAD-X with the help of OPENMP techniques.

Cons: On the other hand, for a true assessment of the speed one has to consider that in the case of the purely frozen mode one can completely serialize runs, since no cross talk between particles is required, and thereby gain a tremendous speed-up. The intermittent TWISS is quite a burden because it complicates the re-entry into the MAD-X tracking routines which has been an implementation nightmare, quite feared in the community of code developers. Besides these more technical problems, there is a more general and more serious issue which concerns the possibility that the continuous upgrade of the emittances may introduce some kind of statistical noise because it changes quasi random from turn to turn. This will have to be studied carefully.

Machine Parameters

Table 1 holds the most basic parameters of all machines that have been studied here. It is important to point out that there is a particular problem with the PS which consists of combined function magnets. These cannot easily be split into drift and kicks while keeping the full Hamiltonian intact, but rather this transformation leads to the expanded Hamiltonian. As a result the chromaticity is modified by some 16% for the PS after creating a thin-lens lattice. Therefore, our student Malte Titze has re-derived, from first principles, a thin model of the combined function model [17] that agrees with the full Hamiltonian in the limit of large number of kicks in the splitting of the thick combined function magnet.

Table 1: Machine Parameters

Parameter	SIS18	PS	SPS
Length [m]	216.71	628.32	6911.5
Kin. E. [GeV]	0.0114	2	25.079
Tuneshift	-0.1/-0.1	-0.05/-0.07	-0.1/-0.19
Special Features	Sextupole	Sextupole	Optimal adjusted
	Uncorr. Chromaticity		

PS Experiment

In 2012 we have done SC studies at the PS [8] with special sextupoles excited to allow for a code bench-marking with experiments. In Fig. 2 a measured loss scan is shown as a function of tunes together with 10 tune WPs (white crosses) being used to sample the $Q_x + 2Q_y = 19$ normal sextupole resonance and testing the SC tune-shift of $-0.05/-0.07$. Figure 3 shows the comparison of the measured emittance growth ratio (dashed lines) with those from MAD-X in adaptive mode (solid lines). While the overall agreement is excellent at medium and large horizontal tunes the MAD-X simulations predict a distinct increase of the horizontal emittance when approaching the integer tune that is not found in the experiment. When re-doing the simulations (see Fig.4) either with MICROMAP [6] which only has the frozen mode or with MAD-X in frozen mode there is no such increase to be found. Nevertheless, the understanding is less than evident at this point: on the one hand in discussions [18] – the author of the adaptive mode in MAD-X – we tend to believe that the procedure seems to drive particles onto the integer resonance. This may explain why we could not perform TWISS calculations during the run at $Q_x = 6.039$. On the other hand we are puzzled why we cannot find the

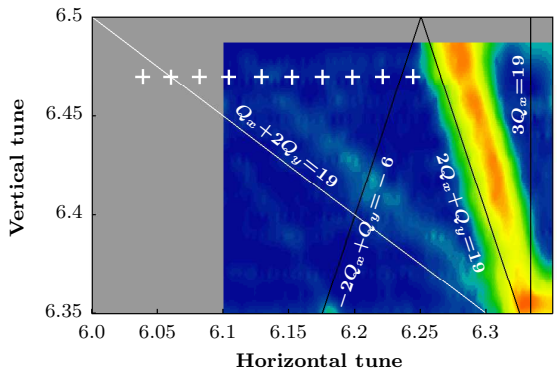

Figure 2: PS SC study with sextupoles excited. The sextupolar resonance $Q_x + 2Q_y = 19$ is shown with a white solid line and the working points used for the systematic study are indicated with the white crosses.

ISBN 978-3-95450-185-4

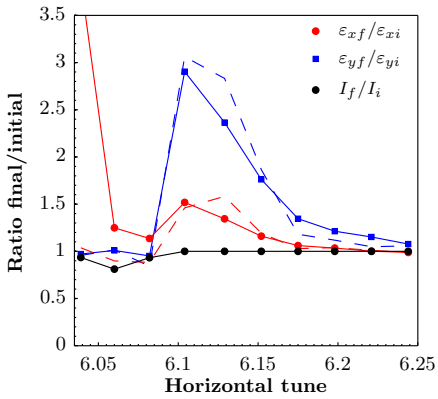

Figure 3: PS Emittance Evolution (adaptive).

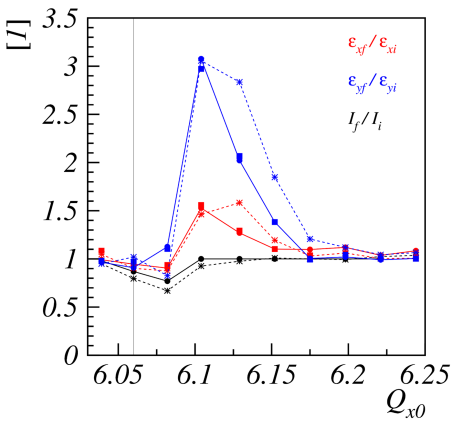

Figure 4: PS Emittance Evolution (frozen).

usual large horizontal emittance blow-up close to the integer resonance as for instance at the SPS (see below). In fact, we have planned simulations with PyORBIT for the PS at these smaller horizontal tunes to determine if this behavior in the adaptive mode is a code feature or if we do not understand something in our experimental set-up. Unfortunately, these studies are not yet ready to be presented here. For a better understanding of the adaptive and frozen mode we have done extensive simulations just at $Q_x = 6.039$ and $Q_x = 6.104$. To this end we have made a systematic check of how the simulations are done: standard MAD-X versus a better model of the combined function magnets and several options to enact the adaptive mode, leading us to present the average and RMS. We used a polar Gaussian distribution in NormalForm space and transferred it to the laboratory system via the full 6D linear transformation. This makes sure that the beam distribution is matched in 6D. We do not make additional adjustments since in the PS experiment we have a similar set-up. The table shows that apparently the adaptive mode is indeed overstating the presence of the integer for the case $Q_x = 6.039$ while the frozen mode is reproducing what is found in the experiment quite well. For $Q_x = 6.104$ the results are mixed in the sense that the frozen mode better agrees for horizontal emittance growth while for the vertical plane the results are better for the adaptive mode. In conclusion we are not completely sure what the optimal approach is in understanding the results from our machines. In fact, this will be covered by the thesis work of Malte Titze [10].

Table 2: Emittance Ratio in the PS Experiment: Adaptive versus Frozen Mode

Q_x	Mode	Experiment
6.039	Frozen	0.97/1.077
	1.07 ± 0.06/0.99	
	Adaptive	
	1.73 ± 0.03/0.97 ± 0.02	
6.104	Frozen	1.553/2.974
	1.54 ± 0.08/2.47	
	Adaptive	
	1.78 ± 0.03/3.18 ± 0.012	

SPS Experiment

Very detailed studies have been launched for the SPS but the full analysis will come in a few weeks only. In Fig. 5 the horizontal emittance blow-up has been recorded when approaching the integer resonance. It shows both the initial emittance and the final one after 3 sec of storage time. Note that the blow-up close to the integer resonance is quite fast and therefore increasing values are measured already for the

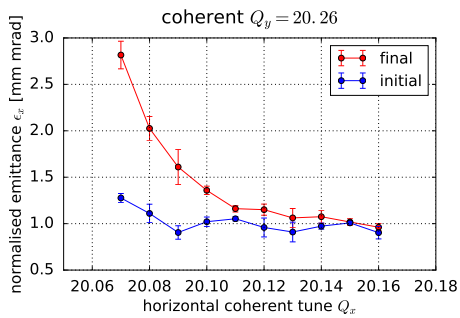

Figure 5: SPS Emittance Evolution Close to the Integer Resonance.

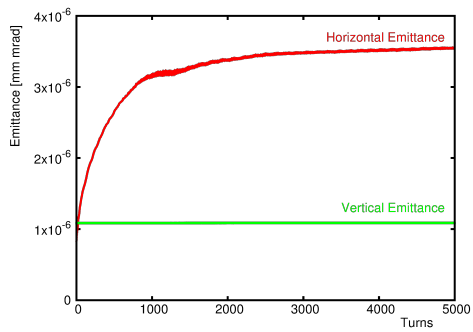

Figure 6: Preliminary Results with PyORBIT for SPS Emittance Evolution at $Q_x = 20.07$.

ISBN 978-3-95450-185-4

initial emittance. Therefore, we should estimate the "real" horizontal emittance to be slightly below $\epsilon_x < 1\mu m$.

Preliminary studies with PyORBIT (2.5D solver, 500k macromacro-particles) confirm that the horizontal emittance blow-up indeed amounts to about a factor of 3 (Fig. 6). Moreover, we are also investigating with MAD-X both frozen & adaptive to see how well the horizontal emittance blow-up can be predicted by either code variant. We must wait until our findings are conclusive and Malte's PhD thesis [10] should provide those results.

THE NOISE ISSUE OF PIC CODES

The grid noise is the standard nuisance of PIC codes and at CERN we are following closely the new developments to overcome this problem by introducing symplectic PIC codes. In fact, we have started our own effort to understand the symplectic violation of PIC codes as presented at this conference [19] and we are actively investigating to create our own symplectic SC module in the future. In the mean-

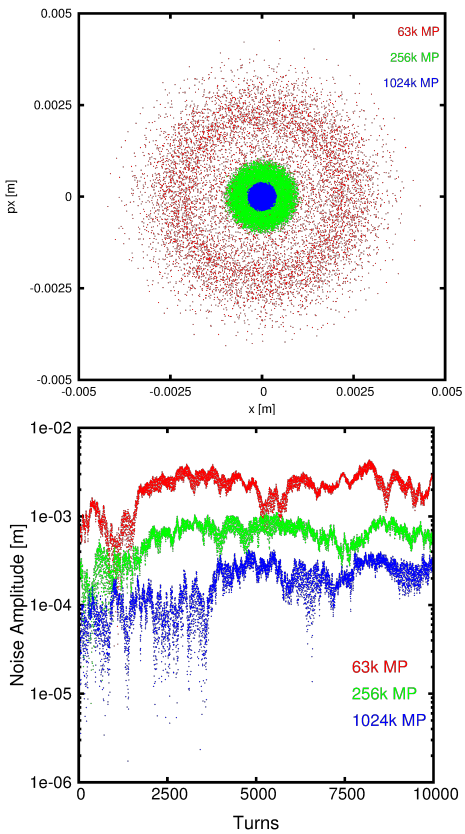

Figure 7: Small Amplitude Jitter study and growth in the horizontal Phase Space with SYNERIA; shown is the artificial phase space of a particle starting with zero amplitude: RED, GREEN & BLUE for 63k, 256k and 1025k Macro-Particles respectively.

time we are looking at the effect of the noise present in today's PIC codes. To this end we have started a zero amplitude particle together with a distribution of particles for 63k, 256k and 1025k Macro-Particles respectively. In absence of noise, e. g. in the case of the frozen mode, this zero amplitude particle should rest at zero indefinitely. In Fig. 7

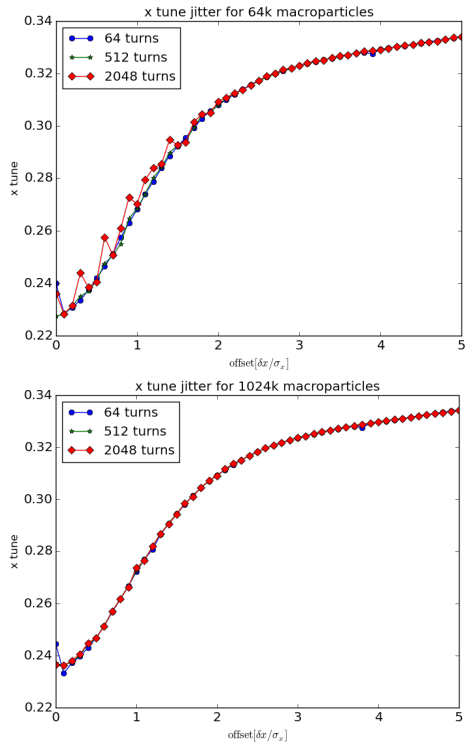

Figure 8: Tune Jitter with SYNERGIA for 64k and 1024K MP respectively.

we find that the noise creates artificial deviations from this expected symplectic behavior that does decrease with the number of macro-particles but nevertheless remains quite large. This is also visible in view of tune jitter (Fig. 8) that unexpectedly becomes larger when the time sequence for the FFT is enlarged. This effect even prevails for the very high number of macro-particle numbers of up to 10^6.

CONCLUSION

The frozen, adaptive symplectic codes are being compared with the intrinsically noisy PIC codes. Surprisingly the PIC codes are doing quite well to predict general parameters like emittance blow-up. Despite best efforts it is still too early to call the shots of which code variants are best suited to understand our experimental data. However, we have made tremendous progress and in a year or two we should have a definite answer to this question. We are also fully involved in understanding the non-symplectic nature of PIC codes and creating CERN's next symplectic PIC tracker. Moreover, the experimental procedures and data quality are rigorously improved for all CERN LHC pre-injectors.

The international collaborations have proven incredibly fruitful in this effort! We are determined to continue with this collective effort until we have a better understanding of SC effects in the presence of non-linear lattices and the codes to deal with them.

ISBN 978-3-95450-185-4

REFERENCES

[1] J. Coupard *et al.*, "LHC Injectors Upgrade, Technical Design Report, Vol. I: Protons", LIU Technical Design Report (TDR), CERN-ACC-2014-0337.

[2] V. Kapin, Fermilab, F. Schmidt, CERN, "MADX-SC Flag Description", CERN-ACC-NOTE-2013-0036, http://cern.ch/Frank.Schmidt/report/MADX-SC.pdf.

[3] L. Deniau, G. Roy, and F. Schmidt, "Integration of MADX-SC into the general MAD-X version", (2013), http://mad.web.cern.ch/mad/.

[4] Andrei Shishlo *et al.*, "The Particle Accelerator Simulation Code PyORBIT", Procedia Computer Science, Volume 51, 2015, pp.1272–1281.

[5] E. Stern *et al.*, "SYNERGIA", https://cdcvs.fnal.gov/redmine/projects/synergia2/wiki;
J. Amundson *et al.*, "High Performance Computing Modeling Advances Accelerator Science for High Energy Physics", *IEEE Comput.Sci.Eng.* 16 (2014) no.6, pp.32-41.

[6] G. Franchetti *et al.*, "MICROMAP LIBRARY", http://web-docs.gsi.de/~giuliano/micromap_manual/micromap_reference_manual.html.

[7] G. Franchetti, "The GSI Bench-Marking Suite", http://web-docs.gsi.de/~giuliano/research_activity/trapping_benchmarking/main.html.

[8] G. Franchetti *et al.*, "Space charge effects on the third order coupled resonance", to be published in *Phys. Rev. ST Accel. Beams* and presented at HB'16, Malmö, Sweden, paper TUAM6X01, this conference.

[9] H. Bartosik *et al.*, "Space Charge Studies with high Intensity single Bunch Beams in the CERN SPS", in *Proc. of IPAC'16*, Busan, Korea, paper MOPOR021, pp. 644-647, doi:10.18429/JACoW-IPAC2016-MOPOR021

[10] M. Titze, "On the Impact of Non-Symplecticity of Space Charge Solver", PhD Thesis (see [19]).

[11] P. Spiller and G. Franchetti, *Nucl. Instrum. Methods Phys. Res.*, Sect. A **561**, 305 (2006).

[12] Joint GSI-CERN Space Charge Workshop, held at CERN, April 2013, https://indico.cern.ch/event/221441/.

[13] Space Charge Collaboration Meeting, held at CERN, May 2014, http://indico.cern.ch/event/292362/.

[14] Y. Alexahin, "Computation of Eigen-Emittances (and Optics Functions!) from Tracking Data", presentation given at the Space Charge Joint GSI/CERN workshop held at CERN (2013).

[15] V. Kapin, Y. Alexahin, "Space Charge Simulation Using MADX with Account of Synchrotron Oscillations", in *Proc. of RuPAC'10*, Protvino, Moscow region, Oct 27, 2010, pp. 204-206.

[16] N D'Imperio *et al.*, "Experience with OpenMP for MADX-SC", CERN-ACC-2014-0075, BNL C-A/AP/515 (2014).

[17] M. Titze, "Approach to combined-function magnets via symplectic slicing", *Phys. Rev. ST Accel. Beams* 19.054002 (2016).

[18] Y. Alexahin, private communication.

[19] M. Titze, "On the Impact of Non-Symplecticity of Space Charge Solvers.", presented at HB'16, Malmö, Sweden, paper MOPR029, this conference.

ISBN 978-3-95450-185-4

CODE DEVELOPMENT FOR COLLECTIVE EFFECTS

K. Li*, H. Bartosik, G. Iadarola, A. Oeftiger, A. Passarelli, A. Romano, G. Rumolo, M. Schenk,
CERN, Switzerland,
S. Hegglin, ETH Zürich, Switzerland

Abstract

The presentation will cover approaches and strategies of modeling and implementing collective effects in modern simulation codes. We will review some of the general approaches to numerically model collective beam dynamics in circular accelerators. We will then look into modern ways of implementing collective effects with a focus on plainness, modularity and flexibility, using the example of the PyHEADTAIL framework, and highlight some of the advantages and drawbacks emerging from this method. To ameliorate one of the main drawbacks, namely a potential loss of performance compared to the classical fully compiled codes, several options for speed improvements will be mentioned and discussed. Finally some examples and applications will be shown together with future plans and perspectives.

INTRODUCTION

Collective effects can lead to beam instabilities and brightness limitations and, thus, have a considerable detrimental impact on the performance of high brightness machines. Numerical modeling and simulations are a fundamental tool in understanding the physics of collective effects in circular particle accelerators. Moreover, they are a valuable means to evaluate and propose mitigation techniques to improve these limitations.

With the push towards higher brightness and higher energy these limitations play an increasingly important role. They involve several effects, among them impedance driven instabilities, electron cloud effects, the impact of long-range and head-on beam-beam collisions and single and multi-bunch effects.

In the past, simulation tools were often geared to modeling certain types or subsets of these effects. Meanwhile, the understanding of the individual effects has improved by a large amount and the combination of the different effects is now becoming increasingly important. To systematically study these combined effects on the beam stability, it is mandatory to bring together all the specific features of collective effects simulation codes.

In this paper we will investigate modern approaches to code development for collective effects. We will briefly illustrate the numerical modeling of collective effects in circular accelerators and then mention some general concepts and strategies for modern code style. We will then embark into a more specific discussion on the utilization of modern programming languages where we will use the example of the PyHEADTAIL framework. We will try to give an objective view on the advantages this type of approach can provide and show how to cope with potential limitations. Finally, we will present some specific applications illustrating the particular usefulness of this type of approach.

BASIC MODEL OF THE ACCELERATOR-BEAM SYSTEM

The numerical model that we will adopt to illustrate some of the concepts is the macroparticle model. Macroparticle models provide a direct and intuitive mapping of physics onto computer systems. Nearly any physical effect linked to particle beam dynamics can be easily implemented which makes these models extremely flexible and powerful. Macroparticles are essentially a numerical representation of a cluster of spatially neighbouring physical particles. As such, they follow the same dynamics following the same equations of motion that hold for physical particles.

A macroparticle system's dynamics is fully described by the evolution of its six phase space variables, the generalized coordinates and canonically conjugate momenta. Hence, a physical particle system, or a particle beam, can be easily represented via a macroparticle system on a computer system as an allocated chunk of memory where for each macroparticle all values of the six phase space variables are stored.

The accelerator is represented as a concatenation of elements each individually performing a distinct particle tracking. On a computer system, this can be represented by dedicated functions or methods that act on a macroparticle system in a defined and specific manner. Typically, a ring is split into a set of segments. A particle beam is transported from one segment to another by means of linear transfer matrices based on the machine optics in the transverse planes. In the longitudinal plane, tracking is performed assuming linear synchrotron motion, but also multi-harmonic RF systems can be easily taken into account as long a symplectic integration scheme is employed to assure numerical stability. Nonlinearities are treated via effective machine parameters such as chromaticity or detuning with amplitude by adjusting the phase advance of each individual macroparticle correspondingly after tracking along one segment. At each segment node, collective interactions can take place such as the application of different forms of wake field kicks, beam – electron cloud interaction, space charge kicks etc.

Typically, these effects are correlated with the longitudinal position of particles within the beam. To make the computations numerically efficient, a beam is longitudinally binned into a set of slices via a 1D particle-in-cell (PIC) algorithm. A single slice is then thought to be representative for all the macroparticles contained within. Collective

* kevin.shing.bruce.li@cern.ch

ISBN 978-3-95450-185-4

effects are correspondingly applied to the macroparticles on a slice-by-slice basis.

This type of modeling is illustrated in Fig. 1. Looking at this model, it inherently exhibits a modular structure and it becomes somewhat natural to follow the same modular architecture also for the code design itself.

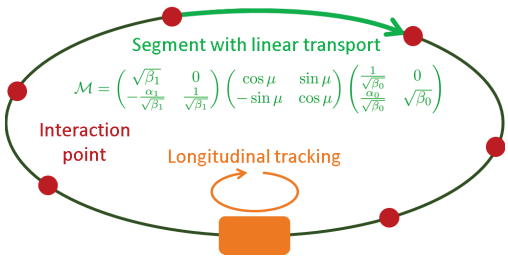

Figure 1: Illustration of the typical numerical model of the accelerator-beam system for collective effects. α, β denote the Twiss parameters, μ the phase advance between the interaction points (red).

MODERN APPROACHES AND PROGRAM ARCHITECTURES

General Concepts

Modern programming languages have support for multiple programming paradigms. This gives flexibility in the choice of programming style in order to describe and control the underlying numerical model in the most suited manner.

There are some minimum requirements, apart from the obvious one that the underlying physics should be correctly modeled, that can be specified for modern computer simulation codes. A key guideline should be to keep them as short and as simple as possible. In addition, they should be designed in a modular way and they should be usable in a dynamic manner. We will explain what we mean by these requirements in more detail in the following.

Writing short and simple code keeps the code base compact and concise and results in programs that are usually much more straightforward to read and to understand, making it easier to maintain and to extend and, at the same time, less susceptible to errors. The philosophy here is not to produce code bloat of which the quality and capabilities is measured by the number of lines of code but instead to write this code in as few lines as possible while capturing all the essentials of the underlying physical processes. Although this process does require some effort it usually pays off in the long run.

A modular architecture was already identified in the previous section to be well-suited to describe and to set up an accelerator-beam system simulation. The idea here is to have an orthogonal set of code blocks that can be developed independently and that can be combined to allow for a nearly infinite spectrum of simulation scenarios to be carried out. Each of these code blocks should follow the guiding philosophy of being compact and concise and ideally self-documenting in order to make them easily accessible, maintainable and usable. The concept of object-oriented programming blends in perfectly with the idea of a modular architecture. One can independently instantiate different objects that represent different elements of a machine. Each object can have its own interface, properties and methods to then manipulate the macroparticle beam.

Finally, requiring the simulation codes to be usable in a dynamic manner means several things. For one, the code should be fast both in development time as well as in execution time. Incremental and interactive development allows for efficient and effective implementation of complex physical processes. Code optimizations and parallelization allow for speed gains during execution.

Technologies nowadays are changing extremely fast and simulation codes should be able to adapt accordingly. For this, the classical static and heavy code basis is not well suited and should instead be replaced by more lightweight and flexible code.

Choice of Programming Language

Most of the requirements stated above can be satisfied by several modern programming languages. For the purpose of illustration and because it was the choice made for PyHEADTAIL, we will use the Python programming language [1] as an example. Python is a high-level, interpreted and dynamic programming language with a very large user community. It supports multiple programming paradigms, including object-oriented, imperative and functional programming or procedural styles. Its design philosophy is to foster short and simple code with an emphasis on code readability.

In terms of modular architecture, the layout and structure forms the backbone of the code design. Python's package and module management provide an easy and natural way of implementing any given structure with only few constraints. Thus, one is left with the pure architectural task of crafting the different parts of the code and their interactions. Python's strong support for object-oriented programming allows to build on this structure and to include additional functionality provided by the Python class mechanism such as instantiation of objects, inheritance, special methods, abstract classes etc.

Code development itself becomes very easy, for one due to the strongly reduced number in lines of code needed along with the very expressive language and syntax of Python. On the other hand, Python is an interpreted language. This makes the programming procedure essentially interactive. Online inspection and interaction with the program become possible making programming much more efficient and reliable. Programs are developed and tested at the same time almost naturally encouraging test-driven development with all its benefits.

A potential problem remains due to the very fact that Python is an interpreted language which is dynamically typed. This comes with considerable overhead during execution of the program and can render the simulation code

ISBN 978-3-95450-185-4

significantly slower compared to fully compiled simulation codes. We will address this issue in the next section.

Example of PyHEADTAIL

PyHEADTAIL [2] is a project that was started at CERN at the beginning of 2014. It is based on the well established HEADTAIL code [3]. However, being more a framework than a pure simulation code it builds on the very principles stated above. As such, it is predominantly written in Python and aims for a compact and concise code base making extensive use of Python's powerful expressiveness. It is built in a strictly modular way. The basic building blocks are a particles package, several packages containing machine elements and some utilities packages.

The particles package manages macroparticle systems which representing the physical particle beams. Essentially, this is a collection of data structures to keep track of the macroparticle system's dynamics and the evolution of its six phase space variables along with some specialised methods to help handling these data structures. It also contains all the methods for the generation of different macroparticle distributions and is mainly used to instantiate a bunch or beam object.

Machine elements are derived from an abstract base class and as such must all contain a *track* method. This method is always called on a bunch or beam object and manipulates the underlying data structures in accordance to the machine element that the object represents. There are classes that describe single particle tracking such as the ones contained in the longitudinal tracking module describing synchrotron motion. The multipoles module describes non-linear kicks in the thin lens approximation. There are other classes that simulate collective effects such as from wake fields or space charge. The architecture is set up in a way to minimize dependencies and to support the straightforward implementation of additional packages, modules or classes in order to streamline the code design and development. It is continuously being improved.

In providing the structure and classes that allow a modular composition of basic building blocks for customized simulations, the question may arise how to create a suitable inputfile syntax that can support and exploit this feature. We found that it is not necessary to create a new syntax and input files as used in the classical computer simulation codes such as MAD-X [4] or MAFIA [5]. Instead, it would be much easier to build on a syntax that is already available and widely known – the Python syntax itself. The input file becomes essentially a Python script and along with this comes the full power of the Python programming language injected up to the level of inputfile writing.

With this approach for example Python control flows become available in the input file. Examples are conditional execution of different parts of the input file (e.g. having a trigger on file i/o) or dynamic change of object attributes (i.e. resembling the implementation of trim functions). Any missing functionality can be easily programmed at the level of the input file. This can serve as a test and can later be reworked up to form a new module, for example. We will show some use cases in the last section.

Figure 2 shows the typical workflow in setting up and running a PyHEADTAIL simulation.

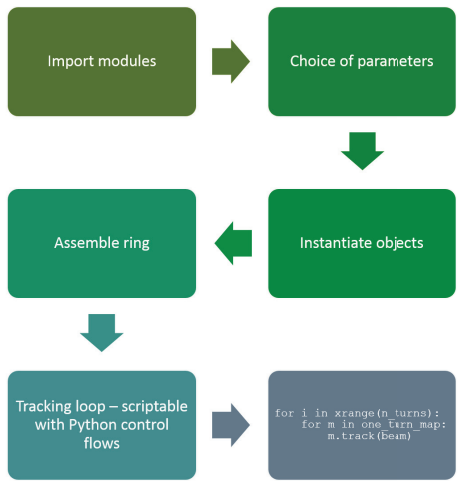

Figure 2: Typical workflow when setting up a PyHEADTAIL simulation.

PERFORMANCE CONSIDERATIONS

We mentioned in the previous section that the advantages provided by an interpreted language typically come with the price of performance loss in execution speed. Fortunately, there are ways out of this limitation at least for the case of Python.

First, Python contains a large set of third party libraries specialized for scientific computing, most importantly to be mentioned here, the NumPy and SciPy packages [6]. The core functionality of NumPy is its *ndarray* (for n-dimensional array) data structure. These arrays are strided views on contiguous memory buffers and they are homogeneously typed [1]. Any arithmetic operation on an ndarray is then automatically propagated down to a lower level such that the inner loops are performed on the level of the compiled language. This is called vectorization [2]. Algorithms that are not expressible as a vectorized operation will typically run slowly because they must be implemented in "pure Python". For these, Python can be interfaced with compiled languages such as Fortan or C routines, for example, to speed up computationally demanding parts of the code and thus to overcome performance bottlenecks. There are basically two different strategies for extending Python in this manner.

Python can be extended to use it as a "glue" language in which the core programming language is another, usually lower level compiled language, and Python is just used at the high level to stich different components of the core program together in a script. Different tools can be used for this

[1] A new package called Blaze attempts to generalize the NumPy functionalities to distributed and heterogeneous data structures and out-of-core computations [7]

[2] This should not be confused with the automatic vectorization provided by modern CPUs via SIMD instruction sets.

ISBN 978-3-95450-185-4

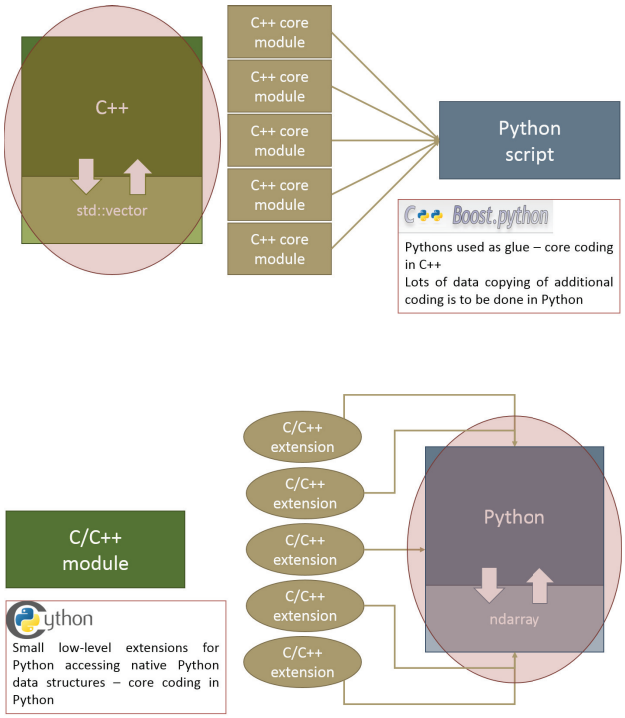

Figure 3: Comparison of the two strategies using Python as a "glue" language (top) and using Python as the core programming language (bottom) with the lower level language being C++ in this example. The core programming language is encircled in red in each case along with the basic data structure used.

with SWIG [8] or Boost.Python [9] being among the most popular. While most of the advantages mentioned earlier about having the input file actually written as a Python script still hold, the core programming is performed with a lower level language, e.g. C++, and the core data structures are the constructs of this language (i.e. for C++ the std::vector). For most scientists this makes the fundamental principle of writing short and simple code a lot more challenging. The other option is to use Python as the core programming language and to use lower level compiled languages only for the parts that actually pose a performance bottleneck. There are several tools available for Python that can be used for this purpose, among them statically compiling ones such as F2PY [10], ctypes which is part of the Python standard library, Cython [11] or alternatives that interoperate with NumPy, including scipy.weave, numexpr [12] or Numba [13]. Figure 3 shows and illustrative comparison of the two approaches.

In fact, PyHEADTAIL emerged from another project that was started already in 2012 and actually followed the first approach. This was cobra-HEADTAIL [14] which had its core written in C++, exporting modules to Python via Boost.Python. It was more cumbersome to add code written in pure Python and to exploit the advantages provided by NumPy since the basic data structures were C++ std::vectors. For this reason and after some research on the ndarray data structure it was finally decided to move to the second approach and to migrate to PyHEADTAIL.

Finally, parallelisation techniques exist for Python to further boost the performance both by multi-threading via OpenMP [15] (where the global interpreter lock, or GIL, needs to be released) and by multi-processing via mpi4py [16]. In addition, parallelsiation on the GPU is easily added with libraries such as PyCUDA [17] or can be added as CUDA [18] extensions via Cython or even via the CUDA just-in-time (JIT) compilation offered by Numba [13].

APPLICATIONS, PRESENT STATUS AND PERSPECTIVES

One of the big advantages that comes with running simulations in a scripting language is the dynamic control over the simulation process. For example, it is possible to access instance variables representing simulation parameters and to modify them at run time. This allows to seamlessly implement trim functions into the simulation. In principle, real machine cycles can thus be realistically simulated. One example where dynamically changing parameters have been employed is the creation of longitudinally hollow bunches in the CERN Proton Synchrotron Booster (PSB) used for space charge mitigation [19]. Here, the phase loop offset is modulated around the synchronous phase to excite a dipolar parametric resonance, effectively depleting the bunch core in longitudinal phase space. Figure 4 shows the function for phase loop offset modulation. The same function was implemented in the simulation to reproduce the dynamics during the formation of those observed in the experiments (Fig. 5).

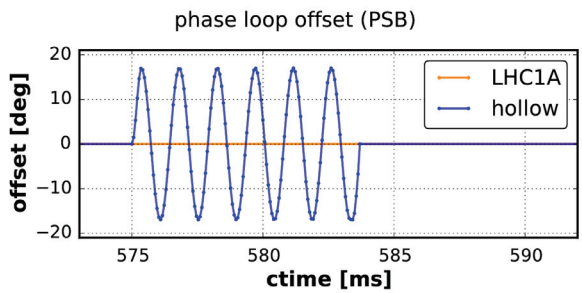

Figure 4: Trim function for the phase loop offset (blue curve).

The advantage provided by the modular design of PyHEADTAIL was exploited when interfacing PyHEADTAIL with PyPIC and PyECLOUD [20] to include the treatment of electron-cloud effects. PyPIC includes a set of Poisson solvers based on the particle-in-cell (PIC) algorithm including, for example, FFT methods using integrated Green's functions or finite-difference time-domain (FDTD) solvers which are able to handle complex boundaries using Shortley-Weller stencils. PyECLOUD is a build-up simulation code to simulate the formation of electron-clouds though multipacting. It therefore contains, among others, a sophisticated multipacting model and very detailed implementation of

ISBN 978-3-95450-185-4

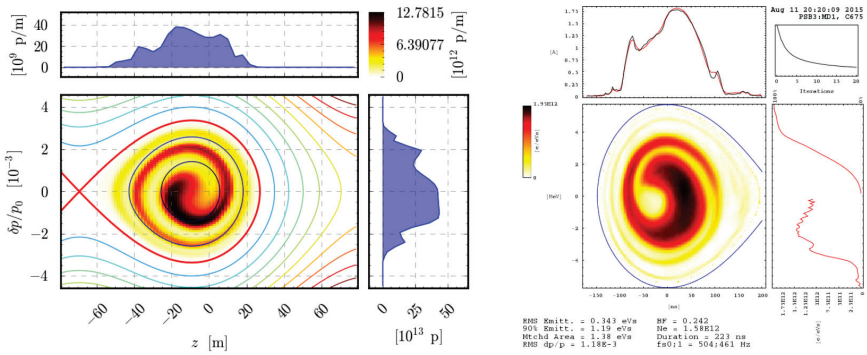

Figure 5: Comparison of the longitudinal phase spaces as obtained in simulation and measured in the experiments. Note that the horizontal axis on the left plot indicated position whereas on the right plot it indicates time.

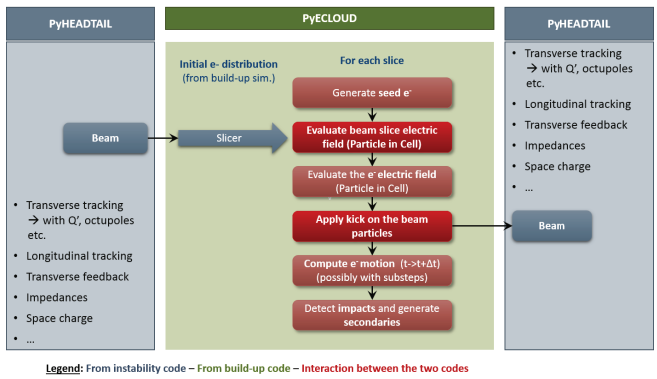

Figure 6: A graphical illustration of how PyHEADTAIL interacts with PyPIC and PyECLOUD.

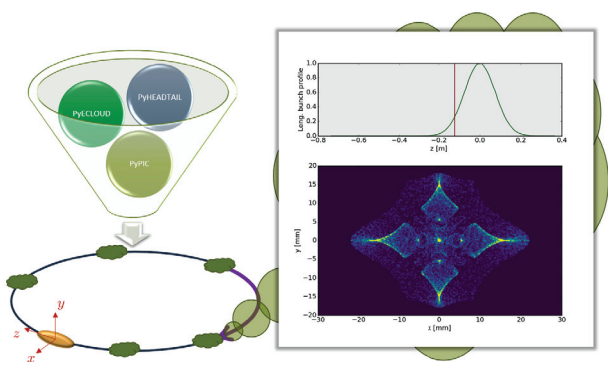

Figure 7: Snapshot of a simulation including electron clouds in quadrupoles. The plot shows the electron density distribution in an LHC vacuum chamber.

the electron dynamics within magnetic fields. PyPIC and PyECLOUD have been widely used in the past to study the formation of electron clouds in different machines with their specific beams and has also been benchmarked against experiments [21]. To include electron cloud effects to study them as collective effects it is therefore natural to reuse all the existing features of the two projects. Thanks to the orthogonal design of PyHEADTAIL no additional knowledge of any of the other modules was necessary for the successful integration of PyPIC and PyECLOUD. This made the inclusion of an entire separate code seamless and drastically reduced the probability of introducing any bugs in any of the working routines. Figure 6 illustrates how the different parts of the codes interact with each other.

Equipped with this additional feature, PyHEADTAIL was used to study electron cloud instabilities in different vacuum chambers with different magnetic field configurations for the Super Proton Synchrotron (SPS) at CERN. It is also being used to study the beam stability in presence of electron clouds in the quadrupoles of the LHC and the HL-LHC, where the high beam energies generate very fast cyclotron motion of the electrons which makes the correct modeling of the electron motion numerically very challenging. Figure 7 shows a snapshot of such a simulation.

Finally, PyHEADTAIL has been partly ported to the GPU using PyCUDA [22]. Following the usual philosophy, this was performed in the least invasive manner possible. To keep the interface unchanged at the user level, an abstraction layer was added in the form of a context manager. This context manager handles all dispatches of the different function calls via the context to the matching platform. That way, the performance of the GPU can be exploited when possible without having to pollute any of the existing programs or scripts.

Efforts are ongoing to include parallelisation at different levels using multi-processing via mpi4py in order to boost

ISBN 978-3-95450-185-4

performance for multi-bunch and electron cloud instability simulations.

REFERENCES

[1] "Python", https://python.org/, Jun. 2016.

[2] E. Métral et al.: "Beam Instabilities in Hadron Synchrotrons", in *IEEE Transactions on Nuclear Science*, vol. 63, no. 2, Apr. 2016, pp. 1001-1050.

[3] G. Rumolo and F. Zimmermann: "Practical user guide for HEADTAIL", *SL-Note-2002-036-AP*, Nov. 2002.

[4] "MAD – Methodical Accelerator Design", mad.web.cern.ch, Jun. 2016.

[5] "Die Finite-Integrations-Theorie und das Programmpaket MAFIA",temf.tu-darmstadt.de,Jun.2016.

[6] "SciPy", scipy.org, Jun. 2016.

[7] T. Oliphant, "Passing the torch of NumPy and moving on to Blaze", technicaldiscovery.blogspot.ch, Jun. 2016

[8] "Simplified Wrapper and Interface Generator", swig.org, Jun. 2016.

[9] D. Abrahams and S. Seefeld, "Boost.Python", boost.org, Jun. 2016.

[10] P. Peterson, "F2PY: Fortran to Python interface generator", sysbio.ioc.ee/projects/f2py2e, Jun. 2016.

[11] "Cython C-Extension for Python", cython.org, Jun. 2016.

[12] "Fast numerical expression evaluator for NumPy", pypi.python.org/pypi/numexpr, Jun. 2016.

[13] "Numba", numba.pydata.org, Jun. 2016.

[14] K. Li, "cobra-HeadTail", 95th ICE section Meeting, Nov. 2013.

[15] "The OpenMP API specification for parallel programming", openmp.org, Jun. 2016.

[16] "MPI for Python", bitbucket.org/mpi4py/mpi4py, Jun. 2016.

[17] A. Klöckner, "PyCUDA", mathema.tician.de/software/pycuda, Jun. 2016.

[18] "NVIDIA CUDA 8", developer.nvidia.com/cuda-zone, Jun. 2016.

[19] A. Oeftiger, "Space Charge Mitigation With Longitudinally Hollow Bunches", *in proc.* HB2016, paper MOPR026.

[20] "(Py)thon (Co)llective (M)acro-(P)article Simulation (L)ibrary with (E)xtendible (T)racking (E)lements", github.com/PyCOMPLETE, Jun. 2016.

[21] G. Iadarola, "Electron cloud studies for CERN particle accelerators and simulation code development", CERN-THESIS-2014-047, 2014.

[22] S. Hegglin, "Simulating Collective Effects on GPUs", MSc thesis, ETH Z¨urich, Switzerland, 2016.

ISBN 978-3-95450-185-4

NUMERICAL MODELING OF FAST BEAM ION INSTABILITIES

L. Mether*, G. Iadarola, G. Rumolo, CERN, Geneva, Switzerland

Abstract

The fast beam ion instability may pose a risk to the operation of future electron accelerators with beams of high intensity and small emittances, including several structures of the proposed CLIC accelerator complex. Numerical models can be used to identify necessary vacuum specifications to suppress the instability, as well as requirements for a possible feedback system. Vacuum requirements imposed by the instability have previously been estimated for linear CLIC structures, using the strong-strong macroparticle simulation tool FASTION. Currently, efforts are being made to improve the simulation tools, and allow for equivalent studies of circular structures, such as the CLIC damping rings, on a multi-turn scale. In this contribution, we review the recent code developments, and present first simulation results.

INTRODUCTION

Beam-induced ionization of residual gas present in the vacuum chamber of an accelerator, leads to the formation of ions and electrons along the beam path. Depending on several beam and machine parameters, such particles can accumulate into ion or electron clouds, which may cause serious beam degradation and the excitation of a two-stream instability. In electron machines with bunched beams, ion clouds build up if ions accelerated by a passing bunch do not have the time to reach the opposing chamber wall before the appearance of the subsequent bunch. In linacs, as well as in circular machines operating with a large clearing gap, the ion clouds can build up only over the passage of a bunch train, but may nevertheless lead to the development of an instability, the fast beam ion instability [1].

The Compact Linear Collider (CLIC) is a proposed TeV-scale high-luminosity linear electron-positron collider currently under study [2]. The collider could, in stages, reach a centre-of-mass energy up to 3 TeV, with roughly 20 km long main linacs. The linacs are designed to operate with trains of 312 or more short bunches with a minimum intensity of $N = 3.7 \times 10^9$, and a bunch separation of 0.5 ns. To maximize the luminosity, the transverse beam emittances, in particular in the vertical plane, need to be very small. These small emittance beams are produced in the CLIC injector complex, which consists of injector linacs, followed by two damping rings for each beam. The damping rings are designed to lower the normalized transverse emittances by several orders of magnitude from the injected values, down to the target extracted values of roughly 500 nm and 5 nm in the horizontal and vertical planes respectively. The beams are then further accelerated in a common linac before being transported through the main transfer lines to the beginning of the main linacs.

Due to the high brightness and the short bunch separation of the CLIC beams, the electron beam is at serious risk of suffering from the fast beam ion instability in several structures along the accelerator complex. Whether an instability can develop depends on if the ion species present in the chamber are trapped by the beam, and the residual gas pressure is sufficiently high to excite an instability. Studies of ion trapping, as well as assessments of pressure thresholds for the onset of instability can successfully be made using numerical models. In the past, such studies have been performed for the major linear CLIC structures: the main linac and the main transfer line, using a dedicated simulation tool, FASTION, which was developed specifically for the purpose [3]. To be able to perform similar studies for the damping rings, a number of outstanding challenges need to be addressed.

In the following section, we describe our tools and procedures for modeling fast beam ion instabilities. We outline the main issues with extending the studies to synchrotrons, and describe the modifications made to accommodate them. Subsequently, we present first results from simulation studies of the instability in the CLIC main damping ring. We also discuss in more detail some of the general challenges related to numerical studies of fast beam ion instabilities, and the strategies and solutions we have adopted in our simulation tools in order to address these. In the final section, we draw some concluding remarks.

SIMULATION TOOLS AND DEVELOPMENT

Macroparticle tracking simulations using the particle-in-cell (PIC) method, are a common tool for numerical studies of collective effects, and the one we employ in our model. Within this framework, the machine lattice is divided into a number of segments, each of which is represented by an interaction point where the electromagnetic beam-ion interaction along the segment is modeled in 2D. Ions are generated bunch by bunch, and the beam-ion interaction is simulated separately for each bunch along the train. In our studies, we use strong-strong simulation tools, *i.e.* both the beam and the ion cloud are represented by sets of macroparticles, which can be time-consuming, but offer a comprehensive model of the phenomenon. The ion macroparticles are regenerated in every interaction point, whereas the beam macroparticles, defined by their phase space variables, are transported between the interaction points using the linear transverse transfer matrices.

FASTION

The FASTION code, written in the C language, was developed at CERN specifically to study the fast beam ion instability in linear CLIC machines. It allows to study a user defined gas composition with different species, defined through their

* lotta.mether@cern.ch

ISBN 978-3-95450-185-4

individual mass, partial pressure and ionization cross section. Ions are generated either through scattering ionization, or, if the beam field exceeds a given threshold, through field ionization. Field ionization is estimated to take place along a large part of the CLIC main linac, greatly increasing the amount of ions generated by the passing beam [4–6]. Longitudinal dynamics are not included in the code, and each bunch is modeled as a transverse 2D distribution. This can be considered a reasonable approximation, given the short bunch length of the CLIC beams, along which the relatively heavy ion distribution would not move significantly. Acceleration is taken into account by assigning a relativistic gamma to each interaction point.

In order to adapt the FASTION code to the CLIC damping rings, it should be extended with a number of features that are generally relevant in electron synchrotrons, *e.g.* radiation damping, a model for a feedback system, detuning parameters such as chromaticity, and perhaps longitudinal dynamics. Another issue that could be interesting to consider is the effect of the applied magnetic fields on the ion motion. In the CLIC main linac, roughly a quarter of the length consists of quadrupoles, the fields of which have not been taken into account in the instability simulations. In the damping ring, quadrupoles take up a similar fraction, and in addition more than 40 % of the length is covered by dipole fields. Due to the proton mass, the effect of the magnetic fields is not expected to be crucial, as it is for electron clouds, but especially the lightest ion species, which could be trapped by the beam in the beginning of the damping process, could undergo a number of cyclotron periods during the passage of a bunch train.

Rather than proceeding with implementing the desired features into the FASTION code, however, we have adopted the approach of implementing the functionality of FASTION into another tool set, the PyECLOUD-PyHEADTAIL simulation set-up, which already includes these as well as several other potentially useful features.

PyECLOUD and PyHEADTAIL

PyECLOUD is a 2D macroparticle code modeling the build-up of electron clouds in accelerators [7]. PyHEADTAIL is a macroparticle tracking code used for simulating various collective effects [8]. The tools are used extensively at CERN for studies of both the current accelerator complex and future projects, and have each been benchmarked against experiments. Both tools are based on earlier numerical codes, ECLOUD and HEADTAIL [9] respectively, which have been rewritten using mainly the Python language, extended and updated with a modular structure to make them more versatile, maintainable and user-friendly. A more detailed description of the implementation and a discussion on the motivation and underlying principles of the design choices are provided in Ref. [8].

Owing to their modular structure and flexible nature, the two codes can be coupled together to simulate the beam dynamics of various electron cloud induced effects [10]. In this set-up, PyHEADTAIL is used to track the beam through various elements along a machine, which also contains a selected number of electron cloud interaction points distributed along the lattice. In each of these interaction points, the state of the beam macroparticles is passed to PyECLOUD, which models in detail the interaction between the beam and an electron cloud (which can be loaded from an earlier dedicated build-up simulation), and subsequently passes the updated beam phase space coordinates back to PyHEADTAIL for continued tracking.

Practical Implementation

Due to the very similar nature of electron- and ion-induced beam effects, the PyECLOUD-PyHEADTAIL simulation set-up could be applied to the simulation of fast beam ion instabilities, with relatively few adjustments. One main distinction is that the ion cloud in each interaction point should be built up from the beginning in real time along the bunch train passage, taking into account the actual position of each bunch. Below we list a few additional modifications that were required for the practical implementation:

- Generalization to arbitrary charge and mass, both for the beam and cloud particles.
- Modification of impacts in PyECLOUD. While secondary emission is an important ingredient for the electron cloud build-up, we have implemented simple perfect absorber boundary conditions for ions reaching the border of the simulation domain.
- Extension of the gas ionization model already present in PyECLOUD as an electron source, to handle the generation of different ion species.

Whereas PyECLOUD is designed to simulate electron cloud build-up along an arbitrary bunch train pattern, PyHEADTAIL had previously been used only with beams of a single bunch. In both tools, however, a bunch is typically divided longitudinally into slices, with collective interactions modeled slice by slice. For the fast beam ion instability simulations it is essential to track the full bunch train, but the interactions can be modeled bunch by bunch, using strictly transverse 2D distributions for the ion and bunch particles, as is done in FASTION. Benefiting once more from the modular design, it was thus possible to set up multi-bunch beam tracking following a similar structure, slicing the beam into bunches for the ion-beam interaction and applying a single kick per bunch.

In principle, it would be possible with only minor additional adjustments, to add a second layer of slicing to resolve the longitudinal bunch structure in the interactions. We have currently not explored this option, however, since we expect the effect to be relatively insignificant, whereas it would significantly increase the execution time, which is already a limiting factor without the additional operations.

On the other hand, enabling PyECLOUD to run with ions in place of electrons also opens up the possibility of dedicated ion build-up studies using a rigid beam field map, and

ISBN 978-3-95450-185-4

separate instability simulations based on their output, which is the current approach for electron-cloud-induced instability studies. This makes it possible to study and estimate the effect on the beam of ion trapping and the build-up of ion clouds over multiple turns, which would currently be computationally too demanding for most practical applications using strong-strong simulations. Such studies could be of interest *e.g.* for light sources operating with short clearing gaps, which may become more sensitive to ion-induced instabilities due to future upgrades to smaller beam sizes.

APPLICATION TO CLIC DAMPING RING

Table 1: Main Damping Ring Parameters in Simulations

Parameter	Symbol, unit	Value
Energy	E [GeV]	2.86
Bunch population	N [10^9]	4.1
Norm. horizontal emittance	$\gamma\epsilon_x$ [µm]	472
Norm. vertical emittance	$\gamma\epsilon_y$ [µm]	4.8
Bunch length (r.m.s.)	σ_s [mm]	1.6
Bunch spacing	ΔT_b [ns]	0.5
Bunches per train	N_b	312
Circumference	C [m]	427.5

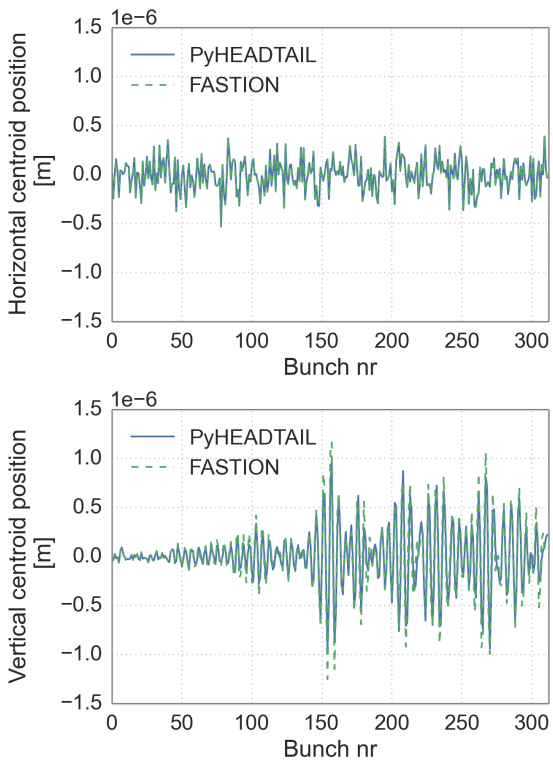

Figure 1: Horizontal and vertical bunch-by-bunch centroid position after one turn of tracking with P = 20 nTorr.

To test the new implementation of ion-induced instabilities within PyECLOUD and PyHEADTAIL, we have set up some simulations for the CLIC main damping ring, to benchmark the results against FASTION simulations. For this purpose we use a simple simulation scenario, excluding any of the effects that motivated the recent development, since these are not available in FASTION. The main parameters used for the study, corresponding to the equilibrium values for the damping ring, are summarized in Table 1. The residual gas consists of a single species, water vapor, with the mass number A =18, which is the lightest species expected to be trapped for the chosen beam parameters.

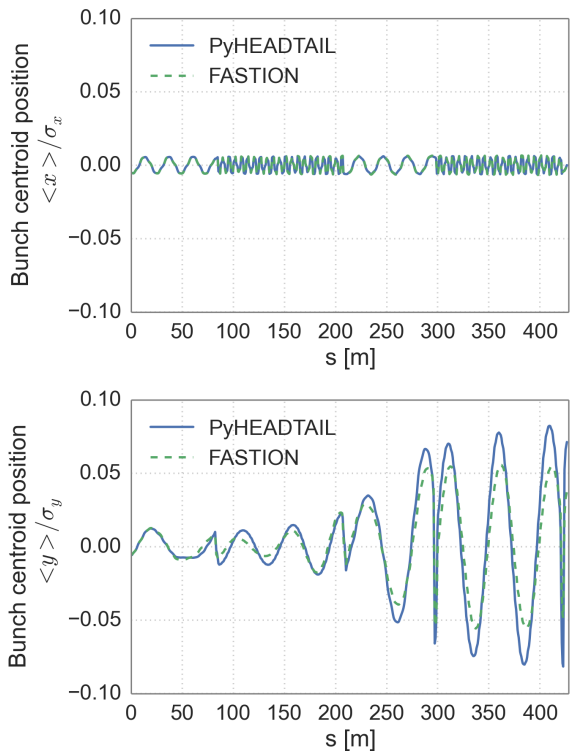

Figure 2: Evolution of the horizontal and vertical centroid position of the last bunch of the train over one turn in the machine with P = 20 nTorr.

In the first study, a bunch train is initialized with identical macroparticle phase space coordinates in each code. The train is tracked for one turn in the machine, which is divided into 677 interaction points, each representing a segment roughly 60 cm long. The residual gas pressure is set to 20 nTorr, which is sufficiently high to induce a growth of unstable motion in a single turn. The transverse bunch-by-bunch centroid position of the full train after one turn of tracking with each code is shown in Fig. 1. There is a clear growth of unstable motion in the vertical plane, whereas the horizontal plane is unaffected, as expected for a flat transverse beam profile. Figure 2 displays the evolution over one turn in the machine of the centroid position of the last

ISBN 978-3-95450-185-4

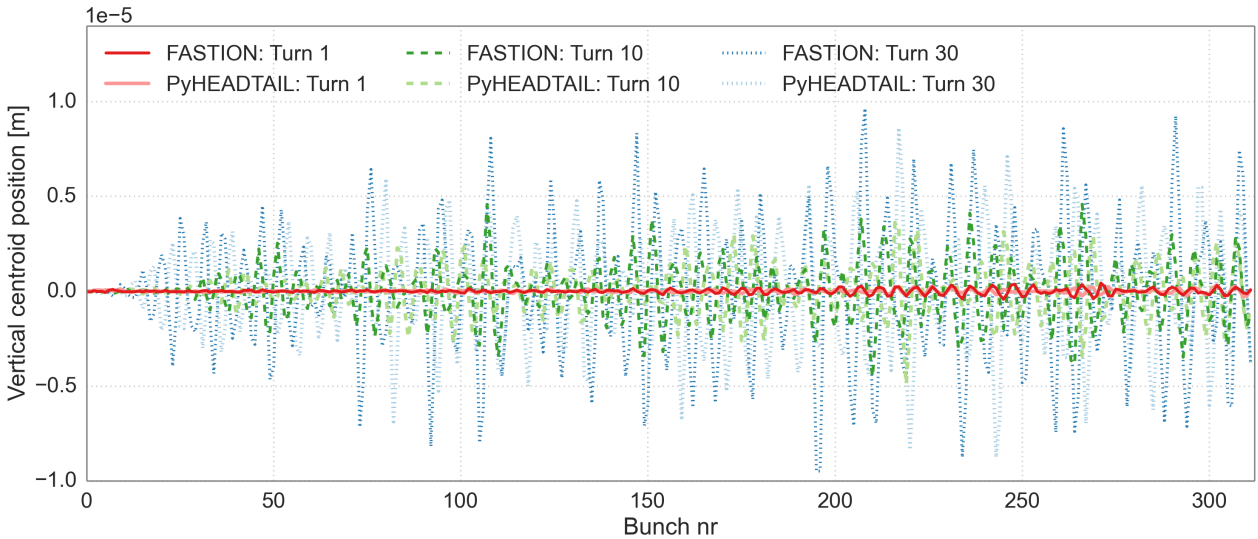

Figure 3: Vertical bunch-by-bunch centroid position after 1, 10 and 30 turns of tracking with P = 10 nTorr.

bunch of the train. In both cases, the results obtained with the two different tools are in good agreement. We believe that the small discrepancies can be attributed to the randomness in the explicit coordinates of the ion distribution generated around each bunch.

A second benchmarking study was performed, with the phase space coordinates of the bunch train macroparticles initialized with different random jitter seeding the instability in each code. The bunch trains were tracked for a hundred turns, with the machine lattice divided into 260 interaction points and the gas pressure set to 10 nTorr. Snapshots of the bunch-by-bunch centroid positions of the full train after one, ten, and thirty turns are displayed in Fig. 3. Even though initialized with different seeds, it can be seen that the growth of unstable motion for a given bunch along the train evolves at a similar pace with respect to the number of executed turns in both cases. A similar agreement can be seen also on the vertical emittance growth of the last bunch of the train, shown in Fig 4.

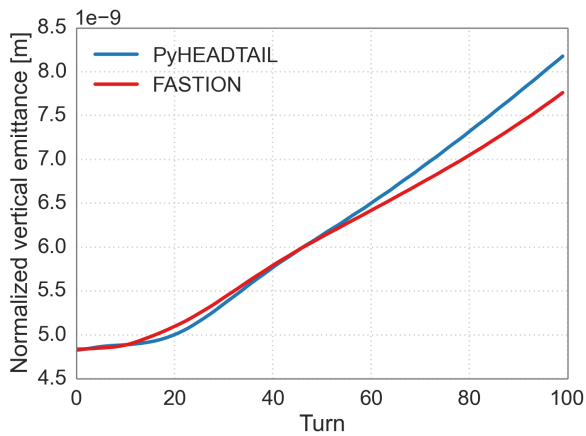

Figure 4: Evolution of the normalized vertical emittance of the last bunch of the train over 100 turns with P = 10 nTorr.

ASPECTS ON PERFORMANCE AND ACCURACY

One of the main challenges with using a strong-strong simulation tool for modeling the fast beam ion instability is the relatively large computational load of each interaction, resulting in long execution times. This becomes a serious limitation especially for studies of the damping rings, where it would be desirable to model the evolution of the instability during the entire damping period, or at least a considerable part at a time, since both the species of ions trapped by the beam and the dynamics responsible for initiating the instability depend crucially on the beam size.

In the CLIC main damping ring the transverse damping time is 2 ms, corresponding to roughly 1400 turns. With a sufficiently small distance between interaction points, which we consider to be ≤ 2 m, simulating one turn around the ring currently takes 20 minutes with FASTION, yielding a run time of 20 days for a full damping time. The PyECLOUD-PyHEADTAIL implementation currently exhibits execution times roughly 50 % slower than FASTION, after some initial optimization. Code profiling studies have shown that a large part of this difference comes from the FFT calculations used in the PIC solver, on which some further optimization is still required. Moreover, to improve the run-time performance further, efforts are under way to create a layer of parallelization that can be used for the ion studies, as well as for electron cloud and other multi-bunch studies.

For particle-in-cell simulations of two-stream instabilities in general, it can be challenging to resolve accurately the electric field of the beam, with a simulation domain spanning

ISBN 978-3-95450-185-4

the size of the surrounding cloud, or even the entire beam chamber. This is especially true for electron and positron machines, which typically have much smaller beam sizes compared to the chamber radius than hadron machines. For fast beam ion instability studies it is particularly important to have a good resolution of the electric fields within the beam, since the variations in the kick given to particles at slightly different locations around the centre of the beam, are an important ingredient in exciting the instability.

Simply increasing the number of PIC grid cells representing the full simulation domain easily leads to unacceptably long execution times, and may require excessive amounts of memory. For very flat transverse beam profiles typical in lepton machines, using rectangular grid cells may be beneficial, but *e.g.* in the case of the CLIC main linac where the beam size becomes extremely small, we found it not to be a sufficient measure to obtain the required resolution with a reasonable execution time. The problem could be addressed through the use of multiple nested grids, such that the grid resolution can be increased around the beam where it is needed, but kept at a lesser resolution elsewhere. In FASTION, a dual-grid solution using an internal, fine grid spanning the area around the beam, and a coarser grid spanning the full simulation domain for ions outside of the beam was implemented. A similar solution, but allowing for an arbitrary number of grids is currently being implemented in PyPIC, the PIC module used by PyECLOUD.

CONCLUSION

In order to ensure that the operation of the damping rings in the proposed CLIC accelerator complex will not be affected by the fast beam ion instability, systematic simulation studies are needed to determine viable vacuum and feedback specifications. To this end, the functionality of the FASTION code has been implemented in a new simulation set-up using the existing simulation codes PyECLOUD and PyHEADTAIL, which include all the necessary features for studying synchrotrons. First studies for the main damping ring have been performed, and the results have been successfully benchmarked against FASTION. Making use of the many features available in the new simulation set-up, the effects on the instability of several different elements can now be estimated, such as the self-space charge of the ions, the electric field boundary for various beam chamber profiles, energy or position dependent detuning and the movement of ions in bending and focusing magnetic fields. Another significant benefit is the shared workload of maintenance and development, which is already bearing fruit in the currently ongoing developments on parallelization and optimization of the PIC methods.

REFERENCES

[1] T. O. Raubenheimer and F. Zimmermann, "Fast beam-ion instability. I. Linear theory and simulations", *Phys. Rev. E*, vol. 52, no. 5, pp. 5487–5498, Nov. 1995.

[2] M. Aicheler *et al.*, "A multi-TeV linear collider based on CLIC technology: CLIC conceptual design report", CERN, Geneva, Switzerland, Report CERN-2012-007, Oct. 2012.

[3] G. Rumolo and D. Schulte, "Fast ion instability in the CLIC transfer line and main linac", in *Proc. 11th European Particle Accelerator Conf. (EPAC'08)*, Genoa, Italy, Aug. 2008, pp.655-–657.

[4] G. Rumolo and D. Schulte, "Update on fast ion instability simulations for the CLIC main linac", in *Proc. 23rd Particle Accelerator Conf. (PAC'09)*, Vancouver, Canada, May 2009, pp. 4658–4660.

[5] J.-B. Jeanneret, G. Rumolo, and D. Schulte, "Vacuum specifications for the CLIC main linac", in *Proc. 1st Int. Particle Accelerator Conf. (IPAC'10)*, Kyoto, Japan, 2010, pp. 3401–3403.

[6] A. Oeftiger and G. Rumolo, "Fast beam-ion instabilities in CLIC main linac: vacuum specifications", CERN, Geneva, Switzerland, Rep. CERN-OPEN-2011-050, Nov. 2011.

[7] G. Iadarola, "Electron cloud studies for CERN particle accelerators and simulation code development", Ph.D.thesis, CERN-THESIS-2014-047, 2014.

[8] K. Li *et al.* "Code development for collective effects", presented at the 57th ICFA Advanced Beam Dynamics Workshop on High-Intensity and High-Brightness Hadron Beams (HB2016), Malmö, Sweden, July 2016, paper WEAM3X01.

[9] G. Rumolo and F. Zimmermann, "Practical user guide for HEADTAIL", Rep. CERN-SL-Note-2002-036-AP, 2002.

[10] G. Iadarola, A. Axford, H. Bartosik, K. Li, and G. Rumolo, "Effect of electron cloud in quadrupoles on beam instability", *Proc. 6th Int. Particle Accelerator Conf. (IPAC'15)*, Richmond, VA, USA, May 2015, pp. 409–411.

ISBN 978-3-95450-185-4

BEAM DYNAMICS ISSUES IN THE FCC*

W. Bartmann, M. Benedikt, M.I. Besana, R. Bruce, O. Brüning, X. Buffat, F. Burkart, H. Burkhardt, S. Calatroni, F. Cerutti, S. Fartoukh, M. Fiascaris, C. Garion, B. Goddard, W. Höfle, B. Holzer, J.M. Jowett, R. Kersevan, R. Martin, L. Mether, A. Milanese, T. Pieloni, S. Redaelli, G. Rumolo, B. Salvant, M. Schaumann, D. Schulte, E. Shaposhnikova, L.S. Stoel, C. Tambasco, R. Tomas, D. Tommasini, F. Zimmermann†, CERN, Switzerland; G. Guillermo, CINVESTAV Merida, Mexico; V. Kornilov, GSI Darmstadt, Germany; O. Boine-Frankenheim, U. Niedermayer, TU Darmstadt, Germany; T. Mitsuhashi, K. Ohmi, KEK, Japan; A. Chancé, B. Dalena, J. Payet, CEA, Saclay, France; P. Bambade, A. Faus-Golfe, J. Molson, LAL Orsay, France; J.-L. Biarrotte, A. Lachaize, IPNO, France; J. Fox, G. Stupakov, SLAC, U.S.A.; J. Abelleira, E. Cruz, A. Seryi, JAI Oxford, U.K.; R. Appleby, U. Manchester, U.K.; M. Boscolo, F. Collamati, A. Drago, INFN-LNF, Italy; J. Barranco, EPFL, Switzerland; S. Khan, B. Riemann, TU Dortmund, Germany

Abstract

The international Future Circular Collider (FCC) study [1] is designing hadron, lepton and lepton-hadron colliders based on a new 100 km tunnel in the Geneva region. The main focus and ultimate goal of the study are high-luminosity proton-proton collisions at a centre-of-mass energy of 100 TeV, using 16 T Nb_3Sn dipole magnets.

Specific FCC beam dynamics issues are related to the large circumference, the high brightness — made available by radiation damping —, the small geometric emittance, unprecedented collision energy and luminosity, the huge amount of energy stored in the beam, large synchrotron radiation power, plus the injection scenarios.

In addition to the FCC-hh proper, also a High-Energy LHC (HE-LHC) is being explored, using the FCC-hh magnet technology in the existing LHC tunnel, which can yield a centre-of-mass energy around 25 TeV.

MOTIVATION AND SCOPE

The Large Hadron Collider (LHC) [2] and its high-luminosity upgrade, the HL-LHC [3], have an exciting physics programme, which, covering the next 20 years, extends through the mid 2030s. Counting from the start of its design study in 1983, more than 30 years were needed to design, build and commission the LHC. Therefore, the community must now urgently start preparing the next accelerator for the post-LHC period, as it has clearly been recognized by the 2013 Update of the European Strategy for Particle Physics [4].

A large circular hadron collider seems to be the only approach to reach energy levels far beyond the range of the LHC, during the coming decades, so as to provide access to new particles with masses up to tens of TeV, through direct production, as well as to obtain tremendously increased production rates for phenomena in the sub-TeV mass range, with the corresponding greatly improved precision and enhanced sensitivity to new physics.

The energy reach of a high-energy hadron collider is simply proportional to the dipole magnetic field and to the bending radius: $E \propto B \times \rho$. Assuming a dipole field of 16 T, achievable with Nb_3Sn technology, the ring circumference must be about 100 km in order to reach the target value 100 TeV for the centre-of-mass energy.

Figure 1 presents a schematic of the FCC tunnel along with a sketch of the hadron collider layout. Prior to FCC-hh installation, the new 100 km tunnel could host a high-luminosity circular e^+e^- collider (FCC-ee). Concurrent operation of hadron and lepton colliders is not foreseen however. In addition, the FCC study considers aspects of *pe* collisions (FCC-he), as could be realized, e.g., by colliding the electron beam from an energy recovery linac (ERL) with one of the two FCC-hh hadron beams.

In the frame of the FCC study another future hadron collider is being studied, the so-called High Energy LHC (HE-LHC). The HE-LHC would be based on FCC-hh magnet technology, but be installed in the existing 26.7 km tunnel, which is presently housing the LHC.

Historically, investigations of an earlier version of the HE-LHC [5] gave birth to the FCC concept.

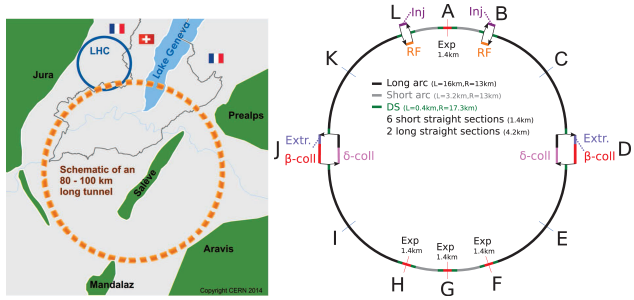

Figure 1: Left: Schematic of a 100 km tunnel for a Future Circular Collider (FCC) in the Lake Geneva basin. Right: Layout of the FCC-hh ring.

* This work was supported in parts by the European Commission under the Capacities 7th Framework Programme project EuCARD-2, grant agreement 312453, and the HORIZON 2020 project EuroCirCol, grant agreement 654305, as well as by the German BMBF.

† frank.zimmermann@cern.ch

ISBN 978-3-95450-185-4

PARAMETERS AND OPTIONS

Table 1 compares key parameters of FCC-hh [6] and HE-LHC (preliminary) with those of LHC and HL-LHC. The FCC-hh design considers parameter sets for two phases of operation [7]: Phase 1 (baseline) aims at a peak luminosity of 5×10^{34} cm^{-2}s^{-1}, and should deliver about 250 fb^{-1} per year on average. In Phase 2 (ultimate) the peak luminosity is increased by almost a factor of six, to about 3×10^{35} cm^{-2}s^{-1}, and the integrated luminosity by a factor of four to 1000 fb^{-1} per year.

The initial proton burn-off time can be computed as $\tau_{\rm bu} = N_b n_b/(L_0 \sigma_{\rm tot} n_{\rm IP})$, where N_b denotes the bunch population, n_b the number of bunches per beam, and $n_{\rm IP}$ the number of high-luminosity interaction points (IPs); $n_{\rm IP} = 2$ for all four colliders under consideration.

For both FCC-hh and HE-LHC there is an option of operating with a reduced bunch spacing of 5 ns, instead of the 25 ns spacing used at the LHC and HL-LHC. The total beam current would be the same, so that for 5 ns spacing the bunch charge is reduced by a factor of 5. To maintain the same luminosity (and the same beam-beam tune shift), the emittance also needs to be reduced by a factor 5, which appears possible — at least during the course of a physics fill — thanks to the strong radiation damping. The main advantage of 5 ns spacing is a factor five lower event pile up per bunch crossing in the particle-physics detectors. Possible disadvantages include much reduced transverse Landau damping and potentially aggravated eletron-cloud effects.

LUMINOSITY EVOLUTION

The four hadron colliders operate in different regimes.

At the LHC, the intensity decreases due to burn off. For the HL-LHC it is held constant by levelling (e.g. dynamic change of $\beta^*_{x,y}$ during a physics fill [8]). In either of these two cases, the transverse emittances do not much evolve during a fill, since the weak radiation damping is roughly balanced by the effects of intrabeam scattering, gas scattering and beam-beam-related phenomena.

By contrast, for the FCC-hh the radiation damping is extremely strong, faster than the burn off. As a result the total beam-beam tune shift , $\Delta Q_{\rm bb}$, and luminosity increase during the physics fill. From a certain moment onwards, the emittance shrinkage may need to be counteracted by controlled noise excitation, especially in Phase 1, in order for the beam-beam tune shift or detector pile-up not to exceed the empirical limits.

For the HE-LHC, the situation is again different. Here, the initial proton burn off is (two times) faster than the emittance shrinkage. In consequence, both the luminosity and the tune shift naturally decrease with time.

Figure 2 presents the evolution of instantaneous luminosity, integrated luminosity, bunch population, emittance, pile up and beam-beam tune shift for both phases of FCC-hh over 24 h of running. Here, we assume that the injected beam corresponds to the baseline parameters and a beam-beam tune shift of $\Delta Q_{\rm tot} \approx 0.01$. In Phase 2 the emittances are

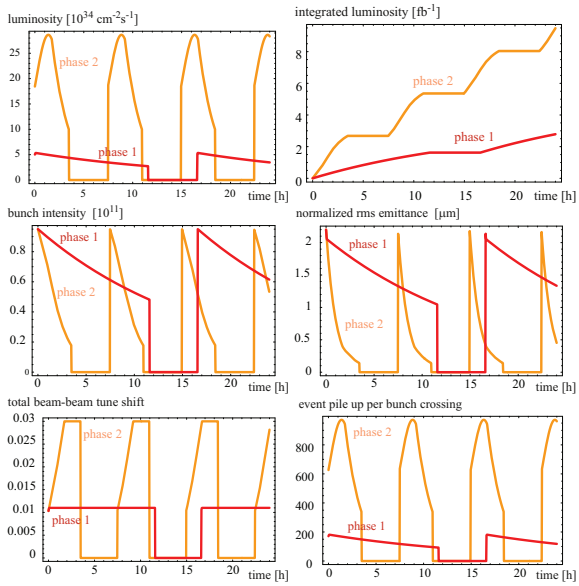

Figure 2: Instantaneous luminosity, integrated luminosity, bunch population, emittance, total beam-beam tune shift, and event pile up as a function of time during 24 hours with 25 ns bunch spacing, for FCC-hh Phases 1 ($\beta^*_{x,y} = 1.1$ m, $\Delta Q_{\rm bb} = 0.01$) and 2 ($\beta^*_{x,y} = 0.3$ m, $\Delta Q_{\rm bb} = 0.03$) [7].

allowed to shrink, the tune shift increases during the fill, until the higher tune-shift limit of $\Delta Q_{\rm tot} = 0.03$ is reached. From this moment onwards the further emittance damping is counterbalanced by a controlled blow up keeping the beam brightness constant. Only the proton burn-off in collision and the natural, or — after reaching the beam-beam limit — controlled emittance shrinkage due to radiation damping are taken into account. Other additional phenomena like gas scattering, Touschek effect, intrabeam scattering, and space charge are insignificant for the 50-TeV beams, in the scenarios considered.

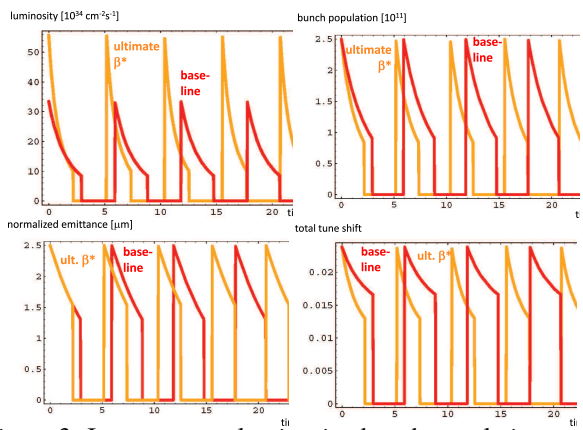

Figure 3: Instantaneous luminosity, bunch population, emittance, and total beam-beam tune shift, as a function of time during 24 hours, for the HE-LHC with 25 ns bunch spacing [9]. Nominal $\beta^*_{x,y} = 0.25$ m and ultimate $\beta^*_{x,y} = 0.15$ m ($\Delta Q_{\rm bb} = 0.025$).

Similar pictures for the HE-LHC, in Fig. 3, reveal the difference in behavior: here the tune shift decreases while

ISBN 978-3-95450-185-4

Table 1: Key Parameters of LHC, HL-LHC, HE-LHC (tentative), and FCC-hh

parameter	FCC-hh	HE-LHC	HL-LHC	LHC (*pp*)
centre-of-mass energy [TeV]	100	25	14	14
injection energy [TeV]	3.3 (1.5?)	0.45	0.45	0.45
ring circumference [km]	100	26.7	26.7	26.7
arc dipole field [T]	16	16	8.33	8.33
number of IPs	2+2	2+2	2+2	2+2
initial bunch population $N_{b,0}$ [10^{11}]	1.0 (0.2)	2.5 (0.5)	2.2	1.15
number of bunches per beam n_b	10600 (53000)	2808 (14040)	2748	2808
beam current [A]	0.5	1.29	1.11	0.58
initial (peak) luminosity/IP [10^{34} cm^{-1}s^{-1}]	5–30	5–34	5 (levelled)	1
max. no. of events per bunch crossing	170–1020 (204)	1070 (214)	135	27
stored energy per beam [GJ]	8.4	1.4	0.7	≈0.4
arc synchrotron radiation [W/m/aperture]	28.4	4.1	0.33	0.17
bunch spacing [ns]	25 (5)	25 (5)	25	25
IP beta function $\beta^*_{x,y}$ [m]	1.1–0.3	0.25	0.15 (min.)	0.55
momentum compaction [10^{-4}]	1.0	3.2	3.5	3.2
initial normalized rms emittance [μm]	2.2 (0.405)	2.5 (0.5)	2.5	3.75
normalized transverse equil. emittance (SR) [μm]	0.05	0.006	0.01	0.001
total cross section σ_{tot} [mbarn]	153	124	111	111
inelastic cross section σ_{intel} [mbarn]	108	100	85	85
transverse emittance damping time τ_ϵ [h]	1.08	4.5	25.8	25.8
initial intensity burn off time τ_{bu} [h]	19.2–3.2	2.3	15.5	40.4

protons are consumed. For HE-LHC, the integrated luminosity barely improves when reducing $\beta^*_{x,y}$ below 0.25 m.

The evolution for 5 ns spacing would look the same as for 25 ns spacing, except that bunch population, transverse emittance and event pile up would all be a factor 5 lower.

SYNCHROTRON RADIATION

At the FCC-hh an unprecedentedly large synchrotron radiation power of about 2.3 MW per beam is emitted in the cold arcs. To efficiently absorb this synchrotron radiation a new beam screen, inserted inside the cold bore of the magnets, is proposed [10, 11]. As shown in Fig. 4, it features two slits with an integrated wedge such that most primary photons generated at 50 TeV beam energy are deflected upward and downward behind the beam screen, where pumping holes are placed, and very few photoelectrons are generated inside the beam screen proper. In addition, the beam screen temperature will be raised, from 5–20 K at the LHC to 40–60 K at the FCC-hh. The higher temperature improves the Carnot efficiency and, thereby, facilitates the removal of the synchrotron radiation heat load.

An unsolved issue is the correction of the dispersion generated from the vertical crossing at one of the two high luminosity experiments. If this dispersion is corrected using vertical orbit bumps along the adjacent short arcs, here the synchrotron radiation fan can miss the beam screen slits. Preliminary simulations show that this would generate only a limited increase of the average gas density around the ring; it could still give rise to significant electron-cloud effects, especially at 5 ns bunch spacing.

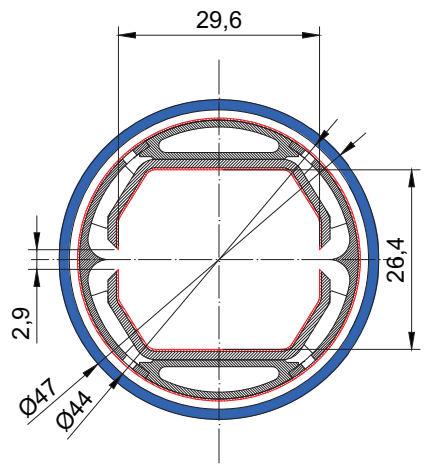

Figure 4: FCC-hh beam-screen design with integrated "folded" antechamber [10, 11].

As in electron storage rings, the eventual balance of the radiation damping by photon quantum fluctuations, in conjunction with the nonzero design dispersion, gives rise to a horizontal equilibrium emittance, ϵ_{eq}, which can here be considered a lower bound on the available emittance range. Its value is given by $\epsilon_{\text{eq}} \approx C_q \gamma^2 \theta_{\text{hc}}^3 F$, where θ_{hc} denotes the bending angle per half cell (0.0165 rad for the LHC, 0.001 rad for the FCC-hh), F is a numerical factor of order 1 which depends on the optics and the filling factor [12] ($F \approx 3.1$ for a FODO cell with 90 degree phase advance and 80% dipole-magnet filling factor in the arcs),

ISBN 978-3-95450-185-4

and $C_q = 55/(32\sqrt{3})\hbar c/(m_p c^2) \approx 2.09 \times 10^{-16}$ m designates the quantum constant for protons. For the hadron colliders which we consider in this paper (LHC, HE-LHC and FCC-hh) the equilibrium emittances from synchrotron radiation are one to three orders magnitude smaller than the initial emittances considered for use in operation (see Table 1). However, for FCC-hh Phase 2 with 5 ns spacing the final emittance at the end of a physics fill will reach this equilibrium emittance value: This type of operation will indeed be limited by the quantum fluctuations.

Synchrotron-light based emittance diagnostics has long been used at electron storage rings and has also proven an efficient non-invasive monitoring tool for the LHC.

The FCC and the HE-LHC will operate with a much smaller geometric emittance, and much higher energy. The FCC-hh will also have a larger bending radius than the LHC. A comparison is given in Table 2, where the parameters for a modern light source (MAX-IV) are included for comparison. The emittances of the various FCC-hh scenarios are much smaller than the horizontal emittance for any storage-ring based light source operating or under construction. For 5 ns spacing, the transverse emittance also becomes smaller than the lowest vertical emittances found in electron-storage rings. Indeed the FCC-hh will produce diffraction-limited light down to wavelengths of $\lambda \sim 4\pi\epsilon \leq 0.1$–$0.01$ nm, thereby becoming a truly "ultimate storage ring". The critical photon energy in the 16 T dipoles, 4.3 keV, corresponds to a wavelength of 0.28 nm.

For the FCC-hh, at a location with large beta function, $\beta \approx 2$ km, the rms beam size will be 200 μm. A synchrotron light monitor based on visible light ($\lambda = 500$ nm) from a standard arc bending magnet can be used over the entire energy range from 3 TeV to 50 TeV [13]. Similar to the existing diagnostics at the LHC, this will allow standard beam profile imaging, SR interferometry [14] for beam-size measurements, and coronograph techniques [15] for beam halo measurement. In addition, at FCC-hh, for beam energies above 30 TeV, hard X-rays (10 keV) will also become available. In this energy range, an X-ray pinhole camera will be a convenient method for monitoring the beam profile and beam size [13]. Pinhole arrays are sometimes used to monitor beam size and divergence simultaneously, e.g. [16].

INJECTOR SCENARIOS

The baseline scheme is to inject at a beam energy of 3.3 TeV from the present LHC, with upgraded ramping (factor 5 higher speed [17]) and decommissioned interaction regions (IRs). The minimum FCC filling time then becomes 40 minutes (4 ramps). Another option, which could also provide an energy of 3.3 TeV, is a 100-km superferric booster in the FCC tunnel itself.

One alternative, with lower injection energy around 1.5 TeV, is based on a superconducting High Energy Booster (HEB) installed in the SPS tunnel. The filling time of 34 minutes (34 ramps) is only marginally lower than for the injection using the LHC. However, the HEB could greatly facilitate operation, avoid superconducting transfer lines, and relax machine protection issues during the injection.

Main concerns related to the lower injection energy of 1.5 TeV are the much increased persistent current effects and reduced beam stability with regard to impedance.

Enhanced persistent-current field errors at 1.5 TeV imply a chromaticity swing of 800–1600 units, which could possibly be reduced either by optimizing the magnet design or by using smaller filaments in the superconducting wire.

Proposed machine studies in LHC [18] and RHIC [19] aim at exploring the possibility of lowering the injection energy for these machines and accelerating a beam through the "b_3 minimum," as proof-of-principle experiments.

OPTICS AND IR

The layout of the FCC-hh machine was illustrated in the right picture of Fig. 1. A full ring optics for FCC-hh is already available, including arcs, IR, injection region with RF section, betatron collimation, energy collimation, and extraction/dump line.

This optics can support β^* values down to 0.3 m or even 0.05 m [20, 21]. It is compatible with the achromatic telescopic squeeze (ATS) scheme [22]. A β^* of 5 cm is the limit determined by beam stay clear considerations [20]. This also turns out to be the minimum useful value with regard to integrated luminosity [21].

The interaction region design is scaled from the LHC/HL-LHC. The free length from the collision point to the first quadrupole is 45 m, i.e. about twice the length at the LHC, which also provides the space needed for forward spectrometer and compensator dipoles. The total length of the final quadrupole triplet exceeds 100 m.

The inside of the final quadrupoles needs to include a ≥15 mm tungsten shield against collision debris to guarantee a magnet lifetime of at least 5 years [23–25].

COLLECTIVE EFFECTS

The low revolution frequency of the FCC enhances the resistive-wall instability. The growth rate of the most affected lowest-frequency mode scales as [26]

$$\frac{1}{\tau} \approx -\frac{I_{\mathrm{beam}}\sqrt{\rho}}{\gamma Q_\beta f_{\mathrm{rev}}^{3/2} b^3} \frac{\mathrm{sgn}(\Delta_\beta)}{\sqrt{|\Delta_\beta|}} \qquad (1)$$

where ρ designates the resistivity of the inner side of the beam screen, Q_β the betatron tune, Δ_β the fractional part of the betatron tune (with values between $-1/2$ and $1/2$), and b the vertical half gap. The FCC-hh half gap is 13 mm instead of 17 mm for the LHC. The betatron tune is about 2 times the LHC tune. The revolution frequency is 4 times lower. At the higher beam-screen temperature of 50 K (compared with 5–20 K at the LHC), the surface copper layer (at $RRR \sim 100$ [27]) has about a 5 times higher resistivity ρ. The FCC-hh resistive-wall instability growth time at the LHC betatron tune of $\Delta_\beta = 0.32$ amounts to 47 turns at an injection energy of 1.5 TeV and 91 turns at 3.3 TeV [28]. The

ISBN 978-3-95450-185-4

Table 2: Emittances and a few other parameters for LHC, HE-LHC (tentative), and FCC-hh, compared with the corresponding values at a modern electron-beam light source (MAX-IV).

parameter	FCC-hh Phase 1 (2)		HE-LHC		LHC (*pp*)	MAX-IV
beam energy [TeV]	50		12.5		7	0.003
bunch spacing [ns]	25	5	25	5	25	10
initial bunch population $N_{b,0}$ [10^{11}]	1.0	0.2	2.5	0.5	1.15	0.3
initial geometric rms emittance [pm]	41	8	188	38	500	200
final geometric rms emittance [pm]	19 (2)	4 (1)	98	20	500	200
wave length at diffraction limit [nm]	0.025–0.5	0.01–0.1	1.2–2.4	0.25–0.48	6.3	2.5
arc bending radius [km]	10.4		2.8		2.8	0.019
critical photon energy [keV]	4.3		0.25		0.044	3.1

corresponding growth rates can be damped by a (possibly distributed) multi-band feedback system [29]. The instability may be further weakened by coating the beam screen with HTS materials like Tl-1223 or YBCO [30]. The single-bunch threshold of the transverse mode coupling instability is about an order of magnitude higher than the nominal bunch charge.

The electron-cloud instability needs to be addressed for the two bunch spacings of 5 and 25 ns. At the shorter spacing, Landau damping of multi-bunch instabilities by octupole magnets in the arcs will be 5 times less effective. Combining the FCC-hh beam-screen design featuring "antechamber" slits with a beam-screen surface layer of low secondary emission yield (obtained, e.g., by means of amorphous carbon coating or laser treatment [31]), may render the electron cloud harmless at any bunch spacing.

Achievable total head-on beam-beam tune shifts are taken to range from 0.01 (Phase 1) to 0.03 (Phase 2) as already demonstrated at the LHC without any noticeable effect on lifetime or emittance evolution.

COLLIMATION AND PROTECTION

A preliminary collimation system design has been developed for the FCC-hh based on scaling arguments [32]. At present the betatron collimation section extends over a considerable length of 2.8 km. Future options include smaller gaps, use of advanced, higher-performance collimator materials, deployment of bent crystals or electron lenses etc.

First simulations of collimation efficiency for the present system indicate a potential problem with losses of off-energy particles in the dispersion suppressors located downstream of the collimator insertions [33–35] and around the high-luminosity collision points. It is planned to add collimators at adequate locations in the dispersion suppressors, like those to be installed for the HL-LHC.

At top energy, the energy stored in the FCC-hh beams is about 20 times higher than for the LHC. Machine protection is critical. Pertinent aspects include the survival of the collimators in standard operation, in presence of regular losses, and in case of the asynchronous firing of a beam dump kicker, and the injection process, where the number of bunches per shot will be more limited than for the LHC.

FCC HEAVY-ION PERFORMANCE

Like the LHC, the FCC-hh could provide collisions of nuclear beams. Table 3 summarizes the principal beam parameters for Pb-Pb and p-Pb collisions [36, 37]. For heavy ions, the synchrotron radiation damping rates are about twice as fast as those of protons while the low-intensity equilibrium emittance is very much smaller (and unlikely ever to be reached). In a typical fill, the luminosity first rises sharply and subsequently decays in a regime governed by the interplay among luminosity burn-off, intra-beam scattering (IBS) and radiation damping [36]. The peak Pb-Pb luminosity at the FCC-hh is about 60 times higher than the design value for the LHC ALICE experiment. As at the LHC, photon-photon and photo-nuclear interactions will generate secondary beams emerging from the interaction points with intensities proportional to luminosity. The power they carry will increase from several tens of watts at the LHC to several kW. Suitable absorbers will have to be included in the dispersion suppressor sections to intercept them and avoid magnet quenches.

Table 3: Selected Beam and Performance Parameters for the FCC-hh in Pb-Pb and p-Pb Modes [36, 37]

operation mode	Pb-Pb	p-Pb
beam energy [TeV]	4100	50
c.m. energy/nucl. $\sqrt{s_{\mathrm{NN}}}$ [TeV]	39.4	62.8
no. of bunches / beam	2072	2072
bunch population [10^8]	2.0	164
transv. norm. emittance [μm]	1.5	3.75
IP beta function $\beta^*_{x,y}$ [m]	1.1	
hor. IBS emit. growth time [h]	23.4	4×10^3
long. emit. rad. damping time [h]	0.24	0.5
init. luminosity [$10^{27}\mathrm{cm}^{-2}\mathrm{s}^{-1}$]	24.5	2052
peak luminosity [$10^{27}\mathrm{cm}^{-2}\mathrm{s}^{-1}$]	57.8	9918

CONCLUSIONS

Future hadron colliders like FCC-hh and HE-LHC will enter a new parameter regime, which implies novel challenges as well as novel opportunities in beam dynamics, and calls for innovative technological approaches.

The rapidly growing global FCC collaboration is developing a cost-effective design with optimized performance.

ISBN 978-3-95450-185-4

REFERENCES

[1] FCC web site http://cern.ch/fcc.

[2] O.S. Brüning *et al.*, LHC Design Report, v.1: the LHC Main Ring," CERN Yellow Report CERN-2004-003-V-1 (2004).

[3] G. Apollinari *et al.*, "High-Luminosity Large Hadron Collider (HL-LHC): Preliminary Design Report," CERN Yellow Report CERN-2015-005 (2015).

[4] *European Strategy Session of Council, 30 May 2013*, CERN-Council-S/106 (2013).

[5] E. Todesco and F. Zimmermann (eds.), "EuCARD-AccNet-EuroLumi Workshop: The High-Energy Large Hadron Collider," CERN Yellow Report CERN-2011-003 (2011).

[6] D. Schulte *et al.*, "Future Circular Collider Study Hadron Collider Parameters," FCC-ACC-SPC-0001, EDMS no. 1342402 (2014)

[7] M. Benedikt, D. Schulte, F. Zimmermann, "Optimizing Integrated Luminosity of Future Hadron Colliders", *Phys. Rev. ST – Accel. Beams* 18, 101002 (2015).

[8] A. Gorzawski *et al.*, CERN-ACC-NOTE-2015-0043 (2015).

[9] M. Benedikt, S. Fartoukh, F. Zimmermann, HE-LHC WG meeting 20 May 2016

[10] R. Kersevan, "Beam Screen Design and Cooling, Vacuum Aspects, Synchrotron Radiation", Review of the FCC-hh Injection Energy, CERN, 16 October 2015, http://indico.cern.ch/event/449449.

[11] C. Garion, "FCC-hh beam screen studies and beam screen cooling scenarios," FCC Week 2016, Rome.

[12] L.C. Teng, "Minimizing the Emittance in Designing the Lattice of an Electron Storage Ring," Fermilab, TM-1269 (1984).

[13] T. Mitsuhashi *et al.*, "Conceptual Design for SR Monitor iin the FCC Beam Emittanxe (Size) Diagnostic," in *Proc. IPAC'16*, Busan, Korea (2016) pp. 133.

[14] G. Trad *et al.*, "Performance of the Upgraded Synchrotron Radiation Diagnostics at the LHC," in *Proc. IPAC'16*, Busan, Korea (2016) p. 306.

[15] T. Mitsuhashi *et al.*, "Design of Coronagraph for the Observation of Beam Halo at LHC," in *Proc. IBIC'15*, Melbourne, Canada (2015), p. 288.

[16] W.B. Peatman, K. Holldack, "Diagnostic Frontend for BESSY II," J. Synchrotron Rad. 5 (1998) 639.

[17] A. Milanese, B. Goddard, M. Solfaroli, "Faster ramp of LHC for use as an FCC High Energy hadron Booster," CERN-ACC-2015-133 (2015).

[18] M. Solfaroli *et al.*, "FCC Related MDs (MD on 225 GeV LHC Injection)," CERN Ext. LSWG Meeting, 18 January 2016.

[19] C. Montag, "Accelerating Protons through the b_3 Minimum in RHIC," BNL intenal note, October 2015.

[20] R. Martin, "β^* Reach Studies," FCC Week 2016, Rome.

[21] X. Buffat, D. Schulte, "Beam Parameter Evolution and Luminosity Performance," FCC Week 2016, Rome.

[22] S. Fartoukh, "Achromatic telescopic squeezing scheme and application to the LHC and its luminosity upgrade," Phys. Rev. ST Accel. Beams 16, 111002 (2013).

[23] M.I. Besana, F. Cerutti, "Collision Debris on the Triplet Quadrupoles," FCC Week 2016, Rome.

[24] M.I. Besana *et al.*, "Assessment and Mitigation of the Proton-Proton Collision Debris Impact on the FCC Triplet," in *Proc. IPAC'16*, Busan, Korea (2016) pp.1410–1413.

[25] R. Martin *et al.*, "Radiation Load Optimization in the Final Focus System of FCC-hh," in *Proc. IPAC'16*, Busan, Korea (2016) pp.1462–1465.

[26] A. Chao, *Physics of Collective Beam Instabilities in High Energy Accelerators*, J. Wiley (1993).

[27] F. Caspers *et al.*, "Surface Resistance Measurements of LHC Dipole Beam Screen Samples," in *Proc. of EPAC'00*, Vienna, Austria (2000).

[28] O. Boine-Frankenheim, "FCC-hh Impedances and Instabilities," FCC Week 2016, Rome.

[29] W. Höfle, "The LHC RF transverse system and perspectives for FCC-hh," FCC Week 2016, Rome.

[30] O. Brüning *et al.*, "High Energy LHC Document prepared for the European HEP strategy update," CERN-ATS-2012-237 (2012);
W. Barletta *et al.*, "Future hadron colliders: From physics perspectives to technology R&D," NIM A 764 (2014) p. 352; also see G. Stupakov, FCC Week 2015 Washington; S. Calatroni, "Status Report on HTS Coating Study," FCC Week 2016 Rome.

[31] R. Valizadeh *et al.*, "Low Secondary Electron Yield of Laser Treated Surfaces of Copper, Aluminium and Stainless Steel," in *Proc. IPAC'16*, Busan, Korea (2016) p. 1089.

[32] M. Fiascaris, "Collimation System Study Overview and Plans," FCC Week 2016, Rome.

[33] M. Fiascaris and S. Redaelli, "Betatron Collimation Efficiency," FCC Week 2016, Rome.

[34] J. Molson *et al.*, "Simulation of the FCC-hh Collimation System," FCC Week 2016, Rome.

[35] M. Fiascaris *et al.*, "First design of a proton collimation system for 50 TeV FCC-hh", in *Proc. IPAC'16*, Busan, Korea (2016) p. 2423.

[36] M. Schaumann, "Potential performance for Pb-Pb, p-Pb, and p-p collisions in a future circular collider, *Phys. Rev. ST Accel. Beams* 18, 091002 (2015).

[37] A. Dainese *et al.*, "Heavy ions at the Future Circular Collider," contribution to forthcoming CERN Report on Physics at FCC-hh, http://arxiv.org/abs/1605.01389.

ISBN 978-3-95450-185-4

STUDIES OF HIGH INTENSITY PROTON FFAGS AT RAL

C.R. Prior*, STFC Rutherford Appleton Laboratory, Didcot, U.K.

Abstract

The paper describes studies of high intensity proton accelerators for a next-generation source of short-pulse spallation neutrons. Along with conventional designs using rapid cycling synchrotrons, the long-term nature of the project provides scope for novel accelerator designs and developing technological ideas. A range of FFAG options is under consideration for the main spallation driver. Theory and simulation in the UK are combined with experimental studies of FFAGs in Japan, and a small prototype FFAG ring is planned to go on the FETS injector at the Rutherford Appleton Laboratory (RAL) for essential R&D. The paper covers the broad scope of the programme and details the success of the study to date.

INTRODUCTION

After several years considering options to upgrade the ageing ISIS spallation neutron source, there is renewed activity at RAL to explore options for a high intensity proton accelerator for next-generation neutron physics. Such a facility is being seen loosely as a successor to ISIS, which, despite its high productivity, is likely to have a limited life-span even with modest upgrades. Conventional designs using rapid cycling synchrotrons have been considered but, being long-term, the project provides opportunities for new proposals and an R&D programme based on developing technological ideas.

Existing spallation neutron sources generate a proton beam on target of up to ~1.5 MW at an energy up to about 3 GeV. The facility with the highest mean beam power is SINQ at PSI [1], with a cyclotron operating in continuous wave mode. SNS at Oak Ridge [2] is based on a pulsed H^- linac filling an accumulator ring via charge exchange injection and routinely produces 1 MW. The neutron facility at J-PARC [3] also operates at the 1 MW level though, in contrast, the accelerating structures rely on a 400 MeV H^- linac and a 3 GeV rapid cycling synchrotron (RCS). The facility with the longest history of producing world-leading science is ISIS [4] at RAL with a total beam power of 160-180 kW. Users benefit from a wide range of instruments around two different neutron production targets. In a few years, ESS will come online as a major neutron source in Europe. As ESS is a long-pulse facility (with a linac driving a proton beam straight into a spallation target), ISIS's aim is to continue to be the main provider of experimental opportunities for short-pulse neutron studies. It can either be progressively upgraded - and this has been the object of studies in the past - or a completely new facility can be designed with a view to the long-term future.

* chris.prior@trinity.ox.ac.uk

ISIS PHASED UPGRADES

Several ideas for upgrading ISIS to the 1-5 MW level of beam power have been proposed in recent years. One is to replace the 70 MeV linac, which is the oldest part of the facility and already suffers from cavity breakdown and beam-loss, with a new linac operating at 180 MeV. Since tune shift depends on $N/\beta^2\gamma^3$, the higher energy would allow an increased number N of protons, provided practical issues such as a revised injection system can be accommodated in the ring. Another idea is to add a second RCS in series with the existing 800 MeV ring and increase the energy of the existing beam to around 3 GeV. The ring, shown in Fig. 1, would initially take the beam from ISIS by bucket-to-bucket transfer; however its design also allows for a completely new 800 MeV H^- linac to be installed at a later date, which would replace the present synchroton. Such a system would use charge-exchange injection at 800 MeV, with phase-space painting to give a distribution that should be robust against intensity effects. Mean beam power at the target would be of the order of 2.5 MW with later upgrades to 5 MW. ISIS could continue to operate during the phased construction. Other options have also been considered, most notably an idea to build a second ring in the existing tunnel, but this would mean the neutron facility closing down for an extended period, so at this stage is not preferred.

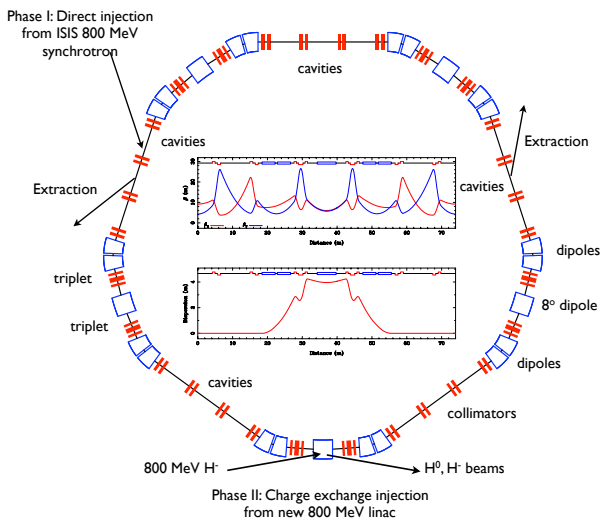

Figure 1: ISIS upgrade RCS showing lattice and optical parameters. Injection in the first phase would be directly from the present 800 MeV RCS, with a new system of H^- painting from a new linac in Phase II.

A further aspect of the proton R&D programme at RAL is the development of a flexible high current H^- injector, known as FETS (Front-End Test Stand) [5]. This project has been important in covering novel ion source design, implementation of a 3-solenoid LEBT, design and construc-

ISBN 978-3-95450-185-4

tion of a 4-vane, 4 m long, 324 MHz RFQ and application of a versatile dual fast-slow beam chopper. The H^- current is typically 60 mA with a pulse length up to 2 ms. Commissioning of the RFQ is about to start aiming for project completion in 2017, and plans for its future use are now being developed. While one application could be as a target test facility, FETS would be invaluable as an injector for a small development ring at RAL. In parallel with the design of a future multi-megawatt neutron source, a low energy ring (up to ~15 MeV, say) could provide essential guidance for the design of the main accelerating ring.

FFAG-BASED PROTON ACCELERATORS

Rapid cycling synchrotrons now provide a well-understood, reliable option for pulsed operation at the 1 MW level with a repetition rate up to about 50 Hz. But they do present challenges, and it is questionable whether conventional designs could take a very great step forward into the affordable multi-megawatt regime. There is the need for fast ramping magnets, eddy currents to be damped, and difficulties such as phasing multiharmonic rf. The H^- injection systems are highly complex, and contain controls to deal with partially stripped H^0 ions and unstripped H^-, ways to reduce stripping foil temperatures and methods of painting to create an intense beam with the correct emittances and transverse distribution. H^- linacs also suffer from intra-beam stripping, a phenomenon first identified at SNS [6].

In a forward-looking scenario we would look to eliminate at least some of these, and we believe the solution lies in fixed field alternating gradient accelerators, or FFAGs. Studies in the 1950's at MURA [7] produced a wealth of knowledge of beam dynamics in electron FFAGs. An FFAG option was proposed for the European Hadron Facility (EHF) in the 1970's, and was carried over into the 1990's study of a short pulse ESS. It was rejected in favour of a linac+accumulator ring scenario because of the cost of R&D and demands from the neutron community for a tried-and-tested - and therefore - trustworthy machine. However FFAG studies have come on in leaps and bounds with the development of technology and new materials such as magnetic alloys in Japan and initiatives in beam dynamics in the USA and the UK.

For future needs, there are several advantages in FFAGs for a spallation source. Stable dc power supplies can be used for the main magnets; fewer accelerating cavities will be required, and horizontal beam extraction will be easier. The repetition rate can be higher than synchrotrons (~ 100 Hz) and quite flexible, restricted only by the rf programme pattern. This leads to increased beam power and the ability to offer a better match to users' requirements. Neutron users do not necessarily want a high repetition rate but as an option this opens possibilities for a wider range of proton driver use: driving a sub-critical nuclear reactor, or splitting the beam so that different areas of physics can be studied using a single accelerator on a single site.

FFAGs have a large momentum acceptance. This allows particles with the injection and extraction momenta to circulate in the ring at the same time. A large horizontal aperture means that the horizontal emittance ϵ_h can be enlarged. Since the tune depression is given by

$$\Delta Q_v = -\frac{N r_p}{\pi \epsilon_v \left(1 + \sqrt{\epsilon_h/\epsilon_v}\right) \beta^2 \gamma^3} \frac{1}{B_f}, \qquad (1)$$

an emittance ratio $\epsilon_h/\epsilon_v = 10$ and a repetition rate of 100 Hz (four times J-PARC), could generate a beam power approaching 10 MW and still maintain acceptable space charge levels. The beam power could be even higher if the linac feeding the RCS operated at a higher energy.

In the absence of ramping, it is also possible to use superconducting or permanent magnets. Energy efficiency will be high; the machine is expected to be robust with high availability; and low operational costs can be achieved.

On the negative side are the non-linear magnetic fields, the perceived increased sensitivity to alignment and magnet field errors and need for a larger vertical injection acceptance. Design issues include the need for a long straight section for injection, the choice of the cell and ring tunes, the space charge field effects, and the protection against beam loss during injection, acceleration and extraction.

Parameter Requirements

For the main spallation driver, a range of FFAG structures is under consideration to meet the optical demands. The features are as far as possible carried over to a companion prototype FFAG ring to go on FETS. Possible parameters for the two scenarios are shown in Table 1. The starting points are assumptions about the injector linac current, the normalised emittance of the incoming beam (the same in both cases), the likely emittances created in the rings and the ring radii. Input energies are the FETS energy, 3 MeV, for the small ring, and 800 MeV, the ISIS top energy for the main ring. The space-charge tune depression is assumed to be $\Delta Q \sim -0.1$; then equation (1) gives the total number of protons N in the rings and the number of turns to be injected to achieve these levels. The ring designs are based around meeting these parameters.

Pumplet FFAG

The idea of pumplet[1] lattices was first developed for the muon accelerators in the neutrino factory [8] and several options followed for proton machines. The type considered in this study is the scaled pumplet whose lattice uses combined-function magnets in an Od(-)oF(+)oD(-)oF(+)od(-)O pattern. (OO) and (o) are respectively, long and short straight sections, (d,D) are horizontally defocusing fields, F is a horizontal focusing field, and (+) and (-) represent normal and reverse bending. A sample cell for the small (FETS) ring is shown in Fig. 2. It has mirror symmetry about the central D(-) magnet. Both

[1] The name comes from the Welsh 'pump', meaning five, indicating the number of magnets making up each cell.

ISBN 978-3-95450-185-4

Table 1: Injection Requirements for the Main Spallation Source Ring and R&D Test Ring

Parameter	Main Ring	Test Ring
Kinetic energy at injection (MeV)	800	3
Linac beam current (mA)	100	1.9
Unnormalised injected emittances (π mm.mrad)	2.70	10.8
Painted horizontal emittance of ring beam (π mm.mrad)	270	270
Painted vertical emittance of ring beam (π mm.mrad)	135	135
Expected tune depression	0.065	0.065
Number of ions N ($\times 10^{11}$)	1950	2.79
Injection interval required, Ne/I (μs)	313.08	23.50
Revolution period at injection, t (μs)	1.29	1.31
Mean radius at injection energy, $\beta ct/2\pi$ (m)	52.00	4.974
Number of injected turns	241	17
Length of injection straight (m)	5.0	1.30

scaling and non-scaling designs have been considered. Orbits in the former are scaled replicas of one another with fixed beam dynamics across the energy range. The scaling property can be ensured through the use of magnet edges aligned on a common centre. Bend radii and quadrupole strengths are common to all elements. Theoretical optimisation to the desired cell tunes is carried out by varying the field gradients and the spacing of the magnet units, which in turn requires changes to the edge angles, and an iterative re-optimisation process.

The design for the FETS ring is scaling and has a circumference of 31.25 m, with 8 pumplet cells, all magnets having the same bending radius 0.91 m, as shown in Fig. 2. The energy range is 3-10 MeV and 1.3 m is provided for the injection straight. The radial orbit excursion is about 43 cm. A similar lattice is proposed for the main ring, a 26-cell pumplet structure with a 7.6 m bending radius. Each cell has a 5 m straight and a total length of 12.57 m, giving a mean ring radius of 52 m. Lattice functions for this pumplet FFAG are shown in Fig. 3. The energy range in this case is 800 MeV to 3.2 GeV. Scaling and non-scaling models have been treated but the markedly reduced vertical β-function means that for the main ring non-scaling is seen as preferable at this stage of the study.

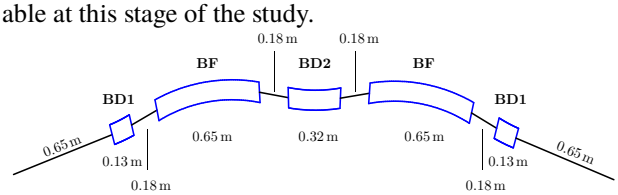

Figure 2: dFDFd pumplet cell, 0.91 m bending radius, part of an eight cell ring with mean radius 4.974 m

The alternative pumplet structure Of(+)oD(-)oF(+)oD(-)of(+)O shows larger β-functions and is ruled out at this stage of the study.

RCS lattice options

RCS pumplet-type lattices have also been examined both for the 3-10 MeV FETS ring and the larger 0.8-3.2 GeV main ring. The pumplet structure is the same as for the FFAGs but the combined-function magnets all have positive bends, which allows the bending radii to be larger and the magnetic fields much reduced. The choice of a pumplet cell is found to give a wide range of betatron tunes, providing flexibility in optimising parameters for injection. There are both advantages and disadvantages in choosing between RCS and FFAG designs. Ring costs will play a role but the crucial aspect is the effectiveness of the ring injection scheme described below.

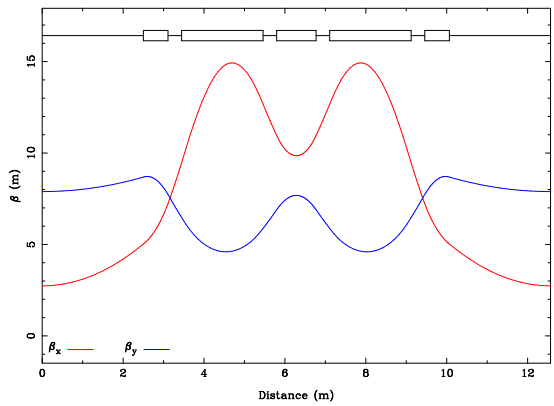

Figure 3: β-functions for the main FFAG pumplet lattice, an enlarged version of the lattice in Fig. 2; the dispersion (not shown) is non-zero throughout.

DF-spiral FFAG

A very recent idea is the DF-spiral FFAG developed by Machida [9]. This combines features of two types of scaling FFAG - radial sector and spiral - that were individually part of the MURA programme. In the radial sector FFAG, the vertical tune depends on the field flutter and there is zero spiral angle; in the spiral FFAG, the tune is adjusted by a non-zero spiral angle and the field flutter parameter is fixed at ≈ 1. Attempts to use one or other of these designs

ISBN 978-3-95450-185-4

for a high energy, high intensity machine have resulted in either large spiral angles or very high fields in the reverse bends. The novel DF-spiral design combines normal and reverse bend magnets with finite spiral angle to create doublet focusing. The reverse bending magnet is positioned on one side of the normal bending magnet so as to enhance the edge focusing in the vertical direction. This provides a practical lattice design, with a reasonably compact size, that could provide cost effective operation, especially if superconducting technology is used. Fig. 4 shows an example of a 0.4-1.2 GeV ring with a radius of 26 m, the same size as the ISIS tunnel. There are also designs for a prototype test ring for FETS (3-27 MeV) and a larger ring with 52 m radius for a high intensity 3 GeV driver.

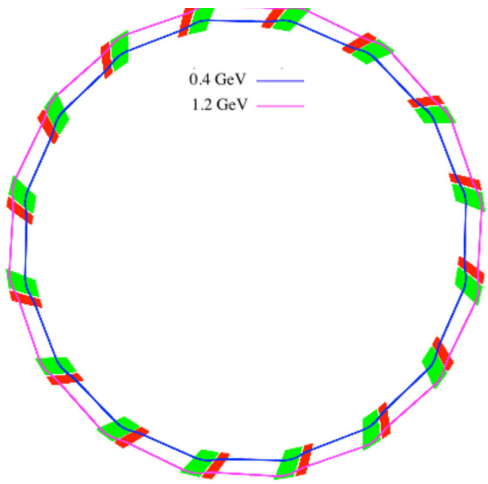

Figure 4: DF-spiral FFAG designed to fit in the ISIS tunnel.

INJECTION

Perhaps the most innovative proposal in this study is the direct use of protons in a Liouvillean injection scheme rather than charge-exchange injection using H^- ions. The use of H^- was proposed about 50 years ago and now represents standard practice in operating proton rings at high intensity. It was implemented in the Fermilab booster, for example, in 1978 [10]. However the injection system is complex because of the need to remove partially stripped and unstripped particles and there are associated issues in dealing with H^- such as foil scattering, foil lifetime and intra-beam stripping in the higher energy stages of the linac [6]. On the other hand, conventional injection into a single phase plane allows only 5-10 turns, which is clearly inadequate (see Table 1). This explains why requirements at the CERN PS-Booster are met through four stacked rings and why the machine is currently being converted to H^- to meet the demands of the next stage of LHC.

But one can in fact do much better. In the 1990's as part of the HIDIF inertial confinement fusion project [11], a two-plane Liouvillean injection scheme was proposed using a tilted electrostatic septum. Injection is then into four-dimensional x-x'-y-y' phase space and allows many more turns to be injected. The suite of codes written to optimise HIDIF has been updated and used to study Liouvillean proton injection schemes into each of the rings described above [12]. The code bases calculations on the geometric properties of linear zero-current beam dynamics, and, from nominal design values, varies tunes and ring and linac β-functions while determining a closed orbit bump programme to minimise beam loss. The model ring is then modified to meet the optimum parameters before the scheme is explored further in a non-linear tracking code with space-charge.

Two conditions are imposed in the optimisation:

$$\frac{\alpha}{\beta} = \frac{\alpha_i}{\beta_i} = -\frac{x'_o - x'_i}{x_o - x_i}, \tag{2}$$

$$\frac{\beta}{\beta_i} \leq \left(\frac{\epsilon}{\epsilon_i}\right)^{1/3}. \tag{3}$$

The subscript i refers to the injected turn; parameters without subscript are for the ring at the injection position; o identifies the closed orbit bump at this point; and ϵ is the painted emittance in the ring. Equation (2) is a 'matching' condition and ensures the incoming turn is positioned in phase space so as to minimise the emittance of the circulating beam in the ring. The second equation (3) is a condition on phase space curvatures that ensures emittances ellipses fit best together. Note that the beams do not (and should not) be 'matched' in the conventional sense that $\beta = \beta_i$ etc.

With these conditions, there are encouraging results that a zero-loss system (ignoring space-charge) could be possible with up to 350 turns for the main ISIS ring and 45-50 turns for the small R&D ring designed for FETS. We have still to explore the injection process using a detailed tracking code with a full injection bump chicane, but these figures are well within the requirements identified in Table 1.

The optimisation code contains a simple feature to account for space-charge tune depression via (1). Assuming no beam loss, N is proportional to the number of turns injected and the emittance factor is given by the painted emittances in the ring. Figure 5 (top left) gives an example of the kind of distribution created and is rectangular in real space because of the correlated painting mechanism. This is for 350 turns injection into the dFDFd pumplet FFAG and shows the septum tilted at an optimised angle of 66.4∘. Figure 5 (top right) shows the variation of the closed orbit as the circulating beam is pulled away from the septum to avoid loss and control the emittance in the ring. The displacement is achieved with four horizontal and four vertical bump magnets. Note that, according to equation (2), if α is non-zero at the injection point, it is necessary to create non-zero $x'_o - x'_i$. One would expect $x'_i = 0$ and it is a simple matter to generate both displacement x_o and angle x'_o in the closed orbit with the kickers. The two lower plots in Fig. 5 show (normalised) horizontal and vertical phase space projections (different colours identify different turns). It remains to study the effects of non-linear space-

ISBN 978-3-95450-185-4

charge, which will fill in the phase space holes and generate emittance growth and halo, and also the effects of dispersion which, as noted above, is non-zero in the FFAG injection straights.

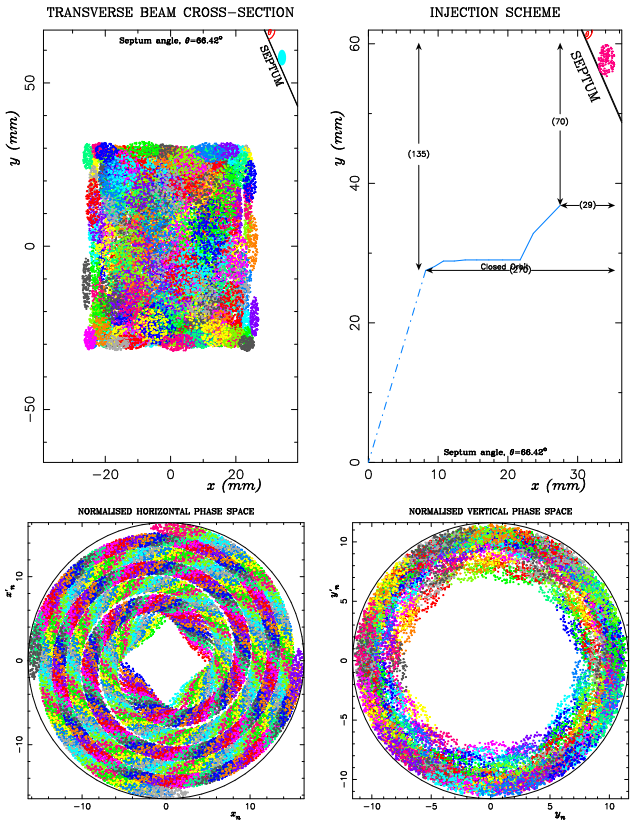

Figure 5: Simulation results for the FFAG main ring pumplet, 350 turns, in the absence of space-charge.

Extrapolating the parameters in Table 1, 350 turns at a repetition rate of 100 Hz would represent 3.6 MW of mean beam power in the ring even at the injection energy, and we might expect to increase this by a factor 4 after acceleration to the final energy. The absolute tune shift is still < 0.1. Thus, the two-plane injection system could be the way forward for future high power proton accelerators and could supersede the accepted norm of H^- charge exchange injection.

Coincidentally, the two-plane injection idea has been adopted by China's HIAF [13] for its B-ring ion accelerator, and there is now a good chance that experimental verification of the theories may be carried out.

EXPERIMENTAL PROGRAMME

Associated with the theoretical study is an experimental programme that has two aspects.

FFAGs at KURRI, Japan

With Kyoto University, we have a Memorandum of Understanding in place to share knowledge, information and training facilities related to FFAG development. This provides opportunities for regular periods of experiment and data-taking on the 150 MeV FFAG at KURRI. Unique techniques have been developed to characterise the proton beam and enhance understanding of FFAG beam dynamics. There are so few machines of this type operating anywhere in the world, and it is essential that we know how to improve and control beam quality if we are to demonstrate the feasibility of high power operation of FFAG accelerators in the future. Details are given in [14].

IBEX Paul trap at RAL

The second experimental aspect of FFAG and other high power studies in the U.K. is the design and construction of a linear Paul trap at RAL. This follows closely in the footsteps of pioneering work by Okamoto [15] at Hiroshima University, who has used the similarity between the equations of a trapped ionised plasma and the motion of a charged particle beam in a strong focusing channel to study beam dynamics in a local table-top environment. The Paul trap's flexibility, compactness and low cost make it a useful tool for the study of a wide range of accelerator physics topics. The RAL team has collaborated with Hiroshima in work that has focused on high intensity collective effects as well as a study of integer resonance crossing in the low intensity regime. A natural extension of this work is to investigate space-charge effects in intense beams in more realistic lattices to aid high power accelerator design and development.

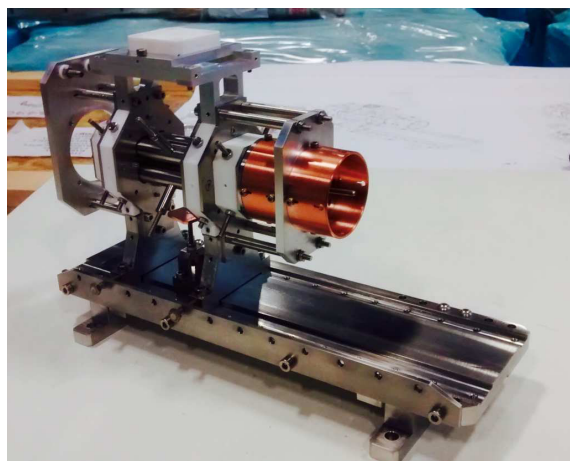

Figure 6: IBEX (Intense Beams Experiment) Paul trap at RAL.

The trap being set up at RAL (shown in Fig. 6) is a modified version of the Hiroshima design and will be used for intense beams studies [16]. Among other features, it is envisaged that it should also be able to model non-linear elements and a wider range of lattice configurations. Plans include modelling the IOTA (Integrable Optics Test Accelerator) at Fermilab [17] and contribute to the development of the MTE extraction system at the CERN-PS [18], where a combination of tune control and non-linear magnets such as octupoles is used to manipulate phase-space and control beam dynamics.

ISBN 978-3-95450-185-4

REFERENCES

[1] M. Seidel, Proceedings of the First International Particle Accelerator Conference, IPAC'10, Kyoto, Japan, May 2010. http://www.psi.ch/sinq

[2] Y. Kang, 'Status and Performance of ORNL Spallation Neutron Source Accelerator Systems', Proceedings of IPAC2016, Busan, Korea.

[3] H. Hotchi et al, 'Recent Progress of 1-MW Beam Tuning in the J-PARC 3-GeV RCS', Proceedings of IPAC2016, Busan, Korea.

[4] D.J. Adams at al, 'Operational Experience and Future Plans at ISIS', Proceedings of HB2016.

[5] A.P. Letchford, 'Status of the FETS project', Proceedings of LINAC2014, Geneva, Switzerland.

[6] J. Galambos et al, 'Increased Understanding of Beam Losses from the SNS Linac Proton Experiment', Proceedings of LINAC2012, Tel-Aviv, Israel.

[7] F.T. Cole, 'O CAMELOT! - A Memoir of the MURA Years', http://accelconf.web.cern.ch/AccelConf/c01/cyc2001/extra/Cole.pdf

[8] M. Bogomilov et al: 'Neutrino Factory', Phys. Rev. ST Accel. Beams 17, 121002 (2014)

[9] S. Machida, 'Scaled Fixed Field Alternating Gradient Accelerators with Reverse bend and Spiral Angle', in preparation.

[10] http://history.fnal.gov/criers/VC_1978_3_23.pdf

[11] C.R. Prior and G.H. Rees, 'Multiturn Injection and Lattice Design for HIDIF'. Proceedings of the 12th International Symposium on Heavy Ion Inertial Fusion, Heidelberg, September 1997.

[12] C.R. Prior, 'MISHIF: A Code to Optimise Multiturn Injection', enquiries should be directed to the author.

[13] J. Yang,' Status and Challenges of the High Intensity Heavy Ion Accelerator Facility (HIAF) in China', Proceedings of HB2016.

[14] S.L. Sheehy et al, 'Characterisation techniques for fixed-field alternating gradient accelerators and beam studies using the KURRI 150 MeV proton FFAG', arxiv.org/abs/1510.07459

[15] H. Takeuchi, K. Fukushima, K. Ito, H. Okamoto and H. Sugimoto, 'Experimental Study of Resonance Crossing with a Paul Trap', PRST-AB **15**, 074201 (2012).

[16] S.L. Sheehy, D.J. Kelliher, S. Machida, C. Plostinar, C.R. Prior, 'Overview of the Design of the IBEX Linear Paul Trap', Proceedings of IPAC'16, Busan, Korea, May 2016.

[17] S. Nagaitsev, 'Nonlinear Focusing in IOTA for Space-Charge Compensation and Landau Damping', Proceedings of HB2016,

[18] A. Franchi and M. gGovannozzi, 'A Novel Technique for Injecting and Extracting Beams in a Circular Hadron Accelerator Without Using Septum Magnets', CERN-ACC-2015-0063.

ISBN 978-3-95450-185-4

PERFORMANCE OF LINAC-4 INSTRUMENTATION DURING COMMISSIONING

U. Raich, CERN, Geneva, Switzerland

Abstract

Linac-4 is CERN's new H- Linac, which will replace the aging Linac-2 proton machine. Linac-4 is being built and commissioned in stages. While the machine is permanently equipped with the standard beam instrumentation necessary to ensure smooth operation, three dedicated measurement benches have also been designed to commission the source and LEBT at 45 keV, the MEBT and its chopper at 3 MeV as well as the first DTL tank at 12 MeV and finally the full DTL at 50 MeV and CCDTL at 100 MeV. The beam after the PIMS structures at the Linac's full energy of 160 MeV will be sent to a beam dump and commissioned with permanently installed instruments. Installation and commissioning of the machine up to the CCDTL is now complete. This contribution will present the results from the various commissioning stages, showing the performance of the various diagnostic devices used and comparing the data obtained to simulations.

ION SOURCE AND LEBT

Beam diagnostic devices measure the total beam current coming from the source with a Faraday Cup and a Beam Current Transformer (BCT) and the transverse beam distribution with a sandwich of horizontal and vertical wire grids.

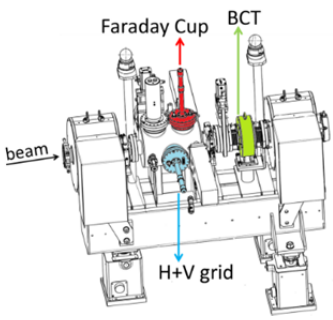

Figure 1: LEBT instrumentation.

As discussed below, the grid signal is dominated by the H- ion net charge deposition (negative) on the wires. Both the metallic wire frame and the wires themselves can be polarized in order to suppress secondary emission and repel low energy electrons emerging from the source.

The wire readout system allows signal sampling at 250 kHz such that the signals on the wires can be compared to the Faraday Cup signal.

As the 45 keV proton is stopped in the wire with a secondary emission yield estimated as ~ 3.5 charges per ion, a positive signal with the same overall shape as the negative Faraday Cup signal is expected. However, what was observed was the black trace in Figure 2.

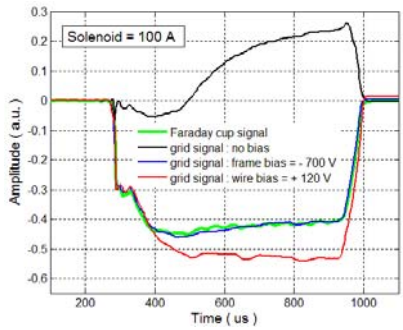

Figure 2: Comparison wire signal to Faraday Cup.

This can be understood as suppression of the secondary emission by strong space charge effects coming from the primary H- beam. When negatively polarizing the wire frame the secondary emission can be further suppressed such that the wire grid works only in charge collection mode and its wire signals (blue) are now negative, following the Faraday Cup signal (green). Polarizing the wires positively has the same effect but attracts additional background electron such that the signal is distorted (red).

In addition to the permanent instrumentation, the LEBT was temporarily equipped with a slit/grid emittance meter moved to various positions along the LEBT to verify the matching to the RFQ acceptance.

THE MEBT OR CHOPPER LINE

The MEBT adapts the 3 MeV H- beam coming from the RFQ to the first cavity of the DTL Linac and implements a fast chopper to adapt the beam longitudinally for injection into the PS Booster. It contains two BCTs, which, in combination with the LEBT BCT, allows the transmission through the RFQ and chopper to be determined. It also contains two L-shaped wire scanners for transverse profile measurement [1].

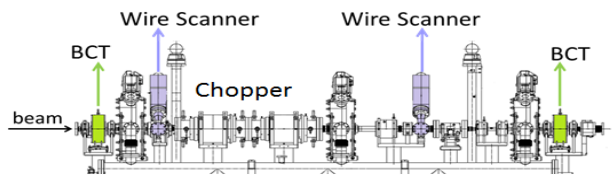

Figure 3: MEBT layout.

The correct functioning of the chopper was first verified with the vertical wire scanner observing the vertical beam deflection when the chopper is switched on, as shown in Figure. 4.

ISBN 978-3-95450-185-4

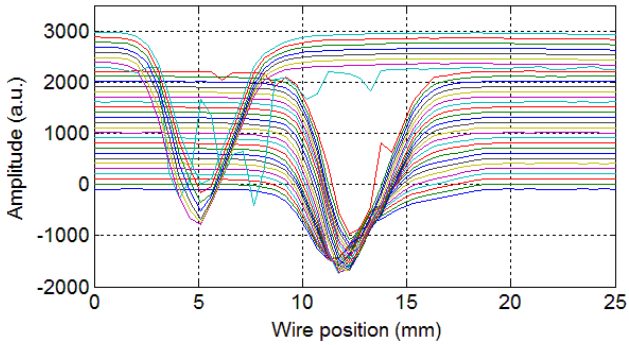

Figure 4: Wire profiles with chopper switched on.

The rise and fall times of the chopper were observed with the MEBT's second BCT, whose electronics can sample the BCT signal with a maximum sampling frequency of 100 MHz. Rise and fall times of less than 10 ns were observed.

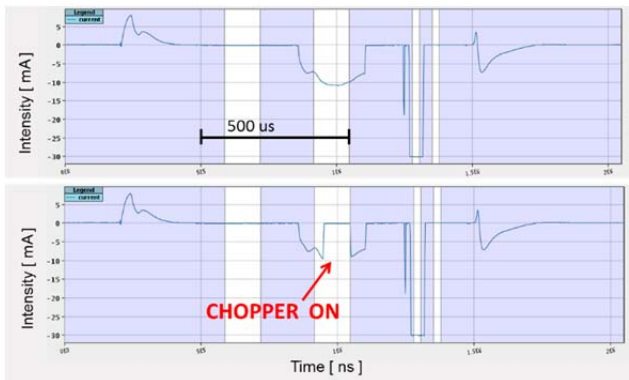

Figure 5: Chopped beam signal seen on transformer (Top–chopper OFF, Bottom: Chopper ON).

THE 3/12 MeV MEASUREMENT BENCH

To fully characterize the beam after the RFQ at 3 MeV and after the first DTL tank at 12 MeV a dedicated temporary measurement bench was designed. It contained

- 2 BCTs
- 3 Beam Position Monitors (BPMs)
- 1 slit/grid emittance meter
- 1 laser emittance meter with diamond detector
- 1 spectrometer magnet and horizontal wire grid
- 1 bunch shape monitor (BSM)

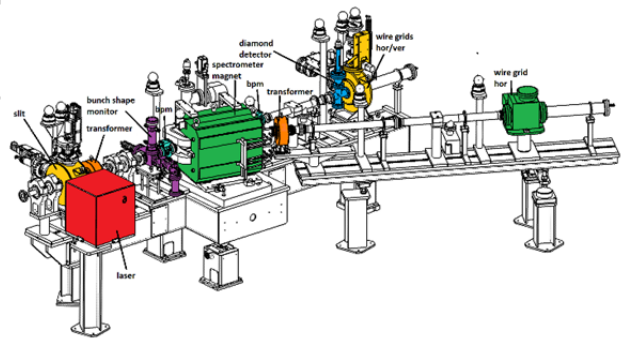

Figure 6: 3/12 MeV measurement bench.

Emittance Meter

In contrast to the LEBT emittance meter the design of the 3/12MeV emittance meter slit was very delicate because of the high thermal load expected on the slit material for a beam of up to 70 mA at 12MeV. A harmonica type design, distributing the heat load onto a larger surface and using carbon on a water cooled copper support was used. Nevertheless it was necessary to limit the pulse length to 100 µs compared to the nominal 400 µs.

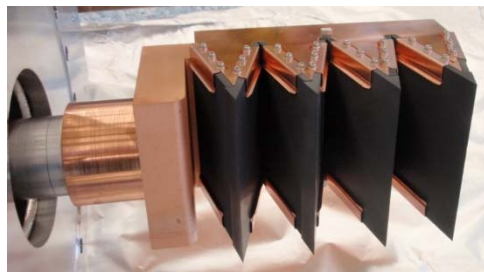

Figure 7: Emittance meter slit design.

The wire grids use carbon wires both due to its high sublimation temperature and since this gave the maximum signal level after considering the competing effects of charge collection and secondary emission. If the beam pulse gets longer than ~ 200 µs thermionic emission is observed to destroy the beam signal [2].
The results from the phase space scans for nominal optics show very good agreement with the expected matched phase space parameters as can be seen in Figure 8 [3].

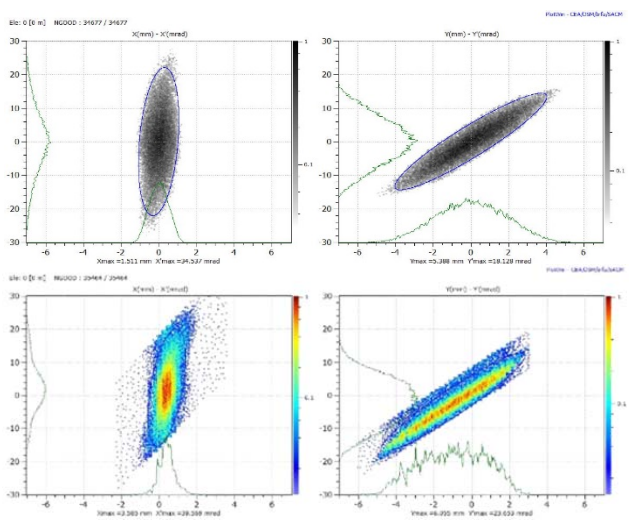

Figure 8: Black: expected matched beam, coloured: measured matched beam.

In addition to the traditional slit/grid device a laser emittance scanner was also employed. A thin laser beam is used to neutralizes part of the H^- ions converting them into H^0 atoms [4]. A spectrometer magnet is used to separate the H^- ions from the H^0 atoms. Moving the laser through the beam and measuring the angular distribution of the H^0 atoms for each laser position allows the phase

ISBN 978-3-95450-185-4

space to be sc anned in a sim ilar fashion to the slit/grid emittance meter (Figure 9).

Comparisons between the two methods show perfect agreement (Figure 10). The laser emittance meter has the advantage of not relying on any material to intercept the beam and can therefore also be used at high energy and during physics production.

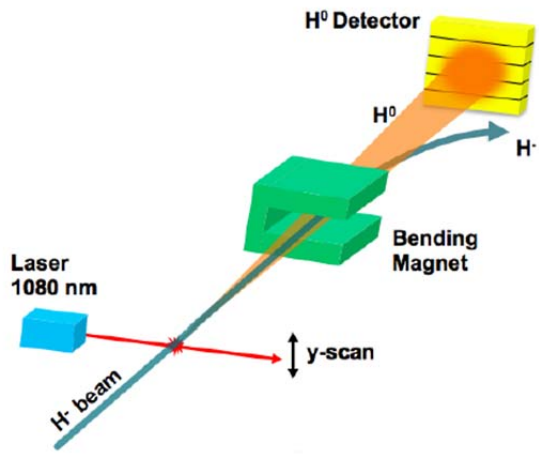

Figure 9: Emittance measurement using the laser wire.

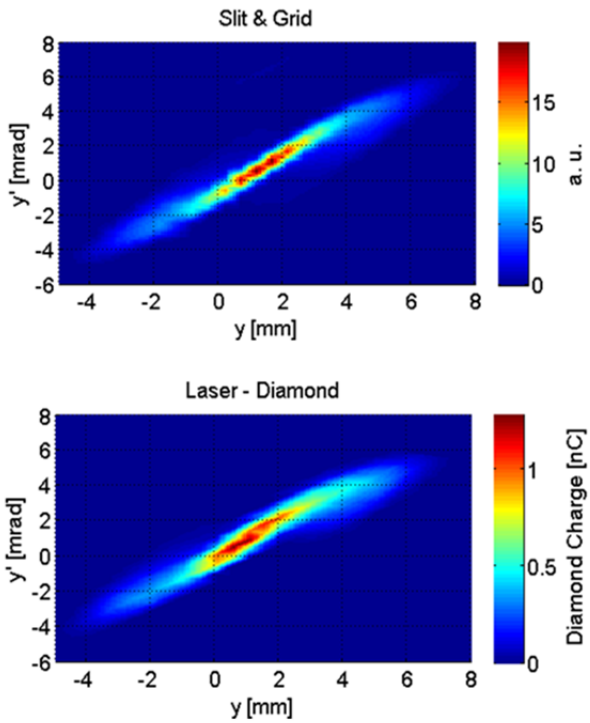

Figure 10: Emittance measurement slit/grid and laser.

Bunch Shape Measurements

The longitudinal charge distribution can be measured with a Bunch Shape Monitor (BSM) build by the Institute for Nuclear Research (INR), Troitsk, Russia. The instrument has a t emporal resolution of ~ 8 ps and can measure the longitudinal shape of the micro-bunc hes every 1 µs al ong the 400 µs beam pulse. It was used on both the 3/12MeV and 50/100 MeV measurement benches to adjust the RF p arameters of the cavities (buncher cavity and accele rating cavities) and will be definitively installed at th e end of the com plete linac in the transfer line to the PS-Booster. A typical measurement result is shown in Figure. 11.

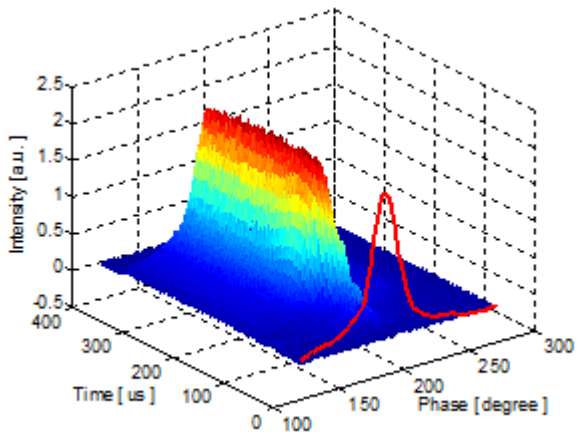

Figure 11: Bunch Shape measurement at nominal RF parameters.

Buncher Cavity Adjustment

The buncher cavity RF parameters were adjusted using the spectrometer line and the BSM. Changing the buncher phase at nom inal RF a mplitude, the centre of the beam distribution was observed with the wire grid in the spectrometer line. The acceleration and deceleration phases (beam at the max/min of the RF wave) and the bunching and debunching phases (beam at the zero crossing of t he RF wave) were determined. The values found were cross-checked with the BSM. Increasing the RF amplitude at the correct bunching phase results in a narrower longitudinal distribution but does not change its centre position (no a verage acceleration). The distinction between bunching and debunching phases is also made by measuring the longitudinal distribution with the BSM, with longer bunches created in the debunching case.

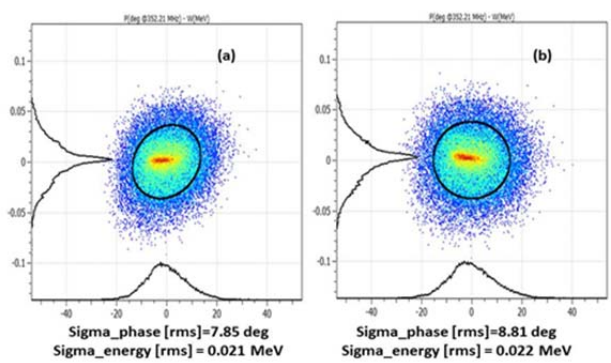

Figure 12: Longitudinal emittance expected (left) and measured (right).

The longitudinal emittance can be measured by varying the buncher RF amplitude with nominal phase settings

ISBN 978-3-95450-185-4

and measuring the longitudinal bunch distribution. This method is similar to the quadrupole scan in the transverse case. Traditionally the emittance and Twiss parameters are found by the matrix inversion technique, which only works when these transformations are linear. In our case, where space charge effects play a major role, only an initial estimation is calculated this way. These calculated Twiss parameters are used to produce a conforming particle distribution with Monte Carlo, which is followed with a tracking program (PATH), taking into account non-linear effects. Subsequently the distribution is iteratively modified until the simulation-result matches the measurement ("forward method") [5][6].

Figure 12 compares the longitudinal phase space plot obtained through the forward method (b) with the one expected (a).

DTL RF-Adjustments

To get a rough idea about the RF settings of the DTL-1 cavity the reference amplitude was set and the beam transmission measured with a BCT in front the cavity and another one behind it. The measurement (dots in Figure 13 was taken with all bunchers in the MEBT switched off (red), and with all bunchers on and compared to the theoretical curves.

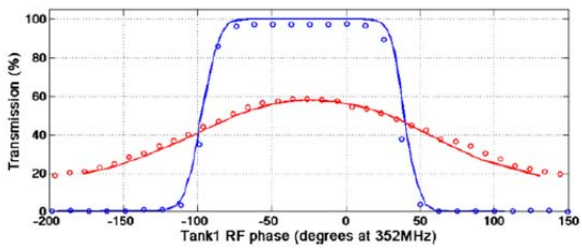

Figure 13: Transmission during phase scan.

Beam Energy Measured with Time of Flight

The BPMs used in Linac-4 are shorted striplines which allow the measurement of beam position, relative intensity and phase with respect to the 352.2 MHz accelerating frequency.

Through phase-comparison between two BPMs the time of flight between these two BPMs, and thus the average beam energy of the particles, can be determined. Using different BPM pairs permits a cross-check of the result.

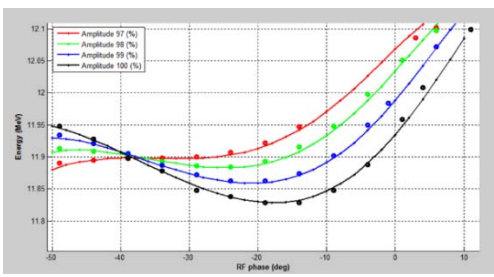

Figure 14: Beam energy versus DTL1 RF amplitude and phase (lines: simulated, points: measured).

The beam energy versus RF phase curve has a characteristic shape for a given RF amplitude. The curves were calculated with simulation programs for several RF amplitudes and compared to the corresponding time-of-flight measurements. Figure 14 shows the excellent result for DTL1. The RF parameters for the other cavities were adjusted using the same method.

50/100 MeV MEASUREMENT LINE

The slit/grid device could not be used at higher energies than 12 MeV because of the high energy-deposition in the slit. Equally, the spectrometer could not handle higher energies because of the limited field in the spectrometer magnet.

For these reasons a different measurement line was designed for 50 and 100 MeV commissioning in which the emittance is measured with 3 profile measurements and the average beam energy is measured using the time of flight between 2 BPMs used as phase probes.

The 50/100 MeV measurement line contains:

- 3 Profiler assemblies with horizontal & vertical wire grids and an L-shaped wire scanner
- 2 BPMs
- 1 BCT
- 1 laser profiler with a diamond detector
- 1 bunch shape monitor

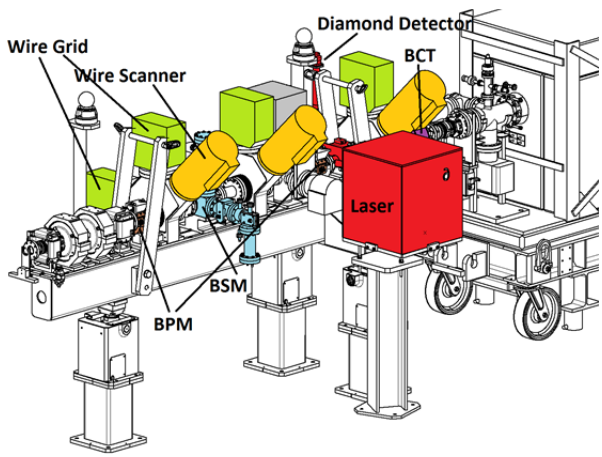

Figure 15: 50/100 MeV measurement line.

This measurement line was first installed after the third DTL tank at 50 MeV and has since been moved to after the CCDTL and the first PIMS module at 105 MeV.

Profile Measurements

When an H^- particle is intercepted by a grid wire it loses its electrons which can then be collected by adjacent wires thus distorting the measured beam profile. In order to estimate this effect, a profile measurement station was designed with a grid and an L-shaped wire scanner very close to each other. Comparing the profile measured with the wire scanner, which is not sensitive to crosstalk, with

ISBN 978-3-95450-185-4

the result from the wire g rid shows a di fference in the order of 1.5% in profile width, most of which is assumed to come from this crosstalk between neighbouring wires in the grid.

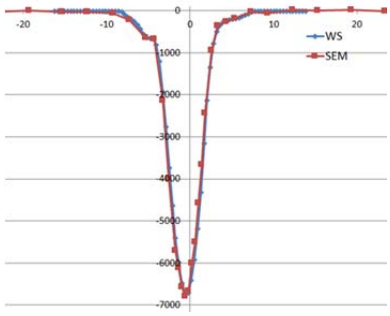

Figure 16: Grid profile (SEM) versus scanner profile (WS).

Laser Profile Measurements

Since there is no spectrometer on t he 100 Me V measurement bench the H^0 atoms created through lase r stripping cannot be separated from the primary H^- beam. It is, however, possible to extract the stripped electrons with a weak bending magnet having little effect on the primary beam. The intensity of these electrons with respect to the laser p osition in the beam provides the beam profile.

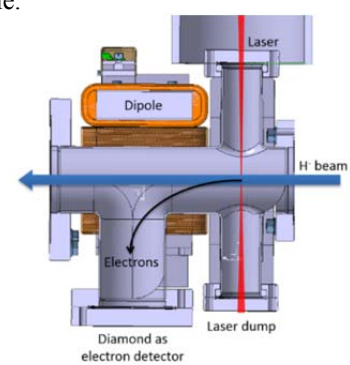

Figure 17: Laser profile.

The laser was installed between two profile measurement boxes containing wire scanners and grids. In this way the laser scanner profile could be compared to profiles from the grids extrapolated to the position of the laser.

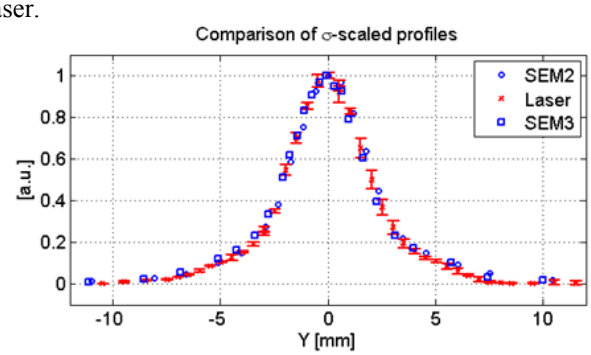

Figure 18: Comparison profiles grid and laser

Transverse Emittance

As the slit/grid method cannot be used above 12MeV a 3-profile method was used to obtain the emittance at 50 and 100MeV. Three beam profiles were measured at a phase advance of 60 degree s from each other and the emittance determined through optics calculations. As for the case of the longitudinal emittance, linear optics cannot be applied, and the “forward method” described above was therefore also used in the transverse case. The comparison between measured (red) and expected (black) Twiss parameters shows remarkable agreement (Figure 19).

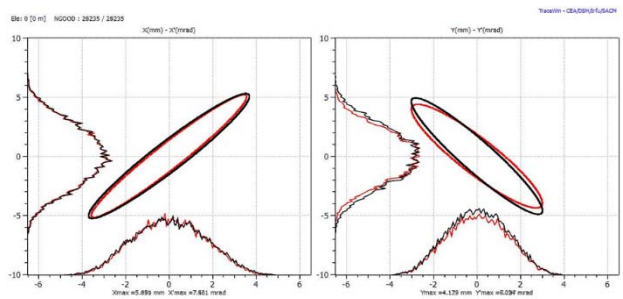

Figure 19: Twiss parameters simulated and extracted from measurements with the forward method.

CONCLUSION

CERN’s new H^- Linac is currently being commiss ioned in stages. The source, LEBT, MEBT with chopper, the DTL and CCDTL structures have all been commissioned with beam, while the PIMS cav ities and transfer line to the PS Booster remain to be commissioned before the end of 2016.

Three temporary measurement lines were designed to fully characterize the beam at 45 keV, 3 and 12 MeV, and 50 and 100 MeV. Many beam parameters were measured with different instruments giving results that showed excellent agreement with theoretical predictions.

This also allowed se veral measurement techniques to be validated, such as tran sverse and longitudinal emittance measurements using the “forward method”, profile measurements using wire scanner, grids and laser stripping and energy measurement through time-of-flight between two BPMs.

ACKNOWLEDGMENTS

Many thanks go to the members of t he CERN BE/BI group for help with mechanics, electronics and software. The CERN BE/ABP group supplied the simulation results and operated the machine during the measurements.

ISBN 978-3-95450-185-4

REFERENCES

[1] V.Dimov, E. Belli, G. Bello di, J-B. Lallement, M. Yarmohammadi Satri, Beam Commissioning of Linac4 up to 12 MeV, Proc. IPAC'15, Richmond USA, May 2015, paper THPF085, pp. 3886-3889.

[2] R. Roncarolo et al., Transverse Profile and Emittance Measurements during the CER N Linac-4 Commissioning at 3 and 12 MeV, Proceedings of Linac 2014 Geneva, Switzerland, paper TUPP035, pp. 506-509.

[3] F. Zocca, E. Bravin, M. Duraffourg, G.J. Focker, U. Raich, F. Roncarolo, CERN Geneva Switzerland Profile and E mittance measurements at the CERN Linac-4 3 Me V Test Stand. Proceedings IBIC 2013, Oxford UK, paper WEPF09 pp. 826 – 829.

[4] T. Hofmann, G.E. Boorman, A. Bosco, E. Bravin, S.M. Gibson, K.O.Kruchinin, U. Raich, F. Roncarolo, F. Zocca, Experim ental Results of Laserwire Emittance Scanner for Li nac-4 at CERN, Nucl. Inst. and Meth. i n Phys. Res. Section A, http://dx.doi.org/10.1016/j.nima.2016.02.018.

[5] J-B Lallement, A.M. Lombardi. P.A.Posocco CERN Linac4 Beam Commissioning Strategy Proceedings of HB2012, Beijing, China, paper TUO3B03 pp. 283-285.

[6] V. Dimov, Emittance Reconstruction Techniques in Presence of Space Charge Applied duri ng Linac4 Beam Commissioning, paper WEPM1Y01, this conference.

ISBN 978-3-95450-185-4

HIGH POWER TARGET INSTRUMENTATION AT J-PARC FOR NEUTRON AND MUON SOURCES

Shin-ichiro Meigo*, Motoki Ooi, Kiyomi Ikezaki, Tomoyuki Kawasaki, Hidetaka Kinoshita, Atsushi Akutsu, Masaaki Nisikawa and Shinpei Fukuta, J-PARC center, JAEA, 319-1195, Japan
Hiroshi Fujimori, J-PARC center, KEK, 305-0801, Japan

Abstract

Since 2008, the Japanese Spallation Neutron Source (JSNS) of J-PARC has produced a high-power proton beam of 300 kW. In order to operate with high intensity beam such as 1 MW, a reliable beam instruments are crucial. We developed profile monitor system by using SiC as sensor wires. Since pitting erosion was found at the vessel of the spallation neutron target at other facility of SNS, the beam current density at the target should be kept as low as possible. To decrease the beam current density at the target, a beam flattering system based on a non-linear optics with octupole magnets was developed. Beam profile at the target obtained with the Multi Wire Profile Monitor (MWPM) showed flat distribution and showed good agreement with the design calculation. Furthermore, the present status of the development of the beam instruments are also described.

INTRODUCTION

In the Japan Proton Accelerator Research Complex (J-PARC) [1], a MW-class pulsed neutron source, the Japan Spallation Neutron Source (JSNS) [2], and the Muon Science facility (MUSE) [3] will be installed in the Materials and Life Science Experimental Facility (MLF) shown in Fig. 1. In 2015, we successfully ramped up beam power to 500 kW continuously[1] and delivered several shots of the 1-MW beam to the targets. To produce a neutron source, a 3 GeV proton beam collides with a mercury target, and to produce a muon source, the 3 GeV proton beam collides with a 2-cm-thick carbon graphite target. To efficiently use the proton beam for particle production, both targets are aligned in a cascade scheme, with the graphite target placed 33 m upstream of the neutron target. For both sources, the 3 GeV proton beam is delivered from a rapid cycling synchrotron (RCS) to the targets by the 3NBT (3 GeV RCS to Neutron facility Beam Transport) [4–6]. Before injection into the RCS, the proton beam is accelerated up to 0.4 GeV by a LINAC. The beam is accumulated in two short bunches and accelerated up to 3 GeV in the RCS. The extracted 3 GeV proton beam, with a 150 ns bunch width and a spacing of 600 ns, is transferred to the muon production target and the spallation neutron source.

Recently, pitting damage became evident in the mercury target container [7], and the extent of the damage is proportional to the fourth power of the peak current density of the proton beam. After operating the beam at high power, significant pitting damage was observed at the spent mercury target vessel at JSNS and at the Spallation Neutron Source (SNS) in Oak Ridge National Laboratory [8,9]. Using linear optics (i.e., quadrupole magnets) for beam transport, the peak current density can be reduced by expanding the beam at the target. However, beam expansion increases heat in the vicinity of the target, where shielding and the neutron reflector are located. Therefore, the peak current density is limited by the heat induced in the vicinity of the target. At the JSNS, the minimum peak current density is expected to be 9 μA/cm^2, which gives a thermal energy density at the target of 14 J/cm^3/pulse [10]. Because the pitting damage goes as the fourth power of the peak density, scanning the beam with a deflecting magnetic field will not mitigate the pitting damage.

Beam profile monitoring plays an important role in comprehending the damage to the target. Therefore it is very important to watch continuously the status of the beam at the target at the JSNS especially for the peak current density. We have developed a reliable beam profile monitor for the target by using Multi Wire Profile Monitor (MWPM). In order to watch the two dimensional profile on the target, we have also developed the profile monitor based on the imaging of radiation of the target vessel after beam irradiation. In this paper, the present status of the beam monitor at the spallation neutron source is described.

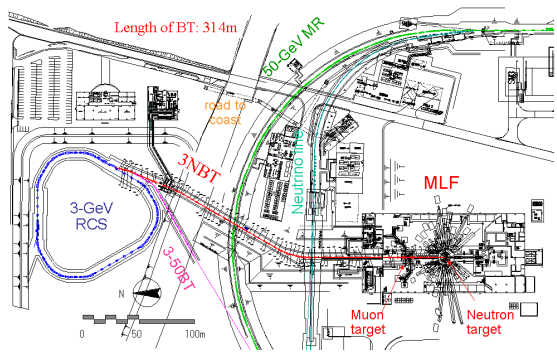

Figure 1: Plan of rapid cycling synchrotron (RCS) at the Materials and Life Science Experimental Facility (MLF) at J-PARC.

BEAM MONITOR SYSTEM AT THE BEAM TRANSPORT TO THE TARGET

Silicon Carbide Sensor Wire

In order to obtain the characteristics of the proton beam, diagnostic system based on a Multi Wire Profile Monitor

* meigo.shinichiro@jaea.go.jp

[1] Recently the power is restricted to 200 kW due to no spare mercury target remaining since February 2016.

ISBN 978-3-95450-185-4

(MWPM) was developed. Principle of the MWPM is simple to observe the amount of the electron emission by the interaction of the beam at the wire. As a material of sensitive wire, usually tungsten wire is selected due to large emission amount of the electron and having high temperature melting point. In the present system, silicon carbide (SiC) was chosen due to the high resistance of the radiation [11], which can survive for 80 DPA. Due to the interaction, the beam loss is caused, which is one of issues of the high intensity proton accelerator and the optimization of the beam loss is important. The angular differential cross section of Rutherford scattering is proportional to square of atomic number of wire material. Therefore wire material with low atomic number has advantage for beam loss. Since the average atomic number of SiC is 10, the differential cross section of SiC becomes 1/55 times of the cross section of tungsten. In order to obtain the angular distribution after scattered by the wire is calculated with revised DECAY-TURTLE [12] by Paul Scherrer Institute (PSI) [13]. It was recognized that SiC wire than tungsten gives less influence on the beam. In order to estimate of the lifetime of monitor wire, the displacement cross section of DPA is calculated with NMTC/JAM [14]. By the calculation, it is found that the DPA cross section of SiC and tungsten for 3-GeV proton is 278 and 7997 b respectably, which shows that DPA of the tungsten is about 29 times larger than SiC. SiC was chosen as wire of as a standard model of the profile monitor at the 3NBT.

Multi Wire Profile Monitor

The view of MWPM is shown in Fig. 2. Along the beam transport line, 15 sets of movable MWPMs are placed to measure the beam profile. The MWPM frame has 31 wires of SiC with the spacing pitch of 6 mm for each horizontal and vertical direction. We employed the SiC wire having diameter of 0.1 mm, which has a tungsten core of 0.01 mm and is coated with 1 μm of pyrolytic carbon. The wire frame made of aluminum oxide with purity more than 95 % is selected due to the high radiation resistance. In order to sustain with the fixed tension, wires are kept by the holder with spring, which gives the unique tension of 0.6 N to the wire. The frame of wires is placed in the vacuum chamber made of titanium, which is selected by the following reason, good vacuum characteristics and low activation. In order to avoid unnecessary irradiation of the wires, the frame can retract and moves like the pendulum motion.

For the actual high intensity beam tuning, it is important to know the beam parameter. The intrinsic parameters of the beam transport was confirmed by observing response of beam position for the kick angle of the steering magnet. By the observation of the beam width with the MWPMs, the Twiss parameter and the beam emittance can be acquired with help of the SAD [15] code.

Monitors Placed at Proton Beam Window

It is very important that continuously observation of the characteristics of the proton beam introduced to the target. Due to the high activations caused by the neutron produced at the target, remote handling technique is necessary to exchange the beam monitor for the target. In order to decrease the radiation produced at the spallation neutron target, shielding above the monitor was required. To decrease the difficulties of the exchange work and decrease of the shielding, we combined the beam monitors with a Proton Beam Window (PBW) for separation between the vacuum region of the accelerator and the helium region around the neutron target. The PBW is better to be placed closer to the target where distance between the target and the PBW is 1.8 m, which gives reliable profile at the target. In Fig. 3, the MWPM placed at the center of vacuum chamber of the PBW is shown. In order to avoid exceed heat at target vicinities, beam halo monitors are placed as well. The chamber of the PBW has inflatable vacuum seal called pillow seal. Due to the pillow seal, the monitors can be changed by the remote handling. Io calibrate sensitivity of each wire, the signal was observed by the scanning the position with narrow width beam. It was found that the difference of individual sensitivity was 6 % at most.

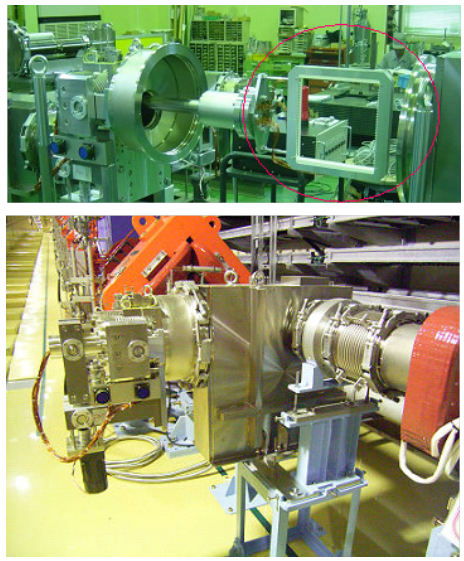

Figure 2: MWPM placed at the beam transport line. (top: MWPM and frame inside the vacuum chamber. Red circle stands for sensor wire head. bottom: MWPM and chamber placed in the beam transport line.)

In an actual beam operation, the heat at the target vicinities such as shielding, which mainly does not have water cooling channel, is important for reduction the peak density. Beam halo monitors attached at the PBW to observe the heat deposition at the target vicinities such as reflector and shielding, which is not allowed to exceed 1 W/cm^3. We placed two types of beam halo monitors to obtain the thermal information by thermocouple and the emission of electron by electrode. Since the emission of electron indicates relative intensity of the beam halo, the beam halo relative intensity, which can be normalized by the following thermal observation, can be obtained by several shots of the beam. To observe the absolute intensity of the halo, the thermocou-

ISBN 978-3-95450-185-4

ple type was implemented, which consists of copper strips coupled with the thermocouple. With 5 minutes of 25 Hz beam operation, the absolute intensity of the beam halo can be determined by the differential of temperature by time. These procedure was normally performed in actual beam operation.

Since wires at the MWPM placed at the PBW are fixed type and continuously irradiated to the beam, long lifetime wire is required. The profile monitor at the PBW is important so that a redundant system using SiC and tungsten wires was applied. In summer of 2013, some spots were observed at the surface of helium side of the PBW, which were thought to be produced by the erosion of nitric acid produced by the radiolysis around the target. We decided to change the 1st PBW already received the integration beam power of 2000 MWh to the new one. Until 2000 MWh, the wires still gave normal signals and after irradiation they were not found serious damage by inspection.

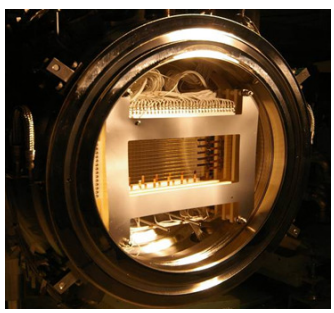

Figure 3: MWPM and beam halo monitors placed at the Proton Beam Window (PBW).

All signals of MWPM is transfer to the local control room by twisted pare cables with high radiation harding. As for the MWPM of the PBW, Mineral Insulator Cables (MICs) are applied because the cables receives quite high radiation does more than 1 MGy. The signal is fed to the inverter amp (Technoland N-GK 160 32ch Inverter AMP) and fed to the charge collective ADC (Technoland C-TS 301B) with the integration time range of 3 μs, which has integration charge range of -3 nC in total and is driven by the CAMAC bus. The signals on the CAMAC bus are read out via crate controller of Toyo CC/NET. All signals is controlled by the EPICS [16] and is data base server based on PSQL server. Each result of the beam profile is fitted by the Gaussian and base distribution for every second. Result of the center position and the width is utilized to watch the status of beam injected to the target.

For the safety, if any anomaly of the beam was found such as offset of the beam position, the beam should be immediately. The machine protect system (MPS) was developed, which cut out the beam immediately if either the beam position exceeded 5 mm offset or the beam peak density exceeded the threshold giving the peak heat density of 14 J/cm^3/pulse at the mercury target. Due to the MPS, high power beam operation such as 1 MW can be performed with high confident. Data of the beam profile for every shots are watched by the control system driven by the EPICS and are stored in data base.

DEVELOPMENT OF BEAM FLATTERING SYSTEM USING NON-LINEAR BEAM OPTICS

Distribution of the beam extracted from the RCS can be described well by a simple Gaussian [6]. For the beam with Gaussian distribution in the phase space, the beam profile becomes a Gaussian at all place with an ordinary linear beam optics. By using non-linear optics, the beam particles located at the edge is bent to the center so that the distribution can become flat. In order to obtain flat shape for each horizontal and vertical direction, two octupole magnets is required. These octupole magnets can be placed at anywhere upstream of the target except the place where the phase advance between the magnet and the mercury target is an integer multiple of π. Since the targets had been irradiated by the beam for 5 years, the radiation dose around the targets is too high to place magnet. Therefore, two octupole magnets (OCT1, OCT2) are placed at upstream of the muon target as shown in Fig. 4.

In briefly, the fundamental of the beam flattering is based on the edge folding by the high order magnet of octupole magnet. By choosing appropriate octupole magnetic field, a flat beam distribution can be obtained as shown in Fig. 5.

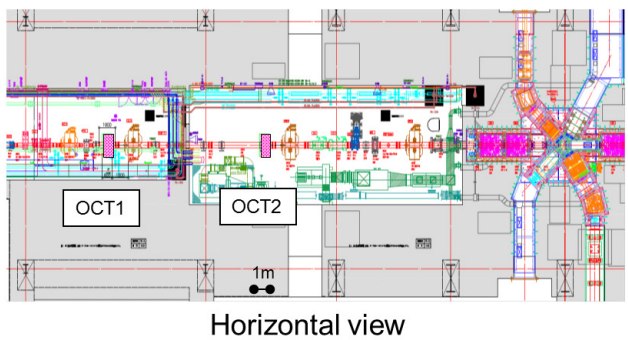

Figure 4: Plan of octupole magnets for beam flattening system, which is to be placed upstream of muon production target shown in right side.

Beam Optics for Flattering System

In order to achieve flat distribution, the required octupole field is proportional to the inverse square of the beta functions at the octupole magnet. Due to the relative high momentum of the present beam, achievement of a large octupole field of the K is difficult. To obtain the flat shape with the realistic K of the octupole, we expand the beam at the octupole magnet to have large β function. Around the octupole magnet, since physical aperture of quadrupole magnets was fixed to 300 mm, the aperture of the octupole magnet is determined to 300 mm. The admittance of the beam was designed to have 324 π mm mrad, which was given by the

ISBN 978-3-95450-185-4

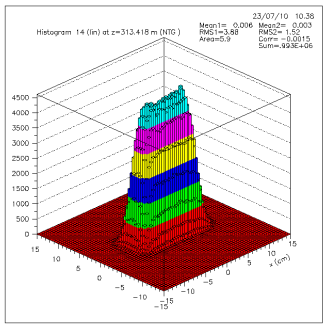

Figure 5: Flat beam distribution at the mercury target by using two set of octupole magnets.

beam collimator placed at the RCS . A study of the RCS [17] showed that the transverse emittance will be as small as 250 π mm mrad. The beam admittance at the octupole was determined to 250 π mm mrad and the beta function at the octupole magnets was chosen to 200 m.

Octupole Magnets

Based on the optics design, two pieces of the octupole magnet shown in Fig. 6 were fabricated. The designed field gradient is 800 T/m^3 with a bore diameter of 0.3 m and 0.6 m in length of pole and the current of 700 A. Using a hall prove, the field gradient was measured. It was confirmed that the magnetic field were in good agreement with the design calculation. In an actual beam operation, the beam centering at the octupole is important to avoid peak at the edge. To perform centering, beam position monitor was installed in each octupole magnet.

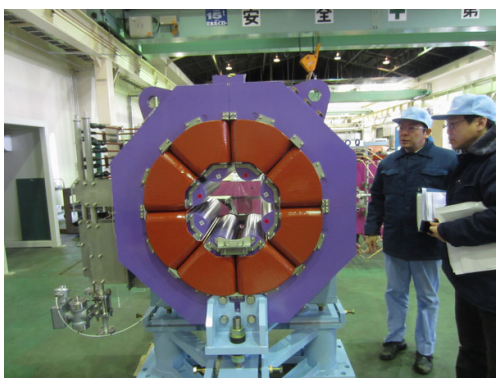

Figure 6: Fabricated octupole magnet with magnetic field gradient of 800 T/m^3.

Beam Profile with Non-linear Optics

In order to obtain the beam profile at the neutron source, SAD code is utilized, which provide beam information by fitting the result given by the MWPM placed at upstream of the octupole magnet. Also revised DECAY-TURTLE [12] by Paul Scherrer Institute (PSI) [13] is utilized to simulate multiple scattering at the muon target. Figure 7 shows results of beam profile for 800 kW beam with and without excitation of the octupole magnets. The beam profile shown in Fig. 7 was observed by the MWPM placed at the PBW. It can be found that considerable flat distribution can be obtained by the non-linear optics. The calculation results with and without excitation are also shown in Fig 7. The calculation results show good agree with the experiment ones with and without octupole magnetic field. It is also confirmed that the calculated beam profile by using the muon target showed good agreement with the experiment for both cases with and without octupole magnetic field. By the calculation result, the peak density can be thought to be reduced by 30% compared with the linear optics.

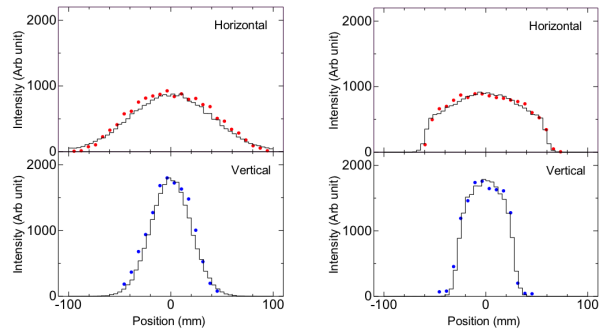

(a) OCT 0A (b) OCT 698A

Figure 7: Beam profile obtained with calculations (line) compared with result by the MWPM (dots) supplying current of (a) 0 A and (b) 698 A to octupole magnet . Upper and bottom figure represents for horizontal and vertical directions, respectively.

DEVELOPMENT NEW BEAM INSTRUMENTS

Lifetime Estimation of the PBW

The MWPM placed at the PBW so that the lifetime estimation of the PBW is important. When the water was leaked from the PBW, enormous efforts and time will be necessary for restoring. If water leaked from the PBW to the vacuum side, the baking procedure will be necessary to reduce the outgas inside vacuum. We chose aluminum alloy as the material of the PBW, because SINQ at PSI had a good result for lifetime as a safety hull material of the target. Post irradiation examination (PIE) was already performed and material property was studied preciously at the SINQ [18] . The lifetime can be thought to be determined by the embrittlement due to the especially helium caused by the spallation reaction. Therefore, helium production rate is important to estimation of the lifetime. To eliminate difference of the proton energy, calculation should be made for He production rate for the proton energy, whereas the SINQ is utilized 590-MeV protons. In order to obtain validate of nuclide production, cross section for residual nuclide was measured using 3-GeV proton with thin aluminum foil (0.5 mm) placed at front of the beam dump. The gamma

ISBN 978-3-95450-185-4

ray caused by the residual nuclide was observed with High Pure Germanium (HP-Ge) detector. Due to high intensity beam, irradiation time was enough to 5 min. Figure 8 shows obtained cross section for ^{27}Al(p,x)^{7}Be reaction compared with other experiment [19–21],calculation code [14] and evaluated nuclear data [22]. It is shown that experimental data with relatively high accuracy can be obtained by well controlled beam and beam monitors with high precision. Using 3-GeV result, calculation code for H and He gas production may be improved. By using developed code, a reliable lifetime of the PBW will be obtained.

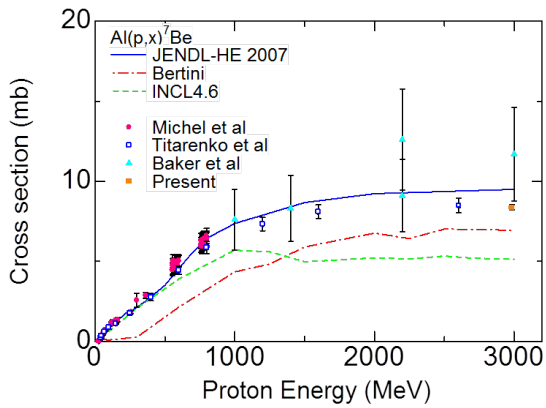

Figure 8: Experimental result of ^{27}Al(p,x)^{7}Be reaction for code validation.

Development of New Profile Monitor

Until now the monitor wire survived up to 2 GWh, which was at attached the first PBW, however, there is no evidence that the MWPM will survive for long duration of 1 MW beam. The lifetime of the PBW is expected as 2 years for 1 MW beam [23], which has proton fluence 2×10^{21} cm^{-2} and the integral beam power of 10 GWh. Furthermore, a target material experimental facility for accelerator driven system (ADS) is planed at J-PARC, where the peak current density will be 5 times higher than the MLF [24]. In order to observe 2D profile, a on-line type profile monitor is desired because the present 2D beam profile by IP can be obtained after the irradiation. Therefore we begun to develop a new beam profile monitors.

By observation of the thermal distribution at the target, the beam profile can be obtained. We developed an infrared camera system with bundled hollow-core fibers having length of 1 m. The hollow-core fibers were made of the quartz capillary-tube coated by polyimide. Since beam monitor is placed at the PBW, the radiation hardening of the monitor is required obviously. The capillary tube is made of inorganic material and the camera can be placed far away from the radiation source so that the infrared system can be thought to have enough high radiation hardening.

Also we developed a profile monitor based on the bundled optical fibers with high radiation hardening (Fujikura FISR-20) having 2x10^{4} pixels and length of 5 m. By painting fluorescence material such as alumina at the target vessel, the beam profile can be observed with fluorescence, which already utilized at the SNS. In future, we will place the present fiber system at the PBW.

To observe temperature anomaly on the target, the image of fibers was obtained with the near infrared filter to cut the visible light. Figure 9 shows the direct image of the near infrared from the ceramic heater as the system demonstration. The present near infrared system may be utilized for diagnostic system of the muon production target. Since the muon production target was the rotating target cooled by the radiation heat having any cooling channel, if the rotation stopped by certain cause then the temperature will arise rapidly eventually introduce break of the target. Due to the rotation target, observation of the temperature by the thermocouple was difficult. Normally the temperature of the target exceeded 1000 °C so that By the near infrared system, the anomaly of the target can be easily detected.

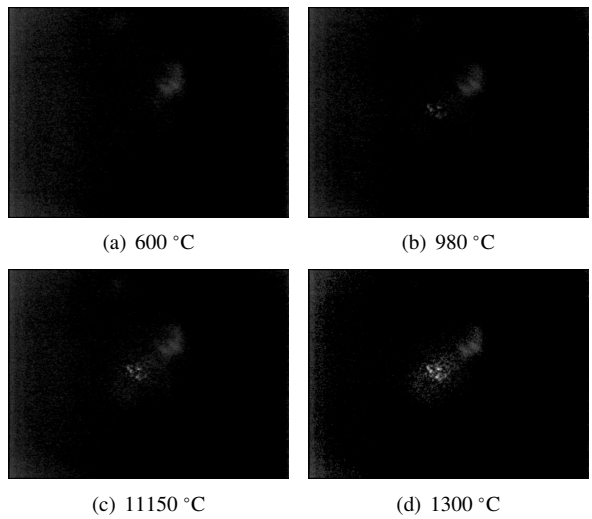

(a) 600 °C (b) 980 °C

(c) 11150 °C (d) 1300 °C

Figure 9: Images obtained by the near infrared beam profile system for various temperature of ceramic heater.

CONCLUSION

For reliable beam operation at the JSNS in J-PARC, beam instruments have been developed.. By using the MWPM, beam parameter such as the emittance and Twiss parameter can be obtained by several shots of the beam. Under the present system, high power beam operation such as 1 MW can be performed with high confident.

In order to reduce peak density of the beam current at the target, a non-linear beam optics with the octupole magnets was developed. By the present system, it was found that the flat shape can be obtained. The calculation simulation shows good agreement with the result obtained with the present profile monitor, which implies that the beam flattening can be achieved by the design of optics having large β function at the octupole magnet and an appropriate phase advance between the octupole and the mercury target. By the cal-

ISBN 978-3-95450-185-4

culation including with the beam scattering on the muon production target, it is shown that the peak current density can be reduced about 30 % of the peak density without the non-linear beam optics.

ACKNOWLEDGMENT

This work is partly supported by the Ministry of Education, Culture, Sports, Science and Technology (MEXT) KAKENHI Grant-in-Aid for Scientific Research (C) Grant no. 26390114.

REFERENCES

[1] The Joint Project Team of JAERI and KEK, JAERI-Tech 99-56, 1999.

[2] Y. Ikeda, Nucl. Instrum. Meth. **A600**, (2009) 1.

[3] Y. Miyake, et al., Physica B **404** (2009) 957.

[4] S. Meigo, et al., Nucl. Instrum. Meth. **A562**, (2006) 569.

[5] S. Sakamoto, et al., Nucl. Instrum. Meth. **A562**, (2006) 638.

[6] S. Meigo, et al., Nucl. Instrum. Meth. **A600**, (2009) 41.

[7] M. Futakawa, et al., J. Nucl. Sci. Technol. **40** (2004) 895.

[8] T. Naoe, et al., J. Nucl. Mater. **450** (2014) 123.

[9] D. A. McClintock, et al., J. Nucl. Mater., **431** (2012) 147.

[10] S. Meigo, et al., MOPEB066, IPAC10 (2010).

[11] G. E. Youngbllood, et al., J. Nucl. Matler. , **258 - 263**, 1551 (1998).

[12] K.L. Brown, Ch. Iselin and D.C. Carey: Decay Turtle, CERN 74-2 (1974).

[13] PSI Graphic Turtle Framework by U. Rohrer based on a CERN-SLAC-FERMILAB version.

[14] K. Niita, et al., JAERI-Data/Code 2001-007 (2001).

[15] K.Oide, et al, Phys. Rev. E **49** , 4474 (1994).

[16] M. Ooi, et al., PO1.024-1, ICALEPCS10 (2005).

[17] H. Hotchi, et al., THPPP080, IPAC12 (2012).

[18] Y. Dai, et al., J. Nucl. Mater., **343**, 184 (2005).

[19] Yu.E.Titarenko, et al., Yadernaya Fizika Vol. **74**, 531 (2011).

[20] R. Michel, et al., Nucl. Instrum. Meth. Phys. Res., Sect. B **129**, 153 (1997).

[21] E.Baker, et al., Phys. Rev. **112**, 1319 (1958).

[22] Y. Watanabe, et al., J. Korean Phys. Soc. **59**, 1040 (2011).

[23] S. Meigo, et al., J. Nucl. Mater. , **450**, 141 (2014).

[24] S. Meigo, et al., J. Nucl. Mater. , **450**, 8 (2014).

ISBN 978-3-95450-185-4

THE APPLICATION OF THE OPTIMIZATION ALGORITHM IN THE COLLIMATION SYSTEM FOR CSNS/RCS

Hongfei Ji#, Sheng Wang, Mingyang Huang, Shouyan Xu
CSNS/IHEP, CAS, Dongguan, 523803, P.R. China
Yi Jiao, Na Wang. IHEP, CAS, Beijing 100049, P.R. China

Abstract

The robust conjugate direction search (RCDS) method, which is developed by X. Huang from the SLAC National Accelerator Laboratory, has high tolerance against noise in beam experiments and thus can find an optimal solution effectively and efficiently. In this paper, the RCDS method is used to optimize the beam collimation system for Rapid Cycling Synchrotron (RCS) of the China Spallation Neutron Source (CSNS). A two-stage beam collimation system was designed to localize the beam loss in the collimation section in the RCS. The parameters of secondary collimators are optimized with RCDS algorithm based on detailed tracking with the ORBIT program for a better performance of the collimation system. The study presents a way to quickly find an optimal parameter combination of the secondary collimators for a machine model for preparation for CSNS/RCS commissioning.

INTRODUCTION

The China Spallation Neutron Source (CSNS) is designed to provide a proton beam with beam power of 100 kW [1, 2]. The accelerator complex consists of an 80 MeV Linac and a 1.6 GeV Rapid Cycling Synchrotron (RCS) [3, 4]. In the RCS, the proton beam is accumulated through an anti-correlated painting scheme within 200 turns, and accelerated to 1.6 GeV in about 20000 turns [5, 6].

For the RCS, the space charge forces are strong and have a large impact on beam dynamics. The emittance growth and halo generation induced by space charge could lead to unacceptably high beam loss [7, 8]. Considering the requirements for hands-on and safe maintenance of the machine, the average particle loss should be controlled to a low level of 1 W/m [9]. To meet this requirement, a two-stage collimation system was designed to localize the beam loss in the collimation section in the RCS [10, 11].

The transverse collimation system consists of one primary collimator and four secondary collimators. The layout of the transverse collimation system and the optical parameters are shown in Fig. 1.

In the RCS, the aperture of each secondary collimator can be varied by adjusting the positions of four movable blocks. Now the RCS is under construction, and the collimation efficiency with different sets of collimator parameters is evaluated with numerical simulation in this study. The collimation process in the presence of space charge is simulated with the Objective Ring Beam Injection and Tracking (ORBIT) code [12, 13]. Moreover, we introduce an algorithm, the Robust Conjugated Direction Search (RCDS) method, in the optimization. This method is effective in optimizing a multi-variable objective online and it has both high tolerance to noise and high convergence speed [14]. It has been used for online optimization of machine performance when the objective function can be measured [14-16].

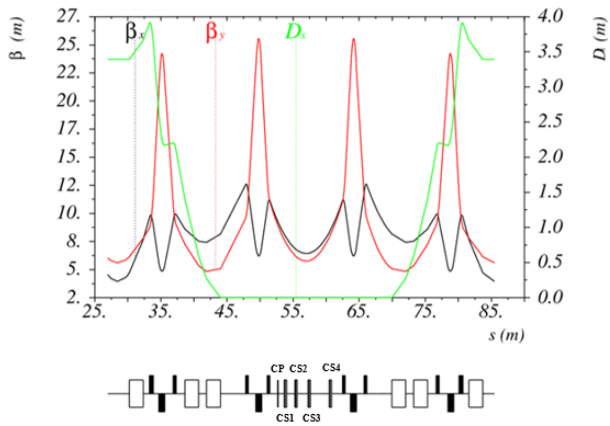

Figure 1: Optical functions along a ring super period of the RCS, and the layout of the transverse collimation system. CP represents the primary collimator. CS1, CS2, CS3 and CS4 represent four secondary collimators in sequence, respectively).

PHYSICS ANALYSIS AND MODELING

To implement the application of the RCDS method in the optimization of the RCS collimation system, the model of an ORBIT instance to simulate the collimation process were determined.

Physical Variables

In this study, the acceptance of the primary collimator is fixed to 350 π mm·mrad all the time, and the secondary collimators are tuned to optimize the performance of the collimation system.

The structure of a secondary collimator is shown in Fig. 2. Each of the secondary collimators is composed of four movable copper blocks with thickness of 200 mm. Two of the blocks are in the vertical direction and the other two, downstream of the vertical blocks, are in the

jihf@ihep.ac.cn

ISBN 978-3-95450-185-4

horizontal direction. All the blocks can be adjusted individually.

Each block has a circular surface based on the equation,

$$\frac{\left(x\cos(\frac{\pi\theta}{180^\circ})+y\sin(\frac{\pi\theta}{180^\circ})\pm c\right)^2}{a^2}+\frac{\left(-x\sin(\frac{\pi\theta}{180^\circ})+y\cos(\frac{\pi\theta}{180^\circ})\right)^2}{a^2}=1, \quad (1)$$

where θ = 0° or 90° corresponds to the horizontal or vertical direction of the block, a is the radius, and c is the distance between the beam center and the geometric center of the block, which can be changed from 34.8 mm to 68.8 mm determined by the mechanical design.

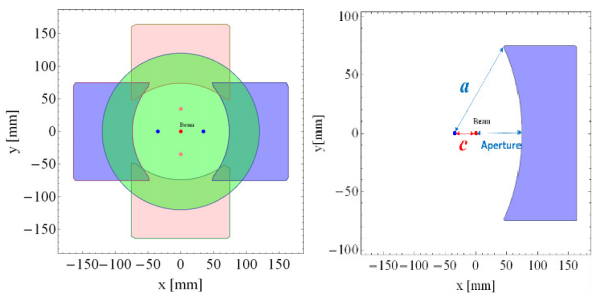

(a) (b)

Figure 2: The structure of a secondary collimator. (a) A second collimator has four blocks (pink: vertical blocks, blue: horizontal blocks) and has a cross section with the ring (green: vacuum chamber of the RCS). (b) The relationship between the parameter *c* and the aperture of the acceptance of the collimator.

The parameter *c* of each block is closely related to the acceptance of the collimator, so this parameter is selected to be the variable for the optimization. Considering the symmetry of beam distribution in simulations, the parameter *c* of the blocks on the same direction of each secondary collimator are same. Then there are eight variables to be tuned for four secondary collimators, i.e., (c_1, c_2, c_3, c_4, c_5, c_6, c_7, c_8), as shown in Fig. 3.

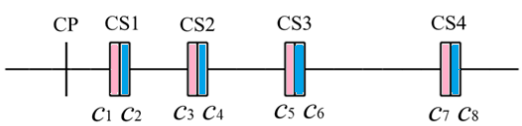

Figure 3: The variables to be tuned in the optimization of the RCDS collimation system.

Objective Function

The goal of the optimization of the collimation system is to localize the beam loss with a high shielding efficiency, and meanwhile, to have a low uncontrolled beam loss, a high cleaning efficiency of the system [17], a high collimation efficiency and a low beam loss around the RCS.

In our study, a single objective function is constructed to measure the performance of the collimation system, which is in the form of

$$f = -\eta_{\text{system}} \cdot R_{\varepsilon_{xm}} \cdot R_{\varepsilon_{ym}} \cdot R_{\varepsilon_{add}} \cdot R_{\varepsilon_{flag}}, \quad (2)$$

where a minus sign is added to form a minimization problem, η_{system} is the cleaning efficiency of the system, $R\varepsilon_{xm}$, $R\varepsilon_{ym}$, $R\varepsilon_{add}$ and $R\varepsilon_{flag}$ are the weight factors [18].

OPTIMIZATION RESULT

In order to confirm the optimization of the performance of the collimation system, we fixed the particle distribution for the input of the acceleration process. A realistic distribution of macro particles was obtained with the acceptances of secondary collimators being set to 500 πmm·mrad due to the transverse acceptance of the ring. The horizontal 99% emittance of the beam distribution is 193 πmm·mrad and the vertical is 219 πmm·mrad.

In the following, the performance of the collimation system during the acceleration process is presented and analyzed. By running an instance with the beam being accelerated for 2000 turns (a series of numerical simulations have been performed to determine the parameters of model [18]) repeatedly, the noise level of the cleaning efficiency was calculated to be 0.7%, and this value was used as the noise of the objective during the optimization. The initial acceptances of secondary collimators were set to 420 πmm·mrad. Based on the optical functions, the initial values of the variables were calculated and listed in Table 1.

Table 1: The Initial Values of the Variables

variables	c_1	c_2	c_3	c_4	c_5	c_6	c_7	c_8
value / mm	52.8	51.6	57.9	55.7	59.5	56.6	50.6	48.2

Having configured the parameters of RCDS and given the initial values of the variables, the simulation was performed to optimize the collimation system for the RCS. Figure 4 shows the objective function for all trial evaluations and the best evaluations. The objective was optimized from −92.8% to −98.2% with the product of the weight factors set to 1. Table 2 shows a comparison of the parameters reflecting the performance of the collimation system between the initial state and the optimal result. The cleaning efficiency, η_{system}, was optimized to 98.2%. The total beam loss along the ring was acceptable for shielding, although it was a little higher than that of the initial state. The uncontrolled beam loss of 1.7×10^{-4} of the total beam was lower. Considering even larger beam loss might be caused by various kinds of errors in the actual conditions, it is more important to reduce the uncontrolled beam loss.

ISBN 978-3-95450-185-4

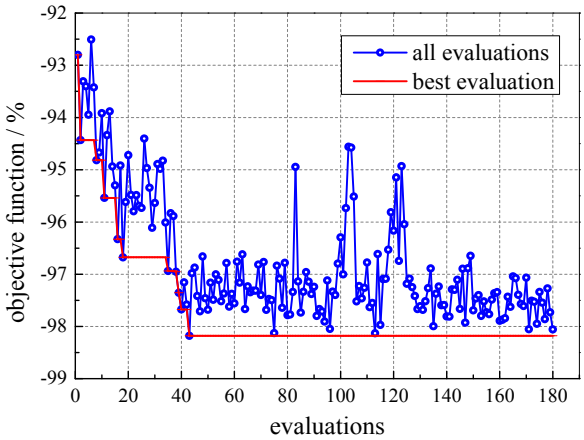

Figure 4: History of all evaluations and the best evaluations during the optimization of the collimation system with the RCDS method.

Table 2: Comparison of parameters reflecting the performance of the collimation system between the initial state and the optimal result. The parameter η_{system} is the cleaning efficiency, η_{co} is the collimation efficiency of collimators, λ_{un} is the uncontrolled beam loss of total beam outside the collimation section during the acceleration, λ_{total} represents the total beam loss as a percentage of total beam along the ring during acceleration, and ε_x (ε_y) is the 99% horizontal (vertical) emittance of the beam.

parameters	η_{system} / %	λ_{un} / 10^{-4}	η_{co} / %	λ_{total} / %	ε_x /πmm·mrad	ε_y /πmm·mrad
initial state	92.8	4.9	91.9	0.7	193	219
optimal result	98.2	1.7	96.3	0.9	193	215

SUMMARY AND DISCUSSIONS

In this paper, we have implemented the RCDS method to optimize the collimation system of CSNS/RCS. The uncontrolled beam loss of the total beam during the acceleration can be reduced to 1.7×10^{-4}, which is lower than that obtained by previous optimization [11]. As a result, an approach was established to efficiently give an optimal parameter combination of the secondary collimators for the present machine model.

ACKNOWLEDGEMENT

We would like to thank X. B. Huang for a lot of helpful discussions.

REFERENCES

[1] CSNS Project Team. China Spallation Neutron Source Feasibility Research Report. Institute of High Energy Physics and Institute of Physics, Chinese Academy of Sciences, 2009 (in Chinese).
[2] J. Wei, H. S. Chen, Y. W. Chen *et al.*, Nucl. Instrum. Methods Phys. Res., Sect. A, 600: 10-13 (2009).
[3] S. Wang, S. X. Fang, S. N. Fu *et al.*, Chin. Phys. C, 33(S2): 1-3 (2009).
[4] J. Wei, S. N. Fu, J. Y. Tang *et al.*, Chin. Phys. C, 33(11): 1033-1042 (2009).
[5] M. Y. Huang, S. Wang, J. Qiu *et al.*, Chin. Phys. C, 37(6): 067001 (2013).
[6] J. Y. Tang, J. Qiu, S. Wang *et al.*, Chin. Phys. C, 30(12): 1184-1189 (2006).
[7] S. Y. Xu, S. Wang, Chin. Phys. C, 35(12): 1152-1158 (2011).
[8] S. Y. Xu, S. Wang, Chin. Phys. C, 36(2): 160-166 (2012).
[9] N. Catalan-Lasheras *et al.*, "Beam loss and collimation at SNS ring", in Proceedings of the Seventh ICFA Mini-Workshop on High Intensity High Brightness Hadron Beams, Lake Como, Wisconsin, 1999.
[10] T. Wei, Q. Qin, Nucl. Instrum. Methods Phys. Res., Sect. A, 566: 212-217 (2006).
[11] N. Wang, M. Y. Huang, S. Y. Xu *et al.*, "Optimization of the Collimation System for the CSNS/RCS", in *Proc. IPAC'12*, New Orleans, Louisiana, USA, p. 538-540 (2012).
[12] J. Galambos *et al.*, ORBIT Use's Manual V.1.0, SNS-ORNL-AP Technical Note 11, March 1999.
[13] J. A. Holmes *et al.*, "Dynamic Space Charge Calculations for High Intensity Beams in Rings", in *Proc. ICAP'98*, SLAC-R-580, p. 179 (1998).
[14] X. B. Huang, J. Corbett, J. Safranek *et al.*, Nucl. Instrum. Methods Phys. Res., Sect. A, 726: 77-83 (2013).
[15] X. B. Huang, J. Safranek, Phys. Rev. ST Accel. Beams, 18: 084001 (2015).
[16] H. F. Ji, Y. Jiao, S. Wang *et al.*, Chin. Phys. C, 39(12): 127006 (2015).
[17] N. Wang, S. Wang, N. Huang *et al.*, "The Design of Beam Collimation System for CSNS/RCS", in *Proc. HB2010*, Morschach, Switzerland, p. 572-575 (2010).
[18] Hongfei Ji, Yi Jiao, Mingyang Huang, Shouyan Xu, Na Wang, Sheng Wang, "Optimization of the Beam Collimation System of the CSNS/RCS with RCDS Method", arXiv: 1603.09020 [physics.acc-ph].

ISBN 978-3-95450-185-4

COLLIMATION DESIGN AND BEAM LOSS DETECTION AT FRIB*

Z. Liu†, F. Marti, S. Lidia, S. Cogan, M. Ikegami, FRIB, East Lansing, Michigan, USA
T. Maruta, J-PARC/JAEA, Ibaraki, Japan
V. Chetvertkova, GSI, Darmstadt, Germany

Abstract

As a multi-charge-state, heavy-ion, superconducting accelerator with a folded geometry, FRIB faces unique beam loss detection and collimation challenges to protect superconducting cavities from beam-induced damage. Collimation is especially important in the Folding Segment 1 where the multiple charge states are created by a charge stripper and selected by a charge selector. The transported ECR contaminants, interaction with the residual gas, and beam halo due to stripping could induced significant beam losses in this region. We have simulated the potential beam losses and planned collimation accordingly. A layered loss detection network is also specifically designed to visualize potential blind zones and to meet the stringent requirements on loss detection. The related sub-systems are designed and procured and are introduced in this paper.

INTRODUCTION

As a superconducting heavy-ion accelerator, FRIB's folded structure adds additional difficulties to the machine protection and loss monitoring [1]. Among these difficulties, Folding Segment 1 (FS1) and low energy linac segment are two special regions:

Due to the charge stripper and charge selector in FS1, there are several additional beam loss sources, such as the ECR contaminants that are separated from primary beam after charge stripper, beam halo created by stripping, and charge exchange with residual gas due to the higher pressure around charge selector. These losses require additional collimation planning in FS1.

Radiation cross talk from high energy linac segments and cavity X-ray background make small loss detection especially challenging in the low energy linac segments [1]. We have designed a bunch of loss detectors to compose a multiple layer beam loss monitoring network. Feasibility study has been carried out for each loss detector and DAQ scheme is designed according to detector sensitivity and MPS requirement respectively.

This paper introduces the collimation system design in FRIB FS1 and detectors in the beam loss monitoring network. The DAQ cards and data acquisition scheme is also introduced.

COLLIMATION AT FRIB FS1

In FS1, the charge stripper and charge selector create five charge states from two, e.g. from $U^{33+\sim34+}$ to $U^{76+\sim80+}$. The five charge states is then transported to Linac Segment 2 (LS2). Figure 1 shows the mechanical drawing of FS1 lattice, on which charge stripper and charge selector are pointed out.

Besides the large intentional beam losses of those charge states that are collimated by charge selector, there are several other potentially significant losses that may need to be collimated.

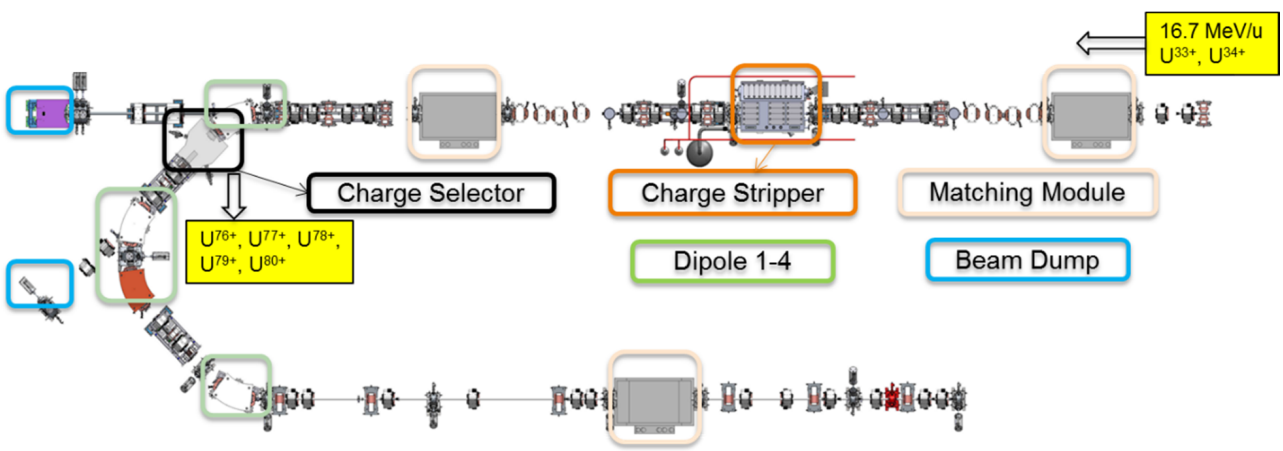

Figure 1: Mechanical drawing of FRIB FS1 lattice. $U^{33+\sim34+}$ becomes $U^{76+\sim80+}$ after charge selector.

Collimation for ECR Contaminants

The most common contaminants are carbon, nitrogen and oxygen that are coming from outgassing of the ECR plasma chamber wall or hardware introduced by a specific run such as an oven. FRIB's high intensity requirement

* This material is based upon work supported by the U.S. Department of Energy Office of Science under Cooperative Agreement DE-SC0000661.
† liuz@frib.msu.edu

ISBN 978-3-95450-185-4

pushes to operate the ion source at high microwave power, which leads to additional outgassing and conditioning. The amount of these contaminants depend on the time available for outgassing, and could be up to 5% of primary particle number in a bad case.

These contaminants, if have the same Q/A as the primary beam before FS1, e.g. N^{2+} contaminants for U^{34+} beam, can be transported through Linac Segment 1 (LS1). After charge stripping, the contaminant has larger Q/A (e.g. N^{7+} Q/A=0.5) than the beam and different focusing and bending path.

Contaminant losses are simulated between the charge stripper and charge selector, with larger Q/As compared with primary $U^{76+\sim80+}$ beam: Q/A = 0.35, 0.40, 0.42, 0.45, 0.50 was simulated [2]. With these simulations, five collimator locations are defined, as shown in Figure 2. According to the transmission plot at the bottom, 90% of Q/A=0.40 contaminants are collimated by the new collimators, only 10% of such contaminants lost in the 1st bending magnet. The vacuum chamber of the 1st bending magnet still need water cooling though.

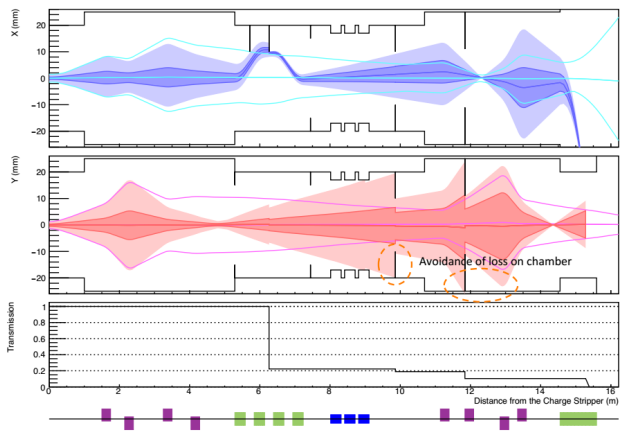

Figure 2: Simulation of Q/A=0.40 contaminant loss with five collimators between charge stripper and charge selector. The small aperture "collimator" in the middle is Halo Monitoring Ring. . The color lines are envelope of uranium beam, dark color represents rms envelope of contaminant particles while pale region represents 100% envelope.

Beam Halo Induced by Charge Stripping

Charge stripping could also create significant beam halo for the primary beam. If no collimation is planned for that, the beam halo could become losses at superconducting cavities downstream in Linac Segment 2 (LS2). To protect critical equipment such as superconducting cavities, collimators should be planned before LS2.

To simulate the potential losses, artificial beam halo was created by increasing the nominal beam size. Particle tracking was then implemented in MAD-X. Collimators are planned before critical equipment such as magnet, superconducting cavities and bellows, as shown in Figure 3.

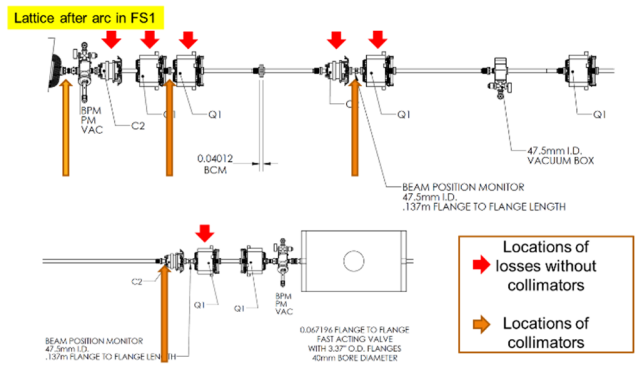

Figure 3: Lattice after arc in FS1 with collimator locations.

Secondary losses, i.e., primaries and fragments that escaped from collimator, were also simulated at collimator. The collimators are determined to be elliptical shape that can cut both horizontal and vertical tails, with apertures about 5-6 times of rms beam size.

Charge Exchange with Residual Gas

Charge exchange with residual gas could be a source of beam losses due to relatively high pressure around charge selector. Figure 4 shows the simulated vacuum profile around the charge selector. Compared with superconducting region (~10^{-9} Torr), the pressure at charge selector could be 3 order of magnitude higher.

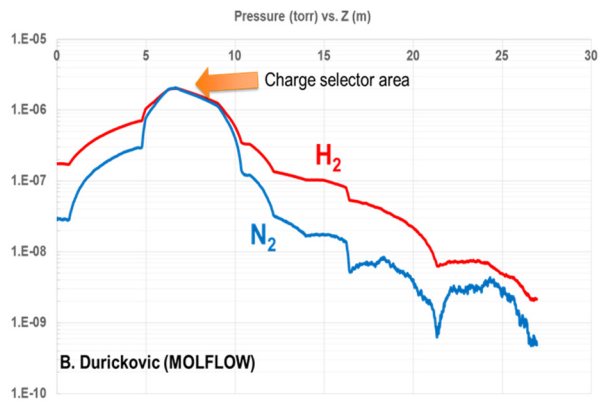

Figure 4: Simulated vacuum profile around charge selector, from the entrance of 1st bending magnet to end of FS1.

We can estimate the fractional charge exchange rate using the electron capture cross section:

$$\frac{N_o - N}{N_o} \sim 1 - e^{-\int_0^L \sigma\, n\, dl}$$

where σ is the electron capture cross section for U^{73+}[3], and $n = p/kT$, for H_2 and N_2 respectively.

The fractional beam loss induced by charge exchange is thus 7 ppb for H_2, and 10 ppm for N_2. Most losses occur at charge selector area and we should plan collimator after it.

The location of collimator can be determined by simulating charge exchange induced losses [2]. Losses mainly caused by U^{81+} that is stripped from U^{80+}. An easy way to simulate the loss location is to assume uniform charge exchange rate over the whole length (from the entrance of 1st bending magnet to end of FS1). A new collimator before

ISBN 978-3-95450-185-4

the 2nd sextupole in the arc, together with previous beam halo collimators, can stop beam losses generated in charge selector area completely [2]. But 6% of other charge exchange particles escape the collimators and goes into LS2 [2]. HMR aperture in LS2 may need to be optimized to protect superconducting cavity.

FRIB LOSS MONITORING NETWORK

Since superconducting cavities are very sensitive to beam losses, FRIB machine protection requirement is made comparable to proton machine: Detector should response to Fast Protection System (FPS) in 15 μs for large fractional loss and be capable to detect 1 W/m or equivalent small losses in the superconducting region.

However, FRIB's special folded structure [1] greatly challenge the conventional BLM system, i.e. the ion chamber. The challenges can be summarized as:

- Heavy ion produces less radiation. Therefore the signal is much smaller for 1 W/m beam loss compared with proton machine
- Cavity X-ray background is high compared with low energy beam loss signal
- Significant radiation cross talk from high energy segments to low energy segment disable loss location determination

To fulfil FRIB machine protection requirement, we developed a multiple layer beam loss monitoring network that is composed of a bunch of beam loss detectors: Differential Beam Current Monitor (DBCM), Ion Chamber (IC), Halo Monitor Ring (HMR) [4], Fast Thermometry System (FTS), Neutron Detector (ND) and Cryogenic System Monitor (Cryo). The layered network is shown as Table 1.

Table 1: Multiple Layer Beam Loss Monitoring Network

Fast Losses (response in 15 μs)			
	Primary	**Secondary**	**Tertiary**
LS1	DBCM	HMR	
FS1	DBCM	HMR	IC
LS2 low E	DBCM	HMR	
LS2 high E	DBCM	IC	HMR
FS2	DBCM	IC	HMR
LS3	DBCM	IC	HMR
BDS	DBCM	IC	

Slow Losses (1 W/m)			
	Primary	**Secondary**	**Tertiary**
LS1	HMR/FTS	HMR/FTS	Cryo
FS1	HMR	IC	
LS2 low E	HMR/FTS	HMR/FTS	Cryo
LS2 high E	IC	HMR/Cryo	
FS2	IC	HMR	
LS3	IC	HMR/Cryo	HMR
BDS	IC		

The neutron detector mainly serves as background detector and will be also helpful for LS1 tuning.

Per machine protection requirement, Table 2 shows example signal amplitudes with acquisition times for IC and HMR, where HMR signal is estimated as consolidated loss over cryomodule and IC signal is based on minimum sensitivity requirement 1.5nA/R/hr. The priority of each loss detector in loss monitoring network is determined by its signal amplitude and acquisition time. For example, ion chamber imposes a limitation on noise requirement of the DAQ card, i.e. 10% of 350 pA in 150 μs, since integration time × 10 corresponds to signal amplitude /√10.

Table 2: Signal Amplitude Estimation, Acquisition Time and Corresponding Loss Level for HMR and IC

SIGNAL	LS1	LS2	LS3	T_{DAQ}	LOSS LEVEL
HMR	10nA	2nA	1nA	1.5s	0.1W/m
	100nA	20nA	10nA	15ms	1W/m
	1μA	200nA	100nA	150μs	10W/m
	10μA	2μA	1μA	15μs	100W/m
IC	N/A	3.5pA	42pA	1.5s	0.1W/m
	N/A	35pA	420pA	15ms	1W/m
	N/A	350pA	4.2nA	150μs	10W/m
	N/A	3.5nA	42nA	15μs	100W/m

FRIB will procure three DAQ cards for loss detectors, i.e. CAENels AMC-PICO-8 card for HMR, IC and ND, Struck SIS8300-L2 card for DBCM, and FRIB Digital Board for general purpose such as interfacing with the Global Timing System (GTS) and Fast Protection System (FPS). These DAQ cards will be installed in a MicroTCA.4 chassis, which is used as the platform for most of the FRIB "fast" diagnostics that interface with FPS and acquire "fast" data (>10 kHz). 75% of FRIB diagnostic devices are covered by these 3 MicroTCA cards.

Among these 3 cards, CAENels AMC-PICO-8 is specifically customized for loss diagnostics while it also serves Faraday Cups, Allison Scanner and Profile Monitor. It is a fast picoammeter that features 8 channels @ 1 MS, with ~35 kHz bandwidth. It has a switchable dynamic range of 16 μA or 130 μA, and a tolerable noise requirement for loss monitors, as shown in Table 3.

Table 3. Noise Requirement and Measurement of CAENels AMC-PICO-8 Card. The noise level was measured with a 150 ft cable.

Sample Time	Noise requirement (35 kHz, 1 μA)	Noise measurement (35 kHz, 16 μA)
1 μs	770 pA	995 pA
15 μs	199 pA	220 pA
150 μs	35 pA	68 pA
100 ms	2.43 pA	2.63 pA

ISBN 978-3-95450-185-4

The measured noise level for 150 µs sampling time is about twice of the requirement, which is 10% of the minimum IC signal. Considering the IC signal is estimated based on minimum IC sensitivity and 20% noise level is still tolerable, we accept the fast picoammeter card as our loss monitor DAQ card.

A common feature for these three cards is background subtraction capability. Depending on the signal, background could be electrical measurement offset, or cavity X-ray background for ion chamber. The power line harmonics (60 Hz, 180 Hz) will also be sampled and subtracted by Struck card for BCM. All three fast DAQ cards are capable to subtract background in the 50 µs beam gap period. This implies the requirement for 35 kHz bandwidth in order to sample at the second half of beam gap, as shown in Figure 5.

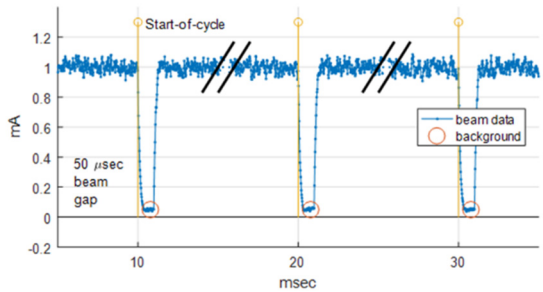

Figure 5: Background sampling at the 2nd half of beam gap.

Rather than DBCM, HMR, IC and ND, FTS only serve slow loss monitoring and does not interface with FPS. Its feasibility has been validated with In-Cryomodule test [5]. Its DAQ system is a commercial temperature monitor and the data will be directly fed into EPICS.

CONCLUSION

In this paper, we have introduced the collimation consideration for FRIB machine, especially at Folding Segment 1, the most concerned area due to charge stripper and charge selector. Ten collimators are planned in FS1 to eliminate losses induced by ECR contaminants, beam halo and charge exchange. These collimations, will protect critical equipment such as magnets, superconducting cavities and bellows. However, such intensive collimations also introduce intentional losses that add difficulty to detect uncontrolled losses. While we can measure beam current at several locations and monitor the change of ratio for unexpected losses, instrumenting collimators in the arc for differential loss monitoring is also encouraged. If the intentional loss is stable on the time scale of few seconds, we should be able to subtract it for small loss monitoring at FS1.

The FRIB loss monitoring network, composed of different layers of loss detectors, was introduced to overcome radiation cross talk issue and fulfil 1 W/m machine protection requirement for superconducting region. We have defined the requirement for DAQ system according to the machine protection requirement, priority of detectors in the network, and detector signal estimations. The DAQ cards that meets the requirement were introduced. We are now on the track for pre-installation/integration tests. The commissioning of loss monitors and feasibility of loss network will be reported in the future.

ACKNOWLEDGMENT

T. Maruta and V. Chetvertkova provide their simulation and collimation design result for this paper.

The authors want to thank A. Hussain, Z. Zheng and Colleagues in FRIB Diagnostics group for generous help and fruitful discussions.

The authors also want to thank FRIB management team for support of this work.

REFERENCES

[1] Z. Liu *et al*., "Beam Loss Monitor System for the Low-Energy Heavy-Ion FRIB Accelerator", in *Proc. IBIC'13*, Oxford, UK, paper MOPC46.

[2] T. Maruta *et al*., "Simulation Study on the Beam Loss Mitigation in the 1st Arc Section of FRIB Linac", submitted to LINAC'16, East Lansing, MI, USA (2016).

[3] V. P. Shevelko *et al.*, *NIM* B 278 (2012) 63.

[4] Z. Liu *et al*., *NIM* A 767 (2014) 262-266.

[5] Z. Zheng *et al.*, "Cryogenic Thermometers as Slow Beam Detectors", in *Proc. IBIC'15*, Melbourne, Australia, paper MOPB073.

ISBN 978-3-95450-185-4

A COUPLED RFQ-IH-DTL CAVITY FOR FRANZ: A CHALLENGE FOR RF TECHNOLOGY AND BEAM DYNAMICS

R. Tiede, M. Heilmann*, D. Mäder†, O. Meusel, H. Podlech, U. Ratzinger, A. Schempp, M. Schwarz, IAP, Goethe-University Frankfurt, Germany

Abstract

For the 'Frankfurt Neutron Source at the Stern-Gerlach-Zentrum' (FRANZ) facility an inductively coupled combination of a 4-Rod-type Radio-Frequency-Quadrupole (4-Rod-RFQ) and an 8 gap interdigital H-type (IH-DTL) structure will provide the main acceleration of an intense proton beam from 120 keV to 2.0 MeV. The RFQ-IH combination with a total length of about 2.3 m will be operated at 175 MHz in cw mode. The expected total power need is around 200 kW. Due to the internal inductive coupling only one RF amplifier is needed, which significantly reduces the investment costs. At present the RFQ is installed separately in the beam line for conditioning up to the design rf power and for measuring the beam quality behind the RFQ. In parallel, the IH-DTL is rf tuned together with a dummy RFQ outside the FRANZ cave. This paper will present the status of the project with emphasis on key questions like beam dynamics constraints, rf tuning issues and technological challenges resulting from the high thermal load in cw operation.

INTRODUCTION

At the FRANZ facility on the campus of the Frankfurt University physics faculty, a 2 MeV proton primary beam will produce 1 – 200 keV neutrons by the ^{7}Li(p,n)^{7}Be reaction with a maximum neutron yield at 30 keV. For such lower neutron energies, the FRANZ facility will provide intensities by two to three orders of magnitude larger than from existing accel. driven intense neutron sources [1].

The facility will mainly serve to nuclear astrophysics experiments [2], namely:

- Measurement of the differential neutron capture cross sections dσ/dE, with relevance to the stellar nucleosynthesis (slow neutron capture process). For this purpose, time-of-flight (TOF) measurements are needed and the FRANZ facility has to deliver 1 ns short proton bunches with a repetition rate of 250 kHz. In the so called "compressor mode" it is aimed to produce a neutron flux of $1 \cdot 10^7$ /cm^2/s at the sample.
- Measurement of integrated neutron capture cross sections. In the so called "activation mode" the facility is designed to produce 10^{11} n/cm^2/s in cw operation.

In order to fulfil these ambitious specifications, an intense primary proton beam of several mA (for the activation mode) and up to 140 mA (for the compressor mode) must be accelerated to 2.1 MeV with an energy variation of ± 0.2 MeV. In the first operation phase of FRANZ, the maximum proton beam current will be limited to 50 mA. However, the in house developed filament driven source already delivered a 200 mA d. c. proton beam. The time structure needed for the TOF measurements will be applied by a chopper array integrated to the LEBT section, which will form macro pulses with a flat top of 50 ns and 250 kHz repetition rate. Behind the main linac, a Mobley type "bunch compressor" will merge 9 consecutive micro bunches as delivered by the linac and bunch the proton beam to the final length at target of around 1.1 ns.

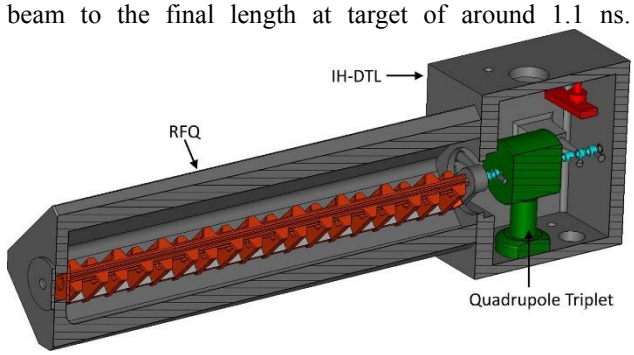

Figure 1: Coupled RFQ-IH-DTL cavity.

Table 1: Parameters of the Coupled Cavity

Parameter	Value	
f [MHz]	175	
I [mA]	50 (140)	
coupling factor k	0.004	
	4-Rod-RFQ	**IH-DTL**
energy range [MeV]	0.12 – 0.7	0.7 – 2.0
total length [m]	1.7	0.6
rf losses [kW]	95 (140)	60 (60)
4-Rod-RFQ		
electrode volt. [kV]	62 (75)	
R_p [kΩm]	70	
no. of stems	18	
IH-DTL		
eff. gap volt. [kV]	80 – 350 (80 - 350)	
$R_{shunt,eff.}$ [MΩ / m]	62	
no. of gaps	8	

This paper focuses on the discussion of all points of interest related to the main accelerator component, an inductively coupled 4-Rod-RFQ & IH-DTL combination (see Figure 1): from beam dynamics to rf tuning aspects and right up to mechanical design challenges due to the high thermal load on the cavities at cw operation.

* GSI Helmholtzzentrum, Darmstadt, Germany
† BEVATECH, Frankfurt, Germany

ISBN 978-3-95450-185-4

After a careful assessment of several alternatives (see next chapter), the inductive coupling was chosen because it helps reducing rf amplifier costs and utility space, but also minimizing the length of the inter tank section, which is an advantage in high current beam dynamics.

CAVITY COUPLING OPTIONS

The most natural solution would have been an RFQ resonator up to the end energy of 2 MeV. This cavity would be about 3 meters long and require a 300 kW amplifier. This is why, mainly for costs reasons, the more efficient combination of an RFQ up to 700 keV followed by the IH-DTL up to 2 MeV has been chosen. In this case, feeding each resonator cavity by its own amplifier unit is the natural solution with the highest degree of flexibility with respect to rf tuning and cavity control. However, in case of two independent cavities, two cw amplifiers would have been needed, in the power class between 100 kW (IH-DTL) and 200 kW (4-Rod-RFQ). This option has been rejected from the start, by lack of budget and of the needed utility space on site. This is why different alternative solutions have been carefully investigated [3], [4]. All alternatives described below have in common that only one amplifier in the power class of 250 kW would be needed.

Power Splitter

By using a splitter, the power from one amplifier can be divided according to the needed RFQ-DTL amplitude ratio as defined in advance. However, the power ratios are then fixed and cannot be easily rematched. The splitter itself would be an expensive, custom-made item. Moreover, one has to fight against reflections at the splitter unit and difficult phase matching between 4-Rod-RFQ and IH-DTL.

Phase Shifter

The full rf power is coupled into one of the cavities (e.g. the 4-Rod-RFQ), then partly out coupled and critically coupled to the second cavity (IH-DTL) by means of the phase shifter unit. The rf phase relation between both structures can be adjusted by length variation of the coaxial transmission line. However, the phase matching is rather sensitive.

Galvanic Internal Coupling

The full rf power is again coupled into the RFQ and then transferred to the IH-DTL by a bridge directly connected to the last RFQ and the first DTL stem. The positions of the connections to both stems basically define the voltage amplitude ratio U_{IH}/U_{RFQ}. This option has been investigated in detail and seriously considered in the early project phase [5]. However, it has been finally abandoned because of a missing technical solution for the sophisticated, coaxial water cooling system needed for absorbing the thermal losses along the coupling bridge.

Inductive Internal Coupling

The inductive coupling is accomplished by just opening the connection flange between both structures. Thus the magnetic field can penetrate through the coupling cell (see Figure 2) and can induce a common (i.e. coupled) resonance of both connected cavities. This concept allows for a flexible tuning of the resonance frequency and the RFQ-DTL amplitude ratio, and hence it was finally chosen for the FRANZ RFQ-DTL combination.

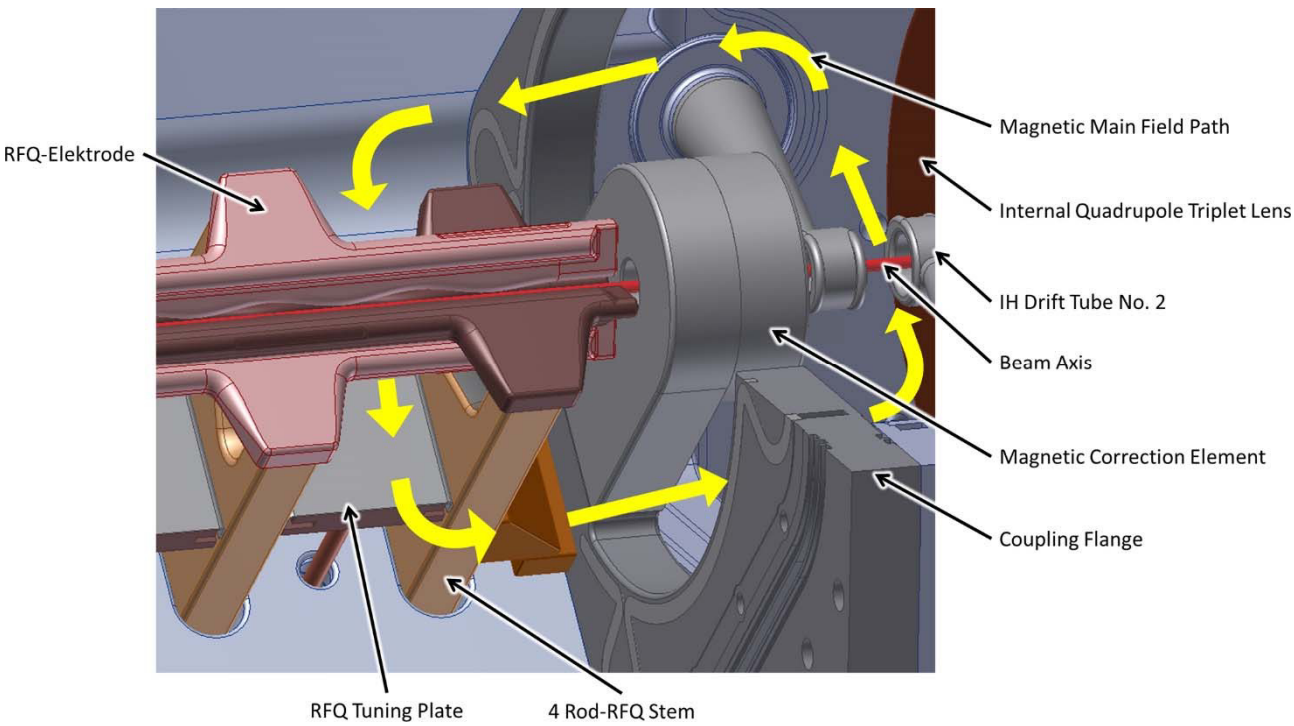

Figure 2: Detail view of the coupling flange between Four Rod RFQ and IH DTL. The qualitative pathway of the magnetic field lines (in yellow) in case of the zero mode is shown.

ISBN 978-3-95450-185-4

TUNING OF THE INDUCTIVE COUPLED RFQ-IH-DTL COMBINATION

The theory of eigenmodes in a series of n inductive coupled resonant circuits is described in many textbooks, e.g. by T.P. Wangler [6]. In our case the eigenvalue problem must be solved for only two coupled oscillators. Assuming that both cavities are independently tuned to the same resonance frequency f_0 before coupling, then after coupling the following two coupled resonances appear:

$$\omega_1 = \omega_0 \cdot \sqrt{\frac{1}{1+k}} \quad \text{with } i_2 = i_1, \text{“zero mode”} \tag{1}$$

$$\omega_2 = \omega_0 \cdot \sqrt{\frac{1}{1-k}} \quad \text{with } i_2 = -\, i_1, \text{“}\pi\text{ mode”} \tag{2}$$

The bandwidth is then given as follows:

$$\delta\omega = \omega_2 - \omega_1 \approx \omega_0 \cdot k \tag{3}$$

with k being the coupling factor ($k = M / L$).

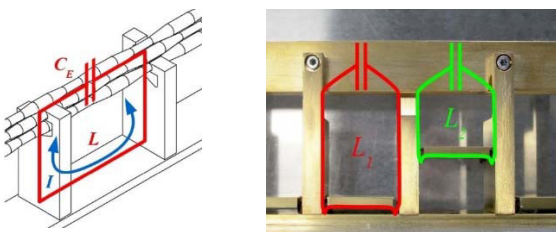

Figure 3: Adjusting the resonance of Four-Rod-RFQ cells by changing the tuning plates' positions.

Based on these considerations, the tuning procedure of the coupled 4-Rod-RFQ IH-DTL combination has been performed in the following steps [3], [4], [7]:

- Tuning of the uncoupled cavities to the same resonance frequency f_0. The 4-Rod-RFQ can be described as a chain of coupled $\lambda/2$ resonators. The inductance of each cell can be tuned by changing the position of the contacting tuning plates (see Figure 3). By these means, the FRANZ RFQ has a tuning range of several MHz, limited only by the required field flatness. The IH-DTL has a tuning range of ± 2 MHz by static tuners, also limited by the voltage distribution.

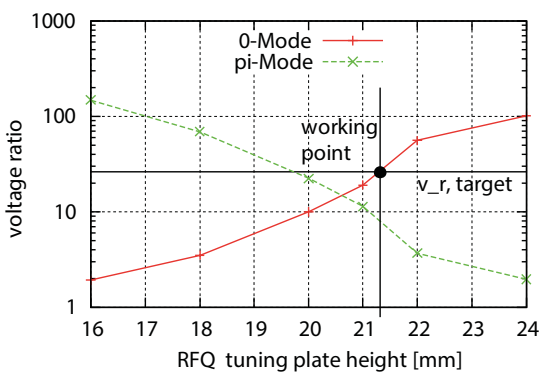

Figure 4: U_{IH}/U_{RFQ} adjustment by RFQ tuning plates.

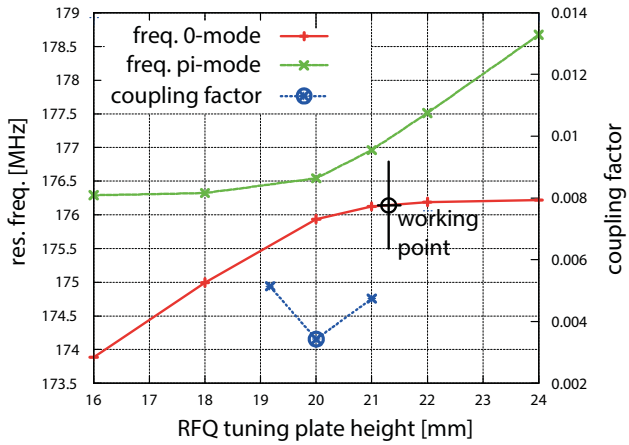

Figure 5: Mode separation and dependence of the coupling factor on the position of the last RFQ tuning plate.

- Couple the cavities and use the tuning knobs as described before for setting the desired U_{IH}/U_{RFQ} voltage ratio. The target value was 25.4. As seen from Figure 4, the voltage ratio can be matched effectively by only changing the position of the last RFQ tuning plate.
- Rebalance the field flatness in the RFQ and the voltage distribution in the IH-DTL and simultaneously adjust the coupled cavity resonance to f_1 = 175 MHz. This final step can be performed by using all RFQ tuning plates and the movable RFQ and DTL tuners (only small displacements needed for fine adjustment).

The described tuning procedure has been investigated on a cold model cavity. Key results are shown in Figure 4 and Figure 5 [3], [7]. Microwave Studio simulations would be too time consuming in this case, because of the complicated mesh and lack of symmetries. After optimization of the coupling parameters by measurements, CST MWS simulations were used for cross checking.

As shown in Figure 4 and Figure 5, the zero and the pi mode act in an opposite way, as expected from theory, and moreover they are separated by a minimum of 0.6 MHz and by about 1.0 MHz at the working point. Finally, the feasibility of the cavity coupling with good accuracy and high tuning ability could be demonstrated (see Figure 6).

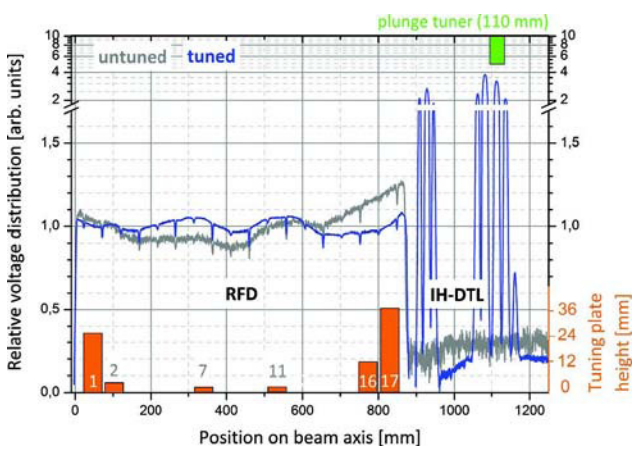

Figure 6: Demonstration of the successful inductive coupling (blue line) based on cold model measurements.

ISBN 978-3-95450-185-4

STATUS OF THE RFQ AND IH-DTL STRUCTURES

A technological challenge for both the RFQ and the IH-DTL structure of the FRANZ project is given by the high thermal load due to cw operation. This is why extensive rf and thermal simulations were necessary in the design phase of both cavities. Based on the results, improved cooling and contacting techniques had to be developed, as for example: The RFQ cooling channels were done by electroforming technology; the contact pressure between the tuning plates and the stems was improved by using specially shaped shims instead of the conventional spring contacts.

For the validation of the new technology, a short (0.4 m long) prototype RFQ was built and power tested. Figure 7 shows the encouraging power test result: At the maximum power level of 46 kW (i.e. 115 kW/m, 2.5 times higher than ever achieved for cw operated 4-Rod-RFQs) the reflected power (in red) is still less than 1%. Long term stability was also demonstrated in a 200 hours run at 31 kW (i.e. 78 kW/m, which is the FRANZ 4-Rod-RFQ design value) [8].

For the IH-DTL, extensive simulations of the heat distribution were performed, resulting into max. surface field reduction and the development of a cavity walls and stems cooling concept [4], [9].

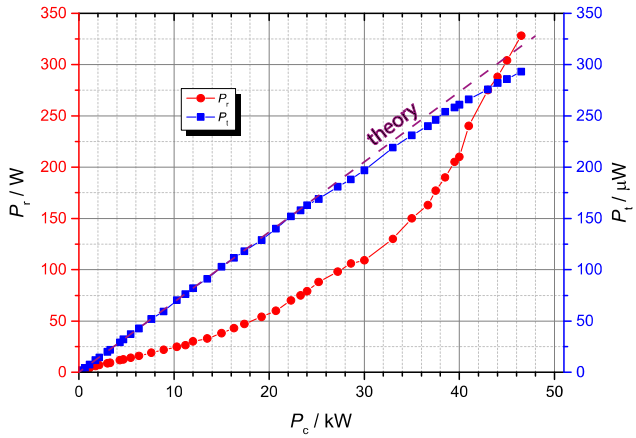

Figure 7: Power test results on the short RFQ prototype cavity. Pickup (P_t, blue) and reflected (P_r, red) power as function of the cavity power.

At present, both cavities and all subsidiary components (e.g. the coupling flange with integrated steering magnet unit) are ready for installation (see Figure 8). The 4-Rod-RFQ has been rf tuned as a "stand alone" cavity and is now under high power rf conditioning. For the IH-DTL rf tuning measurements are performed by using a RFQ dummy, in order to prepare the coupled mode operation. The final steps will be the coupling of both cavities, installation in the FRANZ cave and first tests with beam.

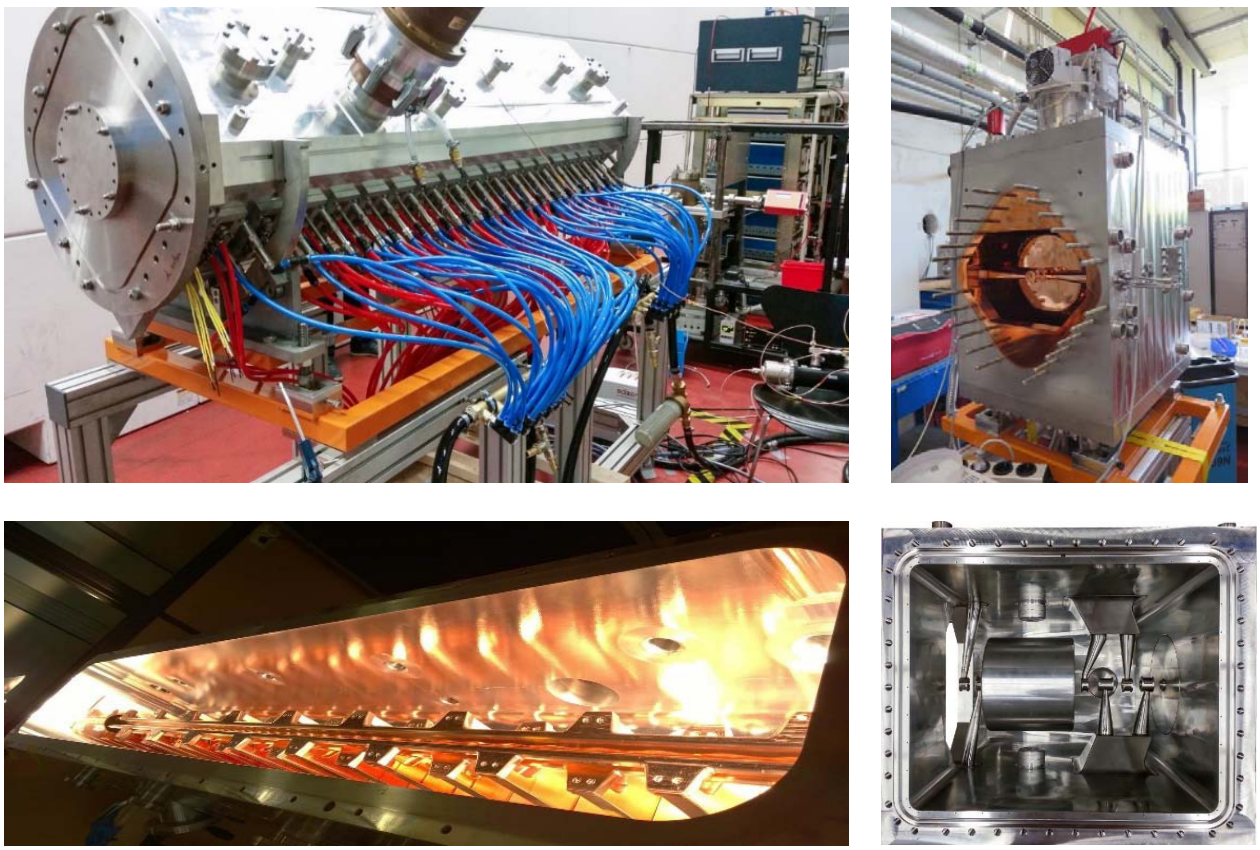

Figure 8: RFQ and IH-DTL ready for power testing and installation into the FRANZ cave.

ISBN 978-3-95450-185-4

BEAM DYNAMICS ISSUES

The RFQ beam dynamics design has been performed with the PARMTEQ code (results not shown in this paper). The RFQ output distribution is used as an input for the DTL simulations performed with the in-house developed code LORASR. The results are shown in Figure 9 and Figure 10. In the simulations the subsequent quadrupole triplet lenses as well as the rebunching CH-type cavity are included. The transverse beam dynamics is defined by a quadrupole triplet channel, whereas the longitudinal motion is that of a separated function linac: a combination of main acceleration sections at $\phi_s = 0$ deg and rebunching gaps at negative synchronous phase.

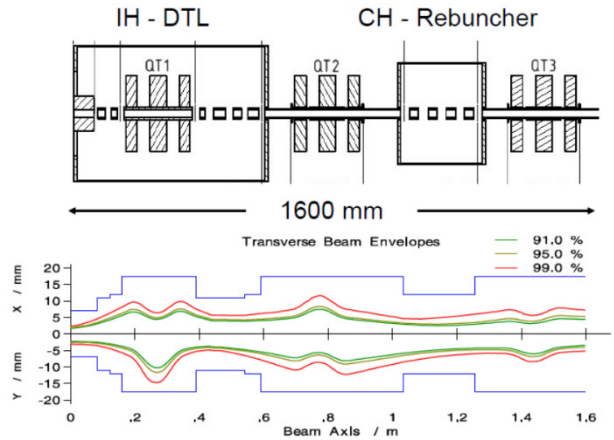

Figure 9: Transverse beam envelopes along the IH cavity and the subsequent transport and bunching section.

The major beam dynamics constraint to be considered is the fixed RFQ-DTL rf phase relation. This is why the drift between the RFQ electrode ends and the first DTL gap has to be matched with high precision. However, the RFQ output phase and beam energy might diverge, depending on the achievable coupled RFQ-DTL rf tuning accuracy.

This is why detailed error sensitivity simulations are necessary and can start as soon as the final coupled cavity rf tuning data will be available. First cross check simulations as shown in Figure 10 are very promising: The lattice shows high robustness with respect to very large offsets in phase (10 deg) and beam energy (5 %).

CONCLUSION

A novel, inductively coupled RFQ-IH-DTL combination will serve as the main linac component for the FRANZ project, accelerating a 50 mA proton beam from 120 keV to 2.0 MeV in cw operation. The basic structure parameters have been defined after detailed numerical simulations and measurements on a scaled model.

At present all components were delivered and are tuned and rf conditioned separately, in preparation for the coupled mode operation. An extended beam dynamics error study is under preparation in order to define the needed coupled cavity tuning accuracy.

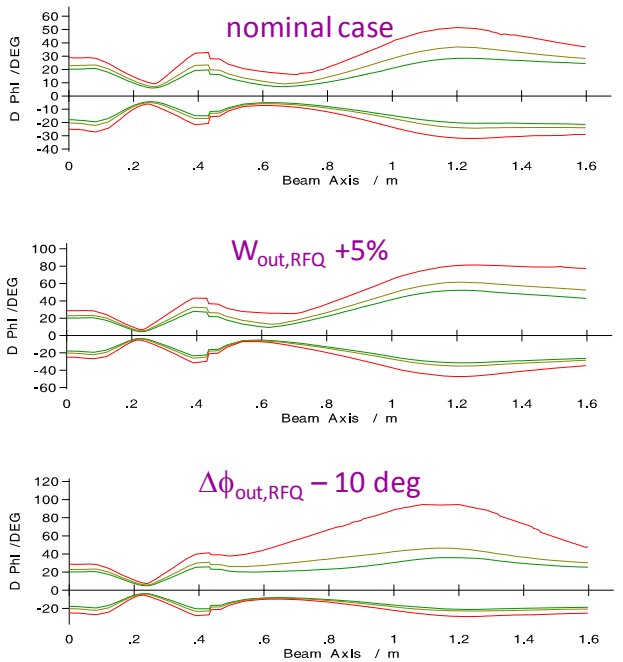

Figure 10: Error sensitivity of longitudinal beam dynamics with respect to starting phase and RFQ output energy variation.

ACKNOWLEDGEMENT

The presenter would like to thank all the co-authors – some of them with new affiliations – for their manifold contributions and efforts to bring the main FRANZ accelerator components to the present state, close to first operation with beam in the coupled cavity mode.

REFERENCES

[1] U. Ratzinger *et al.*, "The Frankfurt Neutron Source FRANZ", in *Proc. IPAC'10*, Kyoto, Japan, 2010, paper MOPEC059, pp. 597-599.

[2] R. Reifarth et al., "Neutron Reactions in Astrophysics", *J. Phys. G: Nucl. Part. Phys.*, vol. 41, p. 053101 (2014).

[3] D. Mäder, "Kopplung der Beschleunigerkavitäten RFQ und IH-DTL am FRANZ-Projekt", Master thesis, Inst. for Applied Physics, Frankfurt University, Germany, 2011.

[4] M. Heilmann, "Kopplung von 4-Rod-RFQ und IH-DTL für das FRANZ-Projekt", Ph.D. thesis, Inst. for Applied Physics, Frankfurt University, Germany, 2016.

[5] A. Bechtold *et al.*, "A Coupled RFQ-Drift Tube Combination for FRANZ", in *Proc. LINAC'08*, Victoria, Canada, 2008, paper MOP001, pp. 46-48.

[6] T. P. Wangler, "Coupled-Cavity Linacs", in *RF Linear Accelerators*, Wiley-VCH, 2008, pp. 98-121.

[7] M. Schwarz, "Hochfrequenzabstimmung und Feldoptimierungen des gekoppelten 1:2 RFD-IH-Modells für FRANZ", Bachelor thesis, Inst. for Applied Physics, Frankfurt University, Germany, 2012.

[8] S. Alzubaidi et al., "The Frankfurt Neutron Source FRANZ", *Eur. Phys. J. Plus (2016) 131: 124.*

[9] M. Heilmann *et al.*, "A Coupled RFQ-IH Cavity for the Frankfurt Neutron Source FRANZ", in *Proc. LINAC'12*, Tel-Aviv, Israel, 2012, paper THPB008, pp. 858-860.

ISBN 978-3-95450-185-4

OVERVIEW OF THE CSNS LINAC LLRF AND OPERATIONAL EXPERIENCES DURING BEAM COMMISSIONING

Zhencheng Mu†, Jian Li, Xin An Xu, Zonghua Zhang, Lin Yan Rong, Zhe Xin Xie, Wenzhong Zhou, Mei Fei Liu, Ma Liang Wan, Bo Wang, Yuan Yao, Chinese Spallation Neutron Source (CSNS), Dongguan, China

Abstract

The CSNS proton linear accelerator (Linac) will deliver 81MeV proton beam to RCS ring. The Linac is comprised of H- ion source, RFQ, two Buncher cavities (MEBT), four DTL accelerators and one Debuncher cavity (LRBT). The RFQ accelerator is powered by two 4616 tetrodes, the maximum output power of each tube is 350kW. Three 25kW solid state amplifiers supply RF power to two Buncher cavities and one Debuncher cavity, repectively. The RF power sources of four DTL accelerators are four 3MW klystrons. Each RF power source owns a set of digital LLRF control system in order to realize an accelerating field stability of ±1% in amplitude and ±1° in phase. The front four LLRF control systems have been used in the beam commissioning of CSNS Linac in the end of 2015. This paper will introduce the design and the performance of the digital LLRF control system.

INTRODUCTION

In the CSNS 81MeV proton linear accelerator (Linac), the RF power sources consist of two 350kW 4616 tetrodes, three 25kW solid state amplifiers, five 3MW klystrons (including spare one). Now, the 4616 tetrodes, two solid state amplifiers and the first Klystron power source have already supplied RF power to the corresponding accelerating cavities for the ageing process and beam commissioning. The installation and test of the rest three klystron power sources are still in process. The block diagram of the Linac RF system is shown in Figure 1 [1].

The RF field are controlled by eight almost the same digital LLRF controllers which are installed in cabinets. The prototype of the digital LLRF control system was developed in the 352MHz RFQ of IHEP, the design team have gathered much experiences from the operating process of the prototype. Based on the good design experiences of the prototype, the improvement and commissioning of the eight on-line LLRF hardwares are completed quickly, software algorithms are also completed with some elaborate improvements on time.

As shown in Figure 2, each LLRF control system consists of the 324MHz RF reference line, analog module (AM) and clock distribution module (CDM), digital control module (DCM) and the high power protection module (HPM). Because the AM and CDM are absolutely analog components, most analog components are susceptible to ambient temperature, so we put these two modules into a temperature stabilizing chamber. The DCM is mainly responsible for the stability of the RF field amplitude and phase, HPM can quickly cut off the RF drive in case of arc in the RF distribution system, VSWR over threshold or cavity vacuum fault, and so on. The field control algorithms and high power protection logics are designed through digital signal processing in FPGA and DSP. Various control parameters can be set from IPC human-computer interface through embedded Ethernet communication. The block diagram of the digital LLRF control system is showed in Figure 2.

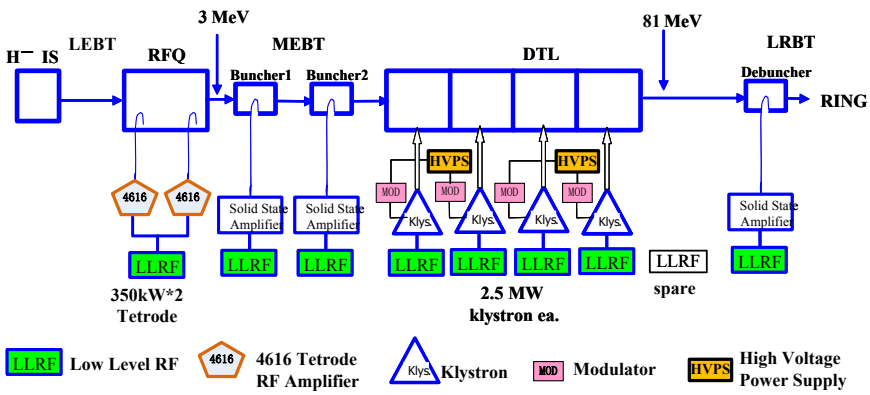

Figure. 1: Block diagram of the CSNS Linac RF system.

† muzc@ihep.ac.cn

ISBN 978-3-95450-185-4

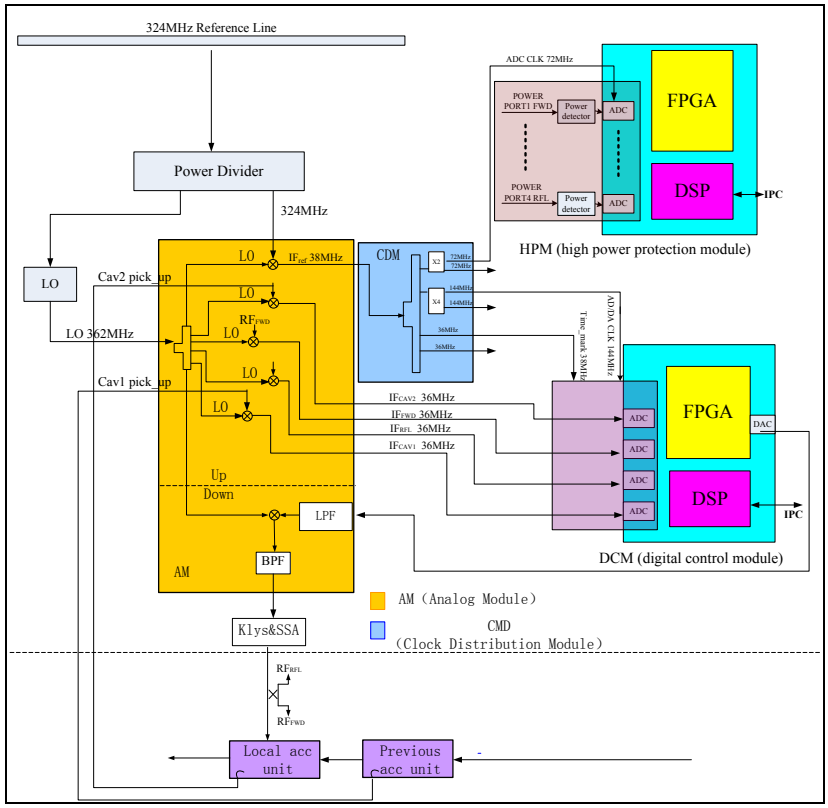

Figure 2: Overview of the digital LLRF control system.

THE 324MHz REFERENCE LINE [2]

The 324MHz reference signal of the Linac is from the reference line system, and the reference signal is from the main oscillator, the reference line stretches along the sub-tunnel of CSNS Linac, Figure 3 shows the whole structure of the sub-tunnel. The phase stable cable is wrapped in a constant temperature water jacket, the variation range of the water temperature is limited within $\pm 0.1^\circ$. The reference signal is picked up through a Narda 3000 coupler, and transferred to each LLRF station through Andrew phase stable cable.

Figure 3: The 324MHz reference line of the CSNS Linac.

THE AM AND CDM

As shown in Figure 2, the AM consists of four down conversion channels and two up conversion channels, The frequencies of the LO and IF are 360MHz and 36MHz, respectively. The clocks distribution module generates three clocks: 144MHz, 36MHz and 72MHz. The 144 MHz and 36MHz clocks are used as the 4 channel ADC sampling clock of the DCM, and 72MHz clock is used as the 8 channels ADC sampling clock of the HPM. In order to achieve the higher control precision of the RF filed amplitude and phase, the analog up-down conversion unit and the clocks distribution module are put into a temperature stabilizing chamber, as shown in Figure 4, the two units are installed parallel inside the chamber, it adopts the air cooling semi-conductor refrigeration technology to keep the temperature stable. The temperature variation range inside chamber is less than ± 0.1℃.

Figure 4: Temperature stabilizing chamber.

ISBN 978-3-95450-185-4

HIGH POWER PROTECTION MODULE (HPM)

The high power protection module owns eight power detector channels, as shown in Figure 5, the power detector array are installed in the chassis beside the HPM digital signal processing board. The forward/reflected RF signals which are picked up by the directional couplers along power transmission line are sent into the power detector channels, and the DC pulses are sampled by 72MHz ADCs, the high power VSWR protection logics are realized in FPGA. The maximum protection threshold of the VSWR can be set in IPC through human-computer interface, and the RF switch will cut off the the RF drive in case of VSWR over set value. Total VSWR interlock number during the accelerator operating period is recorded in database. The arc sentry and the fiber probes are purchased from AFT, the arc protection logics are also designed in FPGA.

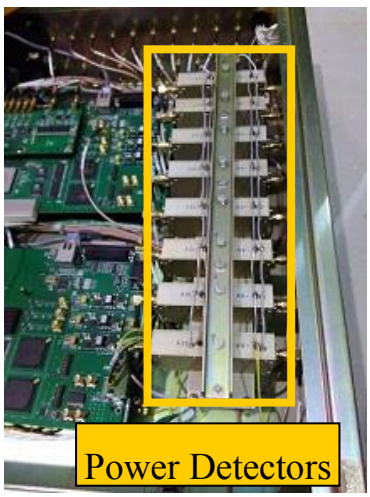

Figure 5: Power detector array of the HPM.

INTRODUCTION OF THE DIGITAL FEEDBACK CONTROL

The picture of the digital feedback control board is shown in Figure 6, the mother board of the digital feedback controller consists of a Stratix II FPGA and two TI C6713 DSPs, ADC sampling daughter board with four AD sampling channels is mounting on the mother board.

Figure 6: Digital feedback control board.

The frequency of the ADC sampling clock is 144MHz, the forward/reflected RF signals and the cavity pick-up signal are down-converted to 36MHz IF signals by mixers, the digital I, Q, -I, -Q sequences of the three IF signal are sent into FPGA, the I, Q components of the forward/reflected RF signals is just used to calculate the phases which are the judgment basis of the cavity detuning. The I and Q components of the 36MHz cavity pick-up signal are produced by sampling it with 144MHz clock, then a series of digital signal processing is performed, including rotational matrix, digital PI controller and NCO, etc. Reference tables of the feedback control loop can be set from IPC, one is step mode, the other is exponential mode. The FB ON and OFF can be set in the human-computer interface in IPC. If the FB is off, the reference table will drive the RF power source directly, otherwise, the digital feedback control loop begins to take effect. The feedback loop suppresses various disturbances including the power sources noises, high voltage drop, beam loading, and so on. In actual operating, we gradually increase the Kp, Ki parameters as long as the oscillation doesn't appear.

A fixed feedforward table is used to compensate the beam loading effect, and the feedforward compensation is triggered by the synchronous beam pulse, we can adjust the delay time of the pulse, make the feedforward driving precisely synchronized with the beam loading in cavity. The fixed value of the table can be adjusted in IPC. After the feedback and feedforward process, I/Q components are finally sent into numerically controlled oscillator (NCO), NCO outputs the 36MHz digital IF signal.

THE DIGITAL FREQUENCY CONVERSION TECHNOLOGY FOR WARM-UP CAVITY

The digital frequency conversion technology tunes the output frequency of the power sources to match the RF cavities during the RF start-up. It is carried out by NCO IP core in FPGA, by using this technology, the RF start-up time in cavity obviously decreased, the cavity field building process is quickly and smoothly.

Two types of frequency conversion mode can be selected, the auto frequency conversion mode and the manual mode. In the auto-mode, we calculate the detuned frequency from the operating frequency of the cavity by the phase decay curve during the damped oscillation after the end of RF pulse [3].

$$\Delta\omega = \frac{\partial\theta}{\partial t}$$

Then we change the frequency of the NCO sine and cosine function according to the Δω, output frequency of the RF power source will be consistent with the resonant frequency of the cavity, and the RF power can be fed into the cavity quickly with less reflected power. The RF pulse waveform of the power source output is shown in Figure

ISBN 978-3-95450-185-4

7, and the amplitude modulation results from the mechanism of frequency conversion.

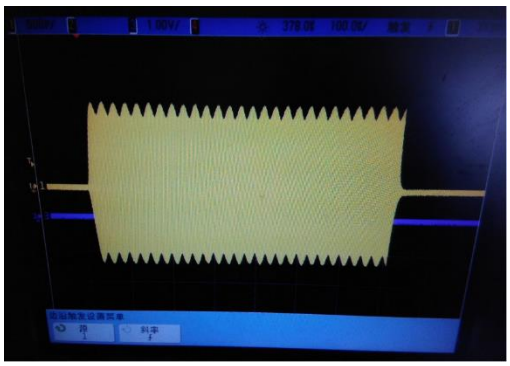

Figure 7: RF pulse waveform with frequency conversion.

PERFORMANCE OF THE DIGITAL FEEDBACK CONTROL

The hardware installation and software development of the eight LLRF control system is completed, the LLRF systems of RFQ, two Buncher cavities and DTL1 have been used in the high power ageing process and the beam commissioning. As previously mentioned in the abstract, the required performance of the cavity field error is less than ±1% in amplitude and ±1° in phase, according to the actual operating experiences, the control precision satisfies the specified performance, Figure 8 shows the control results of the cavity field in RFQ, we can see that a good stability of the RF field has been achieved about ±0.4% in amplitude and ±0.5° in phase when the amplitude is set to 6270 and the phase is set to 0°, and the pulse width of the RF is 700μs, beam width 500μs, beam intensity 10mA.

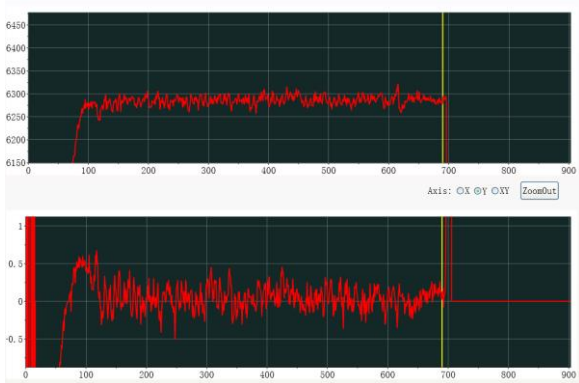

Figure 8: Performance of the LLRF control system in RFQ.

SUMMARY

Next, we will complete the debug of the rest LLRF control systems, and the long term stability of the LLRF system still need time to test. We want to improve it with chassis and CPU in the future, the cPCI chassis with Vxworks OS will be a choice.

REFERENCES

[1] Jian Li, et al., "CSNS LINAC RF System Design and R&D Progress", in *proc. of the Linear Accelerator Conference (Linac2010)*, Tsukuba, Japan, 2010, paper THP046, pp. 863-865.

[2] Hengjie Ma, "SNS LINAC RF Control: Reference System and Phase Measurement", SNS LLRF Tech Note 3, 2002, unpublished.

[3] Z. Fang, et al, "Recent Progress in the LLRF FPGA Control System of the J-PARC Linac. ", in *Proc. of Particle Accelerator Society Meeting*, JAEA, Tokai, Naka-gun, Ibaraki, Japan, 2009, pp. 1053-1055.

ISBN 978-3-95450-185-4

PRESENT STATUS OF THE HIGH CURRENT LINAC AT TSINGHUA UNIVERSITY AND ITS APPLICATION*

Q.Z. Xing, S.X. Zheng, X.L. Guan, C. Cheng, T.B. Du, H.Y. Zhang, L. Du, R. Tang, L. Wu, H.P. Jiang, Q.Z. Zhang, C.T. Du, Q.K. Guo, D. Wang, C.X. Tang, X.W. Wang†, Key Laboratory of Particle & Radiation Imaging (Tsinghua University), Ministry of Education, Beijing 100084, China
also at Laboratory for Advanced Radiation Sources and Application, Tsinghua University, Beijing 100084, China
also at Department of Engineering Physics, Tsinghua University, Beijing 100084, China
W.Q. Guan, Y. He, J. Li, NUCTECH Co. Ltd., Beijing 100084, China

Abstract

The CPHS (Compact Pulsed Hadron Source) linac at Tsinghua University, is now in operation as an achievement of its mid-term objective. Presently the RFQ accelerator is operated stably with the beam energy of 3 MeV, peak current of 26 mA, pulse length of 100 μs and repetition rate of 20 Hz. After the maintenance the transmission rate of the RFQ accelerator had been recovered from 65% to 91%. The applications of the proton and neutron beams are introduced in this paper.

INTRODUCTION

Since the first 3 MeV/44 mA proton beam of the CPHS (Compact Pulsed Hadron Source) linac at Tsinghua University was achieved in March 2013, the proton beam has been delivered to bombard the Beryllium target to produce neutrons for various applications [1][2]. The whole linac contains the ECR Ion Source (IS), the 4-vane Radio Frequency Quadrupole (RFQ) proton accelerator (shown in Fig. 1), RF power supply and distributor, and beam transport. In the first half year of 2017 the Drift Tube Linac (DTL) is expected to be installed downstream the RFQ accelerator to upgrade the beam energy to the designed value of 13 MeV.

Figure 1: 3MeV RFQ accelerator at Tsinghua University.

Based on the proton and neutron beams, various applications mainly includes the development of the neutron detectors (B_4C-coated straw-tube and gadolinium-doped Micro-Channel Plate (MCP)) and biological dosemeters, and neutron imaging. Furthermore, a proton irradiation station is being planned to provide the 13 MeV proton beam with a flux of 10^8~10^9 p/cm^2/s for the experimental simulation of the space radiation environment.

OPERATION STATUS OF THE HIGH CURRENT 3MeV PROTON LINAC

The operation time of the CPHS facility in 2016 was ~300 hrs. The present main parameters together with the designed values of the proton beam are listed in Table 1. The RFQ accelerator is operated stably with the beam energy of 3 MeV, peak current of 26 mA, pulse length of 100 μs and repetition rate of 20 Hz. The peak current is measured near the outside surface of the target station. The current of the proton beam at the entrance of the RFQ has decreased from 60 mA (year 2013) to 44 mA (year 2016).

Table 1: Main Parameters of the Proton Beam Passing into the Target Station

Parameter	Designed Value	Present Value
Beam Energy (MeV)	13	3
Peak Current (mA)	50	26
Beam Pulse Width (μs)	500	100
Repetition Rate (Hz)	50	20

Neutrons are produced by proton beam bombarding the 1.2 mm-thick Beryllium target. The Be target has been redesigned to be mounted on a 2 mm-thick aluminium plate since it had broken twice after only several-hour operation on the repetition rate of 50 Hz. The possible reason of the crack was evaluated to be the thermal stress under high repetition rate. The new target with Al plate mounted had worked well in 2014 with the repetition rate of 20 Hz. Increasing the repetition rate to 50 Hz to test the new target with the proton beam will be carried out in the future.

MAINTENANCE AND UPGRADE OF THE 3MeV LINAC

The maintenance and upgrade of the CPHS linac are carried out as the following, among which the first five has been accomplished:

* Work supported by National Natural Science Foundation of China (Project 11575098).
† wangxuewu@tsinghua.edu.cn

ISBN 978-3-95450-185-4

1. Field retuning of the RFQ accelerator to enhance the transmission rate.
2. Insert one chopper into the LEBT to decrease the rising and falling time of the beam pulse.
3. Re-layout of the power source supply of the IS/LEBT to avoid the sparking.
4. Upgrade the control system by adopting the EPICS environment.
5. Adopt parameter scanning during beam commissioning.
6. Monitor the temperature distribution of the Be target.
7. Upgrade the beam energy to 13MeV by the DTL accelerator.
8. Recovery of the output current of the proton beam to ~60mA at the exit of the ECR source.

Re-tuning of the RFQ Accelerator

In order to deal with the transmission rate degradation of the RFQ accelerator, the field distribution inside the RFQ cavity was checked, and the field tuning was performed and the relative error of the quadrupole field was reduced from 7.3% to 2.6% (Fig. 2).

The resonance frequency of the RFQ was adjusted to 325.01 MHz from 325.12 MHz. After the RFQ was recommissioned, the transmission rate of the RFQ raised to 91% by the end of 2015.

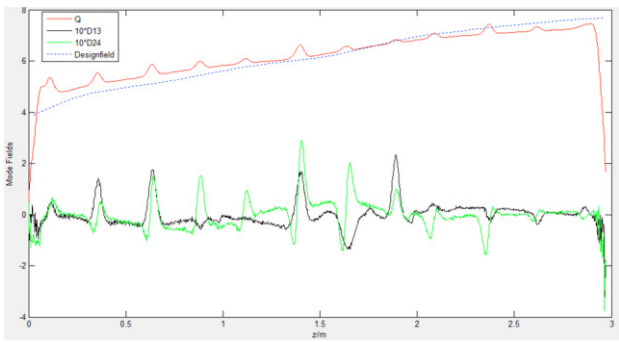

(a) Before re-tuning

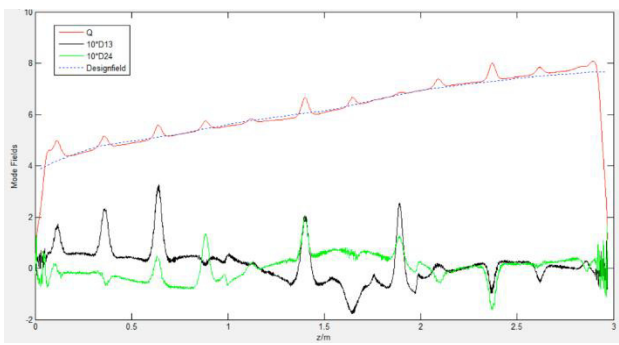

(b) After re-tuning

Figure 2: Field distribution of the CPHS RFQ.

LEBT Chopper

One electrostatic chopper has been added at the end of LEBT. The rising and falling time of the beam pulse with the chopper had been decreased to 1~3 μs. The chopped particles are mostly lost before entering into the RFQ cavity.

Parameter Scanning

The measured currents from the ACCT and Faraday cups have been sampled and hold, then acquired by the EPICS system. Multi-dimensional parameter scanning has been achieved on the currents of the two solenoids and four steering magnets. Figure 3 shows the transmission rate of the CPHS RFQ (in different color) changes with the currents of the two solenoids.

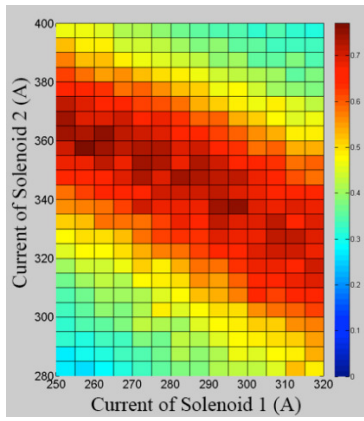

Figure 3: Transmission rate of the CPHS RFQ with the currents of the two solenoids.

Monitoring the Be Target

In order to obtain the profile of the proton beam bombarding on the target, the temperature distribution of the Be target had been monitored by one infrared camera, as shown in Fig. 4. One mirror will be added to prevent the camera from the damage of the neutrons. More study will be carried out on the relationship between the beam profile and the accelerator parameters.

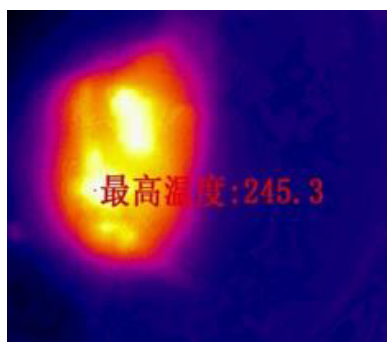

Figure 4: Temperature distribution of the Be target with the proton beam bombarding on it.

DTL Development

The CPHS DTL is under development. Ten test drift tubes (five aluminium tubes and five copper ones) were fabricated, and the alignment experiments are being carried out with the test drift tubes, as shown in Fig. 5. It is expected to finish the formal manufacture by the end of 2016 and finish the installation of the DTL by July 2017.

ISBN 978-3-95450-185-4

Figure 5: Alignment experiment with the test drift tubes.

PROTON APPLICATION

Development of 2D Profile Measurement

Based on the CT algorithm, 2D profile measurement of the proton beam is under development by the rotatable multi-wires [3]. Twenty carbon wires with the diameter of 30 μm are aligned and mounted on one board. The development of the electronics system for the measurement of the twenty wires simultaneously has been completed. With the position step of 0.1 mm and angle step of 5°, the 2D profile of the proton beam has been acquired in 20 minutes at the position of about six meters downstream the RFQ accelerator, as shown in Fig. 6. The dynamic range of the measurement in one-dimensional can reach ~10^4.

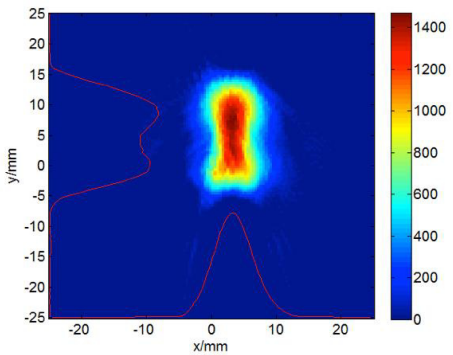

Figure 6: 2D profile of the proton beam downstream the CPHS RFQ measured by the rotatable multi-wires.

Proton Irradiation Station

A proton irradiation station is been planned to provide the future 13 MeV proton beam with a flux of 10^8~10^9 p/cm^2/s for the experimental simulation of the space radiation environment. The main objective is to decrease the flux by 10^6~10^7 by adopting one collimator (Fig. 7) and adjusting the currents of the solenoids and quadrupoles. The irradiation station will be located at the end of the straight line of HEBT.

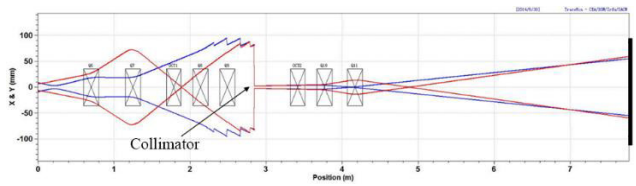

Figure 7: Beam profile in the HEBT for proton irradiation.

NEUTRON APPLICATION

The application of the neutrons mainly consists of the neutron imaging, and the development of the neutron detectors (B_4C-coated straw-tube and gadolinium-doped Micro-Channel Plate (MCP)) [4]. Furthermore, experiments related to biological dosemeters has been carried out based on the CPHS facility. Figure 8 shows the neutron imaging line and neutron beam test line.

Figure 8: The neutron imaging line (left) and neutron beam test line (right).

CONCLUSION

CPHS facility at Tsinghua University can provide 3 MeV proton beam and corresponding neutron beam to users. The beam energy will be enhanced to 13 MeV in the year of 2017. A proton irradiation station is planned at the end of the straight line of HEBT.

REFERENCES

[1] J. Wei *et al.*, "The Compact Pulsed Hadron Source Construction Status", IPAC'10, Kyoto, MOPEC071, p. 633 (2010); http://www.JACoW.org/.

[2] X.W. Wang *et al.*, "Status report of CPHS and neutron activities at Tsinghua University", *IL NUOVO CIMENTO* 38 C (2015) 185.

[3] L. Du *et al.*, "Beam dynamics and experiment of CPHS linac", HB2014, East Lansing, THO2LR02, p. 355(2014); http://www.JACoW.org/.

[4] Q.Z. Xing *et al.*, "Present Status of the High Current Proton Linac at Tsinghua University and Its Beam Measurements and Applications", HB2014, East Lansing, TUO3AB01, p. 208 (2014); http://www.JACoW.org/.

ISBN 978-3-95450-185-4

DESIGN AND PROTOTYPING OF THE SPOKE CYROMODULE FOR ESS

P. Duthil†, D. Reynet, G. Olry, S. Brault, P. Duchesne, N. Gandolfo, E. Rampnoux, D. Longuevergne, M. Pierens, F. Chatelet, S. Bousson, Institut de Physique Nucléaire d'Orsay, UMR 8608 CNRS/IN2P3 – Univ. Paris Sud, BP1, 91406 Orsay- France
C. Darve, N. Ellas, European Spallation Source, Lund, Sweden

Abstract

A cryomodule integrating two superconducting radiofrequency double Spoke cavities and their power couplers is now being assembled at IPNO. It is the prototype version for the Spoke section which will be operated for the first time in a linear accelerator for the European Spallation Source. It will be the most powerful neutron source feeding multidisplinary researches. This cryomodule provides the environment for operating the two β = 0.5 cavities at full RF power in a saturated superfluid helium bath at a temperature of 2 K. For this operation, the prototype cryomodule includes all the interfaces with radiofrequency powering, cryogenics, vacuum systems, beam pipe and diagnostics. It will be tested by 2016 at IPNO by use of a test valve box which is also a prototype for the future cryogenic distribution system of the Spoke section, another contribution to ESS. Both prototypes will then be tested at full power in FREIA facilities at Uppsala University.

THE EUROPEAN SPALLATION SOURCE

The ESS Linac

The European Spallation Source (ESS) [1] is now designed to be the most powerful neutron source dedicated to multidisciplinary researches. It is an intergovernmental research project, carried out by 17 european countries, which started to be built in 2014 in Lund, Sweden, and will be fully operational by 2025.

The ESS machine is based on a linear particles accelerator (linac) placed in a tunnel and which accelerates protons from a source to a tungsten target located on the ground surface. From the collisions of the protons onto this target, fast neutrons are produced and then moderated before feeding multiple physics experiment lines.

The ESS linac operates in a pulsed mode with a pulse duration of 2.86 ms and a repetition frequency of 14 Hz. It shall accelerate protons up to an energy of 2 GeV to produce a 5 MW beam with a peak current of 62.5 mA. For that purpose, it benefits from a 312 m long section integrating superconducting radiofrequency (SRF) accelerating cavities. Electromagnetic waves are produced by klystrons and distributed into the tunnel along a network of waveguides to the RF power couplers which radiate this wave into each cavity. The cavity then acts as an electromagnetic resonator and produces an accelerating electrostatic field phased in time with the protons bunches traveling withinthe high vacuum of the beam pipe. All SRF cavities are made of bulk niobium and are operated in a superfluid helium bath at a temperature of about 2 K. This cryogenic environment is ensured by a surrounded dedicated horizontal cryostat, named cryomodule, and which also combines other functionalities and interfaces to run the cavities and transport the beam: magnetic shielding, support and alignment, RF powering, vacuum systems and beam interfaces.

Ordered by proton energy or by the ratio β of the speed of a particle (within the accelerating device) to the speed of light, this SRF linac section includes:

- 26 double Spoke type cavities with β = 0.50 and paired in 13 cryomodules;
- 36 elliptical 6-cell type cavities with β = 0.67 and grouped by 4 within 9 cryomodules;
- 84 elliptical 5-cell type cavities with β = 0.86 and grouped by 4 within 21 cryomodules.

A cryogenic distribution system (CDS) runs all along the ESS linac tunnel to distribute or transform the needed cryofluids – helium at different thermodynamic states – produced by the cryoplant located at one end of the ESS machine. Consisting in a multichannel cryoline, this CDS also integrates 43 valve boxes aiming at managing the cryogenic distribution process of each cryomodule.

The Spoke Section

Between the Drifted Tube Linac (DTL) – which ends the warm section of the ESS linac – and the medium beta (elliptical cavities) linac (MBL), a 56 m long portion with 26 double Spoke SRF cavities shall increase the protons beam energy from 90 to 216 MeV. The Institut de Physique Nucléaire d'Orsay (IPNO) is responsible for the supply of most of this Spoke section pictured on Fig. 1: the 13 cryomodules and the cryodistribution system containing 13 valves boxes.

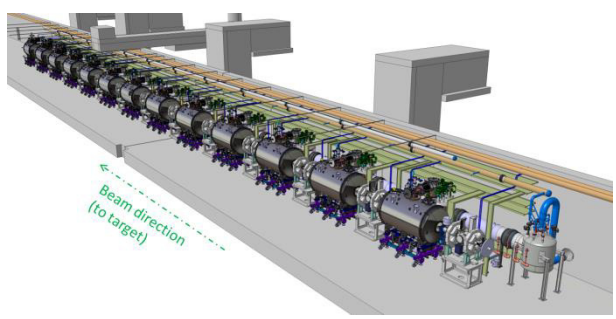

Figure 1: Spoke section of the ESS linac.

IPNO is also in charge of prototyping this section by designing, constructing one prototype cryomodule and one prototype valve box and testing them at IPNO. This valve box is also part of the facilities which will be

† duthil@ipno.in2p3.fr

ISBN 978-3-95450-185-4

used to qualify the prototype and the 13 series Spoke cryomodules at full RF power at Uppsala University (Sweden) [2].

PROTOTYPING THE RF COMPONENTS

Double Spoke Cavities

The double Spoke cavity [3] is 994 mm long with an internal diameter of 481 mm. It contains n = 3 accelerating gaps and its accelerating length is Lacc = $\beta \times n \times \lambda / 2$ = 0.639 m, where $\lambda = c / f$ is the wavelength of the 352.21 MHz electromagnetic wave. One advantage of this type of cavity is a stiff geometric configuration: it can achieve low Lorentz detuning factor and is less sensitive to pressure fluctuations. Because it has frequency modes well separated, High Order Modes (HOM) are intrinsically filtered making it robust to beam instabilities. With an expected quality factor of $1.5 \cdot 10^9$, those double Spoke cavities shall produce the ESS nominal accelerating field of 9 MV/m, which was very challenging in 2009 at the time of the accelerator design update. Their design was performed by IPNO taking care of optimizing the shape of the cavity (e.g. Spoke bars, coupler location) for RF/mechanical purposes as well as for cost consideration. The nominal thickness of the bulk niobium was chosen to be 4.2 mm and stiffeners were added at each cavity end cups as well as inside the Spoke bars. The helium tank is made of 4 mm thick titanium grade 2 sheets and standard dish ends. It is linked to the cavity by two welded rings to improve the mechanical behaviour of the assembly limiting local stress and reducing the Lorentz factor to K_L = -5.5 Hz/MV²/m². The tuning sensitivity (along the beam axis) is 130 kHz/mm.

Three prototypes were manufactured: 2 by the Italian company Zanon and one by the French SDMS. They were all prepared at IPNO facilities and different procedures tested. The preparation baseline includes an ultrasonic degreasing for the first cleaning following the manufacturing. Then a chemical etching of the inner cavity surface is achieved to remove a layer of niobium of about 200 µm (3.4 kg). During this 8 hours etching, position of the cavity is changed. The mix of hydrofluoric, nitric and phosphoric acids is maintained at a temperature below 15 °C by use of a cooling system placed on the acid storage vessel and by a water flow circulating within the helium tank. Cavity is then rinsed inside an ISO 4 class clean room with a high pressure ultra-pure water jet moving up and down and rotating within the cavity. Each cavity and each preparation procedure were evaluated by testing the performances of the cavity in a vertical cryostat. All cavities were equipped with their helium tank allowing the possibility of mounting their cold tuning system. It can be noted that IPNO also designed a new vertical cryostat for the simultaneous test of two SRF cavities. It will be constructed by 2017 and will be used to qualify the ESS series double Spoke cavities.

During the tests in vertical cryostat, performances of all prototype cavities were measured to exceed the ESS nominal specifications as shown on Fig. 2 where the quality factor Q_0 of the three (named) cavities is plotted versus the accelerating field.

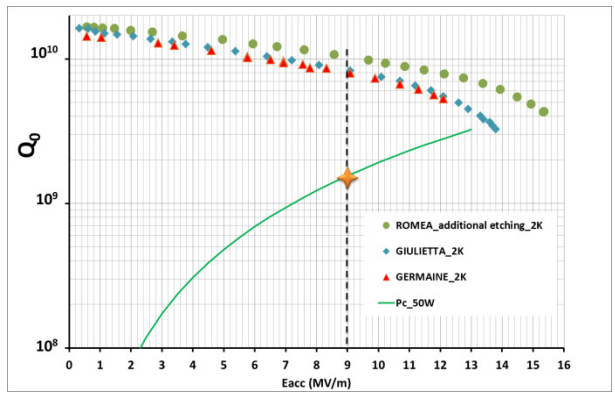

Figure 2: Prototypes of the double Spoke cavities: measured performances in vertical cryostat.

However the thermal cycling of the cavities during this intensive experimental campaign induced a degradation of the quality factor. It is considered that this effect is due to the hydrides formation on the inner surface of the cavities during cool-down. Hydrides formation also induces defects on the surface that remain even after a warm-up at room temperature. Those generated defects then create favoured sites stimulating new hydrides formation during the successive cool-downs. Surface recovery induces a heat treatment at high temperature. An ultra-high vacuum furnace was hence installed at IPNO and was qualified up to 1400 °C by measuring the residual pressure levels and the temperatures at several locations during different thermal cycles. Prototype cavities (with their helium tank) will hence be heat treated at 600 °C to degas hydrogen responsible for hydrides occurrence. This temperature is indeed limited by the brazing of stainless steel flanges onto the niobium cavity. Until now, preliminary annealed heating tests were carried out on samples: niobium rectangular or disk samples and a 1.3 GHz niobium cavity with titanium supports. For one sample having a Residual Resistivity Ratio (RRR) of 320 before being annealed, a RRR of 300 was obtained afterward.

352 MHz RF Power Couplers

The power coupler [4] feeds each cavity with the 400 kW RF electromagnetic wave. It is a coaxial waveguide which links the cavity to the ambient environment: air at room temperature. The outer conductor is attached to the cavity and the inner conductor, made of copper, ends as an antenna inside the cavity. Its design includes a single ceramic window made of high purity alumina. It separates the ultra-high vacuum of the cavity from the ambient air. To limit the heat flowing from the room temperature environment to the cavity operated at 2 K, the outer conductor of this coupler is made of stainless steel with an inner coating of 30 µm thick copper layer. It also consists in a double wall tube within which supercritical helium flows at a temperature ranging from 5 to 300 K. A mass flow of 40 mg/s reduces most of the diffusing and radiating heat flowing to each cavity at 2 K to 1.75 W. When

ISBN 978-3-95450-185-4

the RF is operated, the penetration of the magnetic field into the copper layer induces substantial additional heat loads that are evacuated by increasing the helium flow by 6 mg/s.

Four power couplers were manufactured by two French companies: PMB and SCT. The qualification of those couplers to the ESS nominal operating conditions involved the design and construction of a dedicated conditioning bench. It consists in a RF resonant cavity made of stainless steel whose inner surface is coated with copper. The outer surface is equipped with a brazed water channel to maintain the cavity at a controlled temperature when RF power is dissipated onto the inner surface. In clean room, two couplers are mounted onto the top of this cavity. After baking, ultra-high vacuum of 10^{-9} mbar is achieved inside the cavity at room temperature by use of a turbomolecular pump. Mass flow rates and temperatures of the different water circuits cooling the cavity, the couplers antennas and ceramic windows are controlled. The RF wave is produced by a 352.21 MHz klystron and its power and time pulse is controlled. The wave propagates via waveguides, into the RF cavity via the upstream coupler and out from it via the second coupler. Downstream, a sliding RF short-circuit is used inducing full RF reflection at its location. This place is then changed to modify the position of wave anti-nodes along the couplers. Directional couplers are used at the inlet and outlet of the cavity to measure the RF power. Each power coupler is equipped with an arc detector and with an electron pickup to evaluate multipacing. 3D multipactor effect within the Spoke power coupler (and within the Spoke cavity) was previously assessed by use of a new software developed at IPNO and named MUSICC 3D [5]. By identifying several multipacting barriers with the numerical analysis, TiN coating of the inner surface of the ceramic window of the ESS Spoke couplers was realised. Until now, suppression of multipactoring by use of a high voltage bias is not implemented on those prototypes.

Different conditioning tests were carried out at CEA Saclay where a 352.21 Hz klystron was available and where the IPNO test bench was installed (see Fig. 3). During a test at 250 kW, one ceramic window was broken and analyses are now carried out to understand the origins of this failure. One coupler is conditioned at the ESS nominal operating conditions. It will now be mounted onto a prototype SRF Spoke cavity and tested in a horizontal cryostat, named HNOSS, in the FREIA facilities at Uppsala University. Coupling factor between the cavity and the RF coupler will be measured and the efficiency of the supercritical helium heat intercept evaluated.

A new power test station was installed at IPNO, in the Supratech technical infrastructure, and commissioned. Named SPARE, it is able to deliver RF power up to 2.8 MW (1.5 ms, 50 Hz or 3 ms, 14 Hz) at 352 MHz for the needs of several accelerator projects. It will be used for the conditioning of the series ESS Spoke couplers.

Figure 3: IPNO conditioning bench for the Spoke RF power couplers installed at CEA Saclay.

Cold Tuning Systems

Each cavity is equipped with a double lever type fast / slow cold tuning system (CTS) which uses a push pull action on the beam pipe to deform the cavity along the beam axis. This aims at accurately tuning the resonance frequency of the cavity after cool-down and to compensate microphonics (pressure waves) and Lorentz force detuning. Slow and large displacements up to 1.28 mm are achieved by a stepper motor yielding a tuning range of about 170 kHz with a resolution of 1.1 Hz. Fast tuning over a range of about 800 Hz involves two piezo-actuators. Two pairs of CTS prototypes were constructed in order to test different piezo-actuator stack lengths. Several bearings (with or without dry lubricant) were also implemented. A dedicated test bench is now being designed at IPNO to qualify the 26 series ESS Spoke CTS and to operate CTS over long-time periods for reliability analysis of their components.

A PROTOTYPE SPOKE CRYOMODULE

A prototype Spoke cryomodule is now assembled at IPNO [6]. It will contain a string of two (among the three) double-Spoke prototype cavities contained in their helium tanks. This cryomodule is dedicated to provide the cryogenic environment needed to operate the cavities at 2 K in a saturated helium bath and all needed interfaced.

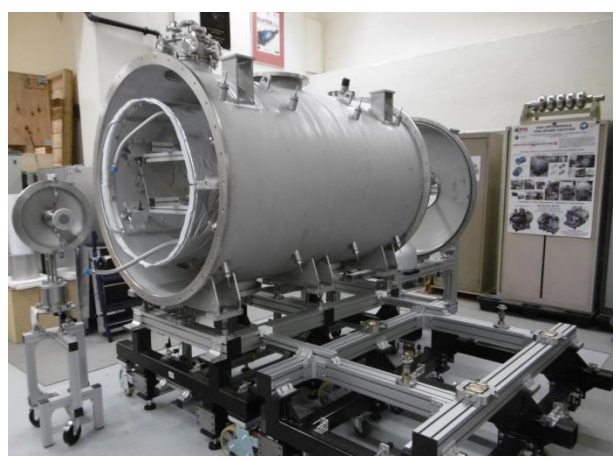

Figure 4: Vacuum vessel of the prototype Spoke cryomodule with the thermal shield.

Its cryostat functionality implicates the use of a vacuum vessel made of stainless steel (304 L) having a diameter of 1.288 m (see Fig. 4). From one UHV gate valve to the

ISBN 978-3-95450-185-4

other one closing the beam pipe, the cryomodule is 2.86 m long. A unique thermal shield made of 2 mm thick aluminium alloy 6082 sheets and covered with 30 layers of MLI protects the string of cavities form the radiant heat. On the ESS machine it will be operated at a temperature between 37 and 53 K with supercritical helium at a pressure ranging from 10 to 19.5 bara. However, for the tests of this prototype at IPNO as well as at Uppsala University, saturated nitrogen at a pressure of about 1.2 bara will be used. This thermal shield was hence designed to cope with both cryofluids. It was already operated twice inside the cryomodule vacuum vessel to verify the mechanical behaviour and to measure the liquid nitrogen consumption which was in agreement with the expected heat load of about 25 W. The distribution of the different cryofluids – saturated normal and superfluid helium; saturated nitrogen – for the test and qualifying operations is done by a piping network inside the cryomodule. However it is managed by the valve box connected to the cryomodule by a branch multichannel cryoline named the cryogenic jumper. To simplify the assembly of the Spoke cryomodule, all cryogenic control valves needed for the cryogenic process were indeed moved into the valve box. Hence the cryomodule contains only cryogenic control transmitters such as thermometers, pressure transmitters, superconducting liquid level sensors and vacuum gauges.

The support of the string of cavities involves 16 antagonist radial rods and 4 longitudinal rods, all made of Ti6Al4V titanium alloy. Their interfaces, out of the vacuum vessel, shall allow for the alignment correction of the cavities even if vacuum is achieved within the cryomodule or if the cavities are cold. 8 fiducials, mounted onto the two cavities, can be optically targeted from 4 windows placed on the vacuum vessel dish ends to diagnostic and control the alignment.

Each cavity will be entirely enclosed in a magnetic shield made of a double layer of Cryophy® and actively cooled. During cool-down, a flow of helium will indeed be diverted from the helium supply line and will flow inside a cooper serpentine placed between the two shield layers to cool it quicker than the cavity. It is thus expected that the magnetic shield reaches a large magnetic permeability before the Meissner transition of a cavity, avoiding trapping magnetic field. After the cavity is superconducting, the magnetic shield will no longer be actively cooled and left thermally anchored to the cavity helium tank.

Two mock-up cavities, made of stainless steel were built in order to validate different concepts of the prototype cryomodule. The external envelope of those cavities is very similar to the helium tank of the real Spoke cavities including interfaces for the magnetic shields, cold tuning system and coupler. The inner envelope is simplified although it includes two cylinders featuring the Spoke bars. The inner and outer envelopes constitute the helium tank which has the same volume as the one of the prototypes: 48 L. The inner cavity volume is not subjected to ultra-high vacuum as for the Spoke cavities but is connected to the insulation vacuum of the cryomodule. First, those mock-up cavities are now used to qualify the tooling which was designed and constructed for the assembly phases of all the components of the cryomodule outside the clean room. Secondly, by being equipped with the double magnetic shield of the Spoke cavities, they help characterizing the shielding at room and cryogenic temperature. To that end, three flux gates magnetometers are used to measure the Earth's magnetic field components inside the mock-up cavity. A support made of peek is used to translate those sensors allowing an accurate measurement at different locations inside the cavity and comparison with our numerical simulations. This field mapping will be performed at liquid nitrogen temperature using several flux gates by the end of summer 2016. Then, we expect to have additional measurements at liquid helium temperature. Thirdly, they will be used to check the conformity of the cryogenic process to the ESS requirements. They will act as cryogenic reservoirs, being cooled-down, filled with liquid normal and superfluid helium. They will also be equipped with electrical heaters, consisting of etched-foil resistive heating elements laminated between layers of flexible polyimide insulation, to quantify the cooling capacity of the valve box and the cryomodule and to check the regulation loops of the cryogenic control and command system.

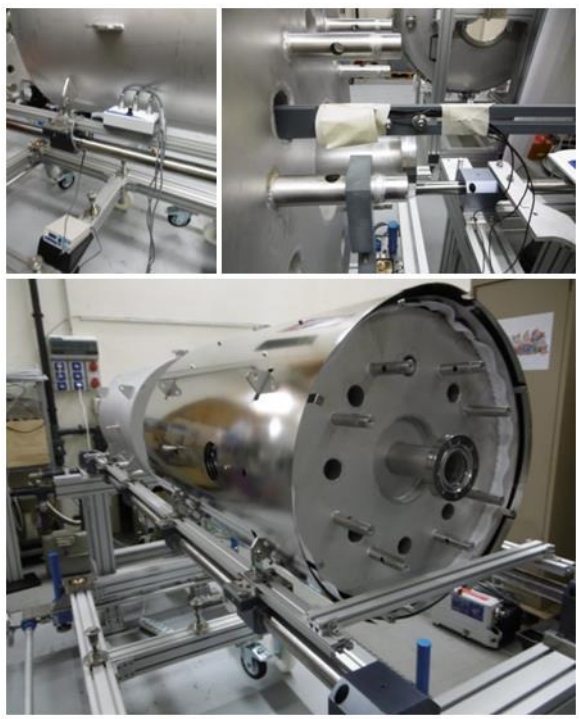

Figure 5: String of two mock-up cavities being assembled on the cryostating tooling and equipped with the Spoke double magnetic shield (bottom). Measurement, by use of fluxgates magnetometers, of the residual Earth's magnetic field within the mock-up cavities (top).

A PROTOTYPE/TEST VALVE BOX

IPNO is in charge of the supply of the cryogenic distribution system for the Spoke section of the ESS linac [7]. It includes the construction of 13 valve boxes for managing the cryofluids distribution into each Spoke cryomod-

ISBN 978-3-95450-185-4

ule. Specifically for the Spoke section, part of the cryogenic diagnostics belongs to the cryomodule whereas all programmable logic controller driven devices such as cryogenic valves are part of the valve boxes only. The consequence is that the production of saturated superfluid helium from the pressurized liquid delivered by the ESS cryoplant is accomplished locally inside each Spoke valve box by isobaric subcooling in a heat exchanger and isenthalpic expansion within a Joule-Thomson valve.

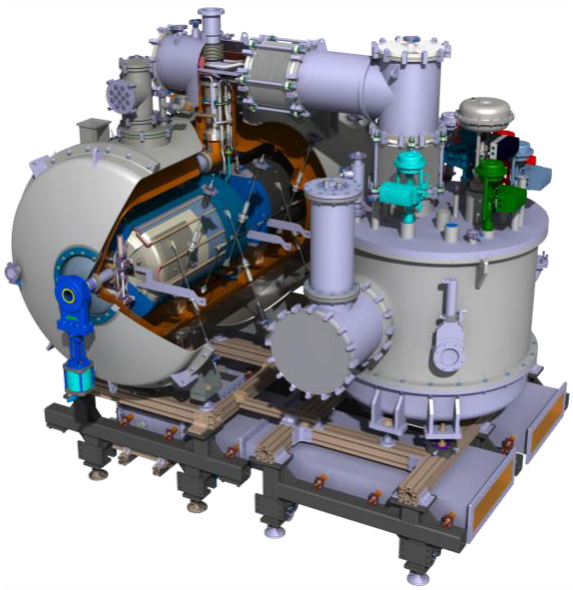

Figure 6: Prototype Spoke cryomodule and valve box.

A prototype valve box was designed by IPNO and is being built. It aims at validating the cryogenic design, the construction, as well as qualifying the prototype Spoke cryomodule (see Fig. 6). The cryogenic tests of those prototype Spoke cryomodule and valve box will be carried out at IPNO. Then, tests at full RF power will be performed in the FREIA facilities of the Uppsala University. But this valve box will also be used for the tests of the 13 series Spoke cryomodules at Uppsala. Hence, it is a complex compromise between a demonstrator and a test bench. It shall integrate the cryogenic operating modes of the ESS linac while functioning with laboratory infrastructures delivering cryofluids differing – by nature or by thermodynamic state – from those supplied by the ESS cryoplant.

The test valve box will hence be feed with saturated helium instead of pressurized subcooled liquid as for the series. It thus integrates a phase separator. The liquid phase will be used to cool-down the cold mass of the cryomodule (magnetic shields, string of cavities and piping) and to produce superfluid helium for 2 K operations. Part of the saturated vapour phase will be used to flow and intercept heat along the couplers double wall tubes instead of using supercritical helium as it will be done on the ESS Spoke section. However this supercritical helium cooling will be tested separately at Uppsala during the RF tests of a single prototype Spoke cavity equipped with a prototype RF power coupler and mounted into the HNOSS horizontal cryostat.

The saturated superfluid helium surrounding the cavities is set at a temperature of 2 K by maintaining and rigorously controlling the bath pressure to 31 mbar. The helium vapours resulting from the vaporization of helium due to heat loads are pumped through the very low pressure line (VLP) of the cryomodule and valve box by use of the laboratory infrastructure vacuum pumping roots. For the prototypes, this VLP ranges from a DN 50 to 63. It is oversized to allow for extra cooling power during the tests and to get the possibility of operating the prototype cryomodule below 2 K for RF tests purposes. The test valve box will be installed at IPNO by this summer to perform the first cryogenic tests.

CONCLUSION

A prototype ESS Spoke cryomodule containing two double-Spoke cavities $\beta = 0.5$ was designed and is now assembled at IPNO. Most of the components of this cryomodule were qualified separately, by use of dedicated test benches, procedures and tooling. Three prototype cavities passed successfully the vertical cryostat tests by being operated above the ESS requirements. Hydrogen degasing operation is now foreseen by heat treatment in a vacuum furnace which was recently installed and qualified at IPNO. One prototype RF power coupler was conditioned at nominal operating conditions and will be installed on a prototype Spoke cavity for RF tests in a horizontal cryostat at Uppsala University. In the meantime, the cryomodule is assembled at IPNO with a string of two mock-up cavities which will be used for the validation of the assembly tooling and procedure, the magnetic shielding concept and the cryogenic process. A valve box was also designed and is constructed to be the prototype of the future cryogenic distribution system of the ESS Spoke section. It will be used at IPNO for the cryogenic experimental campaign of the prototype Spoke cryomodule and then at Uppsala University for the runs at full RF power. This test valve box will also be part of the qualifying bench of the 13 series cryomodules. A preliminary control and command system for managing the cryogenic process is now being implemented at IPNO facilities for the first cryomodule test. It is the basement of the one needed to operate the Uppsala test bench which is also designed by IPNO in collaboration with Uppsala University. This control and command system is built on an EPICS/PLC architecture and includes all the instrumentation controllers for cryogenic processing. It is foreseen as a prototype for the future control and command system of the whole ESS linac which could be supplied by IPNO.

REFERENCES

[1] *ESS Technical Design Report*, 2013, http://europeanspallationsource.se/accelerator-documents

[2] R. Yogi *et al.*, "Uppsala High Power Test Stand for ESS Spoke Cavities," *in Proc. LINAC2012*, Tel-Aviv, Israel, pp. 711-713.

ISBN 978-3-95450-185-4

[3] P. Duchesne *et al.*, "Design of the 352 MHz, beta 0.50, Double-Spoke cavity for ESS", in *Proc. SRF'13*, Paris, France, Sept. 2013, pp. 1212-1217.

[4] E. Rampnoux *et al.*, "Design of 352.21 MHz RF power input coupler and window for the European spallation source project", in *Proc. SRF'13*, Paris, France, Sept. 2013, pp. 1069-1072.

[5] T. Hamelin, "Validation d'un nouveau logiciel de simulation tridimensionnel du Multipactor par le calcul et l'expérimentation", Ph.D. thesis, Université de Paris Sud – paris XI, Orsay, France, 2015.

[6] D. Reynet *et al.*, "Design of the ESS Spoke cryomodule", in *Proc. SRF'13*, Paris, France, Sept. 2013, pp. 357-60.

[7] P. Duthil *et al.*, "The ESS Spoke cryomodule and its test valve box", presented at 26th International Engineering Conference (ICEC26), New Delhi, India, paper 8-O-2A-1, unpublished.

ISBN 978-3-95450-185-4

ANALYZING AND MATCHING STUDY OF MIXED HIGH INTENSITY HIGHLY CHARGED ION BEAMS*

X.H. Zhang, Y.J. Yuan#, X.J. Yin, Y. Yang, L.T. Sun, H.W. Zhao, C.Qian
Institute of Modern Physics, CAS

Abstract

Electron cyclotron resonance (ECR) ion sources are widely used in heavy ion accelerators for their advantages in producing high quality intense beams of highly charged ions. However, it exists challenges in the design of the Q/A selection systems for mixed high intensity ion beams to reach sufficient Q/A resolution while controlling the beam emittance growth. Moreover, as the emittance of beam from ECR ion sources is coupled, the matching of phase space to post accelerator, for a wide range of ion beam species with different intensities, should be carefully studied. In this paper, the simulation and experimental results of the Q/A selection system at the LECR4 platform are shown. The formation of hollow cross section heavy ion beam at the end of the Q/A selector is revealed. A reasonable interpretation has been proposed, a modified design of the Q/A selection system has been committed for HIRFL-SSC linac injector. The features of the new design including beam simulations and experiment results are also presented.

INTRODUCTION

The advances in electron cyclotron resonance (ECR) ion sources that are being achieved by producing high current beams of highly charged ions have made the design of the associated charge to mass ratio Q/A selection system more challenging. In the future, the total ion beam current extracted from an ECR ion source could reach several 10 mA. Serious space charge effect will reduce the resolution of the Q/A selector by increasing the beam size in the slit position and degrading the beam quality. Moreover, the coupled asymmetric beam extracted from the sextupole magnet field used to confine ECR plasma makes the analyzing more complicated. When the beam transmits through a Q/A selector line, the effects of aberrations and coupling in magnetic elements will be obvious, which will also deteriorate the beam quality and reduce the resolution of the system.

The Q/A selection system of LECR4 is designed taking account of all kinds of ion beams produced by the ion source, i.e. from proton to uranium ion beam. However, commissioning results [1] show that the beam quality of high intensity heavy ion beams is rather poor. Studies [2] have been carried out to investigate the possible causes. This study is focusing on the space charge effect on the Q/A selection system. Recent simulations and experimental results at the LECR4 platform are reported and discussed in this paper. The research on LECR4 has provided basis for the design of a new Q/A selection system for LECR4. The features of the new design including beam experiments are also presented in this paper.

*Work supported by the National Natural Science Foundation of China (No. 11575265, 11427904) and the "973" Program of China (No. 2014CB845501).
#yuanyj@impcas.ac.cn

EXPERIMENTS AND SIMULATIONS AT LECR4

Experimental Setup

LECR4[3] is an ECR ion source to provide ion beams from Carbon to Uranium for HIRFL-SSC linac injector[4,5]. It uses unique liquid evaporation cooling method at room temperature coils to reach maximum 2.5 T magnetic field.

Fig. 1 shows the original layout of the Q/A selection system of LECR4. It mainly consists of a solenoid lens, a double focusing 90° analyzing magnet, two slits mounted for both the horizontal and the vertical directions, and beam diagnostic devices in a diagnostic chamber, including a faraday cup, a fluorescent target, and an Allison type emittance measurement device. The solenoid lens is directly attached to the extraction flange of the source body to provide an initial focusing and control the size of the beam into the analyzing magnet. Furthermore, the solenoid takes on the responsibility of the tuning flexibility of the system to deal with all kinds of ion species produced by the ion source.

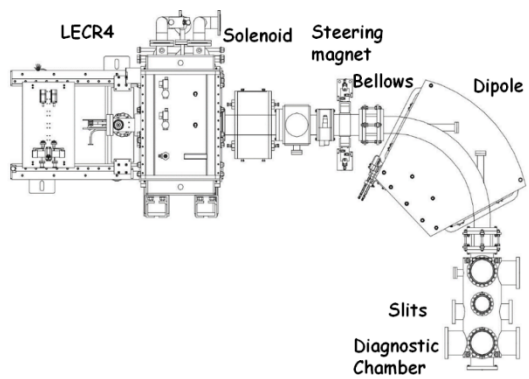

Figure 1: Layout of the multi-component A/Q selection system for LECR4.

LECR4 Beam Emittance

In the original beam line design, nonlinear forces, such as space charge effect and aberrations in magnets [6], were not fully taken into account, resulting in bad transmissions for high current ion beams. Recent simulation results show that the second-order aberration

ISBN 978-3-95450-185-4

in the analyzing magnet appears to be a prior cause leading to the obvious beam phase space aberration and emittance blow-up. However, the focusing solenoid lens at the ion source exit could take effect to adjust the beam angle and size in the analyzing dipole, so as to mitigate the degradation of the beam brightness. Fig. 2 shows the measured beam profile of $^{209}Bi^{27+}$, $^{209}Bi^{28+}$, $^{209}Bi^{29+}$ and the measured beam emittance of $^{209}Bi^{28+}$ at the diagnostic chamber. As is shown, the beam profile seems hollow in the x-y space, but the measured beam emittance has good performance at the exit of A/Q selection system, in the case of drain current of 2.4 mA. Fig. 3 shows the measured beam profile and beam emittance of $^{209}Bi^{28+}$, $^{209}Bi^{29+}$ at the diagnostic chamber with drain current of 5.8 mA. As is shown, the adjacent heavy ions $^{209}Bi^{28+}$, $^{209}Bi^{29+}$ cannot be separated at the slits as the beam profile becomes too large due to the space charge effect of low energy high intensity heavy ions beam. Fig.3(b) shows the corresponding beam emittance measured in the diagnostic chamber.

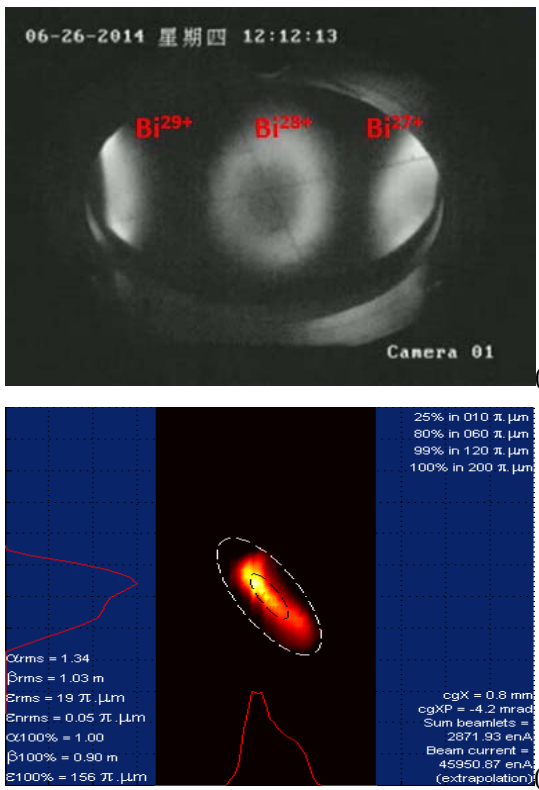

Figure 2: Measured $^{209}Bi^{27+}$, $^{209}Bi^{28+}$, $^{209}Bi^{29+}$ beam profile (a) and beam emittance (b) of $^{209}Bi^{28+}$ at the exit of A/Q selection system. Extraction voltage for the ion source is of 23 kV, microwave frequency is of 18 GHz and drain current is of 2.4 mA.

Space Charge Effect of Mixed Heavy Ions Beam on the Momentum Resolution of the Q/a Selection System

For each Q/A selector, the goal is to achieve high momentum resolution and at the same transmission as well as low beam emittance. To obtain a relatively high resolution ion separation, usually the beam optics of the Q/A analysis system is based on that a beam waist should be formed at the location of the slits. However, there are several factors deciding the position of the beam waist. The factors include the initial beam conditions at the ion source exit, the focusing strength of the solenoid, the structure parameters of the analyzing magnet, space charge effect, and so on. To have better understanding of the space charge effect on the location of the beam waist formation and the momentum resolution of the beam selection system, simulations of multi-charge mixed heavy ion beams are carried out with both high and low current ^{209}Bi beams. For LECR4, single solenoid design is not enough to make the beam waist at the slits location in the case of variable beam currents and initial beam conditions.

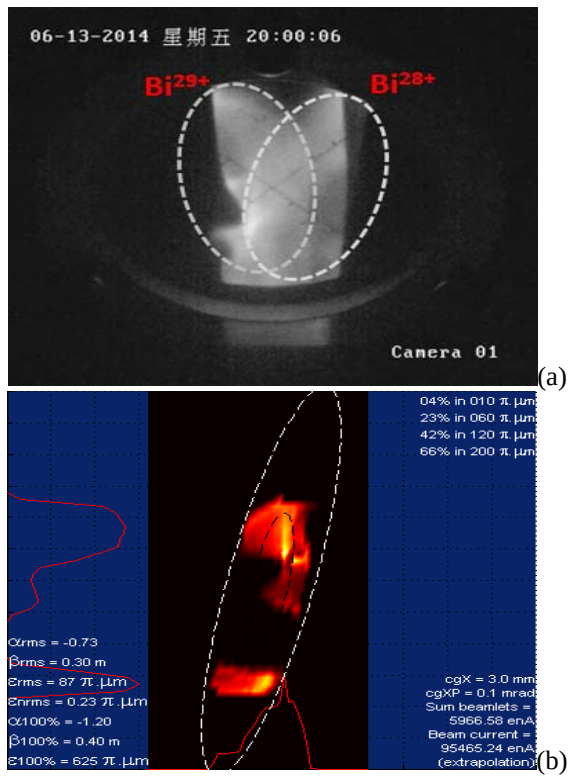

Figure 3: Measured $^{209}Bi^{28+}$, $^{209}Bi^{29+}$ beam profile (a) and beam emittance (b) of $^{209}Bi^{28+}$ at the exit of A/Q selection system. Extraction voltage for the ion source is of 23 kV, microwave frequency is of 18 GHz and drain current is of 5.8 mA.

In the tuning of the ECR injection beam line of single solenoid design, it is repeatedly noted that the analysed beam had a pronounced tendency to be hollow. One explanation of the beam hollow is “short focusing” [7,8] by the magnetic solenoid of beam components with charge/mass ratios higher than the desired beam. Higher Q/A beam components are brought to sharp foci before reaching the analysis magnet. These foci inside the column of desired beam lead to a high space-charge condition driving the lower Q/A beam radially outwards.

In order to expeditiously test the hollow formation hypothesis and make a first attempt to eliminate it, a PIC code has been developed based on Beampath[9] for

ISBN 978-3-95450-185-4

simulation of high intensity mixed heavy ions beam transport. The simulation particles include beams of 26 different ion types, Bismuth ions with the charge state of 19+ to 37+ and Oxygen ions with the charge state of 1+ to 7+, which is given by the measured beam charge state distribution from LECR4. The extraction voltage of the ion source is set to 23 kV and the space charge neutralization factor is supposed to be nearly 0.82, for a good agreement with the experimental results.

The initial beam parameters are calculated indirectly through the forward-tracking & back-evolution method, according to the measured beam emittance at the slits position. Fig. 4 shows The x-x',y-y' and x-y phase space of $^{209}Bi^{27+}$, $^{209}Bi^{28+}$, $^{209}Bi^{29+}$ at the exit of A/Q selection system without space charge. According to the results, the beam hollow didn't appear in the case of no space charge and the heavy ions with the adjacent charge states can be separated clearly at the slits position. While for high current beam, when strong space charge dominates the beam transmission, only one solenoid in a certain range is not enough to control the beam waist position, and the beam waist moving downstream (far away from the ion source). Corresponding beam simulations have also demonstrated a similar phenomenon, as shown in Fig. 5. It has a good consistency with the experimental results as in Fig. 3.

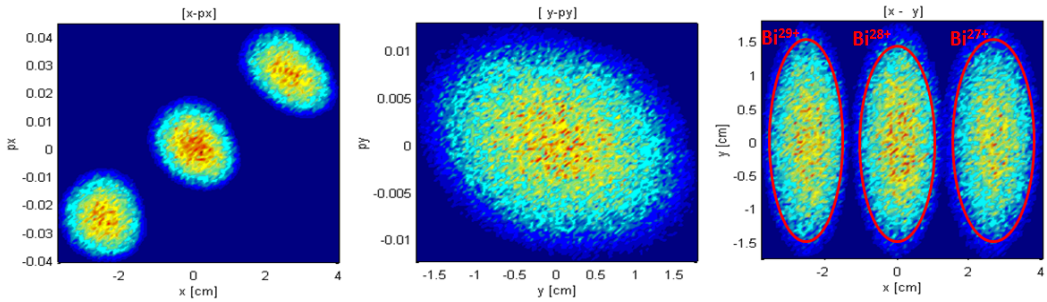

(a) (b) (c)

Figure 4: The x-x' (a),y-y' (b) and x-y (c) phase space of $^{209}Bi^{27+}$,$^{209}Bi^{28+}$,$^{209}Bi^{29+}$ at the exit of A/Q selection system without space charge effect.

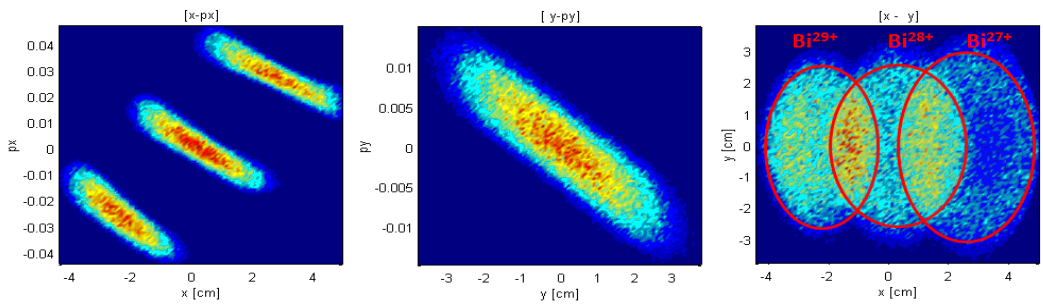

(a) (b) (c)

Figure 5: The x-x' (a),y-y' (b) and x-y (c) phase space of $^{209}Bi^{27+}$,$^{209}Bi^{28+}$,$^{209}Bi^{29+}$ at the exit of A/Q selection system with the total beam current of 5.8 mA and space charge neutralization factor of 0.82.

A MODIFIED DESIGN OF Q/A SELECTION SYSTEM

Based on the research of LECR4 Q/A selector, an updating selection system for LECR4 has been designed to handle the higher beam intensities. Fig.6 shows the schematic design of the new Q/A selection system. As the actual beam envelope and beam waist cannot be controlled with a single solenoid lens, an additional solenoid is introduced before the dipole magnet. Considering the spatial arrangement in the beam line, the solenoid is placed at the entrance of the steering magnet. Double solenoids provide more flexibility for the Q/A selection system to match for a variety of ion species. Moreover, the two solenoids with opposite polarity have the capability to counteract the beam coupling in the transverse phase space from the ECR ion source. In this scheme, the first solenoid is used to control the beam diameter in the beam channel and the second plays a supplementary role to adjust the position of the beam waist at the slits, especially for those high-current heavy-ion beams. For the modified Q/A selector, the focusing strength of the first solenoid is reduced which results in larger beam profiles and lower space charge forces, it helps to eliminate the hollow formation. The utilization of the two solenoids could tactfully solve the conflict between the beam transmission and the resolution of the system.

ISBN 978-3-95450-185-4

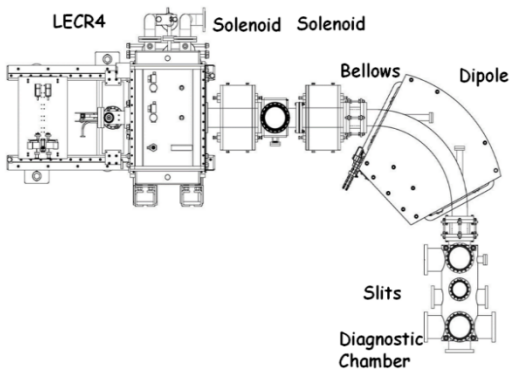

Figure 6: Layout of the updating ion selection system for LECR4.

In order to verify the momentum resolution and beam transmission of the new Q/A selection system, simulations are performed with $^{209}Bi^{28+}$ beam. The revised PIC code is employed to carry out the multi-species ion tracking. Realistic 3D magnetic fields of the solenoid lens and analyzing magnet along the beam line are imported in the simulation. Adopting the realistic fields in the simulation will help to verify the beam line design. The total beam current extracted from the ion source is of 5.5 mA, with an assumed space charge compensation degree of 82%. We assumed all ion species have the same initial conditions as in the simulations for Fig.4 and 5. Fig. 7 shows the simulated particle distribution on the focal plane for different charge states, which indicates a good separation for ions with different mass-to-charge ratios and the beam hollow disappears as the field strength of the first solenoid is reduced.

The new Q/A selection system has been constructed and the beam commissioning is done. Fig.8 shows the measured beam profile of $^{209}Bi^{28+}$ and the measured beam emittance of $^{209}Bi^{28+}$ at the beam diagnostic chamber. As is shown, double solenoids have enough capability to form a beam waist at the position of the slits to ensure adequate ion separation. The measured beam profile is similar to the simulation results in Fig.7. The phase space distributions of the particles in the x-x' and y-y' seem to be in a better condition compared to that with the single solenoid design, but obvious high order aberrations are shown on the x-y plane, which indicates that the effect of high-order aberrations and nonlinear space charge of mixed heavy ions beam cannot be ignored and need to be further investigated deeply.

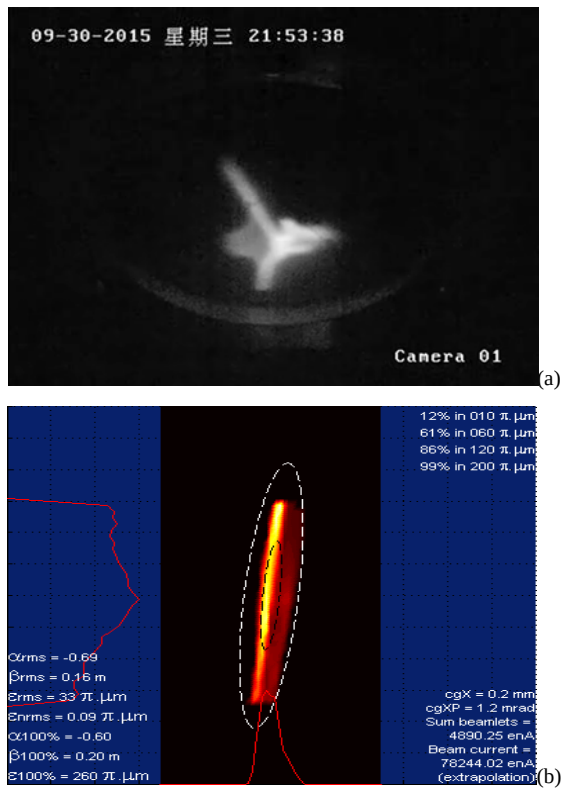

(a)

(b)

Figure 8: Measured $^{209}Bi^{28+}$ beam profile (a) and beam emittance (b) of $^{209}Bi^{28+}$ at the exit of A/Q selector system. Extraction voltage for the ion source is of 23 kV, microwave frequency is of 18 GHz and drain current is of 5.5 mA.

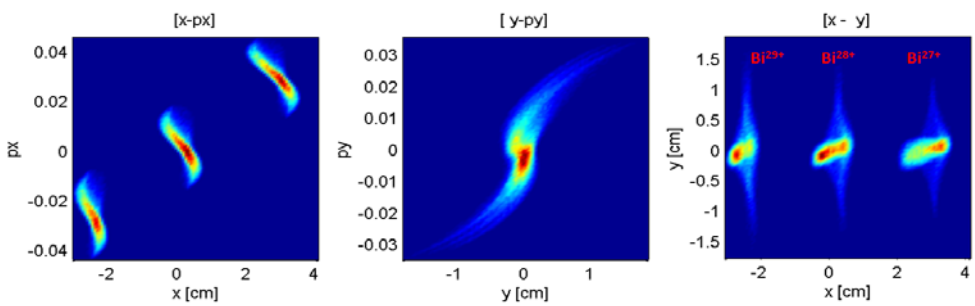

(a) (b) (c)

Figure 7: The x-x' (a), y-y' (b) and x-y (c) phase space of $^{209}Bi^{27+}$, $^{209}Bi^{28+}$, $^{209}Bi^{29+}$ at the exit of A/Q selector system with the total beam current of 5.5emA and space charge compensation degree of 82%.

ISBN 978-3-95450-185-4

SUMMARY AND OUTLOOK

Simulations and experiments have been carried out to investigate the original Q/A selection system at LECR4. The results show that, for high-intensity ion beams, the momentum resolution of the system is deteriorated due to the space charge effect and the beam hollow appears under strong solenoid field, driven by space charge defocused field of the multi-species ions. The updated Q/A selection system with additional solenoid has been designed and tested. Test results show that the matching problem for various species of ion beams is well solved; the modified selector has sufficient Q/A resolution and works well.

REFERENCES

[1] Y. Cao, W. Lu, W. H. Zhang, S. Sha, Y. Yang, B. H. Ma, H. Wang, Y. H. Zhu, J. W. Guo, X. Fang et al., Rev. Sci. Instrum. 83, 02B726 (2012).

[2] Y. Yang, L. T. Sun, Q. Hu, Y. Cao, W. Lu, Y. C. Feng, X. Fang, X. Z. Zhang, H. W. Zhao, and D. Z. Xie, Rev. Sci. Instrum. 85, 02A719 (2014).

[3] W. Lu, et al.,"High intensity high charge state ion beam production with an evaporative cooling magnet ECRIS"，Review of Scientific Instruments, 87(2):02A738, February 2016.

[4] C. Xiao, Y. He, Y.J. Yuan, et al.," Particle-in-cell mode beam dynamics simulation of the low energy beam transport for the SSC-linac injector[J] ", Chinese physics C, 2011, 35(5): 500.

[5] X. Yin, et al, The R&D status of SSC-LINAC, IPAC 2014.

[6] Yang Y, Sun L T, Feng Y C, et al.,"Studies on a Q/A selector for the SECRAL electron cyclotron resonance ion source[J]" ,Review of Scientific Instruments, 2014, 85(8): 083301.

[7] Stetson J W, Machicoane G, Marti F, et al.," A comparison of electrostatic and magnetic focusing of mixed species heavy ion beams at NSCL/MSU[C]" Proceedings of the 2005 Particle Accelerator Conference. IEEE, 2005:2281-2283.

[8] Kazarinov N.,"Hollow beam formation in the intense multi-component heavy ion beam caused by beam self-field[J]", Physics of Particles and Nuclei Letters, 2010, 7(3): 201-208.

[9] Batygin, Yuri. BEAMPATH User Manual. United States: N. p., 2012. Web. doi:10.2172/1055311.

ISBN 978-3-95450-185-4

THE BEAM DELIVERY SYSTEM OF THE EUROPEAN SPALLATION SOURCE*

H.D. Thomsen†, S.P. Møller, Dept. of Physics and Astronomy, Aarhus University, Aarhus, Denmark

Abstract

The European Spallation Source (ESS) will apply a fast beam scanning system to redistribute the proton beam transversely across the spallation target surface. The system operates at sweep frequencies of tens of kHz and efficiently evens out the time-averaged beam intensity within a nominal beam footprint, thus reducing the level of beam-induced material damage. A modular design approach divides the raster action in each direction across 4 independent magnet-supply systems to distribute the magnetic load, ease the peak output power per modulator, and in general reduce the impact of single point of failures (SPOFs). The state of the magnet design and power supply topology will be discussed.

INTRODUCTION

Several present and future accelerator projects at the intensity frontier feature an accelerator (linac or cyclotron) that delivers a MW-class beam to a fixed target for *e.g.* secondary beam production or reactors. Common to all such projects is the importance of the accelerator–target interface, where many challenges and compromises are to be dealt with, and the Accelerator-to-Target (A2T) section of the ESS is no exception. To be able to sustain the considerable beam power, the beam is here expanded to a substantial size to minimize the local power deposition and radiation-induced material degradation across the target shroud and accelerator vacuum windows, if relevant. The replacement frequency of such components and the capacity of their associated cooling systems can be reduced even more by applying schemes to produce transverse beam current profiles that are close to uniform with an extent that matches the edges of beam confinement regions, beyond which only fractions of beam are tolerated. These sophisticated Beam Delivery Systems (BDSs) include both a linear expansion (relying on magnetic quadrupoles) and a system to intentionally distort the time-averaged beam profiles by applying *e.g.* non-linear or AC dithering fields. Several facilities have considered such systems, as will be discussed. Given the considerable beam currents often involved, excessive uncontrolled primary beam losses may ensue, if these systems are not properly designed or the incoming beam is significantly different from the assumptions made in the design phase.

Non-Linear Magnets

To flatten high-power ion beams using a system of non-linear magnetic lenses has long been studied [1], [2], [3], [4], [5], [6] and even applied at *e.g.* the NASA Space Radiation Laboratory, BNL [7], [8]. The scheme will be applied to existing (J-PARC [9]) and future facilities (CSNS, C-ADS, IFMIF [10]). The systems include either pure multipole elements ($O(2n)$ pole elements with $n \geq 3$, *i.e.* sextupoles, octupoles, *etc.*.) or rely on more specialized combined function magnets, *e.g.* the so-called dipole pairs [1] or step-like field magnets [4] which are based on relatively similar magnet topologies. Considering *e.g.* a horizontally Gaussian beam profile with an elliptical phase space distribution (x, x') , a properly applied octupole magnetic field ($B_y(x, y) \propto x^3$) will introduce a symmetric horizontal focusing force affecting in particular the beam tails, causing a characteristic S-shape in the phase space. Although the solution can provide close to uniform distributions by applying DC fields, there are several caveats.

Overfocusing: Unless compensated, the strong non-linear forces can severely overfocus halo particles, which may lead to excessive losses before the beam reaches its intended destination. Saturating the field strengths at large excursions, either by combined-function magnet design or introducing *e.g.* dodecapoles, can compensate for this [1].

Lack of flexibility: Non-linear magnets are usually designed with a narrow band of not only beam RMS sizes in mind, but also kurtosises, *i.e.* beam quality, something that can be very difficult to predict before the accelerator is constructed and commissioned. Combined-function magnets offering several degrees of freedom [11] can perhaps efficiently cover a span of kurtosises.

Beam-magnet alignment: In particular the pure non-linear magnets are very sensitive to beam-magnet displacement, giving rise to steering errors and beam profile artefacts, *e.g.* the characteristic "ears" near the profile edges, in case of octupoles [1].

Aperture vs. field: Designing the non-linear magnets also involves the trade-off between having a sufficient impact on the beam, while retaining sufficiently large apertures to avoid beam losses. This balance becomes increasingly difficult with an intense, rigid beam.

Coupling: To enable flattening of both the horizontal (H) and vertical (V) profile, dedicated H and V non-linear lenses should be applied at locations where the beam RMS size aspect ratio is large, ($\sigma_x/\sigma_y \gg 1$ in the H multipole and vice versa) to avoid H–V coupling. The scheme thus requires magnetic elements between the two non-linear elements. Depending on the beam emittance and tuning accuracy, the beam waists cannot provide complete H-V decoupling, thus rendering tuning complicated.

* Work supported by European Spallation Source ERIC
† heinetho@phys.au.dk

ISBN 978-3-95450-185-4

To assess the concept of applying a multipole-based BDS for a high-power accelerator, the Los Alamos National Lab (LANL) Accelerator Production of Tritium (APT) project, two prototype magnets were constructed for testing at the 800 MeV LANSCE/LAMPF [11]. Both magnet prototypes were 500 mm long 12-pole magnets with three independent families of coils to vary the octupole and dodecapole components while cancelling the quadrupole component. A large beam aspect ratio (3 mm / 25 mm) was assumed when designing the non-cylindrical aperture. Using Hall probes at LANL and a rotating coil system at BNL, the measured field profiles were found to match the calculated values quite well [11]. Even so, "prompt beam-loss radiation was detected near the two nonlinear octupoles" when testing with a pulsed proton beam of 0.1 µA average current or 80 W average power [12]. The observed loss rates would be intolerable, if scaled to APT's 170 MW average beam power. Even before the prototype testing, it was decided to use a linear raster system for the APT instead. This may have had an impact on the beam time allotted for the multipole testing where more extensive commissioning of the system could perhaps have improved the loss levels. The main drivers were the more straightforward tuning of the system and reduction of the expected beam losses.

Much like the LANL story, a great effort was put into studying a multipole-based BDS for the ESS [13], in particular balancing the obtained flattening of beam profiles and the induced losses. To compensate for the latter, a collimator close to the target was intended to intercept of the order of tens of kW of primary beam, even when assuming a nominal beam from the accelerator. The ESS multipole studies confirmed that tuning the non-linear elements was extraordinarily sensitive to the input beam distribution, specifically the magnitude and extent of the beam's tails, or halo. To optimize the settings would involve a series of time-consuming particle tracking simulations. The concept's sensitivity towards beam quality can be considered as a considerable risk, when designing a new facility, in particular when aiming for unprecedented machine parameters or application of novel acceleration technologies, whereas it may be more straightforward to retrofit them into an existing beam line [9]. Due to the reasons above, the ESS BDS was changed to be raster-based in mid-2013.

Raster Systems

As an alternative to non-linear magnets, a set of AC dipole raster magnets can be applied to introduce suitable H and V displacement waveforms at a downstream location, *e.g.* a target surface, such that the beam centroid is swept in a two-dimensional (2D) displacement pattern. A true raster pattern would necessitate a rapid scan in one direction, while the orthogonal scan would be a slower series of steps that match the rapid scan period. This scheme thus demands two distinct magnet and power supply designs. Instead, a common design can typically be used, if the H and V raster waveforms have either identical frequencies but are dephased (thus generating a circle or ellipse) or frequencies corresponding to coprime harmonics, thus generating a Lissajous-like pattern, with a ratio close to but different from unity. Independent linear DC beam optics (*i.e.* quadrupoles) sets the size of the beamlet that is scanned in a controlled pattern, and the resulting time-averaged beam intensity distribution would be a convolution of the displacement pattern and the beamlet profile. The uniformity of the resulting distribution will depend on the spacing between the respective sweeps relative to the beamlet size. The raster waveform amplitude thus sets the size of the central uniform area, while the beamlet RMS size determines the shape and extent of the distribution edges. A pattern containing several sweeps in both directions of a suitably sized beamlet can thus produce effective distributions that inherently suppresses the impact of variations in the incoming beam's profiles. This attractive BDS feature is quite contrary to a system based on multipoles.

Since the scanning pattern will have an inherent finite cycle period, raster systems are most appropriate for accelerators providing long-pulsed or CW beam, and both MYRRHA [14] and SINQ [15] are designing circular raster systems operating at tens to hundreds of Hz to reduce the peak current density on the beam windows and targets. Apart from being designed to be a CW machine, there is a great resemblance between the beam parameters of the APT and the ESS. The raster system designed and prototyped for the APT has thus served as a great inspiration. Whereas the APT system was designed to operate in the 500 Hz–600 Hz range [16], [17], [18], the ESS system will operate at considerably larger frequencies, 10 kHz–40 kHz [19], [20].

Table 1: Nominal Beam Parameters and Requirements at the ESS Target Surface [20]

Parameter	Unit	Value
Average beam power	MW	5.0
Final kinetic energy	GeV	2.0
Beam rigidity	T.m	9.29
Peak beam current	mA	62.5
Average beam current	mA	2.5
Pulse repetition rate	Hz	14
Duty cycle	%	4
Pulse duration	ms	2.86
Maximum beam offset $\langle x \rangle$	mm	±5
Maximum beam offset $\langle y \rangle$	mm	±3
Nominal $\langle J(x, y) \rangle$	µA/cm^2	56
Maximum $\langle J(x, y) \rangle$	µA/cm^2	71
99.0% H × V footprint	mm^2	160 × 60
99.9% H × V footprint	mm^2	180 × 64
Min. $\sigma_x \times \sigma_y$	mm^2	50
Min. hor. raster frequency	kHz	35

The ESS Beam on Target Requirements

The nominal and required beam parameters at the rim of the ESS target wheel rotating at 0.4 Hz [20] can be inspected in Table 1. The listed parameters, *e.g.* the beam

ISBN 978-3-95450-185-4

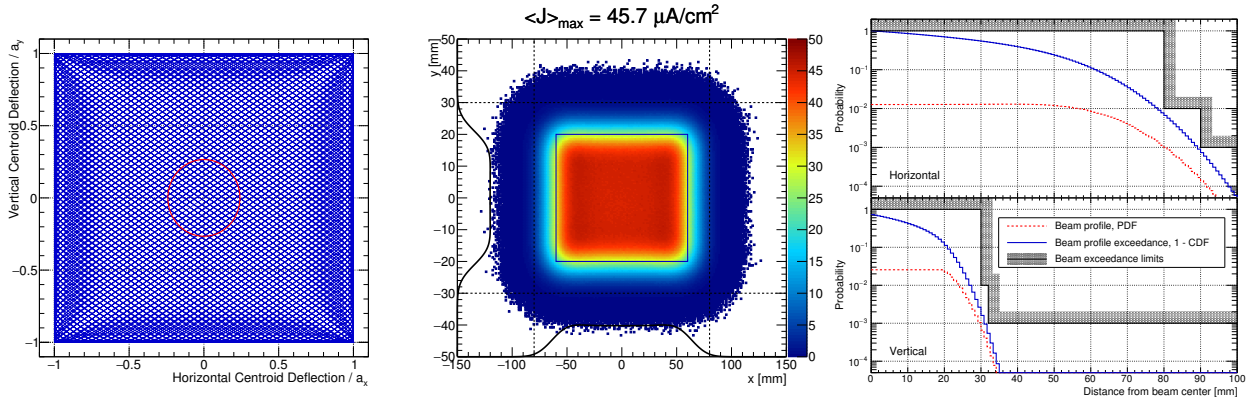

Figure 1: Left panel: A $f_x/f_y = 113/83$ raster pattern compared to the 1-RMS beam size ellipse. Middle panel: A simulation of $\langle J(x,y)\rangle$ with the projected profiles (black curves) and raster pattern outline (blue box). $(a_x, a_y, \sigma_x, \sigma_y) = (60, 20, 12, 4.5)$ mm. The dashed lines mark the 99% confinement zone. Right panel: Diagrams showing the horizontal and vertical PDF and CCDF = 1 − CDF compared to the confinement requirements of Table 1.

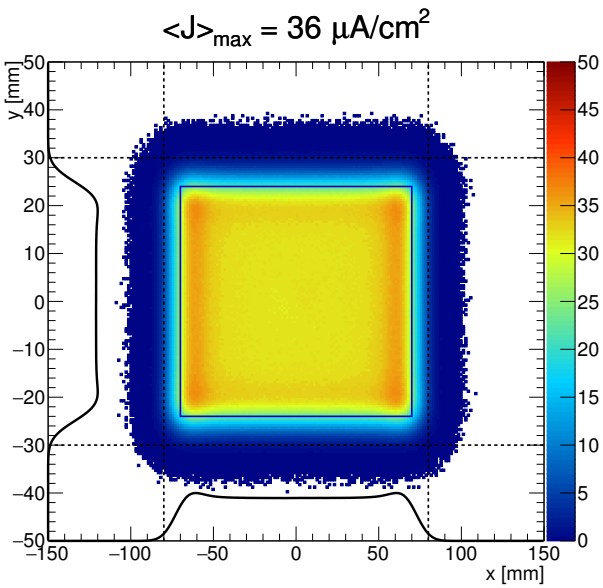

Figure 2: $(a_x, a_y, \sigma_x, \sigma_y) = (70, 24, 7, 3)$ mm.

profile offset from nominal center, $\langle x\rangle$ and $\langle y\rangle$, relate to the pulse-averaged delivered beam, *i.e.* covering a full nominal $(14\,\mathrm{Hz})^{-1}$ beam pulse cycle. The time-averaging does not take the rotation of the target into account. The average current density $\langle J(x,y)\rangle = \int J(x,y,t)\mathrm{d}t$ is a representation of a two-dimensional PDF scaled with the average beam current. It should be emphasized that there are no requirements regarding the distribution's flat top uniformity per se, but that the combination of limiting $\langle J(x,y)\rangle$ while setting confining footprints, truly entails a method to make the profiles very close to uniform.

Optimizing Parameters

With a raster-based system, the degrees of freedom in tailoring the resulting distribution are the raster frequencies (f_x, f_y), the displacement amplitudes (a_x, a_y), and the DC beamlet beam RMS size (σ_x, σ_y). If the sweep frequencies are chosen such that the raster pattern is finely meshed with a centroid path spacing less than (σ_x, σ_y), the time-averaged pulse will not contain artefacts, *i.e.* intensity modulations, due to the raster pattern. For such raster distributions, the amplitudes determine the full width at half maximum (FWHM) of the distribution, *i.e.* the general edge of the distribution. The sharpness of the edge around this point, and the extent of the distribution's tails relative to the amplitudes, will be characterized by the choice of (σ_x, σ_y). To keep the beam confined while providing sufficient rastering is thus a matter of optimizing *e.g.* (a_x, σ_x) where the parameters should be treated as inversely correlated. As an additional constraint, a considerable minimum beamlet cross section $\sigma_x \times \sigma_y > 50\,\mathrm{mm}^2$ is required to ensure that the shroud of the rotating target is unlikely to rupture in the event of a complete failure of the raster system.

Raster patterns have been generated by sampling 2^{16} points from triangle waveforms over a 2.86 ms duration. The pure waveforms are passed through a 1st order Butterworth filter with an upper cutoff frequency $f_{c,2} = 200$ kHz. Assuming prime harmonics of the fundamental pulse frequency, $f_x = 113/2.86\,\mathrm{ms} = 39.6\,\mathrm{kHz}$ and $f_y = 83/2.86\,\mathrm{ms} = 29.1\,\mathrm{kHz}$, the coordinates of the raster pattern is used for Monte Carlo simulations of the resulting beam distribution. At each centroid coordinate, 10^4 protons are sampled from a 2D Gaussian with (σ_x, σ_y) and the data is projected onto a 2D histogram and scaled to represent $\langle J(x,y)\rangle$. This quantity is minimized by searching in the two decoupled parameter spaces (a_x, σ_x) and (a_y, σ_y). It is important to stress that a_x and σ_x are controlled independently in the real accelerator, by the raster system and DC quadrupoles, respectively. An example of the Monte Carlo simulations is represented in Fig. 1. To evaluate the confinement of the simulated protons, the distribution profiles (*i.e.* PDFs), and the resulting exceedance (tail distribution, or complementary cumulative density function (CCDF)) are evaluated and compared to the 99% and 99.9% limits, cf. right

ISBN 978-3-95450-185-4

panel of Fig. 1. In both H and V, the exceedance of the beam profiles is seen to closely match these limits. In the example, $(a_x, a_y, \sigma_x, \sigma_y) = (60, 20, 12, 4.5)$ mm, *i.e.* $\sigma_x \times \sigma_y = 54\,\text{mm}^2$. The local intensity could further be reduced if smaller beamlet cross sections would be tolerated. As the beamlet sizes are lowered, however, the profiles begin to exhibit distinctive intensity ridges ridges that are characteristic of the finite bandwidth of the raster waveforms, cf. Fig. 2, which causes the beam to linger near the edges. The horizontal waveform is particularly affected since $f_x/f_{c,2} > f_y/f_{c,2}$. Although there is a benefit in $\langle J(x,y)\rangle$ from the smaller beamlet cross section, there is thus a limited benefit in seeking lower numbers, which in addition would severely increase the impact of a full failure of raster system. It should be emphasized that it has not been studied whether the DC beam optics of the ESS A2T is able to provide *e.g.* $(\sigma_x, \sigma_y) = (7, 3)$ mm at the target surface.

SYSTEM DESCRIPTION

At the required raster frequencies of >35 kHz in the horizontal direction [20], full magnetic field waveform control becomes unfeasible. Instead, it is exploited that when applying a voltage waveform across a purely inductive load, the resulting current waveform passing through the load will be of a temporal shape that is equivalent to the integral of the voltage waveform. The required symmetric triangle current waveform can thus be generated by applying a square voltage waveform across the load. The load in this context, *i.e.* the raster magnets and the cables carrying the AC currents, can be designed to resemble a predominantly inductive load, while still maintaining a low enough inductance to permit AC currents at tens of kHz.

A modular design approach is followed by distributing the required raster action over a string of colinear Raster Scanning Magnets (RSMs) placed in pairs of identical field direction, $(B_yB_y)(B_xB_x)(B_xB_x)(B_yB_y)$, *i.e.* a set of four acting in H, four acting in V, with a central point of symmetry. Each of the RSMs in a set are to be synchronized within ±200 ns and divide the field amplitude evenly. Although this would enable powering the RSMs in a set with a single supply, each RSM is powered by a dedicated modulator. The individual powering reduces the magnetic load on the RSMs and the peak output power of each modulator, but it is also a straightforward approach to reduce the impact of element failures by implementing redundancy. By operating the system at a duty cycle of only 5%, appropriately more than the 4% beam pulse duty cycle, active cooling of magnets and modulators is unnecessary, thus providing a higher reliability.

Magnet Design

A cross section and isometric view of a H RSM (*i.e.* with a vertical field component) can be seen in Fig. 3. The magnet design features a NiZn ferrite-based yoke to accommodate the considerable operating frequency. Several commercially available ferrites, *e.g.* CMD5005 from National Magnetics

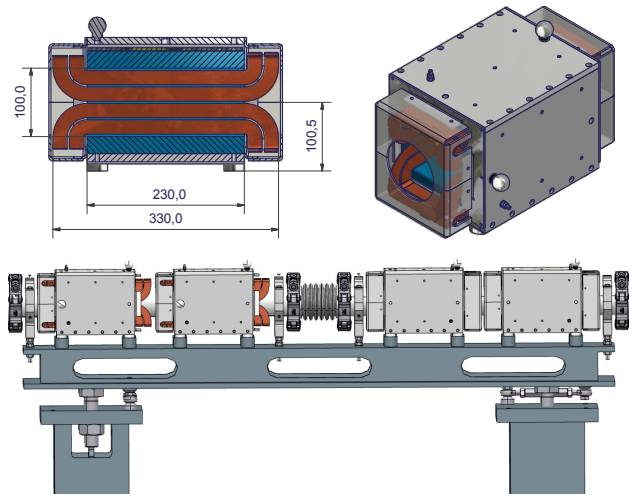

Figure 3: Sagittal cross section of a RSM with dimensions in mm (left, top panel) and isometric view of a complete RSM (right, top panel). Ferrite parts are shown in turquoise and are held in place by spring-loading them against a metallic housing. The bottom panel shows a 4-magnet setup based on a girder that rests on a pair of supports.

Table 2: Top Level Parameters and Specifications of a RSM

Parameter	Unit	Value
Min. magnet aperture	mm	100
Magnetic length	mm	300
Turns per coil	—	2
Peak strength	mT.m	5
Nom. strength $B\ell$ (H / V)	mT.m	1.5 / 2.6
Nom. deflection (H / V)	mrad	0.16 / 0.28
Max. current (peak-to-peak)	A	±340
Max. voltage (peak-to-peak)	V	±650

Group (formerly Ceramic Magnetics), offer sufficiently low eddy current losses and a high frequency response. The Cu coils are cut from a 1 mm thick OFHC plate and bent into 2-turn bedstead coils. The plate thickness is chosen as a trade-off between minimizing eddy current power losses, the Cu skin depth is $\delta_x = 0.3\text{ mm} \times \sqrt{40\text{ kHz}/f_x}$, while maintaining structural integrity considering being subjected to the AC magnetic forces. A window-frame magnet yoke design is chosen to provide very uniform fields across almost the entire magnet aperture, thus minimizing the pole width and avoiding the pole shims involved in an H-magnet. This topology not only minimizes the magnet production cost but also reduces the power supply specifications. One potential disadvantage of the considerable extent of the magnetic fields inside the magnet aperture is that the AC fields would induce eddy current in the actual coils, which in turn could result in power losses and field strength and quality degradation. This effect has not yet been studied but pushes for as thin coils as mechanically possible. The magnet parameters can be found in Table 2. The magnet gap of 100 mm is chosen to avoid significant physical aperture restriction in the

ISBN 978-3-95450-185-4

ceramic vacuum chambers along the RSMs. Having set this figure, the physical length should be chosen appropriately larger to reduce the impact of the inevitable fringe field's inferior field quality. Additionally, the system's stored energy (and thus the concomitant supply's VA rating) will be inversely proportional to the magnet length. The current design features a 230 mm magnet yoke, the longest possible to avoid spatial conflicts.

To facilitate installation, alignment/realignment, and the replacement of principal elements, a girder-based support stand is proposed. There will be two stands holding 4 RSMs each, cf. bottom panel of Fig. 3. High-precision RSM position slots are expected to be machined along the girder, thus avoiding the need for individual RSM alignment, while the girder is used to align the 4 RSMs simultaneously. In case of having to replace a RSM or a vacuum chamber, the vacuum system can be disconnected using quick-CF flanges, and the entire girder can be hoisted out for maintenance, thus minimizing maintenance crew's occupation and exposure to activated components in the accelerator tunnel.

While raster magnets can be produced to sustain the radiation levels that are expected in the tunnel, the power supplies will contain electronics with radiation resistance that are not suitable for radiation zones. The power supplies will thus need to be located at an appropriate distance from the tunnel. The power cables connecting each magnet and supply are foreseen to be 30 m long.

Power Supply Design

Each RSM is powered by a dedicated supply, or modulator, based on a capacitor-charging supply (input converter) and an H-bridge (output converter) to generate the required square voltage waveform across the RSM. More details can be found in [21]. The four semiconductor power switches constituting the H-bridge could be either IGBTs or MOSFETs. Besides, each supply will contain local control electronics (a microprocessor for internal control and communication with the Integrated Control System (ICS)) and a feedback/regulation controller. The latter will be a FPGA to regulate the signals for the switch drivers and the waveform amplitudes, *i.e.* the capacitor voltage. The rise time of the H-bridge switches, t_r, is believed to be the major contributor to $f_{c,2}$, being of the order of $t_r \simeq 250\,\mathrm{ns}$. A previous study found that the minimum value of $f_{c,2}$ should be the fifth harmonic, or 200 kHz [21].

Fault Detection & Mitigation

In particular when consisting of dynamic elements, closely monitoring the performance of the BDS is imperative to prevent component damages and support the 95% availability requirement of the ESS. Potential malfunctions should be foreseen and mitigated internally, if possible. Simple preventive measures like monitoring internal component temperatures, the capacitor voltage, controller state, *etc.* will be an integral part of the local protection functions implemented in each supply. A pretrigger initiates a RSM supply preparatory phase that precedes each raster pulse. The phase duration should allow for extensive system verification that produces an active "ready for beam?" signal to the ESS Run Permit System (RPS). Detection of a local state that could give rise to a non-nominal beam condition shall provoke an interlock signal for the ESS Beam Interlock System (BIS), which can inhibit further beam production and transport at low energies. Apart from the internal local protection functions implemented in each supply, a dedicated ESS RSM Fault Detection Unit (FDU) is to monitor the performance of the RSMs and interfaces to the RPS and BIS. Each RSM will feature a Bdot loop, which typically consists of a single wire back-leg or pole-face winding. A current that is proportional to the rate of change in magnetic flux through the loop will be induced. The resulting voltage square waveforms are a direct consequence of the magnetic fields and thus constitute a valuable indicator of the system's performance in terms of perturbing the beam. Additionally, each supply could contain Idot loops (a current transformer) that measures the rate of change in cable current, *i.e.* ideally also a square waveform. Such signals are obvious input candidates for the RSM FDU, as has been done in other raster magnet applications [22].

Even if a failure should remain undetected, the detailed design study is attempting to push the 4-fold redundancy to as high a level as reasonable and purge the system of single point of failures (SPOFs). In case of a sudden and complete failure in one RSM subsystem, 75% amplitude should be maintained in the affected direction, giving rise to a 33% increase in $\langle J(x, y)\rangle$, which is tolerable for longer durations, cf. Table 1. Even in the catastrophic event of a complete failure of the entire RSM system, letting an unrastered beamlet on the target, the sheer target rotation will allow for mitigation times as long as $\simeq 2\,\mathrm{s}$ [20], assuming $\sigma_x \times \sigma_y > 50\,\mathrm{mm}^2$.

To support the 95% availability requirement, a considerable field strength amplitude contingency of almost 100% in each subsystem, cf. Table 2, enables continued operation in a degraded mode having even a few of the RSM subsystems offline.

OUTLOOK & CONCLUSION

A raster-based BDS is being designed to provide a beam that conforms to the ESS beam-on-target requirements. Although studies of the application of DC multipoles have been made previously, the raster-based system is found to be superior in several aspects. This should, however, be expected to depend considerably on the parameters and requirements of the facility in question. As of June 1st, 2016, a contract has been signed with the vendor that also carried out a feasibility study of the system, Danfysik. Although the parameters appear practical from simulations, a complete two-magnet pre-series will be constructed and tested ultimo 2017. The full series should finish production by the end of 2018 and be installed at ESS in March, 2019.

ISBN 978-3-95450-185-4

REFERENCES

[1] B. Blind, "Production of uniform and well-confined beams by nonlinear optics," *Nucl. Inst. and Meth. in Phys. Research B*, vol. 56-57, Part 2, pp. 1099–1102, 1991.

[2] E. Urakabe, Y. Fujita, K. Hiramoto, *et al.*, "Beam-profile control using an octupole magnet," *Japanese Journal of Applied Physics*, vol. 38, pp. 6145–6149, 1999.

[3] F. Meot and T. Aniel, "Principles of the non-linear tuning of beam expanders," *Nucl. Inst. and Meth. in Phys. Research A*, vol. 379, no. 2, pp. 196–205, 1996.

[4] J. Tang, H. Li, S. An, and R. Maier, "Distribution transformation by using step-like nonlinear magnets," *Nucl. Inst. and Meth. in Phys. Research A*, vol. 532, no. 3, pp. 538–547, 2004.

[5] J. Tang, G. Wei, and C. Zhang, "Step-like field magnets to transform beam distribution at the CSNS target," *Nucl. Inst. and Meth. in Phys. Research A*, vol. 582, no. 2, pp. 326–335, 2007.

[6] Y. Yuri, N. Miyawaki, T. Kamiya, W. Yokota, K. Arakawa, and M. Fukuda, "Uniformization of the transverse beam profile by means of nonlinear focusing method," *Phys. Rev. ST Accel. Beams*, vol. 10, p. 104 001, Oct. 2007.

[7] N. Tsoupas, L. Ahrens, S. Bellavia, *et al.*, "Uniform beam distributions at the target of the NASA Space Radiation Laboratory's beam line," *Phys. Rev. ST Accel. Beams*, vol. 10, p. 024 701, 2 Feb. 2007.

[8] N. Tsoupas, S. Bellavia, R. Bonati, *et al.*, "Results from the Commissioning of the NSRL Beam Transfer Line at BNL," in *Proc. EPAC 2004, Lucerne, Switzerland*, 2004, pp. 2879–2881.

[9] S. Meigo, A. Akutsu, K. Ikezaki, M. Ooi, and H. Fujimori, "Beam Flattening System based on Non-linear Optics for High Power Spallation Neutron Target at J-PARC," in *Proc. IPAC'14*, 2014, p. 896.

[10] Z. Yang, J. Tang, P. P. Nghiem, and N. Chauvin, "Using Step-Like Nonlinear Magnets for Beam Uniformization at IFMIF Target," in *Proceedings of HB2012, Beijing, China*, 2012, p. 424.

[11] D. Barlow, R. Shafer, R. Martinez, *et al.*, "Magnetic design and measurement of nonlinear multipole magnets for the APT beam expander system," in *Proc. PAC'97*, May 1997, pp. 3309–3311.

[12] R. E. Shafer, "Comment on "uniformization of the transverse beam profile by means of nonlinear focusing method"," *Phys. Rev. ST Accel. Beams*, vol. 11, p. 039 001, 3 Mar. 2008.

[13] A. Holm, H. D. Thomsen, and S. P. Møller, "The Layout of the High Energy Beam Transport for the European Spallation Source," in *Proc. IPAC'12 New Orleans, USA*, 2012, p. 475.

[14] H. Saugnac, J. Biarrotte, L. Perrot, D. Vandeplassche, and A. Ferrari, "High Energy Beam Line Design of the 600 MeV, 4 mA proton Linac for the MYRRHA Facility," in *Proc. IPAC'11*, 2011, p. 2721.

[15] T. Reiss, D. Reggiani, M. Seidel, V. Talanov, and M. Wohlmuther, "Simulation of a beam rotation system for a spallation source," *Phys. Rev. ST Accel. Beams*, vol. 18, p. 044 701, 4 Apr. 2015.

[16] C. R. Rose and R. E. Shafer, "A 200-A, 500-Hz, triangle current-wave modulator and magnet used for particle beam rastering," in *Proc. PAC'97*, 1997, pp. 1293–1295.

[17] S. Chapelle, E. L. Hubbard, S. T. L., M. E. Schulze, and R. E. Shafer, "Development of a Raster Electronics System for Expanding the APT Proton Beam," in *LINAC'98*, May 1998, p. 612.

[18] S. Chapelle, S. T. L., D. J. LeBon, M. E. Schulze, and R. E. Shafer, "Testing of a Raster Magnet System for Expanding the APT Proton Beam," in *Proc. of PAC'99*, 1999, p. 3758.

[19] T. Shea, K. Andersen, P. Bentley, *et al.*, "Design Considerations for the ESS Accelerator-to-Target Region," in *Particle Accelerator Conference, 2013*, 2013, p. 300.

[20] E. Pitcher and T. Shea, "Beam on target requirements," European Spallation Source, Tech. Rep. ESS-0003310, 2015.

[21] H. Thomsen and S. Møller, "The Design of the Fast Raster System for the European Spallation Source," in *Proc. IPAC'14*, 2014, p. 2118.

[22] R. Sheffield and M. E. Schulze, "Raster Magnet System for Expanding the APT Proton Beam," Los Alamos National Laboratory, Tech. Rep. LA-UR-99-5820, 1999.

ISBN 978-3-95450-185-4

EMITTANCE RECONSTRUCTION TECHNIQUES IN PRESENCE OF SPACE CHARGE APPLIED DURING THE LINAC4 BEAM COMMISSIONING

V. A. Dimov, J.B. Lallement, A. M. Lombardi, CERN, Geneva, Switzerland
R. Gaur, RRCAT, Indore, India

Abstract

The classical emittance reconstruction technique, based on analytic calculations using transfer matrices and beam profile measurements, is reliable only if the emittance is conserved and the space charge forces are negligible in the beamline between the reconstruction and measurement points. The effects of space charge forces prevent this method from giving sound results up to a relativistic beta of about 0.5 and make it inapplicable to the Linac4 commissioning at 50 and 100 MeV. To compensate for this drawback we have developed a dedicated technique, the forward method, which extends the classical method by combining it with an iterative process of multiparticle tracking including space charge forces. The forward method, complemented with a tomographic reconstruction routine, has been applied to transverse and longitudinal emittance reconstruction during the Linac4 beam commissioning. In this paper we describe the reconstruction process and its application during Linac4 beam commissioning.

INTRODUCTION

The characterization of the beam emittance is essential during each commissioning stage of a linac to validate the settings and correct operation of the linac part being commissioned and predict the beam behaviour and potential beam losses downstream.

At Linac4, during the commissioning of the low energy part, a slit-grid emittance meter installed on a movable diagnostic bench [1] was used for the direct measurement of the transverse phase spaces. The bench was consecutively used for the beam measurements at 3MeV and 12MeV [2]. The longitudinal beam profiles were measured using a bunch shape monitor (BSM) [3] and longitudinal emittance was reconstructed from the measured profiles using forward method [4, 5].

At higher beam energies, the technical realization of a slit becomes challenging. Therefore, indirect emittance measurement methods based on reconstructing the emittance from profile measurements are preferred. The effects of space charge forces prevent the classical emittance reconstruction methods which depend on analytical calculations from giving sound results. Therefore, two methods, namely forward method and hybrid phase space tomography, were developed, validated and applied to the Linac4 commissioning for the emittance reconstruction in the presence of space charge. For the Linac4 50MeV and 100MeV commissioning stages, the diagnostic bench shown in Fig. 1 has been used. Transverse emittances were reconstructed at the entrance of the bench from the measured profiles at three locations along the bench with secondary electron emission (SEM) grids. The quadrupole magnets at the entrance of the bench are essential for obtaining optimum beam sizes at the SEM grids for the reconstruction. The longitudinal emittance was reconstructed at the entrance of a cavity upstream of the bench by varying the cavity settings and measuring the longitudinal bunch profile with the BSM shown in Fig. 1.

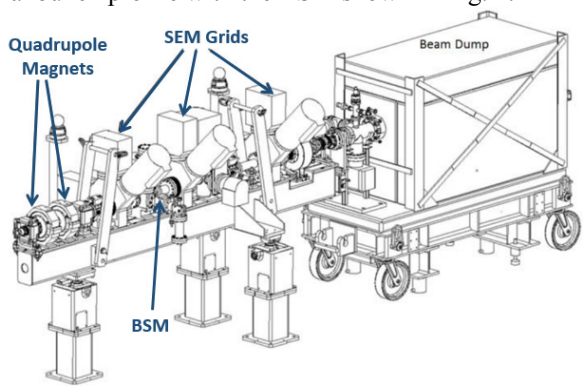

Figure 1: The Linac4 high energy diagnostic bench.

The 50MeV commissioning stage was completed in 2015 and the 100MeV commissioning stage was completed recently [6]. During each stage, the forward method and tomographic reconstruction were used to construct an estimate of the particle distribution in both transverse and longitudinal phase spaces.

The followings sections summarize the forward method with relevant references, discuss the tomographic reconstruction in detail and present the results of their applications to the measurement data.

EMITTANCE RECONSTRUCTION IN STRONG SPACE CHARGE REGIME

The classical emittance reconstruction techniques, based on analytic calculations using transfer matrices and beam profile measurements are not reliable in strong space charge regime. Therefore, two methods are developed and applied during the Linac4 commissioning to estimate the emittance of the beam in the presence of space charge.

The Forward Method

The forward method is a technique which aims at reconstructing the emittance of a particle beam from profile measurements in the presence of space charge. It was validated theoretically [7, 8] and experimentally [5] during the Linac4 commissioning.

ISBN 978-3-95450-185-4

The method is based on iteratively varying the Twiss parameters of the beam and tracking it to the measurement locations by including space-charge effects and comparing the measured and simulated rms beam sizes. The process continues until the simulated beam sizes converge to the measured ones.

During the Linac4 50 and 100 MeV beam commissioning, the forward method was applied to the transverse and longitudinal emittance reconstruction. The details and results will be given in the next sections.

The forward method is relatively simple, though it was proved to be powerful. At the same time, using only the rms beam size calculated from the measured profiles puts limit on the detail that can be recovered from the beam profile measurements. A more sophisticated method, phase tomography, can be used for the reconstruction of phase space density to make use of all the possible information that can be gathered from the profile measurements.

Hybrid Phase Space Tomography

In beam physics, phase space tomography refers to the process of calculating the distribution of particle density in 2-D phase space from its 1-D projections obtained from the beam profile measurements. Tomography has been used in the field of accelerators for several decades for the reconstruction of the transverse and longitudinal phase space density [9-14]. In most of the cases, it was applied to the low current or high energy beams were the nonlinear effects like space-charge can be ignored.

The standard phase space tomography is based on linear mapping of several measured beam profiles onto the initial phase space to estimate the distribution of particle density. The measured profiles are mapped onto the phase space at the reconstruction place and the initial estimate of the distribution of particle density is obtained. The projections of the reconstructed phase space on the measured data are calculated and compared with the measured profiles. The reconstructed distribution of density in the phase space is modified iteratively until the projections of the reconstructed phase space agree with the measured profiles.

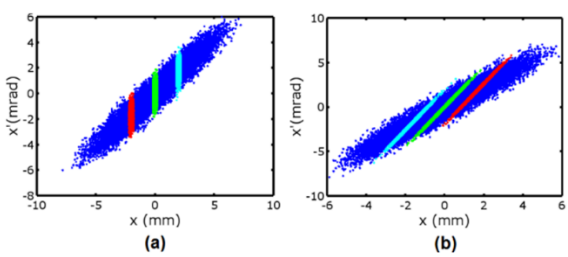

Figure 2: Horizontal phase space (a) at the third SEM grid with rays of particles (around -1, 0 and 1mm), (b) initial phase space at entrance of the diagnostics bench with the initial coordinates of the rays (no space-charge).

Figure 2a shows the horizontal phase spaces of the beam at the third SEM grid of the diagnostic bench (Fig. 1) after particle tracking without space-charge starting from the entrance of the bench. Selected rays of particles can be imagined as the particles hitting to the SEM grid wires having horizontal position of -1, 0 and 1mm. Figure 2b shows the initial phase space and the coordinates of the particles forming the rays in Fig. 2a which is identical to mapping of the coordinate of the wires onto the initial phase space. For the linear mapping of the wire positions onto the initial phase space, the transfer matrix from the reconstruction place to the profile monitor is necessary and sufficient.

When the space-charge effects are not negligible, linear mapping of the measured beam profiles onto the initial phase space is not possible. Figure 3a shows the phase space of the beam at the third SEM grid after tracking with the space-charge effects included. Figure 3b shows the initial phase space and the coordinates of the particles forming the rays in Fig. 3a. As it can be seen from the plots, when the space-charge is included, the mapping is no longer linear and the wire positions at the measurement place does not represent a line in the initial phase space anymore.

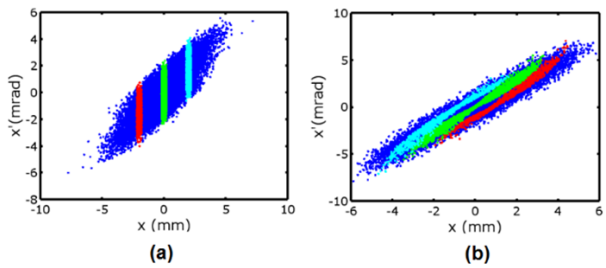

Figure 3: Horizontal phase space (a) at the third SEM grid with rays of particles (around -1, 0 and 1mm), (b) initial phase space at the entrance of the diagnostics bench with the initial coordinates of the rays (with space-charge).

In the longitudinal plane, the motion is nonlinear even if the space charge forces are ignored. Figure 4a shows the longitudinal phase space of a test beam after tracking through the Linac4 third drift tube linac (DTL) tank (Fig. 7) without space-charge. Figure 4b shows the longitudinal phase space at the entrance of the DTL tank and the initial coordinates of the particles forming the rays shown in Fig. 4a. The plots in Fig. 4 shows that even if the space-charge is neglected, the rays of particles having the same phase do not transform linearly onto the initial phase space.

ISBN 978-3-95450-185-4

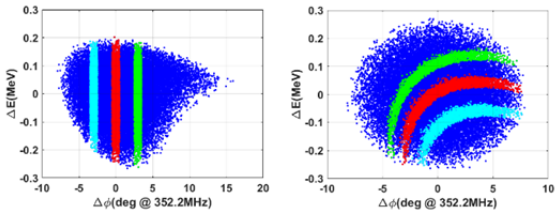

Figure 4: Longitudinal phase space (a) at the DTL exit with rays of particles (around -3, 0 and 3deg), (b) initial phase space at the entrance of the third DTL tank with the initial coordinates of the rays (without space-charge).

A hybrid phase space tomography technique which combines tomography with the multi-particle tracking including space-charge was developed, validated and applied during the Linac4 commissioning to the reconstruction of the transverse and longitudinal phase space density.

The method is iterative and based on tracking a test beam from the reconstruction place to the measurement locations and comparing the simulated beam profiles with the measured ones and modifying the initial particle distribution accordingly.

A script was written in Octave [15] by interfacing it with Travel [16] to automatize the iterative process. The multi-particle tracking is done by Travel, and the data analysis is done by Octave.

In Travel, each particle is tagged and the tag is not changed as the particles are tracked. Therefore, anywhere along the beam line, it is possible to find the coordinates of each particle in the initial phase space. This feature simplifies the process of mapping any area in the final phase space onto the initial phase space even if the transformation is not linear (see Fig. 2, 3 and 4).

The detailed process for the transverse phase space tomography at the entrance of the diagnostic bench (Fig. 1) using the measured beam profiles is as follows:

- The binned data of beam profile measurements are given as an input the script.
- A multi-particle beam (test beam) with uniform distribution and large emittance in both transverse phase spaces is generated at the entrance of the bench. For the longitudinal distribution, the distribution predicted by particle tracking upstream of the linac is used.
- The test beam is tracked to the SEM grid locations with the optics settings that were used while taking the measurements.
- The measured profiles are normalized and compared to the beam profiles obtained from the simulations.
- Each bin in the measured profiles is visited and the simulated particles falling on the bin are selected. Each particle is given a weight according to the measured signal at this bin and the number of particles falling into it. Particles falling outside of the measured profiles are given zero weight.
- At the end of the comparison, each particle gets three weights (one from each SEM grid) for each plane. The weights are combined independently in horizontal and vertical planes by summing three weights if all the weights are nonzero, else the combined weight is set to zero.
- At this point, the distribution of new particle density in each transverse phase space is defined and the information is carried in the initial coordinates and the weight of each particle for the corresponding plane.
- In order to generate a new particle distribution for the next iteration, each phase space is divided into rectangular cells (cell number is defined by the user).
- Using rotation matrix, the coordinates of the particles are transformed so that the major axis of the rms ellipse in each phase space is aligned with the horizontal axis. This decreases the computation time, increases the resolution and avoids generation of phase space distributions with sharp edges.
- Each cell is visited and the total weight in this cell (relative particle density) is calculated by summing all the weights of the particles inside the cell.
- Comparing the density in each cell, the new number of particles inside the cell is computed. If necessary, the number of particles inside each cell is modified by adding or removing particles randomly. The total number of particles in the beam is kept constant in each iteration.
- After the particle generation is complete, the coordinates of the particles are transformed back to obtain the initial ellipse orientation.
- The new particle file is generated and the new iteration is started.
- At each iteration, the measured profiles and the simulated profiles (after normalizing) from the reconstructed beam are compared. For each bin of the measured profile, absolute difference of the measured and simulated signal is calculated. The integral of this function (discrepancy) gives an idea about the convergence (Fig. 6).

The accuracy of the method was tested theoretically at 50 MeV with an H^- beam of 20 mA. A reference beam at the entrance of the diagnostic bench was simulated to the SEM grids and the beam profiles are obtained. A test beam was generated with uniform particle distribution in the transverse phase spaces and a longitudinal distribution identical to that of the reference beam. Using the procedure explained above, the horizontal and vertical phase spaces were reconstructed from the beam profiles. Figure 5 shows the phase space plots of the reference and the reconstructed beams.

ISBN 978-3-95450-185-4

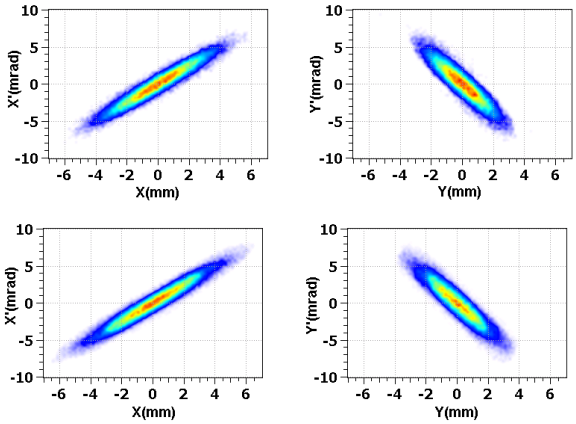

Figure 5: Transverse phase space plots of the reference beam (top row) and the reconstructed beam (bottom row).

The Twiss parameters of the reference and reconstructed beams are given in Table 1. In this specific test, the reconstruction method was able to predict the rms emittances with an error less than 3% and the other Twiss parameters less than 10%. The accuracy of the reconstruction may be increased by introducing more profiles for the reconstruction.

Figure 6 shows the evolution of discrepancy between the measured and simulated profiles after each iteration. Experience with the method showed that the variation of the curves are similar for different reconstructions. After about eight iterations, the method converges to a solution and during the next iterations the variation in the phase spaces is very small.

Table 1: Twiss Parameters (Emittance is Normalized) of the Reference and Reconstructed Beams at 50 MeV with 20 mA Beam Current

Parameter	Reference	Reconstructed
ε_x (rms)	0.39 π.mm.mrad	0.40 π.mm.mrad
α_x	-3.47	-3.81
β_x	2.86 mm/π.mrad	3.14 mm/π.mrad
ε_y (rms)	0.35 π.mm.mrad	0.36 π.mm.mrad
α_y	2.35	2.49
β_y	1.28 mm/π.mrad	1.39 mm/π.mrad

In order to have accurate calculation of the space-charge effects, it is important to use a realistic longitudinal distribution for the initial beam at the first iteration. For this specific test, two transverse phase spaces were reconstructed simultaneously. However, it is possible to reconstruct only one transverse phase space at a time. In that case, the accurate description of the other transverse phase space and longitudinal phase space is important for the accuracy of the reconstruction.

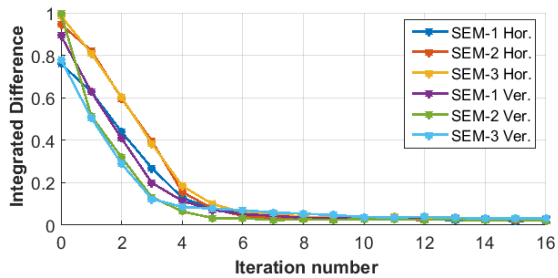

Figure 6: Discrepancy between the measured and simulated profiles after each iteration.

In the case of Linac4 transverse emittance measurements, the profiles were taken at three locations along the beam line. However the method can also be applied to different cases. For instance, when a focusing element is varied and the profiles are measured at the same location. Likewise, it can be applied to the longitudinal phase space where the phase and/or amplitude of an RF cavity is varied and the phase or momentum profile is measured downstream. The former is the basis of the longitudinal emittance measurements during the Linac4 commissioning.

A similar method which uses turn-by-turn particle tracking is being used at CERN for the longitudinal emittance measurements in the PS Booster [17, 18].

50 MEV COMMISSIONING STAGE

During the 50 MeV beam commissioning stage, the diagnostic bench shown in Fig. 1 was installed downstream of the third DTL tank (Fig. 7) which accelerates the beam from 30MeV to 50MeV. The forward method and tomographic reconstruction was applied to the measurement data at 50MeV H^- beam with 20 mA beam current.

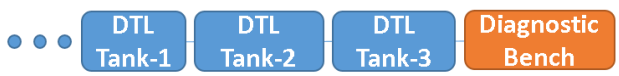

Figure 7: A sketch of part of Linac4 during 50 MeV commissioning.

Transverse Emittance Measurements

The forward method and the hybrid phase space tomography were applied to a set of horizontal and vertical beam profiles measured along the diagnostic bench for the transverse emittance measurements. Figure 8 shows the reconstructed transverse phase spaces with the forward method (top row) and phase space tomography (bottom row).

ISBN 978-3-95450-185-4

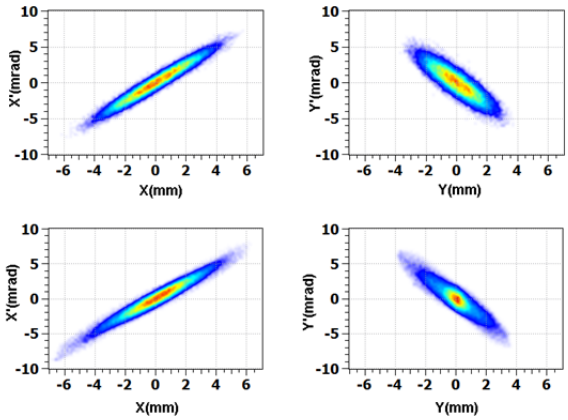

Figure 8: Reconstructed transverse phase spaces. Top row: forward method, bottom row: tomographic reconstruction.

The reconstructed rms emittances are ε_x= 0.32 π.mm.mrad and ε_y= 0.36 π.mm.mrad from the forward method and ε_x= 0.33 π.mm.mrad and ε_y= 0.32 π.mm.mrad from the phase space tomography. The other Twiss parameters in each plane have less than 10% difference. The particle distribution reconstructed with the tomographic method has differences compared to what was initially assumed for the forward method.

Longitudinal Emittance Measurements

The longitudinal phase space density of the beam was reconstructed at the entrance of the DTL tank-3 (Fig. 7) from the longitudinal bunch profiles. The profiles were measured with the BSM on the diagnostic bench by varying the RF phase of the tank. The forward method and the hybrid phase space tomography were applied to the same measurement data. The reconstructed longitudinal phase spaces are given in Fig. 9. The reconstructed rms emittances are 0.29 π.deg.MeV and 0.33 π.deg.MeV with forward method and phase space tomography respectively.

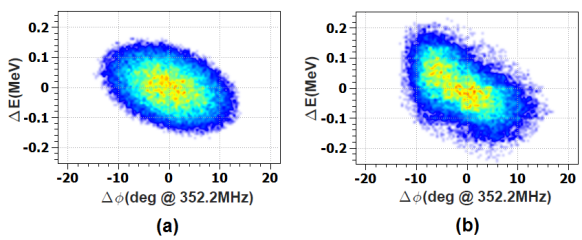

Figure 9: Reconstructed longitudinal phase space, (a) forward method and (b) tomographic reconstruction.

100 MEV COMMISSIONING STAGE

During the 100 MeV beam commissioning, the high energy diagnostic bench was connected to the first tank of the Pi-Mode Structure (PIMS), as shown in Fig. 10.

Figure 10: A sketch of part of Linac4 during 100 MeV commissioning.

Parallel to the process of setting the cavities [6], the transverse phase spaces of the beam were reconstructed at the entrance of the diagnostic bench (Fig. 10) at 50 MeV and 80 MeV beam energies. During the measurements at 50 MeV, all the cavities after the DTL tank-3 were turned off. Likewise, during the measurements at 80 MeV, all the cavities after the fourth module of the Cell-Coupled Drift Tube Linac (CCDTL) were turned off. The Twiss parameters of the reconstructed beams from the forward method and tomographic reconstruction differ less than 10 % at each beam energy.

In order to compare the beams reconstructed with phase space tomography, the reconstructed beam at 50 MeV was backtracked [19] to the exit of the DTL tank-3 with the CCDTL and PIMS cavities turned off and then tracked forward to the reconstruction place with the first four CCDTL cavities are on. The distance between the DTL tank-3 exit and the diagnostic bench was around 27 m.

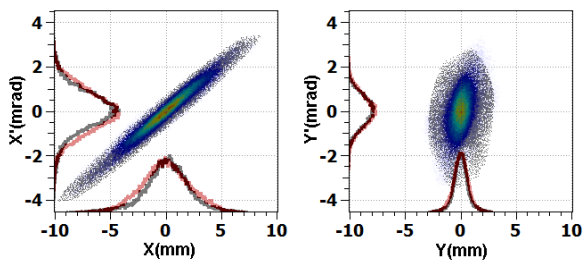

Figure 11: Comparison of phase space plots of the beams measured at 80MeV (grayscale) and measured at 50 MeV then tracked to 80MeV (colour scale).

In Fig. 11, the transverse phase space plots of the beam measured at 80 MeV are overlapped with the phase space plots of the beam measured at 50 MeV and tracked to 80MeV. As it can be seen from the figure, the particle distribution obtained from two sets of measurements at different energies and brought to the same conditions by simulations agree very well. The twiss parameters of the two beams are compared in Table. 2. All the parameters, expect α_y, are very close. The big percentage difference in α_y may come from the fact that it is close to zero.

ISBN 978-3-95450-185-4

Table 2: Twiss Parameters (Emittance is Normalized) of the Beams Measured at 80MeV and Measured at 50 MeV then Tracked to 80MeV

Parameter	50 MeV tracked to 80 MeV	Measured at 80 MeV
ε_x (rms)	0.22 π.mm.mrad	0.23 π.mm.mrad
α_x	-4.5	-4.6
β_x	10.7 mm/π.mrad	10.6 mm/π.mrad
ε_y (rms)	0.26 π.mm.mrad	0.27 π.mm.mrad
α_y	-0.49	-0.19
β_y	1.03 mm/π.mrad	1.02 mm/π.mrad

The agreement of the phase space plots given in Fig. 11 and the parameters given in Table 2 confirms the correct operation of the focusing channel along the beamline where the 50 MeV measured beam was first backtracked and then forward tracked.

At the 100 MeV commissioning stage, the measured emittance of the beam in transverse planes is smaller than what was measured at 50 MeV stage. This is mostly due to the fact that the profile measurements were taken when the transmission through the linac was not optimized.

CONCLUSION

The "forward method" and the "hybrid phase space tomography" were developed, validated and successfully applied during the Linac4 commissioning. These methods allow measurement of the emittance based on the observation of transverse/longitudinal profiles also under the effect of space charge. Both methods give sound and consistent results with each other for the prediction of the rms ellipse parameters. Moreover, the hybrid phase space tomography allows reconstruction of the distribution of particle density in a phase space from the measured beam profiles. These methods, which can be applied to any linac during commissioning and operation, were essential for the Linac4 50 MeV and 100 MeV beam commissioning. The comparison of the measured emittance, at different locations along the linac, with the expected values enabled validation of the operational machine settings and the reconstructed beam distribution was instrumental for the preparation of the next commissioning stages. Both methods will be used during the beam commissioning at 160 MeV and permanently during the operation of Linac4 at the end of the linac, as well as at the PS Booster injection.

REFERENCES

[1] F. Zocca et al., "Beam diagnostic measurements at 3MeV of the Linac4 H^- beam", *in Proc. IPAC'14*, Dresden, Germany, Jun. 2014.

[2] V. Dimov et al., "Beam commissioning of Linac4 up to 12MeV", in *Proc. IPAC'15*, Richmond, VA, USA, May 2015, pp. 3886-3889.

[3] A.V. Feschenko., "Methods and instrumentation for bunch shape measurements", *in Proc. PAC'01*, Chicago, USA, June 2001, 517-521.

[4] G. Bellodi et al., "Longitudinal beam profile measurements in Linac4 commissioning", *in Proc. Linac'14*, Geneva, Switzerland, Sept. 2014, 108-110.

[5] J.B. Lallement et al., "Linac4 transverse and longitudinal emittance reconstruction in the presence of space charge", *in Proc. Linac'14*, Geneva, Switzerland, Sept. 2014, 913-915.

[6] A.M. Lombardi, "The Linac4 project", presented at HB'16, Malmo, Sweden, July 2016, paper MOAM2P20, this conference.

[7] J-B. Lallement, A.M. Lombardi and P.A. Posocco, "Linac4 beam commissioning strategy", *in Proc. HB'12*, Beijing, China, Sept. 2012, 283-285.

[8] J-B. Lallement, A.M. Lombardi and P.A. Posocco, "Emittance reconstruction technique for the Linac4 high energy commissioning", CERN, Geneva, Switzerland, CERN-ATS-Note-2012-079, Oct. 2012.

[9] J.S. Fraser, "Beam analysis tomography", *IEEE Trans. Nucl. Sci.*, vol. NS-26, no. 1, pp. 1641-1645, Feb. 1979.

[10] C. T. Mottershead, "Maximum entropy diagnostic tomography", *IEEE Trans. Nucl. Sci.*, vol. NS-32, no. 5, pp. 1970-1972, Oct. 1985.

[11] C.B. McKee, P.G. O'Shea and J.M.J. Madey, "Phase space tomography of relativistic electron beams", *Nucl. Instr. Meth.*, vol. A 358, pp. 264-267, 1995.

[12] K.M. Hock and A. Wolski, "Tomographic reconstruction of the full 4D transverse phase space", *Nucl. Instr. Meth.*, vol. A 358, pp. 264-267, 1995.

[13] D. Reggiani, M. Seidel and C.K. Allen, "Transverse phase-space beam tomography at PSI and SNS proton accelerators", in *Proc. IPAC'10*, Kyoto, Japan, May 2010, pp. 1128-1130.

[14] Y.-N. Rao and R. Baartman," Transverse phase space tomography in TRIUMF injection beamline", in *Proc. IPAC'11*, San Sebastian, Spain, Sept. 2011, pp. 1144-1146.

[15] `https://www.gnu.org/software/octave/`

[16] A. Perrin and J.F. Amand, "Travel v4.06 user manual", CERN, 2003.

[17] S. Hancock and M. Lindroos, "Longitudinal phase space tomography with space charge", *Phys. Rev. ST Accel. Beams*, vol. 3, p. 124202, Dec. 2000.

[18] `http://tomograp.web.cern.ch/tomograp/`

[19] V. Yildiz, "CERN Linac4 beam dynamics studies and commissioning up to 12 MeV", Ph.D. thesis, Phys. Dept., Bogazici University, Istanbul, Turkey, 2015.

ISBN 978-3-95450-185-4

MODEL BENCHMARK WITH EXPERIMENT AT THE SNS LINAC

A. Shishlo†, A. Aleksandrov, Y. Liu, M. Plum, ORNL, Oak Ridge, TN 37831, USA

Abstract

The history of attempts to perform a transverse matching in the Spallation Neutron Source (SNS) superconducting linac (SCL) is discussed. The SCL has 9 laser wire (LW) stations to perform non-destructive measurements of the transverse beam profiles. Any matching starts with the measurement of the initial Twiss parameters, which in the SNS case was done by using the first four LW stations at the beginning of the superconducting linac. For years the consistency between data from all LW stations could not be achieved. This problem was resolved only after significant improvements in accuracy of the phase scans of the SCL cavities, more precise analysis of all available scan data, better optics planning, and the initial longitudinal Twiss parameter measurements. The presented paper discusses in detail these developed procedures.

INTRODUCTION

The SNS SCL is the world's first of the kind high power hadron superconducting linac. It accelerates H^- ions from 186 MeV to 1 GeV with 81 six-cell niobium elliptical superconducting RF cavities [1]. There are two types of superconducting cavities in SNS: the first is optimized for relativistic beta of 0.61 (medium beta subsection), and the second is optimized for beta of 0.81 (high beta). The cavities are enclosed in 23 cryomodules with inside temperatures of 2 K. There are 3 and 4 cavities per module for the medium and high beta sections respectively. Between modules there are doublets of quadrupoles to provide the transverse focusing.

Commissioning of the superconducting linac started in July 2005, and in 2009 SNS reached 1 MW beam power. During the power ramp up, an unexpected beam loss in the SCL was encountered. Eventually, this beam loss was reduced to the acceptable level by empirically lowering the field gradients of the SCL quadrupoles without understanding the loss mechanism. That led to efforts by the accelerator physics group to understand and to control the beam sizes in the SNS superconducting linac. Later the mechanism of the unexpected beam loss was identified as the Intra Beam Stripping (IBSt) process [2,3]. This explained our success in the loss reduction, but it did not give us the model-based control over the beam sizes in the SCL. This paper describes our path in developing such a model-based SCL optics control.

In the present paper we are going to describe three basic components that allowed us to successfully benchmark the model against the measured SCL beam parameters. First, we developed a procedure to measure the initial transverse Twiss parameters with acceptable accuracy. Second, we speeded up the SCL RF cavity tuning process and improved the accuracy of the phase scan data analysis. Finally, we developed an original method of measuring the longitudinal Twiss parameters based on the Beam Position Monitor signals.

† shishlo@ornl.gov

SNS SCL DIAGNOSTICS

In contrast to normal conducting linacs, the SNS superconducting linac is not allowed to have insertable destructive beam diagnostic devices to avoid surface contamination of the SCL cavities. Instead of wire scanners the SCL has 9 laser wire (LW) profile monitors [4]. As shown in Fig. 1, four of them are placed at the beginning of each of two (medium and high beta) sections, and the last one is at the end of SCL.

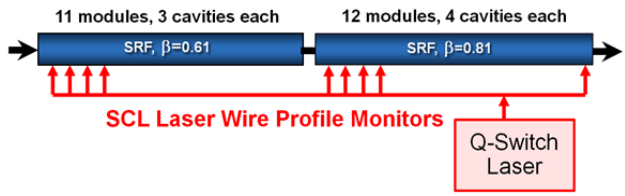

Figure 1: Positions of the 9 laser wire stations in the SNS SCL.

The LW system distributes the laser beam to intercept the H^- ion beam, which removes the second electron. This creates neutral hydrogen, which will be eventually lost inside the SCL. The photo-detached electrons are collected, and their total charge is measured [4]. This signal is proportional to the density of the ion beam. By using a system of mirrors the laser beam can be moved in vertical and horizontal directions providing the ion beam profiles in both planes. The amount of beam loss created by the LW system is negligible, and it can be used even during 1 MW operations.

In addition to the LW system, the SCL has 32 stripline beam position monitors (BPMs) installed along the linac between cryomodules and in the cavity-free part of SCL. The BPMs measure the transverse positions of the beam, the arrival phases of the H^- bunches, and the amplitudes of the 402.5 MHz harmonics (the bunch frequency) of the sum of all four stripline quadrant signals. This amplitude signal can be used for beam peak current measurements or for a longitudinal Twiss parameter analysis, as will be shown below.

The SNS superconducting linac also has a distributed system of Beam Loss Monitors (BLMs), but we are not going to discuss beam loss related issues in this paper.

BEAM TRACKING MODELS

Several accelerator codes were used for the SCL data analysis. Two codes used in the first SCL transverse matching attempt [5] were a "Particle In Cell" (PIC) code IMPACT [6] and an "envelope" tracking Online Model (OM) from the SNS programming infrastructure XAL [7].

ISBN 978-3-95450-185-4

The problem with using the IMPACT code was a long calculation time needed for analysis [6]. It took tens of hours to calculate the initial transverse Twiss parameters from the four first LW profiles. Therefore, IMPACT could be used only for offline analysis, which was difficult to combine with biweekly accelerator physics study time and with conditions in the warm (upstream) part of the linac changing daily to keep beam loss and RF systems tripping rate low.

The Online Model is an envelope tracking accelerator code similar to TRACE3D. The OM tracks the envelope parameters through the SCL lattice using transport matrices for each quadrupole, for each RF gap in the accelerating cavities, and for each drift space. The space charge kicks are accumulated in the total transport matrix describing the transformation of the envelope from the beginning to an arbitrary point in the SCL. The parameters of the lattice, such as the quadrupole field gradients, are synchronized with the control system. The field gradients and phases of the superconducting cavities should be supplied to the model after an analysis of the SCL phase scans.

It takes only a few minutes to analyse LW data at the beginning of the SCL with the Online Model, but for a long time we could not get agreement between this model and the full set of LW data [5]. At that time, the OM was considered to be inappropriate to track beam parameters through the whole SCL. In [5] it was also stated that there is a difference in matching parameters predicted by the IMPACT and the OM codes. Later we found that these differences are caused by parameters of the RF system used by each model. If we use consistent parameters in the models the results will be the same. The Fig. 2 shows the benchmark of the Online Model with the PyORBIT code, which is another PIC code developed at SNS.

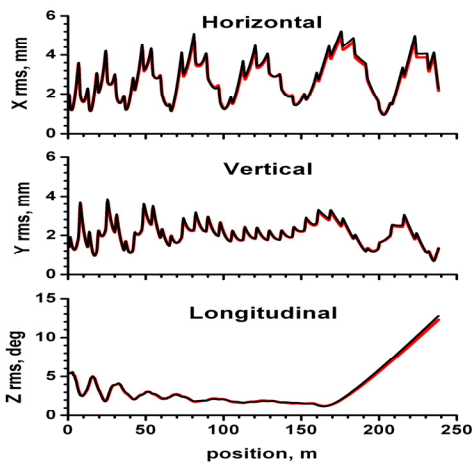

Figure 2: RMS sizes of the beam along the SNS superconducting linac. The black curve is for the PyORBIT code, and the red is for the OpenXAL Online Model.

Because of its nature the OM is more convenient than the PIC based codes for RMS size analysis. Of course we must always be vigilant regarding the linearity of all elements in the lattice and possible envelope instabilities. Fortunately the SNS SCL is a good example of this type of lattice. All analysis described in this paper was performed by using the OpenXAL Online Model.

TRANSVERSE TWISS PARAMETERS

For PIC codes the initial Twiss parameters are found by using the general non-linear fitting method to reproduce RMS sizes from the multiple profile measurements. To find the Twiss by using the Online Model we use a more direct technique described in [8]. Let's consider one plane. The transformation coordinates of the particle between the beginning of the lattice and the profile measurement device are defined by the transport matrix from OM

$$\begin{pmatrix} x_1 \\ x_1' \end{pmatrix} = \begin{pmatrix} m_{1,1}^{(1)} & m_{1,2}^{(1)} \\ m_{2,1}^{(1)} & m_{2,2}^{(1)} \end{pmatrix} \cdot \begin{pmatrix} x_0 \\ x_0' \end{pmatrix} \qquad (1)$$

where x and x' are the transverse coordinates of the particle at the initial and LW position points, and m is the transport matrix between these points.

By squaring of both sides of the first equation of the system (1) and averaging over the whole ensemble of particles in the bunch, we have the expression for the squared RMS beam size

$$\left\langle x_1^2 \right\rangle = m_{1,1}^{(1)2} \left\langle x_0^2 \right\rangle + 2m_{1,1}^{(1)} m_{1,2}^{(1)} \left\langle x_0 x_0' \right\rangle + m_{2,2}^{(1)2} \left\langle x_0'^2 \right\rangle$$

By using several profile monitors or modifying the optics of the lattice we can get as many different transport matrices and equations for the RMS beam sizes as we want (let's say N). Combining the all equations we get the following matrix equation for our problem

$$\begin{bmatrix} \left\langle x_1^2 \right\rangle \\ \cdots \\ \left\langle x_N^2 \right\rangle \end{bmatrix} = \begin{bmatrix} m_{1,1}^{(1)2} & 2m_{1,1}^{(1)} m_{1,2}^{(1)} & m_{2,2}^{(1)2} \\ \cdots & \cdots & \cdots \\ m_{1,1}^{(N)2} & 2m_{1,1}^{(N)} m_{1,2}^{(N)} & m_{2,2}^{(N)2} \end{bmatrix} \begin{bmatrix} \left\langle x_0^2 \right\rangle \\ \left\langle x_0 x_0' \right\rangle \\ \left\langle x_0'^2 \right\rangle \end{bmatrix}$$

This is a typical linear Least Square Problem with the measured RMS sizes on the left side and the unknown initial beam correlation parameters on the right side. The solution gives the Twiss parameters and their errors if the RMS size errors are known [8].

The described algorithms should work directly if there is no space-charge force in the bunch dynamics. In the presence of space charge the transport matrices will be dependent on the initial Twiss parameters for the longitudinal and transverse directions, and on the beam peak current. As for the longitudinal Twiss parameters, we can blindly use the design parameters, or we can use methods described in this paper later. For the transverse parameters the transport matrix dependency makes the equations transcendental, and there is no exact analytic solution for them.

To find the initial Twiss parameters in the presence of strong space charge a two-step method was used. In the first step, a general nonlinear fitting package was used to

ISBN 978-3-95450-185-4

find the parameters that reproduce the measured profiles with minimal deviations. Then the transport matrices generated by the OM for these initial Twiss parameters were used in the matrix equation to get a new set of these parameters and their error estimation. If these two sets were close enough assuming their errors, we concluded that the problem was solved. This method does not guarantee a unique solution, because the fitting routine can find several local minima. This situation can be resolved by increasing the number of measurements with the lattice configurations providing the reduced errors. These additional measurements should be planned ahead by using the preliminary estimation for the initial Twiss. The rule of thumb from Ref. [8] is a $90^0/(N-1)$ betatron phase advance between each measurement. The exact effect of each additional measurement should be estimated. Unfortunately in general even these measures cannot guarantee a uniqueness of the solution and correctness of the error estimation. However, this should not stop us from trying this approach.

Based on the described algorithm we re-analysed the LW data from our previous measurements in [5] and found that we had bad optics for the Twiss parameter analysis, and errors for the parameters were too big to make them useful for the Online Model. Later we performed a series of measurements with different optics settings for the first four LW stations in the SCL. To be confident we eliminated the space charge effect by attenuating the beam right after RFQ, and switching off all RF cavities in the first four cryomodules. The result of comparison between LW data and the OM simulations is shown in Fig. 3.

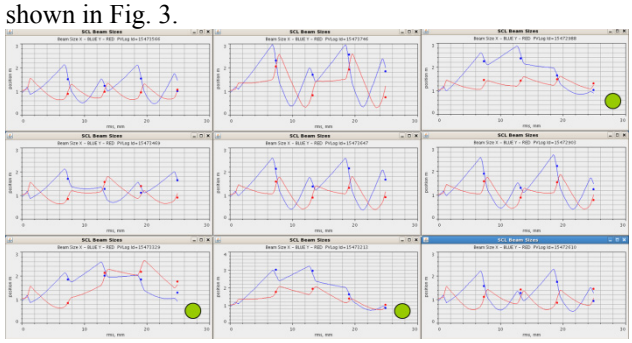

Figure 3: RMS sizes of the beam in the first four cryomodules. The blue/red color is for horizontal/vertical sizes. Points are for LW measurements, and curves are results of the XAL Online Model.

Figure 3 shows the RMS beam sizes for 9 different combinations of quadrupole fields between the first 4 SCL cryomodules. Three of these combinations use optics that follow the Twiss parameters error minimization rules, and they are marked by green dots. These measurements were used to find the initial Twiss that was used for the rest of the random quad settings. Figure 3 demonstrates that the XAL Online Model can be successfully used for the initial Twiss measurements, and the laser wire stations give us the correct RMS sizes of the beam. It also points out that to use the Online Model for the production optics, we have to pay attention to other parameters of the OM, such as the RF parameters and the initial longitudinal Twiss (to treat the space-charge effects correctly).

RF CAVITY PARAMETERS IN THE SCL

To perform realistic simulations with the Online Model we have to specify the correct field gradient and phase for each RF cavity in the SCL. Each SCL cavity in the OM is a combination of six accelerating gaps. The phase of the cavity's model is defined as the phase of the synchronous particle at the first cavity's gap. Until recently to get correspondence between the cavity model parameters and the live machine we used a cavity phase scan. This involves collecting the phases of two BPMs right after the cavity. During the scan the cavity phase changes from -180^0 to $+180^0$, all downstream cavities have the RF pulse blanked so they will not affect the beam, and the number of bunches in the pulse train is limited to about 200 to avoid beam loading of the cavities.

The phase of the beam measured by the BPM is defined by the time of arrival (the distance divided by the velocity)

$$\varphi_{BPM}^{(i)} = \Delta\varphi_{RF}^{(i)} + \frac{z^{(i)}}{\beta c}\cdot\omega_{BPM} \quad i = 1,2 \qquad (2)$$

where β, $z^{(i)}$, ω_{BPM}, $\Delta\varphi_{RF}^{(i)}$ are the relativistic parameter of the beam and the position, frequency, and phase offset relative to the RF synchronization line of the BPM, respectively.

For two synchronized BPMs (with the same phase offset) the velocity (and the energy of ions) of the beam can be found directly from the measured BPM phase difference. Comparing the measured and simulated BPM phase difference as a function of the cavity phase we find the model parameters. This method had a drawback. The two BPMs must be synchronized, which requires the BPMs' electronics to be located in the same crate, and limits distance between them in the lattice. This can lead to relatively big errors in the RF model parameters.

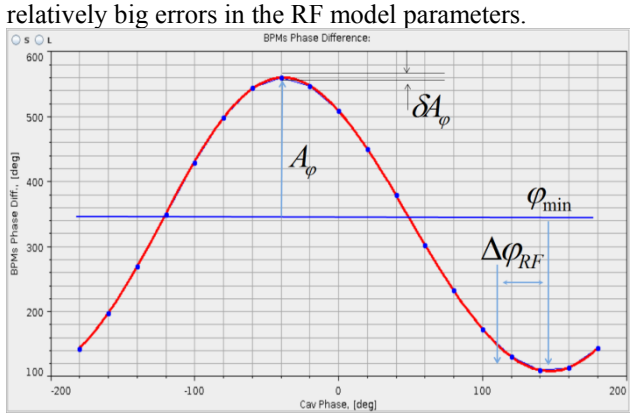

Figure 4: BPMs' phase difference vs. SCL cavity phase. Points are measured values and the curve is a result of the XAL Online Model.

Figure 4 shows a typical picture of the cavity phase scan results. The cavity phase for maximal acceleration (see $\varphi_{\min}$ in Fig. 4) is defined by the minimal difference

ISBN 978-3-95450-185-4

between BPMs phases. The error in this parameter is defined by

$$\delta\varphi_{\min} \approx \frac{1}{\sqrt{N}} \frac{\delta A_\varphi}{A_\varphi} \approx \frac{1}{\sqrt{N}} \frac{\delta\phi_{BPM}}{A_\varphi} \quad (3)$$

where N, A_φ, $\delta\phi_{BPM}$ are the number of cavity phase points, the amplitude of the "sine"-like curve in Fig. 2, and the BPM phase measuring error respectively.

In turn A_φ is defined by the distance between BPMs Δz, the relativistic beam parameters γ and β, and a maximal energy that the cavity can give to the beam $\Delta E_{\max}$

$$A_\varphi \approx \Delta z \cdot \frac{1}{(\gamma\cdot\beta)^3} \cdot \Delta E_{\max} \quad (4)$$

The formula (4) shows that to reduce the error in the cavity phase settings, it is better to use two distant BPMs even sacrificing the synchronization between them.

Eventually we developed a three stage SCL RF settings process:

- First, we scan the phase of the SCL cavities one by one, recording phases of all BPMs. For each cavity we set the phase by subtracting the design synchronous phase from the maximal acceleration phase (see Fig. 4). The phase scan curve is approximated by a two harmonics function. At this stage we do not need the model and synchronized BPMs.
- Second, after completing the phase scans we send beam into the SNS ring and use it as a device to measure the energy. After the final beam energy is known we analyse the BPMs' phase offsets in (2) for all BPMs after the last RF cavity. Then we track these offsets upstream in the SCL analysing the whole scan data. We do need the model at this stage, but at the end we have all BPMs synchronized (phase offsets are known) and ready to use in the model-based analysis. The BPMs' phase offsets calculated during this stage can be saved and used in the future.
- In the last stage we use the scan data with synchronized BPMs to get the model RF parameters for each cavity. The initialized model allows us to retune the SCL linac in a matter of seconds in the case of emergency when, for instance, one of the cavities should be shut down.

The process described above was automated by implementation into an OpenXAL application called "The SCL Tuner Wizard". Automation eliminated possible human errors and sped up the scan procedure. Today it takes about 40 minutes to tune the SCL RF system and to initialize the Online Model compared to about 8 hours in the past.

One of the useful features of the SCL Tuner Wizard is its ability to perform a "non-destructive" scan of an existing configuration. In these types of scans we perform all phase scans as usual, but at the end we do not set new phases to the cavities. We just keep the phase that we had. The rest of analysis is performed as usual. These "non-destructive" scans were used to analyse the 1 MW production tunes when all RF settings, including the SNS normal conducting linac, were considered as "fair game" to reduce the beam loss in the SCL. Fig. 5 shows the synchronous phases of the cavities for one of the 1 MW production settings. In Fig. 5 we see that the real cavity phases in the SCL are far from the initially set -18^0, which would be used in the transverse size matching procedure without the aid of the fast "non-destructive" scan. This factor was another contribution to our failure to perform SCL beam matching in the past.

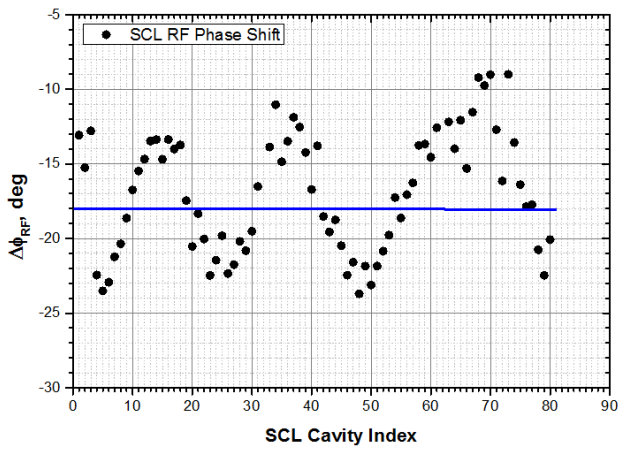

Figure 5: The synchronous phases of the SCL cavities on 2014.03.04. The points are measured phases, and the blue line defines -18^0 phases that were set before the beam loss reduction linac parameter tweaking.

MEASUREMENTS OF INITIAL LONGITUDINAL TWISS PARAMETERS

To correctly account for the space-charge effects in the OM model we have to know the longitudinal RMS bunch size along the entire SCL. The realistic SCL RF cavity parameters will allow the model to track the longitudinal size through the SCL if we know initial longitudinal Twiss parameters. At SNS we developed an original method to measure these parameters based on the BPM signals [9]. One of the BPM signals in SNS is proportional to the amplitude of the harmonics of a summed beam signal from all four stripline electrodes. The frequency of the harmonics is called the BPM frequency. This signal is defined by the formula

$$u_\omega = C \cdot J_\omega / I_0(\omega R/(\beta\gamma c)) \quad (5)$$

where C is a calibration constant, J_ω is an amplitude of the beam current harmonic at the BPM frequency ω; R is the radius of the pickup aperture; c is the speed of light; β and γ are relativistic factors; and I_0 is the modified Bessel function.

In the case of a Gaussian longitudinal bunch density distribution the J_ω is defined by the longitudinal RMS length of the bunch s_z

ISBN 978-3-95450-185-4

$$J_\omega \approx \exp(-(\omega \cdot s_z)^2 / 2) \quad (6)$$

According to formulas (5,6) the BPM amplitude signal can be used to measure the longitudinal bunch length if we calibrate the BPMs. Considering BPMs as analogues of wire scanners and RF cavities as "quadrupoles" acting in the longitudinal phase space, we used the algorithms described for the transverse directions to find the Twiss parameters at the entrance of each RF cavity [9].

Figure 6 shows the RMS bunch length along the SCL measured for the 1 MW production RF and quadrupole settings. This picture demonstrates that longitudinally we have un-matched beam, which also was not expected in our matching attempts in the past.

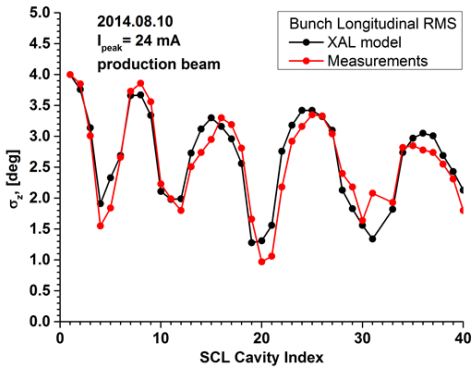

Figure 6: The RMS bunch length along the SCL. Measurements were performed by using the method described in [9].

XAL ONLINE MODEL BENCHMARK

Eventually all three components of the Online Model initialization (transverse and longitudinal Twiss parameters and the SCL RF settings analysis) were integrated into the OpenXAL SCL Tuner Wizard application. It allowed obtaining consistent measurements for offline analysis. Fig. 7 shows a snapshot of the application with a benchmark between the Online Model and a set of Laser Wire data for all 9 stations. As we can see, the agreement between the Online Model and measured data is much improved. Therefore, we can declare a victory and can say that we are ready to try matching in the SCL again. Now it will be based on the benchmarked OpenXAL Online Model.

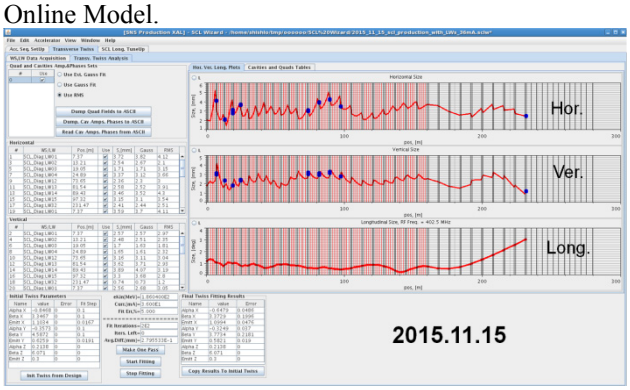

Figure 7: Snapshot of the SCL Tuner Wizard application with the LW measured beam RMS sizes along the SCL as blue dots and red lines as results of Online Model simulations.

CONCLUSION

The successful benchmark of the OpenXAL Online Model was performed with transverse RMS beam sizes measured by the Laser Wire stations in the SNS superconducting linac. It has been achieved by careful measurements of the lattice and beam parameters for the model initialization. The successful model benchmark opens an opportunity for another attempt of beam matching in the SNS SCL.

ACKNOWLEDGMENT

This manuscript has been authored by UT-Battelle, LLC, under Contract No. DE-AC0500OR22725 with the U.S. Department of Energy. This research was supported by the DOE Office of Science, Basic Energy Science, and Scientific User Facilities. The United States Government retains and the publisher, by accepting the article for publication, acknowledges that the United States Government retains a non-exclusive, paid-up, irrevocable, world-wide license to publish or reproduce the published form of this manuscript, or allow others to do so, for the United States Government purposes. The Department of Energy will provide public access to these results of federally sponsored research in accordance with the DOE Public Access Plan (http://energy.gov/downloads/doe-public-access-plan).

REFERENCES

[1] S. Henderson *et al.*, NIM A, Vol.763 (2014), pp 610-673.

[2] V. Lebedev *et al.*, "Intrabeam Stripping in H^- Linacs," in *Proc. LINAC'10*, Tsukuba, Japan, September 12-17, 2010, pp. 929-931.

[3] A. Shishlo *et al.*, Phys. Rev. Lett. 108, 114801 (2012).

[4] Y. Liu *at al.*, Phys. Rev. ST Accel. and Beams 16, 012801 (2013).

[5] Y. Zhang, "Experience and Lessons with the SNS Superconducting Linac", in *Proc. IPAC'10*, Kyoto, Japan, (2010), pp. 26-30.

[6] J. Qiang *et al.*, J. Comp. Phys., Vol.163 (2000) 434.

[7] J. Galambos, *et al.*, "The SNS Application Programming Infrastructure", in *Proc. EPAC'04*, Lucerne, Switzerland, (2004), pp. 2855-2857.

[8] M. G. Minty, F. Zimmermann, "Measurements and Control of Charged Particle Beams", Springer-Verlag Berlin Heidelberg 2003, "Particle Acceleration and Detection" series. p. 104.

[9] A. Shishlo, A. Aleksandrov, Phys. ST Accel. and Beams 16, 062801 (2013).

ISBN 978-3-95450-185-4

HPSIM - ADVANCED ONLINE MODELING FOR PROTON LINACS*

L. J. Rybarcyk†, Los Alamos National Laboratory, Los Alamos, NM, 87545, USA

Abstract

High-power proton linacs seek to operate with low and stable losses. This aspect is carefully evaluated with multi-particle beam dynamics codes during the design stage. However, it is just as important to evaluate the performance of the actual operating linac, which is typically more tedious and complicated when using these same design codes. To improve this situation, we have developed a high-performance, multi-particle online modeling tool, HPSim, with the goal of providing near real-time simulation results for our 800-MeV proton linac at Los Alamos. This presentation will cover the motivation, code features, benefits and applications.

INTRODUCTION

High-power linacs, like the 800-MeV proton linac at the Los Alamos Neutron Science Center are designed and operated to achieve low and stable beam loss. During the accelerator design phase, envelope and multi-particle codes, such as TRACE 2-D & 3-D [1], PARMILA [2], TRACK [3], TRACEWIN [4], and others are used to create the linac layouts and evaluate them for losses. While the envelope codes are being used as online models for the operating machines, the multi-particle codes, until very recently [5], have not. This has been due in part to a combination of performance and computer resource issues associated with using these codes in a control room setting.

The typical multi-particle code, like those mentioned above and others, e.g. IMPACT [6], etc. used to successfully simulate proton beams in linacs, offer benefits and advantages not available from an envelope code. However, using these to simulate beam in an operating linac can be tedious and complicated. This is because all of the relevant beam and machine parameters and settings for a *single snapshot* of the operation must be transferred to the input format used by the code. Only then can a simulation be performed from which results can be compared to measurements under those same conditions.

Routine use of accurate online multi-particle simulations to setup, track and study performance of an operating linac would be beneficial. This is especially true for new and existing high-power linacs where detailed knowledge of the beam distribution along the linac can provide new insight into issues that produce beam spill. HPSim was developed for this purpose.

MOTIVATION

The LANSCE accelerator utilizes both proton and H- beams and delivers them to several user facilities for basic and applied research. The pulsed accelerator operates with a typical maximum beam duty factor of 120 Hz x 625 μs for each species. Initially, the beams are accelerated to 750 keV using Cockcroft-Walton (C-W) style injectors. The high-current DC beams are subsequently bunched prior to injection into our 201.25-MHz 100-MeV drift tube linac (DTL) using two 201.25 MHz single-gap cavities. This scheme enables us to routinely achieve ~80% longitudinal capture of the standard proton and H- beams. However, this approach also results in significant longitudinal tails on each beam. These tails are clearly seen in the simulated longitudinal phase space of the proton beam at the entrance and exit of the DTL, as shown in Figure 1. To operate the DTL in a manner that produces the lowest beam spill along the entire side-coupled cavity linac (CCL) and further downstream, operations staff have found a new set of phase and amplitude set points for the DTL that are significantly different from design. The phase and amplitude set points of the DTL were empirically determined over years of high-power (800 kW) beam operation and are similar even under today's ~100 kW operation.

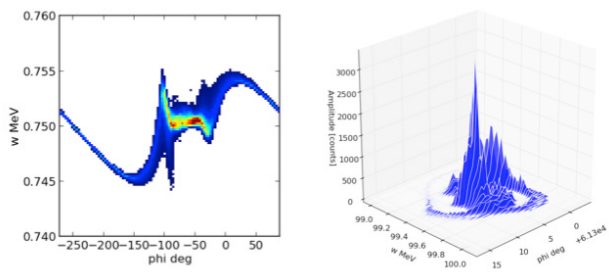

Figure 1: Simulated longitudinal phase space distributions for the LANSCE proton beam at the entrance (left) and exit (right) of the DTL.

The annual tune-up process for the LANSCE linac involves the typical physics-based approach of using envelope and previously established single- and multi-particle model results to determine good starting points for focusing magnets and accelerator modules along the linac. Once this phase is complete, the process becomes much more empirical and the operators resort to tweaking many of the newly established RF set points in order to further reduce beam loss along the accelerator. This is the same approach used at many other accelerator facilities as mentioned in a previous HB workshop [7].

Our first-hand experience, as well as those at other similar facilities, motivated us to develop HPSim. The existing envelope and single-particle models cannot provide the needed insight into the actual beam distribution expected from a particular set of accelerator operating set points. However, to be effective in an accelerator control room setting, the code needs to be fast and accurate with the ability to access the control system to minimize the

* Work supported by the United States Department of Energy, National Nuclear Security Agency, under contract DE-AC52-06NA25396.
†lrybarcyk@lanl.gov

ISBN 978-3-95450-185-4

overhead of setting up the simulation. HPSim meets these requirements.

HPSIM

The new **H**igh-**P**erformance **Sim**ulator, HPSim, was developed as a new stage in online modeling and simulation of proton linacs. It is designed to provide more accurate beam dynamics simulations than the envelope model, faster performance than typical multi-particle simulations that run on desktop workstations, and utilize a connection to the accelerator's EPICS [8] control system.

Physics Model

The physics model used in the code is derived from the PARMILA (Phase And Radial Motion in Ion Linac Accelerators) linac design and simulation code. PARMILA is a well-established tool that has been used in the community for decades and was used to design and/or simulate the LANSCE, SNS and other linacs. It is multi-particle in nature and presently uses a 2D r-z particle-in-cell (PIC) algorithm to produce the nonlinear space-charge force on the beam macroparticles in the bunch. It is a "z code" that employs transfer maps in the beam transport regions. The particle transformation across the rf gap is represented as a "drift + kick-at-the-midplane + drift" and uses the transit-time-factor formulation [9]. It has been compared and benchmarked against other codes and shown to be in good agreement [10].

HPSim, however, has some notable differences. First, it was written to only simulate beam in ion linacs and does not produce a design. The layout must be generated by another code, e.g. PARMILA for the linac geometry and design field information and SUPERFISH [11] for the cell-data and transit-time-factors for each rf gap. Second, to better and more easily simulate real world, non-ideal linac operation, it keeps track of the particles' absolute phase, which is essential when tracking particles in scenarios where an intermediate accelerating section of the linac is operationally turned-off. An example would be when a superconducting section of the linac is taken offline and the downstream module set points adjusted to restore acceleration for maximum available energy, which is done at SNS. Another example, from LANSCE, when delivering beam at an intermediate CCL output energy, one or more downstream modules can be repurposed to bunch the beam and reduce the phase spread of the final beam for neutron time-of-flight experiments. Third, transit-time-factors can be functions of β to be more accurate for particles that are off-energy in an rf-gap. Fourth, the space-charge routine focuses on particles that are in the bucket, to improve the simulation where sizable off-energy beam is present. Fifth, the space-charge algorithm employs a scaling feature that allows the previously calculated field table to be reused when the beam is not too different in energy or size. This improves the performance without a noticeable degradation in accuracy in situations where these quantities are changing slowly between successive space-charge kicks, e.g. in our CCL.

Presently, HPSim supports several standard ion linac elements. Quadrupole focusing magnets use the hard-edge model with a single space-charge kick in the middle. Steering magnets are impulse correctors. Empty spaces are simple drifts with an overall user defined maximum interval between space-charge kicks. A buncher cavity is a single RF gap. A DTL or CCL RF cell is a single gap with a space-charge kick in the middle. The DTL structure is an Alvarez style with quad magnets in the drift tubes. The CCL structure comprises multicell tanks with quad magnets located in between them. It also supports circular and rectangular transverse apertures and a space-charge compensation factor that is used to reduce the effective current in the beam where neutralization is present.

GPU Accelerated

Our goal was to have HPSim be fast enough to perform a simulation in seconds to a small fraction of a minute and be available 24/7 in the LANSCE control room. The cost was also a consideration. This led us to choose state-of-the-art graphics processing unit (GPU) hardware to achieve the desired performance and availability at minimal cost. Although GPU technology was developed for the gaming industry, its power is now being harnessed for scientific computations, e.g. the ORNL Titan, one of the world's fastest supercomputers. In addition, to take full advantage of the GPU power, HPSim was developed from scratch, using a modern programming approach.

The GPU technology is also very cost effective. A single NVIDIA Tesla K20c has 2496 CUDA cores, 5 GB RAM with peak double/single precision performance of 1.17/3.52 Tflops and a street price of ~$3K US.

HPSim Code Design and Performance

Code Design The code design was developed with the philosophy that it should be fast enough for a control room setting and yet easy to use with the same control interface as the actual machine. This led us to create a code with several distinctive aspects. First, the number crunching simulation kernels are written in NVIDIA CUDA C and C++, which take full advantage of the GPU's performance [12]. Details of the implementation are given elsewhere [13]. Second, the user interface is available as Python/C APIs for ease-of-use, which hides all the complex code from the user's experience and enables one to communicate with the code through powerful, yet easy to use, Python scripts. This also allows the user to take advantage of the extensive collection of numerical and visualization libraries available for Python. The hierarchical structure of the code is shown in Figure 2. Third, since the linac design is fixed and the model is meant to be controlled through the same variables as that of the real machine, the representation of the linac and control parameters all reside in a database.

The code is divided into several major components, which reside on either the CPU(host) or GPU(device), as shown in Figure 3. A data server is used to acquire real machine parameter data via EPICS and update a flat-file

ISBN 978-3-95450-185-4

like serverless SQLite database. The database contains the linac design, as well conversion rules and calibration quantities required to transform each control parameter engineering value into a calibrated physics model quantity. The database provides the beamline model that is written to special CPU-side memory, aka "pinned", that can be efficiently accessed by the GPU. To maximize performance, the beam distribution is created and resides on the device, as do all the simulation kernels that represent the element transformations and space-charge algorithms. In the online mode, output from the simulation is then produced in graphical form using OpenGL as either 2D quantitative plots or a 3D particle distribution along the linac. In the offline mode, Python modules are available to analyze and plot the beam results.

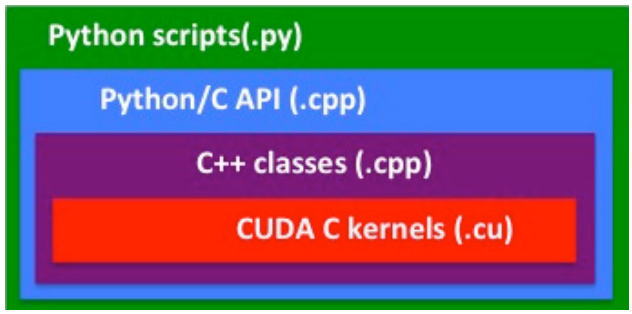

Figure 2: Hierarchical structure of HPSim code.

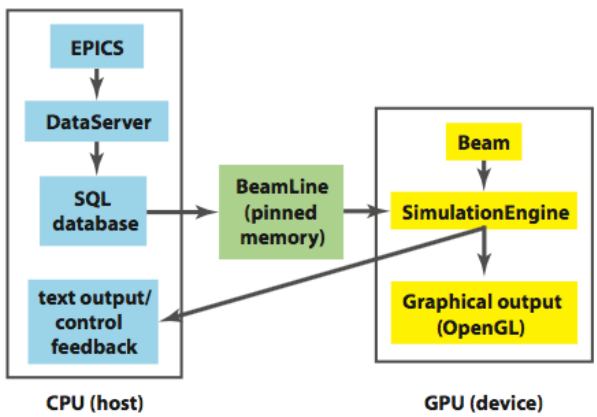

Figure 3: High-level code structure and data flow indicated by arrows.

Code Performance The performance of HPSim exemplifies the speedup possible when employing GPU technology. A comparison of code performance was made on same-era hardware, i.e. an Intel Xeon E5520 2.27 GHz CPU and an NVIDIA GTX 580 GPU (Fermi architecture). We observed a maximum speedup of ~160 for beam transported without space-charge and ~45 for the space-charge routine alone.

The performance in simulating the LANSCE linac is very impressive and is based upon a single NVIDIA K20c GPU in a Linux workstation. Starting with a DC waterbag beam distribution of 64K macro-particles located in the 750-keV low-energy-beam-transport (LEBT) and transporting them up to the end of the 800-MeV CCL takes ~5.5 seconds. This problem space is ~800 m in length and contains over 5100 RF gaps, 400 quads and 6000 space-charge kicks.

Model Calibration

The model must be calibrated for a meaningful and accurate prediction of beam in the linac. All necessary calibration information is held in the database. This enables control set points to be transformed on the fly into physics quantities in the model. Typical devices that require calibration are focusing and steering magnets and rf bunchers and accelerating modules (combination of accelerator cavities/tanks driven by a single amplifier). At LANSCE, EPICS provides engineering quantities associated with the devices that power/control the accelerator and beamline components. These EPICS values, e.g. power supply current (amps) that drives a quadrupole magnet, LLRF cavity phase (degrees) and amplitude (a.u.) set points are then converted to physics model quantities, e.g. quadrupole gradient (T/m), and accelerating cavity phase (deg) and amplitude E0 (MV/m), respectively.

The magnet calibrations are typically done offline in a mapping facility where integral field measurements versus current are made. These calibration curves are stored in the database.

The buncher cavity field amplitude calibration can also be done offline. Using a combination of EM cavity field modeling results to determine the theoretical E_0TL, Q_u and P_{cav} and measurements of the cavity Q along with amplifier output power vs. amplitude set point will produce the effective gap voltage vs. amplitude set point. A beam-based measurement can then be used to determine the phase offset that calibrates the cavity phase with respect to the other rf devices in the linac.

The accelerator modules must be calibrated with beam-based measurements, from which cavity field phase offsets and amplitude scale factors are determined. The measurements that are used at LANSCE are phase scans. The location and width of the phase scan distributions are related to the cavity phase and amplitude, respectively. For the DTL and LEBT bunchers the phase scan procedure measures the beam current of particles with energies above a specified threshold as a function of the phase setting of the tank or buncher being scanned. The measured and simulated distribution produced by scanning LANSCE DTL module 1 with only the last (main) LEBT buncher on is shown in Figure 4. It should be noted that reproducing these kinds of measurements is not possible with a single particle or envelope code. For the CCL, the phase scan is based upon beam phase measurements versus module phase. Fitting the data also provides a field phase offset and amplitude scale factor for each module. The measured and simulated phase scan results for the first module of the CCL are shown in Figure 5.

Online & Offline Modes

HPSim functions in two different modes. In the online mode, a stand-alone executable that uses a predefined input beam runs in a continuous loop. As the actual machine parameters are adjusted, the data server copies the

ISBN 978-3-95450-185-4

updated values into the SQLite db. At the start of each pass, the updated model values are placed into pinned memory. This allows the simulation to automatically track the changes in the machine parameters and reflect them in the simulation results. The graphical 2D display is updated after each pass and includes quantities like output beam phase space distributions and profiles and rms widths, emittances and loss profiles along the linac. The EPICS data can also be obtained from a soft IOC, which is a stand-alone copy of the machine parameters and not actually tied to the operating machine hardware.

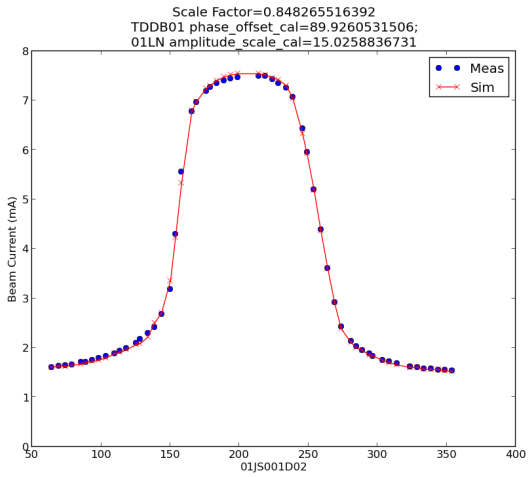

Figure 4: Measured and simulated phase scan of LANSCE DTL tank 1.

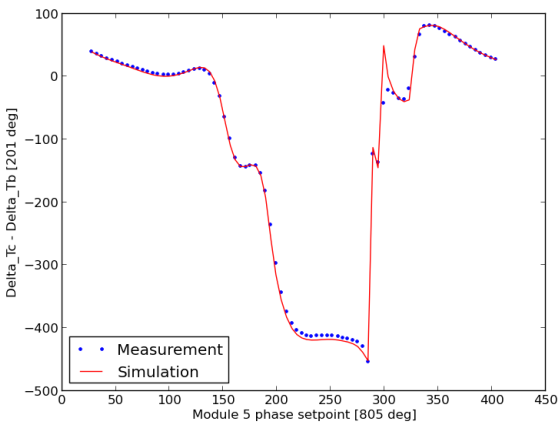

Figure 5: Measured and simulated phase scan of the first LANSCE CCL module.

HPSim can also be operated in an offline mode. This is valuable for the calibration activities that require additional analysis, e.g. fitting. In this mode, the user interacts with the code via Python scripts. HPSim is simply meant to simulate the beam from point A to point B in the linac under specified operating condition. All post-processing is done on the output beam with user-created Python scripts. This approach also gives the user the freedom to explore new ideas in tuneup and operation without the need to modify the HPSim lower-level code directly.

Applications

Machine Tuning and Monitoring The original motivation for creating HPSim was to provide the operations staff with a fast and more realistic beam simulation tool that would help with the tune-up and operation of the LANSCE linac. In this regard, it can function as a virtual beam diagnostic, providing information where none is available. This is especially helpful in high-power linacs, where measurements may not be possible due to the interceptive or deleterious nature of many beam diagnostics. Figure 6 is an example of the 2D online mode showing beam along and out of the LANSCE CCL. During typical operations, the machine parameters are adjusted to minimize beam losses. HPSim could provide additional insight into the source of the beam spill.

Machine Set Point Optimization In an operating linac, set point optimization with regard to a desired state is usually done leading up to and following the transition to high power. The process involves physics model based setup followed by empirically searching a high-dimensional parameter space for optimal values. The offline mode of HPSim works well for this application. Using HPSim in offline mode with the multi-objective particle swarm optimization (MOPSO) and multi-objective genetic algorithm (MOGA), we were able to determine a set of buncher and DTL RF phase and amplitude set points that produce less beam loss and smaller beam emittances in simulation than operating at design set points [14]. Although this exact solution has not yet been experimentally verified, the optimized DTL RF cavity field amplitudes are in fact very close to the typical operating levels.

Virtual Accelerator and Test Bed The simulator can also serve as a virtual accelerator providing a test bed for evaluating new approaches and techniques for the linac where realistic beam information or control of the machine set points is desired. An example that was tested with the simulator was a model-independent automatic accelerator tuning method [15]. This real-time control method enables simultaneous tuning of several parameters, even where coupling is present, to achieve good beam quality. Having HPSim available allowed the initial successful demonstration of this technique to proceed without the risk to the machine or commitment of accelerator resources, i.e. development time and expense.

STATUS AND FUTURE PLANS

To date, HPSim has been used for offline studies and model calibrations of the LANSCE linac, as well as in a few isolated troubleshooting efforts in the accelerator control room. During its development, the code has been thoroughly tested against PARMILA and also compared with various experimental measurements. It will be further incorporated into the LANSCE startup later this year. In addition, we are planning to make HPSim available as

ISBN 978-3-95450-185-4

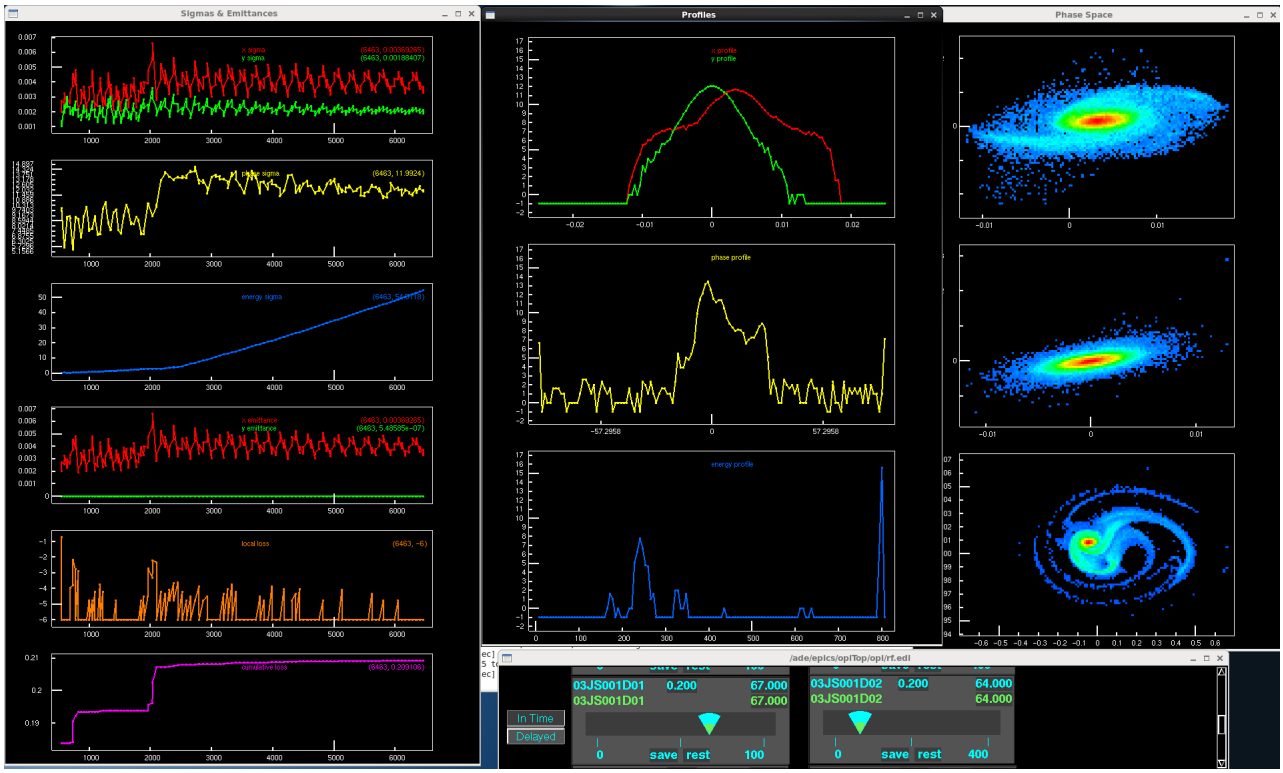

Figure 6: Screen shot of HPSim 2D online graphical output of H- beam transported along the LANSCE CCL. The display includes beam rms widths, emittances, and losses (left), output beam profiles (center) and output beam phase-space distributions (right). The EPICS sliders for DTL Tank 3 amplitude and phase controls are shown at the bottom.

an open source code for the benefit of the wider accelerator community.

ACKNOWLEDGEMENT

The author would like to thank his colleague, Dr. Xiaoying Pang, who has been instrumental in the development of the new HPSim online modeling tool, Scott Baily for providing EPICS support and Bob Garnett and the AOT Division leadership for their support of this work.

REFERENCES

[1] K. R. Crandall, D. P. Rusthoi, "TRACE3D manual," 3rd Ed., LANL publication, LA-UR-97-886, (1997).
[2] H. Takeda and J.H. Billen, "PARMILA," LANL publication, LA-UR-98-4478, (Revised 2005).
[3] B. Mustapha et al., "TRACK: The New Beam Dynamics Code," PAC 2005, Knoxville, Tennessee, May, 2005, TPAT028, p. 2053 (2005); http://www.JACoW.org
[4] TRACEWIN web site http://irfu.cea.fr/Sacm/logiciels/index.php
[5] C. E. Peters et al., "Integration of the TRACK Beam Dynamics Model to Decrease Linac Tuning Times," ICALEPCS2015, Melbourne, Australia, Oct. 2015, MOPGF092, p. 291, (2015).
[6] J. Qiang et al., "An Object Oriented Parallel Particle-In-Cell Code for Beam Dynamics Simulation in Linear Accelerator," Journal of Computational Physics, 163, pp. 434-445, (2000).
[7] J. Galambos et al., "Summary of the Commissioning, Operations and Performance Working Group of the HB-2010 Workshop," HB2010, Morschach, Switzerland, Sept. 2010, FROP04, p. 703, (2010).
[8] EPICS, http://www.aps.anl.gov/epics
[9] Internal Report: "RF-gap Transformation in PARMILA," AOT-ABS: 12-018 (TN), (2012).
[10] S. Nath et al., "Comparison of Linac Simulation Codes", PAC'01, Chicago, 2001, TOPB003, p. 214. (2001).
[11] J. H. Billen and L. M. Young, "POISSON/SUPERFISH Reference Manual," LANL publication, LA-UR-96-1834, 1996, (Revised 2004).
[12] NVIDIA Corporation, CUDA C Programming Guide, (2014).
[13] X. Pang and L. Rybarcyk, "GPU Accelerated Online Beam Dynamics Simulator for Linear Particle Accelerators," Computer Physics Communications, 185, pp. 744-753, (2014).
[14] X. Pang and L. Rybarcyk, "Multi-Objective Particle Swarm and Genetic Algorithm for Optimization of the LANSCE Linac Operation," Nucl. Instr. Meth. A, 741, 124, (2014).
[15] A. Scheinker et al., "Model Independent Particle Accelerator Tuning," Phys. Rev. ST Accel Beams, 16, 102803, (2013).

ISBN 978-3-95450-185-4

H- BEAM DYNAMICS STUDY OF A LEBT IN XIPAF PROJECT WITH THE WARP CODE

R. Tang, Q.Z. Xing, L. Du, Q.Z. Zhang, T.B. Du, H.Y. Zhang, X.L. Guan, X.W. Wang, C.X. Tang*,†,
Key Laboratory of Particle & Radiation Imaging (Tsinghua University),
Ministry of Education, Beijing 100084, China
also at Laboratory for Advanced Radiation Sources and Application,
Tsinghua University, Beijing 100084, China
also at Department of Engineering Physics, Tsinghua University, Beijing 100084, China
Y. He, J. Li, NUTECH Co.Ltd, Beijing 100084,China

Abstract

The 7 MeV H- linac injector of Xi`an Proton Application Facility (XiPAF) is composed of an ECR ion source, a Low Energy Beam Transport line (LEBT), a Radio Frequency Quadrupole accelerator (RFQ) and a Drift Tube Linac (DTL). The 1.7 m-long LEBT is used for matching a 40 μs pulse width 6 mA peak current beam to the entrance of the RFQ accelerator. The peak current and pulse-width of the 50 keV H- beam extracted from the ion source is 10 mA and 1 ms respectively. In the LEBT, an adjustable aperture is used for scraping the peak current of the beam to 6 mA, and an electric chopper is used for chopping the beam pulse width to 40 μs. These elements make the space charge compensation problem more complicated. A careful simulation of the space charge compensation problem of the H- beam has been done by considering the beam particles interacting with the residual gas with the help of WARP PIC code. To achieve the requirements of the LEBT in XiPAF, the type and pressure of the residual gas is given according to the simulation results.

INTRODUCTION

Xi`an Proton Application Facility (XiPAF) is a new proton project which is located at Xi`an City, Shanxi Province of China. This facility is being constructed for single-event-effect experiments. It provides proton beam with the maximum energy of 230 MeV. The accelerator facility of XiPAF mainly contains a 7MeV H- linac injector and a proton synchrotron accelerator. The 7 MeV H- linac injector of Xi`an Proton Application Facility (XiPAF) is composed of an ECR ion source, a Low Energy Beam Transport line (LEBT), a Radio Frequency Quadrupole accelerator (RFQ) and a Drift Tube Linac (DTL). The H- beam current extracted from the ECR source is 10 mA. The space charge effect of this intense beam makes a huge impact on the beam transport. In general, the 50 keV H- beam ionizes the residual gas and traps the positive ions. This process named SCC (space charge compensation) decreases the space charge effect greatly. In the LEBT design of XiPAF, the degree of SCC is assumed as 85% [1]. With the help of WARP PIC code, the residual gas ionization and stripping process is added into the H- beam dynamics simulation. This more accurate simulation is expected to provide guidance for the LEBT commissioning in the future.

*work supported by the Major Research plan of the National Natural Science Foundation of China (Grant No. 91126003).
†tang.xuh@tsinghua.edu.cn

LEBT DESIGN

The actual length of the LEBT is about 1.7 m. With the beam waist as the entrance, the length of the beam dynamics simulation is 1.8 m. Figure 1 shows the layout of the LEBT. The LEBT is used to match the beam between the exit of the ion source and the entrance of the RFQ accelerator. Table 1 shows the symmetric beam parameters at the exit of the ion source and the acceptance of the RFQ accelerator. The Twiss parameters at the exit of the ion source are estimated to be α=0 and β=0.065 mm/mrad.

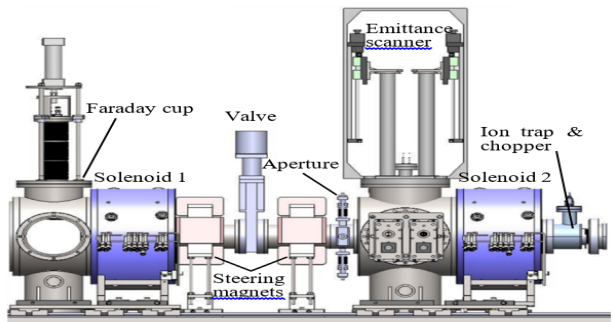

Figure 1: Layout of the Low Energy Beam Transport line (LEBT) of XiPAF.

Table 1: Beam Parameters Requirement

	ECR exit	RFQ entrance
Particle species	H-	H-
Particle energy	50 keV	50 keV
Peak current	10 mA	6 mA
Pulse width	1 ms	40 μ s
α	0	1.052
β	0.065 mm/mrad	0.0494 mm/mrad
Normalized RMS emittance	0.2 π mm• mrad	0.2 π mm• mrad

ISBN 978-3-95450-185-4

The LEBT is mainly composed of two solenoids, an adjustable aperture and an electric chopper. The aperture is used to decreasing the peak beam current. It can decrease the beam emittance as well. The chopper is used to chop the long beam pulse to 40 μs [1].

SIMULATION MODEL

The residual gas molecules in the vacuum area of the LEBT are ionized by the 50 keV negative hydrogen beam particles. The secondary electrons are expelled from the beam area by the space charge force. And the secondary ions are trapped by the beam potential trap. The beam potential trap is decreased as the number of trapped ions increases. This is called Space Charge Compensation (SCC). The space charge compensation time is determined by the residual gas type, the density of gas molecules (n) and the speed of the beam particles (v_{beam}), as given in Eq. (1). σ is the ionization cross section, which is determined by the gas type and the kinetic energy of the beam particles. While there is no available data for negative hydrogen beam, the ionization cross section data for 50keV proton is used in the following simulation [2].

$$\tau = \frac{1}{n \cdot \sigma \cdot v_{beam}} \quad (1)$$

As the ionization continues, the beam potential trap decreases gradually and the secondary ions start to move out of the beam area. At last, there is a balance between the loss and production of the secondary ions. Then, the space charge compensation reaches stable [3]. The degree of space charge compensation is defined as Eq. (2), where ϕ_{beam} is the beam potential created by the non-compensated beam, and ϕ_{scc} is the beam potential created by the compensated beam.

$$\eta = 1 - \frac{\phi_{scc}}{\phi_{beam}} \quad (2)$$

The electrons of the negative hydrogen beam particles can be stripped off by the residual gas molecules. Only one electron stripping process is considered in the following simulation, as given in Eq. (3), where X represents for different gas molecules.

$$H^- + X \rightarrow H + X + e \quad (3)$$

WARP code has been developed to model high current and high brightness beams for heavy-ion inertial fusion studies [4]. It is an open source code and has many models including all sections of particle accelerator. There are many Monte Carlo modules available including the residual gas ionization and stripping process. The code has been cross-checked with Tracewin code. In the H- dynamics simulation with space charge compensation, a very simple and direct method has been proposed. This simulation method is divided into four steps at each time step, as shown in Figure 2.

1, the H- beam particles are injected at the entrance of the simulation area (z=0 m) with the same parameters as the ion source exit.

2, the secondary electrons and ions are added into the simulation area by the Monte Carlo module. The density of those new secondary particles is determined by the cross section data, the density of the residual gas and the density of the beam particles. A uniform distribution of the gas particles is assumed.

3, the space charge induced electromagnetic field is calculated by solving the Poisson equation ($\nabla^2 \emptyset = -\rho/\varepsilon$). ρ is the density of the charge, which is contributed by all the charged particles (including the beam particles and the secondary particles, which is produced in this time step or left before this time).

4, beam transports for one step time considering the solenoids magnetic field together with the field calculated in step 3.

The simulation is a cycle composed of above four steps. It won`t stop until the beam transportation time equals to the required value. The simulation volume is one cylinder with the radius of 80 mm and height of 1800 mm. All kinds of particles out of this area will be not concerned. The cross section data used in the simulation is given in Table 2 [5] [6]. Because of the large simulation time cost, the time step is set to 6.46 ns, and the mesh size of the LEBT area is 2 mm*2 mm*20 mm. The number of the injected macropartilces is 4×10^3 for each time step. The typical number of the beam macroparticles tracked in the simulation area is about 5×10^5.

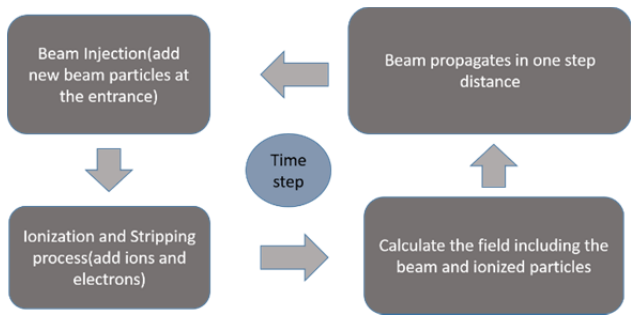

Figure 2: Diagram of simulation flow.

Table 2: Cross Section Data for 50keV H- Beam

Gas type	Ionization(1e-16/cm^2)	Stripping(1e-16/cm^2)
Ar	10.18	15
N2	9.77	12
H2	4.45	6

SIMULATION RESULTS

According to Eq. (1) and Eq. (2), the space charge compensation is closely related to the residual gas type and pressure. Ignoring the aperture, the simulation results with only argon gas injection are below.

The argon gas molecule is ionized into Ar^+ and an electron. Before the space charge compensation reaching stable, almost all of the Ar^+ particles are trapped by the beam potential. The number of Ar^+ particles is proportional to the beam transportation time [2]. This is the space charge compensation buildup process. The time is called SCC buildup time. Figure 3 shows the SCC buildup process with different gas pressure. The left plot

ISBN 978-3-95450-185-4

shows the total emittance (the emittance is the same in x and y direction for the symmetric beam) related to the beam transportation time. The right plot shows the ion numbers related to the beam transportation time.

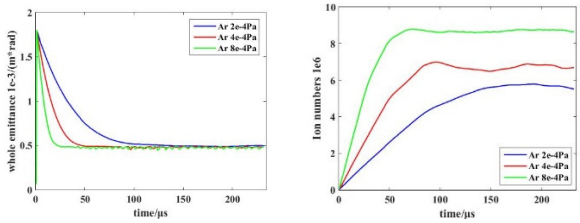

Figure 3: Total emittance vs beam transportation time (left) and ion numbers vs beam transportation time (right).

Before the space charge compensation built up, the beam phase space at the exit of the LEBT changes with the beam transportation time. This unstable beam needs to be chopped and the chopped beam pulse width must be larger than the buildup time. Figure 4 shows several beam phase spaces (at the exit of LEBT) in x direction.

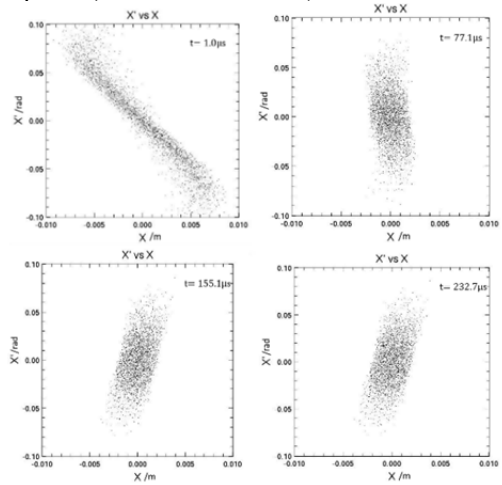

Figure 4: beam phase spaces (at the exit of the LEBT) in x direction at different time (gas pressure of 2e-4 Pa).

After the space charge compensation built up, the beam reaches stable. The degree of the space charge compensation is calculated by Eq. (2). Figure 5 shows the potential map in the LEBT with different pressure.

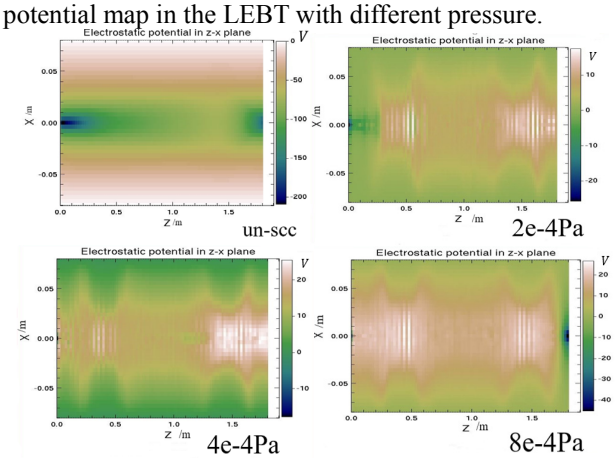

Figure 5: potential map in the LEBT (at t=232.1 μs, un-scc means there is not space charge compensation).

Because of the magnetic field of the two solenoids, the potential at the entrance and exit area of the LEBT changes a lot in the transverse directions. Focusing on the middle area of the LEBT, the degree of space charge compensation is ~105%, ~115% and ~120% for 2e-4 Pa, 4e-4 Pa and 8e-4 Pa respectively. The SCC buildup times are ~25 μs, ~60 μs and ~150 μs for 2e-4 Pa, 4e-4 Pa and 8e-4 Pa gas pressure respectively.

Those simulation results above are based on a simple LEBT model with only two solenoids. Considering the aperture between the solenoids, the simulation results changes as the beam current decreased after the aperture. The radius of aperture is 13.4 mm, and the results are below.

Argon gas injection: Figure 6a, 6b, 6c shows the results with the pressure of 3.5e-5 Pa at time=969.6 μs. The beam current after the aperture is about 7 mA. According to the phase space results, a bigger focusing force is needed to match the beam into the RFQ accelerator. Figure 6d shows the beam phase space in x direction at 5e-5 Pa pressure and t=624.6 μs. A smaller focusing force is needed and the beam current is also about 7mA at the LEBT exit. These simulation results suggests that with the pressure range of $3.5{\sim}5 \times 10^{-5}\ Pa$ for the injected argon gas, ~800 μs beam pulse needs to be chopped at the beam head and the radius of aperture shall be smaller.

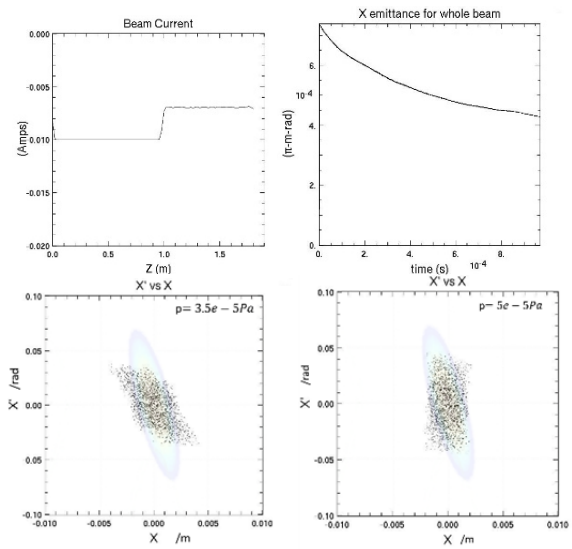

Figure 6: Simulation results at 3.5e-5 Pa and t=969.6 μs. (a. beam current (left top); b. total emittance (right top); c. phase space (left bottom); d. phase space at 5e-5 Pa pressure (right bottom) and at t=624.6 μs; the shadow in phase space plot represents the RFQ acceptance)

Nitrogen gas injection: Figure 7a, 7b, 7c shows the results the pressure of 3.5e-4 Pa at time=624.6 μs. The beam current after the aperture is about 6 mA. A bigger focusing force is needed to match the beam into the RFQ accelerator. Figure 7d shows the beam phase space in x direction at 1e-4 Pa pressure and t=232.7 μs. It meets the RFQ acceptance requirement and the beam current is also about 6 mA at the exit of the LEBT. These simulation results suggests that the pressure range of the injected

ISBN 978-3-95450-185-4

nitrogen gas is $0.5{\sim}1\times10^{-5}\,Pa$, ~600 μs beam pulse needs to be chopped at the beam head.

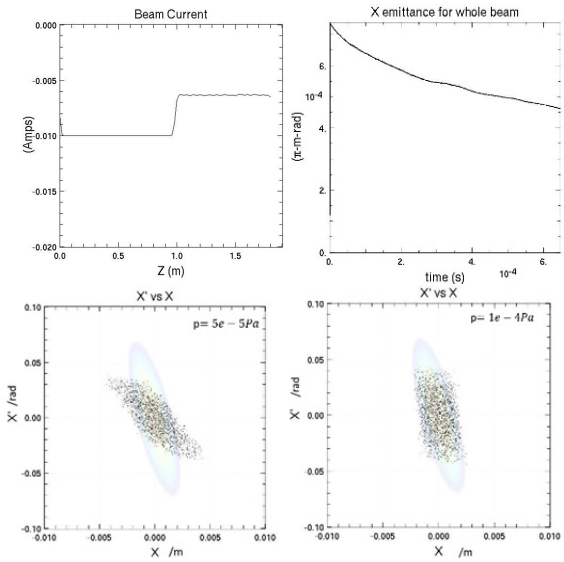

Figure 7: Simulation results at 5e-5 Pa and t=646.6 μs. (a. beam current (left top); b. total emittance (right top); c. phase space (left bottom); d. phase space at 1e-4Pa pressure and at t=232.7 μs(right bottom); the shadow in phase space plot represents the RFQ acceptance).

Hydrogen gas injection: Figure 8a, 8b, 8c shows the results the pressure of 3.5e-4 Pa at time=232.7 μs. The beam current after the aperture is about 6 mA. A bigger focusing force is needed to match the beam into the RFQ accelerator. Figure 8d shows the beam phase space in x direction at 5e-4 Pa pressure and t=232.7 μs. A smaller focusing force is needed and the beam current is also about 6 mA at the LEBT exit. These simulation results suggests that the pressure range of the injected hydrogen gas is $3.5{\sim}5\times10^{-4}\,Pa$, ~150 μs beam pulse needs to be chopped at the beam head.

CONCLUSION

This paper presents a simple and direct space charge compensation simulation method with WARP PIC code. With the design parameters of a LEBT in XiPAF project, H- beam dynamics has been studied by adopting this simulation model. Without the aperture, the space charge compensation with argon gas is simulated. The space charge compensation build-up time is about ~25 μs, ~60 μs, ~150 μs for 2e-4 Pa, 4e-4 Pa and 8e-4 Pa, while the degree of space charge compensation is ~105 %, ~115 % and ~120 % respectively. Adding the aperture, the beam dynamics simulations for the negative hydrogen have been carried out via injecting hydrogen, nitrogen and argon gas separately. To achieve the requirements of the design of the LEBT in XiPAF, the simulation results suggest: 1) the pressure range of the injected argon gas is $3.5{\sim}5\times10^{-5}\,Pa$, ~800μs beam pulse needs to be chopped at the beam head and the radius of aperture should be smaller; 2) the pressure range of the injected

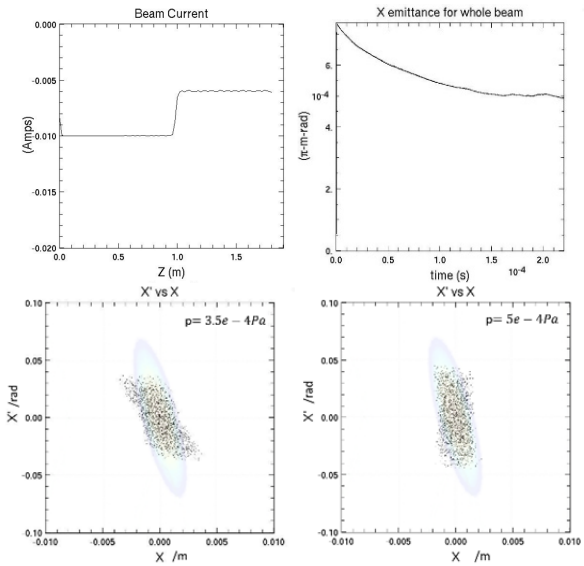

Figure 8: Simulation results at 3.5e-4 Pa and t=232.76 μs. (a. beam current (left top); b. total emittance (right top); c. phase space (left bottom); d. phase space at 5e-4 Pa pressure and at t=232.7 μs(right bottom); the shadow in phase space plot represents the RFQ acceptance)

nitrogen gas is $0.5{\sim}1\times10^{-4}\,Pa$ and ~600 μs beam pulse needs to be chopped at the beam head; 3) the pressure range of the injected argon gas is $3.5{\sim}5\times10^{-4}\,Pa$, ~150 μs beam pulse needs to be chopped at the beam head. These results will provide guidance for the LEBT commissioning in the future.

ACKNOWLEDGEMENTS

The authors wish to thank to Frédéric Gerardin and Jean-Luc Vay for their guidance on WARP code.

REFERENCES

[1] Ruo T, Du L, Du T, et al. Design of the Low Energy Beam Transport Line for Xi ‘an Proton Application Facility[C]//7th International Particle Accelerator Conference (IPAC'16), Busan, Korea, May 8-13, 2016. JACOW, Geneva, Switzerland, 2016: 1343-1345.

[2] Valerio-Lizarraga C A, Leon-Monzon I, Scrivens R. Negative ion beam space charge compensation by residual gas[J]. Physical Review Special Topics-Accelerators and Beams, 2015, 18(8): 080101.

[3] Soloshenko I A. Problems of intense negative ion beam transport[J]. Review of scientific instruments, 2004, 75(5): 1694-1698.

[4] Grote D P, Friedman A, Vay J L, et al. The warp code: modeling high intensity ion beams[J]. Lawrence Berkeley National Laboratory, 2005.

[5] Rudd M E, DuBois R D, Toburen L H, et al. Cross sections for ionization of gases by 5-4000-keV protons and for electron capture by 5-150-keV protons[J]. Physical Review A, 1983, 28(6): 3244.

[6] Thomas E W, Hawthorne S W, Meyer F W, et al. Atomic Data for Controlled Fusion Research[J]. ORNL, 1985.

ISBN 978-3-95450-185-4

STUDY ON SPACE CHARGE COMPENSATION OF LOW ENERGY HIGH INTENSITY ION BEAM IN PEKING UNIVERSITY*

S. X. Peng[1, †], A. L. Zhang[1, 2], H. T. Ren[1], T. Zhang[1], J. F. Zhang[1], Y. Xu[1], J. M. Wen[1], W. B. Wu [1], Z. Y. Guo[1], J. E. Chen[1,2]
[1]State Key Laboratory of Nuclear Physics and Technology & Institute of Heavy Ion Physics, School of Physics, Peking University, Beijing, China
[2]University of Chinese Academy of Sciences, Beijing, China

Abstract

To better understand the space charge compensation processes in low energy high intensity beam transportation, numerical simulation and experimental study on H^+ beam and H^- beam were carried out at Peking University (PKU). The numerical simulation is done with a PIC-MCC model [1] whose computing framework was done with the 3D MATLAB PIC code bender [2], and the impacts among particles were done with Monte Carlo collision via null-collision method. Issues, such as beam loss caused by collisions in H^+, H^- beam and ion-electron instability related to decompensation and overcompensation in H^- beam, are carefully treated in this model. The experiments were performed on PKU ion source test bench. Compensation gases were injected directly into the beam transportation region to modify the space charge compensation degree. The results obtained during the experiment are agree well with the numerical simulation ones for both H^+ beam [1] and H^- beam [1]. Details will be presented in this paper.

INTRODUCTION

The space charge compensation occurred by tapping opposite polarity of the particles could come from the secondary particles produced by gas ionization or supplied by specific device. For gas ionization, it takes time for a particle of the beam to produce a neutralizing particle on the gas. It is expressed as,

$$\tau = \frac{1}{\sigma_i n_g \beta_B c} \quad (1)$$

where σ_i is the ionization cross section of the incoming particles on the gas and n_g is the gas density in the beam line. The gas space charge compensation only applies to those beam whose pulse length is longer than τ, for example CW beam or long-pulse beam. For those short pulsed beam, the opposite polarity of the particles should be initiatively provided and sustained by specific device without transient time limit, such as Electron Volume [3] and Gabor Lens [4]. In this paper, we will focus on the space charge effect and space charge compensation of CW beam and long-pulse beam. Study on space charge compensation can help us to understand the processes during the compensation and guide accelerator design. Experiment research as well as numerical simulation are complementary ways on this study. To simulate the process of space charge compensation within an ion beam, the space charge effect should be treated by taking into account either through a linear analytical model or by treating the beam fully three-dimensional through particle-in-cell (PIC) methods. At PKU, a Monte Carlo collision (MCC) [5] package including the null collision method has been developed as an addition to the usual PIC charged particle scheme. This PIC-MCC code done with 2D MATLAB code has been used to simulate the space charge compensation of H^+ beam. The simulation results had a good agreement with the experimental ones when dealing with Ar compensating H^+ beam [1]. Recently, this PIC-MCC simulation code was improved to 3D model and had been used in the H^- beam after considering the difference of positive and negative ion beams [2]. Again, the results obtained by H^- beam experiment were coincident well with the numerical results. Space charge effect and space charge compensation, and experiment and simulation of space charge compensation will present in the paper.

*Work supported by the National Natural Science Foundation of China (11575013, 11305004)
†E-mail address: sxpeng@pku.edu.cn.

SPACE CHARGE EFFECT

Space charge is the most fundamental of the collective effects whose impact generally is proportional to the beam intensity. The defocusing force of space charge effect will lead to emittance growth ($\Delta\varepsilon_{rms}$) [5]. It can be expressed by the generalized perveance K,

$$\Delta\varepsilon_{rms} = \sqrt{\varepsilon_{rms,final}^2 - \varepsilon_{rms,start}^2} = \sqrt{\frac{<X^2>K\Delta W_{nl}}{8}} \quad (2)$$

Here X is the position of the ions in the beam, ΔW_{nl} is the normalized non-linear field energy which mainly determined by the density distribution of the ion beam. The generalized perveance K, a dimensionless parameter, is defined as,

$$K = \frac{qI}{2\pi\epsilon_0 m_0 c^3 \beta^3 \gamma^3} \quad (3)$$

The perveance K refers to the magnitude of space-charge effects in a beam, and it will largely determine the particle trajectories in drift region. In equation (3), I is the density of the beam, while we approximate that $\Delta W_{nl} \propto I$, from equation (1) we get $\Delta\varepsilon_{rms} \propto I$, which means the emittance growth is proportional to beam current.

Figure 1 showed the perveance K under different energy in several high current projects [6]. As shown in Fig. 1, in low energy region (100 keV) the perveance K is 5×10^{-3}, five orders higher than that in the high energy region (100 MeV). From equation (1) we know that $\Delta\varepsilon_{rms}$ is proportional to $\sqrt{K}$. This means the emittance

ISBN 978-3-95450-185-4

growth $\Delta\varepsilon_{rms}$ caused by space charge effect in low energy is hundreds times larger than it in the high energy region. Therefor the following discussion will focus on the low energy part of accelerator.

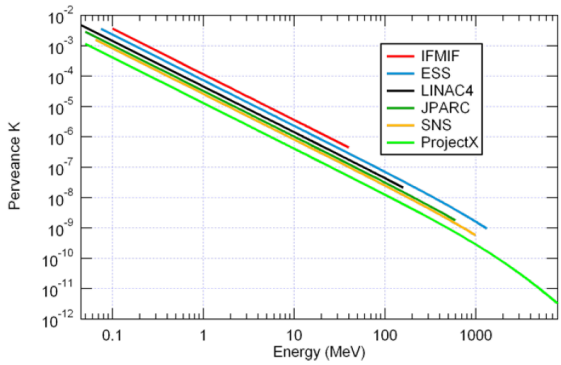

Figure 1: The perveance K under different energy in several projects [6].

Low energy beam transportation (LEBT) is a beamline that connects ion source and the accelerating structure whose energy is usually tens kV to hundreds kV. Emmittance growth will be the significant problem according to Figure 1 and equation (2). The space charge in LEBT of the high intensity accelerators should be compensated carefully.

SPACE CHARGE COMPENSATION

The most common way for space charge compensation in low energy parts of accelerator is gas ionization, and the gas could come from residual gas or initiatively injecting. Figure 2 is an example [7]. When a proton beam is propagating through the gas of the beam line, the proton beam will ionize the molecules of residual gas or injected gas within the vacuum pipe, the electrons will be absorbed to the beam core while the ions are expelled from the beam core, this results that the beam will be neutralized, it's so called space charge compensation.

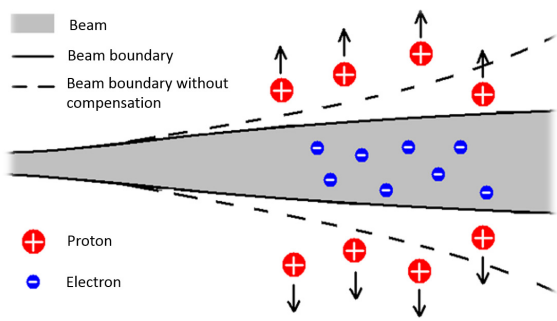

Figure 2: Proton beam compensated with gas ionization [7].

The space charge compensation can be particularly different from each other under different electromagnetic environment. The ions that generated within an ion source body are formed as an ion beam through a beam extraction system. When an extraction electric field applied on the ion source, the wanted sign particles will be extracted from the plasma while the opposite charge particles will be decelerated and reflected towards the plasma. To avoid the compensating particles lost towards the ion source, an accel-decel extraction system has to be used in GSI [8]. The experimentally observed beam profiles using viewing targets and the simulation using the three-dimensional 3D simulation code KOBRA3-INP [9] have a good agreement. Figure 3 showed a simulation result concentrating on magnetic field line and extraction aperture from KOBRA3-INP.

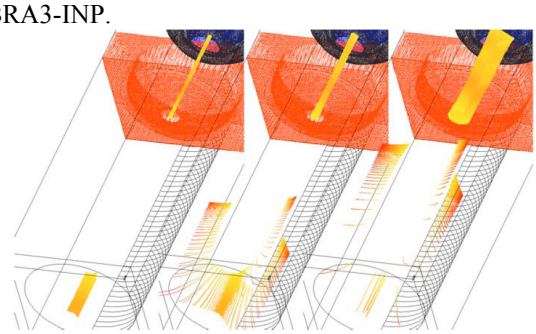

Figure 3: Magnetic field lines going on different radius through the extraction aperture:1 mm, 2 mm, and 6 mm [9].

Once the beam is extracted from the ion source, it has to be transported and matched by the low energy beam transportation (LEBT) to the first accelerating structure such as a RFQ. The focus can be done with electrostatic or magnetic elements [10].

Electrostatic LEBT mainly consists of axisymmetric electrostatic focusing components. The lenses are affecting the beams by the electric field they generated so to adjust the beam transmission parameters to achieve the goal of matching the beam emittance with the cavity acceptance. The electrostatic LEBT is compatible with fast beam chopping as there is no transient time for the space charge compensation. The beam is propagating in electrostatic LEBT without any space charge compensation because the neutralizing particles are repelled by the electric field induced by the focusing elements. The injector developed by PKU for the DWA (Dielectric Wall Accelerator) [11] is a typical electrostatic injector, which consists of an ion source and a 20 cm six electrodes LEBT. The SNS (Spallation Neutron Source) injector shown in Figure 4 is composed by an H^- ion source with a 12 cm long electrostatic LEBT equipped with two Einzel lenses.

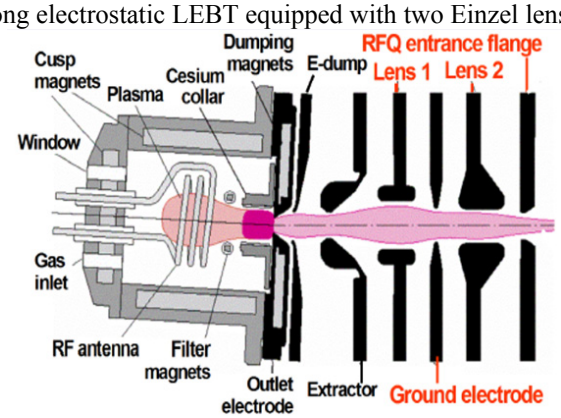

Figure 4: The electrostatic LEBT of SNS [12].

ISBN 978-3-95450-185-4

Nowadays, it is commonly accepted that an optimal LEBT for high current accelerator applications consists of focusing solenoids with space charge compensation. Such magnetic LEBT is spark free and low sensibility to beam loss, and beam diagnostics and mass separation can be easily inserted. However, the pulse rise time in magnetic LEBT which dominated by the transient time of the space charge compensation should be no shorter than hundreds of μs. Two-solenoid Magnetic LEBTs have been successfully used for high current (>100 mA) proton beam [13, 14]. Figure 5 showed a schematic view of the designed two-solenoid magnetic LEBT in SNS. It consists of solenoids S1 and S2 that focus the H^- beam into the RFQ entrance at the right, separated by 50 cm used for pumping and beam diagnostics.

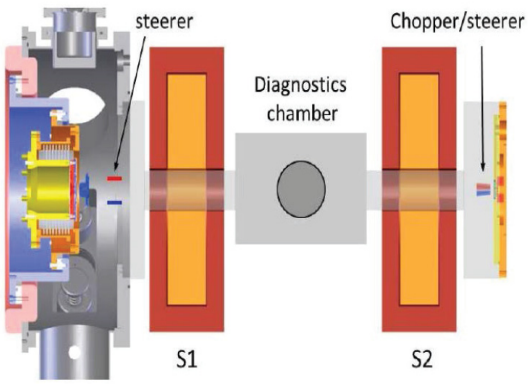

Figure 5: The two-solenoid magnetic electrostatic LEBT of SNS [15].

SIMULATION FOR SPACE CHARGE COMPENSATION

Simulation codes can take space charge compensation into account either by a linear analytical model (as for example presented in Reiser [16]) or by treating the beam fully three-dimensional through numerical simulation methods [1]. The original analytical formula about space charge compensation was presented in 1968 by Nezlin M V [17]. Then, in 1977 Gabovich published a detailed review article on the processes involved in compensation and decompensation of positive and negative high intensity ion beams considering dynamic and decompensation of the ion beams as well as collective processes in the beam plasma [18]. With the development of computer technology, numerical simulation becomes more and more reliable. Numerical simulation codes for space charge compensation had been developed in many lab, such as WARP [19] developed in Lawrence Berkeley National Laboratory (LNBL), SOLMAXP [20] which were developed at CEA/Saclay, and IBSimu [21] 3D simulation code developed at CERN. However, the collisions in those codes are not calculated accurately enough. At PKU, a PIC-MCC code concentrated on collisions had been developed in PKU. Beam loss and instability caused by collisions were careful treated within this code. Its scheme of PIC-MCC simulation is shown in Figure 6. This is similar to the input/output routines of any other numerical tool.

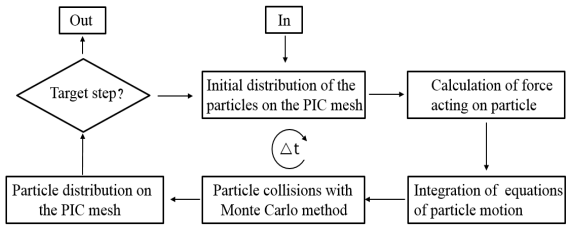

Figure 6: Scheme of the PIC-MCC simulation in PKU.

In order to verify the PIC-MCC model, experiments were performed on PKU Ion Source Test Bench. Figure 7 is a photo of this bench [22]. It consists of a set of microwave system, the permanent magnet 2.45 GHz ECR ion source, a tri-electrode extraction system, and a beam diagnostic section with a Faraday Cup (FC1) that integrates a set of slit-grid emittance measurement device. Compensation gas is injected in the same section of FC1. Mass Flow Controller was used to control the compensation gas flow.

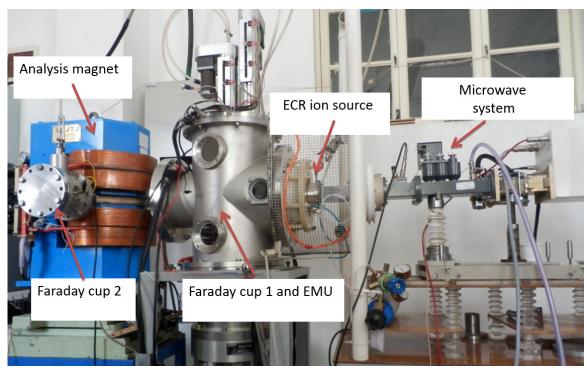

Figure 7: Skeleton diagram of PKU ion source test bench [22].

COMPARISON OF EXPERIMENTAL RESULTS AND SIMULATION ONES ON SPACE CHARGE COMPENSATION

H^+ Beam Results

The PIC-MCC model for H^+ beam is concentrate on the scattering effect which can cause particle loss. Collisions in the simple hydrogen model are,

(1) $H^+ + Ar \rightarrow H^+ + Ar$ (Elastic Scattering)
(2) $H^+ + Ar^+ \rightarrow H^+ + Ar^+$ (Electromagnetic Scattering)
(3) $H^+ + Ar \rightarrow H^+ + Ar^*$ (Excitation)
(4) $H^+ + Ar \rightarrow H^+ + Ar + e$ (Ionization)
(5) $H^+ + e^- \rightarrow H^+ + e^-$ (Electromagnetic Scattering)
(6) $H^+ + H_2 \rightarrow H^+ + H_2$ (Elastic Scattering)
(7) $H^+ + H \rightarrow H^+ + H$ (Elastic Scattering)
(8) $H^+ + H^+ \rightarrow H^+ + H^+$ (Electromagnetic Scattering)

The ionization and electromagnetic scattering (2), (3), (4), (5), (8), is included in the part of PIC. (1), (6), (7) should be calculated with MCC. Null collisions method is used to reduce the computational work.

ISBN 978-3-95450-185-4

Experiment of the space charge compensation using Ar in H^+ beams is presented in this paper. Ion beams were transported through 300 mm of drift section under various vacuum conditions. The simulation result is shown in Figure 8. Comparisons between the 2D PIC-MCC simulations (Figure.9) and the experiment showed the numerical results had a good agreement with the experiment. By studying the scattering effect, we found out an appropriate compensation circumstance to get the best efficiency in Low-energy Beam Transport.

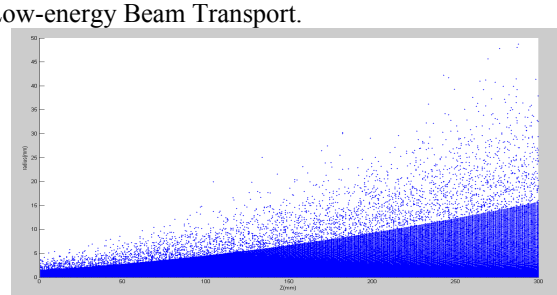

Figure 8: 2D simulation result for H^+ beam. (compensate with 0.05sccm Ar.)

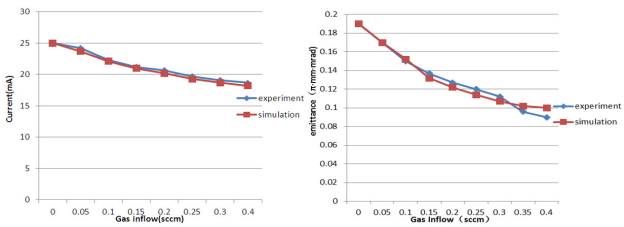

Figure 9: Current (left) and emittance (right) comparison between experiment and simulation for H^+ beam.

H⁻ Beam Results

The 2D PIC-MCC was improved to simulate the space charge compensation of H^- beam in PKU. The biggest difference between compensation of positive and negative ion beams are the masses of the electrons and ions produced by gas ionization. In a negative ion beam, the space charge effect is neutralized by heavy positive ions while positive beam is neutralized by light electrons. The results are that the negative beam maybe overcompensated because the ion is harder to be moved than the electrons. Experiments were done at PKU ion source test bench. Compensation gas He and Ar were injected directly into the beam transport region to modify the space charge compensation degree.

Processes in H^- beam compensated with Ar are,

(1) $H^- + Ar \rightarrow H^- + Ar^*$
(2) $H^- + Ar \rightarrow H^- + Ar^+ + e$
(3) $H^- + Ar \rightarrow H^+ + Ar^+ + 3e$
(4) $H^- + Ar \rightarrow H^+ + Ar + 2e$
(5) $H^- + Ar^+ \rightarrow H^+ + Ar^+ + 2e$
(6) $H^- + H_2 \rightarrow H^- + H_2^*$
(7) $H^- + H_2 \rightarrow H^- + H_2^+ + e$
(8) $H^- + e \rightarrow H^+ + 2e$

Simulations were done with the 3d particle-in-cell [23] code bender. The code provides three solvers for Poisson's equation: a 3d finite-difference Poisson solver which allows handling of boundary conditions on arbitrary geometric objects, an r-z finite-difference solver and a solver using a Fast Fourier Transform. Collisions are handled via the null-collision method. The residual gas is assumed as an ideal gas at constant temperature and pressure.

The 2D PIC-MCC was improved to a 3D MATLAB PIC-MCC code. Figure 10 showed an example of the 3D simulation result of H^- beam transport 50 mm to faraday cup. In this case, the beam focal point, the electron temperature is 10.8 eV, the max electron density on axis is about 5.8 $\times 10^{15}$ m^{-3}, the Debye length is about 1.7 mm and the plasma frequency is about 2.7 GHz.

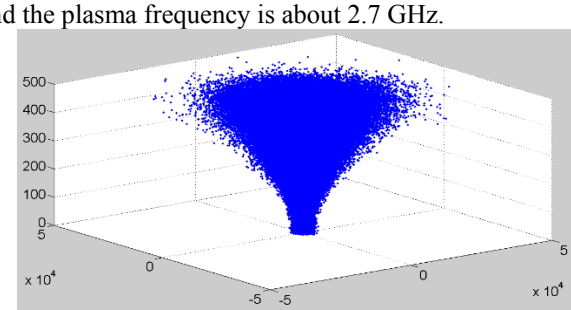

Figure 10: Simulation for H^- beam transport 50 mm to faraday cup. (x, y label represents the PIC meshgrid, z is the time step.)

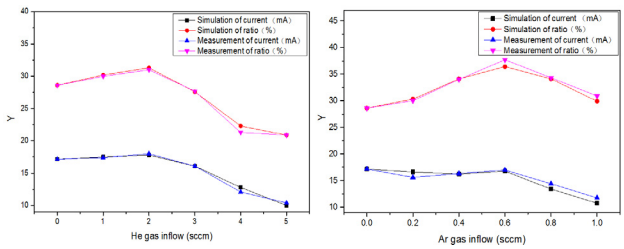

Figure 11: Simulation and experiment comparison on current and ratio for H^- beam.

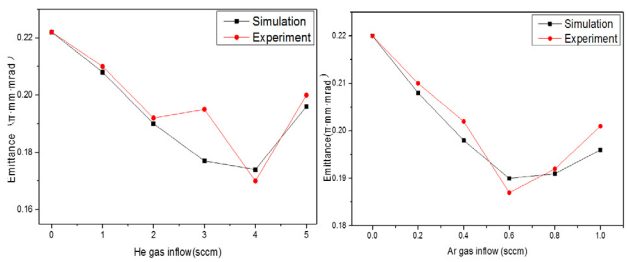

Figure 12: Simulation and experiment comparison on emittance for H^- beam. The minimum emittance is the location where it is believed the space charge compensation is optimum. For He 4 sccm, while for Ar is 0.6 sccm.

Figure 11 showed that the simulation results of current of H^- and ratio of H^- to total beam current have good agreement with the experimental ones. Emittances are calculated and compared in Figure 12. Both He and Ar can reduce the space charge effect in H^- beam transportation. However, to get the best emittance result more than 6 times He inflow (4 sccm) is needed than Ar (0.6 sccm). The simulation results agrees well with the experiments and it will help us to find a good compensation circum-

ISBN 978-3-95450-185-4

stance to avoid the decompensation and overcompensation region in H^- beam.

SUMMARY

In this paper we reviewed the space charge compensation in LEBT. Until now, the beam dynamics simulations of LEBTs have been done with particle tracking codes. The PIC-MCC code developed in PKU had been used to model the space charge compensation, and it has a good agreement with the experiment which was performed on PKU ion source test bench. The simulation result agrees well with the experiments. That helps us to understand the process during the compensation in H^+ beam and H^- beam, and guides us to find a good compensation circumstance to improve the transmission efficiency for LEBT. It has been demonstrated that numerical simulation code PIC-MCC developed in PKU can be used for injectors design of high intensity accelerators.

REFERENCES

[1] A. L. Zhang *et al.*, "Simulation study of space charge compensation in low energy beam transport", *In proceedings of CPAC'14,* Wuhan, China, 2014, AT007.

[2] A. L. Zhang *et al.*, "Study on space charge compensation in negative hydrogen ion beam", *Review of Scientific Instruments,* 2016, 87(2): 02B915.

[3] V. Shiltsev et al., "The use of ionization electron columns for space-charge compensation in high intensity proton accelerators", AIP Conf. Proc. 2009, 1086(FERMILAB-CONF-08-395-APC): 649-654.

[4] O. Meusel et al., "Low energy beam transport for HIDIF". Nuclear Instruments and Methods in Physics Research Section A: Accelerators, Spectrometers, Detectors and Associated Equipment, 2001, 464(1): 512-517.

[5] N. Chauvin et al., "Simulation and measurements in high intensity LEBT with space charge compensation", 2012.

[6] J. Struckmeier et al., "On the stability and emittance growth of different particle phase-space distributions in a long magnetic quadrupole channel", 1984.

[7] P. N. Lu, "Researches of space charge compensation in low-energy-high-intensity ion beam and emittance measurement in high-power ion beam", Peking University (Nuclear technology and application) Master, 2012 :6-7.

[8] P. Spädtke, "Sophisticated computer simulation of ion beam extraction for different types of plasma generators", Review of Scientific Instruments, 2004, 75(5): 1643-1645.

[9] P. Spädtke, "TINSCHERT K, LANG R, et al., "Prospects of ion beam extraction and transport simulations (invited)", Review of Scientific Instruments, 2008, 79(2): 02B716.

[10] S. X. Peng et al., "Review on low energy high current ion injector", Journal of Anhui Normal University (Natural Science) Vol.37, No.3, May, 2014: 205-211.

[11] S. X. Peng *et al.*, "Proton injector acceptance tests for a Dielectric Wall Accelerator (DWA): Characterization of Advanced Injection System of Light Ions (AISLI)", *Nuclear Instruments and Methods in Physics Research Section A: Accelerators, Spectrometers, Detectors and Associated Equipment,* 2014, 763: 120-123.

[12] R. Keller *et al.*, "Design, operational experiences and beam results obtained with the SNS H^- Ion source and LEBT at Berkeley Lab", *Lawrence Berkeley National Laboratory,* 2002.

[13] M. P. Stockli, T. Nakagawa, "Ion injectors for high-intensity accelerators", *Reviews of Accelerator Science and Technology*, 2013, 6: 197-219.

[14] N. Chauvin *et al.*, "Source and injector design for intense light ion beams including space charge neutralization", *Proc. of LINAC*, 2010, TH302.

[15] B. X. Han *et al.*, "Physics design of a prototype 2-solenoid LEBT for the SNS injector", *Proceedings of the 2011 Particle Accelerator Conference*. 2011: 1564-1566.

[16] M. Reiser, "Theory and design of charged particle beams", *John Wiley & Sons*, 2008:120-124.

[17] M. V. Nezlin, "Plasma instabilities and the compensation of space charge in an ion beam", *Plasma Physics*, 1968, 10(4): 337.

[18] M. D. Gabovich "Ion-beam plasma and the propagation of intense compensated ion beams", *Soviet Physics Uspekhi*, 1977, 20(2): 134.

[19] D. P. Grote *et al.*, "The warp code: modeling high intensity ion beams", *Lawrence Berkeley National Laboratory*, 2005.

[20] R. Duperrier, "HIPPI 2008 Annual Meeting", CERN, Meyrin, 2008.

[21] C. A. Valerio lizarraga *et al.*, "Negative ion beam space charge compensation by residual gas", *Physical Review Special Topics Accelerators and Beams*, 2015, 18(8): 080101.

[22] H. T. Ren *et al.*, "Milliampere He2+ beam generator using a compact GHz ECRIS", *Science China Physics*, Mechanics and Astronomy, 2013, 56(10): 2016-2018.

[23] V. Vahedi and M. Surendra. "A Monte Carlo collision model for the particle-in-cell method: applications to argon and oxygen discharges.", *Computer Physics Communications* 87.1–2 (1995), pp. 179–198.

ISBN 978-3-95450-185-4

SIMULATION OF SPACE-CHARGE COMPENSATION OF A LOW-ENERGY PROTON BEAM IN A DRIFT SECTION

Daniel Noll*, Martin Droba, Oliver Meusel, Ulrich Ratzinger, Kathrin Schulte
Institute for Applied Physics, Goethe University, Frankfurt am Main, Germany

Abstract

Space-charge compensation provided by the accumulation of particles of opposing charge in the beam potential is an important effect occuring in magnetostatic low energy beam transport sections of high-intensity accelerators. An improved understanding of its effects might provide valuable input for the design of these beam lines.

One approach to model the compensation process are Particle-in-Cell (PIC) simulations including residual gas ionisation. In simulations of a drifting proton beam, using the PIC code *bender* [1], some features of thermal equilibrium for the compensation electrons were found. This makes it possible to predict their spatial distribution using the Poisson-Boltzmann equation and thus the influence on beam transport.

In this contribution, we will provide a comparison between the PIC simulations and the model as well as some ideas concerning the source of the (partial) thermalization.

SIMULATION OF A DRIFT SECTION

The drift of a 120 keV, 100 mA proton beam over 50 cm through a system enclosed by repeller electrodes on −1.5 kV and filled with Argon gas at 1×10^{-5} mbar was simulated. The code *bender*, the simulation model, the reasons for the choice of this system as well as the behaviour during compensation build-up were presented in previous contributions [1, 2].

Figure 1 depicts the charge densities of all simulated species – the beam protons, the residual gas ions (Ar^{1+}) and the compensation electrons – in the steady-state of the simulation. The globally averaged compensation outside of the area affected by the repellers reaches $\eta_{\mathrm{part}} \approx 86.2\,\%$. Beyond the mean effect of the compensation, a shift in the focus of the beam, which is also easily explained by a scaling of the current, some additional effects are present.

In the focus, the beam becomes hollow. As can be observed in the total charge density, the beam edge is not well compensated, especially in the focus point but also elsewhere in the system. Some electrons have enough energy to be able to form an area of negative charge density close to the beam edge. In most parts of the system, the residual gas ions are immediately expelled by the radial electric field. However, within the focus, the Argon ions accumulate to a density of approximately 300 µC m^{-3} – surprising, since the radial electric fields should be largest in the focus.

Figure 2 shows the distribution of total particles energies H in arbitrarily selected places throughout the volume. For

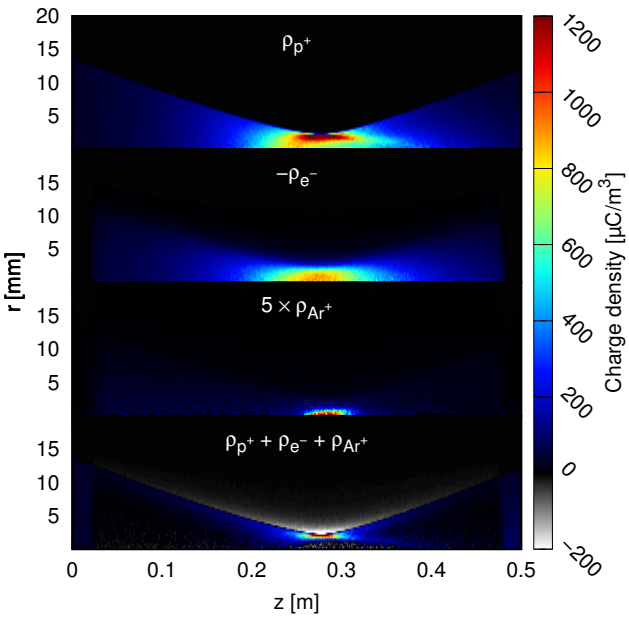

Figure 1: Charge densities for the different particle species in the simulation: beam protons, compensation electrons, residual gas ions and the netto charge density.

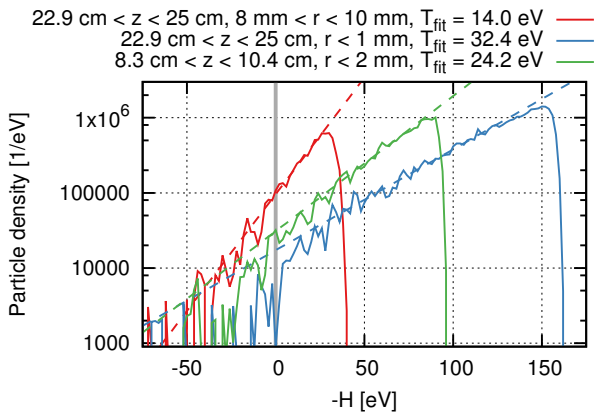

Figure 2: Distribution of total particle energy H (kinetic plus potential energy) at various arbitrarily chosen positions. For $H < 0$, the curves follow the dashed exponential curves. Positive H are underpopulated due to particle loss.

$H < 0$, these follow an exponential dependence

$$H(r, v) = H_0 \exp(-H/(k_\mathrm{b}T)) = H_0 \exp\left(-p^2/(2m_\mathrm{e}k_\mathrm{b}T) + e\varphi(r)/(k_\mathrm{b}T)\right). \quad (1)$$

For $H \geq 0$, particles are not confined and are gradually lost, leading to an underpopulation. The Boltzmann distribu-

* noll@iap.uni-frankfurt.de

ISBN 978-3-95450-185-4

tion in Eq. (1) also predicts Gaussian velocity distributions. These were also observed in the simulation. An example, resolved radially, taken from the center of the system is shown in Fig. 3. Towards larger radii, their width decreases and the curves look more "cut-off", probably due to particle losses.

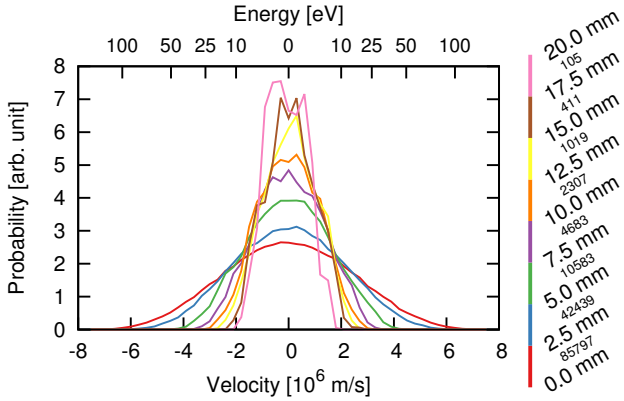

Figure 3: Electron velocities in a slice around $z = 25\,\mathrm{cm}$ resolved radially and normalized independently. The small numbers in the caption give the number of macroparticles contained in each ring.

Therefore, the results show some features of a system in thermal equilibrium. But neither is there equipartitioning – the temperatures differ between the transversal and the longitudinal plane – nor are the temperatures constant spatially. Nevertheless, the assumption that the electrons distribute according to Eq. (1) allows us to understand the features previously found in Fig. 1.

POISSON-BOLTZMANN EQUATION

When the electrons are known to be Boltzmann distributed, their distribution in space can be found by solving

$$\nabla^2\varphi(r) = -\frac{1}{\epsilon_0}\left(\rho_{\mathrm{beam}}(r) + \rho_{\mathrm{comp}}\exp\left(\frac{e\varphi(r)}{k_\mathrm{b}T}\right)\right).$$

By scaling the coordinates by the Debye length $\lambda_\mathrm{d} = \sqrt{\epsilon_0 k_\mathrm{b} T/(ne^2)}$ and the potential by the temperature, $\tilde{\phi} = e\phi/(k_\mathrm{b}T)$, [3] we get

$$\tilde{\nabla}^2\tilde{\varphi} = f_{\mathrm{beam}}(\tilde{r}) - \mu\exp(\tilde{\varphi}), \qquad (2)$$

where $f_{\mathrm{beam}}(\tilde{r}) = \rho_{\mathrm{beam}}(\tilde{r})/(ne)$ is the beam profile. λ_d and the compensation degree incorporated in

$$\mu = \eta_{\mathrm{part}}\int \exp(\tilde{\varphi}(r))\,\mathrm{d}V\left(\int f_{\mathrm{beam}}(r)\,\mathrm{d}V\right)^{-1},$$

are the only free parameters of the model. Equation (2) can be solved by introducing a parameter t,

$$\frac{\mathrm{d}\varphi}{\mathrm{d}t} = \tilde{\nabla}^2\tilde{\varphi} - f_{\mathrm{beam}}(\tilde{r}) + \mu\exp\tilde{\varphi}(\tilde{r})$$

and applying the Crank-Nicolson method [4, p. 1045] for the linear terms on the right hand side and the forward Euler method for the exponential term.

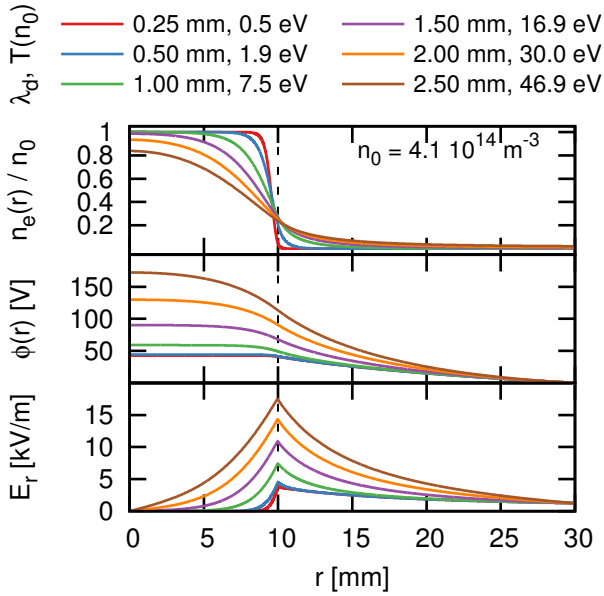

Figure 4: Electron density n_e relative to the beam density n_0, remaining potential ϕ and electric field, when electrons at temperature T confined in a 100 mA, 120 keV proton beam are treated using Eq. (2). Compensation degree is 90 %.

Figure 4 displays the electron density, potential and electric field found from the solution of Eq. (2) for a 100 mA, 120 keV proton beam with 1 cm radius, compensated to $\eta_{\mathrm{part}} = 90\,\%$ by thermal electrons. The algorithm was also included into the beam transport code *tralitrala* as a space-charge solver to be able to look at the influence of the non-linear fields produced by the electrons. Figure 5 shows the emittance growth observed in a 50 cm drift of an initially parallel and homogeneous 50 mA, 120 keV proton beam ($\epsilon_{\mathrm{rms}} = 25\,\mathrm{mm\,mrad}$, $\alpha = 0$, $\beta = 1\,\mathrm{m}$).

For low temperatures, the electrons are concentrated around the beam axis and are able to fully compensate the beam within some radius. The charge density effectively becomes that of a hollow beam, i.e. the electric field is zero in the core of the beam and rises quadratically at the edge. Such a situation does not lead to emittance growth, when the beam is either close to fully or not compensated. However, at intermediate values of η_{part}, where the quadratic electric field affects a large part of the beam, a growth in emittance up to 15 % can be observed.

For higher temperatures, the radial electron density begins to decrease earlier, leading to some electric field over a wide part of the beam. This produces some emittance growth, but not as large as for very low temperatures. Additionally more and more electrons are located outside the beam radius, leading to the negative charge densities also observed in the *bender* simulation.

At very large temperatures, the electron distribution tends towards a homogeneous background, providing nearly no effective compensation but also not leading to any emittance growth. Such a situation is unlikely to occur, since electron losses on the beam pipe would become too large.

ISBN 978-3-95450-185-4

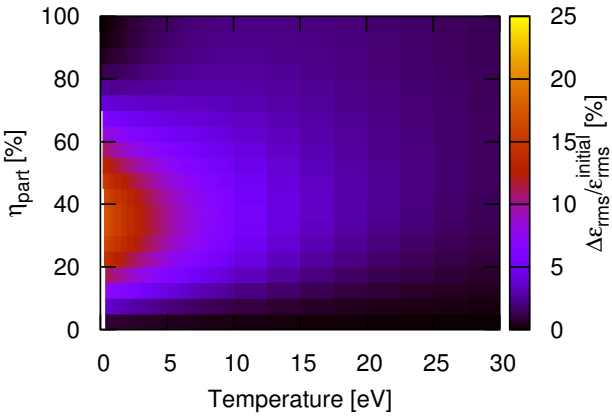

Figure 5: Emittance growth in a 50 cm beam transport of a homogeneous beam, when electrons at given temperature and compensation degree are incorporated in the simulation. Source of the emittance growth are the non-linear fields observed in Fig. 4.

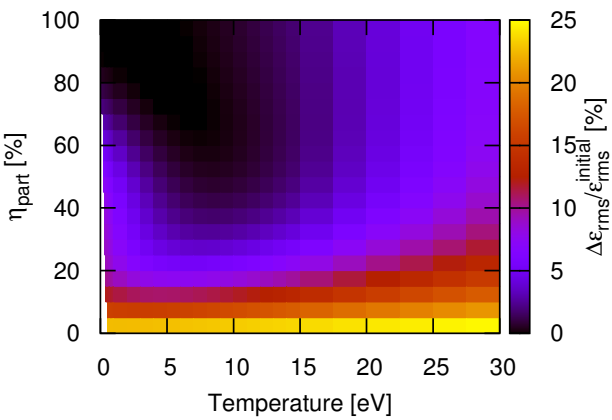

Figure 6: Same parameters as Fig. 5, but for a beam with a Gaussian distribution.

Simulations with rms equivalent parameters were made for a beam with a Gaussian distribution in phase-space. Figure 6 shows the calculated emittance growth. The largest growth is observed for an uncompensated beam, which is a result of redistribution due to non-linear field energy. In the presence of a small number of electrons, the growth is much reduced. In Fig. 6 for example, $\Delta\epsilon_{rms}/\epsilon_{rms} < 10\,\%$, for $\eta_{part} > 40\,\%$ over the length of the drift. Around $\eta_{part} = 60\,\%$, $T = 8\,\mathrm{eV}$, the electrons distribute in a way that the resulting electric field is approximately linear. This leads to the surprising minimum in the emittance growth.

Figure 7 shows the charge density from a similar calculation of the system previously simulated using *bender*. The properties $T(z)$ and $\eta_{part}(z)$ of the electrons were extracted from the full simulation, but their radial distribution calculated from Eq. (2).

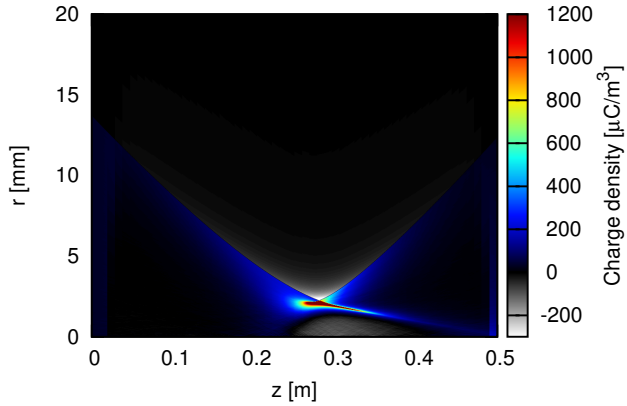

Figure 7: Total charge density in a 2d simulation of the same system as in Fig. 1, when electric fields are calculated from Eq. (2) using the same temperature $T(z)$ and longitudinal compensation degree distribution $\eta_{part}(z)$ extracted from the full simulation.

Both the formation of the negative charge density beyond the beam edge as well as the formation of a hollow beam is present. The latter can be identified as a result of the sharp increase of the electric field at the edge of the beam. This reduces the angle of convergence for the particles leading to an increase in density after some drift. Beyond the focus point, these areas are still observed continuing towards the axis.

The Poisson-Boltzmann model does not include the secondary ions. This makes it possible for a negative charge density to form inside the area around $z = 30\,\mathrm{cm}$ close to the beam axis. In this area, in the *bender* simulation, residual gas ions are not accelerated from the system anymore but confined instead.

Therefore, all features previously identified in the PIC simulation can be explained by the presence of Boltzmann distributed electrons. Hence, the question of its origin becomes important.

STOCHASTICAL HEATING IN A TEST SYSTEM

In the PIC simulation, we observed that the energies of the electrons fluctuate randomly, over a scale of several electronvolts in short-term, but on average increasing continously. When their kinetic energy increases to values larger than the potential, these electrons are lost. Due to this, we suspected that energy is not conserved by the simulation.

To test this hypothesis, a test system was generated by solving Eq. (2) in spherical coordinates for a confining potential of Gaussian shape with $\sigma = 1\,\mathrm{cm}$. The resulting charge density is displayed in Fig. 8. To avoid particle loss, the system parameters were chosen so that the confined particles are well removed from the boundary of the system, taken to be at $R = 10\,\mathrm{cm}$. Particle distributions with a thermal energy distribution and the calculated densities profile were

ISBN 978-3-95450-185-4

then loaded into *bender* and simulated for up to 1.5 ms (30 million steps) in some cases.

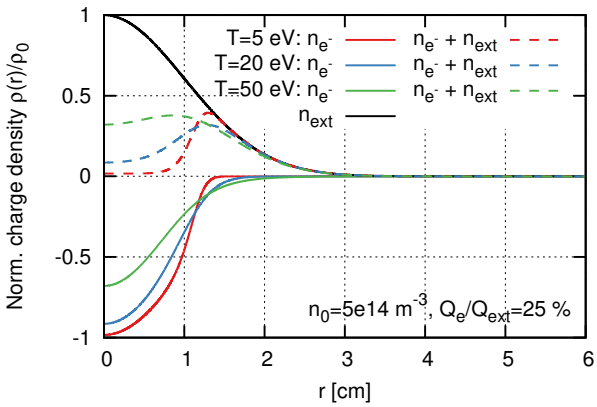

Figure 8: Electron charge density in a Gaussian shaped confining potential for various temperatures.

The density profile should remain stable by design. At a high number of particles, this was also observed. For low-resolution simulations however, a slow increase in the size of the cloud is present. The origin of this expansion is the linear increase in average particle energy shown in Fig. 9.

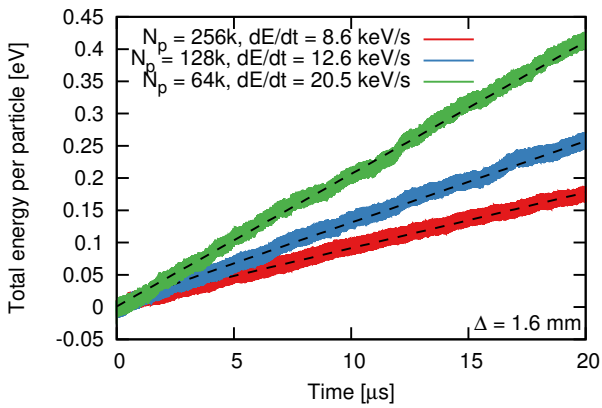

Figure 9: Energy increase in the test system (see Fig. 8) due to stochastical heating.

The rate of energy increase mainly depends on the number of macroparticles used and to a lesser degree on the resolution of the simulation grid. A range of parameters were simulated and the corresponding energy increase rate displayed in Fig. 10.

A possible explanation for the heating can be found in [5, p. 314-318]. Repeating their argument, if we assume that all errors in the simulation contribute to a random error δE in the electric field that has zero time average $\overline{\delta E} = 0$ but a variance $\overline{\delta E^2} \neq 0$, then the kinetic energy change in the simulation between two timesteps is

$$\Delta T = T_{i+1} - T_i = \frac{1}{2} m \left(\overline{(v_i + \delta v)^2} - \overline{v_i^2} \right) \quad (3)$$

$$= \frac{1}{2} m \left(2 v_i \overline{\delta v} + \overline{\delta v^2} \right) = \frac{1}{2} \frac{q^2}{m} \overline{\delta E^2} \delta t^2. \quad (4)$$

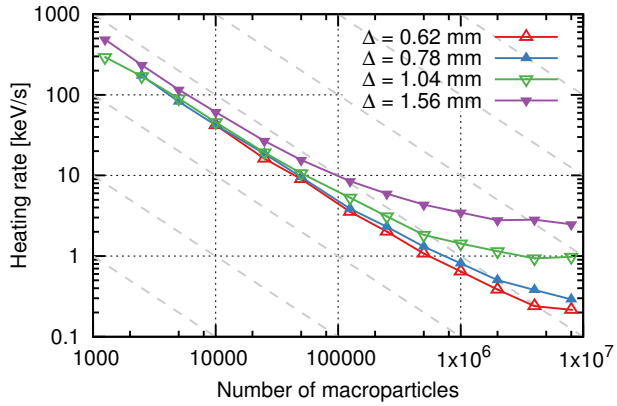

Figure 10: Observed heating rate for different numbers of macroparticles and grid spacings Δ. Dashed lines indicate $O(N^{-1})$ behaviour.

Equation 4 therefore predicts a constant increase in energy, which is what is observed. For a low number of macroparticles, we can assume the error to be statistical and therefore $|\delta E| \sim 1/\sqrt{N}$. Then, the heating rate is inversely proportional to the number of macroparticles N. This is observed in Fig. 10. Depending on the grid resolution at some point, some other (unidentified) process becomes relevant.

Therefore, we can assume a numerical heating to be present in the simulation, with a heating rate dependent on the parameters of the simulation.

In hindsight, the choice of system was not ideal, because a dependence on plasma parameters such as the Debye length is hard to find given the small extent of the system.

NUMERICAL INFLUENCES IN THE DRIFT SIMULATION

Figure 11 shows the temperatures found in the drift system, when the number of beam macroparticles inserted per step (and therefore the charge per macroparticle) is changed. As the electron temperature decreases, more electrons remain closer to the beam axis and the amount of negative charge outside the beam is lower. This allows more electrons to accumulate. Therefore, the decrease in temperature is linked to an increase in total compensation degree of the system. This can be seen in Fig. 11.

We assume that the observed dependence on the number of macroparticles is a result of the stochastical heating previously observed in the demonstration system. Due to particle losses, instead of a continous increase of system energy, an equilibrium forms. The losses could then also be responsible for the appearance of the Boltzmann energy distribution.

When the electric field of the beam is not recalculated in every step from beam particles but fixed to a field taken from a previous simulation, the observed (transversal) temperatures at the center of the system shrink from 27 eV to 11.8 eV. When residual gas ions are also excluded, the results is 8.3 eV. Therefore, a significant contribution of the heating comes from the beam particles.

ISBN 978-3-95450-185-4

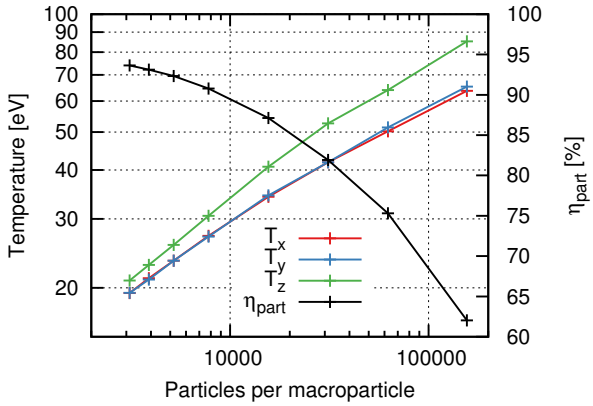

Figure 11: Dependence of the observed electron temperatures and the compensation degree on the number of macroparticles used to represent the particle species in the *bender* simulation.

To make the results of this kind of simulation physical, the numerical heating needs to be removed by some means. We then expect the compensation degree to reach values close to 100 %.

Then, physical heating processes such as Coulomb collisions between beam particles and the compensation electrons can be introduced. An estimation for the heating from these collision, given by Doelling [6, p. 19],

$$P = \frac{e^2}{4\pi\epsilon_0^2 m_e}\frac{n_\mathrm{b} q_\mathrm{b}^2}{v_\mathrm{b}}\ln(\Lambda)\left[\mathrm{erf}\left(\frac{v_\mathrm{b}}{v_\mathrm{t}}\right) - \frac{2}{\sqrt{\pi}}\left(1+\frac{m_e}{m_b}\right)\frac{v_\mathrm{b}}{v_\mathrm{t}}\exp\left(-\left(\frac{v_\mathrm{b}}{v_\mathrm{t}}\right)^2\right)\right],$$

$v_t = \sqrt{2k_\mathrm{b}T/m_\mathrm{e}}$, indicates that for exemplary parameters taken from the simulation ($T = 25\,\mathrm{eV}$), the heating rate $P = 19.5\,\mathrm{keV\,s^{-1}}$ is in the same order of magnitude of the numerical heating described in the previous section. Therefore, final results may, in some ways, not deviate much from those with the unphysical heating.

CONCLUSION

Simulations of space charge compensation in a short drift section were performed using the newly-developed Particle-in-Cell code *bender*. Beyond the reduction in space-charge forces, several features such as the formation of a hollow beam or the accumulation of residual gas ions in the focus were found. These were linked to the presence of a Boltzmann energy distribution for the electrons. Results from simulation using different simulation parameters and from a numerical experiment indicate that the observed energy distributions are of numerical origin.

REFERENCES

[1] D. Noll, M. Droba, O. Meusel, U. Ratzinger, K. Schulte and C. Wiesner, "The Particle-in-Cell Code Bender and Its Application to Non-Relativistic Beam Transport", in Proc. HB2014, East Lansing, USA, November 2014, paper WEO4LR02, pp. 304-308.

[2] D. Noll, M. Droba, O. Meusel, U. Ratzinger, K. Schulte and C. Wiesner, "Investigation of Space-Charge Compensation in Low-Energy Beam Transport (LEBT) Sections Using a Particle-In-Cell Code", in Proc. LINAC2014, Geneva, Switzerland, September 2014, paper MOPP065, pp. 205-207.

[3] R. G. Lefrancois, T. S. Pedersen, A. H. Boozer and J.P. Kremer, "Numerical Investigation of Three-Dimensional Single-Species Plasma Equilibria on Magnetic Surfaces", Physics of Plasmas, 12, 072105 (2005).

[4] Press, H. P. et al., "Numerical Recipes", Cambridge University Press, 2007.

[5] R. W. Hockney and J. W. Eastwood, "Computer Simulation Using Particles", CRC Press, 1988.

[6] Dölling, R., "Raumladungskompensation driftender intensiver Strahlen niederenergetischer Ionen und Techniken zu ihrer Vermessung", Dissertation, Johann-Wolfgang Goethe Universität Frankfurt am Main, 1994.

ISBN 978-3-95450-185-4

REUSE RECYCLER: HIGH INTENSITY PROTON STACKING AT FERMILAB*

P. Adamson†, Fermi National Accelerator Laboratory, Batavia, IL, USA

Abstract

After a successful career as an antiproton storage and cooling ring, Recycler has been converted to a high intensity proton stacker for the Main Injector. We discuss the commissioning and operation of the Recycler in this new role, and the progress towards the 700 kW design goal.

INTRODUCTION

Fermilab's Recycler is a 3319.4 m circumference permanent magnet ring, installed in the Main Injector tunnel at Fermilab. It consists of strontium ferrite gradient magnets and in the straight sections strontium ferrite quadrupoles. It was designed as a storage ring for antiprotons, and with the use of electron cooling it was a key factor in the delivery of increased luminosity during the later years of the Tevatron operation.

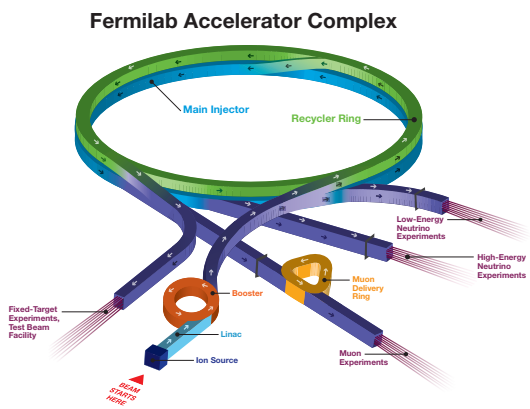

Figure 1: The Fermilab Accelerator complex in the NOνA era.

In a 16 month long shutdown, between May 2012 and September 2013, Recycler was converted for use as a proton stacker as part of the NOνA project [1]. The stochastic and electron cooling systems were removed, the section of ring used for electron cooling was rebuilt with a standard FODO lattice to match the rest of the ring, and the transfer lines used for antiproton transfer between Recycler and Main Injector were replaced with a new transfer line with larger acceptance. A new injection line to accept protons from the Booster was built, a 53 MHz rf system was installed, and new BPM cables and electronics capable of supporting 53 MHz operation was added. The Main Injector loss monitor system was modified to enable it to be continuously active (with Recycler used as a pre-stacker for Main Injector, high-intensity protons will be continuously present in the Main Injector tunnel.)

Recycler's most challenging task is the slip-stacking and delivery of high intensity beam to the Main Injector for NuMI. The NOνA project [2] design goal is for a 700 kW proton beam (48.6×10^{12} protons every 1.333 s.) In addition, Recycler stacks lower-intensity beam for transfer to Main Injector for resonant extraction to Switchyard 120 (the SeaQuest experiment, and the Fermilab Testbeam Facility), and beginning in 2017, it will rebunch protons into 2.5 MHz buckets for delivery to the Muon Campus (first Muon g-2, then μ2e.) In normal operation, roughly 10% of the time is devoted to Switchyard 120, so 630 kW would be delivered to the NuMI target at the design intensity.

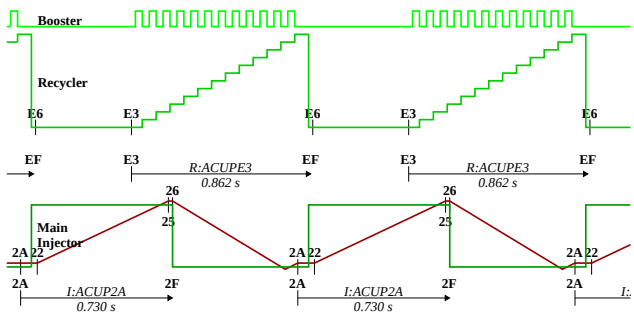

Figure 2: Relative timing of Booster, Recycler and Main Injector cycles for NOνA-era NuMI operation. Beam in each machine is shown in green, and Main Injector momentum in red. The start and end of cycle clock events for MI and Recycler are also shown.

The NOνA upgrade increases the beam power available at 120 GeV principally by reducing the cycle length. By moving the slip-stacking process from the Main Injector to the Recycler, the long front porch is eliminated, and the Main Injector can be kept ramping up and down at its maximum rate. As shown in Fig. 2, the Recycler starts stacking for the next NuMI pulse before the previous pulse has left the Main Injector.

PERFORMANCE OF RECYCLER TO DATE

The NOνA ANU upgrades only provided the capability to transform the Recycler into a high intensity stacking ring. Significant work was required to realize this capability.

Figure 3 shows the NuMI beam power as a function of time since the end of the NOνA shutdown. During the 240 kW period at the start of the plot, the operational beam was

* Operated by Fermi Research Alliance, LLC under Contract No. De-AC02-07CH11359 with the United States Department of Energy.

† pa@fnal.gov

ISBN 978-3-95450-185-4

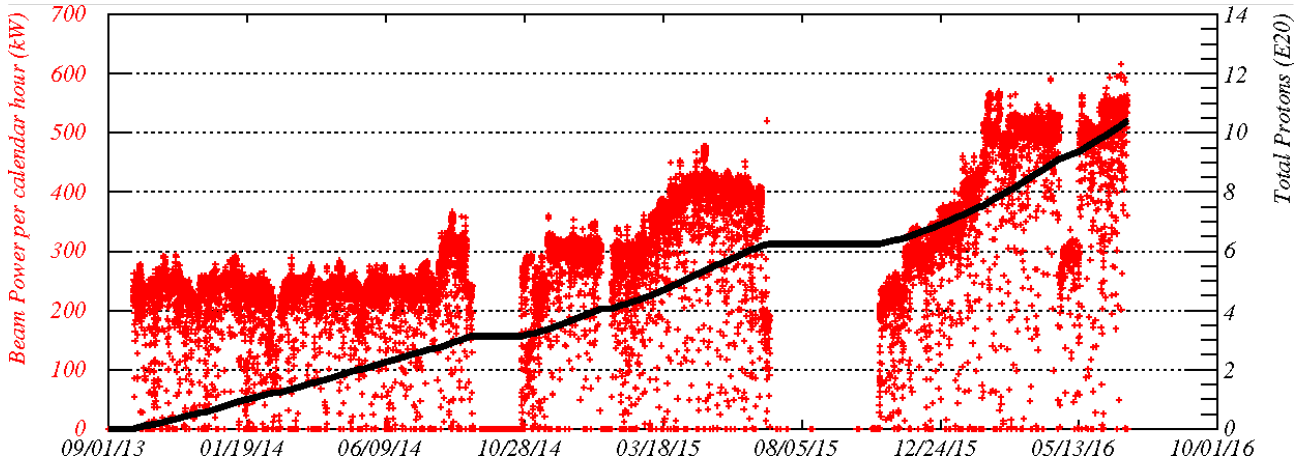

Figure 3: Hourly average beam power to NuMI and total protons delivered. The plot begins with the Main Injector only, at around 240 kW, while the initial commissioning of the Recycler was taking place. The increase to 300 kWbefore the 2014 summer shutdown is provided by the Recycler in 6-batch boxcar mode; subsequent steps to around 400 kW, 500 kW, and finally 550 kW in June 2016 are due to "2+6", "4+6" and "6+6" slip-stacking respectively. The best calendar hour averaged 615 kW, achieved while Switchyard 120 was not operating.

using only the Main Injector. This period contained all the initial commissioning of the Recycler: correction of gross aperture errors, commissioning of rf systems, transverse dampers, and instrumentation, and an initial period of "beam scrubbing". Once it was possible, running 6-batch "boxcar" stacking in the Recycler allowed us to decrease the cycle spacing from 1.66 s to 1.33 s, and increase the power to 300 kW.

Once this was possible, the process of commissioning slip-stacking [3] could begin. We describe the various modes of slip-stacking as "2+6", "4+6", or "6+6": in 2+6 slip-stacking, we inject two batches from the Booster, decelerate them, and allow them to slip against six further batches, producing at the time of recapture (on transfer into the Main Injector) two double-intensity batches and four singles. The initial 2+6 mode allowed us to deliver 400 kW; this was the largest number of batches usable for slip-stacking without an increase in the Booster beam pulse rate.

In order to deliver the design 700 kW beam, it was necessary to upgrade the Linac and Booster to increase the possible proton throughput. These upgrades were performed under the umbrella of the Proton Improvement Plan (PIP) [4–6]. Shortly before the 2015 summer shutdown, Booster became capable of delivering beam at 15 Hz, and so supporting the 4+6 and 6+6 slip-stacking modes.

At this point, we ran the 4+6 slip-stacking mode at 525 kW, producing the unacceptably high per-cycle losses shown in Fig. 4. The next few months were spent systematically improving locations with poor apertures, and conducting detailed measurements of stopbands [7] in the Recycler in order to find a better working point. After these improvements, we returned to 4+6 slip-stacking at 525 kW, achieving beam loss in the ring that was reduced by a factor of close to four, as shown in Fig. 5.

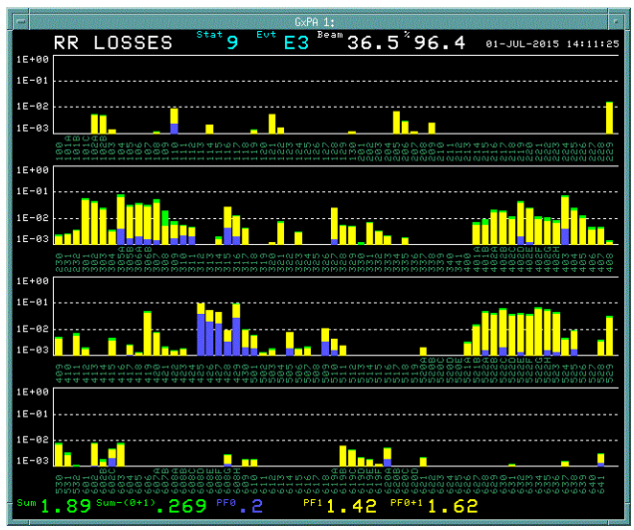

Figure 4: Loss around Recycler for 525 kW operation July 2015.

Following this successful effort, we began studies with the 6+6 mode, culminating in operating routinely at 550 kW during June 2016, with a peak hour at 615 kW and a demonstration of the design beam power of 700 kW (see Fig. 6.)

COLLIMATION

Following our experience in the Main Injector [8], we plan to control the remaining losses associated with beam lifetime with a collimation system. In the 2016 summer shutdown, we will install a two-stage collimator, with a primary scraping foil edge, and two large (20 ton) steel and marble secondary collimators. The system will be similar to that already installed in the Main Injector [9]. The intent is that this collimation system should contain the majority of the losses from Fig. 5. The exception is the loss at the 401-

ISBN 978-3-95450-185-4

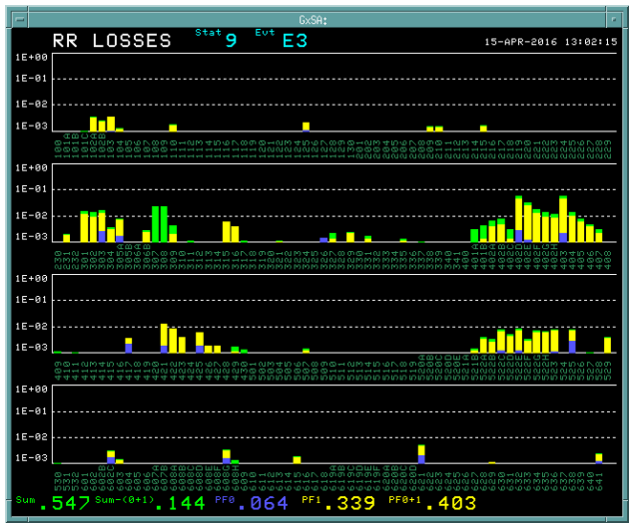

Figure 5: Loss around Recycler for 525 kW operation April 2016.

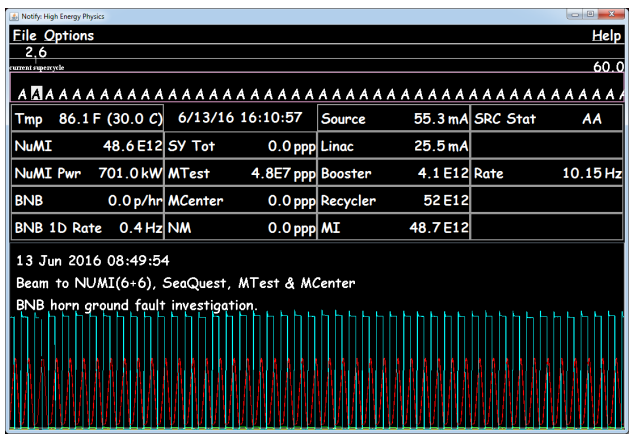

Figure 6: On June 13th, 2016, we demonstrated operation at the NOνA design 700 kW level. Some work remains to be done on loss control before we operate consistently at this level.

402 region: these are single-turn losses caused by tails from the operation of the gap clearing kicker [10] system removing beam from the injection gap, and is directly proportional to the amount of uncaptured (DC) beam present.

The installation of the collimation system is tightly constrained by available space. In order to contain the resultant hadronic shower, the secondary collimator must extend around two feet from the beam pipe in the transverse directions. In most parts of the ring, Recycler is only one foot from the ceiling. There are two locations with high ceilings in the tunnel—where the ring meets the old transfer lines to the Tevatron for protons (locations 523-529) and antiprotons (613-619). The former location is occupied by the new extraction line from Recycler to deliver 2.5 MHz protons to the Muon Campus, so we are led to select the latter.

VACUUM

In its incarnation as an antiproton storage ring, the Recycler vacuum was maintained at ultra-high levels (1×10^{-10} torr or better) with Titanium Sublimation Pumps. This level of vacuum isn't necessary now the beam remains in the ring for less than a second, and the use of TSPs presents some difficulties. Primarily, the titanium in the TSPs is a consumable, and is nearing the end of its life—something must be done. The use of TSPs presents additional downsides: to use TSPs, it is necessary to first bake the beam pipe after breaking vacuum to remove any adsorbed water. The heater tape for the bake-out is also reaching the end of its life, and would need to be replaced wholesale were this capability to be required; the requirement to bake also adds an extra week or so to the overhead associated with breaking vaccum.

We choose instead to convert the Recycler to a fully ion-pumped design, adding two additional ion pumps per half-cell to match the vacuum design of the Main Injector. A total of 600 pumps mus be installed. To minimize the required cutting and welding, and subsequent alignment work, we cut into the TSP cans themselves and weld on vacuum ports. In the three-month 2015 summer shutdown, we were able to complete about a third of the ring. An additional third will be completed in each of the 2016 and 2017 shutdowns.

RECYCLER FAST HORIZONTAL INSTABILITY

As previously reported in [11], when we started operating the Recycler to deliver beam to NuMI, in August 2014, we observed at high intensities a fast horizontal instability in the few hundred machine turns after injection, with a growth rate of 10-15 machine turns. The instability, shown in figure 7, is only driven in the horizontal plane—at our normal operating point, there is some coupling of this motion to the vertical plane. It has a strong dependence on linear charge density (bunch length). With such a rapid growth rate, the transverse damper system is unable to control the instability.

This is a single-batch effect: the instability only affects the newly-injected batch, and does not transfer to other batches already in the machine. In fact, existing beam in the machine provides extra stability. In August 2014, the intensity threshold for the instability was observed to be around 25% higher when injecting into a machine which already contained one or more batches of beam than when injecting into an empty ring. The stabilizing effect depends only on the total number of protons already present in the machine—the distribution of those protons into a smaller number of high intensity bunches or a larger number of low intensity bunches is observed to have no effect.

Since the 2014 fall shutdown, the instability threshold was observed to have increased, and no longer occurred for normal operations—either boxcar stacking or slip-stacking at any intensity up to 700 kW. During 2015, it was possible to force the instability to occur by manipulating bunch rotation in the Booster to create shorter bunches, rendering it

ISBN 978-3-95450-185-4

accessible to special machine studies. In 2016, after additional ion pumps had been installed in a third of the ring, and higher-intensity beam had caused additional "scrubbing" of the beam pipe and reduced the secondary electron yield (SEY) [12], we are no longer able to generate the instability.

We have identified the instability as caused by electron cloud. We have some evidence that suggests the presence of electrons [12, 13], and measure tune shifts that are consistent with a model of electron cloud buildup [14]. We assume that a small fraction of the electrons produced in the gradient magnets are trapped in the magnetic bottle formed by the converging magnetic field lines, providing a seed for the electron cloud that persists until the beam passes again on the next turn. This cloud seed would be dispersed by below-threshold bunches, explaining why we were able to run in August 2014 with the second and subsequent batches over the instability threshold, but the first batch under it. We note that this instability seems to share some features with an instability at high field in the CERN PS, also a combined function machine, which has also been identified as due to electron cloud [15].

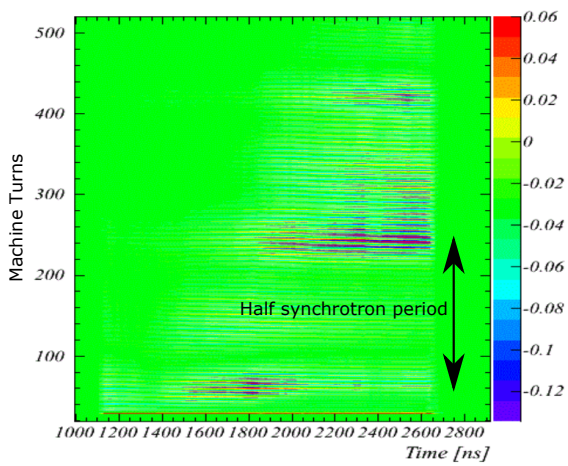

Figure 7: The fast recycler instability in the horizontal plane. The color scale represents horizontal motion, in arbitrary units. Shown is the first injected batch (1.6 μs) for about 500 turns after injection. The incoming beam is not perfectly matched to the rf bucket here, and the instability is seen to occur at bunch length minima, and in the center and the end of the batch.

The instability does not trouble 700 kW operation. We observe that as we increase the beam intensity, we continue to "scrub" the 316L stainless steel beam pipe and reduce its SEY, and so expect that we will be able to increase the per-pulse intensity by some further amount without encountering this instability.

CONCLUSION

Using the Recycler as a slip-stacker for the Main Injector, and running the ultimate 6+6 mode of slip-stacking, we have achieved a consistent sustained performance at the 615 kW level, and have demonstrated operation above 700 kW. A collimation system will be installed in Recycler this summer, which should control the losses at high intensity, and so permit sustained 700 kW operation. The Recycler vacuum system is in the process of being upgraded to be fully ion-pumped, providing a sustainable vacuum system for the future. As we continue to push the beam power beyond the design 700 kW, it will remain important to control the activation of the tunnel components in order to be able to perform maintenance effectively.

REFERENCES

[1] D. S. Ayres *et al.*, "The NOvA Technical Design Report," FERMILAB-DESIGN-2007-01.

[2] P. Derwent, "Accelerators for Intensity Frontier Research," Proceedings of IPAC2012, New Orleans, Louisiana, USA (2012), pp. 4185-4189.

[3] K. Seiya *et al.*, "Multi-batch Slip Stacking in the Main Injector at Fermilab," Proceedings of PAC07, Albuquerque, New Mexico, USA (2007), pp. 742-744.

[4] W. Pellico *et al.*, "FNAL—The Proton Improvement Plan (PIP)," Proceedings of HB2014, East Lansing, Michigan, USA (2012).

[5] K. Seiya, "Booster Upgrade for 700kW NOvA Operations," Proceedings of HB2014, East Lansing, Michigan, USA (2012).

[6] K. Seiya *et al.*, "Beam studies for the Proton Improvement Plan (PIP)—Reducing beam loss at the Fermilab Booster", THPF131, Proceedings of IPAC'15, Richmond, VA, USA (2015).

[7] R. Ainsworth *et al.*, "Simulations and Measurements of Stopbands in the Fermilab Recycler", in Proc. 7th International Particle Accelerator Conference (IPAC'16), Busan, Korea, paper MOPOY010, pp. 864-866, 2016.

[8] B. C. Brown *et al.*, "The Fermilab Main Injector: high intensity operation and beam loss control," Phys. Rev. ST Accel. Beams 16 (2013) 7, 071001.

[9] B. C. Brown *et al.*, "Fermilab Main Injector Collimation Systems: Design, Commissioning and Operation," Proceedings of PAC09, Vancouver, Canada (2009).

[10] I. Kourbanis *et al.*, "A gap clearing kicker for Main Injector," Proceedings of PAC11, New York, USA (2011).

[11] J. Eldred *et al.*, "Fast Transverse Instability and Electron Cloud Measurements in Fermilab Recycler," Proceedings of HB2014, East Lansing, Michigan, USA (2012).

[12] Y. Ji, L.K. Spentzouris, and R.M. Zwaska, "Secondary Electron Yield Measurement and Electron Cloud Simulation at Fermilab", Proc. 6th International Particle Accelerator Conference, Richmond, VA, USA, paper MOPMA039, pp. 629-632,2015.

[13] J. Eldred *et al.*, "Electron Cloud Measurements in Fermilab Main Injector and Recycler," Proc. 6th International Particle Accelerator Conference, Richmond, VA, USA, paper MOPMA026, pp. 604-607, 2015.

ISBN 978-3-95450-185-4

[14] S. A. Antipov, P. Adamson, S. Nagaitsev, and M.-J. Yang, "Study of Fast Instability in Fermilab Recycler," Proc. 7th International Particle Accelerator Conference (IPAC'16), Busan, Korea, paper TUPOR029, pp. 1728–1730, 2016.

[15] R. Steerenberg *et al.*, "Nominal LHC beam instability observations in the CERN proton synchrotron," Proceedings of PAC07, Albuquerque, New Mexico, USA (2007), pp. 4222-4224.

ISBN 978-3-95450-185-4

THE OPERATION EXPERIENCE AT KOMAC*

Yong-Sub Cho†, Kye-Ryung Kim, Kui Young Kim,
Hyeok-Jung Kwon, Han-Sung Kim, Young-Gi Song
Korea Atomic Energy Research Institute, Korea Multi-purpose Accelerator Complex,
Gyeongju, Gyeongbuk, Republic of Korea

Abstract

A 100-MeV proton linac at the KOMAC (Korea Multi-purpose Accelerator Complex) is composed of a 50-keV microwave ion source, a 3-MeV four-vane-type RFQ, a 100-MeV DTL and 10 target stations for proton irradiation on samples from many application fields. The linac was commissioned in 2013 and the user service started in July 2013 with delivering proton beam to two target stations: one for a 20-MeV beam and the other for a 100-MeV beam. In 2015, the linac has been operated more than 2,800 hours with an availability of greater than 89 %. The unscheduled downtime was about 73 hours, mainly due to troubles of ion source arcing and failures of pulsed high voltage power system. More than 2,100 samples from various fields such as materials science, bio-life, nano technology and nuclear science, were treated in 2015. Currently, a new target station for radioisotope production is under commissioning and a new target station for low flux irradiation experiments is being installed. Operational experiences of the 100-MeV linac during the past 3 years will be presented in the workshop.

INTRODUCTION

KOMAC is located in Gyeongju, which was established as a branch of KAERI (Korea Atomic Energy Research Institute) in 2013. Among the gross area of the KOMAC site is 1,100 m × 400 m which is enough to house a 1-GeV proton accelerator, only 450 m × 400 m was developed for the 100-MeV linac as a 1st stage of the KOMAC as shown in Fig. 1 and the remaining area is reserved for future extension. An accelerator building, a beam application building, a utility building, power station and water treatment building are under operation [1]. The construction of the dormitory building will be finished in October, 2016 and the construction of the administration building starts in September, 2016.

After awarding the operation license, the operation of the 100-MeV linac started in 2013. Since then, two target stations have been opened for users. The operation statistics is reported in the following section. To meet the various and dedicated users' needs, a radioisotope production beam line was developed in 2015 and a low-flux beam line is under construction in 2016, which are described in detail. Finally the operational issues related to the accelerator components and user services are discussed in the paper.

* Work supported by Ministry of Science, ICT & Future Planning of Korean Government.
† choys@kaeri.re.kr

Figure 1: KOMAC site.

100-MeV LINAC OPERATIONS

Accelerator

The main specifications of the 100-MeV linac depending on the energy of the beam line are summarized in Table 1. The characteristic of the linac is that it has two beam extraction points, one is at 20-MeV and the other is at 100-MeV. The designed beam duty up to 20-MeV is 24% and the other section up to 100-MeV is 8%. The accelerator layout is shown in Fig. 2. The ion source is a microwave ion source and magnetic LEBT (Low Energy Beam Transport) is used to match the beam to RFQ. A four-vane-type RFQ is used to accelerate the beam from 50-keV to 3-MeV. Total 11 DTL tanks are used to accelerate the beam from 3-MeV to 100-MeV. The operating frequency of RFQ and DTL is 350 MHz. There are total 9 klystrons to drive the 100-MeV linac. And total 4 modulators are used to drive 2 or 3 klystrons simultaneously. The 4 independent DTL tanks at 20-MeV section are driven by 1 klystron. The resonant frequencies of all the cavities such as RFQ, DTL and MEBT tanks are controlled by independent RCCS (Resonant frequency Control Cooling System).

Table 1: Specifications of the KOMAC Linac

Parameters	20-MeV	100-MeV
Output energy [MeV]	20-MeV	100-MeV
Peak beam current [mA]	20	20
Max. beam duty [%]	24	8
Avg. beam current [mA]	0.1~4.8	0.1~1.6
Pulse length [ms]	0.1~2	0.1~1.3
Max. repetition rate [Hz]	120	60
Max. avg. beam power [kW]	96	160

ISBN 978-3-95450-185-4

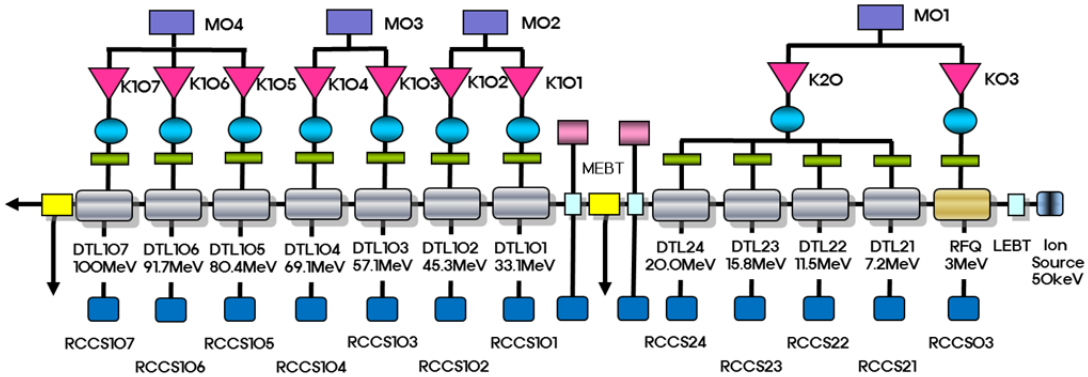

Figure 2: KOMAC linac layout.

The commissioning of the linac was carried out in 2013 and obtained an operation license of 1 kW beam on target. Then the beam power was ramped up to 10 kW with a revised operation license in 2014. The total operation time from 2013 to 2015 was 8,101 hours with accumulated availability was 86.8%. In 2015, the unexpected down time was 73.5 hours, of which the most frequent time consuming failures were modulator interlocks, DTL drift tube failures and the ion source interlocks as shown in Fig. 3.

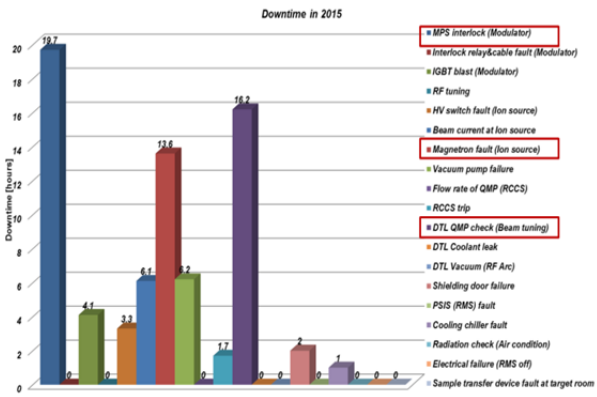

Figure 3: Downtime statistics in 2015.

Beam Service

A total 330 of research projects were proposed from the users during the past 3 years (2013~2015) and the KOMAC could support only 261 projects among them as summarized in Table 2. The numbers of R&D projects proposed are increasing year by year as shown in the Table 2.

Table 2: Service Statistics of the KOMAC Linac

Year	Proposed	Served	Ratio [%]
2013	56	39	69.6
2014	121	103	85.1
2015	153	124	81.0
Total	330	261	79.1

In beam time wise, a total of 768 days were requested, but the KOMAC could supply 460 days which are about 60% for 3 years of operation. A total of 5,058 samples were treated during the same period. The main fields of users are such that 26.4% for bio-life researches, 26.4% for nano/materials science and 22.6% for space and basic science.

BEAM LINE DEVELOPMENT

The 100-MeV beam line layout is shown in Fig. 4. A total of 5 target stations are designed and target rooms were already constructed. A general purpose beam line, which is in operation, is the straight one. Another two beam lines have been developed over the past two years, one is the radioisotope (RI) production beam line and the other is a low-flux beam line. The construction of the RI production beam line was completed in 2015 and the commissioning is underway. The radiation safety inspection will be performed in October, 2016 and the operation starts after obtaining its operation license in 2016. Construction of the low-flux beam line is completed in 2016, and is to be commissioned in 2017.

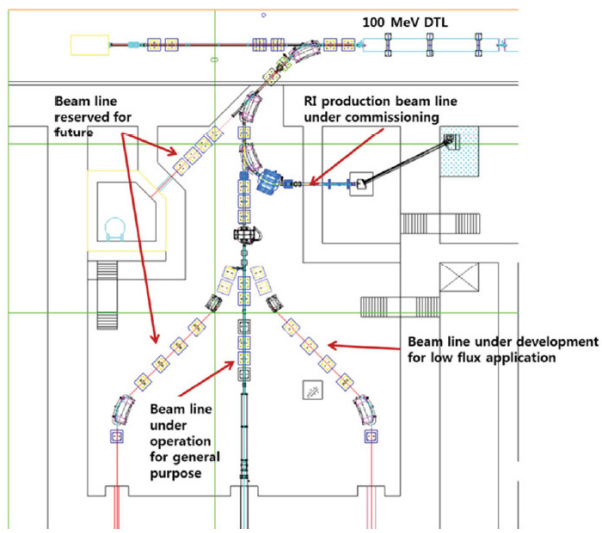

Figure 4: 100-MeV beam line layout.

RI Production Beam Line

The specification of the beam line is summarized in Table 3. The RI beamline is first to produce Sr-82 and Cu-67 by using 100-MeV proton beam. The Sr-82 is used to monitor the blood flow in the cardiac tissue and can be

ISBN 978-3-95450-185-4

produced by using RbCl as a target material. The Cu-67 is used for cancer therapy and can be produced by using ZnO as a target. The separation and purification of the produced RI's are to performed at either HANARO research reactor facilities or Advance Radiation Technology Institute (ARTI), which are also facilities of KAERI [2].

Table 3: Specification of RI Production Beam Line

Parameters	Values
Energy	100 MeV
Peak current	20 mA
Max. duty	3 %
Average beam power	Max. 60 kW
Energy per pulse	1,000 J/pulse
Target diameter	100 mm
Scanning method	Wobbling

The beam line is composed of a beam transport system, a target transport system, a target cooling system and a hot cell. The beam transport line mainly consists of two 45° bending magnets, of which the pole tip field was 1.5 T considering the limited space. The beam window of AlBeMet was installed at the end of the beam transport line. The thickness of the beam window is 0.5 mm and the estimated energy loss in the beam window is less than 1%, which generates maximum heat of 360 W, which is dissipated by a forced air convection cooling system [3].

The target transport system is used to transport target carrier from the hot-cell located outside the target room to the irradiation chamber in the target room. The target carrier is driven by an AC servo motor with chain. The target transport system is full of circulating deionized water, which is used not only to cool the target but also to shield the neutron during beam irradiation.

The hot-cell is divided into two regions, one is used for loading or unloading the target from the target carrier, the other is used to handle the target into the shielding chamber for transportation. The hot-cell is shielded with 150 mm thick lead plate and with 375 mm thick lead glass windows. Two sets of master slave manipulators are installed to handle the target.

An independent cooling skid was installed to cool the target. The cooling capacity is 30 kW, which is considered a maximum power at first stage, and the flow rate is 180 l/min. An air-cooled chiller is used to remove the heat from the skid. The radioactivity monitor and the conductivity meter were installed in the skid to monitor the possible leakage of the radioisotopes from the target. The skid is also located outside of the target room and pipe line is installed from the skid to the target transport system through hot-cell. The pipe line is shielded 5 mm thick lead plate. The target system inside the target room is shown in Fig. 5 and the cooling skid and hot cell are shown in Fig. 6.

Figure 5: Target transport system in the target room.

Figure 6: Cooling system and hot-cell.

We performed a beam test to check the radio isotope production with during commissioning stage. A 100-MeV beam was irradiated to Zn target to produce Cu-67. Peak current during the irradiation was 0.4 mA. The radiation level was 5.5 uSv/hr at the target right after the irradiation. We measured gamma ray spectrum by using HPGe detector and found peaks around 91 keV, 93 keV and 184 keV, which showed the production of Cu-67 as shown in Fig. 7. From the spectrum measurement, we concluded that the overall system is functioning without any major fault [4].

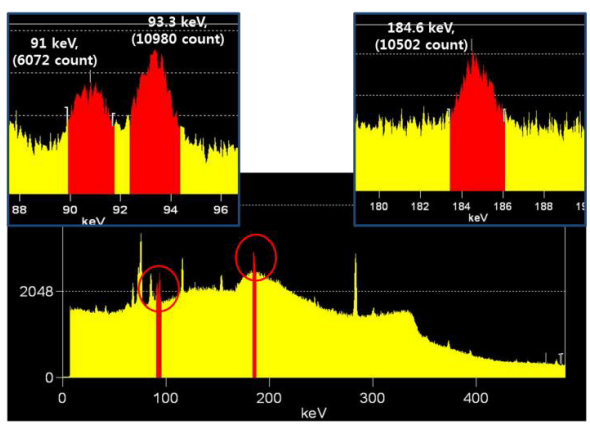

Figure 7: Gamma-ray spectrum from the Zn target.

ISBN 978-3-95450-185-4

Low-Flux Beam Line

The low-flux beam line is designed to deliver low-flux beams to users from simulation of the space radiation, detector development and so on. The users in this field demand a beam with a low-flux and a high-duty cycle because CW-like low-flux is most suitable for such applications. To meet these requirements, we are going to use a high-power collimator to reduce the beam flux to the target while maintaining the reasonable peak current. The design specification of the beam line is summarized in Table. 4 and the beam transport system under installation is shown in Fig. 8 [5].

Table 4: Specification of Low Flux Beam Line

Parameters	Values
Energy	20 ~ 100 MeV
Peak current at accelerator	0.1 mA
Max. duty	8 %
Max. power at collimator	800 W
Beam current at target	10 nA in average
Max. beam power at target	1 W
Target size	100 mm X 100 mm
Uniformity at target	± 5%

Figure 8: Low-flux beam line installation.

A high-power collimator was designed, which has a 15° sloped-corn shape of graphite, which was chosen to minimize neutron production and to have high melting temperature. A hole of 10 mm in diameter is located in the center of the collimator and the beam is guided to the collimator in off-axis direction, then only part of the off-centered beam is transmitted to the downstream through the hole. If the beam center is diverted 40 mm from the center of the collimator, the beam current reduces to 1/1,000 assuming a Gaussian beam profile. The collimator is located downstream of the 25° bending magnet, therefore we are able to control the direction of the beam center into off-axis direction. The collimator was designed to be cooled by water with a cooling channel located at the copper, which is back-plate material of the graphite.

Two sets of octupole magnets are used to produce spatially uniform beam at the target. Two octupole magnets are installed in the beam waist position of each transverse direction to facilitate the beam size adjustment in each direction respectively.

An AlBeMet is used as a beam window. In this beam line the cooling of the window is not necessary, but the size of the window is 300 mm in diameter, which is 3 times larger than that was used in RI production beam line.

OPERATION ISSUES

Several issues found for 3 year operation periods are reported.

Ion Source

The microwave ion source is driven by a 2.45 GHz microwave power. The operation parameters are such that the extraction energy is 50 keV with 20 mA peak current and the duty is 30% (2.5 ms, 120 Hz), which means the ion source is almost in CW operation. Thus we always turn on the plasma and extract a pulsed beam by switching the extraction power supply. 80 stacks of IGBT (Insulated Gate Bipolar Transistor) are used as a high voltage switch [6]. After 1,000 hours of plasma operation, we experienced frequent sparks at the bias electrode which destroyed the switches. It was found that the BN (Boron Nitride) which was used as a microwave window was deposited on the tip of electrodes as shown in Fig. 9, which made the part insulator. And we believed this was the main source for the frequent sparking after several hundred hour operation. To cope with the above issues, we installed a ion source test bench to improve the ion source and also are going to do the preventive maintenance to replace all parts of the ion source at every 6 months.

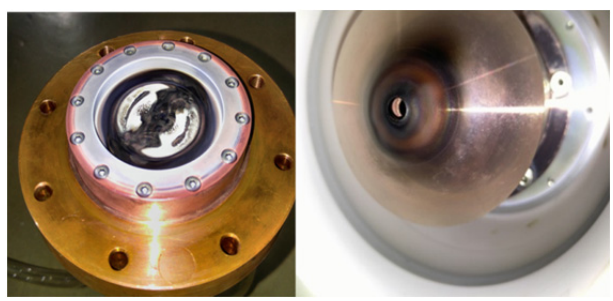

Figure 9: BN window (left) and BN coating on tip of the extraction electrode.

Quadrupole Magnet inside Drift Tube

Two types of DTQs (Drift tube quadrupole magnets) are used. One is a pool-type electromagnet which used an enamelled wire with nickel coated yoke and was immerged in the cooling water. The pool-type magnets were used for DTL from 3-MeV to 20-MeV to save the space inside the drift tube. The other is a magnet which used a hollow conductor which was used for DTL from 20-MeV to 100-MeV [7]. There were failures among the pool-type

ISBN 978-3-95450-185-4

DTQs and eight DTQs were replaced. The inside of the failed DTQs was investigated and we found that enamel coating was separated from the wire and the yoke was covered with rust as shown in Fig. 10. Low resistivity of the cooling water which was supplied by accident for few days and high radiation during beam commissioning seems to be the factors to affect the degradation of the pool type DTQs. We consider changing the pool type magnet into permanent magnet or adding liquid type insulator.

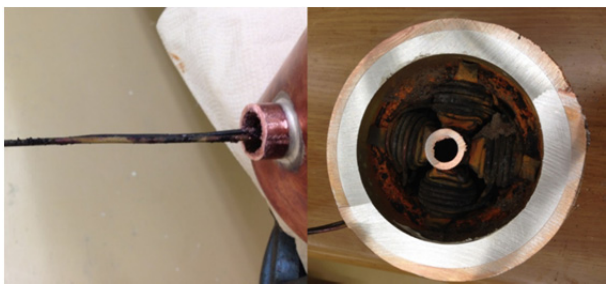

Figure 10: Enamel coating separation from the wire (left) and the yoke covered with rust (right).

Vacuum Pump

One TMP (Turbo Molecular Pump) and three IPs (Ion Pump) are installed per DTL tank. A TMP is used for initial evacuation and after the operation of the IPs, it is turned off and the vacuum of the DTL is maintained with only IPs. The normal vacuum level was from 5E-8 to 10E-8 Torr. After 3-year operation, we observed vacuum-bursts phenomena in the DTL tank as shown in Fig. 11. We suspected the argon instability of the ion pump and operated the TMP during operation which removed the vacuum bursts. Up to now, 3 IPs and a TMP are operating and we are going to replace an IP with a TMP.

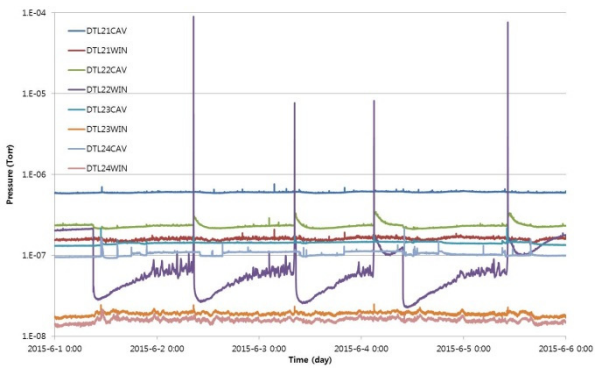

Figure 11: Vacuum burst in the DTL.

RF Network

The characteristics of the KOMAC RF system are such that 4 independent DTL tanks are driven by one klystron and 2 or 3 klystrons are driven by one klystron modulator as shown in Fig. 2. To drive 4 DTL tanks with 1 klystron, we adjusted the power balance from the design stage and installed a phase shifter at each RF transmission line. Also the resonance frequency of each DTL is controlled by an RCCS (Resonance Frequency Control Cooling System). To drive the group of klystrons with a modulator, we grouped the klystron which had the same perveance and the resonance circuit of the modulator was adjusted to the load impedance. By doing this, we could operate the RF system without problems. The normalized beam emittance was measured to be 0.23 π-mm-mrad which agrees well with the design value of 0.20 π-mm-mrad [8,9].

Shielding Door

There were frequency failures of the shielding door of the target room. The shielding door consists of 1.1 m thick concrete and 0.9 m thick steel and its mass is 26 ton. For beam service, the shielding door should be opened and closed in every irradiation. The severe case is the low flux irradiation service which needs few pulses. In this case, the shielding door needs many times of operation. This is one reason to develop a low flux beam line which will be operated without a shielding door.

History Management System of the Component

The history management system of the components was developed to operate the linac efficiently. The system used a QR code and tablet which enables us to scan the information in a distance. The possible distance is decided from the size of the QR code attached in the component. The management system includes specification, maintenance history, drawing and related document.

Diversity of the Beam Requirement from Users

Only two general purpose target rooms have been operating for 3 years, one for 20 MeV beam, the other for 100 MeV beam, and supported users from various fields such as material, bio, space and basic science. Moreover, user requirements are wildly varying in beam energy (from 20 MeV to 100 MeV), peak current, beam size, duty, number of particles (total dose), spatial uniformity of dose, timely uniformity of dose and so on. Therefore, we supply 8-discrete energy of beam to users by turning on or off each DTL tank up to 100 MeV and low-peak beam current down to 0.1 mA with some poor stability. This kind of limitations is to be resolved not only by accumulating more operation data but also operating target room more specifically. (for example high-flux beam line for RI production, low-flux beam line and general purpose.)

CONCLUSION

The operation experiences and status of the KOMAC linac are reported. Two new beam lines are under commissioning or construction in addition to the existing beam lines. Several operational issues are also summarized.

ISBN 978-3-95450-185-4

REFERENCES

[1] Y. S. Cho, in *Proc. LINAC'14*, Geneva, Switzerland, 2014, pp. 413-416.

[2] H. J. Kwon *et al*., *Journal of the Korean Physical Society*, vol. 67, no. 8, (2015, 10) pp. 1387 – 1392).

[3] H. S. Kim *et al*., in *Proc. IPAC'16*, Busan, Korea, 2016, pp. 1349-1351.

[4] S. P. Yun *et al*., in *Proc. IPAC'16*, Busan, Korea, 2016, pp. 1384-1386.

[5] H. J. Kwon *et al*., in *Proc. IPAC'16*, Busan, Korea, 2016, pp. 938-940.

[6] D. I. Kim *et al*., *Journal of the Korean Physical Society*, vol. 62, No. 11, June 2013, pp. 1591-1594.

[7] Y. S. Cho *et al*., *Journal of the Korean Physical Society*, vol. 52, No. 3, March 2008, pp. 721-726.

[8] H. J. Kwon *et al*., *Journal of the Korean Physical Society*, vol. 59, No. 2, August 2011, pp. 623-626.

[9] J. S. Hong *et al*., *Journal of the Korean Physical Society*, vol. 59, No. 2, August, 2011, pp. 635-638.

ISBN 978-3-95450-185-4

INVESTIGATION TO IMPROVE EFFICIENCY AND AVAILABILITY IN CONTROL AND OPERATION OF SUPERCONDUCTING CAVITY AT ESS

Rihua Zeng, European Spallation Source ERIC
Olof Troeng, Lund University, Sweden

Abstract

The higher efficiency and higher availability (fault-tolerant oriented) of RF & Cavity system (with beam loading) to operate at, the more dynamic details needs to be identified, so as to have the abilities (a) to work at nonlinearities, (b) to work close to limitation, and (c) to change operation point quickly and correctly. Dynamic detail identifications rely heavily on high precision measuring and characterizing basic cavity parameters (Q_L, R/Q, dynamic detuning, phase and amplitude) and system behaviours under beam-RF-cavity interactions. It is especially challenging to characterize these dynamics under varying operating points or environment. Advanced technologies in LLRF and ICS providing real time/online characterizing will be the key enablers for addressing such challenges. However, to be successful, the deployment of these technologies must be embedded within local conditions taking into account available resources, existing hardware/software structures and operation modes. Several improvement approaches will be introduced. For example, 15% or more energy efficiency improvement at ESS will be obtained by reduction of power overhead and optimization of operation.

INTRODUCTION

The European Spallation Source is a planned neutron source to be built in Lund, Sweden, with a start of neutron production in 2019. The performance goals are an average beam power at the target of 5 MW, with a 62.5 mA current and a pulse repetition rate and length of 14 Hz and 2.86 ms, respectively. It is to be built as a green plant, which places stringent demands on powers conservation and recycling of energy. This will be achieved by careful design and modern power recapture methods, such as using the cooling water to heat the surrounding municipalities. This also places stringent demands on the low level RF systems, especially as the plant at the same time has an operational goal of 95% availability and a comparably short time from start of final design to commissioning. Here we will describe some of the consequences these demands have on the RF, Cavity and LLRF system, and the proposed solutions and development projects that have started in order to reach this goal.

ENERGY EFFICIENCY

Typically linear accelerators use klystrons as RF power amplifiers, as these can deliver the power to get necessary accelerating gradients in the cavities of the Linac. In feedback control mode, to facilitate the control of the phase and the amplitude of the fields in the cavities, the klystrons are typically run far below saturation in a linear region of operation to leave some power overhead for regulation. Such overhead is not necessary if klystrons are operated in open loop. There are quite some electron machines (MAXIV, PSI, CLIC, etc.) in which klystrons are operated at their saturation point.

To better describe system efficiency, the power overhead in this paper is defined in a wide range: the difference between the maximum RF amplifier output and the power delivered to the beam, including necessary margin for error compensation and transient behaviour in feedback control, and also the power dissipation in RF distribution system. The operation points of klystron in traditional accelerators are often chosen at lower than 70% of saturation (where klystrons input-output power curve are much linear), to ensure adequate power overhead without considering high-order dynamic details. In JPARC, great effort has been put to figure out dynamic details of klystron and normal conducting cavities under heavy beam loading. As a reward for their effort, more of their klystrons are able to work at 85% of saturation level, reducing significantly power consumption. Advanced technologies in modern high performance hardware make these solutions possible, with great flexibility in configuration and short time in implementation.

Within the ESS project we will look into system dynamic details and try every effort to step further, so as to operate the power amplifiers at 90% of their saturation level, as shown in Figure 1.

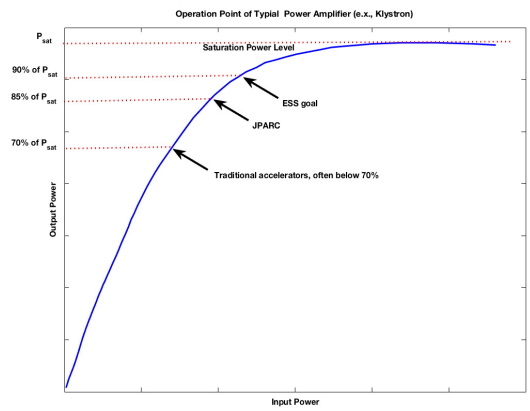

Figure 1: Operation points of klystron in closed loop in different facilities and ESS goal.

The higher efficiency point of power amplifiers we want to operate at, the more dynamic details we have to figure out for both cavity system and RF system. Dynamic detail identifications rely heavily on high precision measuring and characterizing basic cavity parameters (Q_L, R/Q, dynamic detuning, phase and amplitude) and system behaviours under beam-RF-cavity interactions. It

ISBN 978-3-95450-185-4

is especially challenging to characterize these dynamics under varying operating points or environment. Advanced technologies in LLRF and ICS providing real time/online characterizing will be the key enablers for addressing such challenges. Real time calibration and online diagnostic system playing more and more important roles in modern technology, if applied appropriately, would be a very effective and innovative solution to these problems. Different real time/online calibration schemes will be introduced in this paper and discussion will be made to see how well they can be applied at ESS.

More development projects in LLRF system are also looking into the use of different techniques, such as feedback, predistortion and feedforward circuits. Both static and adaptive algorithms will be investigated. As the complete Linac at ESS will incorporate around 155 different RF sources, working at powers from 20 kW to 1.5 MW, a self-learning and adaptive system would minimise the commissioning time for the complete system.

AVAILABILITY

The goal of the availability of the ESS neutron source is 95%. In order to make this possible, the effort to enhance availability must be paid in every corner all over the design, construction, commissioning and operation stages. Two aspects of availability improvement is distinguished in this paper:

- Availability enhancement in system design and development. This includes careful design of overall system, careful selection of reliable components and product, and also possible inclusion of active or passive redundancy.
- Fault tolerance in operation. It acts more a strategy at the system level to mitigate failures that will occur inevitably in final commissioning and operation. One topic often mentioned for fault tolerance design, for example, is to have the possibility to run with one or more cavities in a detuned position when LLRF, Klystron or modulator get failure.

In early design and development stage, it is much easy to integrate availability improvement in design by considering redundancy and overall operation efficiency. For example, one design approach in LLRF system aimed for at the moment is to make use of a common hardware platform for all the LLRF systems and, as far as possible, also for the beam instrumentation systems. This will simplify service and reduce the cost of the necessary inventory of spare parts. The hardware will be built around an FPGA solution, which moves the adaptions to the different parts of the linac from hardware to software. As the FPGA makes it possible to both adjust the actual control layout, as well as the control parameters, to each individual system, any gains found in the development projects running in parallel to the industrial design of the hardware can be utilised. The additional cost of this solution is the necessity to have a very stringent version tracking system, in order to guarantee that each individual LLRF board has the correct code loaded that corresponds to its position in the Linac.

The need, if any, of redundant structures in the LLRF chain will be decided on the experience of other facilities, and on analysis of the prototype hardware. Even though there is not an inherent safety aspect of a high reliability, as in accelerator driven reactor, the goal of the ESS still sets a stringent demand on the hardware and software reliability.

Another important factor to improve availability is to well conditioning and testing individual system before integrating into the whole system with beam. After system design and development, knowledge and experience obtained in testing and conditioning individual system will be crucial to identify manufacturing imperfections and design flaws, to provide feedback on system production, and to develop strategies minimizing mistakes in integration to whole system. There is always larger failure rates in system start up and initial operation, and it costs much less to avoid overlapping this larger failure stage with the period of test and commissioning whole accelerator system with beam. For example, it would be advantageous to be able to run the LLRF system together with the control and timing systems without having to be fully powered up and having a beam in the accelerator. In order to make this possible, the LLRF systems will be designed so that they can be run on their own, with a simulated cavity and beam. This will make it possible to test the whole control system of the Linac before all the parts of the accelerator itself are in place. The model of the cavity and beam will either be implemented in the FPGA, or as a separate circuit connected to it. Both variants have different strengths and risks connected to them.

The possibility to also include simulated faults in these modules, such as Klystron degradation or modulator failure, will make it possible to test the contingency parts of the control system, and prepare the system for the high availability goal.

Availability enhancement is very important but trial and practical, more on system integration perspective to find a systematic solution to variety of problems, and it is hard to cover all in this paper. The following sections of this paper are thus mainly focusing the effort and possible solution to the second availability aspect fault-tolerance in operation, and introduce some general methods that are common to the solution enabling to improve energy efficiency.

Frequent appeared failures in RF and cavity systems showed in other facilities are cavity quench, field emission, software/hardware/configuration errors, the interlock trips of the arc, vacuum, reflection power and temperature, and the failures from klystron, modulators and other key RF components. The failures must be detected and fixed as fast as possible. If the failures cannot be fixed at once, they must be bypassed quickly so as that the system can get recovered as soon as possible. Under this context, insight into system dynamics under different operation conditions, instant online diagnostics for key system parameters and high degree of automated operation are highly required to support early detection of the faults and fast recovery from failures. For example, a

ISBN 978-3-95450-185-4

cavity quench can be handled quickly by lowering the gradient of the troubled cavity in next RF pulse, if dynamic Q_L changes can be captured in real time; For the cavity/modulator/klystron failure, we could recovery the system either in a relatively short time by adjusting the adjacent cavities gradients and phases or by adjusting RF phases in all the downstream cavities, if system dynamics in different operation gradient/synchronous phase are well known in advance.

Most of systems are usually designed and optimized at certain nominal operating point, however, the final operation point in accelerator systems usually needs to be flexible enough to adjust away from design value. It requires also changing operation point quickly and correctly when it comes to the fault tolerance strategies where fast detection and fast recovery are essential. In this sense, similar with what we discussed in energy efficiency section, the higher availability of RF & Cavity system (with beam loading) to operate at, the more dynamic details needs to be identified, so as to have the abilities to work in different operation conditions and to change operation point quickly and correctly. The following sections describes thus more on what the system dynamics are and more how to figure out these dynamics [1].

CAVITY AND RF DYNMICS IDENTIFICATIONS

Dynamic details identifications rely very much on high precision measurement of basic cavity parameters (Q_L, R/Q, dynamic detuning, phase and amplitude) and RF system parameters (saturation curve, rising time, group delay, reflection and matching, etc), and consequent high quality data with high resolution, high precision and completeness.

While a variety of techniques become possible today for such high precision measurement thanks to the high performance hardware, how to calibrate these parameters at varying operating point due to system environment variations still challenging. Real time calibration and online calibration system playing more and more important roles in modern technology seems a very effective and innovative solution to this problem.

Cavity Dynamics in General

Some examples of general cavity dynamics are listed but not limited as follows:

- Cavity pass band modes
- Lorentz force detuning at different cavity field levels
- Lorentz force to cavity tuning transfer function
- Piezo tuner to cavity tuning transfer function (time domain, or frequency domain)
- Moto tuner to cavity tuning transfer function
- Microphonics spectrum
- System open loop matrix
- System closed loop matrix
- Cavity field behaviour close to and at quench
- Multipacting in cavity and power coupler
- Fast fault detection and fault recovery

Cavity Dynamics Online Identification

As mentioned earlier, dynamic details identifications rely very much on high precision and online measurement of basic cavity parameters: amplitude (accelerating cavity voltage)V_c, phase (synchronous phase) φ_b, loaded quality factor Q_L, cavity detuning $\Delta\omega$, and R/Q, which reflects the fundamental static and dynamic field behaviours of a RF powered cavity with beam loading [2]:

$$\frac{dV_{cav}}{dt}+\frac{\omega_0}{2Q_L}\left(1-i\tan\varphi_D\right)V_{cav}=\frac{\omega_0}{4}\left(R/Q\right)I \quad (1)$$

where $\tan\varphi_D$ is the detuning angle,

$$\tan\varphi_D=Q_L\left(\frac{\omega_0}{\omega}-\frac{\omega}{\omega_0}\right)\approx 2Q_L\frac{\Delta\omega}{\omega}$$

In steady state, V_{cav} reaches designed value V_c, and required generator current can be written as [2]:

$$I_{gr}=\frac{2V_c}{\left(R/Q\right)Q_L}+I_b\cos\varphi_b \quad (2)$$

$$I_{gi}=-\frac{2V_c}{\left(R/Q\right)Q_L}\tan\varphi_D-I_b\sin\varphi_b \quad (3)$$

These basic parameters are well discussed in literature but sometime defined in different ways. To make it consistent in this paper, the definitions of these parameters are explained. V_c is the absolute value of the line integral of the electric field seen by the beam along the accelerating axis, which reflects the maximum achievable energy gain for beam acceleration. φ_b is, for a given particle traversing the cavity, the phase shift from RF phase at which it obtain the maximum energy gain. It is equivalent to the phase angle between beam and accelerating voltage in vector diagram. Q_L is defined as 2π times the number of RF cycles needed for stored energy to dissipate on the wall and leak out the from couplers, which measures the 'quality' of cavity resonator, conveys the information of cavity field decay rate, and determines cavity bandwidth. $\Delta\omega$ becomes a key parameter in superconducting cavity due to long RF pulse (~3.5ms) operation along with high gradient level. R/Q relates the stored energy and maximum accelerating voltage acting on the beam, which depends on only the cavity shape for a given resonant mode. However, in proton machine, as the velocity of beam changes with its kinetic energy, even having the same cavity field, the accelerating voltage seen by the beam varies from cavity to cavity. Thus the R/Q has to be considered as R/Q (β) as it changes as beam velocity β varies along the linac [3].

Static coefficients of accelerating voltage V_c to probe power can be determined by phase scan methods, and dynamic voltage is then derived from real time probe power measurement. A high signal to noise ratio of probe power signal and high isolation to other measurement channel are critical to monitor accurately real time voltage variations. Some necessary filtering is also needed to rule out the pass-band mode effect. Power amplifier driv-

ISBN 978-3-95450-185-4

ing current is determined by forward power, where high quality directional coupler with good directivity is essential to minimize mixed reflected power. High precision beam current measurement is another important factor. Beam current variations during pulse and from pulse to pulse must be taken into account and it is better to have it below certain value.

Having adequate and high quality measurement of cavity amplitude V_c, driving current and beam current, as well as timing of beam current, other dynamic parameters beam phase, R/Q, and Q_L can be derived from equation 1 with small enough sampling step and long enough sampling data. It is then able to formulate a linear least square problem for estimation of these parameters, which is described in the other paper in this conference.

For dynamic detuning and Q_L, another widely used and well-proved online diagnostic method in other facilities is worth considering. Derived from the same equation 1, dynamic $Q_L(t)$ and $\Delta\omega(t)$ can be written as:

$$\omega_{1/2}(t) = \frac{1}{2}\frac{d|V_{cav}|^2}{dt} \Big/ \left(|V_{for}|^2 - |V_{ref}|^2\right) \quad (4)$$

$$\Delta\omega(t) = \mathrm{Im}\left(\frac{dV_{cav}}{dt} - 2\omega_{1/2}(t)V_{for} \Big/ V_{cav}\right) \quad (5)$$

Where $\omega_{1/2}(t) = \omega_0(t)/2Q_L(t)$. Dynamic $Q_L(t)$ and $\Delta\omega(t)$ in this way are only related to probe power and forward power, affected probably less by the noise and perturbations. The precision of dynamic $Q_L(t)$ and $\Delta\omega(t)$ depends on how precise the measurement of cavity probe power, cavity forward power and reflected power can be. It is reported that better precision will be achieved if good isolation and correction of forward power and reflected power is made [4, 5].

RF Dynamics in General

Some examples of general cavity dynamics are listed but not limited as follows:

- Power amplifier input-output characteristics (power and phase) at different modulator voltage
- Modulator ripple frequency and amplitude
- Circulator characteristics (return loss, frequency) under different power consumption, different reflection power, and working temperature
- Power amplifier bandwidth variation at different output power level
- Driver amplifier and power amplifier delay, rise time and falling time under different power level
- Phase drift in cables due to temperature or humidity changes

RF Dynamics Online Identification

Benefit from advanced hardware platform and one power amplifier (or two in spoke section) for one cavity system configuration, there are enough RF measurement channels around driver amplifier, before and after power amplifier, as well as around circulator. There is therefore good opportunity to carry out elaborate experimentation and make accurate measurement on individual RF components, and obtain adequate data with high resolution and high accuracy. With good quality of data and complete information of system, similar least square estimation method as mentioned in online cavity dynamic diagnostic would be applicable as well to estimate the real time RF system parameters, thereby giving online diagnostics for RF dynamics.

Another simpler method for online RF dynamic diagnostics would be also interesting. In this method, instead of using a pure pulse shape, appropriate RF input waveform with exponential slop or linear slop in cavity filling time is chosen to feed the klystron, in order to generate all power levels from zero to full power. By measuring RF powers before and after driver amplifier, klystron, and circulator, online characteristics of system dynamic such as nonlinearities, return loss and bandwidth variations would be obtainable. It gives valuable information to operate system at nonlinearities and to frequently change the operating points. The shape of the waveform has to be chosen carefully so as to be long enough to get adequate data sampling but short enough to increase efficiency.

ITERATIVE LEARNING FROM PRACTICE AND MODELLING

As analysed above, online system dynamic seems feasible and promising to address the challenges to achieve higher efficiency and availability, with big benefit from advanced technologies.

However, while algorithm and measurement methodology works ideally with the ideal cavity system, it is generally not possible to get a perfect response in reality, due to the uncertainties and errors such as fabrication errors, installation errors, measurement errors, random noises, feedback system transient responses, system environment variations and operation condition variations. Under these cases, the measurement and even the algorithms expect to be adjustable to maintain the required performances.

Further more, wide spread of cavity parameters make it impossible to employ a single “uniform’ control algorithm and control configuration data even for the same type of the cavities. Instead, adjustments and modifications are needed for each cavity and customized approaches are preferred to reflect cavity’s individual performance and characteristics. Under this context, a large number of data are expected and required for all the cavity systems in ESS linac. A controlled, centralized and searchable database is therefore necessary to save the data effectively and ensure to obtain the data immediately when using them.

When preparing to collect data, it is important to keep in mind which kinds of data are required, and to what extent the data quality should be. Although it is the best way to verify the data and refine the requirements in the normal operating cavities, it is always not practical and too late to generate requirements at final stage. Instead, the data and general data quality required could be estimated earlier from results of test stands or similar cavity

ISBN 978-3-95450-185-4

tests in other accelerator facilities, as well as the prediction of theory models. As an example, the time-domain transfer function data of piezo tuner to cavity detuning would be required to compensate the longer pulse Lorentz force detuning, according to the experiments carried out at Fermilab. Another example is that, the data resolution of better than 100ns can be concluded from theory model prediction for feedforward table to compensate beam-loading effects in normal conducting cavities.

Due to uncertainties in reality, practice (experiment and data) is always different from what predict in theory or model, however, models do provide us a framework for expressing such uncertainty in a precise, quantitative and controlled way, allowing us to exploit this to control individual variables and to make predictions that are optimal according to appropriate criteria. It contributes a lot for system development if we can learn from practice, and reviews the practice with theory/model predictions.

A quick and effective way to combine practice (data, experiment) and model/theory might be as follows:

- Build realistic models (measured transfer functions or high order mathematical models) or modify parameters of existing theory models, based on measured data from specific experiments.
- Adjust parameter values and table values, to obtain "ideal" configuration data for the models. This is achieved by judging if the model predict responses meet design requirement.
- Apply these "ideal" configuration data in real cavity system at test stand or other place available, and measure the response of each sub-system such as klystron-modulate, piezo tuner, motor tuner, and Lorentz force detuning. Elaborate and careful design of experiments for the excitation signals, measure techniques and data processing, are essential here to obtain required response from subsystem under measurement, while isolate or filter responses and cross-talk from other subsystems.
- Check if the measured response meets the design requirements. If not, try to identify the errors in model simulation by studying the effect produced by suspected errors. Correct errors when finding them.
- If the errors cannot be fixed, modify or improve the model to better reflect the effect of errors. Then repeat the second step, to obtain an "optimal" configuration data.
- Repeat or partly repeat above steps if necessary.
- Residual errors will be dealt with adjustable algorithm, which is also useful for the variations of environment and operation conditions.

In this way, the models and "optimal" configuration data will be more realistic and get matured through the process of prototype, test and series production. The cavity system can be much better understand as well. As a result, a more sophisticated system will be available in beam commissioning and normal operating phase so as to be able to operate the cavity system more effectively and efficiently.

In steps above, it is can be seen how an iterative learn process works from practice (data and RF experiments) and from theoretical analysis (model). Test/experiments, data, and models are not independent, but interact with each other for a better system development, which can be seen more clearly in Figure 2.

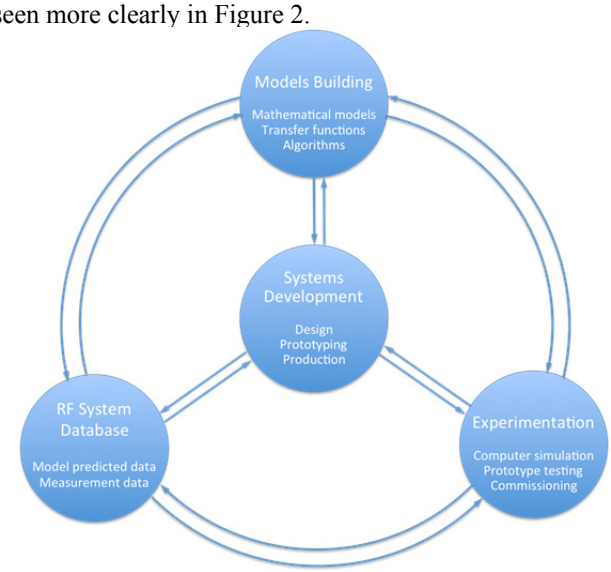

Figure 2: Different RF input waveform to make online RF dynamic diagnostics.

CONCLUSION

Increasing attention has been paid in accelerator for higher energy efficiency and higher availability, with the background of larger and larger scale of accelerator facility emerges. With the advent of advanced technology, it becomes promising to make online diagnostics of key system parameters and thus to gain insight to the system dynamics that was always viewed as black box, which are crucial to improve energy efficiency and availability.

However, to be successful, the deployment of these technologies must be embedded within local conditions taking into account available resources, existing hardware/software structures and operation modes. In spite of the complexity of system, it makes always sense to learn from practice, carrying out experiments, obtaining adequate high quality data, and then verified or guided in model or theoretical framework.

It is important to keep in mind challenges and tough facts expected to face during the phases of commissioning, normally operating and maintaining. It is equally important, if not more, to identify and find suitable solutions to address these challenges, and to understand better system dynamics and get to know its limitations, thereby testing, controlling and operating the system efficiently and effectively.

ISBN 978-3-95450-185-4

REFERENCES

[1] A.J. Johansson and R. Zeng, "Challenges for the Low Level RF Design for ESS", IPAC11, San Sebastian, paper MOPC161, pp. 460-462.

[2] S.Simrock, and M.Grecki. Lectures on LLRF & HPRF, 5th ILC School, 2010, Switzerland.

[3] Zeng, R., W. Schappert, and P. Jönsson, "Application Investigation of High Precision Measurement for Basic Cavity Parameters at ESS", Linac14, Geneva, paper MOPP040, pp 149-151.

[4] W. Schappert and Y. Pischalnikov, "Adaptive compensation for Lorentz force detuning in superconducting RF cavities", SRF 2011, Chicago, paper FRIOA01, pp.940-942.

[5] S. Michizono*, et al.*, "Performance of the LLRF system at S1-Global in KEK", IPAC11, San Sebastian, paper MOPC157, pp.451-453.

ISBN 978-3-95450-185-4

THE PATH TO 1 MW: BEAM LOSS CONTROL IN THE J-PARC 3-GeV RCS

H. Hotchi#, H. Harada, S. Kato, M. Kinsho, K. Okabe, P.K. Saha, Y. Shobuda, F. Tamura, N. Tani, Y. Watanabe, K. Yamamoto, M. Yamamoto, and M. Yoshimoto
J-PARC Center, Japan Atomic Energy Agency, Tokai, Naka, Ibaraki, 319-1195 Japan

Abstract

The J-PARC 3-GeV RCS started a 1-MW beam test in October 2014, and successfully achieved a 1-MW beam acceleration in January 2015. Since then, a large fraction of our effort has been concentrated on reducing and managing beam losses. In this paper, recent progresses of 1-MW beam tuning are presented with particular emphasis on our approaches to beam loss issues.

INTRODUCTION

The J-PARC 3-GeV rapid cycling synchrotron (RCS) is the world's highest class of high-power pulsed proton driver aiming for a 1-MW output beam power. As shown in Fig. 1, a 400-MeV H^- beam from the injector linac is delivered to the RCS injection point, where it is multi-turn charge-exchange injected through a 340-μg/cm^2-thick carbon foil over a period of 0.5 ms. RCS accelerates the injected protons up to 3 GeV with a repetition rate of 25 Hz. Most of the 25-Hz pulses are transported to the material and life science experimental facility (MLF), while only 4 pulses every several seconds are delivered to the following 50-GeV main ring synchrotron (MR).

Recently injector linac upgrades were completed, by which the injection energy was upgraded from 181 MeV to the design value of 400 MeV in 2013, and then the injection peak current was increased from 30 mA to the design value of 50 mA in 2014. Via these series of the injector linac upgrades, RCS now has all the hardware parameters to realize its design performance.

Figure 2 shows the history of the RCS beam operation. RCS was beam commissioned in October 2007 [1] and made available for the user program in December 2008 with an output beam power of 4 kW. Since then, the RCS beam power ramp-up has steadily proceeded following progressions in beam tuning and hardware improvements [2, 3]. The output beam power for the routine user program has been increased to 500 kW to date, though it is temporarily limited to 200 kW at present due to a malfunction of the neutron production target at MLF. In addition to such a routine user operation, RCS has intermittently been continuing high-intensity beam tests toward realizing the design output beam power of 1 MW. As shown by red bars in Fig. 2, RCS started a 1-MW beam test in October 2014 right after completing the injector linac upgrades, and successfully achieved a 1-MW beam acceleration in January 2015.

The most important issue in realizing such a MW-class high-power routine beam operation is to keep machine activations within a permissible level, that is, to preserve a better hands-on-maintenance environment. Thus, a large fraction of our effort has been concentrated on reducing and managing beam losses. This paper presents recent progresses of 1-MW beam tuning especially focusing on our approaches to beam loss issues.

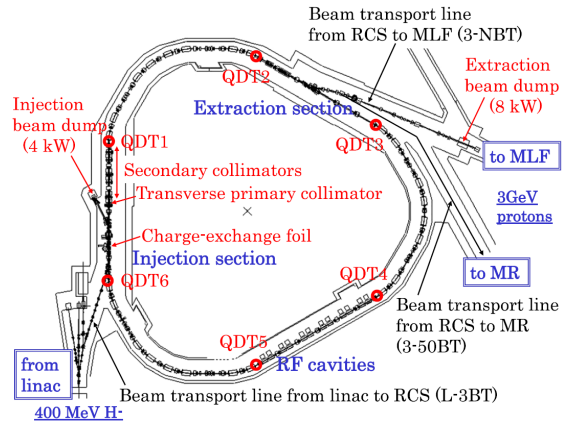

Figure 1: Layout of the J-PARC 3-GeV RCS.

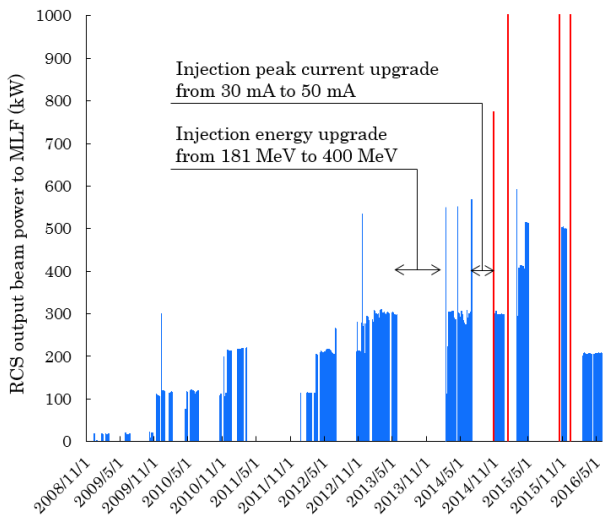

Figure 2: History of the RCS beam power since the start-up of the user program in December 2008.

RESULTS OF THE INITIAL STAGE OF THE 1-MW BEAM TEST

Longitudinal Beam Loss and its Mitigation

As already reported in the last HB workshop [3], the first 1-MW beam test was conducted in October 2014. In this trial, the beam acceleration of up to 770 kW was

#hotchi.hideaki@jaea.go.jp

ISBN 978-3-95450-185-4

achieved with no significant beam loss, but then the 1-MW beam acceleration was not reached due to an over-current of the RF anode power supply. Higher intensity beam needs larger beam loading compensation. Thus, the workload of the RF power supply increases with the ramp-up of the beam intensity.

After this beam test, a quick measure against the RF trip was taken; the resonant frequency of the RF cavity was shifted from 1.7 MHz to 2.1 MHz to decrease the anode current required for the 1-MW beam acceleration. By this treatment, the 1-MW beam acceleration was successfully achieved in January 2015. But then there still remained slight longitudinal beam loss ($<10^{-3}$) coming from a RF bucket distortion caused by beam loading. Such a beam loss occurs through a large momentum excursion, so it is mainly lost in the high dispersion area. The upper plot in Fig. 3 shows the beam loss monitor (BLM) signals in the high dispersion area at the arc section, measured over the whole acceleration time of 20 ms with various beam intensities of up to 1 MW. As shown in the figure, there is no significant beam loss up to 825 kW, but it appears when the beam intensity reaches over 900 kW. RCS employs a multi-harmonic feed-forward (FF) system for beam loading compensation, and it works very well [4]. But, at this stage, the RF anode power supply nearly reached the limit again, and there remained no enough margin for sufficient beam loading compensation for the 1-MW beam. The resonant frequency shift also contributed to this beam loss. RCS normally accelerates two bunches with the harmonic number of h=2. Thus, major parts of wake voltage components are to be the even harmonics (h=2, 4, 6). But, after the resonant frequency shift, the effect of the odd harmonics (h=1, 3, 5) was additionally enhanced, which caused a coupled-bunch-like behaviour, i.e. different longitudinal motions for two bunches [5]. Our FF system covers the odd harmonics as well as the even ones [6], but this phenomenon made the FF tuning more complicated.

After receiving this result, the RF anode power supply upgrade was carried out using the scheduled summer maintenance period in 2015. Then, the resonant frequency was also put back to the original value to make the longitudinal motion more stable. As shown in the lower plot in Fig. 3, the longitudinal beam loss was completely removed by beam loading compensation conducted in October 2015 right after the RF power supply upgrade.

Transverse Beam Loss and its Localization

Most of remaining transverse beam loss was well localized at the collimator section in the dispersion-free long straight insertion. Figure 4 shows the BLM signals at the collimator section, measured for the first 4 ms with various beam intensities of up to 1 MW. As shown in the figure, the beam loss occurs only for the first 1 ms of beam injection, and its beam loss amount simply shows a linear beam intensity dependence. They indicate that the observed beam loss mainly arises from foil scattering during charge-exchange injection. The other beam loss, such as space-charge induced beam loss, was well minimized by the combination of 100π-mm-mrad correlated transverse injection painting and longitudinal injection painting [7-9]. The beam loss for the 1-MW beam was evaluated to be <0.1%. This beam loss rate corresponds to <130 W in power, which is much less than the collimator capability of 4 kW.

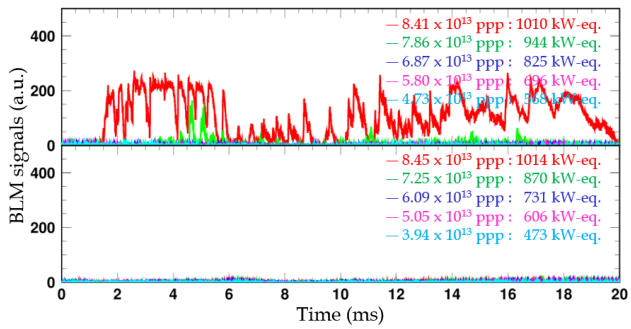

Figure 3: BLM signals in the high dispersion area measured over the whole 20 ms with various beam intensities of up to 1 MW before (upper) and after (lower) the RF power supply upgrade.

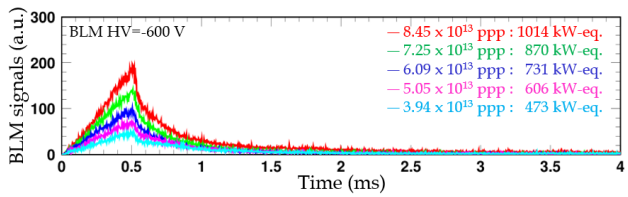

Figure 4: BLM signals at the collimator measured for the first 4 ms with various beam intensities of up to 1 MW, where 100π-mm-mrad correlated transverse injection painting and longitudinal injection painting were applied.

Beam Instability and its Suppression

Beam instability is also an important issue for the 1-MW beam acceleration. In RCS, the extraction pulse kicker is the most dominant impedance source, causing horizontal beam instability depending on the choice of the operational parameters such as the betatron tune and the chromaticity [10, 11]. Thus, for its suppression, the systematic beam instability measurement was done with different tunes and chromaticities at the initial stage of the 1-MW beam test.

Figure 5 shows six sets of tune variations from injection to extraction used for this measurement; the tunes at injection were set at the same point, but after that, they were moved differently toward extraction. Figure 6 shows the time dependence of the turn-by-turn horizontal beam position, measured for the 1-MW beam with the sets of tune variations. The green plots in this figure show the case that the natural chromaticity is fully corrected to zero at injection with dc sextupole fields. In this case, the beam instability occurs for any choice of the tune variation, whereas the growth rate displays a characteristic tune dependence, which is mainly determined by the frequency dependence of the kicker impedance. On the other hand, the red and blue plots are

ISBN 978-3-95450-185-4

the cases of less chromaticity correction; only a quarter of the natural chromaticity is corrected at injection for the blue ones, while no chromaticity correction is applied for the red ones. In this figure, one can find the beam instability is more stabilized by Landau damping through momentum spread as the negative chromaticity becomes larger. This situation allows us to fully suppress the beam instability in combination with tune control even for the 1-MW beam.

Thus, the operational condition to damp the beam instability was revealed through this measurement. Figures 3 and 4, presented above, are the experimental data taken with the stable condition, namely, with the combination of a quarter of the full chromaticity correction and Tune (4), where no instability occurs.

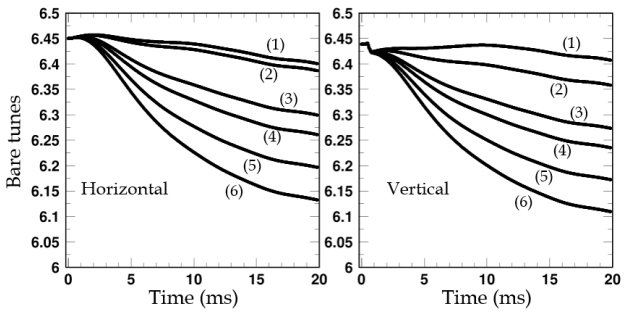

Figure 5: Six sets of tune variations from injection to extraction used for the beam instability measurement.

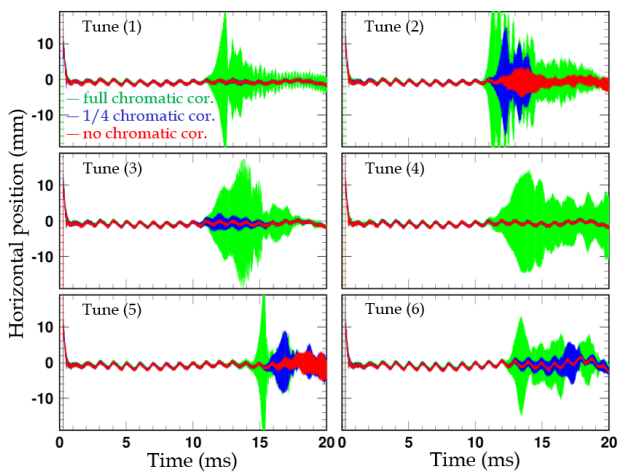

Figure 6: Time dependence of the turn-by-turn horizontal beam position measured for the 1-MW beam with six sets of tune variations (1)–(6) given in Fig. 5; (green) the natural chromaticity is fully corrected to zero at injection with dc sextupole fields, (blue) only a quarter of the natural chromaticity is corrected similarly, and (red) no chromaticity correction is applied.

FURTHER BEAM LOSS MITIGATION BY LARGER TRANSVERSE PAINTING

As already described in the last section, beam loss other than foil scattering beam loss was well minimized. Thus, the next subject is to further reduce the foil scattering beam loss. Most of the foil scattering beam loss is well localized at the collimators, so no serious problem has been encountered to date. But some of them with large scattering angles cause un-localized beam loss, making relatively high machine activation near the charge-exchange foil. It was 15 mSv/h on the chamber surface right after the 400-kW routine beam operation. This value should be 38 mSv/h if the output beam power is increased to 1 MW as is. To preserve a better hands-on-maintenance environment, the machine activation has to be reduced as low as possible.

The amount of the foil scattering beam loss is in proportion to the foil hitting rate during injection. One possible solution to reduce the foil hitting rate is to expand the transverse painting area. As described in [7], in RCS, horizontal painting is performed by a horizontal closed orbit variation during injection. Thus the foil hitting rate decreases as the horizontal painting area becomes wider, because the circulating beam more rapidly escapes from the foil thanks to the larger horizontal closed orbit variation. On the other hand, vertical painting is performed by a vertical injection angle change during injection. Vertical painting also acts to reduce the foil hitting rate through the wider painting area than the vertical dimension of the foil. The painting emittance used thus far is 100π mm mrad, where the average number of foil hits per particle is 41. This number can be reduced to 25 or 15 if the painting emittance is enlarged to 150 or 200π mm mrad.

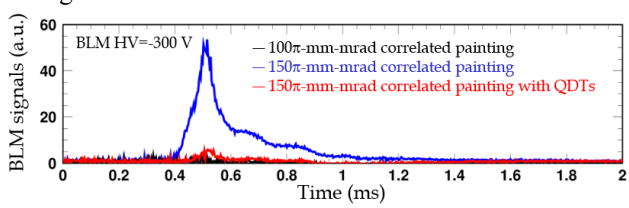

Figure 7: BLM signals at the collimator measured for the first 2 ms with a beam intensity of 850 kW.

Realizing 150π-mm-mrad Transverse Painting

Such a wide-ranging transverse injection painting had not been realized until recently due to edge focusing of pulsed injection bump magnets. The edge focus cause a 30% big beta function beating during injection. This beta function beating makes a distortion of the lattice super-periodicity and additionally excites various random betatron resonances. Such random resonances cause a shrinkage of the dynamic aperture during the injection period, leading to extra beam loss when the transverse painting area is enlarged.

To compensate the beta function beating, we recently installed six sets of pulse type quadrupole correctors (QDT1–6 in Fig. 1) [12], by which the effect of the random resonances can be minimized through the recovery of the super-periodic condition.

To confirm the effectiveness of the correction scheme, we performed a beam test with an 850-kW intensity beam [13]. As shown in Fig. 7, 0.5% significant extra beam loss

ISBN 978-3-95450-185-4

occurred when the transverse painting area was enlarged from 100 to 150π mm mrad, but the beam loss was minimized as expected by introducing QDTs.

The empirical result was well reproduced by the numerical simulation. The more detailed mechanism for the observed phenomena was investigated with the simulated result [13]. Figure 8 shows the transverse phase space coordinates calculated at the end of injection with the painting emittance of 150π mm mrad, where three kinds of transverse beam distributions are plotted; (a) without edge focus, (b) with edge focus, and (c) with the addition of QDTs to (b). In this figure, one can find that beam halo formation is enhanced from (a) to (b) by the edge focus, especially on the vertical plane. This beam halo formation causes the extra beam loss observed in the blue plot in Fig. 7. But, the beam halo is well mitigated from (b) to (c) by QDTs, which causes the beam loss reduction observed in the red plot in Fig. 7.

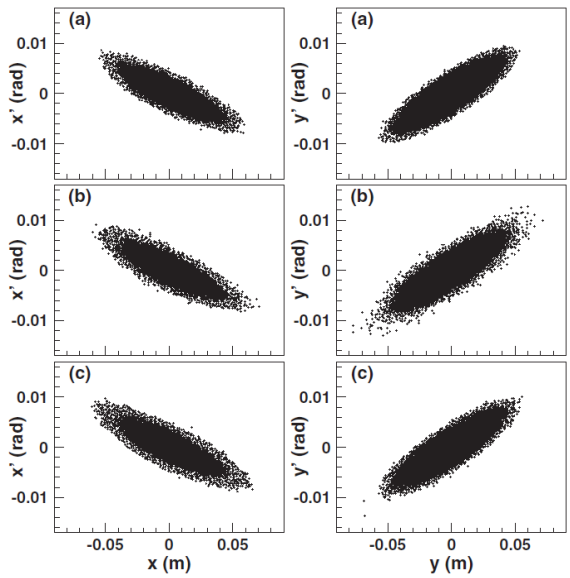

Figure 8: Two-dimensional plot of transverse phase space coordinates calculated at the end of injection with 150π-mm-mrad correlated painting, where three kinds of transverse beam distributions are plotted; (a) without edge focus, (b) with edge focus, and (c) with the addition of QDTs to (b).

Figure 9 shows a tune diagram near the present operating point. The numerical simulation confirmed the beam halo is formed through the combined effect of two resonances; $\nu_x+2\nu_y=19$ and $2\nu_x-2\nu_y=0$. The $\nu_x+2\nu_y=19$ resonance is a third-order random resonance arising from the chromatic correction sextupole field and the intrinsic sextupole field component in the main bending magnets, and it is additionally excited through a distortion of the super-periodicity caused by the edge focus during injection. This sum resonance induces emittance growth on both horizontal and vertical planes with the invariant value of $2J_x-J_y$. On the other hand, the $2\nu_x-2\nu_y=0$ resonance is a fourth-order systematic resonance, which is mainly excited through the octupole component in the space charge field. This difference resonance induces emittance exchange between the horizontal and the vertical planes with the invariant value of J_x+J_y.

Figure 10 shows a typical sample of the turn-by-turn betatron actions of one macro-particle that forms beam halo. In this figure, one can see a characteristic emittance blow-up that implies the combined effect of the two resonances; the horizontal and the vertical actions of the macro-particle gradually grow up along the line of $2J_x-J_y$ =const, while oscillating in a direction parallel to the line of J_x+J_y=const. This analysis confirmed that most of the beam halo is generated through such a single-particle behaviour. In particular, the contribution of the $\nu_x+2\nu_y=19$ resonance is more critical, since the resonance causes more severe beam halo formation on the vertical plane. QDTs act to mitigate the $\nu_x+2\nu_y=19$ resonance through the recovery of the super-periodic condition. That is, it follows that the beam loss reduction achieved in this beam test is mainly led through the mitigation of the vertical beam halo by QDTs.

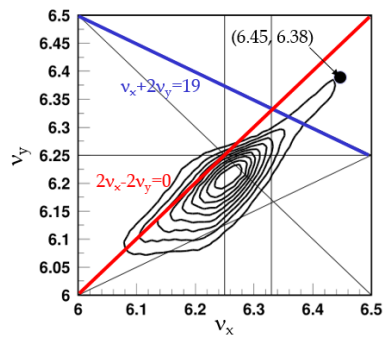

Figure 9: Tune diagram near the present operating point (6.45, 6.38), where the tune footprint was calculated at the end of injection with 150π-mm-mrad correlated painting assuming a beam intensity of 850 kW.

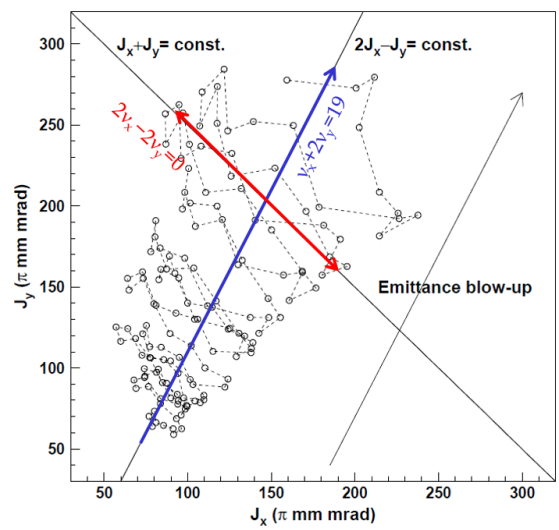

Figure 10: Typical sample of the single-particle behaviour of one macro-particle that forms beam halo; two-dimensional plot of the turn-by-turn betatron actions.

ISBN 978-3-95450-185-4

Realizing 200π-mm-mrad Transverse Painting

The above analysis gave another important suggestion. That is, the further expansion of transverse painting area can be realized by reducing the effect of the $2\nu_x-2\nu_y=0$ resonance, as well as mitigating the $\nu_x+2\nu_y=19$ resonance with QDTs. For this clue, we discussed the introduction of anti-correlated painting, instead of correlated painting used thus far.

In RCS, both correlated and anti-correlated painting are available, in which anti-correlated painting has several advantages for mitigating the effect of the $2\nu_x-2\nu_y=0$ resonance. As shown in the left plot in Fig. 11, in correlated painting, the injection beam is painted along the blue arrow. To the direction of beam painting, the emittance exchange by the $2\nu_x-2\nu_y=0$ resonance occurs in the orthogonal direction like the red arrow. Thus the emittance exchange is directly connected to the emittance growth in this case. On the other hand, in anti-correlated painting, the direction of beam painting is the same as the direction of the emittance exchange as shown in the right plot in Fig. 11. Therefore, the emittance growth caused by the emittance exchange is well suppressed in this case. Another advantage of anti-correlated painting is to make a KV-like distribution. Therefore anti-correlated painting gives less space-charge octupole field component, acting to mitigate the $2\nu_x-2\nu_y=0$ resonance.

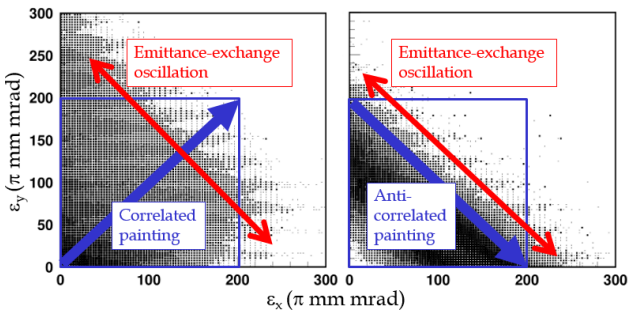

Figure 11: Two-dimensional plot of the beam emittances calculated at the end of injection with 200π-mm-mrad correlated and anti-correlated painting assuming a beam intensity of 1 MW.

Based on the above considerations, we tried to further expand the transverse painting area to 200π mm mrad for the 1-MW beam. Figure 12 shows the experimental result. The first plot (a) is the case of 200π-mm-mrad correlated painting, where 1.9% significant extra beam loss occurred. The beam loss was reduced to (b) as expected by introducing anti-correlated painting. The beam loss was further reduced to (c) by turning off the chromaticity correction, that is, by turning off the sextupole magnets. Less sextupole field mitigates the effect of the $\nu_x+2\nu_y=19$ resonance, which is the main cause of this beam loss reduction. The beam loss was finally reduced to (d) by introducing QDTs, which is caused by the further mitigation of the $\nu_x+2\nu_y=19$ resonance through the recovery of the lattice super-periodicity.

As shown in the plot (d), slight extra beam loss still remains. But we expect the remaining beam loss does not lead to serious issue, because the value is small enough; besides most of the beam loss can be localized at the collimator section. On the other hand, uncontrolled beam loss arising from large-angle foil scattering was reduced drastically by the above efforts. While the original number of foil hits per particle was 41 with 100π-mm-mrad transverse painting, it was reduced to 15 by expanding the transverse painting area to 200π mm mrad, and then to 7 by further optimizing the foil size and its position. This reduced number of foil hits expects that the machine activation near the charge-exchange foil is kept at less than 10 mSv/h on the chamber surface even for the 1-MW beam operation, which is sufficiently within the acceptable level.

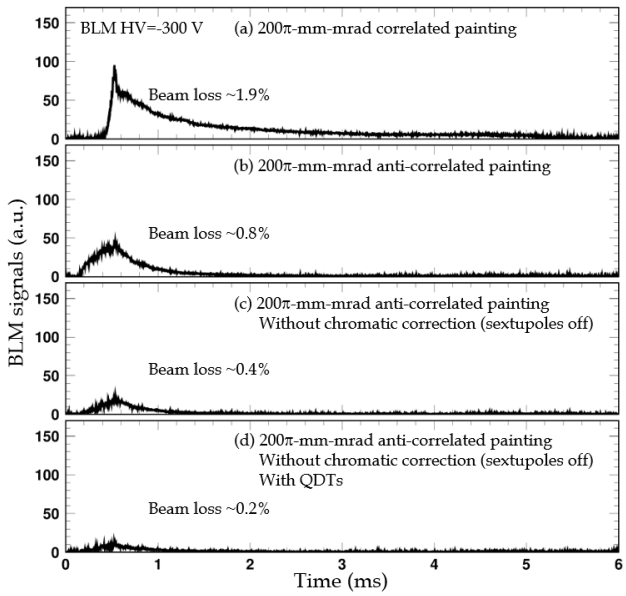

Figure 12: BLM signals at the collimator measured for the first 6 ms with a beam intensity of 1 MW.

SUMMARY

We restarted a 1-MW beam test in October 2015 after the RF power supply upgrade.

By the recent efforts, the 1-MW beam operation is now estimated to be established within a permissible beam loss level. Though it is unfortunate that the routine output beam power from RCS is now limited to 200 kW due to a malfunction of the neutron production target at MLF, RCS beam commissioning in itself is making steady progress toward realizing the routine 1-MW design beam operation.

The further parameter optimization for the 1-MW beam will be continued with more careful attention to beam quality as well as to beam loss.

REFERENCES

[1] H. Hotchi *et al.*, *Phys. Rev. ST Accel. Beams* **12**, 040402 (2009).

ISBN 978-3-95450-185-4

[2] H. Hotchi *et al.*, Prog. Theor. Exp. Phys. **2012**, 02B003 (2012).
[3] H. Hotchi, in *Proc. of HB2014*, East Lansing, MI, USA, 2014, pp. 6–11.
[4] F. Tamura *et al.*, *Phys. Rev. ST Accel. Beams* **14**, 051004 (2011).
[5] M. Yamamoto *et al.*, in Proc. of the 12th Annual Meeting of Particle Accelerator Society of Japan, Tsuruga, Japan, 2015, pp.1008–1012.
[6] F. Tamura *et al.*, *Phys. Rev. ST Accel. Beams* **18**, 091004 (2015).
[7] H. Hotchi *et al.*, *Phys. Rev. ST Accel. Beams* **15**, 040402 (2012).
[8] F. Tamura *et al.*, *Phys. Rev. ST Accel. Beams* **12**, 041001 (2009).
[9] M. Yamamoto *et al.*, *Nucl. Instrum. Methods Phys. Res.*, Sect. A **621**, 15 (2010).
[10] Y. Shobuda *et al.*, in *Proc. of HB2014*, East Lansing, MI, USA, 2014, pp. 369–372.
[11] P.K. Saha *et al.*, in *Proc. of IPAC2016*, Busan, Korea, 2016, pp. 589–591.
[12] H. Hotchi *et al.*, *Nucl. Instrum. Methods Phys. Res.*, Sect. A **778**, 102 (2015).
[13] H. Hotchi *et al.*, *Phys. Rev. Accel. Beams* **19**, 010401 (2016).

ISBN 978-3-95450-185-4

TYPOLOGY OF SPACE CHARGE RESONANCES

Ingo Hofmann*, Technische Universität Darmstadt, Darmstadt, Germany
also at GSI Helmholtzzentrum für Schwerionenforschung GmbH, Darmstadt, Germany
also at Goethe Universität, Frankfurt am Main, Germany

Abstract

The existence of structural space charge resonant effects in otherwise linear periodic focusing systems is well-known, but referred to in a variety of languages and contexts. We show here that for short bunched beams a "classification" in two major groups is possible, e.g. parametric resonances or instabilities on the one hand and single particle type space charge resonances on the other hand. The primary feature of distinction is that for the former the driving space charge force initially exists on the noise level (rms or higher order mismatch) only and gets amplified parametrically, hence an entirely coherent response; for the latter the driving space charge multipole is part of the initial density profile and the coherent response is weak. In the extreme limit of KV beams only parametric resonances (instabilities) exist, and in principle in all orders. For waterbag or Gaussian distributions we find half-integer parametric resonances only up to fourth order, but evidence for single particle resonances in all orders up to tenth have been identified.

INTRODUCTION

With advancing demands on the control of space charge effects for beam dynamics of both linear and circular high intensity accelerators the appearance of purely space charge driven resonances merits careful consideration. The present study considers this space charge case in an otherwise linear periodic focusing lattice. It is based on a recent analysis of the so-called ninety degree and other structural space charge driven stopbands, where it was found that a distinction between single particle type resonant effects and instabilities - here also called parametric resonances - is fundamental [1].

The analytical basis for resonant space charge phenomena in periodic focusing was given by a perturbational Vlasov analysis of structural instabilities of different order for a Kapchinskij-Vladimirskij (KV) distribution of a coasting beam [2]. Our present examples show that this earlier work - though derived for the special case of a 2d KV beam, and under the constraints of a perturbation theory, is still highly relevant and a key to differentiating types of resonant behaviour.

Experimental investigation of this stop-band was undertaken only in 2009, in a dedicated experiment at the UNILAC high intensity heavy ion linear accelerator [3]. This experiment gave evidence of a fourth order resonance as suggested already in an earlier simulation study for a periodic lattice [4], and no indication of a simultaneously occurring envelope instability was found. However, a recent study has shown that the matter is more complex and not independent of the length of the system and the initial mismatch [1]. In particular, the claim of Ref. [5] that the envelope mode is suppressed by the appearance of a fourth order resonance is not supported by our findings. Likewise, we cannot confirm a more recent interpretation that the envelope mode is induced my a mismatch induced by the fourth order resonance [6], which ignores the independence of these modes.

Note that our examples are related to short bunches, where the synchrotron period is not very different from betatron periods; in circular accelerators the synchrotron period is usually very long, which requires special consideration due to possibly different mixing effects. The suggested typology is, however, still applicable.

Resonances driven by space charge in combination with emittance exchange - so-called non-equipartitioned beams [7, 8] - are not part of the present study. They are driven by beam anisotropy rather than the periodic focusing, which leads to a related typology including single particle resonances and anisotropy driven instabilities.

RESONANT PARTICLES AND COHERENT MODES

Single Particle Resonances

The commonly considered resonances in accelerators are based on external forces periodically acting on particles. The origin of these forces usually are systematic and error multipoles of magnets, which provide the driving terms for the resonance.

In a linear lattice with non-uniform space charge density similar driving terms can be given, if one expands the space charge potential in so-called space charge "pseudo-multipoles", which particles cannot distinguish from external forces provided that the space charge terms are well-matched and follow the lattice periodicity.

Resonances in such well-matched beams will be called "single-particle" or "incoherent resonances" reflecting the fact that coherent motion does not affect the resonance condition. Using linac notation the corresponding resonance condition in the $x - x'$-plane (similar in the other planes) can be written as

$$mk_x = 360^0, \tag{1}$$

with $k_x \equiv k_{0,x} - \Delta k_{x,inc}$ the phase advance with space charge, and $k_{0,x}$ without. Note that applied to circular accelerators, these quantities would have to relate to a periodic structure cell. Here, we assume $\Delta k_{x,inc}$ (> 0) is an rms average of incoherent tune shifts and ignore possible spreads depending on amplitudes.

* i.hofmann@gsi.de

ISBN 978-3-95450-185-4

Parametric Resonances

On the other hand, in beams also parametric resonances exist, which are not due to external forces from magnets or space charge, but a system parameter is periodically modulated and drives the resonance.

An example of parametric resonance in accelerators is the single-particle "Mathieu stopband", which prevents single particle transport in periodic focusing and leads to a runaway effect, if the phase advance is 180^0 per focusing period. This example is a special case of the well-known behaviour of a linear differential equation of Hill's type, $d^2x/dt^2 + (\omega^2 + f(t))x = 0$, where ω is the eigenfrequency of the free oscillation and $f(t)$ a parameter of the oscillating system varying periodically with ω_0. The parametric excitation leads to exponential instability of an arbitrarily small initial perturbation, if

$$\omega = \frac{n}{2}\omega_0, \tag{2}$$

where n is a positive integer. The widest stopband is the "half-integer" case, $n = 1$, often called "parametric instability" or "sub-harmonic instability" [9].

Here we are interested in the case, where not a single particle is driven parametrically, but a *coherent eigenmode* of a beam. The lowest order phenomenon is the envelope instability [4,10], where a quadrupolar or envelope eigenmode is driven parametrically.

The corresponding coherent resonance condition for a parametric resonance is written with ω relating to the frequency of a coherent eigenmode of the beam. The order of the motion in the $x - x'$plane is described by m as in Eq. (4), but - in principle - an additional parameter n describing the parametric order according to Eq. (2) is needed. Thus, the resonance condition for a coherent eigenmode in the $x - x'$-plane can be written as:

$$\omega \equiv mk_{0,x} - \Delta k_{m,coh} = \frac{n}{2}360^0. \tag{3}$$

Note that $\Delta k_{m,coh}$ stands symbolically for a *coherent* space charge tune shift to express the fact that there is an underlying coherent motion, which leads to a shift of this resonance with respect to the incoherent one. In most cases it is positive, but negative values cannot be excluded (Ref. [2] and in smooth approximation Ref. [11]). The shift is comparable in size with the incoherent space charge tune shift and depends on the specific eigenmode, hence on m, and possibly on other parameters as well. The shift reflects the fact that coherent and incoherent resonances differ in nature and can be displaced. According to Ref. [2] one needs to take into account that in practice there is also a finite width of stopbands in addition to a shift.

A well-known example of half-integer parametric resonance is the transverse envelope instability of an ellipsoidal bunch in a symmetric periodic FODO array of quadrupoles. We assume a longitudinal focusing provided by two thin rf gaps in the center of both drift spaces in each cell and employ the (3d) KV-envelope equation option of the TRACEWIN code [12]. Parameters are set within a stop-band of instability by assuming $k_{0,x,y} = 100^0$, a moderate space charge leading to $k_{x,y} = 82^0$, and the longitudinal focusing arbitrarily set to $k_{0,z} = 50^0$.

In the above nomenclature the envelope parametric instability case is written as $\omega = 2k_{0,x,y} - \Delta k_{2,coh} = \frac{1}{2}360^0 = 180^0$ and shown in Fig. 1, where the initial exponential phase is followed by a more chaotic pattern of saturation, damping and growth. Details of the lattice and initial envelope are shown in the insert. Note that the three rms emittances are initially chosen equal, which results in bunches slightly elongated from spherical. A necessary condition for instability

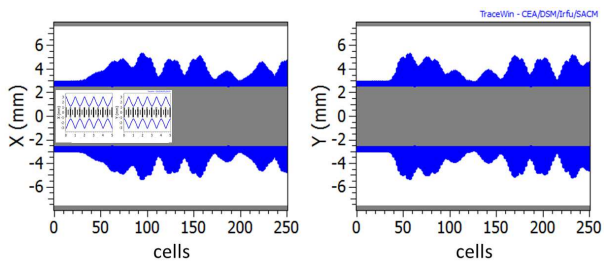

Figure 1: Evolution of KV-envelopes versus cell number for $k_{0,x,y} = 100^0$, $k_{x,y} = 82^0$.

of this mode is $k_{0,x} > 90^0$, while k_x is below 90^0, and similar for y. This enclosure of 90^0 justifies the nomenclature 90^0-stopband.

Higher Order Parametric Instabilities

Here we examine the possibility of higher than $m = 2$ parametric resonances. A third order parametric instability with $m = 3$ and $n = 1$, hence $3k_{0,x,y} - \Delta k_{3,coh} = 180^0$ is expected for a 60^0 stopband in full agreement with the analytical theory of Ref. [2]. Note that a beam symmetric in x and y has no space charge multipole to drive a third order resonance phenomenon, except by parametric instability.

The case is retrieved by our 3d simulations for the example $k_{0,x,y} = 90^0$, and found to exist over the same range of $k_{x,y}$ as predicted in Ref. [2]. For a waterbag distribution and $k_{x,y} = 41.5^0$ the result is shown in Fig. 2. The roughly doubling of rms emittances is accompanied by a three-fold phase space structure as shown on the cell 45 phase space plot. The "triangles" repeat their orientation every second lattice cell, which confirms the 180^0 condition. The growth of the rms emittance in the exponential phase is preceded by a weak sixth order single particle (incoherent) resonance - following the notation $6k_{x,y} = 360^0$ as indicated by the phase space symmetry insert at cell 5 - but quickly overtaken by the lower order parametric case.

This combined third and sixth order phenomenon is similarly encountered in an analogous interplay of second and fourth order as will be discussed in Section .

We also confirm the additional existence of the *half-integer* parametric instability $4k_{0,x,y} - \Delta k_{4,coh} = 180^0$ - also predicted in Ref. [2] - with a stopband near 45^0. We choose $k_{0,x,y} = 70^0$ and take an intensity corresponding to

ISBN 978-3-95450-185-4

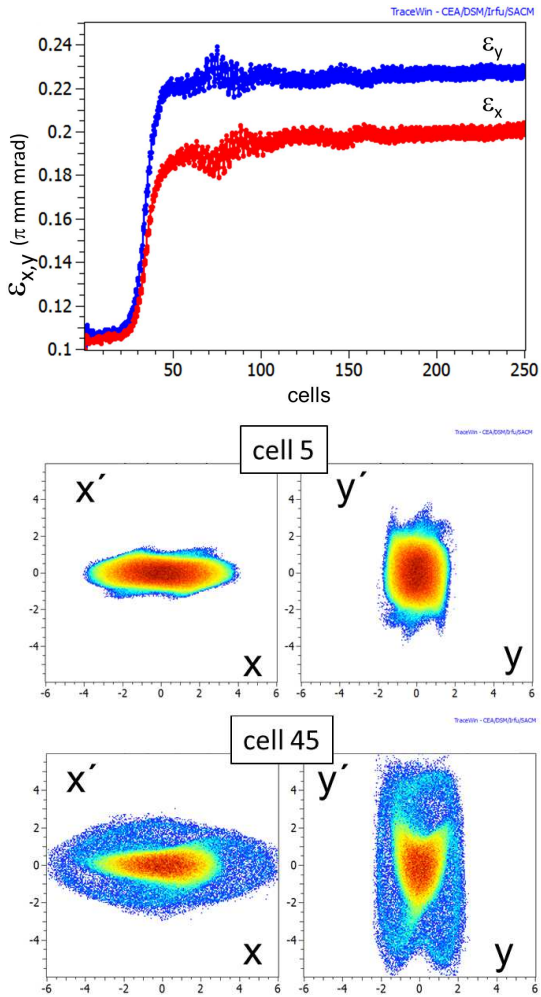

Figure 2: Top graph: rms emittances versus cell number for $k_{0,x,y} = 90^0$, $k_{x,y} = 41.5^0$ for a waterbag distribution. Bottom graph: phase space plots.

$k_{x,y} = 35^0$. For $k_{0,z} = 50^0$ ($k_z = 17^0$) as before we find a weak evidence of this mode, with only 4% emittance growth. However, by raising $k_{0,z}$ to 120^0 we obtain a 40% emittance growth as is shown in Fig. 3, with the phase space insert at cell 20 confirming the fourth order structure. We assume that the roughly 5 times faster effective synchrotron oscillation plays a role and possibly reduces the transverse Landau damping effect, which needs additional study.

Using KV-beams we have also found higher order parametric cases with relatively small emittance effects, but no such evidence was found for waterbag beams. We thus conclude that parametric resonances are insignificant beyond fourth order - at least in the range of parameters studied here.

Ninety Degrees Stopband

We start with a Gaussian distribution truncated at 3.4 σ, transverse tune of $k_{0x,y} = 120^0$ and a space charge depressed tune $k_{x,y} = 70^0$. As shown in Fig. 4 a fourth order phase space structure evolves quickly with 90% of rms emittance growth in less than 10 cells. This can be identified as a single

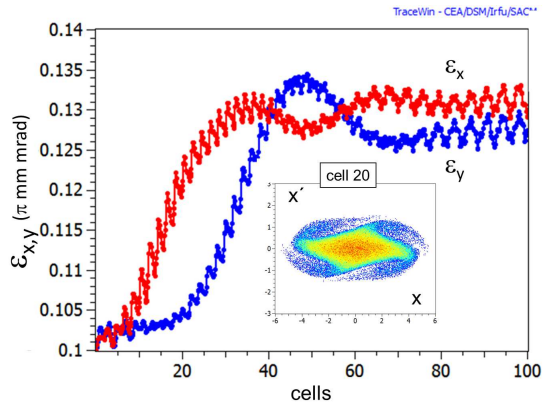

Figure 3: Rms emittances versus cell number for paramteric fourth order mode at $k_{0,x,y} = 70^0$, $k_{x,y} = 35^0$ and waterbag distribution.

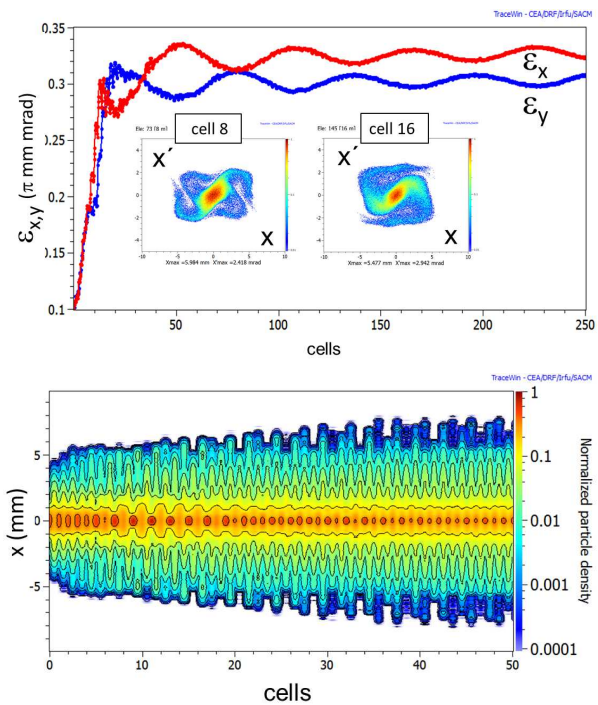

Figure 4: Top graph: rms emittances versus cell number for $k_{0,x,y} = 120^0$, $k_{x,y} = 70^0$ for Gaussian distribution with inserts showing phase space plots. Bottom graph: evolution of density (with contour lines) in x along the lattice.

particle resonance owed to the presence of a strong space charge octupole in the initial Gaussian distribution.

The subsequent evolution to a total growth of over 200% is characterized by a sudden switch to the envelope instability with a dominating two-fold symmetry as shown in the insert at cell 16. The evidence of a growing envelope instability is owed to the fact that the envelope instability is an independent eigenmode, which grows exponentially from the rms mismatch of the initial beam - however small it is. The recently presented argument of Ref. [6] that it grows from a mismatch induced by the preceding fourth

ISBN 978-3-95450-185-4

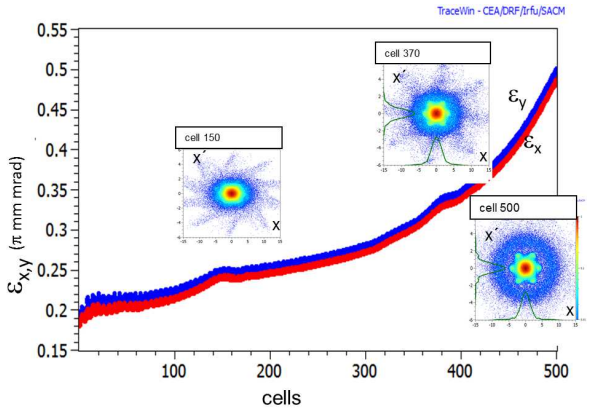

Figure 5: Rrms emittances versus cell number for dynamical ramp of $k_{0,x,y} = 150^0 \rightarrow 130^0$ for Gaussian distribution with inserts showing phase space plots.

order resonance contradicts the fact that the envelope equations - where fourth order effects are entirely absent - already reveal the 90 degree stopband. The extent and shape of it is fully consistent with the PIC simulation result as was shown in Ref. [1].

Results for the evolution of the density in x along the lattice are shown in Fig. 4. They indicate an initial incoherent growth due to the fourth order single particle resonance. A coherent motion takes over between cells 8-10, and a gradual return to more incoherent motion again after 20 cells. The contour lines of peak density in the centre emphasize this transfer of incoherent motion well matched to the lattice to a coherent one, where two cells are needed to perform one period of the strongly excited envelope oscillation.

This coherence is a characteristic of the half-integer parametric resonance as opposed to the incoherent behaviour at single particle resonances.

Higher Order Lattice Harmonics

Above the 90^0 stopband we have not found any evidence of parametric resonances. Theoretically, a 120^0 integer parametric stopband of a third order resonance $3k_{0,x,y} - \Delta k_{3,coh} = 360^0$ could exist, but it must be assumed to be much weaker than the half-integer parametric resonance found above at 60^0.

Instead, a slow ramp of $k_{0,x,y}$ from $150^0 \rightarrow 130^0$ shows that a number of space charge driven single particle resonances exist as shown in Fig. 5. They require, however, higher harmonics h of the lattice function (with space charge) according to

$$mk_{x,y} = 360^0 h. \quad (4)$$

Thus, resonances of 10^{th}, 8^{th} and 6^{th} order are crossed sequentially for $k_{x,y} = 144^0, 135^0, 120^0$ pertaining to $h = 2, 3, 4$. For better identification of the resonant structure and order we have seeded the initial Gaussian distribution with an initial halo seed of 10% of the particles spread out to an rms emittance enhanced by a factor of nine.

	Single particle	Parametric
Driving term	Incoherent (matched) space charge distribution	Coherent space charge
Source	Non-uniform density	Eigenmode
Linac resonance condition	$mk_{xy}=360^0$ h h: lattice harmonic	$mk_{0xy}-\Delta k_{m,coh}$ $=n/2\ 360^0$
Ring resonance condition	$mQ_{xy}=N$ h N: superperiods	$mQ_{0xy}-\Delta Q_{m,coh}$ $=n/2$ N
Range of values identified	m=2...10 h=1...4	m=2,3,4 n=1 (half-integer) h=1

Figure 6: Typology of structural space charge resonances.

SUMMARY ON TYPOLOGY

We have identified two groups of structural resonant space charge effects:

- *Single particle resonances:* The driving space charge term (pseudo-multipole) stems from the matched initial distribution. In the course of the resonance the driving term may change and/or de-tuning may occur. Higher order harmonics of the focusing play a role above the 90^0 stopband. In an initial KV-type distribution space charge multipoles are absent beyond second order, hence the corresponding single particle resonances are also absent.

- *Parametric resonances:* Here the driving space charge term is pumped parametrically from initial noise, if the resonance condition is fulfilled. For non-KV beams we practically only find *half-integer* cases of parametric resonances, and up to fourth order. For initial KV-type distributions, instead, all orders of parametric resonances exist in theory [2] - in simulation limited by resolution.

The distinction single particle versus parametric resonances is not always sharp. Assume a distribution close to a KV, but with weakly non-uniform density. In such a case one can still expect single particle resonances, but a parametric enhancement of the correlated pseudo-multipole as well.

Three parameters characterize the different types of structure space charge resonances (see Fig. 6): m stands for the order of the resonance (space charge potential term order); n for the order in the parametric driving mechanism; h the lattice harmonic, which is theoretically relevant for both, single particle and parametric resonance, but we have not found values different from unity for the latter.

CONCLUSION

This work shows that in high intensity beams two major groups of structural space charge resonant effects exist. They are distinguished by whether the space charge driving term is present in the initial beam, or built up from noise by a parametric process. The latter has no counterpart in externally driven resonances and is of the so-called half-integer parametric resonance or instability type.

ISBN 978-3-95450-185-4

A common feature at different orders is the joint appearance of a parametric resonance and a single particle resonance of twice the order. As an example, the envelope instability and fourth order single particle resonance are independent mechanisms - but not without influencing each other. The associated ninety degree stopband is of particular concern in high current linacs.

The role of the third - here longitudinal - dimension with the synchrotron oscillation as additional mechanism possibly influencing Landau damping must be addressed carefully in future work.

REFERENCES

[1] I. Hofmann and O. Boine-Frankenheim, *Phys. Rev. Lett.* **115**, 204802 (2015).

[2] I. Hofmann, L.J. Laslett, L. Smith, and I. Haber, *Part. Accel.* 13, 145 (1983).

[3] L. Groening, W. Barth, W. Bayer, G. Clemente, L. Dahl, P. Forck, P. Gerhard, I. Hofmann, M. S. Kaiser, M. Maier, S. Mickat, and T. Milosic, *Phys. Rev. Lett.* **102**, 234801 (2009).

[4] I. Hofmann, "Transport and focusing of high-intensity unneutralized beams", in Septier, A. (Ed.), Applied Charged Particle Optics, Part C, 49-140 (C), Academic Press (1983).

[5] D. Jeon, L. Groening, and G. Franchetti, *Phys. Rev. ST Accel. Beams* 12, 054204 (2009).

[6] D. Jeon, J.H. Jang, and H. Jin, *Nucl. Instr. Methods* A, **832**, 43 (2016).

[7] I. Hofmann and O. Boine-Frankenheim, *Phys. Rev. Lett.* **87**, 034802802 (2001).

[8] L. Groening, I. Hofmann, W. Barth, W. Bayer, G. Clemente, L. Dahl, P. Forck, P. Gerhard, M. S. Kaiser, M. Maier, S. Mickat, T. Milosic, and S. Yaramyshev, *Phys. Rev. Lett.* **103**, 224801 (2009).

[9] F. Verhulst, in "Mathematics of Complexity and Dynamical Systems" (ed. A.R. Meyers), Springer, New York, p. 1251-1264 (2011).

[10] J. Struckmeier and M. Reiser, *Part. Accel.* 14, 227 (1984).

[11] I. Hofmann, *Phys. Rev.* E **57**, 4713 (1998).

[12] `http://irfu.cea.fr/Sacm/logiciels/`.

ISBN 978-3-95450-185-4

RESONANCES AND ENVELOPE INSTABILITY IN HIGH INTENSITY LINEAR ACCELERATORS

Dong-O Jeon†, Ji-Ho Jang, Hyunchang Jin, Institute for Basic Science, Daejeon, S. Korea

Abstract

Understanding of space charge effects has grown and recent studies have led to the findings of space charge resonances in high intensity linear accelerators. Lately the sixth order resonance of high intensity linear accelerators was reported, along with the in-depth studies on the interplay of the fourth order resonance and the envelope instability. Experiment studies on space charge resonances were reported. This paper reviews the resonances of high intensity linear accelerators such as the $4\sigma = 360°$, and the $6\sigma = 720°$ resonances, along with the envelope instability.

INTRODUCTION

For high intensity beams, the envelope instability [1, 2] has been long known and the high intensity linac designers have kept $\sigma_o < 90°$ to avoid the envelope instability. However in 2009 researchers found that the space charge fourth order $4\sigma=360°$ resonance was excited rather than the envelope instability [3] and was verified experimentally [4, 5]. Here $\sigma(\sigma_o)$ is the depressed (zero-current) phase advance per cell. These works led to further studies about the fourth order resonance and the envelope instability such as [6]. In 2015 it was reported that the envelope instability grows out of the mismatch induced by the fourth order resonance for a linear accelerator with a constant σ_o lattice [7]. Recently a space charge sixth order $6\sigma=720°$ resonance was found in the high intensity linear accelerators [8].

Space charge coupling resonances were measured in the linear accelerators [9-10, 5] and in the circular accelerators for example in [11].

Recent study showed that the envelope instability can be suppressed or excited after the development of the fourth order resonance by controlling the σ or σ_o of the linac lattice [12].

This paper reviews the space charge resonances in high intensity linear accelerators; their simulation studies and the experiment studies, and the interplay of the fourth order resonance and the envelope instability.

THE FOURTH ORDER SPACE CHARGE RESONANCE

The space charge fourth order $4\sigma=360°$ resonance was found and reported in 2009 [3]. It was observed that the fourth order resonance dominates over the envelope instability. Various studies were done to confirm that it was a resonance including the resonance crossing studies and the frequency analysis. It was shown that the resonance takes effect only for $90°-\Delta\sigma \le \sigma \le 90°$ with a stopband $\Delta\sigma$. No fourth order resonance effect is found beyond 90°.

Figure 1 shows the four resonance islands of this resonance populated with beam particles. And Fig. 2 shows pronounced peaks at the tune of 1/4 (90°/360°) for the $\sigma=85°$ and $\sigma=75°$ lattices. For the lattice with $\sigma=92°$, one does not observe the peak at 1/4. The lattices were designed to maintain a constant σ depressed phase advance per cell.

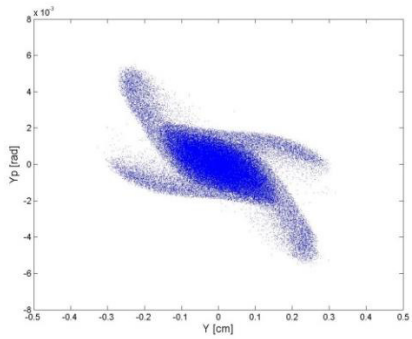

Figure 1: Beam distributions after the development of the fourth order resonance for the $\sigma = 85°$ lattice (Courtesy of [3]).

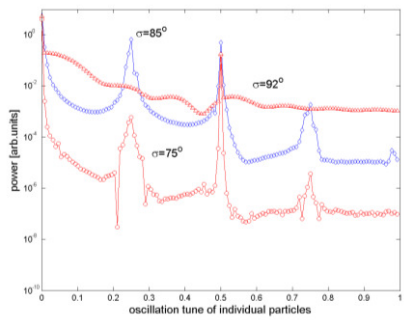

Figure 2: Plot of the FFT power spectrum of the rms beam size for the $\sigma=85°$ and $\sigma=75°$ lattices. One can see the pronounced peak at 1/4 (90°/360°) due to the resonance. (Courtesy of [3])

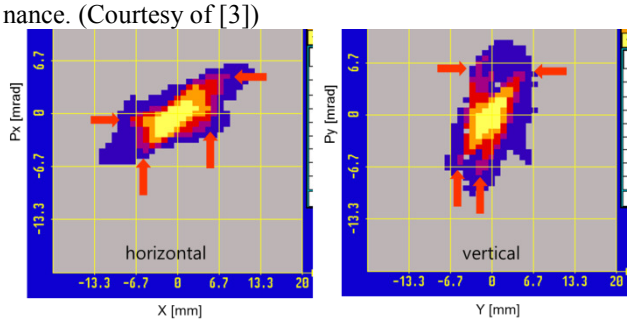

Figure 3: Measured x and y emittance for the lattice with $\sigma_o=100°$ of the GSI UNILAC. Clear evidence of the fourth order resonance is observed. (Courtesy of [4])

† jeond@ibs.re.kr

ISBN 978-3-95450-185-4

This fourth order resonance was verified experimentally through the emittance measurement using the GSI UNILAC and reported in 2009 [4]. Four resonance islands are marked with red arrows in the emittance data shown in Fig. 3.

Another experiment was conducted recently to verify the fourth order resonance through the multiple beam profile measurements using the SNS linac [5]. Figure 4 shows the schematic layout of the CCL and the location of the wire-scanners used for the experiment. Beam profile measurements were done using all the wire-scanners in the CCL that follows the MEBT and the DTL.

Efforts were taken to minimize the halo of incoming beams by using the round beam MEBT optics [13] and by the matching experimentally between sections of the linac [14]. The beam profiles of the incoming beams were measured using the upstream wire-scanner and are shown in Fig. 5. The measured beam profiles are very close to Gaussian and no significant halos are observed. How the matching was done in the experiment is shown in Fig. 6 utilizing the upstream four wire-scanners. Solid dots are measured beam sizes.

Figure 7 shows the beam profiles from the simulation on the left and those from the experiment on the right at the wire-scanner WS304. The measured profiles agree well with the simulated profiles. The pronounced shoulders are due to the beam particles populating the resonance islands. Clear resonance shoulders are observed for the σ=80° lattice, while there are no resonance effects for the σ=65° lattice. The beam shoulders move toward the center while their intensity increase for the σ=88.5° lattice compared with the σ=80° lattice (bottom plots). This is also consistent with the simulation. Beam profiles from the other wire-scanners show a consistent pattern.

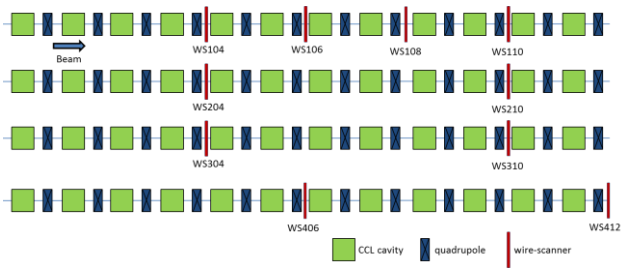

Figure 4: Schematic layout of the SNS CCL (Coupled Cavity Linac) and the location of wire-scanners used in the experiment. (Courtesy of [5])

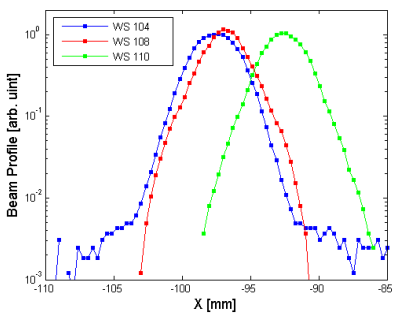

Figure 5: Measured x beam profiles of the incoming beam to the CCL using the upstream wire-scanner; WS104, WS108 and WS110 in Fig. 4. Beam profiles indicate that there is no significant halo in the incoming beam. (Courtesy of [5])

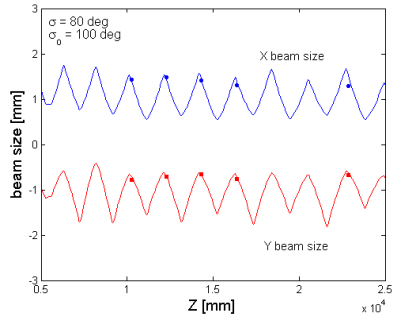

Figure 6: Plot showing how the matching was done. The beam envelope and measured beam sizes are shown.

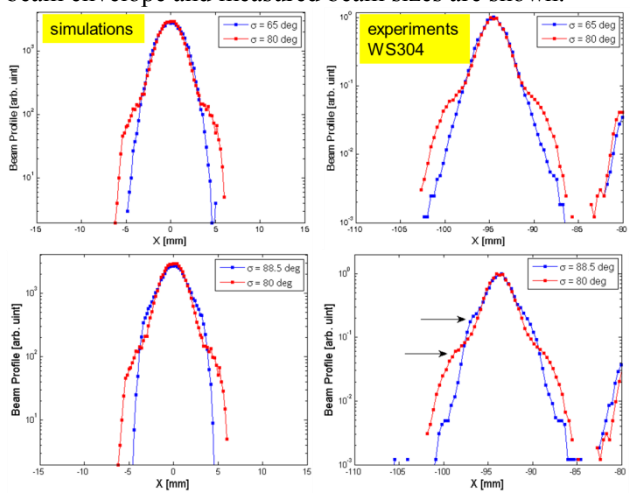

Figure 7: Beam profiles from the simulation on the left and those from the experiment on the right. The top plots show the beam profiles for the σ=65° and σ=80° lattices. The bottom plots show the beam profiles for the σ=80° and σ=88.5° lattices. The beam shoulders move toward the center while their intensity increase for the σ=88.5° lattice compared with the σ=80° lattice. The experiment results are consistent with the simulation.

THE SPACE CHARGE COUPLING RESONANCE

Space charge coupling resonances in linacs were extensively studied and verified in the experiment in the linear accelerators [9, 10, 5] and in the circular accelerators [11]. Recently the emittance exchange due to the coupling resonance was measured using the J-PARC linac [10].

The coupling resonance was experimentally measured using the SNS linac [5]. Figure 8 shows the phase advances for the “Coupled” and “Uncoupled” lattices and the corresponding emittances. Figure 9 shows the beam profiles for the two lattices obtained from the simulation at the wire-scanner WS310. It is shown that the space charge coupling resonance broadens beam profiles as a whole in both planes with little beam profile deformation.

The halo of incoming beam was minimized by the round beam MEBT optics and the matching. Figure 10 shows the measured beam profiles of the 38-mA beam in

ISBN 978-3-95450-185-4

log scale for the "Coupled" (in red) and the "Uncoupled" (in blue) lattices. The top left (right) plot shows the X (Y) beam profiles for the two cases obtained from the wire-scanner "WS310". The bottom left (right) plot shows the X (Y) beam profiles from the wire-scanner "WS406".

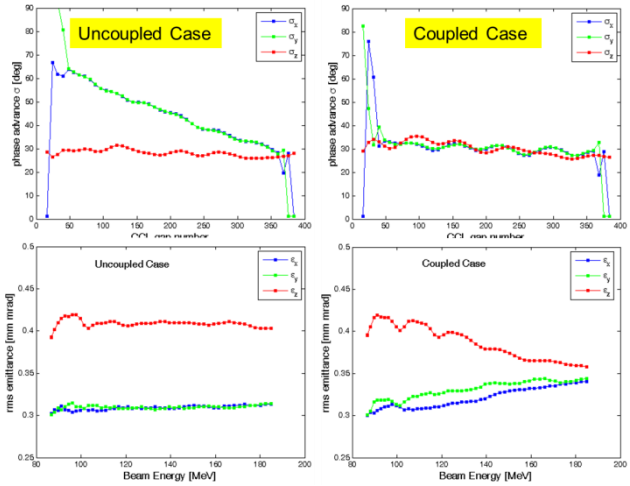

Figure 8: Plots of the phase advances s for the "uncoupled" lattice and the "coupled" lattice (top plots) and those of the corresponding emittances along the linac (bottom plots). For the "Coupled" case, the transverse and longitudinal phase advances almost overlap.

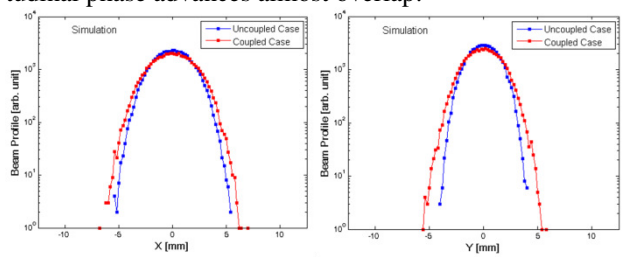

Figure 9: Simulated beam profiles in X and Y planes for the "Coupled" and the "Uncoupled" case at the wire-scanner WS310. One can notice that the space charge coupling resonance (in red) broadens beam profiles in both planes as a whole with little beam profile deformation.

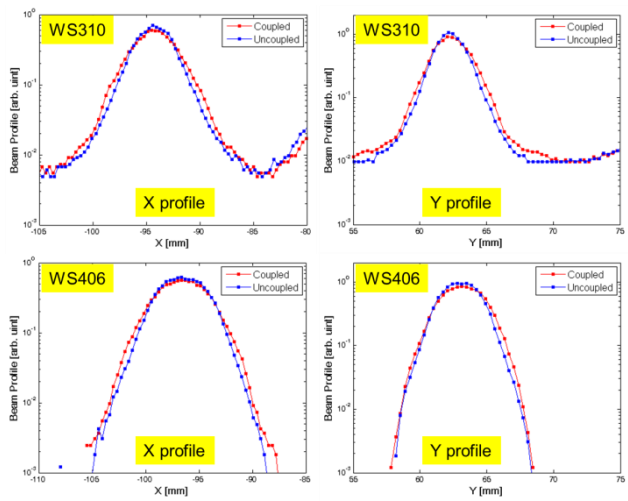

Figure 10: Plots of measured beam profiles from the wire-scanner WS310 and WS406 for the "Coupled" (in red) case and the "Uncoupled" case (in blue). Consistent beam profile broadening is observed as predicted by the simulation. (Courtesy of [5])

Simulations and experiments show that the coupling resonance induces about 20% transverse emittance increase (in Fig. 8) and 10~20% beam profile broadening as a whole in both transverse planes at the downstream wire-scanners (in Fig. 9).

THE SIXTH ORDER SPACE CHARGE RESONANCE

The space charge sixth order $6\sigma=720°$ resonance in high intensity linacs was found and reported in 2015 [8]. This resonance is observed for $120°-\Delta\sigma \le \sigma \le 120°$ with a stopband width $\Delta\sigma$. Transverse rms emittances vs the phase advance σ is shown in Fig. 11. The resonance effect disappears for $\sigma > 120°$, which is a Hamiltonian property. Simulations show a clear emittance growth by this resonance in Fig. 11 and a characteristic six-fold resonance structure in phase space as shown in Fig. 12.

To verify that this is a resonance, a frequency analysis was conducted that shows a clear peak at 1/3 (120°/360°) as shown in Fig. 13. A study was performed of crossing the resonance from above and from below the resonance, even though the results are not presented in this paper.

Canonical perturbation is carried out to show that this resonance arises through perturbation of strong $2\sigma=360°$ (2:1) and $4\sigma=360°$ (4:1) space charge resonances [8].

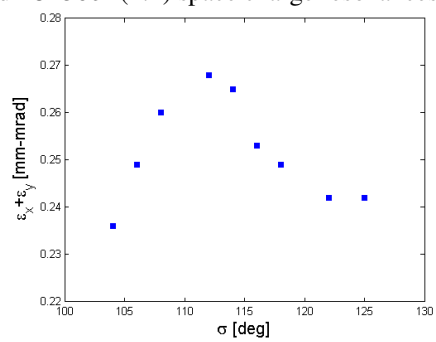

Figure 11: Plot of the transverse rms emittances vs. depressed phase advance per cell σ showing the emittance growth induced by the $6\sigma=720°$ (or 6:2) space charge resonance of linacs. (Courtesy of [8])

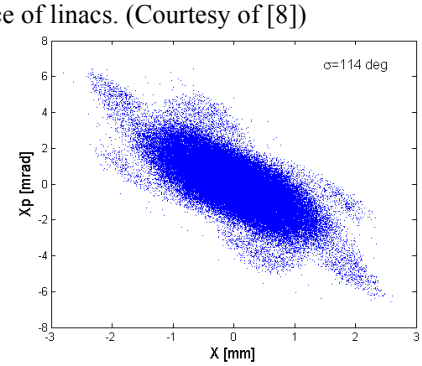

Figure 12: Plot of beam distribution for the lattice with $\sigma=114°$ due to the $6\sigma=720°$ resonance in Fig. 11. (Courtesy of [8])

ISBN 978-3-95450-185-4

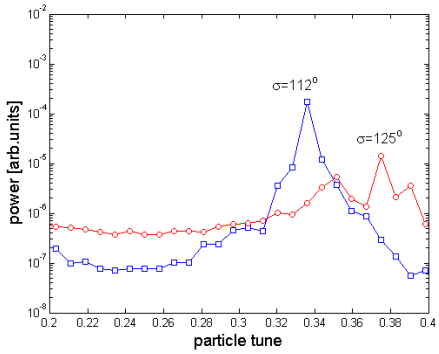

Figure 13: Plot of power spectrum of the frequency analysis on the rms beam size for the σ=112° and 125° lattices. A clear peak at 1/3 (120°/360°) is observed for the σ=112° lattice and no peak is found for the σ=125° lattice beyond σ=120°. (Courtesy of [8])

INTERPLAY OF FOURTH ORDER RESONANCE AND ENVELOPE INSTABILITY

Since the finding of the space charge fourth order 4σ = 360° resonance [3], studies have been carried out to better understand the fourth order resonance and the envelope instability in high intensity linear accelerators [6, 7]. The questions remained unanswered under what conditions the envelope instability got excited or suppressed following the development of the fourth order resonance. Recent studies shed light on this subject [12] and are briefly presented in this paper. Well-matched Gaussian beams were used as input for the simulation.

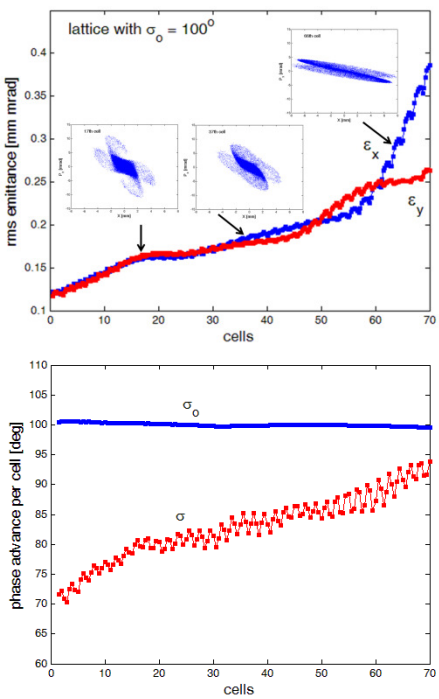

Figure 14: Plots of normalized rms emittances (the top plot) and the plot of σ_o and σ in X plane for the linac lattice with $\sigma_o \approx 100°$. The fourth order resonance structure is observed at the 17th cell and the four-fold structure fades away outside the beam core at the 37th cell, as σ increases approaching 90° and the resonance islands shrink. The emittance growth beyond the 50th cell is associated with the envelope instability that starts to take place when σ increases approaching 90° and the extent of the resonance shrinks. (Courtesy of [12])

Simulations suggest that the envelope instability is excited from the mismatch generated by the fourth order resonance, 1) when σ_o is maintained approximately constant or increases along the linac with $\sigma_o > 90°$ and 2) when the extent of the fourth order resonance shrinks, as σ increases approaching 90°. Here $\sigma(\sigma_o)$ is the depressed (zero-current) phase advance per cell.

Figure 14 shows a case of the linac lattice with a constant σ_o. In this case, σ increases as the beam is accelerated. Initially the fourth order resonance develops from the well-matched initial beam and later the envelope instability develops out of the mismatch generated by the fourth order resonance. The envelope instability is manifested when the extent of the resonance shrinks as σ increases approaching 90°.

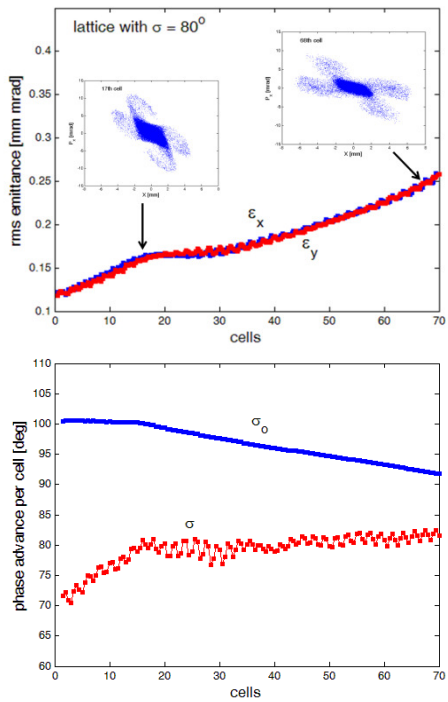

Figure 15: Plot of normalized rms emittances (the top plot) and the plot of σ_o and σ (the bottom plot) in X plane. The downstream lattice is modified to keep $\sigma \approx 80°$ from the 20th cell on. In this lattice with $\sigma \approx 80°$ (from the 20th cell on), one does not observe the envelope instability. The fourth order resonance structure is formed by the 17th cell and persists throughout the linac and the envelope instability is not excited. Maintaining σ constant keeps the resonance islands outside the beam core, which seems to prevent the envelope instability. (Courtesy of [12])

On the other hand, when σ stays almost constant (maintaining the fourth order resonance) or when σ_o decreases

ISBN 978-3-95450-185-4

and gets close to 90° (getting out of the envelope instability), the envelope instability is suppressed and the halo particles formed by the fourth order resonance preserves a four-fold structure in the phase space.

Maintaining σ constant keeps the resonance islands outside the beam core, which seems to prevent the envelope instability. In the lattice with σ ≈ 80° (from the 20th cell on), one does not observe the envelope instability as in Fig. 15. The fourth order resonance structure is formed by the 17th cell and persists throughout the linac and the envelope instability is not excited.

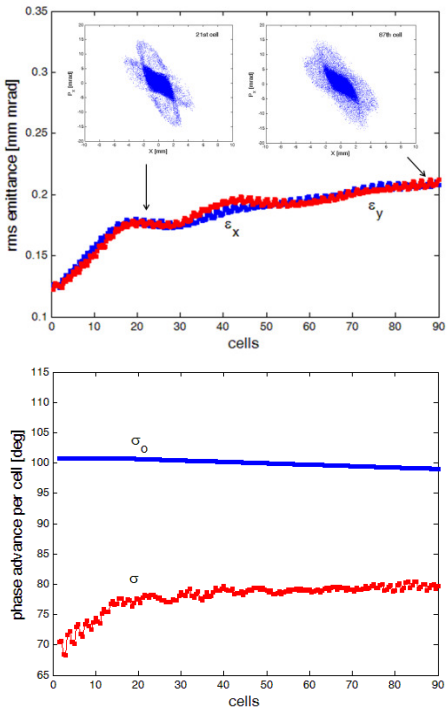

Figure 16: Plots of rms emittances (the top plot) and σ_o, σ (the bottom plot) in X plane. The linac lattice is designed such that both σ_o and σ remain almost constant by reducing the beam acceleration to zero, while the longitudinal focusing is maintained. The σ increases initially until the 16th cell due to the fourth order resonance and the redistribution of the beam, and then very slowly increases from 77° to 80° afterward. This is an ideal case to see whether the fourth order resonance dominates over the envelope instability or not. In this lattice the fourth order resonance persists and the envelope instability is not excited. (Courtesy of [12])

Now a linac lattice is designed such that both σ_o and σ remain almost constant by reducing the beam acceleration to zero (setting synchronous phase to –90°), while the longitudinal focusing is maintained (see Fig. 16). The corresponding σ increases initially until the 16th cell due to the fourth order resonance and the redistribution of the beam, and then very slowly increases from 77° to 80° afterward. As an ideal case to test whether the fourth order resonance dominates over the envelope instability or not, this case shows that the fourth order resonance persists and the envelope instability is not excited.

CONCLUSION

This paper reviews the space charge resonances in high intensity linear accelerators; their simulation studies and the experiments for the fourth order 4σ=360° resonance and the space charge coupling resonances along with the space charge sixth order 6σ=720° resonance.

Recent studies show that when σ stays almost constant (maintaining the fourth order resonance) or when σ_o decreases and gets close to 90° (getting out of the envelope instability), the envelope instability is suppressed and the fourth order resonance preserves a four-fold structure in the phase space.

Simulations suggest that the envelope instability is excited from the mismatch generated by the fourth order resonance, 1) when σ_o is maintained approximately constant or increases along the linac with σ_o > 90° and 2) when the extent of the fourth order resonance shrinks, as σ increases approaching 90°.

ACKNOWLEDGEMENT

This work was supported by the Rare Isotope Science Project of the Institute for Basic Science funded by the Ministry of Science, ICT and Future Planning (MSIP) and the National Research Foundation (NRF) of the Republic of Korea under Contract 2013M7A1A1075764.

REFERENCES

[1] I. Hofmann, L.J. Laslett, L. Smith, and I. Haber, Part. Accel. **13**, 145 (1983).

[2] J. Struckmeier and M. Reiser, Part. Accel. **14**, 227 (1984).

[3] D. Jeon, L. Groening, G. Franchetti, Phys. Rev. ST Accel. Beams **12**, 054204 (2009).

[4] L. Groening et al., Phys. Rev. Lett. **102**, 234801 (2009).

[5] Dong-O Jeon, Phys. Rev. Accel. Beams, **19**, 010101 (2016).

[6] Chao Li and Ya Liang Zhao, Phys. Rev. ST Accel. Beams **17**, 124202 (2014).

[7] I. Hofmann and O. Boine-Frankenheim, Phys. Rev. Lett. **115**, 204802 (2015).

[8] Dong-O Jeon et al., Phys. Rev. Lett. **114**, 184802 (2015).

[9] L. Groening et al., Phys. Rev. Lett. **103**, 224801 (2009).

[10] C. Plostinar et al., Proc. of IPAC2013, Shanghai, China (2103), pp. 3966-3968.

[11] G. Franchetti et al., Phys. Rev. ST Accel. Beams, **13**, 114203 (2010).

[12] D. Jeon, J.H. Jang, H. Jin, Nucl. Instrum. Meth. A. **832** (2016) 43.

[13] D. Jeon et al., Phys. Rev. ST Accel. Beams **5**, 094201 (2002).

[14] D. Jeon et al., Nucl. Instrum. Meth. A **607** (2009) 51.

ISBN 978-3-95450-185-4

USING AN ELECTRON COOLER FOR SPACE CHARGE COMPENSATION IN THE GSI SYNCHROTRON SIS18*

W. D. Stem†, O. Boine-Frankenheim[1], TEMF, TU Darmstadt, Darmstadt, Germany
[1]also at GSI, Darmstadt, Germany

Abstract

For the future operation of the SIS18 as a booster synchrotron for the FAIR SIS100, space charge and beam lifetime are expected to be the main intensity limitations. Intensity is limited in part by the space-charge-induced incoherent tune shift in bunched beams. A co-propagating, low energy electron lens can compensate for this tune shift by applying opposing space-charge fields in the ion beam. In this paper, we study the effect of using the existing electron cooler at the SIS18 as a space charge compensation device. We anticipate beta beating may arise due to the singular localized focusing error, and explore the possibility of adding additional lenses to reduce this error. We also study the effect of electron lenses on the coherent (collective) and incoherent (single-particle) stopbands. Furthermore, we estimate the lifetime of partially stripped heavy-ions due to charge exchange process in the lens.

INTRODUCTION

The future Facility for Antiproton and Ion Research (FAIR) project will include several scientific experiments that require high-intensity (more than 10^{11} ions) primary beams to produce sufficiently high-intensity secondary beams. The incoherent tune shift due to space charge is one of the main intensity-limiting factors standing in the way of this goal. This tune shift, in terms of ion beam parameters, is given by

$$\Delta Q_y^{SC} \approx \frac{N Z^2 r_p}{2\pi A \epsilon_y \beta_0^2 \gamma_0^3 B_f}, \tag{1}$$

where N is the number of particles, Z and A are the charge and mass number of the ion beam, respectively, r_p is the classical proton radius, ϵ_y is the four-times rms beam emittance, γ_0 and β_0 are the relativistic factors of the ion beam, and B_f is the bunching factor.

Many authors estimate a maximum attainable space charge tune shift of 0.2-0.4 [1, 2]. The FAIR reference ion, U^{28+}, will reach a space charge tune shift of 0.25 horizontally and 0.45 vertically at its injection energy. It is clear that a tune shift mitigation process is necessary to obtain the target intensities.

Electron lenses have been studied as a way to compensate for this tune shift [2–5]. Electron lenses are low energy co- or counter-propagating electron beams that provide a localized, amplitude-dependent space charge kick to the ion beam. The tune shift due to co-propagating electron lens with density n_e over interaction length L_e is given by

$$\Delta Q_y^e = -\frac{Z}{A}\frac{\beta_y r_p n_e L_e}{2\gamma_0 \beta_0^2}(1 - \beta_0\beta_e), \tag{2}$$

where β_y is the beta function in the electron lens and β_e is the relativistic factor for the electron beam. The electron density in the cooler n_e is given by

$$n_e = \frac{I_e}{e\pi a^2 \beta_e c}, \tag{3}$$

for electron current I_e, electron charge e, speed of light c, and rms electron beam radius a. For an electron lens to work as designed, the ion beam must be centered inside the electron beam, $\beta_0 \neq \beta_e$ to prevent cooling, the transverse density profiles of the two beams should match, and the electron beam must be pulsed to match the longitudinal density profile of the bunched ion beam.

CHALLENGES

There are numerous challenges one must face when designing an electron lens. Among these are resonances, instabilities, and charge exchange. This paper discusses how we are addressing each of these problems in the SIS18, and how each help to answer the ultimate question: how many electron lenses are necessary for space-charge compensation.

Resonances and Instabilities

The localized focusing structure of the electron lens has an impact on both the coherent (betatron) and incoherent (single particle) stopbands. Equation (2) acts not only on the incoherent tune but also the collective tune of the ion beam. Furthermore, half-integer resonance stopbands due to single particle closed orbit instabilities are determined by the stability criterion [6, 7]. Fig. 1 plots a stability diagram that represents the combined effect of a single electron lens on both the incoherent and coherent tunes of the ion beam. In this simplified case, the electron lens fully compensates for an ion beam that has a space charge tune shift of 0.1 in both planes. The incoherent tune shifts to the standard working point of the SIS18 ($Q_x = 4.2$, $Q_y = 3.3$), while the coherent tune, unaffected by the incoherent space charge tune shift, also shifts by 0.1 in both planes. The result is a compensated beam with a coherent tune offset. Since the instabilities only act only on single particle orbits, Fig. 1 represents an example of stable compensation.

By doing an experimental tune scan, it will be possible to empirically see these instabilities. The results should provide information on how much tune shift each lens should

* Work supported by BMBF contract FKZ:05P15RDRBA
† stem@temf.tu-darmstadt.de

ISBN 978-3-95450-185-4

produce, and thus how many lenses are required for full compensation.

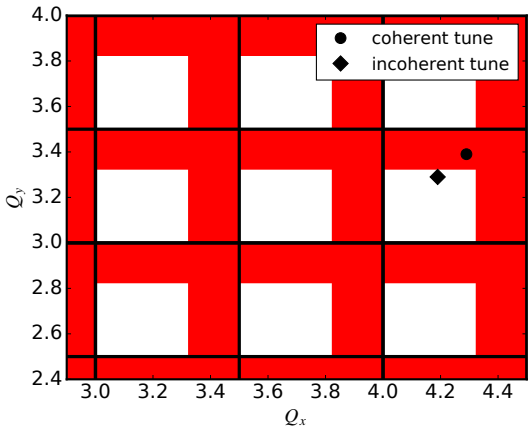

Figure 1: Tune space diagram for an electron lens compensation of 0.1 in the SIS18. The red space represents the single particle closed orbit instability stop bands, and the diamond represents the standard working point of the SIS18.

Charge Exchange

Beam lifetime limitation due to charge exchange inside the electron lens was a concern we explored. Two possible charge exchange mechanisms are ionization and recombination. The FAIR reference ion, U^{28+}, is ionization dominated. The cross section due to ionization of heavy ions by free electrons can be found in Ref. [8]. From there, the lifetime can be calculated using the simple formula, $\tau = 1/(n_e \sigma_e v_r f)$, where σ_e is the ionization cross section, v_r is the relative velocity of the beams, and $f = L_e/C$ is the fractional interaction length of the electron lens.

The calculated cross sections and lifetimes as a function of electron velocity due to ionization in a single electron lens for U^{28+} in the SIS18 are plotted in Fig. 2. The lifetimes due to the ionization mechanism are large compared to the beam lifetime, so we suspect charge exchange will not play a significant role in electron lens space charge compensation.

PRELIMINARY EXPERIMENTS

For the purpose of benchmarking our simulations and calculations, measurements were taken at the GSI synchroton SIS18. The SIS18 electron cooler was re-purposed as an electron lens by modifying the energy and current settings. Goals of the experiments were to measure the coherent tune shift as a function of cooler electron density, to measure the effect of the beam offset on the closed orbit, and to measure beta beat onset, since beta beat can arise from a large axisymmetric focusing error [9]. However, this paper only discusses the coherent tune shift measurement, as the other results are still under analysis.

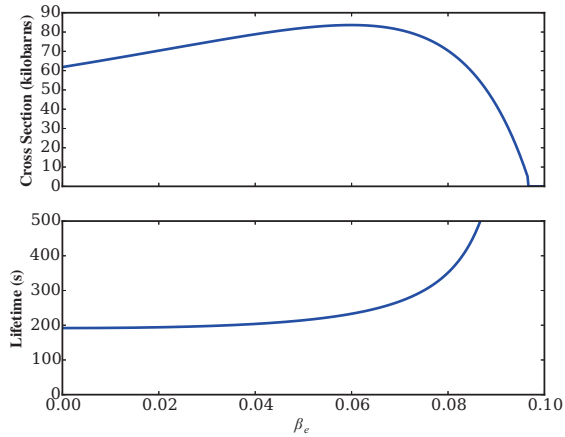

Figure 2: Cross sections and lifetimes as a function of electron velocity due to ionization in a single electron lens for U^{28+} in the SIS18.

Setup and Procedure

Experiments were performed on both coasting and bunched ion beams on a long (5 sec) injection flattop. Noting that Eq. (2) does not depend on ion intensity, a low intensity ($\sim 10^8$ ions) beam was used to eliminate complexity due to space charge. Experiments were performed on two ion species, Xe^{43+} and C^{3+}, but this report only includes results from C^{3+}. The ion beam parameters are shown in Table 1 and the electron beam parameters are shown in Table 2.

Table 1: C^{3+} Parameters

U_{kin}	6.78 MeV/u
β_0	0.12
N_{inj}	(2.0-3.0)x10^8
$\beta_{x,lens}$	8.0 m
$\beta_{y,lens}$	15.0 m
ϵ_x	15.5 mm-mrad
ϵ_y	20.1 mm-mrad
$Q_{x,0}$	4.32
$Q_{y,0}$	3.25

Table 2: SIS18 Cooler Parameters

U_{kin}	6.55 keV
β_e	0.16
f_{exp}	2
L_e	3.4 m
I_e	0.0-0.6 A

Measurements of the ion current were recorded from the current monitor. The beam profile was monitored with the SIS18 residual gas monitor (RGM). The emittances (see Table 1) were calculated from the horizontal and vertical profiles by $\epsilon_{x,y} = (2\sigma_{x,y})^2/\beta_{x,y}$. For these emittances, there is an rms ion beam radius of 5.6 mm horizontal and

ISBN 978-3-95450-185-4

8.7 mm vertical in the electron cooler. With an expansion factor f_{exp} of 2, the electron beam has a rms radius of 9.0 mm. Therefore, so long as the ion beam passes through the center of the cooler, the electron beam will completely encapsulate the ion beam in both planes. This is important, because outside the electron beam, electric fields fall off by $1/r$.

Tune measurements were taken using both Schottky and Base Band Tune (BBQ) [10] methods. Due to the tune spread of the ion beam, the tune signal was difficult to resolve using Schottky. Thus, due to improved sensitivity, the BBQ method was the primary tune diagnostic employed in this experiment.

Results

The results for both coasting and bunched ion beams is shown in Fig. 3. Each fractional tune value is normalized to the 0-current tune shift. The tune shift calculated by equation 1 is plotted as the blue line. The shaded region in each part represents the error in the tune measurement with no electron beam present in the cooler. Electron cooler density was limited due to a 3rd order resonant stopband (1,2,11) for which an experimental tune scan reports high beam loss in the SIS18. Results show favorable agreement with the theory, and it can be seen that as expected there is no difference in the tune shift for coasting and bunched beams.

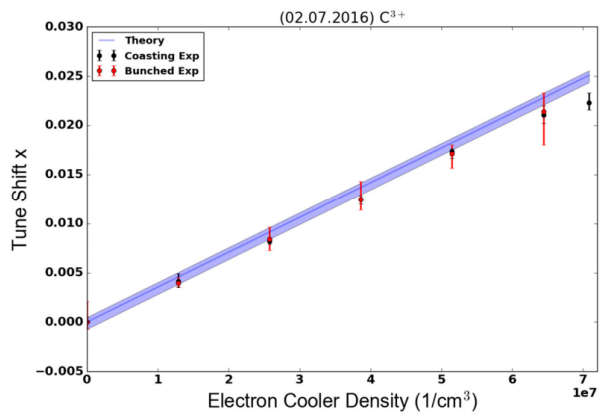

Figure 3: Linear tune shift as a function of electron lens density for both coasting and bunched C^{3+} beams. The theory is a direct calculation from Eq. (2).

CONCLUSIONS AND DISCUSSION

To counteract the intensity-limiting space charge tune shift in the SIS18 when it will be used as an injector for the FAIR SIS100, electron lens techniques will be used. Challenges to overcome include avoiding coherent and incoherent resonance stopbands, limiting beta beat due to localized focusing errors, centering the ion beam in the electron lens, pulsing the electron beam to fit the longitudinal ion beam profile, and more. We do not anticipate charge exchange will be a factor limiting the beam lifetime. Preliminary experiments were performed in the SIS18 electron cooler to benchmark our simulations and calculations, and results for the coherent tune shift show good agreement with theory. In the near future, pyORBIT PIC codes will be used to simulate the incoherent behavior of the beam, and experiments will be performed in the CRYRING [11].

At the HB2016 workshop, S. Nagaitsev proposed new ideas that will provide helpful direction for the future of this work. He introduced a method to measure trapped ions in the electron lens that can compromise the integrity of the fields. He also suggested the use of a McMillan-type electron density profile to eliminate single particle instabilities [12, 13]. These ideas will be explored in future work.

ACKNOWLEDGMENT

We would like to thank C. Dumopoulou, M. Steck, R. Singh, S. Appel, and I. Karpov for providing their expertise and assistance for the tune shift experiments in the SIS18.

REFERENCES

[1] W. T. Weng, "Space charge effects–tune shifts and resonances," in *AIP Conf. Proc.*, 153 (1987), SLAC-PUB-4058, pp. 348-389.

[2] V. D. Shiltsev, *Electron Lenses for Super-Colliders*. Springer, 2016.

[3] A. V. Burov, "Space-charge compensation in proton boosters," in *Proc. of PAC01*, Chicago, USA (2001).

[4] V. D. Shiltsev *et al.*, "Tevatron electron lenses: Design and operation," *Phys. Rev. ST Accel. Beams*, vol. 11, p. 103501, Oct. 2008.

[5] V. N. Litvinenko and G. Wang, "Compensating tune spread induced by space charge in bunched beams," *Phys. Rev. ST Accel. Beams*, vol. 17, p. 114401, Nov. 2014.

[6] M. Aiba *et al.*, "Space-charge compensation options for the LHC injector complex," in *Proc. of PAC07*, THPAN074, New Mexico, USA (2007).

[7] D. A. Edwards and M. J. Syphers, *An Introduction to the Physics of High Energy Accelerators*. WILEY-VCH, 2004.

[8] T. Peter and J. Meyer-ter-Vehn, "Energy loss of heavy ions in dense plasma. II. Nonequilibrium charge states and stopping powers," *Phys. Rev. A*, vol. 43, num. 4, Feb. 1991.

[9] S. Y. Lee, *Accelerator Physics, Second Edition*, World Scientific Publishing Co. Pte. Ltd., 2004.

[10] R. Singh, "Tune Measurements at GSI SIS-18: Methods and Applications," Ph.D. thesis, TEMF, TU Darmstadt, Darmstadt, Germany, 2014.

[11] `http://www.msl.se/MSL_files/cryring.html`

[12] G. Stancari *et al.*, "Electron lenses for experiments on nonlinear dynamics with wide stable tune spreads in the Fermilab integrable optics test accelerator," in *Proc. of IPAC15*, Virginia, USA (2015).

[13] E. M. McMillan, "Some thoughts on stability in nonlinear periodic focusing systems," UCRL–17795, California, USA (1967).

ISBN 978-3-95450-185-4

SPACE CHARGE EFFECTS IN FFAG *

M. Haj Tahar, F. Méot , BNL, Upton, Long Island, New York, USA

Abstract

Understanding space charge effects in FFAG is crucial in order to assess their potential for high power applications. This paper shows that, to carry out parametric studies of these effects in FFAG, the average field index of the focusing and defocusing magnets are the natural parametrization. Using several classes of particle distribution functions, we investigate the effects of space charge forces on the non-linear beam dynamics and provide stability diagrams for an FFAG-like lattice. The method developed in this study is mainly applicable to systems with slowly varying parameters, i.e slow acceleration.

INTRODUCTION

Since the early 1990s, cyclotrons and linacs have been proposed to address the mission of coupling a high power proton accelerator with a spallation target in an Accelerator Driven Subcritical Reactor (ADSR) application. However, due to the recent revival of interest in using FFAG accelerators, the question then arises as to what sort of improvement can the FFAG technology bring. In an effort to demonstrate the high beam power capability of FFAG, studies of the collective effects such as the space charge effects have been undertaken and plans for high intensity experiments are ongoing [1]. Benchmarking work has also been undertaken to validate the simulation results. The following study is in major part induced by the successful benchmarking work so far [2].

AVERAGE FIELD INDEX OF THE FOCUSING/DEFOCUSING MAGNET

In a FFAG accelerator, it is not possible to define a single closed orbit. Instead, the beam moves outwards, and therefore, all parameters are likely to change with the energy of the reference particle. For that reason, it is particularly misleading to replace the equation of motion with a transfer matrix since the betatron amplitude functions continuously change with the energy. For instance, in a scaling FFAG where the tunes are to remain constant, $\beta_{x,y} \propto R$ where R is the radius of the closed orbit [3].

In order to carry out parametric study of space charge effects in non-linear FFAG lattices, the idea is to vary the strength of the applied forces on the beam. For that reason, an extension of the mean field index k as defined by Symon [4], is to introduce its azimuthal variation by defining the mean field index of the focusing (F), defocusing (D) magnets and the drift ($drift$) in the following way:

$$k_i = \frac{R}{B_i}\frac{dB_i}{dR} \quad ; \quad i = F, D, drift \tag{1}$$

where B_i is the vertical component of the magnetic field in the median plane of the FFAG that is averaged over the width of the element. Since the drift space between the magnets is likely to contain the fringe fields, it may be important to assign a mean field index to it to determine its effect on the beam dynamics. However, in the ideal case, $k_{drift} = 0$, which we will assume in the following for simplification, yet without loss of generality. Now, assuming that the k values have no radial dependence, Eq. (1) can be integrated and the magnetic field expressed in cylindrical coordinates:

$$B(R,\theta) = B_{F0} \times \left(\frac{R}{R_0}\right)^{k_F} \times F_F(\theta) + B_{D0} \times \left(\frac{R}{R_0}\right)^{k_D} \times F_D(\theta) \tag{2}$$

where F_F and F_D are the fringe field factors that describe the azimuthal variation of the field in the F and D magnets respectively. It is important to note that the field is a separable function in radial and azimuthal coordinates since the fringe fields merge to zero in the drift space between the magnets as can be seen in Fig. 1 below. Also, note that if $k_F = k_D$, the field writes in the standard form of a scaling FFAG. The lattice considered for this study is a radial sector KURRI-like DFD triplet [1]. Now assuming that all orbits

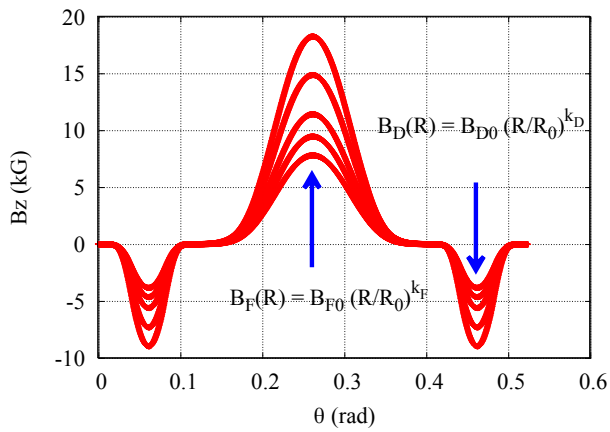

Figure 1: Magnetic field along several closed orbits.

are similar, i.e assuming a linear motion around the closed orbits in which only the path length and the field index may change with the radius, it can be shown that the square number of betatron oscillations in the transverse plane is a linear combination of the k_i values [3]. However, this result is not valid in the general case as shown in [3]: by using the Bogoliubov-Krilov-Mitropolsky (BKM)'s method of averages [5], one can compute approximately the frequencies of the betatron oscillations and their dependence on the average field index of the F and D magnets. To the first order

* Work supported by Brookhaven Science Associates, LLC under Contract No. DE-AC02-98CH10886 with the U.S. Department of Energy.

ISBN 978-3-95450-185-4

in the BKM's method, this yields:

$$\nu_x^2(R_E) = \sum_i \beta_i(R_E) - \sum_i \alpha_i(R_E) \times k_i(R_E) \quad (3)$$

$$\nu_y^2(R_E) = \sum_i \alpha_i(R_E) \times k_i(R_E) + \mathcal{F}^2 \quad (4)$$

where $\mathcal{F}$ is the magnetic flutter defined by

$$\mathcal{F}^2 = \frac{\langle B^2 \rangle - \langle B \rangle^2}{\langle B \rangle^2} = \frac{\langle F^2 \rangle - \langle F \rangle^2}{\langle F \rangle^2} \quad (5)$$

α_i and β_i are defined as the 1^{st} and 2^{nd} order index of similarity of the closed orbits:

$$\alpha_i(R_E) = \frac{-1}{2\pi/N} \int_{\theta_i} \mu(R,\theta) d\theta = \frac{-1}{2\pi/N} \int_{\theta_i} \frac{R}{\rho} d\theta \quad (6)$$

$$\beta_i(R_E) = \frac{1}{2\pi/N} \int_{\theta_i} \mu(R,\theta)^2 d\theta = \frac{1}{2\pi/N} \int_{\theta_i} \left(\frac{R}{\rho}\right)^2 d\theta \quad (7)$$

and R_E refers to the radius of the closed orbit of energy E. This study shows that perturbing the k_i values of the magnets creates a closed orbit change such that the indices of similarity of the orbits as well as the magnetic flutter become energy dependent. The tunes follow as well and two regimes can be distinguished:

- If $k_D < k_F$ then the phase advance per cell is a decreasing function of the energy in both planes.
- If $k_D > k_F$ then the phase advance per cell is an increasing function of the energy in both planes.

In order to better understand these results, we define two new quantities in the calculation, the average as well as the rms values of the tunes over the closed orbits to quantify the average focusing strength of the applied forces on the beam and for any tune variation:

$$\nu_{x,y}^m = \langle \nu_{x,y} \rangle = \frac{1}{NCO} \sum_{i=1}^{NCO} \nu_{x,y,i} \quad (8)$$

$$\nu_{x,y}^{rms} = \langle \nu_{x,y}^2 \rangle^{1/2} = \left(\frac{1}{NCO} \sum_{i=1}^{NCO} \left(\nu_{x,y,i} - \nu_{x,y}^m \right)^2 \right)^{1/2} \quad (9)$$

We also define $\kappa = k_D - k_F$, the difference of the average field index of the F and D magnet. Particle tracking in ZGOUBI [6] is performed in order to solve the non-linear equation of motion using truncated Taylor expansions of the field and its derivatives up to the 5^{th} order: the closed orbits are first obtained, then the phase advance per cell is computed for each. A scan on k_F and k_D provides the stability diagrams in Fig. 2 (in order to remain within the allotted length of the paper, we only show the results in the vertical plane): qualitatively, in the case where $k_F = k_D = k$, the results are in good agreement with the Symon formula ($\nu_y^2 \approx -k$): increasing k increases the horizontal tune and decreases the vertical one. Besides, the RMS tune exhibits the expected behavior in the vicinity of the line $k_F = k_D$ where it becomes negligible. One can also observe that for large k values, increasing κ makes the orbits quickly unstable, thus the stability diagram shrinks. This result is expected since the second order term in the field expansion becomes non negligible for large k so that the system is no longer slowly (linearly) responding to perturbations:

$$B(R) = B_0 \times (\frac{R}{R_0})^k = B_0 \times (1 + \frac{x}{R_0})^k \quad ; \quad x \ll R_0$$
$$= B_0 \times \left[1 + k\frac{x}{R_0} + k(k-1)(\frac{x}{R_0})^2 + O\left((\frac{x}{R_0})^3\right) \right]$$

However, in the vicinity of the central line, i.e $\kappa = 0$, one key finding is that the RMS tunes are proportional to κ:

$$\nu_{x,y}^{rms} \approx a_{x,y} |k_F - k_D| = a_{x,y} |\kappa| \quad (10)$$

This result, combined with the previous observation that the tunes follow two regimes depending on whether $\kappa > 0$ or < 0 is particularly useful as it demonstrates that alternating κ does allow to obtain a non-scaling fixed tune FFAG. This proves that the two cardinal conditions of a scaling FFAG (similarity of the orbits and constancy of the field index with respect to the momentum) are sufficient but non necessary conditions to obtain a fixed tune FFAG. However, this result will be further discussed in a later publication.

SPACE CHARGE EFFECTS IN FFAG

In order to investigate the effects of space charge forces on the non-linear beam dynamics of FFAGs, the idea is to vary the (k_F, k_D) values which act upon the phase advance per cell in both planes as described in Eq. (3) and (4). This approach is in particular relevant to scaling FFAG: since it is impossible to make a field which corresponds exactly to the ideal one, i.e $k_F = k_D$, it is important to investigate the beam stability due to field errors in presence of space charge forces.

Procedure

- We build the model by generating a median plane field map for a given (k_F, k_D) as illustrated in Fig.1. Tracking is performed using ZGOUBI: Median plane antisymmetry is assumed and the Maxwell equations are accommodated which yields the Taylor expansions for the three components of the magnetic field.
- Search for NCO closed orbits between injection and extraction using the built-in fitting routines in ZGOUBI. NCO was chosen to be 30 in order to have good statistics and ensure the convergence of the calculated quantities. The energy range of the protons is chosen between 11 MeV and 100 MeV suitable for the KURRI 150 MeV FFAG.
- For each closed orbit, the matching condition ensuring a periodic motion around the closed orbit is obtained

ISBN 978-3-95450-185-4

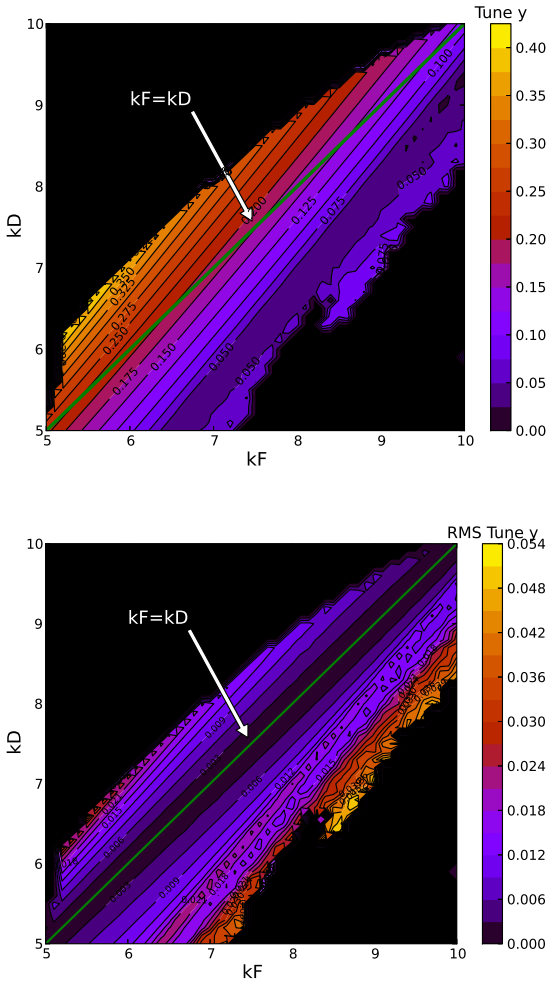

(b) RMS tune variations.

Figure 2: Contour plot of the average (a) and rms (b) tune variations in the vertical plane as a function of the scaling factors k_F and k_D: as can be observed from (b), the rms tune variations increase with increasing $|\kappa|$.

and the matched distribution is generated and tracked over several turns (120 turns). One assumes a symmetric beam distribution, i.e, $\epsilon_x = \epsilon_y = \epsilon$. The damping of beam emittances with momentum is taken into account.

- For each closed orbit, the number of betatron oscillations of the distribution is computed using the ZGOUBI Discrete Fourier Transform (DFT):

$$\nu^{co}_{x,y} = \left\langle \nu_{x,y} \right\rangle = \frac{1}{Npar} \sum_{i=1}^{Npar} \nu_{x,y,i} \quad (11)$$

$$\sigma^{co}_{\nu_{x,y}} = \left(\frac{1}{Npar} \sum_{i=1}^{Npar} \left(\nu_{x,y,i} - \nu^{co}_{x,y} \right)^2 \right)^{1/2} \quad (12)$$

Eqs. (8) and (9) are then invoked in order to calculate the average tune of the lattice as well as rms tune over the closed orbits.

- The same steps are repeated in presence and in absence of the space charge effects: given that the emittance growth time is much shorter than the synchrotron period, our numerical simulation consists of a frozen longitudinal phase space. This provides the tune depression. We assume that the FFAG is operating in emittance-dominated regime. Therefore, the space charge is treated as a small perturbation.

The closed orbits formalism that we use for our analysis is mainly valid under the assumption that all orbits are slowly changing with time, i.e the acceleration rate is small enough that the damping of the betatron oscillations can be considered adiabatic. This is essentially the case for the KURRI FFAG in which the energy increase $\Delta E = 2keV/turn$ is extremely slow that the tunes are independent of the acceleration rate.

KV Beam Distribution

For a fast parametric study, a frozen space charge model is employed. One has to keep in mind though that the KV model does not include non-linear effects that increase the emittance. This test is particularly useful to validate the model built. As described in [7], each particle in the distribution experiences a linear space charge kick given by:

$$\Delta x' = \frac{2Q}{(r_x + r_y) r_x} x \Delta s \quad (13)$$

$$\Delta y' = \frac{2Q}{(r_x + r_y) r_y} y \Delta s \quad (14)$$

where Q is the generalized perveance (dimensionless) defined by:

$$Q = \frac{q\lambda}{2\pi\epsilon_0 m_0 c^2 \beta^2 \gamma^3} = \frac{I}{I_0} \frac{2}{\beta^3\gamma^3} \approx 6.45 \times 10^{-8} \frac{I[A]}{(\gamma^2 - 1)^{3/2}} \quad (15)$$

In order to calculate the space charge tune shift, we recall the Laslett tune shift formula applied to a KV beam:

$$\Delta\nu_y = \frac{1}{4\pi} \oint_0^C \beta_y(s) \frac{2Q}{r_y(r_x + r_y)} ds \quad (16)$$

After simplification, and recalling the symmetry of the beam, this yields :

$$\frac{\Delta\nu_y}{\nu_{y_0}} \approx \frac{1}{2\pi} \frac{Q}{\epsilon^2} \frac{r_y^3}{r_x + r_y} \approx \frac{RQ}{\epsilon} \frac{\nu_{y_0}^{-3/2}}{\nu_{x_0}^{-1/2} + \nu_{y_0}^{-1/2}} \quad (17)$$

where ν_{y_0} is the undepressed vertical betatron tune and R is the average radius of the particle orbit in the accelerator. Interchanging x and y gives the horiontal tune shift.
Introducing the normalized emittance $\epsilon_n = \beta\gamma\epsilon$ yields the scaling $\Delta\nu_y \propto R/(\beta\gamma^2)$.

ISBN 978-3-95450-185-4

Case of scaling FFAGs Assuming that $\kappa = 0$, thus the undepressed phase advance per cell is constant, one applies the procedure described above to a scaling FFAG case by varying the average field index k of the magnets as well as the linear charge density λ of the beam, thus the perveance Q. The results of tracking using the space charge module implemented in ZGOUBI are shown in Fig. 3. In order to interpret the results, we inject the approximated tune formula: $\nu_{x_0}^2 \approx k+1$ and $\nu_{y_0}^2 \approx -k+\mathcal{F}^2$ into Eq. (17). This yields:

$$\frac{\Delta\nu_y}{\nu_{y_0}} \approx \frac{RQ}{\epsilon} \frac{(-k+\mathcal{F}^2)^{-3/4}}{(k+1)^{-1/4}+(-k+\mathcal{F}^2)^{-1/4}} \approx f(k,Q) \quad (18)$$

and a similar result can be obtained for the horizontal plane. A contour plot of the previous formula (Fig. 4) shows good agreement with the tracking results: increasing the k value increases the horizontal focusing and decreases the vertical one. Thus the tune shift exhibits the opposite behavior. Besides, the tune shift is quasi linear with respect to the perveance term, which is a good indication that the beam matching is well ensured as well. Some differences are observed between the analytical formula and the tracking results, mainly in the vertical plane: this is due to our assumption that the magnetic flutter $\mathcal{F}$ is independent of the k-value of the lattice, which is only an approximation.

The above results hold for the average tune of the lattice. However, one shall recall that the tune excursion of a scaling FFAG in presence of space charge forces can be non negligible and scales as $R/(\beta\gamma^2)$. Therefore, one main question to answer is whether one can find a FFAG lattice that maintains the fixed tune property in presence of space charge. For that reason, the non-scaling FFAG case is treated next.

Case of non-scaling FFAGs In the general case of a non-scaling FFAG where the similarity of the orbits is no longer valid, the previous approach is repeated for a fixed Q value equivalent to $I = 0.5mA$ at injection. The results are shown in Figs. 5 and are in good agreement with Eq. (17).

Now, back to the previous question: given that the space charge tune shift is larger at injection and decreases with the energy, for a scaling FFAG, the KV tune excursion is necessarily an increasing function of the energy in both planes. Therefore, the idea of the following method is to introduce a perturbation of the average field index of the magnets $(\delta k_F, \delta k_D)$ in such a way as to counteract the space charge effects, and thus produce a constant tune. As shown earlier, if $\kappa < 0$, this condition can be satisfied since the bare tune is a decreasing function of the energy in both planes. The problem writes in the following way:

$$\begin{cases} \nu_x = \nu_{x_0} + \delta\nu_x(\delta k_F, \delta k_D) + \delta\nu_x(\text{space charge}) \\ \nu_y = \nu_{y_0} + \delta\nu_y(\delta k_F, \delta k_D) + \delta\nu_y(\text{space charge}) \end{cases}$$

where all quantities are energy dependent. In order to determine $(\delta k_F, \delta k_D)$, one equates the RMS tune excursion of the KV beam $\nu_{x,y}^{rms}(sc)$ with the RMS tune excursion of the bare tunes. Recalling Eq. (10) for the latter, and solving for κ, this yields:

$$\kappa \in \left[\frac{\nu_x^{rms}(sc)}{a_x} : \frac{\nu_y^{rms}(sc)}{a_y} \right] \quad (19)$$

In order to test the previous scheme, we choose a lattice corresponding to $k_F = k_D = 7.6$. If we choose to maintain k_F fixed, then Eq. (19) yields $k_D \in [7.0 : 7.11]$. The results are shown in Fig.6 which proves the validity of this method.

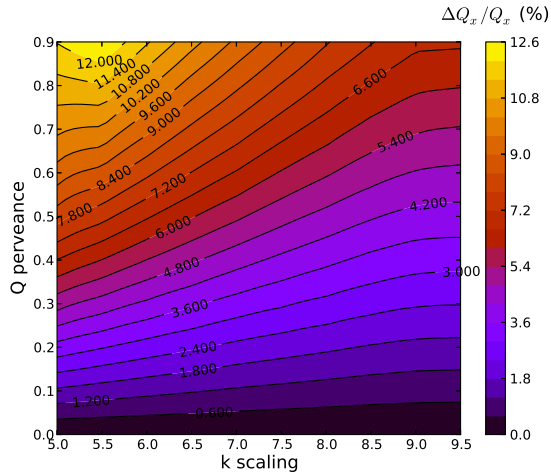

(a) Horizontal plane.

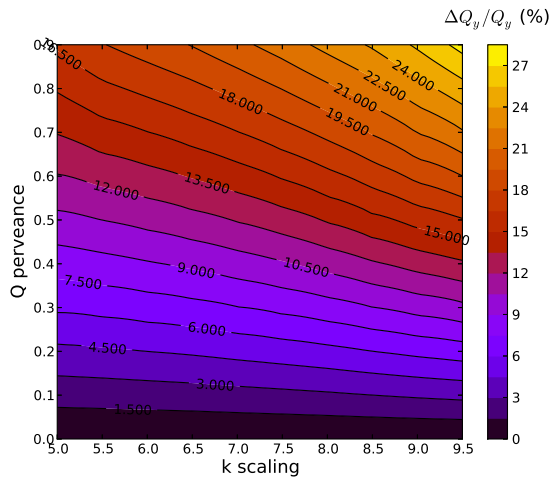

(b) Vertical plane.

Figure 3: Contour plot of the space charge tune shift for a scaling FFAG as a function of the average field index k and the perveance Q (from tracking).

Gaussian Beam

For a Gaussian beam distribution the situation is more complicated due to the large tune spread: while the betatron tune shift is the largest for the core particles, the large amplitude particles experience a near zero tune shift. Therefore, the previous approach of perturbing the field index of the magnets does not remediate the tune spread of the beam.

ISBN 978-3-95450-185-4

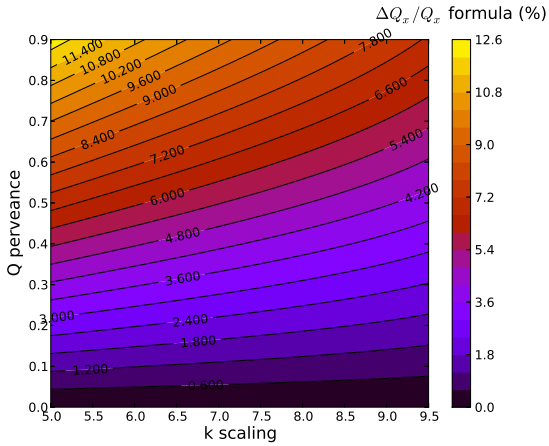

(a) Horizontal plane.

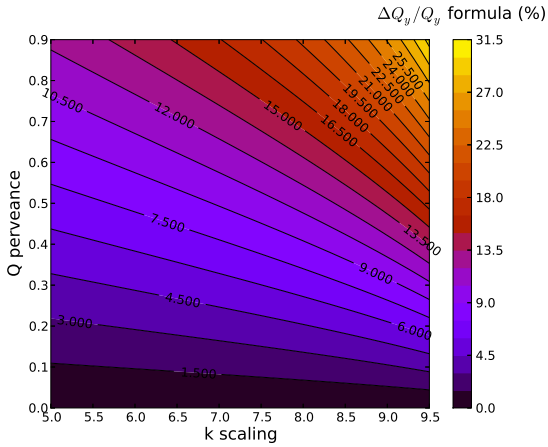

(b) Vertical plane.

Figure 4: Contour plot of the space charge tune shift for a scaling FFAG as a function of the average field index k and the perveance Q (analytical formula 18).

However, it remains valid for the core of the distribution which can be positioned in the tune diagram in a way to avoid harmful resonance crossings.

DISCUSSION AND PLANS

Presently, efforts are made to produce distributions with the linear space charge forces: uniform 3D ellipsoids are the only distributions whose internal force fields are linear functions of position [8]. Therefore, the ellipsoidal model is consistent with a KV distribution in the transverse phase space and a Neuffer distribution in the longitudinal phase space [9]. These two distributions are adequate approximations for the bunch modelling and can be correlated with other distributions via the concept of rms equivalent beams. So, the previous results of the KV beam model should hold in a more realistic case where the linear space charge forces are achieved. Future plans include the study of the resonance effects on the non-linear beam dynamics of FFAGs.

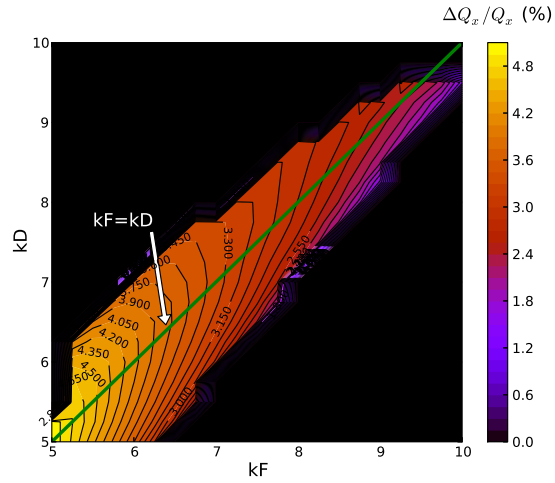

(a) (k_F, k_D) diagram.

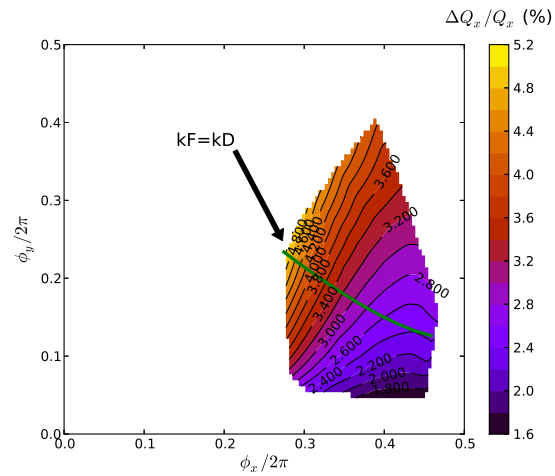

(b) Phase advance diagram.

Figure 5: Contour plot of the horizontal space charge tune shift (a) for a non scaling FFAG as a function of the average field index (k_F, k_D) and the equivalent phase advance diagram (b).

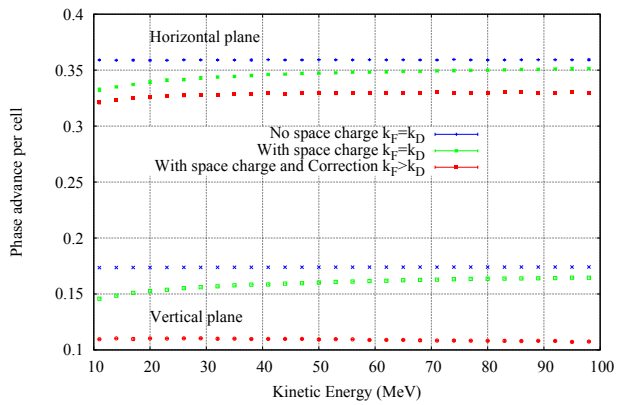

Figure 6: Phase advance per cell before and after perturbation of the average field index of the D-magnet: before correction $(k_F, k_D) = (7.6, 7.6)$ while after correction $(k_F, k_D) = (7.6, 7.11)$.

ISBN 978-3-95450-185-4

REFERENCES

[1] S. L. Sheehy *et al.*, "CHARACTERISATION OF THE KURRI 150 MeV FFAG AND PLANS FOR HIGH INTENSITY EXPERIMENTS", presented at the 57th ICFA Advanced Beam Dynamics Workshop on High Intensity, High Brightness and High Power Hadron Beams (HB2014), Michigan, USA, November 2014, paper MOPAB27, pp 89–93.

[2] S. L. Sheehy *et al*, "Progress on simulation of fixed field alternating gradient accelerators", MOPJE077, IPAC'15, Virginia, USA, May 2015, paper MOPJE077, pp 495–498.

[3] M. Haj Tahar and F. Méot, "Transverse beam dynamics in nonlinear Fixed Field Alternating Gradient accelerators", BNL AP-Technote: C-A/AP/559, March 2016.

[4] K.R. Symon *et al.*, "Fixed-Field Alternating-Gradient Particle Accelerators", *Phys. Rev.*, vol. 103, no. 6, pp 1837–1859, Sep 1956.

[5] N.N. Bogoliubov and Y.A. Mitropolskii, "Asymptotic methods in the theory of nonlinear oscillations", Gordon and Breach, New York (1961).

[6] F. Méot, "Zgoubi Users Guide", Report CA/AP/470, BNL C-AD (2012).

[7] M. Haj Tahar *et al.*, "Space charge studies in FFAG using the tracking code ZGOUBI", MOPMN008, IPAC'15, Virginia, USA, May 2015, paper MOPMN008, pp 717–719.

[8] O. Luiten, S. Van der Geer, M. De Loos, F. Kiewiet, M. Van Der Wiel, Physical Review Letters, vol. 93, no. 9, p 094802, Aug 2004.

[9] M. Reiser, "Theory and Design of Charged Particle Beams", Wiley Series in Beam Physics and Accelerator Technology, Wiley-VCH, Berlin (2008).

ISBN 978-3-95450-185-4

USE OF RF QUADRUPOLE STRUCTURES TO ENHANCE STABILITY IN ACCELERATOR RINGS

M. Schenk[1*], A. Grudiev, K. Li, K. Papke, CERN, CH-1211 Geneva, Switzerland
[1]also at EPFL, CH-1015 Lausanne, Switzerland

Abstract

The beams required for the high luminosity upgrade of the Large Hadron Collider (HL-LHC) at CERN call for efficient mechanisms to suppress transverse collective instabilities. In addition to octupole magnets installed for the purpose of Landau damping, we propose to use radio frequency (rf) quadrupole structures to considerably enhance the aforementioned stabilising effect. By means of the PyHEADTAIL macroparticle tracking code, the stabilising mechanism introduced by an rf quadrupole is studied and discussed. As a specific example, the performance of an rf quadrupole system in presence of magnetic octupoles is demonstrated for HL-LHC. Furthermore, potential performance limitations such as the excitation of synchro-betatron resonances are pointed out. Finally, efforts towards possible measurements with the CERN Super Proton Synchrotron (SPS) are discussed aiming at studying the underlying stabilising mechanisms experimentally.

INTRODUCTION

To push the limits of the Large Hadron Collider (LHC) [1] and its future upgrade HL-LHC [2] towards higher luminosities, the machine must be able to handle beams with significantly increased brightnesses and intensities. Amongst others, these parameters are limited by the presence of transverse collective instabilities induced by the transverse beam coupling impedance of the accelerator structure. A successful stabilising mechanism for the so-called slow head-tail instabilities is the effect of Landau damping [3]. It is present when there is a spread in the betatron frequency, or tune, of the particles in the beam as discussed in detail e.g. in [4] and references therein. This so-called incoherent tune spread is a result of non-linearities in the machine. Partially, they are of parasitical nature, i.e. originating from non-linear space-charge forces, non-linearities in the magnetic focusing systems, beam-beam interactions at collision, etc. In addition, they are often introduced by design through dedicated non-linear elements for better control and efficiency. Magnetic octupoles are commonly used for the latter purpose. They change the betatron tunes of a particle depending on its transverse actions. In LHC for instance, families of 84 focusing and 84 defocusing, 0.32 m long superconducting magnetic octupoles are installed and successfully used to suppress a variety of instabilities [5, 6]. Nevertheless, LHC operation in 2012 at an energy of 4 TeV and a bunch spacing of 50 ns, as well as in 2015 at 6.5 TeV and 25 ns has shown that these Landau octupoles (LO) need to be powered close to their maximum strength in order to guarantee stable beams [7]. With the HL-LHC upgrade, the bunch intensity will be increased from $1.15 \cdot 10^{11}$ p$^+$/b to $2.2 \cdot 10^{11}$ p$^+$/b which will potentially lead to more violent instabilities. At the same time, the normalised transverse emittances will be reduced from 3 μm (LHC operational) to 2.5 μm, and the beam energy will be increased from 6.5 TeV to 7 TeV, thus rendering the LO less effective.

An rf quadrupole operating in a transverse magnetic quadrupolar mode TM_{210} was proposed as a more efficient device for introducing a non-vanishing betatron tune spread in the beams of a high energy particle accelerator like (HL-)LHC [8]. A first numerical proof-of-principle study was presented in [9]. The quadrupolar focusing strength of such a device has a harmonic dependence on the longitudinal position of the particles in the bunch. As a result, the betatron tunes of a particle are changed as a function of its longitudinal position. Since in high energy hadron colliders, the longitudinal emittance is much larger than the transverse ones, the rf quadrupole is able to generate a betatron tune spread more efficiently than magnetic octupoles.

The publication is structured as follows. Firstly, the working principle of an rf quadrupole as well as the PyHEADTAIL macroparticle tracking code are introduced. Thereafter, the applicability of an rf quadrupole for HL-LHC as well as the excitation of synchro-betatron resonances are discussed. Finally, experimental studies of the concerned stabilising mechanism are proposed for the SPS.

THEORY

Radio Frequency Quadrupole

A bunch of electrically charged particles of momentum p traverses an rf quadrupole along the z-axis. Given that the thin-lens approximation holds, a particle i located at position z_i measured with respect to the zero crossing of the main rf wave ($z = 0$) experiences both transverse and longitudinal kicks

$$\Delta \mathbf{p}_\perp^i = pk_2 \left(y_i \mathbf{u}_y - x_i \mathbf{u}_x \right) \cos\left[\frac{\omega z_i}{\beta c} + \varphi_0 \right], \quad (1)$$

$$\Delta p_\parallel^i = \frac{\omega p k_2}{2\beta c} \left(x_i^2 - y_i^2 \right) \sin\left[\frac{\omega z_i}{\beta c} + \varphi_0 \right]. \quad (2)$$

x_i and y_i are the transverse coordinates of the particle, ω denotes the rf quadrupole angular frequency, $\mathbf{u}_{x,y}$ are the unit vectors along the x and y coordinates respectively, and φ_0 is a constant phase offset of the rf quadrupole wave with respect to $z = 0$. It has been added for reasons of generality. β and c denote the relativistic beta and the speed of light respectively. k_2 is the amplitude of the normalised integrated

* michael.schenk@cern.ch

ISBN 978-3-95450-185-4

quadrupolar strength of the cavity

$$k_2 = \frac{q}{\pi r p c} \int_0^{2\pi} \left\| \int_0^L \left(E_x - c B_y \right) e^{j\omega z/\beta c} dz \right\| \cos\varphi \, d\varphi, \tag{3}$$

with q the electric charge of the particle, L the length of the cavity and $[r, \varphi, z]$ the cylindrical coordinates. E_x and B_y denote respectively the horizontal component of the electric and the vertical component of the magnetic field vectors. Throughout this article, k_2 is expressed in magnetic units [Tm/m] using the conversion $b^{(2)} = B_0 \rho k_2$, where the product $B_0\rho$ denotes the magnetic rigidity of the particle beam.

A particle that is subject to the transverse quadrupole kicks given in Eq. 1 experiences a change of its betatron tunes $Q^i_{x,y}$ [10]

$$\Delta Q^i_{x,y} = \pm \beta_{x,y} \frac{b^{(2)}}{4\pi B_0 \rho} \cos\left[\frac{\omega z_i}{\beta c} + \varphi_0 \right], \tag{4}$$

where $\beta_{x,y}$ are the transverse beta functions of the accelerator at the location of the kicks. To obtain an incoherent betatron tune spread that is as large as possible and does not average out over one synchrotron period, the rf quadrupole is operated with a phase of $\varphi_0 = 0$ or $\varphi_0 = \pi$. Choosing $\varphi_0 = 0$ means that the device is focusing (defocusing) in the horizontal (vertical) plane for particles at $z_i = 0$. The situation is reversed for $\varphi_0 = \pi$. Equivalently, operating the cavity in one of these two modes means that particles located at $z_i = 0$ enter the device (anti-)on-crest of the rf wave. It is worth mentioning that this approach is different from the one described in [11, 12] where an rf quadrupole is proposed to increase the threshold of the transverse mode coupling instability (TMCI), also known as the strong head-tail instability [4]. For the latter, the cavity is operated at zero-crossing of the rf wave for particles at $z_i = 0$.

In the following, $\varphi_0 = 0$. Equation 4 can be expanded into a Taylor series in z_i

$$\Delta Q^i_{x,y} = \pm \beta_{x,y} \frac{b^{(2)}}{4\pi B_0 \rho} \left[1 - \frac{1}{2} \left(\frac{\omega z_i}{\beta c} \right)^2 + O(z_i^3) \right]. \tag{5}$$

Given that the wavelength of the rf wave is much larger than the bunch length σ_z, i.e. $\omega \sigma_z / \beta c \ll 1$, the higher order terms $O(z_i^3)$ can be neglected. Assuming linear synchrotron motion, averaging over one synchrotron period T_s reveals that the rf quadrupole changes the betatron tune as a function of the longitudinal action J^i_z of the particle

$$\left\langle \Delta Q^i_{x,y} \right\rangle_{T_s} \approx \pm \beta_{x,y} \frac{b^{(2)}}{4\pi B_0 \rho} \left[1 - \frac{1}{2} \left(\frac{\omega}{\beta c} \right)^2 \beta_z J^i_z \right], \tag{6}$$

where β_z is the longitudinal beta function.

Equation 5 shows the z_i^2 dependence of the betatron tune change caused by an rf quadrupole (first order). For comparison, the betatron tune change introduced by a non-zero second order chromaticity $Q''_{x,y}$ is given by

$$\Delta Q^i_{x,y} = \frac{Q''_{x,y}}{2} \delta_i^2, \tag{7}$$

where δ_i is the relative momentum deviation $\Delta p_i / p$ of the particle. Hence, similarly to the rf quadrupole, the average betatron tune change over one synchrotron period is dependent on the longitudinal action J^i_z of the particle. In the following this is referred to as betatron detuning with *longitudinal* amplitude which stands in contrast to betatron detuning with *transverse* amplitude introduced for instance by magnetic octupoles.

PyHEADTAIL

PyHEADTAIL is a macroparticle tracking software under development at CERN [13]. It is the successor of the well-established HEADTAIL code [14] and allows to study the formation of collective instabilities in circular accelerators and to evaluate appropriate methods for their mitigation. The model assumes linear periodic transport in the transverse planes from one section to the next along the accelerator ring. In the longitudinal plane, the code supports linear synchrotron motion or multi-harmonic rf systems. All the impedance contributions of the accelerator structure are lumped in one point where the wake kicks are computed and applied on a longitudinal slice-by-slice basis. The effect of chromaticity, including higher orders, as well as detuning with transverse amplitude originating from magnetic octupoles are modelled as a change in the individual phase advance of every macroparticle in the bunch (incoherent detuning). The rf quadrupole effect, on the other hand, is modelled as localised kicks computed according to Eq. 1 and 2. PyHEADTAIL has been successfully benchmarked against LHC measurements for a head-tail instability that can be suppressed by LO [9].

APPLICABILITY FOR HL-LHC

PyHEADTAIL is used to assess the potential gain of an rf quadrupole for HL-LHC. The goal is to evaluate the performance of an ensemble of 800 MHz superconducting rf quadrupole cavities [8] in presence of the LHC LO. The beta functions at the location of the rf quadrupole kicks are set to a conservative $\beta_{x,y} = 200$ m according to [8]. To begin with, only single-bunch instabilities are studied for operational flat-top beam and machine parameters [2], the major

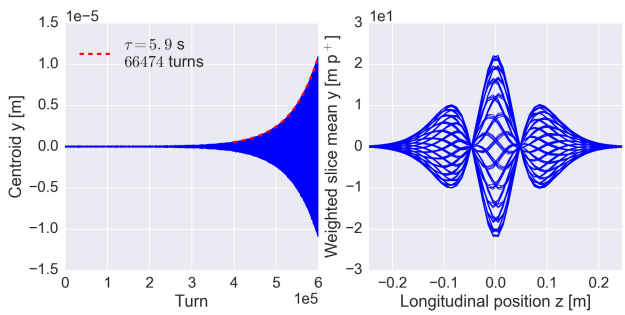

Figure 1: PyHEADTAIL output for HL-LHC at a chromaticity of $Q'_{x,y} = 10$. *Left:* Vertical bunch centroid motion with an exponential fit (red line) and the corresponding instability rise time τ. *Right:* Acquired bunch position monitor data.

ISBN 978-3-95450-185-4

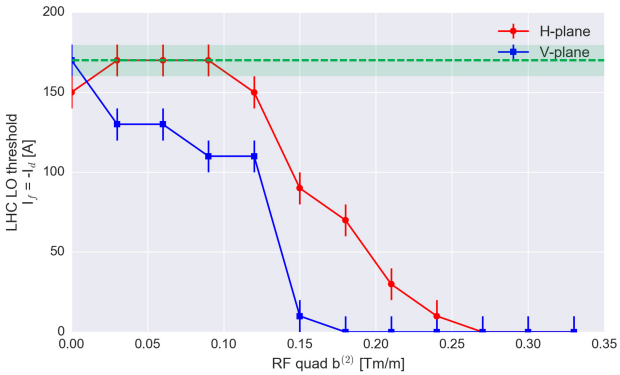

Figure 2: LO current required for HL-LHC operation at a chromaticity of $Q'_{x,y} = 10$ vs. rf quadrupole strength. The green dashed line marks the stabilising current when using LO alone.

ones being summarised in Tab. 1. A first order chromaticity of $Q'_{x,y} = 10$ is chosen for the study as it is a likely working point judging from past LHC operation. Furthermore, an ideal bunch-by-bunch transverse feedback system with a damping time of 50 turns is included in the machine setup. Throughout the study, the latest HL-LHC dipolar impedance model is used.

In a first step, the instability expected for the given machine configuration is characterised. The simulation setup is hence chosen such that both the rf quadrupole and the LO are switched off. The results are summarised in Fig. 1. The vertical centroid position acquired over $6 \cdot 10^5$ turns is shown on the left and the bunch position monitor data is given on the right. The latter is an overlay of 200 consecutive traces and clearly illustrates the head-tail pattern. After carrying out a frequency analysis on the centroid motion, the instability can be characterised as a head-tail mode with azimuthal and radial mode numbers of 0 and 2 respectively. This result is consistent with experimental observations made in the LHC at 6.5 TeV [5].

PyHEADTAIL indicates that beam stabilisation with LO alone is achieved when they are powered at focusing and defocusing currents of $I_f = -I_d = 170 \pm 10$ A respectively. Figure 2 summarises the effect of an rf quadrupole system on the required stabilising current in the LO for the instability shown in Fig. 1. The green dashed line represents the required LO current in absence of an rf quadrupole. The gain in margin for stabilisation with the additional rf quadrupole system is significant in both planes. Although there is only a small effect on the threshold current $I_{f,d}$ up to a cavity strength of about $b^{(2)} = 0.1$ Tm/m, the numerical model suggests that for $b^{(2)} \approx 0.25$ Tm/m the LO would no longer be required to suppress the instability. Given the preliminary cavity design, the latter strength can already be provided by two rf cavities [8]. Further optimisations of the cavity geometry in terms of kick strength and impedance are currently ongoing. Apart from the strong decrease of the required LO current with rf quadrupole strength, the plot illustrates that there is an asymmetry in the behaviour for stabilisation in the

Table 1: Main Machine and Simulation Parameters used for the HL-LHC Studies with PyHEADTAIL.

Parameter	Symbol	Value
Bunch intensity	N_b	$2.2 \cdot 10^{11}$ p$^+$/b
Beam energy	E	7 TeV
Chromaticity	$Q'_{x,y}$	10
Transverse normalised emittance	$\epsilon_{x,y}$	2.5 μm
Longitudinal emittance	ϵ_z	2.5 eVs
Number of macroparticles		$8 \cdot 10^5$ p
Number of turns		$6 \cdot 10^5$ turns

two planes. The vertical plane behaves more favourably even if the required stabilising LO current without rf quadrupole is slightly larger than in the horizontal plane (higher vertical impedance). This is a consequence of the asymmetric nature of the incoherent tune spreads (compare Eq. 6) combined with the fact that the rf quadrupole is focusing in one plane and defocusing in the other for a given longitudinal position. Indeed, it has been verified that the asymmetry can be inverted by operating the rf quadrupole with $\varphi_0 = \pi$ instead of $\varphi_0 = 0$ (Eq. 1 and 2). These effects are currently under study and are addressed in more detail below in the section on experimental studies in the SPS.

SYNCHRO-BETATRON RESONANCES

The numerical simulations that are carried out to define possible scenarios for an rf quadrupole proof-of-principle experiment in the SPS at CERN revealed that this type of cavity can excite synchro-betatron resonances (SBR). Such resonances have also been studied and reported by [12] for an rf quadrupole aiming at increasing the TMCI threshold. Figure 3 shows the growth rates (top) and the fraction of losses

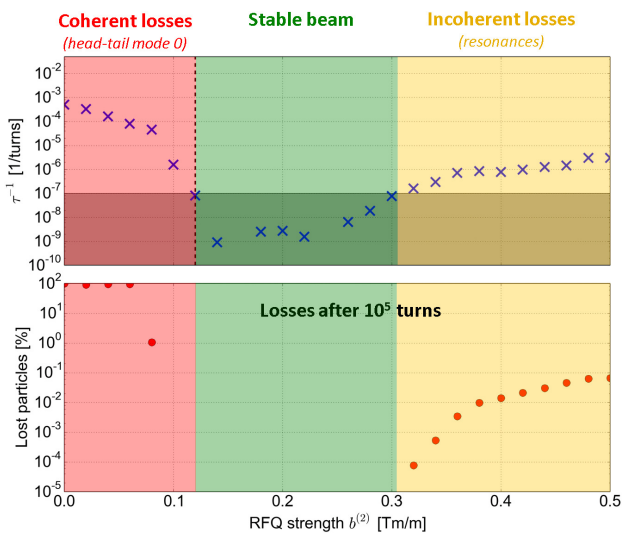

Figure 3: PyHEADTAIL results for a mode 0 head-tail instability in the SPS. *Top:* Instability growth rate vs. rf quadrupole strength. *Bottom:* Fraction of lost particles over 10^5 turns.

ISBN 978-3-95450-185-4

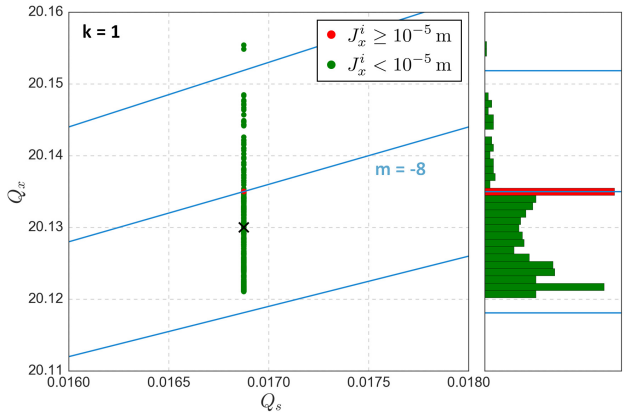

Figure 4: Subset of the tune parameter space (Q_s, Q_x) around the SPS working point (black cross). Shown are the SBR lines (blue) expected from Eq. 8 as well as the incoherent tune spread induced by an rf quadrupole for particles of high (red) and low (green) horizontal action.

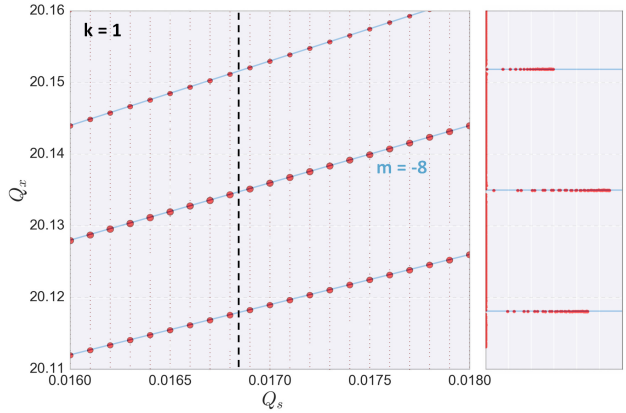

Figure 5: Subset of the tune parameter space (Q_s, Q_x) as in Fig. 4. Shown are tracking results from a 2D scan in (Q_s, Q_x) (red) overlaid with the expected SBR lines (blue). The plot on the right shows a detailed view of the results for a fixed value of Q_s (black dashed line).

over 10^5 turns (bottom) as a function of the rf quadrupole strength $b^{(2)}$ for a vertical mode 0 head-tail instability in the SPS. Three regimes can be distinguished: (i) at low $b^{(2)}$ the coherent instability can still develop and even if the growth rate is reduced almost the whole beam is lost after 10^5 turns (red), (ii) at intermediate $b^{(2)}$ the beam is stabilised and no losses are observed over the given number of turns (green), and (iii) at high $b^{(2)}$ only a small fraction of the beam is lost (yellow). The focus lies on the latter regime where the observed losses can be explained by SBR excited by the rf quadrupole. The condition for SBR for a particle i oscillating at tunes Q_x^i, Q_y^i, and Q_s^i is given by [15]

$$k \cdot Q_x^i + l \cdot Q_y^i + m \cdot Q_s^i = n, \quad k, l, m, n \in \mathbb{Z}. \tag{8}$$

In a first approximation, the rf quadrupole does not couple the horizontal and vertical planes (see Eq. 1 and 2). Hence, without loss of generality one can set $l = 0$ and treat the transverse planes independently. Equation 1 shows that the rf quadrupole gives a horizontal kick dependent on the coordinates $x_i(t)$ and $z_i(t)$, which describe respectively the betatron and synchrotron oscillations in time. Given that the particle tunes Q_x^i and Q_s^i fulfil the resonance condition in Eq. 8, the resulting kick $\Delta p_x^i(t)$ leads to an amplitude growth of the particle motion over time. The same arguments are valid for the vertical plane.

To prove the presence of SBR in a first step, a tracking simulation was performed over 200 synchrotron periods using linear synchrotron motion, a fixed rf quadrupole strength and a set of 1000 macroparticles. Particles with a high horizontal action J_x^i at the end of the simulation were separated from the rest and their individual tunes were analysed by means of the SUSSIX code [16]. The distribution of the tunes is shown in Fig. 4 in a subset of the tune space (Q_s, Q_x) around the SPS working point (black cross). The incoherent tune distribution is introduced by the rf quadrupole. The green dots mark particles maintaining a constant horizontal action, while those marked red exhibit a strong amplitude growth over time. The SBR lines (blue) expected from Eq. 8 are overlaid and show excellent agreement with tracking results. Even though this method is good enough to prove the excitation of SBR through an rf quadrupole, it is very time-consuming due to the SUSSIX tune analysis over the number of particles. In addition, the limited number of macroparticles cannot give a complete picture of all the potential resonance lines. To study and scan the tune space (Q_s, Q_x) more systematically, which is important especially in view of evaluating the presence of SBR for HL-LHC, the tool has been modified such that only one particle is tracked at a time, but for many different working points (Q_s^i, Q_x^i). For every tune setting, the amplitude of the particle motion is analysed and fitted with an exponential function to obtain the growth rate. The results are shown in Fig. 5. Red markers represent tracking results and their size is proportional to the measured amplitude growth rate of the betatron motion. The plot illustrates again the excellent agreement between the tracking code and the analytical formula (blue) and serves as a successful benchmark of the developed tool.

EXPERIMENTAL STUDIES IN THE SPS

As described in the theory section of this article, the betatron detuning introduced by a non-zero second order chromaticity $Q''_{x,y}$ is dependent on the longitudinal amplitude of the particles, similarly to the rf quadrupole (Eq. 6). Hence, studying the effect of a non-zero $Q''_{x,y}$ on beam stability will lead to a better understanding of the underlying mechanisms driven by betatron detuning with longitudinal amplitude. Other than the rf quadrupole, where a prototype must first be designed, built and installed in an accelerator, $Q''_{x,y}$ can in principle be controlled immediately by changing the optics of the machine. It thus makes experimental studies possible on a shorter time scale and allows to validate the numerical model on which the rf quadrupole results are based.

ISBN 978-3-95450-185-4

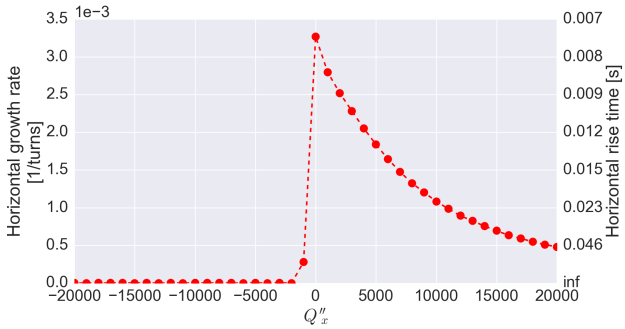

Figure 6: PyHEADTAIL results showing growth rate vs. Q''_x for a mode 0 head-tail instability in the horizontal plane of the SPS.

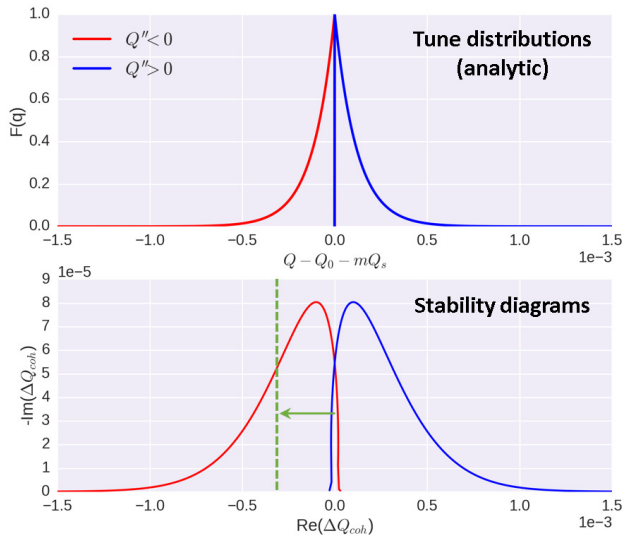

Figure 7: *Top:* Analytical incoherent tune distribution for positive and negative Q'' respectively. *Bottom:* Corresponding stability diagrams. The green dashed line represents $\mathrm{Re}\,(\Delta Q_{coh}) < 0$ caused by a dipolar impedance.

At CERN, the SPS is the most suitable machine for this kind of experiments. At present, there are ongoing studies towards improving the non-linear optics model of the accelerator in order to be able to control the horizontal second order chromaticity Q''_x reliably [17]. The idea is to vary Q''_x by using the magnetic octupoles installed in the high dispersion regions of the accelerator. Powering these elements means, however, that detuning with transverse amplitude is introduced in the machine as well. Naturally, the latter needs to be compensated for to disentangle beam stabilisation through detuning with transverse and longitudinal amplitude respectively. MAD [18] simulations of the SPS optics model show that such a compensation can indeed be achieved by means of the magnetic octupoles located in the low dispersion regions.

In parallel, PyHEADTAIL studies are under way to define possible scenarios for experiments as well as the required beam and machine parameter values. The accurate impedance model of the SPS [19] allows to obtain a clear idea of the expected instability growth rates and the amount of Q''_x required for beam stabilisation. Figure 6 shows an example of the dependence of the growth rate of a horizontal mode 0 head-tail instability in the SPS as obtained from PyHEADTAIL simulations. The operating point is a bunch intensity of $5 \cdot 10^{10}$ p$^+$/b and a first order chromaticity of $Q'_x = -2$. The plot illustrates that already a small amount of negative Q''_x leads to beam stabilisation. On the other hand, for positive Q''_x the instability cannot be suppressed within the scanned range of values. This strong asymmetry can be understood better when considering the shape of the incoherent tune spread introduced by second order chromaticity as well as the stability diagram (SD) for Landau damping. The latter can be obtained by solving the dispersion integral for betatron detuning with longitudinal amplitude. It has been derived by Scott Berg and Ruggiero [20] and can be integrated numerically. Figure 7 illustrates the analytic tune distribution (top) as well as the SD for a mode 0 head-tail instability in the plane of complex coherent tune shifts ΔQ_{coh} (bottom), both for positive and negative Q''_x respectively. The interpretation of an SD is such that head-tail instabilities characterised by a ΔQ_{coh} situated below the curve are suppressed by the presence of the corresponding incoherent tune spread. The real part of the coherent tune shift caused by a dipolar impedance is negative as indicated by the green arrow. This explains not only why much better stabilisation behaviour is expected for negative Q''_x, but also why stabilisation with positive Q''_x is much more difficult. Both observations are in qualitative agreement with tracking results. Nevertheless, the quantitative comparison with PyHEADTAIL simulations still remains to be done.

CONCLUSIONS

The potential advantages of an rf quadrupole for HL-LHC have been evaluated numerically by means of PyHEADTAIL simulations for a likely flat-top machine working point. It has been shown that a few rf cavities would be sufficient to reduce the stabilising Landau octupole current to zero. Synchro-betatron resonances can, however, be a possible performance limitation and need to be understood in detail in particular for the HL-LHC tune working point. The necessary tools for systematic studies are now available and benchmarked. The first steps towards experimental studies of the underlying stabilising mechanism in the SPS have been discussed. The second order chromaticity serves as a convenient means to study the effect of betatron detuning with longitudinal amplitude experimentally, making a validation of the numerical models of beam stabilisation through an rf quadrupole possible.

ACKNOWLEDGEMENTS

The authors would like to thank G. Arduini, H. Bartosik, X. Buffat, E. Métral, and G. Rumolo for enlightening discussions and valuable inputs to the presented studies.

ISBN 978-3-95450-185-4

REFERENCES

[1] O. S. Brüning et al., *LHC Design Report*, CERN-2004-003, 2004.

[2] G. Apollinari et al., *High-Luminosity Large Hadron Collider (HL-LHC): Preliminary Design Report*, CERN, Geneva, 2015.

[3] L. Landau, *On the vibration of the electronic plasma*, J. Phys. USSR **10**, 1946.

[4] A. W. Chao, *Physics of Collective Beam Instabilities in High Energy Accelerators*, Wiley Series in Beam Physics and Accelerator Technology, Wiley, 1993.

[5] L. R. Carver et al., *Current status of instability threshold measurements in the LHC at 6.5 TeV*, Proceedings of IPAC16, Busan (Korea), 2016.

[6] E. Métral, B. Salvant, and N. Mounet, *Stabilization of the LHC single bunch transverse instability at high-energy by Landau octupoles*, Tech. Rep. CERN-ATS-2011-102, 2011.

[7] E. Métral et al., *Measurement and interpretation of transverse beam instabilities in the CERN Large Hadron Collider (LHC) and extrapolations to HL-LHC*, this conference.

[8] A. Grudiev, *Radio frequency quadrupole for Landau damping in accelerators*, Phys. Rev. ST Accel. Beams **17**, 011001, Jan 2014.

[9] A. Grudiev et al., *Radio frequency quadrupole for Landau damping in accelerators: analytical and numerical studies*, Proceedings of HB2014, East-Lansing (USA), 2014.

[10] A. W. Chao et al., *Handbook of Accelerator Physics and Engineering*, 2nd edition, World Scientific, Singapore, 2013.

[11] V. V. Danilov, *Increasing the transverse mode coupling instability threshold by RF quadrupole*, Phys. Rev. ST Accel. Beams **1**, 041301, Jun. 1998.

[12] E. A. Perevedentsev and A. A. Valishev, *Synchrobetatron dynamics with a radio-frequency quadrupole*, Proceedings of EPAC2002, Paris (France), 2002.

[13] E. Métral et al., *Beam Instabilities in Hadron Synchrotrons*, IEEE Transactions on Nuclear Science, 2016.

[14] G. Rumolo and F. Zimmermann, *Electron cloud simulations: beam instabilities and wakefields*, Phys. Rev. ST Accel. Beams **5**, 121002, Dec. 2002.

[15] A. Piwinski, *Synchro-Betatron Resonances*, in 11th International Conference on High-Energy Accelerators: Geneva, Switzerland, July 7-11, 1980, edited by W. S. Newman, Birkhäuser Basel, 1980.

[16] R. Bartolini and F. Schmidt, *A Computer Code for Frequency Analysis of Non-Linear Betatron Motion*, Tech. Rep. SL-Note-98-017-AP, CERN, Geneva, 1998

[17] H. Bartosik et al., *Improved methods for the measurement and simulation of the CERN SPS non-linear optics*, Proceedings of IPAC16, Busan (Korea), 2016.

[18] Methodical Accelerator Design `mad.web.cern.ch`.

[19] C. Zannini et al., *Benchmarking the CERN-SPS transverse impedance model with measured headtail growth rates*, Proceedings of IPAC15, Richmond (USA), 2015.

[20] J. S. Berg and F. Ruggiero, *Stability diagrams for Landau damping*, LHC-Project-Report-121, 1997.

ISBN 978-3-95450-185-4

EARLY TESTS AND SIMULATION OF QUASI-INTEGRABLE OCTUPOLE LATTICES AT THE UNIVERSITY OF MARYLAND ELECTRON RING *

Kiersten Ruisard †, Heidi Baumgartner, Brian Beaudoin, Irving Haber, David Matthews, Timothy Koeth
[1] Institute for Research in Electronics and Applied Physics, University of Maryland, College Park, USA

Abstract

Nonlinear quasi-integrable optics is a promising development on the horizon of high-intensity ring design. Large amplitude-dependent tune spreads, driven by strong nonlinear magnet inserts, lead to decoherence from incoherent tune resonances. This reduces intensity-driven beam loss while quasi-integrability ensures contained orbits. The experimental program at the University of Maryland Electron Ring (UMER) will explore the performance of a strong octupole lattice at a range of operating points. Early measurements use a distributed octupole lattice, consisting of several small octupole inserts. We vary lattice tune to change the quasi-integrable condition as well as probe behavior near different resonant conditions. Simulation results show there should be invariant conservation under carefully chosen conditions. We discuss the effect of steering errors on the lattice performance and on-going efforts to reduce these errors. We also discuss plans for a single-channel insert.

INTRODUCTION

Beam resonances that drive particle losses and beam halo present a significant challenge for high intensity accelerators, limiting beam current due to risk of damage and/or activation. While landau damping can control resonant effects, the addition of weak nonlinearities to a linear lattice can introduce resonant islands and chaotic phase space orbits, which reduce dynamic aperture and lead to destructive particle loss. Theory predicts that lattices with one or two invariants and sufficiently strong nonlinear elements should suppress tune and envelope resonances without loss of stable phase space area [1].

In [1], the small-angle Hamiltonian for transverse motion of a particle in an external linear focusing system is given by

$$H_N = \frac{1}{2}\left(p_x^2 + p_y^2 + K(s)\left(x^2 + y^2\right)\right) + V(x, y, s) \quad (1)$$

where $V(x, y, s)$ is a generic nonlinear term. In the normalized frame, the Hamiltonian becomes

$$H_N = \frac{1}{2}\left(p_{x,N}^2 + p_{y,N}^2 + x_N^2 + y_N^2\right) + \kappa U(x_N, y_N, s) \quad (2)$$

where $x_N = \frac{x}{\sqrt{\beta(s)}}$ and $p_N = p\sqrt{\beta(s)} - \frac{\alpha x}{\sqrt{\beta(s)}}$.

In order for $U(x_N, y_N)$ to be an invariant quantity (and therefore for H_N to be conserved), $\beta_x = \beta_y$ inside the nonlinear element and the nonlinear element strength parameter $\kappa(s)$ depends on $\beta(s)$. In particular, for an octupole element $\kappa \propto \frac{1}{\beta(s)^3}$.

For an elliptic nonlinear magnet, the transverse motion of a particle will be fully integrable with two conserved invariants, the normalized Hamiltonian and an additional quadratic term. The theory of the integrable lattice will be tested at the IOTA ring, currently under construction at Fermilab [2, 3]. The proposed lattice consists of a transversely symmetric ($\beta_x = \beta_y$) beam in an axially varying nonlinear insert, linked by linear sections of $n\pi$ phase advance that provide external focusing and image the beam between nonlinear sections, for pseudo-continuous motion of particles through the nonlinear insert. This lattice is illustrated in Fig. 1.

The goal of the nonlinear optics program at UMER is to test a quasi-integrable octupole lattice, experimentally demonstrating increased transverse stability and halo mitigation, predicted in [4]. While IOTA aims to test a fully integrable nonlinear solution, UMER does not have the precision necessary to verify integrability [2]. The strength of UMER lies in its flexibility to accommodate variable space charge beams with flexible focusing schemes. For the quasi-integrable lattice, the conserved H_N will result in chaotic but bounded motion, while still providing large amplitude-dependent tune spreads to reduce resonant behavior.

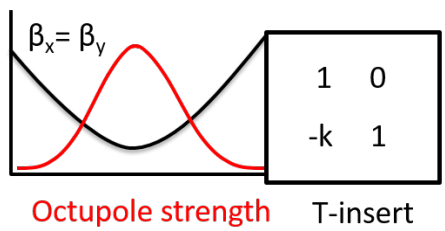

Figure 1: Ideal nonlinear lattice composed of $\beta_x = \beta_y$ channel and ideal thin lens transfer matrix.

This paper will discuss preliminary testing of a distributed octupole lattice, conducted in parallel with preparations for the more robust single-channel design.

EXPERIMENTAL SETUP

UMER is a 10 keV, 11.52 meter circumference ring designed for the study of high intensity beam dynamics. The

* Work and travel supported by NSF GRFP, NSF Accelerator Science Program, DOE-HEP and UMD Graduate School ICSSA award.
† kruisard@umd.edu

ISBN 978-3-95450-185-4

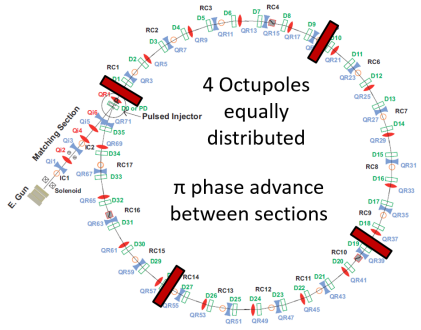

Figure 2: N4 octupole lattice imposed on alternative lattice, large blocks indicate octupole positions.

facility consists of an electron source and pulsed dipole injection into the ring, containing 36 FODO cells and 36 dipole magnets. At present, the ring has 5 available beam current settings, ranging from 0.6 mA to 100 mA, with corresponding tune depressions of 0.85 - 0.14. Transport of the 0.6 mA (or "pencil") beam is largely emittance dominated, while higher currents are space charge dominated. [5] A 60 μA beam is currently being characterized for use in the nonlinear experiments.

The Nonlinear Optics project at UMER has examined two variants of the quasi-integrable octupole lattice [1]. One test lattice, referred to as the single-channel lattice, will have one long octupole insert (64 cm, or 6% of the ring) over a symmetric beam waist. [6] This will resemble the octupole and elliptic lattices at the IOTA ring.

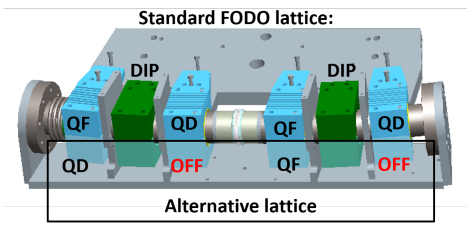

Figure 3: Two standard UMER FODO cells (blue quadrupoles and green dipoles). In the Alternatice lattice, the crossed quadrupoles are unpowered, leaving a vacancy for octupole elements.

The primary focus of this paper is the second consideration, an N4 distributed octupole lattice. The nonlinear inserts are comprised of 4 short octupoles distributed at even intervals about the ring (90^o points, see Fig. 2). This configuration utilizes a mode of UMER operation known as the "alternative lattice" in which the total number of FODO cells in the ring is halved (by removing half of the quadrupoles). The two lattices are illustrated in Fig. 3. The nominal tune of the ring is also approximately halved, from $\nu \approx 6.7$ to ≈ 3.8. The alternative lattice uses printed circuit octupoles with the same aspect ratio as the standard UMER PC quad, which are seated in unused quadrupole mounts at the mid-point of the FODO cell.

The lattice can be tuned to have a tune of $4 + \delta 2\pi$, where δ indicates the phase advance through the octupoles. For a turn length of 11.52 m, effective octupole length of 5.2 cm and tune near 4, the phase advance through the octupoles will be near $\psi = 0.07 * 2\pi$.

The N4 lattice is natively suited to the UMER structure, allowing the installation of octupoles with minimal disruptions to the ring (utilizing existing mounts and power supplies). However, it is a coarse approximation of the quasi-integrable octupole lattice and it is expected that these approximations will limit the extent to which the Hamiltonian H_N is conserved.

A key liberty taken with the quasi-integrable theory is the requirement that $\beta_x = \beta_y$ throughout the nonlinear element. In the N4 case, $\beta_x \approx \beta_y$, with differences on order 15%. The other approximation is that the PC octupole is fringe-dominated, meaning the longitudinal profile is not flat top and therefore the magnet cannot perfectly meet the requirement that $V_{oct} = 1/\beta^3 =$ constant. Theoretical calculations of the UMER magnets predict that fringe fields cancel due to the relatively short magnet length. [7] It is yet to be seen if this cancellation will help preserve the nonlinear invariant. Octupole models used in simulations shown here utilize a hard-edged approximation.

Printed Circuit Octupole Magnets

UMER utilizes air core flexible printed circuit magnets for focusing and steering. The printed circuits are cost-effective, lightweight and stackable, making any combination of multipoles possible. They can operate in DC or pulsed mode, and are easily tunable with no hysteresis as well as inexpensive and rapid to prototype.

The first generation of printed circuit octupoles has been produced and initial characterization made. The PC circuits, pictured in Fig 4, are made in two double-layered halves, which fit inside the standard UMER quadrupole mount. Based on the similarity to existing UMER PC quadrupoles and dipoles, each magnet should easily be able to sustain 2 A DC with the existing mounts and up to 10 A with addition of water cooling. Maxwell 3D calculations show $75T/m^3/A$ peak fields in the octupole, with the 16-pole as the next significant multipole, against theoretical predicts that the 24-pole is the next highest allowed multipole. [7]

The magnet has been characterized using an integrated rotating coil measurement. A long coil rotating at 1 Hz sends EMF signal to an oscilloscope. The resulting scope FFT can be seen in Fig. 5. The large dipole contribution is primarily due to the earth's magnetic field. Sextupole and quadrupole terms are minimized by adjusting the transverse position of the octupole.

DISTRIBUTED OCTUPOLE LATTICE SIMULATIONS

Simulations of N4 distributed lattices in the Elegant and Warp codes predict enhanced stability near the ideal tune operating point.

ISBN 978-3-95450-185-4

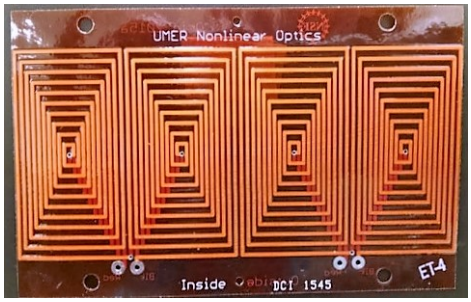

Figure 4: Half of a UMER printed circuit octupole magnet.

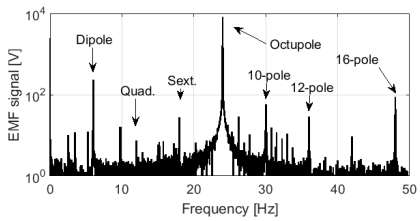

Figure 5: FFT measurement of octupole from rotating coil measurement.

Elegant

The idea of the distributed octupole lattice was first explored in the Elegant code, which allows beam tracking through third order matrices and symplectic elements. [8] Frequency map analysis shows the dynamic aperture is largest for an evenly distributed N4-octupole lattice With an octupole strength of $200T/m^3$, which corresponds to approximately 2.66 A in the physical octupoles, we see a tune shifts up to $\Delta\nu \approx 0.07$. This comes at the cost of operating near the integer resonance band.

The Elegant calculation was run at $\delta\psi_x = 1.06 * 2\pi$, $\delta\psi_y = 1.08 * 2\pi$ between octupoles (ring tune of $\nu_x = 4.45$, $\nu_y = 4.54$), slightly displaced from the ideal $\delta\psi_x = \delta\psi_y = 2\pi$ between octupoles. At this offset, the integer resonance band $\nu_x = \nu_y$ is visible in both configuration and tune space as an evacuated band, as seen in Fig. 6. This integer band is destructive and cannot be mitigated by increasing octupole strength to drive up tune spread; The maximum externally induced tune spread is fixed, while the dynamic aperture decreases with octupole current (and amplitude dependent tunes scale accordingly).

A comparable analysis for single channel design was done in Elegant. The single channel octupole is expected to have a maximum tune shift of roughly twice what is expected in the N4 lattice ($\delta\nu \approx 0.23$), and less apparent sensitivity to the $\nu_x = \nu_y$ band.

WARP

We use the WARP PIC code to track the invariant quantity (Hamiltonian) in the nonlinear lattice [9]. We first model an ideal quasi-integrable octupole channel, in which octupoles are perfectly scaled as β^{-3} across a 64 cm drift (equivalent 20 degree section of UMER), and the remaining 340 degrees of the ring is condensed to a thin-lens axisymmetric focusing

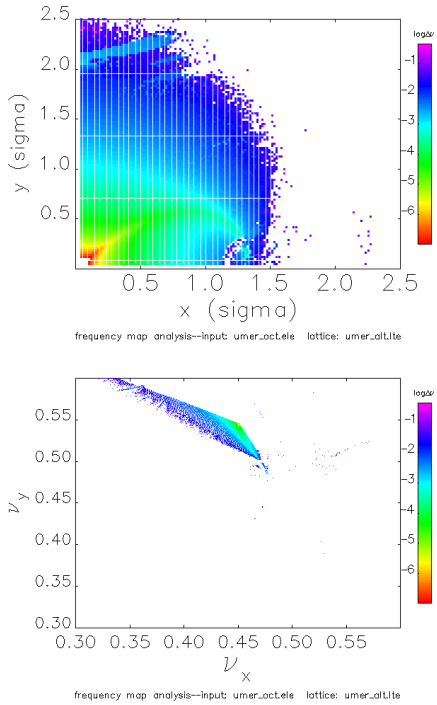

Figure 6: Frequency Map Analysis of N4 lattice in configuration and tune space.

kick. This system is discussed in more detail in previous presentations [6]. For 100 passes through this octupole channel, we see a particle of $\langle H_N \rangle = 1E-5$ experience RMS variations of $2.8E-10$ without octupoles (jitter apparently due to computational noise) and variations of $1.5E-8$ for maximum octupole current of 2 A. These values can be compared to Table 1. Despite low-frequency oscillations, the particle energy appears to be well-bounded as expected, see Fig. 7.

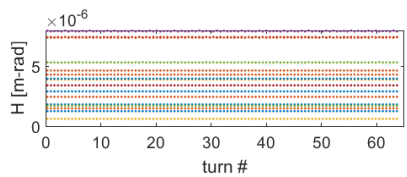

Figure 7: Conserved invariant H_N for simple quasi-integrable octupole lattice, WARP simulation.

N4 distributed lattice In comparison, invariant tracking through the N4 distributed lattice shows much larger amplitude oscillations in H_N, most likely due to the approximations on the nonlinear portion of the lattice. For the WARP model, we use hard edged elements in the alternative lattice configuration. Octupoles of length 5.2 cm and peak strength $75T/m^3/A$ are placed at 2.88 m intervals.

Two cases are considered: The historically utilized alternative lattice operating point $I_F = I_D = 0.87A$, which has a tune (as calculated in WARP) of $\nu_x = 3.88$, $\nu_y = 3.83$

ISBN 978-3-95450-185-4

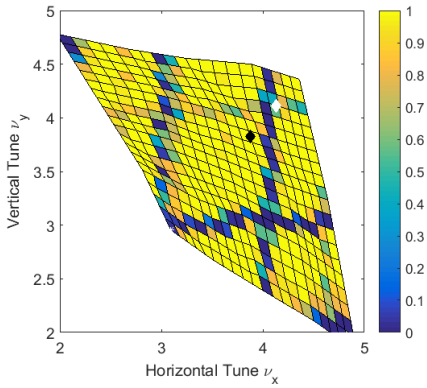

Figure 8: Tune scan, simulated with WARP. Color axis shows particle survival over a range of operating points. Black marker indicates operating point $\nu_x = 3.88$, $\nu_y = 3.83$, while white marker indicates $\nu_x = 4.13$, $\nu_y = 4.11$.

and $I_F = 0.938A$, $I_D = 0.944A$, with tunes $\nu_x = 4.13$, $\nu_y = 4.11$. The two operating points are marked in Fig. 8.

One expects the invariant to be perfectly conserved in the linear case ($I_{oct} = 0$). Also, decrease of dynamic aperture with increasing octupole strength is can be seen through high-amplitude unstable chaotic orbits leaving the system. Recall, for the nonlinear invariant to be conserved, particles must have continuous motion through the octupole elements otherwise chaotic, unbounded orbits are permitted. [1] In the case continuous motion (or quasi-continuous, allowing for linear inserts between octupoles) cannot be maintained, we expect the invariant quantity to be less bounded. As seen Fig. 9 and Fig. 10, particles seem to gain stability as the external focusing nears the $\nu_x = \nu_y = 4.07$ condition. However, simulations at this operating point yield poor results, and the invariant is not well conserved.

While the Hamiltonian is not well conserved, long term stability (past the tested 50 turns) may be possible. A natural extension of this work is to include predicted experimental errors into the invariant calculation, as well as extend consideration to a wider range of operating points.

PRELIMINARY MEASUREMENTS

Alternative Lattice Tune Scan

In preparation for N4 lattice testing, measurements are taken on the alternative lattice to gauge beam losses over a variety of operating parameters. The tune scan technique, described in more detail in [10], measures variations in beam losses as a function of quadrupole strength in two families of quadrupoles (horizontally focusing and defocusing, notated as I_F and I_D). Fig. 11 shows beam survival measurements of the 0.6 mA beam for a range of quadrupole values. Transformation to tune-space was done using WARP simulations with hard-edged elements and a thin-lens model of dipole edge focusing. The obvious integer resonance bands are used to orient the measurement in tune-space. An offset of

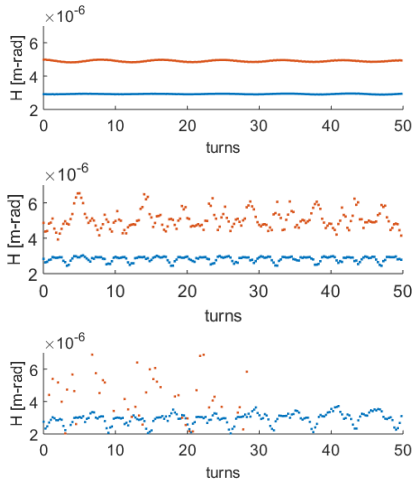

Figure 9: Invariant H_N for N4 distributed lattice at $\nu_x = 3.88$, $\nu_y = 3.83$.

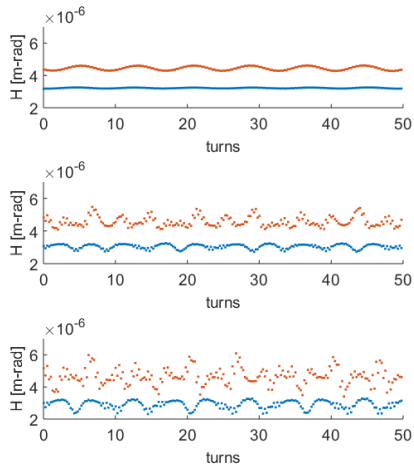

Figure 10: Invariant H_N for N4 distributed lattice at $\nu_x = 4.13$, $\nu_y = 4.11$.

$\nu_x = -0.45$ and $\nu_y = -0.35$ from the WARP prediction is necessary to line up integer bands.

The tunescan shows broad bands at the even integer tune resonances. As this N4 lattice is intended to be run at $\nu_x = \nu_y = 4+\delta$, tuning the beam closer to this operating point will be necessary if any beneficial effect is to be observed over the integer band losses. With octupoles on (Figs. 11,12), no apparent increase in dynamic aperture is seen.

Errors: Beam Matching and Steering The beam matching quadrupoles and steering correctors were optimized to a single operating point, at $I_F = I_D = 0.87$ A. It is expected that the accrued errors in the match and the steering grow with greater distance from the ideal operating point, although it is not clear that they accrue anisoptropically.

The steering solution for this operating point had first turn horizontal offsets in the quadrupoles of RMS 0.5 mm with a maximum of 1.3 mm. Vertically, RMS offsets are 3.2 mm with maximum value of approximately 8.5 +- 0.5 mm. The contribution of these steering errors can be seen in the width

ISBN 978-3-95450-185-4

Table 1: Invariant Tracking in N4 Lattice

$\nu_x = 4.13$ I_{oct} [A]	$\nu_y = 4.11$ $\langle H_N \rangle$	RMS variation	% variation peak to peak
0	3.22E-6	2.3E-8	2.4
0.5	3.17E-6	4.2E-8	6.2
2.0	3.05E-6	1.1E-7	17.6
4.0	2.91E-6	2.1E-7	33.5
$\nu_x = 3.88$ I_{oct} [A]	$\nu_y = 3.83$ $\langle H_N \rangle$	RMS variation	% variation peak to peak
0	2.92E-6	1.5E-8	2.3
0.5	2.90E-6	3.5E-8	6.8
2.0	2.82E-6	1.0E-7	20.8
4.0	2.93E-6	1.4E-7	59.9

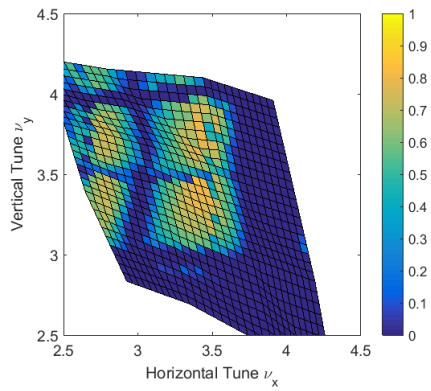

(a) Alternative lattice tune scan

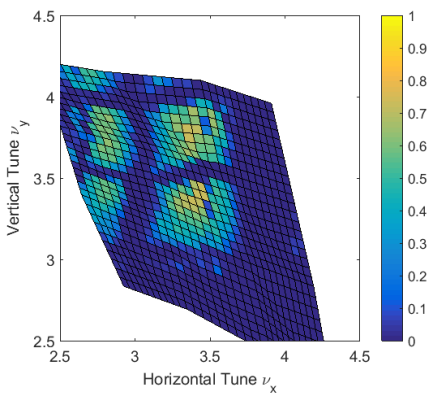

(b) N4 lattice tune scan with octupoles powered at 0.5 A

Figure 11: Tune scan data for 0.6 mA "pencil" beam, beam survival plot at 25 turns. Color axis is peak beam current normalized to 10th turn.

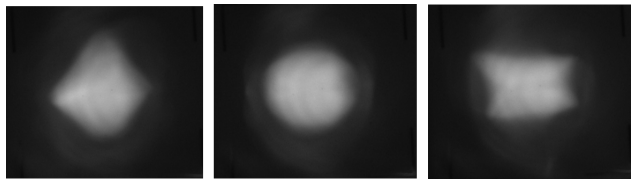

Figure 12: Beam profile after 1 pass through octupole, imaged using phosphor screen. From left to right: $I_{oct} > 0$, $I_{oct} = 0$, $I_{oct} < 0$.

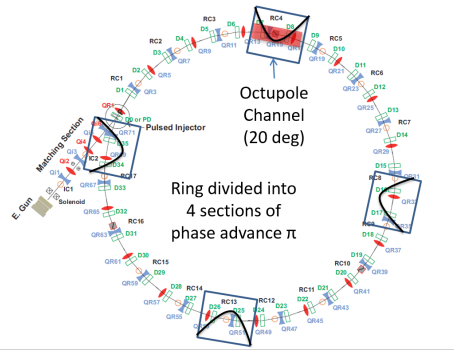

Figure 13: Single octupole lattice layout, with 4 symmetric $\beta_x = \beta_y$ points, one of which will accommodate the octupole insert.

of the integer resonance bands in the tune scan data (Fig. 11). More precise control of the steering will likely improve this characteristic by reducing the steering error for all operating points.

The beam match was not well-tuned, with percent RMS variations of 33% in the horizontal and 28% in the vertical. More accurate matching solutions have been demonstrated in UMER, up to standard deviations of 0.17 mm horizontally and 014 mm vertically for the 6 mA beam. [11]

CONCLUSION

In conclusion, UMER is equipped to test quasi-integrable octupole lattices. Insight has been built into the behavior of the N4 octupole lattice, which has potential to be an approximate testbed for quasi-integrable dynamics. However, the proximity to an integer resonance band may ultimately limit its usefulness and implementation, at least with short octupole elements. On UMER, the large $\nu_x = 4$ band overshadows any resonant loss mitigation induced by the octupoles.

Additional work to improve the matching and steering errors near the desired tune operating point may increase the viability of the N4 lattice. However, the emphasis of future work will be on implementing the single-channel lattice on UMER, by modifying a 20 degree ring section to accommodate a long octupole insert, as depicted in Fig. 13.

REFERENCES

[1] V. Danilov and S. Nagaitsev, "Nonlinear acclerator lattices with one and two analytic invariants," *Phys. Rev. ST Accel*

ISBN 978-3-95450-185-4

Beam, vol. 13, p. 084002, 2010.

[2] A. Valishev *et al.*, "Beam physics of integrable optics test accelerator at Fermilab," presented at the Int'l Particle Accel. Conf. (IPAC'12), New Orleans, LA, USA, May 2012, paper TUPPC090, pp. 1371-1373.

[3] S. A. Antipov *et al.*, "Quasi-integrable nonlinear optics experiments at IOTA," presented at the 16th Advanced Accelerator Concepts Workshop (AAC'14), San Jose, California, July 2014, unpublished.

[4] S.D. Webb *et. al*, "Effects of nonlinear decoherence on halo formation" (unpublished). submitted to Phys. Rev. Lett., 2012.

[5] S. Bernal *et al.*, "Beam experiments in the extreme space-charge limit on the University of Maryland Electron Ring," *Phys. Plasmas*, vol. 11, p. 2901, 2004.

[6] K. Ruisard *et al.*, "Nonlinear optics at the University of Maryland Electron Ring," presented at the 16th Advanced Accelerator Concepts Workshop (AAC'14), San Jose, California, July 2014, unpublished.

[7] M. Venturini, "Lie methods, exact map computation, and the problem of dispersion in space charge dominated beams," Ph.D thesis, Phys. Dept, University of Maryland College Park, 1998.

[8] M. Borland, "elegant: a flexible SDDS-compliant code for accelerator simulation," Advanced Photon Source LS-287, Sept. 2000.

[9] A. Friedman *et al.*, "Computational methods in the Warp code framework for kinetic simulations of particle beams and plasmas," *IEEE Trans. Plasma Sci.*, vol. 42, no. 5, p. 1321, May 2014.

[10] S. Bernal *et al.* "Coherent phenomena over a broad range of beam intensities in the electron storage ring UMER," presented at the Particle Accel. Conf. (PAC'09), Vancouver, Canada, 2009, paper FR5PFP063, pp. 4455-4457.

[11] H. Zhang, "Experimental study of beam halo in intense charged particle beams," Ph.D thesis, Phys. Dept, University of Maryland College Park, 2014.

ISBN 978-3-95450-185-4

SPACE CHARGE EFFECTS AND MITIGATION IN THE CERN PS BOOSTER, IN VIEW OF THE UPGRADE

E. Benedetto, F. Schmidt, CERN, Geneva, Switzerland
V. Forte, CERN and University Blaise Pascal, Clermont-Ferrand, France
M. Cieslak-Kowalska, CERN and EPFL, Lausanne, Switzerland

Abstract

The CERN PS Booster (PSB) is presently running with a space charge tune spread larger than 0.5 at injection. Since the High Luminosity LHC (HL-LHC) will require beams with twice the intensity and brightness of today, the LHC Injector Upgrade (LIU) Project is putting in place an upgrade program for all the injector chain and, in particular, it relies on the important assumption that the PS Booster can successfully produce these beams after the implementation of the 160 MeV H- injection from Linac4. This contribution describes the studies (measurements and simulations) that have been carried out to confirm that the PSB can indeed perform as needed in terms of beam brightness for the future HL-LHC runs. The importance of the mitigation measures already in place, such as the correction of the half-integer line, and the effects of non-linear resonances on the beam are also discussed.

INTRODUCTION

The PSB is the first synchrotron in the LHC proton injector chain and it is where the beam brightness is defined. The future increase of the PSB injection energy from 50 MeV to 160 MeV with Linac4 gives a factor $(\beta\gamma^2)^{160MeV}/(\beta\gamma^2)^{50MeV} = 2.04$ reduction of the space charge tune spread for the present beams. The baseline of LIU is to keep the same tune spread at the PSB injection energy and to inject twice as many protons in a given emittance [1]. In the first part of the paper we summarize the studies that are leading to the beam brightness predictions for the upgrade to 160 MeV, additional details in [2,3]. The simulations, compared with measurements at 50 MeV, are done with PTC-Orbit [4,5]. In the second part we discuss the mitigation measures in place against space charge for both the present situation and the upgrade. Finally we discuss our first attempt to include non-linear errors in our model.

BEAM BRIGHTNESS

Present Machine, 50 MeV p+ Injection

Measurements of LHC beams in the PSB show that, after optimization of the injection settings, the points of the emittance as a function of intensity lay on a straight line [6, 7], indicating that we are running at constant brightness. The brightness here is defined as (Ex+Ey)/2/Np, where Ex, Ey are the normalized rms transverse emittances and Np is the number of protons.

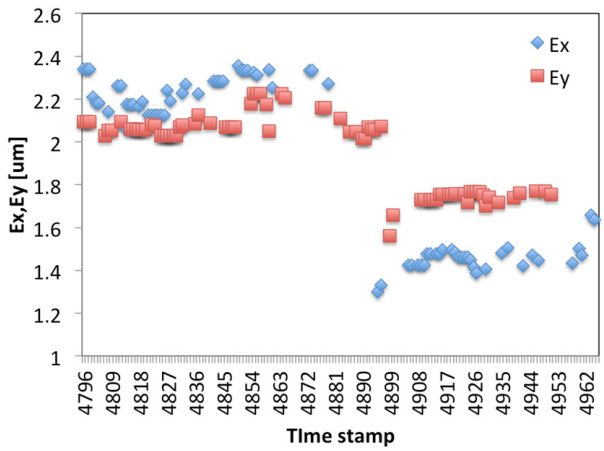

Figure 1: Measured horizontal and vertical rms normalized emittance, averaged over the 4 PSB rings, for Qx=4.28 (<496) and after the change to Qx=4.42 (>496). The vertical tune is fixed at 4.45.

Moreover, in operation we see an important reduction of the horizontal emittance, when the working point is moved from Qx=4.28 to Qx=4.42, as shown in Fig. 1.

In the present PS Booster, the beams emittances are determined by space charge effects and by the multi-turn injection process itself.

In order to prove that the emittances strongly depend on the distance of the working point from the integer lines, we launched PTC-Orbit simulations with a simple model that does not include the proton multi-turn injection process, but only looks at the evolution of an initially matched beam, in a pure linear lattice.

Figure 2 shows the emittance evolution versus time when starting from an initial Gaussian beam of 1.5 µm, for two working points similar to the ones used in operation. We find good qualitative agreement with the measurements. In particular, the horizontal emittance is strongly reduced when going to a larger working point. In this case the vertical emittance is also slightly increasing, since the vertical tune is smaller.

For what concerns the longitudinal plane, the beam is injected in coasting mode and then the voltage of the two RF cavities, h=1 and h=2 (in anti-phase) is raised to V=8kV within 7 ms in an accelerating bucket. This is an important ingredient in the space charge simulations because the bunching factor is going down from 1 to 0.4, thus the line density is increasing. Figure 3 shows the initial and final profiles, from simulations.

ISBN 978-3-95450-185-4

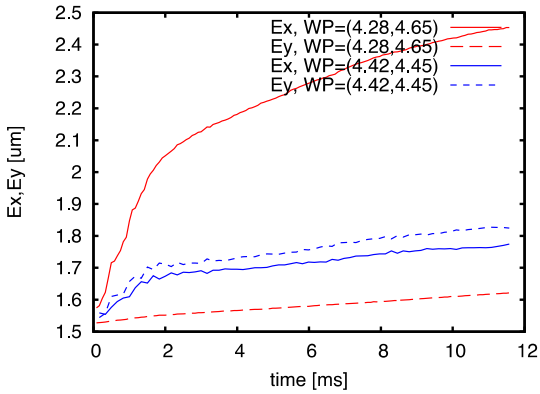

Figure 2: Simulated (simple model) horizontal and vertical rms normalized emittance evolution for two different working points: (4.28,4.65) and (4.42,4.45).

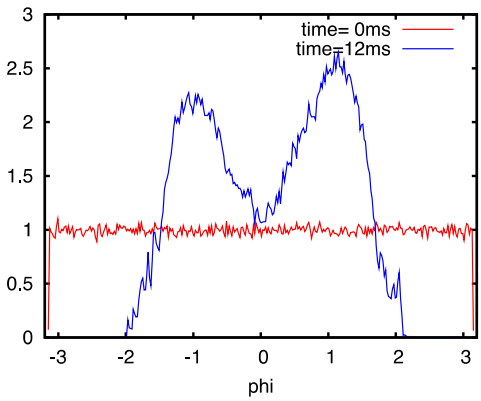

Figure 3: Longitudinal profile at injection (coasting beam) and after the RF capture in double harmonics.

Upgrade to 160 MeV, H- Injection

Applying a simple scaling law, one expects a factor 2 improvement in the PS Booster brightness curve by going from the present 50 MeV injection energy to 160 MeV, to take into account the increase in $\beta\gamma^2$.

Figure 4 shows the emittance versus intensity and the comparison of our simulations with the measurements [6, 7]. The points in red correspond to the two simulations at 50 MeV injection energy discussed in the previous section (Fig. 2), for the working points (4.28, 4.60) and (4.42, 4.45). In green and in orange the simulation at 160 MeV are plotted, assuming the two working points (4.33, 4.55) and (4.43, 4.60), in comparison with the measured line scaled by the factor 2. Raising the horizontal tune increases the beam brightness by reducing the slope of the emittances versus intensity. The curves were obtained for a longitudinal emittance of 1.2 eVs, additional margin will come from an increase of the longitudinal acceptance at injection [2].

The model included in these simulations [2,3] is once more very simple: it does not include the H- charge-exchange injection, but it starts from a matched Gaussian distribution in the transverse planes and looks at the beam dynamics during the fall of the chicane magnets, which takes 5 ms.

Quadrupolar perturbations varying with time are modelled, due to the edge effects and to feed-down effects of eddy-currents induced sextupolar components in the rectangular chicane magnets. To compensate for the beta-beating (and the excitation of the half-integer line), two main quadrupoles at a proper phase advance with respect to the injection region are trimmed with a special function, as described in [8].

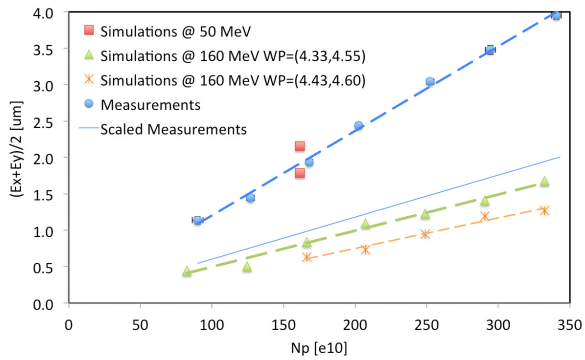

Figure 4: Semi-sum of the normalized rms emittances versus intensity. Blue points: measurements [4]; blue line: measurements slope scaled by 2; green and orange: simulations at 160 MeV injection energy, for two working points; red: simulations at 50 MeV, as in Fig. 2.

Refined Analysis

As a second step, we have included in the simulations the H- charge-exchange multiturn injection, studying different painting schemes [9]. In particular Fig. 5 shows the results of simulations in which the phase space painting is achieved by programming a constant amplitude for the painting bump and by applying an injection offset in both the horizontal and vertical plane.

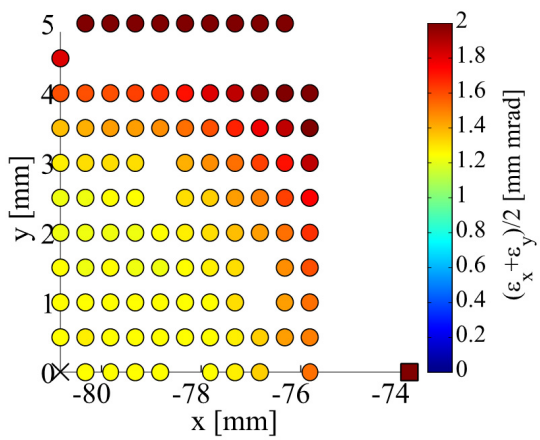

Figure 5: The simulated final emittance (semi-sum of the normalized rms emittances) after 10 ms tracking with respect to the injection offset in x and in y [9]. The beam intensity is Np=3.42e12 and the bare tune is (4.43, 4.60).

The main message from this study is that indeed the details of the injection process are in the shadow of the

ISBN 978-3-95450-185-4

space charge effects and that there is a large span of initial offsets that allow to produce the same transverse emittance. In particular, an emittance of <1.4 μm (the LIU goal is 1.7 μm for an intensity of 3.42e12 protons) can be achieved with an offset of up to 3 mm in both planes. The result is relevant in defining the tolerances with respect to injection offset errors.

MITIGATION MEASURES

Since a space charge tune spread of more than 0.5 [10] is our bottleneck in the brightness of the LHC beams and is affecting losses at low energy for the high-intensity users, the PS Booster relies on several mitigation measures to increase its reach.

RF System

One of the most important measures implemented in the present machine is the use of a second harmonics cavity (h=2) in anti-phase and about the same voltage for the main cavity (h=1) in order to flatten the beam profile and reduce the line density, thus the space charge tune spread.

Presently, the protons from Linac2 are first injected in coasting mode. Then the beam is adiabatically captured and accelerated. With Linac4, thanks to the chopping system, which will remove about 40% of the pulse, the beam will be injected directly into an accelerating bucket, thus reducing the time spent at low energy.

Transverse Painting

The transverse painting in the horizontal plane (and vertical injection offset) is particularly relevant for PS Booster high intensity beams, for which up to 1.6e13 protons have to be injected in about 100 turns [11].

Long term space charge tracking studies [12] have been performed to study the long term evolution of the painted profiles, taking into account the design of a new beam absorber/collimator to localize losses.

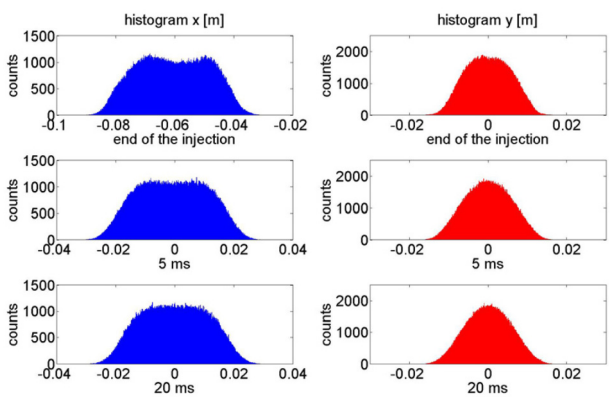

Figure 6: Horizontal (left) and vertical (right) beam transverse distribution at the end of the injection process (~100 μs), after 5 ms and 20 ms. Beam intensity is 1.6e13 protons and the final normalized rms emittances are 13 μm and 6μm.

Figure 6 shows the transverse profile evolution, up to 20ms after injection, which meet the constrains of having a vertical emittance smaller than 6 mm in the vertical plane, imposed by a bottleneck in the extraction line [13], and no more than 5-6% losses at low energy.

Choice of Working Point

The choice of the injection working point is fundamental for the production of high brightness beams, as discussed in earlier in the paper. In the PS Booster, the tunes are varying during the acceleration, from around (4.3, 4.6) at injection down to (4.20,4.20) at extraction.

Today, with the conventional multi-turn proton injection from Linac2, for the high intensity beams which need about 10 turns injected, we are limited in the choice of the horizontal tune, which should be a compromise between the goal to accommodate the largest space charge tune spread and the efficiency of the process itself, i.e. low losses at the septum.

For the LHC beams, for which only 2 injection turns are needed, we already see the advantages of going to a larger horizontal tune, both in measurements and in simulations. With the new H- charge-exchange injection scheme, the constrain of the septum and the one imposed by the Liouville theorem will not be there any more and it will be possible to inject onto the same phase space, at ideally any working point.

Half-Integer Correction

In order to go to tunes above 4.5 in the vertical plane, we need a good compensation of the half integer resonance otherwise strong losses are observed in operation.

We have a dedicated set of normal quadrupoles, powered in pairs with a proper phase advance, in such a way that they form an orthogonal base to correct for the half integer without exciting the integer lines.

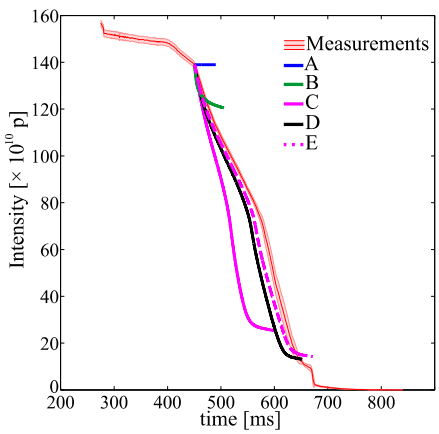

Figure 7: Intensity evolution vs. time. Measurements in pink. Simulation: (A) with only space charge but no errors; (B) no space charge; (C) with quadrupolar errors (programmed Qy =4.53); (D) with quadrupolar and misalignment errors (Qy=4.53); (E) with quadrupolar errors (Qy =4.525).

Figures 7 to 9 show the studies that we did [14, 15] to understand the effect of the half-integer on the beam. A

ISBN 978-3-95450-185-4

special cycle was prepared to accelerate the beam and keep it on a 160 MeV flat-top in order to study the PS Booster at the future injection energy. The beam was brought to a working point of (4.28, 4.53) with the normal quadrupoles correctors switched-on, in order to compensate the 2Qy=9 line. Strong losses occurs when the quadrupoles are switched off, starting at t=500ms from the start of the cycle. The pink line in Fig. 6 shows the measured intensity evolution. One can notice already some losses before, due to the non-perfect compensation that was achieved at the time. The black line is the result of simulations that include the PSB model, at the best of our knowledge, i.e. with misalignments and an effective set of quadrupolar errors [14]. A very good agreement was obtained with the measurements. The transverse profiles stay constant, while in the longitudinal plane one can see (Fig. 7) the equivalent in double harmonics of the bunch shortening phenomena, seen when particles at large synchrotron amplitude interact with a resonance line [15].

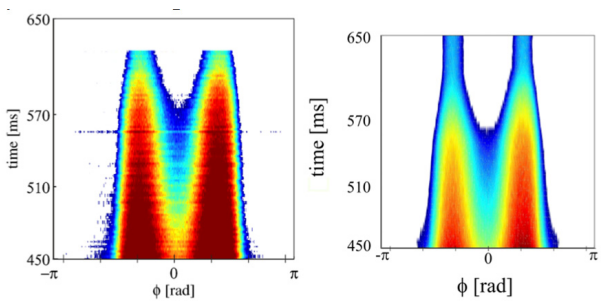

Figure 8: Waterfall plot of the measured (left) and simulated (right) longitudinal bam profile.

Our interpretation of the losses is that particles performing large excursions in the space charge necktie under synchrotron motion interact with the 2Qy=9 line, getting trapped/scattered and eventually getting lost.

As a consequence, the tune footprint shrinks, bringing other particles to interact with the line. The change of slope in the losses, at around t=570ms, also reproduced in simulations, occurs when particles inside the inner separatrix of the double harmonics bucket start interacting with the resonance.

Further studies [16] put in evidence the dependence of the loss rate on the beta-beating, as shown in Fig. 8, where 10 different seeds of errors were generated, with the same standard deviation of measurements.

Non-linear Correctors

A large set of high order multipoles, to correct for normal and skew sextupolar errors, one family of sextupoles for chromaticity correction, one family of octupoles and skew quadrupoles are available in the machine, but only the sextupolar correctors and the skew quadrupoles are used in operation and empirically adjusted to minimize losses for the high intensity beams.

Figure 10 illustrates the extra emittance blow-up in case sextupolar errors are included in the simulations for the 160 MeV brightness predictions.

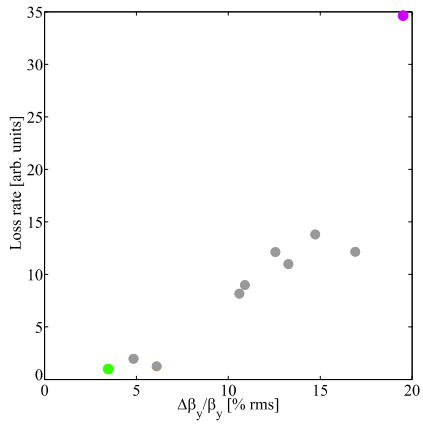

Figure 9: Loss rate vs. vertical beta beating, computed from different error seeds.

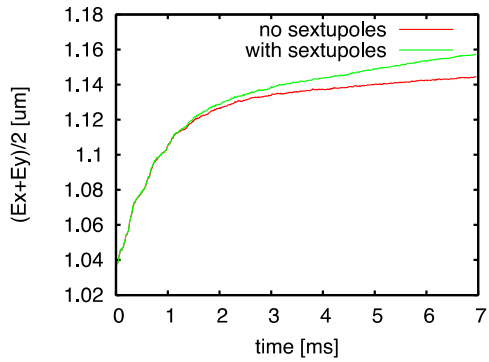

Figure 10: Emittance evolution vs. time, assuming no sextupolar errors in the lattice and with errors. Simulations at 160 MeV, Np=260 e10 p, WP (4.33,4.55).

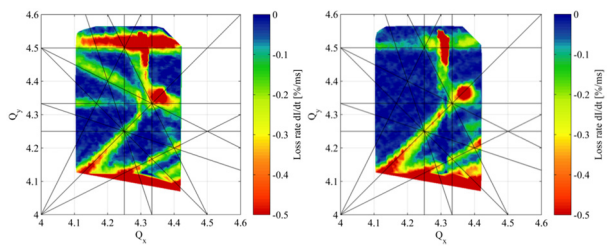

Figure 11: Tune scans. Left, bare machine, Right, after empirical correction [16].

The errors are implemented in our model by powering with the opposite sign the set of correctors empirically found to compensate the lines of Fig. 11 (left). Table 1 lists the resonance driving terms amplitude, as computed with MAD-X, showing that both coupling resonances and integer lines are excited by the sextupolar errors.

Table 1: Driving Terms

Normal		**Skew**	
h3000 =	0.01	h2010 =	0.06
h2100 =	0.06	h2001 =	0.07
h1020 =	0.03	h1110 =	0.17
h0011 =	0.12	h0030 =	0.07
h0002 =	0.04	h0021 =	0.18

ISBN 978-3-95450-185-4

Following this analysis it is interesting to note that the main magnets in the PS Booster carry a non-negligible normal 3rd order component, intrinsic to the dipole itself. In Table 2 the values are listed.

Table 2: Driving Terms Excited by the Main Dipoles

Normal	
h3000 =	0.01
h2100 =	0.02
h1020 =	0.006
h0011 =	0.01
h0002 =	0.02

OPTICS MACHINE STUDIES

Efforts are ongoing to improve the machine model including non-linear terms.

Systematic studies from turn-by-turn Beam Position monitors will most likely be possible from next year onwards, when the electronics will be available. Preliminary analysis of data coming from the few monitors already equipped with turn-by-turn readings has been started. The goal is mainly to commission the hardware and to validate the method of the AC Dipole excitation in a low-energy ring [17].

Measurements of the non-linear chromaticity were made and compared with MAD-X (ptc_normal) assuming a model which includes only the main bends, quadrupoles and the chromaticity sextupoles family. Detailed analysis is ongoing, but a preliminary table showing the comparison are presented in Table 2. By looking at the output of the Control Room application (Fig. 12), one can already appreciate that only the first and second order terms are relevant. Measurements have been taken on the 160 MeV flat-top special machine cycle, for two different working points. The first one is a "standard" one, i.e. (4.20, 4.32), the second one has been prepared in an ad-hoc manner to be (3.32, 3.81). Table 3 summarizes the results, showing a reasonable agreement with the model.

Table 3: Non-linear Chromaticity

Q	Q'	Q"	Measured Q'	stdev
Standard working point				
4.20	-3.35	45	15.1	5.7
4.30	-6.84	87	44.4	13.7
Low working point				
3.32	-2.81	78	48.3	3
3.81	-4.97	116	112	34

CONCLUSIONS

We have shown predictions for the future brightness of the LHC beams in the PS Booster, after the upgrade to 160 MeV, based on space charge tracking simulations being bench-marked with measurements in the present machine. The driving mechanism for the final emittances is space charge related, while the details of the injection process remains in the shadow.

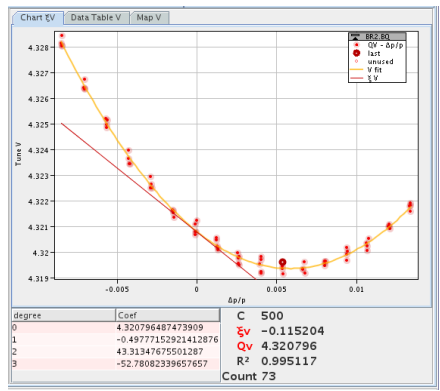

Figure 12: Screenshot of the Chromaticity measurement application in the Control Room.

The PS Booster can count on a series of mitigation measurements and in the paper we have started exploring the impact of the multipole correctors that are available but currently only used empirically. After completing the analysis of the half integer problem we are now moving our focus to the non-linear terms. To do so we investigated the impact of uncorrected sextupolar errors on the brightness curve. Moreover we have measured non-linear chromaticity in order to improve our non-linear model. In the future we expect help from turn-by-turn position measurements that most likely will open the way to more specific measurements.

ACKNOWLEDGMENT

The authors would like to thank J. Abelleira, C. Bracco, A. Garcia, G. P. Di Giovanni, B. Mikulec, G. Rumolo for useful input and discussions.

REFERENCES

[1] G. Rumolo *et al.*, "Expected Performance in the Injectors at 25ns without and with Linac4", in Review of LHC and Injector Upgrade Plans Workshop, 29-31 October 2013, Archamps, France.

[2] E. Benedetto *et al.*, "Transverse Emittance Preservation Studies for the CERN PS Booster Upgrade", in *Proc. HB2014*, East Lansing, MI, USA, 10-14 November 2014, paper THO4LR05, pp 428-432.

[3] E. Benedetto *et al.*, "CERN PS Booster Upgrade and LHC Beams Emittance", in *Proc. IPAC'15*, Richmond, VA, USA, 2015, paper THPF088, pp. 3897-3900.

[4] J.D. Galambos *et al.*, ORBIT User Manual Version 1.10, 2011.

[5] E. Forest *et al.*, "Synopsis of the PTC and ORBIT Integration", KEK. Internal Report (A), 4 November 2007.

[6] B. Mikulec, "Performance reach of LHC beams", in LIU Beam Studies Review, 28 August 2012, CERN, Geneva, CH, http://indico.cern.ch/event/200692/

[7] K. Hanke, *in Proc*. Chamonix 2016

[8] E. Benedetto *et al.*, "Detailed Magnetic Model Simulations of the H- Injection Chicane Magnets for the

ISBN 978-3-95450-185-4

CERN PS Booster Upgrade, Including Eddy Currents, and Influence on Beam Dynamics", in *Proc. IPAC'14*, Dresden, Germany, 2014, paper TUPRI027, pp. 1618-1620

[9] V. Forte *et al*., "3D Emittances Tailoring Techniques and Optimization with Space Charge for the Future CERN PS Booster Operations with Linac4", in *Proc. IPAC'16*, Busan, Korea, 2016, paper MOPOR025, pp. 660-663.

[10] B. Mikulec *et al*., "Tune Spread Studies at Injection Energies for the CERN Proton Synchrotron Booster", in *Proc. HB2012*, 17-21 September 2012, Beijing, China, paper MOP249, pp. 175-179.

[11] C. Bracco *et al*., "LHC Injectors Upgrade for the HL-LHC", in *Proc. HB'16*, Malmo, Sweden, July 2016, paper TUPM4X01, this conference.

[12] M. Cieslak-Kowalska *et al.,* "Evolution of High Intensity Beams in the CERN PS Booster after H- Injection and Phase Space Painting", in *Proc. IPAC'16*, Busan, Korea, 2016, paper MOPOR024, pp. 656-659

[13] J. Abelleira, CERN engineering note, EDMS number 1537199 (2015).

[14] V. Forte *et al*., "The CERN PS Booster Space Charge Simulations with a Realistic Model for Alignment and Field Errors", in *Proc. IPAC'14*, Dresden, Germany, 2014, paper TUPRI029, pp. 1624-1626.

[15] G. Franchetti *et al*., PRST-AB 13, 114203 (2010)

[16] V. Forte, Ph.D. thesis - 2016. Université Blaise Pascal, Clermont-Ferrand, France

[17] M. McAteer *et al*., "Simulation and Observation of Driven Beam Oscillations with Space Charge in the CERN PS Booster", in *Proc. IPAC'14*, Dresden, Germany, 2014, paper THPRO081, pp. 3073-3075.

ISBN 978-3-95450-185-4

STRIPLINE BEAM POSITION MONITORS WITH IMPROVED FREQUENCY RESPONSE AND THEIR COUPLING IMPEDANCES

Y. Shobuda, J-PARC Center, JAEA, Ibaraki, JAPAN,
Y. H. Chin, K. Takata, T. Toyama, KEK, Tsukuba, Ibaraki, JAPAN
K. G. Nakamura, Kyoto University, Kyoto, JAPAN

Abstract

In J-PARC MR, there is a concern that electron cloud instabilities may appear and limit the beam current at future higher power operations. For the case, we have developed a wider-band beam position monitor by deforming the electrode shapes. The modification of the electrode can be done without significant enhancement of the beam coupling impedance. For typical electrode shapes, we show the coupling impedances as well as the frequency responses of the electrodes.

INTRODUCTION

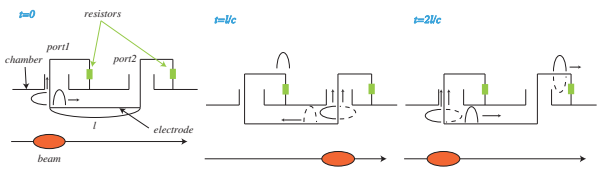

Figure 1: Flow chart of the induced pulses at a BPM.

Stripline beam position monitors (BPMs) are widely used for measurements of beam position signals in study of beam instabilities. The electrode is placed inside of the chamber. Figure 1 schematically shows the principle of the working of the BPMs.

Based on two-dimensional theory, the frequency response of the BPM is analytically given by the transfer function $F(\omega)$ as [1]

$$F(\omega) = i\omega \int_0^{\frac{2l}{c}} \frac{1}{2} k(\frac{ct}{2}) e^{-i\omega t} dt = \frac{i\omega}{c} \int_0^l k(z) e^{-i\frac{2\omega}{c}z} dz, \quad (1)$$

where i is imaginary unit, ω is angular frequency, $k(z)$ is the coupling function to the fields at point z, l is the electrode length and the velocity of the beam is approximated by the speed of light c.

For the electrode in a shape of rectangle, the transfer function is calculated as

$$F(\omega) = k_0 \frac{(1 - e^{-i\omega\frac{2l}{c}})}{2}, \quad (2)$$

by extracting the z-dependence from the coupling function $k(z) = k_0$. The distinctive feature of this function is that the absolute value has sharp notches with its interval: $f_n = nc/2l$, where n is integer (see the red lines in Fig.2).

The origin of these notches can be qualitatively understood as follows. As Fig.1 shows, when a beam arrives at the front-end of the electrode ($t = 0$), the beam excites two currents with opposite polarities. One current flows to the downstream with the beam, while the other does to the upstream side and enters the port1.

When the beam reaches the back-end of the electrode ($t = l/c$), new currents with opposite polarities (the dashed-pulse) are additionally excited there. The total signal to the port 2 is cancelled by superposing the currents (the solid and the dashed pulses at $t = l/c$).

When successive pulse trains come with their interval $2l/c$, the subsequent pulse (the solid pulse at $2l/c$) compensates the prior signal (the dashed pulse) crated by the predecessor pulse as in the figure at $t = 2l/c$. Finally, all beam-induced signals with the frequency : f_n cannot be detected at all outside the chamber.

THE IDEAL ELECTRODE SHAPE

To avoid the demerit of the rectangular electrode, no pair of image currents should be generated by the leaving pulse. It is enabled by narrowing the electrode toward downstream and carefully reclining the electrode to the chamber, to preserve the characteristic impedance Z_c of the electrode.

In 1970's Linnecar suggested an exponential electrode for better frequency characteristic [2]. When the coupling function $k(z)$ is given by

$$k(z) = k_0 e^{-\frac{az}{l}}, \quad (3)$$

the transfer function $F(\omega)$ is calculated as

$$F(\omega) = k_0 \frac{i\omega l(1 - e^{-a - i\frac{2\omega l}{c}})}{c(a + \frac{i2\omega l}{c})}, \quad (4)$$

where a is a positive dimensionless parameter defining the degree of the exponential tapering of the electrode. The blues line in the left figure of Fig.2 shows the transfer functions for the Linnecar's exponential electrode with $a = 2.63$ and $l = 190$ mm. We can find that the notches appearing in the red line (rectangle electrode) diminish in the blue line, while Linnecar's exponential electrode theoretically keeps oscillating at high frequency as

$$F(\omega) \sim \frac{k_0}{2}(1 - e^{-a - i\frac{2\omega l}{c}}). \quad (5)$$

As Eq.(1) shows, the transfer function $F(\omega)$ can be interpreted as the Fourier transform of the step function, which

ISBN 978-3-95450-185-4

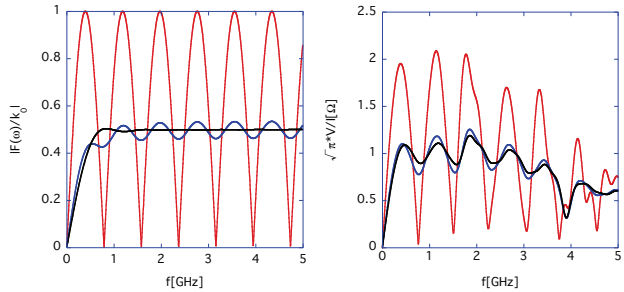

Figure 2: The theoretical (left) and the simulation (right) results of the transfer function $|F(\omega)|$.

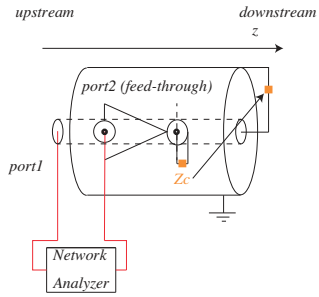

Figure 3: A schematic of the setup for the measurement of the transfer function.

exists only between zero to l, where the coupling function $k(z)$ plays a window function role [3]. From a mathematical point of view, the optimization of the electrode shapes is simplified to the issue how to choose the window function. Finally, we find that a polynomial function [4] :

$$k(z) = k_0 \frac{(l-z)^\sigma}{l^\sigma}, \tag{6}$$

with $\sigma = 2.63$, is the best choice for the purpose. The transfer function is given by

$$F(\omega) = -\frac{k_0}{2} \frac{e^{-i\frac{2\omega l}{c}}(\Gamma[1+\sigma] - \Gamma[1+\sigma, -i\frac{2\omega l}{c}])}{(-i\frac{2\omega l}{c})^\sigma}, \tag{7}$$

where $\Gamma(z)$ and $\Gamma(a,z)$ are the Γ- and the incomplete Γ-functions, respectively. Contrary to the exponential case, the formula approximated by

$$F(\omega) \sim \frac{k_0}{2}(1 - \frac{e^{i(\frac{\pi\sigma}{2} - \frac{2\omega l}{c})}\Gamma[1+\sigma]}{(\frac{2\omega l}{c})^\sigma}), \tag{8}$$

damps and approaches $k_0/2$ at high frequency. Overall behavior of the result is shown in the black line in the left figure of Fig.2. The frequency characteristic of the transfer function becomes much flatter for the polynomial function.

The simulation is performed by CST Studio [5]. In this simulation, four electrodes are placed 90 degree apart in the chamber with $a_1 = 65$ mm radius and 5 mm thickness. The respective electrodes are sophisticatedly reclined in order that Z_c of the electrode preserves 50 Ω along the electrode. In the simulations, the transfer function is obtained by dividing the Fourier transform of the beam-induced voltage at the upstream port by that of the beam current. The blue, the red and the black lines in the right figure of Fig.2 show the results for the exponential, the rectangular and the polynomial electrodes, respectively. As theoretically expected, the amplitude fluctuation is most suppressed in the polynomial results.

The transfer function $F(\omega)$ is obtained by the measurement of S_{21} in the setup shown in Fig.3. The downstream side of the chamber is terminated with the matched resistor. One port of the Network Analyzer (NA) is connected to the port at the entrance of the chamber, while the other port is connected to the wider end of the electrode.

In J-PARC MR [6], exponential electrodes with $l = 306$ mm are used for the intra-bunch feed-back system. Since it was difficult to bend them exponentially as required for a good impedance matching, we kept them straight as a flat plate.

The left figure of Fig.4 shows the measurement results of S_{21} for the exponential electrode. While the peak to peak modulation is about 30 % below 1 GHz, it is drastically worsen at high frequency. The right figure of Fig.4 shows the simulation results with $l = 280$ mm. The blue line shows the case that the electrode is put straight as a flat plate, while the red line shows the one that the electrode is precisely reclined to preserve Z_c. The peak to peak modulation on the blue line is worsen to about 30 % below 1 GHz, apart from about 23 % on the red line.

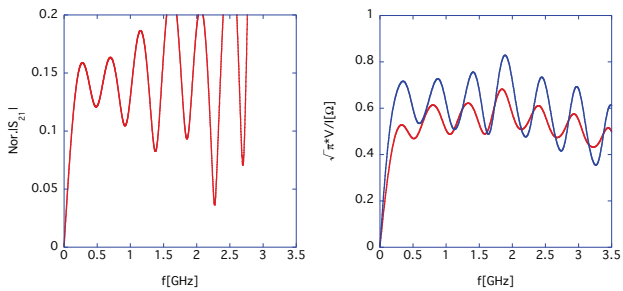

Figure 4: Measured S_{21} (left) for the exponential electrode, and simulation results (right).

From these results, the precise bent of the electrode is a key issue to make maximum use of the merit of electrode shapes, which is quite difficult in practice. Consequently, we start with a simple shape and gradually increase its complexity to improve the frequency performance.

THE TRANSFER FUNCTION OF ELECTRODES TAPERED BY LINEAR FUNCTIONS

The simplest shape next to the rectangle electrode is a triangle. It requires no sophisticatedly bending to attain a good impedance matching.

The coupling function of the triangle electrode is given

ISBN 978-3-95450-185-4

by [7]

$$k_{triangle}(z) = k_0 \frac{(l-z)}{l}. \quad (9)$$

Accordingly, the transfer function is calculated as

$$F(\omega) = \frac{k_0}{2} \frac{i(1 - i\frac{2\omega l}{c} - e^{-i\frac{2\omega l}{c}})}{\frac{2\omega l}{c}}. \quad (10)$$

The red line in the left figure of Fig.5 shows the theoretical result of the triangle electrode with $l = 280$ mm. The blue line shows the result for the exponential one, for reference. Except the large overshoot at low frequency, the triangle electrode has a better frequency characteristic compared with that for the exponential electrode.

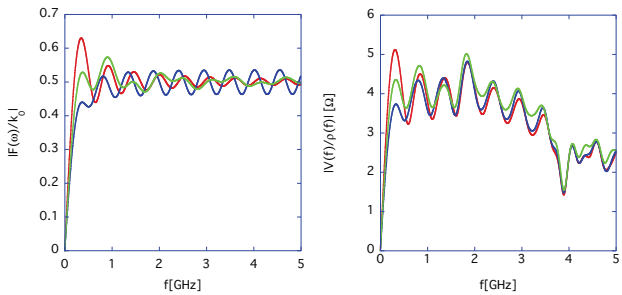

Figure 5: The theoretical (left) and the simulation (right) results of the transfer functions.

By introducing one more complexity in the shape, this overshoot effect can be mitigated. Let us replace the long, straight sides of the triangle by a three-point polyline. This deformation transforms the triangle to a concave pentagon. The concave pentagon electrode needs to be bent only once at the middle point of the polylines for a good impedance matching. Thus, its fabrication and setup remain to be easy.

The coupling function is given by

$$k_{pentagon}(z) = \begin{cases} k_0(1 - \frac{(1-y_0)z}{x_0}), \text{for } z \le x_0, \\ -k_0 \frac{y_0(z-l)}{(l-x_0)}, \text{for } z > x_0, \end{cases} \quad (11)$$

where x_0 and y_0 specify a middle point location. Theoretically, the optimal position of the middle point provides

$$x_0 = \frac{8.5}{20} l, y_0 = \frac{7.5}{20}. \quad (12)$$

The theoretical transfer function of the concave pentagon electrode is shown by the green line in the left figure of Fig.5. The simulation results for all shapes of electrode are shown in the right figure of Fig.5. The overshooting effect in the triangle electrode is suppressed in the concave pentagon electrode. Moreover, the frequency characteristic of the concave pentagon (green) is surprisingly similar to that of the exponential electrode (blue).

WORKING OF THE APRON PLATES

The signal strength in the simulation result (the right figure of Fig.5) starts to be declined beyond the first transverse magnetic (TM) waveguide mode:

$$f_c = \frac{0.114}{a_1 (= 65\text{mm})} (\simeq 1.76\text{GHz}). \quad (13)$$

This is due to a large gap between the chamber wall and the upstream end of the electrode. Some of the image current running on the chamber surface before the electrode jump to the electrode over this gap as a displacement current. For short wavelength modes, this gap prevents a smooth flow of the displacement current and thus the image current running on the electrode loses some parts of high frequency components.

By attaching a plate perpendicular to the upstream edge of the plate (See the left picture of Fig.6. From hereon, we call this plate "an apron".), this gap for the image current can be reduced. The right figure of Fig.6 shows the simulation results with the apron for the triangle (red) electrode, the exponential one (blue) and the concave pentagon one (green). Comparing that with the right figure in Fig.5, we find that the signal strength is maintained up to the second TM mode :

$$f_c = \frac{0.262}{a_1} (\simeq 4\text{GHz for } a_1 = 65 \text{ mm}). \quad (14)$$

The apron plate is effective to sustain a signal strength up to higher frequency as a chamber has a smaller radius [7].

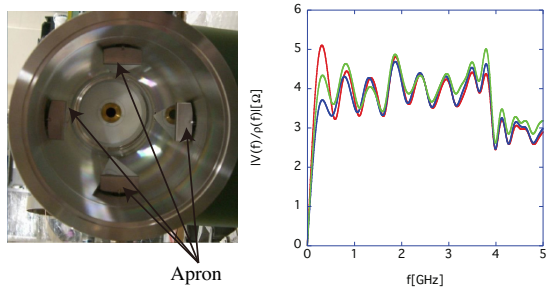

Figure 6: A photo of the apron on the triangle electrodes (left), and the simulation results (right) for $l = 280$ mm.

MEASUREMENTS OF THE TRANSFER FUNCTIONS

Measurements are done by preparing for four types of electrodes (the triangle and the concave pentagon electrodes with and without the apron.). A schematic picture of the setup is shown in Fig.3. The inner conductor is installed in the chambers with 134 ϕ, where the 306 mm long four electrodes are housed. The inner conductor and the chambers make a coaxial structure with $Z_c = 50\ \Omega$. The chamber is sandwiched between two conical tapered coaxial section to suppress reflection effects while keeping a constant 50 Ω characteristic impedance for the NA operation.

The transmission coefficient S_{21} is measured with 4-port Agilent Technologies ENA Series E5071C. The calibration is done by 2-port electric calibration module 85092b [8].

ISBN 978-3-95450-185-4

The measurement results are shown in Fig.7. The red and the green lines show the results for the triangle and the concave electrodes, respectively. The left and the right figures show the results without and with the apron, respectively. The overshooting effect appearing in the red lines diminishes in the green lines. As the right figure shows, the apron is effective to suppress the signal fluctuations.

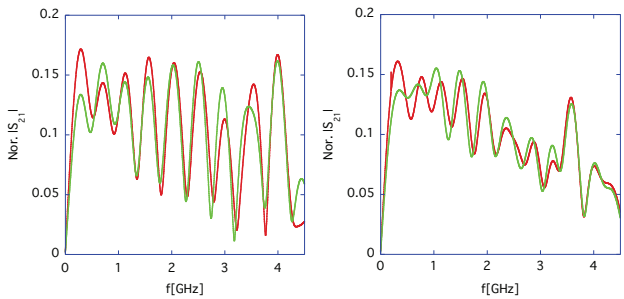

Figure 7: Measured S_{21} without (left) and with (right) the apron.

We measured the impedance distribution along the electrode by time domain reflectometry method, where the down stream port on the electrodes are terminated by 50 Ω resistor, and the upstream port is connected to a Tektronix DSA8200 Sampling Oscilloscope [9]. The measurement results for the triangle (left) and the concave pentagon(right) electrodes are shown in Fig.8. To the goal of the excellent impedance matching, more significant efforts are worthy to be made in the fabrication process. We expect that the gradual decline of the signal strength in the right figure of Fig.7 will be recovered by improving the impedance mismatch along the electrodes.

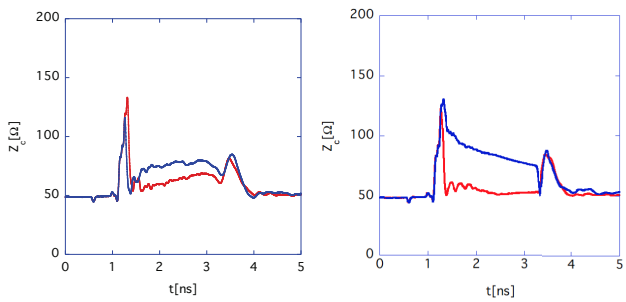

Figure 8: Measurement results of the impedance distribution along the triangle (left) and the concave pentagon (right) electrodes with (blue) and without (red) the apron.

IMPEDANCES OF THE ELECTRODES

Now, let us investigate the beam-coupling impedances of the electrodes. The longitudinal impedance Z_L is measured by connecting the second port of the NA to the exit of the chambers both housing the electrodes and housing no electrode (as a reference pipe). Both ends of all electrodes are terminated by the matched resistors.

The measured S_{21} are converted to Z_L by using the standard log-formula [10]:

$$Z_L = -2Z_c \log \frac{S_{21}}{S_{21}^{(ref)}}, \tag{15}$$

where S_{21} and $S_{21}^{(ref)}$ are the transmission coefficients for the device under test and for the reference pipe, respectively.

At first, we theoretically derive the formula of Z_L based on the transmission line model. We assume port 1 and 2 are located at $z = 0$ and $z = l$, respectively. Equations are given by

$$\frac{dV_1}{dz} = -i\omega L(z) I_1 - i\omega M(z) I_{inner}, \tag{16}$$

$$\frac{dI_1}{dz} = -i\omega \frac{L_{inner}}{c^2(L(z)L_{inner} - M(z)^2)} V_1 + i\omega \frac{M(z)}{c^2(L(z)L_{inner} - M^2(z))} V_{inner}, \tag{17}$$

$$\frac{dV_{inner}}{dz} = -i\omega L_{inner} I_{inner} - i\omega M(z) I_1, \tag{18}$$

$$\frac{dI_{inner}}{dz} = i\omega \frac{M(z)}{c^2(L(z)L_{inner} - M(z)^2)} V_1 - i\omega \frac{L(z)}{c^2(L(z)L_{inner} - M(z)^2)} V_{inner}, \tag{19}$$

where $L(z)$, V_1 and I_1 are the self-inductance, the voltage and the current of the electrode, respectively, L_{inner}, V_{inner} and I_{inner} are the self-inductance, the voltage and the current of the inner conductor, respectively, and $M(z)$ is the mutual inductance between the inner conductor and the electrode.

It is quite difficult to solve Eqs.(16)-(19) exactly. Let us make the approximations to solve them : the coupling between the inner conductor and the electrode is weak ($M^2 \ll LL_{inner}$), and regard M as a perturbation and solve them iteratively. Finally, the transmission coefficient S_{21} is approximately calculated, and Z_L is given by

$$Z_L = \frac{2n_{NE}\omega^2}{Z_c} \int_0^l dz'' \int_0^{z''} dz' M(z') M(z'') e^{i\frac{2\omega}{c}(z'-z'')}, \tag{20}$$

where n_{NE} the number of the electrodes in the chamber (In this description, the negative value of the imaginary part corresponds to be inductive impedances. For comparison with a simulation result, the sign is made opposite in the red dashed line of Fig.9).

For the exponential electrode, the mutual inductance is approximated as

$$M(z) \simeq \frac{Z_0}{2\pi c} \log[\frac{a_1}{a_1 - \Delta e^{-\frac{a}{l}z}}], \tag{21}$$

where Δ is the distance between the electrode and the chamber at $z = 0$. The difference of the electrode shapes

ISBN 978-3-95450-185-4

is confined in the z-dependence of the logarithmic function, by which we expect that the impedances do not significantly depend on the electrode shapes.

The theoretical (red) and the simulation (blue) results for the exponential electrode are shown in the left figure of Fig.9. The theoretical result shows that it is inductive, and that the wake function behaves like the δ'-function, as shown by the simulation result in the right figure.

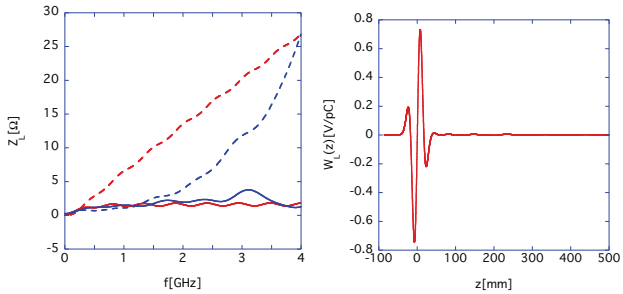

Figure 9: The theoretical (red) and the simulation (blue) results of Z_L (left) for the exponential electrode ($a = 2.63$, $l = 280$ mm), and the simulation result of the wake function (right). The solid and the dot lines show the real and the imaginary parts of the impedance.

Here, let us investigate the impedance dependence on the electrode shapes. The scaled picture of the simulation results below 1GHz are shown in Fig.10. The Z_L is shown in the upper figure. The Z_T are shown in the lower figure, as well. The left and the right figures show the results without and with the apron, respectively. The red, the blue and the green lines show the results for the triangle, the exponential and the concave pentagon electrodes, respectively. The amount of the value of the impedances for all shapes is the same order of magnitudes, as theoretically expected. Moreover, the simulation results suggest that the impedances do not strongly depend on the existence of the aprons.

The measurement results of Z_L are shown in Fig.11. The left and the right figures show the results without and with the apron, respectively. The impedances with the aprons are enhanced compared to those without the aprons within a factor or two, because the electrodes with the aprons are more apart from the chamber wall than those without them, violating impedance-matching (refer to Fig.8). Figure 10 suggests that this impedance enhancement should be reduced by improving the impedance-mismatch along the electrodes.

SUMMARY

The high frequency performance of the exponential electrode in J-PARC MR (Fig.4) can be improved by replacing it with the concave pentagon electrode with the apron (Fig.7). The apron plate on the wider end of the electrode helps to maintain the signal strength up to the second TM-mode. The merit of the concave pentagon with the apron is that, its fabrication is easier than that of the exponential

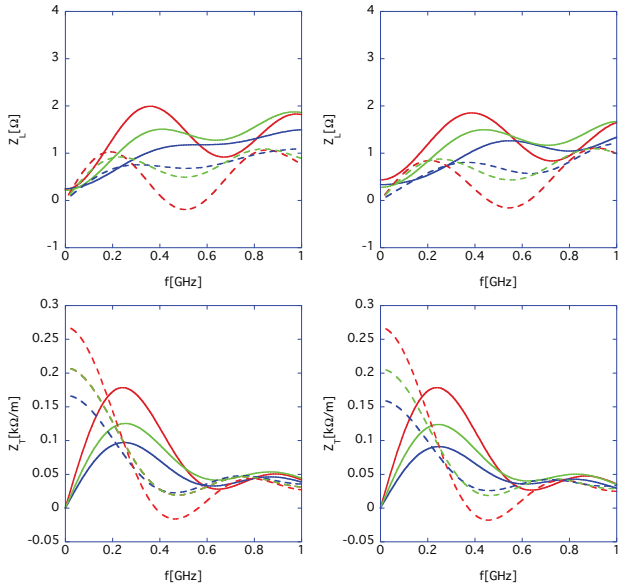

Figure 10: The simulation results of Z_L (upper) and Z_T (lower) without (left) and with (right) the apron. The solid and the dashed lines show the real and the imaginary parts of the impedances, respectively.

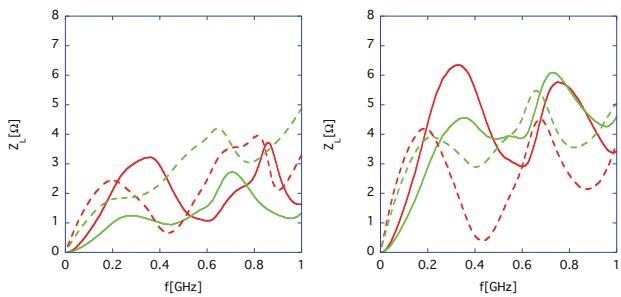

Figure 11: Measured Z_L for the triangle (red) and the concave (green) electrodes, respectively. The solid and the dashed lines show the real and the imaginary parts of the impedances, respectively.

electrode.

The simulation results suggest that the impedances do not significantly depend on the electrode shapes, and whether the aprons are attached on the electrodes. We expect that the significant efforts to improve the impedance-mismatch along the electrodes will realize the better frequency performance as well as the lower coupling impedances.

ACKNOWLEDGMENTS

This work was partially supported by MEXT KAKENHI Grant No. 25105002.

ISBN 978-3-95450-185-4

REFERENCES

[1] B. M. Oliver, Proc. I.R.E., Vol 42, No. 11, 1686, (1954)

[2] T. Linnecar, CERN-SPS-ARF-SPS/78/17, CERN, (1978)

[3] F. G. Harris, Proceedings of the IEEE, Vol. 66, 51, (1978).

[4] Y. Shobuda and Y. H. Chin, PRST AB 17, 092801, (2014)

[5] CST STUDIO SUITE, http://www.cst.com

[6] http://j-parc.jp/index-e.html

[7] Y. Shobuda *et al*, Phys. Rev. AB 19, 021003, (2016)

[8] $http://www.home.agilent.com/$

[9] $http://jp.tek.com/$

[10] *Handbook of Accelerator Physics and Engineering*, edt by A. Chao *et al*, (Singapore, World Scientific, 2013)

ISBN 978-3-95450-185-4

BEAM COMMISSIONING OF C-ADS LINAC INSTRUMENTATION*

Y.F. Sui#, J.S. Cao, H.Z. Ma, L.D. Yu, Y. Zhao, J. He, X.Y. Zhao, S.J. Wei, Q. Ye, J.H. Yue, L. Wang
Key Laboratory of Particle Acceleration Physics and Technology, IHEP, Chinese Academy of Sciences, Beijing, 100049, China

Abstract

The China Accelerator Driven Subcritical system (C-ADS) linac, which is composed of an ECR ion source, a low energy beam transport line (LEBT), a radio frequency quadrupole accelerator (RFQ), a medium energy beam transport line (MEBT) and cryomodules with SRF cavities to boost the energy up to 10 MeV. The injector linac will be equipped with beam diagnostics to measure the beam position, the transverse profile and emittance, the beam phase as well as beam current and beam losses. Though many are conventional design, they can provide efficient operation of drive linac. This paper gives an overview and detail in beam commissioning of C-ADS linac beam instrumentation.

INTRODUCTION

The Chinese ADS project is aimed to solve the nuclear waste problem and the resource problem for nuclear power plants in China. With its long-term plan lasting until 2030th, the project will be carried out in 3 phases: Phase I of R&D facility, Phase II of experiment facility and Phase III of industry demonstration facility. The driver linac of the CADS consists of two injectors to ensure its high reliability. Each of the two injectors will be a hot-spare of the other. Although the two injectors that are installed in the final tunnel will be identical, two different design schemes, named injector I and II respectively are being pursued in parallel by the Institute of High Energy of Physics (IHEP) and the Institute of Modern Physics (IMP) [1]. This paper aims to introduce the instrumentation beam commissioning of the injector I. The Injector I ion source is based on ECR technology. The beam will be extracted with an energy of 35 keV. The ion source will be followed by a Low Energy Beam Transportline (LEBT), which consists of 2 solenoids, a fast chopper system and a set of beam diagnostics including CTs and faraday cup. A Radio Frequency Quadrupole (RFQ) will accelerate the beam up to 3.2 MeV and will be followed by the first Medium Energy Beam Transport line (MEBT1), fully instrumented and also equipped. The next section is two cryogenic modules named CM1 and CM2 with seven cold beam position monitors in each, which accelerate beam up to about 10 MeV. The last section is the second Medium Energy Beam Transport line (MEBT2). The drift tubes between magnets provide the gap for diagnostics.

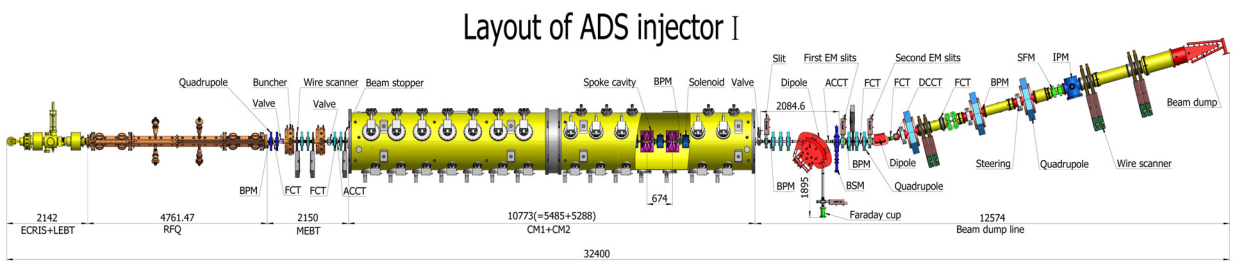

Figure 1: Beam instrumentation layout in C-ADS linac.

INSTRUMENTATION OF INJECTOR I

The injector I linac is equipped with beam diagnostics to measure the beam position, the transverse profile, the beam emittace, the beam energy as well as beam current and beam losses. This will provide efficient operation of drive linac and ensure the beam loss at a low level. A list of the different type of monitors using in the injector I linac is presented in Table 1.

According the geometry of pick-ups, three type of BPMs are hired to measure the beam position in the injector I linac. There are 25 BPMs of which 14 is cold BPM installed in two cryostats. Measurement of the particle beam position of CADS injector I proton linac is an essential part of beam diagnostics. The BPMs could provide information about both the center of mass position and the beam phase that can be used to detect energy on line by using the time-of-flight (TOF) method [2]. The sum signal of BPM could be used for beam loss measurement which can be detected by a Differential Beam Current Monitor (DBCM) measuring beam current difference at two locations along the accelerator, especially for the beam energy is lower than 10MeV [3].

For the beam profile monitor in injector I, four wire scanners using solid material as a probe inside the beam to sample the charge at different location is installed in MEBT1 and the start of MEBT2. Three pairs of wire scanner is installed downstream of the first SFM (step-like field magnet). For the beam profile is expanded quickly, one wire scanner can only measure one direction beam dimension. Although the double slits is for emittace

*Work supported by China ADS Project (XDA03020000) and the National Natural Science Foundation of China (NO. 11205172, NO. 11475204)
#syf@ihep.ac.cn

ISBN 978-3-95450-185-4

measuring specially, the wire scanners are also used for check the result with Q-magnet scan method for checking the result of double slits. Two non-invasive beam profile measurement methods were developed for the CADS main Linac in which beam is very intensive. One is an IPM (ionization beam profile monitor), and the other is electron scanner.

Table 1: List of Beam Instrumentation in C-ADS Linac

Device	Accuracy	Resolution	Quantity
Beam position monitor	±100um	30 um	25
Wire scanner	±0.5mm	50 um	4+3
Beam emittace unit	10%	-	2
Beam current monitor	1.5%	0.01mA	5
Beam loss monitor	1%	-	8
Beam energy monitor	±1deg	0.5deg	3
IPM	1mm	200 um	1
Electron scanner	1mm	300um	1

Kinds of Current transformers (CTs) are used measure the beam current. Three different kinds of CTs are used in the linac for different purpose. FCTs are for checking bunch shape with fast rise time and measuring the beam phase by using the time-of-flight (TOF) method. ACCTs are used for beam transmission monitor and beam pulse current. NPCT measures beam current in CW mode.

A double-slits emittance mertre is equipped to measure beam emittance in both horizontal and vertical. The first slits are made of tungsten with a cooling system. To ensure the slits safety, the heat analysis is carried out and the result is shown in Fig.2

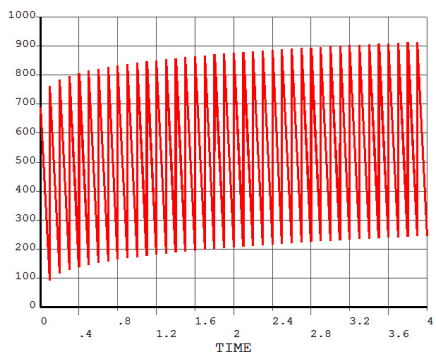

Figure 2: The time (x-axis in unit second) versus temperature(y-axis in unit degree) of first slit in beam, with the beam duty factor 0.1% and 10Hz pulse repetition rate.

The beam loss monitor is the most important diagnostic system for proton linac. The purpose of the beam loss monitor is to avoid the accelerator damage and excessive machine activation by beam loss. Ionization chambers will be the main beam loss detector. However, at low energies, ionization chambers are not effective to detect beam loss due to the self-shielding from the copper cavities and the low energy particle can't penetrate the shielding. The differential current measurement between two beam position monitor will be the primary input to the fast machine interlock system. Also the ports signal of beam position pick-ups are used for the fast machine interlock system if the voltage exceeds some thresholds [4].

BEAM COMMISSIONING

The injector I beam commissioning is including five stages. The first stage is ion source and LEBT. RFQ and MEBT1 tuning is the second stage, the third stage is test cryomodule commissioning. Each formal cryomodule beam test is one stage. This paper presents the RFQ and CM1 beam test result and the beam parameters of the RFQ.

RFQ and MEBT1 Tuning

In MEBTI, there are three wire scanners, two FCTs, six BPMs, and an ACCT, the location of beam instrumentations in MEBT1 are shown in Fig.1 .The RFQ commissioning starts from May 15th, 2014. After about two months conditioning, 99.97% RF duty factor was reached with pulse width of 12.5ms, repetition frequency of 79.975Hz and 250kW in cavity power [5]. In the period of RFQ commissioning, the emittance of RFQ is obtained by double slits shown in Fig.3. Three wire scanners installed in MEBT1 with two Q-magnets between each other. The quad-scan and the multi wire scanners emittance measurement method are also used to check the result of double slits. Also the beam energy measured with the FCTs is reported. The transmission is based on the proportion of ACCT at entrance to the ACCT at the exit. The transmission reached 90% with beam shooting through the RFQ with 90% duty factor. The beam position is monitored, and finished the beam based alignment(BBA) to determine the offset of BPM pick-ups.

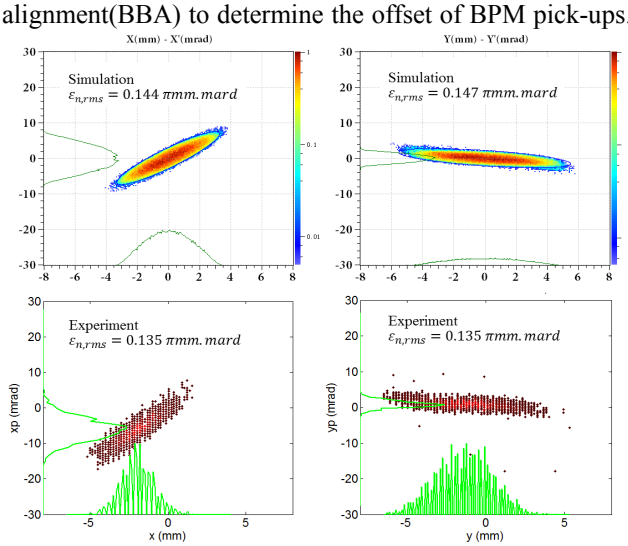

Figure 3: The measured beam emittance of RFQ (bottom) with double slits versus the simulation result (upper).

ISBN 978-3-95450-185-4

CM1 Beam Commissioning

The SC (Super Conduct) section including two cryomodules, named CM1 and CM2, which boost the proton from 3.2MeV to 10Mev.The first CM was installed in the tunnel after the Test cryomodule was commissioned. The fisrt CM houses 7 spoke cavities, 7 solenoids and 7 cold BPM. The cold BPMs are used to scan beam phase and determine cavity phase in CM1 tuning. Beam based phase scan is the most simple and effective method for measuring cavity phase and amplitude. For the first cavity phase measurement, we detuned the second cavity and use the two following BPMs to measure energy after calibrating the offset between the BPMs [6]. The phase scan result is listed in Fig.4. The beam energy is checked by energy analysis station including a dipole magnet, two slits and an end-type faraday cup. Also the beam emittance of CM1 is shown in Fig.5 measured by double slits emittance meter.

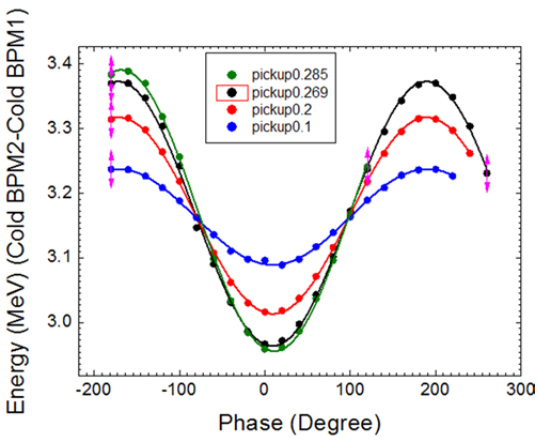

Figure 4: The beam energy versus SRF cavity phase with different amplitude (in different color) in NO.1 cavity of CM1.

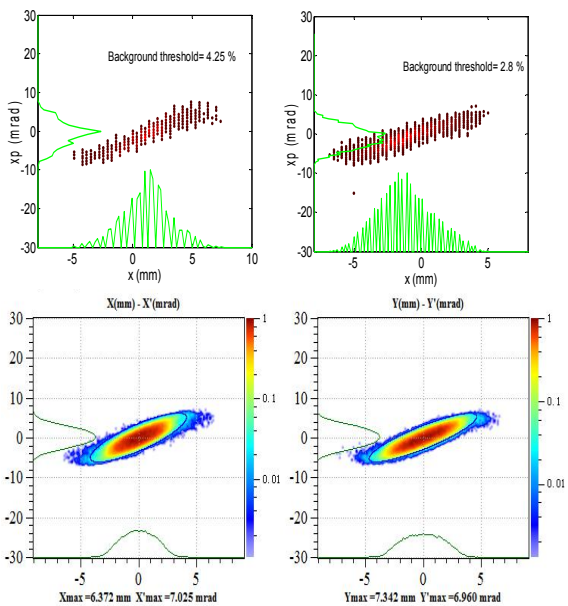

Figure 5: The measured beam emittance of CM1 (upper) with double slits versus the simulation result (bottom).

CONCLUSION

The beam instrumentation system works well in beam commissioning of injector and is very helpful in beam tuning. The required parameters of beam are all acquired for the injector tuning. For the important beam parameters, such as beam energy, beam emittance, beam current, the result are checked with at least two methods. Cold BPMs are carefully test and works well in cryostat. In the SRF cavities tuning, the cold BPMs play important roles in determining the phase of cavities. As an intensity accelerator, Fast Protection System (FPS) should be developed to prevent permanent damage to the machine. For the beam diagnostics, the beam position signal and the beam loss signal are feed to FPS as the inputs. In the future the BPM sum signal will be used as the Differential Beam Current Monitor and set as an input to FPS.

REFERENCES

[1] Jingyu Tang and Zhihui Li (ed.), "Conceptual Physics Design of the C-ADS Accelerators", IHEP-CADS Report/2012-01E.

[2] Y. F. Sui *et al.*, "Design and Simulation of Beam Position Monitor for the CADS Injector I Proton Linac", in *Proc. IBIC'13*, Oxford, UK, Sept. 2013, paper WEPC17.

[3] A. Aleksandrov, "Beam Instrumentation for High Power Hadron Beams", in Proc. NA-PAC'13, Pasadena, CA, USA, paper TUYBA1.

[4] Y. F. Sui *et al.*, "Overview of Beam Instrumentation for the CADS Injector I Proton Linac", in *Proc. IPAC'15*, Richmond, VA, USA, May 2015, paper MOAB2.

[5] Y. Yan *et al.*, "Commissioning of the China-ADS Injector-I Testing Facility", in *Proc. IPAC'16*, Busan, Korea, May 2016, paper WEOBA02.

[6] C. Meng *et al.*, "Superconducting Cavity Phase and Amplitude Measurement in Low Energy Accelerating Section", in Proc. IPAC'16, Busan, Korea, May 2016, paper MOPOY030.

ISBN 978-3-95450-185-4

MEASUREMENTS OF BEAM PULSE INDUCED MECHANICAL STRAIN INSIDE THE SNS* TARGET MODULE

W. Blokland†, M. Dayton, Y. Liu, B. Riemer, M. Wendel, D. Winder, Oak Ridge National Laboratory, Oak Ridge, USA

Abstract

Because several of the SNS targets have had a shorter lifetime than desired, a new target has been instrumented with strain sensors to further our understanding of the proton beam's mechanical impact. The high radiation and electrically noisy environment led us to pick multi-mode fiber optical strain sensors over other types of strain sensors. Special care was taken to minimize the impact of the sensors on the target's lifetime. We also placed accelerometers outside the target to try correlating the outside measurements with the internal measurements. Remote manipulators performed the final part of the installation, as even residual radiation is too high for humans to come close to the target's final location. The initial set of optical sensors on the first instrumented target lasted just long enough to give us measurements from different proton beam intensities. A second set of more rad-hard sensors, installed in the following target, lasted much longer, to give us considerably more data. We are developing our own rad-hard, single-mode fiber optic sensors. This paper describes the design, installation, data-acquisition system, the results of the strain sensors, and future plans.

INTRODUCTION

The Spallation Neutron Source uses neutron scattering to study the structure and properties of materials and macromolecular and biological systems. Proton beam pulses of less than 1 μs long, up to 24 μC, hit a stainless steel vessel filled with mercury at 60 Hz for a total power of up to 1.4 MW to generate the neutrons. The beam creates an initial pressure field of up to ~34 MPa that leads to tension and cavitation of the mercury as the pressure wave interacts with the target vessel.

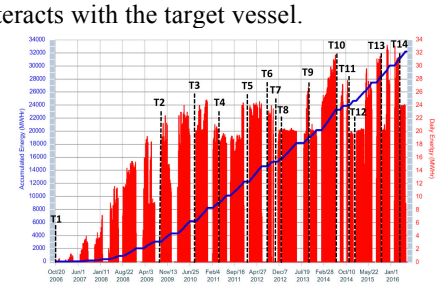

Figure 1: The SNS production runs.

The reliability of the target vessel is critical for minimizing interruptions to the operation schedule. It was initially thought that the lifetime of a target would be limited by the erosion of the target wall, due to the cavitation of the mercury during the proton beam impact, and by reaching the SNS administrative radiation damage limit of the vessel's steel at about 5000 MWHrs.

However, at higher proton beam powers, we did start seeing target failures before the radiation damage limit. Four out of seven premature target failures were due to weld failures from fatigue, while two were due to cavitation erosion, and one could not be determined. Figure 1 shows the quick succession of installation of targets 10, 11, and 12.

We decided to measure the strain on the actual target vessel wall to better understand the limitations to the target lifetime: Do the pulses induce a higher strain on the target than expected and does the repetition rate of the beam hit a resonance? Once we have a strain measurement system in place, we can see if certain mitigation methods are effective. In particular, we are interested in how effective injecting gas bubbles is at reducing the pressure wave. Also, we know that during operation an internal baffle erodes and a partial, non-critical, crack occurs. We hope that with a long-lasting strain sensor, we can find the point in time when this crack occurs.

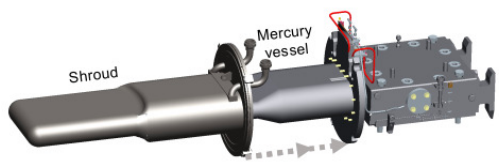

Figure 2: The target layout showing the shroud sliding over the mercury vessel.

The pulse-induced strain on liquid metal targets has been measured previously for the SNS target at LANL [1] and for displacement measurements of the J-PARC target [2], but not for the actual SNS target during beam impact. The SNS target has a double containment design, see Figure 2, and the outer shroud is structurally independent from the inner mercury vessel. Therefore, measurements on the outer surface, as done at J-PARC, will not give meaningful results. Based on the experience from the LANL experiment, we selected commercially available fiber optic strain sensors [3]. These sensors are small enough to fit in the interstitial space between the shroud and mercury vessel, have enough bandwidth (100kHz) to see the pressure wave, and do not suffer from electromagnetic noise from the beam and surrounding equipment. The optical sensors work on the Fabry-Perot interferometer principle, where one measures the phase shift of the light reflecting in the cavity as the length of the cavity changes along with the material, in our case the vessel wall, to which it is attached.

* ORNL is managed by UT-Battelle, LLC, under contract DE-AC05-00OR22725 for the U.S. Department of Energy. This research was supported by the DOE Office of Science, Basic Energy Science, Scientific User Facilities.
† blokland@ornl.gov

ISBN 978-3-95450-185-4

DESIGN CONSIDERATIONS

Introducing new material inside the target module requires careful consideration. The impact on its lifetime must be minimal, but it also cannot affect the existing method of detecting leaks. If there is a hole in the inner mercury vessel, the mercury will collect at the bottom of the shroud, where there are two bare wires that will now get shorted out. The newly introduced materials should not be able to short these wires nor insulate these wires. The high radiation field at the vessel wall does heat the fiber but not enough to melt it. The high radiation, between 1E12 (front) to 1E8 (back) R/hr. at 1.4 MW, also limits our choice in how to fasten the sensors. We did not find glues rated for 5000 hours at those radiation levels, and opted to use the same Stycast 2850FT epoxy that was used to glue the bare wires, thus not introducing a new material inside the interstitial space.

INSTALLATION

Optical Strain Sensors Installation

We installed eight strain sensors distributed along the vessel wall at the target's manufacturing facility [4]. The fibers were routed through a narrow, ¼ inch tube that also had to be epoxied to separate the helium gas in the interstitial space from the air around the target. The epoxy was cured using heat lamps. Figure 3 shows on the left, the curing of the epoxy; in the middle, the glued sensors on the top of the mercury vessel; on the right, the lowering of the mercury vessel into the water shroud.

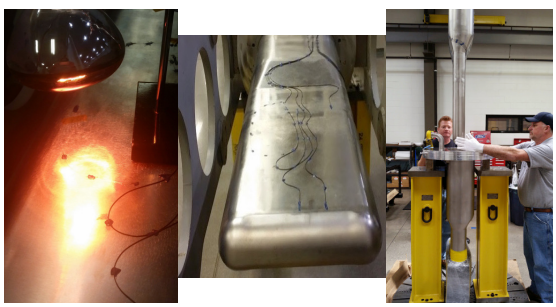

Figure 3: The installation of the optical strain sensors.

Accelerometers

Besides the optical strain sensor, we also installed two rad-hard accelerometers, one on the target mount (right behind the mercury vessel) and one on the mercury return piping several meters away from the target. These accelerometers are expected to survive much longer than the optical strain sensors.

Functional Test

To test the sensors, we drew a vacuum in the interstitial space to put a static strain on the mercury vessel to compare the sensor measurements with simulations. This test shows us not only which sensors are operational, but also how well they agree with the static strain simulation. We place high trust in the static strain calculation, as this does not involve liquid mercury dynamics.

This functional test also showed us that the new optical processor had a different scale factor than the older optical processor used in the LANL experiments. The results are shown in Figure 4. In general, the results match very well, except for sensor 6, which shows an opposite sign of strain change.

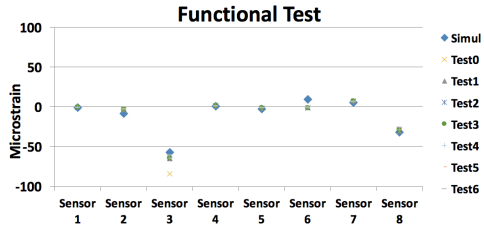

Figure 4: The functional test results.

Signal Routing from Target to Equipment

To install a new target, it must be moved into the service bay. The service bay has very high radiation levels and is contaminated. To avoid introducing contamination to the electronics, we split the cabling in two parts, one section rolls in with the target and is already connected to the sensors, while the second cable is fed from the outside to the inside of the hot cell. A connector box allows the manipulator operators to connect the two cables. Ahead of installation time, the operators practiced using a test manipulator to prepare for the actual installation. The connectors were reinforced with a metal bracket to prevent the mechanical manipulators from potentially crushing them. Even fine work, such as removing small dust caps from the fiber connectors, was performed without any problems (Fig. 5).

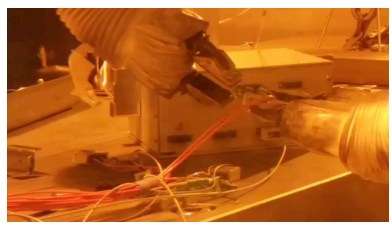

Figure 5: Manipulators connect the fiber-optic cables.

Sensors

We have now run with two instrumented targets. The first target, T13, was instrumented with eight non-rad-hard, multi-mode optical sensors, see Figure 6, and two accelerometers. The multi-mode fiber optic strain sensors are not meant for use in high radiation areas. But in our case, the residual radiation ranges from 100 to more than 100,000 Rad/hr depending on how long the beam was turned off and the location inside the target.

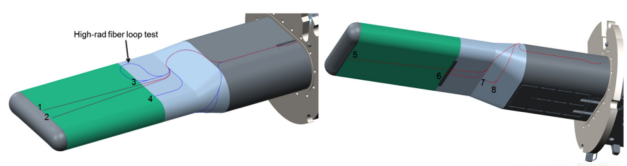

Figure 6: The layout of the installed sensors of T13.

ISBN 978-3-95450-185-4

The target is typically inserted several days before beam is turned on because all the cooling and mercury flow lines have to be connected and the accelerator has to be setup before beam can be sent to the target. Thus the sensor and fiber cables in the target are already potentially exposed up to the order of 1 MRad, even before beam has been sent to the target.

Much higher radiation resistance is to be found in single-mode fiber. To investigate super rad-hard optical fiber, we installed one run of single-mode fiber in a loop to measure transmission, and one run with a dead-end to measure the reflection as a function of radiation exposure. Laser light of milli-watt level at 1320 nm is sent through the fiber and the returned light power is measured.

For the second instrumented target, T14, we used rad-hard, high OH (hydroxyl) content, multi-mode fiber, two accelerometers, and two prototype super rad-hard, single-mode optical strain sensors developed at SNS [5].

ACQUISITION SYSTEM

To minimize signal attenuation, the cable lengths are kept as short as possible, requiring an electronics rack, equipped with accelerator timing and networking signals, to be installed in the manipulator gallery directly outside the service bay. This equipment rack holds the optical signal processor (OSP) that converts the optical signal into an analog electric signal. These electric signals, the two accelerometer signals, and the single mode fiber power signals, are all sampled by two digitizers in a PXI-crate (PCI eXtensions for Instrumentation). The software is LabVIEW based. A backup optical processor and a backup scope were installed and the data-acquisition system was thoroughly tested to make sure that we would capture the first pulse.

RESULTS

T13 Experiment

The T13 experiment started with single pulses of different intensities ranging from 10 µC to 24 µC. We also did a few pulse trains of 10 pulses to look at a possible build-up of strain. While the acquired data is immediately shown on the screens, an offline program was created to organize and analyze the data, see Figure 7.

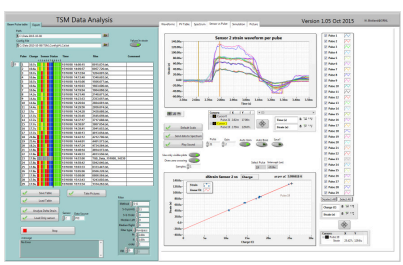

Figure 7: The offline data analysis program.

The analysis program arranges the acquired data files in columns on the left side, while on the right side it shows the strain waveforms per pulse or per sensor and can calculate the strain per beam pulse charge for each sensor by calculating the peak-to-peak strain versus intensity of several beam pulses. The program can also read simulation files and compare the measured strain waveforms to simulated strain waveforms.

T13 Multi-Mode Optical Strain Measurements

The longest lasting optical sensor, sensor 4, survived for about 80 pulses for a total of about 1.3 mC, which is equivalent to 1.5 s at 850 kW. The accelerometers survived the full production run but are also installed in a much lower radiation area. Results are shown in Figure 8 and Figure 9 and show on the top, the strain waveforms for various intensity pulses; in the middle, the fit to calculate the strain per beam pulse charge; and on the bottom, the comparision to the simulation [6]. Signals from sensors 1 and 5 should be very similar, as their locations are similar but one on top and one on the bottom. The measurements are not perfect: We see that the strain signals are failing, most likely due to radiation induced attenuation in the fiber. The output signal of the OSP starts jumping in levels and then gets a very large offset, and finally shows nothing but noise. The jumping of the signal can be seen in the sensors 3 and 5 waveforms. Sensor 6 was dead. Typically, we see a linear relation between the measured strain and beam intensity, but the intersection does not always run through zero. To further investigate, we did perform lower intensity measurements for T14.

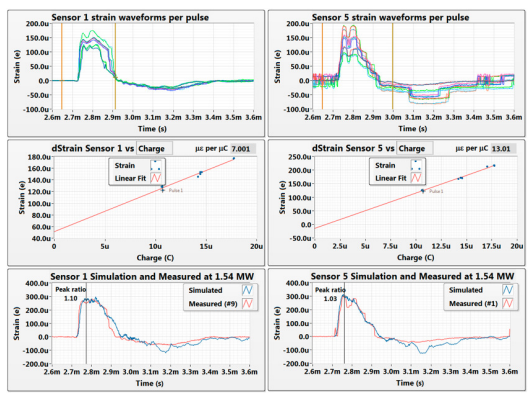

Figure 8: Results from sensors 1 and 5.

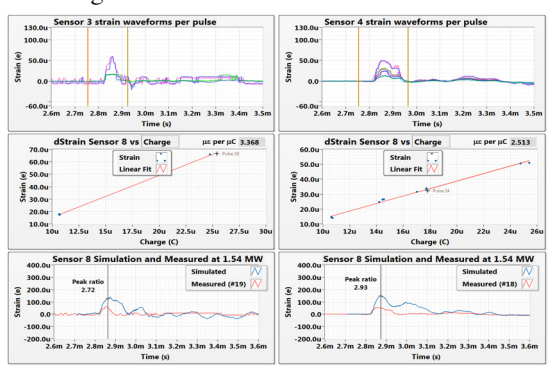

Figure 9: Results from sensors 3 and 4.

In most cases, the shape of the simulated waveform is similar to that of the measured waveform, but the two don't always agree in intensity. This can be due, e.g. in

ISBN 978-3-95450-185-4

sensor 7, to the fact that the location of the sensor is not well represented in the finite-element simulations or that it is near a simulation boundary. In some cases, the simulation results highly depend on the position, see Figure 10.

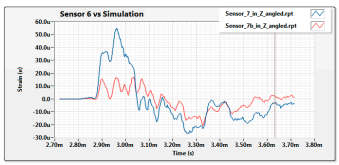

Figure 10: Simulations done near the position of sensor 7.

To look at any possible pulse-to-pulse interaction or strain build-up, we measured the strain during 10 consecutive pulses of 17.8 µC (equivalent to the 1 MW beam). Figure 11 shows the strain waveforms of sensors 4 and 8 during the 10 pulses. The signals show some reflections or resonances, but these do not seem to lead to an increase in peak-to-peak strain, and die down slowly.

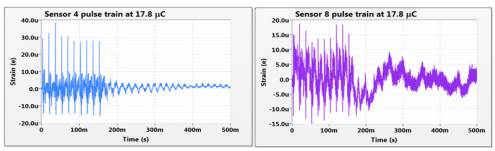

Figure 11: The pulse trains do not show a build-up.

T13 Accelerometer Measurements

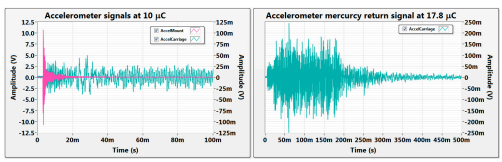

Figure 12: The signals from the accelerometers.

The accelerometer signals are shown in Figure 12. The signal of the one mounted on the mercury return is much smaller, as it is many meters away from the target and sees many reflections of the pressure wave. The accelerometer on the target mount saw good signals, but saturated at intensities above 10 µC. We have not yet derived useful information from the accelerometers from T13.

T13 Single-mode Fiber Attenuation

Figure 13 shows the attenuation as a function of time for the two fiber signals, as well as the accumulated beam energy on target. The calculated Radiation Induced Attenuation is equivalent to 0.4 dB/km/MRad and peaks at 0.9 dB/km/MRad. The peak dose amount is 83.6 GRad and the peak dose rate is 329 kRad/s at 800 kW beam power, [5]. From these results, we can estimate at least a two-week lifetime for the single-mode sensors.

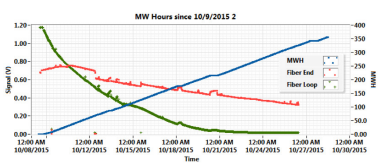

Figure 13: Attenuation of the single mode fiber.

T14 Experiment

For the T14 experiment, we replaced the regular multi-mode fiber with a high OH content multi-mode fiber that is more rad-hard. Of the 8 installed multi-mode fibers, only 5 survived the initial installation, while 2 out of 4 single-mode sensors survived. In addition, two thermocouples were installed, as shown in Figure 14. Due to the need to ensure that electrically conductive material could not reach the leak detectors, the thermocouples had to be located some distance from the beam impact area.

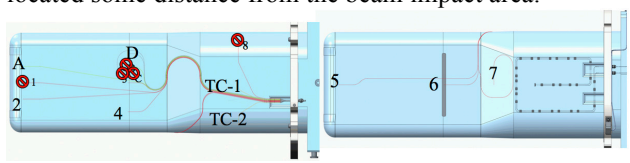

Figure 14: T14 sensor locations.

T14 Multi-Mode Optical Strain Measurements

The high OH multi-mode fiber sensor lasted beyond our expectations. The life-time of the multi-mode sensors was so much improved that the analysis program had to be rewritten to handle the large amount of data. The analysis is still in progress. We only show our initial results.

The longest performing sensors, 4 and 7, have lasted well over two weeks. Sensor 4 showed a slowly descreasing amplitude of the measured strain, but it still produced a signal for more than a month, see Figure 15. That time span is long enough to start looking for the possible breaking of the mercury vessel baffle, aka a change in the waveform. The improvement over the non rad-hard fibers is about 100,000 in terms of radiation exposure.We also found that the fibers tend to recover after a few days without beam on the target and that resetting the OSP helps regain a signal.

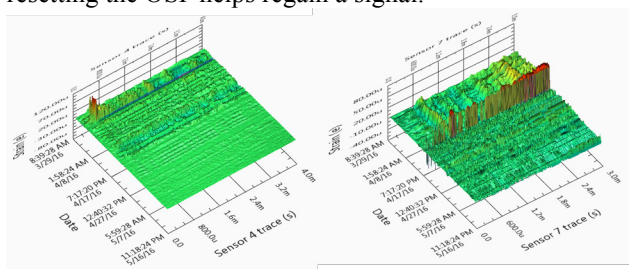

Figure 15: Lifetime of the multi-mode sensor signals.

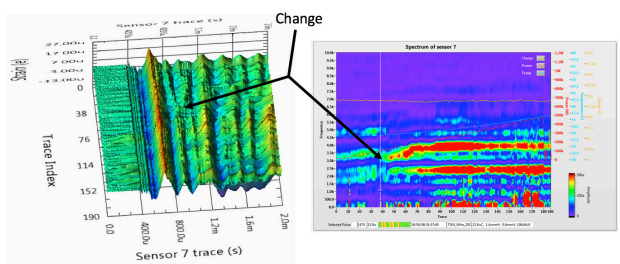

Figure 16: Possible event during ramp-up.

Figure 16 shows a change in the waveform of sensor 7 at about one week after the production start. Sensor 4

ISBN 978-3-95450-185-4

shows a similar change around the same time, April 6th at 2 am. We will investigate if this represents a change in the target's internal structure.

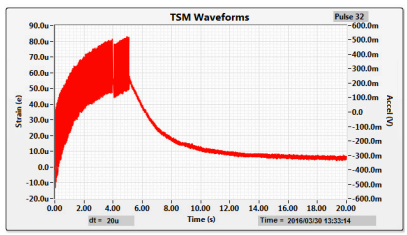

Figure 17: Build-up of static strain at 300 pulses.

An interesting result shown in Figure 17 is a static build-up of strain during a train of 300 pulses, most likely due to the local rise of the vessel temperature.

T14 Thermo-Couple Results

Figure 18 shows that the simulated and measured temperature responses are very similar, both in increase, about 0.3 C, and in decay time-constant. The temperature response is much slower than the strain response because the thermo couple is farther away from the beam impact area.

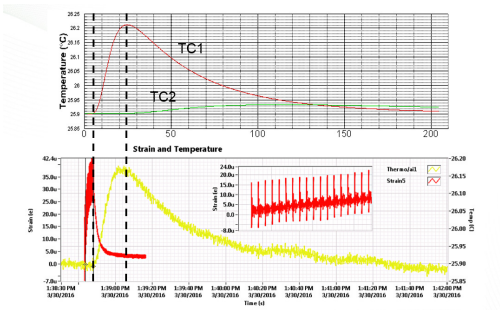

Figure 18: Simulated (top) and measured temperature (bottom) response.

T14 Accelerometer Measurements

The new accelerometer on the target mount is less sensitive than the previous ones and is no longer saturating. The data is being analyzed, but also shows some specific points in time where the signal changes.

T14 Single-Mode Optical Strain Measurements

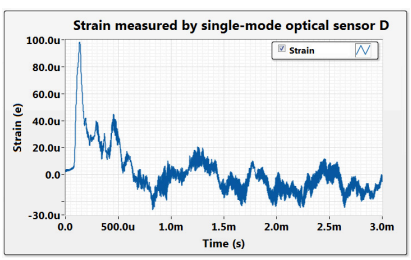

Figure 19: Single-mode fiber strain measurement.

The sensor located in the front edge of the target vessel survived for about 3 days while the sensor located in the middle of the vessel was able to provide strain measurements over 5 weeks. The signal from Sensor D is shown in Figure 19.

CONCLUSIONS

In the case of T13, we found that the strain responses are linearly proportional to the beam charge despite the non-linear (cavitating) mercury behavior, and that this is consistent with other experimental data. The simulated and measured strain data at forward and central locations, 1 and 5, agree very well in both magnitude and dynamic character, while the dynamic response is predicted well at other locations, except for sensors 7 and 8. The simulation has more high frequency content than what is observed, perhaps missing a dampening effect. The signals measured in the back are quite lower than the simulation predicted; this can be due to a dampening effect and also to the sensitivity of the simulation to location. We see some reverberation, mostly in the sensors in the back, but not build-up in the peak-to-peak response and thus at this point, we do not see an unanticipated build-up of dynamic strain endangering the life-time of the target.

We haven't fully analyzed the data from T14 yet; we are in the process of validating the single mode fiber sensor data. We do see that the temperature response is as expected.

SUMMARY

After a year-long effort by many people, we have results. While a year seems like a long time, given all the preparations and deadlines associated with target manufacturing, the time constraint in developing the measurements was actually fairly tight. The T13 instrumentation lived just long enough to give us data. We are still analyzing the T14 data. With the rad-hard, multi-mode prototype super-rad hard single-mode, we now have long-term measurement capability.

FUTURE

We plan to further develop the prototype single-mode optical strain sensors and integrate their data acquisition with the multi-mode sensors. In addition, we plan to install metal strain gauges to see if we can overcome the expected electrical noise and provide another method for measuring the strain.

ACKNOWLEDGMENTS

The authors wish to thank the many people who helped make these measurements a possibility; in particular Bob Sangrey and Jeff Bryan for the sensor installation as well as the many others who helped with tasks ranging from installing the necessary infra-structure in the manipulator gallery to cable hook-ups in the service bay.

REFERENCES

[1] B. Riemer *et al.*, "Small gas bubble experiment for mitigation of cavitation damage and pressure waves in short-pulse mercury spallation targets," *Journal of Nuclear Materials,* Volume 450 (2014) 192.

ISBN 978-3-95450-185-4

[2] T. Wan, T. Naoe, M. Futakawa, "In-situ structural integrity evaluation for high-power pulsed spallation neutron source – Effects of cavitation damage on structural vibration," *Journal of Nuclear Materials*, Volume 468, January 2016, P 321-330, ISSN 0022-3115, http://dx.doi.org/10.1016/j.jnucmat.2015.07.052.

[3] E. Pinet, "Fabry-Perot Fiber-Optic Sensors for Physical Parameters Measurement in Challenging Conditions," Journal of Sensors Volume 2009, Article ID 720980, 9 pages doi:10.1155/2009/720980.

[4] D. Winder, B. Sangrey, J. Bryan, "Target System, MTX-009 Sensor Installation," ORNL, Oak Ridge, USA,Internal Report 106010101-TR0007, Internal Report, March 2015.

[5] Liu *et al.*, "Radiation-Resistant Fiber Optic Strain Sensors for SNS Target Instrumentation", in Proc. 7th International Particle Accelerator Conference (IPAC'16), Busan, Korea, May 2016, paper MOPMR055, pp. 371-373, ISBN: 978-3-95450-147-2, doi:10.18429/JACoW-IPAC2016-MOPMR055, http://jacow.org/ipac2016/papers/mopmr055.pdf, 2016.

[6] B. Riemer, "Benchmarking dynamic strain predictions of pulsed mercury spallation target vessels," *Journal of Nuclear Materials*, Volume 343, 1 August 2005, P 81–91, doi:10.1016/j.jnucmat.2005.01.026.

ISBN 978-3-95450-185-4

R&D ON MICRO-LOSS MONITORS FOR HIGH INTENSITY LINACS LIKE LIPAc

J. Marroncle*, P. Abbon, A. Marchix, CEA Saclay, DRF/DSM/IRFU, Gif sur Yvette, France
M. Pomorski, CEA Saclay, DRT/LIST/DM2I/LCD, Gif sur Yvette, France

Abstract

Before approaching the micro-loss monitor concept, we propose to present the high intensity Linac for which the R&D program was done, LIPAc (Linear IFIMIF Prototype Accelerator). This later is the feasibility accelerator demonstrator for the International Fusion Materials Irradiation Facility (IFMIF). IFMIF aims at providing a very intense neutron source (10^{18} neutron/m^2/s) to test materials for the future fusion reactors. This challenging accelerator LIPAc (1.125 MW deuteron beam) is in installation progress at Rokkasho (Japan).

Then, we will focus on the feasibility study of the beam optimization inside the SRF Linac part. Commissioning of such high beam intensity has to be done with a different approach based on detection of micro-losses, CVD diamonds, set inside the cryomodule linac. This is mandatory to keep beam losses below 1W/m for hands-on maintenance purposes.

INTRODUCTION

This paper deals with the R&D on µLoM (micro-Loss Monitor) which was attempted for beam fine tuning of high intensity Linac while maintaining losses below 1W/m for maintenance hands-on purpose. Beam dynamics team working on the Linear IFMIF prototype Accelerator, LIPAc, warned about the feasibility for fulfilling this requirements with the foreseen diagnostics. Thus, they proposed to introduce the new concept of beam micro-losses and required monitors for measuring them.

After a swift introduction to LIPAc and its commissioning plans, this R&D program devoted to µLoM will be presented. Firstly micro-loss concept will be defined, emphasizing their importance for beam optimization. Therefore the step by step study will be investigated like, counting rate estimates and their potential background contributions, experimental neutron tests for rate validation and a proposition for signal processing before to conclude.

IFMIF CONTEXT

The International Fusion Materials Irradiation Facility (IFMIF) [1], a project involving Japan and Europe in the framework of the "Broader Approach", aims at producing an intense flux of neutrons, in order to characterize materials envisaged for future fusion reactors. This neutron source will be a combination of two deuteron beam accelerators (125 mA – 40 MeV cw) and a liquid lithium target. Therefore, these two 5 MW accelerators impinging the Li target will produce a huge neutron flux (10^{18} neutrons/m^2/s). Downstream, dedicated cells will be implemented to test the material sample responses submitted to mechanical and thermal stresses in these very harsh conditions. Shielding structures are optimized in order to roughly reproduce the neutron energy spectrum expected in fusion reactors.

IFMIF project has to face to many challenges, thus an intermediate phase of validation was decided which consists to design and built an accelerator prototype, a 1/3-scaled Li loop target and parts of test cells.

The prototype accelerator LIPAc (Linear IFMIF Prototype Accelerator) is a 1-scaled IFMIF accelerator up to the first Superconducting Radio Frequency Linac (SRF), delivering 9 MeV deuteron beam at 125 mA cw. A high beam transport line will be installed to lead safely the beam toward a high power beam dump able to handle 1.1 MW. This accelerator is in commissioning and assembling progress at Rokkasho (Japan).

GENERAL COMMISSIONING PLANS

LIPAc accelerator components have been mainly designed and manufactured in Europe by European Institutions (CEA Saclay, CIEMAT Madrid, INFN Legnaro and SCK-CEN) under F4E management, who is also responsible of other activities. LIPAc building was constructed by QST (National institutes for Quantum and Radiological Science and Technology), who takes also in charge the supply of conventional facilities, the control system, the protection and the timing system.

The accelerating components (Fig. 1) are the injector delivering a deuteron beam at 100 keV (A), the RFQ (175 MHz) to bunch and accelerate up to 5MeV (B) and the superconductive Linac increasing the energy up to 9 MeV (C). These components are connected through beam transport lines (LEBT, MEBT, HEBT) tuned and qualified by various diagnostic monitors [2] and the beam is absorbed into the HPBD (High Power Beam Dump) (phase D) to stop safely the 1.1 MW beam power.

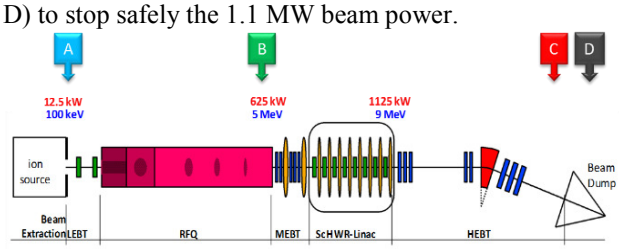

Figure 1: commission plan with the 4 phases.

* Jacques.marroncle@cea.fr

ISBN 978-3-95450-185-4

The commissioning of the accelerator is based on a staged approach divided in 4 Phases [3].

- Phase A [4][5]: commissioning with 100 keV deuteron beam of 140 mA. Installation has already begun in 2014 for the injector and in 2015 for its commissioning. First beam was produced with H^+ at the same generalized perveance, meaning half energy and half current, to keep constant the space charge effect expected for a deuteron beam, and to mitigate activation. After various proton beam measurement, injector comes to be familiar to jump to deuteron beam during 1 week. Finally, at 100 keV a 152 mA deuteron beam was extracted from the source at 10% duty cycle with ε=0.23 π.mm.mrad; beam intensity measured on the beam stopper was about 110 mA, recently increased up to 130 mA. Encouraging results which have to be repeated this year with other condition settings.
- Phase B: installation of the RFQ [6] started in April 2016, and still in progress. In September, the bead pull measurements and the final tuning should be reached before the installation of the RFQ in its nominal position. The Mean Energy Beam Transport line [7] and a D-Plate with a low power beam dump will be attached downstream before to start the RFQ commissioning in June 2017 up to end 2017.
- Phase C and D: will resume operation after the rest of the beam line installation and the SRF Linac. Phase C commissioning concerns pulsed beam while cw will be done during phase D after the HPBD installation.

All these activities will end by December 2019.

DEVELOPMENT OF MICRO-LOSS MONITORS FOR SRF LINACS

Beam tuning of high intensity Linacs requires a peculiar attention to beam losses which have to be kept below 1 W/m. The µLoMs, which should be inserted in the cryomodule, were designed to insure the SRF Linac commissioning strategy and monitoring.

As mastering the beam losses in the SRF Linac has been identified as crucial, we investigated which and how potential loss sensors could be used. After a brief SRF Linac description [8], the feasibility study of µLoM will be presented step by step showing that the selected system should work in this radiative environment.

SRF Linac Description

The SRF Linac will accelerate deuteron beams from 5 to 9 MeV. It consists in one large cryostat hosting 8 identical structures, each composed of:

- 1 half wave resonator (HWR) with its own tuner for precise resonant frequency tuning, where a 175 MHz, 100 kW total RF power is injected,
- 1 solenoid equipped with steerers,
- 3 micro-loss detectors or µLoM around the solenoid vacuum chamber,
- 1 button BPM in front of the solenoid.

All these structures are superconductive and have their own helium vessel maintained at 4.45 K.

To protect the SRF Linac against beam losses, 8 BLMs (Beam Loss Monitor – Ion chambers LHC-type) will equipped the vacuum tank of the cryomodule.

All design, tests and procurements of the entire cryomodule including its RF couplers are done at CEA Saclay and will be completed by May 2017. Assembling of the cryomodule should start later in 2017 at Rokkasho, in a dedicated clean room, under the responsibility of F4E.

SRF Linac Tuning And Fine Tuning

Unlike for classical accelerators where the tuning of the MEBT and the SRF Linac consists in minimizing emittance growth, for high intensity accelerators, like LIPAc, it aims at minimizing the beam external halo (the so-called "halo matching" method to decrease losses as low as 10^{-6} of the beam or 1 W/m) [9]. In order to perform this matching, the necessary beam diagnostics have been identified (BPMs, BLMs and µLoMs) which may be implemented.

The tuning strategy relies on the principle that the number of independent diagnostics should be larger than or at least equal to the number of tuneable parameters, which are those of the MEBT quadrupoles and bunchers, together with the SRF Linac solenoids and cavities [10]. After a first dipolar tuning done with steerers aiming at minimizing trajectory deviations detected by BPMs, a quadrupolar tuning can be performed by minimizing losses detected by BLMs installed around the MEBT and the SRF Linac. As those ones are located relatively far from the beam, particle losses on the vacuum chamber would trigger several of them at once, making that the number of independent diagnostics is less than the actual number. That is why, at this step, it is foreseen to adjust only the MEBT setting, while letting the SRF Linac setting at its nominal values.
Then, in the ultimate step, referred to as fine tuning, in order to satisfy hands-on maintenance requirements, micro-losses (less than 10^{-6} of the beam) detected by µLoM will be minimized. As those ones are close to the beam, it is expected that they are enough correlated to loss locations. In this step, all the tuneable parameters of the MEBT and the SRF Linac will be adjusted. This is necessary on the one hand, and feasible in the other hand. This has been simulated by using the Particle Swarm Optimization algorithm [11]. A fine tuning at this level of precision is expected to be made frequently, as regard to the reproducibility of the accelerator components.

Ideal Criteria For µLoM

We consider beam energies below few tens of MeV where only neutrons and γ may escape from the beam structures (pipe, cavity wall…), dictating µLoM choices. Hereunder is a list of requirements for such µLoMs:

- sensitivity to beam losses better than 10^{-6} of the beam power,
- stability at cryogenic temperature since monitors are closely installed to the beam inside the cryomodule for better beam loss localizations,
- radiation tolerant,
- high counting rates because beam fine tuning is an iterative process whose effects need to be evaluated for

ISBN 978-3-95450-185-4

each single beam settings. Indeed, it requires a quite swift measurement (~1 minute per each tuning step) for achieving the final tuning in a reasonable duration time,
- reliability, like for all cryomodule components for which maintenance is a difficult and long operation,
- response to neutron better than to γ, as superconducting cavities may produce photons in the energy range [10 keV - few MeV]. Ideal µLoM should have a weak γ response avoiding confusion between high γ beam losses and γ cavity emission by-products,
- reasonable price.

CVD Diamonds As µLoM

CVD Diamonds fulfill the previous criteria but the last, thus they have been selected as the most promizing sensor for µLoM. Main characteristics of mono crystalline CVD Diamonds are listed in the following Table 1.

Table 1: Mono Crystalline CVD Diamond Characteristics For µLoMs

Size	$4 \times 4 \times 0.5$ mm^3
Active area	3×3 mm^3
Density	3.52 g/cm^3
Resistivity	10^{13}-10^{16} Ω.m
ε_r	~5.7
e$^-$/hole production	~13.2 eV
Band gap	5.5 eV
Radiation hardness	~500 MRad for 24 GeV proton

A thin conductive coating (Al, 200 nm) was deposited on the diamond for electric polarization (about 1V/µm diamond thickness). As sketched on Fig. 2, a particle may induce reactions (ionization, recoil, nuclear…) on diamond materials creating e$^-$/hole pairs which drift toward electrodes under the electric field influence. Electric current is then measured with an appropriate electronics.

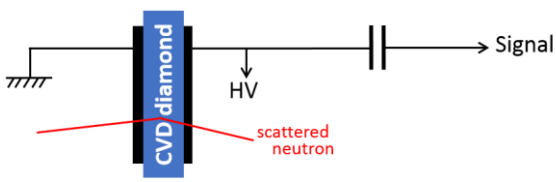

Figure 2: sketch of the diamond working principle.

CVD Diamonds Cryogenic Tests

In 2010, no information was available about the diamond behavior at cryogenic temperature. Since diamonds will be fixed to the SRF Linac solenoids cooled at 4.5 K, characterization of crystal diamond responses at cryogenic temperature was necessary.

For this reason, cryogenic tests were done in 2 steps with a ^{252}Cf source radiating γ and fission neutrons bombarding diamond cooled in a liquid nitrogen Dewar (77 K) [12] in a first time, and in a liquid helium cryostat (4.5 K) in a second time [13].

For both conditions we have observed a normal diamond behavior which validates our choice allowing to resume our R&D activities about counting rate expectations.

By end 2011, it was organize a workshop on cryogenic BLM at Cern [14] where cryogenic data were available, but low α particle energy exhibit anomaly which was not understood.

Counting Rate Estimates

Expected rates for γ and neutrons were evaluated for of 1W/m beam losses for insuring hands-on maintenance in the SRF Linac (5 to 9 MeV). The simulated spectra (using MCNPX 2.5.0 [15]) for both incident particles shown on Fig. 3, take into account the cavity and solenoid materials of the cryomodule, while the simulated diamond responses are given on Fig. 4 for a 3×3 mm^2 active diamond surface. This later correspond to the conductive quoting surface deposited on both sides of the diamond; at present, deposition may be extended to roughly the whole diamond surface. This is an interesting gain (16/9~2) in term of counting rates, particularly appreciated at low duty cycle beam mode.

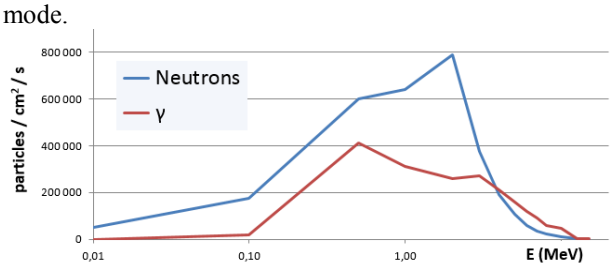

Figure 3: incident neutrons and γ spectra impinging diamond for SRF Linac condition for 1 W/m beam losses.

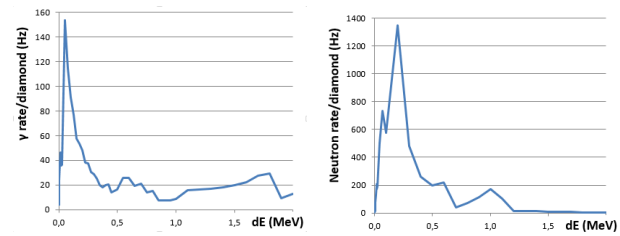

Figure 4: γ (left) and neutrons (right) spectra of energy deposited in diamond at SRF Linac for 1 W/m beam losses.

The 1 W/m contributions are extracted from these data for both particles and summarized on Table 2.

Table 2: Neutrons And γ Counting Rates (kHz) Versus Energy Thresholds (keV)

Threshold (keV)	**70**	**100**	**200**	**300**	**400**	**500**
Neutron (kHz)	3.7	3.2	1.8	1.3	1.1	0.9
Photons (kHz)	1.2	1.1	0.9	0.8	0.7	0.6

During thermal tests, we got thresholds about 50 and 100 keV, but due to the very low diamond capacitance with respect to the FEE cable length, threshold should be of the order of 200 or 300 keV!

Although the µLoMs are designed for full beam power, they are also expected to give wealthy indications during first tuning processes that will occur mainly at low duty cycle. Considering the extreme case of the very first commissioning phase at reduced duty cycle as low as 10^{-4} leading to only 16 counts/mn for 1W/m and 200 keV threshold. These rates could actually be higher because losses in these very first phases are very likely higher than 1 W/m, and

ISBN 978-3-95450-185-4

when going to higher duty cycle 10^{-3}, the counts would be hopefully multiplied by 10.

We have also checked that background contributions coming from the beam dump would represent less than 5% of the 1 W/m losses.

µLoM Beam Test With Neutrons

In order to validate the simulated counting rates previously presented we have tested in 2011 our µLoMs with various neutron energies. It was done with a Van de Graaf facility installed at CEA center of Bruyères-le-Châtel (France) which allows delivering 0.6, 0.75, 1.2, 2.1, 3.65, 6 and 16 MeV neutron beam energies using different beam / target combinations. They were produced in pulsed beam mode with a γ contaminations, which was efficiently discriminated by time of flight technique as seen on Fig. 5.

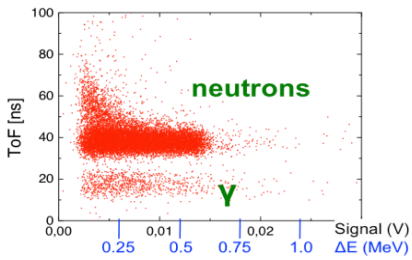

Figure 5: neutrons and γ time of flight discrimination for 2.1 MeV neutrons.

On Fig. 6 are plotted experimental data for $E_{neutron}$ = 0.6, 0.75, 1.2 and 2.1 MeV (dashed lines) while simulated ones are in solid lines. It clearly appears that experimental thresholds are about 100 keV. Finally, the quite good agreement between experimental and simulated data gives us a better confidence for the calculated counting rates.

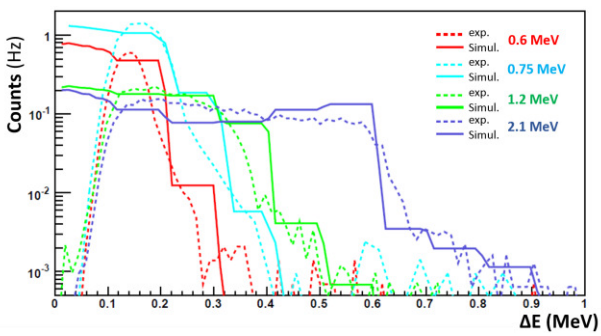

Figure 6: experimental and simulated neutron energy deposits in µLoM for different neutron incident energies.

X-Rays And γ Contaminations

As written previously, ideal µLoM should have a better response for neutron than for γ. The reason is that superconductive accelerators may emit X-rays and γ mainly due to high electric fields applied on the superconductive cavity surfaces. Indeed, electron emissions will generate photons when electrons impinge material. Their energies depend on electron energies, which can be strongly increased by the cavity radio frequency power when it is phase-correlated to electrons.

The goal of µLoM is to measure losses coming from the beam, but cryo-cavities. Since these 2 photon contributions can't be discriminate, it is preferable to choose a photon low efficiency µLoM. Therefore, a low-Z material, as diamond, is a quite good candidate.

Note that the photon emission probability of superconductive cavities increases as the accelerating electric field applied: nominal value for LIPAc is 4.5 MV/m while it is 6.5 MV/m for Spiral2 for instance.

In 2013, we have set a diamond close to a cryostat inside which a Spiral2 cavity was tested. The energy deposit in the diamond was measured with an MCA (Multi-Channel Analyser). Data tacking was done at different test periods. We have noticed that generally electric field increases smoothly with low parasitic emission, but less often we have observed really important photon emissions.

This is illustrated in Table 3 where the 1 W/m is the simulated contribution of neutrons plus photons (photons are in parenthesis). The 3rd column are measured rates for normal cavity behaviour; note that the mean contribution represents less than 5% of the 1 W/m losses. This is totally different for the last column where cavity emissions are higher to the 1 W/m!

Table 3: Counting Rates (CR) At 100 And 200 keV Threshold For Superconductive Cavity Emissions

Runs	**"1W/m"**	few "good" runs	"bad" run
CR@Th=100 keV	**4400** (1200)	203	6340
CR@Th=200 keV	**2700** (1100)	77	2813

To conclude, except for specific cavity processes µLoM measurement should not be drawn under photon emission cavities.

Front-End Electronics (FEE)

Preliminary study has been performed, mainly to check that adequate solution may be implemented. FEE sometimes can't be installed inside the accelerator vault due to high radiation background like for LIPAc.

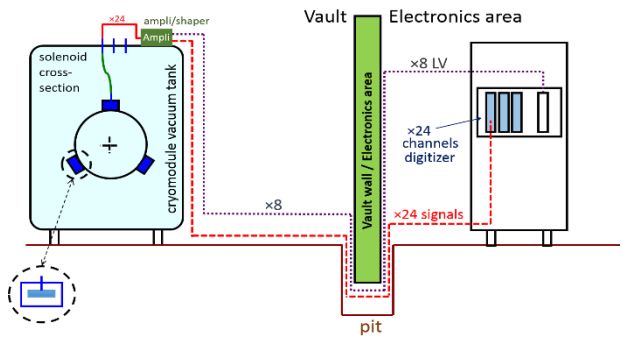

Figure 7: LIPAc vault and electronics area separated by a concrete wall for radiation shielding purpose.

However, diamond capacitance is really tiny (about 2 pF) and minimizing the cable length is of greatest importance for reducing its contribution. To keep the ratio signal/noise above a reasonable threshold, a first broadband amplifier (BW>1 GHz, Gain≥40 dB) made of radiation tolerant components must be installed in the vault. The length of the cables connecting this amplifier to the diamond have to be minimized, but not less than 3.5 m for

ISBN 978-3-95450-185-4

LIPAc. Then, the 50 Ω output amplifier signal may be transported through a long cable to reach the second FEE level for data processing, located outside the vault (see Fig. 7).

We have measured a diamond signal with a ^{60}Co source radiating 2 γ (1.17 and 1.33 MeV). Their simulated diamond response is expected about 0.9 – 1 MeV. A broadband Cividec amplifier (BW>2 GHz – Gain=40 dB – output impedance = 50 Ω – 1 MGy radiation tolerant) [16] connected through a 3 m cable to the µLoM was used. Such a signal is displayed on Fig. 8.

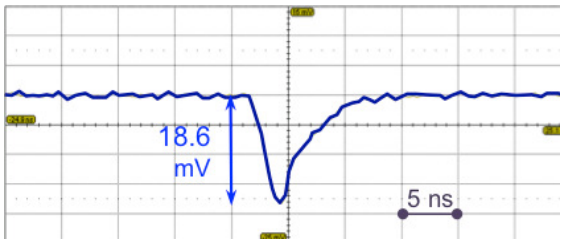

Figure 8: oscilloscope display for diamond signal submitted to a ^{60}Co source.

For LIPAc, we proposed to attach 3 µLoMs per solenoid, in order to be as close as possible to get the best loss locations. The accelerator vault is separated to the rest of the facility by a concrete wall for radiation shielding purposes.

For each µLoM, a radiation tolerant amplifier/shaper provides a signal which is transported to a digitizer. A CAEN digitizer as V1720 card (12 bits, 8 channels, 250 MHz sampling) [17], will process signal as soon as its amplitude is higher than a settable threshold, giving then access to the deposited charge in the µLoM.

During commissioning or monitoring periods, evolution of micro-losses may be followed thanks to µLoM which will be of great help for the machine operation group in charge of the accelerator tuning and defining working points in safe conditions.

CONCLUSION

A R&D program about µLoM for beam optimization of high Linac intensity like LIPAc was initiated on IFMIF/EVEDA framework, as monitoring the very low beam losses is mandatory for achieving fine tuning.

CVD diamonds were identified as good candidates for such loss detections and deeply investigated in the frame of dedicated R&D program. This study has demonstrated how they nicely fulfil the main requirements related to radiation tolerance, operation at cryogenic temperatures, counting rates sensitivity to background particles. Thanks to the various tests performed, missing experimental values have been obtained and full characterization of the sensor for the purpose of loss measurements has been completed. A digitizing processing signal was also designed to measure the energy deposit spectra. All these elements argue for mono crystalline CVD diamond as a good candidate for µLoM.

ACKNOWLEDGEMENT

Authors want to thanks P.A.P. Nghiem and N. Chauvin from CEA Saclay for the numerous and fruitful discussions about µLoM and beam dynamics.

REFERENCES

[1] J. Knaster *et al.*, "Challenges of the Current Prototype Accelerator of IFMIF/EVEDA", in *Proc. 7th Int. Particle Accelerator Conf. (IPAC'16)*, Busan, South Korea, May 2016, paper MOZB02, pp. 52-57.

[2] J. Marroncle *et al.*, « IFMIF-LIPAc Diagnostics and its Challenges », in *Proc. Int. Beam Inst. Conf. (IBIC'12)*, Tsukuba, Japan, Oct. 2012, paper WECC01, pp. 557-565

[3] P. Cara *et al.*, "The Linear IFMIF Prototype Accelerator (LIPAc) Design Development Under The European-Japanese Collaboration", in *Proc. IPAC'16*, Busan, South Korea, May 2016, paper MOPOY057, pp. 985-988.

[4] R. Gobin *et al.*, "Installation and first operation of the IFMIF Injector at the Rokkasho site", in *Proc. ICIS'15*, New York, USA, Aug. 2015, paper MONPS05.

[5] B. Bolzon *et al.*, "Intermediate Commissioning Result of the 70 mA/50 keV H^+ and 140 mA/100 keV D^+ ECR Injector of IFMIF/LIPAc"", in *Proc. IPAC'16*, Busan, South Korea, May 2016, paper WEPMY033, pp. 2625-2627.

[6] P. Mereu *et al.*, "Mechanical Integration of the IFMIF-EVEDA Radio Frequency Quadrupole", in *Proc. IPAC'16*, Busan, South Korea, May 2016, paper THPY025, pp. 3712-3715.

[7] I. Podadera *et al.*, "RF Design of the Re-buncher Cavities for the LIPAC Deuteron Accelerator", in *Proc. IPAC'11*, San Sebastian, Spain, Sept. 2011, paper MOPC047, pp. 184-186.

[8] H. Dzitko *et al.*, "Technical and logistical challenges for IFMIF-LIPAC cryomodule construction, in *Proc. SRF'15*, Whistler, Canada, Set. 2015, paper FRB01, pp. 1453-1459.

[9] P.A.P. Nghiem *et al.*, *Laser and Particle Beams, vol. 32, pp. 639-649, 2014*.

[10] P.A.P. Nghiem *et al.*, "Advanced Concepts for Very High Intensity Linacs", in *Proc. IPAC'16*, Busan, South Korea, May 2016, paper THYA01, pp. 3155-3160.

[11] N. Chauvin *et al.*, "Halo Matching For High Intensity Linacs and Dedicated Diagnostics", presented at HB2014, East Lansing, USA, Nov. 2014, paper TUO2AB02, unpublished.

[12] J. Marroncle *et al.*, "Micro-Loss Detector for IFMIF-EVEDA", in *Proc. DIPAC'11*, Hamburg, Germany, May 2011, paper MOPD42, pp. 146-148.

[13] J. Marroncle *et al.*, "µ-Loss for LIPAc", presented in "Cryogenic Beam Loss Monitors Workshop", `http://indico.cern.ch/event/156472/`, Cern, Switzerland, Oct. 2011.

[14] H. Pernegger *et al.*, "Diamond TCT measurement down to 60 K", presented in "Cryogenic Beam Loss Monitors Workshop", `http://indico.cern.ch/event/156472/`, Cern, Switzerland, Oct. 2011.

[15] D. B. Pelowitz, ed., "MCNPX™ User's Manual," Version 2.5.0, Los Alamos National Laboratory report LA-CP-05-0369, April 2005.

[16] Cividec, `https://cividec.at/`

[17] CAEN, `http://www.caen.it/csite/CaenProd.jsp?idmod=570&parent=11`

ISBN 978-3-95450-185-4

NEW ARRANGEMENT OF COLLIMATORS OF J-PARC MAIN RING

M. J. Shirakata†, S. Igarashi, K. Ishii, Y. Sato, and J. Takano
J-PARC/KEK, Tokai/Tsukuba, Ibaraki, Japan

Abstract

The beam collimation system of J-PARC main ring has been prepared in order to localize the beam loss into the specified area, especially during the injection period. At the first time, it was constructed as a scraper-catcher system in horizontal and vertical planes which consisted of one halo-scraper and two scattered protons catchers, whose the maximum beam loss capacity was designed to be 450 W in the beam injection straight of the ring. In 2012, the scraper was replaced by two collimators with a movable L-type jaw for both planes. Two catchers remained at the same places, and they were used as collimators. This large change of design concept of main ring collimation system was required in order to increase the beam loss capacity more than 3 kW. The system worked well but unexpected loss spots still remained in the following arc and straight sections. The four-axis collimator was developed with movable jaw in horizontal, vertical directions adding tilt functions which has high cleaning efficiency. We have four four-axis collimators, two two-axis collimators, and two original catchers. The most effective arrangement of collimators was investigated in this report.

INTRODUCTION

The Japan Proton Accelerator Research Complex (J-PARC) is a multi-purpose accelerator facility in Tokai village of Ibaraki, Japan [1]. The 3 GeV beam from the rapid cycling synchrotron (RCS) is utilized in muon and many neutron beam lines. The main ring (MR) has been providing 30 GeV beam to the neutrino and hadron experiments since early 2009. The recent beam power has achieved 416 kW for the T2K neutrino oscillation experiment, which corresponds to 2.15e+14 protons per 2.48 s cycle [2]. We have about 2.7e+13 protons per bunch. It is important to localize the beam losses for the maintenance, and to handle the beam loss amount for the machine protection. In order to localize the beam losses, MR has the beam collimation system to remove the halo component from the circulating beam.

ORIGINAL DESIGN

The beam collimation system of J-PARC MR has been updated since 2011. The first collimation system started as a single scraper-catchers system which was an ordinary one for the ring accelerators for horizontal and vertical planes. As there are 216 quadrupole magnets in MR, the ring is addressed from address 001 to 216 by using their sequential number. We call as the insertion-A (INS-A) from QDX216 to QDX016 which corresponds to address 001 to 016. The beam collimation system was installed in INS-A as shown in Fig.1, where QFRs and QDRs indicated the focusing and defocusing quadrupole magnets with address numbers, respectively. It consisted of one halo-scraper, catcher-1, and catcher-2 which were often called as Col-1, Col-2, and Col-3. STR means a steering magnet. The scraper was installed in address 007, catchers were installed in address 008 and 010. The designed beam loss capacity was 450 W but we prepared the 1 kW capable system to have a leeway in an actual beam operation. The original collimation system was designed for the tune (νx, νy) = (22.41, 20.80) which was called as a mid-tune in 2006. The actual operating point was set to (22.40, 20.75) until May 2016.

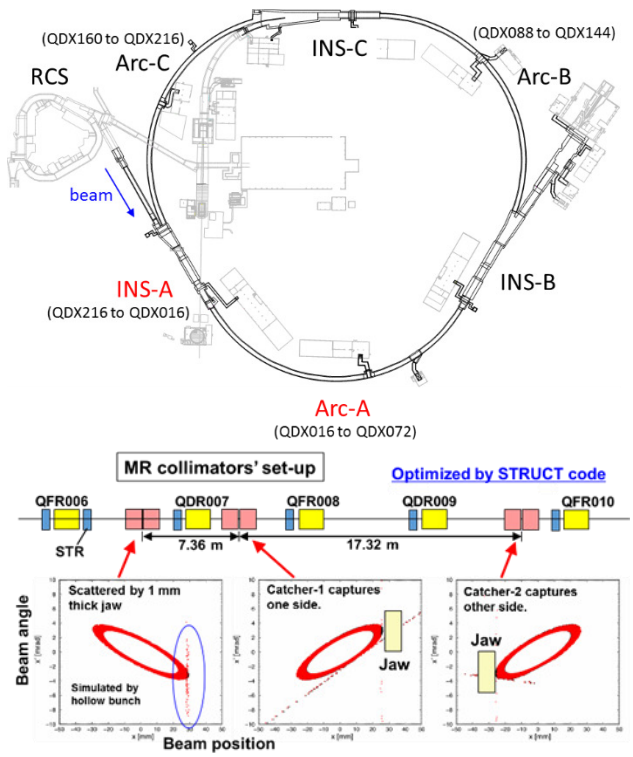

Figure 1: Schematic view of J-PARC MR and a layout of the original beam collimation system.

The scraper and catchers have a same radiation shield system. They have two cubic iron shields placed next to each other on beam line. Upstream shield can move to horizontal direction, and the other can move to vertical direction. Their movable range is +/-12 mm. Vacuum pipe which has scraper jaws or catcher jaws moves with the radiation shield. The vacuum pipe has a transverse position shift ability at the jaw positions by double bellows prepared at the middle and both ends. The beam loss distribution during the fast extraction (FX) operation in the circumference as a function of MR address number is

† masashi.shirakata@kek.jp

ISBN 978-3-95450-185-4

shown in Fig.2. We have to take care that the gain of beam loss monitors (BLMs) from 213 to 020 were set to be 1/8 compared to the others. The amounts of beam loss around the catchers were 8 times higher in this scale. The specific beam loss spots in the Arc-A were addresses 026, 030, 033, and 037. The addresses 026 and 033 correspond to QFX026 and QFX033 which are focusing quadrupole magnets in the missing bend section where we have a dispersion peak. These beam losses seemed mainly due to off-momentum protons and unavoidable because we didn't have any momentum collimation system. The losses at addresses 030 and 037 found that they occurred in the bending magnets BM030 and BM037 from the results of residual radiation survey, which were upstream side of QDX030 and QDX037, respectively. Though they were suspected to be a leakage from catchers, the origin was not identified. The maximum beam loss point was address 011 which was the following cell of catcher-2.

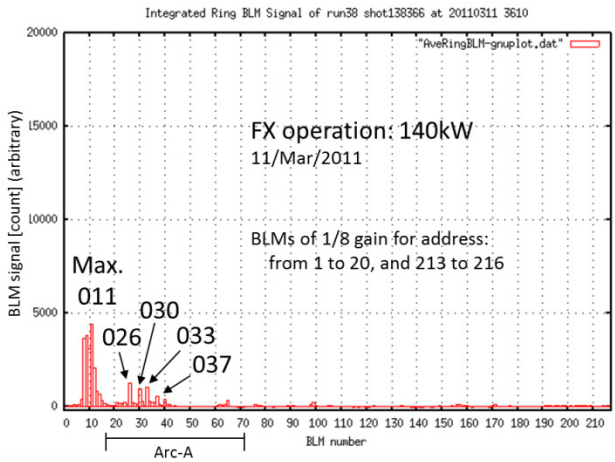

Figure 2: Beam loss distribution in the early days.

FIRST UPDATE

The first update started in 2011 introducing the movable wall-type radiation shield and secondary absorbers made of iron, and remodelling of water cooling system [3] for higher radiation capacity of collimator area. The update of beam collimation system itself was altered in 2012.

Scheme Change

The update plan started from investigating how to add one or more scraper-catchers system. We got the following results:

- Only one more scraper-catchers can be installed.
- Maximum beam loss capacity of collimation system will be limited to 2 kW which is not sufficient.
- As the MR operating point will largely change in future, we have to hold flexibility for tune, that is, betatron phase advance.

The beam loss capacity is limited by the concrete thickness of the accelerator tunnel as shown later. We decided to change the base design of beam collimation system in order to achieve the 3 kW beam loss capacity, that was, we threw the scraper away.

Solid Collimator

In order to remove the halo component at the one-passing of the beam, a collimator with thick jaw was developed. It is an ordinary type of a collimator in the beam transport line, and we call it as a solid collimator in this report. A solid collimator is shown in Fig.3. It consists of a solid iron base with LM guide rail and exchangeable mover unit with a special beam pipe. The central part of a mover unit transversely moves by the slide and lift-up system on the unit top. The beam pipe has a 300 mm long L-type jaw for both planes in the middle, and double bellows at each end in order to displace the jaw to horizontal and vertical directions. The solid collimator was designed to have shorter length than a catcher in order to install two modules in one cell which meant a space between quadrupole magnets. Thus, this collimator is often called as a short collimator. The beam loss capacity is 500 W for one unit.

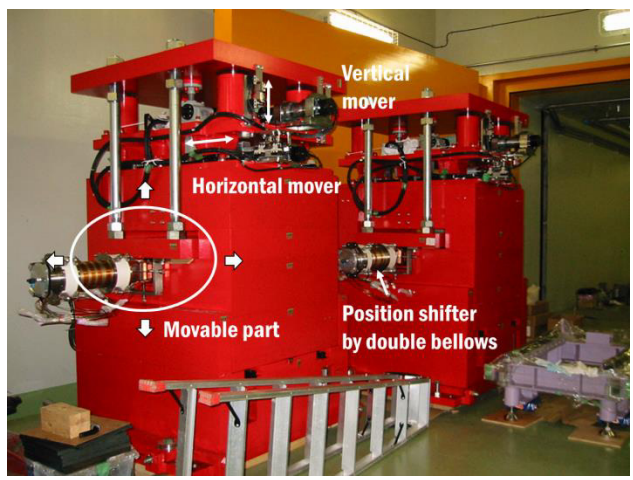

Figure 3: A solid collimator.

Replacement of the Scraper

The scraper was replaced by two solid collimators during three months summer shutdown period in 2012. The remained two catchers were also used as solid collimators. Then, we called them as Col-A, Col-B, Col-2, and Col-3 in this configuration from upstream side of the beam line, in order to avoid confusion from the collimator numbering. The system worked well and the beam loss distribution during the FX operation is shown in Fig.4. The specific beam loss spots existed at addresses 023, 033, and 037. As the beam loss at address 023 newly appeared in this configuration, it was a side effect of the scheme change. The protons scattered by some collimator jaws seemed to make this beam loss because the betatron phase advances in horizontal and vertical planes were about 160+2nπ degrees between them and BM023. The beam loss at address 011 which was the maximum beam loss point largely reduced due to the secondary absorbers installed in 2011.

ISBN 978-3-95450-185-4

The measured dose rate of a residual radiation at the entrance of QFN017 found to be much higher, though the beam loss signal was not remarkable. The scattered protons change their momentum about 0.1% when they passed through a thin material such as a halo-scraper. On the other hand, the protons scattered at the jaw edges of solid collimators lost their momentum up to more than 10%. The off-momentum protons deviated from the design orbit in BM017 which is the first bending magnet of Arc-A, and hit the QFN017. This is also a side effect of the scheme change. It is better to prepare the hadron shield to protect QFN017.

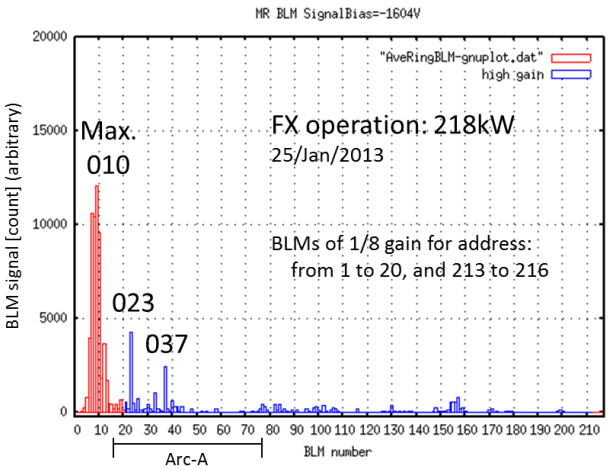

Figure 4: Beam loss distribution after the beam collimation system update in 2012.

SECOND UPDATE

The second update started in 2013. In this case, four solid collimators were additionally installed in addresses 008 and 009, removing the catcher-1 from address 008. Though the installation was planned in September 2013, it was postponed to the January 2014 because of an accident occurred in hadron experimental hall. The polarity and length of jaws were investigated and optimized [4] by using STRUCT code [5]. The material of jaw changed from tantalum to tungsten. The newly installed collimators were called as Col-C, Col-D, Col-E, and Col-F. The total beam loss capacity increased to 3.5 kW with seven collimators. The layout of collimators was confirmed to satisfy the boundary condition on the surface of accelerator tunnel as shown in Fig.5 by PHITS code [6].

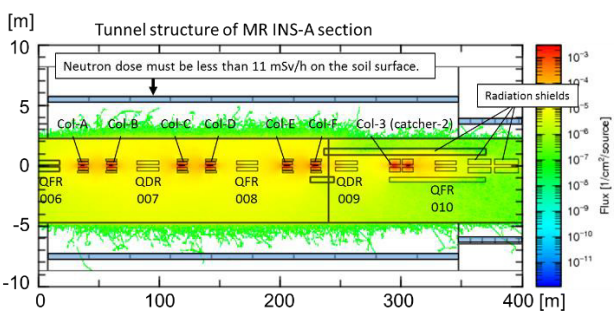

Figure 5: Neutron distribution with seven collimators.

The parasitic beam losses caused by collimator jaws were investigated and it was found that the beam loss tend to occur especially at addresses 023, 030, 037, and 044 where the lattice had a same structure BMnnn + QDXnnn. The fundamental beam responses with seven collimators were studied in April and May [7]. However, a vacuum problem was found on the collimator ducts produced in 2013. The second update was cancelled. Col-C, D, E, F were removed from the beam line, and catcher-1 was reinstalled to the original position, that is, the beam collimation system returned to the configuration in October 2012.

THIRD UPDATE

As the result of investigation with respect to the beam-jaw angle, it suggested that the controllable incline of collimator jaw was important to suppress the loss spots in downstream area.

Four-axis Collimator

The rotation and tilt mechanism were added to the solid collimator in order to change a beam-jaw angle in both planes. We call it as a four-axis collimator. A four-axis collimator is shown in Fig.6. A range of rotation and tilt are set to +/-5 mrad which required by the tunability for MR operating points. The mover unit of this collimator was designed to have compatibility to the existing solid iron base.

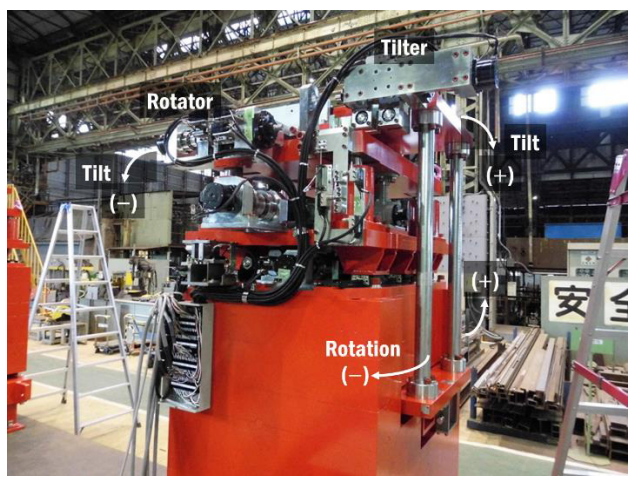

Figure 6: A four-axis collimator.

The beam loss improvement due to the jaw incline system is shown in Fig.7. In this case, only Col-CH was inserted. When a beam-jaw angle was improper, unexpected beam losses appeared not only in Arc-A but also Arc-B. The beam loss distribution in Fig.7 shows the zoom up window below the usual scale one. When the beam-jaw angle was matched, unexpected beam losses were largely suppressed. As shown in Fig.8, some beam loss points have the minimum plateau. On the other hand, some points go to an opposite way like address 026. We optimized the jaw incline for the total beam loss.

ISBN 978-3-95450-185-4

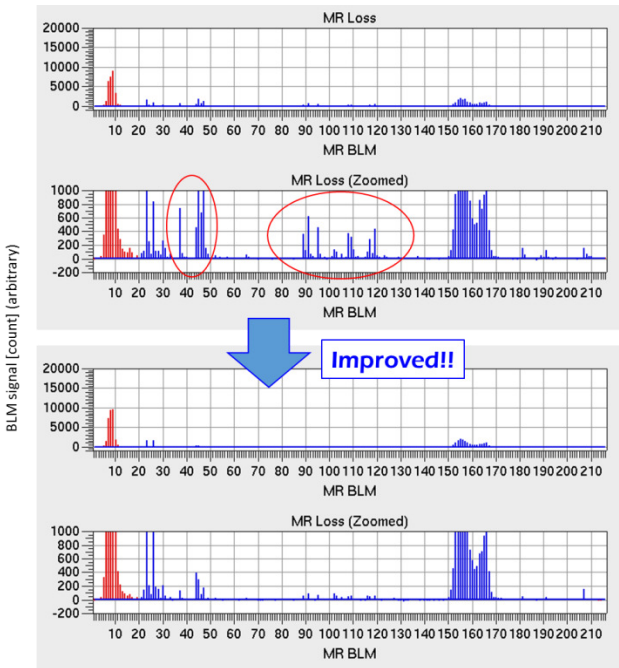

Figure 7: Effect of beam-jaw angle.

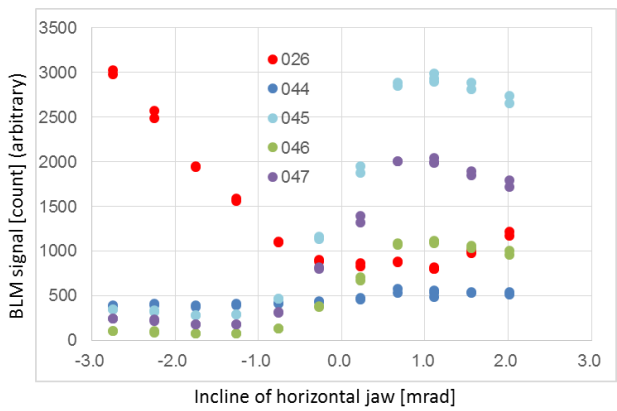

Figure 8: Beam losses as a function of jaw incline.

Operation at (21.35, 21.43)

Since May 2016, we have changed the operating point from (νx, νy) = (22.40, 20.75) to (21.35, 21.43) for the FX operation toward the higher beam power beyond 400 kW. The responses of each collimator jaw were investigated, again. At the beginning, Col-AH and Col-AV were set to the aperture of 70π mm mrad. Here, we call the horizontal jaw of Col-A as Col-AH, the vertical jaw of Col-A as Col-AV, in same way for other collimators hereafter. The specific beam loss spots are addresses 023, 026, 030, 033, 044, 082-084, 102, 116-124, 130, 131, 137, 147, 148, 174, and 202 as shown in Fig.9a. Because the signals from addresses 154 to 168 are reflections from the beam dump, we can ignore them. The mechanism of beam losses in Arc-B and after (from 102 to 202) is not well known. The beam loss at address 023 can be eliminated by using Col-BV as shown in Fig.9b. It is a good thing of this operating point because it was difficult on the previous tune.

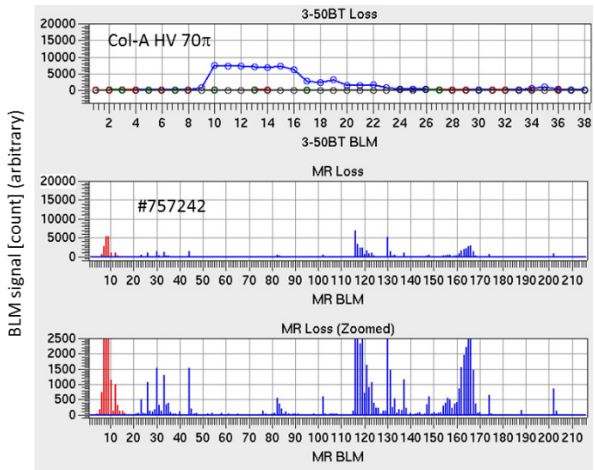

Figure 9a: Beam loss distribution with only Col-A (H and V) on the operating point (21.35, 21.43).

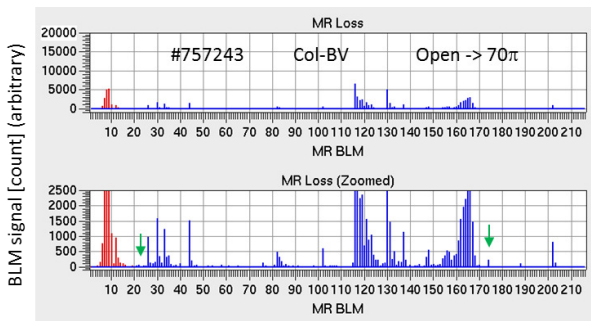

Figure 9b: Effect of Col-BV. Beam loss at address 023 disappeared.

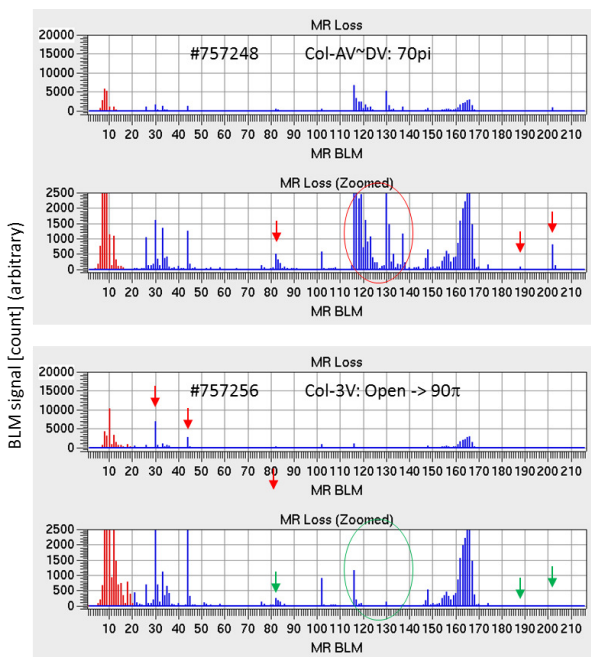

Figure 9c: Effect of Col-3V.

The beam losses from addresses 082 to 203 can be eliminated by using Col-3V as shown in Fig.9c. After the same method was repeated in horizontal plane, the final beam loss distribution with five collimators is shown in

ISBN 978-3-95450-185-4

Fig.9d. The parasitic beam loss spots survived at addresses 030, 044, 102, and 116. The beam losses at addresses 030, and 116 can be reduced by inserting Col-3V more, however, beam losses at addresses 044, 102, around 018, and around 036 increase. Though the Col-3V should be a key device, we cannot use it effectively, because it makes significant parasitic beam losses in the following section especially in Arc-A. It should be replaced by a four-axis collimator. For the user-run of 416 kW FX operation, all the collimators were retuned and the Col-3H and Col-3V were eased.

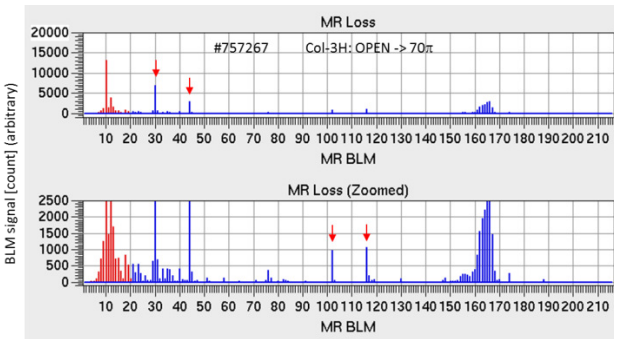

Figure 9d: The final beam loss distribution with all (five) collimators.

FOURTH UPDATE (FUTURE)

We summarize the available devices for the beam collimation: two catchers (Col-2 and Col-3), two solid collimators (Col-A and Col-B), and two four-axis collimators (Col-C and Col-D). Then we assume that we can prepare more two four-axis collimators, that is, we will have up to Col-F for short collimators. The MR operating point will be chosen to (21.35, 21.43) in the next beam time, however, it might be changed in several years later.

Re-arrangement

The requirements for the next update of beam collimation system are taken into account. Though the roll of Col-3 is important, the side effect producing parasitic beam losses is a large problem. It should be replaced by a four-axis collimator. As Col-A and Col-B don't have a incline mechanism, they release scattered protons in the lower reaches. It is good that they remain at the uppermost stream part of beam collimation system. In order to catch the leak protons from Col-A and Col-B by the following collimators, the jaw polarity of Col-C or Col-D should be turned to the opposite side. The catchers should be used before address 009. It is possible to install a catcher and a four-axis collimator in one cell. When we reuse a catcher, the side effect should be considered carefully because the leakage of scattered protons seems to be large. Then, it is good not to use a catcher if the beam loss capacity of collimation system was secured sufficiently.

CONCLUSION

The fourth update is planned in 2018. It consists of the following procedures:

1. Col-3 will be removed.
2. Col-C will be moved to the address 010 instead of Col-3. It will be called as Col-F
3. New Col-C which has a jaw in opposite side will be installed.
4. New Col-E will be installed at upstream side of QDR009.
5. Proton and neutron absorber will be prepared between BM017 and QFN017 in order to protect QFN017.

The final layout of the beam collimation system is shown in Fig.10.

Now, another plan is also under consideration, and we are preparing the beam test in this winter which uses the new halo-scraper. The fourth update will be decided in next year taking that result into account.

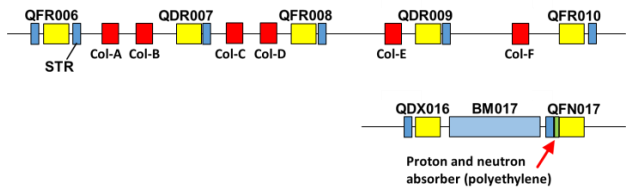

Figure 10: Final layout of beam collimation system.

REFERENCES

[1] Y. Yamazaki et al., "Accelerator Technical Design Report for J-PARC", http://hadron.kek.jp/~accelerator/TDA/tdr2003/index2.html.

[2] S. Igarashi, MOAM6P60, Proc. of HB2016, Malmö, Sweden, Jul. 2016, in this conference.

[3] M. J. Shirakata et al., THPS035, Proc. of IPAC2011, San Sebastián, Spain, Sep. 2011, pp. 3496-3498.

[4] J. Takano et al., WEPS018, Proc. of PASJ9, Osaka Univ., Japan, Aug. 2012, pp. 394-396.

[5] A. Drozhdin, N. Mokhov, "The STRUCT Program User's Reference Manual", FNAL, Dec. 1999.

[6] T. Sato, K. Niita, N. Matsuda, S. Hashimoto, Y. Iwamoto, S. Noda, T. Ogawa, H. Iwase, H. Nakashima, T. Fukahori, K. Okumura, T. Kai, S. Chiba, T. Furuta and L. Sihver, Particle and Heavy Ion Transport Code System PHITS, Version 2.52, J. Nucl. Sci. Technol. 50:9, 913-923 (2013)

[7] M. J. Shirakata et al., WEP016, Proc. of PASJ12, Tsuruga, Fukui, Japan, Aug. 2015, pp. 441-443.

ISBN 978-3-95450-185-4

PATH TO BEAM LOSS REDUCTION IN THE SNS LINAC USING MEASUREMENTS, SIMULATION AND COLLIMATION

A. Aleksandrov, A. Shishlo

Oak Ridge National Laboratory, Oak Ridge, TN 37830 USA

Abstract

The SNS linac operation at its design average power currently is not limited by uncontrolled beam loss. However, further reduction of the beam loss remains an important aspect of the SNS linac tune up and operation. Even small "acceptable" beam loss leads to long term degradation of the accelerator equipment. The current state of model-based tuning at SNS leaves an unacceptably large residual beam loss level and has to be followed by an empirical, sometimes random, adjustment of many parameters to reduce the loss. This talk will discuss a set of coordinated efforts to develop tools for large dynamic range measurements, simulation and collimation in order to facilitate low loss linac tuning.

INTRODUCTION

The SNS linac has demonstrated successful operation at the design average beam power of 1.4 MW with acceptable uncontrolled beam loss [1]. However, beam loss mechanisms study and mitigation methods development remains to be on top of the accelerator physics and beam instrumentation tasks list for the following reasons:

- The "acceptable" uncontrolled beam loss is typically defined by the possibility of hands-on maintenance on the accelerator equipment, which corresponds to a dose rate of <100 mRem/hour at 30 cm from the beam pipe, a few hours after beam shutdown. The actual residual activation of the SNS linac is typically lower than that but the long term damaging effect to the equipment in the tunnel from the prompt radiation is important as well. The observed slow degradation of the plastic cable insulation and water hose materials is certainly due to irradiation. Degradation of the superconducting cavities performance is observed as well and in many cases can be correlated to elevated beam loss in the vicinity. Further beam loss reduction is certainly beneficial for long term stable operation.
- The last step in the process of low-loss linac set up involves manual tweaking of many parameters. This step is poorly documented and can be done by only few experienced people. It can be time consuming in case of a significant change of the linac configuration. A knowledge based set up procedure is highly desirable
- The SNS power upgrade and the Second Target Station plans envision doubling the average beam power and adding another beam pulse flavor. This will require cutting the fractional beam loss at least by half to keep the prompt radiation and activation levels on the same level.
- Model-based methods of beam loss control are crucial for future high power linacs. The SNS linac is an ideal test bench for beam instrumentation and loss mitigation methods development.

Reduction of the beam loss in the SNS Super Conducting Linac (SCL) using knowledge of beam dynamics rather than blind tweaking is our first goal. This paper describes the tools and methods we think will be required to achieve this goal.

BEAM LOSS IN SCL

The main mechanism of beam loss in SCL is believed to be the intra-bunch stripping [2]. The rate of loss is proportional to the bunch density therefore increasing the transverse and longitudinal bunch core sizes is an effective way of beam loss reduction. A low loss SCL optics configuration with enlarged bunch size was found empirically and is still in use for high power operation. Only recently a reliable model of RMS beam dynamics in SCL was established [3], which shows not perfectly RMS matched beam for the current optics. The mismatch causes the beam size maximum and minimum to deviate from the average. The increased bunch size maximum prevents further enlargement of the average size; the decreased bunch minimum size creates local bunch density peaks with larger loss rate. We expect to reduce the intra-beam stripping losses using the model to find a better matched optics. However, any further attempt to increase the average RMS bunch size will be limited by the beam halo touching the beam pipe. The current ratio of the beam pipe aperture to the maximum loss limited transverse bunch size is about $^{76mm}/_{7mm} \approx 11$, indicating presence of a significant halo. As a result, having an accurate control of the RMS bunch size is not enough for decreasing the intra-beam stripping - the halo also needs to be controlled.

The exact origin of the halo is not known but we can tell for sure that at least part of it comes from the injector. The easiest method of reducing this part is collimation (or scraping) of the large amplitude particles in the MEBT (a 2.5MeV transport line between the RFQ and the linac).

It is also possible the halo is formed during acceleration in the warm linac due to effect of the space charge. Matching the bunch RMS Twiss parameters to the lattice is believed to mitigate this effect. If the perfect match is not possible or the halo is formed even in the RMS matched beam then the minimum loss is achieved as a compromise between matching the RMS parameters to

ISBN 978-3-95450-185-4

minimize the intra-beam stripping and matching the halo Twiss parameters to minimize the halo size in SCL. Two of the above mitigation techniques, the halo matching and the MEBT collimation, require or benefit from using halo measurement and computer modeling as will be discussed in the following sections.

We do not discuss the RMS bunch size measurement and modeling techniques in this paper because they are well covered in another presentation at this workshop [3].

HALO MEASUREMENT AND MODELING

The halo, as defined below, has a relatively low charge density. However, the actual number of particles in the halo can be large for high intensity beams. Therefore, in many situations it is not difficult to detect the halo or quantify its density in "more" or "less" terms. The loss monitors of various kinds do this quite reliably in all high intensity accelerators. In the context of this paper we are interested in the different kind of measurements, ones which can be used in computer modeling of the halo. The detailed particle distribution in 6D phase space is generally required to initiate particle tracking using Particle-In-Cell (PIC) codes. In many practical cases, however, an assumption of no coupling between the horizontal, vertical and longitudinal planes can provide sufficient accuracy allowing use of a set of three independent 2D phase space measurements. An experimental verification of this assumption will be discussed in the later sections.

Halo Definition

We will use the definition of halo recently agreed upon by a representative group of beam instrumentation experts [4]. In short, the beam charge distribution inside the vacuum chamber can be separated to three parts: the beam core, the beam halo and the transition (the transition is often called "shoulders", "tails" etc.). These parts are characterized by the charge density relative to the peak density. The boundaries are not defined exactly but for the majority of the cases the beam core boundary is at about 10^{-2} level, the beam halo is at 10^{-4} -10^{-6} level and below. The low boundary of the halo region is decreasing with higher intensity beams, obviously, but the 10^{-4} -10^{-6} range represents a good reference number for a large range of today's accelerators and is the current state-of-the art in beam measurements. In the context of this paper we add to the halo definition a notion that the halo extends far from the beam core, it has a negative effect on an accelerator operation, and this effect has to be mitigated.

Direct Phase Space Measurement at Low Energy

The 2D phase space can be measured relatively easily at low energy (particles have to have sub-millimeter range in a solid material) using the slit-slit scan technique. A general measurement set up is shown in Fig. 1. A similar slit-grid arrangement is often used but the slit-slit arrangement allows achieving the required dynamic range much easier [5] because of the possibility of using a single high quality detector. In addition, this configuration allows using various mitigation techniques to suppress the effect of slit scattering - the main factor limiting the dynamic range of the system. For example, the SNS MEBT emittance scanner uses a Faraday cup located downstream of the DTL tanks. The H^- particles convert to proton when scattered by the slit edge, arrive to the DTL entrance in the decelerating phase and therefore are lost before reaching the detector. An example of a large dynamic range profile generated from the measured 2D emittance is shown in Fig.2. The measurements using large bandwidth current detector are shown by the solid lines; the measurements using charge integration from a neutron detector are shown by the circles. As one can see the systems has sufficient dynamic range for measuring halo if good temporal resolution is not required.

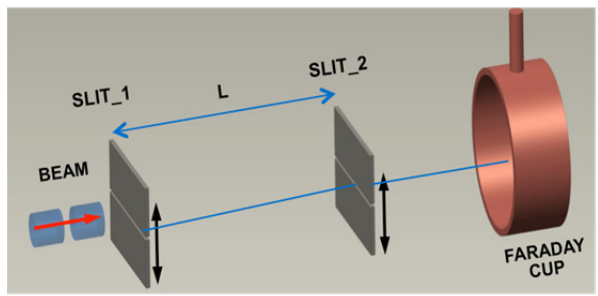

slit-slit emittance scanner

Figure 1: A schematic view of a slit-slit emittance scanner.

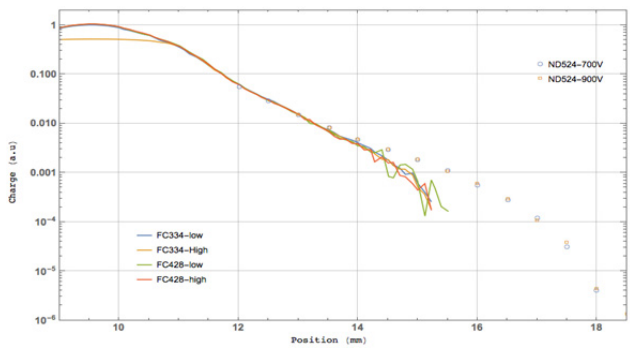

Figure 2: An example of large dynamic measurement with the SNS MEBT slit-slit system.

Direct Phase Space Measurement at High Energy

The only method for direct emittance measurement at high energy successfully demonstrated to date is the laser wire emittance scanner [6]. This method is suitable for H^- beams only. The best currently achieved dynamic range of 10^3 can be possibly improved by an order of magnitude but further extension to the halo region is limited by the laser beam quality. Nonetheless, this diagnostic can be very useful for benchmarking other techniques described below.

Reconstruction of 2D Phase Space Distribution from a Set of 1D Projections

The so-called phase space tomography allows finding the 2D emittance using several 1D projections (profiles)

ISBN 978-3-95450-185-4

measured at different angles in phase space. The method has been demonstrated for transverse and longitudinal phase space. The dynamic range of the reconstructed 2D emittance depends on the dynamic range of the profiles and the method of reconstruction. An example of a reconstruction with 10^3–10^4 dynamic range which used four profiles measured by a wire scanner with 10^4 dynamic range and several iterations of the MENT algorithm is shown in Fig. 3. A reasonably good agreement is observed down to the 10^{-4} level. This result is very encouraging but further development of the method is required to extend the dynamic range to the halo region.

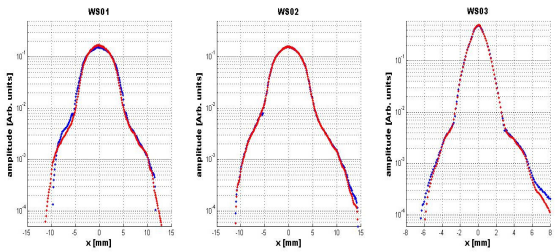

Figure 3: Comparison of measured (red) and obtained from results of 2D emittance reconstruction with large dynamic range (blue).

An example of using the reconstruction technique for measuring the effect of a transverse collimation in the MEBT on the beam distribution at the end of SCL is shown in Fig.4. The panel (a) shows the horizontal emittance measured by the MEBT emittance scanner with no collimators. The panel (b) shows the emittance with the left collimator plate inserted to intercept ~1-2% of the beam charge. The panel (c) shows the particle distribution generated from the emittance obtained using the MENT reconstruction for four profiles measured in the HEBT. The red dots correspond to the case with no collimation and the blue dots correspond to the case with one scraper inserted. The emittance reduction is obvious from the plot. The collimated distribution looks symmetric left to right despite a significant asymmetry in the initial distribution. The most plausible explanation is a complete homogenization of the distribution due to non-linear forces during transport through the linac. But it is also possible that the emittance reconstruction process is not accurate enough to reveal the asymmetry. This example emphasizes the importance of measurements benchmarking when dealing with low level details of beam distribution. The laser emittance measurements can be used to validate the MENT reconstruction at least within the dynamic range of 10^3–10^4.

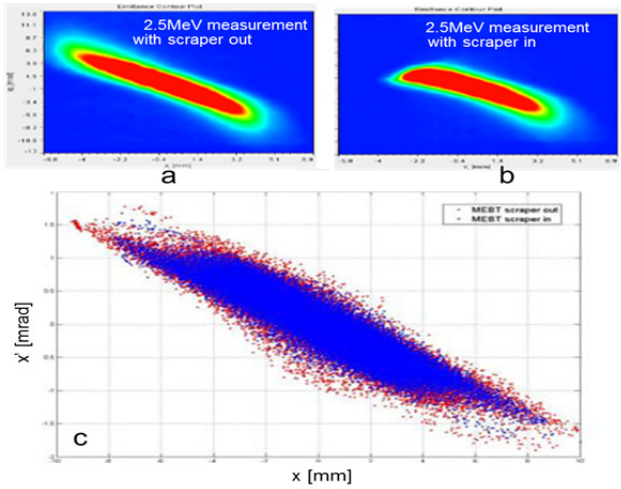

Figure 4: An example of emittances reconstruction from 1D profiles as explained in the text.

Characterization of Particles Distribution in Phase space

A convenient way of visualizing general properties of the 2D phase space distribution is plotting the phase space density vs. the normalized radius according to the following procedure:

- generate N particles using measured 2D phase space distribution as a probability function as illustrated by the panels (a) and (b) in Fig. 5.
- transform the particles coordinates x, x' to new coordinates: $x_n = {}^{x}/_{\sqrt{\beta_{RMS}}}$;
- $x_n' = {}^{\alpha_{RMS} \cdot x}/_{\sqrt{\beta_{RMS}}} + x'\beta\gamma\sqrt{\beta_{RMS}}$, where

  $\alpha_{RMS}, \beta_{RMS}$ are the RMS Twiss parameters, $\beta = {}^{v}/_{c}$, and γ is the relativistic factor
- calculate $r = \sqrt{x_n^2 + x_n'^2}$
- count number of particles N_r within $r \cdot dr$ circular bands as illustrated by the panels (c) and (d) in Fig.5.
- plot $n(r) = {}^{N_r}/_{2\pi r dr}$ vs. r in semi log scale as illustrated by the panel (d) in Fig.5.

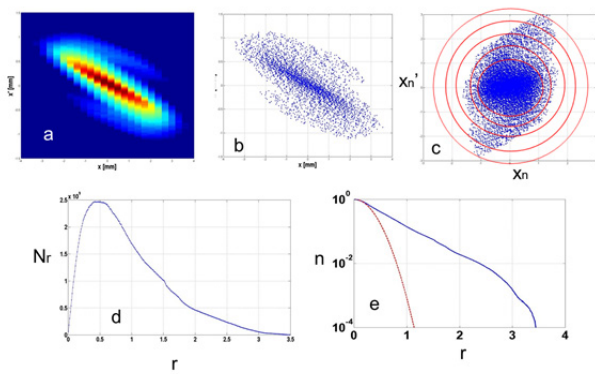

Figure 5: An illustration of making a phase space density plot generation as explained in the text.

ISBN 978-3-95450-185-4

The plot of n vs. r is independent of the beam energy or location along the beam line. It can be used for comparing general distribution properties for different accelerators or even different particles species. An example of phase space density plots for the distributions from Fig. 4c is shown in Fig. 6. A reduction of the tail in the HEBT due to scraping in the MEBT is clearly seen but the dynamic range is not sufficient to make any conclusion about the halo.

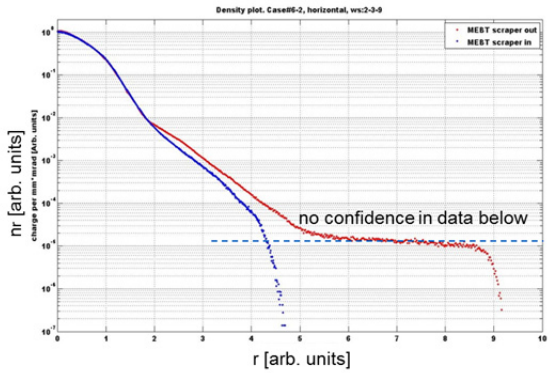

Figure 6: A phase space density plot for beam distributions in Fig.4c.

BEAM LOSS REDUCTION USING COLLIMATION AT LOW ENERGY

There is experimental evidence of beam halo already present in the SNS MEBT. This means it is created in the ion source and the RFQ, which do not have any practical means of beam distribution control. The most efficient way to clean the beam from the halo formed in the injector is to collimate it at as a low an energy as possible while the particles can be still stopped by a relatively thin block of a material. A typical low energy collimator is shown in Fig. 7. The problem usually is to find a free space in the beam line. As a result the collimators are often placed where space is available and the beam line optics needs to be adjusted for effective collimation, i.e. the halo needs to have the correct orientation in phase space. This is much easier to achieve if 2D emittance measurements of the halo are available as illustrated by Fig. 8 where the vertical emittance at the scrapers location in the SNS MEBT is shown. The scraper edges shown by the dashed lines are at 90° in phase relative to the halo, which explains why the vertical scraper at this location turned out to be not useful for reducing beam loss. In order to make the collimator efficient the emittance needs to be rotated by 90° while preserving other constraints of the MEBT optics: phase advance between the RFQ exit and the horizontal collimators, the required Twiss parameters at the MEBT exit, the available quadrupole magnets strength. An example of the MEBT optics modification satisfying the requirements is shown in Fig. 9 and the corresponding emittance rotation in Fig. 10. It was not easy to find this solution even with help of a model and is practically impossible by an empirical tuning. It has not been proved experimentally yet that this new optics allows for lower losses in SCL compared to the original optics. The scraper efficiency should be better but it is possible that more halo will be created due to the large vertical beam size variation.

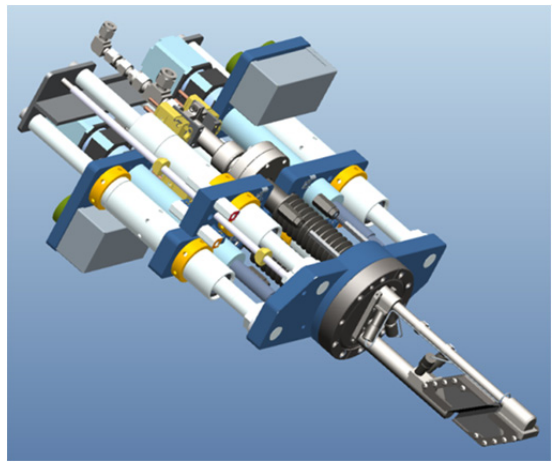

Figure 7: A model of the SNS MEBT vertical scarper.

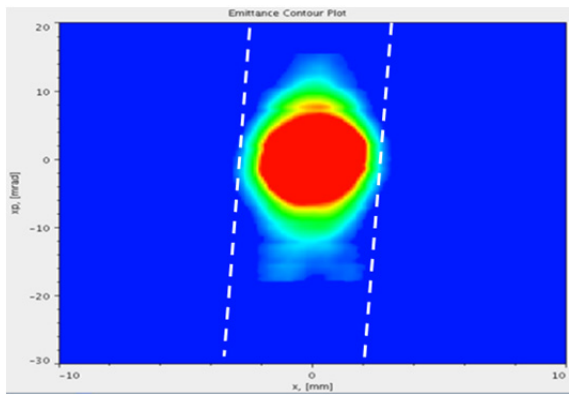

Figure 8: The measured vertical MEBT emittance orientation relative to the scraper edges (dashed lines).

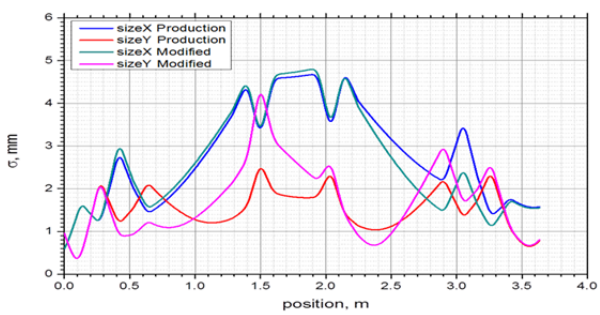

Figure 9: The measured vertical MEBT emittance orientation relative to the scraper edges (dashed lines).

ISBN 978-3-95450-185-4

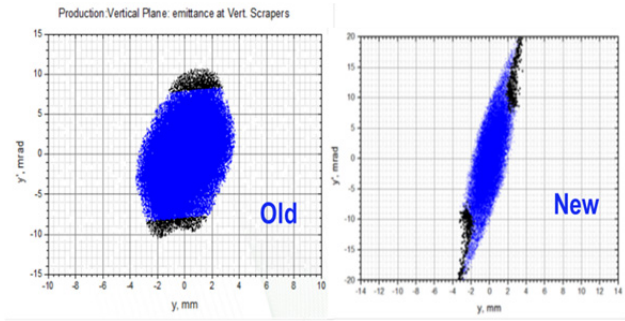

Figure 10: The measured vertical MEBT emittance orientation relative to the scraper edges (dashed lines).

SUMMARY AND FUTURE PLANS

A number of measuring tools, data processing techniques and simulation codes [3] are been developed to facilitate model based beam loss reduction in SNS SCL. There need to be a way to characterize the beam halo in a form suitable for use in simulation codes. Ultimately, the 6D phase space distribution is required but only 1D or 2D projections can be measured with sufficiently large dynamic range. We are equipping two experimental facilities for directed development and exploration of methods of beam distribution reconstruction from lower dimensionality projections – one for low beam energies, and one for high beam energies.

1. The SNS HEBT beam line having a straight section containing several individually settable quadrupole magnets, five large dynamic range wire scanners and a laser wire emittance scanner is an ideal test bench for large dynamic range MENT or other reconstruction methods development. A layout of the beam line is shown in Fig.11.
2. The SNS BTF [7] has equipment for direct measurement of 6D phase space distribution. This experiment will verify the accuracy of the assumption of un-correlated degrees of freedom in the input beam and provide a benchmark tool for various methods of constructing 6D distributions out of lower dimensionality projections. A FODO beam line is being designed to repeat the Los Alamos LEDA experiment on halo development [8]. This experiment will test the importance of RMS core matching for preventing halo formation in a beam transport line. A layout of the SNS BTF is shown in Fig. 12.

ACKNOWLEDGEMENT

This manuscript has been authored by UT-Battelle, LLC, under Contract No. DE-AC0500OR22725 with the U.S. Department of Energy. The United States Government retains and the publisher, by accepting the article for publication, acknowledges that the United States Government retains a non-exclusive, paid-up, irrevocable, world-wide license to publish or reproduce the published form of this manuscript, or allow others to do so, for the United States Government purposes. The Department of Energy will provide public access to these results of federally sponsored research in accordance with the DOE Public Access Plan (http://energy.gov/downloads/doe-public-access-plan).

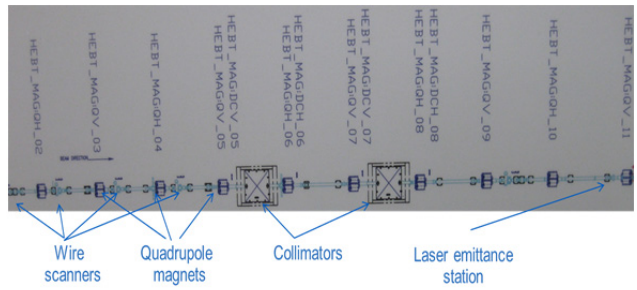

Figure 11: A layout of a beam line for large dynamic range tomographic reconstruction techniques development.

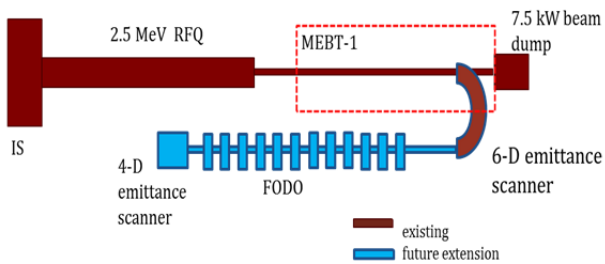

Figure 12: A layout of the SNS Beam Test Facility.

REFERENCES

[1] S. Cousineau, 'A Fifteen Years Perspective on the Design and Performance of the SNS Accelerator,' presented at High Brightness 2016 Workshop (HB2016), Malmo, July 2016, paper MOAM4P40.

[2] A. Shishlo *et al*., Phys. Rev. Lett. 108, 114801 (2012).

[3] A. Shishlo, 'Model Benchmark With Experiment at SNS Linac,' presented at High Brightness 2016 Workshop (HB2016), Malmo, July 2016, paper WEPM2Y01.

[4] A.S. Fisher, "Summary of the 2014 Beam-Halo Monitoring Workshop", in *Proc. IBIC'15,* paper THBLA01, pp. 630-636.

[5] A. Aleksandrov *et al.*, "Diagnostics Tools for Beam Halo Investigation in SNS Linac", *Proc. LINAC'12,* paper THPB013, pp. 873-875.

[6] Y. Liu *et al*., *NIM* A 675(2012).

[7] A. Aleksandrov *et al*., "Status of New 2.5 MeV Test Facility at SNS", in *Proc. LINAC'14,* paper THPP108, pp.1105-1107.

[8] C. Allen *et al.*, *PRST-AB* 5, 124202, 2002.

ISBN 978-3-95450-185-4

SIMULATIONS AND DETECTOR TECHNOLOGIES FOR THE BEAM LOSS MONITORING SYSTEM AT THE ESS LINAC

I. Dolenc Kittelmann*, T. Shea, ESS, Lund, Sweden

Abstract

The European Spallation Source (ESS), which is currently under construction, will be a neutron source based on 5 MW, 2 GeV superconducting proton linac. Among other beam instrumentation systems, this high intensity linac requires a Beam Loss Monitoring (BLM) system. An important function of the BLM system is to protect the linac from beam−induced damage by detecting unacceptably high beam loss and promptly inhibiting beam production. In addition to protection functionality, the system is expected to provide the means to monitor the beam losses during all modes of operation with the aim to avoid excessive machine activation. This paper focuses on the plans and recent results of the beam loss studies based on Monte Carlo (MC) simulations in order to refine the ESS BLM detector requirements by providing the estimations on expected particle fluxes and their spectra at detector locations. Furthermore, the planned detector technologies for the ESS BLM system will be presented.

INTRODUCTION

The ESS is a material science facility, which is currently being built in Lund, Sweden and will provide neutron beams for neutron−based research [1]. The neutron production will be based on bombardment of a tungsten target with a proton beam of 5 MW average power. A linear accelerator (linac) [2] will be used to accelerate protons up to 2 GeV and transport them towards the target through a sequence of a normal conducting (NC) and superconducting (SC) accelerating structures (Fig. 1).

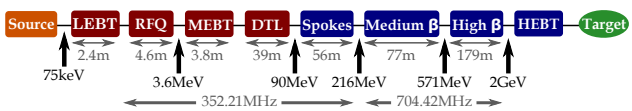

Figure 1: The ESS linac layout. Red color represents the NC and blue the SC parts of the linac.

Rapid startup and reliable operation of the linac requires a certain suite of beam instrumentation. As part of this suite, the BLM system will detect high beam losses potentially harmful to the linac components and inhibit beam production before damage occurs. Additionally, the system provides information about the particle rates during all linac modes of operation in order to enable tuning and keep the machine activation low enough for hands−on maintenance.

ESS BLM DETECTOR TECHNOLOGIES

The ESS BLM system will employ 3 types of detectors. In the SC parts of the ESS linac, parallel plate gas ionization chambers (ICs) developed for the LHC BLM system [3] will be used (Ionization Chamber based BLM − ICBLM). These were chosen due to their availability as part of a joint procurement with CERN and other facilities. Background due the RF cavities must be taken into account when using ICs in a linac. This background is mainly due to the electron field emission from cavity walls resulting in bremsstrahlung photons created on the cavity or beam pipe materials [4]. The background levels are difficult to predict numerically as they depend on the quality of the cavities, beam loading, operation conditions and time. It is planned to asses this experimentally at the ESS RF test stand in Uppsala with the spoke cavities and at the CEA Saclay with the elliptical cavities. Nevertheless, simplified energy spectra estimations show that photons with energies up to tens of MeV can be expected [5]. With a characteristic cut−off value for the photons of ∼2 MeV for the LHC ICs [3], background sampling and subtraction is needed for the ICBLM system. In addition to the primary IC-based system, some Cherenkov radiation detectors may also be deployed. These offer inherent rejection of the RF cavity background.

BLM detectors are planned also in the MEBT and DTL sections of the NC ESS linac. Here the particle fields outside the tanks and beam pipe are expected to be dominated by the neutrons and photons. With RF cavity background still a possible source of photons in these sections, a neutron sensitive detector should be considered. Special micromegas detectors are in development [6] by the micromegas team from the CEA Saclay, designed to be sensitive to fast neutrons, but not to thermal neutrons, X−rays or γ−rays.

ESS BLM SIMULATIONS

MC simulations for tracking of the lost protons are needed in order to address several points crucial for the design of a BLM system, namely: system response time limit, detector locations and dynamic range of the system. In addition to this, they provide a tool for determination of the initial machine protection threshold settings used during the startup period. Furthermore, the MC simulations serve to estimate the anticipated response of the system during the fault studies that will verify the BLM system response. The focus of this chapter are the aforementioned first three simulation tasks, while the last two are not discussed here.

Most of the results presented here are focused on the NC linac, and will provide a basis for the nBLM specifications. The anticipated neutron and photons spectra at the detector locations are required to finalize the micromegas detector design. Previous efforts focused primarily on the SC linac; thus some preliminary results valid for the ICBLM already exist.

* irena.dolenckittelmann@esss.se

ISBN 978-3-95450-185-4

The Geant4 (version 10.00.03, QGSP_BIC_HP physics list) simulation framework [7] developed by the ESS neutron detector group has been used to perform the ESS BLM simulations. No tracking cuts have been employed, while production cuts were set to 10 µm for e^+, e^- and photons.

A Geant4 based ESS linac geometry (Fig. 2) has been created with certain element models (quadrupole magnets, spoke and elliptical cavities and mid parts of the elliptical cryomodules) adapted and changed where needed from the existing ROOT [9] based ESS linac model used for shielding calculations [10]. Magnetic field maps [11] outside the beam pipe for the quadrupole magnets in the SC linac are included in the simulation due to their important impact on the simulation results for the detectors placed close to the these magnets. The linac elements' apertures, lengths and positions follow the values in the 2015 baseline beam physics lattice of the ESS linac. Due to their importance for the low energy parts of the neutron spectra, tunnel walls are included in the simulations. Current simplifications to the geometry include:

- Simplified quadrupole magnet geometry in the yoke and coil length.
- Simplified model of the DTL gaps, where 1−2 cylindrical shapes on each side of the gap are used. The value of (gap length)/(cell length) is the same for all cells in one tank and taken as the average value in the tank.
- Model for cavities in HB sections is calculated by scaling part of the MB cavity profile.
- The following elements are currently not included: post−couplers in the DTL, beam instrumentation devices, correctors, supports, MEBT chopper and chopper dump, spoke cavity insertions.

Certain set of inputs are needed in order to perform the BLM simulations. Ideally one would have a list of accidental beam loss scenarios with corresponding loss maps together with a list of the elements that must be protected along with their damage thresholds. In addition to this, the anticipated loss maps during the normal operation are needed as the lowest detectable BLM signal levels are expected during these periods. However, due to the large number of possible accidental scenarios and operating conditions, some simplifications and assumptions are needed. These are considered in the following subsections in connection to the discussions of the worst case accidental beam loss scenario and detector locations.

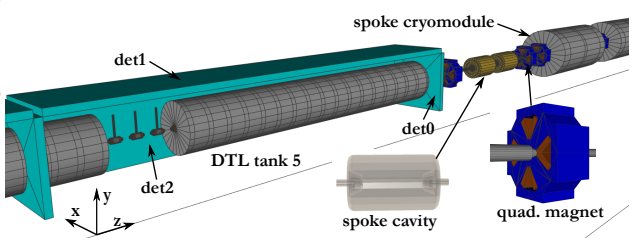

Figure 2: Geant4 based geometry of the ESS linac used in the BLM simulations, focused on the last tank of the DTL section. Phantom detector modules surrounding the tank are marked as det0, det1 and det2. Parts of the volumes are opened for a better view.

Response Time

The required response time of the BLM system was set in the past to ∼5 µs in the NC (MEBT and DTL) and ∼10 µs in the SC parts of the linac [12]. The numbers are based on simplified melting time calculations, where a beam of protons with a uniform profile hits a block of material under perpendicular incidence angle. No cooling is considered in these calculations. The numbers have recently been checked with the updated beam parameters and a Gaussian beam profile. These results support the 10 µs requirement in the SC parts of the linac, and as mentioned below, other damage mechanisms to the SC cavities may mandate an even lower latency. In the NC section, the calculated melting time values of 3−4 µs imply even stronger demands on the response time (Fig. 3). The latter has additionally been confirmed with a MC simulation.

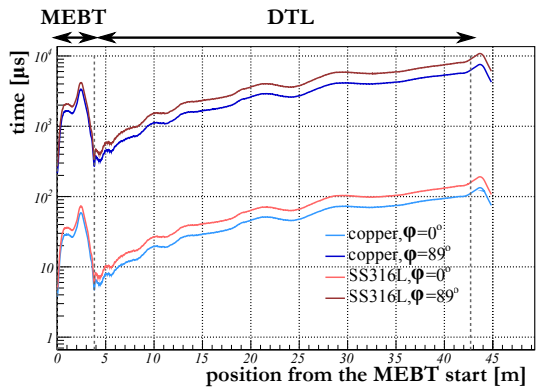

Figure 3: Time to melt a block of copper (blue) or stainless steel (red) under constant irradiation with a proton beam under perpendicular incidence (φ=0°) or a very shallow angle.

Worst case accidental beam loss scenario Melting time depends on the beam incidence angle; thus, the validity of the assumption of the perpendicular incidence as the worst case scenario can be argued. This poses a question on what the worst case accidental loss is, which translates to the need to understand what is the least shallow incidence angle of the most focused beam that can be expected to hit the aperture. This is expected to occur for a particular case of incorrect settings for a set of corrector magnets. Time consuming beam dynamics simulations are required in order to asses this. Therefore the following strategy to find the worst case angle has been suggested [13] and adopted here:

- Increase one of the initial coordinates x, x', y or y' at the beginning of a linac section until the beam centroid starts touching the aperture.

ISBN 978-3-95450-185-4

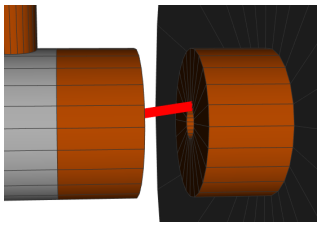

Figure 4: Example of beam hitting a tube in the DTL tank 1 (incidence angle set to 150 mrad).

- The highest deflection found along the section is taken as the worst case angle.

An assessment of this type has been performed [13] for the DTL and HEBT sections (Table 1).

Table 1: Worst Case Beam Incidence Angle (Courtesy of R. Miyamoto)

ESS Linac section	Peak x' or y' [mrad]
DTL tank 1	50
DTL tank 2−3	15
DTL tank 4−5	10
HEBT	20

Implications on the response time Depending on the gap distance, an incidence close to perpendicular is potentially possible in the first DTL tank due to the almost flat surfaces between the gaps (Fig. 4). Given the worst case angle as currently understood, this is geometrically possible though highly improbable as it requires the incidence angle larger than about 3 times the worst case one in the simplified DTL geometry used in the BLM simulations. This deserves further studies with a more accurate mechanical model of the DTL.

In order to determined the time response limit in the SC sections, it is foreseen to check the beam pipe melting time with a focused beam under worst case angle discussed above. However a degradation of the cavities is observed at the SNS after losing a <15 µs pulse of 26 mA beam about 10 times per day [14]. This motivates setting the response time limit for the ESS SC linac significantly lower than 15 µs.

Detector Locations

The most suitable set of detector locations and their count ensures that the system is not blind to any of the accidental losses. In the absence of a complete list of accidental losses, the following strategy is assumed in order to select detector locations:

- A set of localized loss scenarios is considered, each with a selected beam energy, incidence angle and loss location along the linac section under investigation.
- The incidence angle is varied from ∼1 mrad up to the worst case angle as discussed in the previous subsection, while the lost proton energy is varied from the lowest anticipated to the nominal value. The lowest anticipated energy depends on the section in question and is planned to be assessed in the near future.
- By using phantom detectors (with vacuum as the volume material) surrounding the section, a simulation for each of the loss scenarios is run to produce hit maps of incoming neutrons (in case of nBLM) or all particles (in case of ICBLM).
- Hit map mean and RMS values along the section length are extracted for each of the loss scenarios and compared with the origin of the loss. The best detector locations can be extracted by comparing the results from all simulation runs.

A strategy for selecting the detector locations based on optimization methods combined with genetic algorithms has been tried in the past, though only for the case of the ICBLMs. It is planned to augment this work in the near future with the above mentioned strategy, however as previously mentioned, the current efforts are focused on the nBLMs due to the need to develop specifications for this detector design.

As an example, some preliminary hit maps are presented in Fig. 5 for two detector volumes placed around the DTL tank 1. Here, a focused beam was generated at 3 different locations along the tank. A beam angle of 50 mrad with respect to the z−axis was selected while the nominal energy at the loss location was taken as the proton energy. The mean values along the z−axis agree to ∼0.02−0.8 m with the loss location for both of the detectors, while RMS values of ∼1.4.−1.5 m are observed. The same observations holds if a detector volume is placed below the tank, though as expected, this detector yields the lowest hit rate. These results look promising in the view of the BLM system's capability to localize the loss locations, and they justify the need for further simulation.

Dynamic Range

Once the detector locations are known, the dynamic range of the BLM system can be determined by studying two extreme cases:

- **Highest expected hit rate.** This case marks the worst case accidental loss. By assuming the worst case angles discussed in subsection focused on the response time, the simulated particle hit rate can be used to estimate the upper limit of the system's dynamic range.
- **Lowest expected hit rate.** Typically the lower limit of a BLM system dynamic range is set to a fraction of a 1 W/m, which is arguably coming from the activation limit for the hands−on maintenance. To support tuning and optimization, it is also useful to asses the expected signals for example operating scenarios, when certain areas may have loss levels well below the activation

ISBN 978-3-95450-185-4

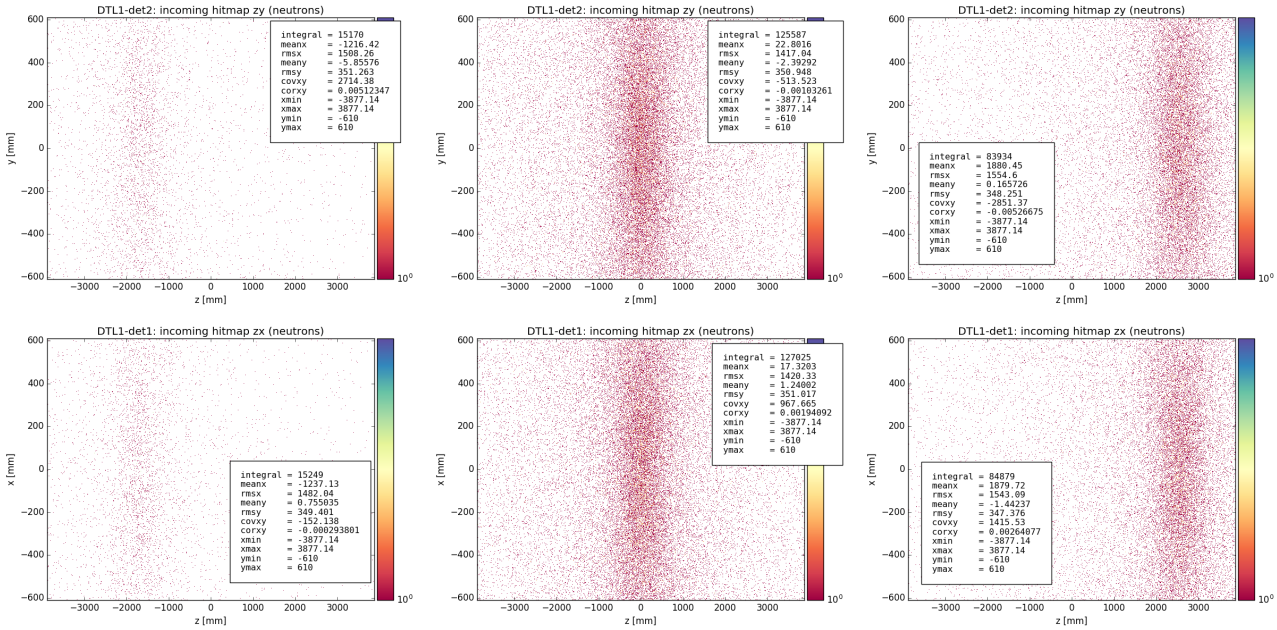

Figure 5: Simulated neutron hit maps for 3 different loss locations along the DTL tank 1 scored in detector volumes det2 (top) and det1 (bottom). See Fig. 2 for the detector locations.

limit. The lower end of the dynamic range can than be set to a fraction of this signal.

Expected loss map during normal operation Beam dynamics error studies have been performed on the 2015 baseline beam physics lattice of the ESS linac [15, 16]. Here the errors were applied to 10000 machines, each with 600000 macro−particles. The error tolerances were set to 100 % of the nominal values, except for the dynamic error (RF jitter), where it was increased to 200 %. The results of this study (Fig. 6) are used as the input to the BLM MC simulation of lost protons and are assumed to represent a realistic scenario of ESS linac beam loss during normal operation.

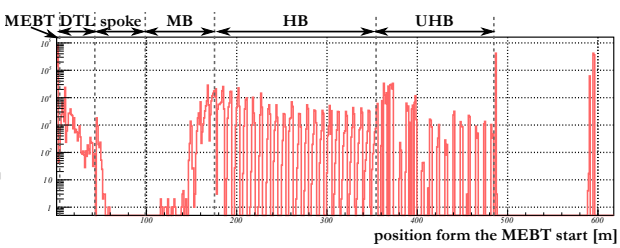

Figure 6: Distribution of the lost protons along the ESS linac resulting from the ESS linac error study [15, 16], which served as an input loss map for the BLM simulation of the linac normal operation.

Normal operation versus 1W/m loss In order to assess the difference between the normal operation and 1 W/m loss, BLM MC simulations of lost protons have been performed for both cases with the following settings:

- **Normal operation loss.** Lost protons were sampled from the lost particle distributions (azimuth and polar angle of the particle momentum, azimuth angle of the particle position and particle energy) obtained from the aforementioned mentioned error study. This approach offers no limitation on the statistics of the BLM simulation and no need for assumptions on the lost particle distributions. Correlation was observed between the azimuth angles for the lost proton position and momentum direction, which was taken into account in the simulation as well.

- **1 W/m loss.** A uniform distribution of lost protons was assumed along the linac. Particle momentum polar angle from the beam axis was fixed to 1 mrad while the particle position azimuth angle was sampled uniformly around the aperture. Particle energy was set to the nominal value at the lost proton location.

The linac geometry used included MEBT and DTL sections together with the first 4 cryomodules of the Spoke section.

The simulated neutron spectra in units of neutrons/s hitting a detector volume for the case of the normal operation and 1W/m loss in the DTL tanks are shown on Fig. 7. For the case of the uniform loss, an increase in incoming neutrons with the tank number is observed which can be attributed to the increase of the neutron production cross−section with increasing proton energy. On the other hand, the normal operation results exhibit the lowest neutron fluxes in the last two tanks. The latter can be explained by emittance decrease with increasing beam energy. By comparing the results for the two loss scenarios, it can be seen that all 1 W/m spectra

ISBN 978-3-95450-185-4

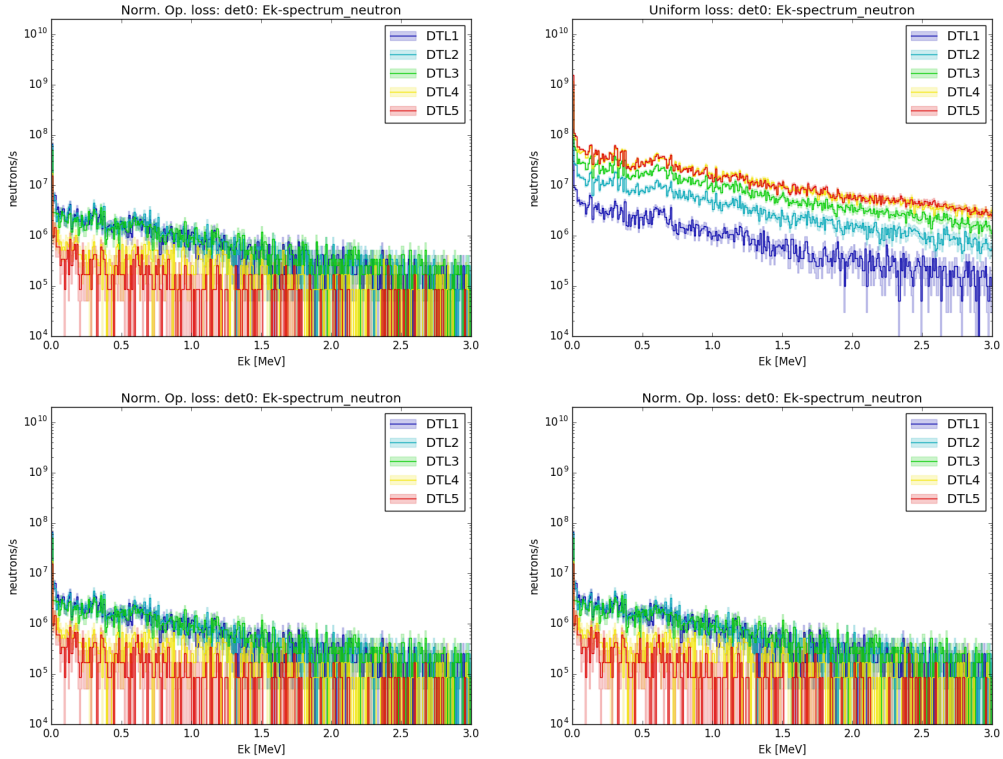

Figure 7: Simulated neutron energy spectra hitting the detector volume det0 (top) and det1 (bottom) for the case of normal operation (left) and 1W/m (right) loss. Different color marks the different DTL tank. See Fig. 2 for the detector locations.

lie above the corresponding ones for the case of normal operation. The difference increases with the tank number from 0 to ~1.5 order of magnitude. The exception is the det0 in the DTL tank1, where the 1 W/m curve is approximately similar to or lies slightly below the corresponding normal operation results.

Dynamic range specification Following the discussion above, once the nBLM detector locations are fixed, the lower limit of the dynamic range for the case of the nBLMs can be set to a fraction of the neutron flux expected during the normal operation. The upper limit on the other hand can be estimated by assuming total beam loss. Since protection should be provided under conditions with maximum damage potential, a focused beam under worst case incidence angle is assumed.

For the case of the ICBLMs, preliminary values have been set in the past [17] by requiring the BLM to able to measure 1 % of the 1 W/m loss during normal operation and up to 1 % of the total beam loss. This gave an estimation for the IC output current range, which was found to be from ~800 mA to few mA. It is planned to re−asses these values in the near future once the ICBLM detector locations are set as well.

SUMMARY

The 3 types of detector technologies planned for the ESS BLM system were presented. In SC parts of the linac ICs will be used as the primary BLM detectors (ICBLMs). It is foreseen to explore an option to use a Cherenkov radiation sensitive detectors as complementary BLMs to the ICBLMs in the SC parts. The advantage of these detectors lies in their low sensitivity to the RF cavity background. On the other hand, novel neutron sensitive micromegas detectors will be used as the BLMs in the NC parts of the linac.

The second part of the paper was focused on the MC simulations of lost protons, which are a necessary tool when building a BLM system. In the past all simulation efforts were focused on the SC linac. Currently the focus has turned to the NC parts due to the need for the inputs in order to design the nBLM detectors.

Strategies to determine the specifications (response time, dynamic range and detector location) of the ESS BLM system were discussed. Selected preliminary results for the NC linac parts were presented together with the past results which were exclusively focused on the SC linac.

ACKNOWLEDGEMENT

The authors would like to thank M. Eshraqui, Y.I. Levinsen and R. Miyamoto (ESS) for their help in the form of beam physics discussions and studies needed to perform the BLM MC simulations. Additionally the authors wish to thank R. de Prisco (ESS) and I. Tropin (FNAL) for the help with the ESS linac geometry. Authors are also thankful to T. Kittelmann (ESS) for providing the support with the Geant4 computing framework.

ISBN 978-3-95450-185-4

REFERENCES

[1] "ESS: Technical Design Report", ESS report ESS-0016915 (2013).

[2] M. Eshraqi *et al.*, "The ESS Linac", in *in Proc. IPAC'14*, Dresden, Germany, paper MOXAP07.

[3] M. Stockner *et al.*, "Classification of the LHC BLM Ionization Chamber", in *Proc. DIPAC'07*, Venice, Italy, paper WEPC09.

[4] E. Donoghue *et al.*, "Studies of Electron Activities in SNS-Type Superconducting RF Cavities", in *Proc. SRF'05*, Ithaca, NY, USA, paper TUP67.

[5] B. Cheymol, "ESS wire scanner conceptual design", ESS report ESS-0020237 (2016).

[6] T. Papaevangelou, "Micromegas detector applications for beam diagnostics", CERN BI seminar, CERN, Geneva, Switzerland (2016), http://indico.cern.ch/event/540799/

[7] T. Kittelmann *et al.*, "Geant4 Based Simulations for Novel Neutron Detector Development" CHEP 2013, Amsterdam, Netherlands (2013), doi:10.1088/1742-6596/513/2/022017, http://iopscience.iop.org/article/10.1088/1742-6596/513/2/022017/meta

[8] GEANT4 collaboration, http://geant4.web.cern.ch/geant4

[9] https://root.cern.ch/

[10] N. Mokhov *et al.*, "ESS accelerator prompt radiation shielding design assessment", ESS report ESS-0052477 (2016).

[11] ESS reports ESS-0040133, ESS-0040134

[12] L. Tchelidze, "How Long the ESS Beam Pulse Would Start Melting Steel/Copper Accelerating Components?", ESS report ESS/AD/0031 (2012) http://docdb01.esss.lu.se/DocDB/0001/000168/001/Time_Response_Requirements_BLM.pdf

[13] R. Miyamoto, private communication.

[14] W. Blokland *et al.*, "A new differential and errant beam current monitor for the SNS accelerator", in *Proc. IBIC'13*, Oxford, UK, paper THAL2.

[15] Y.I. Levinsen, "ESS 2015 Baseline Lattice Error Study", ESS report ESS-0049433 (2016).

[16] Y.I. Levinsen *et al.*, "Beam Dynamics Challenges in the ESS linac", presented at HB'16, Malmö, Sweden, paper TUAM3Y01.

[17] L. Tchelidze *et al.*, "Beam Loss Monitoring at the European Spallation Source", in *Proc. IBIC'13*, Oxford, UK, paper WEPC45.

ISBN 978-3-95450-185-4

DESIGN AND BEAM DYNAMICS STUDIES OF A MULTI-ION LINAC INJECTOR FOR THE JLEIC ION COMPLEX*

P.N. Ostroumov#, A.S. Plastun, B. Mustapha and Z.A. Conway
ANL, Argonne, IL 60439, U.S.A

Abstract

The electron-ion collider (JLEIC) being proposed at JLab requires a new ion accelerator complex which includes a linac capable of delivering any ion beam from hydrogen to lead to the booster. We are currently developing a linac which consists of several ion sources, a normal conducting (NC) front end, up to 5 MeV/u, and a SC section for energies > 5 MeV/u. This design work is focused on the beam dynamics and electrodynamics studies performed to design efficient and cost-effective accelerating structures for both the NC and SC sections of the linac. Currently, we are considering two separate RFQs for the heavy-ion and light-ion beams including polarized beams, and different types of NC accelerating structures downstream of the RFQ. Quarter-wave and half-wave resonators can be effectively used in the SC section.

INTRODUCTION

Recently, we have proposed a pulsed multi-ion linac with a normal conducting (NC) front-end up to 5 MeV/u and a superconducting (SC) section for higher energies as an injector for the JLab electron-ion collider (JLEIC) [1]. Separate radio-frequency quadrupole (RFQ) sections for heavy ($A/Z \leq 7$) and light ($A/Z \leq 2$) ions (polarized or non-polarized) and high-performance superconducting quarter-wave and half-wave coaxial resonators make the injector linac capable of effectively accelerating any ion species from hydrogen (up to 135 MeV) to lead (up to 44 MeV/u). This linac can be used for other purposes during the idle time of the booster ring; for example, isotope production.

LINAC LAYOUT

A block-diagram of the injector linac is shown in Figure 1 and the basic design parameters are listed in Table 1. The JLEIC ion linac will use both heavy and light ion sources including polarized H^+, $^2H^+$, $^3He^{2+}$, $^7Li^{3+}$ ion sources. The emittance of polarized beams is usually larger than the emittance of heavy-ion beams. For this reason, we propose to build two separate RFQs.

RFQ

Both RFQs operate at 100 MHz and accelerate ions up to 500 keV/u. Both of them produce low longitudinal emittance while the light-ion RFQ has larger transverse acceptance which is required for polarized light-ion beams.

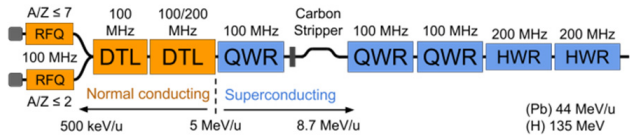

Figure 1: A schematic drawing of the JLEIC ion linac.

Table 1: Main Parameters of the Linac

Parameter	Value	Units
Ion species	H^+ to Pb	
Fundamental frequency	100	MHz
Kinetic energy of protons & lead ions	135&44	MeV/u
Maximum pulse current		
Light ions ($A/q \leq 2$)	2	mA
Heavy ions ($A/q > 2$)	0.5	mA
Pulse repetition rate	up to 10	Hz
Pulse length		
Light ions ($A/q \leq 2$)	0.5	ms
Heavy ions ($A/q > 2$)	0.25	ms
Maximum pulsed beam power	260	kW
# of QWR cryomodules	3	
# of HWR cryomodules	2	
Total length	~55	m

A higher injection energy into the light-ion RFQ allows us to mitigate beam space charge effects. Parameters of the RFQs are presented in Table 2. There are several possible electromagnetic and mechanical designs for the RFQ resonator such as a four-rod structure, a compact 4-vane RFQ resonator with magnetic coupling windows [2, 3] and the so-called "4-ladder" structure [4].

DTL

The drift tube accelerating section (DTL) is conceived to accelerate any ion species up to 5 MeV/u for injection into the superconducting part of the linac. We are considering either IH-DTL with triplet focusing [5, 6] or a spatially-periodic radio-frequency quadrupole focusing structure (see Figure 2) [7]. Both accelerating structures are highly efficient in this energy range, especially in pulsed

*This work was supported by the U.S. Department of Energy, Office of Nuclear Physics, under Contract DE-AC02-06CH11357. This research used resources of ANL's ATLAS facility, which is a DOE Office of Science User Facility.
#ostroumov@anl.gov

ISBN 978-3-95450-185-4

Table 2: Main Parameters of the RFQs

Parameter	Units	Heavy-ion RFQ	Light-ion RFQ
Frequency	MHz	100	
Energy range	keV/u	10 - 500	15 - 500
Highest A/q		7	2
Length	m	5.6	2.0
Average radius	mm	3.7	7.0
Voltage	kV	70	103
Transmission	%	99	99
Quality factor		6600	7200
Pulsed RF power	kW	210	120
Output long. emittance (Norm., 90%)	π keV/u ns	4.5	4.9

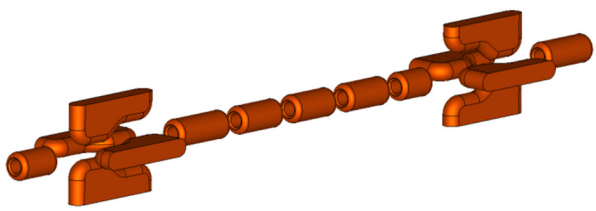

Figure 2: Spatially-periodic RF quadrupole focusingr channel.

linacs. The IH-DTL structure is a proven option as it is used in recently built heavy-ion injectors. The RF focusing DTL (Figure 2) provides similar real-estate accelerating gradient while avoiding significant longitudinal emittance growth.

The peak surface electric field assumed for the DTL design is ~2.5 Kilpatrick units, which is compatible with the pulsed operational mode of the injector [8]. Estimated pulsed RF power for the first DTL tank is 900 kW and 3 MW for the second one.

SC Section

The ion beams will be subsequently accelerated by the SRF section of the linac which comprises two different types of accelerating cavities to cover the velocity range from 0.1c to 0.5c where c is the speed of light. The QWRs and HWRs operating at 100 MHz and 200 MHz respectively are similar to those that have been developed recently at ANL for the ATLAS upgrade and the FNAL PIXE project. Photos of the QWR and HWR resonators developed and successfully operated at ANL are shown in Figure 3 and 4. Based on our experience, we propose to operate the JLEIC linac at peak surface fields up to ~86 mT and ~58 MV/m. In the low duty-cycle pulsed operating regime, these fields can be readily achieved and maintained in operation. Operating in pulsed mode reduces the dynamic heat load to a level where the static load dominates our cryogenic losses. Because of this we are planning on operating at 4.5 K to reduce the overall power requirements for the cryogenic system

The linac comprises 35 SC cavities housed in 5 cryomodules, with the RF parameters listed in Table 2. The cavity parameters were approximated from previously built QWRs and HWRs and refined with MWS simulations [9].

Figure 3: 72.75 MHz quarter wave resonator.

A dog-leg magnet system is foreseen after the stripping foil to dump unwanted charge states in a designated area. The economic acceleration of lead ions to 44 MeV/u requires a stripper in the linac with a stripping energy of ~8.7 MeV/u. The stripping efficiency of lead ions to the most abundant charge state 62+ is 17.5%. The linac can be rephased to accelerate any ion from proton to lead. Though this linac was originally designed to provide optimal voltage gain for lead ions, due to the wide velocity acceptance of the proposed cavities, lighter ions can be accelerated to higher velocities. Figure 5 shows the cavity effective voltage for lead ions and protons as a function of beam energy.

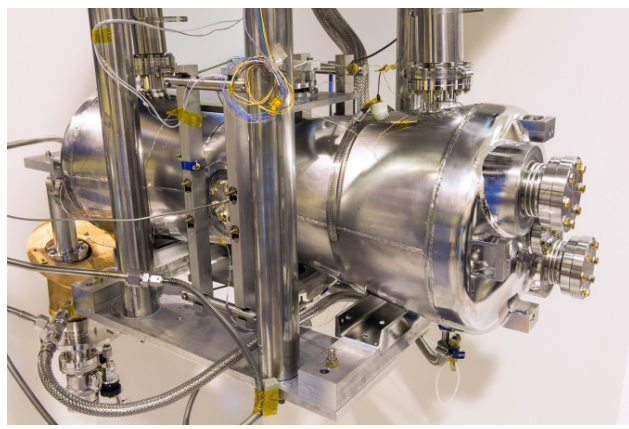

Figure 4: 162.5 MHz half wave resonator.

BEAM DYNAMICS

Beam dynamics simulations for the linac have been performed with the TRACK code [10] using 3D electromagnetic field distribution. The MEBT dipoles and mass separator after the first cryomodules as well as the stripper effects are not yet included in the simulations.

Transverse RMS envelopes of the beam along the injector linac with RF focusing structure are shown in Figure 6. Total transmission of both light and heavy ion beams are kept above 98% with some controlled losses in the RFQ to

ISBN 978-3-95450-185-4

Table 2: Design Parameters of SRF Resonators for JLEIC Ion Linac

Parameter	Units	QWR	HWR
β_{OPT}		0.15	0.30
f	MHz	100	200
Length ($\beta_{OPT}\lambda$)	cm	45	45
E_{PEAK}/E_{ACC}		5.5	4.9
B_{PEAK}/E_{ACC}	mT/(MV/m)	8.2	6.9
R/Q	Ω	475	256
G	Ω	42	84
E_{PEAK}	MV/m	57.8	51.5
B_{PEAK}	mT	86.1	72.5
E_{ACC}	MV/m	10.5	10.5
Phase	deg	-20	-15
Number of cavities		21	14

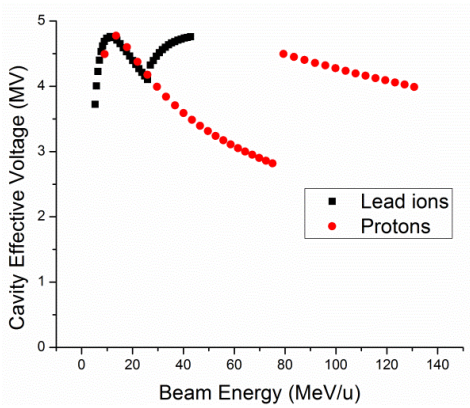

Figure 5: Cavity effective voltage as a function of beam energy.

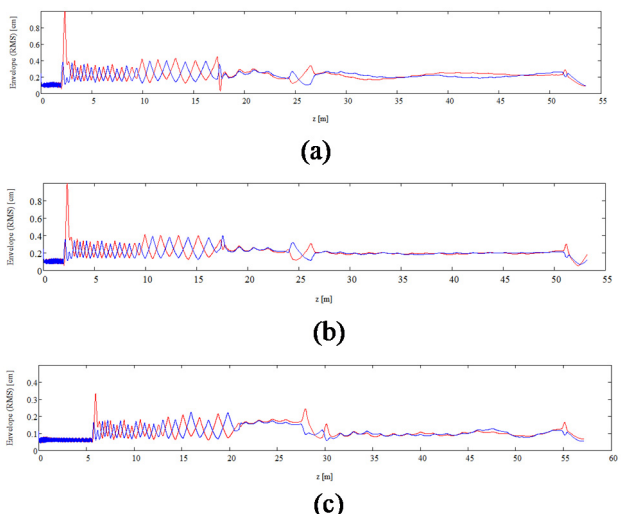

Figure 6: Beam RMS transverse envelopes along the linac: (a) – H^+, (b) – $^2H^+$, (c) – $^{208}Pb^{62+}$.

REFERENCES

[1] P.N. Ostroumov *et al.*, "Pulsed SC ion linac as injector to booster of electron ion collider", in *Proc. of SRF2015*, September 13-18, Whistler, BC, Canada, p. 265.

[2] V.A. Andreev, G. Parisi, "90-apart-stem RFQ Structure for Wide Range of Frequencies", in *Proc. of PAC'93*, May 17-20, Washington, DC, USA, p. 3124.

[3] P.N. Ostroumov, "Development and beam test of a continuous wave radio frequency quadrupole accelerator", *Phys. Rev. ST Accel. Beams*, 15, 110101 (2012).

[4] V.A. Andreev, G. Parisi, "A 90°-apart-stem Low Frequency RFQ", in *Proc. of EPAC'96*, June 10-14, Barcelona, Spain, p. 789.

[5] H.D. Haseroth, "Pb Injector at CERN", in *Proc. of LINAC'96*, August 26-30, Geneva, Switzerland, p. 283.

[6] J. Alessi, "Commissioning of the EBIS-Based Heavy Ion Preinjector at Brookhaven", in *Proc. of LINAC'10*, September 10-17, Tsukuba, Japan, p. 1033.

[7] A.A. Kolomiets, A.S. Plastun, "Spatially periodic radio-frequency quadrupole focusing linac", *Phys. Rev. ST Accel. Beams*, 18, 120101 (2015).

[8] J. Broere *et al.*, "High power conditioning of the 202 MHz IH tank 2 at the CERN Linac3", in *Proc. of the LINAC'98*, August 23-28, Chicago, USA, p. 771.

[9] *CST EM-STUDIO* and *MW-STUDIO*, CST, GmbH, Darmstadt, Germany [http://www.cst.de].

[10] *The beam dynamics code TRACK* [http://www.phy.anl.gov/atlas/TRACK].

ISBN 978-3-95450-185-4

A NEW RFQ MODEL AND SYMPLECTIC MULTI-PARTICLE TRACKING IN THE IMPACT CODE SUITE*

J. Qiang†, Lawrence Berkeley National Laboratry, Berkeley, USA
Z. Wang, H. P. Li, Peking University, Beijing, China

Abstract

The IMPACT code suite is a self-consistent parallel three-dimensional beam dynamics simulation toolbox that combines the magnetic optics method and the parallel particle-in-cell method. It has been widely used to study high intensity/high brightness beams in many accelerators. In this paper, we will report on recent improvements to the code such as the capability to model RFQ in time domain and symplectic multi-particle tracking with a gridless spectral solver for space-charge simulation.

INTRODUCTION

The IMPACT code suite is a parallel three-dimensional multi-particle tracking code to simulate charged particle beam dynamics in high intensity/high brightness accelerators. It includes a time-dependent code, IMPACT-T [1] and a longitudinal position dependent code, IMPACT [2]. Both codes use a particle-in-cell (PIC) method to self-consistently model the space-charge effects in the simulation. It has been used to model high intensity proton/ion linac, high brightness photoinjector, electron linac, proton synchrotron and other accelerators.

A NEW RFQ MODEL

The popular RFQ design code Parmteqm uses position as an independent variable and has a two-dimensional space-charge solver [3]. These approximations might introduce significant errors at lower energy for high intensity proton/ion beams. A new RFQ model is added into the IMPACT-T code with a three-dimensional space-charge solver including space charge effects within the bunch and the effects from neighboring bunches. In the RFQ model, eight term expression was implemented to account for the external accelerating/focusing effects. All coefficients can be obtained from the Parmteqm output file PARIOUT.OUT. Normally, an RFQ consists of different types of cells including radial matching section (RMS) cells, normal cells, and transition cells (including $m = 1$ cell and fringe cell). Inside the normal cells, the potential expression is given by

$$\begin{aligned} U(r,\theta,z) = \frac{V}{2}\{&A_{01}(\frac{r}{r_0})^2\cos(2\theta) + A_{03}(\frac{r}{r_0})^6\cos(6\theta) \\ &+[A_{10}I_0(kr) + A_{12}I_4(kr)\cos(4\theta)]\cos(kz) \\ &+[A_{21}I_2(2kr)\cos(2\theta) + A_{23}I_6(2kr)\cos(6\theta)]\cos(2kz) \\ &+[A_{30}I_0(3kr) + A_{32}I_4(3kr)\cos(4\theta)]\cos(3kz)\} \end{aligned} \quad (1)$$

In the above equation, $0 \le z \le L$, where L is the length of a cell. In the sine and cosine terms, $k = \pi/L$; in the modified Bessel function $I_{2m}(nkr)$ terms, k varies linearly over the cell. In the fringe cell and the RMS cells, the potential expression is given by

$$\begin{aligned} U(r,\theta,z) = &\frac{V}{2}\frac{6A_{01}}{k^2r_0^2}(I_2(kr)\cos(kz) + \frac{1}{27}I_2(3kr) \\ &\cos(3kz))\cos(2\theta) \end{aligned} \quad (2)$$

where $k = \pi/(2L)$, L is length of transition cell. In the transition cell, the potential expression is given by

$$\begin{aligned} U(r,\theta,z) = &\frac{V}{2}[(\frac{r}{r_0})^2\cos(2\theta) - A_{10}I_0(kr)\cos(kz) \\ &-A_{30}I_0(3kr)\cos(3kz)] \end{aligned} \quad (3)$$

where $k = \pi/(2L)$, L is the length of the transition cell. In all of these expressions, the $A_{01}, \cdots, A_{32}$ coefficients values can be calculated by linear interpolation at each z (defining $z = 0$ at the interface).

As an illustration of this new model, we simulated a charged proton beam with 5 mA current at 2.1 MeV transporting through an RFQ designed for the PIP-II project. The final beam phase space distributions at the RFQ exit from the IMPACT-T simulation, from the Toutatis [4] simulation, and from the ParmteqM simulation are shown in Fig. 1. It is seen that the IMPACT-T results agree with the Toutatis and the Parmteqm simulation results quite well.

SYMPLECTIC MULTI-PARTICLE TRACKING WITH A GRIDLESS SPECTRAL METHOD

In the accelerator beam dynamics simulation, for a multi-particle system with N_p charged particles subject to both space-charge self fields and external fields, the approximate Hamiltonian of the system can be written as:

$$H = \sum_i \mathbf{p}_i^2/2 + \frac{1}{2}\sum_i\sum_{j,j\neq i} q\phi(\mathbf{r}_i,\mathbf{r}_j) + \sum_i q\psi(\mathbf{r}_i) \quad (4)$$

where $H(\mathbf{r}_1,\mathbf{r}_2,\cdots,\mathbf{p}_1,\mathbf{p}_2,\cdots,s)$ denotes the Hamiltonian of the system, ϕ is the space-charge Coulomb interaction potential among the charged particles (with appropriate boundary conditions), ψ denotes the potential associated with the external fields. $\mathbf{r}_i$ denotes the canonical spatial coordinates of particle i, and $\mathbf{p}_i$ the normalized canonical momentum coordinates of the particle i. The equations governing the motion of individual particle i follows the Hamilton's equa-

* Work supported by the U.S. Department of Energy under Contract No. DE-AC02-05CH11231.
† jqiang@lbl.gov

ISBN 978-3-95450-185-4

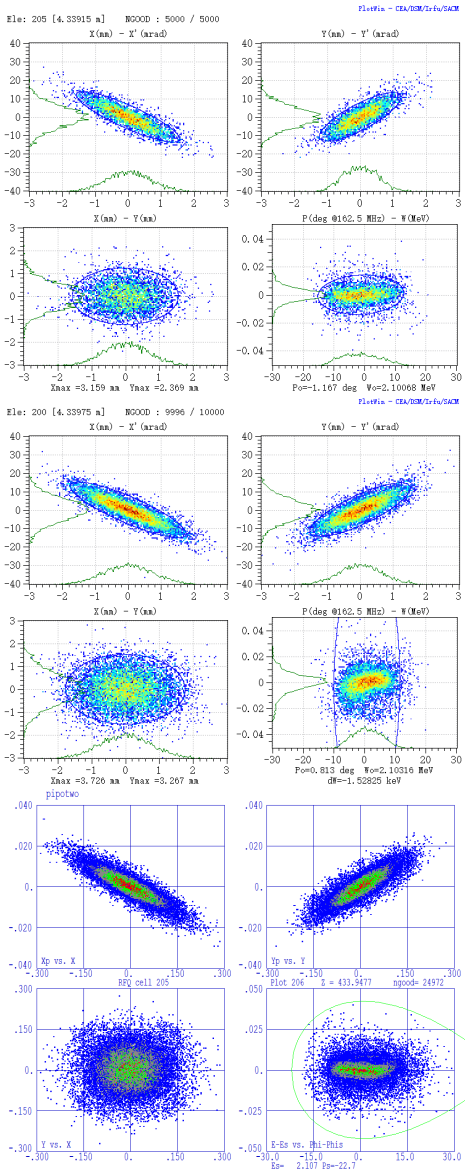

Figure 1: Beam phase space at the RFQ exit from the IMPACT-T simulation (top), from the Toutatis (middle), and from the Parmteqm simulation (bottom).

tions as:

$$\frac{d\mathbf{r}_i}{ds} = \frac{\partial H}{\partial \mathbf{p}_i} \quad (5)$$

$$\frac{d\mathbf{p}_i}{ds} = -\frac{\partial H}{\partial \mathbf{r}_i} \quad (6)$$

Let ζ denote the 6N-vector of coordinates, the above Hamilton's equation can be rewritten as:

$$\frac{d\zeta}{ds} = -[H, \zeta] \quad (7)$$

where [,] denotes the Poisson bracket. A formal solution for above equation after a single step τ can be written as:

$$\zeta(\tau) = \exp(-\tau(: H :))\zeta(0) \quad (8)$$

Here, we have defined a differential operator $: H :$ as $: H : g = [H, g]$, for arbitrary function g, and assumed H is not an explicit function of s [1]. For a Hamiltonian that can be written as a sum of two terms $H = H_1 + H_2$, an approximate solution to above formal solution can be written as [6]

$$\begin{aligned}\zeta(\tau) &= \exp(-\tau(: H_1 : + : H_2 :))\zeta(0) \\ &= \exp(-\frac{1}{2}\tau : H_1 :)\exp(-\tau : H_2 :) \\ &\quad \exp(-\frac{1}{2}\tau : H_1 :)\zeta(0) + O(\tau^3)\end{aligned} \quad (9)$$

Let $\exp(-\frac{1}{2}\tau : H_1 :)$ define a transfer map $\mathcal{M}_1$ and $\exp(-\tau : H_2 :)$ a transfer map $\mathcal{M}_2$, for a single step, the above splitting results in a second order numerical integrator to the original Hamilton equation as:

$$\begin{aligned}\zeta(\tau) &= \mathcal{M}(\tau)\zeta(0) \\ &= \mathcal{M}_1(\tau/2)\mathcal{M}_2(\tau)\mathcal{M}_1(\tau/2)\zeta(0)\end{aligned} \quad (10)$$

Using the above transfer maps $\mathcal{M}_1$ and $\mathcal{M}_2$, higher order numerical integrator can also be constructed [6, 7].

The above numerical integrators Eq. 10 will be symplectic if both the transfer map $\mathcal{M}_1$ and the transfer map $\mathcal{M}_2$ are symplectic. A transfer map $\mathcal{M}_i$ is symplectic if and only if the Jacobian matrix M_i of the transfer map $\mathcal{M}_i$ satisfies the condition:

$$M_i^T J M_i = J \quad (11)$$

where J denotes the $6N \times 6N$ matrix given by:

$$J = \begin{pmatrix} 0 & I \\ -I & 0 \end{pmatrix} \quad (12)$$

and I is the $3N \times 3N$ identity matrix.

For the given Hamiltonian in Eq. 4, we can choose H_1 as:

$$H_1 = \sum_i \mathbf{p}_i^2/2 + \sum_i q\psi(\mathbf{r}_i) \quad (13)$$

Standard charged optics methods can be used to find a symplectic transfer map $\mathcal{M}_1$ for this Hamiltonian with the external field from most accelerator beam line elements [8].

We can choose H_2 as:

$$H_2 = \frac{1}{2}\sum_i \sum_j q\phi(\mathbf{r}_i, \mathbf{r}_j) \quad (14)$$

which is only a function of positions, i.e. $H_2(\mathbf{r})$. The single step transfer map $\mathcal{M}_2$ can be written as:

$$\mathbf{r}_i(\tau) = \mathbf{r}_i(0) \quad (15)$$

$$\mathbf{p}_i(\tau) = \mathbf{p}_i(0) - \frac{\partial H_2(\mathbf{r})}{\partial \mathbf{r}_i}\tau \quad (16)$$

The Jacobi matrix of the above transfer map $\mathcal{M}_2$ is

$$M_2 = \begin{pmatrix} I & 0 \\ L & I \end{pmatrix} \quad (17)$$

[1] For the case that H is an explicit function of s, one can extend the variable space and a similar solution can still be obtained [5].

ISBN 978-3-95450-185-4

where L is a $3N \times 3N$ matrix. For M_2 to satisfy the symplectic condition Eq. 11, the matrix L needs to be a symmetric matrix, i.e.

$$L = L^T \tag{18}$$

Given the fact that $L_{ij} = \partial \mathbf{p}_i(\tau)/\partial \mathbf{r}_j = -\frac{\partial^2 H_2(\mathbf{r})}{\partial \mathbf{r}_i \partial \mathbf{r}_j}\tau$, the matrix L will be symmetric as long as it is analytically calculated from the H_2. If both the transfer map $\mathcal{M}_1$ and the transfer map $\mathcal{M}_2$ are symplectic, the numerical integrator Eq. 10 for multi-particle tracking will be symplectic.

The space charge Coulomb potential in the Hamiltonian H_2 can be obtained from the solution of the Poisson equation. In the following, we consider a coasting beam in a rectangular conducting pipe. In this case, the two-dimensional Poisson's equation can be written as:

$$\frac{\partial^2 \phi}{\partial x^2} + \frac{\partial^2 \phi}{\partial y^2} = -\frac{\rho}{\epsilon_0} \tag{19}$$

where, ρ the charge density distribution of the beam, and ϵ_0 is the dielectric constant in vacuum. The boundary conditions for the electric potential in the rectangular perfect conducting pipe are:

$$\phi(x = 0, y) = 0 \tag{20}$$
$$\phi(x = a, y) = 0 \tag{21}$$
$$\phi(x, y = 0) = 0 \tag{22}$$
$$\phi(x, y = b) = 0 \tag{23}$$

where a is the horizontal width of the pipe and b is the vertical width of the pipe.

Given the boundary conditions in Eq. 20-23, the electric potential ϕ and the source term ρ can be approximated using two sine functions as [9–12]:

$$\rho(x, y) = \sum_{l=1}^{N_l} \sum_{m=1}^{N_m} \rho^{lm} \sin(\alpha_l x) \sin(\beta_m y) \tag{24}$$

$$\phi(x, y) = \sum_{l=1}^{N_l} \sum_{m=1}^{N_m} \phi^{lm} \sin(\alpha_l x) \sin(\beta_m y) \tag{25}$$

where

$$\rho^{lm} = \frac{4}{ab} \int_0^a \int_0^b \rho(x, y) \sin(\alpha_l x) \sin(\beta_m y)\, dxdy \tag{26}$$

$$\phi^{lm} = \frac{4}{ab} \int_0^a \int_0^b \phi(x, y) \sin(\alpha_l x) \sin(\beta_m y)\, dxdy \tag{27}$$

where $\alpha_l = l\pi/a$ and $\beta_m = m\pi/b$. The above approximation follows a numerical spectral Galerkin method since each basis function satisfies the transverse boundary conditions on the wall. For a smooth analytical function, this spectral approximation has an accuracy with the numerical error that scales as $O(\exp(-cN))$ with $c > 0$ and N is the order of the basis function used in the approximation. Substituting above expansions into the Poisson equation and making use of the orthonormal conditions of the sine functions, we obtain

$$\phi^{lm} = \frac{\rho^{lm}}{\epsilon_0 \gamma_{lm}^2} \tag{28}$$

where $\gamma_{lm}^2 = \alpha_l^2 + \beta_m^2$.

In the multi-particle tracking, the charge density $\rho(x, y)$ can be represented by:

$$\rho(x, y) = \sum_{j=1}^{N_p} w \delta(x - x_j) \delta(y - y_j) \tag{29}$$

where w is the charge weight of each individual particle and δ is the Dirac function. Using Eq. 26 and Eq. 28, we obtain:

$$\phi^{lm} = \frac{1}{\epsilon_0 \gamma_{lm}^2} \frac{4}{ab} w \sum_j \sin(\alpha_l x_j) \sin(\beta_m y_j) \tag{30}$$

and the potential as:

$$\phi(x, y) = \frac{1}{\epsilon_0} \frac{4}{ab} w \sum_j \sum_l \sum_m \frac{1}{\gamma_{lm}^2} \sin(\alpha_l x_j) \sin(\beta_m y_j) \sin(\alpha_l x) \sin(\beta_m y) \tag{31}$$

Now, the Hamiltonian H_2 can be written as:

$$H_2 = \frac{1}{2\epsilon_0} \frac{4}{ab} w \sum_i \sum_j \sum_l \sum_m \frac{1}{\gamma_{lm}^2} \sin(\alpha_l x_j) \sin(\beta_m y_j) \sin(\alpha_l x_i) \sin(\beta_m y_i) \tag{32}$$

The one-step symplectic transfer map $\mathcal{M}_2$ of a particle i for this Hamiltonian is given as:

$$p_{xi}(\tau) = p_{xi}(0) - \tau \frac{1}{\epsilon_0} \frac{4}{ab} w \sum_j \sum_l \sum_m \frac{\alpha_l}{\gamma_{lm}^2} \sin(\alpha_l x_j) \sin(\beta_m y_j) \cos(\alpha_l x_i) \sin(\beta_m y_i) \tag{33}$$

$$p_{yi}(\tau) = p_{yi}(0) - \tau \frac{1}{\epsilon_0} \frac{4}{ab} w \sum_j \sum_l \sum_m \frac{\beta_m}{\gamma_{lm}^2} \sin(\alpha_l x_j) \sin(\beta_m y_j) \sin(\alpha_l x_i) \cos(\beta_m y_i) \tag{34}$$

Using a symplectic transfer map $\mathcal{M}_1$ for external field Hamiltonian H_1 from some charged particle optics code and following Eq. 10, one obtain a symplectic multi-particle tracking model including self-consistent space-charge effects.

As an illustration of above symplectic multi-particle tracking model, we simulated a 1 GeV coasting proton beam transporting through a rectangular conducting pipe with a FODO lattice for transverse focusing. The initial transverse density distribution is a Gaussian distribution and given in Fig. 2. We computed the electric field along x axis using above direct gridless spectral solver with 15×15 modes and the electric field from a 2nd order finite difference solver with 129×129 grid points. The results are shown in Fig. 3. The solution of the spectral solver agrees with the finite difference solver very well even with 15×15 modes due to the fast convergence property of the spectral method.

Figure 4 shows the proton beam root-mean-square (rms) envelope evolution through 20 FODO lattice periods. The FODO lattice used in this example consists of two quadupoles and three drifts in a single period. The total length of the period is 1 meter. The 0 current phase advance

ISBN 978-3-95450-185-4

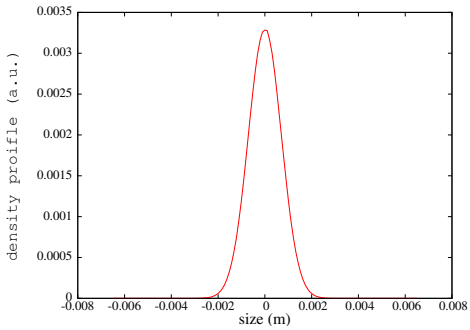

Figure 2: Charge density distribution along x axis.

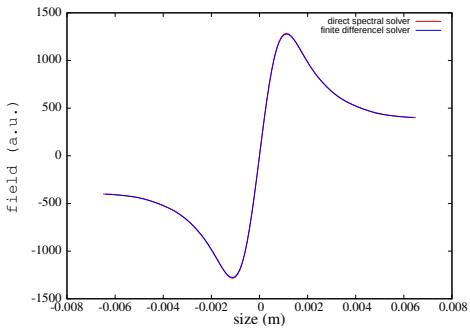

Figure 3: Electric field on x axis from the above direct spectral solver (red) and from the 2nd order finite difference solver (green).

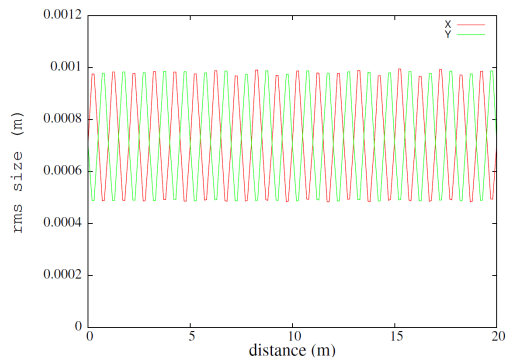

Figure 4: RMS envelope evolution of the beam.

is about 87 degrees and the phase advance with current is about 74 degrees.

The symplectic integrator is normally used for long term tracking since it helps preserve phase space structure during the numerical integration. Figures 5 shows stroboscopic plots (every 10 periods) of $x - p_x$ and $y - p_y$ phase space evolution of a test particle through 100, 000 lattice periods including the self-consistent space-charge forces. As a comparison, we also show in this plot the phase space evolution of the same initial test particle using the standard momentum conservation particle-in-cell (PIC) method with a 2nd order finite difference solver for space-charge calculation. In general, the two models show similar shapes in phase space. However, looking into the details of the phase space, the two models show quite different structures. The single

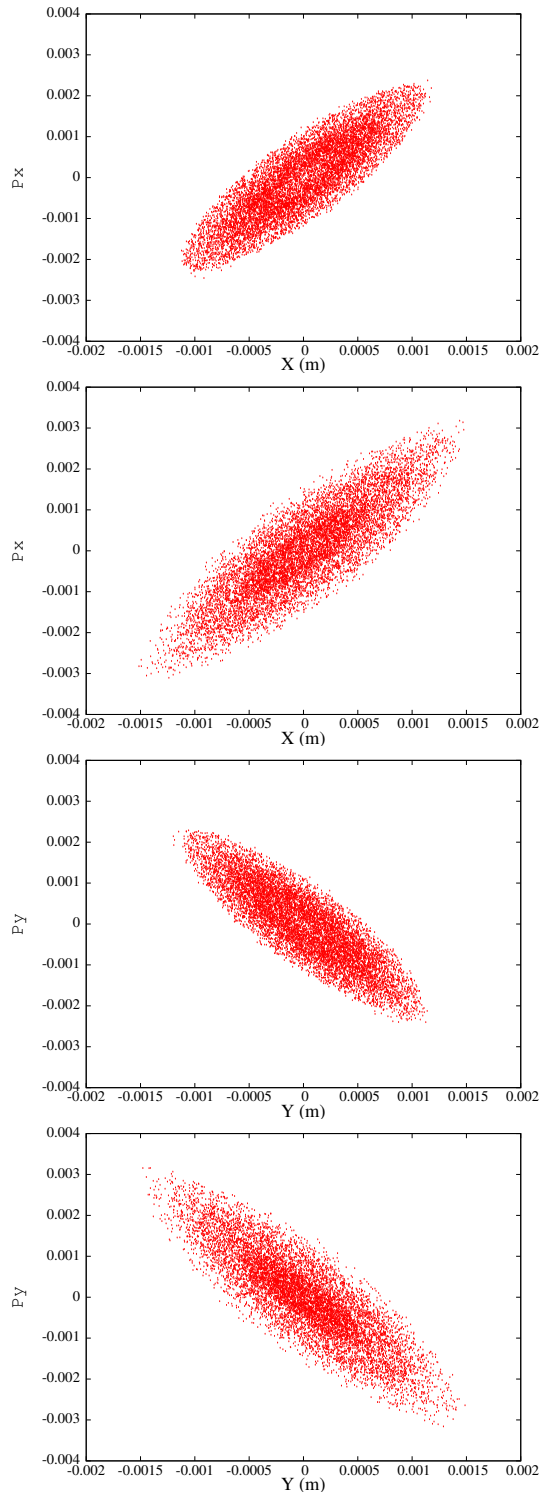

Figure 5: Stroboscopic plot (every 10 periods) of phase space evolution of a test particle from the symplectic-spectral model (top and 3rd) and from the PIC-finite difference model (2nd and bottom).

particle phase space from the PIC model shows a dense core while the symplectic multi-particle model shows a nearly hollow core. Figure 6 shows the 4-dimensional emittance growth evolution from the symplectic model and from the

ISBN 978-3-95450-185-4

PIC model. It is seen that the symplectic model shows a much smaller emittance growth than the PIC model does. This emittance growth is a numerical artifact due to the small number of macroparticles (50, 000) used in the simulation.

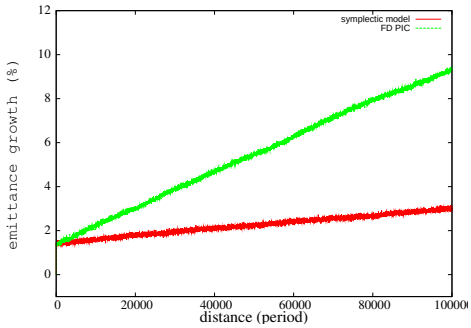

Figure 6: Four dimensional emittance growth evolution from the symplectic multi-particle spectral model (red) and from the PIC finite difference model(green).

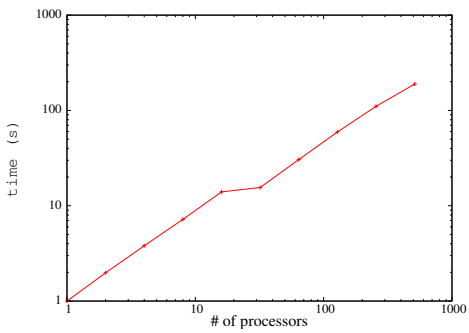

Figure 7: Parallel speedup of the symplectic tracking model on a Cray XC30 computer.

The symplectic multi-particle model with a gridless spectral solver can be used for long-term tracking study including space-charge effects. However, the computational complexity of the model scales as $O(N_l \times N_m \times N_p)$. The standard PIC model can have a computational cost of $O(N_p)+O(N_{grid}logN_{grid})$ when an efficient Poisson solver is used. This suggests that the PIC model should be faster than the symplectic multi-particle model on a single processor. However, the symplectic multi-particle model can be very easily parallelized on a multi-processor computer. One can distribute the macroparticles uniformly across all processors to achieve a perfect load balance. By using a spectral method with exponentially decreasing errors, the number of modes $N_l \times N_m$ can be kept within a relatively small number, which significantly improves the computing speed. Figure 7 shows the parallel speed up of the symplectic multi-particle tracking model as a function of the number of processors for a fixed problem size, i.e. 50, 000 particles and 15×15 modes. It is seen that the model has an almost linear scaling up to 500 processors. This shows that the symplectic multi-particle spectral tracking model can have a good scalability on parallel computers.

CONCLUSION

In this paper, we have shown two improvements to the IMPACT code suite. The new time-dependent RFQ model with 3D space-charge solver enables the IMPACT code suite to simulate low energy high intensity proton/ion beam through an RFQ. The new symplectic multi-particle spectral model also enables the code for long term tracking including space-charge effects.

ACKNOWLEDGEMENTS

We would like to thank Dr. D. Li for the PIP-II RFQ Parmteqm inputs and Drs. G. Franchetti, F. Kesting, C. Mitchell for discussions. This research used computer resources at the National Energy Research Scientific Computing Center.

REFERENCES

[1] J. Qiang, S. Lidia, R. D. Ryne, and C. Limborg-Deprey, *Phys. Rev. ST Accel. Beams* **9**, 044204, 2006.

[2] J. Qiang, R. D. Ryne, S. Habib, V. Decyk, *J. Comput. Phys.* **163**, 434, 2000.

[3] K. R. Crandall *et al.*, LANL Technical Report No. LA-UR-96-1836, 1997.

[4] R. Duperrier, *Phys. Rev. ST Accel. Beams* **3**, 124201, 2000.

[5] E. Forest, "Beam Dynamics: A New Attitude and Framework," *The Physics and Technology of Particle and Photon Beams*, Vol. 8 (Harwood Academic Publishers, Amsterdam, 1998).

[6] E. Forest and R. D. Ruth, *Physica D* **43**, p. 105, 1990.

[7] H. Yoshida, *Phys. Lett.* A **150**, p. 262, 1990.

[8] R. D. Ryne, "Computational Methods in Accelerator Physics," US Particle Accelerator class note, 2012.

[9] D. Gottlieb and S. A. Orszag, *Numerical Analysis of Spectral Methods: Theory and Applications*, Society for Industrial and Applied Mathematics, 1977.

[10] J. Boyd, *Chebyshev and Fourier Spectral Methods*, Dover Publications, Inc. 2000.

[11] J. Qiang and R. D. Ryne, *Comp. Phys. Comm.* **138**, p. 18, 2001.

[12] J. Qiang, *Comp. Phys. Comm.* **203**, p. 122, 2016.

ISBN 978-3-95450-185-4

BEAM ENERGY LOSS IN A BETA=0.09 SRF HWR CAVITY FOR 100 mA PROTON ACCELERATION*

F. Zhu#, H.T.X. Zhong, S.W. Quan, F. Wang, K.X. Liu
Institute of Heavy Ion Physics & State Key Laboratory of Nuclear Physics and Technology,
Peking University, Beijing, 100871, China

Abstract

There's presently a growing demand for cw high current proton and deuteron linear accelerators based on superconducting technology to better support various fields of science. Up to now, high order modes (HOMs) studies induced by ion beams with current higher than 10mA and even 100 mA accelerated by low β non-elliptical Superconducting rf (SRF) cavities are very few. One of the main HOM related issues of the SRF linac is the HOM-induced power. HOM power is the important part of beam energy loss which is used to estimate the cryogenic losses. In this paper, we compare the beam energy loss induced by 100 mA beam passing through a β=0.09 HWR SRF cavity calculated from time domain solver and frequency domain cavity eigenmodes spectrum method.

INTRODUCTION

Compared to normal conducting accelerator, rf Superconducting accelerator has more advantages and the potential to accelerate super high current (for example 100 mA) cw ion beam. The beam pipes can be larger and the operation cost could be much less. Such high current SRF cavities have been adopted by some future facilities. For example, IFMIF has two 125 mA deuteron accelerators [1] and BISOL [2] recently proposed a 50 mA deuteron accelerator as a driver. Peking University (PKU) is developing a β =0.09 HWR SRF prototype cavity for BISOL deuteron acceleration or for 100 mA proton beam acceleration.

Compared to elliptical SRF cavities, quarter wave resonators (QWRs) or half wave resonators (HWRs) have much sparse high order modes. The modes are a little far from the accelerating mode and not easily activated. Normally the effect of the HOMs of QWRs or HWRs can be neglected and the studies of HOMs of HWRs are very few. But for 100 mA beam, whether the beam energy loss induced by the HOMs can be negligible or not still needs study.

All modes contribute to the additional cryogenic load. Cavity loss factor calculation is very important for the total cryo-losses estimation for the SRF cavities. In this paper, we will describe our efforts to characterize the beam-induced power in the β=0.09 HWR cavity for 100 mA beam acceleration, and present the results of calculations made by two independent methods (in time domain and frequency domain) so as to achieve reliable results.

*Work supported by National Basic Research Project (No. 2014CB845504）
#zhufeng7726@pku.edu.cn

TIME DOMAIN ANALYSIS

The power deposited by the beam consisting of bunches following through the cavity with the bunch repetition rate f_{rep} is

$$P=k_{//}Iq= k_{//}q^2 f_{rep}= k_{//}I^2/f_{rep} \quad (1)$$

Where $I=qf_{rep}$ is the average beam current, q is the bunch charge, and $k_{//}$ is the beam energy loss factor.

The time domain calculation of beam energy loss factors is very common and well developed for elliptical cavities and for relativistic beams. Code ABCI can calculate the loss factor of symmetric structure and for relativistic beams [3]. CST can calculate the loss factor of 3D structure, but normally also for relativistic beams. When simulating non-relativistic beams passing through a cavity, one needs to take into account the static Coulomb forces. CST Studio direct wake field solver was used to calculate wake potentials. The total wake potential includes both static (Coulomb forces) and dynamic (beam-cavity interaction) parts. Because static component is not perfectly symmetrical to the bunch centre, the convolution of the bunch profile with the wake potential gives the wrong result for the loss factor. The remedy is to run two consecutive simulations with slightly different pipe lengths, and then the static components of the wake potential will change proportionally to the length while the dynamic part remains the same [4]. Thus, from these two solutions it is possible to subtract the static part and find the wake potential caused by beam-cavity interactions only. We used this method to calculate the wake potentials and further the loss factor for the high current taper type β=0.09 HWR cavity [5]. The structure geometry is illustrated in Figure 1.

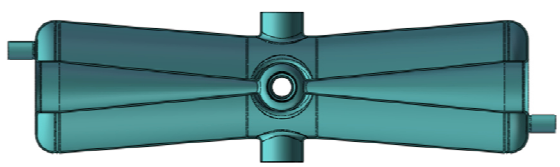

Figure 1: The 162.5 MHz, high current β=0.09 HWR cavity designed by Peking University.

Frequencies of HOMs excited by a non-relativistic beam bunch, passing through an SRF structure, depend on the characteristic size of the EM field distribution on the wall of the beam pipe at the cavity entrance, which is of the order of the beam pipe radius [6]. The beam pipe radius of the HWR cavity is 40 mm, frequencies below 7.5 GHz are present in the bunch field spectrum. It means

ISBN 978-3-95450-185-4

the loss factor doesn't change as the bunch length for the β=0.09 HWR cavity.

CST calculation requires a meshing of the full structure volume, and the total number of mesh elements exceeds ten million for short bunches. The shorter is bunch, the calculation consumes more time. When the bunch length is shorter than 2.5 mm, the CST code can hardly execute the calculation because of time consuming. The beam bunch which we were able to simulate within a reasonable time was 3 mm rms length.

Figure 2 shows the wake potentials before and after the subtraction treatment. The primary wake potential is much higher than the treated one for the low β cavity. Figure 3 shows the dynamic wake potentials got from different lengths of beam pipes. The origin cavity length with beam pipes was 400 mm. The three curves were obtained by subtraction treatment between cavities with different beam pipes (460 mm, 520 mm and 580 mm) and the origin cavity of 400 mm long. These curves are in good consistency.

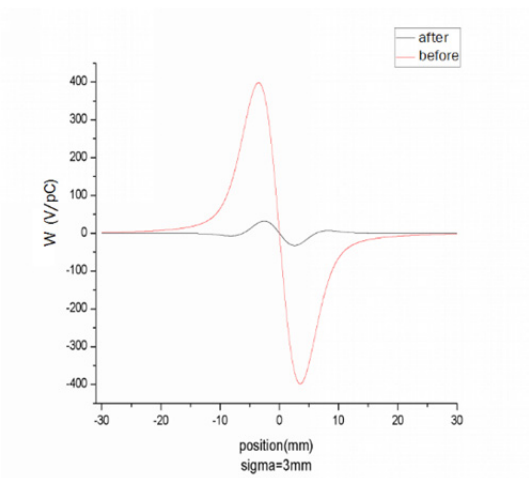

Figure 2: The wake potentials before (the direct result from the CST code) and after (the dynamic wake potential) the subtraction treatment.

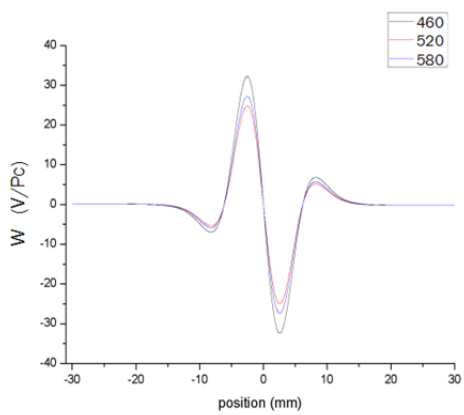

Figure 3: The wake potentials caused by beam-cavity interactions got from different beam pipes.

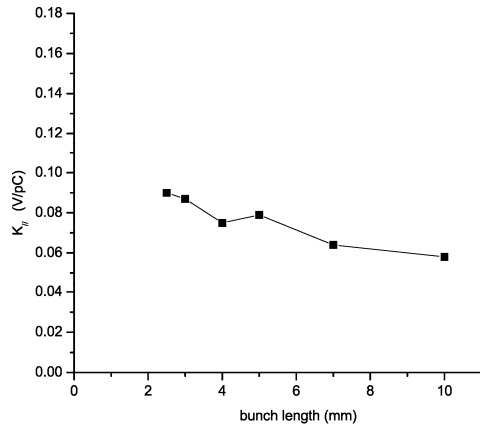

Figure 4: Loss factor $K_{//}$ versus bunch length for β =0.09 HWR cavity.

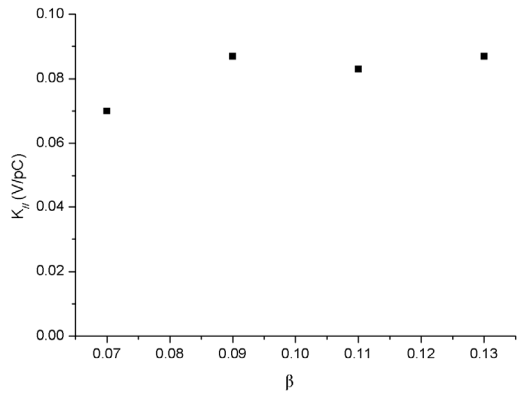

Figure 5: Loss factor versus velocity β for the HWR cavity.

Figure 4 shows the loss factor $k_{//}$ for the β =0.09 HWR cavity changes as the bunch length, $k_{//}$ is in the range of 0.06~0.087 V/pC. $k_{//}$ is about 0.087 V/pC when the rms bunch lengths are 2.5 mm and 3 mm separately. The real bunch which can be accelerated by the β =0.09 HWR cavity can be 2~3 mm. Figure 5 shows the loss factor changes as the beam velocity. The rms bunch length is 3mm. There is no much difference of the loss factors when the ion beam velocity β is in the range of 0.07~0.13. $k_{//}$ is near 0.09 V/pC.

If we choose $k_{//}$ =0.087 V/pC for the β =0.09 HWR cavity, the average beam current is 100 mA, and the bunch repetition rate is 162.5 MHz, then the bunch energy loss is about 5.3 W from equation (1).

FREQUENCY DOMAIN ANALYSIS

Because of the rapid decay of HOM spectrum, the effective HOMs below few GHz will be excited by the non-relativistic beam in the β=0.09 HWR cavity. Table1 gives information of the lowest modes.

The total loss factor k can be represented as an infinite series of all cavity modes' inputs. The loss factor for an individual mode for a Gaussian bunch with rms length σ can be written in the form [7]:

$$k(\beta,\sigma)=\exp\left[-\left(\frac{\omega\sigma}{\beta c}\right)^2\right]\frac{\omega r(\beta)}{4Q} \quad (2)$$

ISBN 978-3-95450-185-4

Table 1: Loss Factors (in V/pC) of the Lowest Modes in the β =0.09 HWR Cavity

Mode	f (MHz)	r/Q	$r_\perp/Q$ (1mm)	$r_\perp/Q$ (10mm)	k (0.09)
1	162.20	255	-	-	0.064
2	315.29	2.8×10^{-7}	6.5×10^{-3}	7.1×10^{-5}	0
3	422.28	16.6	-	-	0.011
4	633.03	7.8×10^{-9}	4.5×10^{-5}	6.7×10^{-7}	0
5	697.30	1.57	-	-	0.0015
6	715.39	0.93	-	-	8×10^{-4}
7	720.03	2.8×10^{-6}		0.32	3×10^{-4}
8	724.25	2.9×10^{-5}	0.13	2.2×10^{-3}	1.5×10^{-4}
9	724.42	1.2×10^{-8}	3.4×10^{-4}	3.2×10^{-4}	0
10	759.78	0.15	-	-	1.2×10^{-4}
11	858.61	1.3×10^{-7}	1.69	2.35	0.0019
12	929.72	1.5×10^{-10}	6.7×10^{-6}	1.4×10^{-6}	0
13	930.07	1.5×10^{-6}	3.9×10^{-3}	8.5×10^{-5}	0
14	944.53	6.9×10^{-11}	1.5×10^{-7}	9.8×10^{-11}	0
15	973.15	0.026	-	-	0
16	1004.43	3.7×10^{-8}	0.098	0.15	1.2×10^{-4}
17	1023.67	1.9×10^{-4}	0.45	0.042	4.4×10^{-4}
18	1226.76	3.6×10^{-4}	0.55	0.008	5×10^{-4}
19	1283.84	-	0.054	-	4.5×10^{-5}
Total					0.078

The definitions of the shunt impedance r/Q of the longitudinal modes and deflecting modes are: $\frac{r}{Q}=\frac{V_{acc}^2}{\omega U}$ for longitudinal modes and $\frac{r_\perp}{Q}=\frac{\left|\int_0^d E_z(\rho=a)e^{i\omega z/v}dz\right|}{(ka)^2\omega U}=\frac{R_a}{Q}\frac{1}{(ka)^2}$ for deflecting modes which has no E_z along the beam axis.

where ω is the circular eigenfrequency, r(β) is the shunt impedance, Q is the eigenmode quality factor and βc is the bunch velocity.

The total loss factor of the HWR cavity for β=0.09 from the frequency domain is 0.078 V/pC. The majority is from the fundamental mode and the contribution of all the other modes gives 0.014 V/pC. The beam energy loss induced by 100 mA beam passing through the cavity obtained by the frequency eigenmodes approach is 4.8 W, and the majority is from the fundamental mode of 3.9 W. The CST eigenmode solver only gives 20 modes for the reference frequency near the fundamental mode frequency. When the reference frequency is much higher than the fundamental mode frequency, the results are not precise even though the program can give more modes. In superconducting cavities, the contribution of the lowest modes is a major concern. Loss factor of 0.078 V/pC does not include those modes with frequencies higher than 1.3 GHz. The time-domain approach is more acceptable. By comparing the frequency domain analysis and the time domain analysis, we can conclude that the beam energy loss induced by the high order modes of the β=0.09 HWR cavity is about 1.4 W. Of all the HOMs, the mode with frequency of 422.28 MHz has the highest r/Q, and the deposited power by this mode is about 0.7 W. Special HOM coupler could be designed to absorb this particular harmful mode.

CONCLUSION

The estimation of the total incoherent beam energy loss of 100 mA beam passing through the PKU β=0.09 HWR cavity was made using two independent methods (in time and frequency domains) for loss factor calculation. Because of the limited modes calculated from the frequency domain approach, the time domain result is a little higher than the frequency domain result. The final amount of incoherent RF losses calculated for a single cavity is about 5.3 W. The energy loss induced by the HOMs is 1.4 W, which gives a little effect on the total cryo-loss budget. The mode with frequency of 422.28 MHz contributes the majority. Thus HOM coupler could be designed to absorb this most harmful mode.

REFERENCES

[1] F. Orsini, P. Bosland, B. Branas, *et al.*, "Study and Realization of the First Superconducting Half Wave Resonator for the SRF Linac of the IFMIF Project", in *Proc. 1st Int. Particle Accelerator Conference (IPAC'10)*, Kyoto, Japan, May 2010, paper MOPEC057.

[2] S.X. Peng, F. Zhu, *et al.*, *Nuclear Instruments and Methods in Physics Research B*, 376: 420-424, 2016.

[3] Y.H. Chin, Report LBL-35258, Berkeley, CA, USA, 1994.

ISBN 978-3-95450-185-4

[4] A. Lunin, V. Yakovlev and S. Kazakov, "Cavity Loss Factors of Non-Relativistic Beams for Project-X", in *Proc. PAC'11*, paper TUP075, New York, USA, 2011.
[5] P.L. Fan, F. Zhu, H.T.X. Zhong, *et al.*, *High Power Laser and Particle Beams*, 28 (2): 045103, 2016.
[6] A. Sukhanov, A. Lunin, V. Yakovlev, *et al.*, "High order modes in Project-X linac", *NIMA*, vol. 734, Part A, 11 January 2014, Pages 9–22.
[7] S.S. Kurennoy, *Phys. Rev. ST Accel. Beams*, vol. 2, 032001, 1999.

ISBN 978-3-95450-185-4

AN ADVANCED PROCEDURE FOR LONGITUDINAL BEAM MATCHING FOR SC CW HEAVY ION LINAC WITH VARIABLE OUTPUT ENERGY

Stepan Yaramyshev[1*], Kurt Aulenbacher[2,3], Winfried Barth[1,2], Viktor Gettmann[1,2], Manuel Heilmann[1,4], Sascha Mickat[1,2], Maksym Miski-Oglu[1,2]
[1]GSI Helmholtzzentrum für Schwerionenforschung, Darmstadt, Germany
[2]HIM, Helmholtz Institute Mainz, Germany
[3]IKP, Johannes Gutenberg-University Mainz, Germany
[4]IAP, Goethe-University Frankfurt am Main, Germany

Abstract

A multi-stage program for the development of a heavy ion superconducting (SC) continuous wave (CW) linac is in progress at HIM (Mainz, Germany), GSI (Darmstadt, Germany) and IAP (Frankfurt, Germany). The main beam acceleration is provided by up to nine multi-gap CH cavities. Due to variable beam energy, which could be provided by each cavity separate, a longitudinal beam matching to each cavity is extremely important. The linac should provide the beam for physics experiments, smoothly varying the output particle energy from 3.5 to 7.3 MeV/u, simultaneously keeping high beam quality. A dedicated algorithm for such a complicate matching, providing for the optimum machine settings (voltage and RF phase for each cavity), has been developed. The description of method and the obtained results are discussed in this paper.

INTRODUCTION

The High Charge State Injector (HLI) in combination with the Universal Linear Accelerator (UNILAC) serves as a powerful high duty factor (up to 25%) accelerator, providing heavy ion beams for the experiment program at GSI [1,2]. Operation of the new GSI Facility for Antiproton and Ion Research at Darmstadt (FAIR) foresees the UNILAC as a heavy ion high intensity injector for the synchrotron SIS18. Therefore beam time availability for Super-Heavy Elements research (SHE) is decreased [3]. To keep the SHE program at GSI on a high competitive level, the development of a heavy ion superconducting (SC) continuous wave (CW) linac is in progress (Fig. 1). Such a machine will provide for significantly higher beam intensities and an increased rate of SHE production [4].

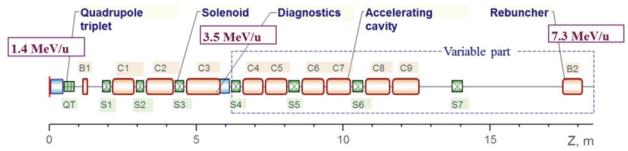

Figure 1: The conceptual layout for SC part of the CW linac at GSI.

SC CW DEMONSTRATOR

The multi-cavity advanced SC Demonstrator is recently under construction at GSI [5-7]. The existing HLI serves as injector and provides heavy ion beams with an energy of 1.4 MeV/u, delivered with a dedicated transport line to the demonstrator cave (Fig. 2).

Besides the room temperature focusing magnetic quadrupoles (triplet and 2 doublets), the setup comprises two rebuncher cavities, beam diagnostics and cold-warm junction of the cryostat. Adequately chosen gradients of the quadrupole lenses make the input beam at the Demonstrator entrance axially symmetric in 4D transverse phase plane for easier further focusing by the solenoids. The rebuncher cavities, operated at 108 MHz, provide for the required longitudinal matching. Therefore the beam 6D matching to the demonstrator is accomplished [8].

The commissioning of the CW-Demonstrator, consisting of two superconducting solenoids and the superconducting CH-cavity, has already started in 2016 [9].

After successful testing of the first cryostat, the construction of an extended cryomodule, which is foreseen to comprise two shorter CH cavities is planned to be tested until end of 2017. Two identical short CH cavities are already ordered; delivery to GSI is expected until summer 2017. The schematic layout of the machine is shown on Fig. 3.

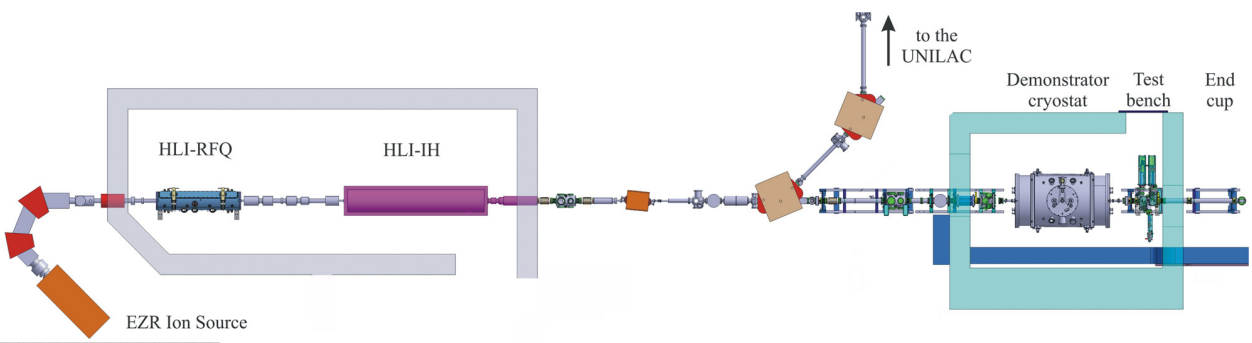

Figure 2: Recent schematic layout of the SC Demonstrator at GSI.

* S.Yaramyshev@gsi.de

ISBN 978-3-95450-185-4

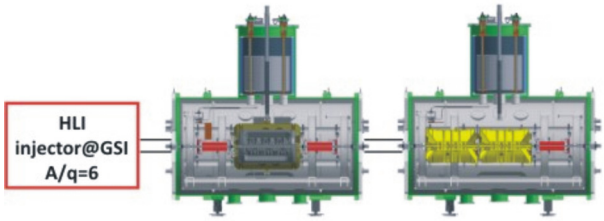

Figure 3. The schematic layout of the linac (expected to be constructed until the end 2017).

LONGITUDINAL BEAM DYNAMICS

As an input for the beam dynamics simulations for the transport line from HLI to the Demonstrator the previously performed simulations for the whole HLI injector have been used. Due to a low beam current (below 1 mA) and relatively high particle energy (above 1.4 MeV/u), the space charge effects could be neglected. Therefore, as a first approach, the longitudinal beam dynamics can be separated from the transverse one.

The capability of the two-buncher system for longitudinal beam matching has been proved and confirmed for a wide range of longitudinal Twiss-parameters at the entrance of the Demonstrator cavity. Beam dynamics simulations have been carried out by means of the codes TRACE-3D [10] and the DYNAMION [11].

The 15-gap CH cavity, as well as the shorter 8-gap CH cavities [12] are designed on the base of KONUS/EQUUS beam dynamics scheme as not fully resonance accelerators. This design feature allows for the desired high accelerating gradient. Although some of the gaps are designed to perform a longitudinal beam focusing at the expense of acceleration. Therefore particle motion in each such accelerating cavity is extremely sensitive to the initial RF phase and the cavity voltage.

The beam dynamics simulations for the cavities has been performed by means of the DYNAMION code, which calculates the shape of an external electrical field in a DTL linac on the base of the real topology of tubes and gaps. A distribution of voltage at each gap along a cavity has been defined by the CST simulations [13], taking into account details of the cavity design and position of the plungers (Fig. 4-5).

Generally the proposed linac should facilitate a variable output energy from 3.5 to 7.3 MeV/u. Also acceleration of ions with mass to charge ratio from 3 to 6 even for higher energies is planned. Therefore the original linac layout has been revised: the number of gaps per cavity has been decreased and number of cavities has been extended from 9 to 13. This layout requires proper settings (voltage and phase) for each of the 13 independently operated cavities, which provide for a required acceleration but sufficiently low emittance growth. Thus the longitudinal beam matching to each cavity is of high importance, hampered by strong dependence of particle motion inside a cavity from beam dynamics in all previous cavities. Therefore a dedicated method for optimization of the matching should be developed, especially due to the numerous scenarios for linac operation.

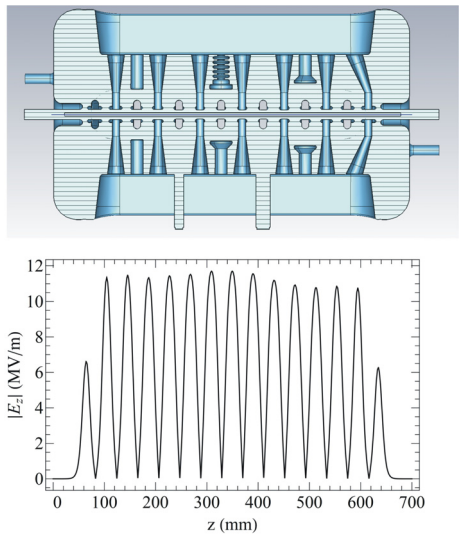

Figure 4. CST model for the 15-gap CH cavity (top) and accelerating electrical field along the cavity (bottom).

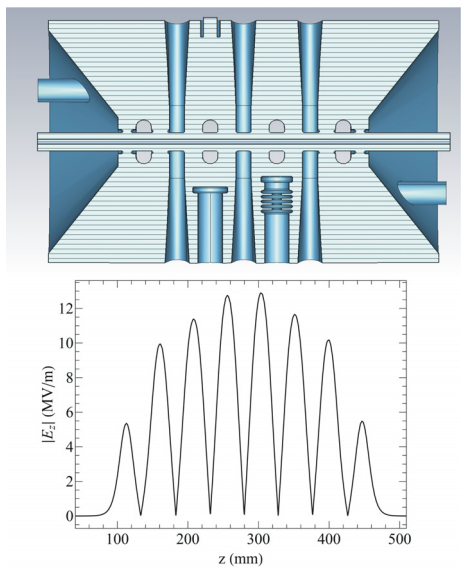

Figure 5. CST model for the 8-gap short CH cavity (top) and accelerating electrical field along the cavity (bottom).

LONGITUDINAL BEAM MATCHING

As particle acceleration in the presented CH cavities is not fully resonance, the input beam parameters, as well as RF phase and voltage of cavity, should be determined to provide for sufficient acceleration and low emittance growth. For instance a strong deformation of an elliptical emittance shape should be limited or even avoided, while such deformation is a typical effect for the KONUS beam dynamics and similar accelerating schemes. Obviously such a deformed beam emittance becomes problematic for further acceleration by subsequent cavities. Also a transverse focusing (by solenoids or magnetic quadrupoles) depends on particle velocity, therefore such longitudinal beam shape potentially drives to a degradation of the transverse beam quality and particle losses.

Thus the matched longitudinal Twiss-parameters, as well as an optimum RF phase of the cavity, should be

ISBN 978-3-95450-185-4

determined for the given (or also optimized) cavity voltage and known longitudinal beam emittance. Fast envelopes codes as TRACE-3D are not applicable for this study due to a strong non-elliptical deformation of the longitudinal beam emittance. Obviously, a direct enumeration of all possible input parameters with full beam dynamics simulations by means of multiparticle codes (10^4-10^6 particles for each run) is extremely time consuming. Therefore the method, already proposed and implemented for a transverse beam matching [14], has been extended for the longitudinal optimization of beam dynamics.

Thus a longitudinal beam phase portrait is represented by only 100 macroparticles, forming an ellipse in the longitudinal phase plane. The ellipse area, divided by π, represents the beam emittance. Transversally all macroparticles could be set on axis due to negligibly low space charge effects and a minor influence of transverse focusing on longitudinal particle motion.

Main parameters of the ellipse could be set randomly:
- Twiss parameters **α** and **β**;
- energy of center;
- coordinate of center.

The last parameter substitutes a variation of the RF phase of the cavity. Therefore a big number of such macroparticle ensembles could be simulated in one run.

Generally an analysis of the output particle distribution could be performed due to dedicated DYNAMION feature of an unique ID number of each macroparticle. The same method could be also implemented to beam dynamics simulations by means of CST Particle Studio.

An example of a typical evolution of the particle ensemble inside the 15-gap demonstrator cavity is shown in Fig. 6. The particles are accelerated to a reasonable energy, while the output distribution is far from elliptical shape.

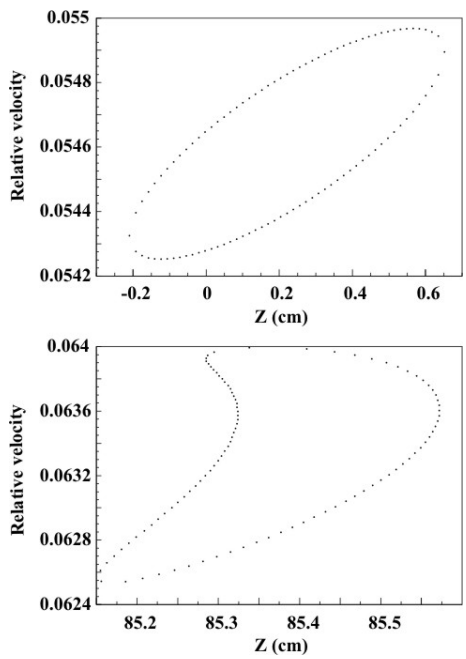

Figure 6. An example of a typical input (top) and output (bottom) 100-particle ensemble.

A series of points (***Z***, ***Z'***) could be approximated by an ellipse, assuming the standard equation:

$$cZ^2 + 2aZZ' + bZ'^2 = 1 .$$

The Twiss-parameters ***α***, ***β***, ***γ*** of such an ellipse could be obtained by means of least squares method:

$$\alpha = a\sqrt{bc - a^2} \ , \ \beta = b\sqrt{bc - a^2} \ , \ \gamma = c\sqrt{bc - a^2} \ .$$

Then the parameter ε_i is enumerated for each particle of the output 100-particle ensemble:

$$\varepsilon_i = \gamma Z^2 + 2\alpha ZZ' + \beta Z'^2 .$$

Three factors are calculated for each output 100-particle ensemble: emittance growth (F_1), deformation of elliptical shape (F_2) and energy gain (F_3):

$$F_1 = \frac{\varepsilon_{\max}}{\varepsilon_{input}},$$

$$F_2 = \frac{\varepsilon_{\max} - \varepsilon_{\min}}{\varepsilon_{input}},$$

$$F_3 = \frac{\beta_{out} - \beta_{in}}{\beta_{in}},$$

where ε_{max} and ε_{min} are the maximum and minimum values of the series ε_i ; ε_{input} is total unnormalized longitudinal beam emittance; β_{in} and β_{out} are the input and output relative velocities, averaged on the 100-particle ensemble.

Without acceleration an elliptical shape of the longitudinal beam emittance is well preserved. But for the maximum acceleration a dramatic deformation of the beam emittance occurs. Generally a combination of factors

$$F_1^p F_2^q F_3^{-s}$$

with the weight coefficients ***p***, ***q***, ***s*** could be constructed and used as mismatch parameter in dependence of the required goal in between of two limits: the highest acceleration or the best beam quality.

The above described algorithm has been implemented by means of the DYNAMION code, adjusted for numerous simulation in a batch mode and using a Monte-Carlo method with random generation of input beam parameters. The dedicated software has been written to analyze the obtained millions of ensembles and to select some hundreds of the best combinations. Fig. 7 shows the lowest mismatch factors F_2 and the corresponding Twiss-parameters. The dashed lines illustrate a clear coincidence of the method.

ISBN 978-3-95450-185-4

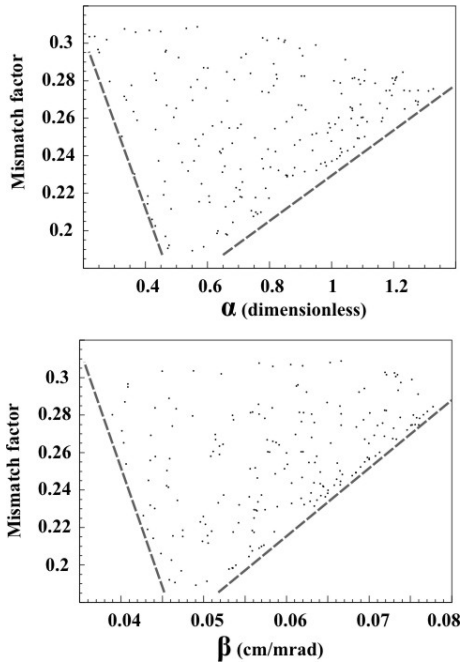

Figure 7. The lowest mismatch factors F_2 and the corresponding Twiss-parameters α (top) and β (bottom).

An example of a well matched input 100-particle distribution is shown on Fig. 8. The particles are accelerated to a reasonable energy and the output distribution is close to an elliptical shape. Therefore the matched input beam characteristics as Twiss-parameters, energy and coordinate (cavity RF phase) are determined.

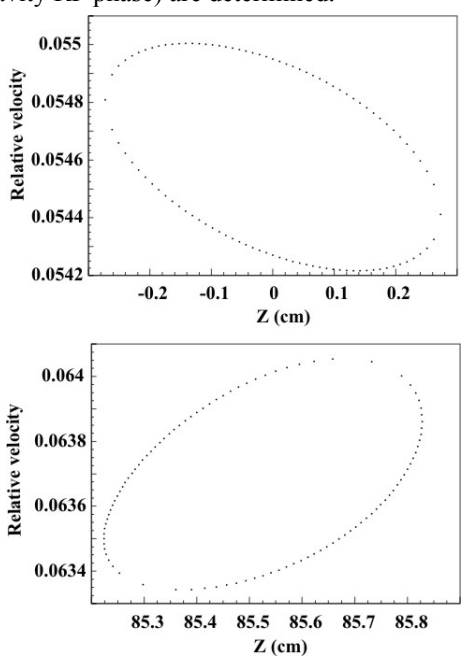

Figure 8. A typical example of the matched input 100-particle ensemble (top) and the corresponding output (bottom).

CONCLUSION

The new heavy ion SC CW linac project, conducted by HIM and GSI, is fully in line with other modern type and high efficient CW linac projects, mainly for proton and light ion acceleration, which are under development at different leading accelerator centers worldwide [15-20].

A dedicated algorithm for the longitudinal beam matching with a DTL cavity is developed. The method is foreseen to be implemented for the new GSI heavy ion SC CW linac, comprised by 13 independently powered multigap cavities, developed at IAP. A flexible constructed mismatch parameter allows for machine optimization for a wide range of the ions with different mass to charge ratio, as well as for the required output beam energy from 3.5 to 7.3 MeV/u and higher (for medium ions).

REFERENCES

[1] W. Barth *et al.*, Proceedings of IPAC2016, Busan, Korea, WEOBA03 (2016).
[2] W. Barth *et al.*, Physical Review ST AB 18(4),·050102 (2015).
[3] W. Barth *et al.*, Proceedings of IPAC'14, Dresden, Germany, THPME004 (2014).
[4] S. Minaev *et al.*, Phys. Rev. ST Accel. Beams, vol. 12, p. 120101 (2009).
[5] M. Miski-Oglu *et al.,* Proceedings of SRF2015, Whistler, BC, Canada, MOPB067 (2015).
[6] F. Dziuba *et al.*, Proceedings of SRF2015, Whistler, BC, Canada, TUPB075 (2015).
[7] M. Schwarz *et al.*, Proceedings of IPAC2016, Busan, Korea, MOPOY023 (2016).
[8] V. Gettmann *et al.*, Proceedings of SRF2015, Whistler, BC, Canada, TUPB020 (2015).
[9] M. Heilmann *et al.*, Proceedings of IPAC2016, Busan, Korea, MOPOY022 (2016).
[10] TRACE-3D Documentation, Los-Alamos National Lab., LA-UR-90-4146.
[11] S. Yaramyshev *et al.*, NIM A, 558/1 (2006).
[12] M. Basten et al., Proceedings of IPAC2016, Busan, Korea, MOPOY019 (2016).
[13] CST Studio Suite, http://www.cst.com/
[14] S. Yaramyshev *et al.*, PhysRev ST AB, 18 5)·(2015).
[15] S.M. Polozov, A.D. Fertman, Atomic Energy, 113, Issue 3, 155–162 (2012).
[16] P.N. Ostroumov, Proceedings of IPAC2015, Richmond, VA, USA, FRXB3 (2015).
[17] L. Weissman *et al.*, Journal of Instrumentation, 10, T1004 (2015).
[18] S. Polozov *et al.,* "Beam Dynamics Simulation and Code Comparison for New CW RFQ Design", presented at HB2016, Malmo, Sweden, July 2016, paper MOPL004, this conference.
[19] D. Berkovits, "SARAF Phase-I Experience with mA Beams", presented at HB2016, Malmo, Sweden, July 2016, paper TUAM1Y01, this conference.
[20] R. Tiede *et al.*, "A coupled RFQ-IH-DTL Cavity for FRANZ: A Challenge for RF Technology and Beam Dynamics", presented at HB2016, Malmo, Sweden, July 2016, paper WEAM1Y01, this conference.

ISBN 978-3-95450-185-4

SUMMARY OF WORKING GROUP A

Wolfram Fischer, BNL, Upton, NY, USA
Giuliano Franchetti, GSI, Darmstadt, Germany
Yong Ho Chin, KEK, Ibaraki, Japan

The working group A, Beam Dynamics in Rings, was structured with the following 6 sections:

1) Collective effects (4 talks),
2) Space charge - beam-beam (4 talks);
3) Code development and benchmarking (4 talks);
4) New machines / New Concepts (4 talks);
5) Theory (4 talks);
6) Emerging talents (6 talks).

A few highlight are given below.

COLLECTIVE EFFECTS

Elias Metral, CERN has presented a status of the collective effect at CERN [1]. The talk concluded that in a machine like LHC, not all the effect can be understood separately. Instead all the possible interplay between the several phenomena need to be analyzed in detail, these effects should include: beam-coupling impedance (collimators, crab cavities); linear and nonlinear chromaticity; Landau octupoles; transverse damper; space charge; beam-beam; electron cloud; linear coupling; tune separation between transverse planes; tune split between the two beams; transverse beam separation between the two beams; noise effects.

Giovanni Rumolo, CERN reviewed the state of the art of the electron cloud effects in the LHC and SPS [2]. The comprehensive talk showed that because of intensive measurements and new simulation tools, a deeper knowledge of the electron cloud in the different CERN accelerators has been reached. For the present 25 ns beam parameters PS and SPS can deliver the required beams within the original specifications. The LHC still suffers from electron clouds. Scrubbing mitigates the electron cloud, and allows for LHC operation, but it is not known up to which point one can rely on scrubbing. Future parameter studies include: in PS e-cloud instabilities should be prevented by transverse feedback system; SPS relies on scrubbing, and relevant chambers will be a-C coated; the HL-LHC will also require studies on scrubbing.

SPACE CHARGE – BEAM-BEAM

Hannes Bartosik, CERN has presented a study of the beam loss in LEIR for high intensity bunched beams [3]. The intensity limitation at LEIR are found experimentally to happen during and after the RF capture. It has been identified that the mechanism driving the beam loss is the interplay of space tune-spread with betatron resonances. It is also found that the vertical emittance is enlarged after RF capture. The mitigation of the beam loss happens by reducing the bunching factor and thereby the space charge tune-spread, and by reducing the excitation of chromatic sextupoles (resonance reduction). These steps have provided a significant reduction of beam loss in LEIR. Plans to further increase the intensity aim at increasing the repetition rate to 10 Hz, the development of a new optics that reduces the strength of low order resonances.

Shinji Machida, STFC presented a study on the effect of space charge on the multi-turn extraction scheme presently running at CERN [4]. The study is motivated by the experimental studies reported in [5, 6], where it appears that the fixed-points in the four islands drift outwards in the phase space when the beam intensity is increased. Simulation studies tracking beam in free space have highlighted that the effect of space charge on the fixed-points is reverted (they move inward in phase space when increasing the beam intensity). The study shows that the effect of the image charge created by the pipe plays the crucial role for unraveling the reverted pattern of the fixed-points. The talk has presented the slope of the fixed-point/intensity for each beam-let when the boundary is included.

CODE DEVELOPMENT AND BENCHMARKING

Frank Schmidt, CERN has presented a code-code benchmarking based on previous HB work [7]. For several codes that implement frozen or PIC space charge algorithm, a comparison of emittance growth over 10^5 turns is made. The physics case is the periodic crossing of one SIS18 resonance. The result of the benchmarking showed that the codes MICROMAP, SIMSONS, MADX and SYNERGIA agree well especially considering the differences in space charge calculation methods, and lattice modeling. In the talk it was shown that code-experiment benchmarking has been performed using the PS experiment data showing a good agreement also for a storage time of half million turns.

Oliver Boine-Frankenheim, GSI has presented a new development in PIC solvers [8]. The issue of simplecticity in particle tracking, which uses PIC is of relevance for long term tracking. In fact, artificial emittance growth is the result of un-physical modeling of the beam dynamics. The talk has presented a review of the methods for avoiding grid heating and artificial noise. A test example using a spectral solver has shown that artificial emittance growth due to grid heating can be avoided. This removes artificial emittance growth at the expenses of heavier computational load. Also Ji Qiang [9] has discussed in WGB a similar integration scheme.

ISBN 978-3-95450-185-4

NEW MACHINES / NEW CONCEPTS

Sergei Nagaitsev, FERMILAB reviewed IOTA [10]. The project is advancing, building space is ready, and the main components of IOTA includes: 20 x/y skew correctors, 8 correctors in dipoles, 20 button BPMs, 30 deg and 60 deg dipoles with synch-light ports, electron-lens sections, and an optical stochastic cooling section.

A very exciting IOTA research program will be centered around nonlinear beam dynamics and advanced beam cooling, in particular on

1) nonlinear integrable optics;
2) space charge compensation;
3) optical stochastic cooling;
4) beam collimation technology development with hollow electron lenses;
5) electron cooling advanced techniques.

Studies for a high intensity proton FFAGs at RAL were presented by **Christopher Prior** [11]. The talk reviewed the ISIS Upgrades option. ISIS has long-served as neutron and muon facility operating at 160-180 kW, with two target stations. There is a continuous program of maintenance, replacements and upgrades with ongoing studies to upgrade to the MW level beam power. ISIS Upgrade options are:

1) a 70 MeV Linac with new tank;
2) replacement of injector with a 180 MeV Linac;
3) phased upgrades for 2.5-3 MW with: a) addition of a 3.2 GeV RCS, b) addition of a new 800 MeV H−ĹŠ Linac.

The future multi-megawatt proton driver aimed specifically at a spallation neutron source (short pulse), including a small test ring that might also have a practical application. FFAGs may be a good choice for a high intensity machine. The main options for the upgrade are:

1) RCS Pumplet, and
2) the DF-Spiral FFAG.

The associated experimental program includes an MoU with Kyoto University (FFAGs at KURRI), and an MoU with Hiroshima University (Paul trap studies of particle accelerators).

THEORY

In the theory section **Ingo Hofmann, GSI/TUD**, attempted to give a global view on the space charge resonances introducing a "typology" of the resonances [12]. The talk categorized two main groups of resonant space charge effects:

1) "Single particle" resonances with driving terms due to the initial space charge profile, the "usual" resonance diagram; and
2) Parametric "half-integer" resonances, which are equivalent to instabilities with driving term pumped from initial noise "stability diagram".

He also concluded that parametric resonances are characterized by coherence in density, hence frozen space charge simulation cannot include these type of effects.

This development should stimulate more experiments to further advance the understanding, which necessarily has to include the synchrotron motion. The discussion of the 3rd order resonance effect has shown, however, different conclusions between Ingo Hofmann [12], and Dong O Jeon [13]; one author called it 3rd order instability, and the other 3rd order parametric resonance. The unraveling of the discrepancy is left to future HB.

Alexei Burov, Fermilab presented a review of head-tail modes with strong space charge [14]. The review started with the work of M. Blaskiewicz on the fast head-tail instability with space charge, and the further development addressing the head-tail modes for strong space charge (A. Burov). Coupled-beam and coupled-bunch instabilities have been treated in the presentation (former work of A. Burov).

Then the presentations addressed numerical work by **V. Kornilov** and **O. Boine-Frankenheim** on head-tail instability and Landau damping in bunches with space charge. The review also discusses the threshold of head-tail instabilities in bunches with space charge (V. Kornilov et al.), and conclude with the latest results on simulation of transverse modes with their intrinsic Landau damping for bunched beams in the presence of space charge (A. Macridin et al.).

A lively discussion followed the talk by **V. Kornilov** on head-tail instability and Landau damping in bunches with space charge [15]. The audience had several comments and an additional early morning session organized Friday from 8:00 to 8:45 has been requested to discuss the topic further. Extra presentation by **Elias Metral** on constant inductive impedance, and by **Alexy Burov** on why there is no Landau damping for the rigid bunch mode have take place during the extra session.

EMERGING TALENTS

The section on emerging talents have covered a broad spectrum of topics such as the space charge effect in FFAGs [16], and how to use electron lenses to compensate space charge [17]. Contribution on nonlinear optics experiment from university [18], and strip-line BPM with improved frequency response [19] have been discussed. The special use of RF quadrupole to enhance stability has been part of the session as well [20].

FINAL CONSIDERATION

The history of space charge effects in ring traces back to prior 1985 at the time when incoherent tune-shift was understood by Lastlett, and the KV distribution was invented. From 1985 to 1990 studies on emittance preservation were performed, especially it started the advent of multi-particle simulations. Theory benefited of Frank Sacherer's innovative work. In the years from 1990 till 2000 the studies developed particle core models, and simulation codes have become more complex and capable. The decade 2000 – 2010 marks the start of the HB workshop series. There is a renewed interest incoherent effects, and systematic machine

ISBN 978-3-95450-185-4

studies started at a number of laboratories including CERN, GSI, J-PARC, and ORNL. The machine modeling has significantly improved. In this decade the beam dynamics analysis also started to include the interplay of several effects.

What are the new trends and the new challenges for this decade?

1 "The computational paradox". From the previous decade the computer power have grow larger and lager, and the advent of new computer languages have allowed the creation of codes that can model accurately a complex accelerator. However, the increase of modeling power leave open all the challenges for understanding the beam dynamics. A new effort for extracting the beam physics from simulation is necessary to give new input to theoretical development.
2 "Coherent vs. Incoherent". In the previous decade a rise of the incoherent effect gain importance in relation with space charge and machine nonlinearities interplay. However it is not clear how coherent and incoherent effects interplay each other, and which beam parameters favor one with respect to the other.
3 The "Transverse - Longitudinal" connection. Transverse, and longitudinal dynamics are often treated as separated areas of studies. However, the trends in the past decades, especially the interplay of effect intertwine these two community. Challenges are in some context arising from the necessity of studying the full 3D dynamics. The experience accumulated in each community is a starting point for a new approach to beam physics in accelerator (also helped by simulation and machine experiment insight).
4 Role of "machine experiment" and the beam dynamics in rings. It is now time for the community to redefine the role of the machine experiments. Some question remain open:
   a) What machine experiments are needed to clarify beam physics this is not well understood?
   b) What is the new beam physics to be addressed?
   c) What machine-code-theory benchmarking is necessary to validate the models?
   d) Is it the beam physics progress uniquely a function of operational needs, or can we progress with new ideas or schemes for advancing the field?

OUTLOOK

The working group A leaves open for the next HB a basket of topics of high relevance:

- What are the machine limits and how can they be addressed? The standard approach to overcome a space-charge limits in rings is still to build a higher energy Linac (the exception to this approach is IOTA).
- After decades of research the community still has no unified language to describe the space charge phenomena.
- There are a number of simulations codes available, and the question arises if the communities efforts should concentrate on fewer codes with more collaborators.

REFERENCES

[1] E. Métral, "General Formula to Deduce the Space Charge Tune Spread From a Quadrupolar Pick-Up Measurement", presented at HB2016, Malmö, Sweden, June 2016, paper MOPR024.

[2] G. Rumolo, H. Bartosik, E. Belli, G. Iadarola, K.S.B. Li, L. Mether, A. Romano, and M. Schenk, "Electron Cloud in the CERN Accelerator Complex", presented at HB2016, Malmö, Sweden, June 2016, paper TUAM4X01.

[3] H. Bartosik, S. Hancock, A. Huschauer, and V. Kain, "Space Charge Driven Beam Loss for Cooled Beams and Mitigation Measures in the CERN Low Energy Ion Ring", presented at HB2016, Malmö, Sweden, June 2016, paper TUAM5X01.

[4] S. Machida, S.S. Gilardoni, M. Giovannozzi, S. Hirlaender, A. Huschauer, and C.R. Prior, "Intensity Effects in the Formation of Stable Islands in Phase Space During the Multi-Turn Extraction Process at the CERN PS", presented at HB2016, Malmö, Sweden, June 2016, paper TUAM7X01.

[5] A. Huschauer, J.C.C.M. Borburgh, S. Damjanovic, S.S. Gilardoni, M. Giovannozzi, C. Hernalsteens, M. Hourican, K. Kahle, G. Le Godec, O. Michels, and G. Sterbini, "Transverse Beam Splitting Made Operational: Recent Progress of the Multi-Turn Extraction at the CERN Proton Synchrotron", presented at HB2016, Malmö, Sweden, June 2016, paper MOPR009.

[6] S. Gilardoni, M. Giovannozzi, and C. Hernalsteens, *Phys. Rev. ST Accel. Beams* **16**, 051001 (2013).

[7] F. Schmidt, Y. I. Alexahin, J. F. Amundson, H. Bartosik, G. Franchetti, J. A. Holmes, A. Huschauer, V. V. Kapin, A. Oeftiger, E. G. Stern, and M. Titze, "Code Bench-Marking for Long-Term Tracking and Adaptive Algorithms", presented at HB2016, Malmö, Sweden, June 2016, paper WEAM1X01.

[8] O. Boine-Frankenheim, "PIC Solvers for Intense Beams: Status and Future Prospects", presented at HB2016, Malmö, Sweden, June 2016, paper WEAM2X01.

[9] J. Qiang, L. Li, and Z. Wang, "A New RFQ Model and Symplectic Multi-Particle Tracking in the IMPACT Code Suite", presented at HB2016, Malmö, Sweden, June 2016, paper THPM7Y01.

[10] S. Nagaitsev, "Nonlinear Focusing in IOTA for Space-Charge Compensation and Landau Damping", presented at HB2016, Malmö, Sweden, June 2016, paper WEAM7X01.

[11] C.R. Prior, "Studies of High Intensity Proton FFAGs at RAL", presented at HB2016, Malmö, Sweden, June 2016, paper WEAM6X01.

[12] I. Hofmann, "Typology of Space Charge Resonances", presented at HB2016, Malmö, Sweden, June 2016, paper THPM1X01.

[13] D. Jeon, J.-H. Jang, and H. Jin, "Resonances and Envelope Instability in High Intensity Linear Accelerators", presented at HB2016, Malmö, Sweden, June 2016, paper THPM4X01.

[14] A.V. Burov, "Head-Tail Modes With Strong Space Charge: Theory and Simulations", presented at HB2016, Malmö, Sweden, June 2016, paper THPM2X01.

ISBN 978-3-95450-185-4

[15] V. Kornilov, O. Boine-Frankenheim, "Head-Tail Instability and Landau Damping in Bunches with Space Charge", presented at HB2016, Malmö, Sweden, June 2016, paper THPM3X01.

[16] M. Haj Tahar, F. Méot, "Space Charge Effects in FFAG", presented at HB2016, Malmö, Sweden, June 2016, paper THPM6X01.

[17] W.D. Stem, O. Boine-Frankenheim, "Using an Electron Cooler for Space Charge Compensation in the GSI Synchrotron SIS18", presented at HB2016, Malmö, Sweden, June 2016, paper THPM5X01.

[18] K.J. Ruisard, H. Baumgartner, B. Beaudoin, I. Haber, T.W. Koeth, and D.B. Matthew, "Early Tests and Simulation of Quasi-Integrable Octupole Lattices at the University of Maryland Electron Ring", presented at HB2016, Malmö, Sweden, June 2016, paper THPM8X01.

[19] Y. Shobuda, Y.H. Chin, K.G. Nakamura, K. Takata, and T. Toyama, "Stripline Beam Position Monitors With Improved Frequency Response and Their Coupling Impedances", presented at HB2016, Malmö, Sweden, June 2016, paper THPM10X01.

[20] M. Schenk, A. Grudiev, K.S.B. Li, and K. Papke, "Use of RF Quadrupole Structures to Enhance Stability in Accelerator Rings", presented at HB2016, Malmö, Sweden, June 2016, paper THPM7X01.

ISBN 978-3-95450-185-4

List of Authors

Bold papercodes indicate primary authors

ISBN 978-3-95450-185-4

ISBN 978-3-95450-185-4

ISBN 978-3-95450-185-4

ISBN 978-3-95450-185-4

ISBN 978-3-95450-185-4

ISBN 978-3-95450-185-4

— Z —

ISBN 978-3-95450-185-4

Institutes List

Aarhus University
Aarhus, Denmark
- Thomsen, H.D.

Allrussian Electrotechnical Institute
Moskow, Russia
- Chikhachev, A.S.

ANL
Argonne, Illinois, USA
- Conway, Z.A.
- Momozaki, Y.
- Mustapha, B.
- Nolen, J.A.
- Ostroumov, P.N.
- Plastun, A.S.
- Reed, C.B.

BEVATECH
Frankfurt, Germany
- Mäder, D.

BNL
Upton, Long Island, New York, USA
- Alessi, J.G.
- Altinbas, Z.
- Beebe, E.N.
- Blaskiewicz, M.
- Brennan, J.M.
- Brooks, S.J.
- Bruno, D.
- Costanzo, M.R.
- Fischer, W.
- Gardner, C.J.
- Gassner, D.M.
- Gu, X.
- Haj Tahar, M.
- Hershcovitch, A.
- Hock, J.
- Huang, H.
- Ingrassia, P.F.
- Jain, A.K.
- Jamilkowski, J.P.
- Kanesue, T.
- Liu, C.
- Luo, Y.
- Marr, G.J.
- Marusic, A.
- Méot, F.
- Mi, C.
- Michnoff, R.J.
- Miller, T.A.
- Minty, M.G.
- Montag, C.
- Pikin, A.I.
- Ptitsyn, V.
- Ranjbar, V.H.
- Raparia, D.
- Robert-Demolaize, G.
- Roser, T.
- Samms, T.
- Sampson, P.
- Schoefer, V.
- Shrey, T.C.
- Smith, K.S.
- Tan, Y.
- Tepikian, S.
- Than, R.
- Thieberger, P.
- Trbojevic, D.
- Tsoupas, N.
- Zaltsman, A.
- Zeno, K.

Brown University
Providence, USA
- Nelson, J.J.

CEA/DRT/LIST
Gif-sur-Yvette Cedex, France
- Pomorski, M.

CEA/IRFU
Gif-sur-Yvette, France
- Abbon, P.
- Chauvin, N.
- Dalena, B.
- Marchix, A.
- Marroncle, J.
- Nghiem, P.A.P.
- Payet, J.
- Uriot, D.

CEA
Gif-sur-Yvette, France
- Chancé, A.

CERN
Geneva, Switzerland
- Albright, S.C.P.
- Arduini, G.
- Argyropoulos, T.
- Bartmann, W.
- Bartosik, H.
- Belli, E.
- Benedetto, E.
- Benedikt, M.
- Besana, M.I.
- Biancacci, N.
- Bohl, T.
- Borburgh, J.C.C.M.

ISBN 978-3-95450-185-4

- Bracco, C.
- Bruce, R.
- Brüning, O.S.
- Buffat, X.
- Burkart, F.
- Burkhardt, H.
- Calaga, R.
- Calatroni, S.
- Carver, L.R.
- Caspers, F.
- Cerutti, F.
- Cieslak-Kowalska, M.
- Coupard, J.
- Damerau, H.
- Damjanovic, S.
- De Maria, R.
- Dehning, B.
- Dimov, V.A.
- Fartoukh, S.D.
- Fiascaris, M.
- Forte, V.
- Fraser, M.A.
- Funken, A.
- Garion, C.
- Gilardoni, S.S.
- Giovannozzi, M.
- Goddard, B.
- Grudiev, A.
- Hancock, S.
- Hanke, K.
- Hirlaender, S.
- Holzer, B.J.
- Hourican, M.
- Huschauer, A.
- Höfle, W.
- Iadarola, G.
- Jowett, J.M.
- Kahle, K.
- Kain, V.
- Kaltenbacher, T.
- Kersevan, R.
- Lallement, J.-B.
- Lamont, M.
- Lasheen, A.
- Le Godec, G.
- Lechner, A.
- Li, K.S.B.
- Lombardi, A.M.
- Manglunki, D.
- Martin, R.
- Martini, M.
- Mataguez, S.
- Meddahi, M.
- Medina Medrano, L.E.
- Mether, L.
- Michels, O.
- Mikulec, B.
- Milanese, A.
- Mirarchi, D.
- Métral, E.
- Oeftiger, A.
- Papke, K.
- Passarelli, A.
- Pieloni, T.
- Quartullo, D.
- Raich, U.
- Redaelli, S.
- Repond, J.
- Roggen, T.
- Romano, A.
- Rumolo, G.
- Salvant, B.
- Schaumann, M.
- Schenk, M.
- Schmidt, F.
- Schulte, D.
- Schönauer, H.O.
- Scrivens, R.
- Shaposhnikova, E.N.
- Sterbini, G.
- Stoel, L.S.
- Tambasco, C.
- Timko, H.
- Titze, M.
- Tomás, R.
- Tommasini, D.
- Velotti, F.M.
- Vollinger, C.
- Vretenar, M.
- Wasef, R.
- Wenninger, J.
- Wildner, E.H.M.
- Zimmermann, F.

CIEMAT
Madrid, Spain
- Oliver, C.

CINVESTAV
Mérida, Mexico
- Guillermo Cantón, G.

Cockcroft Institute
Warrington, Cheshire, United Kingdom
- Welsch, C.P.

CSNS
Guangdong Province, People's Republic of China
- Li, J.
- Li, M.T.
- Liu, M.F.
- Lu, X.H.
- Peng, J.
- Qiu, R.Y.
- Rong, L.Y.
- Sun, J.L.
- Wan, M.L.
- Wang, B.
- Xie, Z.X.

ISBN 978-3-95450-185-4

- Xu, X.A.
- Yang, T.
- Yao, Y.
- Zhang, Z.
- Zhou, W.

DELTA
Dortmund, Germany
- Khan, S.
- Riemann, B.

EPFL
Lausanne, Switzerland
- Banfi, D.
- Barranco, J.
- Cieslak-Kowalska, M.
- Concalves Jorge, P.
- Oeftiger, A.
- Schenk, M.
- Tambasco, C.

ESRF
Grenoble, France
- White, S.M.

ESS Bilbao
Zamudio, Spain
- Bustinduy, I.
- Corres, J.
- de Cos, D.
- de la Cruz, C.
- Harper, G.
- Izaola, Z.
- Miracoli, R.
- Muñoz, J.L.
- Rueda, I.
- Vizcaino, A.
- Zugazaga, A.

ESS
Lund, Sweden
- Cheymol, B.
- Danared, H.
- Darve, C.
- De Prisco, R.
- Dolenc Kittelmann, I.
- Elias, N.
- Eshraqi, M.
- Hartl, M.A.
- Jensen, M.
- Lee, Y.
- Levinsen, Y.I.
- Miyamoto, R.
- Muñoz, M.
- Ponton, A.
- Shea, T.J.
- Thomas, C.A.
- Zeng, R.

ETH
Zurich, Switzerland
- Hegglin, S.

Fermilab
Batavia, Illinois, USA
- Adamson, P.
- Alexahin, Y.I.
- Amundson, J.F.
- Bhat, C.M.
- Burov, A.V.
- Carlson, K.
- Crawford, D.J.
- Derwent, P.
- Garcia, F.G.
- Hendricks, B.
- Holmes, S.D.
- Kapin, V.V.
- Lebedev, V.A.
- Leibfritz, J.R.
- McGee, M.W.
- Mishra, C.S.
- Mitchell, D.V.
- Nagaitsev, S.
- Nobrega, L.E.
- Ostiguy, J.-F.
- Park, C.S.
- Prebys, E.
- Romanov, A.L.
- Ruan, J.
- Shiltsev, V.D.
- Shin, Y.-M.
- Stancari, G.
- Stern, E.G.
- Tan, C.-Y.
- Thangaraj, J.C.T.
- Valishev, A.
- Xiao, M.

FRIB
East Lansing, Michigan, USA
- Cogan, S.
- Fukushima, K.
- Guetschow, P.
- He, Z.Q.
- Ikegami, M.
- Lidia, S.M.
- Liu, Z.
- Lund, S.M.
- Marti, F.
- Maruta, T.
- Maxwell, D.G.
- Nolen, J.A.
- Pozdeyev, G.
- Ren, H.T.
- Shen, G.
- Wei, J.
- Yamazaki, Y.
- Yoshimoto, T.
- Zhao, Q.

ISBN 978-3-95450-185-4

GANIL
Caen, France
- Lagniel, J.-M.

Graduate University, Chinese Academy of Sciences
Beijing, People's Republic of China
- Chen, J.E.

GSI
Darmstadt, Germany
- Adonin, A.
- Barth, W.A.
- Boine-Frankenheim, O.
- Chetvertkova, V.
- Daehn, D.
- Du, X.
- Düllmann, Ch.E.
- Franchetti, G.
- Gettmann, V.
- Groening, L.
- Heilmann, M.
- Hofmann, I.
- Hollinger, R.
- Jäger, E.
- Kaiser, M.
- Kester, O.K.
- Khuyagbaatar, J.
- Kornilov, V.
- Krier, J.
- Mickat, S.
- Miski-Oglu, M.
- Plechov, E.
- Rubin, A.
- Scharrer, P.
- Strašík, I.
- Vinzenz, W.
- Vormann, H.
- Yakushev, A.
- Yaramyshev, S.

HIM
Mainz, Germany
- Aulenbacher, K.
- Barth, W.A.
- Düllmann, Ch.E.
- Gettmann, V.
- Khuyagbaatar, J.
- Mickat, S.
- Miski-Oglu, M.
- Scharrer, P.
- Yakushev, A.

IAP
Frankfurt am Main, Germany
- Ates, A.
- Droba, M.
- Heilmann, M.
- Jameson, R.A.
- Kesting, F.
- Meusel, O.
- Niebuhr, H.
- Noll, D.
- Podlech, H.
- Ratzinger, U.
- Schempp, A.
- Schulte, K.
- Schwarz, M.
- Tiede, R.
- Wagner, J.F.

IBA
Louvain-la-Neuve, Belgium
- Hernalsteens, C.

IBS
Daejeon, Republic of Korea
- Jang, J.-H.
- Jeon, D.
- Jin, H.
- Kim, J.-W.

IHEP
Beijing, People's Republic of China
- An, Y.W.
- Cao, J.S.
- Chi, Y.L.
- Fu, S.
- Geng, H.
- He, J.
- Huang, L.
- Huang, M.Y.
- Huang, N.
- Huang, W.L.
- Huo, L.
- Ji, H.F.
- Jiao, Y.
- Kang, W.
- Li, C.
- Li, F.
- Li, P.
- Li, Y.
- Li, Z.P.
- Liu, R.L.
- Liu, W.B.
- Liu, Y.D.
- Liu, Y.Q.
- Liu, Zh.C.
- Ma, H.Z.
- Meng, C.
- Meng, M.
- Mu, Z.C.
- Peng, J.
- Qin, Q.
- Qiu, J.
- Shen, L.
- Sui, Y.F.
- Tian, J.M.

ISBN 978-3-95450-185-4

- Wang, L.
- Wang, N.
- Wang, S.
- Wei, S.J.
- Wu, X.
- Xu, S.Y.
- Xu, T.G.
- Xu, Zh.H.
- Yan, F.
- Ye, Q.
- Yu, L.
- Yuan, Y.
- Yue, J.H.
- Zeng, L.
- Zhang, J.
- Zhao, X.Y.
- Zhao, Y.L.
- Zhao, Y.
- Zhou, G.Z.

IKP
Mainz, Germany
- Aulenbacher, K.

IMP/CAS
Lanzhou, People's Republic of China
- Chai, W.P.
- Chai, Z.
- Chang, W.
- Chen, W.L.
- Dong, Z.
- Dou, W.P.
- Feng, C.
- Gao, Z.
- He, Y.
- Huang, R.
- Jia, H.
- Kang, X.C.
- Li, J.
- Li, M.
- Li, P.
- Li, S.
- Li, W.L.
- Liu, S.H.
- Luo, C.L.
- Mao, R.S.
- Meng, J.
- Qian, C.
- Sun, L.T.
- Tao, Y.
- Wang, W.S.
- Wang, Z.J.
- Wu, J.X.
- Wu, Q.
- Xia, J.W.
- Xiao, G.Q.
- Xu, H.S.
- Xue, Z.
- Yang, J.C.
- Yang, Y.
- Yin, X.
- Yuan, Y.J.
- Zhang, X.H.
- Zhang, Y.
- Zhao, H.W.
- Zheng, W.H.
- Zhou, X.H.

Indiana University
Bloomington, Indiana, USA
- Lee, S.-Y.

INFN/LNF
Frascati (Roma), Italy
- Boscolo, M.
- Collamati, F.
- Drago, A.

INFN/LNL
Legnaro (PD), Italy
- Bellan, L.
- Comunian, M.
- Fagotti, E.
- Pisent, A.

IPHC
Strasbourg Cedex 2, France
- Bouquerel, E.

IPN
Orsay, France
- Biarrotte, J.-L.
- Blache, P.
- Bousson, S.
- Brault, S.
- Chatelet, F.
- Duchesne, P.
- Duthil, P.
- Gandolfo, N.
- Lachaize, A.
- Longuevergne, D.
- Olry, G.
- Perrot, L.
- Pierens, M.
- Rampnoux, E.
- Reynet, D.
- Rousselot, S.

ISA
Aarhus, Denmark
- Møller, S.P.

ITEP
Moscow, Russia
- Kulevoy, T.

ISBN 978-3-95450-185-4

J-PARC, KEK & JAEA
Ibaraki-ken, Japan
- Maruta, T.
- Toyama, T.

JAEA/J-PARC
Tokai-Mura, Naka-Gun, Ibaraki-Ken, Japan
- Akutsu, A.
- Harada, H.
- Horino, K.
- Hotchi, H.
- Ikezaki, K.
- Kato, S.
- Kawasaki, T.K.
- Kinoshita, H.
- Kinsho, M.
- Meigo, S.I.
- Miura, A.
- Nishikawa, M.
- Okabe, K.
- Ooi, M.
- Saha, P.K.
- Shobuda, Y.
- Takayanagi, T.
- Tamura, F.
- Tani, N.
- Tobita, T.
- Ueno, T.
- Watanabe, Y.
- Yamamoto, K.
- Yamamoto, M.
- Yoshimoto, M.

JAEA
Ibaraki-ken, Japan
- Harada, H.

JAI
Oxford, United Kingdom
- Abelleira, J.L.
- Cruz Alaniz, E.
- Seryi, A.

Johannes Gutenberg University Mainz, Institut of Nuclear Chemistry
Mainz, Germany
- Düllmann, Ch.E.

KAERI
Daejon, Republic of Korea
- Kim, K.Y.

KEK/JAEA
Ibaraki-Ken, Japan
- Fujimori, H.
- Fukuta, S.F.
- Liu, Y.
- Maruta, T.

KEK
Ibaraki, Japan
- Chin, Y.H.
- Igarashi, S.
- Irie, Y.
- Ishii, K.
- Mitsuhashi, T.M.
- Miyao, T.
- Ohmi, K.
- Sato, Y.
- Shirakata, M.J.
- Takano, J.
- Takata, K.
- Yamane, I.

Korea Atomic Energy Research Institute (KAERI)
Gyeongbuk, Republic of Korea
- Cho, Y.-S.
- Kim, H.S.
- Kim, K. R.
- Kwon, H.-J.
- Song, Y.G.

Kyoto University
Kyoto, Japan
- Nakamura, K.G.

LAL
Orsay, France
- Bambade, P.
- Faus-Golfe, A.
- Molson, J.

LANL
Los Alamos, New Mexico, USA
- Rybarcyk, L.

LBNL
Berkeley, California, USA
- Qiang, J.

Lund University
Lund, Sweden
- Troeng, O.

Mainz University
Mainz, Germany
- Scharrer, P.

MEPhI
Moscow, Russia
- Barminova, H.Y.

ISBN 978-3-95450-185-4

- Barth, W.A.
- Kulevoy, T.
- Polozov, S.M.
- Yaramyshev, S.

Michigan University
Ann Arbor, Michigan, USA
- Aldred, C.
- Lorenzon, W.

MSU
East Lansing, Michigan, USA
- LaVere, M.J.

NINT
Xi'an, People's Republic of China
- Chen, W.

Northern Illinois University
DeKalb, Illinois, USA
- Shin, Y.-M.

NSCL
East Lansing, Michigan, USA
- Wong, C.Y.

NUCTECH
Beijing, People's Republic of China
- Guan, W.Q.
- He, Y.
- Li, J.

ORNL RAD
Oak Ridge, Tennessee, USA
- Dayton, M.J.
- Evans, N.J.
- Liu, Y.
- Potts, R.E.

ORNL
Oak Ridge, Tennessee, USA
- Aleksandrov, A.V.
- Blokland, W.
- Cousineau, S.M.
- Dodson, G.W.
- Gorlov, T.V.
- Holmes, J.A.
- Liu, Y.
- Plum, M.A.
- Riemer, B.W.
- Shishlo, A.P.
- Wendel, M.
- Winder, D.E.

PAL
Pohang, Kyungbuk, Republic of Korea
- Lee, H.-S.

PKU
Beijing, People's Republic of China
- Chen, J.E.
- Guo, Z.Y.
- Li, L.
- Liu, K.X.
- Peng, S.X.
- Quan, S.W.
- Ren, H.T.
- Wang, F.
- Wang, Z.
- Wen, J.M.
- Wu, W.B.
- Xu, Y.
- Zhang, A.L.
- Zhang, J.F.
- Zhang, T.
- Zhong, H.T.X.
- Zhu, F.

PSI
Villigen PSI, Switzerland
- Parfenova, A.S.

RRCAT
Indore, India
- Gaur, R.

SLAC
Menlo Park, California, USA
- Chao, A.
- Fox, J.D.
- Stupakov, G.

Soreq NRC
Yavne, Israel
- Berkovits, D.

State Key Laboratory of Intense Pulsed Radiation Simulation and Effect, Northwest Institute of Nuclear Technology
Shannxi, People's Republic of China
- Qiu, M.T.
- Wang, B.C.
- Wang, Y.P.
- Wang, Z.M.
- Yan, Y.H.
- Zhang, H.Z.
- Zhao, C.

STFC/RAL/ASTeC
Chilton, Didcot, Oxon, United Kingdom
- Adams, D.J.

ISBN 978-3-95450-185-4

- Bingham, R.
- Machida, S.
- Plostinar, D.C.

STFC/RAL/ISIS
Chilton, Didcot, Oxon, United Kingdom
- Adams, D.J.
- Gardner, I.S.K.
- Jones, B.
- Kershaw, A.H.
- Letchford, A.P.
- Mathieson, R.J.
- Pertica, A.
- Pine, B.G.
- Prior, C.R.
- Seville, A.
- Smith, H. V.
- Warsop, C.M.
- Williamson, R.E.
- Wright, M.

TEMF, TU Darmstadt
Darmstadt, Germany
- Boine-Frankenheim, O.
- Niedermayer, U.
- Stem, W.D.

The University of Liverpool
Liverpool, United Kingdom
- Welsch, C.P.

TUB
Beijing, People's Republic of China
- Bin, D.T.
- Chen, H.B.
- Cheng, C.
- Du, C.T.
- Du, L.
- Du, T.B.
- Guan, X.
- Guo, Q.K.
- Huang, W.-H.
- Jiang, H.
- Li, G.R.
- Ruo, R.
- Tang, C.-X.
- Tang, R.
- Wang, D.
- Wang, W.
- Wang, X.W.
- Wu, L.
- Xing, Q.Z.
- Yang, Y.
- Yang, Z.
- Yao, H.J.
- Zeng, H.J.
- Zhang, H.Y.
- Zhang, Q.Z.
- Zhang, Q.
- Zheng, S.X.

UMAN
Manchester, United Kingdom
- Appleby, R.B.
- Crouch, M.P.

UMD
College Park, Maryland, USA
- Baumgartner, H.
- Beaudoin, B.
- Haber, I.
- Koeth, T.W.
- Matthew, D.B.
- Ruisard, K.J.

Univ. degli Studi di Padova
Padova, Italy
- Bellan, L.

University of Chinese Academy of Sciences
Beijing, People's Republic of China
- Zhang, A.L.

Université Blaise Pascal
Clermont-Ferrand, France
- Forte, V.

Uppsala University
Uppsala, Sweden
- Ekelöf, T.J.C.
- Olvegård, M.

ISBN 978-3-95450-185-4